Journal of ASTM International
Special Technical Publication

ASTM INTERNATIONAL
Standards Worldwide

STP 1508

Fatigue and Fracture Mechanics

36th Volume

Richard W. Neu
Kim R. W. Wallin
Steven R. Thompson

Guest Editors

In cooperation with ESIS

ESIS
European Structural Integrity Society

Journal of ASTM International
Special Technical Publication STP1508
Fatigue and Fracture Mechanics: 36th Volume

Guest Editors:
Richard W. Neu
Kim R. W. Wallin
Steven R. Thompson

INTERNATIONAL
Standards Worldwide

ASTM International
100 Barr Harbor Drive
PO Box C700
West Conshohocken, PA 19428-2959

Printed in U.S.A.
ASTM Stock #: STP1508

Library of Congress Cataloging-in-Publication Data

ISBN: 978-0-8031-3416-4
ISSN: 1040-3094

Peer Review Policy

Each paper published in this special issue was evaluated in accordance with the *JAI* review process.

The quality of the papers in this publication reflects not only the obvious efforts of the authors and the technical editors, but also the work of the peer reviewers. In keeping with long-standing publication practices, ASTM International maintains the anonymity of the peer reviewers. The ASTM International Committee on Publications acknowledges with appreciation their dedication and contribution of time and effort on behalf of ASTM International.

Citation of Papers

When citing papers from this publication, the appropriate citation includes the paper authors, "paper title", J. ASTM Intl., volume and number, Paper ID, DOI, ASTM International, West Conshohocken, PA, Paper, year listed in the footnote to the paper. A citation is provided as a footnote on page one of each paper.

Printed in Bridgeport, NJ
October, 2009

Foreword

THIS SPECIAL ISSUE OF *JAI*, Special Technical Publication STP 1508, *Fatigue and Fracture Mechanics: 36th Volume*, contains papers presented at the Seventh International ASTM/ESIS Symposium on Fatigue and Fracture (36th ASTM National Symposium on Fatigue and Fracture Mechanics) held November 14-16, 2007 in Tampa, Florida. The symposium was jointly sponsored by ASTM International Committee E08 on Fatigue and Fracture and the European Structural Integrity Society (ESIS).

The symposium was co-chaired by Dr. Richard W. Neu of Georgia Institute of Technology, USA, Dr. Kim R. W. Wallin of the Academy of Finland, Finland, and Mr. Steven R. Thompson of Air Force Research Laboratory, USA.

Contents

Residual Stress Effects on Fracture

Multiscale and Physics-Based Approaches

Reactor Components and Materials

Fatigue Crack Growth

Elevated Temperature and Environmental Effects

Components and Structures

Overview

This book compiles the work of several authors who made presentations at the Seventh International ASTM/ESIS Symposium on Fatigue and Fracture (36th ASTM National Symposium on Fatigue and Fracture Mechanics), sponsored by ASTM Committee E08 on Fatigue and Fracture and the European Structural Integrity Society (ESIS). The symposium was held on November 14-16, 2007, in conjunction with the November 12-13, 2007 standards development meetings of ASTM Committee E08.

The symposium opened with the Jerry L. Swedlow Memorial Lecture given by James A. Joyce of the U.S. Naval Academy. Following his lecture, several papers on related topics involving elastic-plastic fracture mechanics were presented.

Many of the papers presented in the symposium focused on one of three major themes: residual stress effects on fatigue and fracture, multiscale and physics-based approaches, and reactor components and materials. Each of these areas presents their own challenges to the development and application of engineering approaches to predict the structural integrity and remaining life of systems.

A major highlight of the symposium was the extensive number of papers on residual stress effects. ASTM Committee E08 recognizes that residual stresses, both intentionally-applied and manufacturing-induced, can have a significant effect on properties used in durability and damage tolerance design methodologies. These papers aim to ensure that testing standards are robust enough to meet users' needs.

In addition to the major themes, other papers cover the latest research in fatigue crack growth, and in understanding and predicting the effects of elevated temperatures and environment. Finally, several papers deal with fatigue and fracture of specific components, joining methods, surface treatments, and coatings.

Richard W. Neu
Georgia Institute of Technology
Atlanta, Georgia, USA

Kim R. W. Wallin
Academy of Finland
Espoo, Finland

Steven R. Thompson
Air Force Research Laboratory
Wright-Patterson Air Force Base, Ohio, USA

SWEDLOW LECTURE

ASTM Special Technical Publication, Vol. 5, No. 9
Paper ID JAI101512
Available online at www.astm.org

James A. Joyce[1] *and Xiaosheng Gao*[2]

Analysis of Material Inhomogeneity in the European Round Robin Fracture Toughness Data Set

ABSTRACT: The European fracture toughness dataset was developed by ten European laboratories in order to provide an experimental data base sufficiently large to study specimen size and temperature effects on cleavage fracture toughness in the ductile-to-brittle transition regime. The initial Master Curve analysis of this data set was presented by Wallin [*Eng. Fract. Mech.*, Vol. 69, 2002, pp. 451–481. showing a range of T_0 reference values ranging from −80°C to −110°C, with −90°C as an average and a standard deviation of 6.7°C. The initial round robin data set included all scaled C(T) specimens ranging from 1/2T to 4T in scale, but more recently additional specimens have been tested using this material including deep and shallow crack bend specimens (SE(B)) [Link, R. E., unpublished], precracked Charpy size specimens [Wallin, K., *Fracture, Fatigue, and Residual stress—PVP*, Vol. 393, J. Pan, Ed., ASME, New York (1999)], and even some biaxially loaded cruciform specimens [Lidbury, D. P. G., *Fatigue Fract. Eng. Mater. Struct.*, Vol. 29, 2006, pp. 829–849]. These specimens are being analyzed to develop and test constraint analysis tools essential in the application of the Master Curve method to structural applications in the commercial nuclear power industry. The present authors have also developed fracture toughness data on this material over a range of loading rates to investigate the sensitivity of the calibrated Weibull coefficients used in the constraint correction models of Gao and Dodds [*Eng. Fract. Mech.*, Vol., 68, 2001, pp. 263–284] to material loading rates in typical nuclear pressure vessel steels. Clear material inhomogeneity characteristics have developed in this data, and it was felt that a more complete investigation of the inhomogenity in the Euro forging data set

Manuscript received October 30, 2007; accepted for publication August 1, 2008; published online October 2008.
[1] U.S. Naval Academy, Annapolis, MD 21402.
[2] University of Akron, Akron, OH 44325.

Citation: Joyce, J. A. and Gao, X., "Analysis of Material Inhomogeneity in the European Round Robin Fracture Toughness Data Set," *J. ASTM Intl.*, Vol. 5, No. 9. DOI10.1520/JAI101512. Available online at www.astm.org. Also included in JAI Special Issue STP 1508, *Fatigue and Fracture Mechanics: 36th Volume*, R. W. Neu, K. R. W. Wallin, and S. R. Thompson, guest editors, ASTM International, West Conshohocken, PA 2009, pp. 3-29.

should be conducted. Following the proposal of Wallin [*Eng. Fract. Mech.*, Vol. 71, No. 16, 2004, pp. 2392–2346], software was written to investigate whether the subject data set could best be expressed as a bimodal distribution of two combined Master Curve distributions, and this software was then applied to the various individual data sets in the European round robin data. The output of each analysis (e.g., the 2*T* data set) was two T_x values and a probability value p_a, where T_a and T_b are the T_0 values for the two constituents and p_a is the probability of T_a. Using a procedure being developed as an annex to ASTM E1921 which is based on suggestions of Wallin, standard deviations of each of these quantities are estimated and used to judge if the dataset represents inhomogeneous material. The results show that several of the data sets obtained in the original round robin test program are better described by bimodal probability distributions than by the single Weibull distribution of ASTM E1921. Both single specimen datasets, and multi-temperature analysis of the various size specimens appear to show a preference for bimodal probability distributions. Additional sets of precracked Charpy size specimens were then machined from slices of the cross section and the results of testing these specimens shows that some cross sections of the Euro forging demonstrate a clear pattern of toughness variation across the forging cross section, while other cross sections show nearly constant fracture toughness with crack position. A major conclusion of this work is that making "mechanics based" conclusions comparing constraint effects using the Euro forging material is going to be more difficult given the apparent presence of material inhomogeneity in this material as demonstrated very convincingly by the data and analysis presented in this paper.

Origin of the Problem

The Weibull Stress Model

The Weibull stress model originally proposed by Beremin [1] derives from the weakest link statistics and adopts a two-parameter Weibull distribution to describe the cumulative failure probability:

$$P_f(\sigma_w) = 1 - \exp\left[- \left(\frac{\sigma_w}{\sigma_u} \right)^m \right] \tag{1}$$

In this expression, σ_w represents the Weibull stress defined as the integral of a weighted value of the maximum principal (tensile) stress (σ_1) over the process zone for cleavage fracture (i.e., the plastic zone at the crack tip):

$$\sigma_w = \left[\frac{1}{V_0} \int_{V_p} \sigma_1^m \mathrm{d}V \right]^{1/m} \tag{2}$$

In Eq 2, V_p represents the volume of the cleavage fracture process zone, V_0 is a reference volume, m denotes the Weibull modulus which relates to the size distribution of the microscopic cracks in the fracture process zone, and σ_u represents the scale parameter of the Weibull distribution which defines the micro-scale material toughness when the cumulative failure probability is 63.2 %.

The Weibull stress enables construction of a toughness scaling model between different crack configurations based on equal failure probability. Under increased remote loading described by K_J or J, differences in evolution of the Weibull stress $\sigma_w(J)$ reflect the potentially strong variations in crack-front stress fields due to the effects of constraint loss and volume sampling. The inherently 3-D formulation for σ_w defined by Eq 2 readily accommodates variations in K_J or J along the crack front. Constraint corrections then become possible between different crack geometries, applied loading conditions, or both, at identical σ_w values. The quality of fracture toughness predictions using the Weibull stress model relies heavily on the calibrated model parameters m and σ_u. The effect of temperature on the coefficients m and σ_u was investigated by Petti and Dodds [2], who showed a clear dependence of σ_u on temperature, but an insensitivity of the Weibull modulus m on temperature. The effect of loading rate on these same coefficients was investigated by Gao and Dodds [3] using an A515 structural steel. These results showed that σ_u was sensitive to the loading rate while the Weibull modulus was insensitive to rate, at least over the relatively limited range of rates investigated. The data set used for this investigation was limited and an additional data set using the European round robin forging material was initiated and ultimately completed by Gao, Joyce, and Roe [4]. This latter investigation was one of the first instances where concerns of material inhomogeneity in the Euro forging steel appeared to affect the results of the data that were being used in the Weibull stress rate sensitivity investigation.

Three point bend specimens (1/2T SE(B) specimens) were machined with shallow and deep crack geometries from a block of the Euro forging material, as shown in Fig. 1. All tests were conducted according to E1921, except that the loading rate was elevated beyond what is allowed by E1921. Each slice was designated with a letter (ultimately running from A through S) and the layers from the forging centerline were designated (1-2), (3-4), (5-6), and (7-8) as shown in Fig. 1. A further discussion of the cutting of the Euro forging is presented in the following sections, but for this work the (7-8) layer specimens were put aside as having crack positions too close to the forging surface. The deep cracked (5-6) layer specimens then had crack positions within about 45 mm of the forging surface, which was within the region characterized by Heerens and Hellman [5] in the original round robin report as consistent with the general material, at least in terms of tensile and microhardness measurements. In preparing specimens for the original round robin the material within 120 mm of the inside surface was avoided, an option not available to us since only the inner 140 mm of material was made available. This will be looked at further in the following sections. It has been clearly demonstrated since the 1970s that standard tensile mechanical properties, hardness, and Charpy toughnesses vary through the thickness of large section, quench and tempered steel plates and forgings used for nuclear pressure vessels [6] with the maximum strength, hardness, and fracture toughness occurring near the forging surfaces. The Master Curve reference temperature has also been shown to vary in a corresponding fashion by Joyce and Tregoning [7]. For this reason, the

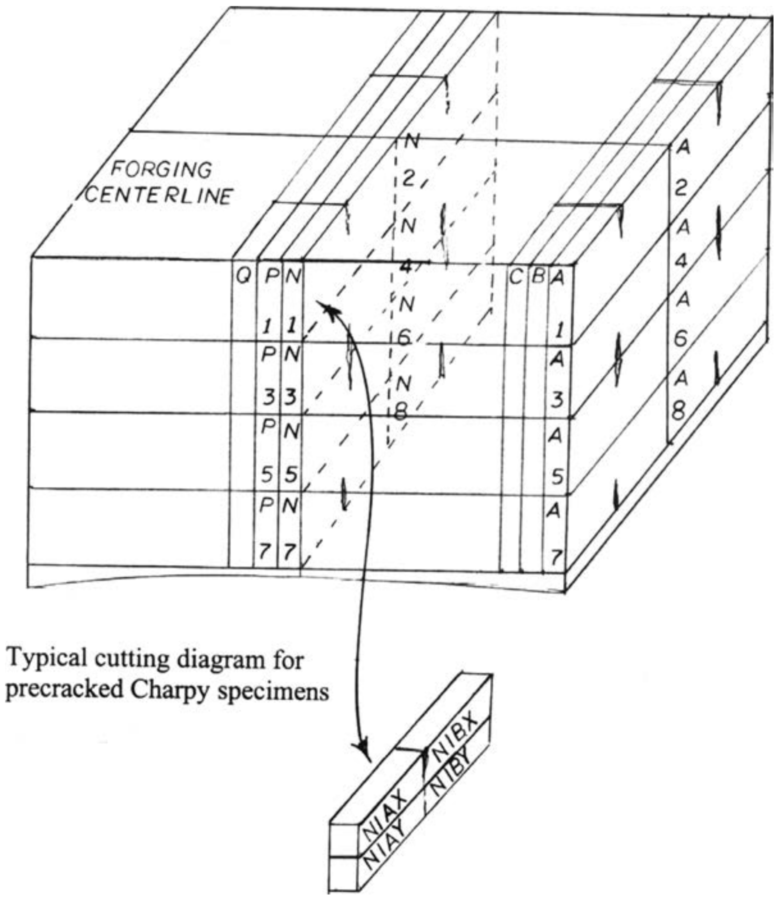

FIG. 1—*Cutting diagram for the Euro forging block made available for testing at NSWC Carderock laboratory and the U.S. Naval Academy.*

European round robin was conducted over a reduced section of the forging thickness and described more fully in a subsequent section.

The first results obtained for the rate investigation are shown in Fig. 2, plotted against a correlation equation suggested by Wallin [8]. The error bars define 2σ confidence bounds as define in E1921. While in the strictest interpretation of E1921 these confidence bounds apply only to the deep crack data sets with $dK/dt < 2.$ MPa$\sqrt{}$m they have been applied in Figs. 2 and 3 to all deep crack data sets. Clearly the data looked consistent and in general agreement with the correlation equation. The specimens at this time had been randomly selected from the various "slices" and layers, but due to a variety of experimental and machining problems, there were not enough specimens to complete the deep crack data set at the intermediate ($dK/dt \sim 100$ MPa$\sqrt{}$m/s) loading rate. Five additional slices were taken and machined into additional deep crack specimens and tested at the $dK/dt \sim 100$ MPa$\sqrt{}$m/s loading rate.

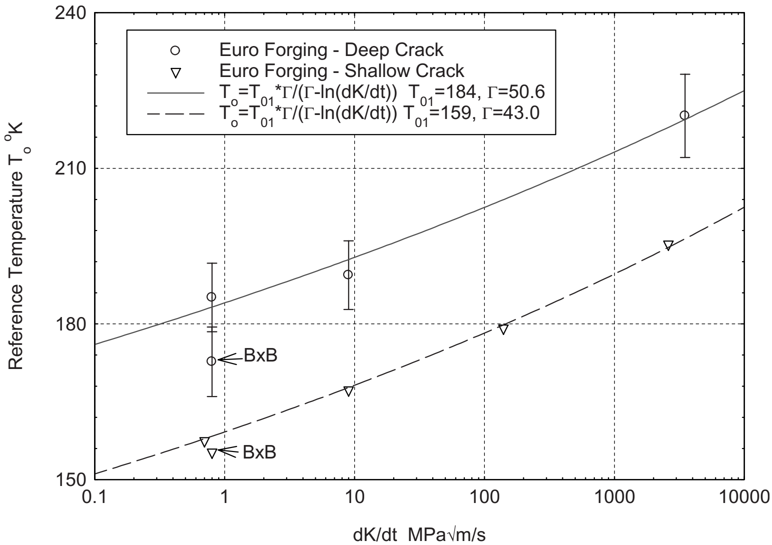

FIG. 2—*Initial data obtained for the Weibull rate effects study.*

The full data set of 22 specimens, using the (1-6) layers, gave the unsatisfying results shown in Fig. 3 and labeled (1-6). Recalculations of T_o using the (1-4), (1-2), and (3-6) layers only are shown as well in Fig. 3. Thoroughly puzzled at this point, a set of nine specimens from the surface (7-8) layer was tested at the same loading rate to obtain an estimate of T_o closer to the forging

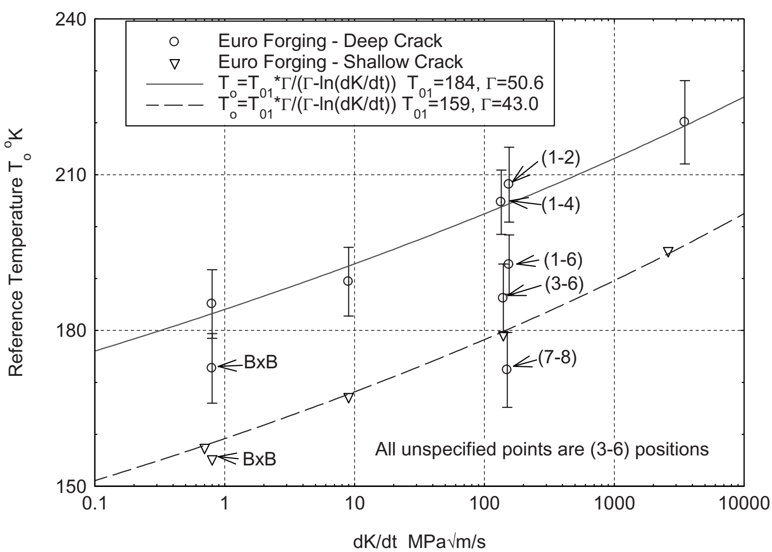

FIG. 3—*Rate data showing effects of material inhomogeneity.*

TABLE 1—*Chemical composition of the 22NiMoCr37 steel* (*wt. %*).

C	Si	P	S	Cr	Mn	Ni	Cu	Mo
0.21	0.24	0.003	0.004	0.003	0.82	0.79	0.049	0.56

inside surface and this result is also presented in Fig. 3. This result clearly shows that, for these slices at least, the toughness is clearly dependent on specimen position through the forging thickness. For the two data sets including specimens from the (5-6) position, T_o is dramatically shifted toward the result that would be expected if only near surface specimens, the (7-8) layer specimens, were tested.

Additional testing, application of the inhomogeneity analysis proposed by Wallin [8], and some sorting and selection of the data were used to complete the investigation of rate sensitivity on the Weibull calibration parameters that was subsequently completed by Gao, Joyce, and Roe [4]. Further testing and analysis was also undertaken to try to get a more complete understanding of the role of inhomogeneity in the Euro forging material, as described in the following sections of this paper.

Description of the Euro Forging Material

The Euro forging material described above and used in this study is from a large forged, quenched and tempered ring segment of 22NiMoCr37 ferritic steel. This material is similar to the A508 pressure vessel steel widely used in North American commercial nuclear power plants. Ten European laboratories have conducted extensive quasi-static fracture tests of this material to generate the Euro fracture toughness data set for studying the specimen size and temperature effects on cleavage fracture toughness in the ductile to brittle transition region. The chemical composition of the 22NiMoCr37 steel is given in Table 1. Heerens and Hellmann [5] provide detailed descriptions of this material and the Euro round robin fracture test program, including the variability of material properties through the thickness of the ring segment.

Figure 4 shows the original cutting plan for the Euro ring forging. The locations of all specimens used for the original round robin were recorded in drawings like that shown in Fig. 5. Extensive work was done by Heerens and Hellman [5] to characterize the uniformity of thick wall forging material. Figure 6, for instance, shows hardness traverses obtained across sub-blocks SX1, SX2, and SX4 along with some tensile data obtained across various sub-blocks. Property variations consistent with what would be expected across such a large section steel cross section were observed, and by restricting the positions of the fatigue cracks it was expected that relatively uniform test results would be obtained. In one instance, unexpectedly large scatter was observed [5] in the 2T data set and additional 1/2T specimens were machined from the broken pieces of 2T C(T) specimens. These 1/2T specimens also showed the same increased data scatter that had been observed in the 2T data set.

Wallin's Master Curve analysis [9] of the original C(T) toughness data generated by the Euro fracture test program leads to an E1921 reference tempera-

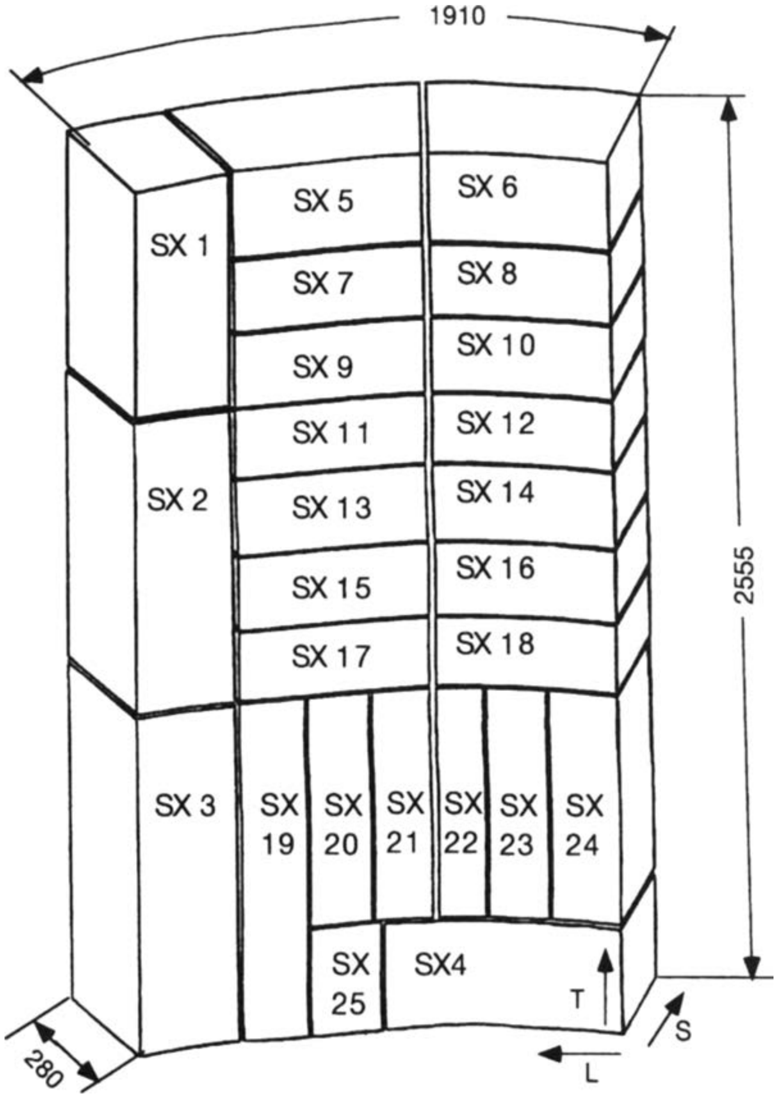

FIG. 4—*Overall cutting plan for the large ring segment of 22NiMoCr37 recognized now as the Euro forging material used for the Euro fracture toughness data set, and for more recent material tests* [*5*].

ture (T_0) of $-90°$C (i.e., the temperature at which the median toughness of a 1T, small scale yielding data set equals to 100 MPa$\sqrt{\mathrm{m}}$). Because of the large scale of this data set it has been used extensively to support developments of aspects of the ASTM E1921 test standard, to support development of the Weibull stress procedure of constraint correction [1–4], to evaluate the effect of biaxial loading on the Master curve reference temperature [10,11], and to develop other

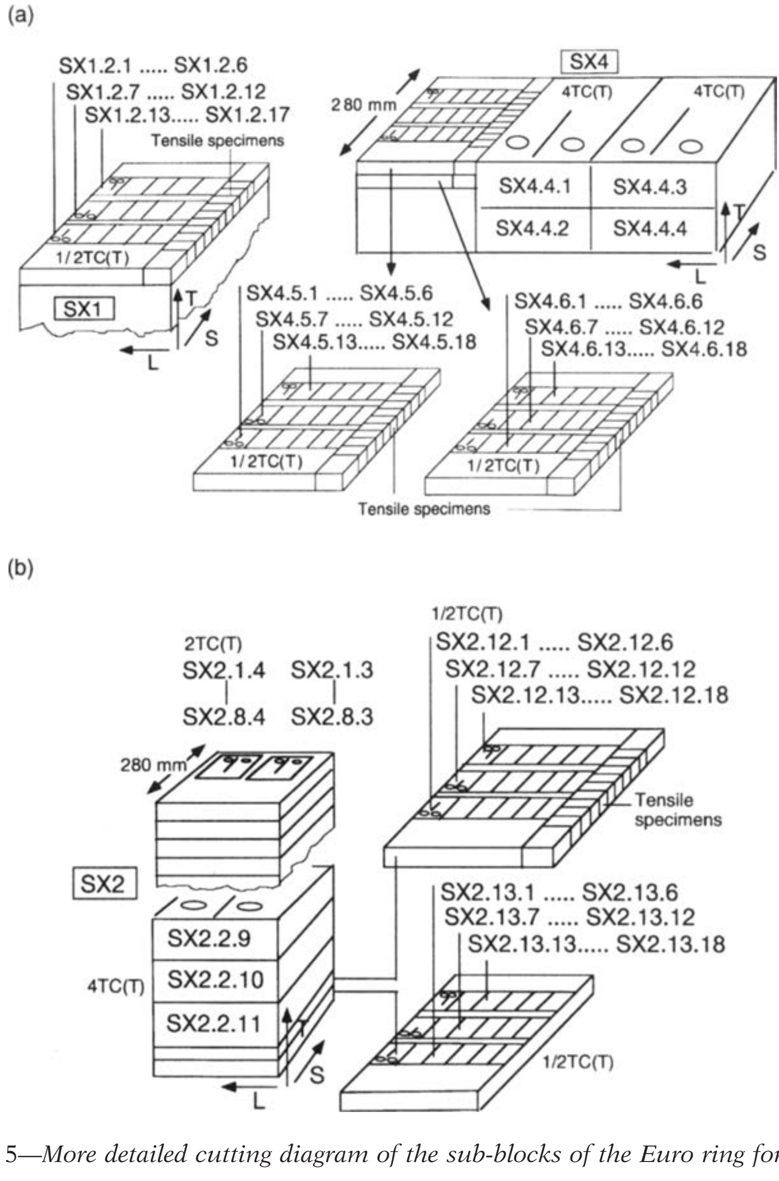

FIG. 5—*More detailed cutting diagram of the sub-blocks of the Euro ring forging.*

techniques of constraint adjustment and correction [12,13].

One piece of the Euro forging material was obtained by NSWCCD Carderock Laboratory specifically to investigate the effect of biaxial loading on the Master Curve reference temperature T_o. Earlier work [14] by Oak Ridge National Laboratory (ORNL) using large cross-section cruciform specimens loaded in bending had suggested that the Master curve reference temperature was dependent on the degree of biaxial loading. This result was not supported

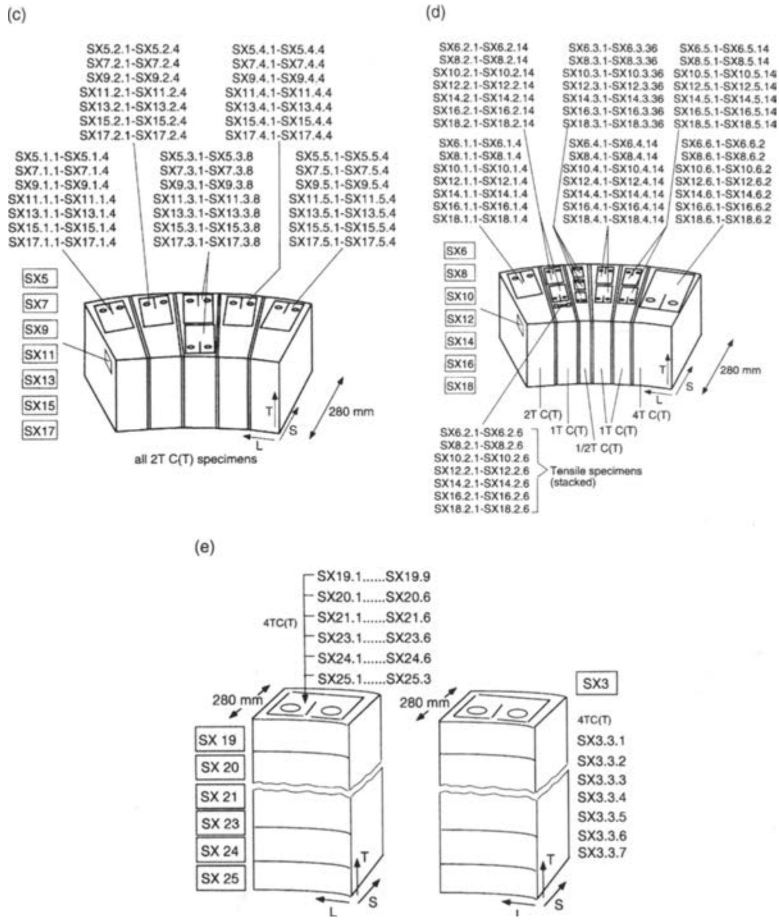

FIG. 6—*More detailed cutting diagram of the sub-blocks of the Euro ring forging.*

by a series of tests conducted at NSWCCD Carderock and at the U.S. Naval Academy using smaller cruciform specimens of two different nuclear vessel type structural steels [11]. Material variability was a concern in these tests, and ORNL had tested a series of large scale Euro forging material cruciform specimens in biaxial loading as part of the VOCALIST [12] project. Very little standard bend specimen data existed for the Euro forging material at that time, so the Euro material was obtained by NSWCCD Carderock to generate shallow and deep crack specimen data for comparison with the large scale Euro forging cruciform tests results of ORNL.

The piece of Euro material that was made available to NSWCCD was approximately 0.33 m by 1 m by 0.14 m thick, representing the inner half of the ring forging 0.28 m thickness shown in Fig. 1. Approximately 2/3 of this material was used to test a series of 1T and 1/2T SE(B) specimens with both deep and shallow crack configurations for comparison with the large scale cruciform results obtained by ORNL. Some of the remaining material was subsequently used to develop a series of data over a range of loading rates to investigate the rate dependence of the Weibull stress model. It was this data, as described more fully below, that first showed that inhomogeneity of the Euro forging material needed to be accounted for if the Euro forging material was to be used to answer "Mechanics" questions. The drawing in Fig. 1 shows the basic cutting plan for these test specimens, with each "slice" of material being designated by slice and layer as the remaining part of this plate was machined and tested.

Concerns about the homogeneity of this segment of the Euro forging material led to the machining of precracked Charpy size specimens from the broken halves of the 1/2T SE(B) specimens that were used for the Weibull coefficient rate characterization. Figure 1 shows how the "A" and "B" halves of the 1/2T SE(B) specimens were machined into "X" and "Y" Charpy specimens, with the layer designations 1 through 8 locating the specimen through the depth of the half thickness of the Euro material. These specimens were all machined with $a/W=0.5$ and tested according to ASTM E1921-06. Two of the original slices were machined in this fashion resulting in 64 specimens, 32 from the "N" slice and 32 from the "P" slice. The various loading rates used for the "Weibull Rate" program study did not allow a direct comparison of the individual slices, but there was enough qualitative evidence to infer that the "P" slice was in some sense tougher that the "N" slice. The results of these tests are described below.

Analysis

Inhomogeneity Analysis

A straightforward type of material inhomogeneity is the assumption that the data population consists of two combined distributions each of which can be described by a Master Curve with its own distinct T_o reference temperature as proposed by Wallin et al. [9]. This consists of assuming that the data population consists of two combined Master Curve distributions with a total cumulative probability distribution given by a bimodal distribution of the form:

$$P_f = 1 - p_a \exp\left[-\left(\frac{K_{Jc} - K_{\min}}{K_a - K_{\min}}\right)^4\right] - (1 - p_a)\exp\left[-\left(\frac{K_{Jc} - K_{\min}}{K_b - K_{\min}}\right)^4\right] \tag{3}$$

where K_a and K_b are the characteristic toughness values for the two constituents and p_a is the probability of the toughness belonging to distribution a.

A draft Annex to the ASTM Standard E1921 has been developed based on the Wallin work, which formalizes the development of the procedure to be used to obtain the two reference temperatures, T_a and T_b, and p_a, where $T_b < T_a$. The valid temperature range for the bimodal distribution is $[T_b - 50°\mathrm{C}, T_a + 50°\mathrm{C}]$. T_a, T_b, and p_a are determined using an appropriate solver that maximizes the logarithm of the likelihood given by:

$$\ln L = \sum_{i=1}^{N} \delta_i \ln f_i + (1 - \delta_i)\ln S_i \tag{4}$$

where:

N = the number of specimen tested,
δ_i = 1.0 if the datum is valid or zero if the datum is a dummy substitute value,
f_i = the datum failure density given below, and
S_i = the datum cumulative surviving probability given below,

$$\begin{aligned} f_i = 4p_a \frac{(K_{Jc(i)} - K_{\min})^3}{(K_a(T_{(i)}) - K_{\min})^4} \\ \times \exp\left[- \left(\frac{K_{Jc(i)} - K_{\min}}{K_a(T_{(i)}) - K_{\min}} \right)^4 \right] + 4(1 - p_a) \frac{(K_{Jc(i)} - K_{\min})^3}{(K_a(T_{(i)}) - K_{\min})^4} \\ \times \exp\left[- \left(\frac{K_{Jc(i)} - K_{\min}}{K_b(T_{(i)}) - K_{\min}} \right)^4 \right] \end{aligned} \tag{5}$$

$$S_i = p_a \exp\left[- \left(\frac{K_{Jc(i)} - K_{\min}}{K_a(T_{(i)}) - K_{\min}} \right)^4 \right] + (1 - p_a)\exp\left[- \left(\frac{K_{Jc(i)} - K_{\min}}{K_b(T_{(i)}) - K_{\min}} \right)^4 \right] \tag{6}$$

and:

$K_{Jc(i)}$ = either a valid K_{Jc} datum or dummy value substitute for an invalid datum. All K_{Jc} input values, valid or dummy K_{Jc}, must be converted to 1T equivalence before entry,
$K_a(T_{(i)})$ = characteristic fracture toughness of population a at the test temperature $T_{(i)}$, and
$K_b(T_{(i)})$ = characteristic fracture toughness of population b at the test temperature $T_{(i)}$.

The accuracy of the obtained parameters depends on the number of data available and is given in terms of standard deviations by:

$$\sigma_{T_a} = \frac{22\,°\mathrm{C}}{\sqrt{N \cdot p_a - 2}} \tag{7}$$

$$\sigma_{T_b} = \frac{16\,°\mathrm{C}}{\sqrt{r - N \cdot p_a - 2}} \tag{8}$$

$$\sigma_{p_a} = \frac{0.35}{\sqrt{N \cdot p_a - 2}} \tag{9}$$

where r is the number of valid data points. The measure of the likelihood that a data set is inhomogeneous is obtained from:

$$MLNH = \frac{|T_a - T_b|}{\sqrt{\sigma_{T_a}^2 + \sigma_{T_b}^2 + \sigma_{\text{exp}}^2}} \tag{10}$$

where σ_{exp} is the experimental uncertainty of the reference temperature and is assumed to be 4°C in the draft E1921 Annex. The data set is likely to be inhomogeneous if MLNH is larger than 2.

Inhomogeneity Analysis of Euro Forging

As described in a previous section, considerable study and care were taken to keep the effects of material variability to a minimum in the development of the Euro forging round robin. All precracks were positioned in a central area of forging which demonstrated uniform tensile mechanical properties and uniform microhardness.

The bimodal inhomogeneity analysis procedure was developed by Wallin but not applied to the Euro forging data set. Many authors have used the subsets of the Euro round robin data set to support analyses related to various aspects of crack tip constraint modeling [1,2,4,10–15]. The present authors were deep into developing additional data sets using small SE(B) specimens obtained from the Euro forging material to investigate the sensitivity of the Weibull stress constraint adjustment procedure to loading rate, when they obtained enough data to become convinced that material inhomogeneity was interfering with the measured data. This was quickly confirmed by applying the Wallin bimodal procedure to the elevated rate data set, but it also caused a reanalysis of the complete Euro round robin data set using the bimodal inhomogeneity technique. The Euro round robin data is available from a GKSS website, and this full data set was downloaded for analysis. All round robin specimens were C(T) specimens of 4T, 2T, 1T, and 1/2T scales. In the following sections each size specimen is looked at individually and, analyzed using the Wallin inhomogeneity approach. Sixty-four additional precracked Charpy size specimens were also machined and tested as part of this study. These specimens were precracked Charpy specimens which were machined from the broken halves of the 1/2T SE(B) specimens that had been used for the Weibull model rate study described briefly previously in this paper. Thirty-two specimens were machined from each of two slices, slices N and P, as shown in the detail in Fig. 1. These specimens were intended to determine whether a toughness gradient existed across the Euro forging that had not been detected using the tensile and hardness measurements conducted as part of the initial round robin (see Fig. 7). These specimens were tested fully in compliance with ASTM E1921.

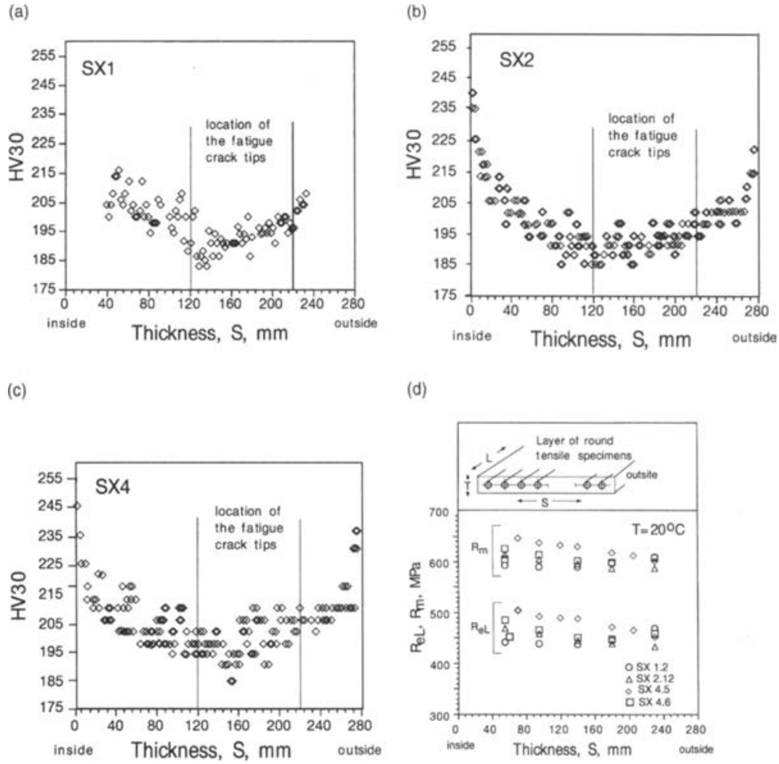

FIG. 7—*Hardness profile (a–c) and tensile data (d) obtained across the wall thickness showing the region used for the Euro round robin fracture tests [5].*

4T C(T) Specimens

Figure 8 shows a standard E1921 Master Curve plot of the 4T round robin specimen data. Tabulated data for this data set is presented in Table 2. T_o reference temperatures calculated for individual test temperature data sets, and for the full set using the ASTM E1921 multi-temperature procedure are very consistent. These specimens did not demonstrate any inhomogeneity as defined by the draft ASTM procedure outlined above. In each case the p_a was very high, resulting in the calculation of σ_{Tb}, being undefined when the argument in the radical in the denominator of Eq 8 became negative. Clearly the Master curve and confidence bounds fit the data distribution well, as shown in Fig. 8. Because of the large size of these specimens, all cracks were very close to the forging centerline in this case, and this combined with the long crack fronts sampling a large amount of material, very little inhomogeneity was experienced in this series of tests.

2T C(T) Specimens

The 2T specimen data set of the Euro round robin is presented in Fig. 9 and Table 3, and these data show a much different result. Comparing the E1921

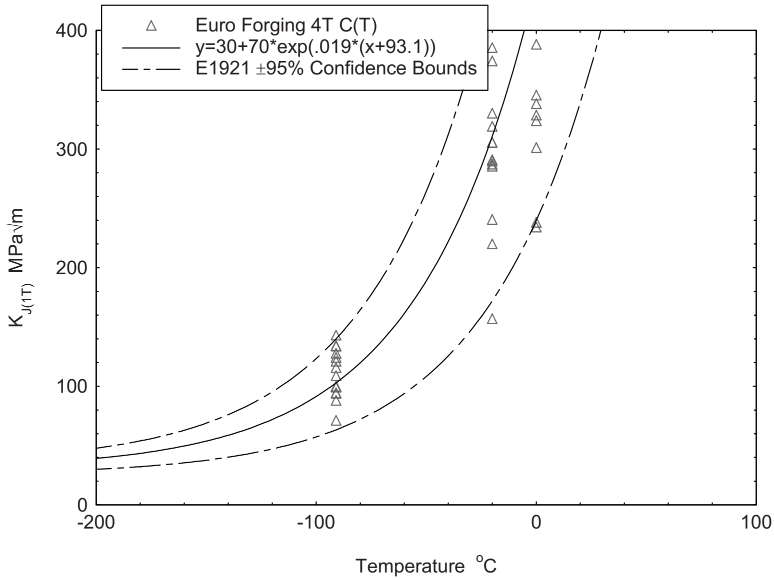

FIG. 8—*The Euro round robin 4T C(T) data set.*

multi-temperature Master Curve and the corresponding ±95 % confidence bounds and the data is not very satisfying in this case with approximately 13 % of the specimens lying outside the ±95 % confidence bounds. None of these specimens showed ductile crack growth or were censored by the E1921 requirements.

The requirements of E1921 would invalidate the result $T_o = -110.6°C$ calculated based on the $-60°C$ data set since $T - T_o > 50°C$, while it would accept the $-40°C$ data set giving $T_o = -85.8°C$ and the $-91°C$ data set result of $T_o = -97.5°C$ since in these cases $T - T_o < 50°C$. The multi-temperature analysis of E1921 leads to the use of only the $-60°C$ and $-91°C$ data sets and gives $T_o = -107.4°C$.

Applying the bimodal analysis demonstrates that the $-60°C$ data set is strongly inhomogeneous. The $-91°C$ and $-40°C$ data sets would be considered homogeneous by the proposed E1921 criteria, but a multi-temperature analysis

TABLE 2—*Homogeneity results, 4T Euro forging specimens.*

Temp., °C	N	r	T_o, °C	T_a, °C	T_b, °C	p_a	MLNH	SX blocks
−91	15	15	−96.2	−96.2	—	1	—	8, 12, 16, 21, 23, 44
−20	15	15	−91.0	−91.0	—	1	—	12, 14, 16, 18, 21, 24, 25
0	15	14	−92.3	−92.3	—	1	—	19, 20, 21, 24
Multi-temp	45	44	−93.1	−93.1	—	1	—	All of the above

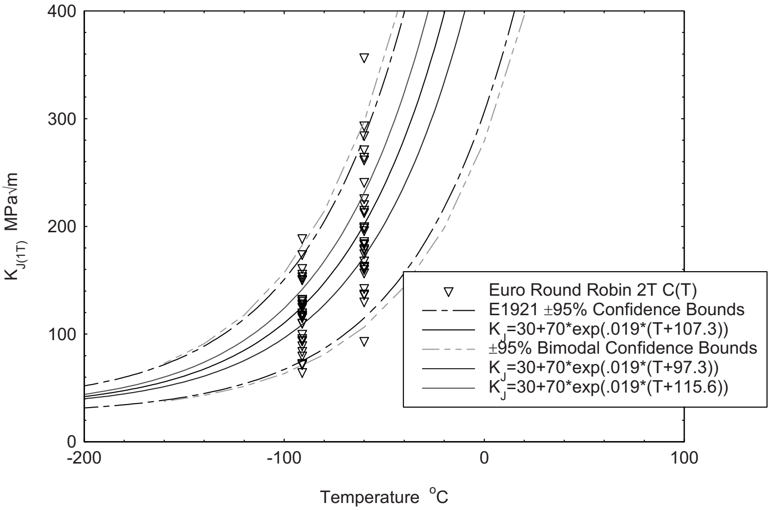

FIG. 9—*Master curve plot of the 2T Euro forging data set.*

results in the full 2T data set being considered inhomogeneous using the proposed MLNH >2.0 criteria. Evaluation of the 95 % confidence bounds for the bimodal analysis using the datum cumulative surviving probability of Eq 6, as shown in Fig. 9, does lead to wider and more satisfying 95 % confidence bounds of the data set with 6.7 % now excluded rather than the 13 % excluded by the E1921 confidence bounds. The $T_a - T_b$ difference is 18.3°C which shifts the lower 95 % confidence bound to the right by about 5°C at the $K_J = 100$ MPa$\sqrt{}$m, which is a significant effect from a regulator's viewpoint.

Looking at the cutting plan it is clear that while the 4T specimens were constrained to having the crack front very close to the forging centerline, the 2T specimens would have had crack positions much closer to the forging surface—generally right at the outer limit allowed by the round robin fatigue crack zone presented in Fig. 7 above. As shown in a following section, this difference in crack position is a likely factor in producing the increased toughness demonstrated in the 2T set of specimens. It is also shown below that when additional

TABLE 3—*Homogeneity results, 2T Euro forging specimens.*

Temp. °C	N	r	T_o, °C	T_a, °C	T_b, °C	p_a	MLNH	SX blocks
−91	30	30	−97.5	−90.4	−130.4	0.96	—	2, 7, 8
−60	30	30	−110.6	−100.0.	−120.1	0.65	2.33	2, 9, 10
−40	30	30	−85.8	−82.3	−89.3	0.56	0.84	2, 11, 12
Multi-temp	60[a]	60	−107.4	−97.3	−115.6	0.61	2.83	2, 7, 8, 9, 10

[a]−40°C data not included since $T - T_o > 50$°C.

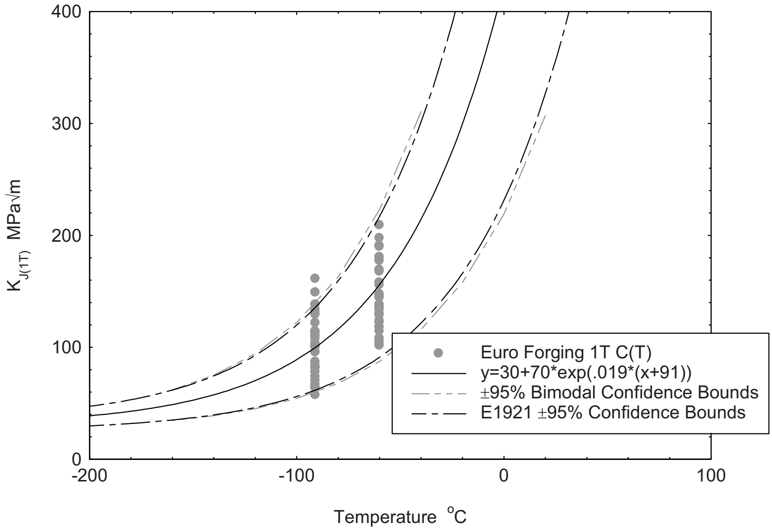

FIG. 10—*Euro forging 1T C(T) bimodal Master Curve.*

1/2T C(T) specimens were cut from 2T specimen halves using specimens originally from blocks SX2 and SX9, the higher toughness results were found again in the resulting data set.

1T C(T) Specimens

A similar but much less dramatic case of apparent material inhomogeneity is found in the 1T data set, as shown in Fig. 10 and Table 4. Here the −91°C single temperature data set demonstrates inhomogeneity and this data set continues to dominate when the multi-temperature calculation is made. The calculated T_a and T_b bracket the E1921 T_o, and there is little difference between the ±95 % confidence bounds based on a single distribution or a bimodal distribution, though the data excluded goes from 4 out of 68 or 5.9 % to 3 out of 68 or 4.4 % when the bimodal, ±95 % confidence bounds are utilized. Here the $T_a - T_b$ difference is 14°C, which shifts the lower 95 % confidence bound to the right by only 2°C at $K_J = 100$ MPa$\sqrt{}$m.

TABLE 4—*Homogeneity results, 1T Euro forging specimens.*

Temp. °C	N	r	T_o, °C	T_a, °C	T_b, °C	p_a	MLNH	SX blocks
−91	34	34	−97.2	−74.2	−98.6	0.23	2.35	8
−60	34	34	−87.5	−87.5	—	1	—	10
−40	32	31	−91.0.	−46.2	−91.2	0.01	—	12
Multi-Temp	68[a]	68	−91.0.	−83.9	−97.9	0.61	2.25	8, 10

[a]−40°C data not included since $T - T_o > 50$°C.

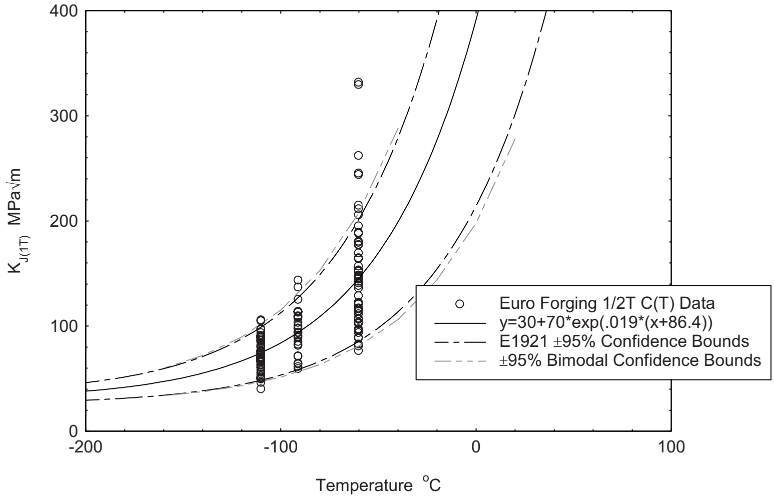

FIG. 11—1/2T *C*(*T*) *Euro round robin data set.*

1/2T *C*(*T*) *Specimens*

Figure 11 and Table 5 show the results of the Euro round robin 1/2T C(T) data sets. Here again inhomogeneity is clearly demonstrated in the data sets tested at −110°C and −60°C. The −60°C data was augmented here by a second set of specimens that the round robin directors subsequently machined from specimens halves of the 2T C(T)'s after these specimen had been recognized as being higher than average in toughness. The second set of 1/2T C(T)'s did show elevated toughness with $T_o = -96°C$, though not nearly as elevated as the results of the 2T specimens described above ($T_o = -120°C$). Combining the two −60°C 1/2T C(T) data sets clearly shows that significant inhomogeneity again exists in the data. Combining all data using the multi-temperature analysis shows that strong inhomogeneity exists in the 1/2T data set with MLNH = 3.38. Very little

TABLE 5—*Homogeneity results,* 1/2T *Euro forging specimens.*

Temp., °C	N	r	T_o, °C	T_a, °C	T_b, °C	p_a	MLNH	SX blocks
−110	55	55	−85.0	−71.3	−86.9	0.20	1.78	1, 2, 4
−91	31	31	−90.9	−90.2	−91.0	0.17	0.07	8
−60	31	29	−79.1	−73.3	−96.0	0.82	1.61	10
−60	31	22	−92.7	−74.2	−97.1	0.26	2.12	2, 9 from 2T C(T)
−60	62	51	−86.6	−76.4	−103.8	0.69	3.32	2, 9, 10
Multi-temp	148	137	−86.4	−71.5	−90.2	0.29	3.38	1, 2, 4, 8, 9, 10
Multi-temp[a]	117	115	−84.6	−70.9	−87.7	0.27	2.82	1, 2, 4, 8, 10

[a]This set excludes the extra specimens machined from the 2T C(T) specimens.

change is noted when the multi-temperature analysis is repeated with the second set of 1/2T C(T)'s at $-60°C$ excluded. In this case the bimodal 95 % confidence bounds better represent the data excluding 10 %, while the E1921 95 % confidence bounds exclude 11.5 % of the data. In this case the $T_a - T_b$ difference is $18.7°C$, corresponding to a shift of the lower 95 % confidence bound to the right by about $5°C$ at $K_J = 100$ MPa$\sqrt{m}$.

Precracked Charpy Data

Analyses of the high rate data obtained by the authors [4] and a review of the original European round robin data set clearly demonstrates that material inhomogeneity is a problem for the Euro forging material. The rate data implied that the position through the forging was a factor in the material inhomogeneity, but this could not be verified using the round robin data because of uncertainty in the positions of many of the specimens and the randomization done in organizing the specimens. To investigate this aspect, precracked Charpy geometry, deep crack bend specimens were machined that were systematically organized to keep track of the specimen location through the plate thickness. Specimen halves from the 1/2T SE(B) specimens originally machined from two "slices" of the Euro forging material were machined into precracked Charpy specimens with $a/W = 0.5$ and tested statically according to ASTM E1921 at $-100°C$. Each 1/2T SE(B) was cut into four precracked Charpy specimens, as shown in the enlargement in Fig. 1, giving a total of 32 specimens per slice. For the initial analysis the near surface specimens machined from the 7-8 layer specimens are not included in the analysis. These specimen results are discussed later in this paper.

The resulting fracture toughness data for the 1-6 layer specimens presented in Table 6 is plotted in Fig. 12. All specimens were tested to cleavage failure, and while some required censoring when evaluating T_o, none showed significant ductile crack extension before failure. Slices N and P were neighbors in the forging since slice "O" was omitted in the rate study specimen machining system to avoid specimen labeling confusion. A review of the high rate 1/2T SE(B) tests did suggest that specimens obtained from the N slice tended to be tougher than average while specimens from the P slice tended to be less tough than average in whatever data set the N or P specimens were a part of.

The results obtained by applying the bimodal inhomogeneity analysis are presented in Table 7 and plotted in Fig. 12. Neither slice can be demonstrated to be inhomogeneous according to the proposed E1921 MLNH criterion, though the plot of the data shown on Fig. 12 appears to be clearly inhomogeneous with a distribution much broader than expected by the E1921 confidence bounds. When the N and P slices are compared it is clear that they are distinctly different, with the T_o values being $-109.2°C$ and $-84.5°C$, respectively.

Combining the data from the two slices results in a strongly bimodal inhomogeneity with $T_a = -66.2°C$, $T_b = -111.4°C$, $p_a = 0.42$, and MLNH = 5.63. Re-analyzing using reduced data sets of (1-4) layer specimens or (5-6) layer specimens results in slight reductions in the MLNH coefficients.

Figure 13 shows a plot of cleavage initiation toughness versus the position

TABLE 6—*Tabulated results of the Euro forging precracked Charpy tests.*

Specimen ID (N Slice)	a/W	K_{Jc}, MPa$\sqrt{m}$	Specimen ID (P slice)	a/W	K_{Jc}, MPa$\sqrt{m}$
HN1AX	0.509	84.9	HP1AX	0.52	74.6
HN1AY	0.516	93.1	HP1AY	0.521	93.8
HN1BX	0.511	125.6	HP1BX	0.53	98.2
HN1BY	0.542	179.6	HP1BY	0.513	85.9
HN2AX	0.511	118.5	HP2AX	0.528	79.2
HN2AY	0.509	158.1	HP2AY	0.546	87.5
HN2BX	0.507	92.8	HP2BX	0.526	84.4
HN2BY	0.506	111.7	HP2BY	0.51	90.3
HN3AX	0.537	101.6	HP3AX	0.533	156.1
HN3AY	0.508	181.6	HP3AY	0.564	171.1
HN3BX	0.495	191.6	HP3BX	0.541	60.0
HN3BY	0.505	122.8	HP3BY	0.531	83.5
HN4AX	0.489	124.9	HP4AX	0.515	79.2
HN4AY	0.510	136.2	HP4AY	0.523	67.0
HN4BX	0.496	113.6	HP4BX	0.539	53.44
HN4BY	0.511	163.2	HP4BY	0.541	138.0
HN5AX	0.510	192.8	HP5AX	0.536	71.3
HN5AY	0.509	196.4	HP5AY	0.505	52.5
HN5BX	0.489	214.4	HP5BX	0.523	95.3
HN5BY	0.499	205.7	HP5BX	0.534	167.5
HN6AX	0.501	119.0	HP6AX	0.510	77.2
HN6AY	0.499	231.6	HP6AY	0.541	77.4
HN6BX	0.511	139.7	HP6BX	0.53	58.7
HN6BY	0.506	249.3	HP6BY	0.528	54.0
HN7AX	0.433	169.0	HP7AX	0.442	51.9
HN7AY	0.446	111.5	HP7AY	0.450	89.0
HN7BX	0.442	196.7	HP7BX	0.465	124.5
HN7BY	0.447	223.3	HP7BY	0.452	88.9
HN8AX	0.452	109.8	HP8AX	0.446	62.9
HN8AY	0.459	77.6	HP8AY	0.440	69.5
HN8BX	0.446	252.6	HP8BX	0.447	61.4
HN8BY	0.431	138.9	HP8BY	0.455	55.6

of the specimen precrack from the forging centerline. The lines are least-squares linear regression trend lines only. While the N and P slices are within 15 mm of each other in the forging, they demonstrate very different properties when cleavage initiation toughness is plotted versus position through the forging. Slice N demonstrates a distinct position dependence with toughness increasing as one moves from center to near the forging quarter thickness location, while the P slice shows little dependence on specimen position, with if

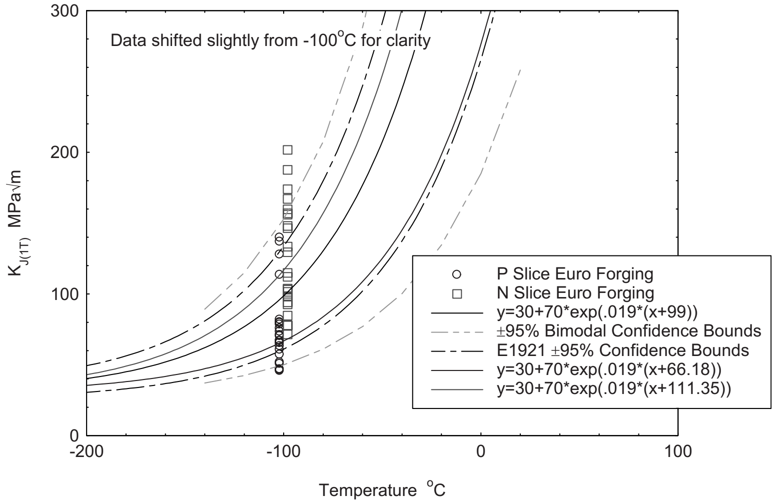

FIG. 12—*Master curve plot of precracked Charpy data showing E1921 and bimodal curve fits and confidence bounds.*

anything, a reverse behavior when compared to slice N. These results show why adding additional specimen slices in the rate study could have produced such unexpected havoc in the resulting data set.

Specimens machined in the (7-8) layers had been set aside until the results shown in Fig. 13 were available, since it was expected that these specimens would demonstrate a different toughness response than specimens machined from the center region of the forging. Specimen halves were now located and machined into precracked Charpy specimens, tested consistently with those describe previously, and the results are shown in Table 6 and in Fig. 14. Rather unexpectedly, the N slice specimens were found to have peaked in toughness at about the 6 layer and the toughness then falls toward the P slice results. The P slice results continued at a rather constant level, falling gradually, on average from the forging centerline to the surface.

It seems clear from the results of the N and P slices that the inhomogeneity is bimodal when combining the two slices with each slice representing one

TABLE 7—*Homogeneity results, precracked Charpy Euro forging specimens, Temp: −100°C.*

N	r	T_o, °C	T_a, °C	T_b, °C	p_a	MLNH	Layers	Slices
48	34	−99.0	−66.2	−111.4	0.42	5.63	1–6	N, P
24	13	−109.2	−109.3	−109.2	1.0	—	1–6	N
24	21	−84.5	−62.8	−121.1	0.82	—	1–6	P
32	25	−95.9	−72.4	−107.1	0.46	3.76	1–4	N, P
16	9	−105.1	−50.8	−121.4	0.38	3.41	5–6	N, P

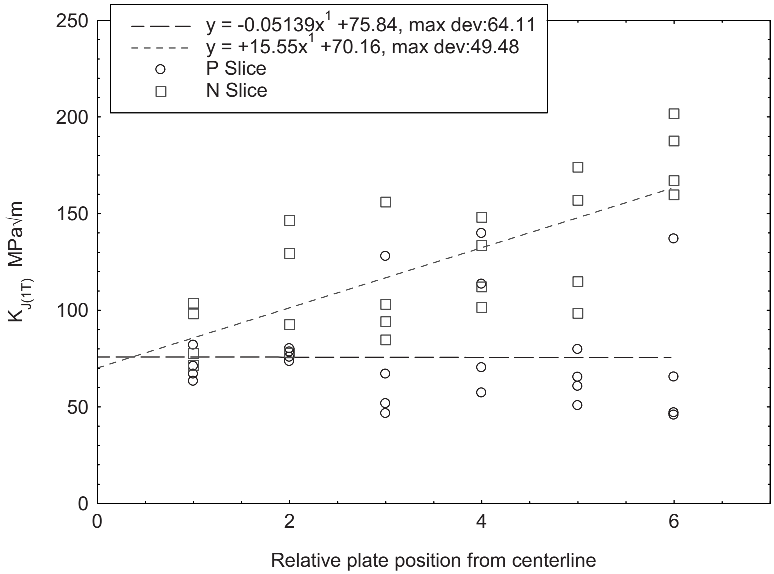

FIG. 13—*Fracture toughness versus relative position from the forging centerline.*

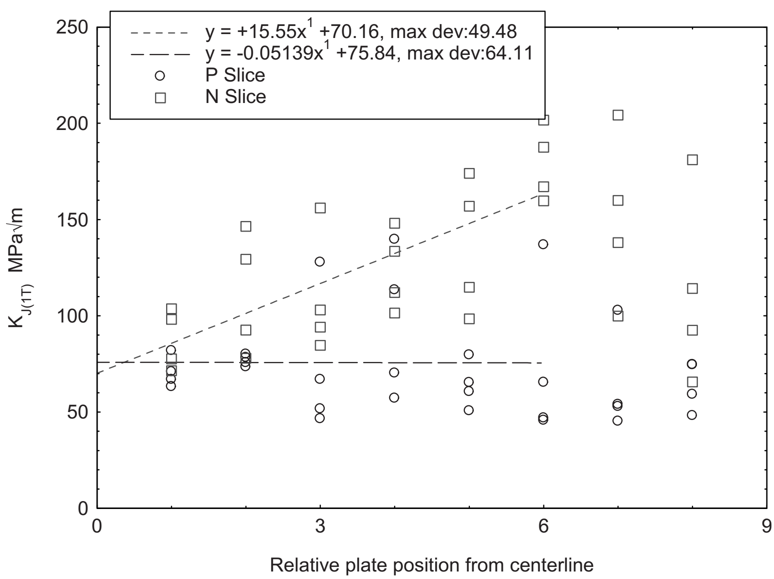

FIG. 14—*Toughness versus relative position for the N and P slices including the near surface (7-8) layers.*

mode. For slice N the toughness is elevated as one moves from the forging centerline to the quarter thickness location, and then falls again toward the outside surface. Slice P demonstrates nearly uniform toughnesses throughout the forging cross section. It seems highly likely that behavior like that of both type of slices repeats throughout the forging, though it is certainly not clear which behavior predominates. Data sets with all precracks located near the forging centerline would be homogeneous, while data sets with precracks located near the forging quarter thickness location would tend to be inhomogeneous.

Comparison with Other Experimental Results for the Euro Forging Steel

Additional data have been developed on the Euro forging material as part of the VOCALIST (Validation Of ConstrAint-based methodoLogy In Structural integriTy) project [12]. The stated objective of the VOCALIST project is to develop analysis procedures to relate specimen geometry data to realistic crack geometries and loading that might be found in critical engineering structures. To advance toward this goal the participants have tested deep and shallow crack bend specimens of the Euro forging material for comparison with the C(T) specimens that were used for the Euro round robin. Besides the standard E1921 specimen geometries the VOCALIST program has obtained ductile-to-brittle transition data on biaxially load cruciform specimens of the Euro forging material as well as center-cracked tension specimens and modified C(T) specimens (POR specimens) containing surface like cracks at the root of machined notches. All tests were conducted using Master Curve-like methods and the results were reported in terms of the reference temperature T_o.

Additional results on shallow and deep SE(B) specimens using the Euro forging material have also been reported by Joyce, Link, and Roe [11], again using the Master Curve approach. The comparable data from these studies is presented in Fig. 15 with T_o plotted against specimen type. The C(T) data are taken directly from the Euro round robin data set. The reference temperature T_o calculated using the full set of E1921 qualified data, labeled in Fig. 15 as "Full RR," is $T_o = -95°C$, though if the 2T specimens and the 1/2T specimens machined from these 2T specimens are removed from the analysis $T_o = -90°C$, which is labeled in Fig. 15 as "Reduced RR."

The deep crack SE(B) results reported by Joyce, Link, and Roe [11] are consistent with the round robin C(T) results, while the VOCALIST SE(B) results, with $T_o = -121°C$, appear low and the difference between the C(T) and the standard deep crack SE(B) is larger than one would expect if it was due only to the constraint difference between these two E1921 specimen types. The "shallow crack effect" reported by Joyce Link, and Roe is approximately 25°C, and this is consistent with what is reported by the VOCALIST project, but again the VOCALIST shallow SE(B) result appears low in comparison with the round robin C(T) results and the precracked Charpy specimen results. The precracked Charpy results appear consistent between the results of this paper, the results reported by Wallin [15] and the VOCALIST project, at least when thickness-

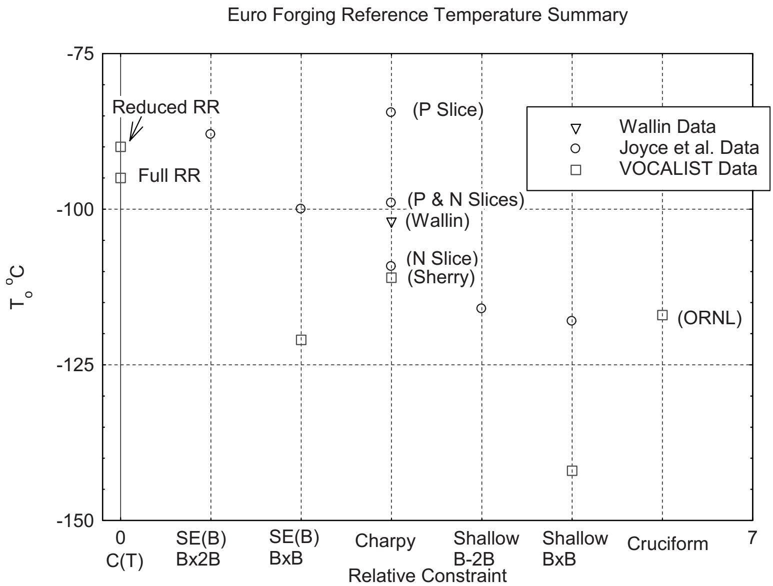

FIG. 15—*Comparison of VOCALIST and other constraint data available for the Euro forging material.*

dependent toughness variations that exist in the Euro forging material are understood.

Tabulated data for the VOCALIST SE(B) data were not made available, so it is not possible to investigate the homogeneity of the VOCALIST SE(B) and precracked Charpy data sets. The Joyce, Link, and Roe SE(B) data sets presented in Fig. 15 all demonstrate homogeneous behavior according to the proposed E1921 Annex requirements, while the precracked Charpy data sets are inhomogeneous, as described previously. The location through the forging thickness where the VOCALIST specimens were machined is also not known.

It seems unlikely that a constraint difference alone is responsible for the 27°C difference between the reference temperatures of the round robin C(T) specimens and the VOCALIST SE(B) results. It is also inconsistent with constraint based expectations that the larger SE(B) specimens would give T_o's so much less than that obtained using precracked Charpy size specimens.

The work presented previously in this paper suggests that material inhomogeneity plays a role in the T_o differences observed in these results, especially in the B by B SE(B) results which appear to be so inconsistent with the other results, and this should be investigated further before intricate constraint models are developed based on these results.

Discussion of the Results

Significant material inhomogeneity exists in the Euro forging material used for the Euro round robin and for aspects of the VOCALIST study. Application of the proposed ASTM E1921 Annex procedure shows distinct inhomogeneity exists at one or more temperatures in the 2T, 1T, 1/2T Euro round robin C(T) geometry data sets, and in the precracked Charpy data sets presented in this work. Inhomogeneity was not found in the 4T data sets, in all likelihood, because for this geometry all precracks were placed at the forging centerline, which does not exhibit material inhomogeneity. The 2T C(T) data sets demonstrated the worst inhomogeneity, apparently because for these specimens the precrack tips were often located near the forging quarter-thickness location, the location that appears to demonstrate the worst inhomogeneity at "slices" where inhomogeneity is present. Inhomogeneity in the test results was not traceable to the European Round Robin test lab in any case. Inhomogeneity was present in some of the sub-blocks shown in Fig. 4 and it is present in the block of material provided to NSWCCD Carderock for testing. Testing done as part of this study has clearly shown that in some areas of the forging the toughness changes rapidly as the precrack position is moved from the centerline toward the forging quarter thickness position, and in other areas the toughness is insensitive to the precrack position through the forging cross section. In the "P slice" data developed here, which did not demonstrate a through thickness toughness variation, bimodal inhomogeneity was still present, as currently proposed by the draft E1921 Inhomogeneity Annex.

The Euro forging ductile-to-brittle transition temperature is difficult to characterize because of the large amount of material inhomogeneity present. Individual data sets of the round robin give E1921 T_o reference temperatures ranging from $-79.1°C$ to $-110.6°C$, roughly consistent with the P and N slice results of $-84.5°C$ and $-109.2°C$, respectively. If the sole objective was to assure the safety of a pressure vessel the highest $T_o=-79.1°C$ could be adopted for all safety analyses.

The large variation in T_o makes it difficult to use this material and the existing round robin data set to make comparisons of crack tip constraint by testing low constraint specimens, for example, shallow crack bend specimens, single edge notch tension specimens, or biaxial cruiform specimens, since the differences caused by constraint can be of the same order as the $25°C$ resulting from inhomogeneity alone. Placing all low constraint geometry specimen cracks at the forging centerline, and comparing the results with the 4T C(T) round robin results would be the most effective comparison.

Conclusions

The forging material used for the European Master Curve round robin is inhomogeneous and care must be taken in interpreting results obtained using this material. Larger data sets of each specimen and loading configuration should be tested and care should be taken to position the precrack at consistent positions through the plate thickness. It should be expected that the measured T_o is dependent on the position of the precrack relative to the plate thickness and understood that differences in T_o of up to $75°C$ have been observed in E1921 valid data sets obtained from this forging. The restrictions used for the original Euro round robin reduced this variation dramatically to about $32°C$. This variation is considerably larger than the 20°C variation suggested as "typical" for homogeneous materials by E1921. The data sets that contributed most to this larger than expected variability were the 2T specimen data sets that demonstrated higher toughnesses and hence lower T_o values than the other specimen data sets. Basically, 4T specimens had their precracks located near the forging centerline, 1T and 1/2T specimens had their precracks distributed between the forging centerline and quarter thickness location, while the 2T specimens had their precracks all near the forging quarter-thickness location. Work presented here has shown that some forging cross sections show substantial variations in fracture toughness between the forging centerline and the forging quarter-thickness location, and this material inhomogeneity would have the largest effect on the 2T data sets.

Application of the single temperature procedure of the draft E1921 Inhomogeneity Annex to the Euro round robin data sets shows that several data sets are inhomogeneous according to the inhomogeneity standard presently proposed. The 4T data sets, which had the precrack at the forging centerline for all specimens, are shown to be much more homogeneous than the other data sets. Applying the multi-temperature method of the proposed E1921 Inhomogeneity Annex to the 2T, 1T, and 1/2T C(T) data sets of the Euro round robin results in the conclusion that these data are all inhomogeneous.

Careful testing of cross-section slices using precracked Charpy specimens presented here shows that at some cross sections the Euro forging fracture toughness increases approximately linearly between the forging centerline and the forging quarter thickness position, and then falls off again toward the forging surface. In other cross sections the fracture toughness is not dependent on crack tip location. Combined data sets including data from near the forging quarter-thickness location results in bimodal inhomogeneity as defined by the draft E1921 Inhomogeneity Annex.

The Euro forging material does not appear to be a good choice for studies like the VOCALIST project because the material inhomogeneity invariably will confuse or at least complicate the determination of the effects of constraint on T_o. The inhomogeneity observed in the Euro forging material is not unexpected for a large forging but the observed difference, $T_a - T_a = \sim 18°C$ is large compared to the constraint effect on T_o anticipated for various crack and loading configurations, and it is difficult to separate the two effects in an experimental study like that conducted in the VOCALIST project. The Euro forging is a good material to demonstrate the value of the addition of inhomogeneity analysis procedures to the ASTM E1921 standard. In order to obtain estimates of the effect of constraint on T_o, it appears that an experimental program conducted on a homogeneous model material will be necessary. Obtaining a material that is homogeneous and available in large section sizes is certainly a challenge. Continued research must be directed to develop methods and model materials to evaluate and characterize material inhomogeneity in large section structural materials.

Acknowledgments

This program was performed at the U.S. Naval Academy under the program "Elastic-Plastic Fracture Mechanics Technology for LWR Alloys," C. Roe program manager. The program is sponsored by the Office of Nuclear Regulatory Research of the U.S. Nuclear Regulatory Commission (NRC). The NRC technical monitor is Dr. Mark Kirk. The authors would like to acknowledge the help of Mr. Derek Baker of the U.S. Naval Academy who did the machining of the tests specimens utilized in this program. The use of material testing and computer resources at the U.S. Naval Academy is also appreciated.

References

[1] Beremin, F. M., "A Local Criterion for Cleavage Fracture of a Nuclear Pressure Vessel Steel," *Metall. Trans. A*, 14A, 1983, pp. 2277–2287.

[2] Petti, J., and Dodds, R. H., "Calibration of the Weibull Stress Scale Parameter, σ_u, Using the Master Curve," *Eng. Fract. Mech.*, Vol. 72, 2004, pp. 91–120.

[3] Gao, X., and Dodds, R. H., "Loading Rate Effects on Parameters of the Weibull Stress Model for Ferritic Steels," *Eng. Fract. Mech.*, Vol. 72, 2005, pp. 2416–2425.

[4] Gao, X., Joyce, J. A., and Roe, C., "An Investigation of the Loading Rate Dependence of the Weibull Stress Parameters," *Eng. Fract. Mech.*, Vol. 75, 2008, pp. 1451–1467.

[5] Heerens, J., and Hellmann, D., "Development of the Euro Fracture Toughness Dataset," *Eng. Fract. Mech.*, Vol. 69, No. 4, 2002, pp. 421–450.

[6] Canonico, D. A., and Berggren, R. G., "Tensile and Impact Properties of Tick-Section Plate and Weldments," *Nucl. Eng. Des.*, Vol. 17, No. 1, 1971 pp. 4–15.

[7] Joyce, J. A., and R. L. Tregoning, "Investigation of Specimen Geometry Effects and Material Inhomogeneity Effects in A533B Steel," ECF14, Krakow, 2002.

[8] Wallin, K., "Effect of Strain Rate on the Fracture Toughness Reference Temperature T_o for Ferritic Steels," In *Recent Advances in Fracture* R. K. Mahidhara, Ed., The Minerals, Metals and Materials Society, Warrendale, PA, 1997, pp. 171–182.

[9] Wallin, K. et al., "Master Curve Analysis of Inhomogeneous Ferritic Steels," *Eng. Fract. Mech.*, Vol. 71, No. 16, 2004, pp. 2329–2346.

[10] Yin, S., Bass, R., Williams, P., Ludwig, M., and Keim, E., "Effect of Shallow Flaws and Biaxial Loading on Transition Temperatures Using a Weibull Stress Model," ASME Pressure Vessel and Piping Conference, PVP Vol.-475, San Diego CA, pp. 77–84.

[11] Joyce, J. A., Link, R. E., and Roe, C., "An Experimental Investigation of the Effect of Biaxial Loading on the Master Curve Transition Temperature in RPV Steels," *Eng. Fract. Mech.*, Vol. 74, 2006 pp. 2824–2843.

[12] Lidbury, D. P. G. et al., "Validation of Constraint-based Methodology in Structural Integrity of Ferritic Steels for Nuclear Reactor Pressure Vessels," *Fatigue Fract. Eng. Mater. Struct.*, Vol. 29, 2006, pp. 829–849.

[13] Sherry, A. H., Hooten, D. G., Beardsmore, D. W., and Lidbury, D. P. G., "Material Constraint Parameters for the Assessment of Shallow Defects in Structural Components. Part II: Constraint-based Assessment of Shallow Defects," *Eng. Fract. Mech.*, Vol. 72, 2005 pp. 2396–2415.

[14] Bass, B. R., McAfee, W. J., Williams, P. T., and Pennell, W. E., "Fracture Assessment of Shallow-flaw Cruciform Beams Tested Under Uniaxial and Biaxial Loading Conditions," *Nucl. Eng. Des.*, Vol. 188, 1999, pp. 259–288.

[15] Wallin, K., "Quantitative Experimental Method for Studying Brittle Fracture Constraint Loss in CT and 3PB Specimens," *Fracture, Fatigue, and Residual Stress–PVP Vol. 393*, Pan J., Ed., American Society of Mechanical Engineers, New York, 1999.

ELASTIC-PLASTIC FRACTURE MECHANICS

ASTM Special Technical Publication, Vol. 5, No. 10
Paper ID JAI101546
Available online at www.astm.org

Juan R. Donoso,[1] *Katherine Vasquez,*[1] *and John D. Landes*[2]

The Significance of a Crack Growth Law for a *C(T)* Fracture Specimen Undergoing Stable Crack Extension

ABSTRACT: A new method of construction of the *J-R* curve has been proposed recently that makes use of a postulated crack growth law relating stable crack extension, Δa, to plastic displacement, v_{pl}. An analytical treatment of both the J-Δa curve and the force-displacement, P-v, curve, is now possible even under circumstances in which the sole inputs are the P-v curve and the initial and final crack size values. Based upon this crack growth law concept, and on the common and the concise format equations of Donoso and Landes, an alternative way of estimating the amount of stable crack growth is presented. This alternative method, which allows for the evaluation of the crack size at any value of force or displacement along the P-v curve, has been applied to some examples of *C(T)* fracture test specimens that have crack extension values obtained by the unloading compliance method. The results are quite encouraging, and the method is extended here to cases in which there are no crack extension measurements available.

KEYWORDS: stable crack growth, common format, elastic-plastic fracture, normalization

---

Manuscript received November 29, 2007; accepted for publication October 6, 2008; published online November 2008.
[1] Professor and Student, Materials Science Department, Universidad Santa Maria, Valparaiso, Chile; e-mail: juan.donoso@usm.cl
[2] Professor, MABE Department, The University of Tennessee, Knoxville, TN; e-mail: landes@utk.edu

Citation: Donoso, J. R., Vasquez, K., and Landes J. D., "The Significance of a Crack Growth Law for a *C*(*T*) Fracture Specimen Undergoing Stable Crack Extension," *J. ASTM Intl.*, Vol. 5, No. 10. DOI10.1520/JAI101546. Available online at www.astm.org. Also included in JAI Special Issue STP 1508, *Fatigue and Fracture Mechanics: 36th Volume,* R. W. Neu, K. R. W. Wallin, and S. R. Thompson, guest editors, ASTM International, West Conshohocken, PA 2009, pp. 33-53.

Nomenclature

a_c = Critical crack size
a_o = Initial crack size
a_f = Final crack size
B = Thickness of a fracture toughness test specimen
b = Ligament size
b_o = Initial ligament size
b_c = Critical ligament size
C = Coefficient of geometry function for plasticity
c_f = Elastic compliance for the final crack size
D = Parameter equal to $\Omega^* \cdot \sigma^*$
G = Geometry function
J = Total value of the J integral
J_{Ic} = Plane strain fracture toughness
J_Q = Provisional value of J_{Ic}
$J_{Q\exp}$ = Experimental value of J_Q
l_0; l_1 = Coefficient and exponent of crack growth law
m = Exponent of geometry function in plasticity
n = Exponent of hardening function
P = Force
P_f = Force at final point in a test
P_f^* = Corrected value of force at the final point of the test
$P_{\max}$ = Maximum force in a force-displacement graph
v = Displacement (general)
v^* = Total displacement at the intersection point of two P-v curves
v_c = Critical displacement; displacement at which $P = P_{\max}$
v_{el} = Elastic displacement
$v_{el,f}$ = Final value of elastic displacement
v_f = Final (total) displacement
v_n = Normalized plastic displacement, equal to v_{pl}/W
v_{pl} = Plastic displacement
$v_{pl,f}$ = Final value of plastic displacement
W = Width of a fracture toughness test specimen
Δa = Crack extension
Δa_c = Critical value of crack extension
Δa_f = Final measured value of crack extension
Ω^* = Common Format constraint factor
σ^* = Coefficient of the plasticity hardening function

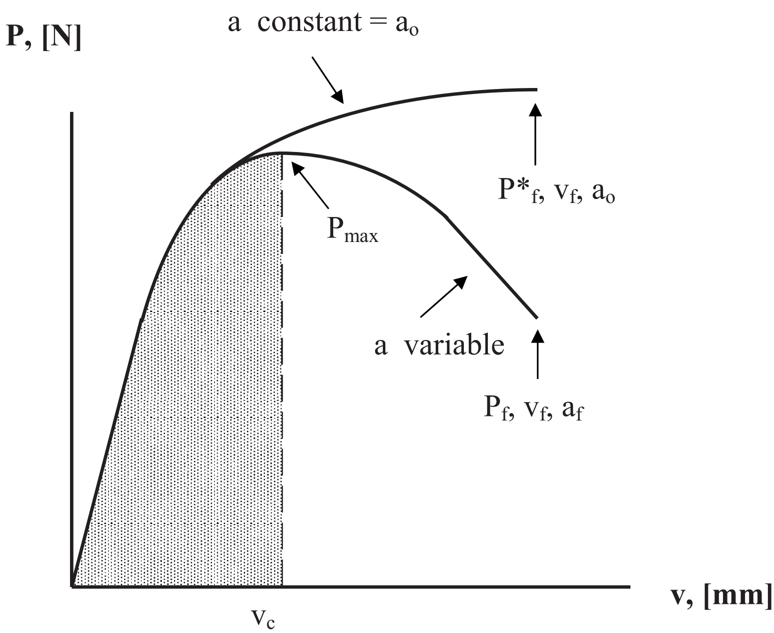

FIG. 1—*Schematic P-v curves for constant and variable crack size.*

Introduction

The fracture toughness of a ductile material may be evaluated, following the guidelines of E 1820, either as a point value, designated provisionally as J_Q—to become J_{Ic}, provided certain size and constraint requirements are met—or as a complete fracture toughness resistance curve. If the latter option is taken, a J-based resistance curve—the J-R curve—may be obtained from a single specimen fracture test, in which the actual crack length is measured concurrently with the test by means of elastic compliance changes or other techniques.

Recently, Pehrson and Landes [1] were able to show empirically that J_Q, the single fracture toughness point value, correlates well with the value of J at maximum force for $C(T)$ specimens of size $W = 50$ mm, i.e., $J_Q \approx J(P_{max})$. Moreover, they suggest that $J_{Ic} = J(0.99P_{max})$ with a high degree of statistical confidence. Although the value of J_Q is dependent on size (W), Pehrson and Landes's results show that one can run a fracture test, analyze the force-displacement (P-v) data, and obtain a reasonable estimate for a major fracture property—J_{Ic}—related to the initiation of the stable crack extension process, without the concern of how the crack size evolves in the test beyond maximum force.

A fracture test is often carried out to displacements well beyond those for maximum force. Figure 1 shows a schematic P-v curve with maximum force P_{max}. This curve is labeled as *a variable*, to reflect the fact that a specimen that displays such a curve undergoes stable crack extension. The test is willfully

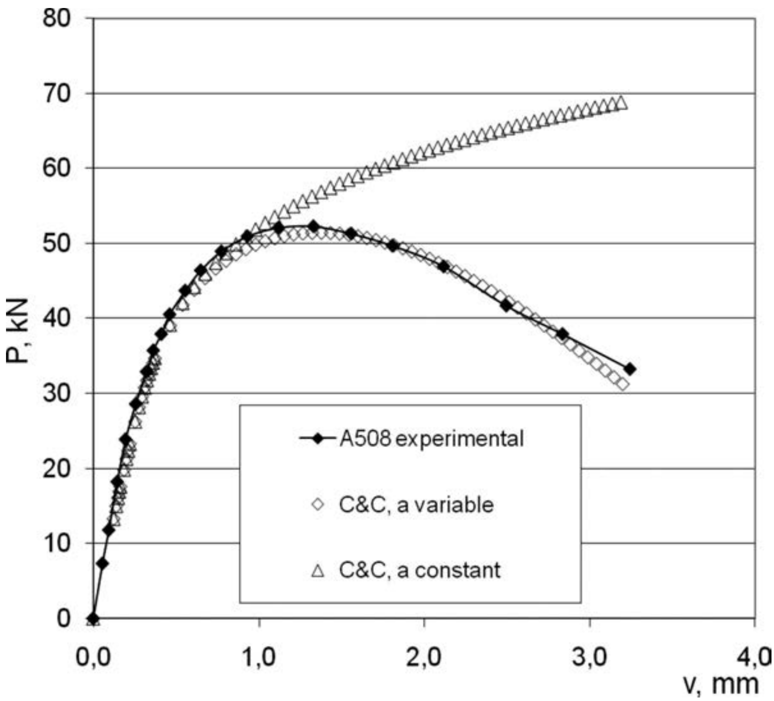

FIG. 2—*P-v curves for a 1T-C(T) A 508 specimen.*

terminated at a point designated as P_f, v_f, a_f, meaning that the force and displacement at the final test point are (P_f, v_f), and the crack size is a_f. The stable crack growth amount at the end of the fracture test is $\Delta a = a_f - a_o$.

The force for the *a variable* curve first increases, then decreases. The maximum force is attained at a displacement labeled as v_c, so that J_Q (J at $P_{\max}$ for a specimen with $W = 50$ mm) may be calculated as [1,2]

$$J_Q = \frac{m}{Bb} \int_0^{v_c} P dv. \tag{1}$$

There is a second curve abutting the first, designated as *a constant*. This is the curve the specimen would show in the absence of crack growth, i.e., it represents the behavior of a blunt notch specimen with initial crack size a_o. For such a situation, the force—ideally—goes on increasing, following a well known power-law pattern given by the conjunction of the common format equation [3] and the concise format [4].

Figure 2, taken from Ref. 5, shows a *P-v* curve for an ASTM A 508 steel *C*(*T*) specimen. In this figure, three curves are included. The solid points joined by the continuous line are the experimental data points for the A 508 specimen. Two C&C curves are shown—C&C being the acronym for common and concise formats—one for *a variable*, being coincident with the A 508 experimental curve, and another for *a constant*. This latter curve has also been obtained with the C&C Formats with a crack size equal to the initial specimen crack size, a_o.

A couple of questions might be asked in light of Pehrson and Landes's findings:

(1) If the single point critical value of J, J_{Ic}, may be obtained with the aid of $P_{\max}$, what then is the use of the force-displacement data for $v > v_c$?;

(2) On the other hand, if the full J-R curve is sought and the concurrent measurement of crack size with the fracture test is not viable—for any number of reasons—can we get an estimate of the values of crack size as a function of either force or displacement beyond maximum force?

The significance of the maximum force on the P-v curve, and its relation with J_{Ic}, cannot be underestimated [1]. However, the events that take place after the attainment of maximum force in a fracture toughness test of a ductile material seem of equal importance. This paper will focus on how stable crack extension data may be inferred, with only the knowledge of maximum load, initial and final crack sizes, and the datum (P_f, v_f), as shown in Figs. 1 and 2.

The DZL Original Crack Growth Model

Donoso, Zahr, and Landes (DZL) [5] proposed a novel way of obtaining the J-R curve using the common [3] and concise formats [4] (C&C). Among several advantages, the use of these formats has made it possible to relate the maximum force on a P-v curve to the crack extension values, for a specimen that undergoes stable crack growth [6]. In order to show how maximum load on a P-v curve is related to the crack extension process, the required C&C relations for this analysis are presented next.

The common and concise formats developed by Donoso and Landes are calibration functions that relate the force, P, to the displacement, v, and the crack length, a, of a fracture toughness specimen. The common format deals with the plastic component of the displacement, v_{pl} [3], whereas the concise format is used in the elastic regime, in which $v = v_{\mathrm{el}}$ [4].

These P-v-a relations are based upon the concept of load separation [7] into a geometry function and a deformation function. The geometry function depends on crack size and does so through a power law relation on the normalized ligament size b/W. The deformation function, on the other hand, depends on v_{pl}/W through a power law relation in the common format and linearly on v_{el}/W in the concise format. Since a test specimen undergoing stable crack extension shows a large amount of plastic displacement compared to the elastic one, the primary analysis is done using the common format.

The common format equation (CFE) was proposed by Donoso and Landes [3] to describe the force-plastic displacement relationship for a blunt-notch fracture specimen. As such, it relates the applied force P with two variables representing the nonlinear deformation of a fracture specimen with a stationary crack: v_{pl}/W, the plastic component of the force-line displacement, normalized by the specimen width W, and b/W, the normalized ligament size (ligament size b in lieu of the crack size a). The CFE also includes a term that denotes the out-of-plane constraint, Ω^*, and is written as

$$P = \Omega^* \cdot B \cdot C \cdot W \cdot (b/W)^m \cdot \sigma^* \cdot (v_{\mathrm{pl}}/W)^{1/n}, \tag{2}$$

where B = specimen thickness; C and m = the geometry function parameters, and σ^* and n are material properties, which are obtained from a material stress-strain curve [8], or directly from the specimen normalized force-normalized displacement curve.

For a nongrowing crack, the crack (or ligament) size is constant, and P and v become the variables of the calibration function, at constant crack size. When there is stable crack extension, however, the crack size a also becomes a variable, so that a separate relation between a and v_{pl} is needed. For such purpose, DZL proposed a "crack growth law" [5] to account for the relation between stable crack extension Δa and plastic displacement v_{pl}. The assumed crack growth law is a two-parameter power law equation relating the change in normalized crack size, $\Delta a/W$, with normalized plastic displacement, $v$pl$/W$, i.e.,

$$\frac{\Delta a}{W} = l_0 \left(\frac{v_{\mathrm{pl}}}{W} \right)^{l_1}. \tag{3}$$

In Eq 3, l_0 is a coefficient to be determined—as will be explained presently—and l_1 an exponent, which for $C(T)$ specimens is of the order of 2.0 [5].

The term Δa, crack extension, may also be written in terms of the change in ligament size, that is, $\Delta a = b_o - b$, where b_o is the initial ligament size (b_o is equal to W minus the initial crack size, a_o). Thus, Eq 3 gives the following expression for the current ligament size, b:

$$\frac{b}{W} = \frac{b_o}{W} - l_0 \left(\frac{v_{\mathrm{pl}}}{W} \right)^{l_1}. \tag{4}$$

Substitution of Eqs 3 and 4 into Eq 2 yield the following expression for the CFE in terms of only the plastic displacement when there is stable crack growth

$$P = DBCW \left[\frac{b_o}{W} - l_0 \left(\frac{v_{\mathrm{pl}}}{W} \right)^{l_1} \right]^m \left(\frac{v_{\mathrm{pl}}}{W} \right)^{1/n}, \tag{5}$$

where D = product of the parameters σ^* and Ω^*.

On the other hand, substitution of Eqs 3 and 4 into Eq 2, gives the CFE for a crack growth situation in terms only of crack extension, Δa,

$$P = DBCW \left[\frac{b_o - \Delta a}{W} \right]^m \left(\frac{1}{l_0} \frac{\Delta a}{W} \right)^{1/(nl_1)}. \tag{6}$$

Equation 5 is the DZL model relation for the force versus plastic displacement curve for stable crack growth. Equation 6, on the other hand, shows the relation between force and crack length alone, when there is stable crack growth. The shape of both relations clearly indicates the existence of a maximum value for P in terms of plastic displacement [Eq 5] or crack size [Eq 6].

Following the procedure of E1820, a fracture toughness test plot is usually given as force versus total displacement (often including the unloading-reloading lines), with the stable crack extension data given as a function of total displacement, as a complement to the P-v output. The alternative look at the J-R curve construction proposed by DZL, includes the crack growth law, Eq 3,

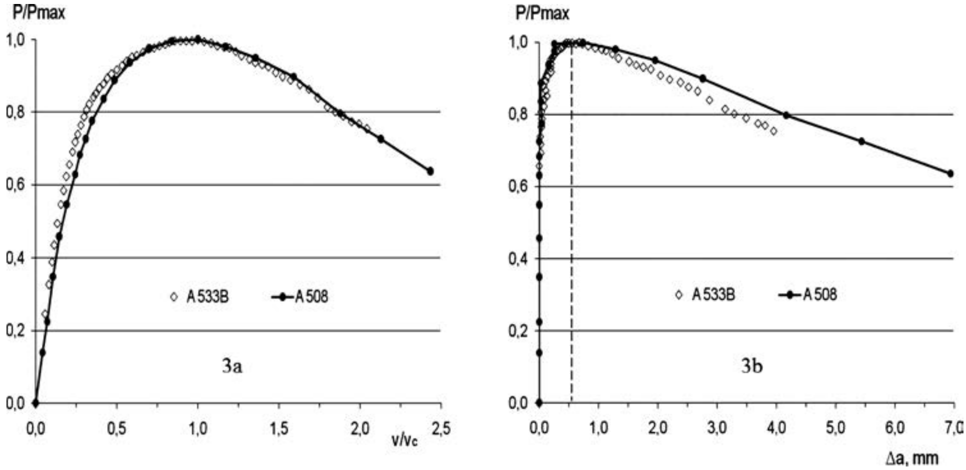

FIG. 3—*Force divided by maximum force, P/P_{max}, as a function of v/v_c [Fig. 3(a), left] and as a function of Δa [Fig. 3(b), right], for A 533B and A 508 C(T) specimens.*

and the relation between force and plastic displacement for a crack growth situation, Eq 5. Both Eqs 3 and 5 relate Δa and P to the plastic component of the displacement; the elastic displacement, on the other hand, may be obtained with the use of the concise format [5].

Figure 3 shows the comparative behavior of two $C(T)$ specimens with regard to stable crack extension, obtained from the original P-v-a data: A 508 [5] and A 533B [9], both of which were included in the J-Δa analysis of Ref. [5]. Figure 3(a) (left) shows force normalized by maximum force, $P/P_{\max}$, plotted against the ratio of the total displacement normalized by the displacement at maximum force, v/v_c (see Fig. 1 for nomenclature). Figure 3(b) (right), on the other hand, shows $P/P_{\max}$ plotted against the amount of stable crack extension, Δa, generated during the tests. Thus, these two plots reflect, somehow, the P-v-a relations of Eq 5 [Fig. 3(a)] and of Eq 6 [Fig. 3(b)].

Looking at Fig. 3(b), if one uses Pehrson and Landes's criterion for the $1T$-$C(T)$ specimen [1], then J_Q could be obtained at a value of crack extension of $\Delta a_c \approx 0.55$ mm for A 533B. In fact, for this specimen (CT-10) Joyce and Link [9] give a value of J_{Ic} of 240 (N/mm) at a value of Δa of 0.556 mm. Also, from Figs. 3(a) and 3(b), one can expect that at a given $P/P_{\max}$ beyond maximum force, any value of the total displacement should give rise to a different Δa behavior response for the two specimens.

Figure 4 shows the amount of stable crack growth Δa normalized by W, as a function of normalized displacement, v/W, for the two specimens, A 508 and A 533B. Two sets of curves are shown, one for the elastic displacement (left side of the figure) and the other for the plastic displacement. The elastic values are smaller than the plastic ones, are similar for both specimens, and their rate of change with crack extension is rather low. On the other hand, it is clear that at any given value of $\Delta a/W$, the A 533B specimen gives a normalized plastic displacement $v_n = v_{\rm pl}/W$ larger than that of the A 508, in agreement with what is

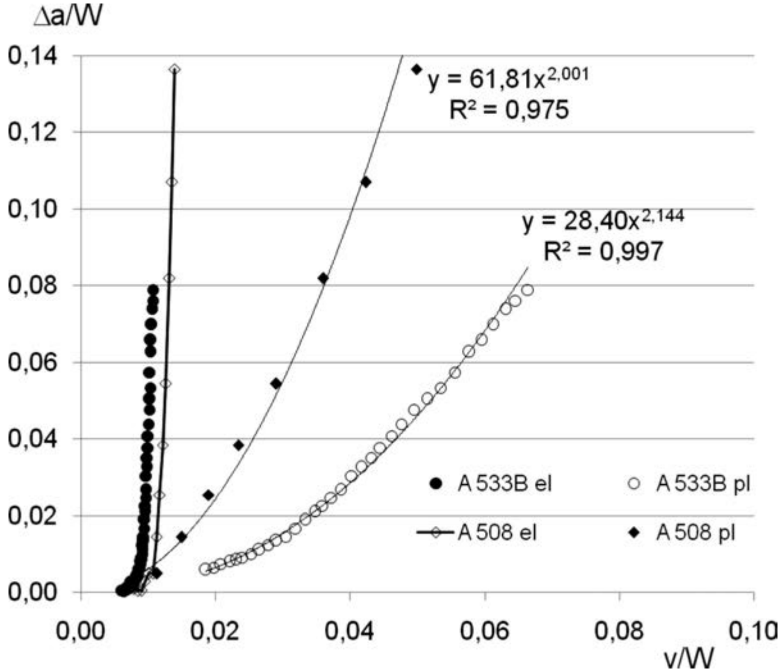

FIG. 4—*The crack growth law for the $C(T)$ specimens of Fig. 3.*

shown in Figs. 3(*a*) and 3(*b*). The dependence of v_n with $\Delta a/W$—in other words, the crack growth law of Eq 3—is shown in Fig. 4 for both specimens by means of power-law fits. For the A 508 specimen, the coefficient l_0 is larger than that for the A 533B specimen, implying thus less amount of normalized plastic displacement with unit crack extension. It is important to notice that $l_1 = 2.001$ for A 508 and 2.144 for A 533B, values which are close to that used earlier in the DZL model, i.e., $l_1 = 2.0$ [5].

An Alternative Crack Growth Model for a $C(T)$ Specimen

The original DZL model used a value of the exponent l_1 of the crack growth law, Eq 3, of the order of 2.0 for the $C(T)$ specimens data examined [5]. The value of the coefficient l_0, on the other hand, was obtained by calibration with the final point of the test. Using the notation of Fig. 1, the values of the set P_f, v_f, a_f were employed to obtain l_0 as

$$l_0 = \left(\frac{\Delta a_f}{W}\right)\left(\frac{v_{\mathrm{pl},f}}{W}\right)^{-l_1}, \tag{7}$$

where the plastic component of Eq 11 at the end of the test, $v_{\mathrm{pl},f}$, is

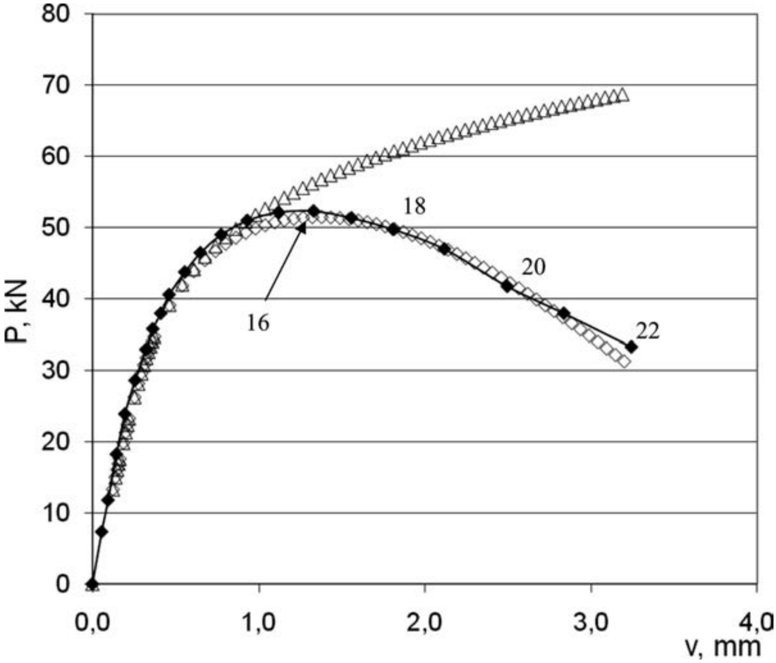

FIG. 5—*P-v curves for 1T-C(T) A 508 specimen.*

$$v_{\mathrm{pl},f} = v_f - v_{\mathrm{el},f}, \tag{8}$$

and the elastic displacement, $v_{\mathrm{el},f}$, is

$$v_{\mathrm{el},f} = c_f P_f. \tag{9}$$

In Eq 9, c_f is the elastic compliance—a function of the final value of the crack size, a_f—at the test final point.

In order to introduce the alternative way to obtain values of crack extension, let us use the example of the A 508 specimen. Figure 5 shows the same *P-v* curves for A 508 as Fig. 2, without the legend. The A 508 experimental curve has 22 data points—including the pair at the origin—of which the last seven have been numbered in Fig. 5 every other one, backwards from 22 to 16. In this case, maximum force is produced at point 16.

What if the test had been terminated at point 20 instead of 22? Or terminated at any other point between the final point and that at maximum force? The original data for this A 508 specimen includes the crack size at any (P,v) point on the experimental curve, determined from unloading compliance measurements.

Figure 6 shows, once again, the experimental *P-v* curve for the A 508, plus eight *a constant* curves, all of them constructed with the C&C formats. The upper curve of Fig. 6 is the same *a constant* C&C curve for which $a = a_o$. Each one of the remaining seven curves of Fig. 6 has a crack size equal to the crack size the specimen has at each of the selected experimental points labeled 16–22.

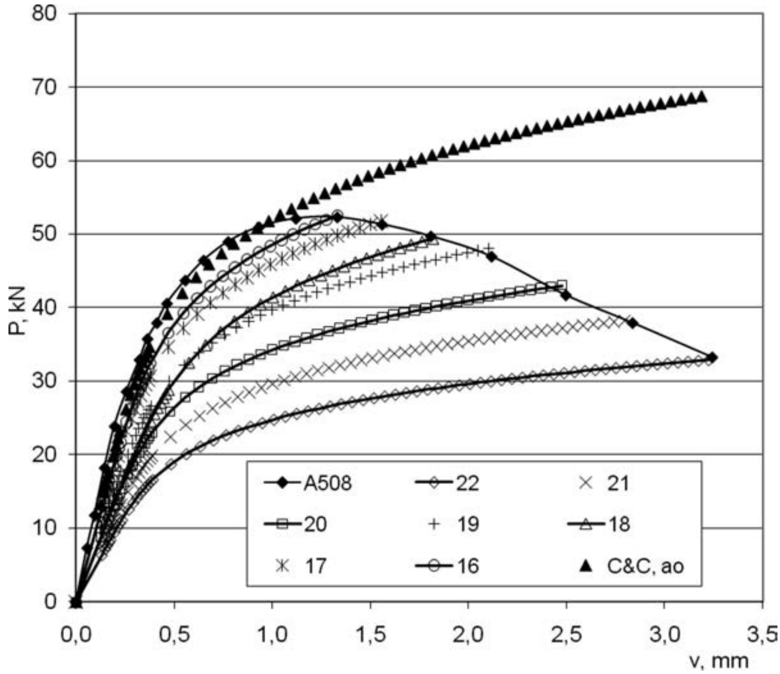

FIG. 6—*Experimental P-v curve for the A 508 specimen of Fig. 5, and eight C&C curves of known crack sizes.*

These curves are, in fact, the equivalent of the uppermost curve (C&C, $a = a_o$) but adapted to the corresponding crack sizes at each one of the points 16–22. Thus, each curve has its own elastic slope and geometry function, both of which depend on crack size. Each curve, on the other hand, has been drawn up to the intersection point with the experimental A 508 curve.

All points from 16 to 22 on Fig. 6 have their P_j, v_j, a_j sets of data well identified, for any point "j" on the P-v curve ($j = 16, 17, \ldots, 22$). The C&C construction of the seven *a constant* curves has been done with full knowledge of the corresponding crack size a_j, at the point P_j, v_j. Within some margin of error, all seven curves intersect the experimental curve at, or very near to, each of the selected points, 16–22. If this construction has a meaning, let us then work the construction process backwards: assume a certain crack size—say a crack size in between those experimentally measured—then draw the curve and look for the corresponding P-v intercept.

This has been done and is shown in Fig. 7. Here, a certain crack size has been assumed, and on this basis, a C&C curve has been constructed for that crack size. The crack sizes have been calculated from the known values as the average of the sizes of two neighboring points (16–22), and therefore the curves have been labeled as j/k. Thus, "17/18" means a crack size calculated as $0.5(a_{17} + a_{18})$.

The full result of this method is presented in Fig. 8, in the form of crack

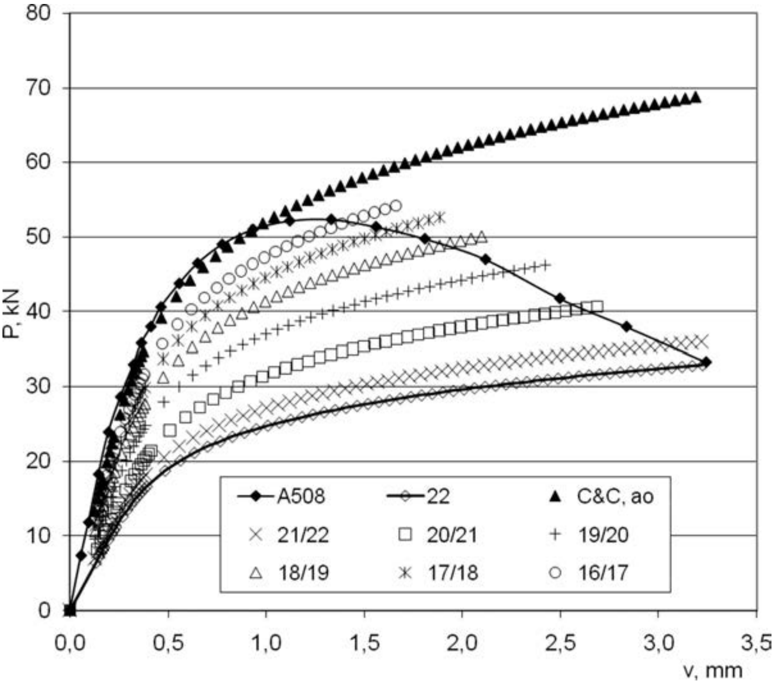

FIG. 7—*Experimental P-v curve for 1T-C(T) A 508 specimen, and seven intersecting C&C curves of known crack sizes of values j/k.*

size against total displacement. Here, three sets of data are included: the × symbols are the experimental values; the open symbols (○) represent the solutions obtained by the intercept method using the original known crack sizes (Fig. 6), and the triangle symbols (▲) identify the solutions for the assumed crack sizes of values j/k (Fig. 7). The results shown in Fig. 8 indicate that this "intercept method" works well in predicting crack sizes at any point on the curve beyond maximum force.

Figure 9, on the other hand, shows the crack growth law of Eq 3 plotted for the points obtained with the method (both data points j and j/k of Figs. 6 and 7, represented by open symbols), together with the original experimental points. The power law fit for the method gives $l_0 = 50.12$ and $l_1 = 1.934$, and has to be compared to the values $l_0 = 61.81$ and $l_1 = 2.001$ of Fig. 4.

The rationale behind this method will be explained presently, by using as an example curve "18" from Fig. 6: the intercept between the *a variable* curve (the experimental A 508 curve) and the *a constant* curve (curve 18) will be analyzed in order to assure that the method has a solid analytical foundation. Let us recall first that curve 18 has been constructed with the C&C Formats by knowing the crack size in advance; that is, curve 18, for this material, size and geometry, is a unique function of that crack size. Furthermore, should elastic unloading take place at any point along curve 18, the slope of the line would be the same as the initial slope, characteristic of the crack size.

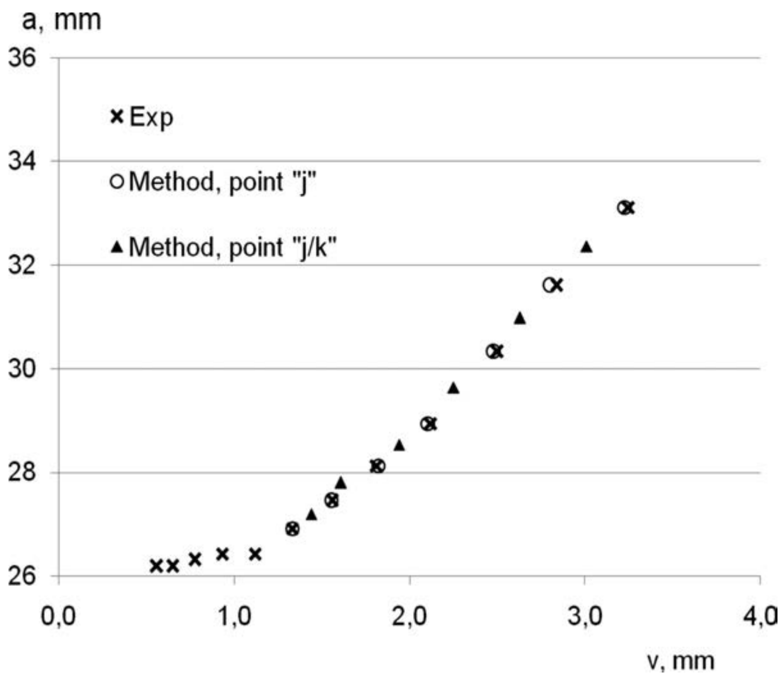

FIG. 8—*Plot of crack size, a, versus total displacement, v, for A 508.*

Figure 10 shows the two curves, intersecting each other at a point close to a force value of 50 kN. The corresponding total displacement has been labeled as v^*. For the experimental curve, the following relation holds:

$$v^* = v_{x,\mathrm{el}} + v_{x,\mathrm{pl}}, \tag{10}$$

where x stands for the fact that the crack size is an unknown—to be determined—at that point. For curve 18, on the other hand, the displacement is

$$v^* = v_{18,\mathrm{el}} + v_{18,\mathrm{pl}}. \tag{11}$$

The two displacements must be equal at the intersection point, so

$$v_{x,\mathrm{el}} + v_{x,\mathrm{pl}} = v_{18,\mathrm{el}} + v_{18,\mathrm{pl}}. \tag{12}$$

Now, at the intersection point, curve 18 has an elastic displacement given by the force at that point (50 kN), and by the elastic compliance corresponding to crack size 18. On the other hand, the A 508 curve, of which we know that at the intersection point has a crack size of value 18, must have an elastic displacement equal to the elastic displacement of the C&C curve.

In fact, if crack size 18 has been experimentally measured on the A 508 specimen by the unloading compliance method, then the elastic slope of the *a constant* curve 18 should be the same as the slope of the unloading line. Thus, if $v_{x,\mathrm{el}} = v_{18,\mathrm{el}}$, then by Eq 12,

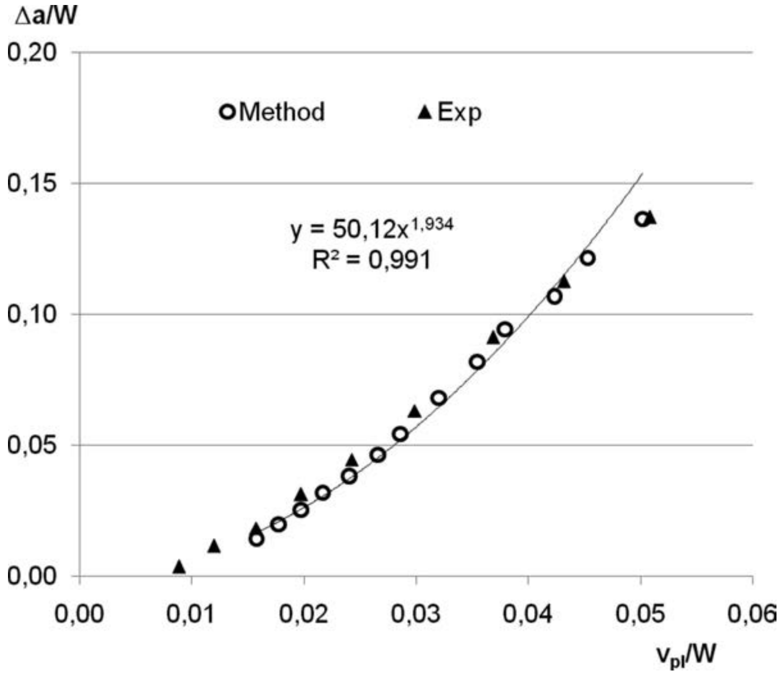

FIG. 9—*The crack growth law for the A 508 data of Fig. 8.*

$$v_{x,\mathrm{pl}} = v_{18,\mathrm{pl}}. \tag{13}$$

Equation 13 indicates that the plastic displacements at the intersection point are equal, no matter how the two curves arrive to that point: the experimental curve, following the "loading" path, and the *a constant* curve, following the deformation path, without crack growth. This is quite significant for the experimental curve because the path followed to reach point 18 is the result of a competition between a strain hardening process and a stable crack extension process. The balance between the two processes leads to instability, giving rise to the maximum force, to be followed then by a stable increase in crack size.

Applications of the Alternative Crack Growth Model

Two examples of *P*-*v* data included in Pehrson and Landes work [1], and one generated at our facilities were used to test the approach. The first is labeled as SPEC4 and has known stable crack extension behavior. The second specimen is designated as specimen SX 18.4.13, and it only has initial and final values of crack size available. The third specimen was fabricated from a cast martensitic stainless steel impeller of nominal composition 13 % Cr–4 % Ni, and is designated as MS 13-4.

Figure 11(*a*) (left side) shows the complete experimental *P*-*v* curve for SPEC4 with nine elastic unloading-reloading cycles performed to determine

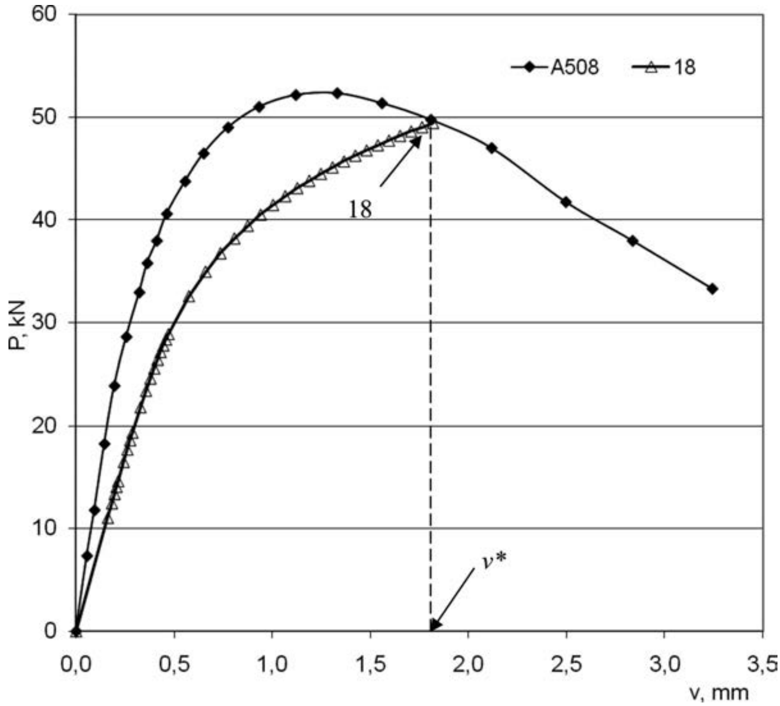

FIG. 10—*Experimental P-v curve for the A 508 specimen, and one C&C "a constant" intersecting curve that has crack size 18.*

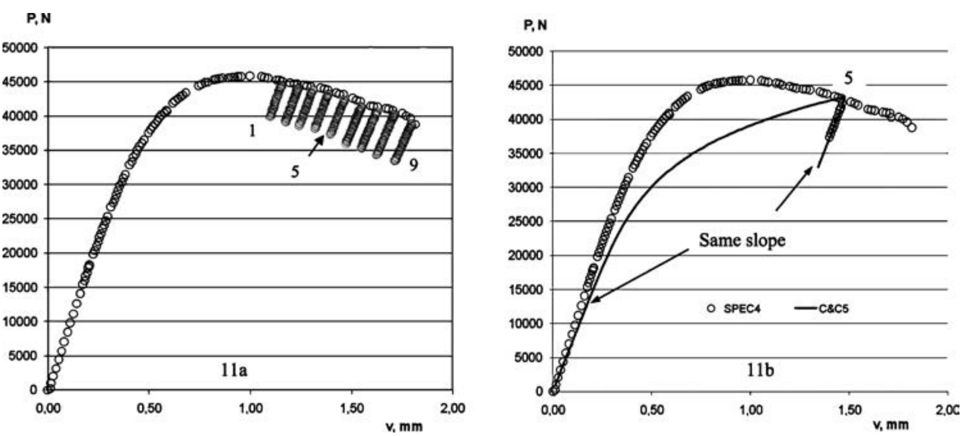

FIG. 11—*Original experimental P-v curve for SPEC4, with nine unloading-reloading cycles (left) and one intersecting C&C curve for cycle No. 5 (right).*

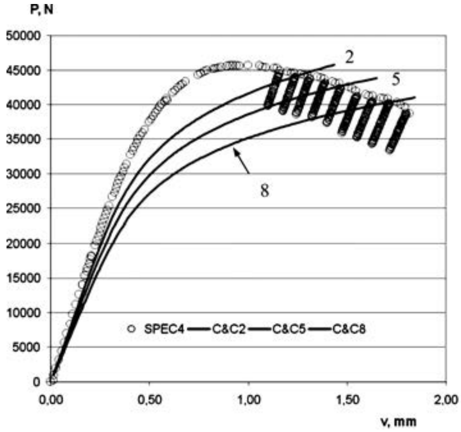

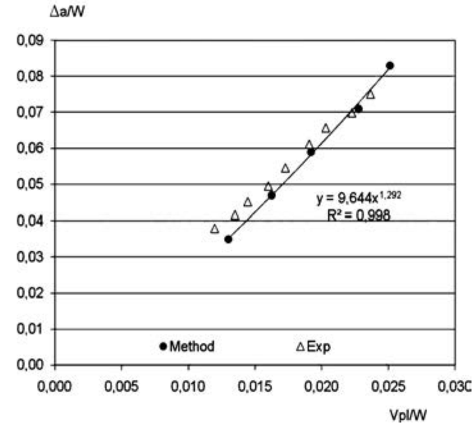

FIG. 12—*The intercept method applied to SPEC4: Experimental and intersecting C&C curves for cycles 2, 5, and 8 (left) and the crack growth law (right).*

crack size at the locations labeled 1,…,5,…,9. Figure 11(*b*) (right side) shows the same experimental curve but stripped of all cycles save cycle No. 5. A C&C curve with crack size corresponding to that given by the inverse compliance solution of cycle No. 5, has also been drawn, including the unloading line, whose slope is the same as the initial elastic slope of the C&C curve.

This fact gives further support to the notion expressed earlier, in relation with the equality of the elastic displacements of both the C&C curve and the experimental curve at the intersection point. Thus, the plastic displacements of both the C&C and the experimental curve at the point of intersection are also equal, so the intercept method presented here is able to produce sound values of stable crack extension as a function of displacement.

Figure 12(*a*) (left side) shows a recreation of Fig. 11(*a*), with the C&C curves for unloading cycles 2, 5, and 8. Figure 12(*b*) (right side), on the other hand, shows the comparison of the nine experimental values (△) with data obtained with the method (●). The correspondence between both sets of data points is good; however, the crack growth law behavior of this specimen ($l_1 \approx 1.3$) deviates somewhat from the previous values of A 508 and A 533B, i.e., $l_1 \approx 2.0$.

So far, only examples of fracture tests which include crack extension data have been shown. Now, the method will be applied to P-v data for 1T-$C(T)$ specimens for which no crack size measurements are available, save for the initial and final crack sizes, both measured after the tests. The first is SX-18.4.13 [1], whereas the second is MS 13-4.

Figure 13 shows the experimental curve (full line, labeled 18413) and the various C&C curves (left): the *a constant* curves for both the initial crack size, a_o (○) and final crack size, a_f (•); five other similarly generated curves for crack sizes in between a_o and a_f ("3" to "7"), and the C&C curve (×) that should replicate the experimental curve with the aid of the crack growth law shown on the right side of Fig. 13.

Two significant issues should be noted in Fig. 13: first, the crack growth law

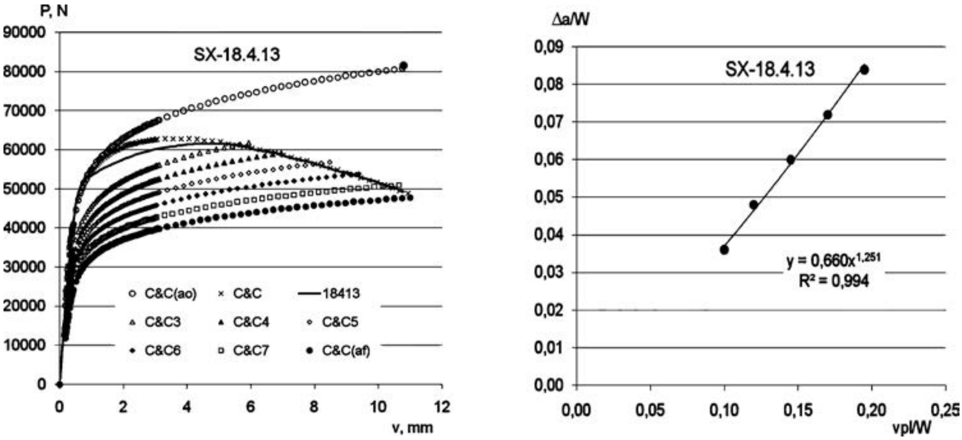

FIG. 13—*The intercept method applied to SX-18.4.13: Experimental and intersecting C&C curves (left) and the crack growth law (right).*

has a value of l_1 of 1.25. This means that the rate of change of plastic displacement with crack extension is almost linear, and the *P*-*v* curve ought to reflect that fact. Second, the C&C curve derived from the analysis only matches the experimental curve for displacements that are larger than the critical displacement. This is probably so because the original specimen test data show an subdued yield point at $v \approx 1$ mm, a fact the C&C model is unable to reproduce.

Figure 14, on the other hand, illustrates the experimental behavior of the 13-4 martensitic stainless steel 1*T*-*C*(*T*) specimen, shown by the continuous, jagged line (left side). Again, two *a constant* curves have been drawn for both the initial crack size a_o (△) and final crack size a_f (▲). The five C&C curves

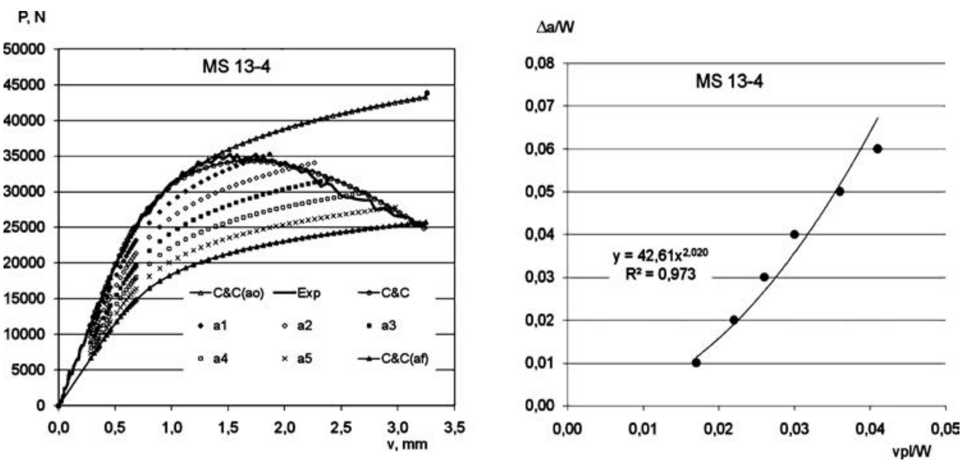

FIG. 14—*The intercept method applied to MS13-4: Experimental and intersecting C&C curves (left) and the crack growth law (right).*

TABLE 1—*Values of D and n for all specimens.*

Specimen	D, MPa	n
A 508	370	5.60
A 533B	350	5.65
SPEC4	350	6.20
SX 18.4.13	305	7.75
MS 14-3	560	6.90

constructed with the crack sizes a_1–a_5 have produced the crack extension values used for drawing the curve shown on the right side, in which $l_1 \approx 2$. The C&C curve generated with the *a variable* values obtained with the crack growth law (○) matches fairly well with the experimental curve of the 13-4 specimen.

The alternative method used to determine the stable crack extension values, introduced in this work, and described above with the aid of Figs. 5–14, can be summarized by means of the following steps:

(1) Characterize the P_n-v_n behavior of the specimen-material, obtaining the values of D and n of the common format equation. Table 1 shows the values of D and n for all specimens reported in this work.
(2) Construct two bordering curves with the C&C formats (elastic + plastic), one with the initial ligament size (known), and the other with the final ligament size (also known).
(3) Define a discrete number of ligament sizes in between the two known values, and construct C&C curves with constant ligament (the *a constant* curves), which intersect the experimental curve at various points.
(4) The crack size of the experimental curve at each of the intersection points will be equal to the crack size of the corresponding *a constant* (constant ligament) curve.
(5) The intersection point defines not only the crack size, but the force and total displacement along the experimental curve as well.
(6) A discrete set of values of crack extension Δa and plastic displacement v_{pl}, obtained with the method, will give rise to the crack growth law, Eq 3. Once the parameters l_0 and l_1 are known, a more complete set of data may be surmised in order to generate Δa and J values for the construction of the full J-R curve.

In order to show the applicability of the intercept method for J-R curve construction, J-Δa data have been calculated for the A 508 specimen, on the basis of the procedure outlined above. A similar J-R curve comparison for this same specimen was included earlier in the DZL crack growth law paper [5], in which the crack extension values were estimated by using the final point of the test as the calibration point, the CG law parameters being those shown in Fig. 4 (i.e., $l_0 = 61.81$ and $l_1 = 2.001$). Figure 15 shows the experimental J-R curve for the A 508 specimen, marked with open symbols (O), and calculated with the E 1820 methodology using the originally measured crack sizes. On the same plot, the J-Δa data points obtained with the CG law solution based on the intercept method, are shown by dark triangles (▲), and appear to follow closely the ex-

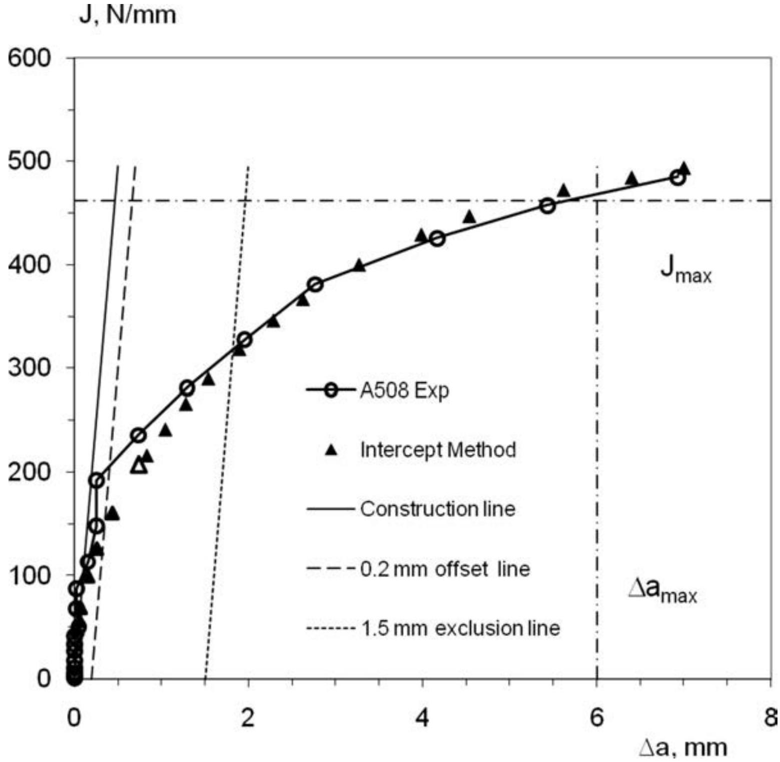

FIG. 15—*Experimental and intercept method J-Δa curves for the A 508 specimen.*

perimental points. These data points were calculated with the crack growth law parameters $l_0 = 50.12$ and $l_1 = 1.934$, as given by Fig. 9.

Figure 15 shows the typical E 1820 plot structure, including the boundaries set by the lines J_{max} (462 N/mm) and Δa_{max} (6.0 mm) for the A 508 specimen. It also includes the construction line, the 0.2 mm offset line, and the 1.5 mm exclusion line, the 0.15 mm exclusion line being left out for clarity purposes. The points labeled "intercept method" comprise actually two sets of data: for $J > J_{Q\,exp} \approx 210$ N/mm (given by the intercept between the experimental curve and the 0.2 mm offset line), the points correspond to those of Fig. 9 on a one-to-one basis. The point at $J = J_{Q\,exp} \approx 210$ N/mm, has been outlined by an open triangle (△) to indicate that it is the point at which $P \approx P_{max}$. Finally, all points for which $J < J_{Q\,exp}$ have been estimated with the crack growth law, following the procedure explained at length in Ref. [5].

It was pointed out above that the *J-R* curve constructed with the crack extension data estimated by the intercept method is similar to the experimental curve. There is one marked difference, however, at the experimental point for which $J \approx 190$ N/mm. In fact, this point has a value of crack extension $\Delta a \approx 0.2$ mm, there being another data point at the same Δa, but with a smaller value of $J \approx 150$ N/mm. This makes the experimental *J-R* curve to show a "cusp" where there should be a smooth curvature. If one interpolates the value of crack extension for the experimental point at $J \approx 190$ N/mm, giving $\Delta a \approx 0.5$ mm, then $J_{Q\,\mathrm{exp}} \approx 180$ N/mm. The data points that make up the intercept method *J-R* curve, on the other hand, are disposed in a fully regular fashion, giving a conservative value of $J_Q \approx 160$ N/mm.

Concluding Remarks

A new method of construction of the *J-R* curve was proposed by DZL [5] that made use of the notion of a crack growth law relating stable crack extension, Δa, normalized by W, to the normalized plastic displacement, v_{pl}/W. The crack growth law was proposed in the form of a power-law type relation with two parameters: a coefficient, l_0, and an exponent, l_1.

Of these two parameters in the original DZL proposal, the coefficient l_0 was substituted on the basis of one known calibration point (highlighted in Fig. 1), which is the final point of the test: total displacement, v_f, and force, P_f. Thus, the crack growth law model had only one adjustable parameter, namely the exponent, l_1. The value of l_1 that seemed to accommodate best the experimental values of force and displacement (i.e., to best reproduce the experimental *P-v* curve) was 2.0. This value was used in a couple of examples of *P-v* data of 1*T*-*C*(*T*) specimens of A 508 and A 533B steels with known values of crack extension along the test, giving a very good fit between the experimental *P-v* curve and the C&C *a variable* curve.

It was then proposed that an analytical treatment of both the *P-v* curve and the resulting J-Δa curve would be possible even under circumstances in which the sole inputs are the *P-v* curve and the initial and final crack size values, without crack extension values measured concurrently with the fracture test. In order to accomplish this however, the concept of the crack growth law needed a more solid analytical foundation and empirical proof of its significance. This has been the core subject of this work.

Based upon this crack growth law concept, and on the common and the concise format equations of Donoso and Landes [2–4], an alternative way of generating the amount of stable crack growth has been introduced. The method, called the "intercept" method, has shown here to produce reasonable crack extension values when using *P-v-a* data in which crack sizes at various *P-v* points along the test were experimentally measured by the unloading compliance method.

The intercept method developed in this work is based upon the fact that the C&C format equations are able to generate *a constant P-v* curves, of given known crack sizes of values in between the initial crack size, a_o, and the physically measured final crack size, a_f. The intercept of these blunt-notch *P-v* curves with the experimental curve will give a value of total displacement and force at which the experimental curve will have a crack size equal to that of the corresponding C&C curve. From this intercept, the value of the plastic displacement at each point may be calculated, and thus, by using the C&C approach, a full set of crack extension values may now be available.

The method, which allows for the evaluation of the actual crack size at any value of force or displacement along the experimental *P-v* curve, was extended here to some examples of 1*T-C*(*T*) fracture test specimens for which there are no crack extension measurements available, save for the initial and final crack sizes. The results obtained are quite encouraging, and suggest more work along these lines.

Furthermore, in order to show the applicability of the intercept method for *J-R* curve construction, the J-Δa data points calculated with the crack growth law solution based on the intercept method for A 508, were plotted together with the experimental points for this specimen. The values estimated with the proposed method follow quite closely the experimentally observed behavior.

The crack growth law, of which it might be said that it is a convenient and useful tool, may not always have the exponent $l_1 = 2.0$. Some of the examples shown along this paper have values of l_1 close to unity, i.e., the rate of generation of plastic displacement with crack extension is almost linear. Nonetheless, the use of a crack growth law, regardless of the value of l_1, should prove to be of great help obtaining crack size values where there are none available. Thus, a *J-R* curve construction may now be derived from *P-v* data that only has as a complement the initial and final crack sizes.

Acknowledgments

The financial support of FONDECYT Project No. 1060415, FONDECYT Visiting Grant No. 7070100 for Professor J. D. Landes, and Project No. USM/DGIP 21.06.21 are gratefully acknowledged.

References

[1] Pehrson, B. P. and Landes, J. D., "A Direct Estimate of JIc From the Load Versus the Load-Line Displacement Record," *Fatigue Fract. Eng. Mater. Struct.*, Vol. 30, No.2, 2007, pp. 73–86.

[2] Donoso, J. R. and y Landes, J. D., "A Unifying Principle for Evaluating Fracture Toughness in the Elastic and Plastic Regimes with Two-Dimensional Fracture Specimens," *Fatigue and Fracture Mechanics, 30th Volume*, Paris, P. C., and Jerina, K. L., Eds., ASTM STP 1360, American Society for Testing and Materials, West Conshohocken, PA, 2000, pp. 34–50.

[3] Donoso, J. R. and y Landes, J. D., "Common Format for Developing Calibration Curves in Elastic-Plastic Fracture Mechanics," *Eng. Fract. Mech.*, Vol. 47, No. 5, 1994, pp. 619–628.

[4] Donoso, J. R. and y Landes, J. D., "Advantages of the Concise K and Compliance Formats in Fracture Mechanics Calculations," *Fatigue and Fracture Mechanics, 32nd Volume*, Chona, R., Ed., ASTM STP 1406, American Society for Testing and Materials, West Conshohocken, PA, 2001, pp. 261–278.

[5] Donoso, J. R., Zahr, J., and Landes, J. D., "Construction of J-R Curves Using the Common and Concise Formats," *Fatigue and Fracture Mechanics, 34th Volume*, Daniewicz, S. R., Newman, J. C., and Schwalbe, K.-H., Eds., ASTM STP 1461, ASTM International, West Conshohocken, PA, 2005, pp. 323–339.

[6] Donoso, J. R. and Landes, J. D., "An Instability Analysis for a Crack Growth Situ-

ation Based on the Common Format," ECF15, 15th European Conference on Fracture, Stockholm 2004.

[7] Ernst, H. A., Paris, P. C., and Landes, J. D., "Estimations on J-Integral and Tearing Modulus T From a Single Specimen Test Record," *Fracture Mechanics; Thirteenth Conference 743*, Roberts, R., Ed., ASTM STP, ASTM International, West Conshohocken, PA, 1981, pp. 476–502.

[8] Donoso, J. R. and y Landes, J. D., "The Role of Constraint on the Calibration Functions for the Prediction of Ductile Fracture Behavior in Structural Components," *Int. J. Fract.*, Vol. 63, 1993, pp. 275–285.

[9] Joyce, J. A. and Link, R. E., "Effects of Tensile Loading on Upper Shelf Fracture Toughness," Report NUREG/CR-6051, US Nuclear Regulatory Commission, Washington, DC, March 1994.

ASTM Special Technical Publication, Vol. 5, No. 3
Paper ID JAI101467
Available online at www.astm.org

Enrico Lucon[1] *and Marc Scibetta*[1]

Assessing the Loading Rate for a Fracture Toughness Test in the Ductile-to-Brittle Transition Region

ABSTRACT: For fracture toughness tests in the ductile-to-brittle transition region, ASTM E1921-05 requires specimens to be loaded using a loading rate dK/dt between 0.1 and 2 $MPa\sqrt{m}/s$ during the initial elastic portion. It has been proposed that the standard allow testing at higher loading rates, including precracked Charpy specimens tested on an instrumented pendulum machine (impact toughness tests). The revised standard would require test results (K_{Jc} or T_o) to be reported along with the relevant loading rate, and should therefore provide guidance on how to assess the value of dK/dt in a relatively simple but reliable manner. Various options for measuring the loading rate have been investigated in this paper for several fracture toughness tests performed at different loading rates (quasi-static, dynamic, and impact). For each loading rate, three different toughness levels have been considered: low, medium, and high. Three considerably different materials have been selected: two RPV steels (JRQ, JSPS) and a ferritic/martensitic 9 % chromium steel (EUROFER97). It is found that the preferable option is given by the ratio between K_{Jc} and time at the onset of cleavage, whereas the elastic value K_{el}/t_{el} or the average dK/dt can be used when partial unloadings are performed.

KEYWORDS: ductile-to-brittle transition region, loading rate, impact toughness tests

Manuscript received October 3, 2007; accepted for publication February 18, 2008; published online March 2008.

[1] SCK•CEN, Institute for Nuclear Material Science, Boeretang 200, B-2400 Mol, Belgium.

Citation: Lucon, E. and Scibetta, M., "Assessing the Loading Rate for a Fracture Toughness Test in the Ductile-to-Brittle Transition Region," *J. ASTM Intl.*, Vol. 5, No. 3. DOI10.1520/JAI101467. Available online at www.astm.org. Also included in JAI Special Issue STP 1508, *Fatigue and Fracture Mechanics: 36th Volume,* R. W. Neu, K. R. W. Wallin, and S. R. Thompson, guest editors, ASTM International, West Conshohocken, PA, 2009, pp. 54-65.

TABLE 1—*Rate estimation for SE(B) and C(T) specimens (Table 3 from ASTM E1921-05).*

SE(B) Specimen Rate Estimation			C(T) Specimen Rate Estimation		
a/W	$\frac{t_M \dot{K}}{\sigma_Y \sqrt{W}}$	$\frac{E\dot{\Delta}_{LL}}{\frac{dK}{dt}\sqrt{W}}$	a/W	$\frac{t_M \dot{K}}{\sigma_Y \sqrt{W}}$	$\frac{E\dot{\Delta}_{LL}}{\frac{dK}{dt}\sqrt{W}}$
0.45	0.346	5.064	0.45	0.412	3.475
0.50	0.333	5.263	0.50	0.386	3.829
0.55	0.318	5.522	0.55	0.361	4.212
0.60	0.302	5.851	0.60	0.336	4.635
0.65	0.283	6.267	0.65	0.312	5.118
0.70	0.263	6.798	0.70	0.287	5.696

Introduction

For fracture toughness tests in the ductile-to-brittle transition region, the current ASTM Standard E1921-05 requires specimens to be loaded using a loading rate dK/dt between 0.1 and 2 MPa$\sqrt{\text{m}}$/s during the initial elastic portion. A table is also provided, which allows estimating the testing machine loading rate associated with this allowable range, both in terms of time to control load t_M or specimen load-line displacement rate $\dot{\Delta}_{LL}$. It has been proposed that the standard allow testing at higher loading rates, including precracked Charpy specimens tested with an instrumented pendulum machine (impact toughness tests). The revised version of ASTM E1921 would require test results (K_{Jc} or T_o) to be reported along with the relevant loading rate (dK/dt), and should therefore provide guidance on how to assess the value of dK/dt in a relatively simple but reliable manner.

Possible Options for Evaluating dK/dt in a Fracture Toughness Test

The loading rate is not constant during a fracture toughness test, particularly once plasticity is evident in the force/displacement record. However, for practical purposes it is necessary to specify a single value of dK/dt to be associated to the individual test result and reported with the measured data. This might also be prescribed in a future revision of ASTM E1921 or in the future ISO standard on impact toughness tests. In this paper, the following five options have been investigated.

(a) Average value of dK/dt, calculated using each individual force/time data point in a test up to cleavage or test termination. This option is the most time-consuming from a computational point of view. In practical terms, for the Nth data point, $dK = K_N - K_{N-1}$ and $dt = t_N - t_{N-1}$.

(b) Ratio between stress intensity factor and corresponding time at cleavage or test termination (K_c/t_c). Since K_c is always calculated, the only additional parameter that needs to be evaluated is t_c.

(c) Estimation based on Table 3 of ASTM E1921-05 (reproduced in Table 1), which is intended to help the user choose the appropriate value of load-line displacement rate ($\dot{\Delta}_{LL}$) or t_M (time to control force P_M) corresponding to the required loading rate dK/dt. In Table 1, a is the crack size, W the specimen width, σ_Y the yield strength at the test temperature, $\dot{K}$ or dK/dt the loading rate, and E the Young's modulus. By fitting the values in the third or sixth column as a function of a/W and solving the relationship for dK/dt, the loading rate can be easily calculated since all remaining variables (a, W, E, and load-line displacement rate) are known.

(d) Ratio between stress intensity factor and corresponding time within the linear elastic region of the test record (K_{el}/t_{el}). This option requires only the determination of K_{el} and t_{el} at an arbitrarily chosen point along the linear elastic slope.

(e) Value of loading rate dK/dt at the instant preceding cleavage fracture (or test termination); i.e., if N corresponds to the instant of cleavage, the loading rate to be considered would be $(dK/dt)_{N-1}=(K_{N-1}-K_{N-2})/(t_{N-1}-t_{N-2})$.

Investigations Performed

The study consisted in analyzing data from 27 fracture toughness tests. More specifically, three steels with significantly different characteristics were chosen:

- EUROFER97 (9Cr reduced activation ferritic/martensitic steel, presently considered as the European reference structural material for future fusion reactors) [1];
- JRQ (A533B reactor pressure vessel steel, used by the International Atomic Energy Agency for several Coordinated Research Projects) [2,3];
- JSPS (Japanese RPV steel of A533B type, artificially embrittled by increasing the sulphur content in order to obtain low toughness properties in the unirradiated condition) [3].

Chemical composition and basic mechanical properties are given in Tables 2 and 3 for the three investigated steels.

Three displacement (loading) rate regimes were examined:

- quasi-static (machine crosshead displacement rate 0.2 mm/min; sampling time 1 s; digital precision A/D converter = 24 bit);
- intermediate/dynamic (displacement rate = 150 mm/min; sampling time = 0.2 ms; digital precision A/D converter = 24 bit);
- impact (tests performed on precracked Charpy specimens using an instrumented pendulum with impact velocities in the range 1.2–1.6 m/s; sampling time = 0.5 μs; digital precision A/D converter = 12 bit);

Tests were performed in accordance with ASTM E1921-05 (quasi-static and dynamic rates) and the ESIS TC5 Test Procedure [4] (impact rates). Typical test records for the three loading rates are shown in Fig. 1 (JRQ steel in mid-transition regime, K_{Jc} = 99 to 133 MPa$\sqrt{m}$).

Three different fracture toughness levels were considered (typical examples of test records are shown in Fig. 2 for the lowest loading rate, i.e., 0.2 mm/min):

TABLE 2—*Chemical composition (wt. %, Fe balance) of the steels investigated.*

Steel	C	Ni	Cr	Mo	Cu	Si	S	V	P	Mn	W	Ta
EUROFER97	0.12	0.007	8.99	<0.001	0.022	0.07	—	0.19	<0.005	0.44	1.1	0.14
JRQ	0.18	0.84	0.12	0.51	0.14	0.24	—	0.002	0.017	1.42	—	—
JSPS	0.24	0.43	0.08	0.49	0.19	0.41	0.023	—	0.028	1.52	—	—

TABLE 3—*Room temperature tensile properties (measured in accordance with ASTM E08M) and Master Curve reference temperature (measured from bend-type samples in accordance with ASTM E1921) for the steels investigated.*

Steel	R_{p02}, MPa	R_m, MPa	A, %	RA, %	T_o, °C
EUROFER97	557	670	20	80	−112
JRQ	455	609	20	73	−70
JSPS	461	640	18	59	−5

- lower transition regime (K_{Jc} = 41–88 MPa$\sqrt{m}$);
- mid-transition regime (K_{Jc} = 98–133 MPa$\sqrt{m}$);
- upper transition regime (K_{Jc} = 138–241 MPa$\sqrt{m}$).

For the sake of clarity, the three regions of the ductile-to-brittle transition regime are schematically represented in Fig. 3.

In order to illustrate four of the five investigated approaches, the force/time record for one of the tests (JRQ steel, 0.2 mm/min, K_{Jc} = 174 MPa$\sqrt{m}$) is shown in Figs. 4 and 5 together with the evolution of the loading rate and the stress intensity factor, respectively. Options (a) and (e) are depicted in Fig. 4, while Fig. 5 illustrates options (b) and (d).

As far as option (c) is concerned, the loading rate for a SE(B) specimen can be estimated from the left-hand side of Table 1 using:

$$\frac{dK}{dt} = \frac{E\dot{\Delta}_{LL}}{Y\sqrt{W}} \tag{1}$$

where E is in MPa, $\dot{\Delta}_{LL}$ is in m/s, W is in m, and Y is a function of a/W obtained by fitting a third-order polynomial curve through the values in the third column of Table 1 and is given by:

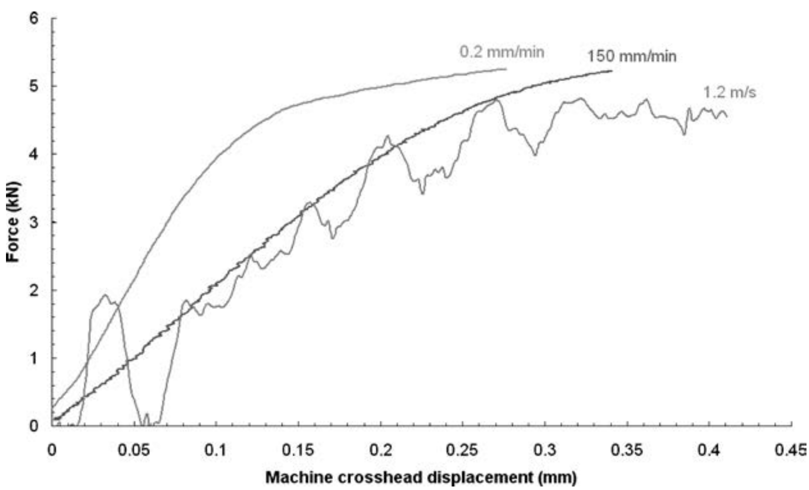

FIG. 1—*Typical test records for three different loading rates (JRQ steel).*

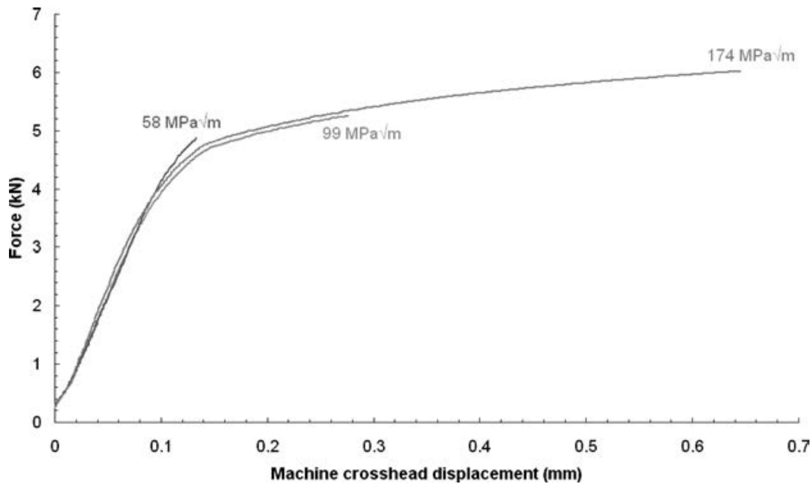

FIG. 2—*Typical test records for the three toughness levels (JRQ steel,* 0.2 mm/min).

$$Y\left(\frac{a}{W}\right) = 24.15\left(\frac{a}{W}\right)^3 - 25.31\left(\frac{a}{W}\right)^2 + 11.72\left(\frac{a}{W}\right) + 2.272 \quad (2)$$

Results Obtained

The values of loading rate calculated using the five options previously listed for the 27 fracture toughness tests considered are presented in Table 4.

As an example, results for tests conducted in the lower transition regime (K_{Jc}=41 to 88 MPa $\sqrt{m}$) are illustrated in more detail using histograms in Fig. 6 (quasi-static loading rates), Fig. 7 (intermediate/dynamic), and Fig. 8 (impact).

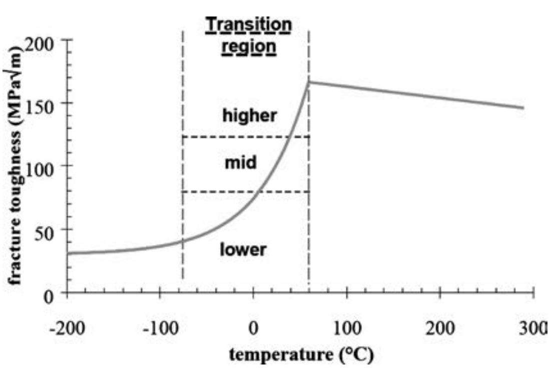

FIG. 3—*Schematic representation of the fracture toughness/temperature curve for a ferritic steel.*

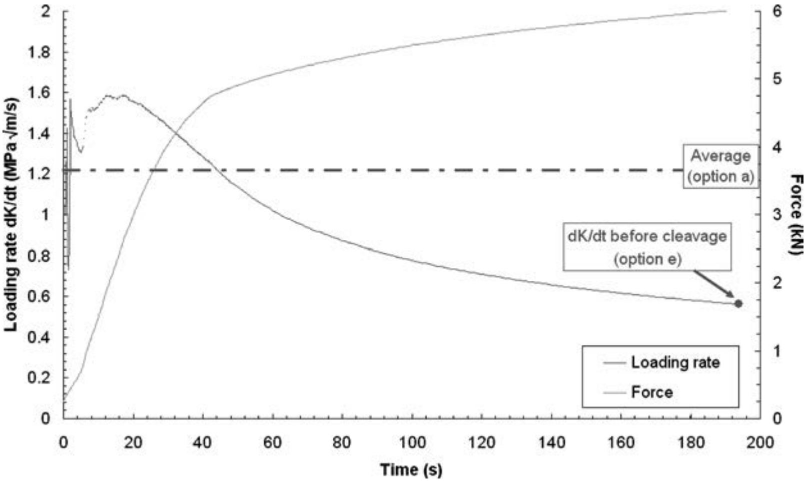

FIG. 4—*Loading rate and test record for a JRQ specimen tested at* 0.2 mm/min. *Options* (*a*) *and* (*e*) *are illustrated.*

Discussion

It is clear, from the investigations performed and also from a merely intuitive standpoint, that the loading rate changes continuously during a fracture toughness test and no "unique" value of dK/dt can be defined. However, the results obtained show that options (a) and (b) (and (d) as well, but only in the lower transition regime) provide substantially equivalent results and appear sufficiently representative of the effective loading rate for practical purposes.

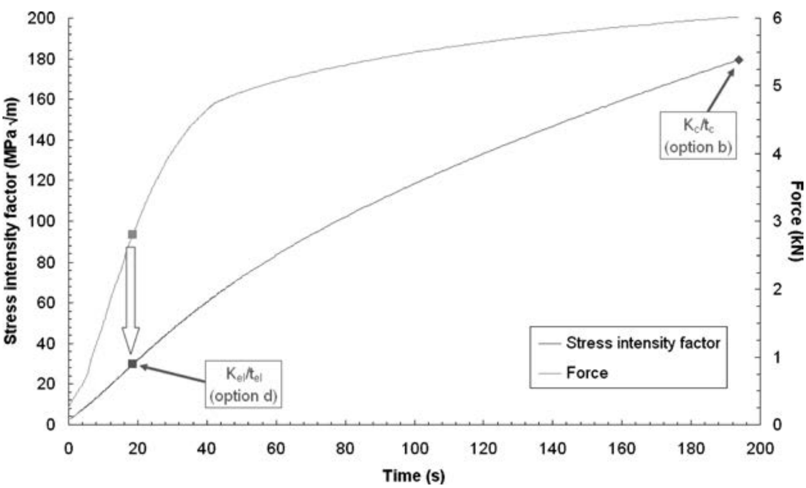

FIG. 5—*Stress intensity factor and test record for a JRQ specimen tested at* 0.2 mm/min. *Options* (*b*) *and* (*d*) *are illustrated.*

TABLE 4—*Values of loading rate calculated using the 5 different options.*

			Loading rate, MPa$\sqrt{}$m/s				
Material	Test speed	K_{jc} (MPa$\sqrt{}$m)	Average	K_{jc}/t_c	E1921-05	K_{el}/t_{el}	dK/dt(cl)
EUROFER97	0.2 mm/min	47	**0.66**	0.72	1.38	0.69	0.79
		106	**0.72**	0.74	1.36	0.69	0.65
		184	**0.69**	0.69	1.33	0.67	0.41
JSPS		53	**1.14**	1.23	1.23	1.27	1.07
		102	**1.09**	1.07	1.26	1.47	0.71
		201	**0.80**	0.73	1.32	1.64	0.39
JRQ		58	**1.34**	1.42	1.39	1.43	1.39
		100	**1.36**	1.25	1.38	1.55	1.36
		174	**1.22**	0.93	1.38	1.60	0.56
EUROFER97	150 mm/min	54	**635**	654	974	634	1615
		99	**742**	752	972	638	1507
		192	**647**	654	985	694	426
JSPS		63	**751**	761	974	673	1728
		98	**760**	777	969	683	−83
		146	**587**	595	950	651	−16
JRQ		60	**674**	693	998	643	−181
		99	**753**	764	967	673	48
		155	**621**	630	932	708	834
EUROFER97	1.6 m/s	41	$\mathbf{8.31 \times 10^5}$	8.40×10^5	6.55×10^5	8.42×10^5	5.54×10^5
		98	$\mathbf{6.78 \times 10^5}$	6.04×10^5	6.51×10^5	6.47×10^5	2.70×10^5
		188	$\mathbf{6.25 \times 10^5}$	5.04×10^5	6.35×10^5	6.34×10^5	1.40×10^5

TABLE 4— (*Continued.*)

Material	Test speed	K_{jc} (MPa$\sqrt{}$m)	Loading rate, MPa$\sqrt{}$m/s				
			Average	K_{jc}/t_c	E1921-05	K_{el}/t_{el}	dK/dt(cl)
JSPS	1.5 m/s	75	$\mathbf{6.40\times10^5}$	6.47×10^5	5.77×10^5	6.38×10^5	9.97×10^5
		100	$\mathbf{5.53\times10^5}$	5.56×10^5	5.79×10^5	6.18×10^5	5.58×10^5
		138	$\mathbf{4.80\times10^5}$	4.82×10^5	5.83×10^5	6.54×10^5	4.29×10^5
JRQ	1.2 m/s	88	$\mathbf{3.90\times10^5}$	3.88×10^5	4.83×10^5	3.86×10^5	6.10×10^5
		133	$\mathbf{3.85\times10^5}$	3.85×10^5	4.75×10^5	4.38×10^5	2.51×10^4
		188	$\mathbf{2.90\times10^5}$	2.90×10^5	4.74×10^5	4.30×10^5	6.15×10^4

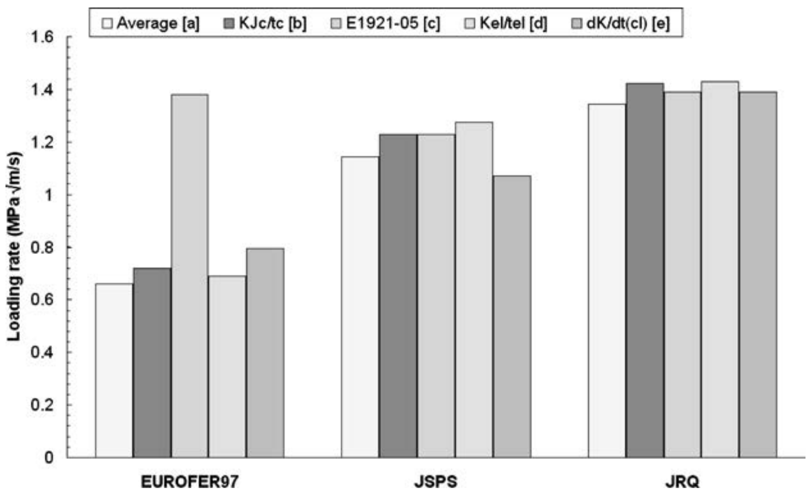

FIG. 6—*Comparison between different approaches for evaluating the loading rate under quasi-static conditions for tests conducted in the lower transition regime.*

In particular, K_c/t_c (option b) offers a straightforward and convenient way to estimate the overall loading rate in a fracture toughness test and, with respect to the average value of dK/dt (which can significantly vary during the test, see Figs. 4 and 9), it offers the advantage of being calculated in relation to the actual fracture event. Moreover, a similar approach is suggested by both ASTM E399-06 (Annex A10) and ASTM E1820-06 (Annex A13). However, one notable exception are tests where partial unloadings are performed in order to evaluate

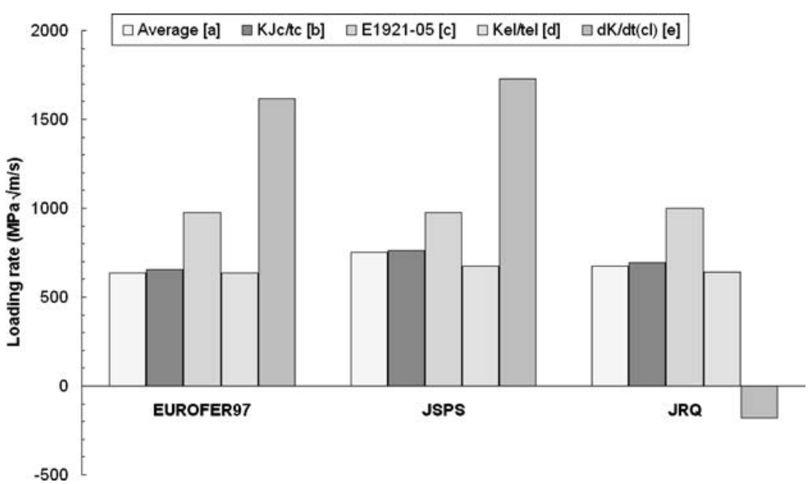

FIG. 7—*Comparison between different approaches for evaluating the loading rate under dynamic/intermediate conditions for tests conducted in the lower transition regime.*

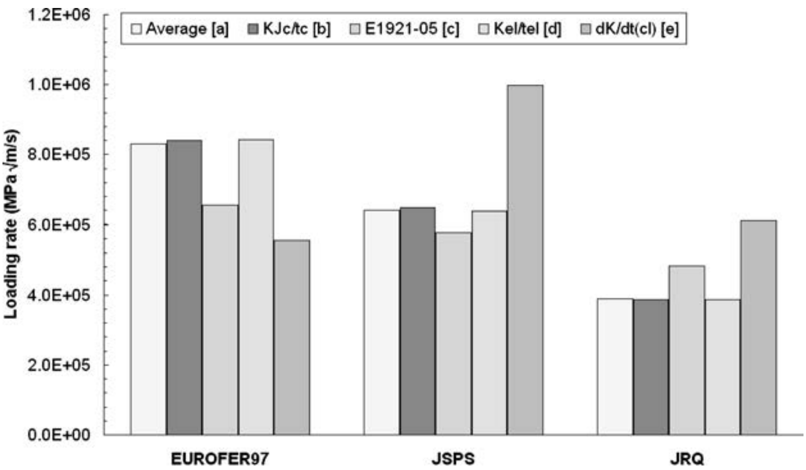

FIG. 8—*Comparison between different approaches for evaluating the loading rate under impact conditions for tests conducted in the lower transition regime.*

the current crack size; in this case, the time spent during the partial unloadings should be subtracted from the time to cleavage (t_c) used to calculate the loading rate. From a practical point of view, it might be advisable to use for such tests one of the other two approaches; i.e., average dK/dt (option a) or K_{el}/t_{el} (option d).

The two approaches that clearly emerge from our investigation as unsatisfactory and therefore should not be recommended are:

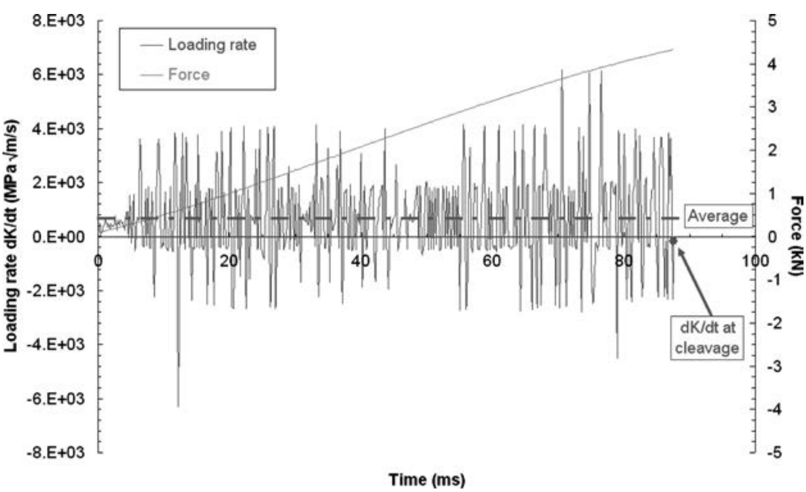

FIG. 9—*Loading rate and test record for a dynamic test* (150 mm/min) *on the JRQ steel.*

- the use of Table 3 from ASTM E1921-05 (option c), which often overestimates the average loading rate of the test, and
- the value of dK/dt just before cleavage (option e), which can produce erratic or even negative results since the actual loading rate in some cases oscillates around its mean value, particularly for higher test velocities (an example in Fig. 9).

Conclusions

- Based on the investigations performed, the ratio between stress intensity factor and time at cleavage (or test termination), i.e., K_c/t_c, can be used to effectively estimate the average loading rate dK/dt in fracture toughness tests, since:
  (a) it is sufficiently close to the average loading rate of the test; and
  (b) it requires a minimum of additional computation (i.e., only the determination of the time at cleavage t_c).
- However, in case partial unloadings are performed during the test (for instance, during the linear elastic portion), K_c/t_c should not be used and other options (average dK/dt excluding the unloading periods or K_{el}/t_{el} evaluated before the first unloading) should be chosen.
- The use of Table 3 from ASTM E1921-05 can grossly overestimate the average loading rate and is therefore not recommended. The reasons for this poor performance are not clear.
- Since the actual loading rate in a test tends to fluctuate around the average value, using dK/dt just before cleavage can lead to erratic results, including (albeit only in the case of dynamic tests) negative values that have no physical meaning.

The results obtained do not appear to depend on material type or loading rate.

Acknowledgments

The collaboration of the technical staff of the Institute of Nuclear Material Science of SCK·CEN is gratefully acknowledged.

This work is partially sponsored by Electrabel/Tractebel Engineering, whose support is kindly appreciated.

References

[1] van der Schaaf, B. et al., "The Development of EUROFER Reduced Activation Steel," *Fusion Eng. Des.*, Vol. 69, 2003, pp. 197–203.

[2] *Reference Manual on the IAEA JRQ Correlation Monitor Steel for Irradiation Damage Studies*, IAEA, Vienna, Austria, 2001, IAEA-TECDOC-1230, available at http://www-pub.iaea.org/MTCD/publications/PDF/te_1230_prn.pdf.

[3] Lucon, E., Scibetta, M., and van Walle, E., "Assessment of the Master Curve Approach on Three Reactor Pressure Vessel Steels," *Int. J. Fract.*, Vol. 119, 2003, pp.161–178.

[4] ESIS TC5, "Proposed Standard Methods for Instrumented Pre-Cracked Charpy Impact Testing of Steels and Other Metallic Materials," European Structural Integrity Society, Draft 25.4, December 2005.

ASTM Special Technical Publication, Vol. 5, No. 5
Paper ID JAI101532
Available online at www.astm.org

Xian-Kui Zhu,[1] *Brian N. Leis,*[1] *and James A. Joyce*[2]

Experimental Estimation of *J-R* Curves from Load-CMOD Record for SE(B) Specimens

ABSTRACT: Fracture resistance of ductile materials is often characterized by a *J-R* curve, and measured using the fracture toughness testing standard ASTM E1820 (Standard Test Method for Measurement of Fracture Toughness). The recommended elastic unloading compliance method or resistance curve test method requires simultaneous measurements of applied load (*P*), load-line displacement (LLD), and crack-mouth opening displacement (CMOD) from a single test for the single-edge notched bend [SE(B)] specimen. The *P*-CMOD record is used to determine crack extension, and the *P*-LLD record in conjunction with the crack extension is used to calculate the *J*-integral. However, it is well known that while highly accurate CMOD measurements can be made, the measurement of LLD is less accurate and more difficult because of transducer mounting difficulties, specimen load point indentions and load train deflections, or a combination thereof. Extensive finite element analyses showed that the LLD-based *J* equation may give inaccurate results for a shallow-cracked SE(B) specimen because its geometry factor η may depend on the strain hardening exponent. In contrast for the same geometry, the CMOD-based η factor is insensitive to the hardening exponent, and thus a CMOD-based *J* equation could be more accurate to be used in the determination of *J-R* curves. Based on the energy principle, this paper proposes a CMOD-based *J* equation for a growing crack using an incremental function similar to the present ASTM E1820-06 formulation that

Manuscript received November 7, 2007; accepted for publication March 28, 2008; published online May 2008.

[1] Senior Research Scientist and Senior Research Leader, respectively, Battelle Memorial Institute, 505 King Avenue, Columbus, Ohio 43201, e-mail: zhux@battelle.org
[2] Professor,Mechanical Engineering Department, U.S. Naval Academy, 590 Holloway Road, Annapolis, Maryland 21402.

Citation: Zhu, X.-K., Leis, B. N. and Joyce, J. A., "Experimental Estimation of *J-R* Curves from Load-CMOD Record for SE(B) Specimens," *J. ASTM Intl.*, Vol. 5, No. 5. DOI10.1520/JAI101532. Available online at www.astm.org. Also included in JAI Special Issue STP 1508, *Fatigue and Fracture Mechanics* (*36th ASTM National Symposium on Fatigue and Fracture Mechanics*), R. W. Neu, K. R. W. Wallin and S. R. Thompson, guest editors, ASTM International, West Conshohocken, PA, 2008, pp. 66-15.

is applicable to the J calculations for a *J-R* curve testing. The proposed CMOD-based J formulation contains two geometry factors, i.e., CMOD-based η and γ, and can consider the crack growth correction. The solutions of four geometry factors are presented for the SE(B) specimens with a wide range of crack length. The proposed formulation is then applied to determine *J-R* curves for HY80 steel using the load-CMOD record for SE(B) specimens, and the results are compared with those using the traditional LLD-based formulation. The comparison shows close agreement between these two formulations. It is recommended that the proposed formulation be used in ASTM E1820 to determine more accurate *J-R* curves and reduce test costs as well.

KEYWORDS: fracture toughness testing, *J-R* curve, crack extension, load-line displacement (LLD), crack mouth opening displacement (CMOD), SE(B) specimen

Introduction

The J-integral proposed by Rice [1] in the late 1960s symbolizes the birth of elastic-plastic fracture mechanics theory and method. Now the J-integral is used as a principal parameter for characterizing fracture behavior of ductile materials, and the J-based fracture mechanics method has been extensively applied to structural integrity management, flaw assessment, material performance evaluation, and fitness for service analysis for various engineering structures, such as the nuclear pressure vessels and piping, oil and gas pipelines, and high-pressure storage tanks. Originally, the parameter J represents the intensity of crack-tip singularity of HRR field [2,3]. Since the introduction of the multiple-specimen technique by Begley and Landes [4,5] in the early 1970s, the J-integral has become a material parameter because it can be determined experimentally using a variety of specimens. The experimental value of J was then accepted as the fracture toughness of materials at crack initiation in the earliest fracture toughness testing standard ASTM E813 (Standard Test Method for JIC, A Measure of Fracture Toughness).

Significant effort has been devoted in the development of effective fracture testing methods for measuring the material toughness parameter J. To save test costs, in the early 1970s, Rice et al. [6] developed the single specimen technique which allows the calculation of J from a single load-displacement record for different configurations, where the J-integral was expressed as the function of a geometry factor, the remaining ligament and the area under the load-displacement curve for a given specimen. Their expression of J for the single-edge notch bend [SE(B)] specimen with deep cracks under pure bending has been broadly used for bending geometries. Merkle and Corten [7] suggested a modified expression of J to consider the tensile effect on the compact tension [CT] specimen. Sumpter and Turner [8] further proposed a general equation of J for the SE(B) specimens that is applicable to all crack sizes.

At the same time, many investigators explored whether the J-integral can be used as the controlling parameter in the presence of crack growth. In the late 1970s, Hutchinson and Paris [9] proposed that a J-controlled crack growth region exists near the crack tip for a limited amount of crack extension. Consequently, it became common practice to characterize the fracture resistance of materials against crack growth using the *J*-resistance curve, or *J*-*R* curve. This fracture resistance curve has been used to characterize the material capability against fracture initiation, stable crack growth, and unstable crack tearing. At that time, the *J* was estimated using the original crack length only, and the crack extension was determined using the elastic unloading compliance method [10]. In the early 1980s, Ernst et al. [11] suggested a simple and effective method for determining correct values of *J* for a growing crack by following the actual path of the load-displacement record. Their expression of *J* is an incremental function, and contains two geometry factors η and γ with the crack growth correction considered. Since then, this incremental expression has been widely used as an accurate equation to estimate the *J* values in the *J*-*R* curve testing, in conjunction with use of different measuring methods, including the elastic unloading compliance method, the key curve method [12], the electric potential drop method [13], and the normalization method [14] for determining crack extension. To date, this incremental equation of *J* is still adopted worldwide in various fracture testing codes, including ASTM E1820-06 and all its predecessors in the determination of *J*-*R* curves.

For a SE(B) specimen, the elastic unloading compliance method recommended in ASTM E1820 requires simultaneously recording three sets of test data, i.e., load (*P*), load-line displacement (LLD), and crack mouth opening displacement (CMOD) from a single specimen during the fracture testing to develop a *J*-*R* curve. The *P*-CMOD record is used to estimate the crack extension, and the *P*-LLD record with the crack extension is used to calculate the *J* values. However, it is well known that it is usually difficult to accurately measure LLD for the SE(B) specimen in a fracture test. Although the LLD can be measured remotely, it requires correction for specimen Brinell hardening and nonlinear machine compliance. If mounted on the specimen, the LLD gages suffer effects from specimen load-point indentation, friction between specimen surfaces and gage legs, specimen geometry changes during test and problems mounting the apparatus. In contrast, CMOD gages are much more precise, more accurate, more repeatable, more sensitive, and more easily mounted on the specimen than LLD gages. On the other hand, extensive finite element results [15–19] have shown that the LLD-based *J* estimation equation may give inaccurate estimations of *J* for some materials because the LLD-based geometry factor η for the SE(B) specimen is more sensitive to the strain hardening exponent for shallow-cracked SE(B) specimen geometries with $a/W < 0.3$, where a is the crack length and W is the specimen width. In contrast for these same geometries, the CMOD-based η factor is insensitive to the hardening exponent, which implies that the *J* estimation could be more accurate if the *P*-CMOD record is used. In fact, Sumpter [20], Morrison and Karisallen [21], and Wang et al. [22] have used the load versus CMOD records for the SE(B) specimens in the experimental determination of *J* or it critical value J_C for different metals.

To improve the test quality and accuracy of an experimental *J*-*R* curve, the current ASTM standard E1820-06 has included a CMOD-based *J* equation that is valid for stationary cracks. This CMOD-based J equation is good for the J calculations in the basic test method. If it is used for the J calculations for a growing crack as required in the resistance curve test method, the calculated J values shall be corrected for crack growth using the procedure from an empirical method proposed by Wallin and Laukkanen [23]. However, the procedure is complicated because it includes an initial crack growth correction, a power-law curve fit with the initial J-R curve, and a final crack growth correction for each test. To our knowledge, an incremental CMOD-based J estimation equation for a growing crack that can correct the J integral for crack growth is not available. The development of this relationship would result in more accurate and more cost effective J calculations in J-R curve testing.

So motivated, the present paper proposes an incremental CMOD-based J estimation equation for a growing crack to determine a J-R curve using the P-CMOD record in reference to the energy principle. As similar to the LLD-based J equation, the CMOD-based J equation is developed with two geometry factors, i.e., CMOD-based η and γ and the crack growth correction is considered. The expressions of CMOD-based η and γ factors are discussed in details for SE(B) specimens with various crack sizes. The proposed CMOD-based formulation is then applied to determine J-R curves from the load-CMOD record of SE(B) specimens for HY80 steel. The J-R curves are then analyzed and compared with those determined from the traditional LLD-based formulation. It should be noted that this paper focuses on the SE(B) specimens for moderately short to deep cracks in the CMOD-based formulation that is generally capable of also addressing very shallow cracks of $a/W < 0.25$, a topic which will be the subject of a subsequent paper.

Review of the LLD-Based J Estimation Method

Rice [1] proposed the parameter J-integral for a nonlinear elastic material as a measure of the crack-tip singularity intensity of HRR field [2,3]. Begley and Landes [4,5] first recognized that the J-integral and its critical value can be evaluated experimentally from the interpretation of J as the energy release rate given by:

$$J = -\frac{dU}{Bda} \tag{1}$$

where U is the strain energy and B is the specimen thickness. Using multiple specimens with different crack lengths, they obtained the load-displacement records, and the J is then determined using Eq 1. The major disadvantage of the multiple-specimen method for determining J is that five to ten specimens are needed to develop the calibration of J versus displacement. Therefore, a technique for establishing the J from a single specimen is very desirable so as to reduce test costs. A method for estimating the J from a single load-displacement record was proposed first by Rice et al. [6]. For convenience, they introduced two alternative, but equivalent forms of J as:

$$J = \frac{1}{B}\int_0^P \frac{\partial \Delta}{\partial a} dP \tag{2a}$$

or

$$J = -\frac{1}{B}\int_0^\Delta \frac{\partial P}{\partial a} d\Delta \tag{2b}$$

where P is the total generalized load or force of the component and Δ is the associated load-point or load-line displacement (LLD). For a deeply-cracked SE(B) specimen, J is equivalent to:

$$J = \frac{2}{bB}\int_0^\Delta P d\Delta = \frac{2A_{LLD}}{bB} \tag{3}$$

where b is the remaining ligament and A_{LLD} is the area under the P-Δ record. Note that Eq 3 was developed initially for the deeply-cracked SE(B) specimen in pure bending, where the generalized load is the applied moment M, and the load-point displacement is the relative rotation θ of the beam ends. It was found that Eq 3 is applicable to three-point bend and compact specimens with deep cracks because their remaining ligament supports primarily a bending moment due to an applied load P. For a bending specimen with different sized cracks, Sumpter and Turner [8] proposed a general expression of Eq 3 as:

$$J = \frac{\eta_{LLD}}{bB}\int_0^\Delta P d\Delta = \frac{\eta_{LLD} A_{LLD}}{bB} \tag{4}$$

where η_{LLD} is an LLD-based geometry factor that is a function of a/W only, where a is the crack length and W is the specimen width. This expression gives a very convenient way for evaluating the J for any bending specimens from a single P-LLD record.

A total LLD, Δ, can be separated into an elastic component Δ_{el} and a plastic component Δ_{pl}:

$$\Delta = \Delta_{el} + \Delta_{pl} \tag{5}$$

At any given point in the P-LLD record, the elastic component of LLD can be calculated as the load times the elastic load-line compliance, and the plastic component of LLD is calculated from Eq 5. Substitution of Eq. 5 into 2b gives:

$$J = J_{el} + J_{pl} \tag{6}$$

in which the elastic component of J can be directly calculated from the stress intensity factor K, as used in ASTM E1820 for a plane strain crack:

$$J_{el} = \frac{K^2(1-\nu^2)}{E} \tag{7}$$

where E is the Young's modulus and ν is the Poisson ratio. The plastic component of J is determined from Eqs 2a and 2b or 4 as:

$$J_{pl} = \frac{1}{B}\int_0^P \frac{\partial \Delta_{pl}}{\partial a} dP = -\frac{1}{B}\int_0^{\Delta_{pl}} \frac{\partial P}{\partial a} d\Delta_{pl} = \frac{\eta_{LLD} A_{LLD}^{pl}}{bB} \tag{8}$$

where A_{LLD}^{pl} is the plastic component of area under the measured P-Δ curve.

All expressions introduced above are valid only for stationary cracks. For a growing crack, the J estimation should consider the crack growth correction. Since the J-integral was developed on the basis of deformation theory of plasticity, it is independent of the loading path leading to the current values of LLD and a, provided that J-controlled crack growth conditions [8] are satisfied. Accordingly, the deformation theory based J value is a function of two independent variables: Δ and a. From Eq 8, Ernst et al. [11] derived the complete differential of J_{pl} as:

$$dJ_{pl} = \frac{\eta_{LLD} P}{bB} d\Delta_{pl} - \frac{\gamma_{LLD}}{b} J_{pl} da \tag{9}$$

with

$$\gamma_{LLD} = \eta_{LLD} - 1 - \frac{b}{W}\frac{\eta'_{LLD}}{\eta_{LLD}} \tag{10}$$

where the prime denotes the partial differential with respect to a/W, i.e., $\eta'_{LLD} = \partial \eta_{LLD} / \partial(a/W)$. Integrating Eq 9, one has:

$$J_{pl} = \int_0^{\Delta_{pl}} \frac{\eta_{LLD} P}{bB} d\Delta_{pl} - \int_{a_0}^{a} \frac{\gamma_{LLD}}{b} J_{pl} da \tag{11}$$

This equation holds for any loading path leading to the current values of a and Δ_{pl}, including the actual loading path for a growing crack.

Figure 1 illustrates a typical P-Δ_{pl} curve for a growing crack. This figure includes the deformation paths for an original crack length a_0 and also for two arbitrarily fixed crack lengths a_i and a_{i+1}. Since the J_{pl} in Eq 11 is valid for any loading path leading to the current values of a_i and Δ_{pl}^i, its value at point A (or B) can be determined by following path OA (or OB) for the fixed crack length a_i to the corresponding Δ_{pl}^i (or Δ_{pl}^{i+1}) in the actual P-LLD curve. Because $da = 0$ on this loading path, from Eq 11, one has:

$$J_{pl}^A = \frac{\eta_{LLD}^i}{b_i B}\int_0^{\Delta_{pl}^i} P d\Delta_{pl} \tag{12}$$

and

$$J_{pl}^B = J_{pl}^A + \frac{\eta_{LLD}^i}{b_i B} A_{\Delta pl}^{i+1,i} \tag{13}$$

where $A_{\Delta pl}^{i+1,i}$ represents the area under the P-Δ_{pl} curve between Δ_{pl}^i and Δ_{pl}^{i+1} with an error of the area of triangle ΔABC. Integration of Eq 11 along BC obtains an approximate result:

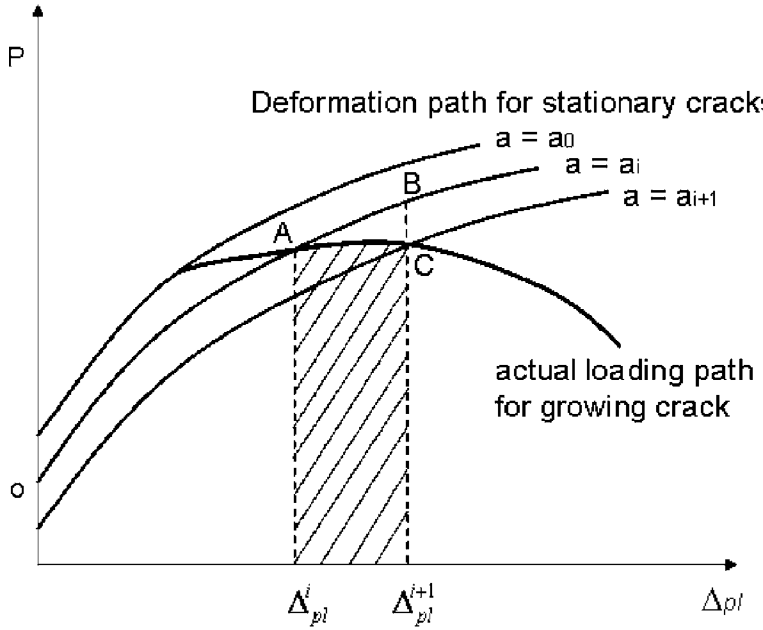

FIG. 1—*Typical load versus plastic displacement curves for static and growing cracks.*

$$J_{pl}^{C} = J_{pl}^{B}\left(1 - \frac{\gamma_{LLD}^{i}}{b_i}(a_{i+1} - a_i)\right) \tag{14}$$

From Eqs 12 to 14, one obtains:

$$J_{pl(i+1)} = \left(J_{pl(i)} + \frac{\eta_{LLD}^{i}}{b_i B} A_{\Delta pl}^{i+1,i}\right)\left(1 - \frac{\gamma_{LLD}^{i}}{b_i}(a_{i+1} - a_i)\right) \tag{15}$$

This incremental expression is the LLD-based J estimation equation that was adopted in ASTM E1820-06 and all its predecessors, where the specimen thickness B is replaced by the net thickness B_N for specimens with side grooves. The simultaneous measurement of the load, LLD and CMOD (used for measuring crack extension) permits the determination of a J-R curve from a single test.

Formulation of CMOD-Based *J* Estimation

Following the similar route for deriving the LLD-based J equation, this section formulates an incremental CMOD-based J estimation. A total CMOD, V, is separated into an elastic component V_{el} and a plastic component V_{pl}. At any given point in the P-CMOD record, the V_{el} can be calculated as the load times the elastic CMOD compliance, and the V_{pl} is obtained from $V_{pl} = V - V_{el}$. As such, the total J can be decomposed into an elastic component J_{el} and a plastic component J_{pl}, as shown in Eq 6. The J_{el} is defined in Eq 7, whereas the J_{pl} is determined next.

For a stationary crack, using the P-V_{pl} record, the plastic component of J can be expressed as:

$$J_{pl} = \frac{\eta_{CMOD} A_{CMOD}^{pl}}{bB} = \frac{\eta_{CMOD}}{bB} \int_0^{V_{pl}} P dV_{pl} \tag{16}$$

where A_{CMOD}^{pl} is the area under the measured P-V_{pl} curve. Without loss of generality, it is assumed that the ratio of V_{pl} and Δ_{pl} is a function of a/W:

$$\frac{V_{pl}}{\Delta_{pl}} = \lambda(a/W) \tag{17}$$

From Eqs 8, 16, and 17, three equivalent expressions for this new geometry factor are obtained:

$$\lambda = \frac{V_{pl}}{\Delta_{pl}} = \frac{A_{CMOD}^{pl}}{A_{LLD}^{pl}} = \frac{\eta_{LLD}}{\eta_{CMOD}} \tag{18}$$

Since J_{pl} is now the function of V_{pl} and a, its complete differential is obtained as:

$$dJ_{pl} = \frac{\eta_{CMOD} P}{bB} dV_{pl} - \frac{\gamma_{CMOD}}{b} J_{pl} da \tag{19}$$

where

$$\gamma_{CMOD} = \lambda \, \eta_{CMOD} - 1 - \frac{b}{W}\left(\frac{\lambda'}{\lambda} + \frac{\eta'_{CMOD}}{\eta_{CMOD}}\right) \tag{20}$$

Substituting Eq 18 into 20, it is interesting to find that $\gamma_{CMOD} = \gamma_{LLD}$.

Integrating Eq 19 gives the plastic component of J in reference to the CMOD-based geometry factors:

$$J_{pl} = \int_0^{V_{pl}} \frac{\eta_{CMOD} P}{bB} dV_{pl} - \int_{a_0}^{a} \frac{\gamma_{CMOD}}{b} J_{pl} da \tag{21}$$

This integral holds for any loading path leading to the current values of a and V_{pl}.

A typical P-V_{pl} curve for a growing crack can be illustrated as similarly as in Fig. 1, where a loading path for an original crack length a_0 and two deformation paths for arbitrarily fixed crack lengths a_i and a_{i+1} are included. Since the integral J_{pl} in Eq 21 is path-independent, its value at point A can be determined by following path OA for the crack length a_i up to Δ_{pl}^i in the actual path of P-CMOD curve. Note that "path-independent" is used here to evaluate the J-integral following the loading path of load versus plastic displacement plots. Because $da = 0$ on this loading path, from Eq 21, we have:

$$J_{pl(i)} = J_{pl}^{A} = \frac{\eta_{CMOD}^{i}}{b_i B} \int_{0}^{V_{pl}^{i}} P dV_{pl} \tag{22}$$

where the integral represents the area under the curve OA. Likewise, at point B, we obtain:

$$J_{pl}^{B} = J_{pl}^{A} + \frac{\eta_{CMOD}^{i}}{b_i B} A_{Vpl}^{i+1,i} \tag{23}$$

where $A_{Vpl}^{i+1,i}$ represents the area under the curve AB and is approximated as the area under the actual path of P-V_{pl} records between V_{pl}^{i} and V_{pl}^{i+1} with an error of the area of triangle ΔABC. To determine J_{pl}^{C} for the fixed crack length a_{i+1} and displacement V_{pl}^{i+1}, integrating Eq 21 along the curve BC where V_{pl} is constant obtains the following expression:

$$J_{pl(i+1)} = J_{pl}^{C} = J_{pl}^{B}\left(1 - \frac{\gamma_{CMOD}^{j}}{b_i}(a_{i+1} - a_i)\right) \tag{24}$$

where the first-order approximation is used in the calculation of integration. From Eqs 22 to 24, we obtain the following CMOD-based J estimation equation for a growing crack:

$$J_{pl(i+1)} = \left(J_{pl(i)} + \frac{\eta_{CMOD}^{i}}{b_i B} A_{Vpl}^{i+1,i}\right)\left(1 - \frac{\gamma_{CMOD}^{j}}{b_i}(a_{i+1} - a_i)\right) \tag{25}$$

Equation 25 is an incremental function in the form similar to Eq 15. In the derivation of these two equations, the actual loading path is approximated by the artificial step lines for small crack extensions, and the apparent error is the area of triangle ΔABC in Fig. 1. When the crack extension or the increment of plastic displacement between two loading points is sufficiently small, the error is small and both equations are "accurate." To compare the relative accuracies of Eqs 15 and 25, it is needed to compare the errors in J from the triangle ΔABC, or equivalently compare $\eta_{CMOD}^{i} A_{CMOD}^{\Delta ABC}/b^i B$ and $\eta_{LLD}^{i} A_{LLD}^{\Delta ABC}/b^i B$, where $A_{CMOD}^{\Delta ABC}$ and $A_{LLD}^{\Delta ABC}$ are the areas of triangle ΔABC, respectively, using P-CMOD and P-LLD records. At the deformation path from A to B, it follows from Eq 18 that $A_{Vpl}^{i,i+1} + A_{CMOD}^{\Delta ABC} = \lambda_i (A_{\Delta pl}^{i,i+1} + A_{LLD}^{\Delta ABC})$. This equation leads to:

$$\frac{\eta_{CMOD}^{i} A_{CMOD}^{\Delta ABC}}{b^i B} - \frac{\eta_{LLD}^{i} A_{LLD}^{\Delta ABC}}{b^i B} = \frac{1}{2b^i B}(P_i + P_{i+1})(\lambda_i - \lambda_{i+1})\Delta_{pl}^{i+1}\eta_{CMOD}^{i} \le 0 \tag{26}$$

where $\lambda_i - \lambda_{i+1} \le 0$ for a growing crack with $a_{i+1} \ge a_i$ is used. Note that this inequality will be demonstrated by Eq 31 and Fig. 3 in the next section. Equation 26 indicates that the error in J from the triangle ΔABC using CMOD is less than the error using LLD. This implies that Eq 25 has a higher accuracy than Eq 15. It is known that for the SE(B) specimens in three-point bending, the applied load P increases with b^2 because its limit load is $P_L = 1.455 b^2 B \sigma_Y / S$, where S is the beam span. Accordingly, the error difference of J in Eq 26 could become larger when the ligament b is larger, or the crack length is shorter. Therefore, the CMOD-based J in Eq 25 should be larger than the LLD-based J

in Eq 15 at each loading point, and their difference would get smaller as the crack becomes deeper. As a result, it is expected that the proposed CMOD-based J formulation would be much more accurate than the LLD-based J formulation, particularly for specimens with initially short cracks where an accurate LLD measurement can be more difficult. Therefore, the CMOD-based J formulation is the better way to determine J-R curves for SE(B) specimens.

Recall that the LLD-based Eq 15 requires simultaneous measurements of P, LLD, and CMOD, whereas the CMOD-based Eq 25 requires only measurements of P and CMOD (note that crack extension can be determined from P-CMOD record in the elastic unloading compliance method) in the determination of a J-R curve from a single test on the SE(B) specimen. Obviously, the test procedures are simplified and the test costs are reduced in the proposed CMOD-based formulation. In general, this incremental CMOD-based J formulation is applicable to any laboratory specimen with any crack length, provided that the two related geometry factors are known for that specimen. In case CMOD is equal to LLD, such as for the compact tension [CT] specimen, Eq 25 is identical to Eq 15, and thus the CMOD-based J formulation is equivalent to the LLD-based J formulation.

Determination of Geometry Factors for SE(B) Specimen

For the fracture standard ASTM E1820-06 recommended SE(B) specimens with deep cracks of $0.45 \leq a/W \leq 0.70$ under three-point bending, all predecessor versions adopted $\eta_{LLD}=2$ and $\gamma_{LLD}=1$, while E1820-06 used $\eta_{LLD}=1.9$ and $\gamma_{LLD}=1$ in the LLD-based J Equation 15. However, the latter set of the geometry factor values does not satisfy Eq 10, and so it should not be used. It is thus suggested herein to use:

$$\eta_{LLD} = 1.9 \quad \text{and} \quad \gamma_{LLD} = 0.9 \tag{27}$$

Through detailed finite element analysis (FEA), Kirk and Dodds [15] determined a CMOD-based factor η_{CMOD} for the SE(B) specimen under three-point bending for a wide spectrum of crack lengths and strain hardening exponents. They found that η_{CMOD} is insensitive to the strain hardening exponent, and their FEA results were fitted by the following curve:

$$\eta_{CMOD} = 3.785 - 3.101(a/W) + 2.018(a/W)^2, \quad 0.05 \leq a/W \leq 0.7 \tag{28}$$

This equation was adopted in the fracture standard ASTM E1820-06 and E1290-02 (Standard Test Method for Crack-Tip Opening Displacement (CTOD) Fracture Toughness Measurement) for the standard SE(B) specimen. In addition, Nevalainen and Dodds [16], Kim et al. [17], and Donato and Ruggieri [18] also performed detailed FEA calculations and obtained the FEA results of η_{CMOD} for the SE(B) specimens for different crack lengths and strain hardening exponents. Similarly, their FEA results of η_{CMOD} are less sensitive to the strain hardening exponent, as shown in Fig. 2, where the slip line field (SLF) solution developed by Wu et al. [24,25] is also included for comparison. It is seen that except for the FEA results of Kirk and Dodds for $a/W > 0.5$, the other FEA results match well with the SLF solution that is believed to be accurate for deep

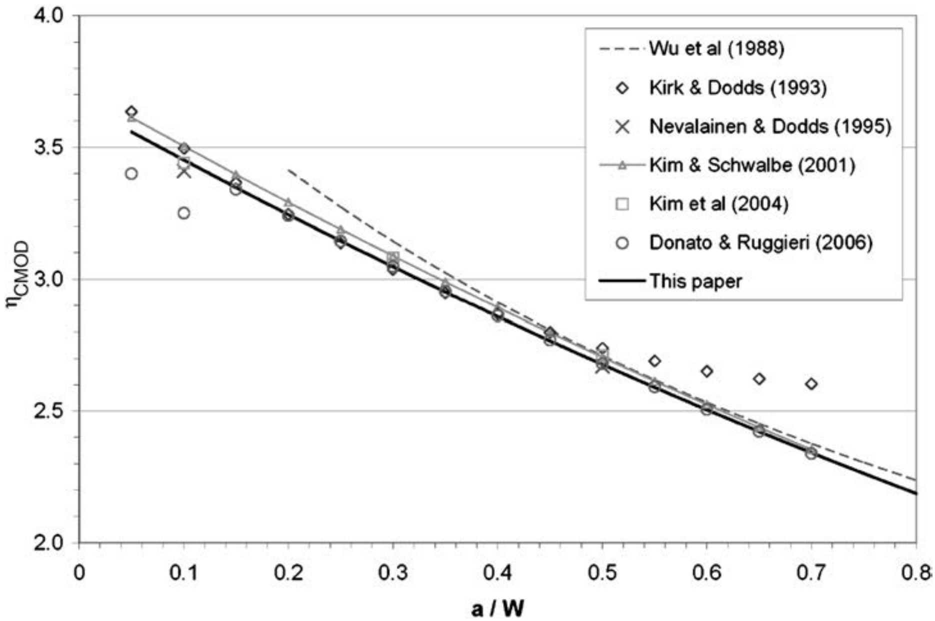

FIG. 2—*Variations of the geometry factor* η_{CMOD} *with* a/W.

cracks with $a/W > 0.3$. The reasons for the deviation of the FEA results of Kirk and Dodds with $a/W > 0.5$ is not understood but they significantly deviate from the accurate SLF solution and the other FEA trend. Thus, Eq 28 is acceptable only up to $a/W = 0.5$, and the general use of Eq 28 in ASTM E1820-06 is inappropriate. Actually, Kim and Schwalbe [19] already pointed out the errors and gave an alternative solution by fitting the FEA results of Kirk and Dodds for shallow cracks and the SLF solutions for deep cracks as follows:

$$\eta_{CMOD} = 3.724 - 2.24(a/W) + 0.408(a/W)^2, \quad 0.05 \le a/W \le 0.7 \tag{29}$$

Figure 2 shows that the results of Eq 29 agrees closely with the correct FEA results and SLF result with a slight overestimation. By fitting all valid FEA results, excluding those of Kirk and Dodds for $a/W > 0.5$ and Donato and Ruggieri for $a/W \le 0.1$, an improved quadratic curve is found as:

$$\eta_{CMOD} = 3.667 - 2.199(a/W) + 0.437(a/W)^2, \quad 0.05 \le a/W \le 0.7 \tag{30}$$

As demonstrated in Fig. 2, the new relationship for η_{CMOD} in Eq 30 is in excellent agreement with all correct FEA results and the SLF solutions. Accordingly, this new expression of η_{CMOD} is more accurate, and can be used for SE(B) specimens for all crack lengths of interest. Since it has higher accuracy, the proposed expression of η_{CMOD} in Eq 30 is recommended for use in all related ductile fracture testing standards, including ASTM E1820, E1290, and E1921 (Standard Test Method for Determination of Reference Temperature, T_0, for Ferritic Steels in the Transition Range).

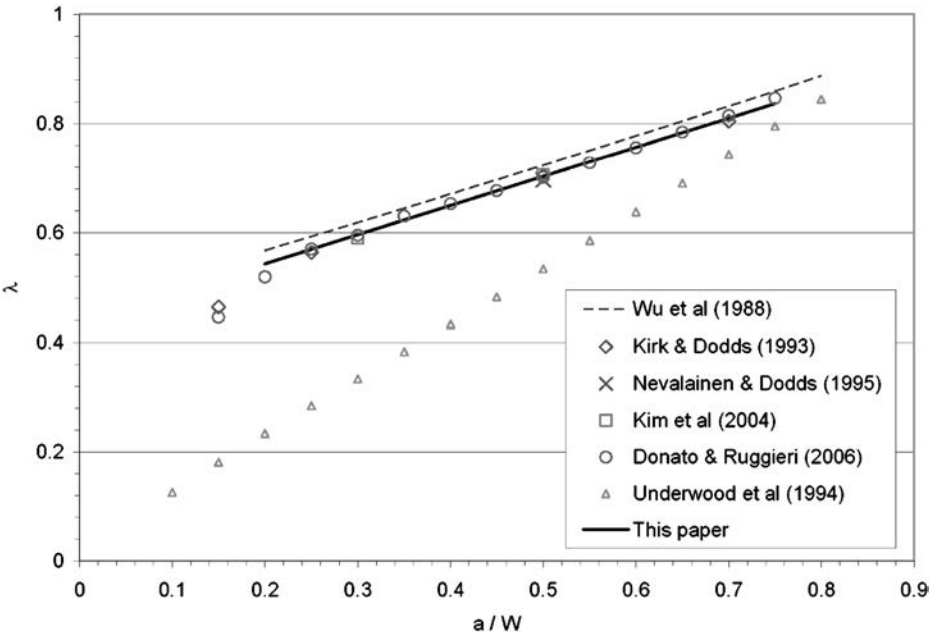

FIG. 3—*Variations of the geometry factor* λ *with* a/W.

Figure 3 plots the variation of the geometry factor λ with a/W. In this figure, the FEA results from Kirk and Dodds [15], Nevalainen and Dodds [16], Kim et al. [17], and Donato and Ruggieri [18] are calculated using $\lambda = \eta_{LLD}/\eta_{CMOD}$, and the SLF solutions of Wu et al. [25] are obtained using the relationship $\lambda = V/\Delta$ for perfectly-plastic materials. These FEA results are in close agreement for $a/W \geq 0.25$, but deviate gradually from the linear trend when $a/W < 0.25$. By curve fitting of the FEA results of λ versus a/W for $a/W \geq 0.25$, a linear relationship of the form:

$$\lambda = 0.436 + 0.534(a/W), \quad 0.25 \leq a/W \leq 0.7 \tag{31}$$

is found to be adequate. This equation, in conjunction with Eq 18, can be used to check the experimental accuracy of LLD and CMOD measurements in the elastic unloading compliance method, or to infer LLD from CMOD data for determining J using the LLD-based formulation, and vice versa. In addition, Fig. 3 includes the analytic results of Underwood et al. [26]. Clearly, this solution is inaccurate because it deviates far below the FEA results.

From Eqs 30 and 31, we have the LLD-based geometry factor:

$$\eta_{LLD} = [0.436 + 0.534(a/W)][3.667 - 2.199(a/W) + 0.437(a/W)^2], \quad 0.25 \leq a/W \leq 0.7 \tag{32}$$

This equation is equivalent to the following quadratic curve:

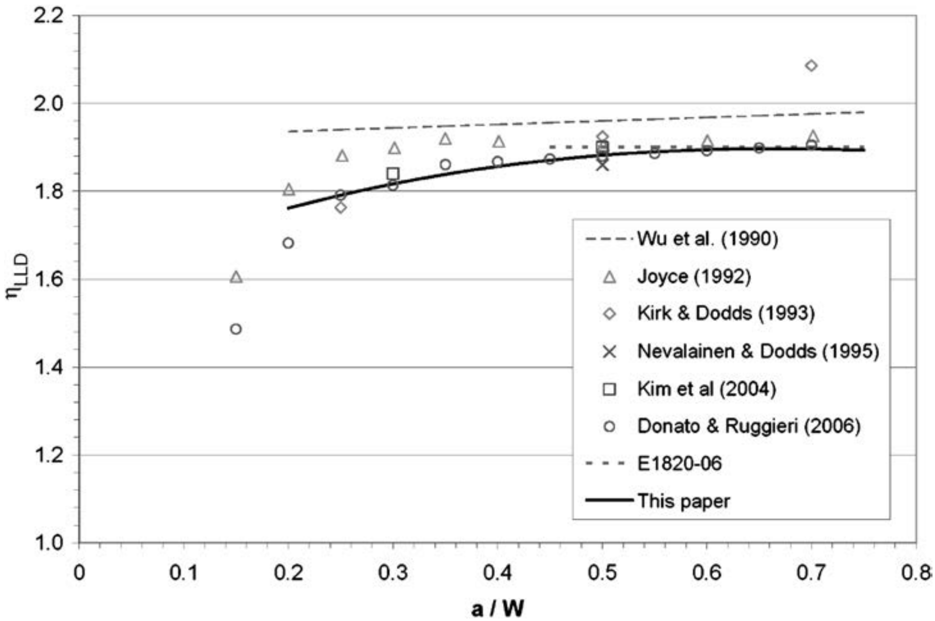

FIG. 4—*Variations of the geometry factor η_{LLD} with a/W.*

$$\eta_{LLD} = 1.620 - 0.850(a/W) - 0.651(a/W)^2, \quad 0.25 \le a/W \le 0.7 \tag{33}$$

Figure 4 shows the variation of η_{LLD} with a/W determined from Eq 33. Also included in this figure are the SLF solutions by Wu et al. [25] and the FEA results by Joyce [27], Kirk and Dodds [15], Nevalainen and Dodds [16], Kim et al. [17], and Donato and Ruggieri [18]. It indicates that our solutions in Eq. 33 match well with the FEA results for $a/W \ge 0.25$, and are nearly identical to $\eta_{LLD} = 1.9$ that is used in ASTM E1820-06 for deep cracks within the range of $0.45 \le a/W \le 0.7$. Therefore, the use of $\eta_{LLD} = 1.9$ rather than 2 in the new standard E1820-06 is more reasonable and accurate for the SE(B) specimen in three-point bending. Note that the geometry factor η_{LLD} strongly depends on the strain hardening exponent for short cracks with $a/W < 0.25$, as demonstrated in Refs. [15–18,28].

The factor γ_{CMOD} and γ_{LLD} are similarly obtained by substituting Eqs 30 and 31 into Eq 20 or substituting Eq 33 into Eq 20, and the results are shown in Fig. 5. These calculated results are almost identical to the following quadratic curve:

$$\gamma_{CMOD} = 0.131 + 2.131(a/W) - 1.465(a/W)^2, \quad 0.25 \le a/W \le 0.7 \tag{34}$$

Figure 5 shows that γ_{CMOD} or γ_{LLD} approaches to 0.9 only for very deep cracks with $a/W > 0.6$. This indicates that the small slope of the function η_{LLD} has bigger influence on the γ factor. For instance, at $a/W = 0.5$, the "accurate" solution $\eta_{LLD} = 1.882$ and $\eta'_{LLD} = 0.199$ from Eq 33, and $\gamma_{CMOD} = 0.829$ from Eq 34. The approximate solution $\eta_{LLD} = 1.9$ overestimates the "accurate" solution of

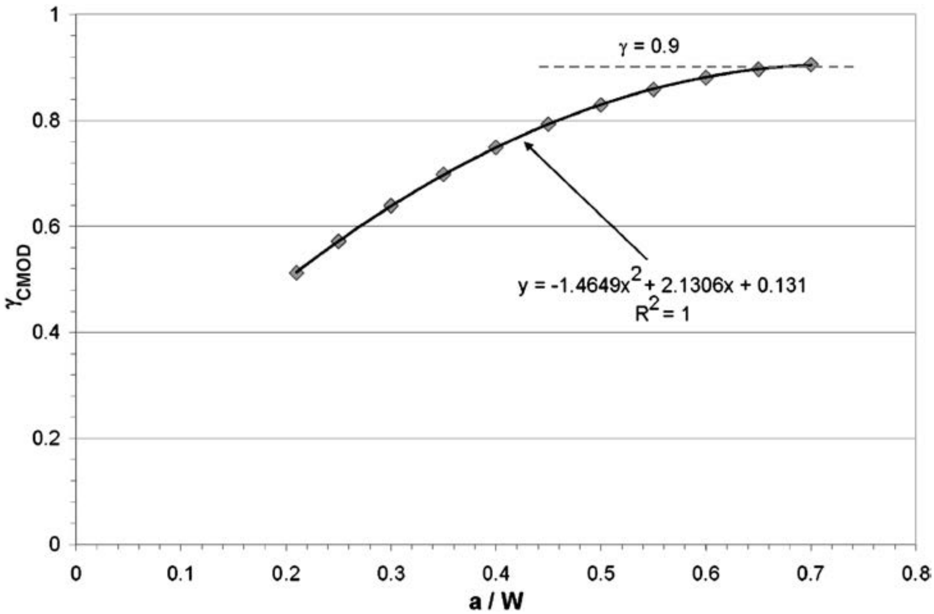

FIG. 5—*Variations of the geometry factor* γ_{CMOD} *with* a/W.

$\eta_{LLD}=1.882$ by only 0.96 %; however, $\gamma_{CMOD}=0.9$ overestimates the "accurate" solution of $\gamma_{CMOD}=0.829$ by 8.56 %. Nevertheless, the larger value of γ will allow conservative estimation of J. Therefore, one may use:

$$\gamma_{CMOD} = \gamma_{LLD} = 0.9, \quad 0.45 \le a/W \le 0.7 \tag{35}$$

in both the CMOD-based J Eq 25 and the LLD-based J Eq 15 for the standard SE(B) specimens, as specified in ASTM E1820-06. The following section applies these two formulations to determine *J-R* curves for an HY80 steel using the SE(B) specimens.

Applications to Determining *J-R* Curves for HY80 Steel

Joyce and his coworkers [27,29,30] tested a series of 1T SE(B) specimens with a wide range of crack lengths from short to deep at room temperature. In their tests, all SE(B) specimens were loaded in three-point bending, with a bend span of 203 mm, a span to width ratio of 4, and a thickness to width ratio of 0.5. The specimens were manufactured with two side-grooves of a total 20 % thickness reduction to promote the plane strain deformation along the crack front. The material used was an HY80 steel with the 0.2 % offset yield stress of 630 MPa, the ultimate tensile stress of 735 MPa, the Young's modulus $E=207$ GPa and the Poisson ratio $\nu=0.3$. Detailed chemistry and tensile properties for this steel were presented in Ref [27]. The test data for most of these specimens can be found in Ref [30].

The standard elastic unloading compliance method was used in all their tests for determining the instantaneous crack length and crack extension. For each specimen, the load, LLD and CMOD data were simultaneously recorded during the test. Figures 6(*a*) and 6(*b*) show the raw experimental data of the load-LLD record and the load-CMOD record, respectively, for the initial crack lengths $a_0/W = 0.704$, 0.606, 0.550, 0.549, 0.393, and 0.286. Except for the last two cracks, the other four are the standard deep cracks as defined in E1820. Comparison of these two figures indicates that the total LLD is larger than the total CMOD at each loading point, and the *P*-LLD curve is relatively fatter in shape than the *P*-CMOD curve for each crack.

With the measured crack length and the *P*-LLD record, the *J*-integral is calculated from Eq 15 for each specimen. Likewise, using the measured crack length and the *P*-CMOD record, the *J*-integral is estimated from Eq 25 for each specimen. Figures 7(*a*) to 7(*b*) compare the *J*-*R* curves determined from the LLD- and CMOD-based formulations, respectively, for two deep cracks of $a_0/W = 0.704$ and 0.606. Figures 7(*c*) and 7(*d*) compare the *J*-*R* curves for two moderately short cracks of $a_0/W = 0.393$ and 0.286. It is seen that these two formulations have close agreement for the two deep cracks, and good agreement for the two short cracks with slightly higher values of *J* estimated using the CMOD-based formulation. These observations are consistent with the experimental results by Morrison and Karisallen [21], where their *J* values were calculated without considering the crack growth correction. These observations also confirm our early prediction that the CMOD-based *J* is larger than the LLD-based *J* at each loading point for a growing crack, and their difference goes larger when the crack becomes shorter. In addition, detailed examination of experimental data indicates that the ratio of CMOD- and LLD-based plastic displacements or plastic areas is higher than that determined from Eq 31 for most tests. This may show the measurement errors for LLD and CMOD, or the discrepancy between actual measurements and ideal FEA results for the geometry factors. Anyway, the results in Figs. 7(*a*)–7(*d*) verify the correctness and efficiency of the proposed CMOD-based formulation and the related geometry factors for the SE(B) specimens.

To obtain consistent fracture toughness J_{IC}, E1820 suggests a *J* validity requirement for the maximum crack extension as $\Delta a_{max} = 0.25 b_0$. Accordingly, the maximum crack extension for the HY80 SE(B) specimens shown in Fig. 7 should be 3.75, 5.00, 7.71, and 9.10 mm, respectively, for $a_0/W = 0.704$, 0.606, 0.393, and 0.286. Comparing these values with the measured data of crack extension as shown in Figs. 7(*a*)–7(*d*) indicates that except for the deep crack of $a_0/W = 0.606$, the maximum crack extensions for the other three cracks are close to those required in ASTM E1820. For the special case of $a_0/W = 0.606$, the *J*-*R* curve is developed with much larger crack extension. Although being far beyond the *J*-controlled crack growth, it might still be within the two-parameter controlled crack growth, and provides more usable fracture resistance data of *J* versus crack growth, and enables to perform a complete crack growth failure analysis including crack initiation, stable crack growth and unstable crack tearing for an actual crack in the HY80 steel with an anticipation of large crack extension.

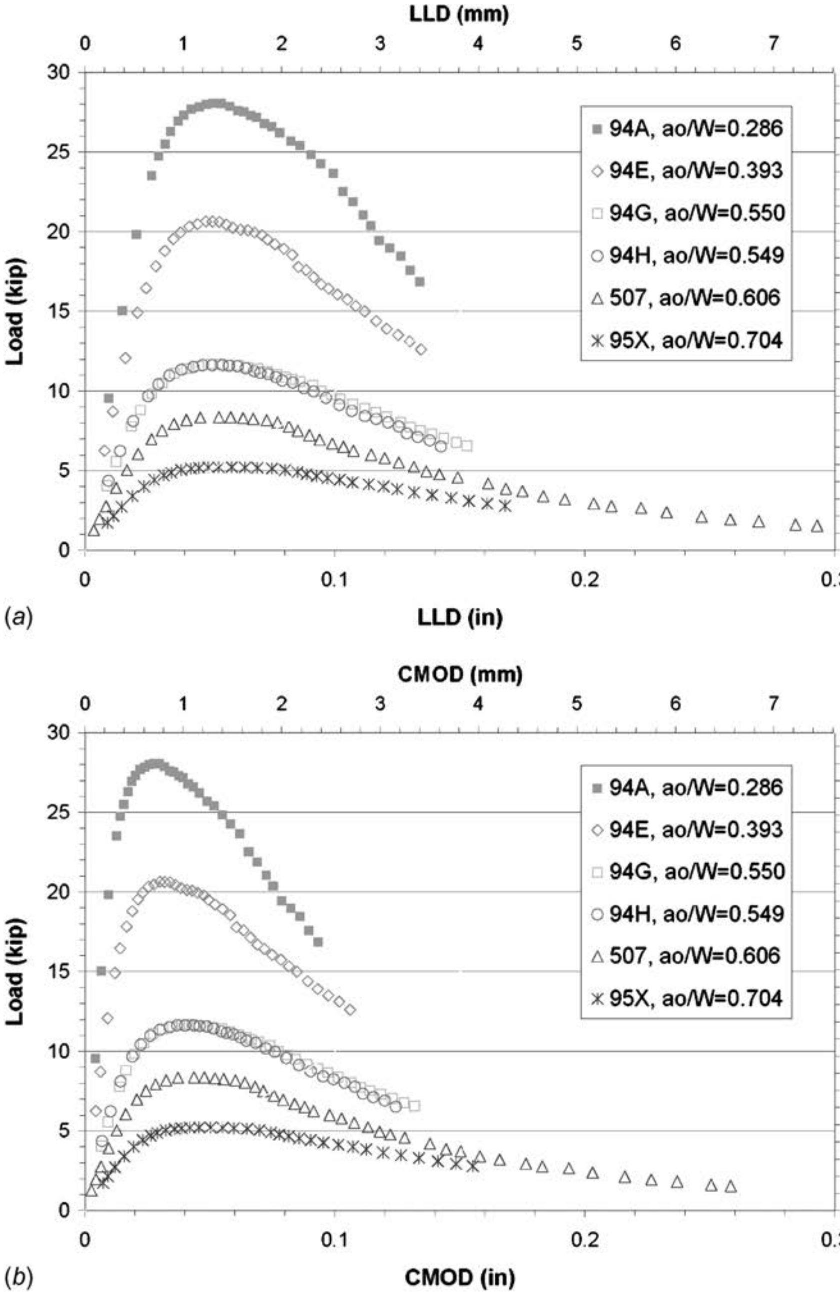

FIG. 6—*Experimental data of load-displacement record for six SE*(*B*) *specimens* (*a*) *P-LLD record;* (*b*) *P-CMOD record.*

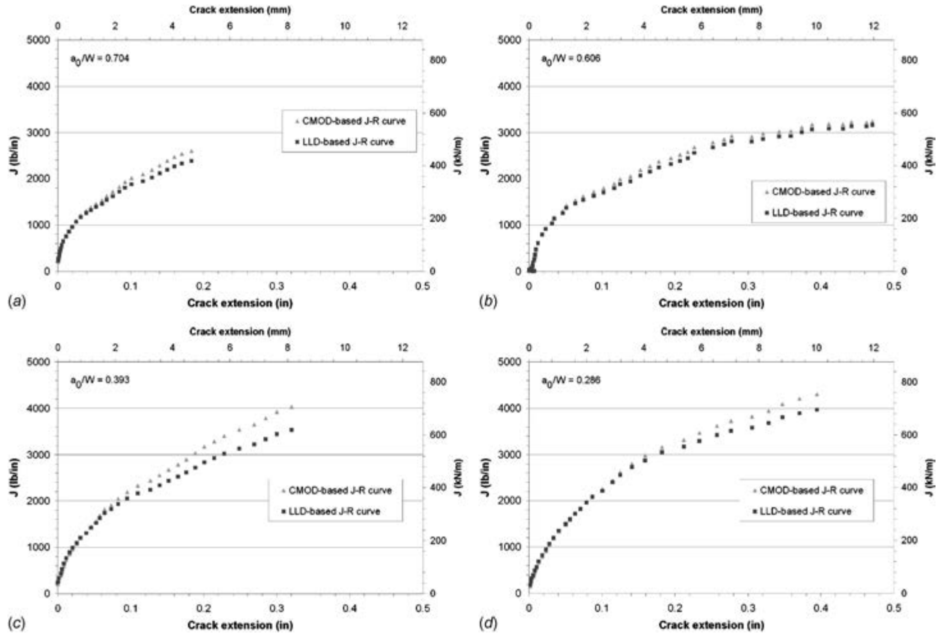

FIG. 7—*Comparisons of J-R curves determined by the CMOD- and LLD-based formulations for the HY80 SE(B) specimens with* (*a*) $a_0/W = 0.704$; (*b*) $a_0/W = 0.606$; (*c*) $a_0/W = 0.393$; (*d*) $a_0/W = 0.286$.

Figures 8(*a*) and 8(*b*) show the experimental *J-R* curves determined, respectively, using the LLD-based formulation and the CMOD-based formulation for all six cracks considered for the HY80 SE(B) specimens. The blunt line and the 0.2 mm offset line are also included in Fig. 8. Within the crack extension of 2 mm, the *J-R* curves determined by the two formulations are nearly identical to each other for these specimens. This infers that the fracture toughness at crack initiation determined using the proposed CMOD-based formulation is equivalent to that using the traditional LLD-based formulation. In addition, the scatter range of *J-R* curves in Fig. 8(*b*) is slightly larger than that in Fig. 8(*a*). This may reflect the nature of constraint (or crack size) effect on the fracture resistance curve and the higher accuracy of the CMOD-based Eq 25 or it may be caused by displacement measurement errors. Therefore, it can be concluded that the proposed CMOD-based formulation performs well and suggests that it can be used, and maybe should be used to determine more accurate *J-R* curves.

Conclusions

Based on the energy principle, this paper developed an incremental CMOD-based *J* equation for a growing crack to be used in the experimental determination of *J-R* curves for one single test on the SE(B) specimen. Its expression is similar to the traditional LLD-based *J* equation for a growing crack, rather than

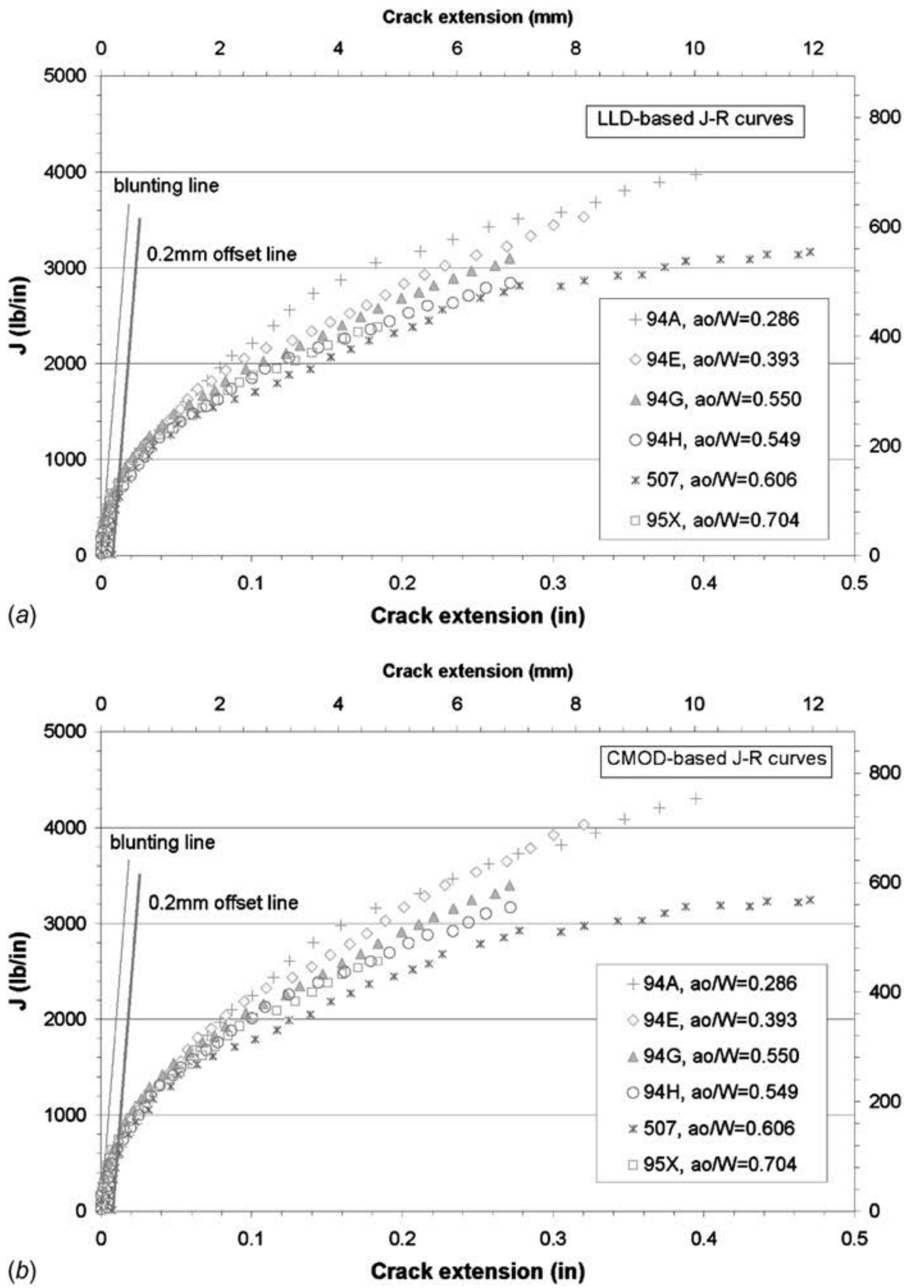

FIG. 8—*The experimental J-R curves for the HY80 SE*(*B*) *specimens* (*a*) *LLD-based J-R curves;* (*b*) *CMOD-based J-R curves.*

the available CMOD-based *J* equation for a stationary crack, presently used in

ASTM E1820-06. The newly proposed formulation contains two geometry factors, and can accurately correct the crack growth effect on the J integral. Moreover, the rigorous mathematical error analysis indicated that the proposed CMOD-based J equation has higher accuracy than the traditional LLD-based J equation. As a result, the complicated procedures suggested in E1820-06 for the crack growth correction of CMOD-based J evaluations are not needed. This has the added advantage that the LLD measurement is no longer required for a ductile fracture toughness test. Therefore, test procedures can be simplified and test costs can be reduced if the proposed formulation is adopted in a J-R curve test on the SE(B) specimen. In general, the proposed CMOD-based J formulation is applicable to any laboratory specimen with any crack length, provided that the two related geometry factors are known for that specimen.

Based on the FEA results, the solutions for the geometry factors: η_{CMOD}, γ_{CMOD}, λ, η_{LLD}, γ_{LLD} for the SE(B) specimen were given using data regressions over a wide range of crack length ratio. The comparisons showed that the η_{CMOD} in Eq 28 presently used in E1820-06 is inaccurate for $a/W > 0.5$, and thus the use of Eq 28 in E1820-06 is inappropriate. In contrast, the proposed new solution of η_{CMOD} in Eq 30 is more accurate and can be used for all cracks of interest: $0.05 < a/W < 0.7$. The proposed solutions of λ in Eq 31, η_{LLD} in Eq 33, and γ_{CMOD} or γ_{LLD} in Eq 34 are valid and accurate for cracks with $a/W \geq 0.25$. As such, it is suggested to use the η_{CMOD} in Eq 30, $\eta_{LLD}=1.9$, and $\gamma_{LLD}=0.9$ for the SE(B) specimens with standard deep cracks in E1820-06.

The proposed CMOD-based J formulation was applied to determine J-R curves from the load-CMOD record for SE(B) specimens in the HY80 steel. These J-R curves were then compared with those determined by the LLD-based formulation for different crack sizes. The results showed close agreement of the J-R curves between these two formulations, with a general trend that the CMOD-based J-R curve is higher than the LLD-based one for each specimen. The trend is consistent with the results predicted in the mathematical analysis on the errors for these two methods. With this validation, it is strongly recommended to use the incremental CMOD-based J formulation and the geometry factors proposed in this paper in all related facture testing standards, including ASTM E1820, E1920, and E1921 to determine more accurate fracture toughness or J-R curves.

Acknowledgments

The partial support from a Battelle IR&D program to this work is acknowledged. The authors are very grateful to the anonymous reviewers for their useful suggestions.

References

[1] Rice, J. R., "A Path Independent Integral and the Approximate Analysis of Strain Concentration by Notches and Cracks," *J. Appl. Mech.*, Vol. 35, 1968, pp. 379–386.

[2] Hutchinson, J. W., "Singular Behavior at the End of a Tensile Crack in a Hardening

Material," *J. Mech. Phys. Solids*, Vol. 16, 1968, pp. 13–31.

[3] Rice, J. R. and Rosengren, G. F., "Plane Strain Deformation Near a Crack Tip in a Power Law Hardening Material," *J. Mech. Phys. Solids*, Vol. 16, 1968, pp. 1–12.

[4] Begley, J. A. and Landes, J. D., "The J-integral as a Fracture Criterion," *Fracture Mechanics*, ASTM STP 515, ASTM International, West Conshohocken, PA, 1972, pp. 1–23.

[5] Landes, J. D. and Begley, J. A., "The Effect of Specimen Geometry on J_{IC}," *Fracture Mechanics*, ASTM STP 515, ASTM International, West Conshohocken, PA, 1972, pp. 24–39.

[6] Rice, J. R., Paris, P. C., and Merkle, J. G., "Some Further Results of J-integral Analysis and Estimates," *Progress in Flaw Growth and Fracture Toughness Testing*, ASTM STP 536, ASTM International, West Conshohocken, PA, 1973, pp. 231–245.

[7] Merkle, J. and Corten, H., "A J-integral Analysis for the Compact Specimen, Considering Axial Force as Well as Bending Effects," *J. Pressure Vessel Technol.*, Vol. 96, 1974, pp. 286–292.

[8] Sumpter, J. D. G. and Turner, C. E., "Method for Laboratory Determination of J_C (Contour Integral for Fracture Analysis)," *Cracks and Fracture*, ASTM STP 601, ASTM International, West Conshohocken, PA, 1976, pp. 3–18.

[9] Hutchinson, J. W. and Paris, P. C., "Stability Analysis of J-Controlled Crack Growth," *Elastic-Plastic Fracture*, ASTM STP 668, ASTM International, West Conshohocken, PA, 1979, pp. 37–64.

[10] Clarke, G. A., Andrews, W. R., Paris, P. C., and Schmidt, D. W., "Single Specimen Tests for J_{IC} Determination," *Mechanics of Crack Growth*, ASTM STP 590, ASTM International, West Conshohocken, PA, 1976, pp. 27–42.

[11] Ernst, H. A., Paris, P. C., and Landes, J. D., "Estimations on *J*-integral and Tearing Modulus *T* from a Single Specimen Test Record," *Fracture Mechanics: 13th Conference*, ASTM STP 743, ASTM International, West Conshohocken, PA, 1981, pp. 476–502.

[12] Joyce, J. A., Ernst, H., and Paris, P. C., "Direct *J-R* Curve Analysis: A Guide to the Methodology," *Fracture Mechanics: 12th National Symposium*, ASTM STP 700, ASTM International, West Conshohocken, PA, 1980, pp. 222–236.

[13] Bakker, A., "A DC Potential Drop Procedure for Crack Initiation and R-Curve Measurements During Ductile Fracture Tests," *Elastic-Plastic Fracture Test Methods: The User's Experience*, ASTM STP 586, ASTM International, West Conshohocken, PA, 1985, pp. 394–410.

[14] Landes, J. D., Zhou, Z., Lee, K., and Herrera, R., "Normalization Method for Developing *J-R* curves with the LMN Function," *J. Test. Eval.*, Vol. 19, 1991, pp. 305–311.

[15] Kirk, M. T. and Dodds, R. H., "*J* and CTOD Estimation Equations for Shallow Cracks in Single Edge Notch Bend Specimens," *J. Test. Eval.*, Vol. 21, 1993, pp. 228–238.

[16] Nevalainen, M. and Dodds, R. H., "Numerical Investigation of 3-D Constraint Effects on Brittle Fracture in SE(B) and C(T) Specimens," *Int. J. Fract.*, Vol. 74, 1995, pp. 131–161.

[17] Kim, Y. J., Kim, J. S., Cho, S. M., and Kim, Y. J., "3-D Constraint Effects on J Testing and Crack Tip Constraint in M(T), SE(B), SE(T), C(T) Specimens: Numerical Study," *Eng. Fract. Mech.*, Vol. 71, 2004, pp. 1203–1218.

[18] Donato, G. H. B. and Ruggieri, C., "Estimation Procedure for J and CTOD Fracture Parameters Using Three-Point Bend Specimens," *Proceedings of the 6th International Pipeline Conference*, Sept. 25–29, 2006, Calgary, Canada, Paper Number: IPC2006-10165.

[19] Kim, Y. J. and Schwalbe, K. H., "On Experimental J Estimation Equations Based on CMOD for SE(B) Specimen," *J. Test. Eval.*, Vol. 29, 2001, pp. 67–71.

[20] Sumpter, J. D. G., "J_C Determination for Shallow Notch Welded Bend Specimens," *J. Mech. Phys. Solids*, Vol. 26, 1987, pp. 479–493.

[21] Morrison, J. and Karisallen, K. J., "An Experimental Comparison of J and CTOD Estimation Formulas," *Eng. Fract. Mech.*, Vol. 51, 1995, pp. 145–149.

[22] Wang, Y. Y., Reemsnyder, H. S., and Kirk, M. T., "Inference Equations for Fracture Toughness Testing: Numerical Analysis and Experimental Verification," *Fatigue and Fracture Mechanics: 28th Volume*, ASTM STP 1321, ASTM International, West Conshohocken, PA, 1997, pp. 469–484.

[23] Wallin, K. and Laukkanen, A., "Improved Crack Growth Corrections for *J-R* Curve Testing," *Eng. Fract. Mech.*, Vol. 71, 2004, pp. 1601–1614.

[24] Wu, S. X., Mai, Y. W., and Cotterell, B., "Plastic Rotation Factors of Three-Point Bend and Compact Tension Specimens," *J. Test. Eval.*, Vol. 16, 1988, pp. 555–557.

[25] Wu, S. X., Mai, Y. W., and Cotterell, B., "Plastic η-Factor of Fracture Specimens with Deep and Shallow Cracks," *Int. J. Fract.*, Vol. 45, 1990, pp. 1–18.

[26] Underwood, J. H., Troiano, E. J., and Abbott, R. T., "Simpler J_{IC} Test and data Analysis Procedures for High-Strength Steels," *Fracture Mechanics, 24th Symposium*, ASTM STP 1207, ASTM International, West Conshohocken, PA, 1994, pp. 410–421.

[27] Joyce, J. A., "J-Resistance Curve Testing of Short Crack Bend Specimens Using Unloading
Compliance," *Fracture Mechanics: 22nd Symposium*, ASTM STP 1131, ASTM International, West Conshohocken, PA, Vol. I, 1992, pp. 904–924.

[28] Zhu, X. K. and Joyce, J. A., "J-Resistance Curve Testing of HY80 Steel Using SE(B) Specimens and Normalization Method," *Eng. Fract. Mech.*, Vol. 74, 2007, pp. 2263–2281.

[29] Joyce, J. A., Hackett, E. M., and Roe, C., "Effect of Crack Depth and Mode of Loading on the *J-R* Curve Behavior of a High-Strength Steel," *Constraint Effects in Fracture*, ASTM STP 1171, ASTM International, West Conshohocken, PA, 1993, pp. 239–263.

[30] Joyce, J. A. and Link, R. E., "Application of Two Parameter Elastic-Plastic Fracture Mechanics to Analysis of Structures," *Eng. Fract. Mech.*, Vol. 57, 1997, pp. 431–446.

ASTM Special Technical Publication, Vol. 5, No. 6
Paper ID JAI101550
Available online at www.astm.org

Xin Wang[1]

On the Quantification of the Constraint Effect Along a Three-Dimensional Crack Front

ABSTRACT: In this paper we examined the characterization of constraint effects for surface cracked plates under uniaxial and biaxial tension loadings. First, three-dimensional (3D) modified boundary layer analyses were conducted using the finite element method to study the constraint effect at a typical 3D crack front. The analyses were carried out using small geometry change formulation and deformation plasticity material model. Elastic-plastic crack front stress fields at a constant J and various T-stress levels were obtained. Three-dimensional elastic-plastic analyses were performed for semi-circular surface cracks in a finite thickness plate, under remote uniaxial and biaxial tension loading conditions. In topological planes perpendicular to the crack fronts, the crack stress fields were obtained. Then, J-Q and J-T two-parameter approaches are used in characterizing the elastic-plastic crack-tip stress fields along the 3D crack front. It is found that the J-Q characterization provides good estimate for the constraint effect for crack-tip stress fields. Reasonable agreements are achieved between the T-stress based Q-factors and the Q-factors obtained from finite element analysis.

KEYWORDS: elastic-plastic fracture mechanics, constraint effects, T-stress, Q-factors, surface cracked plate, biaxial loading

---

Manuscript received November 22, 2007; accepted for publication May 2, 2008; published online June 2008.
[1] Associate Professor, Department of Mechanical and Aerospace Engineering, Carleton University, Ottawa, Ontario, Canada,
K1S 5B6.

Citation: Wang, X., "On the Quantification of the Constraint Effect Along a Three-Dimensional Crack Front," *J. ASTM Intl.*, Vol. 5, No. 6. DOI10.1520/JAI101550. Available online at www.astm.org. Also included in JAI Special Issue STP 1508, *Fatigue and Fracture Mechanics: 36th Volume*, R. W. Neu, K. R. W. Wallin, and S. R. Thompson, guest editors, ASTM International, West Conshohocken, PA, 2009, pp. 87-102.

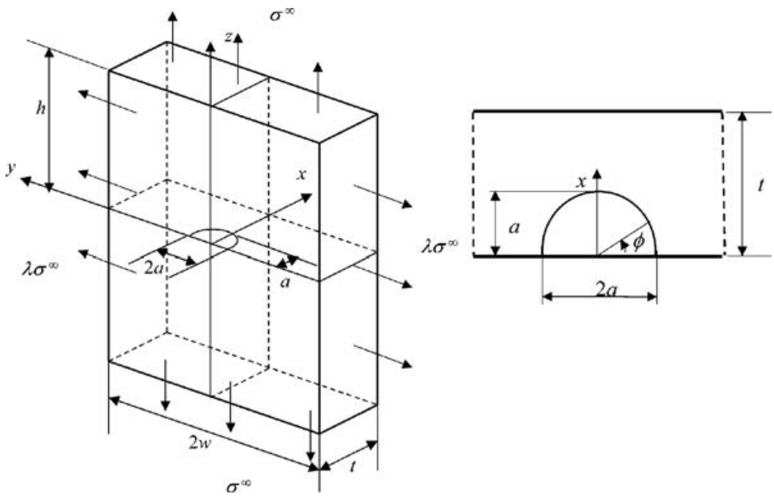

FIG. 1—*Surface cracked plate under biaxial loading; λ is the biaxial ratio.*

Introduction

It has been well established that elastic-plastic fracture mechanics using the J-integral works well only for crack-tip stress/strain fields that are under high constraint conditions [1,2]. For low constraint conditions, an additional parameter is required to quantify the constraint effects. Significant efforts and progress have been made in the past 15 years in quantifying the effect of constraint on fracture using a two-parameter methodology. In this methodology, the first parameter measures the degree of crack-tip deformation, as characterized by J (or equivalently crack-tip opening displacement). The second parameter characterizes the degree of crack-tip constraint. The most commonly used second parameters are T-stress, Q-factor, and A_2-term, corresponding to the J-T, J-Q, and J-A_2 characterizations [1–3]. It has been shown that two-parameter approaches provide effective characterization of plane-strain elastic-plastic crack-tip fields in a variety of crack configurations and loading conditions. Recently developed life assessment and structural integrity procedures have incorporated frameworks that including the constraint effect [4].

However, most of the developments have been based on the analyses using two-dimensional (2D) plane-strain models. The understanding of constraint effects in three-dimensional crack configurations, typically encountered in engineering practice, and the corresponding two-parameter characterization is still quite limited. In many 3D crack geometry configurations and loading conditions, the crack front conditions could deviate from the plane-strain conditions and both the *in-plane* (perpendicular to the crack front) and the *out-of-plane* (parallel to the crack front) constraint effects must be properly accounted for. For example, surface cracks in nuclear pressure vessels experience complex biaxial stress states under pressurized thermal shock conditions. Figure 1 shows a surface cracked plate under biaxial loading conditions, which presents a good model for these situations. In these cases, both in-plane and out-of-plane conditions will play important roles at the crack-tip stress fields. Therefore, the applicability of the two-parameter characterization needs to be further studied. Several experimental and numerical research programs have been conducted to investigate biaxial loading effects [5,6]. It is necessary to carry out additional detailed numerical analyses to investigate the crack-tip stress fields along a 3D crack front under both uniaxial and biaxial loading conditions. Based on these analyses, the two-parameter quantifications of the stress fields can be assessed.

In this paper, we focus on the *J-Q* and *J-T* two-parameter approaches for 3D crack configurations. First, three-dimensional modified boundary layer (MBL) analyses were conducted using the finite element method to study the constraint effect at a typical 3D crack front. The analyses were carried out using small geometry change formulation and deformation plasticity material model. Elastic-plastic crack front stress fields at a constant J and various T-stress levels were then obtained. Three-dimensional elastic-plastic analyses were then performed for semi-circular surface cracks in a finite thickness plate, under remote uniaxial and biaxial tension loading conditions. In topological planes perpendicular to the crack fronts, the crack stress fields were obtained and assessed. Then, *J-Q* and *J-T* two parameter approaches are used in characterizing the elastic-plastic crack-tip stress fields along the 3D crack front.

Theoretical Background

The elastic T-stress, the second term of the asymptotic series [7] for the stress field in linear elastic material, has been used to characterize the constraint (see [1,8]). It has also been shown in [2] that a two-parameter description, using J and a constraint parameter Q, fully characterizes the near tip stress and strain states in wide range of crack geometries. The parameter Q is determined from a finite element analysis and is the difference between the actual hoop stress and reference hoop stress. In this section, the *J-T* and *J-Q* characterizations of crack-tip stress fields are summarized.

J-T and J-Q Theories

In both *J-T* and *J-Q* theories, the plane-strain crack-tip stress field is constructed using the modified boundary layer formulation in which the remote tractions are given by the first two terms of the Williams series expansion solution under plane-strain conditions [7]:

$$\sigma_{ij} = \frac{K_I}{\sqrt{2\pi r}}\begin{bmatrix} f_{11}(\theta) & f_{12}(\theta) & 0 \\ f_{21}(\theta) & f_{22}(\theta) & 0 \\ 0 & 0 & f_{33}(\theta) \end{bmatrix} + \begin{bmatrix} T & 0 & 0 \\ 0 & 0 & 0 \\ 0 & 0 & \nu T \end{bmatrix} \tag{1}$$

Here, r and θ are polar coordinates centered at the crack tip with $\theta = 0$ corresponding to a line ahead of the crack and normal to the crack front, shown in Fig. 2. K_{I} is the Mode I stress intensity factor of the crack. The term T is the T-stress, and ν is the Poisson's ratio.

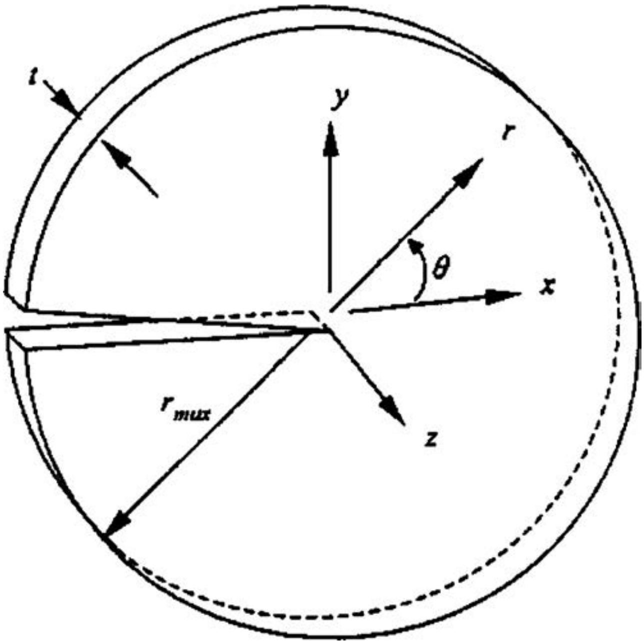

FIG. 2—*Three-dimensional modified boundary layer model.*

Fields of different crack tip stress triaxialities can be induced by applying different combination of K and T in an elastic-plastic finite element analysis, the boundary layer analysis. These fields can be organized into a family of crack-tip stress fields parametrized by

$$\sigma_{ij} = \sigma_0 \tilde{f}_{ij}\left(\frac{r}{J/\sigma_0}, \theta; \frac{T}{\sigma_0}\right) \tag{2}$$

That is, the parameter T/σ_0 provides a convenient means to investigate the constraint effect. It has been shown that this method can be used to quantify the elastic-plastic crack-tip stress fields for a wide range of crack geometries under small scale loading and contained loading conditions (see [1,8]).

However, it has been realized that the results of Eq 2 cannot be applied for large scale yielding conditions since the elastic solution of Eq 1 will not be valid under those loading conditions. Recognizing this limitation, O'Dowd and Shih [2] identified the family of stress fields by the parameter Q, which arises in the plasticity analysis. It can be written as

$$\sigma_{ij} = \sigma_0 g_{ij}\left(\frac{r}{J/\sigma_0}, \theta; Q\right) \tag{3}$$

The function of g_{ij} can be obtained from the modified boundary layer analysis, and the equation holds for finite width crack geometries under large yield conditions.

Through numerical and analytical analyses, the stress field represented by Eq 3 can be represented by

$$\sigma_{ij} = (\sigma_{ij})_{T=0} + Q\sigma_0\delta_{ij} \quad \text{for } |\theta| \leq \pi/2 \tag{4}$$

where δ_{ij} is the Kronecker delta. The Q-parameter can be obtained by subtracting the stress field for the $T=0$ reference state from the stress field of interest. The most commonly used definition of Q is

$$Q \equiv \frac{\sigma_{yy} - (\sigma_{yy})_{T=0}}{\sigma_0} \quad \text{at } \theta = 0 \quad \text{and} \quad \frac{r\sigma_0}{J} = 2 \tag{5}$$

where σ_0 is the yield stress. For the modified boundary layer solutions, T and Q are uniquely related.

Both T- and Q-parameters have been used as constraint parameters; using these as a basis on which the resistance to fracture for different geometries can be accounted, a more realistic fracture assessment can be obtained. For example, the recently developed structural integrity assessment procedures for European industry (SINTAP [4]) have suggested procedures for failure assessments that include the constraint effect. However, most of the development has been based on analyses using 2D plane-strain models.

Three-Dimensional Aspects

It is important to realize that the J-T and J-Q theories have been developed using plane-strain stress fields. Real cracks are three dimensional and the stress state will vary along the crack front. In addition to the *in-plane* (plane perpendicular to the crack front) loading and geometry effects characterized using plane-strain models, the loading and geometry effects from *out-of-plane* (plane parallel to the crack front) need to be considered. For example, surface crack in a finite thickness plate (Fig. 1), the biaxial versus uniaxial loading influence on the constraint effect needs to consider both *in-plane* and *out-of-plane* effects.

Several researchers investigated the quantification of stress fields using J-T and J-Q theories for surface cracks in uniaxial and biaxial loading conditions [8,9]. It has been observed that under uniaxial tension and bending loading conditions, J-T characterizes the stress fields up to contained yielding conditions [8]. Dodds et al. [9] considered one surface crack geometry ($a/c=0.33$, $a/t=0.25$) and found that J-Q characterization works well for both uniaxial and biaxial loading conditions. Several experimental programs were also conducted to investigate the effect of out-of-plane loading on constraint effects [5,6]. Further studies are required to assess the validations/limitation of the constraint quantification along crack front. In the following sections, a detailed finite element analysis is conducted to assess the J-T and J-Q characterizations for surface cracks. Both uniaxial tension and biaxial tension loadings are considered.

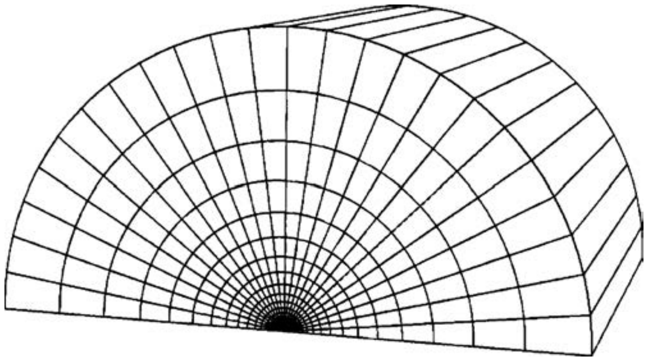

FIG. 3—*Finite element model for the modified boundary layer analysis.*

Finite Element Analysis

Three-dimensional finite element analyses are conducted to obtain the crack-tip stress fields for the modified boundary layer models and for surface cracked plate specimens. The finite element models use conventional small-strain theory. In this section, the details of the models are outlined, beginning with those aspects common to both the small-scale yielding (SSY) and surface cracked plate analyses.

Material Properties and Crack-Tip Models

The material model used is the deformation plasticity theory, Ramberg-Osgood model provided in ABAQUS [10]:

$$\frac{\varepsilon}{\varepsilon_0} = \frac{\sigma}{\sigma_0} + \alpha\left(\frac{\sigma}{\sigma_0}\right)^n \tag{6}$$

where α is a material constant, n is the strain hardening exponent, σ_0 is a normalizing stress, and $\varepsilon_0 = \sigma_0/E$. For all the analyses, $\alpha = 1$, $E = 207$ GPa, $\sigma_0 = 200$ MPa, $\nu = 0.3$, and $n = 10$ were used.

The finite element analyses are made using ABAQUS, version 6.4 [10], with 20-noded isoparametric three-dimensional solid elements. At the crack tip, three-dimensional prism elements (a degenerate cube with one face collapsed) are used. The mid-side nodes are retained at the mid-side points. Initially coincident nodes along the crack front are unconstrained, which gives a $1/r$ singularity appropriate for elastic-plastic crack analysis and allows blunting deformation of the crack tip. A domain integral method is used to calculate the J-integral values at the crack tip [10].

Modified Boundary Layer Models

Figure 3 shows the finite element mesh used in modified boundary layer models analyses. A sharp crack with tip located at $r = 0$ is modeled. Symmetric boundary conditions are applied on the crack plane. Since we are analyzing a typical 3D crack front, the thickness along the z-direction is modeled to be large. The radial extent of the disk is assumed as $r_{max}=t$, where t is the disk thickness. In the plane perpendicular to the crack front (x-y plane), the element size is gradually increased with radial distance from the crack front. Forty radial elements are used with the radial length of the smallest element is about 10^{-3} of the maximum disk radius. There are 24 sectors within the angular region from 0 to π along the circumference and one-element layer through the half thickness.

The loadings are applied by displacement boundary conditions through the stress intensity factor K_I and T-stress. They are applied uniformly on the finite element model across the disk thickness at $r=r_{max}$. The values of displacement components u_x and u_y are calculated from the plane strain K_I-T stress fields represented in Eq 1:

$$u_x = \frac{K_I}{2\mu}\sqrt{\frac{r}{2\pi}}\cos\left(\frac{\theta}{2}\right)\left[\kappa - 1 + 2\sin^2\left(\frac{\theta}{2}\right)\right] + \frac{1-\nu}{2\mu}Tr\cos\theta \tag{7}$$

$$u_y = \frac{K_I}{2\mu}\sqrt{\frac{r}{2\pi}}\sin\left(\frac{\theta}{2}\right)\left[\kappa + 1 - 2\cos^2\left(\frac{\theta}{2}\right)\right] + \frac{(-\nu)}{2\mu}Tr\sin\theta \tag{8}$$

where μ is the shear modulus, ν is Poisson's ratio, $\kappa=3-4\nu$, T is the far-field T-stress, and K_I is the far-field stress intensity factor. The stress intensity factor is related to the far-field J-integral as

$$J = \frac{1-\nu^2}{E}K_I^2 \tag{9}$$

To simulate the plane-strain condition, the condition of out-of-plane displacement component, i.e., $u_z=0$, is used in the analyses. A wide range of analyses for loading of the same J and varying T/σ_0 ratio were carried out. Through these calculations, the crack-tip stress distributions parametrized by J and T are investigated.

Surface Cracked Plate

Three-dimensional finite elements are used to model the symmetric quarter of a plate containing a semi-circular surface crack. The geometry and co-ordinate system used are shown in Fig. 1. The two loading conditions, uniaxial ($\lambda=0$), and biaxial ($\lambda=1$) tension loadings, are considered. Loads are applied to the far ends of the plate (see Fig. 1). The geometry considered is $a/c=1.0$ and $a/t=0.2$, i.e., a shallow semi-circular surface crack. The h/w ratio is fixed to 1, and w/c ratio is fixed to 16 in the calculations. The large w/c ratio used is to exclude the effect from free boundary in the width direction. A typical finite element mesh is plotted in Fig. 4. A total of 18 elements are used along the crack front. The core element is divided into 30 rings of increasing size with eight elements of equal spacing of θ for each ring. The intense refinement in r is necessary to provide resolution needed for crack-tip stress characterizations.

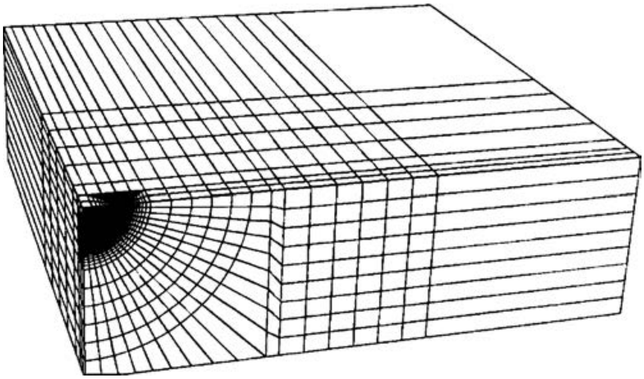

FIG. 4—*Three-dimensional finite element mesh for analyses of surface cracked plate.*

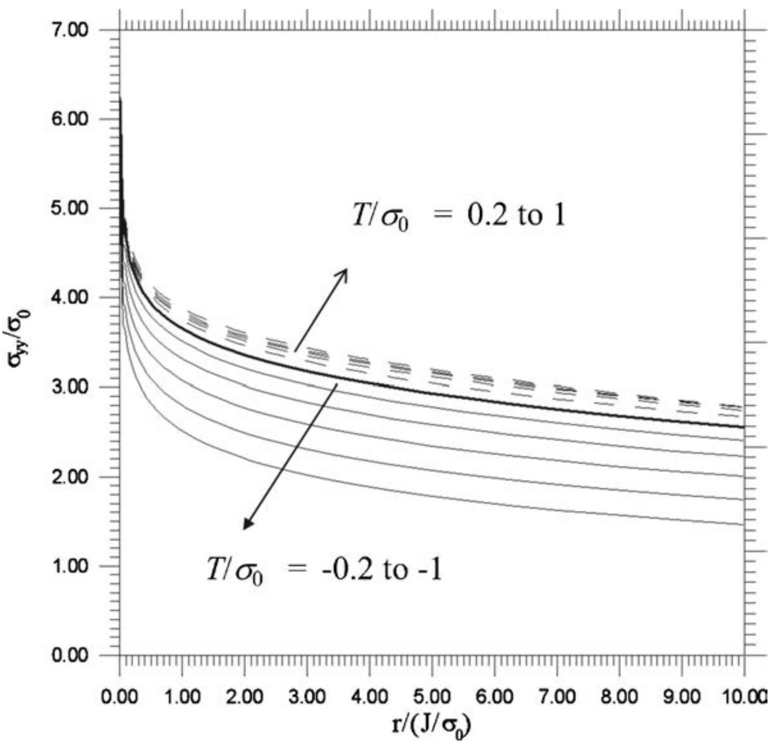

FIG. 5—*Normalized crack-opening stress distribution at various values of T/σ_0. The thick line is the results for $T/\sigma_0 = 0$.*

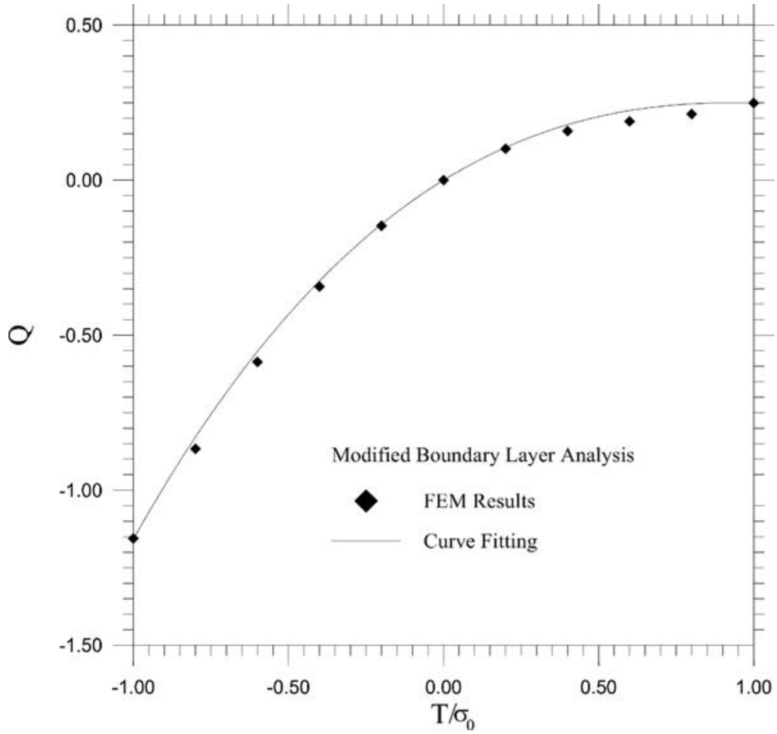

FIG. 6—*Relationship between Q and T obtained from modified boundary layer analyses.*

The loading remote level increases from small to moderate yielding conditions.

Results of Crack-Tip Stress Fields and Analysis

Modified Boundary Layer Models

Elastic-plastic crack-tip stress fields of modified boundary layer (MBL) solutions were obtained by systematically varying the T-stress level ($-1 \leq T/\sigma_0 \leq 1$) while keeping the stress intensity factor K_I (and J) constant.

Figure 5 shows the variation of normalized crack-opening stress σ_{yy} ($\theta = 0$) versus normalized distance from the crack tip under varying T/σ_0 ratios. Here the distance is normalized by J/σ_0, which is the relevant length scale around the crack tip (in the order of crack-tip opening displacement). Very similar results were obtained from early calculations using plane-strain models (see [1,2,8,9]). Substantial stress reduction is seen at negative T-stress. Moderate stress elevation is observed at positive T-stress.

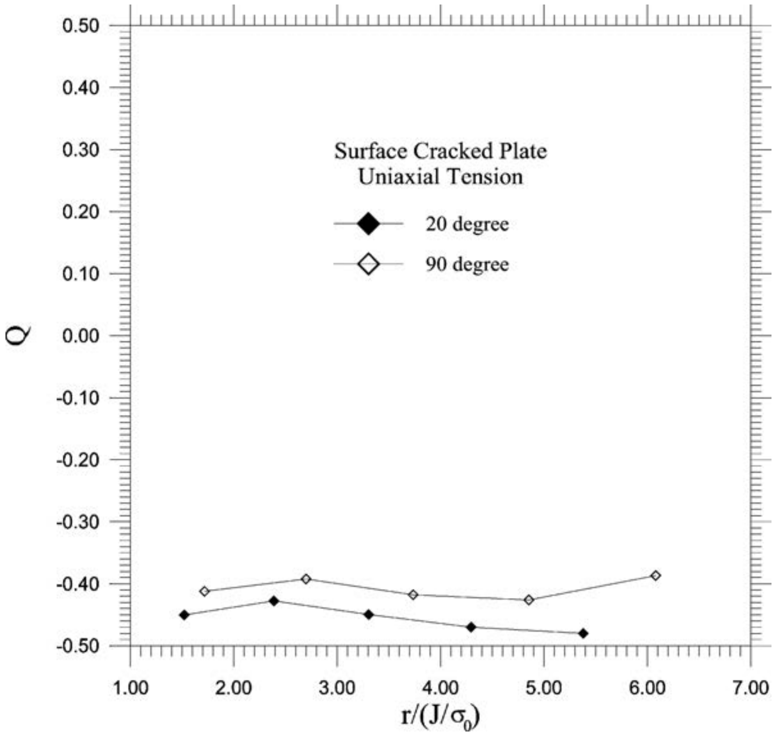

FIG. 7—*Evolution of Q-factor in surface cracked plate ahead of crack tip at* $\phi=20°$ *and 90°, for uniaxial tension.*

Based on the observations of [1], the plane-strain stress variation with respect to T-stress as shown in Fig. 5 can be fitted into the following form for any normalized distance in the range of $1 \leq J/\sigma_0 \leq 6$:

$$\sigma_{ij}^{\mathrm{MBL}} = (\sigma_{ij}^{\mathrm{SSY}})_{T=0} + A_n\left(\frac{T}{\sigma_0}\right) + B_n\left(\frac{T}{\sigma_0}\right)^2 + C_n\left(\frac{T}{\sigma_0}\right)^3 \tag{10}$$

where A_n, B_n, and C_n are constants dependent on the strain-hardening exponent n.

Based on Eq 5, the Q-factor can also be calculated from this set of data at $r/(J/\sigma_0)=2$. Comparing Eqs 10 and 5, the Q-factor is obtained:

$$Q = A_n\left(\frac{T}{\sigma_0}\right) + B_n\left(\frac{T}{\sigma_0}\right)^2 + C_n\left(\frac{T}{\sigma_0}\right)^3 \tag{11}$$

Figure 6 shows plot of Q- versus T-stress using the data from Fig. 5 at $r/(J/\sigma_0)=2$. It is clear the J-T and J-Q characterizations are equivalent for modified boundary layer models. Least-squares fitting was conducted and the constants A_n, B_n, and C_n are determined as 0.6164, −0.4549, and 0.0867, respectively, for the present strain-hardening exponent ($n=10$).

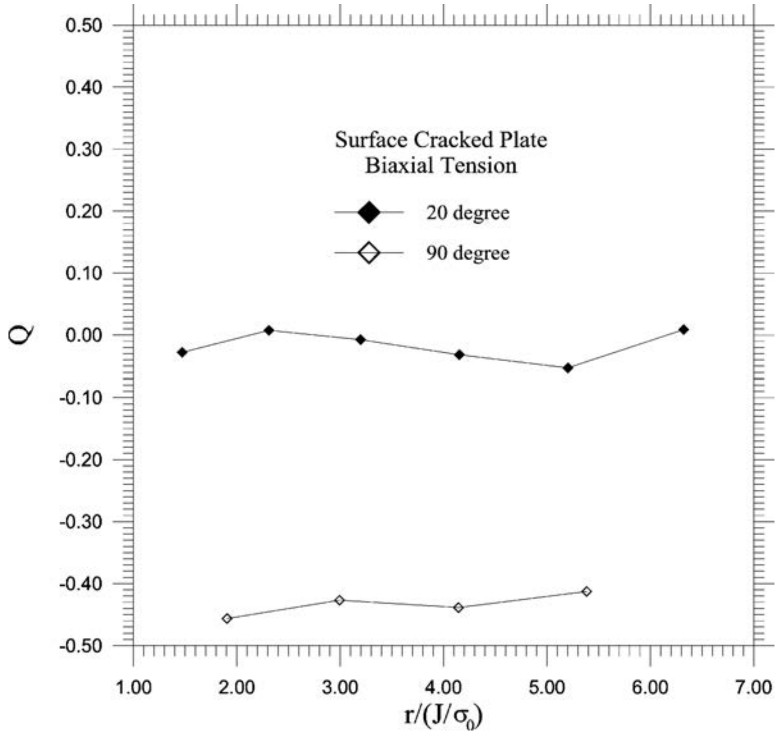

FIG. 8—*Evolution of Q-factor in surface cracked plate ahead of crack tip at* $\phi = 20°$ *and* $90°$, *for biaxial tension* ($\lambda = 1$).

Surface Cracked Plate

Uniaxial and biaxial tension loadings are applied to the surface cracked plate model, and the remote load σ^{∞} is increased up to $0.7\sigma_0$, corresponding to a moderate yielding condition. Figures 7 and 8 show the resulting Q-factor obtained along the radial lines normal to the crack front at two crack locations: $\phi = 20°$ and $90°$ for uniaxial and biaxial loadings, respectively. It can be seen that the Q-factors are nearly independent of the radial dependence, indicating the Q-theory is adequate in quantifying the constraint effects along the crack front. Note that only results for $\sigma^{\infty} = 0.7\sigma_0$ are presented here. Similar results were obtained for lower loadings. Due to the applied stress in the second direction, the biaxial loading generates a significant increase in the constraint level around the crack front near the surface point (as shown at $\phi = 20°$).

Figure 9 shows the resulting Q-factors along the crack front for both uniaxial and biaxial loadings. It is observed under both loadings, the constraint level are nearly the same around the deepest point of the crack ($\phi = 90°$). However, away from the deepest point, the constraint level increases under biaxial loading and it remains the similar level under uniaxial loading.

It is important to point out that the crack front J-integral distributions are different for uniaxial and biaxial loading conditions. Figure 10 shows the nor-

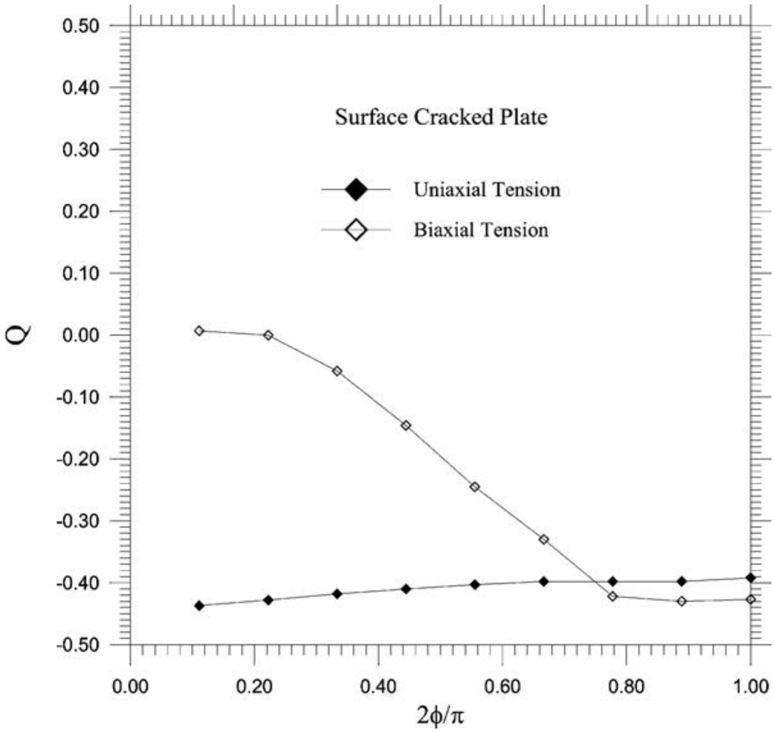

FIG. 9—*Distribution of Q-factor along the crack front for* $\sigma^{\infty} = 0.7\sigma_0$ *under uniaxial and biaxial* $(\lambda = 1)$ *loadings.*

malized fully plastic J-integral (h_1 factor) from [11] for the present crack geometry ($a/c = 1$, $a/t = 0.2$) under uniaxial and biaxial loadings ($\lambda = 1$). It is clear that under same external loading (σ^{∞}) the J-integral is generally smaller under biaxial loadings comparing to uniaxial loadings. When combined with the Q-factor solutions, we can conduct fracture assessment using the J-Q locus of the given material. The effects of the biaxial loading on the failure of surface cracked plates can be investigated extensively. It is expected that the increase of constraint level away from the deepest point under biaxial loading will play an important role in determining the load carrying capacity.

Estimation of Q Using the Elastic T-Stress

It has been shown at the beginning of this section that there is a one-to-one relationship between T and Q under small to contained yielding conditions. For the material in the present paper, the T-Q curve has been fitted by a cubic polynomial in Eq 11. This approximation method can be used to estimate the Q-factors.

Recently, T-stress solutions for a wide range of surface crack geometries in finite thickness plates were obtained from three-dimensional finite element

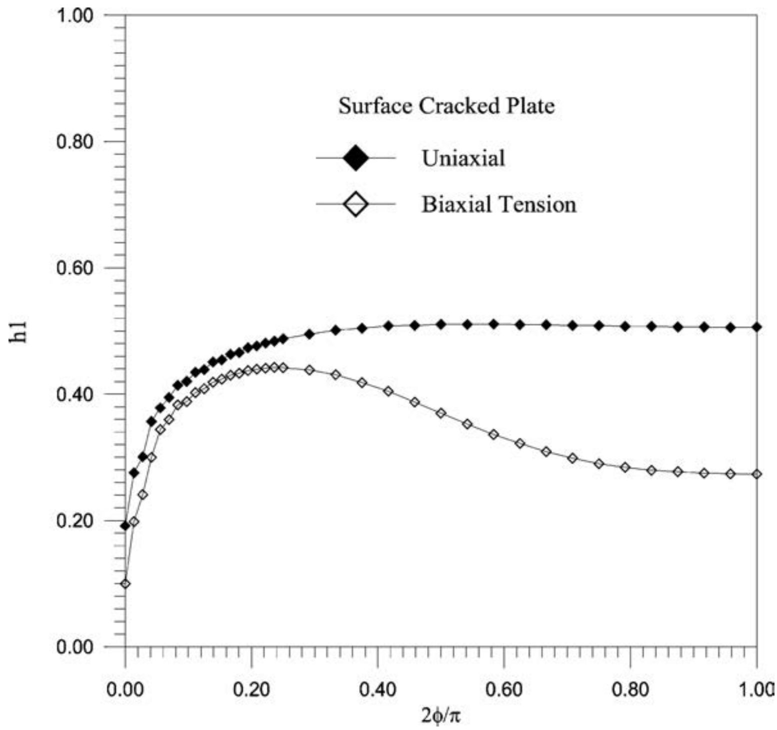

FIG. 10—*Normalized fully plastic J-integral solutions* (h_1) *for uniaxial and biaxial tension* ($\lambda=1$) *loadings from Ref. 11.* $J_p=h_1\alpha\sigma_0\varepsilon_0 a(\sigma_\infty/\sigma_0)^n$.

analyses [12–14]. The T-stress results were obtained for any point along the crack front for a wide range of ratios of a/c and a/t. The results for biaxial tension loading were presented in [14]. For biaxial tension loading of ratio λ, as shown in Fig. 1, the T-stress for general point along a semi-circular crack, represented by the parametric angle ϕ, can be calculated directly by:

$$T(\phi,\lambda) = \sigma_z V(\phi) + \sigma_z \lambda \cos^2 \phi \tag{12}$$

where $V(\phi)$ is the normalized T-stress for the uniaxial tension case, available from [12]. From Eq 12, it can be seen that the T-stress at the deepest point ($\phi=90°$), under biaxial tension is the same as the corresponding T-stress under uniaxial loading. However, for all other points along the crack front, moving away from the deepest point, the T-stress is gradually larger for the biaxial case than the values for uniaxial case. Therefore, the predicted constraint level is generally higher along the crack front for the biaxial case. Figure 11 shows the T-stress variations along the crack front for the present crack geometry ($a/c=1$, $a/t=0.2$).

For any given surface cracked plate under biaxial loading, Eq 12 can be used to calculate the corresponding T-stress distribution along the crack front, and then Eq 11 can be used to estimate the Q-factor distributions. Figure 12

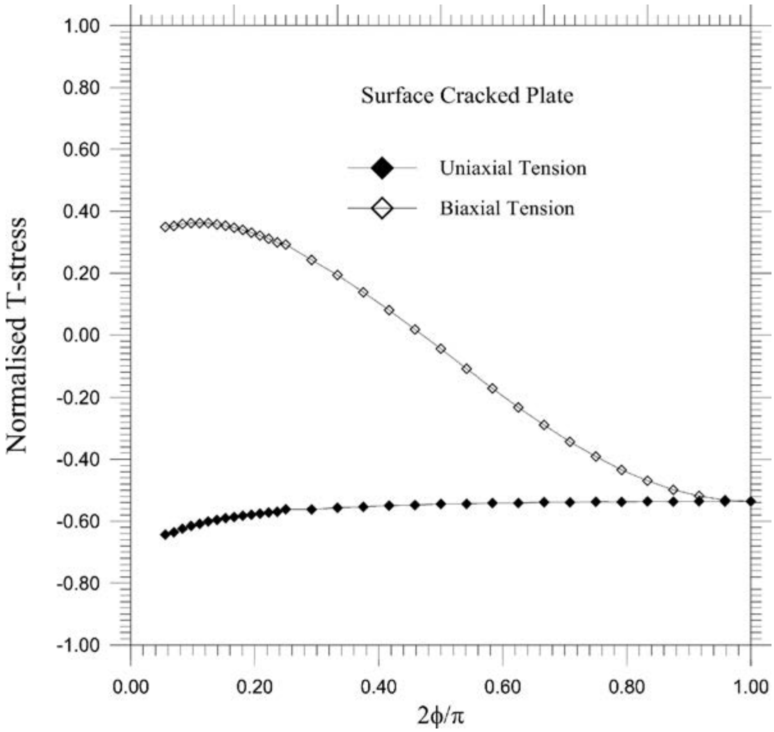

FIG. 11—*Normalized T-stress, $V = T/\sigma^{\infty}$, along the crack front for $\lambda = 0$ and 1.*

shows the comparisons between the results of T-stress based Q-factors and the Q-factors obtained from present finite element calculations. For the present load level $\sigma^{\infty} = 0.7\sigma_0$, reasonable agreements are achieved. For uniaxial loading, the T-stress based Q-factors predict the same trend and similar low level of constraint. For biaxial loading, the T-stress based Q-factors predict the constraint increase away from the deepest point as well. Therefore, the T-stress based Q-factors give reasonable estimate of the crack-tip constraint conditions, but cautions are needed since the T-stress based approach overestimates the Q-factors slightly for both uniaxial and biaxial loading conditions.

Conclusions

This paper has examined the characterization of constraint effects for surface cracked plates under uniaxial and biaxial tension loadings. Three-dimensional finite element analyses are conducted to calculate the crack-tip fields for modified boundary layer models and surface cracked plate models. Both the J-Q and J-T two-parameter characterization are considered. The following conclusions are summarized.

(1) For semi-circular cracks in finite thickness plates, the J-Q characterization provides good estimate for the constraint effect for crack-tip stress

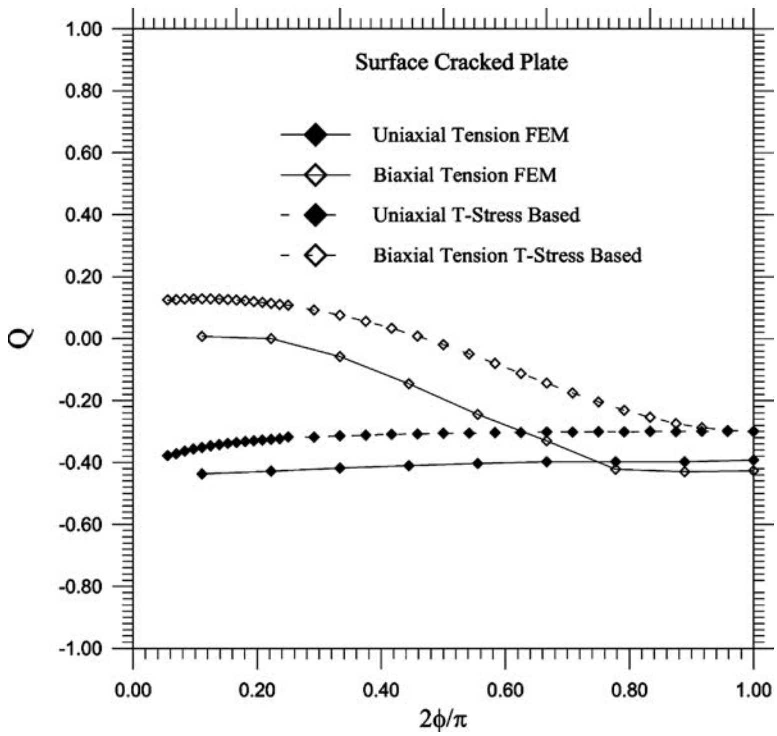

FIG. 12—*Comparison of T-stress based Q-factors and Q-factors from finite element analyses for uniaxial and biaxial* ($\lambda = 1$) *loadings.*

fields. For the crack geometry considered, it is found that under both uniaxial and biaxial loadings, the constraint level are nearly the same around the deepest point of the crack. However, away from the deepest point, the constraint level increases under biaxial loading and it remains the similar level under uniaxial loading. When combined with J-integral solutions for the corresponding loadings, constraint based fracture assessment can be conducted to investigate the biaxial loading effect.

(2) The Q-factors are also obtained using the T-stress solutions based on the T-Q relationship. It is found that reasonable agreements are achieved between the results of T-stress based Q-factors and the Q-factors obtained from finite element calculations. In other words, the J-T characterizations can be used to estimate the constraint conditions for both uniaxial and biaxial loadings. However, the T-stress based Q factor results for both uniaxial and biaxial loading should be used with caution because it overestimates the Q-factors slightly.

(3) Further studies are required to investigate the effects of higher level loads, crack aspect ratio ($a/c < 1$), and deep cracks ($a/t > 0.2$).

Acknowledgments

The author gratefully acknowledges the financial support from the Natural Sciences and Engineering Research Council (NSERC) of Canada and Ontario Centres of Excellence (OCE). Thanks also go to Hibbit, Karlsson and Sorensen, Inc. for making ABAQUS available under an academic license to Carleton University.

References

[1] Betegon, C., and Hancock, J. W., "Two-Parameter Characterization of Elastic-Plastic Crack Tip Fields," *J. Appl. Mech.*, Vol. 58, 1991, pp. 104–110.

[2] O'Dowd, N. P., and Shih, C. F., "Family of Crack Tip Fields Characterized by a Traiaxiality Parameter—I. Structure of Fields," *J. Mech. Phys. Solids*, Vol. 39, 1991, pp. 989–1015.

[3] Chao, Y. J., Yang, S., and Sutton, M. A., "On the Fracture of Solids Characterized by One or Two Parameters, Theory and Practice," *J. Mech. Phys. Solids*, Vol. 42, 1994, pp. 629–647.

[4] Ainsworth, R. A., Sattari-Far, I., Sherry, A. H., Hooton, D. G., and Hadley, I., "Methods for Including Constraint Effects Within SINTAP Procedures," *Eng. Fract. Mech.*, Vol. 67, 2000, pp. 563–571.

[5] Bass, B. R., McAfee, W. J., Williams, P. T., and Pennell, W. E., "Fracture Assessment of Shallow-Flaw Cruciform Beams Tested Under Uniaxial and Biaxial Loading Conditions," *Nucl. Eng. Des.*, Vol. 188, 1999, pp. 259–288.

[6] Lidbury, D. P. G., Sherry, A. H., Bass, B. R. et al., "Validation of Constraint-Based Methodology in Structural Integrity of Ferritic Steels for Nuclear Reactor Pressure Vessels," *Fatigue Fract. Eng. Mater. Struct.*, Vol. 29, 2006, pp. 829–849.

[7] Williams, M. L., "On the Stress Distribution at the Base of a Stationary Crack," *J. Appl. Mech.*, Vol. 24, 1957, pp. 111–114.

[8] Wang, Y. Y., "On the Two-Parameter Characterization of Elastic-Plastic Crack Front Fields in Surface Cracked Plates," in: *Constraint Effects in Fracture*, ASTM STP 1171, E. M. Hackett, K. H. Schwalbe, and R. H. Dodds, Eds., American Society for Testing and Materials, West Conshohocken, PA, 1993, pp. 120–138.

[9] Dodds, R. H., Shih, C. F., and Anderson, T. L., "Continuum and Micromechanics Treatment of Constraint in Fracture," *Int. J. Fract.*, Vol. 64, 1993, pp. 101–133.

[10] *ABAQUS Manual*, Version 6.6, Hibbitt, Karlsson & Sorensen, Inc., Pawtucket, RI, 2006.

[11] Wang, X., "Fully Plastic *J*-integral Solutions for Surface Cracked Plates Under Biaxial Loading," *Eng. Fract. Mech.*, Vol. 73, 2006, pp. 1581–1595.

[12] Wang, X., "Elastic *T*-stress Solutions for Semi-Elliptical Surface Cracks in Finite Thickness Plates," *Eng. Fract. Mech.*, Vol. 70, 2003, pp. 731–756.

[13] Wang, X., and Bell, R., "Elastic *T*-stress Solutions for Semi-Elliptical Surface Cracks in Finite Thickness Plates Subject to Non-Uniform Stress Distributions," *Eng. Fract. Mech.*, Vol. 71, 2004, pp. 1477–1496.

[14] Wang, X., and Yu, X., "On the Constraint-Based Failure Assessment of Surface Cracked Plates Under Biaxial Loading," *J. ASTM Int.*, Vol. 2, 2005 ID JAI12038. Also in *Fatigue and Fracture 34th Volume*, ASTM STP 1461, S. R. Daniewicz, J. C. Newman, K. H. Schwalbe, Eds., American Society for Testing and Materials, West Conshohocken, PA, 2005, pp. 245–259.

RESIDUAL STRESS EFFECTS ON FATIGUE

ASTM Special Technical Publication, Vol. 5, No. 8
Paper ID JAI101610
Available online at www.astm.org

Patrick J. Golden,[1] *Dennis Buchanan,*[2] *and Sam Naboulsi*[3]

Influence of Residual Stresses on Fretting Fatigue Life Prediction in Ti-6Al-4V

ABSTRACT: The objective of this work was to evaluate life prediction methodologies involving fretting fatigue of turbine engine materials with advanced surface treatments. Fretting fatigue tests were performed on Ti-6Al-4V dovetail specimens with and without advanced surface treatments. These tests were representative of the conditions found in a turbine engine blade to disk attachment. Laser shock processing and low plasticity burnishing have been shown to produce deep compressive residual stresses with relatively little cold work. Testing showed these advanced surface treatments improved fretting fatigue strength by approximately 50 %. In addition to advanced surface treatments, several specimens were also coated with diamond-like carbon applied through a nonline-of-sight process capable of coating small dovetail slots in an engine disk. Testing with this coating alone and combined with advanced surface treatments also significantly improved fretting fatigue strength due to a decreased coefficient of friction along with the compressive residual stresses. This work presents a mechanics based lifing analysis of these tests that takes into account the local plasticity and the redistribution of residual stresses due to the contact loading. The use of superposition of the residual stresses into the contact stress analysis results in unconservative crack growth life predictions. Finite element analyses were conducted to predict the redistribution of residual stresses due to the contact loading. The

Manuscript received December 4, 2007; accepted for publication June 30, 2008; published online July 2008.

[1] Materials and Manufacturing Directorate, Air Force Research Laboratory, Wright-Patterson AFB, OH.
[2] Structural Integrity Division, University of Dayton Research Institute, Dayton, OH.
[3] The Institute for Computational Engineering and Sciences, The University of Texas, Austin, TX.

Citation: Golden, P. J., Buchanan, D., and Naboulsi, S., "Influence of Residual Stresses on Fretting Fatigue Life Prediction in Ti-6Al-4V," *J. ASTM Intl.*, Vol. 5, No. 8. DOI10.1520/JAI101610. Available online at www.astm.org. Also included in JAI Special Issue STP 1508, *Fatigue and Fracture Mechanics: 36th Volume,* R. W. Neu, K. R. W. Wallin, and S. R. Thompson, guest editors, ASTM International, West Conshohocken, PA, 2009, pp. 105-121.

redistributed residual stresses were used to make improved crack growth life predictions when possible. The results showed very little redistribution of residual stresses for the advanced surface treatments, however, a significant change in shot peened residual stress gradients was predicted.

KEYWORDS: fretting, fatigue, crack growth, surface treatments, residual stress

Introduction

Fretting occurs in many aerospace components such as the dovetail attachments of turbine blades and disks in turbofan engines or lap joints in aircraft structures. Designers often seek palliatives such as coatings or shot-peening to reduce the negative effects of fretting on the life of a component. Typically, however, the positive effect of these palliatives is not taken into account in the design life of a component. Instead it may be treated as an additional margin of safety. As the retirement age of aerospace vehicles continues to grow, the expected maintenance cost and burden also continues to increase. This drives the need for new palliatives and design methods that will allow safe increases in component usage before repair or replacement. One option is advanced surface treatments such as laser shock processing (LSP) or low plasticity burnishing (LPB). These methods of inducing a layer of compressive residual stresses on a component, although more costly than shot-peening, may allow designers to use improved analysis methods to take credit for residual stresses in design as proposed by Prevey and Jayaraman [1], for example.

In order to take design credit for a process such as LSP or LPB it must be satisfactorily shown that the compressive residual stresses are sufficiently retained throughout the life of the component. Thermal relaxation, plastic deformation, or other sources of damage such as fretting or foreign object damage could all potentially reduce or even reverse the effects of the compressive residual stresses. It is known that plasticity in fretting contacts plays an important role in the understanding of crack nucleation and propagation of cracks. Waterhouse [2] observed that many antifretting palliatives may be disrupted by plastic deformations. Plastic deformation in the substrate of a coated material, for example, may result in a loss of coating adhesion and effectiveness. Intentionally induced compressive residual stresses by methods such as shot-peening could also be disrupted by this plasticity.

Martinez et al. have also proposed that the loss of residual stresses in a fretted material may be an indicator to fatigue damage [3]. Martinez et al. tested shot-peened fretting samples, some of which were interrupted prior to failure, and made an array of residual stress measurements on the surface across the fretting scar. The results showed that the compressive residual stresses relaxed in the fretted region. It appears that this may be a different mechanism than the local plastic zone being proposed in the current work since the relaxation appears over a wide region. Instead, accumulation of damage on the surface (microcracking, scarring, etc.) may be responsible for the relaxation of residual stresses throughout the fretted region. Since only surface residual stress measurements were taken, it is not clear if this was only a surface phenomenon or if relaxation extended into the depth.

In previous work, the current authors applied a mechanics based life prediction analysis to a series of fretting fatigue tests that included bare specimens, coated specimens, and specimens treated with LSP or LPB [4]. The conclusion of this work was that mechanics based predictions were accurate and conservative for bare Ti-6Al-4V specimens and also for coated specimens meaning that all of the predicted lives to failure were shorter than the actual lives to failure. In the LSP and LPB treated specimens, the fracture mechanics analysis predicted in all cases tested that short cracks would grow into a decreasing stress intensity factor range until crack arrest occurred. Thus, no specimen failures were predicted. In reality, several of the test specimens with LSP and LPB did fail, therefore, the predictions were not conservative. The objective of this paper was to investigate the possibility that redistribution of compressive residual stresses due to plastic deformations contributed to the nonconservative failure predictions in the LSP and LPB treated fretting specimens. A hypothetical shot-peened (SP) specimen was also analyzed. The influence of different levels of compressive residual stress retention was also studied. The approach was to conduct elastic-plastic contact finite element method (FEM) analyses to determine the level of plasticity and residual stress redistribution in the fretting experiments.

Experiments

The material used in this study was a Ti-6Al-4V alloy from the United States Air Force National High Cycle Fatigue program [5]. The material was $\alpha+\beta$ forged then solution treated and overaged at 932°C for 75 min, fan cooled, and mill annealed at 704°C for 2 h. The resulting microstructure was approximately 60 % primary α and 40 % transformed β. All of the test specimens were machined from this material. The elastic modulus was 116 GPa and the 0.2 % offset yield stress was 930 MPa. The ultimate tensile strength was 980 MPa. Monotonic and cyclic stress-strain curve fits were generated for this material and are plotted in Fig. 1. The cyclic stress-strain curve were fit to the stress-strain hysteresis loops from multiple strain controlled low cycle fatigue tests measured at the half life of the specimens. These stress-strain curves will be used in the elastic-plastic contact models described later.

A photograph of the dovetail fretting experimental setup is shown in Fig. 2. Development and testing with this fixture has been discussed previously by Conner and Nicholas [6] and Golden and Nicholas [7]. The steel fixture worked by pulling together a dovetail shaped test specimen and two fretting pads that had precisely machined surface profiles. Several surface profiles have been tested including cylindrical and flat with rounded edges with varying dimensions. All of the fretting pads in this work were machined to a flat with rounded edges profile with a 3 mm flat and 3 mm radii. There were several key features to this setup that separate it from other fretting fatigue apparatus. First, the specimen was dovetail shaped which resulted in cyclic loading of both the normal P and shear Q contact forces rather than only cyclic Q. Second, the

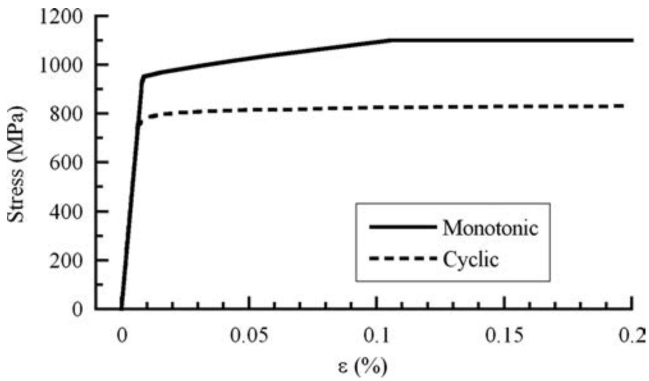

FIG. 1—*Monotonic and cyclic stress versus strain curves used in the finite element analysis.*

fixture was designed with replaceable fretting pads. Each experiment only required replacement of the pads rather than the entire fixture as with other dovetail fatigue experiments [8]. Finally, it was not possible to obtain direct measurement of the contact forces *P* and *Q* unlike many other fretting fatigue test setups that do allow direct measurement of the contact forces through

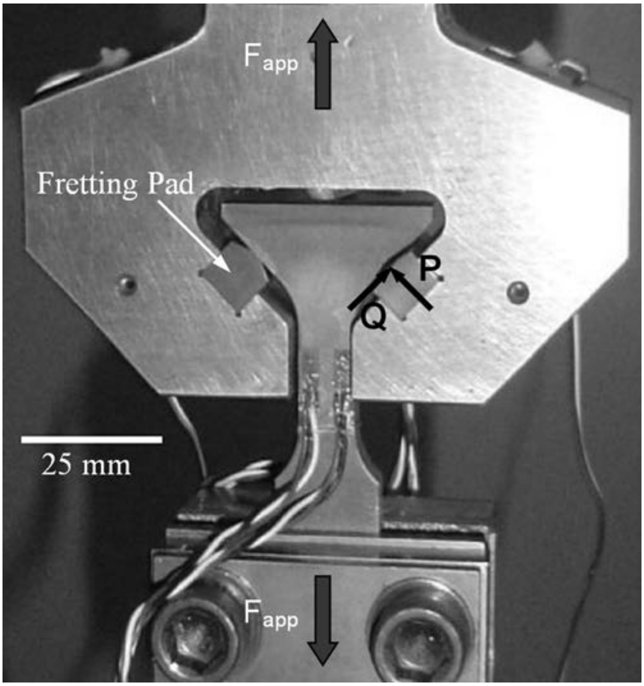

FIG. 2—*Photograph of the dovetail fretting fatigue setup.*

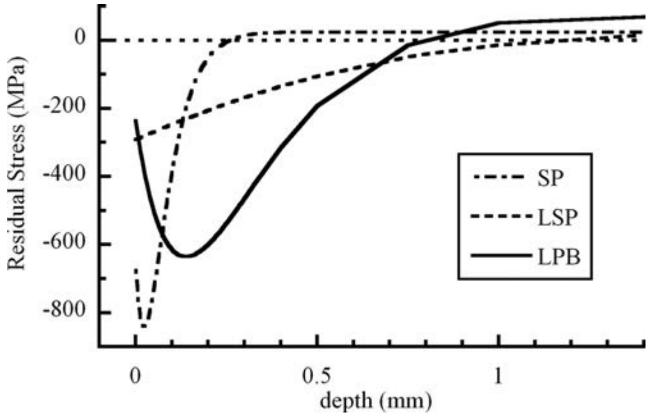

FIG. 3—*Residual stress profile curve fits. The LSP and LPB curves were fit to measurements made in this work. The SP curve is fit to typical* 6–8 A *intensity peening data on Ti-6Al-4V.*

placement of load cells in the load path [9]. Instrumentation of the contact loads, however, was critical to allow validation of life prediction methods. Instrumentation was achieved through the addition of strain gages to the fixture in location of peak strain. Calibration of the contact forces to the strain gages was achieved through finite element modeling of the fixture as discussed in Golden and Nicholas [7].

The focus of this effort was to test and model the effects of coatings and residual stress surface treatments on dovetail fretting. LSP and LPB were each applied to six specimens in the regions of contact. Half of these and an additional five untreated specimen were also coated with diamond-like carbon (DLC). Several specimens were sent post-test for destructive measurement of the in-depth residual stresses. The measurements were made using x-ray diffraction in a region of the specimens just outside of the fretting scars. In-depth measurements were made by layer removal with electropolishing. The results were shown previously in Golden et al. [10] and curve fits of those results are plotted in Fig. 3. Also plotted is a typical residual stress profile of a shot-peened Ti-6Al-4V specimen peened with steel shot at 6–8 A intensity. These profiles were used in the stress analysis and life prediction described later. Note that the shot-peening profile has a significantly higher magnitude than both the LSP or LPB profiles, but the LSP and LPB processes provide a much deeper layer of compressive residual stress.

Room temperature tests at a load ratio $R=0.1$ were conducted at several load levels on bare Ti-6Al-4V, LSP treated, LPB treated, DLC coated, LSP +DLC, and LPB+DLC. The results were plotted in Fig. 4 and have been described previously in Golden et al. [10]. Both the residual stress treated specimens and the DLC treated specimens each extend the life by an order of magnitude. When DLC was combined with LSP or LPB none of the specimens were able to be failed. The fatigue load limit of the fixture was exceeded before failure of the specimens could occur. The contact loads and average friction

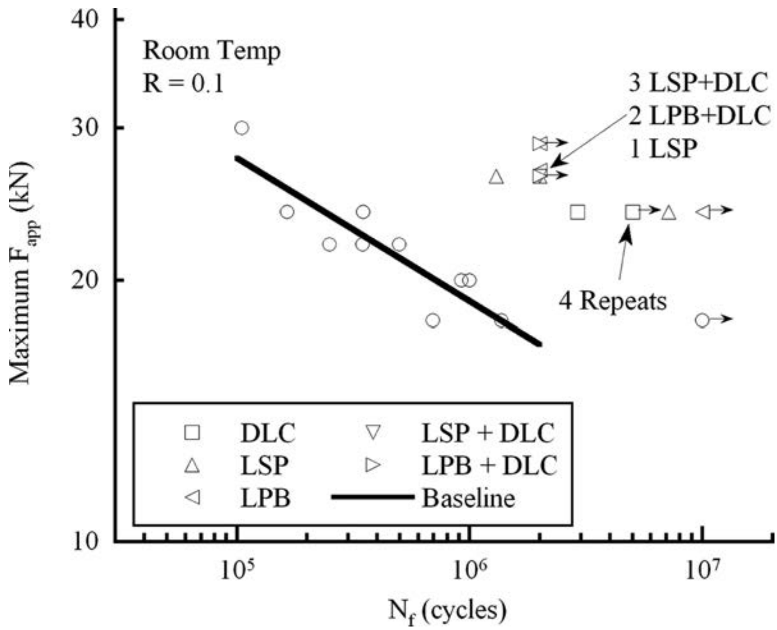

FIG. 4—*Results of the dovetail fretting fatigue tests with advanced surface treatments and diamond like carbon coating.*

coefficients for each of these tests were measured and will be used in the stress analysis and life prediction described below.

Analytical Procedures

Several different analysis procedures have been applied in this work. The overall objective of this research was to develop and demonstrate effective deterministic analysis methods that will allow accurate life prediction in a dovetail geometry. These methods accounted for changes in friction and residual stress due to surface treatments and processing. The mechanics based approach taken was dependent on the quality of the contact force measurement or prediction as well as the stress analysis tools. In this study, the contact forces were determined experimentally as discussed above. In general, however, the contact forces and the bulk stresses would be predicted from the results of a global FEM model. In either case, the local contact stresses were then calculated using the contact geometry and forces as input to a singular integral equation (SIE) solution (described below). In the case of applied surface treatments and/or local plasticity the residual stresses must be superimposed with the applied stresses. The effects of redistribution of residual stresses were a focus of the elastic-plastic contact modeling conducted in this work. Once the complete stress field had been calculated, standard nucleation and fracture mechanics life prediction methods were applied.

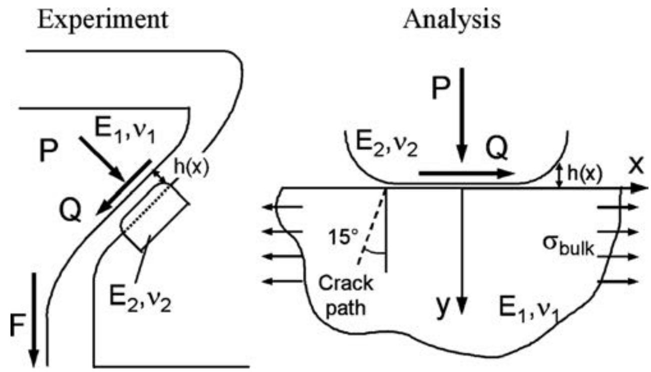

FIG. 5—*Schematic of an equivalent geometric representation of an actual dovetail used in the singular integral equation solution to the contact problem.*

Figure 5 shows two schematics that represent the contact in the current experimental setup and the equivalent geometry used in the contact mechanics analysis. In the experiment, the dovetail specimen was pulled down into the contact pad, by force F. This results in the reaction forces P and Q and moment M (not shown) between the specimen and pad. The contact pad had a surface profile that was described by $h(x)$. In this case, the profile was a 3 mm flat with 3 mm radii at the edges of contact. In general, the configuration could have two materials; the specimen $(E_1, \nu_1))$ and the pad (E_2, ν_2), but in this study the materials were both Ti-6Al-4V. Although the contact forces were known from the experiment, the bulk stresses in the contact region were not. Prior studies [11,12] have described a method to extract the bulk stress from the FEM analysis in the contact region of a dovetail configuration. In short, the bulk stress was the FEM stress solution minus the contact stresses. Once the contact stresses were determined analytically as described below, they were subtracted from the FEM stress results to obtain the bulk stress. The reason a FEM and a SIE analytical solution were both used was that each had an advantage and a disadvantage in terms of accuracy and efficiency. The FEM solution accounted for all of the specimen or component geometric features and boundary conditions, whereas the SIE solution did not. The SIE solution was very fast and accurate at obtaining the very steep edge of contact stress gradient, whereas the FEM solution had long computational times and it was often not possible to obtain a converged stress solution at the edge of contact, particularly in three-dimensional models.

The second schematic in Fig. 5 shows the configuration used in the SIE analysis. A MATLAB script named CAPRI was used to solve the SIE that describes the contact between two similar materials with a gap function $h(x)$. CAPRI was written at Purdue University to calculate the normal and shear contact tractions and the subsurface stresses for an arbitrary indenter that is pressed into a semi-infinite body [13]. The influence of the bulk stress plays a role in the calculation of the contact tractions, but must be a known input and is not an output of the analysis. Thus, there is often a need for a FEM analysis to deter-

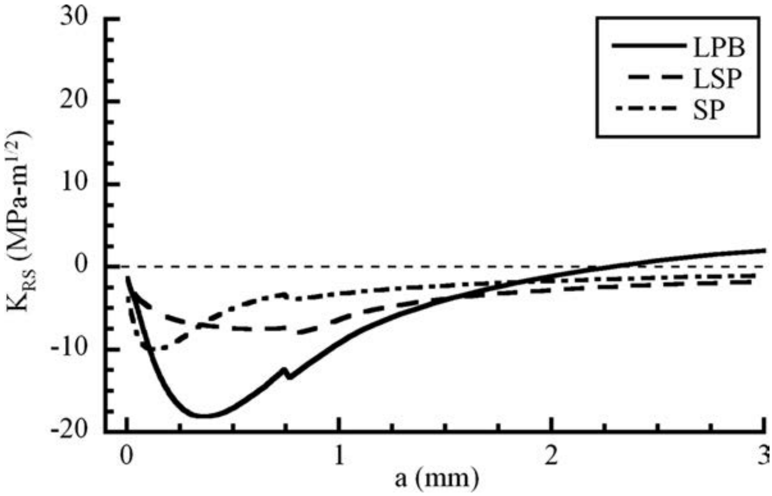

FIG. 6—*Stress intensity factor due to residual stress gradients.*

mine the bulk stress as described above. Once the SIE contact stress analysis including the bulk stress is complete, stress gradients can be extracted along the expected crack growth paths as shown in Fig. 5.

After the stress gradients were extracted the next step was to calculate nucleation and fracture mechanics stress intensity factor K. Nucleation was not the focus of this effort, however, an equivalent stress methodology to calculate nucleation life based on surface stresses had been applied in prior work [14]. This model includes the multiaxial components of stress and used a stressed area approach to account for the local stress peak at the edge of contact. K solutions were calculated using the weight function methodology. Mode I surface crack and through crack weight function K solutions were written in MATLAB to efficiently work with the output of CAPRI [11,15,16]. Negative K_I values were allowed to be calculated in the case of the residual stress gradients and were plotted in Fig. 6 and referred to as K_{RS}. Clearly negative values of K_{RS} are not real. They are only being used in combination with K_I calculated from the applied stresses to account for the change in stress state in the body and its affect on the crack due to the residual stresses. Superposition of K_{RS} with the maximum and minimum applied K_I resulted in a total ΔK_I that had a shift in R that was also a function of crack length. An effective stress intensity factor range, ΔK_{eff}, was then used to account for this changing R as calculated in Eq 1. Figure 7 is a plot of ΔK_{eff} versus crack size. Here, m is an exponent fit from crack growth data at R values of −1, 0.1, 0.5, and 0.8 [5] and equals 0.72 for positive R and 0.275 for negative R. The crack growth rate and propagation life was then calculated from ΔK_{eff} using the sigmoidal crack growth law shown in Eq 2. Here B, P, Q, d, K_{th}, and K_c were constants fit to the crack growth data with values of −18.1, 3.71, 0.235, −0.0066, 4.21 MPa$\sqrt{m}$, and 66 MPa$\sqrt{m}$, respectively [5]. The crack growth rate da/dN data were in units of m/cycle

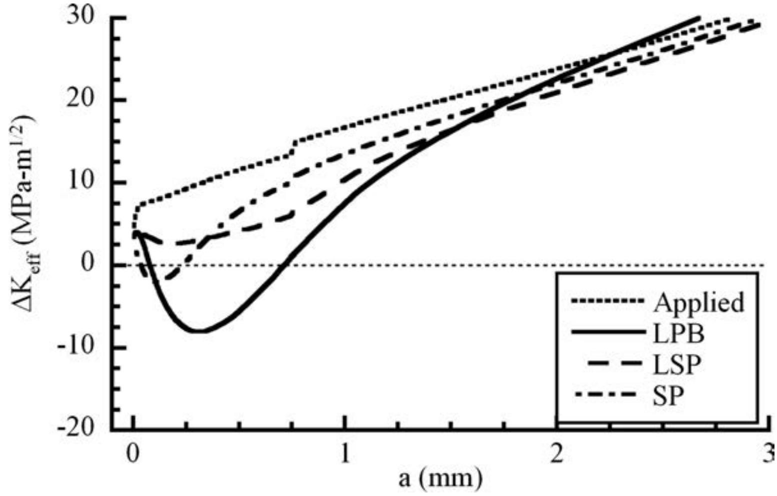

FIG. 7—*Stress intensity factor range for combined applied load and residual stress.*

$$\Delta K_{\mathrm{eff}} = K_{\max}(1 - R)^{m}, \tag{1}$$

$$\frac{da}{dN} = 0.0254 \times \exp^{B}\left(\frac{\Delta K_{\mathrm{eff}}}{K_{\mathrm{th}}}\right)^{P}\left[\ln\left(\frac{\Delta K_{\mathrm{eff}}}{K_{\mathrm{th}}}\right)\right]^{Q}\left[\ln\left(\frac{K_c}{\Delta K_{\mathrm{eff}}}\right)\right]^{d}. \tag{2}$$

A finite element model was generated to represent the dovetail fretting fatigue experiment loading conditions and is shown in Fig. 8. A simplified geometry of a two-dimensional (2D) plate and contact pad was chosen rather than modeling the actual dovetail geometry. The maximum and minimum contact forces, P, Q, and M, from the experiments were applied to the top surface of the contact pad in a cyclic manner. Five load cycles were found to be sufficient to stabilize the elastic-plastic response. Constraints were applied to the fretting pad to distribute the applied loads and to control its rotation. The bulk stress

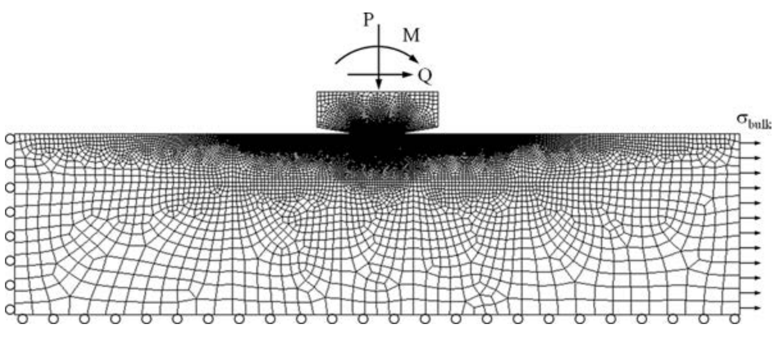

FIG. 8—*Finite element model used to represent the loading conditions in the dovetail fretting tests.*

was applied to the end of the plate, which represented the fretting specimen. The plate was 15 mm deep by 60 mm long and had roller constraints on the edges opposite the contact and bulk stress as shown in Fig. 8. The model was analyzed in ABAQUS and was meshed with 2D plane strain four-node bilinear elements. The element size in the contact region was 5 μm by 5 μm which was sufficient to capture the very high stress peaks at the edge of contact and the plastic zone that developed. The nonlinear combined isotropic/kinematic model provided in ABAQUS was used. The cyclic and monotonic stress strain curves plotted in Fig. 1 were the only data available for this analysis. The model was run using both sets of data with very little difference in results for these problems. The results shown in the following section were analyzed using the cyclic stress-strain curve.

Results and Discussion

The results of this work consist of the output of the elastic-plastic contact finite element analysis, changes in the residual stress profiles, and the resulting influence on life predictions. The life predictions in this work are focused entirely on crack propagation including short crack growth, rather than nucleation plus propagation. Prior work [17] has shown that at the end of interrupted fretting fatigue tests in Ti-6Al-4V cracks were often found very early in the expected life of the specimens. Also, nucleation life predictions on these experiments [11] have previously been shown to be on the order of 10 % of the total life or less. This was expected since the stresses at the edge of contact were typically well above yield in an elastic analysis, and then rapidly decreased. This lead to early crack nucleation followed by relatively slow early crack growth. Additionally, all of the analysis in this work was limited to mode I fracture mechanics. Again, previous analysis on these experiments [11] as well as on other fretting fatigue experiments [18] have shown that any mode II contribution to crack growth was expected to be quite small. Although the calculated value of K_{II} was significant, ΔK_{II} was not. This, however, did not imply that all cracks grew perpendicular to the surface. In fact, the experiments showed that the macroscopic cracks grew approximately 15–25° from normal in a direction away from the center of contact. This was accounted for in the fracture mechanics calculations.

In these experiments, many of the treated specimens ended as run-outs and did not fail. It was predicted from the stress analysis, nucleation model, and fracture mechanics that despite the compressive residual stresses and/or the low friction coatings that cracks would still form at the edge of contact and grow a short length before arresting. This, in fact was the case as demonstrated in Fig. 9. Fig. 9 is a scanning electron microscopy micrograph showing a crack that grew from the edge of contact in a specimen treated with LPB. The section was mounted, ground, and polished in the specimen thickness direction. The crack was nearly 100 μm deep in this cross section which was near the maximum depth found for this crack. The fracture mechanics analysis with the El Haddad short crack correction [19] for this specimen predicts crack arrest at a depth of approximately 60 μm when the full residual stress gradient is super-

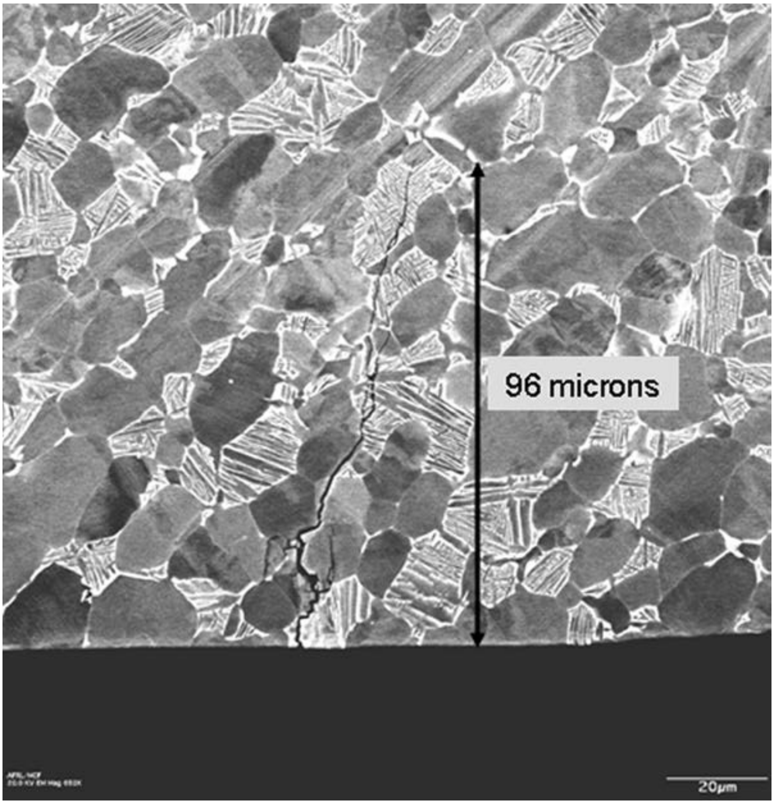

FIG. 9—*Profile of a crack located at the edge of contact found post-test in a run-out experiment that had been processed with LPB.*

imposed with the applied stress gradient. The actual crack length is longer than the predicted crack arrest which is generally consistent with the unconservative fracture mechanics life predictions for these experiments that was discussed earlier. The observation of a crack in this and other run-out specimens did, however, validate the analytical results that showed cracks can nucleate, grow, and arrest under fretting fatigue. This has been observed in run-out tests with and without residual stresses due to LSP or LPB.

The contact finite element analysis with plasticity and initial residual stress distribution was conducted for the LSP, LPB, and SP conditions. Several different loading conditions were analyzed. These load cases used minimum and maximum values of P, Q, M, and bulk stress taken directly from the experiments. They were representative of the range from the least to most severe load cases found in the actual experiments. Multiple steps of maximum and minimum load were run until the plastic zone stabilized. Five cycles was found to be sufficient. Analyses with both the cyclic and the monotonic stress-strain curves were run and compared, but since the plasticity was so localized the difference was very small. The final result of interest was the change in the initial residual

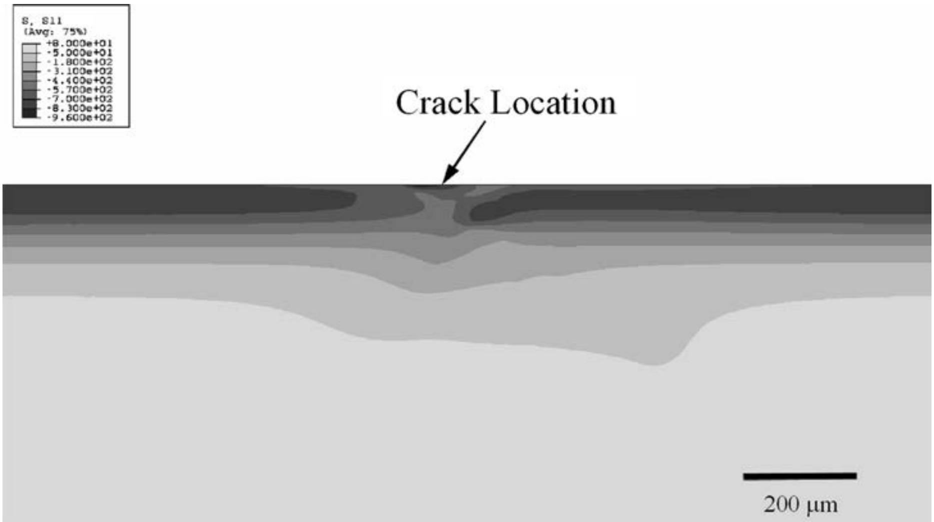

FIG. 10—*Contours of shot-peen residual stress,* σ_{xx}*, at the edge of contact after stress redistribution. Contours range from* +80 (*light*) *to* −960 MPa (*dark*) *in* 130 MPa *increments.*

stress in the model, so the final load step in the analysis was unloading to zero applied loads. Fig. 10 is an example of redistributed shot-peen residual stresses in the specimen. The fretting pad is not shown. The surface to the right of the crack location is under the contact. The component of stress shown is the normal stress parallel to the surface. The effected zone was an approximately 300×300 μm area at the edge of contact. It is observed that a significant amount of redistribution was predicted to occur in this very small volume. This could significantly affect crack growth predictions for shot peened specimens in the short crack regime. A plot of the redistributed SP residual stress is shown in Fig. 11(*a*). This stress was taken along a path from the edge of contact into the depth and was compared to the original SP residual stress gradient. The distribution peak was significantly pushed into the tensile direction for the first 70 μm. This result is important because this peak is what is responsible for leading to potential early crack arrest and providing a fatigue benefit. Fig. 11(*b*), however, shows that for the LPB treated specimens a very different redistribution of the residual stress gradient occurred. The LSP treated specimens had a nearly identical trend. Here, the near surface stresses were pushed more compressive. Slightly deeper, the residual stress becomes more tensile to compensate.

The mechanisms for the different results in SP and LSP or LPB specimens can be explained as followed. The modeling showed that the high compressive stress due to contact during the negative shear reversal can combine with the compressive residual stresses to result in a localized plastic zone as was hypothesized. This can be observed in the finite element results shown in Figs. 10 and 11(*a*). The compressive yield results in a region of residual stresses that are

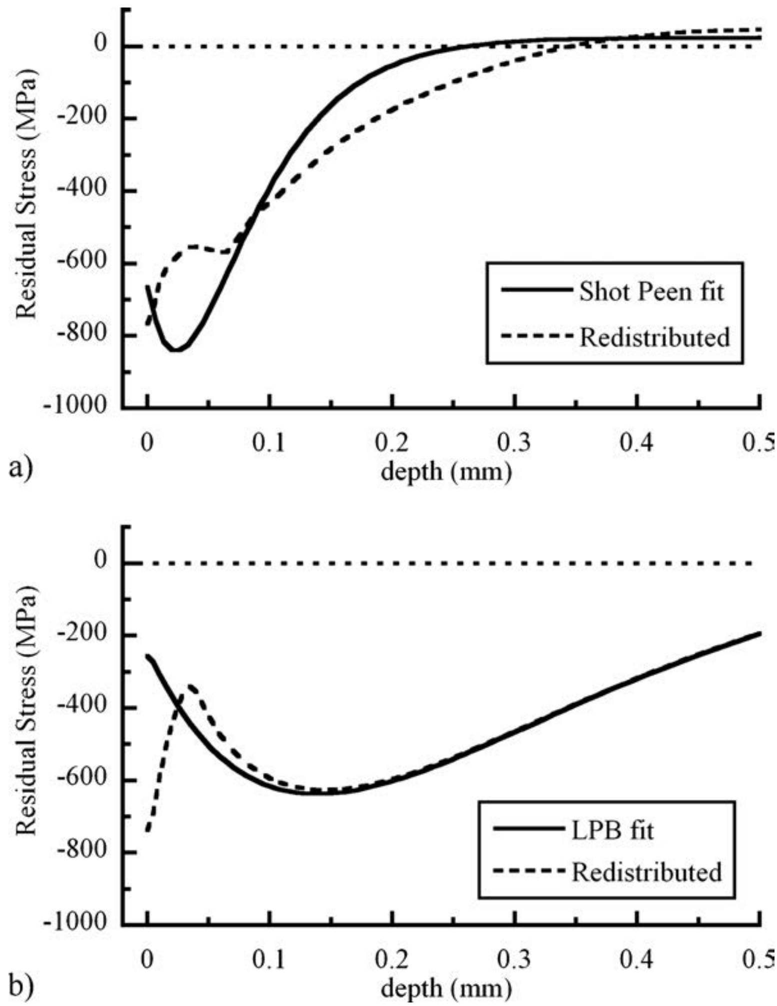

FIG. 11—*Predicted redistribution of residual stress at the edge of contact for typical contact loading case for both* (*a*) *shot peening and* (*b*) *LPB.*

shifted in the tensile direction near the surface (20 μm deep). Tensile yield occurs in the shot peened example [Fig. 11(*a*)] due to the high tensile stress due to contact during the positive shear reversal. This results in more compressive residual stresses at the surface (0–5 μm). The compressive yield zone was larger (60–70 μm deep) than the tensile, however, so there is a zone of more tensile residual stress (5–70 μm). Beyond 70 μm the residual stresses become more compressive to compensate. In the LPB treated samples, yielding was not predicted to occur during the negative shear reversal. The highest compressive stresses due to the applied loading occurred very near the surface, while the highest compressive residual stresses occur deeper in the material than those due to shot peening. The two compressive stress peaks (applied and residual) did not sufficiently overlap to result in a predicted plastic zone in the case of LPB. This is reflected in the predicted redistribution shown in Fig. 11(*b*). Here, the redistribution was caused entirely by the tensile yield that occurs at the surface in the edge of contact during the positive shear reversal. The compressive residual stresses due to LPB were smaller near the surface than those due to shot peening which also resulted in a larger predicted tensile plastic zone. Residual stress measurements of the specimens at the edge of contact were never performed. It was believed by the authors that the minimum x-ray spot sizes available using the x-ray diffraction technique were much too large to capture any expected localized change in residual stress. This may be an area of future work to either help confirm the analysis results or better explain the experimental results.

These predictions were based entirely on homogeneous material properties. The predicted plastic zone depths, however, were on the order of only a few grains. The local microstructure was not taken into account in the analysis. Goh et al. [20] showed that crystal plasticity may result in quite different results in predictions of localized plastic zones. In their simulations of plasticity under a fretting contact they showed that in the case of homogeneous material properties a small zone of cyclic plasticity develops surrounded by a larger zone that reaches an elastic shakedown condition. Much like the results predicted in this work. When the same material was modeled with crystal plasticity, however, a much deeper zone of ratcheting and cyclic plasticity was predicted. Although this type of analysis has not been conducted for the experiments in this work, Goh's results suggests that a more accurate analysis using crystal plasticity could result in a larger and deeper influence on residual stress redistribution.

The results of this work lead to the questions of how much of a reduction in the residual stress gradient is required to lead to life predictions that match the experimental results. Is a redistribution of residual stresses alone enough to explain the unconservative life predictions, or are some other sources of uncertainty in the analysis more important? To help answer these questions the life prediction analyses were repeated with different levels of residual stress gradients. The SP, LSP, and LPB gradients were each scaled to 100, 80, 50, 35, 20, and 0 % and the analyses were repeated for all of the respective fretting experiments. The SP gradients were applied to the uncoated LSP and LPB experiments for comparison since there were no shot peened experiments to analyze. An example of the results of this analysis is shown in Fig. 12. Crack growth to failure was predicted from a range of initial flaw sizes. In this example, 50 % of the LPB residual stress gradient or higher was predicted to result in no failure for initial crack depths smaller than approximately 0.5 mm. Shorter crack lengths were either below the crack propagation threshold or grew for a short time then arrested. Approximately 35 % of the LPB residual stress gradient resulted in a finite life prediction of approximately 2 million cycles. Since the actual specimen was a 10 million cycle run-out, the predicted remaining level of residual stresses in the specimen was between 35 and 50 %. A similar analysis was conducted on all of the LSP and LPB experiments and also the hypothetical SP samples. The predicted remaining level of residual stresses in the LSP specimens was 50–80 %. The predicted remaining level of residual stresses

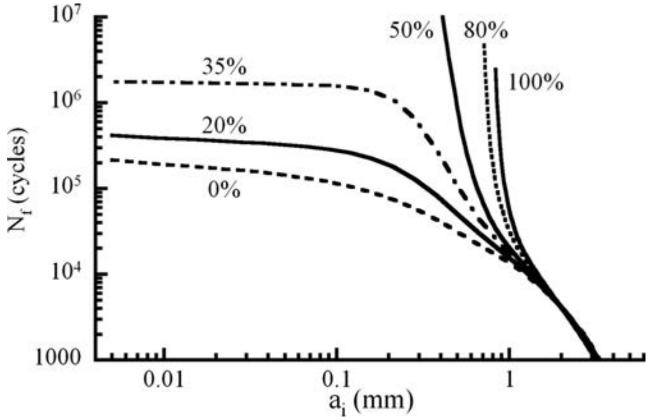

FIG. 12—*Predicted remaining life as a function of crack length and percent retained residual stress due to LPB for a typical fretting experiment.*

in the SP specimens that would result in some specimens failing was 35–50 %.

One additional observation from these analyses has been that the SP residual stress gradient could be predicted to be just as effective at preventing growth of fretting fatigue cracks as the LSP or LPB residual stress gradients. Even though the LPB gradient was much deeper than the SP gradient, it appeared that the magnitude and depth of the SP gradient is sufficient to prevent cracks of significant depth (0.3 mm) from growing in these experiments, if the original residual stresses remain unaltered. What the elastic-plastic contact analysis in this work showed, however, was that the SP residual stress gradients appeared to be more easily altered due to redistribution from local plasticity than the LSP or LPB residual stresses. Additionally, prior research showed that shot peened Ti-6Al-4V was more susceptible to thermal relaxation than either LSP or LPB [21]. This was explained as being a result of the much higher level of cold work imparted on the material in shot peening than in LSP or LPB. A thorough understanding of the loading and thermal conditions and the possibility of tensile or compressive local yielding are important factors to consider when designing a fatigue critical location with SP, LSP, or LPB.

Conclusions

Mechanics based life predictions of LSP and LPB treated fretting fatigue experiments resulted in unconservative life predictions. An elastic-plastic contact analysis was conducted to determine the influence of plastic deformations on the residual stresses. The compressive stress from the applied loading at the edge of contact during the reverse shear cycle was predicted to be elastic under the test conditions in these experiments. When the applied compression was combined with shot-peening compressive residual stresses, however, a compressive yield zone formed that redistributed the compressive residual stresses in the tensile direction. This compressive yield zone did not form in the case of

LSP or LPB treated samples because the peak compression was either deeper in the material or because the peak magnitude of compression was smaller than for shot-peening. Based on the results of the finite element modeling, it could not be concluded that redistribution of the residual stresses due to plasticity was the source of the unconservative life predictions on these experiments. Further analysis using crystal plasticity models, however, could reveal that local plasticity does result in redistribution of residual stresses in LSP or LPB.

The elastic-plastic contact analysis of shot-peened specimens showed a significant redistribution of the residual stresses at the edge of contact. Although no experiments were conducted with shot-peening in this work, this result suggests extreme caution must be applied before taking design credit for shot peening residual stresses with fretting.

Life predictions were conducted on all of the fretting experiments with different levels of retained residual stresses. Predictions were then made to determine the level of retained residual stresses that would make the predicted lives match the actual fretting fatigue lives. The level of retained residual stresses in the LPB specimens that correlated with the experimental results was 35–50 %. In the LSP specimens, the level of retained residual stresses that best correlated with the experiments was 50–80 %. This would be a significant reduction in residual stress that the analysis did not support. This lead the authors to believe that other sources of uncertainty besides the residual stresses not considered in the current deterministic analysis may be driving the unconservative life prediction results.

References

[1] Prevey, P., and Jayaraman, J., "A Design Methodology to Take Credit for Residual Stresses in Fatigue Limited Designs," *J. ASTM Int.*, Vol. 2, No. 8, 2005, Paper ID JAI12546.

[2] Waterhouse, R. B., "Plastic Deformation in Fretting Processes—A Review," Hoeppner, D. W., Chandrasekaran, V., and Elliott, C. B., Eds., *Fretting Fatigue: Current Technology and Practices*, ASTM STP 1367, ASTM International, West Conshohocken, PA, 2000.

[3] Martinez, S. A., Sathish, S., Blodgett, M. P., Mall, S., and Namjoshi, S., "Effects of Fretting Fatigue on the Residual Stress of Shot Peened Ti-6Al-4V Samples," *Mater. Sci. Eng., A*, Vol. 399, 2005, pp. 58–63.

[4] Golden, P. J., and Shepard, M. J., "Life Prediction of Fretting Fatigue with Advanced Surface Treatments," *Mater. Sci. Eng., A*, Vol. 468–470, 2007, pp. 15–22.

[5] Gallagher, J. P. et al., AFRL-ML-TR-2001-4159, "Improved High-Cycle Fatigue (HCF) Life Prediction," Wright-Patterson Air Force Base, OH, January 2001.

[6] Conner, B. P., and Nicholas, T., "Using a Dovetail Fixture to Study Fretting Fatigue and Fretting Palliatives," *J. Eng. Mater. Technol.*, Vol. 128, 2006, pp. 133–141.

[7] Golden, P. J., and Nicholas, T., "The Effect of Angle on Dovetail Fretting Experiments in Ti-6Al-4V," *Fatigue Fract. Eng. Mater. Struct.*, Vol. 28, 2005, pp. 1169–1175.

[8] Ruiz, C., Boddington, P. H. B., and Chen, K. C., "An Investigation of Fatigue and Fretting in a Dovetail Joint," *Exp. Mech.*, Vol. 24, 1984, pp. 208–217.

[9] Hills, D. A., and Nowell, D., *Mechanics of Fretting Fatigue*, Kluwer, London, 1994, pp. 153–168.

[10] Golden, P. J., Hutson, A. L., Sundaram, V., and Arps, J. H., "Effect of Surface Treatment on Fretting Fatigue of Ti-6Al-4V," *Int. J. Fatigue*, Vol. 29, 2007, pp. 1302–1310.

[11] Golden, P. J., and Calcaterra, J. R., "A Fracture Mechanics Life Prediction Methodology Applied to Dovetail Fretting," *Tribol. Int.*, Vol. 39, 2006, pp. 1172–1180.

[12] Rajasekaran, R., and Nowell, D., "Fretting Fatigue in Dovetail Blad Roots: Experiments and Analysis," *Tribol. Int.*, Vol. 39, 2006, pp. 1277–1285.

[13] Murthy, H., Harish, G., and Farris, T. N., "Efficient Modeling of Fretting of Blade/Disk Contacts Including Load History Effects," *J. Tribol.*, Vol. 126, 2004, pp. 56–64.

[14] Murthy, H., Rajeev, P. T., Farris, T. N., and Slavik, D. C., "Fretting Fatigue of Ti-6Al-4V Subjected to Blade / Disk Contact Loading," Developments in Fracture Mechanics for the New Century, 50th Anniversary of Japan Society of Materials Science, Osaka, Japan, 2001, pp. 41–48.

[15] Shen, G., and Glinka, G., "Weight Functions for a Surface Semi-Elliptical Crack in a Finite Thickness Plate," *Theor. Appl. Fract. Mech.*, Vol. 15, 1991, pp. 247–255.

[16] Glinka, G., and Shen, G., "Universal Features of Weight Function for Cracks in Mode I," *Eng. Fract. Mech.*, Vol. 40, 1991, pp. 1135–1146.

[17] Hutson, A. L., Neslen, C., and Nicholas, T., "Characterization of Fretting Fatigue Crack Initiation Processes in Ti-6Al-4V," *Tribol. Int.*, Vol. 36, 2003, pp. 133–143.

[18] Nicholas, T., Hutson, A., John, R., and Olson, S., "A Fracture Mechanics Methodology Assessment for Fretting Fatigue," *Int. J. Fatigue*, Vol. 25, 2003, pp. 1069–1077.

[19] El Haddad, M. H., Smith, K. N., and Topper, T. H., "Fatigue Crack Propagation of Short Cracks," *J. Eng. Mater. Technol.*, Vol. 101, 1979, pp. 42–46.

[20] Goh, C. H., McDowell, D. L., and Neu, R. W., "Plasticity in Polycrystalline Fretting Fatigue Contacts," *J. Mech. Phys. Solids*, Vol. 54, 2006, pp. 340–367.

[21] Shepard, M. J., Prevey, P. S., and Jayaraman, N., "Effects of Surface Treatment on Fretting Fatigue Performance of Ti-6Al-4V," 8th National High Cycle Fatigue Conference, 2003.

ASTM Special Technical Publication, Vol. 5, No. 7
Paper ID JAI101661
Available online at www.astm.org

Kristina Langer,[1] *Scott VanHoogen, and Jeffery Hoover II*

Fatigue Response of Aluminum Aircraft Structure under Engineered Residual Stress Processing

ABSTRACT: Advanced surface treatment methods for imparting beneficial residual compressive stresses into fatigue-prone metallic components such as laser shock processing (LSP) and low plasticity burnishing (LPB) have proven highly effective in prolonging the life of titanium turbine engine blades. The objective of the current effort was to experimentally evaluate whether similar life enhancement benefits are possible for metallic aircraft structures. Under this initiative, aluminum test specimens were processed using three engineered residual stress techniques, referred to as LSP 1, LSP 2, and LPB, and subsequently fatigue tested under uniaxial, constant amplitude loading conditions. Evaluation of the test results indicated that both the LSP and LPB processes, if carefully designed and applied, have the potential to increase the fatigue life of aircraft structural components.

KEYWORDS: residual stress, laser shock processing, low plasticity burnishing, aircraft structures

Introduction

Advanced surface treatment methods for imparting beneficial residual compressive stresses into fatigue-prone metallic components, such as laser shock processing (LSP) and low plasticity burnishing (LPB), have proven to be highly effective in prolonging the life of turbine engine blades in U.S. military aircraft (see, for example, Ref. [1]). Whether similar fatigue life enhancements are pos-

Manuscript received April 10, 2008; accepted for publication June 13, 2008; published online July 2008.
[1] Air Force Research Laboratory, Air Vehicles Directorate, Wright-Patterson Air Force Base, OH 45433.

Citation: Langer, K., VanHoogen, S., and Hoover II, J., "Fatigue Response of Aluminum Aircraft Structure Under Engineered Residual Stress Processing," *J. ASTM Intl.*, Vol. 5, No. 7. DOI10.1520/JAI101661. Available online at www.astm.org. Also included in JAI Special Issue STP 1508, *Fatigue and Fracture Mechanics: 36th Volume,* R. W. Neu, K. R. W. Wallin, and S. R. Thompson, guest editors, ASTM International, West Conshohocken, PA 2009, pp. 122-133.

sible for airframe components, however, has been a subject of considerable debate. Because aircraft structural components typically utilize very different material systems, can have very complex structural geometries, and experience complex and often variable loading spectra, many of the "tried and true" methodologies used to extend the life of turbine engine components may not necessarily perform in a similar fashion when applied to airframe components. To address these issues, the Air Force Research Laboratory (AFRL) conducted a feasibility study to provide first-order test data in support of a quantitative evaluation of LSP and LPB processes for fatigue life enhancement of airframe structures. Within this program, two primary test issues were identified:

- Can LSP and LPB increase the fatigue life of aircraft structural components?
- Is additional research in LSP and LPB for aircraft structures warranted?

Although both of the processing techniques used in this study are designed to introduce deep residual compressive stress fields into metallic components, the mechanisms employed by LSP and LPB are quite different (see Ref. [2] for a concise overview of mechanical surface treatments). With LSP, the residual stresses are induced via a high amplitude (5–10 GPa, typically), short duration (10–50 ns, typically) pressure pulse generated through laser-induced vaporization of a sacrificial opaque coating on the surface of the target material. The propagation of the highly localized shock wave through the material causes dynamic yielding and plastic deformation which result in deep (on the order of 1–2 mm) residual compressive stresses. In contrast, LPB is a quasi-static process in which a freely rolling spherical ball is passed along the surface of the material. The hydraulically controlled normal force applied to the ball causes plastic deformation of the surface which results in residual compressive stresses after the ball passes.

Exploratory fatigue experiments using two specimen configurations and three residual stress processes were conducted to address the test issues. As discussed in the following sections, data considered in the evaluation were the overall fatigue responses (cycles to failure) and through-the-thickness residual stress profiles.

Three residual stress processing techniques were used in the evaluation, two LSP techniques (designated as LSP 1 and LSP 2) and one LPB technique. Each technique was provided by a separate vendor. Each vendor was provided specimens, the loading spectra, and detailed finite element models. All processing-specific details, including processing area, process specifications, system settings, etc., were left to the discretion of the vendors. For proprietary reasons, processing details were not released to AFRL. See Ref. [2] for a discussion of the relationship between process control parameters and the induced stress fields.

Overview of Experiments

To ensure an Air Force relevant test program, the design of the laboratory specimens was inspired by historical aircraft usage data for fatigue-prone

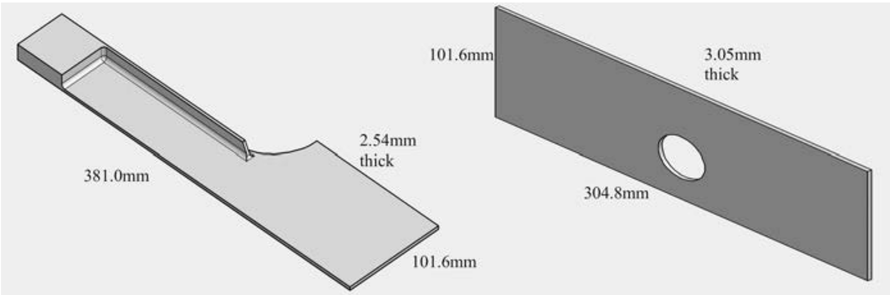

FIG. 1—*Specimen geometries.*

structural components. Key elements of typical airframe components were considered, including

- Material type
- Complex geometry
- Complex load paths
- High stress gradients
- Low cycle fatigue
- Damage tolerant design

Using these design considerations, two specimen configurations were selected (Fig. 1). Both specimens were fabricated from Al 2024-T851, a high strength aluminum alloy typically used for aerospace structural applications. The first specimen, referred to as Part A, was inspired by a canopy sill component and is characterized by a highly complex geometry. Because of the asymmetric design, axially applied loading resulted in a coupled bending and axial response with a localized stress concentration located along the fillet at the base of the flange. The second specimen, Part B, was inspired by a fuselage bulkhead cutout. It was designed to have a simpler geometry consisting of a flat panel with an offset circular through-hole but a much more challenging loading spectrum (fully reversed axial loading).

Fatigue responses were evaluated using both smooth and pre-cracked specimens with the pre-cracks introduced at the high stress locations prior to residual stress processing. For these tests, a small (nominal 0.02 in. [0.5 mm]) notch was cut into the specimens and then grown to 0.05 in. (1.27 mm) nominally under constant amplitude fatigue loading ($R = 0.1$).

All specimens were tested under constant amplitude loading using an MTS servo-hydraulic axial test frame. For Part A, uniaxial tension with a stress ratio of 0.01 was used. For Part B, fully reversed loading (stress ratio of –1.0) was used. In keeping with the stated test design philosophy, the loading spectra were developed so that failure would occur in the low cycle fatigue regime. For the unprocessed state (e.g., no residual stress processing), the target number of cycles to failure was designed to be 30 000. This correlated to loading spectra with stress amplitudes of 11.4 ksi (78.6 MPa) for Part A and 11.5 ksi (79.3 MPa) for Part B. In addition, each specimen configuration was tested using a second constant amplitude loading spectrum with the amplitude increased by 10 %. The objective of the increased loading was to obtain a preliminary assessment of the sensitivity of the LSP and LPB processes to small variations in the applied loads.

The primary test variables considered (Table 1) were the residual stress process (none, LSP 1, LSP 2, and LPB), the pre-crack status (with and without the 0.05 in. [1.27 mm] precrack]), and the loading condition (nominal loading and 10 % increased loading, shown as "Med" and "High," respectively). Either three or six repetitions per test case were used as indicated.

In addition, for Part B, the effects of small satellite holes drilled in the vicinity of the main hole were also considered, as shown in Table 2. This is a common procedure used in the assembly of aircraft structural components during which small holes are drilled on-site to accommodate the fastening of a collar or other fitting inserted through the main hole. The objective of these tests was to evaluate whether post-drilling (that is, drilling after the residual stresses have been imparted), can affect the efficacy of the processes.

For both specimen types, processing was applied primarily to the specimen faces in the through-thickness direction. One exception was the LSP 2 processing of the simple specimen in which processing was also applied radially along the face of the circular through-hole.

The following primary data were collected:

- Residual stress profiles: Through-thickness residual stress distributions were measured using X-ray diffraction with layer removal (see, for example, Ref. [3]).
- Fatigue data: The number of cycles to failure was collected for each specimen tested. For Part A, scanning electron microscopy (SEM) was also conducted on representative samples to assess crack initiation characteristics.

Results and Discussion

For the smooth (i.e., no pre-crack) simple test specimens, the average numbers of cycles to failure, normalized by the baseline averages (26 987 cycles for the medium load case and 15 195 cycles for the high load case) are shown in Fig. 2. Also shown for reference are bars indicating maximum and minimum values for each process type.[2] As is shown, very little fatigue life benefit, on average, was observed for the specimens with LSP-induced residual stress fields for either the medium or high load cases. In addition, some of the specimens experienced decreases in fatigue life on the order of 15–30 %. For the specimens with LPB-induced fields, average increases on the order of 3× were observed. The scatter in the data however was fairly significant, ranging from a minimum of 1× to a maximum of approximately 5×.

These observations raised the question as to whether LPB processing was somehow "better" than LSP processing in enhancing the fatigue response of this specimen set or whether the observed differences in fatigue life were due to differences in the way in which the processing was applied. To address this

[2]Tabulated data documenting individual specimen test results are considered proprietary information and are not included in this article.

TABLE 1—*Primary test matrix.*

Part A (R = 0.01)					Part B (R = −1.0)				
Test Case	Process	Load Level	Pre-Crack	Repetitions	Test Case	Process	Load Level	Pre-Crack	Repetitions
1a.1	None	Med	yes	3	1b.1	None	Med	yes	3
1a.2			no	6	1b.2			no	6
1a.3		High	yes	3	1b.3		High	yes	3
1a.4			no	6	1b.4			no	6
1a.5	LSP 1	Med	yes	3	1b.5	LSP 1	Med	yes	3
1a.6			no	6	1b.6			no	6
1a.7		High	yes	3	1b.7		High	yes	3
1a.8			no	6	1b.8			no	6
1a.9	LSP 2	Med	yes	3	1b.9	LSP 2	Med	yes	3
1a.10			no	6	1b.10			no	6
1a.11		High	yes	3	1b.11		High	yes	3
1a.12			no	6	1b.12			no	6
1a.13	LPB	Med	yes	3	1b.13	LPB	Med	yes	3
1a.14			no	6	1b.14			no	6
1a.15		High	yes	3	1b.15		High	yes	3
1a.16			no	6	1b.16			no	6

TABLE 2—*Test matrix for post-drilled holes.*

Part B (R = −1.0)				
Test Case	Process	Load Level	Holes	Repetitions
4a.1	None	Med	yes	3
4b.2		High	yes	3
4b.3	LSP 1	Med	yes	3
4b.4		High	yes	3
4b.5	LSP 2	Med	yes	3
4b.6		High	yes	3
4b.7	LPB	Med	yes	3
4b.8		High	yes	3

issue, the LSP 2 vendor processed a new set of simple specimens using the geometry of the LPB-processed zone as a template. In this case, rather than processing around the entire circumference of the hole as was done for the initial specimen set, the LSP 2 vendor processed only a small region in the vicinity of the stress concentration. These specimens were then fatigue-tested under the same loading conditions as the initial specimens. The results are shown in Fig. 3. As can be seen, this second round of LSP processing resulted in an average life increase of over four times the baseline life, outperforming all of the initial specimens including those processed using LPB. These results suggest that both the LSP and LPB processing techniques have potential for enhancing the fatigue life of aluminum structural components, with proper design and application of the engineered fields as critical elements for achieving success.

For the pre-cracked simple test specimens, the average fatigue responses, normalized by the baseline average responses (1276 cycles to failure for the medium load case and 1215 cycles for the high load case) are plotted in Fig. 4. Also shown for reference are bars indicating the maximum and minimum values for each process. As can be observed, increased average life was observed for all of the processed specimens with gains ranging from about $3.5\times - 30\times$ for the medium load case and about $2\times - 13\times$ for the high load case. Unlike the

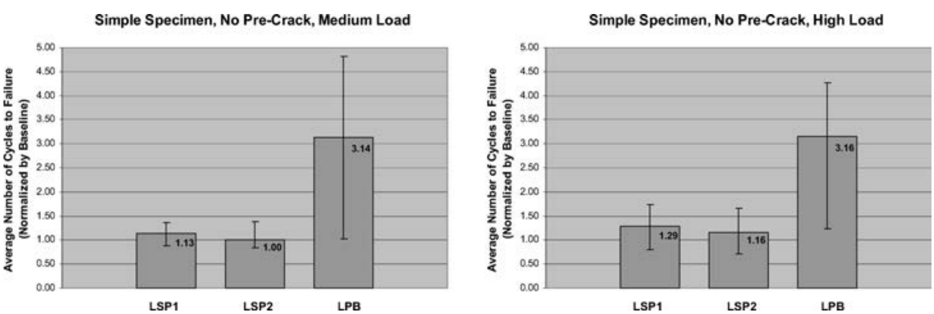

FIG. 2—*Comparison of average fatigue response (Part B, no pre-crack).*

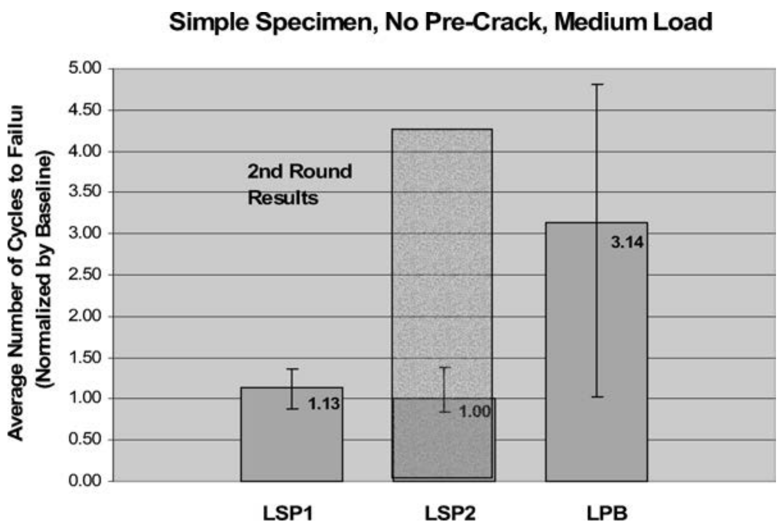

FIG. 3—*Second round of LSP 2 results.*

smooth specimens, none of the individual data points dropped below 1×. These results suggest that the engineered residual stress fields could be particularly beneficial in extending the life of cracked components.

The average fatigue response for the specimens with small satellite holes drilled through the induced stress fields is shown in Fig. 5. As can be seen, post-drilling holes in close proximity to the processed regions resulted in significant stress relief. These results suggest that structural components requiring this sort of fabrication might not be good candidates for residual stress processing.

To glean further insights, residual stress profiles in the through-thickness direction were measured using X-ray diffraction with layer removal for a small number of processed specimens. Measurements were obtained at two locations on the top side of the specimen and the corresponding locations on the bottom side in both the longitudinal and transverse directions, as shown in Fig. 6.

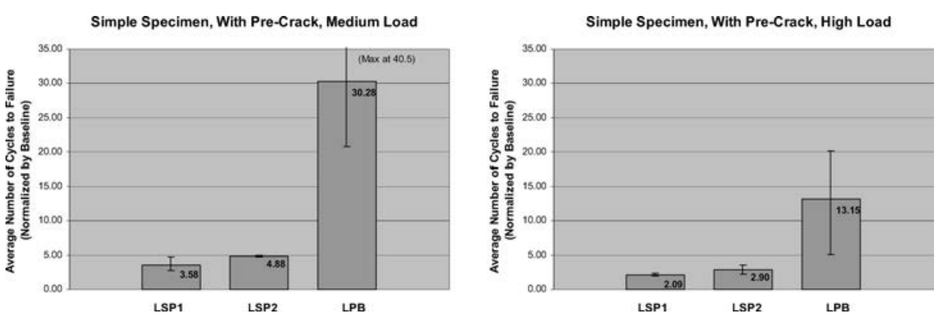

FIG. 4—*Comparison of average fatigue response (Part B, pre-cracked).*

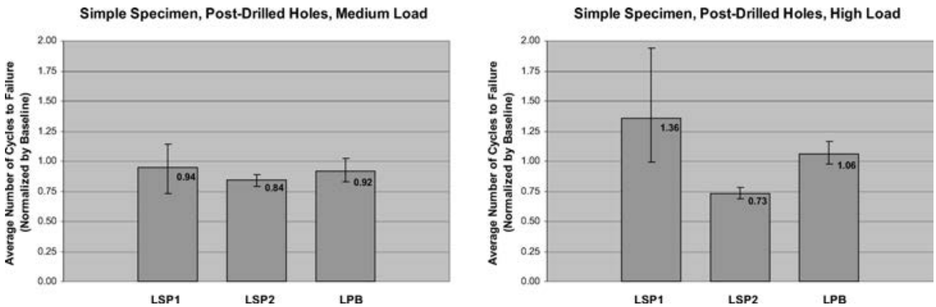

FIG. 5—*Comparison of average fatigue response* (*Part B, post-drilled holes*).

Because the specimen geometry is symmetric in the thickness direction, the top and bottom designations were chosen arbitrarily. Two specimens were evaluated for each processing technique (one for the topside measurements and one for the bottom). In addition, baseline measurements were obtained using an unprocessed specimen.

The residual stress data for "Location A, Longitudinal," the high stress point in the specimens, are plotted in Fig. 7. The data show the "top" and "bottom" face residual stress profiles are very similar in shape and magnitude indicating that the residual stress distribution is symmetric about the mid-plane of the plate. The depth of the induced stresses was approximately 0.025–0.030 in. (0.64–0.76 mm). Magnitudes of the compressive fields varied

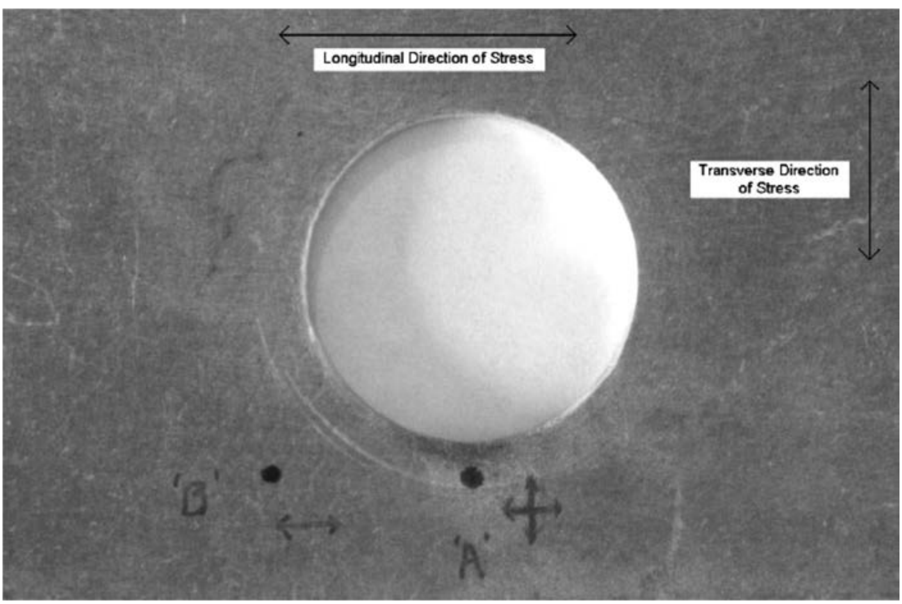

FIG. 6—*Locations for X-ray diffraction measurements* (*Part B*).

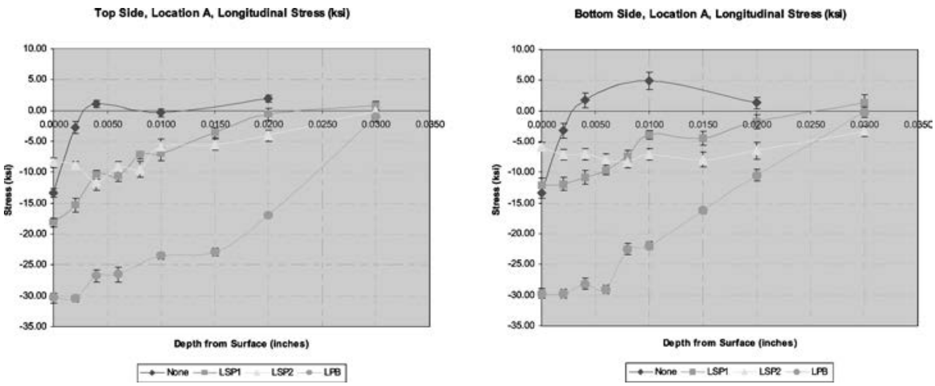

FIG. 7—*Distribution of longitudinal component of stress in the through-thickness direction* (*Part B*).

from about 5–20 ksi (83–138 MPa) for the LSP processing and about 30 ksi (207 MPa) for the LPB processing. (Note that residual stress distributions were not obtained for the modified LSP processing.)

The average fatigue responses of the complex specimens are shown in Fig. 8. The average number of cycles to failure has been normalized by the baseline average (30 6422 cycles for the medium load case and 16 979 cycles for the high load case). Also shown for reference are bars indicating the maximum and minimum values for each process type. As can be seen, the average response of the smooth complex specimens was similar in nature to that of the smooth simple specimens with little to no fatigue life benefit observed on average, for the LSP-processed specimens and significant benefit associated with the LPB processing. Based on the results of the second round of testing conducted on the simple specimens however, it is likely that with proper design and application, all of the processing techniques could demonstrate the same potential for life enhancement.

The fatigue test results for the pre-cracked, complex specimens are shown in Fig. 9. The average baseline response was 1583 cycles to failure for the medium load case and 610 cycles to failure for the high load case. The ob-

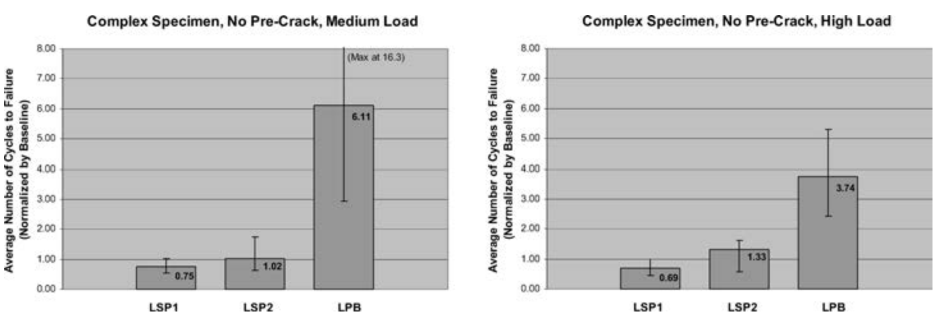

FIG. 8—*Comparison of average fatigue response* (*Part A, no pre-crack*).

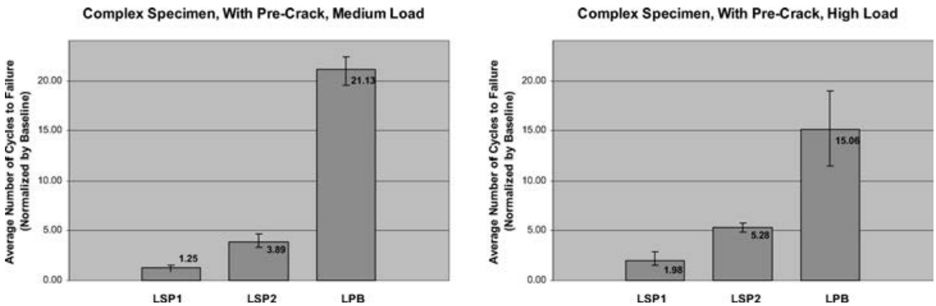

FIG. 9—*Comparison of average fatigue response* (*Part A, pre-cracked*).

served life enhancements for these specimens were quite significant, on the order of 2–5× for the LSP-processed specimens and 15–20× for LPB.

Through-thickness residual stresses were measured using X-ray diffraction with layer removal to gain insight into the observed fatigue responses. Measurements were obtained at two locations on the top side of the specimen and two locations on the bottom side in both the longitudinal and transverse directions, as shown in Fig. 10. Two specimens were evaluated for each processing technique (one for the topside measurements and one for the bottom). In addition, for the bottom side, baseline measurements were obtained for an unprocessed specimen. The residual stress data for "Location 2, Longitudinal," the high stress point in the specimens, are plotted in Fig. 11. The induced LSP 1 stresses are fairly shallow and even show a small amount of tension at the surface. This observation is in line with the corresponding fatigue response for these specimens which indicated (on average) a loss of life. For the LSP 2 and LPB specimens, more classic stress profiles were measured with maximum compression magnitudes of about 40–60 ksi (275–414 MPa) compression and corresponding depth of about 0.02 in. (0.5 mm).

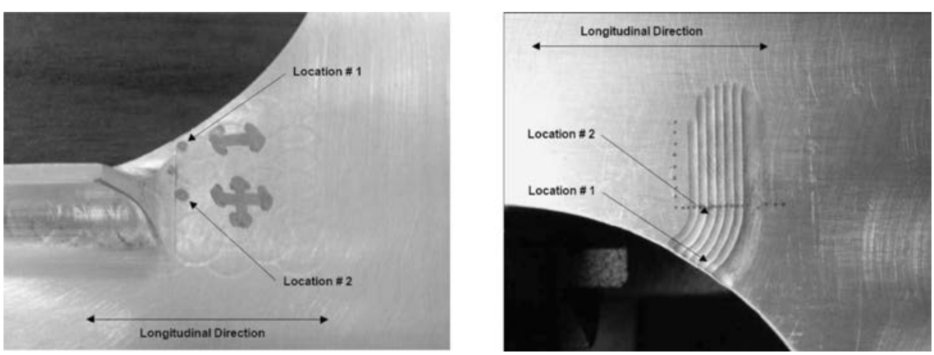

FIG. 10—*Locations for X-ray diffraction measurements* (*Part A*).

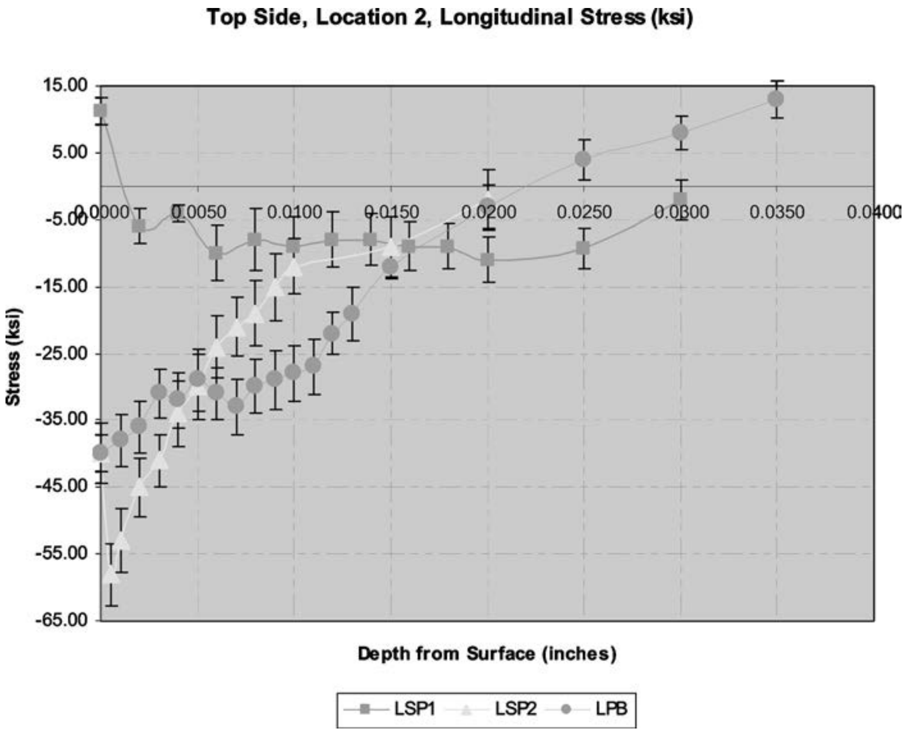

FIG. 11—*Through-thickness longitudinal stresses* (*Part A, top*).

Conclusions

This test program was developed to address two primary issues regarding the potential application of advanced surface treatments (in particular, laser shock processing and low plasticity burnishing) for enhancing the fatigue life of aluminum aircraft structural components. The first issue was to evaluate whether the LSP and LPB processes have the potential to increase the fatigue life of structural components. The second issue was to evaluate whether additional research in LSP and LPB for aircraft structures is warranted. The simple answer to both questions, as demonstrated by the test results, is yes.

Regarding the first issue, clear evidence was obtained to support the concept of fatigue life enhancement for aircraft structures using LSP and LPB processes. In the case of tension-only loading of a geometrically complex fatigue specimen, increases in fatigue life were demonstrated for some portion of the test matrix. Life increases were especially significant for specimens that contained a small pre-crack in the high stress area prior to processing. Also observed was the ability of the processed specimens to retain significant fatigue life increases even under a 10 % increase in the amplitude of the loading spectrum. Somewhat surprisingly, similar trends were observed for the case of fully reversed loading on geometrically simple specimens. Conventional wisdom suggests that engineered residual stress processing is typically less effective for fatigue life extension in parts subjected to fully reversed loading due to cyclic plasticity effects. However, under the current test program, life increases on the order of 3× for the LPB-processed smooth specimens and 2–30× for the LSP- and LPB-processed precracked specimens were observed.

Regarding the second issue, several areas for additional research were identified. First, in some cases, the introduction of the residual stresses resulted in a loss of fatigue life. A better understanding of the relationship between the engineered residual stress processing and the resultant impact on fatigue response needs to be established for aircraft structural applications. Second, the measured average fatigue life of the specimens was highly dependent on the design of the residual stress fields, with results varying widely between vendors. This indicates a need for process specifications and application standards by which to define a uniform process. Third, considerable scatter in the fatigue response (greater than the scatter in the baseline specimens) of some of the test series were observed. Because this could impact the structural reliability of a processed component, further research in this area is warranted. Finally, additional test variables of importance to aircraft structural applications, such as specimen thickness, stress ratio, bending, variable amplitude spectrum loading, etc., need to be investigated.

References

[1] Tenaglia, R. D. and Lahrman, D. F., "Preventing Fatigue Failures with Laser Peening," *The Advanced Materials and Process Technology Information Analysis Center (AMPTIAC) Quarterly*, Vol. 7, No. 2, 2003, pp. 3–7.

[2] Zhuang, W. and Wicks, B., "Mechanical Surface Treatment Technologies for Gas Turbine Engine Components," *J. Eng. Gas Turbines Power*, Vol. 125, 2003, pp. 1021–1025.

[3] Prevéy, P. S., "X-Ray Diffraction Residual Stress Techniques," *Metals Handbook, American Society for Metals*, 1986, pp. 380–392.

ASTM Special Technical Publication, Vol. 5, No. 9
Paper ID JAI101537
Available online at www.astm.org

H. Leitner,[1] *B. Oberwinkler,*[2] *H.-P. Gaenser,*[2] *and M. Stoschka*[2]

Influence of the Peening Intensity on the Fatigue Behavior of Shot Peened Titanium Components

ABSTRACT: Although mechanical surface treatments are commonly used in engineering practice for their beneficial effect on fatigue life, little quantitative data are available from published literature. This paper presents the first results of a long-term research program that aims to develop quantitative design guidelines for the influence of mechanical surface treatments on the fatigue life of structural lightweight components. To gain a detailed understanding of the effects of mechanical surface treatments on surface roughness, residual stress distribution, and resulting fatigue strength, extensive experimental work as well as accompanying fracture analyses have been performed. Four-point rotating bending tests and alternating torsional tests were performed on a Ti-6Al-4V titanium alloy. Both smooth and notched specimen geometries were investigated. The heat-treated and machined specimens were subjected to a shot peening process with varying shot intensities within the recommendations of the MIL-S-13165C and MIL-P-81985 specifications. It was observed that shot peening can result in both an improvement as well as a deterioration in fatigue strength, depending on the shot peening intensity and the type of loading. For the assessment of the fatigue failure mechanisms, detailed investigations of the surface layer were included in the research program.

KEYWORDS: Ti-6Al-4V, surface layer, fatigue, shot peening

Manuscript received November 8, 2007; accepted for publication August 18, 2008; published online September 2008.
[1] Chair of Mechanical Engineering, University of Leoben, 8700 Leoben, Austria, e-mail: heinz.leitner@unileoben.ac.at
[2] Mechanical Engineering, University of Leoben, 8700 Leoben, Austria.

Citation: Leitner, H., Oberwinkler, B., Gaenser, H.-P., and Stoschka, M., "Influence of the Peening Intensity on the Fatigue Behavior of Shot Peened Titanium Components," *J. ASTM Intl.*, Vol. 5, No. 9. DOI10.1520/JAI101537. Available online at www.astm.org. Also included in JAI Special Issue STP 1508, *Fatigue and Fracture Mechanics: 36th Volume*, R. W. Neu, K. R. W. Wallin, and S. R. Thompson, guest editors, ASTM International, West Conshohocken, PA 2009, pp. 134-146.

TABLE 1—*Chemical composition in wt. %.*

Material	Ti	Al	V	C	Fe	O_2	H_2	N_2
Lamellar	balance	6.24	3.83	0.015	0.17	0.150	0.0038	0.0035
ASTM B348 spec.	balance	5.5–6.75	3.5–4.5	<0.10	<0.40	<0.20	<0.0125	<0.05

Shot Peening of Ti-6Al-4V

Ti-6Al-4V is the most common titanium alloy as far as its fatigue behavior is concerned. However, all of the results documented have only a very narrow range of validity with respect to heat treatment conditions and microstructure, owing to the strong influence of the microstructural parameters on the resulting fatigue behavior. This becomes particularly apparent if one studies the inconsistencies in the results communicated in the literature regarding the effects of surface treatments on the fatigue behavior of Ti-6Al-4V. The type of loading and the specimen geometry must also be known exactly as the effect of surface treatment on fatigue strength is always localized in the surface layer and depends on the stress gradient.

Gray et al. [1] tested unnotched rotating bending specimens peened with an intensity of 0.28 A (mm), which exhibit an increase in the fatigue limit of 23 %, at 10^7 load cycles, over unpeened specimens. Wagner et al. [2] as well as Franz and Obricht [3] obtained improvements in the fatigue limit of ~15 %, at 10^7 load cycles. Wohlfahrt [4] reported a decrease in the fatigue limit in combination with an increase in the slope of the S/N curve at 0.25 A (mm) peening intensity. However, with additional glass bead shot peening the fatigue limit was increased by 25 % compared to milled specimens. In many of the references found, detailed information about the microstructure and the surface layer is missing or at least incomplete. In summary it may be stated that the literature shows a considerable fatigue strength optimization potential due to shot peening of up to 25 %. Shot peening with inappropriate parameters (e.g., shot peening intensity too high) may easily result in a decrease in the fatigue strength. Results describing the effect of shot peening on torsional fatigue and experiments in the very high cycle fatigue (VHCF) regime, i.e., fatigue data at more than 10^8 load cycles are extremely rare. The majority of the documented experiments were performed in the high cycle fatigue (HCF) range, i.e., between 10^4 load cycles up to a maximum cycle count of 10^7. In the low cycle fatigue (LCF) region, i.e., below 10^4 load cycles, the residual stresses are relieved due to cyclic plastification. For this reason shot peening is not so common. Taking this information as a starting point, a systematic parametric investigation of the effects of shot peening on the fatigue behavior of Ti-6Al-4V was initiated.

Material Characterization

Table 1 presents the chemical composition of the investigated Ti-6Al-4V material. The material corresponds to the ASTM B348, "Standard Specification for Titanium and Titanium Alloy Bars and Billets" and was delivered as β-rolled

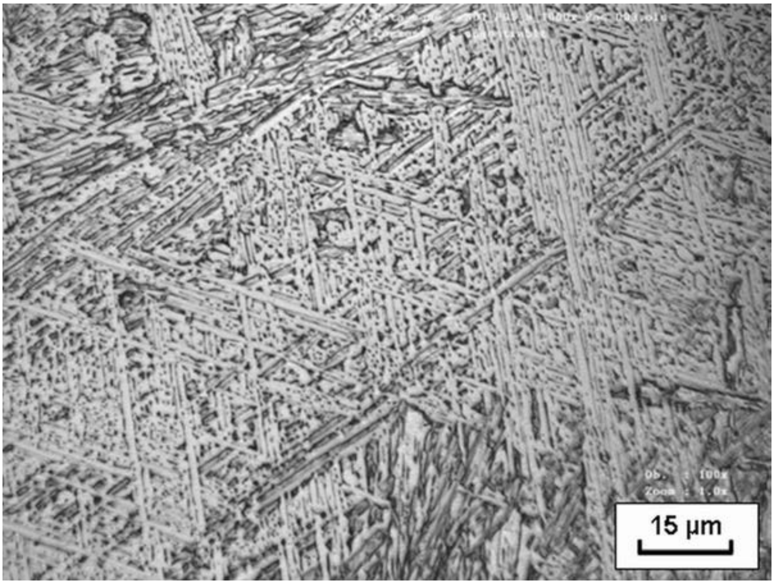

FIG. 1—*Micrograph of the fine lamellar microstructure.*

cylindrical bars, 18 mm in diameter and 4 m in length. The fine lamellar microstructure results from a rolling at 1050°C and air cooling and is a typical microstructure for β-processed components.

Figure 1 shows the micrograph of the fine lamellar microstructure. The quasi-static strength of the material was determined by tensile tests, cf. Table 2.

Test Procedure

Specimens manufactured from Ti-6Al-4V with lamellar microstructure and shot peened with varying intensities were tested under different loading conditions, i.e. tension/compression, rotating bending and torsion, cf. Table 3. The peening intensities were chosen in the range recommended by MIL-S-13165C and MIL-P-81985 [5,6]. Table 3 shows a summary of the conditions investigated. Coverage of 200 % was chosen for all experiments. The shot used was a steel ball shot, size classification 0.35 mm with hardness HV 640 (labeling StD-G3-0.35-HV640).

TABLE 2—*Quasistatic strength of lamellar Ti-6Al-4V.*

Microstructure	Young's Modulus E [MPa]	Yield Strength $R_{p0.2}$ [MPa]	Ultimate Tensile Strength R_m [MPa]	Ultimate Strain A_5 [%]	Reduction of Area After Fracture Z [%]
Lamellar	110800	885	938	14.45	30.8

TABLE 3—*Test program.*

Microstructure	Peening Intensity	Loading Conditions	Stress Concentration Factor K_t
Lamellar	Unpeened	Rotating bending	1.02
Lamellar	Unpeened	Alternating torsion	1.02
Lamellar	$I = 0.16$ A (mm)	Rotating bending	1.02
Lamellar	$I = 0.16$ A (mm)	Rotating bending	1.70
Lamellar	$I = 0.16$ A (mm)	Alternating torsion	1.02
Lamellar	$I = 0.25$ A (mm)	Rotating bending	1.02

The experiments were performed at room temperature in ambient air. All tension/compression tests were run on a servo-hydraulic test stand at a stress ratio of $R = -1$ and a frequency of 30 Hz. The rotating bending tests were carried out on a rotating bending test machine. The tests under alternating torsional loading were performed on a purpose-designed test rig capable of realizing arbitrary combinations of rotating bending and torsional loadings, including arbitrary phase shifts and frequency ratios.

Both the literature, [7–10], as well as the test results in this paper validate that there is no fatigue limit up to at least 10^8 load cycles, because some specimens failed at a number of load cycles above 10^7. Therefore, the experimental data points were fitted by a two-slope S/N curve model initially developed to describe the fatigue behavior of aluminum cast alloys [11]. In this model the slope of the S/N curve in the high cycle fatigue regime is five times as high as in the finite life region, i.e., $k_2 = 5k_1$. The ratio $k_2 = 5k_1$ was chosen as the best fit for a large amount of test series. The data analysis was divided in two steps. At first the slope k_1 of the S/N curve was be determined by the help of a lognormal distribution. Only load levels with exclusive failed specimens were included. In the second step the load levels with a mixture of failed specimens and run-outs or solely run-outs were used to calculate the fatigue limit regarding 10^7 load cycles. Through this point the second S/N curve k_2 was drawn. By extending both S/N curves the point of intersection was defined.

Shot peening does not significantly affect the scatter of the fatigue data. Therefore, to describe the characteristic effects of shot peening all S/N curves in this paper correspond to a survival probability of 50 %. The detailed analysis including the scatter of the fatigue test results can be found in [12].

All residual stress measurements were performed by X-ray diffraction in combination with the $\sin^2 \psi$ method. The presented residual stresses are measured data points without any smoothing.

Rotating Bending Tests under Varying Peening Conditions

Figure 2 shows the results of the rotating bending fatigue tests of unpeened specimens and of specimens peened with intensities of 0.16 A (mm) and 0.25 A (mm), respectively.

Due to the lamellar microstructure of the material, the S/N curve for the unpeened reference specimens displays relatively low fatigue strength of

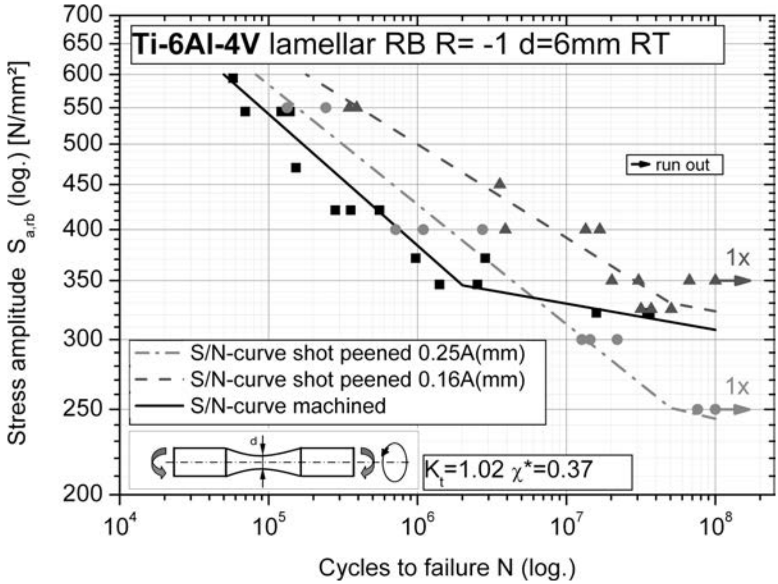

FIG. 2—*Rotating bending S/N curves for machined versus shot peened specimens.*

330 MPa at 10^7 load cycles, compared to strengths as high as 600 MPa for equiaxed or bimodal microstructures [2,3,12]. The fatigue strength increase due to shot peening with 0.16 A (mm) is particularly significant in the finite life region with about 18 % enhancement compared to the unpeened specimens at 10^7 load cycles. At higher cycle counts the advantage of shot peening is not that significant and decreases to approximately 4 % at 5×10^7 load cycles.

For a peening intensity of 0.25 A (mm) the situation is quite different. For cycle counts below 6×10^6, the fatigue strength is also slightly improved; however, for higher cycle counts it falls below the strength of the unpeened reference specimens, getting as low as 250 MPa at 5×10^7 load cycles. Apparently this behavior is due to a change of the damage mechanism, which will be discussed in more detail in section here after.

Figure 3 deals with the effect of notches on the fatigue behavior. It can be observed that, for the unpeened material, unnotched and notched specimens show almost identical fatigue strength with only a slight increase in the finite life regime. This means that the material is highly notch sensitive. Shot peening of the notched specimens—using the optimum peening intensity of 0.16 A (mm) as determined above—augments the fatigue strength significantly for any number of cycles, and by as much as 80 % at the endurance limit.

In addition to the rotating bending tests, alternating torsion experiments with unpeened and peened specimens were performed, cf. Fig. 4. A significant enhancement was achieved at load cycles of up to 2×10^7. Due to testing time restrictions it was not possible to carry out tests up to 10^8 load cycles. However, considering the rotating bending results, it may be assumed also that for tor-

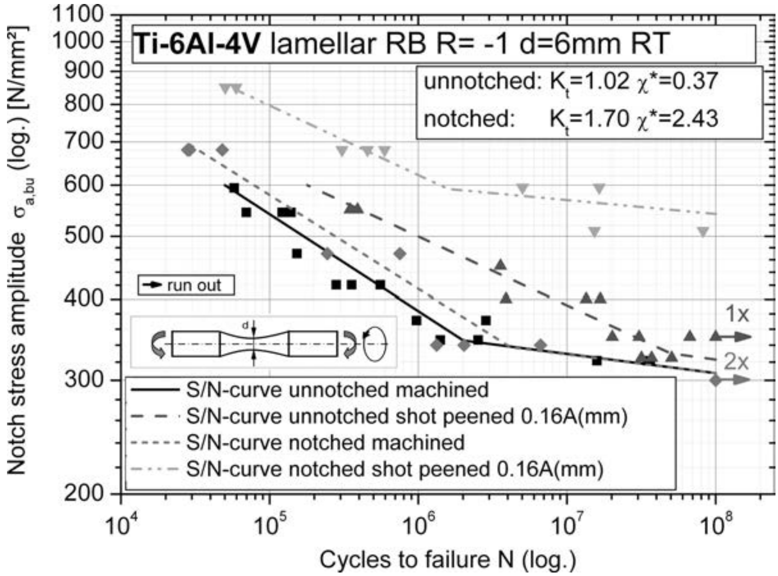

FIG. 3—*Rotating bending S/N curves of notched and unnotched specimens shot peened with different intensities.*

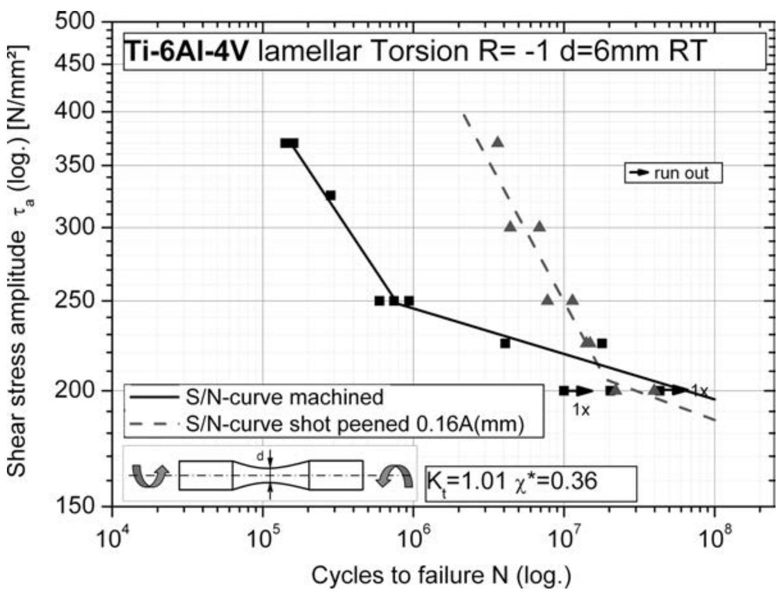

FIG. 4—*Effect of shot peening on the fatigue limit of specimens loaded in torsion.*

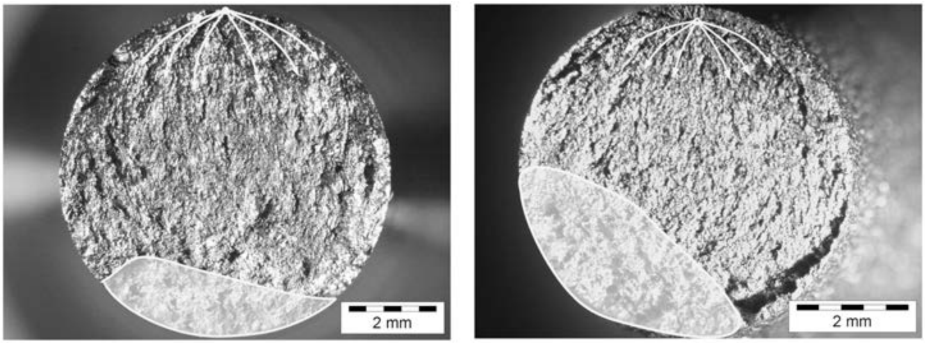

FIG. 5—*Fracture surface of:* (*left*) *an unpeened specimen;* (*right*) *a peened specimen.*

sional loading, shot peening results neither in an improvement nor in a degradation of the fatigue strength in the VHCF regime.

Fracture Analysis

Figures 5 and 6 present typical normal stress controlled fracture areas of the rotating bending tests. The crack initiation positions are marked by the common origin of the arrows. For all unpeened specimens the initial crack is found at the surface of the specimen Fig. 5 (left), in case of the peened specimens the crack initiation is observed below the surface at a depth of 0.2–0.3 mm, Fig. 5 (right). Figure 6 shows optical and secondary electron images (SEI) of the crack initiation site for the shot peened specimen shown in Fig. 5 (left), including the positions from which the EDX analyses were taken, see also Table 4. The crack initiation site can be observed in Fig. 6 (left) in detail. Figure 6 (right) shows a SEI image of the crack initiation location inclusive the sites for the energy dispersive X-ray EDX analysis. The EDX analysis confirms that the chemical composition at the crack initiation site was Ti-6Al-4V and not a material imper-

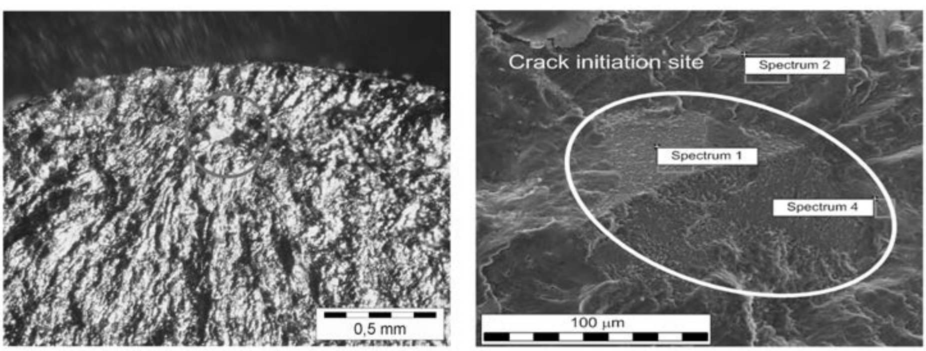

FIG. 6—*Crack initiation site for the peened specimen:* (*left*) *optical micrograph;* (*right*) *SEI.*

TABLE 4—*Results of the EDX analysis of the sites shown in Fig. 6 (right).*

Spectrum	Ti [wt %]	Al [wt %]	V [wt %]
Spectrum 1	88.2	7.5	4.3
Spectrum 2	90.4	5.6	4.0
Spectrum 4	88.0	8.1	3.9

fection, e.g., a nonmetallic inclusion. The paths of the arrows indicate the fatigue crack propagation. The crack growth rate increases due to the continuous decrease of the remaining intact cross section, leading to a coarsening of the fracture surfaces. This process finally leads to unstable crack growth and forced rupture exhibiting a granular crystalline surface, marked in Fig. 5 by the shaded areas. With increasing load, the cross section affected by forced rupture increases.

A fracture surface of a specimen loaded in torsion is shown in Fig. 7. The crack initiation starts shear stress controlled perpendicular to the specimen axis. During crack propagation the crack growth process changes into a normal stress controlled mode, at 45° to the specimen longitudinal axis.

Characterization of the Surface Layer

Crack initiation takes place typically at the surface or close to the surface. For a deeper understanding of the shot peening mechanism, the surface layer was analyzed extensively. Figure 8 presents a micrograph of the surface layer of a specimen shot peened with 0.16 A (mm) intensity. The lamellar microstructure is plastically deformed up to a depth of 10–15 μm due to the shot peening process, see Fig. 8. With increasing shot peening intensity, the depth of the plastically deformed layer increases too. Specimens peened with 0.25 A (mm) show a surface layer with a plastically deformed zone of approximately 20 μm depth.

One of the most important parameters for an interpretation of a shot peening process is the residual stress distribution in the surface layer. Figure 9

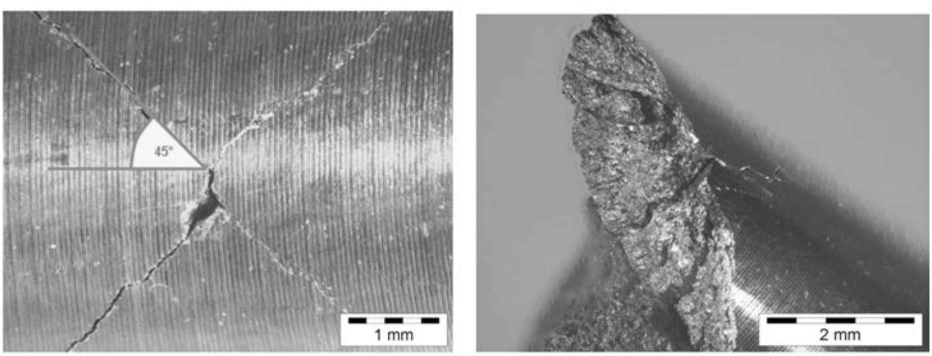

FIG. 7—*Specimen loaded in torsion: (left) fracture path; (right) fracture surface.*

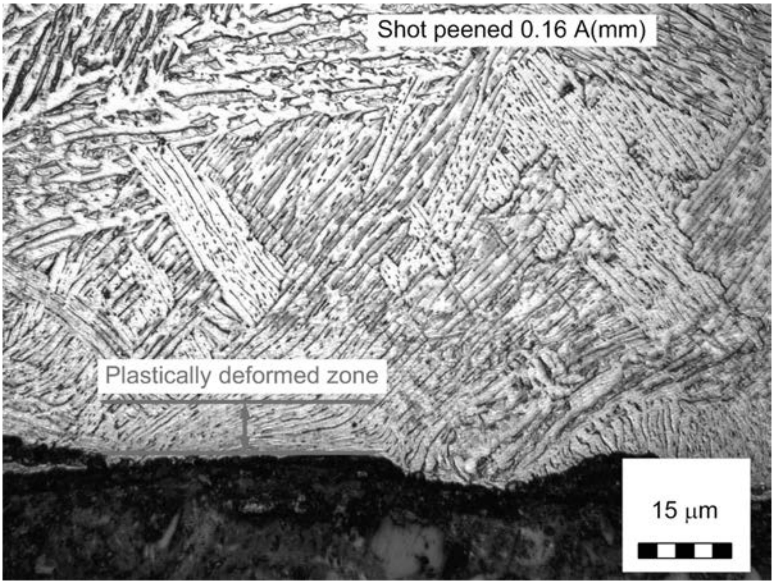

FIG. 8—*Optical micrograph of a surface layer of a specimen peened with* 0.16 A (mm).

depicts residual stress distributions in specimens peened with 0.16 A (mm) and 0.25 A (mm) measured before cyclic loading. In addition, residual stress measurements were performed after cyclic loading to investigate the residual stress relief. For 0.16 A (mm) peening intensity the residual stresses at the surface are

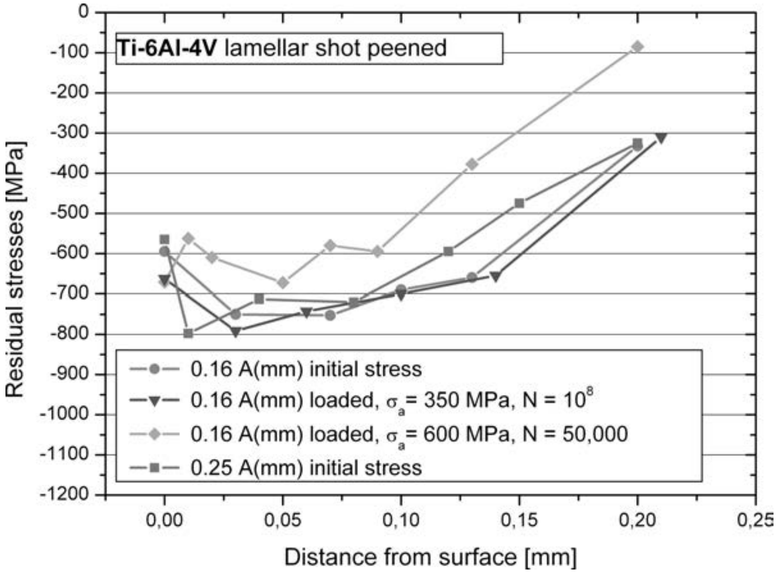

FIG. 9—*Residual stress distribution in the shot peened surface layer.*

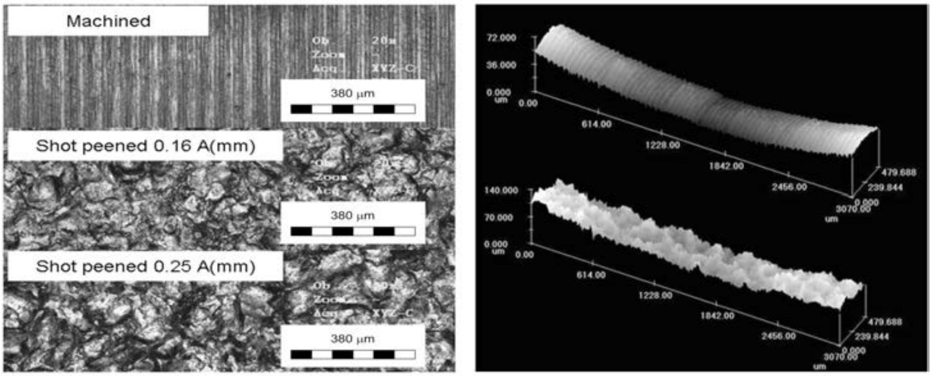

FIG. 10—*Comparison of the surface roughness of machined and shot peened specimens.*

at a residual stress level of −570 to −600 MPa. A shot peening intensity of 0.25 A (mm) does not lead to higher compressive residual stresses compared to 0.16 A (mm). It is important to note that residual stress measurement with X-ray diffraction is always afflicted with a considerable scatter (typically 30–50 MPa). The 0.16 A (mm) specimens showed no stress relief at relatively low load levels in the HCF regime, but a considerable stress relief at higher loads. It can be supposed that the stress relief under cyclic loading is caused by microplasticity. The effect increases with an increase of the load level and is known from investigations on different shot peened materials [13–15].

Figure 10 shows three-dimensional images of machined as well as shot peened surfaces. The surface roughness increases significantly with higher peening intensity. The roughness values are given in Table 5; R_a is the arithmetic mean height and R_z the mean height according to [16].

Finally, microhardness measurements were performed at the surface layer of the shot peened specimens. No considerable mircrohardness variations were observed.

Discussion

Rotating bending and alternating torsion experiments on shot peened Ti-6Al-4V specimens have been performed and the results may be summarized and interpreted as follows:

- Shot peening gives, under optimum process conditions, compressive residual stresses ranging from −600 to −800 MPa in a surface layer of

TABLE 5—*Peening intensity versus surface roughness.*

	R_z [μm]	R_a [μm]
Machined	2.61	0.82
Shot peened 0.16 A (mm)	6.96	2.36
Shot peened 0.25 A (mm)	8.47	2.90

0.1–0.15 mm thickness (Fig. 9). In HCF, no residual stress degradation is observed; this ties in well with the widespread assumption that, at or near the endurance limit, no gross cyclic plasticity must occur. On the other hand, under LCF loading, the residual stress degradation is quite pronounced, due to a large amount of cyclic plasticity.

- Shot peening with an intensity of 0.16 A (mm) leads to a marked improvement in the fatigue strength, whereas an intensity of 0.25 A (mm) results even in a degradation of the fatigue life in the HCF/VHCF regime. This is explained easily by overpeening. As is shown in Fig. 9, an intensity of 0.25 A (mm) does not yield significantly higher compressive stresses compared to 0.16 A (mm), but results—due to increased plastic deformation of the surface layer—in higher initial ductile damage, leading to reduced fatigue resistance. In addition, the surface roughness for the 0.25 A (mm) specimens is much higher (cf. Table 5 and Fig. 10), which is also known to have an adverse effect on the fatigue resistance [17].
- Shot peening increases the fatigue resistance in the lower HCF ranges; however, the VHCF behavior near the endurance limit is left almost unchanged in the case of alternating load.
  - The behavior near the endurance limit may again be explained by the absence of the required gross plasticity: in the presence of residual compressive stresses of ~−600 MPa near the surface, the yield limit in compression of −885 MPa and the ultimate strength of 940 MPa (i.e., the strength after severe plastic deformation, such as found in the surface layer) are reached with superimposed alternating bending stresses of 285 MPa and 340 MPa, respectively. This means that for a shot peened specimen the endurance limit will be in a range, due to the higher yield strength of the deformed surface layer, close to 340 MPa.
  - In the LCF regime, the allowable alternating stresses are higher, as the residual stresses have already decreased during the first few cycles (Fig. 9).
  - In the HCF regime, no residual stress degradation is observed, cf. Fig. 10; this means that cyclic plasticity will occur, and will lead to the initiation of fatigue cracks. However, fatigue crack growth is significantly delayed due to stress-induced crack closure in the presence of residual compressive stresses, which explains—together with the increased yield limit of the deformed surface layer—the fatigue strength increase in the HCF regime due to shot peening.
- In the shot peened specimens, failure is often observed to result from subsurface crack initiation sites at a depth of 0.2–0.3 mm. This means that in these cases the fatigue resistance of the surface layer (characterized by higher yield strength and compressive residual stresses) is higher than that of the material below (without plastic deformation and residual stresses).
- Likewise, in alternating torsion, shot peening results in an increased fatigue resistance in the lower HCF ranges, whereas the VHCF behavior is again nearly unaffected. Fatigue cracks initiate in Mode II (i.e., per-

pendicular to the specimen axis), but switch later to Mode I propagation (i.e., at 45° to the axis). Here, the same line of argumentation may be applied as in the case of rotating bending:

- Failure initiation in the VHCF regime is due to incipient cyclic plastification. Consequently, the fatigue limit in torsion corresponds—by way of the von Mises yield criterion—to $1/\sqrt{3}$ times the fatigue limit in tension: at 10^8 cycles, $190\ \text{MPa} \approx 340\ \text{MPa}/\sqrt{3}$.
- Final failure occurs by fatigue crack growth in Mode I, which is known to be significantly delayed by compressive stresses. The compressive residual stresses induced by shot peening therefore lead to a fatigue life increase in torsion just as in (rotating) bending.

- Notched specimens show a much more pronounced fatigue strength increase in the VHCF regime due to shot peening than unnotched specimens, although a comparison of unpeened notched and unnotched specimens shows that the material is highly notch sensitive. One of the standard concepts for explaining the effect of residual stresses as well as reduced notch sensitivity is the critical distance method (CDM), where it is assumed that the damage relevant stress is obtained by averaging over a critical distance, or a critical material volume. If one were to assume that stresses are to be averaged over 0.05 to 0.1 mm, this would result in lower notch sensitivity as well as in an increase in the effect of compressive residual stresses (which increase from -600 MPa to -800 MPa within the first 0.05 mm). The impact of the described behavior is influenced by both the stress gradients of the residual stresses and the applied loading. The increased fatigue strength of notched shot peened specimens stands in contrast to a fully notch sensitive material. These somewhat contradictory findings are now subject to further investigations.

Conclusions

- Variation within the range of the shot peening intensity according to MIL-S-13165C and MIL-P-81985 specifications can lead to both a significant increase or decrease in the HCF strength of lamellar Ti-6Al-4V.
- The effect of shot peening on the fatigue behavior is significantly influenced by the combination of the stress gradient due to external loading (geometry and type of loading) and the distribution of the residual stresses caused by shot peening.
- Under alternating torsion loads, shot peening shows similar effects on the fatigue behavior as for rotating bending loads. In the HCF regime the fatigue strength is increased significantly, whereas the VHCF region is nearly unaffected.
- In the lower HCF regime the compressive residual stresses induced by shot peening are reduced throughout the cyclic loading. At load levels causing VHCF the residual stress state is persistent.
- Under rotating bending loading both the crack initiation and the crack propagation of the investigated material are normal stress controlled. By contrast, fatigue crack initiation under torsional loading is caused by shear stresses but fatigue crack growth is normal stress dominated.

Acknowledgments

The authors would like to thank the Austrian Ministry of Economy and the Federal Governments of Vienna, Styria, Tyrol, Upper Austria, and Lower Austria for funding of this research work in the framework of the Austrian Aeronautics Research Program.

References

[1] Gray, H. et al., "Influence of Surface Treatment on the Fatigue Behavior of Ti-Alloys at Room and Elevated Temperatures," *6th World Conference on Titanium*, 1989.

[2] Wagner, L., and Lütjering, G., "Influence of Shot Peening on Surface Integrity of Some Machined Aerospace Materials," ICSP-1, Paris, 1981, www.shotpeening.org/ICSP

[3] Franz, H. E., and Obricht, A., "Optimization of Shot Peening to Improve the Fatigue Strength of Ti-6Al-4V," ICSP3, *Shot Peening: Science, Technology, Application* Vol. 2, 1987, pp. 439–446, www.shotpeening.org/ICSP

[4] Wohlfahrt, H., "Kugelstrahlen und Dauerschwingverhalten," ICSP-1, Paris, 1981, www.shotpeening.org/ICSP

[5] U.S. Army, "Military Specification—Shot Peening of Metal Parts, MIL-S-13165C," 1998.

[6] U.S. Army, "Military Specification—Peening of Metals, MIL-P-81985," 1974.

[7] *Fatigue Data Book*, "Light Structural Alloys," Library of Congress Cataloging-in-Publication Data, ASM International, 1995, ISBN 0-87170-607-9.

[8] U.S. Dept. of Defense, "MIL-HDBK-5," 1991.

[9] U.S. Dept. of Defense, "MIL-HDBK-5E," 1987.

[10] Bower, A., "The Effect of Testing Direction on the Fatigue and Tensile Properties of a Ti-6Al-4V Bar," *2nd International Conference on Titanium*, reported in *Fatigue Data Book*: Light Structural Alloys, Library of Congress Cataloging-in-Publication Data, ASM International, 1995, ISBN 0-87170-607-9.

[11] Leitner, H., "Simulation des Ermüdungsverhaltens von Aluminiumgusslegierungen," Dissertation, University of Leoben, 2001.

[12] Oberwinkler, B., "Schwingfestigkeit von Ti-6Al-4V—Betrachtung mehrerer Einflussgrößen," Diploma thesis, University of Leoben, 2007.

[13] Torres, M. A. S., and Voorwald, H. J. C., "An Evaluation of Shot Peening, Residual Stress and Stress Relaxation on the Fatigue Life of AISI 4340 Steel," *Int. J. Fatigue*, Vol. 24, 2002, pp. 877–886.

[14] Capello, E., Davoli, P., Filippini, M., and Foletti, S., "Relaxation of Residual Stresses Induced by Turning and Shot Peening on Steels," *J. Strain Anal. Eng. Des.*, Vol. 39, No. 3, 2004, pp. 285–290.

[15] Jiang, X. P., Man, C.-S., Shepard, M. J., and Zhai, T., "Effects of Shot-peening and Re-shot-peening on Four-point Bend Fatigue Behavior of Ti-6Al-4V," *Mater. Sci. Eng., A*, Vol. 468–470, 2007, pp. 137–143.

[16] International Organization for Standardization, "ISO 4287: Geometrical Product Specifications (GPS)—Surface Texture: Profile Method—Terms, Definitions and Surface Texture Parameters," 1997.

[17] Forschungskuratorium Maschinenbau (FKM): *Analytical Strength Assessment*, 5th ed., 2003, ISBN 3-8163-0425-7.

ASTM Special Technical Publication, Vol. 5, No. 4
Paper ID JAI101587
Available online at www.astm.org

Shankar Mall,[1] *J. L. Ng,*[1] *and E. Madhi*[1]

Fretting Fatigue Behavior of Shot-Peened Ti-6Al-4V and IN100

ABSTRACT: Shot-peened titanium alloy Ti-6Al-4V and nickel-based super alloy IN100 were subjected to plain and fretting fatigue under cylinder-on-flat contact condition at room temperature. Measurement of compressive residual surface stress from shot-peening before and after fretting showed relaxation, which was significant in IN100 and near the contact surface. The fretting fatigue life of IN100 did not improve significantly due to shot-peening, while there was considerable improvement for Ti-6Al-4V and relatively less relaxation of the residual surface stress. Further, fretting had a relatively more detrimental effect on the fatigue performance of Ti-6Al-4V than in the case of IN100. A critical plane-based fatigue crack initiation model, a modified shear stress range parameter, was computed from finite element analysis for two levels of residual surface stress relaxation: no relaxation and complete relaxation. This analysis suggested that not only crack initiation but also propagation should be considered to characterize fretting fatigue behavior of shot-peened specimens; however, it showed an appropriate trend with the measured fretting fatigue life and agreement with several other experimental observations.

KEYWORDS: fretting fatigue, residual surface stress, shot-peening, stress relaxation, crack initiation parameter, titanium alloy, nickel-based super alloy

Manuscript received November 26, 2007; accepted for publication February 28, 2008; published online April 2008.

[1] Department of Aeronautics and Astronautics, Air Force Institute of Technology, Wright-Patterson AFB, OH 45433.
Corresponding author e-mail: Shankar.Mall@afit.edu

Citation: Mall, S., Ng, J. L., and Madhi, E., "Fretting Fatigue Behavior of Shot-Peened Ti-6Al-4V and IN100," *J. ASTM Intl.*, Vol. 5, No. 4. DOI10.1520/JAI101587. Available online at www.astm.org. Also included in JAI Special Issue STP 1508, *Fatigue and Fracture Mechanics: 36th Volume*, R. W. Neu, K. R. W. Wallin, and S. R. Thompson, guest editors, ASTM International, West Conshohocken, PA, 2009, pp. 147-163.

Introduction

Fretting fatigue involves mating components under cyclic load that causes the localized relative motion at contact surface(s). This develops contact stresses that along with relatively small applied cyclic stresses lead to premature crack initiation and failure, and hence reduction in fatigue life. Failures from fretting fatigue are observed in many applications. One such case is the dovetail joint; i.e., interface of the disk slot and blade attachment in the fan compressor or turbine section of a gas turbine engine. Fretting fatigue causes not only significant reduction in aircraft and engine components' service life and premature failure in several instances but also increases maintenance costs. Therefore, the fretting fatigue is one major concern to the gas turbine engine community.

Considerable attention has been given to several aspects of fretting fatigue in an effort to better understand as well as to mitigate its effects in practical applications [1–3]. One of the most common techniques to enhance the plain fatigue as well as fretting fatigue performance is shot-peening, which involves the bombardment of the material surface with small, hard steel balls. This creates a residual compressive stress-state near the shot-peened surface. At the same time, a tensile stress within the interior is also created. The residual compressive stress plays a critical role in fatigue crack initiation and crack propagation retardation. Further, the residual stress can relax under cyclic loading condition but more so during fretting fatigue. The induced surface residual stress along with its relaxation also modifies the contact stress-state.

Fretting fatigue behavior of several important engineering materials, such as carbon steel, high strength steel, stainless steel, Ni-Mo-V steels, aluminum alloys, titanium alloys, nickel-based super alloys, etc., have been reported [1–3]. Titanium and nickel-based super alloys are utilized widely in both land-based and aero-based gas turbine industries. There are several fretting fatigue studies of titanium alloys reported in the literature [1–7]. However, very few studies are available on fretting fatigue behavior of nickel-based alloys. One such study involved the investigation of the fretting fatigue of nickel-based alloys, Inconel® 600 and Inconel 800 when in contact with carbon steel and 410S stainless steel in a steam environment at 265°C [8]. On the other hand, nickel-based alloys have been also used as one of the contacting materials (i.e., fretting pad) to investigate the fretting fatigue behavior of titanium alloy [9–12]. Another study involved the fretting fatigue behavior of a single crystal nickel alloy in contact with polycrystalline nickel alloy (IN100) at 610°C [13]. Furthermore, there are several fretting fatigue studies of shot-peened titanium alloys [14–16]. On the other hand, the authors are not aware of any such study of nickel-based alloys.

The objective of this study is twofold: (i) to characterize fretting fatigue behavior of a shot-peened nickel-based alloy by conducting experiment and their analysis, and (ii) to compare this with a shot-peened titanium alloy available from previous studies [14–16]. Titanium and nickel-based alloys are used in both disks and blades of gas turbine engines at different locations and temperatures, but they are subject to fretting fatigue during their usage. Therefore, the comparison of their fretting fatigue behaviors, especially similarities and differences, is of importance to the gas turbine designers and maintenance technologists. This study involved only room temperature, ambient laboratory condition as a first step in this direction. Further, the study looked into the relaxation and role of residual surface stress on the fretting fatigue crack initiation behavior through finite element analysis using a critical plane-based fatigue crack initiation parameter.

Experiments

Material and Specimen Details

Two test materials, Ti-6Al-4V and IN100, from titanium and nickel-based alloys, respectively, were used in this study. They were selected without any specific consideration except that they are the representative materials from each group that are commonly used in gas turbine engines. A forged alpha-beta titanium alloy Ti-6Al-4V was obtained as the plate. It contains 6 wt.% Al and 4 wt.% V, and its elastic modulus, yield strength, and ultimate strength are 126 GPa, 930 MPa, and 980 MPa, respectively. IN100 was obtained as a disk manufactured from powder metallurgy (P/M) and extrusion processes. It consisted of 60 wt.% Ni, 15 wt.% Co, 9.5 wt.% Cr, 5.5 wt.% Al, 4.75 wt.% Ti, 3 wt.% Mo and remaining other constituents. Its elastic modulus, yield strength, and ultimate strength are 196 GPa, 1150 MPa, and 1520 MPa, respectively. Dog-bone type specimens, machined by a wire electrical discharge machining method, had a thickness of 6.4 mm, width of 6.4 mm, and length of 127 mm. Specimens were ground to obtain a smooth surface finish, and then were shot-peened as per SAE Materials Specification (AMS) 2431 with standard cast steel shots of 4.3 mm diameter. The shot-peening intensity was 7 ± 1A and 12 ± 1A for Ti-6Al-4V and IN100, respectively. The surface coverage was 100 % for all specimens. A cylinder-on-flat contact configuration was used in this study. Fretting pads had 9.53 by 9.53 mm^2 cross section with 50.4 mm end radius and were not shot-peened. The pads were ground to an 8 RMS surface finish.

Residual stress on the surface of the shot-peened specimen was measured via X-ray diffraction technique before and after the fretting fatigue test. The X-ray diffraction measurements of residual stress were conducted using a two-angle sine-squared technique, in accordance with SAE J784. The surface area irradiated in these measurements was 0.5 by 5 mm^2. Residual stresses were also measured at several depths below the contact surface by iterative removal of thin layers of material by electropolishing and subsequent X-ray measurements. The distribution of these measured residual stresses is shown in Fig. 1.

Test Details

A servo-hydraulic fatigue test machine equipped with a fretting test setup was used (Fig. 2). The details of fretting test setup and fretting test procedure are documented in previous studies [4–6]. Several experiments were conducted under axial tension-tension fatigue loading condition at different stress levels with a constant stress ratio of 0.1. The cyclic axial force on the specimen was

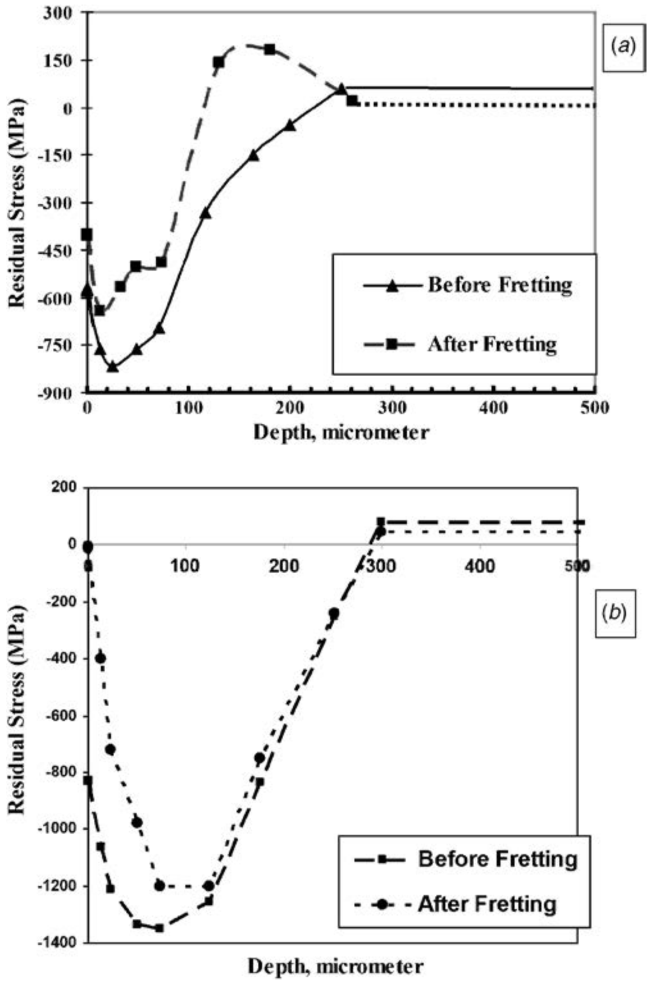

FIG. 1—*Residual stress before and after fretting:* (*a*) Ti-6A1-4V *and* (*b*) *IN100.*

applied in its length direction with constant amplitude at frequency of 10 Hz. A pair of pads was pressed on both sides of the specimen through the fretting fixture. The normal contact force P on the pad was 1335 N and 4000 N for Ti-6Al-4V and IN100 specimens, respectively. The tangential force Q was generated by pads. It was determined from the measured forces on the each side of the specimen [4–6]. The tangential force increased initially in a fretting test, but it stabilized between 100 to 500 cycles in a test. Axial and tangential forces were recorded throughout the test. The experimentally stabilized value of tangential and contact forces (Q/P) ratios ranged from 0.4 to 0.6 in this study. All tests involved the partial slip condition that was verified from the hysteresis loops between axial stress and tangential force. These were of the slender elliptical shape representative of the partial slip condition.

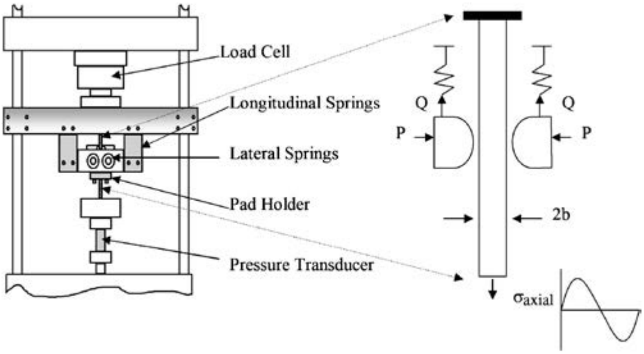

FIG. 2—*Fretting fatigue setup.*

Finite Element Analysis

Finite element analysis (FEA) of all tested specimens was conducted using a commercially available finite element code ABAQUS. Details of the analysis can be found elsewhere [17]. Finite element model of fretting fatigue specimen and cylindrical pad was created using four-noded, plane strain elements along with master-slave contact elements on the contact surface between fretting pad and specimen. A mesh with an element size of 0.0062 by 0.0062 mm^2 was used in the contact region between pad and specimen. This mesh size was gradually increased in regions away from the contact zone. The element size was selected after performing a convergence test. The selected mesh size resulted in a difference of less than 5 % in the contact region stress-state between the analytical and FEA in a semi-infinite domain; i.e., in a specimen with a very large thickness [18]. All specimens were analyzed using the measured axial, contact, and tangential forces. Normal contact force P was applied in the first step. In the second step, the stabilized value of the maximum tangential force Q_{max} and maximum axial stress were applied to match the experimental maximum cyclic loading condition. Finally in the third step, the stabilized value of minimum tangential force Q_{min} and minimum axial stress were applied to match the experimental minimum cyclic loading condition. Shot-peening effects were incorporated by adding the residual stresses to the longitudinal and transverse normal components of computed stress-state from the finite element analysis at all locations of the specimen. It was assumed that the shot-peening introduced only normal longitudinal and transverse stresses not the shear stress, and these stresses from the shot-peening were assumed equal to each other.

Results and Discussion

Damage Mechanisms

Fretting scar and fracture surface of fretting fatigued specimens were investigated using optical and scanning electron microscopes. All specimens from

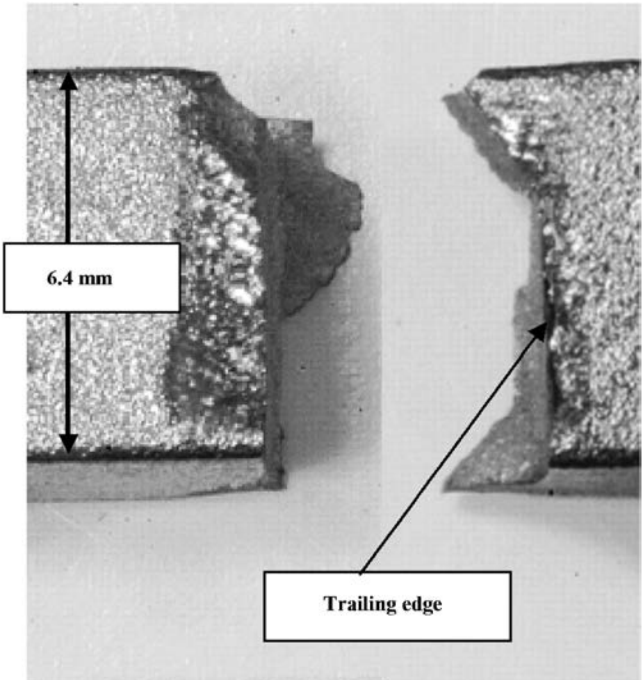

FIG. 3—*Crack initiation location on fretting scar in* Ti-6A1-4V.

both Ti-6Al-4V and IN100 materials fractured typically near the trailing edge of contact, as shown in Fig. 3 for a Ti-6Al-4V specimen. Besides the failure location on the fretting scar, the crack initiation location on the fracture surface is also an important consideration. Examination of the fractured surfaces with scanning electron microscopy showed that crack initiation location was at the contact surface in both Ti-6Al-4V and IN100 materials. Figure 4 shows this feature. Crack initiation location is on the contact surface of specimen, where there are river patterns and discoloration. Another important feature of the crack initiation is its orientation on the contact surface. For this purpose, several specimens were sectioned along the longitudinal direction and perpendicular to the fracture surface, then mounted in epoxy, and ground and polished near the crack initiation location. In both Ti-6Al-4V and IN100 materials, cracks initiated initially at either +45° or −45° with a variation of ±10° from perpendicular to the applied loading direction, and then became perpendicular to the applied fatigue loading direction over a short distance ranging from 30 μm to 100 μm. Figure 5 shows this feature in both materials. Similar damage characteristics were observed in both unpeened Ti-6Al-4V and IN100 specimens [4–6].

Fatigue Life

Figure 6 shows the applied stress range versus fretting fatigue life (S-N) results of Ti-6Al-4V and IN100 for both unpeened and shot-peened conditions as well

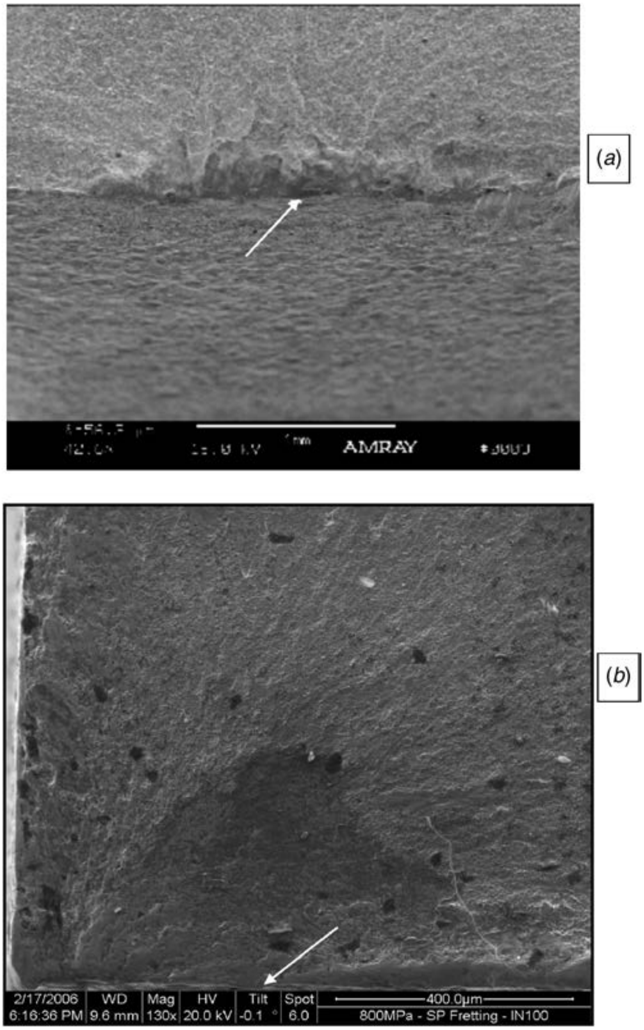

FIG. 4—*Crack initiation location on contact surface in* (*a*) Ti-6A1-4V *and* (*b*) *IN100* (*arrow shows contact surface*).

as the corresponding plain fatigue results for the unpeened specimens. These S-N results are shown on the basis of the applied stress range. Both materials clearly illustrate decrease in the fatigue strength with fretting. In many metallic materials, the magnitude of this reduction in the presence of fretting has been reported in the range of 30 %–60 % relative to plain fatigue [1–3]. So, in essence, the fretting fatigue behavior of both Ti-6Al-4V and IN100 follows the same general process of degradation relative to plain fatigue. Further, there is definitely a more detrimental effect on the fatigue performance of Ti-4Al-4V in comparison with IN100 in the presence of fretting. This is shown more clearly

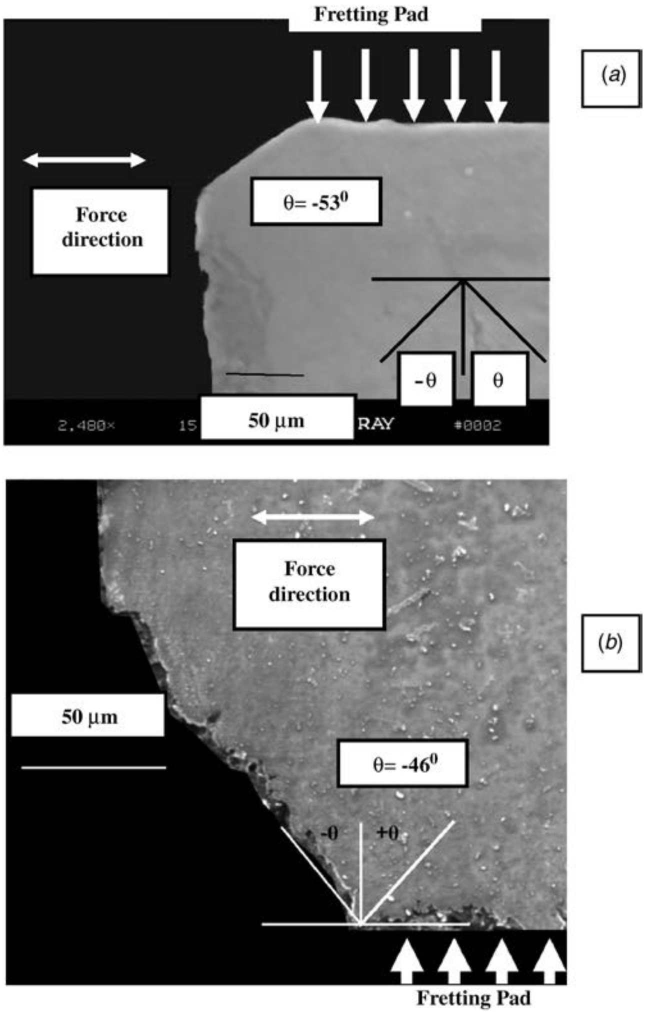

FIG. 5—*Crack initiation orientation on contact surface:* (*a*) Ti-6A1-4V *and* (*b*) *IN100.*

in Fig. 7, where the S-N results are illustrated on the basis of normalized stress range, where the applied stress range is normalized by the yield strength of each material. As can be seen in this figure, the normalized fretting fatigue strengths for 5×10^6 cycles are about 50 % and 20 % for Ti-6Al-4V and IN100, respectively; while these values for the plain fatigue are about 70 % and 60 %, respectively for the two materials.

Further, there is an improvement in the fretting fatigue life of Ti-6Al-4V due to shot-peening, and this is relatively more pronounced in the high cycle regime; i.e., for fatigue life greater than 10 000 cycles. This is not the case in IN100 where improvement from shot-peening is almost the same in both low and high cycle regimes. Furthermore, shot-peening of intensity equal to 12A

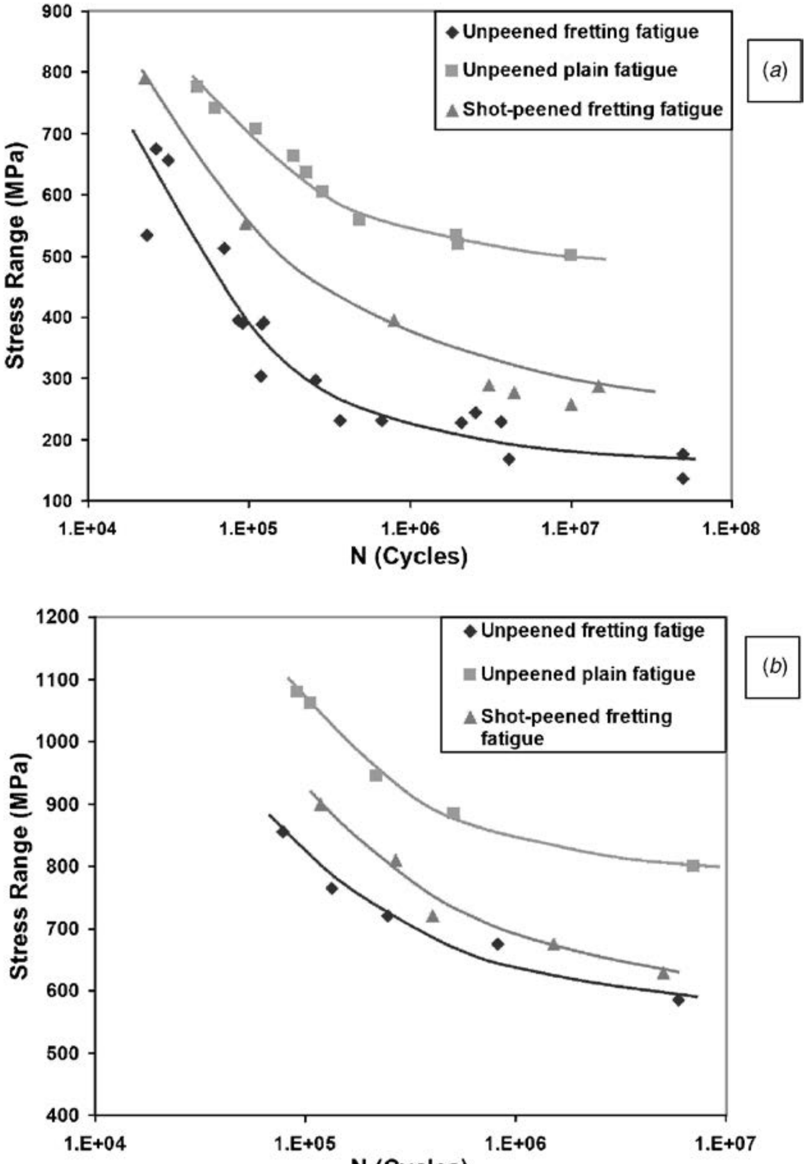

FIG. 6—*Stress range versus cycles to failure:* (*a*) Ti-6A1-4V *and* (*b*) *IN100* (*all curves are trend lines*).

generated relatively less improvement in IN100 than in Ti-6Al-4V shot-peened with 7A intensity. These features of the tested materials could depend upon the induced residual surface stress from the shot-peening and its relaxation characteristics as discussed in the next section. Further, the fatigue-life diagrams

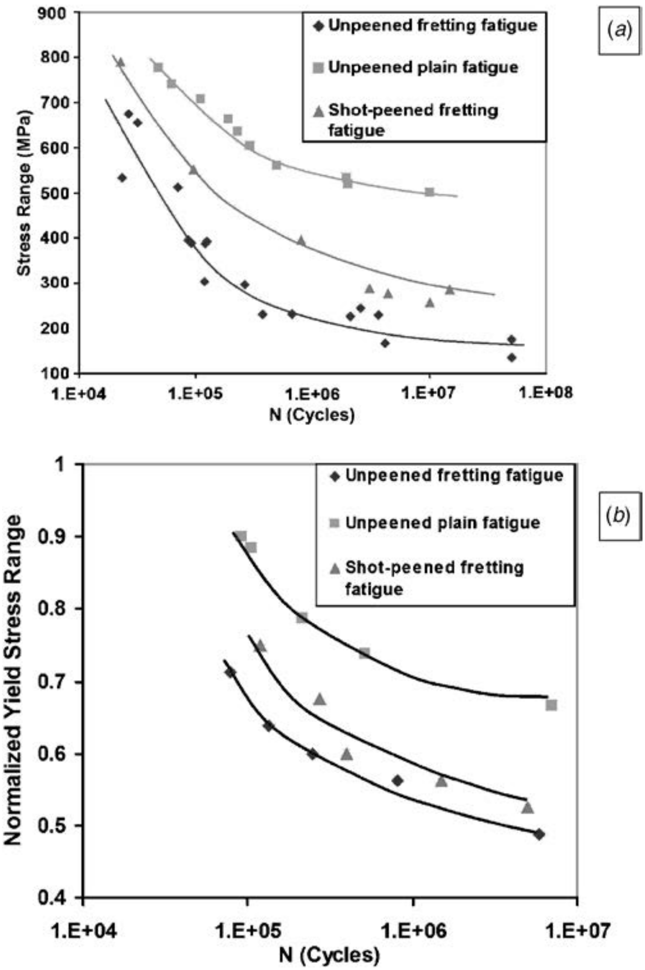

FIG. 7—*Normalized stress range versus cycles to failure:* (*a*) Ti-6A1-4V *and* (*b*) *IN100* (*all curves are trend lines*).

shown in Figs. 6 and 7 are based on the applied stress range on the specimen. They do not account for the contact stresses that also play a role on the fretting fatigue behavior of a material. It is obvious that the contact stress should be incorporated. This can be done through what is referred to as the critical plane-based fatigue parameters since they take into account the multi-axial stress state in the contact region. This is discussed later.

Residual Stress

Figure 1 shows the residual stress profiles of shot-peened Ti-6Al-4V and IN100 specimens that had 7A and 12A intensities, respectively. This figure shows residual compressive stress distributions along a vertical distance (or depth) away from the contact surface before and after the fretting test. Its values at the contact surface before fretting fatigue test were approximately −600 MPa and −820 MPa for Ti-6Al-4V and IN100 specimens, respectively. These values of residual stress increased initially inside the material, and then decreased. The major difference between these two cases are that shot-peening with greater intensity generated greater residual compressive stresses (−820 MPa versus −600 MPa) and deeper (up to ~300 μm for 12A versus ~175 μm for 7A); i.e., over the greater material volume below the contact surface. Further, it should be mentioned that the residual surface stress were measured up to a depth of about 250 μm–300 μm, which spanned a region generally with compressive residual stress. Further, these measurements away from the contact surface were done by the successive removal of material from the surface that may have some effect on the redistribution of internal stresses especially at greater depths. Therefore, this procedure is generally restricted to a region in the vicinity of the surface. Hence, these measurements were restricted near the contact surface.

As mentioned earlier, shot-peening also induces a compensatory tensile stress below the contact surface in order to balance the internal force in the material. Thus, the stresses at depths more than 250 μm–300 μm in Fig. 1 were calculated such that the total internal compressive force is balanced by the total internal tensile force in the specimen that involved the force balance over the areas under the positive and the negative stresses [17]. These tensile stresses were approximated as a constant value inside the specimen, as shown by dotted lines in Fig. 1.

Further, it has been observed that residual stresses from shot-peening are relaxed during fretting fatigue. This was also the case in the present study with both Ti-6Al-4V and IN100, as shown in Fig. 1. There was considerable relaxation of residual stresses especially near contact surface in the case of IN100, and it was almost fully relaxed at the contact surface after fretting fatigue. On the other hand, relaxation (i.e., reduction) of residual compressive stresses from fretting fatigue ranged from 20 % to 40 % at all locations below the contact surface as well as on the contact surface in Ti-4Al-4V. This clearly suggests that IN100 is prone to more relaxation than Ti-6Al-4V in spite of greater initial residual stresses in IN100. However, this relaxation behavior appears to be primarily in the vicinity of the fretting action that is generally up to about 100 μm from the contact surface in the case of IN100, while it is almost equal at all depths in Ti-6Al-4V. It should be mentioned here that relaxation behavior could depend upon many factors, such as shot-peening intensity, number of fretting fatigue cycles, applied stresses, etc., which should be investigated further. Such full characterization would require a significant number of tests and greater effort than undertaken in this study.

Fatigue Parameter

The stress state in contact region subjected to fretting fatigue is of a multi-axial nature. In order to characterize the crack initiation under such a situation one of the authors of the present paper and his colleagues have proposed a critical plane-based parameter, a modified shear stress range (MSSR) parameter that has been shown to be effective in terms of predicting fretting fatigue life from the plain fatigue data as well as the orientation and location of crack initiation in the unpeened titanium alloy Ti-6Al-4V tested with various contact geometries [6]. This parameter involves a combination of shear and normal stresses on the critical plane. This parameter will be utilized in the present study with shot-peened Ti-6Al-4V and IN100 specimens to study the effects of residual stress on the fretting fatigue crack initiation behavior.

To compute the MSSR parameter, shear stress was calculated on all planes with angles $-\pi/2 \leq \theta \leq \pi/2$ (Fig. 5) using:

$$S_{12}|_{\theta} = -\frac{S_{11} - S_{22}}{2}\sin 2\theta + S_{12}\cos 2\theta \tag{1}$$

where; S_{11}, S_{22}, and S_{12} are the longitudinal, transverse, and shear stresses, respectively, and θ is the orientation from a vertical to the applied axial force direction (1 – direction) of the specimen. By differentiation of Eq 1, and then equating it to zero, the angle of the plane where the shear stress is maximum was determined:

$$\theta|_{S_{12\max}} = -0.5\arctan\left(\frac{S_{11} - S_{22}}{2 \cdot S_{12}}\right) \tag{2}$$

The shear stress range on the plane was then computed:

$$\Delta S_{12} = S_{12\max} - S_{12\min} \tag{3}$$

Here, $S_{12\max}$ and $S_{12\min}$ are shear stresses due to maximum and minimum applied axial forces on the specimen, respectively. $S_{12\max}$ is given as:

$$S_{12\max} = -\frac{S_{11}|_{S_{b\max}} - S_{22}|_{S_{b\max}}}{2}\sin 2\,\theta|_{S_{12\max}} + S_{12}|_{S_{b\max}}\cos 2\,\theta|_{S_{12\max}} \tag{4}$$

or, in terms of stresses directly after substituting $\theta|_{S_{12\max}}$ from Eq 2 and simplification:

$$S_{12\max} = \frac{1}{2}\sqrt{S_{11}^2 - 2S_{11}S_{22} + S_{22}^2 + 4S_{12}^2} \tag{5}$$

A similar expression for $S_{12\min}$ involves the corresponding terms for the minimum applied axial force. From these, the value of the maximum shear stress range, its location, and the plane where it is acting, i.e., the critical plane, were obtained. Since the mean stress or stress ratio also affects the fatigue behavior, this effect on the critical plane was accounted for by a technique proposed by Walker [19]. $\Delta S_{12\text{crit}}$ was then calculated from:

$$\Delta S_{12\text{crit}} = S_{12\max}(1 - R_{\tau})^{m} \tag{6}$$

where $S_{12\max}$ and $R_{\tau}=S_{12\min}/S_{12\max}$ are the maximum shear stress and shear stress ratio on the critical plane, respectively. A fitting parameter m was determined to be 0.45 in a previous study [6]. Finally, the MSSR parameter was calculated by combining $\Delta S_{12\text{crit}}$ and the maximum normal stress on the critical plane of maximum shear stress range as:

$$MSSR = A(\Delta S_{12\text{crit}})^B + C[\,(S|_{S_{12\max}})|_{S_{b\,\max}}]^D \tag{7}$$

where $(S|_{S_{12\max}})|_{S_{b\,\max}}$ is the normal stress on the critical plane at the maximum applied force on the specimen, and is expressed as:

$$(S|_{S_{12\max}})|_{S_{b\,\max}} = \tfrac{1}{2}(S_{11}|_{s_{b\,\max}} + S_{22}|_{S_{b\,\max}}) + \tfrac{1}{2}(S_{11}|_{s_{b\,\max}} - S_{22}|_{S_{b\,\max}})\cos 2\,\theta|_{S_{12\max}} + S_{12}\sin 2\,\theta|_{S_{12\max}} \tag{8}$$

A, B, C, and D are the constants determined in a previous study [6]: $A=0.75$, $B=0.5$, $C=0.75$, and $D=0.5$.

Two levels of relaxation of residual stress from shot-peening were assumed in this study as these are limiting conditions. These were either full relaxation or no relaxation, and will be referred to as 0 % RS and 100 % RS, respectively. In other words, 100 % of residual stress (100 % RS) belongs to an initial value in the shot-peened specimen, i.e., before relaxation or before a fretting test, and 0 % of residual stress (0 % RS) represents the complete relaxation. Further, the 0 % RS case is the same as an unpeened specimen. The MSSR parameter was calculated at all locations for all specimens without any relaxation (100 % RS) and with complete relaxation (0 % RS) of residual stress as the two limiting cases.

The computed MSSR was analyzed to investigate the fretting fatigue crack initiation behavior as well as the role of shot-peened induced residual stress. The MSSR parameter predicted well the crack initiation location that matched closely with the experimental results. It was near the trailing edge and at the contact surface. In addition, the predicted crack initiation angle was ±45° with variation of ±10°, which matched very well again with the experimental results. Further, these predictions about location and crack initiation angle did not change due to addition of the residual stresses. Thus, these features from the MSSR parameter were the same for either the unpeened or shot-peened condition for both Ti-6Al-4V and IN100.

The computed MSSR parameter values versus fretting fatigue life (MSSR-N data) from all fretting tests (shot-peened and unpeened) of both materials for the two shot-peened limiting cases, 100 % RS and 0 % RS, as well as the unpeened specimens, are shown in Fig. 8. In addition, the similar relationships from the plain fatigue are shown in this figure. Firstly, it can be observed that MSSR versus N data for fretting fatigue and plain fatigue of unpeened specimens for both materials are in agreement with each other. This shows that this critical plane-based parameter represents well the fretting fatigue behavior. This also shows that IN100 has better plain and fretting fatigue resistance than those of Ti-6Al-4V, which is also evident based on the stress range basis, as seen previously in Fig. 6. Further, the MSSR parameter shows that there is an improvement in fretting fatigue life due to shot-peening when there is no relaxation of residual stress (i.e., 100 % RS versus unpeened) in both materials. However, the full relaxation of residual stresses lead to practically little or no improvement in the IN100 material, as predicted by the critical plane-based

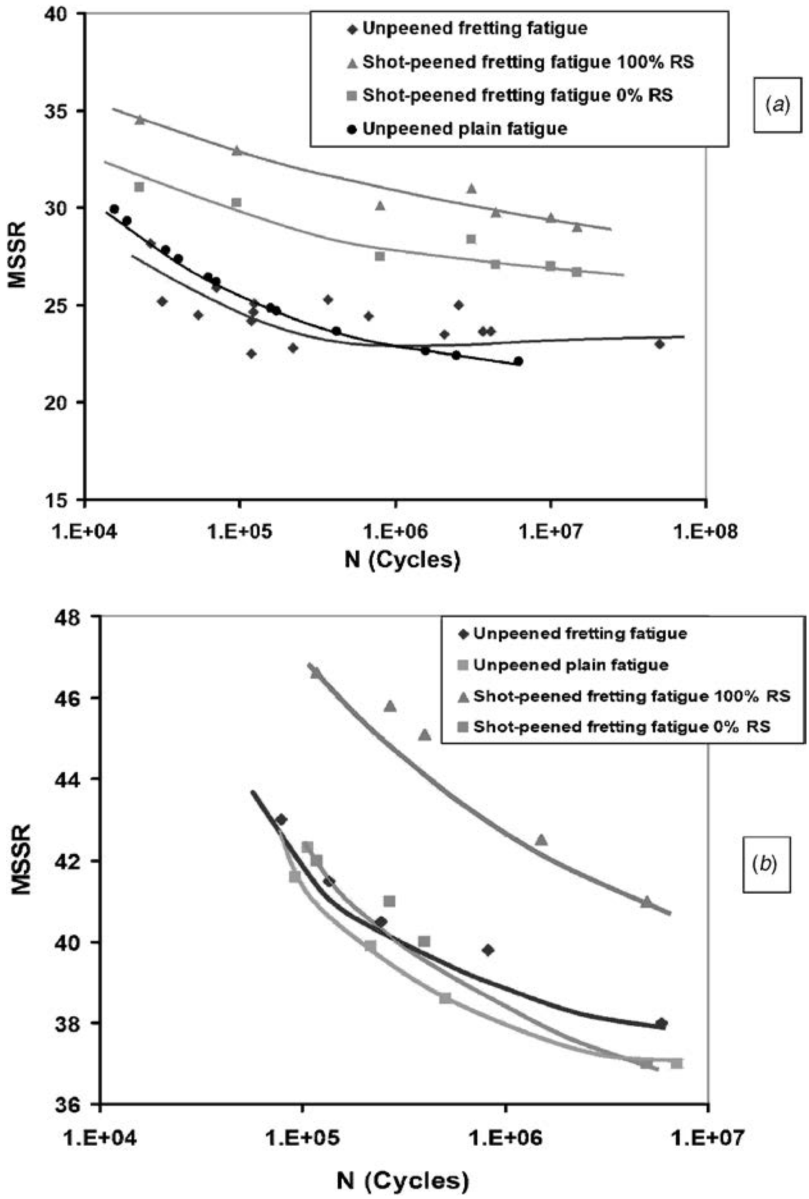

FIG. 8—*MSSR versus cycles to failure:* (*a*) Ti-6A1-4V *and* (*b*) *IN100* (*all curves are trend lines*).

fatigue crack initiation parameter, which is also evident from the measured experimental total life data (i.e., stress range versus fatigue life in Fig. 6). On the other hand, in the case of Ti-6Al-4V, the critical plane-based fatigue crack initiation parameter MSSR shows that there is an improvement in fretting fatigue life due to shot-peening in spite of the relaxation of residual stress. In reality, the stress relaxation is somewhere in between these two limiting conditions, i.e., in-between no relaxation (100 % RS) or complete relaxation (0 % RS), as shown in Fig. 1. If this consideration is included in the analysis, then the MSSR approach would show even more improvement in the fretting performance of Ti-6Al-4V than what is shown in Fig. 8. Moreover, the difference between these two sets of data, i.e., improvement in fretting fatigue life due to shot-peening, would also depend on the difference in number of cycles for crack initiation versus that for crack propagation in specimens with and without shot-peening.

It has been shown in a previous study that crack initiation consisted of about 90 % to 95 % of the total life or complete specimen rupture [4]. This was estimated from the *post-mortem* analysis of striations on fractured specimens as well as from crack growth analysis [4]. However, this would not be the case in shot-peened specimens due to the presence of residual compressive stresses that would cause longer crack initiation period and slower crack propagation rate and these characteristics would depend also upon the hardness, strength, etc. of the material. Thus, these two sets of S-N data (based MSSR parameter) from the unpeened and shot-peened specimens are expected to be apart from each other, which is not in the case of IN100. This suggests that crack initiation part was probably contributing relatively more than the crack propagation part in IN100, which might be expected since there was relatively much more relaxation of residual stress especially near the contact surface. On the other hand, crack propagation phase was probably contributing relatively more in Ti-6Al-4V shot-peened specimens. This phenomenon has been shown qualitatively in previous studies [20,21]. However, there may be several other factors. Therefore, further studies are needed to characterize the fretting fatigue behavior in shot-peened materials and the present study is a step in the direction.

Conclusions

Fretting fatigue behavior of shot-peened titanium alloy Ti-6Al-4V and nickel-based super alloy IN100 under cylinder-on-flat contact condition at room temperature was investigated. Residual stress measurements before and after fretting test showed that it relaxed during fretting fatigue. Further, this relaxation near the contact surface was considerable in IN100. Therefore, shot-peening generated a small improvement in the fretting fatigue life of IN100. On the other hand, shot-peening improved considerably the fretting fatigue life of Ti-6Al-4V in spite of the relaxation of the residual surface stress. A critical plane-based fatigue crack initiation parameter, modified shear stress range (MSSR), was computed from finite element analysis. It showed the appropriate trend with the measured fretting fatigue life. Further, cracks always initiated at the contact surface near the trailing edge of the fretted region and were correctly predicted by the MSSR parameter. In addition, the MSSR parameter correctly predicted the orientation of fretting fatigue crack initiation on the contact surface that was in excellent agreement with the experimental counterpart. Finally, fretting had a relatively more detrimental effect on the fatigue performance of Ti-6Al-4V than in the case of IN100.

References

[1] *Standardization of Fretting Fatigue Test Methods and Equipment*, ASTM STP 1159, M. H. Attia and R. B. Waterhouse, Eds., ASTM International, West Conshohocken, PA, 1992.

[2] *Fretting Fatigue: Current Technologies and Practice*, ASTM STP 1367, D. W. Hoeppner, V. Chandrasekaran, and C. B. Elliot, Eds., ASTM International, West Conshohocken, PA, 2000.

[3] *Fretting Fatigue: Advances in the Basic Understanding and Applications*, ASTM STP 1425,
S. E. Kinyon, D. W. Hoeppner, and Y. Mutoh, Eds., ASTM International, West Conshohocken, PA, 2003.

[4] Lykins, C. D., Mall, S., and Jain, V. K., "Combined Experimental-Numerical Investigation of Fretting Fatigue Crack Initiation," *Int. J. Fatigue*, Vol. 23, 2001, pp. 703–711.

[5] Lykins, C. D., Mall, S., and Jain, V. K., "A Shear Stress-Based Parameter for Fretting Fatigue Crack Initiation," *Fatigue Fract. Eng. Mater. Struct.*, Vol. 24, 2001, pp. 461–473.

[6] Namjoshi, S. A., Mall, S., Jain, V. K., and Jin, O., "Fretting Fatigue Crack Initiation Mechanism in Ti-6Al-4V," *Fatigue Fract. Eng. Mater. Struct.*, Vol. 25, 2002, pp. 955–964.

[7] Iyer, K. and Mall, S., "Effects of Cyclic Frequency and Contact Pressure on Fretting Fatigue Under Variable-Amplitude Loading," *Fatigue Fract. Eng. Mater. Struct.*, Vol. 23, 2000, pp. 335–346.

[8] Attia, M. H., "Fretting Fatigue of Some Nickel-Based Alloys in Steam Environment at 265°C," *Fretting Fatigue: Current Technology and Practices*, ASTM STP 1367, D. W. Hoeppner, V. Chandrasekaran, and C. B. Elliott, Eds., ASTM International, West Conshohocken, PA, 2000, pp. 231–246.

[9] Hansson, T., Kamaraj, M., Mutoh, Y., and Peterson, B., "High Temperature Fretting Fatigue Behavior in an XDTM γ-base TiAl," *Fretting Fatigue: Current Technology and Practices*, ASTM STP 1367, W. Hoeppner, V. Chandrasekaran, and C. B. Elliott, Eds., ASTM International, West Conshohocken, PA, 2000, pp. 65–79.

[10] Miyoshi, K., Lerch, B. A., Draper, S. L., and Raj, S. V., "Evaluation of Ti-48Al-2Cr-2Nb under Fretting Fatigue Conditions," *Fretting Fatigue: Advances in Basic Understanding and Applications*, ASTM STP 1425, Y. Mutoh, S. E. Kinyon, and D. W. Hoeppner, Eds., ASTM International, West Conshohocken, PA, 2003, pp. 323–337.

[11] Lee, H. and Mall, S., "Effect of Dissimilar Mating Materials and Contact Force on Fretting Fatigue Behavior of Ti-6Al-4V," *Tribol. Int.*, Vol. 37, 2004, pp. 35–44.

[12] Lee, H., Jin, O., and Mall, S., "Fretting Fatigue Behavior of Ti-6Al-4V with Dissimilar Mating Materials," *Int. J. Fatigue*, Vol. 26, 2004, pp. 393–402.

[13] Murthy, H., Garcia, D. B., Matlik, J. F., and T. Farris, T., "Fretting Fatigue of Single Crystal/Polycrystalline Nickel Subjected to Blade/Disk Contact Loading," *Acta Astronaut.*, Vol. 57, 2005, pp. 1–9.

[14] Namjoshi, S. A., Jain, V. K., and Mall, S., "Effect of Shot-Peening on Fretting-Fatigue Behavior of Ti-6Al-4V," *J. Eng. Mater. Technol.*, Vol. 124, 2002, pp. 222–228.

[15] Lee, H., Jin, O., and Mall, S., "Fretting Fatigue Behavior of Shot-Peened Ti-6Al-4V at Room and Elevated Temperature," *Fatigue Fract. Eng. Mater. Struct.*, Vol. 26, 2003, pp. 767–778.

[16] Lee, H. and Mall, S., "Stress Relaxation Behavior of Shot-Peened Ti-6Al-4V under Fretting Fatigue at Elevated Temperatures," *Mater. Sci. Eng., A*, Vol. 366, 2004, pp. 412–420.

[17] Sabelkin, V., Martinez, S. A., Mall, S., Sathish, S., and Blodgett, M. P., "Effects of Shot Peening Intensity on Fretting Fatigue Crack Initiation Behavior of Ti-6A1-4V," *Fatigue Fract. Eng. Mater. Struct.*, Vol. 28, 2005, pp. 321–332.

[18] Hills, D. A. and Nowell, D., *Mechanics of Fretting Fatigue*, Kluwer Academic Publishers, Dordrecht, 1994.

[19] Walker, K., "The Effect of Stress Ratio during Crack Propagation and Fatigue for 2024-T3 and 7075-T6 Aluminum," *Effects of Environment and Complex Load History on Fatigue Life*, ASTM STP 462, ASTM International, West Conshohocken, PA, 1970, pp. 1–14.

[20] Shkarayev, S. and Mall, S., "Computation Modeling of Shot-Peening Effects on Crcak Propagation Under Fretting Fatigue," *J. Strain Anal. Eng. Des.*, Vol. 38, 2003, pp. 495–506.

[21] Fadaq, H. A., Mall, S., and Jain, V. K., "A Finite Element Analysis of Fretting Fatigue Crack Growth in Ti-6Al-4V," *Eng. Fract. Mech.*, Vol. 75, 2008, pp. 1384–1399.

ASTM Special Technical Publication, Vol. 5, No. 3
Paper ID JAI101528
Available online at www.astm.org

Minwoo Kang,[1] *Kentaro Irisa,*[1] *Yuuta Aono,*[1] *and Hiroshi Noguchi*[1]

Prediction of the Fatigue Limit of Prestrained Carbon Steel Under Tensile Mean Stress

ABSTRACT: The effect of tensile mean stress on the fatigue limit of carbon steel was investigated. Annealed 0.1 % and 0.5 % carbon steel specimens were subjected to monotonic tension to produce prestrain. Fatigue tests were performed using a servohydraulic fatigue test machine. The experimental results showed that tensile mean stress degraded the fatigue limit. However, the tensile mean stress did not affect the decrease in the surface hardness as a result of fatigue loading for the specimen without a defect. In the case of the specimen with a defect, the decrease in the hardness was small and did not depend on the mean stress or stress amplitude. Formulae for predicting the fatigue limit of prestrained carbon steel specimens under tensile mean stress were proposed. The results calculated using the formulae showed good agreement with the experimental results.

KEYWORDS: prestrain, fatigue limit, mean stress, carbon steel, hardness, residual stress

Introduction

Structural members and parts for practical use are subjected to plastic deformation during manufacturing. It has been reported that this plastic deformation, which is called prestrain, affects the static and cyclic properties of metallic

Manuscript received November 7, 2007; accepted for publication January 28, 2008; published online March 2008.

[1] Department of Mechanical Engineering Science, Kyushu University, Moto-oka 744, Nishi-ku, Fukuoka, 819-0395, Japan, e-mail: kjs1108@mech.kyushu-u.ac.jp

Citation: Kang, M., Irisa, K., Aono, Y. and Noguchi, H., "Prediction of the Fatigue Limit of Prestrained Carbon Steel Under Tensile Mean Stress," *J. ASTM Intl.*, Vol. 5, No. 3. DOI10.1520/. Available online at www.astm.org. Also included in JAI Special Issue STP 1508, *Seventh International ASTM/ESIS Symposium on Fatigue and Fracture Mechanics* (*36th ASTM National Symposium on Fatigue and Fracture Mechanics*), R. W. Neu, K. R. W. Wallin and S. R. Thompson, guest editors, ASTM International, West Conshohocken, PA, 2008, pp. 164-182.

materials [1–6]. Many previous studies on the effect of prestrain on fatigue have also been reported [1–9]. In our previous study, we investigated the effect of prestrain on the fatigue limit of carbon steels and proposed formulae for predicting the rotating bending fatigue limit ($R=-1$) [10]. In general, the modified Goodman equation, the Gerber parabola, and the Morrow equation have been used to consider the effect of tensile mean stress in fatigue design for non-strained metallic materials [11,12]. However, there have been a few in which the effect of tensile mean stress on the fatigue limit of prestrained carbon steels is investigated and a method of predicting the fatigue limit is proposed. When we consider real conditions used for most prestrained mechanical structural members and parts, the effect of tensile mean stress on the fatigue limit of prestrained carbon steel must be considered for safe and rational fatigue design.

The aim of the present study is to investigate the effect of tensile mean stress on the fatigue limit of prestrained carbon steels and to propose formulae for predicting the fatigue limit under tensile mean stress. Axial loading fatigue tests under tensile mean stress were performed using tensile-prestrained annealed 0.1 % carbon steel and annealed 0.5 % carbon steel specimens. A hardness test and the observation of the specimen surface during fatigue tests were carried out. In addition, formulae for predicting the fatigue limit were proposed on the basis of the test results.

Experiment

The materials used in this study were annealed 0.1 % carbon steel and annealed 0.5 % carbon steel, hereafter called S10C and S50C, respectively. Table 1 lists the chemical compositions and mechanical properties of the test materials. Prestrain is defined as the remaining plastic strain after tensile plastic deformation. Figure 1 shows the shapes and dimensions of the prestrain and fatigue specimens. Figure 2 shows the procedure for preparing and testing the specimens. All the specimens were electropolished to remove the work-hardened layer and to make it easier to observe changes in the surface state. Static tensile tests were performed to apply prestrain to the specimens. The prestrains applied to the specimens were 12 % for S10C and 10 % for S50C. The specimens were heated at 100°C for 1 h after prestraining to prevent any time-dependent variation in the static and fatigue characteristics as a result of strain aging [13,14]. The prestrained specimens used for the fatigue test are shown in Figs. 1(*b*) and 1(*c*), before the fatigue test. The central part of the specimen was preserved to retain the effect of prestrain. To make the specimen with a defect, as shown in Fig. 1(*c*), an artificial defect was introduced using a microdrill (diameters 500 μm) on the central part of the fatigue specimen, shown in Fig. 1(*b*), after heating. The fatigue tests were performed using a servohydraulic fatigue test machine (50 kN, 30 Hz) at room temperature. The fatigue limits were determined at intervals of 5 MPa. All fatigue tests were carried out at 25 Hz. The surface hardness of the specimens was measured using a micro-Vickers hardness tester to determine the variation of the hardness before and after fatigue tests. The measuring load was 4.9 N. An X-ray diffraction residual

TABLE 1—*Chemical compositions and mechanical properties.*

		Chemical composition (wt %)							Mechanical properties			
Material	Heat treatment	C	Si	Mn	P	S	Cu	Prestrain %	E (GPa)	σ_u (MPa)	σ_y (MPa)	ϕ (%)
S10C	Annealing 900°C, 1 h	0.13	0.22	0.39	0.01	0	0.09	0	207	378	221	42
								12	200	465	401	18.3
S50C	Annealing 833°C, 1 h	0.54	0.28	0.77	0.02	0.02	0.06	0	200	620	335	4.6
								10	200	738	—	—

E: elastic modulus, σ_u: tensile strength, σ_y: yield strength (lower),
ϕ: engineering fracture strain (gauge length: 25 mm)

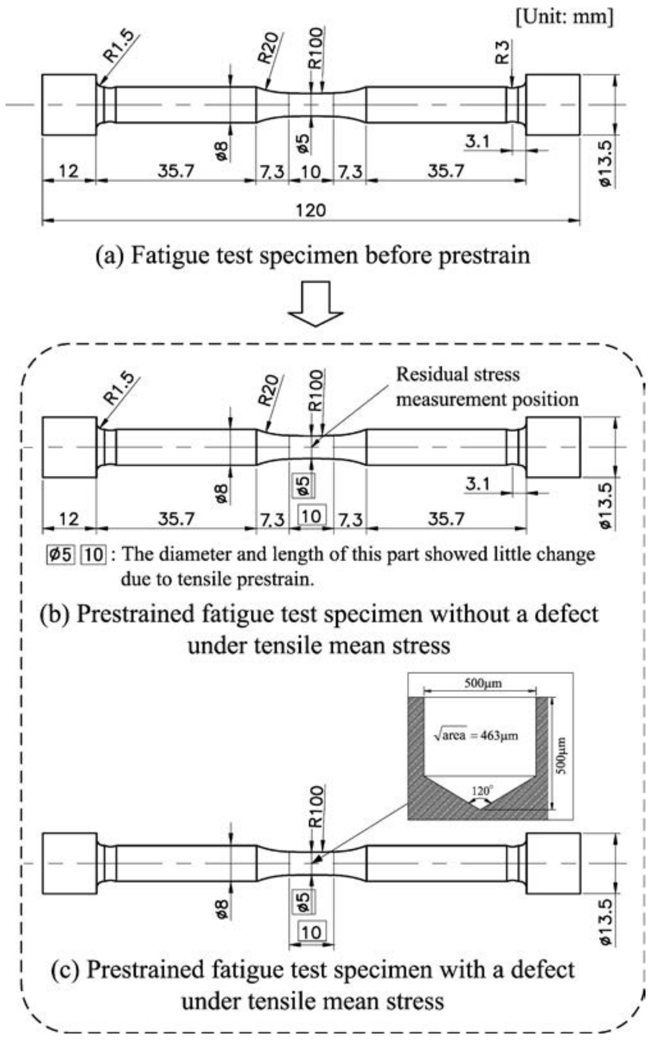

FIG. 1—*Shapes and dimensions of prestrain and fatigue specimens. Dashed lines in* (*a*) *represent the shape of the fatigue specimen after remachining. Defect size,* $\sqrt{\text{area}}$*, is the square root of the area obtained by projecting the crack onto a plane perpendicular to the specimen axial direction.*

stress measurement apparatus was used to measure the surface residual stress in the axial direction of the specimens before fatigue tests. The X-ray tube of CrKα type was operated at 40 kV and 30 mA. The shift of α-Fe(211) diffraction profile was detected. The X-rays were counted for 60 s at each step at angles of ψ equal to 0, 13.6, 19.5, 24.1, 28.1, 31.8, 35.3, 38.6, 41.8, and 45.0°. Here, ψ is the angle between the normal to the specimen surface and the normal to the diffractive face. The diffraction angle 2θ without strain was 156.4° and the

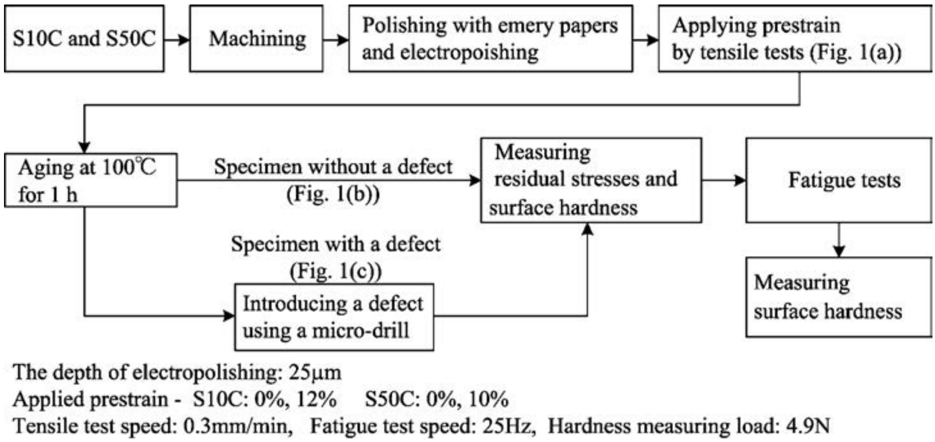

FIG. 2—*Procedure for preparing and testing specimens.*

stress factor of the X-ray diffraction method was −318.0 MPa/deg. An X-ray beam with a diameter of 0.5 mm was focused on the central part of specimens without a defect. In the case of specimens with a defect, the X-ray beam was focused on the vicinity of the defect (500 μm far from the edge of the defect) to consider the relaxation of residual stress as a result of introducing the defect. The replica method was used to monitor the formation of fatigue cracks and the propagation behavior on the specimen surface.

Fatigue Limit of Prestrained Specimens Under Tensile Mean Stress

Figure 3 shows the fatigue limit of prestrained S10C specimens under tensile mean stress. The fatigue limits of specimens without a defect are 210, 210, and 185 MPa at a mean stress of $\sigma_m = 0$, 145, and 230 MPa, respectively. The results show that as mean stress increases, the fatigue limit decreases. In the case of specimens with a defect, the same tendency is shown. The fatigue crack formation and propagation behavior of the specimens at the fatigue limit stress are shown in Figs. 4 and 5. The fatigue limits of all the prestrained S10C specimens without and with a defect are determined by the nonpropagation of a fatigue crack, as shown in the figures. As mean stress increases, the length of the nonpropagating crack on the specimens without and with a defect decreases. This result is in agreement with the result of another study [15]. It is thought that this phenomenon is related to the decrease in the threshold stress intensity factor ΔK_{th} as a result of increasing stress ratio R or mean stress σ_m [16]. When the crack size is small (threshold stress is equal to fatigue limit, $\sigma_{\mathrm{th}} = \sigma_w$), ΔK_{th} depends on the crack length [16,17]. Therefore, it is thought that R or σ_m decreases ΔK_{th} and the length of the nonpropagating crack.

Variation of Surface Hardness and Fatigue Limit in Prestrained Specimen

To investigate the macroscopic change in material properties, the surface hardnesses of the prestrained S10C specimens before and after fatigue tests were

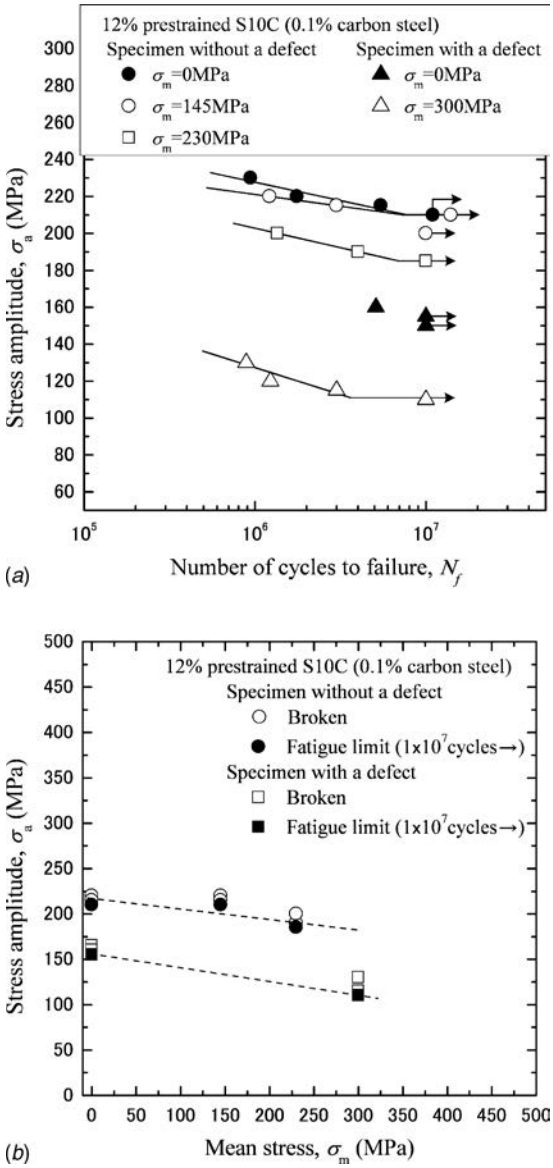

FIG. 3—*Fatigue limit of prestrained S10C specimens. The fatigue limit decreases with mean stress.* (*a*) *S–N curves of prestrained S10C specimens.* (*b*) *Relationship between fatigue limit and mean stress.*

measured, as shown in Table 2 and Fig. 6. The load of the hardness test was 4.9 N. The hardnesses shown in the table and figure were average hardnesses measured at 10 points and the scatter of these values was within ±10 %. In the case of the specimens with a defect, the points used to measure the hardness

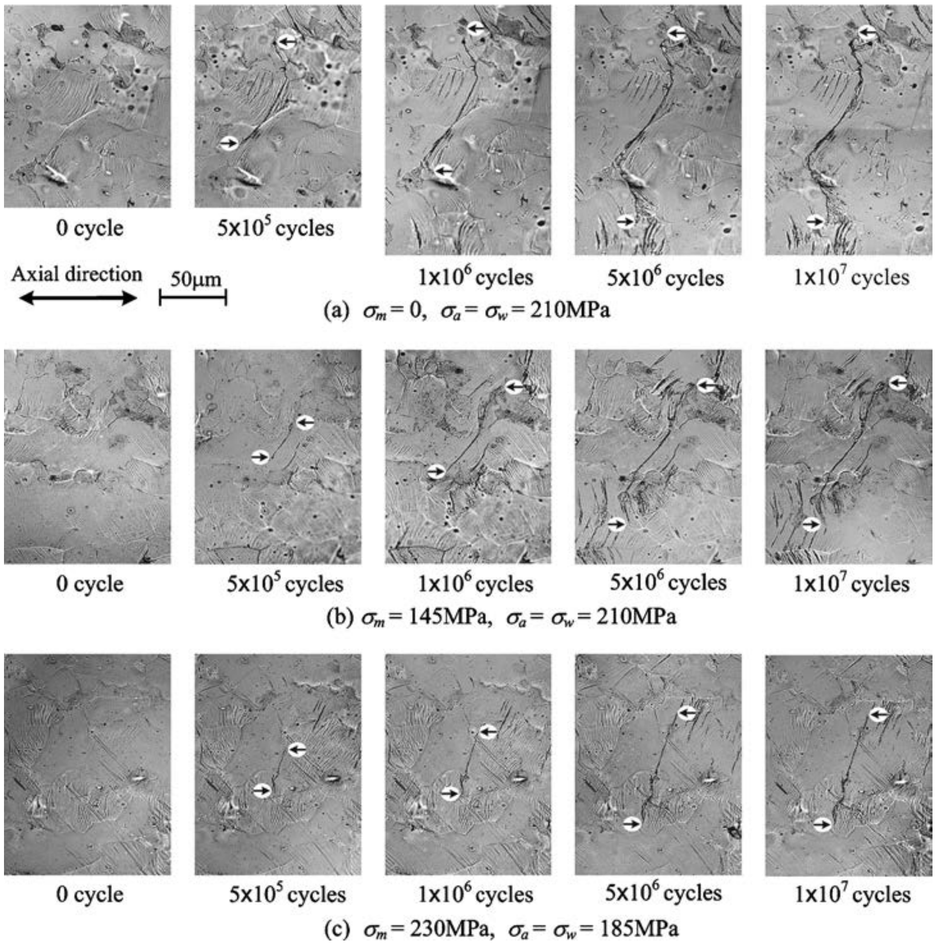

FIG. 4—*Fatigue crack formation and propagation of prestrained S10C specimens without a defect at fatigue limit stress. σ_a: stress amplitude, σ_w: fatigue limit, σ_m: mean stress.*

were far from the defect to prevent the effect of plastic deformation due to stress concentration in the vicinity of the defect. The hardness data given in Table 2 are separated into stress amplitude σ_a [Fig. 6(*a*)] and mean stress σ_m [Fig. 6(*b*)] and plotted in Fig. 6. The hardness of all the specimens decreased after the fatigue test. For specimens without a defect, the hardnesses after the fatigue test decreased with increasing stress amplitude, as shown in Fig. 6(*a*). In addition, considering that the hardnesses of the specimens for which $\sigma_a = 160$ MPa, $\sigma_m = 0$ MPa, and $\sigma_a = 160$ MPa, $\sigma_m = 290$ MPa are the same in Fig. 6(*b*), it is clear that the decrease in hardness after the fatigue test is not related to the tensile mean stress but to the stress amplitude. The hardnesses of the specimens with a defect decreased to HV = 160 after the fatigue test, regardless

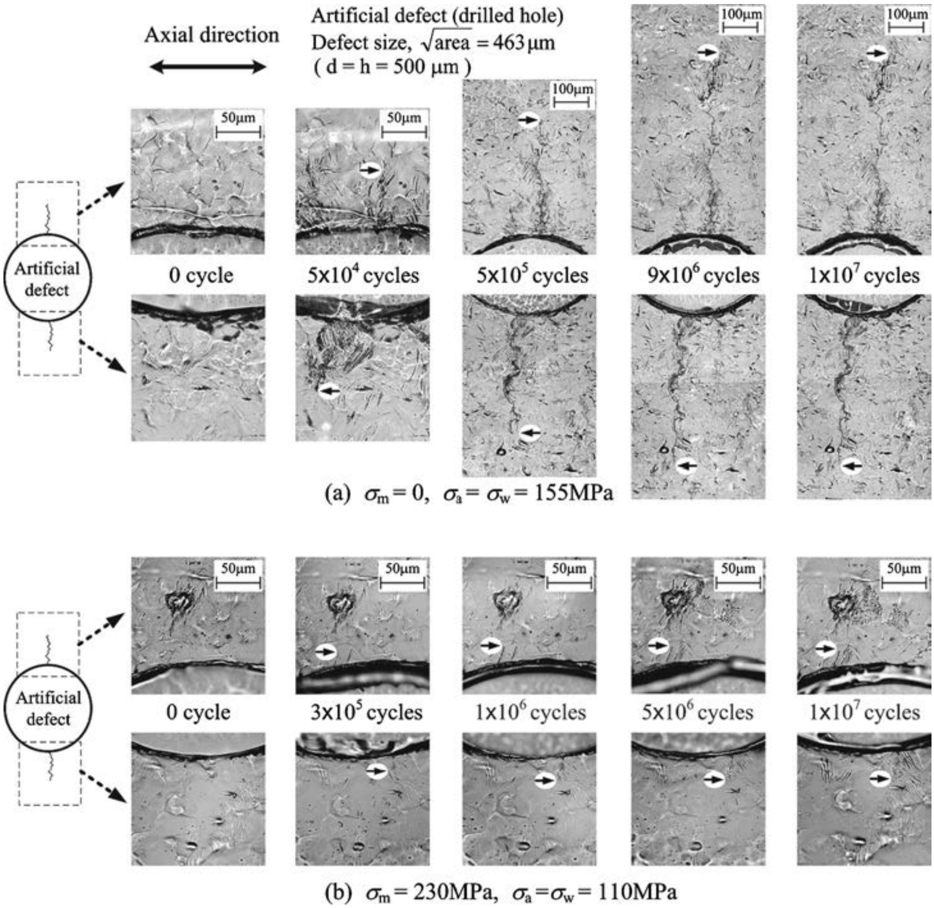

FIG. 5—*Fatigue crack formation and propagation of prestrained S10C specimens with a defect at fatigue limit stress.* σ_a*: stress amplitude,* σ_w*: fatigue limit,* σ_m*: mean stress.*

of the stress amplitude and tensile mean stress, but these values are greater than those of the specimens without a defect. This result signifies that the macroscopic cyclic softening (decrease in hardness) caused by fatigue loading in the prestrained specimens with a defect is smaller than that in the prestrained specimens without a defect.

Figure 7 shows the variation in hardness induced by fatigue loading for a prestrained specimen during the fatigue test. The mean stress σ_m and stress amplitude σ_a were 0 and 230 MPa, respectivley. The hardness of the prestrained specimen decreases rapidly in the early stage ($0.05 \sim 0.1N_f$) and then decreases slowly. This result says that the cyclic softening (decrease in hardness) is saturated within 10 % of the specimen life. When we consider that the crack formation life in nonstrained low-carbon steel and prestrained low-carbon steel without a defect is generally about 20 ~ 30 % (up to grain size)

TABLE 2—*Surface hardnesses of prestrained S10C specimens before and after fatigue tests.*

				Surface hardness, HV			
Material	Defect size $\sqrt{area}$(μm)	Mean stress σ_m (MPa)	Stress amplitude σ_a (MPa)	Before fatigue test	After fatigue test	After/ Before	N_f
	—	0	160	163	156	0.96	1.0×10^7
12 %	—	0	230	163	154	0.94	3.4×10^6
prestrained	—	0	260	163	153	0.94	8.4×10^5
S10C	—	145	210	163	155	0.95	$1.4\times10^7\rightarrow$
	—	230	190	163	155	0.95	4.0×10^6
	—	230	200	163	155	0.95	1.4×10^6
	—	290	130	163	156	0.96	$1.0\times10^7\rightarrow$
	—	290	160	163	156	0.96	$1.0\times10^7\rightarrow$
12 %	463	0	150	163	160	0.98	$1.0\times10^7\rightarrow$
prestrained	463	0	155	163	160	0.98	$1.0\times10^7\rightarrow$
S10C	463	300	110	163	160	0.98	$1.0\times10^7\rightarrow$

Defect size, $\sqrt{area}$(μm): square root of the area obtained by projecting the defect onto a plane perpendicular to the specimen axial direction. N_f: number of cycles to failure. $\rightarrow$: test stopped due to no failure.

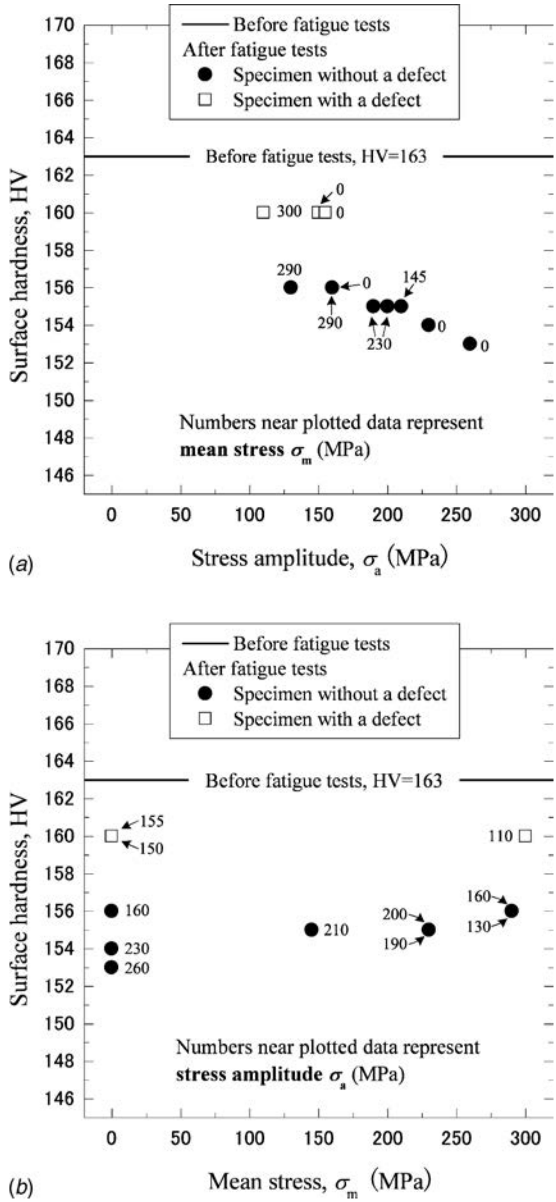

FIG. 6—*Variation of surface hardness in prestrained S10C specimens before and after fatigue tests* ($\sigma_a < 1.2\sigma_w$). (*a*) *Surface hardness versus stress amplitude.* (*b*) *Surface hardness versus mean stress.*

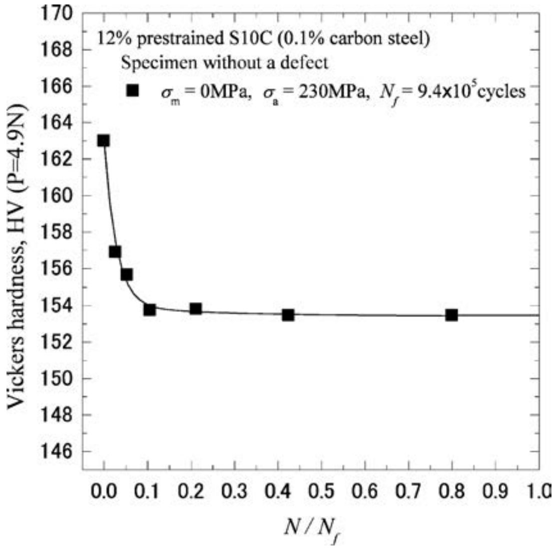

FIG. 7—*Change in surface hardness with fatigue. N: number of fatigue cycles, N_f: number of cycles to fatigue fracture.*

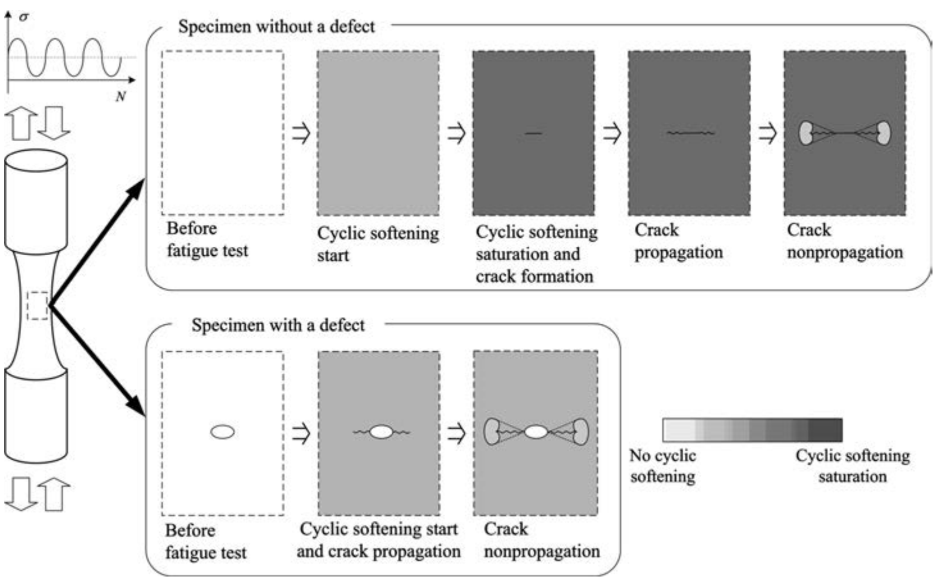

FIG. 8—*Schematic illustration of relation between cyclic softening and fatigue behavior in specimen without and with a defect.*

[18,19] and 40 % (up to about 50 μm in length) [20] of the specimen life, it is thought that the crack is formed after the saturation of the cyclic softening. In contrast, it is reported that the crack formation life is about 2~8 % of the life of medium carbon steel with a defect [21]. The crack formation life of the specimen with a defect is shorter than that of the specimen without a defect.

Figure 8 schematically shows the difference between the cyclic softening behavior for the specimen without a defect and the specimen with a defect. In the case of the specimen without a defect, the hardness decreases with cyclic loading. After the cyclic softening has been saturated, a fatigue crack is formed, propagates, and stops. The hardness, which was decreased by cyclic softening, affects the arrest of the fatigue crack. In other words, this decreased hardness affects the fatigue limit. In the case of the specimen with a defect, the cyclic softening and fatigue crack initiation from the defect seem to occur at almost the same time, then the crack propagates. Nisitani and Takao [19,22] reported that most of the fatigue damage is concentrated at the tip of the fatigue crack when the crack propagates. This phenomenon explains why the decrease in the hardness of the specimen with a defect is smaller than that in the specimen without a defect. Namely, the decrease in the hardness is small in the specimen with a defect because of the early crack initiation from the defect and the concentration of the fatigue damage at the tip of the crack, and this decrease in hardness, which occurs before the cyclic softening is not yet saturated, affects the fatigue limit of the specimen with a defect.

Prediction of the Fatigue Limit Under Tensile Mean Stress

In the fatigue limit and surface hardness sections, the fatigue tests, the observation of fatigue crack and measurement of the surface hardness before and after the fatigue tests were performed using prestrained S10C specimens. In summary, we obtained the following experimental results.

(1) Tensile mean stress degrades the fatigue limit of the prestrained specimen (refer to Fig. 3).
(2) The length of the nonpropagating crack decreases with the increase in tensile mean stress. This means that tensile mean stress affects ΔK_{th} related to the crack nonpropagation (refer to Figs. 4 and 5).
(3) The decrease in surface hardness as a result of fatigue loading in prestrained specimen without a defect is not affected by tensile mean stress (refer to Table 2 and Fig. 6).
(4) In the case of prestrained specimen with a defect, the decrease in surface hardness as a result of fatigue loading is small compared to that of the prestrained specimens without a defect regardless of stress amplitude and tensile mean stress (refer to Table 2 and Fig. 6).

Figure 9 shows a schematic of the relationship between the surface hardness and fatigue limit of carbon steels. The slope of the tensile-prestrained carbon steel (Line ②) is smaller than that of nonstrained carbon steel (Line ①). In general, this phenomenon is caused by cyclic softening [23–25]. The fatigue limit of prestrained carbon steel increases at a certain rate with increasing hardness due to prestrain. However, the fatigue limit decreases with generation

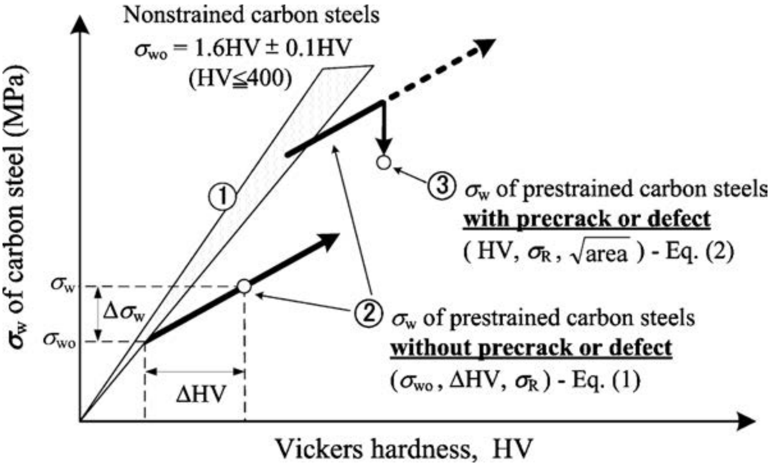

FIG. 9—*Schematic illustration of relationship between hardness and fatigue limit of prestrained carbon steels. HV: Vickers hardness.* σ_{wo}*: fatigue limit of nonstrained carbon steels.* σ_w*: fatigue limit of prestrained carbon steels* [*10*].

of precrack as a result of prestrain beyond a certain hardness level (Dot ③). In a previous study [10], we have suggested formulae Eqs 1 and 2 for predicting the rotating bending fatigue limit of prestrained carbon steels without and with a defect by considering the cyclic softening phenomenon. We derived the formulae from test results using annealed 0.1 % carbon steel (HV = 119) and quenched and tempered 0.5 % carbon steel (HV = 546). Equation 1 is for the case when precrack or defect does not exist. This equation involves the effect of the decrease of the surface hardness due to fatigue loading (as shown in Fig. 8) and the effect of the surface residual stress as a result of prestrain at the fatigue limit. Equation 2 is for the case when precrack or defect exists on the specimen surface after applying prestrain and involves the effect of the surface hardness and surface residual stress as a result of prestrain and the defect size at the fatigue limit. Equation 2 is based on the equation proposed by Murakami [26]. The hardness used in Eq 2 is not the decreased hardness after fatigue loading but the hardness immediately after prestrain. The decrease in the hardness is ignored in this equation because it is small in the specimen with a defect (as mentioned in the surface hardness section and shown in Fig. 8). We now discuss and propose formulae for predicting the fatigue limit of prestrained carbon steel under tensile mean stress on the basis of these equations and the experimental results

$$\sigma_w = \sigma_{wo} + 0.77(\Delta\mathrm{HV}) - 0.18\sigma_{wo}\frac{0.75\sigma_R}{\sigma_u} \quad (\sigma_m = 0) \tag{1}$$

$$\sigma_w = \frac{1.43(\mathrm{HV} + 120)}{(\sqrt{\mathrm{area}})^{1/6}}\left(\frac{\sigma_w}{\sigma_w + 0.75\sigma_R}\right)^{\alpha} \quad (\sigma_m = 0) \tag{2}$$

where

σ_w = fatigue limit of prestrained specimen,
σ_{wo} = fatigue limit of nonstrained specimen,
ΔHV = change in Vickers hardness upon applying prestrain,
σ_R = surface residual stress of the specimen in the axial direction induced by prestrain,
σ_u = tensile strength,
HV = Vickers hardness of prestrained specimen,
α = $0.226 + \mathrm{HV} \times 10^{-4}$,
$\sqrt{\text{area}}$ = the square root of the area obtained by projecting the crack or defect onto a plane perpendicular to the specimen axial direction.

Prestrained Specimen Without a Defect

Experimental results 1, 2, and 3, which are listed above, reveal that tensile mean stress does not affect the decrease in surface hardness as a result of fatigue loading, but it affects the limit of crack nonpropagation in the prestrained specimen without a defect. Thus, the fatigue limit decreases with the increase in tensile mean stress, although tensile mean stress does not affect the decrease in surface hardness (Fig. 6). Therefore, to predict the fatigue limit of a prestrained specimen without a defect under tensile mean stress, it is necessary to consider the effects of surface hardness and tensile mean stress on crack propagation and nonpropagation. Equation 1 involves the effect in the decrease of the surface hardness due to fatigue loading and the effect of the surface residual stress as a result of prestrain on the fatigue limit. Murakami [26] has proposed Eq 3, which predicts the fatigue limit of a nonstrained metal with a defect within ±15 % error. The first term of this equation, $1.43(\mathrm{HV}+120)/(\sqrt{\text{area}})^{1/6}$, represents the effects of the hardness, HV, and defect size, $\sqrt{\text{area}}$, on the threshold stress intensity factor range, ΔK_{th}, when the mean stress σ_m is zero. The second term of the equation, $((1–R)/2)^{\alpha}$, represents the effect of the stress ratio R or mean stress σ_m on ΔK_{th}. This term is based on Eq 4 [12,27] and was determined from experimental data. Therefore, we combine Eq 1 with the second term of Eq 3 to propose a formula, given by Eq 5, that predicts the fatigue limit of prestrained carbon steel under tensile mean stress,

$$\sigma_w = \frac{1.43(\mathrm{HV}+120)}{(\sqrt{\text{area}})^{1/6}}\left(\frac{1-R}{2}\right)^{\alpha}, \quad R = \frac{\sigma_m - \sigma_w}{\sigma_m + \sigma_w} \tag{3}$$

$$\Delta K_{\text{th}(R\neq 0)} = (1-R)^{(1-\gamma)}\Delta K_{\text{th}(R=0)} \tag{4}$$

where

R = stress ratio,

σ_m = mean stress,
$\Delta K_{th(R\neq0)}$ = threshold stress intensity factor range when $R\neq0$,
$\Delta K_{th(R=0)}$ = threshold stress intensity factor range when $R=0$,
γ = empirical constant depending on material.

$$\sigma_w = \left(\sigma_{wo} + 0.77(\Delta\mathrm{HV}) - 0.18\sigma_{wo}\frac{0.75\sigma_R}{\sigma_u}\right)\cdot\left(\frac{\sigma_w}{\sigma_w+\sigma_m}\right)^{\alpha} \quad (\sigma_m \geqslant 0) \tag{5}$$

Figures 10(a) and 10(b) show the experimental results and the results calculated using Eq 5 for S10C and S50C using the data in Table 3. The predicted results for both prestrained materials are in agreement with the experimental results within 11 % error, as shown in Table 3.

Prestrained Specimen with a Defect

From experimental result 4, it is thought that the fatigue limit of the specimen with a defect can be predicted by considering only the effect of mean stress on ΔK_{th}. Equation 2 is a formula that was proposed to predict the fatigue limit of prestrained carbon steel with a defect when the mean stress is zero. This equation is based on Eq 3. Surface residual stress as a result of prestrain is regarded as the mean stress in the equation. When the effect of the mean stress is considered, Eq 6 can be obtained from Eq 2,

$$\sigma_w = \frac{1.43(\mathrm{HV}+120)}{(\sqrt{\mathrm{area}})^{1/6}}\left(\frac{\sigma_w}{\sigma_w+0.75\sigma_R+\sigma_m}\right)^{\alpha} \quad (\sigma_m \geqslant 0) \tag{6}$$

Figures 10(a) and 10(b) show the experimental results and the results calculated using Eq 6 for S10C and S50C. When Eq 6 was calculated, the surface residual stress in the vicinity of the defect (* mark in Table 3) was used to consider the relaxation of the residual stress as a result of introducing the defect on the specimen. The predicted results for both prestrained materials show good agreement with the experimental results within 14 % error, as shown in Table 3.

The proposed prediction formulae have a limitation on their application, shown by the dash-dotted lines in Figs. 10(a) and 10(b). When the sum of the stress amplitude and the mean stress is equal to the tensile strength of the material, $\sigma_a+\sigma_m=\sigma_B$, monotonic fracture occurs instead of fatigue fracture. Therefore, Eqs 5 and 6 can only be applied when $\sigma_a+\sigma_m<\sigma_B$.

Conclusion

The effect of tensile mean stress on the fatigue limit of prestrained carbon steel was investigated. The main results obtained are as follows:

(1) Tensile mean stress does not affect the decrease in the surface hardness caused by fatigue loading in the prestrained specimen without a defect.
(2) The decrease in surface hardness as a result of fatigue loading is small in the specimen with a defect compared with that in the prestrained

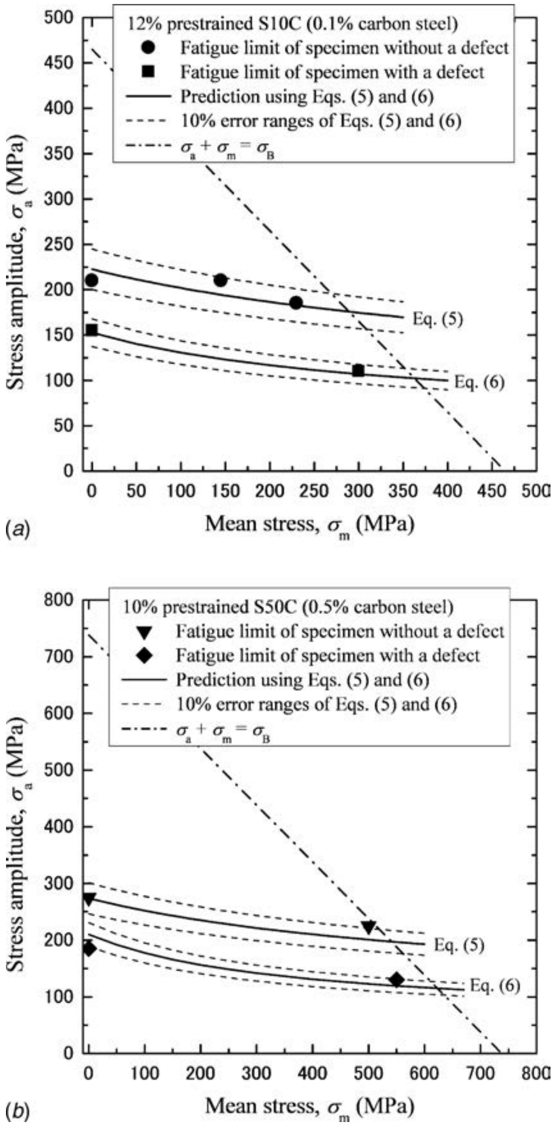

FIG. 10—*Calculation results* [*using Eqs 5 and 6*] *and experimental data of fatigue limit for prestrained S10C and S50C specimens. The dash-dotted lines in the graphs indicate the limit of application of Eqs 5 and 6.* (*a*) *Prestrained S10C specimens.* (*b*) *Prestrained S50C specimens.*

specimen without a defect, regardless of stress amplitude and mean stress.

(3) The fatigue limits of specimens both without and with a defect decrease with tensile mean stress. This means that the tensile mean stress

TABLE 3—*Surface hardness, surface residual stress and fatigue limit data of specimens.*

Material	Prestrain %	HV (P=4.9 N)	Residual stress σ_R (MPa)	Defect size $\sqrt{area}$ (μm)	Mean stress σ_m (MPa)	Fatigue limit, σ_w (MPa) Exp.	Eq 5	Eq 6	Error %
S10C	0	119	0	—	0	185	—	—	—
	12	163	−56	—	0	210	223	—	6
				—	145	210	194	—	−8
				—	230	185	183	—	−1
			−36*	463	0	155	—	153	−1
				463	300	110	—	107	−3
S50C	0	177	0	—	0	230	—	—	—
	10	221	−198	—	0	275	274	—	0
				—	500	225	201	—	−11
			−144*	463	0	185	—	210	14
				463	550	130	—	119	−8

HV: surface hardness of the specimen before fatigue test. σ_R: surface residual stress on the central part of the specimen. *: surface residual stress in the vicinity of the defect (500 μm far from the edge of the defect) in the specimen with a defect.

affects ΔK_{th}, which is related to the crack opening/closure behavior of the formed fatigue crack, although the tensile mean stress does not affect the variation of the hardness.

(4) On the basis of the experimental results, formulae for predicting the fatigue limit of prestrained carbon steels under tensile mean stress were proposed for specimens without and with a defect.

References

[1] Radhakrishhan, V. M. and Baburamani, P. S., "Initiation and Propagation of Fatigue Crack in Pre-strained Material," *Int. J. Fract.*, Vol. 12, No. 3, 1976, pp. 369–380.

[2] Frost, N. E., "The Fatigue Strength of Specimen Cut from Pre-loaded Blanks," *Metallurgia*, 57, 1958, pp. 279–282.

[3] Frost, N. E., Marsh, K. J., and Pook, L. P., *Metal Fatigue*, Dover Publications, Inc., New York, 1999, pp. 331–332.

[4] Lanning, D. B., Nicholas, T., and Haritos, G. K., "Effect of Plastic Prestrain on High Cycle Fatigue of Ti-6Al-4V," *Mech. Mater.*, 34, 2002, pp. 127–134.

[5] Frost, N. E., "The Effect of Cold Work on the Fatigue Properties of Two Steels," *Metallurgia*, 62, 1960, pp. 85–90.

[6] Harvey, P., Bonenberger, R. J., and Wolla, J. M., "Effects of Sequential Cyclic and Monotonic Loadings on Damage Accumulation in Nickel 270," *Int. J. Fatigue*, Vol. 20, No. 4, 1998, pp. 291–300.

[7] Nagase, Y. and Kanri, T., "Effects of Small Prestrain on the Fatigue Behavior of Spheroidal Pearlite Steel," *Fatigue Fract. Eng. Mater. Struct.*, Vol. 15, No. 2, 1992, pp. 213–223.

[8] Fujimura, K., Nisitani, H., and Fukuda, S., "Changes in Residual Stress and Successive Observations by Electron Microscope in the Fatigue Test of Prestrained or Shot-Peened Carbon Steel" (in Japanese), *Trans. Jpn. Soc. Mech. Eng., Ser. A*, Vol. 59, No. 568, 1993, pp. 3006–3013.

[9] Kage, M. and Nisitani, H., "The Effect of Tensile Prestrain on the Fatigue Strength of Strength-Anisotropic Rolled Steel," *Bull. JSME*, Vol. 20, No. 149, 1977, pp. 1359–1366.

[10] Kang, M., Aono, Y., and Noguchi, H., "Effect of Prestrain on and Prediction of Fatigue Limit in Carbon Steel," *Int. J. Fatigue*, Vol. 29, Issues 9–11, 2007, pp. 1855–1862.

[11] Norman, E. D., *J. Mech. Behav. Mater.*, 1997, pp. 370–374.

[12] Stephens, R. I., Fatemi, A., Stephens, R. R., and Fuchs, H. O., *Metal Fatigue in Engineering*, John Wiley & Sons, Inc., New York, 2001, pp. 51, 74–79, 157.

[13] Nisitani, H., Teranishi, T., Takeno, T., Yamada, S., and Tanaka, S., "Effect of Prestrain on Notched Fatigue Strength of 0.45%C Steel," (in Japanese), *Trans. Jpn. Soc. Mech. Eng., Ser. A*, Vol. 64, No. 626, 1998, pp. 2502–2507.

[14] Edwards, C. A., Jones, H. N., and Walters, B., "A Study of "Strain-Age-Hardening" of Mild Steel," *J. Iron Steel Inst.*, Vol. 139, No. 1, 1939, pp. 341–385.

[15] Nisitani, H. and Goto, M., "Effect of Mean Stress on Crack Initiation and Initial Crack Propagation in Axial Fatigue of an Annealed 0.45%C Steel" (in Japanese), *Trans. Jpn. Soc. Mech. Eng., Ser. A*, Vol. 50, No. 460, 1984, pp. 1926–1935.

[16] Suresh, S., Fatigue of Materials, Cambridge Univ. Press, Cambridge, UK, 2003, pp. 343–345, 545–547.

[17] Tanaka, K., Nakai, Y., and Yamashita, M., "Fatigue growth threshold of small cracks," *International Journal of Fracture*, Vol. 17, No. 5, 1981, pp. 519–533.

[18] Nisitani, H., Fujimura, K., Fukuda, S., and Fukuda, T., "Relation between Fatigue Damage and Half-Value Breadth of X-Ray Diffraction Lines in Fatigue Processes of Carbon Steels" (in Japanese), *Trans. Jpn. Soc. Mech. Eng., Ser. A*, Vol. 55, No. 510, 1989, pp. 192–197.

[19] Nisitani, H. and Takao, K., "Successive Observations of Fatigue Process in Carbon Steel, 7: 3 Brass and Al-alloy by Electron Microscope" (in Japanese), *Trans. Jpn. Soc. Mech. Eng., Ser. A*, Vol. 40, No. 340, 1974, pp. 3254–3266.

[20] Nagase, Y. and Izumisawa, M., "Effect of Small Prestrain on the Fatigue Strength of Low Carbon Steel" (in Japanese), *Trans. Jpn. Soc. Mech. Eng., Ser. A*, Vol. 54, No. 504, 1988, pp. 1474–1481.

[21] Murakami, Y., Harada, S., Tani-isi, H., Fukushima, Y., and Endo, T., "Correlations among Propagation Law of Small Cracks, Manson-Coffin Law and Miner Rule under Low-Cycle Fatigue" (in Japanese), *Trans. Jpn. Soc. Mech. Eng., Ser. A*, Vol. 49, No. 447, 1983, pp. 1411–1418.

[22] Nisitani, H. and Takao, K., "Successive Observations of Fatigue Process in Low Carbon Steel by Electron Microscope," Proc. of Int. Conf. on Mechanical Behavior of Materials, Kyoto, Vol. 2, pp. 153–164, 1972.

[23] Nisitani, H., Tanaka, S., Yamada, S., and Teranishi, T., "Relation between Microcracks and the Coaxing Effect of Pre-Strained Low Carbon Steel" (in Japanese), *Trans. Jpn. Soc. Mech. Eng., Ser. A*, Vol. 54, No. 498, 1988, pp. 190–195.

[24] Nisitani, H. and Takase, T., "Behavior of Fatigue Cracks in Annealed or Pre-Strained 0.21%C Steel Specimens under Two-Step Loading" (in Japanese), *J. Soc. Mater. Sci. Jpn.*, Vol. 33, No. 369, 1984, pp. 666–672.

[25] Nisitani, H. and Nomura, S., "Bending Fatigue of Notched Specimens Taken from Steel Pre-Strained by Tension or Torsion" (in Japanese), *Trans. Jpn. Soc. Mech. Eng., Ser. A*, Vol. 41, No. 350, 1975, pp. 2761–2767.

[26] Murakami, Y., *Metal Fatigue: Effects of Small Defects and Nonmetallic Inclusions*, Elsevier Science Ltd., Oxford, UK, 2002, pp. 57–108.

[27] JSME, Fatigue Design Handbook (in Japanese), Yokendo Ltd., Tokyo, Japan, 1995, pp. 178–180.

ASTM Special Technical Publication, Vol. 6, No. 4
Paper ID JAI101616
Available online at www.astm.org

Len Reid[1] *and Joy Ransom*[2]

Practical Challenges Testing Coupons with Residual Stresses from Cold Expanded Holes

ABSTRACT: Cold expanding holes in metal components is widely used throughout the aerospace industry to extend fatigue life and damage tolerance. The beneficial residual stresses induced by hole cold expansion arrest or significantly retard the growth of fatigue cracks, and in doing so make fatigue or crack growth life prediction more difficult. Under low stress level/high cycle fatigue testing, residual compressive stresses have been shown to increase the fatigue strength of the material leading to an "infinite life" and consequent "run-out" of test coupons at the test hole or changing the location of failure away from the test hole. While advantageous to aircraft operators, it makes statistical life prediction difficult because the incomplete data have to be censored, leading to a knock-down of the beneficial life attained. Conversely, increasing stress levels toward material yield stress; life improvement factors are more definitive and tend toward unity. This paper reviews the derivation of residual stresses induced by hole cold expansion and discusses benefits to the structure/test coupon and how the residual stress field impacts fatigue life and damage tolerance/durability under cyclic load conditions. Challenges observed when testing coupons that have been processed using hole cold expansion including modification of the crack behavior and its effect on material microstructure, relocation of crack initiation, dynamics of the redistribution of stress and the crack growth mechanism as well as scatter of results, are also discussed with a focus on aluminum materials.

KEYWORDS: split sleeve cold expansion, residual compressive stress field, fatigue life improvement, crack growth

---

Manuscript received December 3, 2007; accepted for publication May 12, 2008; published online April 2009.

[1] Vice President Research & Development, Fatigue Technology Inc., Seattle, WA 98188.
[2] Manager, Materials Test Facility, Fatigue Technology Inc., Seattle, WA 98188.

Citation: Reid, L. and Ransom, J., "Practical Challenges Testing Coupons with Residual Stresses from Cold Expanded Holes," *J. ASTM Intl.*, Vol. 6, No. 4. DOI10.1520/JAI101616. Available online at www.astm.org. Also included in JAI Special Issue STP 1508, *Fatigue and Fracture Mechanics: 36th Volume,* R. W. Neu, K. R. W. Wallin, and S. R. Thompson, guest editors, ASTM International, West Conshohocken, PA, 2009, pp. 183-199.

Introduction

Hole cold expansion has been used to improve the fatigue resistance at a hole for decades. The most common method of inducing residual compressive stresses around holes in metals is by the split sleeve cold expansion method. Effectively, it is achieved when the area around the hole is expanded locally beyond the material's yield point, as shown in Fig. 1. The cold expansion process is performed by placing a pre-lubricated split sleeve on a tapered mandrel, and the mandrel/sleeve combination is fit through the test hole. The puller unit pulls the mandrel back through the hole and sleeve, producing a cold expanded hole. The diameter of the mandrel and sleeve are greater than the hole causing the hole to enlarge and the material near the hole to plastically yield. As the material tries to return to the original steady state position after the mandrel is removed, an annular zone of residual compressive stress is produced around the hole in hoop compression with a balancing tension field outside the compressive zone, as shown schematically in Fig. 2. This residual compressive stress will influence the mean stress as it is applied at the hole during cycling. The zone of residual stress may not reduce the time to crack initiation (cycles to form micro-crack) since this is mainly a function of alternating fatigue stresses, but it does slow crack growth since it is a function of the mean and alternating stress [1].

There are many factors that can influence the ability to achieve a uniform residual compressive zone around a cold expanded hole. The amount of variation of the zone of compression can be significant and will depend on the prevailing different mechanical and physical conditions such as (1) the amount of applied expansion, (2) the material and its elastic-plastic properties, (3) the material thickness and geometry of the part or coupon, and (4) the material response to the radial expansion. The influences of these variations are discussed in a number of papers summarized in the report by McClung [1], which also summarizes reported experimental and finite element simulations of the cold expansion process. The small changes in residual stress and how they behave under fatigue test or in-service cyclic loading has a significant effect on life prediction and correlation of actual test results. Other outside influences also can affect the long term fatigue performance of cold expanded holes. These influences include loading conditions and the possibility of high stress over-

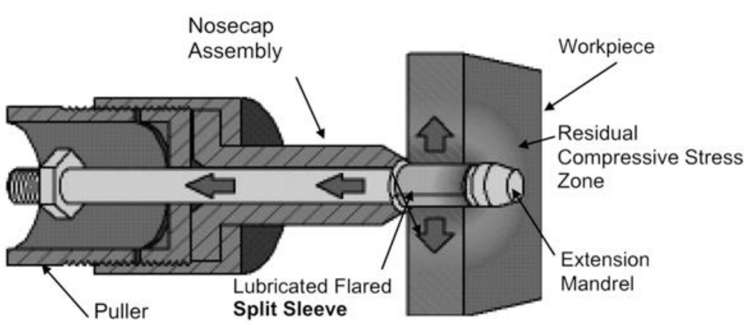

FIG. 1—*Split sleeve cold expansion process.*

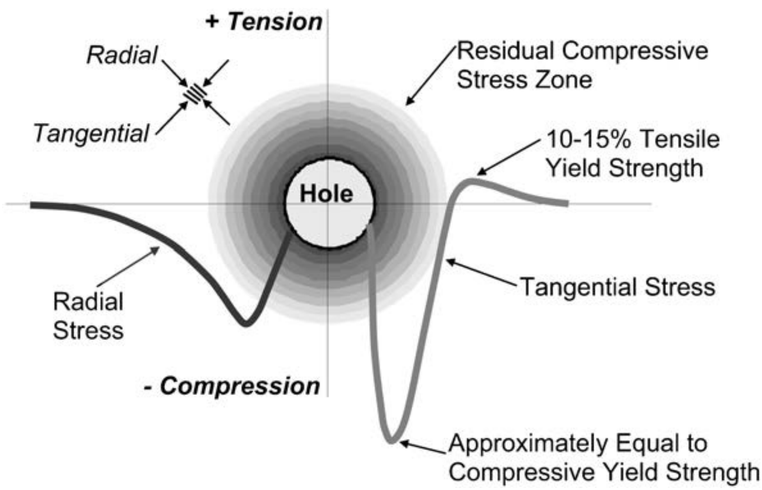

FIG. 2—*Residual compressive stress field created by the split sleeve cold expansion process.*

loads, presence of flaws, environmental conditions, and coupon design. These factors will be discussed in this paper focusing on the performance in aluminum materials.

Nature of Induced Residual Stresses

The nature of the split sleeve cold expansion technique whereby the expansion mandrel is pulled through the lubricated split sleeve causes most of the variation in residual stress around and through the depth of the hole. On the mandrel entry and exit surfaces, the hole is constrained radially but not axially since it is a free surface. A very localized "bulging" is noticeable on these surfaces. Through the thickness, however, the material is constrained axially and therefore the magnitude of the residual stress is larger through the thickness internally than at the free surface edges. In addition, as the mandrel travels through the hole there is a plastic flow of material ahead of the mandrel resulting in a higher applied expansion at the exit face compared to the entry face. From a practical testing aspect, this will affect the location of crack initiation since the crack will generally start on the side corresponding to the mandrel entry where the magnitude of the residual stress is least. The slight surface bulging typically is not a factor in load transfer testing provided the coupons were adequately clamped together during cold expansion. Localized fretting has been detected during high load transfer testing; however, typically the presence of the residual stresses will mitigate crack initiation or growth from the fretting surface.

In general, the location of the opening of the split in the sleeve typically does not matter except in special instances where materials have actual elongation properties less than 3 % (in the grain direction of processing), the hole is near an edge, near another hole, or next to a critical detail. The sleeve ridge

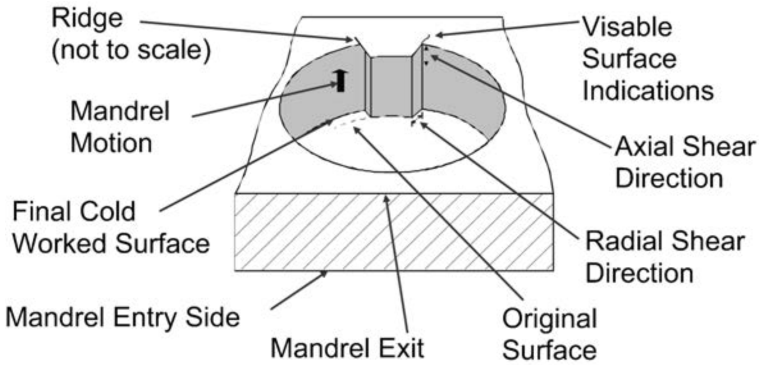

FIG. 3—*Attributes of a split sleeve cold expanded hole* [*8*].

left by the gap in the sleeve during processing, also called a pip (Fig. 3) typically is removed in final reaming operations. Depending on the ream allowance, the location of the pip can influence the location of the fatigue crack. If the pip is at 90° to the load line, the crack typically will start 180° from the location of the pip [2]. To reduce this influence, the pip is generally oriented toward the load line for testing. If the coupon represents a special case (as listed above) the sleeve gap should be oriented similar to what would be recommended for the structural part the coupon is representing.

Factors Influencing Fatigue Life under Test

The nature of the deep residual compressive hoop stress generated by the split sleeve cold expansion method has been shown by a large number of tests and from many years of in-service experience to be extremely beneficial in extending the fatigue life of structures. The most significant observed difference in testing cold expanded coupons, against similar non-cold expanded coupons, is the increased scatter of results with the cold expanded data set. Typically the non-expanded set will record a tighter grouping of failure points. In many cases coupons with cold expanded holes will test to a failure while others will test to a "run-out" condition in the same set of coupons. In general, the influence of the residual stress field is to increase fatigue life or allow operation at higher allowable stresses for the same life, but with greater scatter than in the unprocessed condition.

There are a number of other factors that influence the benefits of the residual compressive hoop stresses induced by the cold expansion process. The following influences will be discussed:

1. Plastically induced overloads, tension or compression
2. Stress-ratio (R, both positive and negative)
3. Spectrum loading
4. Presence and size of flaws/cracks in holes
5. High temperature effects
6. Coupon design

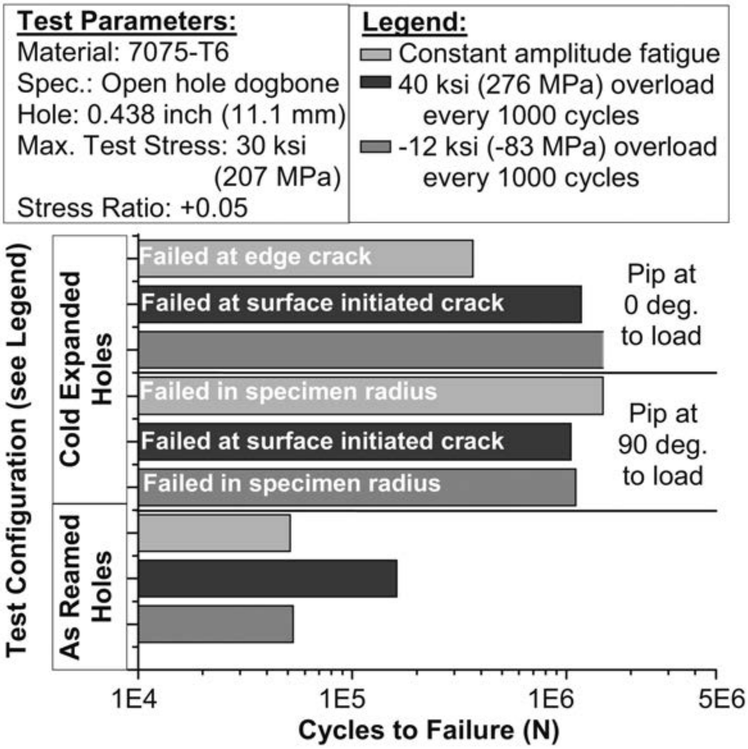

FIG. 4—*Results of overloads on cold expanded holes.*

As noted previously, the residual stress field induced into the material may relax or redistribute due to a variety of mechanisms. Inelastic behavior, caused by compressive or tensile overload, or by possible creep under repeated high load or high temperature operation, can cause redistribution or relaxation of residual stresses over time. Alternately, the coupon design can influence the results by providing alternate crack initiation sites when the hole is shielded by the residual compressive stress field.

Plastically Induced Overloads

Plastically induced overloads, either tension or compression prior to testing or periodically applied during testing, can relax the residual stress field at a hole processed with the split sleeve cold expansion process. In a test program performed at Fatigue Technology Inc. (FTI) to evaluate and quantify the effects of tensile and compressive overloads on specimens with cold expanded holes, testing was terminated after most of the specimens with cold expanded holes failed away from the test hole (Fig. 4) [3]. For these tests, the effects of overloads produced inconsistent results. However, in testing performed by Ball and Doerfler [4] a compressive overload significantly reduced the fatigue life benefit

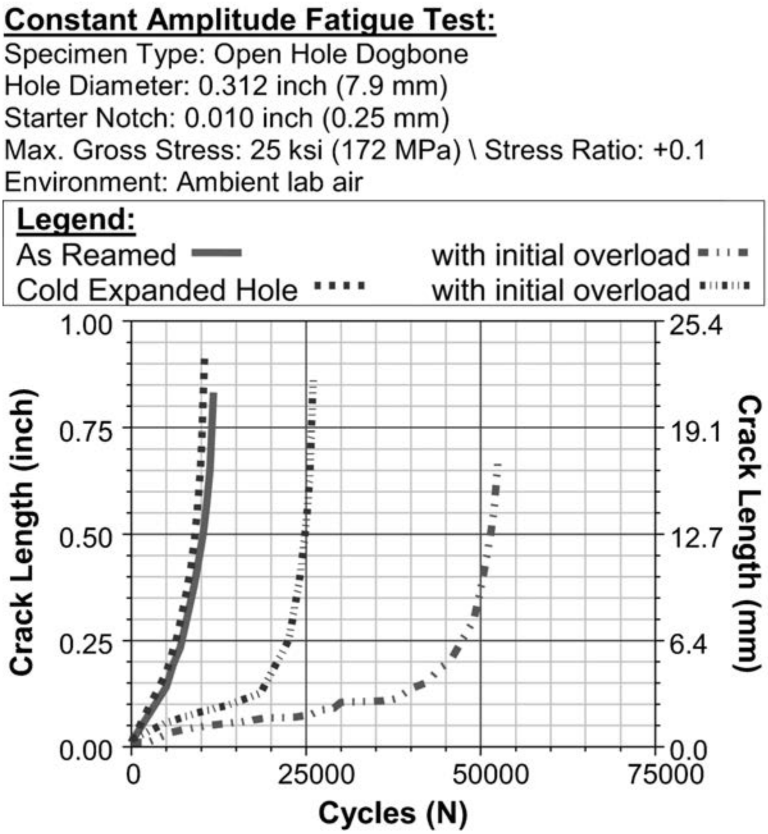

FIG. 5—*Constant amplitude fatigue test after compressive overload.*

from 5 to 2.5 times the baseline coupon (Fig. 5). The induced compression overload can cause reverse yielding at the edge of the hole allowing cracks to initiate and grow. While plastically induced overloads can impact the beneficial effects of the cold expansion residual stress the impact on actual coupon or component life will be influenced by the number of occurrences and the magnitude of the overload strain. Inelastic loading sufficient to alter the induced residual stresses can significantly alter the fatigue performance and residual life prediction.

Stress ratio

Similar to changing the applied maximum stress, changing the stress ratio (R) will change the fatigue life. At low stresses, the stress intensity factor associated with small cracks may not be sufficient to drive the crack through the compressive stress field induced by cold expanding the hole, thereby providing significant fatigue life improvement compared to non-cold expanded holes. Experience has shown that when testing at low stresses the failure location may be

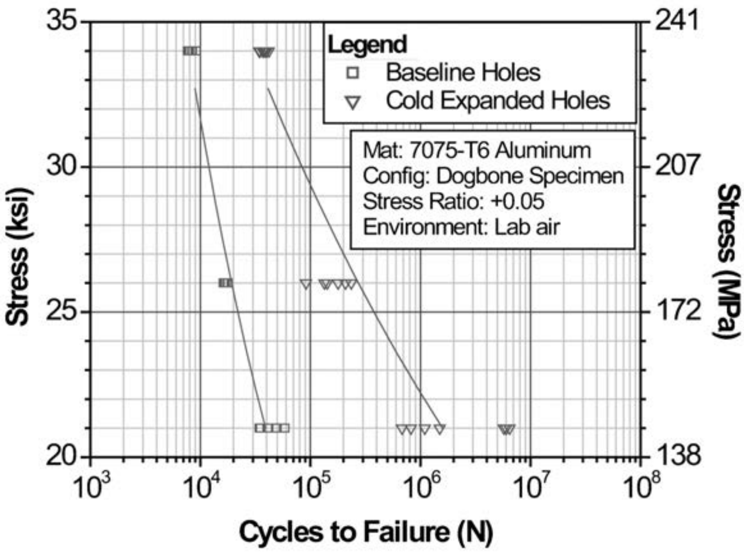

FIG. 6—*Constant amplitude stress-life curves.*

moved away from the hole to the next location of highest stress concentration. The impact of this is that coupons with cold expanded holes appear to have larger scatter bands, or in fact not fail at a reasonable number of cycles, at the low stresses (Fig. 6), making it difficult to analyze the data since many coupons "run-out."

At high stress levels, the difference in fatigue life between parts with and without cold expanded holes becomes less significant. In these cases the part failures for both hole configurations will generally be at the hole. At low stress levels, there is a high likelihood that test specimens will fail away from the hole. Wagner [5] evaluated over 200 specimens in 2024 and 7075 aluminum using cold expansion for new production and as a rework process. The results showed that as the test stress was decreased, the probability of failure away from the hole does increase significantly (Fig. 7).

Rufin [6] performed a test program to develop stress-life (S-N) curves for specimens with cold expanded holes with negative stress ratios (Fig. 8). Reamed open hole specimens were also tested as a comparison dataset. The decrease in stress ratio lowered the fatigue life as expected for both hole configurations. Similar to Wagner [5], at the low stresses specimens tended to fail away from the hole. In the 7075-T651 material, the direction of the crack changed with the lower stress ratios to oblique cracks growing in shear. When calculating the stress-life curve for the cold expanded data, the data are typically censored to remove results for specimens that reached run out. The results are also removed for specimens that fail outside the test area. Figure 8 shows the results using the equations from ASTM E739 to calculate the stress-life curves with and without the censored data. Note that for these results, the author did not censor the data when there were multiple crack initiation sites

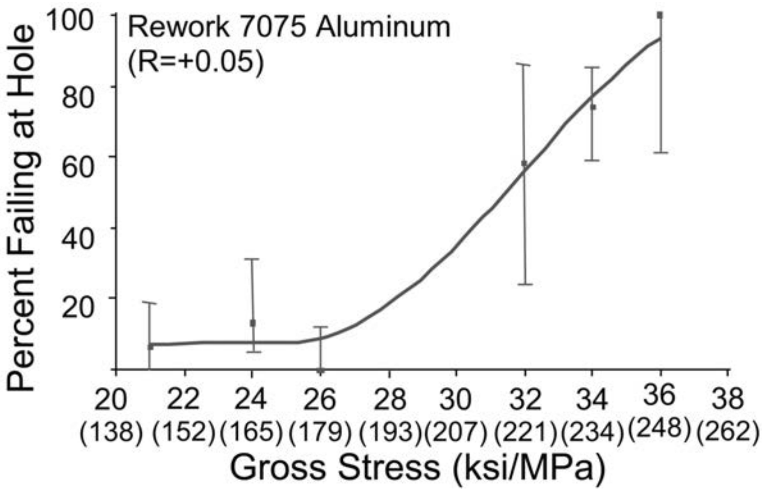

FIG. 7—*Failure locations versus stress.*

or when there were oblique cracks, as there were cracks in these specimens that started from the hole. Censoring data reduces the data set and can make it difficult to provide good comparisons or predictions.

Finding, monitoring or reporting cracks that start on the surface away from the hole edge, or when multiple cracks initiate from the hole, or even when cracks grow along an alternate plane than expected, are problematic when assessing test results. Additionally, when testing coupons at a higher stress level in order to drive a failure in fewer cycles, it could force a failure at the hole instead of failing away from the hole as would have been the case at the lower stress level. These all add to the complexities of interpreting test results.

Variable Amplitude Loading

As previously mentioned, when tests are performed with negative stress ratios the fatigue life of coupons with cold expanded holes is reduced. This is also true when testing is performed using spectrum, or variable amplitude loading that includes compressive loads. Ball and Doerfler [4] performed a spectrum test where the spectrum contained compressive loads (Fig. 9). The spectrum was then clipped and all of the negative loads were set to zero resulting in a tension-only spectrum. In this test, the fatigue life of both the coupons with cold expanded holes and without cold expanded holes was increased when the compression loads were removed from the spectrum.

Presence, Size, and Shape of Flaws or Cracks

It has been shown that cold expansion residual stresses have virtually no effect on crack initiation at an open hole [1,7]. Conversely, the growth of fatigue

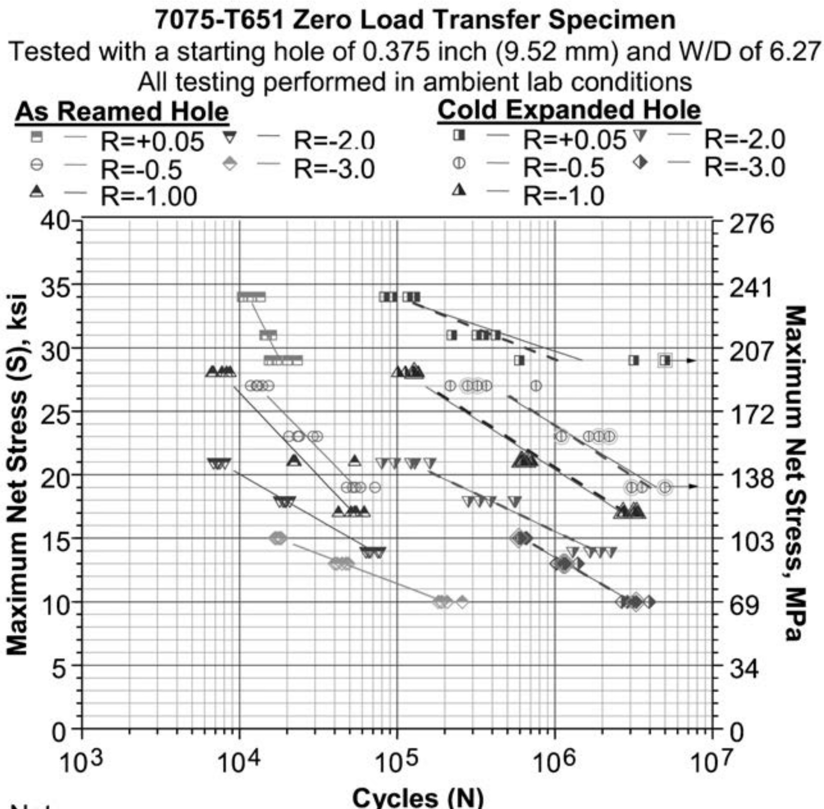

Note:
1. Thin solid lines are average S-N curves based on all data that failed in test area or reached run-out. Curves calculated from ASTM E739.
2. Highlighted data indicates specimen did not fail in test area.
3. Heavy dashed lines are average S-N curves based on data that failed at test hole.

FIG. 8—*Stress-life curves for changing stress ratios* [*6*].

cracks may be significantly delayed, if not arrested completely, by these compressive residual stresses by reducing the stress intensity factor range (ΔK), [8], as well as the stress ratio (R, minimum stress/maximum stress). When associated with crack growth or damage tolerance, the growth of a crack through the residual stress field can cause significant changes in the residual field under some test conditions. In addition, the nature of the compressive hoop stress around the hole acts like a strong clamp on the material around the crack, minimizing crack opening displacement and thereby preventing or retarding crack growth.

Most of the predictive crack growth analysis work [1,4,8,9] uses the stress

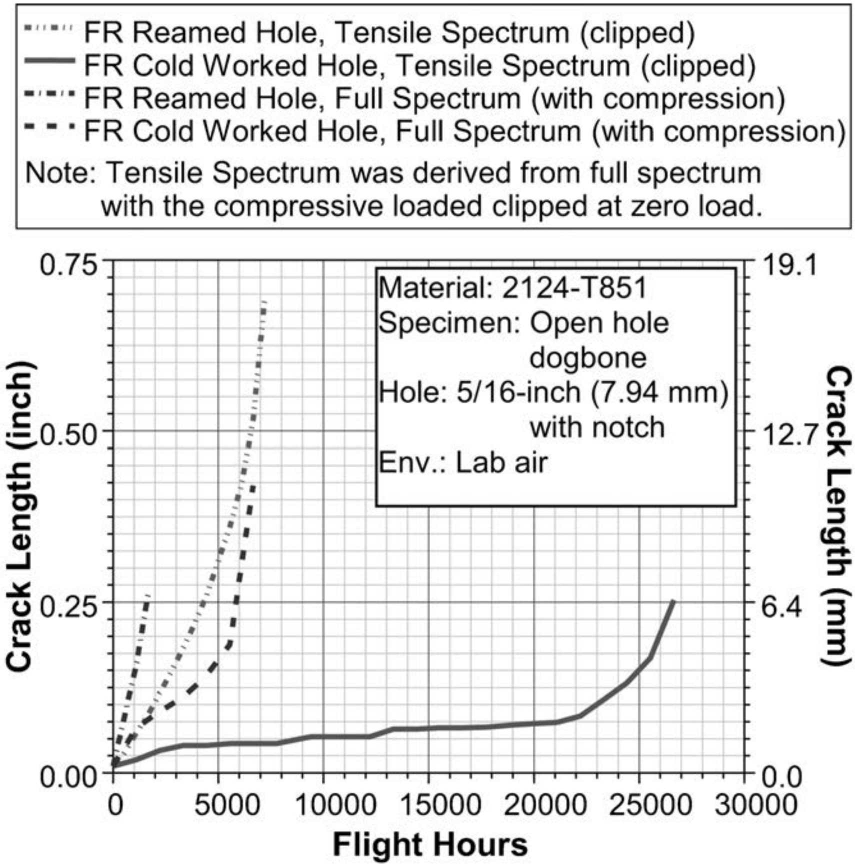

FIG. 9—*Effects of different fatigue loading on fatigue life* [*4*].

intensity *K* methodology for predicting crack growth from cold expanded holes; however, the accuracy and inconsistencies of this method are documented [10]. Traditional crack growth life prediction analysis has assumed fatigue cracks have "conventional" shapes such as the quarter-elliptical corner crack and the straight through thickness crack. These formed the basis for the *K* method solutions. Pell [11] and later Kokaly et al. [12] show that real cracks through the residual stress have complex shapes; most notably "P" shapes, shown in Fig. 10, indicative of highly non-uniform crack growth rates through the thickness.

From a testing and crack growth monitoring perspective this non-uniform crack growth characteristic makes monitoring of cracks almost impossible because the surface crack length is no longer indicative of the crack length through the thickness. This phenomenon also has an impact on the actual crack growth life because the rate of crack propagation is influenced by the material microstructure and the redistribution of the residual stress around the crack and especially at the crack tip. As has been seen in many lot tests, cracks in some coupons are arrested while others are slowed by varying degrees leav-

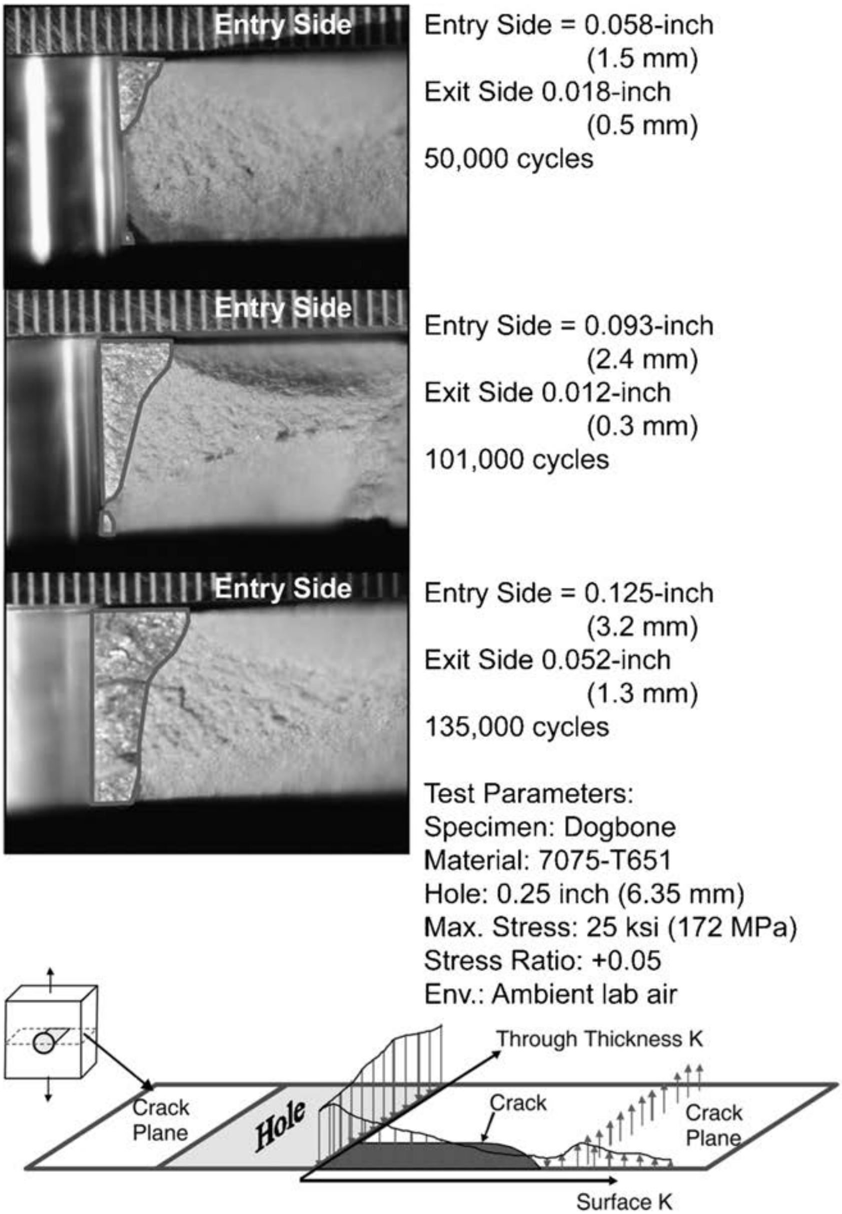

FIG. 10—*"P" crack development with cold expanded hole* [*12*].

ing a scattered series of results. Gathering da/dN versus ΔK data again shows a large scatter in results shown in the fatigue crack growth studies conducted by Priest et al. [13]. The scatter in the experimental results was attributed to the asymmetry of crack growth.

High Temperature Effects

Long exposures to high temperatures can relax the residual stress field produced by the hole cold expansion process. Tests conducted on coupons that were cold expanded and subjected to high temperature by either heat soak at elevated temperature or cycling the coupon at elevated temperature or both, showed some form of relaxation of effective fatigue life improvement compared to coupons tested at ambient temperature. A test conducted on 7050-T7451 [14] before and after thermal aging at 220°F (104°C) for 250 h, showed a relaxation of residual stress of 13.6 % with an estimated relaxation of 17 % at 5000 h. Fatigue properties could significantly change from exposure to elevated temperature depending upon the level of applied cyclic stress. Clark et al. [14] noted a reduction in the fatigue life of thermally aged aluminum parts, but the effects were not quantified.

Coupon Design

In addition to the test parameters and environment, coupon geometry can also affect the results from testing with cold expanded holes. Since the residual hoop stress shields the hole and reduces the effective stress concentration of the hole, many cold expanded coupons in a test will exhibit failure that initiates remote from the hole, such as a free edge or change in coupon geometry. In some cases this could invalidate the test and require censoring of the results. Moving the crack initiation away from the hole can also be an advantage. In a test conducted by FTI [15], the objective was to move the crack initiation away from the hole edge where it was difficult to inspect and required removal of the fastener, or in this case the expanded rivetless nut plate, that was used around the access panel cutout (Fig. 11). Cold expansion residual stresses successfully moved the crack initiation to the adjacent free edge where a surface eddy current technique could easily be used to monitor crack initiation and growth.

Test coupons that incorporate cold expanded holes should be designed to focus the failure to the area of interest which is typically the hole. Regions of high stress concentration away from the hole, such as the grip areas or changes in section or geometry, may attract premature crack initiation or failure outside the test region. To reduce the probability of premature failure in these locations they can be surface shot peened or in the case of the grip attaching holes, these too should be cold expanded.

As noted earlier and shown in Fig. 2, the residual stress induced by cold expansion shields the hole and is balanced by the tensile residual stress zone beyond it. Since the stress concentration at the edge of the hole is greater than that in the tensile stress region, assuming no change in local surface geometry, it is unlikely that cracks would initiate in this region. When cracks have been detected in this region, they are usually associated with aluminum materials that have had the surface treated with anodize or ion vapor deposition (IVD) coating [16,17]. These types of processes require a surface etching prior to application of the coating. This pretreatment exposes the grain boundaries and sets up micro stress concentrations that lead to crack initiation and growth. Cracks typically will propagate normal to the principle stress axis and are visible as “eyebrow” cracks due to the shape of the crack. Depending on the ini-

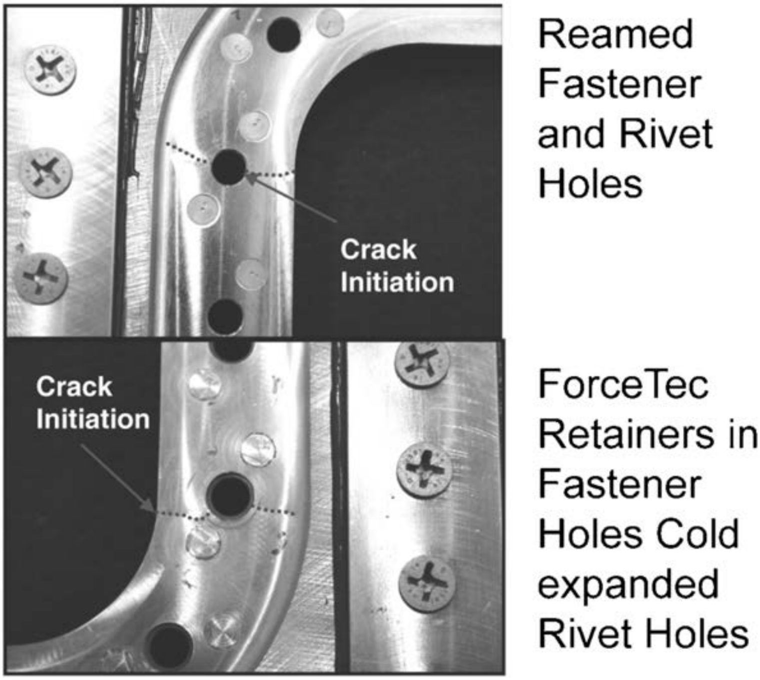

FIG. 11—*Example of specimen where crack initiation site moved with cold expanding holes* [*15*].

tiation point of these eyebrow cracks they will typically grow around the residual hoop stress remote from the hole (Fig. 12). Multiple crack initiation sites may be evident, as shown in the coupon in Fig. 13, in which case the dominant crack can link up to the other cracks. In tests conducted by FTI [16,17] in high strength 7050-T7461 IVD coated aluminum alloy, the non-cold expanded coupons all had crack initiation at the edge of the hole, whereas the cold expanded ones all initiated away from the hole.

Another way specimen geometry can affect the residual zone of compression is when the specimen is scaled down from a large structural component design to a smaller specimen for convenience of shape, simplicity, or loading restrictions. Each of these factors can change the results of testing and produce complications in analyzing the results in comparison to the structure it represents. When a specimen must be scaled down for convenience, additional tests and analysis must be performed to assure that the test results from the scaled down specimen are properly applied to the full scale structure. As previously discussed, increasing test loads, or removing structural details or coatings can mask crack initiation sites away from the hole and can change the predicted fatigue life benefit of cold expanded holes compared to non-cold expanded holes in the test coupons.

A not-so-obvious effect of scaling is the change in the residual stress field produced by the cold expansion process for different hole sizes. Because the

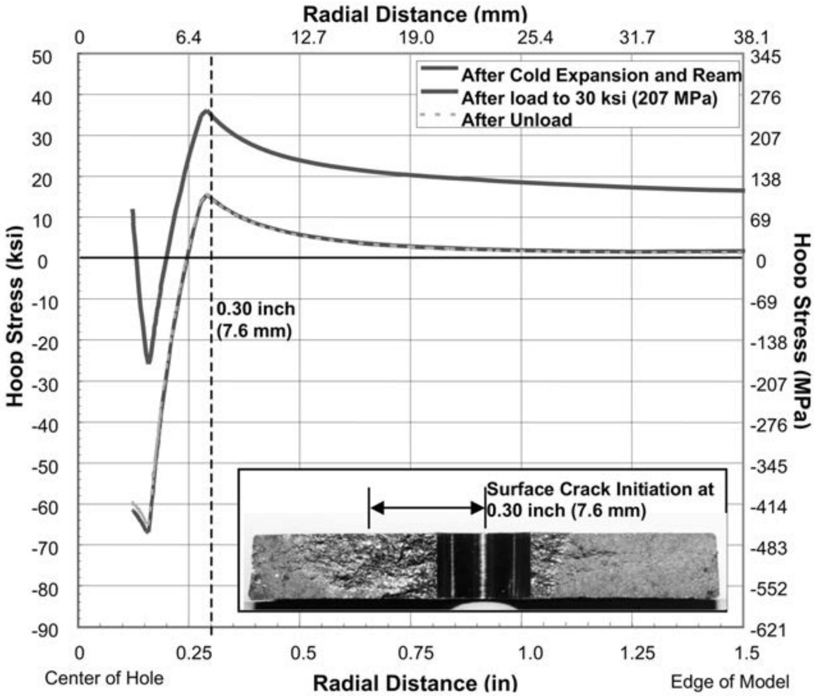

FIG. 12—*Comparison of crack initiation site to maximum tensile ring from cold expansion of hole* [*17*].

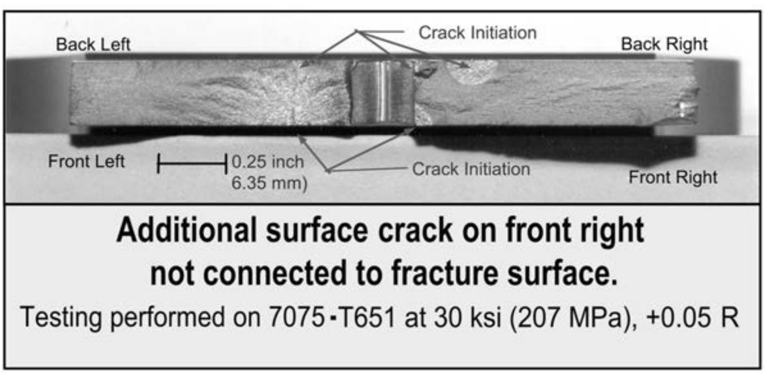

FIG. 13—*Example of failure surface of anodized specimen with cold expanded hole* [*16*].

applied expansion is constant at a nominal 3.5 % for holes up to a 1-in. (25-mm) diameter, the zone of residual stress, typically extending at least one radius away from the hole. Above 1-in. diameter, the applied expansion reduces to maintain a one-sided process thus reducing the zone of residual stress in proportion to the hole. For this reason and other inherent scaling factors, testing of coupons should be as representative of the actual part as possible maintaining the same geometrical proportions for edge margin and part thickness. All these factors will influence crack initiation and growth and ultimately projected life improvement.

Other Materials and Cold Expansion Processes

While this paper focuses on aluminum alloys, similar testing challenges apply to other materials and related cold expansion processes. The affect of residual compressive stresses due to the cold expansion of titanium alloys are discussed in a number of references [18–21]. Rich et al. [20] also discussed the influence of interference fit fasteners in both aluminum and titanium alloys. The combination of residual compressive stresses plus interference fit fasteners further increases fatigue life but also increases scatter of results due to the interaction of the combined processes. Rufin [21] discussed thermal influences on materials used in engine components, including thermal cycling and heat soak. These topics will be the subject of future studies.

Conclusion

There are many challenges when testing coupons with cold expanded holes, as these coupons may be sensitive to factors not typically affecting coupons with non-cold expanded holes because of the presence of the beneficial compressive hoop stress around the hole.

The specimen design should be carefully reviewed to be sure that it will provide results that meet the test requirements such as failures at the test hole or failures in the test area. It is best to design the specimen in the test area to be similar to the structure it is representing, including edge margins, coatings, part thickness, and other geometrical details.

The test loads should also represent the expected in-service applied loads of the structural element that is being evaluated. The presence and influence of the residual compressive hoop stress associated with cold expanded holes has a significant impact on conducting fatigue tests and interpreting fatigue and crack growth test results. The scatter of results is significantly broader for cold expanded hole coupons compared to non-cold expanded coupons, especially at low stresses (high cycle fatigue loading). Comparing non-cold expanded holes to cold expanded holes under low stress conditions, life increase tends toward infinity and endurance may cause suspensions in testing (termination of test prior to failure) or produce failures away from the test hole. The results from these non-test area failures can skew the results in analysis because of the data scatter and reduced number of repetitions that can be used. This can complicate the failure analysis and use of the data for prediction calculations, especially when the results are censored due to "run-out."

With the possibility of multiple crack initiation sites and cracks starting away from the test hole, the methods for recording crack growth from coupons with cold expanded holes may need to be reviewed. Automated crack growth monitoring at the hole edge may not be adequate. Inspection of in-service structure will need to address both crack initiation sites at the hole and possibly adjacent areas to the hole.

The residual stress field produced from cold expanding a hole has been shown to be affected by the coupon geometry and loading conditions. In all cases presented, the cold expansion process does provide fatigue life improvement as compared to coupons with holes that have not been cold expanded though the amount of improvement may be dependent on these conditions.

References

[1] McClung, R. C., "A Literature Survey on the Stability and Significance of Residual Stresses during Fatigue," *Fatigue Fract. Eng. Mater. Struct.*, Vol. 30, 2007, pp. 173–205.

[2] Easterbrook, E. T., "Sleeve Gap Width Investigation," FTI Technical Report #81-4, February 1, 1981.

[3] Wagner, R. V., "Comprehensive Open Hole Rework Test Program," FTI Technical Report 37587, July 30, 1993.

[4] Ball, D. L., and Doerfler, M. T., "Experimental and Analytical Studies of Residual Stress Field Evolution and Fatigue Crack Growth at Cold Expanded Holes," *2003 USAF ASIP Conference*, Savannah, GA, December 2003.

[5] Wagner, R. V., "Fatigue Crack Growth Retardation at Cold Worked Fastener Holes," FTI Technical Report 32291, July 30, 1992.

[6] Rufin, A. C., and Powell, R. L., "The Effect of Split Sleeve Cold Expansion on Holes Subjected to Predominantly Compressive Fatigue Loads," FTI Technical Report #39943, September 24, 1993.

[7] Ball, D. L., and Lowry, D. R., "Experimental Investigation on the Effects of Cold Expansion of Fastener Holes," *Fatigue Fract. Eng. Mater. Struct.*, Vol. 21, 1998, pp. 17–34.

[8] Ozelton, M. W., and Coyle, T. G., "Fatigue Life Improvement by Cold Working Fastener Holes in 7050 Aluminum," *Fatigue in Mechanically Fastener Composite and Metallic Joints*, ASTM International, West Conshohocken, PA, 1986, pp. 53–71.

[9] Stefanescu, D., "Measurement and Prediction of Fatigue Crack Growth from Cold Expanded Holes–Part 2: Prediction of Fatigue Crack Growth from Cold Expanded Holes," *J. Strain Anal. Eng. Des.*, Vol. 39, No. 1, 2004, pp. 41–53.

[10] Pavier, M. J., Poussard, C. G. C., and Smith, D. J., "Effect of Residual Stress Around Cold Worked Holes on Fracture under Superimposed Mechanical Load," *Eng. Fract. Mech.*, Vol. 63, 1999, pp. 751–773.

[11] Pell, R. A. et al., "Fracture of Thick-Section Cold-Expanded Holes With and Without Cracks," *Fatigue Fract. Eng. Mater. Struct.*, Vol. 12, 1989, pp. 553–567.

[12] Kokaly, M. T. et al., "Predicting Fatigue Crack Growth in the Residual Stress Field of a Coldworked Hole," *J. ASTM Int.*, Vol. 2, No. 5, 2005, Paper ID JAI 12556.

[13] Priest, M., Smith, D. J., and Pavier, M. J., "Assessment of Fatigue Crack Growth from Cold Worked Holes," ICAF 1997.

[14] Clark, D. A., and Johnson, W. S., "Temperature Effects on Fatigue of Cold Expanded Holes in 7050-T7451 Aluminum Alloy," *Int. J. Fatigue*, Vol. 25, 2003, pp. 159–165.

[15] Ransom, J., "Underflush ForceTec® (FtCx™) Fastener Study," FTI Technical Report 161695, August 20, 2004.
[16] Ransom, J. S., "Effects of Anodizing on the Fatigue Life of Open Hole Test Specimens," FTI Technical Report 88043, January 10, 2001.
[17] Ransom, J. S., "Effect of Fatigue Life of IVD Coated Aluminum With Cold Expanded and Non-Cold Expanded Holes," FTI Summary 87395, January 10, 2001.
[18] Ozelton, M. W., and Coyle, T. G., "Fatigue Life Improvement by Cold Working Fastener Holes in Aircraft Materials," Northrop Technical Report Number NO00019-82-C-0364, December 1983.
[19] Phillips, J. L., "Sleeve Coldworking Fastener Holes," Air Force Materials Laboratory Technical Report AFML-TR-74-10, February 1974.
[20] Rich, D. L., and Impellizzeri, L. F., "Fatigue Analysis of Cold Worked and Interference Fit Fastener Holes," *Cyclic Stress-Strain and Plastic Deformation Aspect of Fatigue Crack Growth*, ASTM STP 637, ASTM International, West Conshohocken, PA, pp. 153–175.
[21] Rufin, A., "Extending the Fatigue Life of Aircraft Engine Composites by Cold Expansion Technology," The American Society of Mechanical Engineers 92-GT-77, June 1, 1992.

ASTM Special Technical Publication, Vol. 5, No. 5
Paper ID JAI101570
Available online at www.astm.org

Sami Heinilä,[1] *Timo Björk,*[1] *and Gary Marquis*[1]

The Influence of Residual Stresses on the Fatigue Strength of Cold-Formed Structural Tubes

ABSTRACT: Rectangular hollow sections (RHS) are widely used in load-carrying structures due to their good load transfer behavior and aesthetic form. During fabrication of a cold-formed rectangular hollow section (CFRHS), the concave inside corner surfaces experience significant compressive plastic strains. The resulting tensile residual stresses in the corner region significantly reduce the fatigue strength in some design applications. Sections cut from CFRHSs with two different wall thicknesses were studied using distortion fatigue loading and using X-ray diffraction residual stress measurements. Residual stresses and fatigue strengths were virtually identical for the two thicknesses even though the corner radius to thickness ratio was different. Residual stresses were found to significantly influence those corners subjected to compression-compression loading. Fatigue strength of these corners was improved by a stress relief heat treatment, but the treatment had no significant effect on corners subjected to tension-tension loading.

KEYWORDS: fatigue, cold forming, residual stresses, structural tubes

Introduction

Following their introduction more than 40 years ago, rectangular hollow sections (RHS) have become widely accepted in both civil and mechanical engineering applications. Rectangular hollow sections (RHS) are widely used in

---

Manuscript received November 14, 2007; accepted for publication April 11, 2008; published online May 2008.

[1] Lappeenranta University of Technology, Department of Mechanical Engineering, P. O. Box 20, FI-53851 Lappeenranta, Finland, e-mail: sami.heinila@lut.fi

Citation: Heinila, S., Bjork, T., and Marquis, G., "The Influence of Residual Stresses on the Fatigue Strength of Cold-Formed Structural Tubes," *J. ASTM Intl.*, Vol. 5, No. 5. DOI10.1520/JAI101570. Available online at www.astm.org. Also included in JAI Special Issue STP 1508, *Fatigue and Fracture Mechanics: 36th Volume,* R. W. Neu, K. R. W. Wallin, and S. R. Thompson, guest editors, ASTM International, West Conshohocken, PA, 2009, pp. 200-215.

load-carrying structures due to their good load transfer behavior and aesthetic form. During fabrication of a cold-formed rectangular hollow section (CFRHS), the corner regions experience significant plastic strains. The resulting through thickness residual stresses in the corner region can significantly influence the fatigue strength of a structure and, in some design applications, the fatigue strength of the inside corner may be critical [1–7]. Fabricators often desire smaller outside corner radii both for aesthetic reasons and to reduce the amount of preparation required for some welded joint configurations. However, smaller corner radii can cause micro-cracks and reduce the fatigue strength due to the increased stress concentration factor. The forming process may also coarsen the initially smooth surface and enhance both micro-cracking and fatigue crack development on the surface [8].

If the tensile residual stresses in a fabricated component are sufficiently high, a crack can propagate even if the applied local stresses are cyclically compressive. Greasley et al. [9] showed that a Mode I fatigue crack within a tensile welding residual stress field can grow when the cyclic external stresses are compressive. However, in this study the cracks arrested after a period of propagation. Hermann [10] tested compact tension aluminum alloy specimens that were precompressed in order to create a tensile residual stress field ahead of the notch tip. It was shown that the crack length at which a crack arrested increased with increasing levels of the precompression, i.e., an increasing large tensile residual stress field.

The relaxation of manufacturing process-induced residual stresses during cyclic loading is of great importance in understanding the fatigue strength of fabricated structures. It has been reported that the cyclic stress-strain properties of the material, rather than the static yield strength, are related to the relaxation and redistribution of residual stresses [11,12]. The implication is that residual stresses in cyclic softening materials would relax during the stabilization of the cyclic stress strain curve. In cyclic hardening materials, any potential residual stress relaxation would occur within the few first cycles. It has also been observed that relaxation may even occur at stress levels below the cyclic yield stress [12]. Other factors affecting the relaxation include the initial magnitude and gradient of the residual stress field, the degree of cold working, the cyclic stress amplitude, and the mean stress ratio [13,14]. It has been reported that higher strength materials are more resistant to residual stress relaxation than lower strength materials because the relaxation in some cases is associated with the rearrangement of dislocations which depends on the macro- and microplastic strain [15]. The mobility of the dislocations also depends on the initial dislocation density and the initial dislocation arrangement [11].

Experimental Methods

Test Materials

Cold-formed rectangular hollow sections (CFRHS) can be manufactured by either brake pressing or by a roll forming process. Brake pressing is used mainly

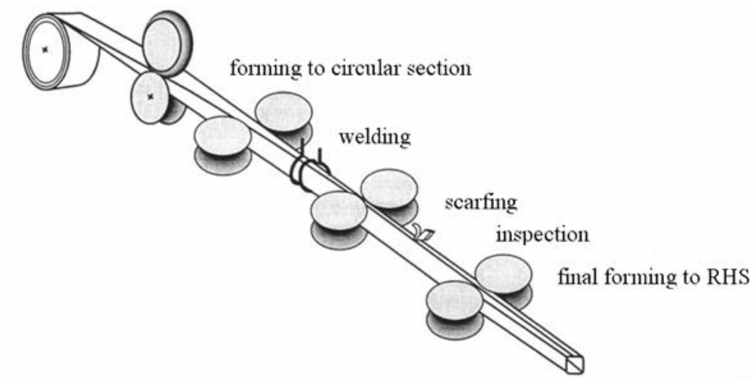

FIG. 1—*Simplified schematic of the two-stage cold roll forming process.*

for small production series or for tapered sections. Roll forming is used for large volume production with constant section profile. Roll forming may be a single process in which an RHS is formed from a strip, but a two-stage process is more common. During two-phase forming the tube is first formed into a circular mother tube and then cold-formed to its final rectangular shape. Although the appearance and nominal properties of sections fabricated from these processes is similar, the residual stress states in the sections can be different significantly depending on the manufacturing process. The greatest difference is that the roll forming process induces residual stresses in both the circumferential and longitudinal directions [16] whereas break pressing induces primarily circumferential residual stresses. During roll forming, the tubes are also mechanically compressed circumferentially during the rectangular forming stage so that the material thickness in the corner region actually increases. By contrast, break pressing is closer to a pure plate bending operation. A simplified schematic illustrating the two-stage cold roll forming process is shown in Fig. 1.

Two phase roll forming was used for the tubes in this current study. Hollow sections were roll formed from structural steel S355 MHJ2H. Nominal yield stress of the material is $f_y = 355$ MPa but the actual yield stress for this material is 460–520 MPa, the measured ultimate strength is 510–620 MPa and measured ultimate strain A_5 is 25–33 % [17,18]. The ultimate strain A_5 is defined as

$$A_5 = \left(\frac{l_u - l_0}{l_0} \right) \cdot 100 \tag{1}$$

where l_u is the final length and l_0 is the initial length of the test specimen. The initial length for A_5 is defined as

$$l_0 = 5d_0 \tag{2}$$

where d_0 is the initial diameter of the circular test specimen.

Due to the cold forming process the material in the corner region of the CFRHS goes through large plastic deformations and thus work hardens. Yield and tensile strengths of the material in the corner regions are typically 25 % greater than for the flat faces and the A_5 is reduced by about 13–15 %. From a structural point of view, the material in the corner region is still sufficiently ductile. The sections were square with outer nominal dimensions of 200 by 200 mm. Wall thickness was either 12.5 or 6 mm. The nominal outer corner radii were 37.5 mm for the 12.5 mm thick section and 12 mm for the 6 mm thick section. Precise dimensions were measured and are given in Table 1 with reference to Fig. 2.

Test Samples

The CFRHSs were received as 3000 mm long tubes. These were then cut into 100 mm long sections for fatigue testing, one 500 mm section for residual stress measurement, and one 500 mm long section which was cut open longitudinally to inspect for inside corner cracks using a dye penetrant method. None of the tubes tested showed any indications of pre-existing cracks.

The edges of the 100 mm long fatigue specimens were machined and the machined edges were slightly chamfered to avoid cracks initiating from the edge. The surfaces of the specimens were cleaned by solvent but not otherwise treated. Strain gages were fixed to the inside radius of one of the corners which were subsequently subjected to tensile stress during fatigue loading. In some tests the opposite corner was also strain gaged.

Residual stresses from the 500 mm long tubes sections were measured using the X-ray diffraction method. The diffraction peak of CrKα hkl (211) and a pin hole collimator with a diameter of 1 mm were used. Measurements were made along the inner surface of each corner as close as possible to the mid-point of the corner radius. Two 500 mm lengths of the CFRHS with 12.5 mm wall thickness were stress relieved at $620°C \pm 10°C$ for 30 minutes. These were subsequently cut into specimens by the procedures just described. Residual stress measurements were performed on one of these specimens. For two of the stress relieved test sections the inside radii of the two corners subjected to tensile loading were mechanically ground and polished with the intention that those corners would resist fatigue crack initiation longer than corners subjected to compressive loading and crack would initiate on corners subjected to compressive loading.

Fatigue Tests

The testing arrangement presented in this paper was chosen due to its simplicity and in order to preserve as much as possible of the original residual stress state in the tube. Because the residual stresses are self-equilibrating through-thickness, longitudinally and around the tube perimeter, any cutting operation causes some degree of residual stress redistribution. For this reason larger specimens would be ideal but the testing arrangement may become complicated and uncertainties in boundary conditions and local stresses may be introduced.

Sections of CFRHS tubes were tested in the distortion test arrangement seen in Fig. 3. The applied force was compressive with a force ratio $R_F = 10$, i.e.,

TABLE 1—*Measured dimensions (in mm) for the rectangular sections used in this study.*

ID	A	B	C	D	a_1	a_2	b_1	b_2	c_1	C_2	d_1	d_2	t_1	t_2	t_3	t_4
CD1	200.7	200.7	201.0	200.9	33.0	32.5	33.0	36.5	36.5	35.0	33.5	34.0	12.49	12.37	12.42	12.33
CD4	199.6	200.3	200.1	200.3	12.5	11.0	10.0	11.0	12.0	13.0	11.0	11.5	5.92	5.92	5.89	5.89

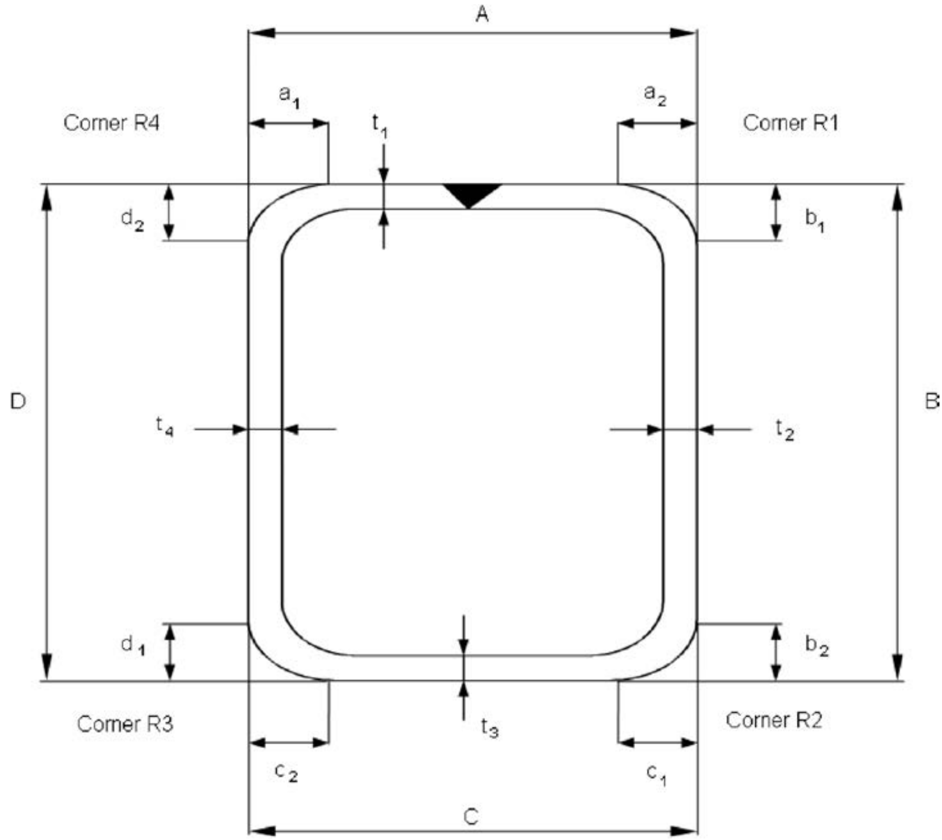

FIG. 2—*Measured dimensions of the tested CFRHS, refer to Table 1.*

minimum force/maximum force. With reference to Fig. 3, the resulting local stress ratio for the two inside vertical corners was $R_\sigma = 0.1$, i.e., tension-tension stress cycle, while the local stress ratio for the two inside horizontal corners was $R_\sigma = 10$, i.e., compression-compression stress cycle. As can be noted from Table 1, there are slight differences in the four corner geometries for a single CFRHS. Specimens were oriented in the test machine so that the inner corner with minimum corner radius was subjected to tensile stress for half of the specimens in a series and compressive stress in the remaining tests. In reality the stress ratios during testing varied slightly from these values due to the dimensional tolerances of the CFRHS sections.

A test was continued until section failure or until five million fatigue cycles had been reached. Frequencies used varied from 3 Hz to 12 Hz depending on the force and the testing machine used. The maximum and minimum values of force, displacement and strain over a time period of ten seconds were recorded every five minutes.

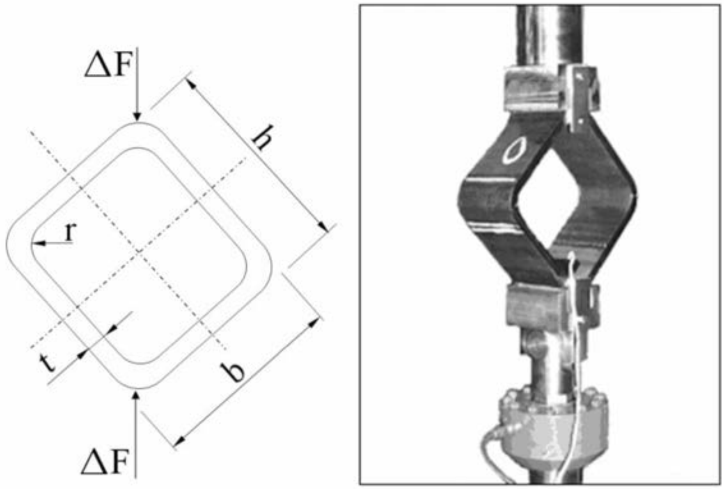

FIG. 3—*Test arrangement for the CFRHS.*

Results

Fatigue Life Calculation

The applied local stress range $\Delta\sigma$ of all the test specimens have been plotted against the number of cycles to failure N_f in Fig. 4 and presented numerically in Table 2. The local stress range has been calculated from the measured strains on the inside surface of one corner of the specimen. The correlation between the stress range and the number of cycles to failure can be expressed as

$$\Delta\sigma = C(N_f)^m \tag{3}$$

The best fit value of m was calculated to be $m = 5.2$ for the 6 mm specimens and $m = 3.1$ for the 12.5 mm thick specimens. If both thicknesses are considered as a single dataset the value is $m = 4.0$. A test result was censored if $N_f > 2 \times 10^6$. The characteristic fatigue strength, $\Delta\sigma_C$, defined as the stress range corresponding to $N_f = 2 \times 10^6$ and 95 % survival probability, for the 6 mm thick specimens was 253 MPa and for the 12.5 mm thick specimens $\Delta\sigma_C = 198$ MPa. If all specimens were considered as a single dataset $\Delta\sigma_C = 226$ MPa. Statistical methods presented by Hobbacher [19]were used to compute $\Delta\sigma_C$.

Fatigue of Specimens Without Heat Treatment

The results of tests of specimens without heat treatment are marked with diamonds in Fig. 4. Several of the nonheat treated specimens failed from one of the inside corners subjected to fully compressive loading. These are denoted with C in column 2 of Table 2. The combination of high tensile residual stresses

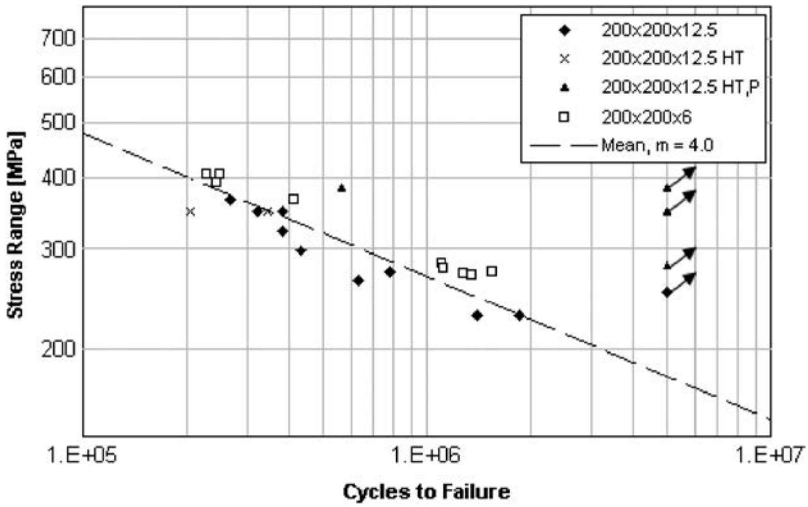

FIG. 4—*Test results for the specimens 200 by 200 by 12.5 and 200 by 200 by 6. Runouts have been marked with arrows. HT=heat treated, HT, P=heat treatment with mechanical polishing of the tensile corners.*

plus cyclic compressive loading was sufficient to make these corners critical. One such crack is shown in Fig. 5. Generally, however, compression cracks did not initiate or did not propagate to failure.

Fatigue of Heat Treated Specimens

In Fig. 4 and Table 2 the heat treated specimens are marked as HT while heat treated plus polished specimens are marked as HT,P. The HT specimens had fatigue strengths similar to the specimens without heat treatment. This is an indication that high tensile residual stresses are not detrimental if the applied loading is tensile, i.e., $R_\sigma=0.1$. No cracking was observed in HT corners subjected to compressive loading, i.e., $R_\sigma=10$. Since only two heat treated specimens without polishing were tested, reliable conclusions cannot be made.

The intention of HT,P specimens was that improving the fatigue life of the inside corners subjected to pulsating tensile stresses by polishing would increase the likelihood of failure occurring in one of the inner corners subjected to cyclic compression loading. However, Table 2 indicates that only one of four HT,P corners failed and this single failure occurred in the polished tensile corner. Fatigue strength in all cases was significantly greater than that of the non-heat treated specimens. The residual stresses of the stress relieved specimens are assumed to be near zero, and confirmation of these using X-ray diffraction measurements is in progress. The significantly increased fatigue strength observed indicates that the tensile residual stresses on the inside surface were significantly reduced. The single HT,P specimen that failed from the tensile corner clearly had fatigue strength greater than the fatigue strength of the non-

TABLE 2—*Test results for the specimens 200 by 200 by 12.5 and 200 by 200 by 6. C denotes failure in the corner subject to compressive stresses.*

	200×200×12.5		
Number	Note	$\Delta\sigma$ [MPa]	N_f thousands
1		349	380
2	C	272	780
3	C	251	5000
4	C	229	1400
5		229	1850
6		349	320
7		297	430
8		368	270
9		264	630
10		322	380
11	HT	321	344
12	HT	321	205
13	HT,P	263	5000
14	HT,P	311	5000
15	HT,P	328	5000
16	HT,P	328	566
	200×200×6		
1		273	1550
2		407	250
3		269	1350
4		406	230
5		283	1112
6		393	245
7		276	1117
8		418	50
9		271	1280
10		368	410

heat treated specimens. More tests would be needed to make any further conclusions on the influence of mechanical polishing of the specimen inside corners.

Residual Stresses

Residual stresses measured using X-ray diffraction are presented in Tables 3 and 4. In Table 3 the sections have the same length, 500 mm, and same outer dimensions but different thicknesses. Data from Table 3 is presented graphically in Fig. 6. There is no significant difference in residual stresses as a function of wall thickness. The average residual stress for the four corners in the

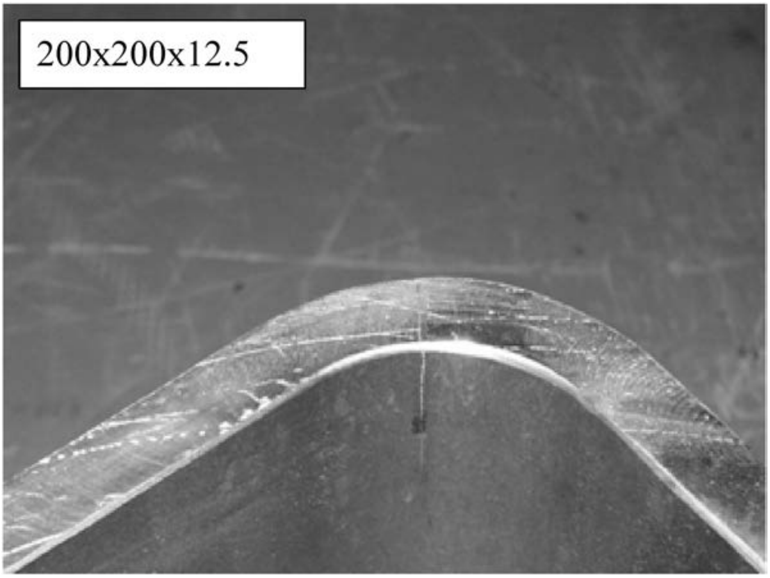

FIG. 5—*Crack initiated on inside surface in corner under compression-compression loading.*

6 mm thick section is only 3 % greater that the average residual stress for the four corners in the 12.5 mm thick section. These values are approximately 25 % of the yield strength of the material in the cold worked corner region. The Full Width Half Maximum (FWHM) values in Tables 3 and 4 represent the

TABLE 3—*Measured residual stresses transverse to the corner radius in specimens with different wall thickness.*

Corner	200 × 200 × 12.5, 500 mm Residual Stress		FWHM
	MPa	± MPa	deg
R1	171	21	2.54
R2	116	36	2.61
R3	126	26	2.58
R4	211	34	2.51
	200 × 200 × 6, 500 mm		
R1	155	7	2.59
R2	135	24	2.59
R3	187	19	2.57
R4	167	31	2.56

TABLE 4—*Measured residual stresses transverse to the corner radius in specimens of two different lengths [15].*

Corner	200×200×10, 500 mm Residual Stress		FWHM
	MPa	± MPa	deg
R1	85	25	2.54
R2	133	17	2.53
R3	119	26	2.60
R4	112	21	2.52
	200×200×10, 100 mm		
R1	−2	27	2.51
R2	14	26	2.53
R3	141	38	2.56
R4	65	36	2.51

width of the intensity profile corresponding to half of the maximum intensity value of X-ray diffraction. These values are given in degrees and relate to the relative plastic deformation at the point of measurement.

Some of the residual stress in CFRHS are self-equilibrating around the section so that any sectioning of the original CFRHS beam causes redistribution of the elastic residual stresses. Detailed modeling and measurements are

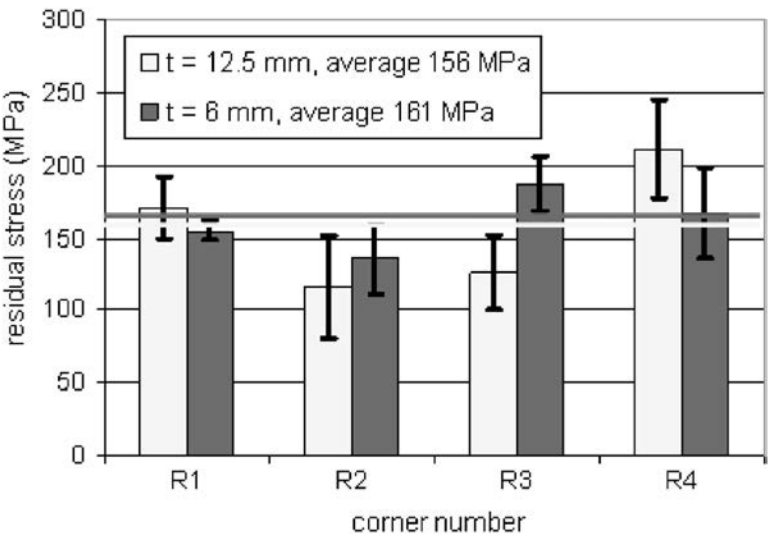

FIG. 6—*Measured residual stresses transverse to the corner radius in specimens with different wall thickness. Measurement uncertainty and average stress for all four corner are also shown.*

beyond the scope of this paper, but any sectioning of the CFRHS beams, either longitudinally or transverse, have been observed to induce small but measurable changes in the profile. For example, a rectangular profile will tend to "ovalize" from the beam ends as the long beam is cut into shorter sections. This is due to longitudinal residual stresses on straight sides of the CFRHS profile that are compressive on the inner surface and tensile on the outer surface [16,20] and tend to bend outwards as is noted e.g., by Weng and Pekoz [20]. As the longitudinal residual stresses redistribute the circumferential residual stresses also redistribute which can be seen from Table 4 in which residual stresses from one 500 mm long section and one 100 mm long section cut from the same mother tube are compared [15]. Note that these CFRHSs had slightly different thicknesses than those specimens fatigue tested in this study. Table 4 shows that three of the four inside corners had significant reductions in the residual stresses while one corner had some increase. The observed increase was smaller than the uncertainty in the measurements. High tensile residual stress transverse to the corner was observed even in the shorter specimen.

Discussion

For CFRHS the ratio of outer corner radius per thickness, r/t, is normally used as a measure of the degree of cold work in the corner region. In this study, the respective ratios were nominally 3 for the 12.5 mm thick sections and 2 for the 6 mm thick sections. From Table 3 and Fig. 6 it can be seen that there was no significant difference in the measured elastic residual stresses as a function of wall thickness. The tangential elastic residual stresses in the inner corner are mainly due to elastic spring back effect in forming and, thus, are more dependent on the yield stress of the material rather than on r or the ratio r/t. The average residual stress for the four corners in the 6 mm thick section ($r/t=2$) is only 3 % greater that the average residual stress for the four corners in the 12.5 mm thick section ($r/t=3$). These values are approximately 25 % of the yield strength of the material in the cold worked corner region. The fatigue life data in Fig. 4 show a small but clear trend that the 6 mm thick specimens had fatigue strengths about 14 % greater than the 12.5 mm thick specimens. This fatigue strength increase with respect to thickness is consistent, e.g., with the increase in fatigue strength with respect to diameter for specimens subjected to rotating bending loading. For example, Dowling suggests a strength increase due to stress gradient of 10–15 % as the diameter decreases from 12.5 to 6 mm [21].

The 12.5 mm and 6 mm thick specimens are evaluated as separate datasets. The exponent for the specimens with a wall thickness of 12.5 mm was $m=3.1$ and for 6 mm was $m=5.2$. It is interesting to note that these two values are similar to those used for fabricated structures. Based on an extensive database, the exponent m in Eq 1 for welded structures is normally assumed to be $m=3$ and for base materials with rolled surfaces, $m=5$ [19]. For ferritic steels, a slope close to 3.0 is normally used as an indication that the crack initiation phase is largely absent. However, the small difference in the S-N slopes for

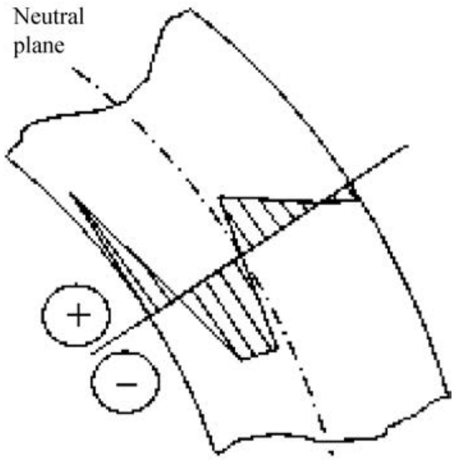

FIG. 7—*Tangential residual stress distribution through wall thickness in the center of the corner of CFRHS.*

different thicknesses is not considered statistically significant due to the relatively small number of tests.

The surface finish on the inside corners of the sections will influence the fatigue strength and produce S-N curves with different slopes. This is dependent on the degree of cold work and the compressive hoop strains induced during the final sizing of the CFRHS as only the outer surfaces of the mother tubes are rolled and the inner surfaces are forced to form without support. Bäckström et al. investigated the surface finish for CFRHS cold formed from the same material as that used in this investigation and with $r/t=2$. Surface defects with depths of 5–20 μm were found in the inside corner region [18]. Corrosion or problems in the manufacturing process, e.g., excessive mill scale during rolling, can increase the size of the surface defects and have been shown to decrease the fatigue strength of CFRHS [15,18].

Analysis of the tangential residual stress distribution through wall thickness due to the roll forming operation has been previously reported by Heinilä et al. [7]. Similar residual stress distributions were obtained, e.g., by Quach et al. [22] for press-braked steel sections. Heinilä et al. [7] made the analysis for a CFRHS geometry and material different from those in this study so the results can only be interpreted qualitatively. Also, the two-dimensional nature of the numerical simulation does not fully represent the 3-D roll forming process. The tangential residual stress pattern is shown in Fig. 7. The tensile residual stress on the inner corner surface and the compressive residual stress on the outer corner have been confirmed in many X-ray diffraction measurements. Tensile residual stresses equal to 25–33 % of the material yield strength are confirmed by other studies [5,15].

In the case of corners subjected to tension-tension loading, the heat treated sections fatigue lives were nearly the same or even slightly less than the fatigue lives of the sections without heat treatment. The complex through thickness stress distribution which alternates between tension and compression will have a mixed effect on crack propagation rate when the external loading is tension-tension. Cracks will tend to initiate relatively quickly but slow down as a region of compressive residual stress is reached. However, residual stresses will be constantly redistributing so as to be self-equilibrating. Residual stress relaxation and redistribution and their effect on fatigue crack growth and the fatigue crack path has not received much research attention. The behavior of fatigue crack path due to residual stress redistribution has been discussed in by Heinilä et al. [5].

Some nonheat treated specimens failed from corners under compressive loading, see Fig. 5. The tensile residual stresses on the inside surface of the corners were high enough to initiate fatigue cracks when the external cyclic stresses were fully compressive. The variation of these tensile residual stresses between different corners can be explained with the slightly different corner radii, normal error in the X-ray diffraction system, and also different residual stress redistribution due to sawing of the test specimens to their length of 100 mm. Change in residual stresses with section length is not investigated further but merely noted as for specimens from the same tube but of different lengths, see Table 4. No cracking was observed in HT corners subject to compressive loading.

Conclusions

Sections cut from CFRHS were fatigue tested using compressive distortion loading. The sections had nominally identical outer dimensions but two different wall thicknesses and different corner radii. Some of the thicker sections were stress relieve heat treated before fatigue testing. X-ray diffraction was used to measure the residual stresses on the inner corners of the sections. The following conclusions based on the results can be made:

1. Tensile residual stresses have significant influence on the fatigue lives of the corners under compressive loading. If tensile residual stresses are present the initiation and advance of fatigue cracks is possible even in corners subjected to external cyclic compressive loading.
2. In heat treated specimens, fatigue crack initiation in corners subjected to cyclic compressive loading was not observed and the fatigue strength of these corners was significantly increased.
3. In the case of corners subjected to tension-tension loading, the heat treated sections fatigue lives were nearly the same the fatigue lives of the sections without heat treatment. The complex through thickness stress distribution which alternates between tension and compression and also changes due to crack propagation. These have a mixed effect on crack propagation rate.
4. The sections had different degrees of cold working as measured by the difference in r/t ratios but the residual stresses showed no significant differences.
5. Sections with smaller wall thicknesses had slightly greater fatigue strength, but the difference can be explained as a thickness stress gradient effect.

References

[1] Karren, K., "Corner Properties of Cold-Formed Steel Shapes," *Journal of the Structural Divisions, Proceedings of the ASCE*, Vol. 93, 1967, pp. 401–432.

[2] Rondal, J., "Residual Stresses in Cold-Rolled Profiles," *Constr. Build. Mater.*, Vol. 1, 1987, pp. 150–164.

[3] Kato, B., and Aoki, H., "Residual Stresses in Cold-Formed Tubes," *J. Strain Anal. Eng. Des.*, Vol. 13, 1978, pp. 193–204.

[4] Webster, G. A., and Ezeilo, A. N., "Residual Stress Distributions and Their Influence on Fatigue Lifetimes," *Int. J. Fatigue*, Vol. 23, 2001, pp. 375–383.

[5] Heinilä, S., Björk, T., and Marquis, G., "Observations on Fatigue Crack Paths in the Corners of Cold-Formed High-Strength Steel Tubes," *Eng. Fract. Mech.*, Vol. 75, 2008, pp. 833–844.

[6] Heinilä, S., Marquis, G., Björk, T., and Lepistö, J., "A Study of Curved Crack Paths in Cold-Formed Corners of High Strength Structural Steel," *Proceedings of International Conference on Crack Paths*, Parma, 14–16 Sept., 2006.

[7] Henilä, S., Björk, T., Marquis, G., and Ilvonen, R., "Numerical Simulation of Cold Forming and Its Effect on the Fatigue Life of Cold-Formed Rectangular Structural Tubes," *Proc., of 4th ECCOMAS Conference*, Jyväskylä, Finland, 24–28 July 2004.

[8] Heinilä, S., Björk, T., Marquis, G., Bäckström, M., and Ilvonen, R., "Fatigue Crack Paths and Life Estimation for Cold-Formed Rectangular Structural Tubes," *Proceedings of ECF15 Conference*, Stockholm, Sweden, 11–13 Aug. 2004.

[9] Greasley, A., and Naylor, S. G. W., "Influence of Residual Welding Stresses on Fatigue Crack Growth Under Compressive Loading," *Eng. Fract. Mech.*, Vol. 24, 1986, pp. 717–726.

[10] Hermann, R., "Fatigue Crack Growth in Ductile Materials under Cyclic Compressive Loading," *Fatigue Fract. Eng. Mater. Struct.*, Vol. 17, 1994, pp. 93–103.

[11] Lu, J., Flavenot, J. F., and Turbat, A., "Prediction of Residual Stress Relaxation during Fatigue," *Mechanical Relaxation of Residual Stresses*, ASTM STP 993, L. Mordfin, Ed., ASTM International, West Conshohocken, PA, 1988, pp. 75–90.

[12] Flavenot, J. F. and Skalli, N., "Effects of Grinding Conditions on Fatigue Behavior of 42CD4 Grade Steel; Comparison of Different Fatigue Criteria Incorporating Residual Stresses," *Mechanical Relaxation of Residual Stresses*, ASTM STP 993, L. Mordfin, Ed., ASTM International, West Conshohocken, PA, 1988, pp. 91–111.

[13] Zhuang, W. and Halford, G., "Investigation of Residual Tress Relaxation Under Cyclic Load," *Int. J. Fatigue*, 23, 2001, pp. 31–37.

[14] Bruno, G. and Nitschke-Pagel, T., "The Residual Stress Relaxation After Fatigue in Fine-Grained Steels," *Appl. Phys.*, Vol. 74 (suppl.), 2002, 1388–1390.

[15] Kokkonen, J. and Björk, T., "Project 7X: Fatigue of High Strength Cold-Formed RHS Corners," CIDECT, Final report 7X-9/06, 2006.

[16] Rondal, J., "Residual Stresses in Cold-Rolled Profiles," *Constr. Build. Mater.*, Vol. 1 No. 3 1987, pp. 150–164.

[17] Björk, T., "Ductility and Ultimate Strength of Cold-Formed Rectangular Hollow Section Joints at Subzero Temperatures," Doctoral Thesis, Lappeenranta University of Technology, Acta Universitatis Lappeenrantaensis, ISSN 1456-4491, 233, 2005.

[18] Bäckström, M., Savolainen, M., Ilvonen, R., and Laitinen, R., "A New Fatigue Test Method for Corners of Structural Hollow Sections," *Proceedings FATIGUE 2002, Special Volume on Design and Analysis of Welded High Strength Steel Structures*, J. Samuelsson, Ed., EMAS, Stockholm, Sweden, 2002.

[19] Hobbacher, A., "Recommendations for Fatigue Design of Welded Joints and Com-

ponents," IIW document XIII-2151-07/XV-1254-07, International Institute of Welding, Paris, 2007.

[20] Weng, C. C. and Pekoz, T., "Residual Stresses in Cold-Formed Steel Members," *J. Struct. Eng.*, Vol. 116, 1990, pp. 1611–1625.

[21] Dowling, N. E., 2007. *Mechanical Behavior of Materials: Engineering Methods for Deformation, Fracture, and Fatigue*," 3rd ed., Prentice Hall, Upper Saddle River, NJ, 2007.

[22] Quach, W. M., "Finite Element Predictions of Residual Stresses in Press-Braked Thin-Walled Steel Sections," *Adv. Mass Spectrom.*, Vol. 28, 2006, pp. 1609–1619.

ASTM Special Technical Publication, Vol. 5, No. 4
Paper ID JAI101612
Available online at www.astm.org

Dale L. Ball[1]

The Influence of Residual Stress on the Design of Aircraft Primary Structure

ABSTRACT: Aggressive performance and weight objectives are driving aircraft manufacturers toward the use of advanced materials and structural concepts that may have inherent, process induced residual stresses in localized, but critical areas. Certification of these structures will require that the influence of these residual stresses be properly accounted for during design. One example of this circumstance is the unitization of lugs and fittings with primary spars and bulkheads. This is being done in order to reduce part count, which, in turn, reduces the necessity for large numbers of fasteners and the associated hole preparation/mating requirements. Such unitization can be achieved through the use of large forgings, which experience has shown may have significant residual stresses in localized areas, even after final machining. For man-rated flight vehicles, primary structural elements are typically designed based on damage tolerance concepts. This requires that fatigue crack growth analysis and testing be used for certification of the structure. Thus, for advanced design concepts based on unitized structure, the influence of residual stress on fatigue crack growth must be addressed. A substantial body of work has been developed over the past three decades by numerous researchers in the field of fracture mechanics with regard to residual stress. In what has become the standard approach to the problem, the residual stress field is used to estimate a residual stress intensity factor (SIF) using weight function or Green's function techniques. The residual SIF is superimposed with the applied SIF due to service loading and the total is then used in an otherwise unmodified, LEFM-based fatigue crack growth analysis. In this paper, we describe current research directed toward the

Manuscript received December 3, 2007; accepted for publication March 24, 2008; published online April 2008.
[1] LM Fellow, Lockheed Martin Aeronautics Co., P.O. Box 748, MZ 8661, Fort Worth, TX 76101

Citation: Ball, D. L., "The Influence of Residual Stress on the Design of Aircraft Primary Structure," *J. ASTM Intl.*, Vol. 5, No. 4. DOI10.1520/JAI101612. Available online at www.astm.org. Also included in JAI Special Issue STP 1508, *Fatigue and Fracture Mechanics: 36th Volume,* R. W. Neu, K. R. W. Wallin, and S. R. Thompson, guest editors, ASTM International, West Conshohocken, PA, 2009, pp. 216-239.

formal inclusion of residual stress effects in the design of aircraft primary structure. This effort has three focus areas. The first is the extraction of confounding residual stress effects during the characterization of the fundamental fatigue crack growth rate behavior of a critical aluminum alloy. The second is the quantification, both by analysis and experiment, of the location, spatial magnitude, and stress magnitude of the residual stress fields in a candidate forged/machined part. The third is the development of improved fatigue crack growth analysis methods that selectively account for the presence of residual stresses. Each of the three focus areas provides a critical ingredient to a proposed design analysis method in which components are analyzed using intrinsic (residual stress free) material data, with residual stresses then explicitly introduced only in those areas where they are known to exist. The discussion includes the results of a trade study on a wing spar showing potential optimization, both in terms of weight savings in over-designed areas, and service life/damage tolerance enhancement in under-designed areas.

KEYWORDS: residual stress, ACR-method, fatigue crack growth analysis, structural design

Nomenclature

a	=	crack dimension in the z-coordinate direction
c	=	crack dimension in the x-coordinate direction
ACR	=	adjusted compliance ratio
C_f	=	closure factor
DAS	=	design allowable stress
FCGR	=	fatigue crack growth rate
G	=	Green's function (stress intensity factor coefficient)
K_I	=	mode I stress intensity factor
LEFM	=	linear elastic fracture mechanics
MSS	=	maximum spectrum stress
n	=	exponent in K_{max} sensitivity relationship
ND	=	nondestructive
p	=	load
r	=	radial coordinate in a right cylindrical coordinate system
R	=	stress ratio
R_{so}	=	generalized Willenborg retardation model overload shutoff ratio
S	=	applied stress
SIF	=	stress intensity factor
t	=	thickness
W	=	width

x, y, z = coordinates in Cartesian coordinate system
α = constraint index
ΔK = stress intensity factor range
ϕ = parametric angle for specifying position on crack front of elliptical or part-elliptical cracks
σ_o = flow stress

Background

Aggressive performance and weight objectives are driving aircraft manufacturers toward the use of advanced materials and structural concepts that may have inherent, process induced residual stresses in localized, but critical areas. Certification of these structures will require that the influence of these residual stresses be properly accounted for during design. One example of this circumstance is the unitization of reinforcements, stiffeners, brackets, and fittings with primary structural components such as spars and bulkheads. This is being done in order to reduce part count, which, in turn, reduces the necessity for large numbers of fasteners and eliminates the associated hole preparation/mating requirements. These benefits generally translate into weight reduction/avoidance when comparing unitized versus comparable assembled structure. Unitization raises a number of issues for structural durability and damage tolerance, notably, reduced repair/replace capability and reduced crack arrest capability. These issues aside, however, the viability of the unitization concept is dependent on the availability of material systems that retain their mechanical properties in very thick sections. Recent developments in aluminum forging technology have addressed this issue [1], paving the way for the production of unitized structural components using large, near net forgings. But experience has shown that these forgings may have significant residual stresses in localized areas, even after final machining.

Historically, the utilization of aluminum forgings for large structural components has been problematic [2,3]. The presence of residual stresses at the coupon level tended to confound the mechanical property data (specifically fracture toughness and fatigue crack growth rate (FCGR)), and at the component level tended to invalidate fatigue crack growth life predictions. In recent aircraft programs, these issues have been addressed by using conservative (left bound) fits to FCGR data for design. This method tends to be very conservative for large portions of finished parts which are residual stress free. On the other hand, it can be unconservative (unsafe) for locations with residual stresses that are greater than those implicit in the design FCGR curves. In both cases, the inaccuracy arises because residual stress effects have not been explicitly addressed.

Bucci and co-workers have recently suggested a design approach that overcomes the issues inherent in large forgings (and in any component with residual stresses for that matter) and have shown that all of the technologies required for its implementation are currently available [4]. In this approach, design fatigue crack growth analyses are conducted using "intrinsic," residual stress-free material data, and residual stresses are explicitly introduced only in those regions where such stresses are known to exist. The approach requires three critical developments. The first is the development of intrinsic material data. In recent work by Donald and co-workers [5], it has been shown that the adjusted compliance ratio (ACR) method can successfully extract residual stress effects during FCGR testing and can thus characterize intrinsic behavior. The second critical development is the characterization of the residual stresses in finished parts made from large aluminum forgings. This characterization includes identifying the location, spatial extent and magnitude of the residual stress fields in a part, and may be achieved by both experimental and analytical means. The recently developed contour method [6,7] will permit quantification of residual stress profiles on critical planes in realistic, complex geometry parts. Finally, the third development requires implementation of residual stress field capability into production fatigue crack growth analysis algorithms. This involves existing fracture mechanics technology and has been accomplished and demonstrated by several researchers [8,9].

The design approach described herein calls for the identification of residual stress zones on candidate parts. A standard residual stress profile, with specified peak and distribution characteristics (including no residual stress), is assigned to each zone. The fatigue crack growth analyses used to support the design process (sizing) for all control points within a given zone are performed using intrinsic material data and explicitly include the residual stress distribution appropriate for that zone. In this way, regions with no residual stress are not unnecessarily penalized (oversized), while regions with high residual stress are sized as required to satisfy service life and residual strength requirements even with detrimental residual stresses present.

First Required Development: Generation of Intrinsic Fatigue Crack Growth Rate Data

The first of the three critical ingredients for the proposed design approach, is the characterization of intrinsic, residual stress-free, fatigue crack growth rate data. A schematic overview of a proposed, six-step process designed to produce such data is shown in Fig. 1. The process generally involves the removal of confounding residual stress effects by processing applied ΔK data using the ACR method and then reconstructing the stress ratio dependence required for production fatigue crack growth analysis by re-introducing $K_{\max}$ sensitivity and closure effects.

The six steps are as follows:

(1) remove residual stress (and closure) effects via the ACR method
(2) remove $K_{\max}$ effect via the ACR method
(3) re-introduce $K_{\max}$ sensitivity
(4) re-introduce plasticity induced closure effects
(5) calibrate constructed FCGR curves based on constant amplitude tests using residual stress-free coupons
(6) validate constructed FCGR curves by correlating fatigue crack growth analysis with spectrum (variable amplitude) with residual stress-free tests.

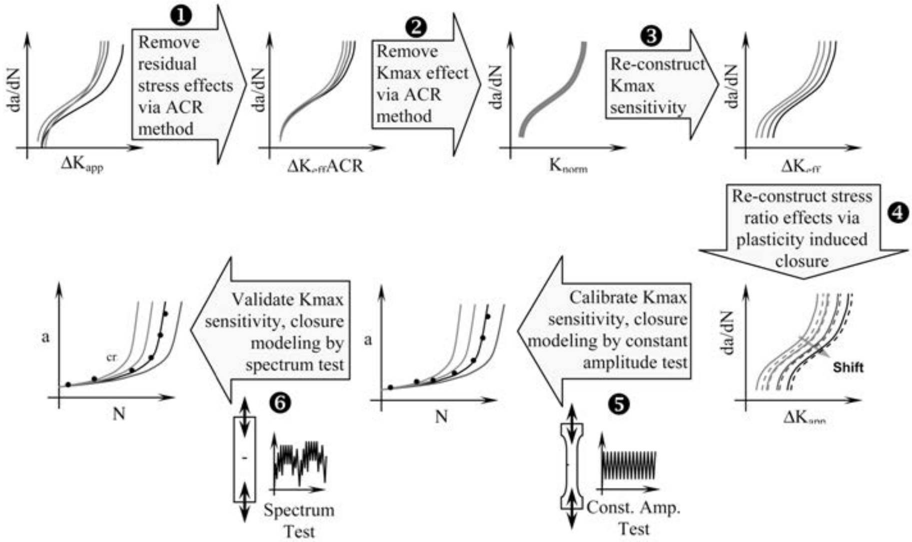

FIG. 1—*Overview of FCGR data reduction approach.*

In recent years, a number of researchers have demonstrated the ability of the adjusted compliance ratio method to reduce applied ΔK (stress intensity factor range) versus da/dN (fatigue crack growth rate) data to intrinsic, ΔK versus da/dN data by removing the effects of tensile residual stresses, the effects of crack closure (both plasticity and roughness induced) and sensitivity to K_{max}. The details of the ACR method have been reported extensively and will not be repeated here [10,11]. The result of applying the ACR method during FCGR testing is a single, intrinsic, da/dN versu K_{norm} curve. An example data set for the forged aluminum material considered in this study is shown in Fig. 2. As shown in Fig. 2(*a*), the ΔK applied data indicate the presence of confounding residual stresses as evidenced by the considerable scatter in the data as well as the apparent crossing of data sets at different applied stress ratios (R). However, as shown in Fig. 2(*b*), application of the ACR method successfully collapses this data to a single K_{norm} versus da/dN curve. Also shown is the mean curve fit to the K_{norm} data; this curve serves as the starting point for step 3 of the reconstruction process.

Many fatigue crack growth analysis algorithms require that the stress ratio dependence of FCGR be included in the definition of material properties. Thus, before the FCGR data shown in Fig. 2(*b*) can be used for analysis, they must be converted back to R-dependent form. In step 3 of the FCGR data reduction approach, K_{max} sensitivity [12] is re-introduced using the expression

$$\Delta K_{int} = K_{norm}(1 - R)^n \qquad (1)$$

where ΔK_{int} represents an intermediate quantity which includes K_{max} sensitivity but not closure. Using the mean da/dN versus K_{norm} curve that has been fit

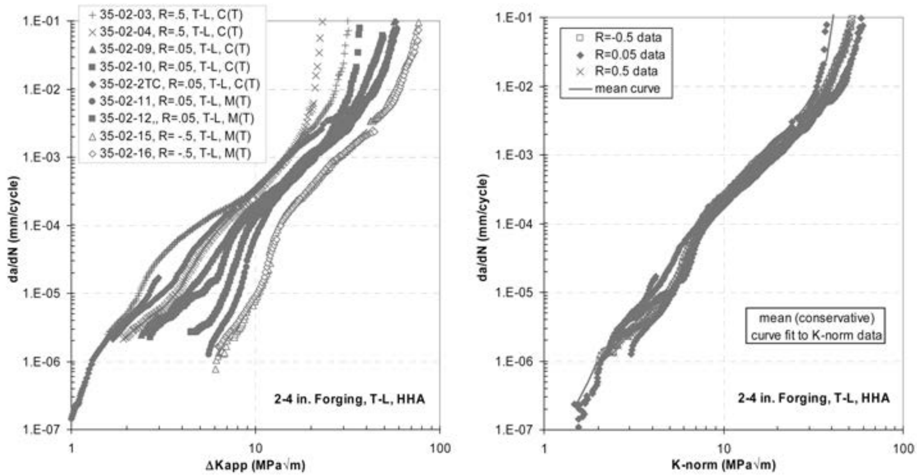

FIG. 2—*Generation of* da/dN *versus* K_{norm} *data for die forging,* 2–4 in.*, T-L, HHA:* (a) da/dN *versus* $\Delta K_{\mathrm{applied}}$ *and* (b) da/dN K_{norm}.

to the test data, ΔK_{int} curves are calculated for a range of R values and an assumed value of n. The result is a family of da/dn versus ΔK_{int} curves, as shown in Fig. 3 (for $n = 0.25$).

The next step in the process is the re-introduction of crack closure effects. While it is recognized that a variety of closure mechanisms are typically at play during fatigue crack growth, only plasticity induced closure is formally addressed in this data reconstruction process. This is primarily for the sake of expediency; the expressions given by Newman for the relationship between closure factor and applied stress ratio [13], which are predicated on the condition that plasticity is the dominant closure mechanism, are very compact and easy to apply. Given each of the da/dN versus ΔK_{int} curves above, the corresponding da/dN versus ΔK_{app} curves may be estimated using the relationship

$$\Delta K_{\mathrm{app}} = \Delta K_{\mathrm{int}} \frac{1 - R}{1 - C_f} \tag{2}$$

where C_f is the closure factor, defined as

$$C_f = \frac{K_{\mathrm{open}}}{K_{\mathrm{max}}} \tag{3}$$

and the relationship between C_f and R was given by Newman as

$$C_f = \max[R, (A_0 + A_1 R + A_2 R^2 + A_3 R^3)] \quad \text{for } R > 0 \tag{4}$$

$$C_f = A_0 + A_1 R \quad \text{for } -2 < R < 0 \tag{5}$$

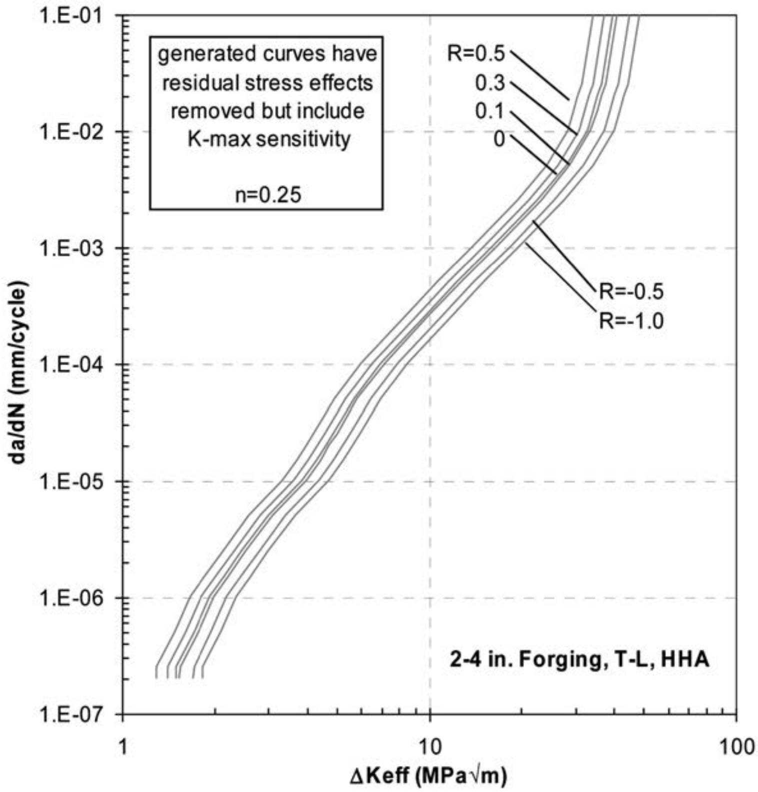

FIG. 3—*Intermediate* da/dN *versus* ΔK_{eff} *mean curves for die forging,* 2–4 in.*, T-L, HHA.*

$$A_0 = (0.825 - 0.34\alpha + 0.05\alpha^2)\left[\cos\left(\frac{\pi}{2}\frac{S_{max}}{\sigma_o}\right)\right]^{1/\alpha} \tag{6}$$

$$A_1 = (0.415 - 0.071\alpha)\frac{S_{max}}{\sigma_o} \tag{7}$$

$$A_2 = 1 - A_0 - A_1 - A_3 \tag{8}$$

$$A_3 = 2A_0 + A_1 - 1 \tag{9}$$

The result of this step is a family of da/dn versus ΔK_{app} curves over a range of stress ratios. A typical set of results, generated using $\alpha = 2$ and $S_{max}/\sigma o = 0.3$, is shown in Fig. 4.

Note that steps 3 and 4 can be combined, and that ΔK_{app} can be calculated directly from K_{norm} as

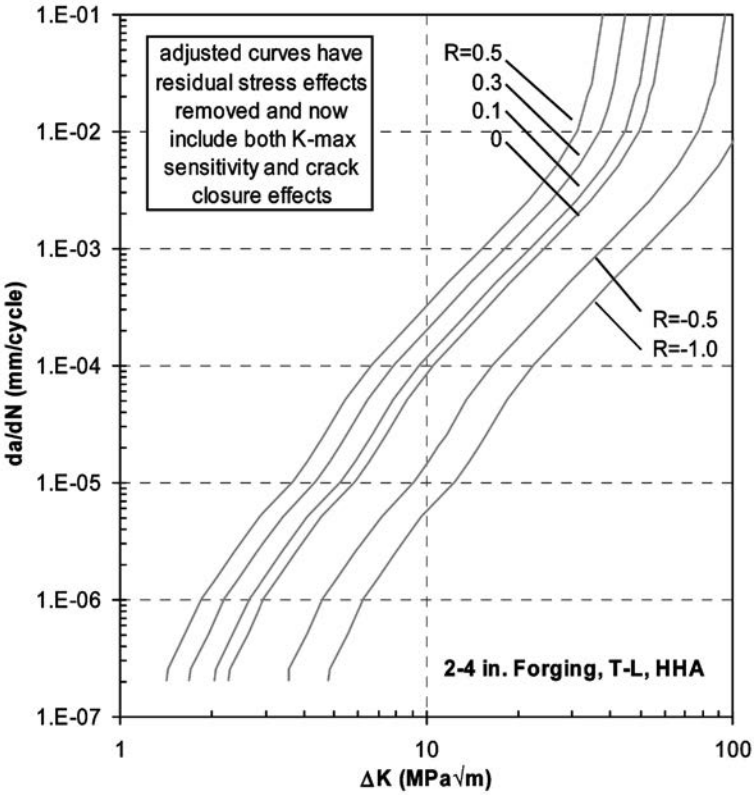

FIG. 4—*Design* da/dN *versus* ΔK_{app} *mean curves for die forging,* 2–4 in., *T-L, HHA.*

$$\Delta K_{\text{app}} = K_{\text{norm}}(1 - R)^n \frac{1 - R}{1 - C_f} \tag{10}$$

As mentioned above, it is recognized that plasticity may not be the only significant closure mechanism operating during fatigue crack growth in the aluminum forgings being addressed here. Since tractable models for all closure mechanisms other than plasticity are not readily available, these mechanisms are not treated explicitly. In step 5 of the data reconstruction process, the combined (net) effect of the other closure mechanisms is determined empirically by comparing FCG analysis results for constant amplitude loading with data taken using residual stress-free coupons. The FCGR mean curves from step 4 are adjusted (calibrated) as required in order to achieve agreement between analysis and test. The amount of calibration required is a measure of the significance of the other closure mechanisms. At the conclusion of the calibration step (step 5), the family of adjusted da/dn versus ΔK_{app} curves are suitable for use in standard fatigue crack growth analysis.

In the final step of the FCGR data reduction-reconstruction process, the

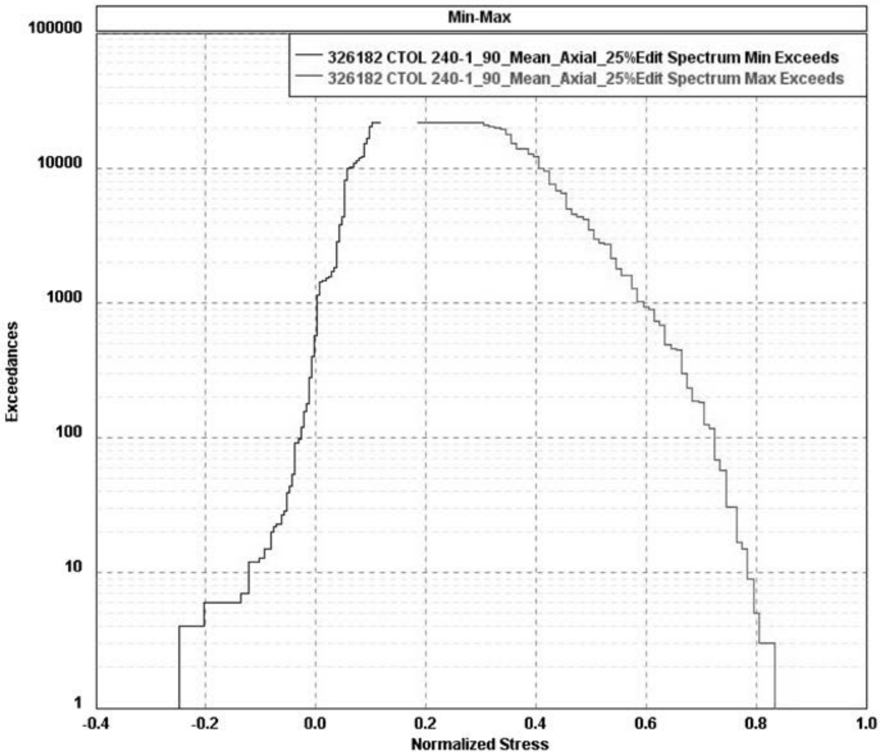

FIG. 5—*WBM spectrum min-max exceedance diagram.*

overall procedure is validated by comparing spectrum fatigue crack growth analyses performed using the adjusted da/dN curves with test data taken using residual stress-free coupons. An example of one such comparison is shown below. A small edge cracked test specimen fabricated from 2–4 in. forged material in the T-L orientation, was subjected to the wing bending moment spectrum shown in Fig. 5. Two corresponding fatigue crack growth analyses were performed. The first utilized a conservative (left bound) FCGR data set according to current design practice. The second utilized the reconstructed, residual stress free data set shown in Fig. 4. (No step 5 calibration was applied to this FCGR dataset.) As shown in Fig. 6, usage of the reconstructed FCGR data in the analysis resulted in a considerable improvement in accuracy.

Second Required Development: Quantification of Residual Stress

The second critical ingredient required for the viability of the proposed design approach is sufficient knowledge of the location, magnitude and internal distribution of residual stresses. Obviously, if residual stresses are going to be explicitly introduced in design fatigue crack growth analyses, these character-

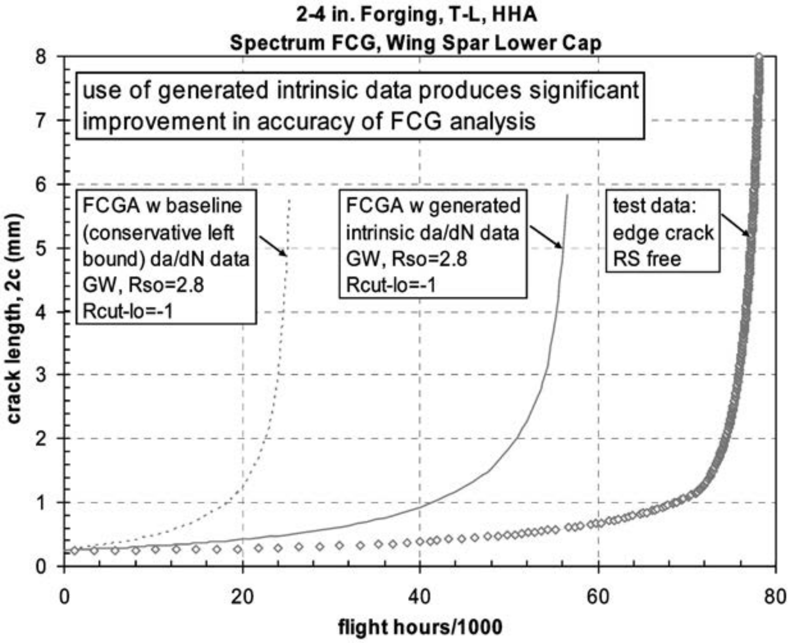

FIG. 6—*Comparison of fatigue crack growth analyses with experimental result for an edge crack in a small, straight sided coupon subjected to WBM spectrum loading.*

istics must be known. In the current program, residual stresses in large aluminum forgings are characterized using both analytical and experimental methods.

Advanced finite element analysis (FEA) techniques are required for analytical determination of residual stresses in finished parts. These analyses require very detailed geometric modeling (very small element size, high level of discretization) as well as sophisticated constitutive modeling. The work of Tanner and Robinson on relatively simple shapes [14,15] provides insight into the computational complexity of these analyses. In order to estimate residual stresses in a finished part, a three-step process is generally required. The first step is the quench from the forging temperature to room temperature. This analysis of thermal cooling involves large, non-linear deformation and elasto-thermo-visco-plastic material behavior. The initial geometric model is based on the as-forged dimensions of the part being analyzed. The second step is the cold compression or cold work step. This is typically an isothermal analysis of the part response to the imposed boundary (surface) displacements or forces expected during the cold work process. Again deformations are large and elasto-plastic material behavior must be accommodated. Finally, the machining step is simulated by removing elements from the model. This is generally an ap-

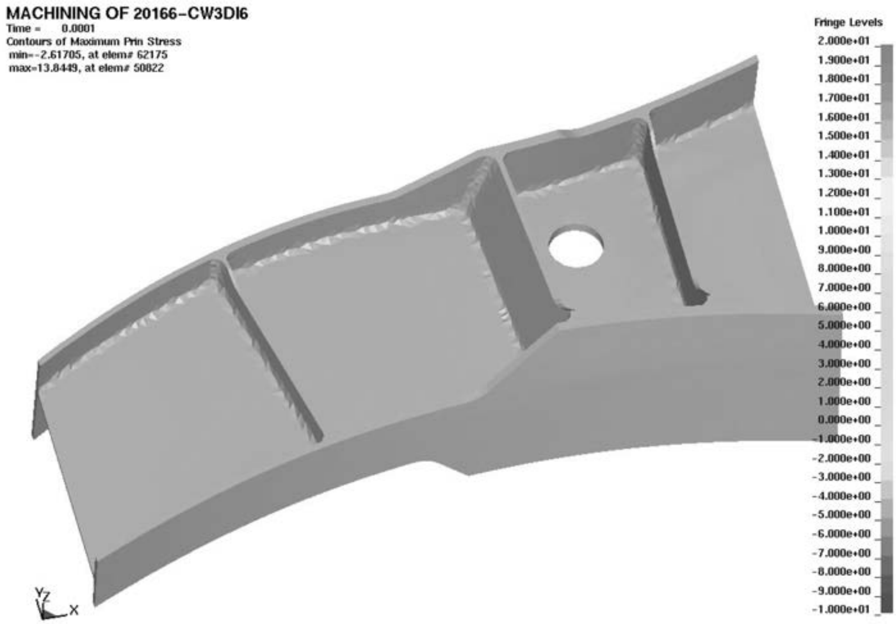

FIG. 7—*FEA calculated max principal stresses in bulkhead segment after quench, cold work and machining* (*Courtesy Alcoa Forgings* [*16*]).

proximation since there is no guarantee that the dimensions (surface positions) of the finished part will correspond exactly with model element boundaries after the quench and cold work steps have been applied.

Preliminary, but very detailed analyses of actual aircraft components (bulkheads) conducted by Alcoa Forgings [16] have indicated that with post-forging cold work, residual stresses can be very low for significant portions (webs, flanges, stiffeners) of the finished parts. Early indications are that after the quench/cold work/machine process, the only significant, detrimental (tensile) residual stresses left are found in highly localized areas like radii and triple points, and that the highest peak stress (max principal) is generally less than 95 MPa (see Fig. 7).

FEA calculated residual stresses depend very heavily on a number of assumptions ranging from heat transfer coefficients (estimated from experimental surface cooling curves) to parameters for the requisite elasto-thermo-visco-plastic constitutive relationships. Clearly, there is still a good measure of "art" involved in these calculations. As a result, FEA results cannot be used without experimental validation.

In the case of large, complex aluminum forgings, experimental determination of residual stresses, particularly in sharp radii and corners, can be challenging. Non-destructive measurement techniques have generally proven to be ineffective. For example, X-ray (XRD) diffraction (XRD) data tend to be confounded by grain size and texturing effects in wrought aluminum alloys; the

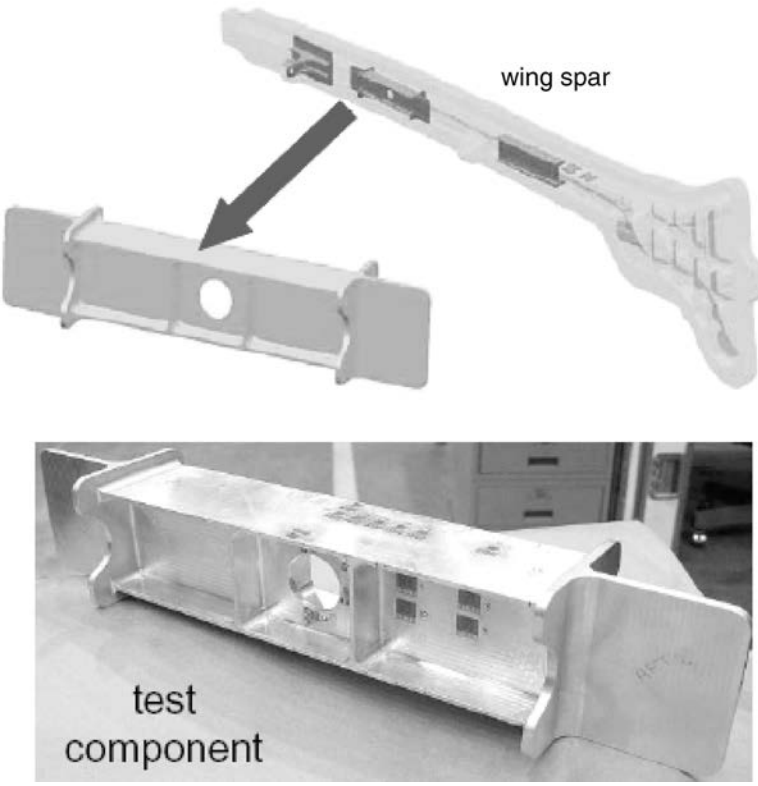

FIG. 8—*Wing spar component subjected to residual stress measurements by hole drilling technique, Alcoa Technical Center* [*18*].

scatter in the data can be larger than the measured residual stresses themselves. XRD also suffers from the inability to resolve high stress gradients in small areas. The indicated stress from a given measurement represents the average over the "footprint" of the X-ray beam.

Most of the experimental data currently available has been taken by destructive means. In support of the current program, the Alcoa Technical Center has conducted extensive testing on components that are representative of new, unitized parts [17] using the hole drilling technique [18]. For example, data were taken at eighteen locations on the wing spar segment shown in Fig. 8. Measurements were made primarily in the webs and spar caps; as with XRD it is not possible to study radii or triple points. In most cases, variation of the stress with hole depth was noted and the average was used. For the component shown, the minimum measured stress was about −40 MPa and the maximum was roughly +60 MPa.

In future work, the ability of advanced techniques such as the contour method [6] will be evaluated for their ability to characterize residual stresses at any location in the part, including tight radii and triple points. The contour method is very attractive because it can provide data both at the surface and within the interior (on a selected plane) of the part being studied.

Third Required Development: Incorporation of Residual Stress in Fatigue Crack Growth Analysis

The traditional LEFM approach for the analysis of fatigue crack growth in the presence of residual stresses [19,20] calls for the calculation of the *initial* residual stress field in the uncracked body and makes the assumption that this stress field remains essentially unchanged during the subsequent fatigue crack growth. With the additional assumption that the bulk material response is elastic, both stresses and stress intensity factors may be superimposed. In particular, the stress intensity factor due to the residual stress field and those due to the applied cyclic stresses may be summed to determine the appropriate total stress intensity factor at each cycle of the analysis. The total SIF is used to calculate fatigue crack growth rate, which in turn is integrated to obtain the crack growth life. With these assumptions, the only additional requirements for the analysis of crack growth are the initial residual stress field and the corresponding residual stress intensity factor versus crack length relationship.

In its basic form, the LEFM approach does not address potential changes in the residual stress distribution due to cyclic plasticity or crack advance. As a result, it is understood that the method provides only a reasonable approximation in situations where the service loading is not too severe (thus avoiding significant alteration of the initial residual stress distribution due to additional plastic deformation) and where crack advance does not significantly relieve the residual stresses. Even with these limitations, the traditional LEFM approach is considered appropriate for design and was adopted for use in the current study.

Stress Intensity Factor Solution Development

Given a residual stress distribution in the uncracked body, which has been defined based on experimental data, by analysis, or both, we require a general stress intensity factor (SIF) solution technique that can accommodate *any* stress distribution. The Green's function method was chosen for use here, in part because it meets the requirement of general applicability but also because Green's functions themselves are readily available for a variety of geometries [21,22]. In this approach, the stress intensity factor at a specified point on the crack front (referred to as the evaluation point) is found as the area integral over the entire crack plane, of the product of the stress distribution acting on that plane and the Green's function for the crack/body geometry being analyzed:

$$K = \int_A \sigma G dA \tag{11}$$

In this context, the Green's function for a given crack/body geometry is the load normalized SIF for a pair of opposing point forces acting on the crack faces for that configuration:

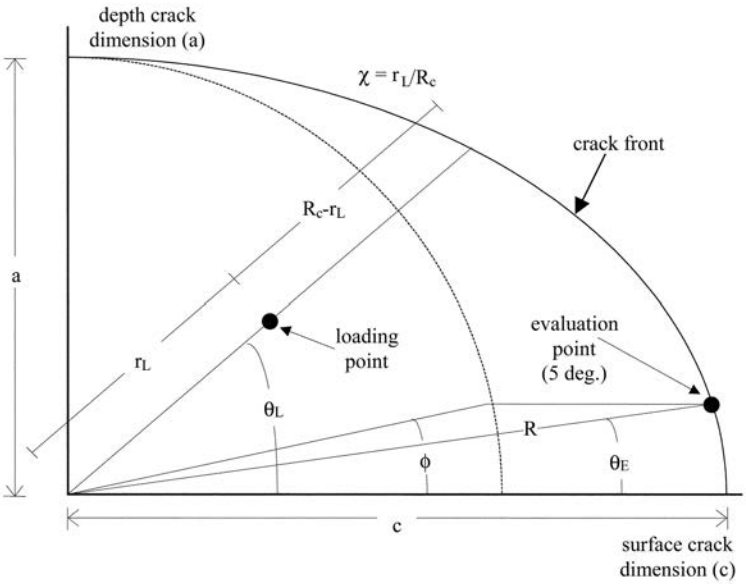

FIG. 9—*Definition of geometric parameters for a semi-elliptical surface crack.*

$$K_{ij} = p_{ij}G \tag{12}$$

The Green's function technique is very powerful because it allows the calculation of SIFs for arbitrary stress distributions, given a known solution for a symmetric point force on the crack face.

The typical configuration for a crack in a radius is that of a semi-elliptical surface crack (see Fig. 9). A Green's function for this configuration was given by the author in [23]:

$$G = \frac{1}{(\pi R_c)^{3/4}}\left[\frac{a_2(1-\xi_i^{a_5})^{a_6}}{1+\xi_i^2-2\xi_i\cos(\Delta\theta_j)}\right] \tag{13}$$

where R_c is the radial distance to the crack front at the angle θ and ξ_i is the normalized radial coordinate: r_i/R_c. The parameters a_2, a_5, and a_6 are transcendental functions of the angular position of the load point; the reader is referred to [23] for details.

The stress distribution in Eq 10 is the normal stress on the critical plane (the plane of the crack). This distribution may be approximated over the crack face using an array of point loads

$$p_{ij} = \sigma(r,\theta)r_i\Delta r_i\Delta\theta_j \tag{14}$$

and the SIF for each point load may be calculated as

$$(K_{\mathrm{I}})_{ij} = p_{ij}G_{ij} \tag{15}$$

The SIF for the total distribution is found by summation

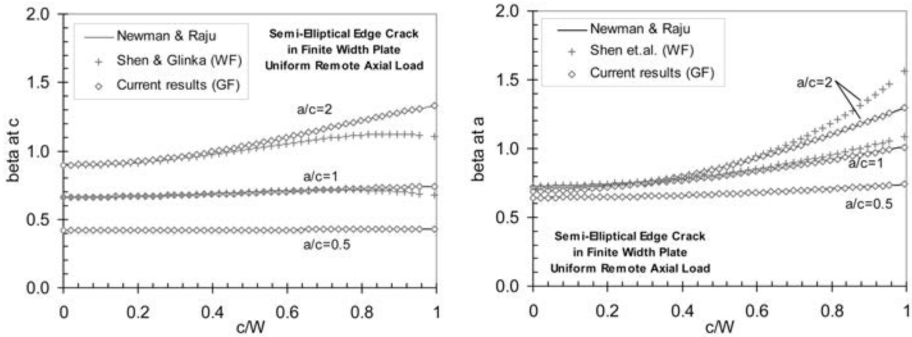

FIG. 10—*Comparison of normalized SIF for a semi-elliptical edge crack in a finite width and thickness plate subjected to uniform remote axial load* [*23*].

$$K_{\mathrm{I}} = \sum_i \sum_j p_{ij} G_{ij} \tag{16}$$

$$K_{\mathrm{I}} = \sum_i \sum_j \sigma(r_i, \theta_j) G_{ij} r_i \Delta r_i \Delta \theta_j \tag{17}$$

which, in the limit, becomes integration

$$K_{\mathrm{I}} = \int_{-\pi/2}^{\pi/2} \int_0^{R_c} \sigma G r \mathrm{d}r \mathrm{d}\theta \tag{18}$$

For fatigue crack growth analysis, it is convenient to write SIF in terms of a reference stress and define a Green's function modifier

$$K_{\mathrm{I}} = S\sqrt{\pi c}\,\beta_{\mathrm{GFC}} \tag{19}$$

$$\beta_{\mathrm{GFC}} = \frac{1}{\sqrt{\pi c}} \int_{-\pi/2}^{\pi/2} \int_0^{R_c} \frac{\sigma}{S} G r \mathrm{d}r \mathrm{d}\theta \tag{20}$$

This expression is evaluated using numerical integration.

The Green's function expressions were evaluated in [23] by calculating SIFs for a configuration for which certain solutions are known. As shown in Fig. 10, the Green's function technique yields accurate results for uniform remote axial loading over the full range of $c/W = 0$ to $c/W = 1$, when compared to those generated using the expressions given in [24]. Also shown in Fig. 10, are normalized SIFs calculated using the weight function technique of Shen and Glinka [25] for the depth (c) direction and Shen, Plumtree and Glinka [26] for the surface (a) direction. In both cases, the current results are in reasonable agreement up to about $c/W = 0.7$. Note that while bi-variant stress distributions can be treated with the current approach, the cited weight function solutions re-

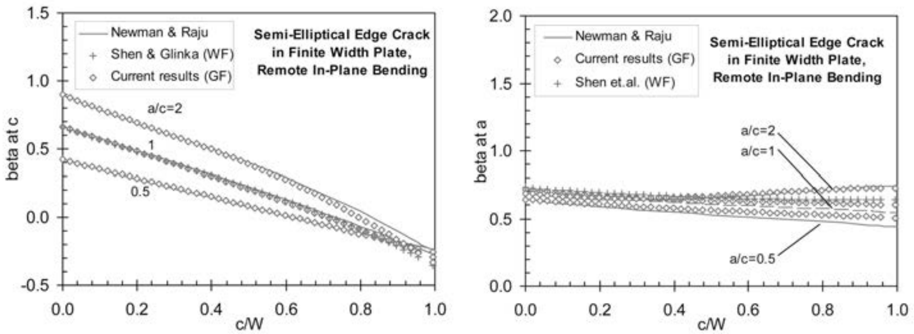

FIG. 11—*Comparison of normalized SIF for a semi-elliptical edge crack in a finite width and thickness plate subjected to remote in-plane bending* [23]*:* (*a*) *depth direction* (phi=0°) *and* (*b*) *surface direction* (phi=85°).

quire uni-variant stress distributions. A similar result is found when comparing the current Green's function and closed form results for in-plane bending (see Fig. 11).

Finally, the stress intensity factors due to applied service loads are superimposed with the residual SIF to find the total or effective SIF:

$$K_{\text{total}} = K_{\text{app}} + K_{\text{residual}} \tag{21}$$

Crack Growth Life Prediction

The remainder of the analysis is carried out in the manner of traditional, LEFM-based fatigue crack growth analysis [27–29]. At each load point in the fatigue history, the total stress intensity factor is determined using the techniques discussed above. Next, load interaction effects are introduced as required. There are numerous empirical models available for this purpose, the one employed in the current study is the Generalized Willenborg model [30]. The effective SIF range for a given load cycle is used to determine the crack growth rate for that cycle; this is typically done using log-log interpolation in a FCGR data table like the one shown in Fig. 4. Once a crack growth rate is determined, the corresponding crack growth increment is known. Starting from a prescribed initial size, the crack size is increased by the calculated crack length/depth increment at each cycle and the process is repeated until instability is reached or until the crack reaches a boundary. The only data over and above that normally required for a traditional fatigue crack growth analysis is the initial residual stress profile.

The algorithm consists of the following primary steps:

(1) calculate the residual SIF,
(2) calculate the total SIF (applied+residual) for cycle i,
(3) check whether calculated SIF exceeds the toughness of the material; if so, stop,
(4) calculate the effective stress intensity factor for cycle i,

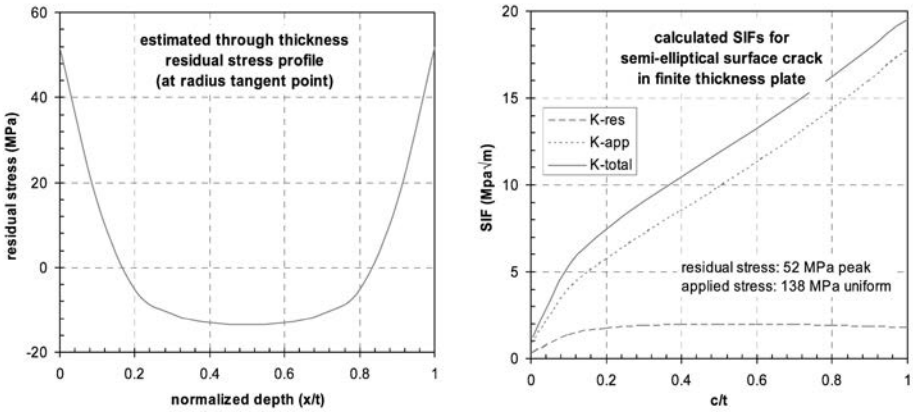

FIG. 12—*Calculated SIFs for a semi-elliptical surface crack in a finite width strip subjected to remote axial load:* (*a*) *residual stress profile* (*through thickness*) *and* (*b*) *calculated SIF* phi = 5°.

(5) calculate crack growth rates and crack growth increments and increment crack size,
(6) check for transition; if crack front of part-through crack has reached a free surface, then re-define the crack geometry as required (e.g., part-through crack to through thickness crack),
(7) check whether maximum crack size has been exceeded; if so, stop,
(8) repeat steps 2 through 7 for the next cycle.

Example SIF and fatigue crack growth calculations were made for a semi-elliptical surface crack in a finite width and thickness section of 7085-T7452 aluminum forging. The plate width and thickness were 127 mm and 12.7 mm, respectively. The initial crack was semi-elliptical with $2c = 0.508$ mm and $a = 0.0254$ mm, and it was centered in the plate. Transition to a through thickness crack occurred when the crack-tip growing in the thickness direction reached the opposite plate surface. A residual stress intensity factor was calculated for the assumed residual stress profile shown in Fig. 12(*a*). The residual SIF, along with the applied SIF for a 10-ksi uniform tensile stress, as well as the sum of the two, is shown in Fig. 12(*b*). Using the crack growth rate parameters from Fig. 4 (which were assumed to be the same in both the crack-length and crack-depth directions), and the wing bending moment (WBM) spectrum whose min-max exceedance curves are shown in Fig. 5, fatigue crack growth lives both with and without the residual stress were calculated. As shown in Fig. 13, introduction of tensile residual stress causes increase in effective SIF and decrease in calculated life.

Design Approach for the Inclusion of Residual Stress Effects

In the existing design approach for forged components, the potential for detrimental residual stresses is incorporated by using conservative (left bound) FCGR data. Depending on control point location and spectrum type, this can

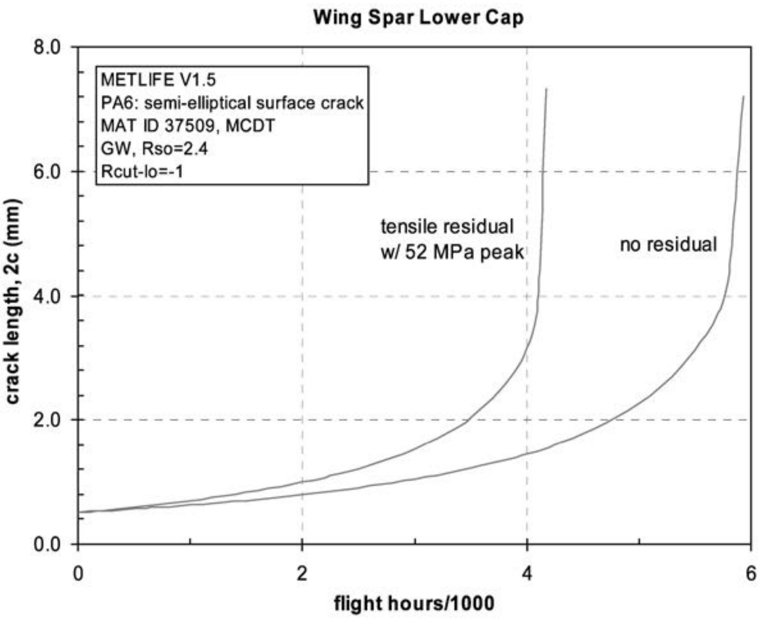

FIG. 13—*Calculated FCG life for a semi-elliptical surface crack in a finite width strip subjected to WBM spectrum loading.*

very conservative for large portions of the finished part that are residual stress free. On the other hand, this approach may produce results that are unconservative (unsafe) for locations with residual stress greater than that implicit in da/dN data. In the first case, the design suffers a weight penalty; in the second, it may fail to meet its durability, damage tolerance requirements, or both.

The more efficient way to utilize product forms or structural concepts that have built-in residual stresses is to explicitly address those residual stresses in the design process. In the proposed design approach, standard residual stress "zones" are identified for machined parts. (There is a precedent for the zoning concept since fracture critical parts are currently zoned for different ND inspection types and levels.) In this process we envision a small of number of standard zones for different details, ranging from large zones with zero residual stress for major portions of webs and flanges, to small zones with significant tensile residual stress for fillets, radii, and triple points. (No zones are defined with, and no benefit is taken for beneficial compressive residual stresses.) Each zone has a standard peak stress and profile. Design fatigue crack growth analyses for control points within each zone are based on intrinsic (residual stress-free) FCGR data and explicitly include the residual stress field specified for that zone. Note that the residual stress is treated as a pre-load stress, meaning that it is not scaled with the spectrum during the process of determining design allowable stress. A schematic of the design process is shown in Fig. 14.

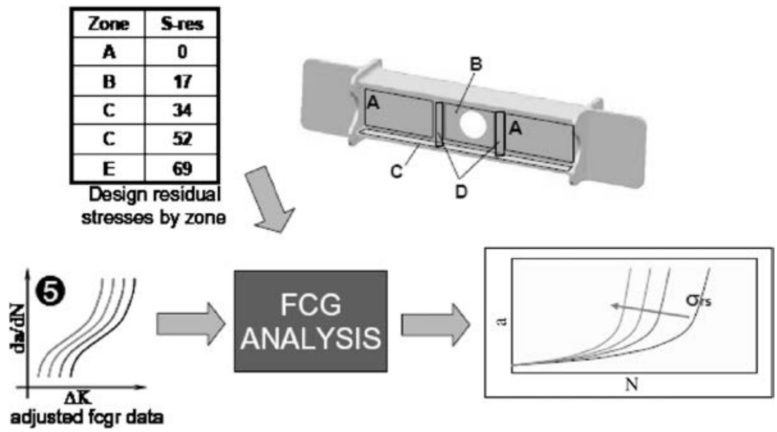

FIG. 14—*Proposed design approach for incorporation of standard residual stress profiles in design fatigue crack growth analysis.*

Shown in Fig. 15 is an example set of profiles and corresponding residual SIF curves for web and flange locations that would support the analysis. In this simplified example, the residual stress in each zone varies in the through-thickness direction (z-direction) only. The residual SIFs associated with each zone may be calculated for several different crack configurations (1D versus 2D) and at multiple points along the crack front for 2D configurations. The results shown in Fig. 15(*b*) are for the point near the surface penetrating crack tip (phi = 5°, see Fig. 9). The approach would apply in a similar way for the individual residual stress fields and SIFs associated with triple points, radii, and fillets.

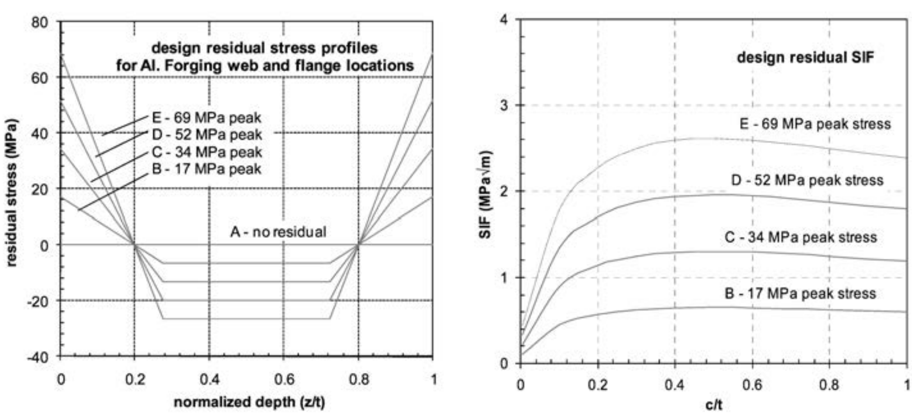

FIG. 15—*Example standard residual stress profiles and calculated residual SIFs for a semi-elliptical surface crack:* (*a*) *standard residual stress profiles - through thickness and* (*b*) *calculated residual SIFs,* phi = 5°.

Example Application—Forged Wing Spar

The potential impact that the proposed design approach might have was evaluated by conducting a very comprehensive parametric analysis of a forged wing spar. This analysis was conducted using the highly automated fatigue design tool described in [31]. After the capability for residual SIF calculation was installed, 970 generic control points were defined, one for almost every element in the coarse grid finite element model of the part. The control points were "generic" in the sense that they all assumed the growth of a semi-elliptical flaw. However, each was unique in that it was based on the fatigue spectrum for the FE element with which it was associated. In all 970 cases, three level-2 analyses were performed. (A level-2 analysis is one in which the fatigue crack growth analysis is run several times with a range of spectrum scale factors; it is used to determine the design allowable stress (DAS) at a control point (CP).)

For the baseline analysis, the DAS at all CPs was determined using conservative (left bound) FCGR data. For the intermediate analysis, all of the control point analyses were run using the intrinsic residual stress free FCGR data. In the third and final step, each of the control point analyses was conducted using the intrinsic FCGR data and the standard residual stress specified for the CP location. (The estimated standard profiles shown in Fig. 15 were used; approximately 90 % of the CPs were assumed to be zone A—zero residual stress.) As expected, the DAS at each control point for the intermediate step increased when compared to the baseline DAS for the same CP (the result of using less conservative da/dN data). However, the CP DAS from the final analysis was in some cases lower than the baseline, and in some cases higher than the baseline, depending on the severity of the residual stress. The results are summarized in Figs. 16 and 17. As shown in Fig. 16, the ratio of DAS_{final} to DAS_{bl} shows an increase for the majority of the control points; 930 out of 970 (96 %) have $DAS_{final}/DAS_{bl} > 1$. The change in the allowable stress can be used estimate the relative change in required local thickness. The control points in Fig. 17 that show a potential decrease in required thickness correspond to the ones in Fig. 16 with $DAS_{final}/DAS_{bl} > 1$. These points indicate regions where potential weight savings exist. Note that this is only a potential since other requirements such as minimum gage or compression stability may override. Of equal importance in Fig. 17 is the small number of control points with an increase in required thickness indicated. This means that at these control points, the conservatism built in to the baseline da/dN is not sufficient to account for tensile residual stresses. The DAS_{final}/DAS_{bl} results are fringe plotted on the wing spar coarse grid FEM in Fig. 18.

Conclusions and Recommendations

- The adjusted compliance ratio (ACR) method was successfully used to determine intrinsic fatigue crack growth rate (FCGR) data for aluminum forgings.
- A method for the construction of design FCGR curves based on K_{max} sensitivity and plasticity induced crack closure has been developed—it will require further validation by test.
- Initial studies of residual stresses in aluminum forgings have been com-

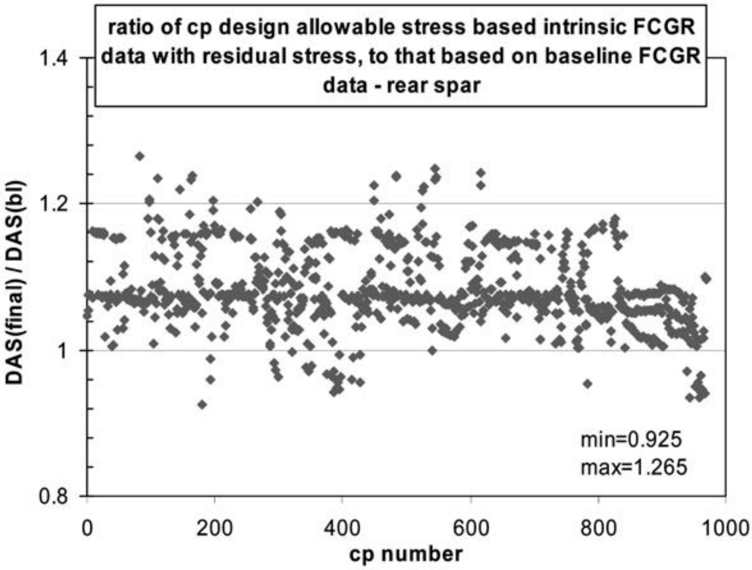

FIG. 16—*Ratio of final design allowable stress to baseline design allowable stress for wing spar.*

pleted; significant, further characterization, both by analysis and by test is required.

- A method for the incorporation of residual stresses in design FCGA has been developed and implemented in design software.
- Parametric studies based on fatigue crack growth analysis indicate that large forgings for aircraft can be optimized using this process (these studies only addressed damage tolerance design requirements).
- The proposed design approach allows selective inclusion of residual stresses—include only where necessary (weight avoidance).
- While the focus of this study has been on built-in residual stresses that occur during material fabrication processes, the approach has equal applicability to structural manufacturing processes such as shot peening, hole cold working, friction stir welding, and low plasticity burnishing, to name a few.

Acknowledgments

This activity was funded under the Lockheed Martin Aeronautics Co. Internal Research and Development Program: "Analysis of Unitized Structures." Special acknowledgment is given to Dr. Robert J. Bucci and Dr. Mark A. James of the Alcoa Technical Center for their significant contributions and assistance, and to J. Keith Donald of Fracture Technology Associates, without whom the characterization of intrinsic material data would not have been possible.

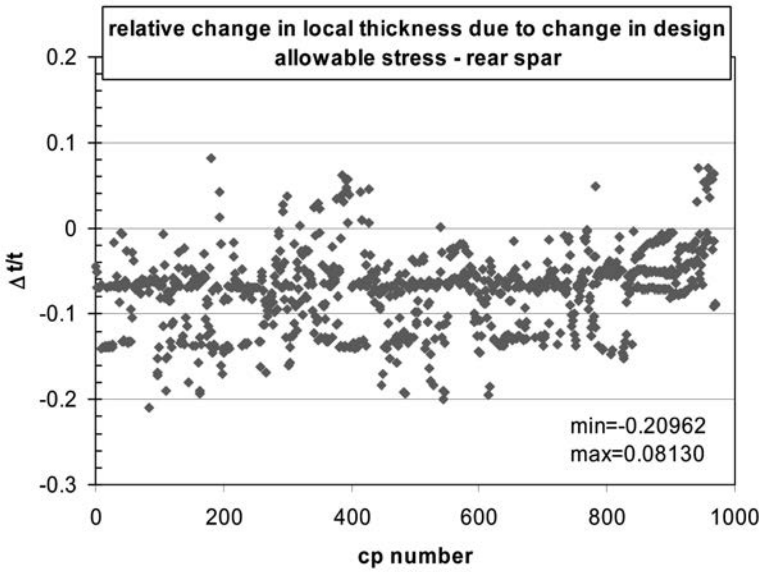

FIG. 17—*Relative change in local required thickness due to change in design allowable stress for wing spar.*

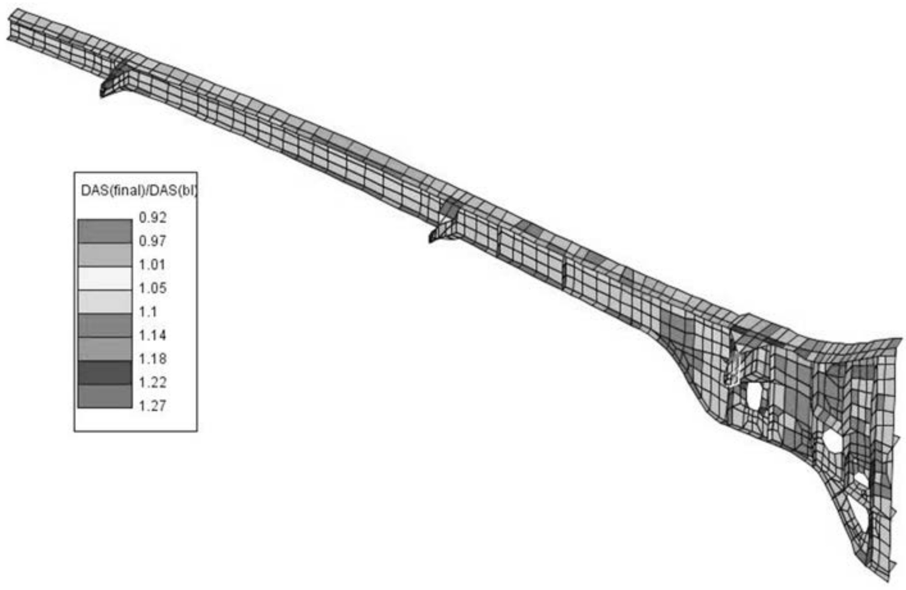

FIG. 18—*Ratio of final design allowable stress to baseline design allowable stress for wing spar.*

References

[1] Mueller, L., Suffredini, L., Bush, D., Sawtell, R., and Brouwer, P., "Alcoa 7085 Forgings, 7th Generation Structural Solutions, 2e," Alcoa Green Letter, Jan. 2005.

[2] Bucci, R. J., "Effect of Residual Stress on Fatigue Crack Growth Rate Measurement," *ASTM STP 743*, ASTM International, West Conshohocken, PA, 1981, pp 28–47.

[3] Bush, R. W., Bucci, R. J., Magnusen, P. E., and Kuhlman, G. W., "Fatigue Crack Growth Rate Measurements in Aluminum Alloy Forgings: Effects of Residual Stress and Grain Flow," *Fracture Mechanics: Twenty Third Symposium*, ASTM STP 1189, R. Chona, Ed., ASTM International, West Conshohocken, PA, 1993, pp 568–589.

[4] Bucci, R. J., James, M. A., Sklyut, H., Heinimann, M. B., Ball, D. L., and Donald, J. K., "Advances in Testing and Analytical Simulation Methodologies to Support Design and Structural Integrity Assessment of Large Monolithic Parts," SAE International, Toulouse, France, 2006.

[5] Donald, J. K., "Introducing the Compliance Ratio Concept for Determining Effective Stress Intensity," *Int. J. Fatigue*, Vol. 19, 1997, pp. 191–195.

[6] Prime, M. B., *J. Eng. Mater. Technol.*, Vol. 123, 2001, pp. 162–168.

[7] Prime, M. B., Newborn, M. A., and Balog, J. A., "Quenching and Cold-Work Residual Stresses in Aluminum Hand Forgings: Contour Method Measurement and FEM Prediction," *Mater. Sci. Forum*, Vols. 426–432, 2003, pp. 435–440.

[8] Glinka, G., "Effect of Residual Stresses on Fatigue Crack Growth in Steel Weldments Under Constant and Variable Amplitude Loads," *Fracture Mechanics*, ASTM STP 677, C. W. Smith, Ed., American Society for Testing and Materials, West Conshohocken, PA, 1979, pp. 198–214.

[9] McClung, R. C., Gardner, B. M., Lee, Y., Pillers, J. E., and Bunch, J. O., "Fatigue Crack Growth Analysis in Complex Residual Stress Fields," AeroMat, Seattle WA, 2006.

[10] Donald, J. K., Bray, G. H., and Bush, R. W., "An Evaluation of the Adjusted Compliance Ratio Technique for Determining the Effective Stress Intensity Factor," *29th National Symposium on Fatigue and Fracture Mechanics*, ASTM STP 1332, T. L. Panontin and S. D. Sheppard, Eds., American Society for Testing and Materials, West Conshohocken, PA, 1998.

[11] Donald, J. K. and Phillips, E. P., "Analysis of the Second ASTM Round Robin Program on Opening-Load Measurement Using the Adjusted Compliance Ratio Technique," *Advances in Fatigue Crack Closure Measurement and Analysis: Second Volume*, ASTM STP 1343, R. C. McClung, J. C. Newman, Jr., Eds., ASTM International, West Conshohocken, PA, 1998.

[12] Bray, G. H. and Donald, J. K., "Separating the Influence of Kmax from Closure-Related Stress Ratio Effects Using the Adjusted Compliance Ratio Technique," *Advances in Fatigue Crack Closure Measurement and Analysis: Second Volume*, ASTM STP 1343, R. C. McClung, J. C. Newman, Jr., Eds., ASTM International, West Conshohocken, PA, 1998.

[13] Newman, J. C., Jr., "A Crack Opening Stress Equation for Fatigue Crack Growth," *Int. J. Fract.*, Vol. 24, 1984, pp. R131–R135.

[14] Tanner, D. A. and Robinson, J. S., "Residual Stress Prediction and Determination in 7010 Aluminum Alloy Forgings," *Exp. Mech.*, Vol. 40, No. 1, 2000, pp. 75–82.

[15] Tanner, D. A. and Robinson, J. S., "Modeling Stress Reduction Techniques of Cold Compression and Stretching in Wrought Aluminum Alloy Products," *Finite Elem. Anal. Design*, Vol. 39, No. 5–6, 2003, pp. 369–386.

[16] Alcoa Forgings, "Bulkhead Residual Stress Analysis," unpublished data, Jan. 2005.
[17] Alcoa Technical Center, "Measurement of Residual Stress in a 7085-T7452 Forging and Test Component," unpublished data, Feb. 2007.
[18] ASTM, Standard E 837-01, "Standard Test Method for Determining Residual Stresses by the Hole-Drilling Strain-Gage Method," *Annual Book of ASTM Standards*, ASTM International, West Conshohocken, PA.
[19] Parker, A. P., "Stress Intensity Factors, Crack Profiles, and Fatigue Crack Growth Rates in Residual Stress Fields," *Residual Stress Effects in Fatigue*, ASTM STP 776, ASTM International, West Conshohocken, PA, 1982, pp. 13–31.
[20] Nelson, D. V., "Effects of Residual Stress on Fatigue Crack Propagation," *Residual Stress Effects in Fatigue*, ASTM STP 776, ASTM International, West Conshohocken, PA, 1982, pp. 172–194.
[21] Tada, H., Paris, P. C., and Irwin, G. R., *The Stress Analysis of Cracks Handbook*, 2nd ed., Del Research Corp., Hellertown, PA, 1985.
[22] Wu, X.-R. and Carlsson, A. J., *Weight Functions and Stress Intensity Factor Solutions*, Pergamon Press, Oxford, 1991.
[23] Ball, D. L., "A Model for the Inclusion of Notch Plasticity Effects in Fatigue Crack Growth Analysis," *Fatigue Testing and Analysis Under Variable Amplitude Loading Conditions*, ASTM STP 1439, ASTM International, West Conshohocken, PA, 2004, pp. 251–277.
[24] Newman, J. C. Jr. and Raju, I. S., "Stress Intensity Factor Equations for Cracks in Three-Dimensional Finite Bodies Subjected to Tension and Bending Loads," NASA-TM-85793, April, 1984.
[25] Shen, G. and Glinka, G., "Weight Functions for a Surface Semi-Elliptical Crack in a Finite Thickness Plate," *Theor. Appl. Fract. Mech.*, Vol. 15, 1991, pp. 247–255.
[26] Shen, G., Plumtree, A., and Glinka, G., "Weight Function for the Surface Point of a Semi-Elliptical Surface Crack in a Finite Thickness Plate," *Eng. Fract. Mech.*, Vol. 40, No. 1, 1991, pp. 167–176.
[27] Gallagher, J. P., Giessler, F. J., Berens, A. P., and Engle, R.. M. Jr., "USAF Damage Tolerant Design Handbook," AFWAL-TR-82-3073, Air Force Wright Aeronautical Labs, Wright-Patterson AFB, OH, May 1984.
[28] Chang, J. B., Hiyama, R. M., and Szamossi, M., "Improved Methods For Predicting Spectrum Loading Effects," AFWAL-TR-81-3092, November 1981.
[29] Chang, J. B., and Engle, R. M., "Improved Damage-Tolerance Analysis Methodology," *J. Aircraft*, Vol. 21, No. 9, 1984, pp. 722–730.
[30] Gallagher, J. P., and Hughes, T. F., "Influence of Yield Strength on Overload Affected Fatigue Crack Growth Behavior in 4340 Steel," AFFDL-TR-74-27, Air Force Flight Dynamics Laboratory, July 1974.
[31] Limer, T. S., Ishee, D. M., Hamilton, J. H., Black, H. W., and Ball, D. L., "An Advanced Software System for the Comprehensive Implementation of Durability and Damage Tolerance Requirements in the Design of New Aircraft Structure," *9th International Fatigue Congress*, Atlanta, GA. USA, May 14–19 2006.

ASTM Special Technical Publication, Vol. 5, No. 8
Paper ID JAI101617
Available online at www.astm.org

Y. Yamada,[1] *J. C. Newman III,*[1] *and J. C. Newman, Jr.*[1]

Elastic-Plastic Finite-Element Analyses of Compression Precracking and Its Influence on Subsequent Fatigue-Crack Growth

ABSTRACT: Compression precracking has been used in a renewed effort to generate fatigue-crack growth rates in the threshold and near-threshold regimes, as an alternative to the traditional load-reduction procedure. But concerns have been expressed on the influence of tensile residual stresses resulting from compressive yielding at the crack-starter notch. This paper uses elastic-plastic, finite-element analyses to study the influence of the tensile residual stresses induced by compression precracking on simulated crack growth under constant-amplitude loading. High-fidelity finite-element models (60 000 to 160 000 DOF) using two-dimensional plane-stress analyses were used to model plastic yielding during compressive loading and simulated fatigue-crack growth through the tensile residual-stress field. The finite-element code was ZIP2D and the course mesh had an element size of 2 μm. A refined mesh had an element size four times smaller (0.5 μm) than the course mesh. Fatigue-crack growth and crack-closure effects were simulated over a wide range in stress ratios (R=0 to 0.8) and load levels, after compression precracking. The crack-tip-opening displacement (CTOD) concept was used to judge the extent of the influence on the tensile residual stresses and the stabilization of the crack-opening loads. It was found that the tensile residual stress field decayed as the crack grew under cyclic loading. Once the crack had reached one compressive plastic-zone size, the tensile residual-stress field had dissipated. However, the stabilization of the

Manuscript received December 5, 2007; accepted for publication July 7, 2008; published online August 2008.
[1] Department of Aerospace Engineering, Mississippi State University, Mississippi State, MS 39762, e-mail: j.c.newman.jr@ae.msstate.edu

Citation: Yamada, Y., Newman III, J. C., and Newman, Jr., J. C., "Elastic-Plastic Finite Element Analyses of Compression Precracking and its Influence on Subsequent Fatigue-Crack Growth," *J. ASTM Intl.*, Vol. 5, No. 8. DOI10.1520/JAI101617. Available online at www.astm.org. Also included in JAI Special Issue STP 1508, *Fatigue and Fracture Mechanics: 36th Volume,* R. W. Neu, K. R. W. Wallin, and S. R. Thompson, guest editors, ASTM International, West Conshohocken, PA, 2009, pp. 240-256.

crack-opening loads and merging of the CTOD values with and without compression precracking was found to be about 1.5 to 2 times the compressive plastic-zone size at $R=0$ loading. The effects dissipated at smaller distances from the notch tip for the higher stress ratios. The present results have validated the crack-extension criterion that had been proposed for use in the compressive precracking threshold test method, beyond which, cracks are growing under constant-amplitude (steady-state) behavior.

KEYWORDS: fatigue-crack growth, compression, residual stresses, load-history effect, crack closure, crack-tip-opening displacement, plasticity

Nomenclature

B = Specimen thickness, mm
c = Crack length, mm
c_n = Notch length, mm
CA = Constant-amplitude loading
CP = Compression precracking
CPCA = Compression precracking followed by constant-amplitude loading
$\mathrm{CTOD_{ca}}$ = Crack-tip-opening displacement for constant-amplitude loading, mm
$\mathrm{CTOD_{cp}}$ = Crack-tip-opening displacement for compression precracked specimens, mm
E = Modulus of elasticity, GPa
K_{cp} = Compressive stress-intensity factor, MPa-m$^{1/2}$
K_{max} = Maximum stress-intensity factor, MPa-m$^{1/2}$
K_{min} = Minimum stress-intensity factor, MPa-m$^{1/2}$
l_e = Minimum element length along crack path, mm
P = Applied load, kN
P_{max} = Maximum applied load, kN
P_{min} = Minimum applied load, kN
P_o = Crack-opening load, kN
r_{cp} = Irwin's plastic-zone size, mm
r_n = Notch-root radius, mm
R = Load ratio ($P_{\mathrm{min}}/P_{\mathrm{max}}$)
W = Specimen width, mm
γ = Coefficient in crack-extension criterion
Δc = Crack-growth increment, mm
ΔK = Stress-intensity factor range, MPa-m$^{1/2}$
ΔP = Load range ($P_{\mathrm{max}}-P_{\mathrm{min}}$), kN
ν = Poisson's ratio
$\rho_{\mathrm{cp\_fea}}$ = Plastic-zone size calculated from finite-element analysis (FEA), mm

σ_o = Flow stress, MPa
σ_{res} = Residual stress, MPa

Introduction

In the early 1970s, a load-reduction test method was developed by Paris et al. [1] to generate fatigue-crack-growth rate data at low stress-intensity factor ranges approaching threshold conditions. Later, Hudak et al. [2] and Bucci [3] finalized the method, which was incorporated into the ASTM E647 fatigue-crack-growth rate testing standard [4]. During the same time, Ohta et al. [5] and Minakawa and McEvily [6] showed a rise in the crack-closure levels as the threshold conditions were approached using load-reduction methods. This rise could have been caused by a variety of crack-tip-shielding mechanisms. The load-reduction test methods had also been shown to exhibit anomalies due to load-history effects from residual-plastic deformations [7,8]. The current load-reduction test method may produce data, which exhibit "fanning" in the threshold regime with stress ratio. (Fanning is a term used to describe more spread in the ΔK-rate data with stress ratio in the threshold regime than in the mid-rate regime.) It is suspected that the load-reduction test method induces remote closure, which prematurely slows down crack growth, and produces abnormally high thresholds for low stress-ratio conditions. The fanning could also be caused by environment, which naturally produces oxide and fretting-debris, or both, and higher closure levels [9,10]. It has also been suspected that crack-surface roughness is more prevalent in the threshold regime, which could also cause higher closure levels at low stress-ratio conditions [10,11] and produce fanning with the stress ratio.

Compression precracking methods [12–15] has been used in a renewed effort to generate fatigue-crack-growth rates in the threshold and near-threshold regimes, as an alternative to the traditional load-reduction procedure [4]. Forth et al. [16], Newman et al. [17], and Ruschau and Newman [18] have shown significant differences between the compression precracking and load-reduction methods on near-threshold crack-growth rate behavior for a variety of materials. However, for compression precracking, concerns have also been expressed on the influence of the tensile residual stresses and the highly deformed crack surfaces resulting from compressive yielding and crack growth at the crack-starter notch.

It is the scope of this paper to use elastic-plastic, finite-element analyses to study the influence of the tensile residual stresses due to compressive yielding at a V-notch in compact specimens made of a high-strength aluminum alloy on the crack-tip-opening displacements (CTOD) and on the stabilization of crack-opening loads under constant-amplitude loading. High-fidelity finite-element models (60 000 to 160 000 DOF) using two-dimensional analyses under plane-stress conditions were used to simulate plastic yielding at a crack-starter notch during compressive loading and simulated fatigue-crack growth through the tensile residual-stress field. The finite-element code was ZIP2D [19], which had been developed at NASA Langley, and enhanced at Mississippi State University.

The course mesh had an element size of 2 μm and the refined mesh element size was four times smaller (0.5 μm), which were the simulated crack-growth increments per cycle in the respective models.

Fatigue-crack growth and crack-closure effects were simulated using highly refined finite-element models over a range in load levels ($\Delta P = 2.2$, 4.4, and 6.6 kN) and stress ratios ($R = 0$ to 0.8), after compression precracking. The crack-tip-opening displacement (CTOD) concept was used to judge the extent of the influence of the tensile residual stresses and the stabilization of the crack-opening loads by comparing CTOD with and without compression precracking. When the CTOD values with and without compression precracking agreed within 1 %, then the influence of the residual stresses had dissipated and the crack-opening stresses had stabilized at their constant-amplitude value. The present results were used to validate a crack-extension criterion, beyond which the crack-starter notch and the tensile residual stress field would have little or no influence on crack-growth rates and the crack-closure behavior would have stabilized under constant-amplitude loading. These results are compared with those obtained by James et al. [20], which used compressive-yielding induced residual stresses and a linear-superposition method to show the impact of the residual-stress field on stress-intensity factors.

Finite Element Analysis Procedure

Elastic-plastic finite-element analyses (FEA) of an elastic-perfectly-plastic material were conducted to study the influence of the tensile residual-stress field induced by compressive precracking (CP) on subsequent fatigue-crack growth during constant-amplitude loading. Two-dimensional (2-D) finite-element models of the compact, C(T), specimens were built using PATRAN-2005 [21] with constant-strain triangular (CST) elements. The finite-element neutral files were exported to create a mesh file for ZIP2D [19] to perform fatigue-crack-growth simulations under constant-amplitude loading. Plane-stress conditions were chosen because the extent of yielding and the influence of the tensile residual-stress field would extend over a larger region than under higher constraint conditions, such as plane strain. Any crack-extension criterion developed to establish "steady state" constant-amplitude crack-growth rate behavior under plane-stress conditions would be conservative, if applied to higher constraint conditions. To understand the influence from CP loading, residual stresses (σ_{res}), crack-opening loads (P_o) and crack-tip-opening displacements (CTOD) were calculated. The finite-element C(T) models had a width $W = 76$ mm, notch height $N = W/32$, notch length $c_n = 0.25W$, and a 45° V-notch with a notch root radius of 0.127 mm. (For ZIP2D, the plate thickness was 7.6 mm.) Typical high-strength aluminum alloy properties, such as those for 7075-T6, were used (modulus of elasticity $E = 70$ GPa; Poisson's ratio $\nu = 0.3$; and flow stress $\sigma_o = 520$ MPa). The material had an elastic-perfectly-plastic stress-strain behavior and neither kinematic nor isotropic hardening was modeled. Moreover, the purpose of this study was to conduct an elastic-plastic treatment of simulated fatigue-crack growth, after compressive yielding, rather than to use linear superposition, which is typically used to account for residual-stress fields. In

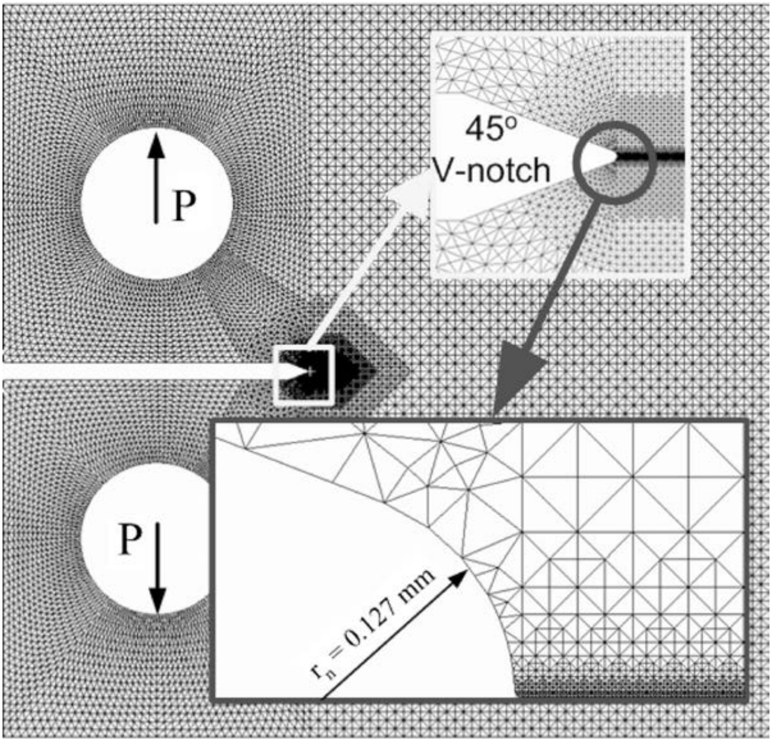

FIG. 1—*Typical finite-element model of compact specimen* (*Mesh 1*).

order to study the convergence of the various crack-tip parameters, two FEA models were developed. Mesh 1 had about 30 k nodes and 60 k elements (~60 k degrees-of-freedom, DOF), whereas Mesh 2 had about 80 k nodes and 150 k elements (~160 k DOF). The minimum element size (l_e) along the crack path was 2 and 0.5 μm for Mesh 1 and 2, respectively. A typical mesh is shown in Fig. 1. In this study, tensile and compressive loads were applied at one single node at the top of the hole instead of simulating a pin-contacting load. Elements near the loaded node were set to elastic conditions, so that the applied loads were redistributed by elastic elements as if the pin-contacting load was modeled and to avoid local yielding at the concentrated load. In actual testing, it is impossible to apply a compressive load at the top of the hole, but it was shown that this loading configuration produced essentially the same stress-intensity factor (SIF) level as block loading applied at the top and bottom edge of C(T) specimen [17]. A minimum compressive precracking (CP) load, −9 kN, which produced a compressive stress-intensity factor of about −22 MPa-m$^{1/2}$ (assuming that the notch was a crack), was used in all cases (maximum load was zero). Three constant amplitude (CA) load ranges ($\Delta P = 2.2$, 4.4, and 6.6 kN) were used over a wide range in load ratios from $R = 0$ to 0.8. These load ranges corresponded to initial stress-intensity factor ranges (ΔK_i) of 5.5, 11, and 16.5 MPa-m$^{1/2}$, respectively. Mesh 1 and 2 experienced more than 5 k and

15 k elements yielding during CP loading, and for the lowest load range about 8 to 12 and 60 to 140 elements yielded at the minimum load, respectively. For the lowest load range and any load ratio, a sufficient number of elements must yield in compression in the crack-tip region to establish the correct crack-closure behavior [19,22,23]. The lowest load range was selected to allow a few elements to yield in compression during crack-growth simulations for Mesh 1. The middle and highest load ranges would cause 4 to 10 times more elements yielding at the crack tip than the lowest load range. (Mesh 2 would also allow about a factor-of-4 more elements to yield in compression than Mesh 1.) Fatigue-crack growth was simulated in ZIP2D by using a very efficient nodal release algorithm at maximum load for each cycle, crack-surface contact or separation due to crack closure or opening were accounted for by using very stiff springs placed along the crack path [19]. Thus, crack-growth rates were constant and were equal to the minimum element length per cycle. For Mesh 1 and 2, the highest and middle load ranges, respectively, corresponded fairly close to the actual fatigue-crack growth rates for a high-strength aluminum alloy. The crack-opening load was monitored at the first node behind the crack-tip node; and the CTOD was monitored at the first and second nodes behind the crack-tip node.

Finite-Element Analysis Results

Convergence Study

Convergence studies were performed using Mesh 1 and 2. First, the residual stresses σ_{res} were calculated at the unloaded condition after −9 kN of compressive load ($K_{cp} = -22$ MPa-m$^{1/2}$) was applied. Figure 2 shows the comparison between Mesh 1 (solid curve) and 2 (dotted curve), and σ_{res} was normalized by the flow stress. Both meshes produced the same residual-stress distribution along the centerline of the specimen, and the compressive plastic-zone size was about 0.5 mm. (For clarity, the figure only shows the upper half of the plastic-zone region.) As a reference, the residual-stress distribution at zero load after a tensile load of $P_{max} = 2.2$ kN (solid curve) is also shown in Fig. 2. Because of the notch-root radius, the low tensile load caused a very small amount of yielding at the notch tip. However, the large compressive load created a tensile residual stress over one-half of the plastic zone and a balancing compressive stress over the remainder of the specimen. There were two sharp kinks in the σ_{res} plot; the first kink was caused by reverse yielding in tension, and the second kink in compressive stress was at the interface of the plastic zone, ρ_{cp_fea}. As shown, the residual-stress field calculated from Mesh 1 and 2 agreed very well, which verified that Mesh 1 was fine enough to calculate the residual-stress field accurately.

Second, fatigue-crack growth simulations were performed with ZIP2D for both CA loading and compression precracking followed by constant amplitude (CPCA) loading using Mesh 1 and 2. The CA loading was $P_{max} = 2.2$ kN at $R = 0$. The crack-opening load P_o normalized by P_{max} is shown in Fig. 3 as a function of normalized crack extension. P_o values under CA loading rapidly rose and stabilized at about 0.58 of P_{max} for both Mesh 1 and 2 (solid and

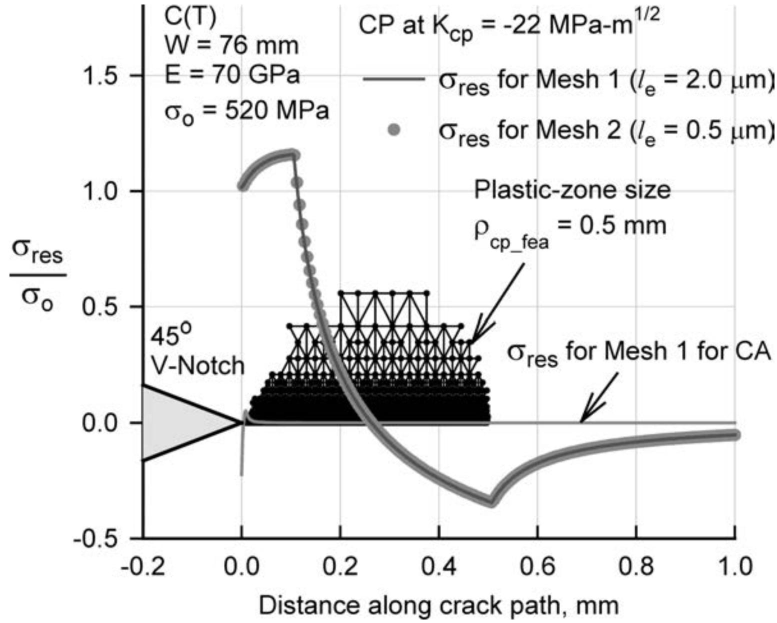

FIG. 2—*Compressive plastic-zone region and comparison of residual-stress distributions from Mesh 1 and 2.*

dashed curves, respectively). These results demonstrate that Mesh 1 had sufficient refinement to model the crack-closure behavior for the low applied load range. For the CPCA loading case, 50 cycles of compression ($P_{max}=0$; $P_{min}=-9$ kN) were applied, which grew the crack about 20 % of the compressive plastic-zone size for Mesh 1. For CP loading, the crack-opening load was negative (not shown) and the crack was grown at the maximum load ($P_{max}=0$) for each cycle. After CP loading, the same CA loading was then applied. In contrast to the CA case, the P_o values for CPCA loading took about one plastic-zone size to stabilize. Results from Mesh 1 showed a smooth curve, but the results from Mesh 2 showed many discontinuities. The reason(s) for these discontinuities were unknown but were not related to the nonuniform element refinement above the crack path. (Further study is required to resolve these problems in the analyses with the finer mesh.) However, the results from Mesh 1 and 2 merged after about 1.5 plastic-zone sizes and, again, demonstrated that Mesh 1 had adequate refinement.

Finally, the CTOD values were calculated for both CA and CPCA loading for Mesh 1 and 2, and the results are compared in Fig. 4. During the crack-growth simulations, the CTOD values at the second node behind the crack tip at the maximum applied load were collected. Mesh 2 was four times finer than Mesh 1, so the distances from the crack tip to the second node were different. (Here only the CTOD ratios for CA and CPCA loading are compared at the same node from the crack tip.) In order to perform convergence studies on CTOD, the CPCA results were normalized by the CA results, so that the crack-extension

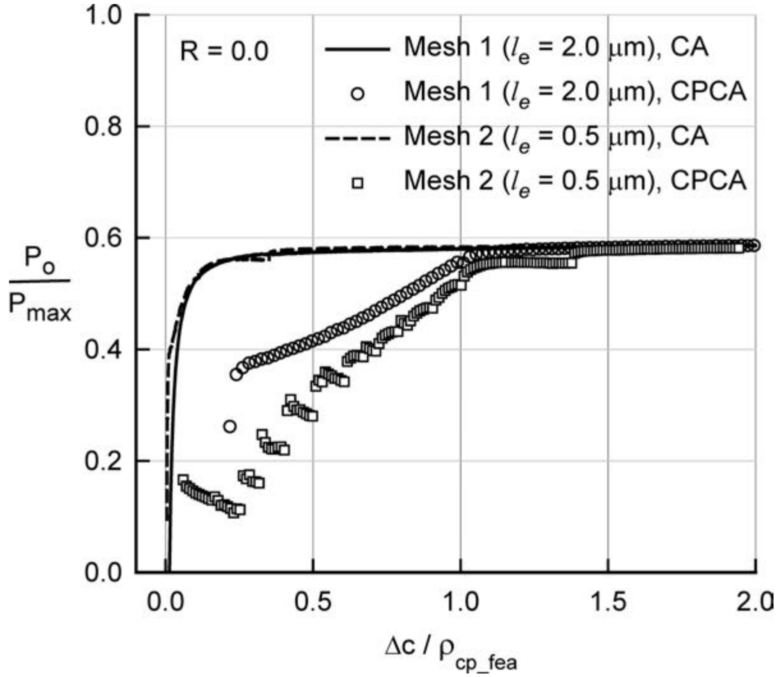

FIG. 3—*Comparison of normalized crack-opening loads from Mesh 1 and 2.*

distance where the CPCA results would merge with the CA results could be easily located. Because of the tensile residual-stress field created by CP loading, the cracks were fully opened at the beginning of the CA loadings. As the crack grew, the influence of CP loading was fading out and the normalized CTOD values were approaching unity. Similar trends were found in the results from Mesh 2, except the CTOD trace showed the same discontinuities. Differences between the results from Mesh 1 and 2 may be due to the number of reverse yielded elements around the crack tip. For this applied cyclic load range, Mesh 1 experienced reverse yielding in about 8 elements, while Mesh 2 had 60 elements. Thus, Mesh 2 may be more precise than Mesh 1, but both results merged to unity at about 1.5 to 2 plastic-zone sizes. Therefore, it was considered that Mesh 1 had sufficient mesh refinement to investigate the influence from CP loading on fatigue-crack growth. In the following sections, all of the parametric studies on different load levels and various load ratios were performed using only Mesh 1 to investigate the influence of CP loading on subsequent crack growth.

Residual Stress Field

In practice, it is common to consider that residual-stress distributions are maintained during fatigue-crack growth and that they do not decay. Hence, linear superposition is traditionally used to account for the influence of re-

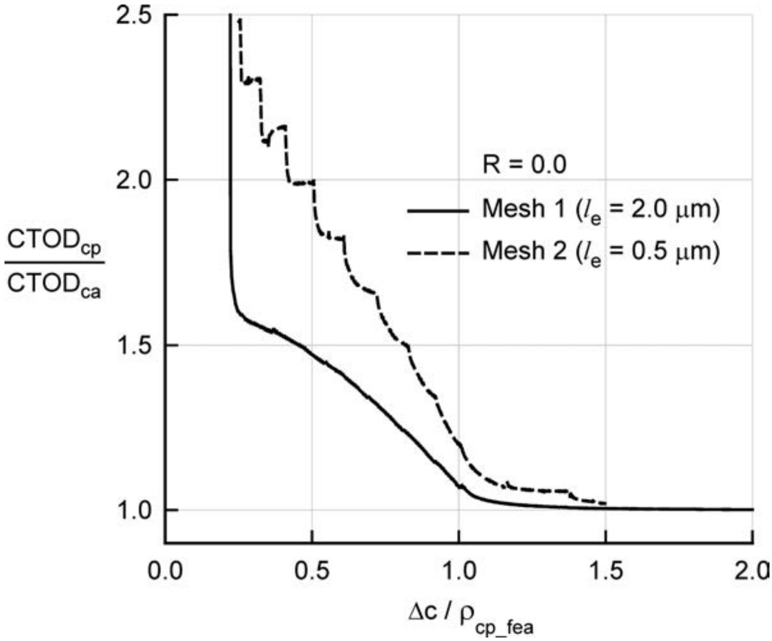

FIG. 4—*Comparison of normalized CTOD from Mesh 1 and 2.*

sidual stresses on fatigue-crack growth. In this section, residual-stress distributions were monitored during simulated fatigue-crack growth at $R=0$ and $P_{max}=2.2$ kN to investigate whether the residual stresses due to CP loading are affected by crack growth. Figures 5(*a*)–5(*d*) show the residual-stress distributions at P_{min} for CA (open symbols) and CPCA (solid curve) when the crack had reached 0.2, 0.5, 1.0, and 1.5 times the plastic-zone size created during CP loading, respectively. Figure 5(*a*) shows the comparison of residual stresses on the 51st cycle, which is the first cycle of CA loading after 50 cycles of CP loadings. The CA loading case shows the typical compressive contact stresses along the crack surface, reverse yielding in the crack-tip region, and the balancing tensile stresses in front of the crack tip. The CPCA loading case shows the compressive precracked region, which is fully open, and the resulting tensile residual stresses. The biaxial stress field around the notch tip causes a slight elevation of the tensile flow stress. The shape change in the compressive residual-stress distribution occurred at the edge of the compressive plastic-zone size. The residual-stress distribution was nearly balanced over about two plastic-zone sizes. When the crack had propagated through one-half of the compressive plastic zone, Fig. 5(*b*), the tensile residual-stress distribution had rapidly decayed. Once the crack tip had reached one compressive plastic-zone size, the crack-tip region was experiencing nearly the same residual-stress distribution as CA loading, as shown in Fig. 5(*c*). However, the CPCA loading case did exhibit some slight compressive contact stresses remote from the crack tip. With further crack propagation, the residual-stress distribution and contact

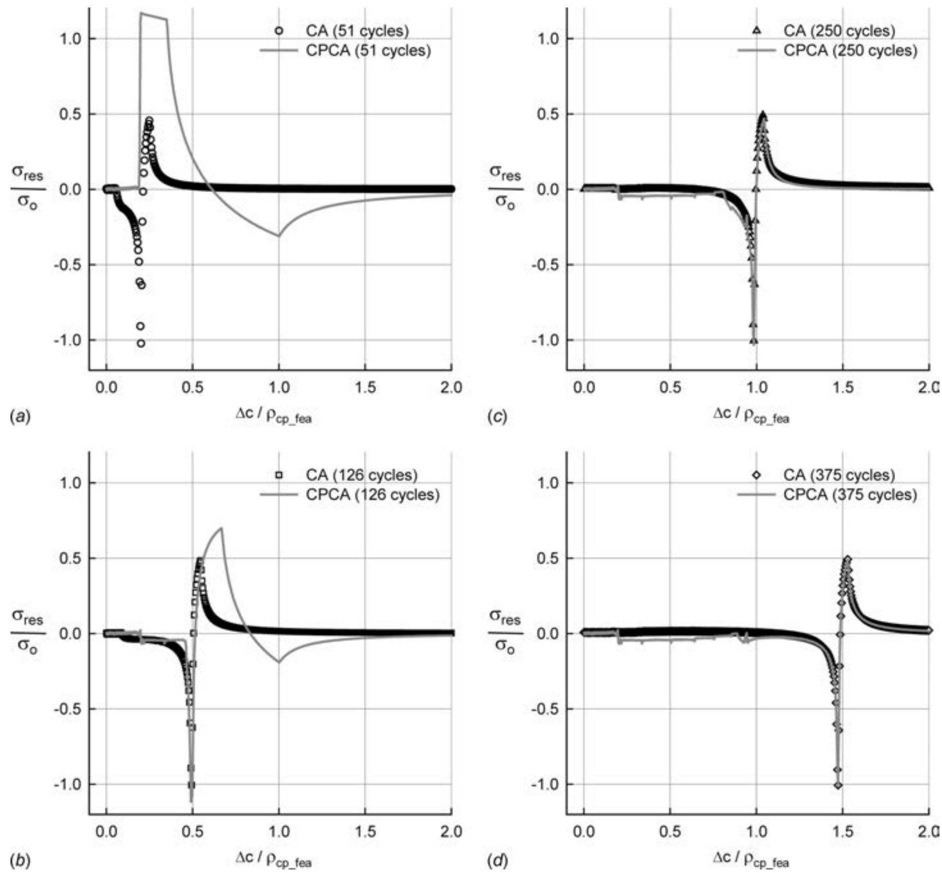

FIG. 5—*Residual stress distributions during simulated fatigue crack growth. (a) Crack tip is located at 20 % of compressive plastic-zone size. (b) Crack tip is located at 50 % of compressive plastic-zone size. (c) Crack tip is located at 100 % of compressive plastic-zone size. (d) Crack tip is located at 150 % of compressive plastic-zone size.*

stresses near the crack-tip region were very similar, as shown in Fig. 5(*d*). The tensile residual stresses created during CP loading were completely removed when the crack had reached about one plastic-zone size. Thus, crack-extension values beyond one plastic-zone size should not be affected by the tensile residual stresses. This is in contrast to the linear-superposition method [20], which showed that the influence of the tensile residual stresses were about two compressive plastic-zone sizes.

Stress Ratio (R) and Load Level Effects on Crack-Opening Loads and CTOD

In the previous section, it was shown that the crack-opening load, P_o, and the CTOD at $R=0$ stabilized in about 1 to 1.5 plastic-zone sizes due to CP loading. In this section, the influence of stress ratio ($R=0$ to 0.8 at $\Delta P=2.2$ kN) and of

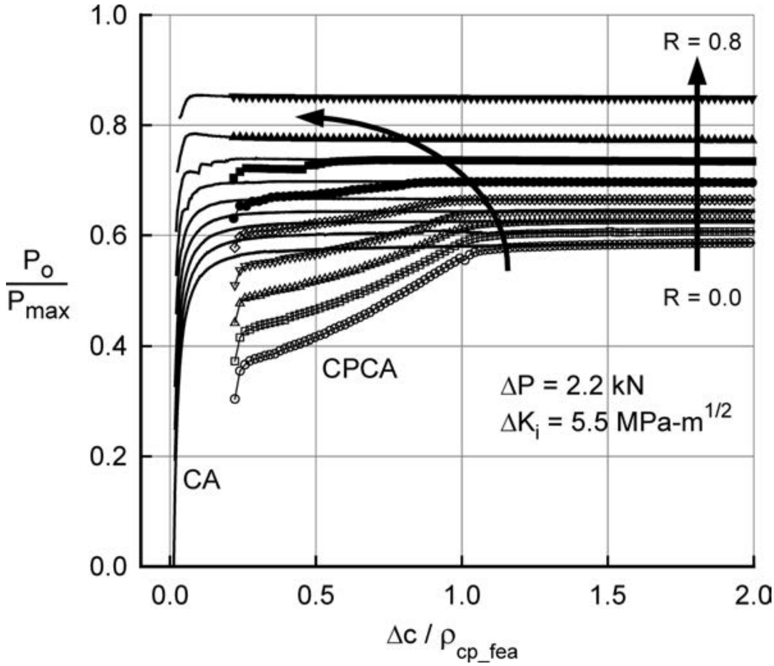

FIG. 6—*Effects of stress ratio* (*R*) *on normalized crack-opening loads.*

load level ($\Delta P = 2.2$, 4.4, and 6.6 kN at $R = 0$) on CA and CPCA loading were investigated. The effects of stress ratio (R) on P_o and CTOD are shown in Figs. 6 and 7, respectively. Figure 6 shows the normalized opening load (P_o/P_{max}) against normalized crack growth ($\Delta c/\rho_{cp\_fea}$). The solid curves are calculations under CA loading and the open symbols are calculations for CPCA loading. Under CA loading, the crack-opening loads stabilized very quickly, but under CPCA loading, the tensile residual stresses caused a delay in the stabilization to about 1 to 1.5 plastic-zone sizes at $R = 0$. For higher stress ratios, the merging between CA and CPCA cases occurred at smaller amounts of crack growth. At high R, like 0.7 and 0.8, the CPCA results agreed with the CA results as soon as the crack began to grow under the tensile CA loading. Figure 7 shows the normalized CTOD for CPCA and CA loading against normalized crack growth ($\Delta c/\rho_{cp\_fea}$). The effects of stress ratio on the normalized CTOD showed a similar trend as the crack-opening loads. For $R = 0$, the merging ($CTOD_{cp}$ within 1 % of $CTOD_{ca}$) occurred when the crack had grown about 1.4 times the compressive plastic-zone size. The merging occurred at smaller amounts of crack extension for higher stress ratios.

The effects of load level for $R = 0$ on crack-opening loads and CTOD are shown in Figs. 8 and 9, respectively. Three load levels were selected for evaluation. The load amplitudes (ΔP) were 2.2, 4.4, and 6.6 kN, which corresponded to initial ΔK levels of 5.5, 11, and 16.5 MPa-m$^{1/2}$. As shown in Fig. 8, the higher load amplitudes caused a slight reduction in the stabilized crack-opening loads,

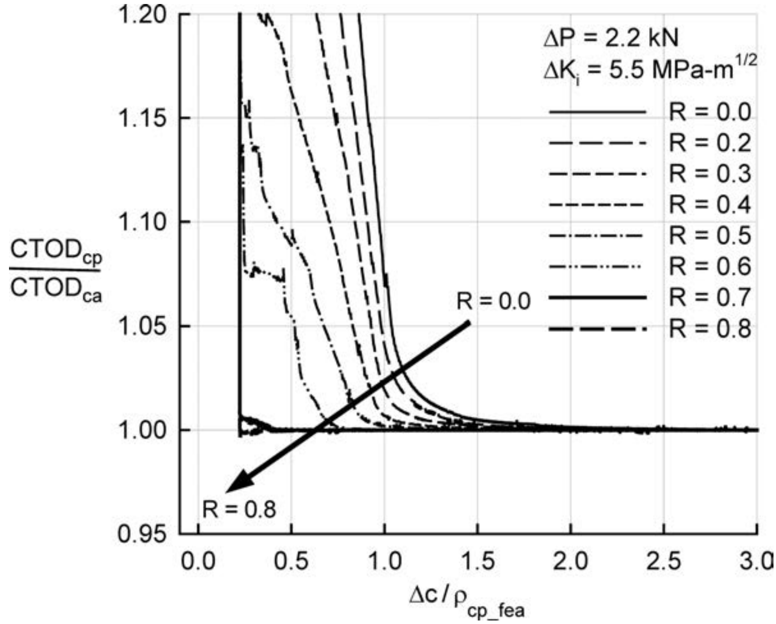

FIG. 7—*Effects of stress ratio* (*R*) *on normalized CTOD.*

similar to applied stress level effects on middle-crack tension specimens [19]. However, the crack growth required for the CPCA loading case to merge with the CA results was nearly independent of the load amplitude and occurred from 1.2 to 1.5 times the compressive plastic-zone size. But as shown in Fig. 9, the normalized CTOD took a larger amount of crack growth to approach unity for the higher load amplitudes. These analyses indicated that the minimum crack growth required to achieve valid fatigue-crack growth rate data (not affected by notching and CP loading) should be based on CTOD for the higher load amplitudes.

Crack-Growth Criterion for Compression Precracked Specimens

One of the objectives of the elastic-plastic finite-element analyses is to establish the amount of crack growth from the notch tip where the CP loading (tensile residual-stress field) would not have a significant effect on crack-growth rates and that the crack-closure behavior would have stabilized. Beyond this crack-growth increment, crack-growth rate behavior would be "steady state" constant-amplitude loading and the crack-growth data would be considered valid (minimal load history effects). Using the FEA results, crack-growth increments where the CPCA and CA results would agree within 1 % are plotted against the stress ratio, *R*, in Fig. 10. The open symbols show the crack-extension values determined from crack-opening behavior; and the solid symbols show the crack-extension values determined from CTOD. In order for

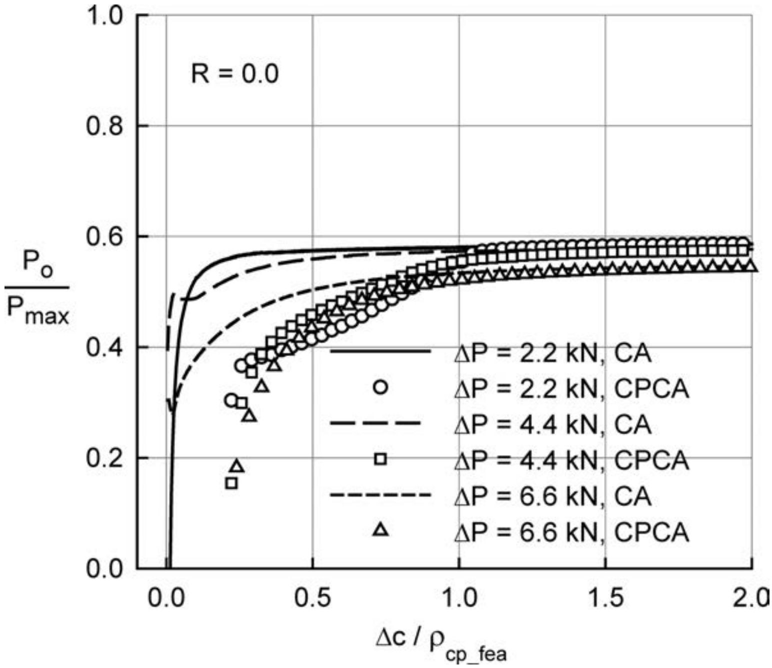

FIG. 8—*Effects of load level on normalized crack-opening loads.*

CPCA loading to produce valid fatigue-crack growth rate data, two criteria were developed. One criterion was based on crack-opening behavior (dashed line in Fig. 10) and is

$$\Delta c = \gamma(1 - R)\rho_{cp\_fea} \tag{1}$$

where $\gamma = 1.5$, and the other criterion was based on CTOD (solid line in Fig. 10 with $\gamma = 2$). Although it was shown that the residual-stress distribution had decayed when the crack-growth increment had reached one compressive plastic-zone size, the influence of CP loading on crack-opening behavior and CTOD extended to longer crack-growth increments. Since the CTOD results produced longer crack-growth increments than crack-opening behavior, the CTOD results have established the criterion for valid fatigue-crack growth data.

It was of interest to compare the current non-linear method with the traditional linear-superposition method to establish the extent of the influence of the tensile residual stresses caused by CP loading. Previous finite-element analyses by James et al. [20] using the traditional method found that crack growth from the notch (Δc) should be two times the Irwin plastic-zone size (5 % difference in the maximum stress-intensity factor with and without residual stresses) for $R = 0.1$ loading. (Note that a 1 % difference in stress-intensity factors from linear superposition would have resulted in a much larger crack-growth increment, maybe three to four times the Irwin plastic-zone size.) The Irwin plastic-zone size [24] was calculated by

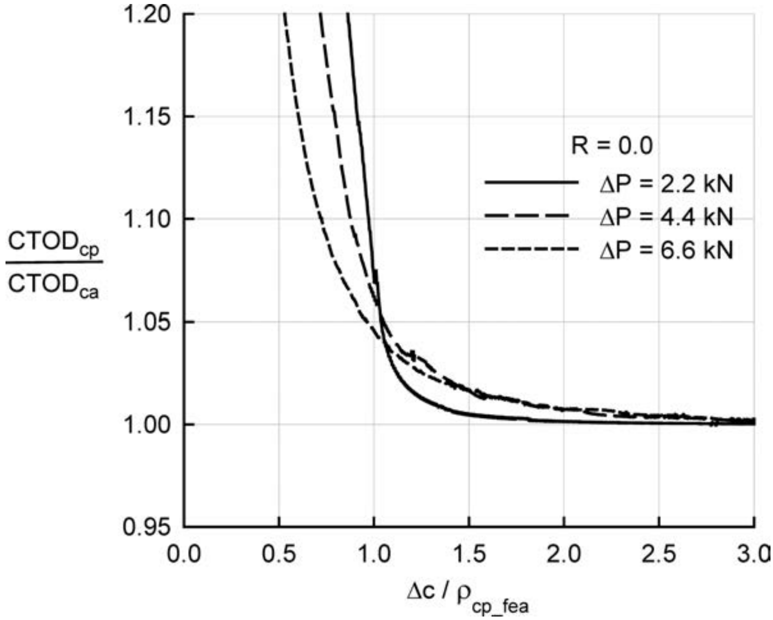

FIG. 9—*Effects of load level on normalized CTOD.*

$$r_{cp} = 1/\pi(K_{cp}/\sigma_o)^2 \tag{2}$$

The linear-superposition method was conservative, in that, it overestimated the influence of the residual-stress distribution on stress-intensity factor ratios. The nonlinear method ($\gamma=2$), which accounted for the decaying residual-stress field, indicated that the effects of CP loading do not extend as far as predicted by the linear method. But note that the differences in the acceptance criteria and parameters used resulted in the same crack extension increment (about 2 compressive plastic-zone sizes) at $R \approx 0$. Note that the acceptance criteria used in the nonlinear method (1 % in CTOD) was much more stringent than that used in the linear-superposition method (5 % in stress-intensity factor).

However, the current nonlinear analyses have not considered the influence of crack-surface roughness and oxide—or fretting-debris induced closure (or shielding) effects and their interactions with the residual-stress field. Thus, in order to be conservative, it is proposed that $\gamma=3$ be used.

Tests on C(T) specimens made of 7050 aluminum alloy [20] at $R=0.1$, using CP followed by constant ΔK loading (referred to as CPCK), shows that steady-rate behavior is achieved at crack-growth increments from 1.3 to 2.5 times Irwin plastic-zone size (r_{cp}), which supports the $\gamma=3$ equation as an upper bound. (The Irwin plastic-zone size was about 15 % larger than the plastic-zone size calculated from the FEA.) Tests on C(T) specimens made of two other aluminum alloys (2324 and 7075) over a wide range in stress ratios [17] support the near linear relationship with stress ratio. Fatigue-crack growth rate data at $R=0.7$ almost immediately fell on what is expected to be the high R curve.

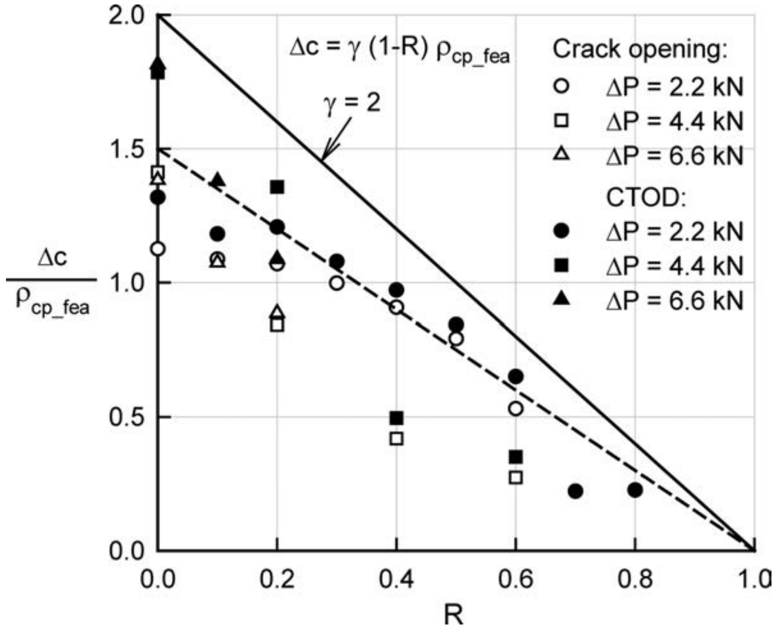

FIG. 10—*Crack-extension location for data unaffected by notching and compression precracking.*

Summary

Elastic-perfectly-plastic finite-element analyses (FEA) were conducted on C(T) specimens to study the influence from compression precracking (CP) and the resulting residual-stress field on the stabilization of crack-opening behavior and the crack-tip-opening displacements (CTOD). High-fidelity finite-element models (60 000 to 160 000 DOF) using two-dimensional plane-stress analyses were used to model plastic yielding during compressive loading and simulated fatigue-crack growth through the tensile residual-stress field. The finite-element code was ZIP2D and the course mesh had an element size of 2 μm. A refined mesh had an element size four times smaller (0.5 μm) than the course mesh. Compressive constant-amplitude loadings were applied and the crack was grown about 20 % of the compressive plastic-zone size from a 45° V-notch for Mesh 1. Then constant-amplitude (CA) loading was applied over a wide range in stress ratios (R) and load levels. The tensile residual-stress field was found to decay as the crack grew. When the crack-growth increment had reached one plastic-zone size, the residual-stress field created by CP loadings was essentially the same as CA loading. This may indicate that residual-stress effects from linear superposition may not be an adequate treatment, and may overestimate the influence. On the other hand, crack opening and CTOD behavior after CP loading merged with CA loading results at larger crack-growth increments. Crack-opening-load stabilization required crack-growth increments about 1.5 times the plastic-zone size to merge with CA results; whereas, the CTOD behavior required about twice the plastic-zone size to agree with CA results within 1 % at $R=0$. Stress ratio and load level effects were also investigated and the analyses showed that higher R-values required less crack growth, but higher loads required more crack growth than lower loads. Merging between the CPCA and CA finite-element analysis results were used to establish a crack-growth criterion for minimum crack extension for valid constant-amplitude fatigue-crack growth data. The criterion produced a linear relationship with stress ratio and indicated that a crack-growth increment two times the compressive plastic-zone size at $R=0$ was sufficient to avoid effects due to compression precracking. However, in order to be conservative, it is proposed that the crack-growth criterion $\Delta c \geq 3\ (1-R) r_{cp}$ be used to generate "steady state" constant-amplitude fatigue-crack growth rate data.

References

[1] Paris, P. C., Bucci, R., Wessel, E., Clark, W., and Mager, T., "Extensive Study of Low Fatigue Crack Growth Rates in A533 and A508 Steels," *National Symposium on Fracture Mechanics: Part I*, ASTM STP 513, ASTM International, West Conshohocken, PA, 1972, pp. 141–176.

[2] Hudak, S. J., Jr., Saxena, A., Bucci, R. J., and Malcolm, R. C., "Development of Standard Methods of Testing and Analyzing Fatigue Crack Growth Rate Data—Final Report," AFML TR 78-40, 1978.

[3] Bucci, R. J., "Development of a Proposed ASTM Standard Test Method for Near-Threshold Fatigue Crack Growth Rate Measurement," *Fatigue Crack Growth Measurement and Data Analysis*, ASTM STP 738, ASTM International, West Conshohocken, PA, 1981 pp. 5–28.

[4] ASTM Standard E647 "Standard Test Method for Measurement of Fatigue Crack Growth Rates," *Annual Book of ASTM Standards*, ASTM International, West Conshohocken, PA, 2006, pp. 615–657.

[5] Ohta, A., Kosuge, M., and Sasake, E., "Fatigue Crack Closure Over the Range of Stress Ratios from −1 to 0.8 Down to Stress Intensity Factor Threshold Level in HT80 Steel and SUS 304 Stainless Steel," *International Journal of Fracture*, Vol. 14, No. 3, 1978, pp. 251–264.

[6] Minakawa, K., and McEvily, A. J., "On Near-Threshold Fatigue Crack Growth in Steels and Aluminum Alloys," *Proceedings of International Conference on Fatigue Thresholds*, Stockholm, Sweden, Vol. 2, 1981, pp. 373–390.

[7] Newman, J. C., Jr., "A Nonlinear Fracture Mechanics Approach to the Growth of Small Cracks," *Behavior of Short Cracks in Airframe Components*, AGARD CP-328, 1983, pp. 6.1–6.27.

[8] Newman, J. C., Jr., "Analysis of Fatigue Crack Growth and Closure Near Threshold Conditions," *Fatigue Crack Growth Thresholds, Endurance Limits, and Design*, ASTM STP 1372, ASTM International, West Conshohocken, PA, 2000, pp. 227–251.

[9] Suresh, S., Zaminski, G. F., and Ritchie, R. O., "Oxide Induced Crack Closure: An Explanation for Near-Threshold Corrosion Fatigue Crack Growth Behavior," *Metallurgical Transactions*, Vol. A12A, 1981, pp. 1435–1443.

[10] Ritchie, R. O., "Mechanisms of Fatigue Crack Propagation in Metals, Ceramics and Composites: Role of Crack Tip Shielding," *Material Science and Engineering*, Vol. 103, 1988, pp. 15–28.

[11] Kirby, B. R., and Beevers, C. J., "Slow Fatigue Crack Growth and Threshold Behaviour in Air and Vacuum of Commercial Aluminium Alloys," *Fatigue and Fracture of Engineering Materials and Structures*, Vol. 1, 1979, pp. 203–216.

[12] Hubbard, R. P., "Crack Growth under Cyclic Compression," *ASME J. Basic Eng.*, Vol. 91, 1969, pp. 625–631.

[13] Topper, T. H., and Au, P., "Fatigue Test Methodology," AGARD Lecture Series 118, The Technical University of Denmark, Denmark, 1981.

[14] Pippan, R., "The Growth of Short Cracks Under Cyclic Compression," *Fatigue and Fracture of Engineering Materials and Structures Journal*, Vol. 9, 1987, pp. 319–328.

[15] Pippan, R., Plöchl, L., Klanner, F., and Stüwe, H. P., "The Use of Fatigue Specimens Precracked in Compression for Measuring Threshold Values and Crack Growth," *J. Test. Eval.*, Vol. 22, 1994, p. 98.

[16] Forth, S. C., Newman, J. C., Jr., and Forman, R. G., "On Generating Fatigue Crack Growth Thresholds," *Int. J. Fatigue*, Vol. 25, 2003, pp. 9–15.

[17] Newman, J. C., Jr., Schneider, J., Daniel, A., and McKnight, D., "Compression Pre-Cracking to Generate Near Threshold Fatigue-Crack-Growth Rates in Two Aluminum Alloys," *Int. J. Fatigue*, Vol. 27, 2005, pp. 1432–1440.

[18] Ruschau, J., and Newman, J. C., Jr., "Compression Precracking to Generate Near Threshold Fatigue Crack Growth Rates in an Aluminum and Titanium Alloy," *Fatigue and Fracture Mechanics: 36th Symposium*, Tampa, FL, 2007.

[19] Newman, J. C., Jr., "A Finite-Element Analysis of Fatigue Crack Closure," *Mechanics of Crack Growth*, ASTM STP 590, ASTM International, West Conshohocken, PA, 1976, pp. 281–301.

[20] James, M. A., Forth, S. C., and Newman, J. A., "Load History Effects Resulting from Compression Precracking," *Fatigue and Fracture Mechanics, 34th Volume*, ASTM STP 1461, ASTM International, West Conshohocken, PA, 2005, pp. 43–59.

[21] PATRAN-2005, MSC Software Corporation, Santa Ana, CA.

[22] McClung, R. C., "Finite Element Perspectives on the Mechanics of Fatigue Crack Closure," *Proceedings of Fatigue '96, 6th International Fatigue Congress*, Berlin, Germany, Vol. 1, 1996, pp. 345–356.

[23] McClung, R. C., "Analysis of Fatigue Crack Closure During Simulated Threshold Testing," *Fatigue Crack Growth Thresholds, Endurance Limits, and Design*, ASTM STP 1372, ASTM International, West Conshohocken, PA, pp. 209–226.

[24] Irwin, G. R., "Analysis of Stresses and Strains Near the End of a Crack Traversing a Plate," *J. Appl. Mech.*, Vol. 24, 1957, pp. 361–364.

ASTM Special Technical Publication, Vol. 5, No. 7
Paper ID JAI101623
Available online at www.astm.org

John J. Ruschau[1] *and James C. Newman, Jr.*[2]

Compression Precracking to Generate Near Threshold Fatigue Crack Growth Rates in an Aluminum and Titanium Alloy

ABSTRACT: The scope of this paper is to determine the fatigue-crack growth rates in the near-threshold regime for both an aluminum and titanium alloy using the compression precracking constant-amplitude (CPCA) test method on compact specimens. Tests were conducted over a wide range of stress ratios ($R = P_{min}/P_{max} = 0.1$ to 0.9). Results were compared with threshold and near-threshold data generated on the same materials using the ASTM E647, "Standard Test Method for Measurement of Fatigue Crack Growth Rates," load-shedding test procedure. On the 7075-T651 alloy, very little difference was observed in threshold values between the load-shedding and CPCA test methods. In contrast, the titanium alloy (Ti-6Al-4V) showed very large differences between the CPCA and load-shedding test results in the near-threshold and threshold regimes for the low stress ratios. Results under high R conditions ($R \geq 0.7$) agreed well between the two-threshold test methods for both materials. On the titanium alloy, the load-shedding test method also produced a specimen width effect on near-threshold behavior, whereas the CPCA test method produced results that were independent of specimen width and produced "steady-state" constant-amplitude data in the near-threshold regime, after the crack had grown several compressive plastic-zone sizes.

KEYWORDS: fatigue, threshold, crack growth, residual stress, aluminum, titanium, compression loading

---

Manuscript received December 5, 2007; accepted for publication May 28, 2008; published online July 2008.

[1] University of Dayton Research Institute, 300 College Park, Dayton OH 45469-0031, e-mail: john.ruschau@wpafb.af.mil

[2] Mississippi State University, Walker Engineering Building, Mississippi State, MS 39762.

Citation: Ruschau, J. J. and Newman, Jr., J. C., "Compression Precracking to Generate Near Threshold Fatigue Crack Growth Rates in an Aluminum and Titanium Alloy," *J. ASTM Intl.*, Vol. 5, No. 7. DOI10.1520/JAI101623. Available online at www.astm.org. Also included in JAI Special Issue STP 1508, *Fatigue and Fracture Mechanics: 36th Volume*, R. W. Neu, K. R. W. Wallin, and S. R. Thompson, guest editors, ASTM International, West Conshohocken, PA, 2009, pp. 257-271.

Introduction

Accurate representation of fatigue-crack thresholds, the region defining crack growth as either very slow or nonexistent, is extremely important for many structural applications. In North America, the threshold crack-growth regime is experimentally defined using ASTM Standard E647 [1], which has been shown to exhibit anomalies due to the load-shedding test procedure for some materials. The current test method defined by ASTM is designed to fully reproduce the range of fatigue-crack thresholds (e.g., low and high stress ratios) needed to characterize loading conditions for many structural applications.

To generate fatigue-crack growth rate data in the near-threshold regime without load-shedding effects, a compression-compression precracking test method, developed by Topper and Au [2], Pippan et al. [3], and others [4,5] is examined. Using this procedure, prenotched specimens were cycled under compression precracking to produce an initial fatigue crack which arrests after small amounts of crack extension. The specimen is then subjected to constant-amplitude fatigue loading under ΔK-increasing conditions to generate fatigue-crack growth rate data in the near threshold regime at the desired stress ratio.

It is the scope of this paper to determine the fatigue-crack growth rates in the near-threshold regime for both an aluminum and titanium alloy using the compression precracking constant-amplitude (CPCA) test method on compact specimens. Tests were conducted over a wide range of stress ratios (R) ranging from 0.1 to 0.9 on a 7075-T651 aluminum alloy and a Ti-6Al-4V STOA titanium alloy. Results are compared with near-threshold and threshold data generated on the same materials using the current ASTM E647 load-shedding test procedure.

Background

Traditionally, the fatigue crack growth threshold, ΔK_{th}, is used as a limit for damage-tolerant design [6], e.g., if the stress-intensity factor for a given crack is below the threshold value, the crack is assumed to be nonpropagating. However, it has been shown by Pearson [7] that small cracks can often propagate at stress-intensity factor levels below the large-crack threshold as defined by the current ASTM standard test procedure E647 [1]. Newman [8,9] has demonstrated that part of the discrepancy between small-crack data under constant-amplitude loading and large-crack data generated with the load-shedding procedure was due to “remote” closure effects on the large-crack data. Thus, the primary anomaly is the large-crack threshold at low stress ratios. Therefore, if fatigue-crack-growth thresholds and near-threshold behavior are to be used in life prediction for cracks growing from material discontinuities or manufacturing defects, then the most accurate representation of the threshold and near-threshold behavior for a material must be defined.

The load-shedding test procedure currently defined in E647 [1] has been shown to often induce high crack-closure loads [10] and remote crack-surface closure [8,11], which prematurely slows down crack growth and produces an abnormally high threshold. Donald and Paris [12] have also shown that closure “away” from the crack tip, possibly due to asperities, may also cause the higher thresholds and difficulty measuring the crack-opening loads during load-shedding tests. During load shedding, the crack-surface displacements are steadily decreasing with longer crack lengths, which give the potential for crack-surface contact and activation of the various closure mechanisms. Several other investigators [13,14] have used other methods to generate threshold values that appear to not be affected by the test procedure.

Thus, some of the fatigue-crack-growth-threshold data in the literature today may be inappropriate due to the load-shedding test procedures that were used to generate these data. A load and environmental history effect, or both, may be causing the load-shedding thresholds to be higher than what would be obtained under steady-state constant-amplitude loading conditions, especially if the initial stress-intensity factor range (ΔK) is much higher than the threshold value. In the literature, these higher thresholds have been attributed to crack-surface roughness, oxide- or fretting-debris accumulation, and plasticity effects. Whether these same closure mechanisms develop at the low stress-intensity factor ranges under constant-amplitude loading is questioned. Another test method is being developed to generate constant-amplitude fatigue-crack-growth-rate data in the threshold and near-threshold regimes with minimal or no load-history effects. The test procedure involves using compression precracking to generate a crack at a sharp V-notch and then to test the specimen under "constant-amplitude" loading. However, the crack must be grown a number of compressive plastic-zone sizes to eliminate the effects of the tensile residual stresses and to stabilize the crack-opening stress history. Thus, the various closure mechanisms will develop as a natural consequence of "constant-amplitude" loading.

Test Specimens and Materials

Two different alloys were evaluated for threshold crack growth rate properties: 7075-T651 aluminum alloy 51 mm (2 in.) thick plate and Ti-6Al-4V titanium alloy 20 mm (0.8 in.) plate. Tensile properties for the aluminum alloy are 545 MPa (79 ksi) yield strength (YS) and 586 MPa (85 ksi) ultimate tensile strength (UTS). The titanium alloy, which is a remnant from the U.S. Air Force (USAF) High Cycle Fatigue program [15], was furnished in the solution treated and overaged (STOA) condition and produced in accordance with AMS 4928. The YS for this alloy was 931 MPa (135 ksi), with UTS equal to 979 MPa (142 ksi).

Compact tension C(T) specimens were machined from the 7075 alloy per the dimensions outlined in ASTM E647 for W = 76 mm (3 in.). Specimen thickness, B, was approximately 5.7 mm (0.225 in.) and the specimens were machined from a section centered about 6 mm from the surface of the thick plate. This location simulated the location of the wing skin material in an integrally stiffened wing panel for a U.S. Navy aircraft. For the titanium alloy, C(T) specimens were machined to sizes of W = 25, 51, and 76 mm (1, 2, and 3 in., respectively), with a thickness, B, of 6.4 mm (0.25 in.) for all widths. Starter notches were machined in all specimens with a notch tip root radius of 0.1 mm (0.004 in.) and included an angle of 60°, as illustrated in Fig. 1.

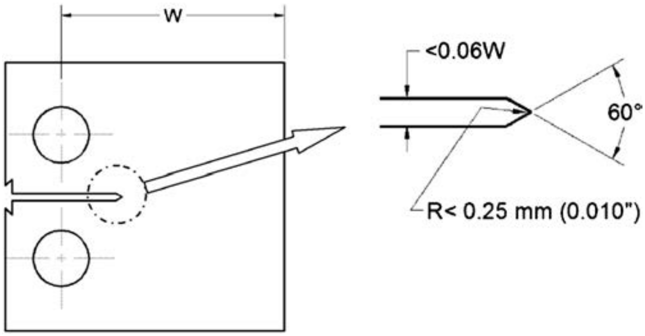

FIG. 1—*Notch details for C(T) configuration.*

Procedures

All tests were performed under laboratory air conditions in a single 22 kN (5 kip) MTS servo-hydraulic test machine. Crack length measurement was accomplished using front face compliance procedures as outlined in E647. Test control was provided by a data acquisition/test control system developed inhouse by UDRI for threshold fatigue crack growth rate (FCGR) testing. For both alloys, crack growth rate testing was performed at stress ratios ranging from 0.1 to 0.9, at a nominal cyclic frequency of 25 Hz. All crack length measurements based on compliance procedures were obtained at the test frequencies to eliminate any potential influence of test interruption caused by frequency changes.

Threshold testing to determine ΔK_{th} was performed using two procedures. The first procedure was the standard load shed (LS) method described in E647 for threshold determination. Initial starting load levels were carefully selected to ensure that growth rates immediately from the starting notch were less than 10^{-8} m/cycle ($4e^{-7}$ in./cycle), as required in the standard. A load shed rate of $C = -0.08$ mm^{-1} (-2 in.$^{-1}$) was maintained in all LS tests. Upon developing rates at or near the target 10^{-10} m/cycle, test control was changed to constant amplitude (CA) loading, ΔK increasing, in order to "trace" back up the growth rate curve to ensure the LS data and the CA data were in agreement. In all cases, the LS and CA methods gave identical results.

The second method utilized was a compression-compression precrack, followed by CA loading and hence referred to as CPCA. In this method, a small fatigue crack is introduced at the tip of the starter notch via compression-compression load cycling. The resulting crack tip is enveloped by a small residual tensile field instead of the typical compressive plastic zone normally resulting from tension-tension loading and in general, free of any crack closure resulting from either crack surface roughness or the compressive plastic zone. Typical crack sizes at the notch tip were 0.2 mm (0.008 in.) for both alloys resulting from compression cycling at $R = 10$. Maximum compression stress intensity factor levels required to produce fatigue cracks within 100 K cycles were -22 MPa$\sqrt{m}$ (-20 ksi$\sqrt{in.}$) for the 7075 alloy and -38 MPa$\sqrt{m}$ (-35 ksi$\sqrt{in.}$) for the Ti-6Al-4V specimens. These maximum compressive load

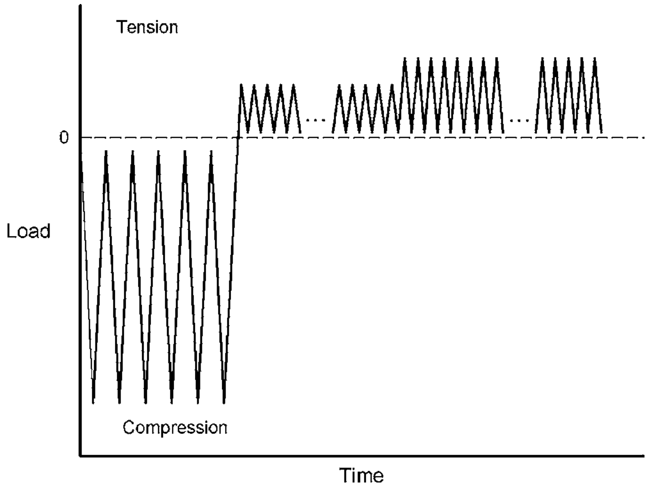

FIG. 2—*Depiction of CPCA loading procedure.*

levels that were found to produce fatigue cracks were estimated from the following relationship:

$$K_{\max,cp}/E = 0.00032\ \sqrt{\ }\mathrm{m}\ \text{(SI units of MPa and m)}$$

or

$$K_{\max,cp}/E = 0.002\ \sqrt{\ }\mathrm{in}\ \text{(ksi and inch units)} \quad (1)$$

where $K_{\max,cp}$, is the maximum compressive stress-intensity factor for precrack, and E = elastic modulus.

Following compression precracking, constant amplitude (CA) loading was performed at or below the anticipated threshold stress intensity ranges until steady state or steadily increasing growth rates occurred. If no appreciable crack growth occurred after approximately 2–3 million cycles, the minimum and maximum loads were increased ~5–10 % (maintaining constant R) and again cycled to examine for crack growth. This procedure is depicted in Fig. 2.

Once steady state crack growth was detected, the fatigue crack was extended by approximately two to three plastic-zone sizes (based on the compressive precrack conditions) from the initial CP crack size prior to taking any growth rate data to eliminate potential transient behavior resulting from the compressive loading and resulting tensile residual stress field [5,16,17]. In most cases, slight but detectable crack growth occurred immediately following the CP procedure at ΔK levels well below the anticipated ΔK_{th} level. In general, these fatigue cracks arrested after minimal crack growth, typically on the order of 0.15 mm (0.006 in.). Once the applied ΔK was equal to or above the ΔK_{th}, steadily increasing crack growth rates occurred and progressed continuously into the mid-region (Region II) portion of the idealized da/dN against ΔK curve, after which the test was terminated.

Threshold testing for both procedures at a given stress ratio were done in pairs (e.g., first a specimen tested under LS procedures, followed immediately by a second test of an identical specimen size under the CPCA procedures) to minimize any laboratory environment influences that might occur over time. Threshold values for both procedures were determined following the ASTM procedure, whereby the stress intensity factor range, ΔK, corresponding to an extrapolated growth rate (linear extrapolation to log da/dN and log ΔK data) of 10^{-10} m/cycle (4e^{-9} in./cycle) is defined as ΔK_{th}. Threshold values obtained for both methods were then compared for consistency.

Results and Discussion

Threshold tests performed with both procedures on the 7075-T651 specimens are shown in Fig. 3 for stress ratios ranging from 0.1 to 0.9. Results clearly demonstrate that for this alloy the two procedures produce similar da/dN data over the range examined. Note that the CPCA data for $R=0.1$ (Fig. 3(*a*)) and $R=0.4$ (Fig. 3(*b*)) shows a number of "crack arrest" points. These data represent the initial low values of ΔK where measurable crack growth occurred, but arrested after minimal growth. Increasing the loads by 5–10 % often led to again minimal crack extension. Only after the ΔK was increased such that $\Delta K_{\text{applied}} > \Delta K_{\text{th}}$ for the test condition did stable crack growth occurred.

Tabulated values of ΔK_{th} for the various stress ratios examined, derived from the current E647 standard for ΔK threshold determination, are furnished in Table 1. Also shown in the table are the deviations in ΔK_{th} between the CPCA and the ASTM LS methods relative to the LS value. Results presented in Table 1 further illustrate that there is little or no difference between the two procedures, as differences of 3 % and less in ΔK_{th} values are well within the anticipated variation for either method. As expected, values of ΔK_{th} decrease linearly with increasing R for the single specimen size examined. Thus, for this particular alloy and specimen configuration, the CPCA method offers fatigue crack growth rate data consistent with the ASTM E647 LS method in the threshold region.

Results for Ti-6Al-4V C(T) specimens of varying width (W) reveal a strikingly different trend. Threshold FCGR data at $R=0.1$ in the threshold region for the LS method are shown in Fig. 4 and show a "fanning out" of data at the lower growth rates as a function of specimen width. Fatigue crack growth rates were measured at much lower ΔK values for the smallest specimen width ($W=25$ mm) relative to the larger specimens, with the largest ($W=76$ mm) having the highest ΔK_{th}. While the data shown in Fig. 4 represents a single test per condition, replicate tests performed for each of the specimen sizes led to similar behavior. At growth rates above 2e-9 m/cycle (8e-8 in./cycle) the three datasets converge. It should be noted that the data developed for the smallest specimen size ($W=25$ mm) did not demonstrate the classic trend of da/dN approaching a vertical asymptote with decreasing ΔK, as witnessed with the other two specimen sizes. Replicate tests of this size behaved in a similar fashion: da/dN decreased with decreasing ΔK linearly (log-log) before arresting following the last load shed, whereby no measurable crack growth occurred.

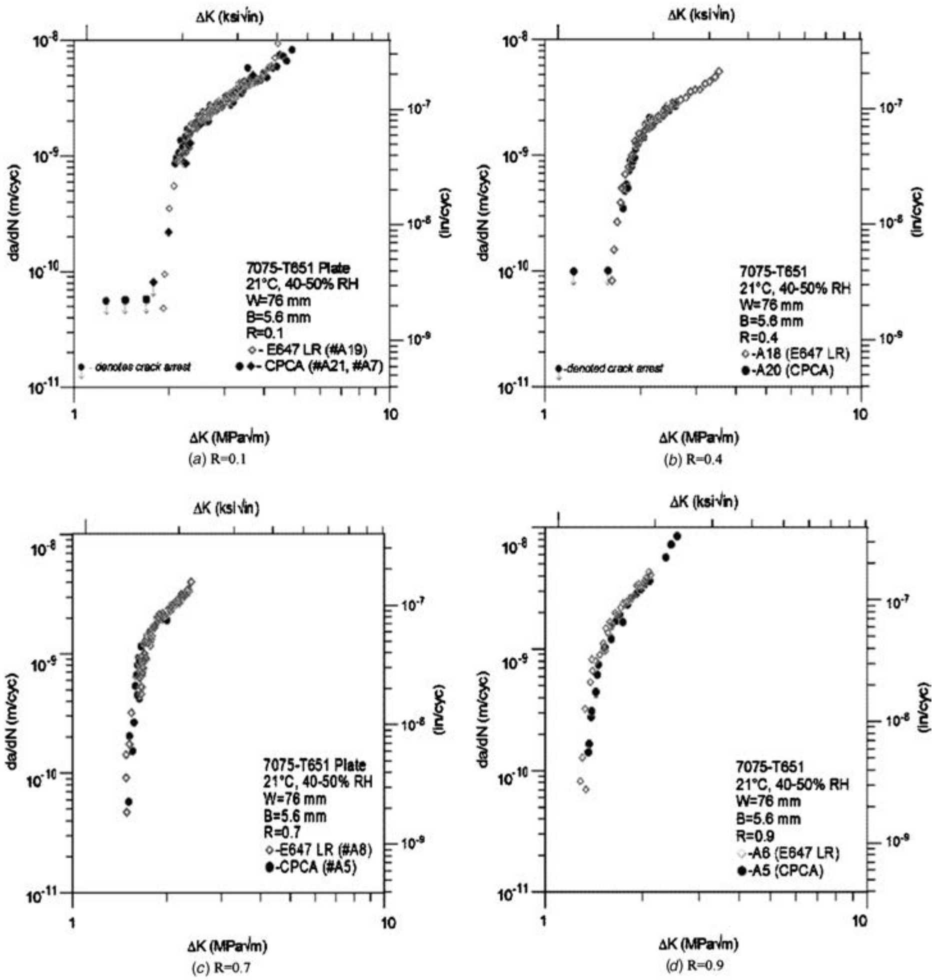

FIG. 3—*FCGR data for 7075-T651 in threshold region: R* = 0.1 (*a*), *0.5* (*b*), *0.7* (*c*), *and 0.9* (*d*).

Consequently, threshold ΔK for this specimen width is defined as the lowest ΔK value for which measurable da/dN was obtained.

Representative compliance curves in the threshold region taken for each of the titanium LS data sets just described are presented in Fig. 5 and help to explain the variation in apparent ΔK_{th} values. While little crack closure is observed in the load-crack-opening-displacement (COD) curve for the smallest specimen width, as shown in Fig. 5(*a*), increasing levels of closure are noted for the increased specimen widths, as seen in Figs. 5(*b*) and 5(*c*). Increasing threshold levels with increasing specimen size is unquestionably due to increasing levels of crack closure. Reasons for the increase in closure with specimen width are uncertain, but may well include crack surface roughness which would pro-

TABLE 1—*Threshold values obtained for LS and CPCA methods for 7075-T651.*

Test Method	Stress Ratio, R	ΔK_{th} (MPa$\sqrt{}$m)	% diff (w/r to LS)
LS	0.1	1.94	...
CPCA	0.1	1.90[a]	−2 %
LS	0.4	1.63	...
CPCA	0.4	1.60	−1 %
LS	0.7	1.49	...
CPCA	0.7	1.54	+3 %
LS	0.9	1.30	...
CPCA	0.9	1.34	+2 %

[a]Average of two tests; all other single test results.

duce longer precrack lengths for the larger specimen widths, as well as the load shed history which produces a region of plastic deformation along the crack surfaces that cause remote closure as the applied loads and crack surface displacements are reduced. Again, it should be restated that all tests were started

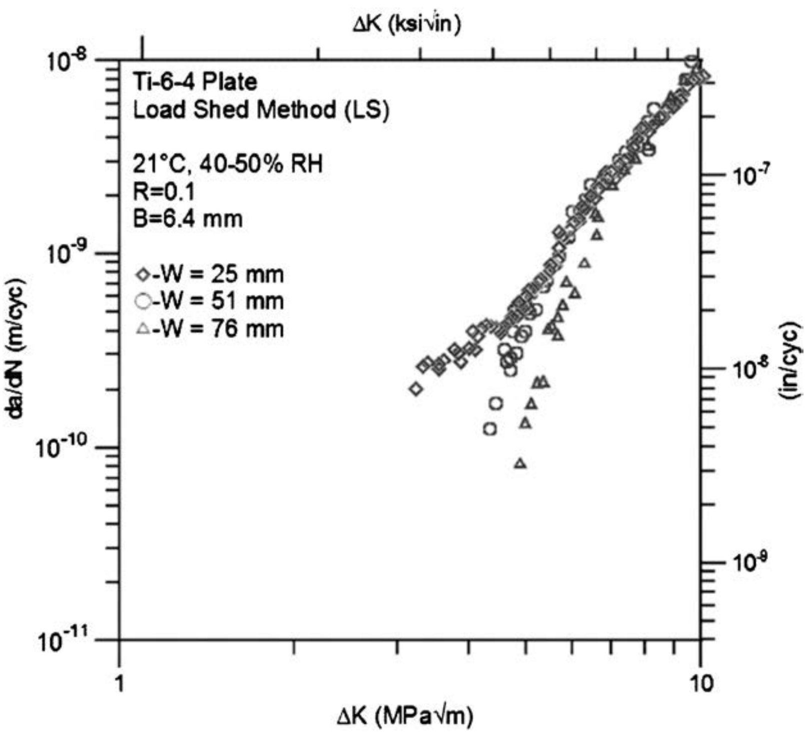

FIG. 4—*FCGR data for Ti-6Al-4V at* $R = 0.1$ *using LS procedure.*

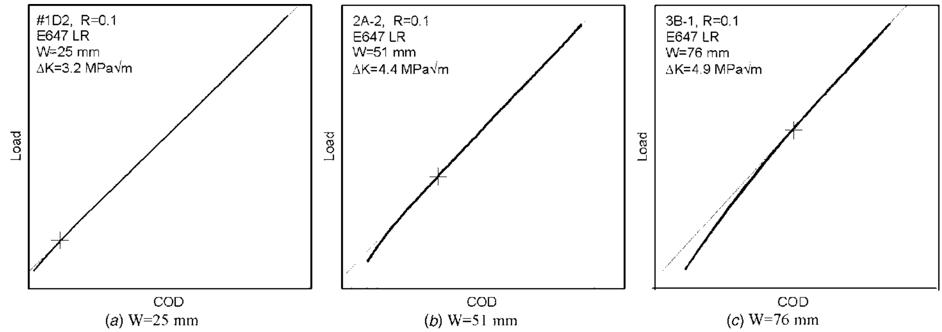

FIG. 5—*Compliance curves at threshold for Ti-6Al-4V at* $R=0.1$ *using LS procedure.*

at ΔK levels corresponding the growth rates at or below 10^{-8} m/cycle (4e-7 in./cycle), as required in the E647 standard.

A cursory attempt was made to estimate ΔK_{eff} from the compliance records shown in Fig. 5 for each of the specimen sizes. The results proved reasonably adequate in correlating the ΔK_{th} for each specimen width into a single effective threshold value. However, when employing the current E647 LS procedures for FCGR testing in the threshold regime, it appears that for this particular material and specimen configuration that ΔK, as defined in the standard, does not uniquely relate crack growth rate behavior.

In contrast, the curves for the three specimen widths using the same CPCA procedures as performed on the 7075 specimens show drastically different behavior as shown in Fig. 6, with no "fanning" or specimen width dependency as was noted with the LS method. Data for the three specimen widths plot directly on top of each other over the same range in growth rates examined. Also presented in Fig. 7 are the compliance traces for the three specimen widths at the threshold conditions, each of which display little or no evidence of crack closure. Again, precrack crack lengths for these three cases are similar and in the range of 0.13 mm (0.005 in.). It is clear from this that the applied ΔK following compressive cycling produces a near closure free starting condition, hence $\Delta K_{\mathrm{applied}} \sim \Delta K_{\mathrm{eff}}$ and the resulting da/dN is only as a function of the applied ΔK, the key assumption in the LEFM approach to life prediction.

Crack growth rate data for the two procedures at the higher stress ratios of 0.4 and 0.7 are also shown in Fig. 8 for the Ti-6Al-4V material. Tabulated threshold values over the range of stress ratios examined are also presented in Table 2. Slight yet consistent differences in ΔK_{th} are also are seen at $R=0.4$, with the CPCA procedure consistently resulting in lower (conservative) ΔK_{th} values relative to the LS method. Similarly, the trend of increasing ΔK_{th} with increasing W for the LS method is slightly evident at the $R=0.4$ test condition. For the single specimen size at $R=0.7$ the two methods yielded similar results, not surprising, as the compliance curves for both methods at high stress ratio ($R=0.7$) were essentially void of any closure.

A concern of any precracking procedure, CP notwithstanding, is the influence of the procedure on ensuing crack growth data. The current ASTM LS

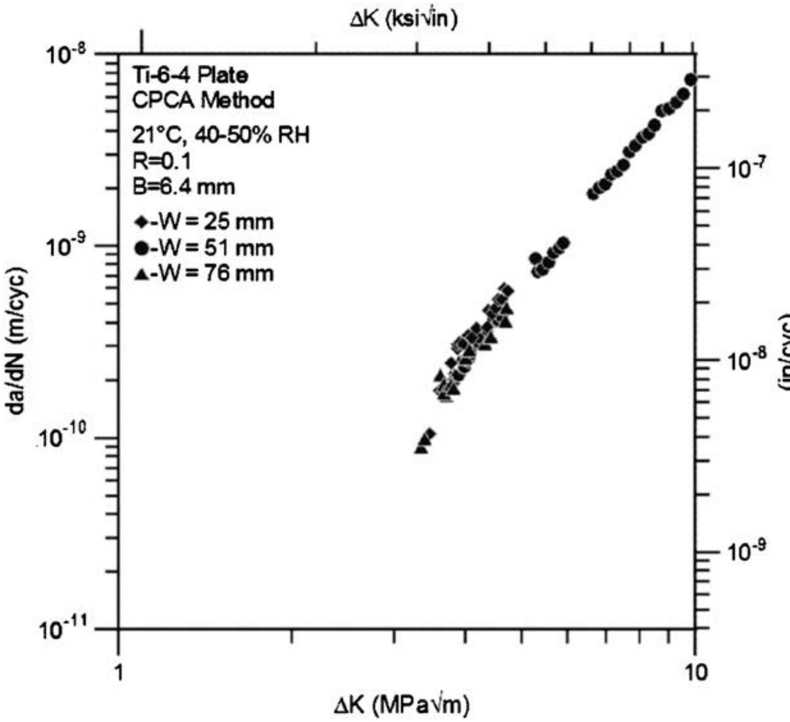

FIG. 6—*FCGR data for Ti-6Al-4V at* $R = 0.1$ *using CPCA procedure.*

procedure requires that during precracking, a crack extension following load shedding be a minimum of $3/\pi(K_{max}/YS)^2$ in order to eliminate potential transient effects. This increment is on the order of three plastic-zone (r_p) sizes. Following this approach and using the plastic-zone size estimated from the maximum compression force used during precracking would require the compression precrack, typically on the order of 0.13 mm (0.005 in.) in length, to

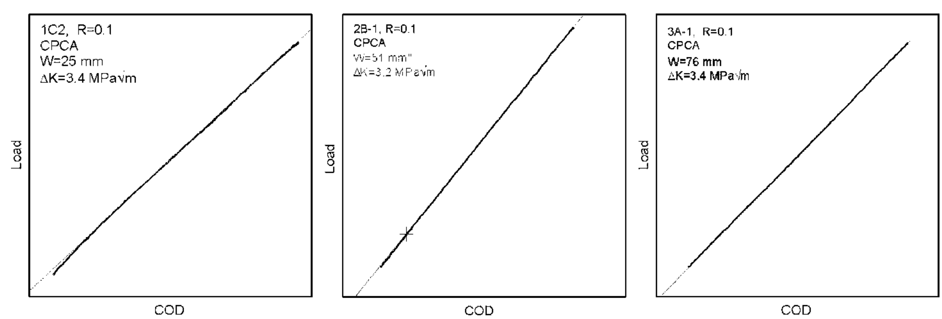

(*a*) W=25 mm (*b*)W=51 mm (*c*)W=76 mm

FIG. 7—*Compliance curves for Ti-6Al-4V at* $R = 0.1$ *using CPCA procedure.*

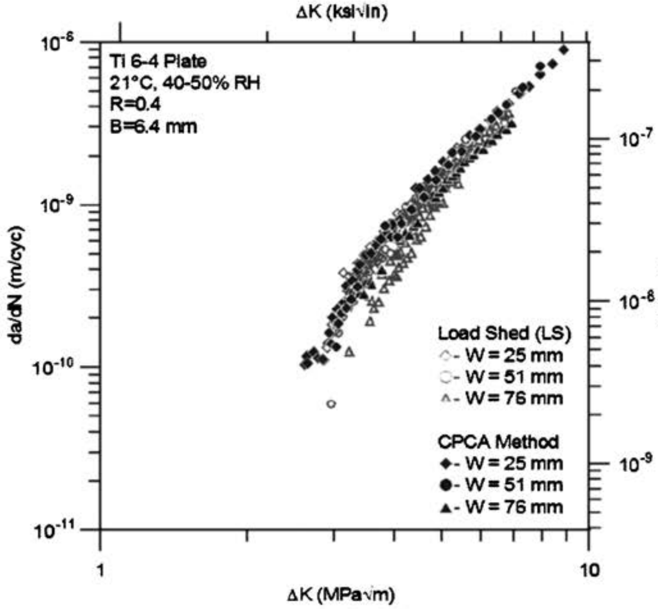

(a) R=0.4

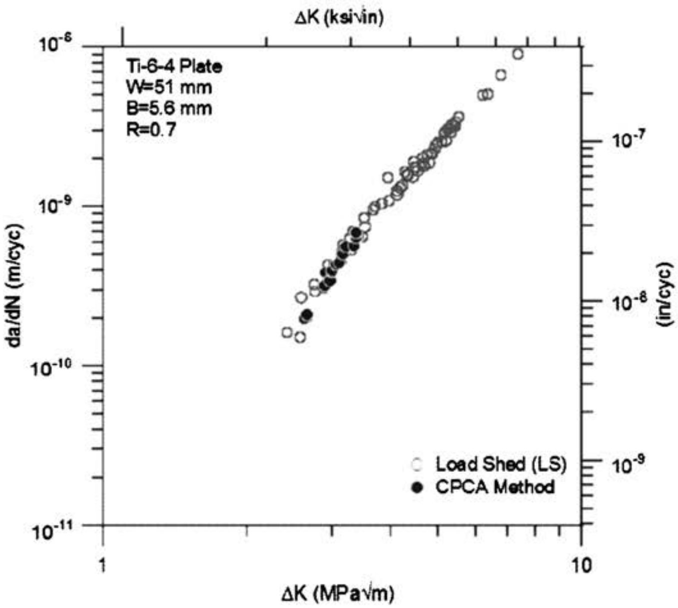

(b) R=0.7

FIG. 8—*FCGR data for Ti-6Al-4V in threshold region:* (*a*) $R = 0.4$ *and* (*b*) $R = 0.7$.

TABLE 2—*Threshold values obtained for LS and CPCA methods for Ti-6Al-4V.*

Test Method	Stress Ratio, R	W (mm)	ΔK_{th} (MPa $\sqrt{m}$)	% diff (w/r to LS)
LS	0.1	25	3.59[a,b]	...
CPCA	0.1	25	3.41	−5 %
LS	0.1	51	4.30[a]	...
CPCA	0.1	51	3.16	−26 %
LS	0.1	76	4.77[a]	...
CPCA	0.1	76	3.42	−28 %
LS	0.4	25	2.81	...
CPCA	0.4	25	2.64	−6 %
LS	0.4	51	3.02	...
CPCA	0.4	51	2.81	−7 %
LS	0.4	76	3.05	...
CPCA	0.4	76	2.62	−14 %
LS	0.7	51	2.50	...
CPCA	0.7	51	2.40	−4 %

[a]Average of two tests; all other single test results.

[b]Lowest value of ΔK prior to crack arrest.

extend approximately 2 mm (0.08 in.) prior to taking reporting valid da/dN data. To examine the need for this excessive crack extension, a single Ti-6Al-4V specimen, $W = 51$ mm (2 in.), was precracked via CP procedures and then immediately subjected to constant ΔK control in the near threshold region at $R = 0.1$. The resulting da/dN behavior for this test is shown in Fig. 9. Shown in the figure is the scaled location of the notch tip and CP crack size, along with the estimated plastic zone size surrounding the end of the CP crack tip. The results in Fig. 9 show that da/dN data taken immediately from the CP crack tip and in the vicinity of the starter notch start out slightly higher, but decrease rapidly to a reasonably steady growth rate after a distance slightly larger than one plastic-zone size. Based on these limited data, it appears that the requirement for crack extension following CP can be reduced to approximately a single r_p as suggested in the following:

$$\Delta a \geqslant 1/\pi \times (K_{\max,cp}/\mathrm{YS})^2 \qquad (2)$$

where, $K_{\max,cp}$, is the maximum compressive stress intensity used in precracking, and YS is the yield or flow stress of the material. Extending the precrack to two or more plastic-zone sizes further ensures that ensuing growth rates are well beyond the influence of the CP procedure.

Conclusions

Based on limited testing of two metallic alloys, it has been shown that the compression precracking method offers a simpler yet accurate alternative to the current ASTM load shed method for developing low crack growth rate data

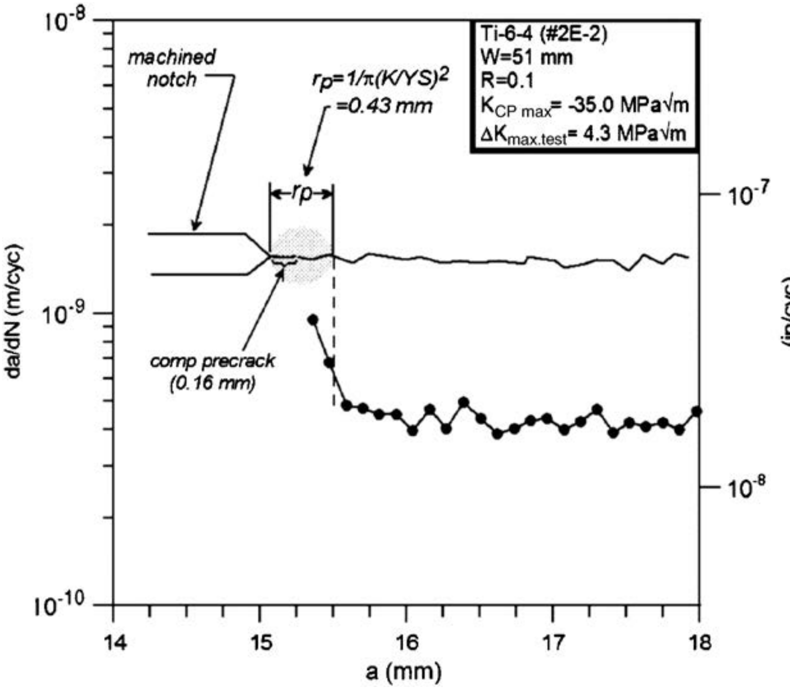

FIG. 9—*Crack growth rate data at* ΔK_{const} *for Ti-6Al-4V following CP.*

in the near-threshold and threshold regimes. Values of ΔK_{th} developed using compression precracking (CP) procedures were similar to or less than the current load shedding (LS) approach. Furthermore, when applying current E647 load shed procedures for threshold testing on the titanium alloy compact C(T) specimens, resulting values of ΔK_{th} were found to be dependent upon specimen width, a clear violation of fracture mechanics concepts that fatigue crack growth rate behavior can be correlated with the alternating stress intensity range, ΔK for a given stress ratio.

On the 7075-T651 alloy, very little difference in threshold stress intensity range was observed between the load-shedding and CPCA test methods. In contrast, the titanium alloy (Ti-6Al-4V) showed large differences between the CPCA and load-shedding test results in the near-threshold and threshold regimes for the low R ratio tests. Results under high R conditions ($R \geq 0.7$) agreed very well between the two-threshold test methods for both materials. On the titanium alloy, the load-shedding test method also produced a specimen width effect on near-threshold behavior, whereas the CPCA test method produced results that were independent of specimen width and produced "steady-state" constant-amplitude data in the near threshold regime, after the crack had grown a number of compressive plastic-zone sizes.

Acknowledgments

The Office of Naval Research under grant N00014-02-1-0379 sponsored this investigation. Special thanks to Dr. A. Vasudevan for his challenging discussions on residual stresses and crack-closure behavior; to Wright-Patterson Air Force Base for providing the titanium alloy material; and to Northrop Grumman Corporation for providing the 7075-T651 aluminum alloy material used in this study.

References

[1] ASTM E647 Standard, "Standard Test Method for Measurement of Fatigue Crack Growth Rates," *Annual Book of ASTM Standards*, ASTM International, West Conshohocken, PA, 2006.

[2] Topper, T. H., and Au, P., *Fatigue Test Methodology*, AGARD Lecture Series 118, The Technical University of Denmark, Denmark, 1981.

[3] Pippan, R., Plöchl, L., Klanner, F., and Stüwe, H. P., "The Use of Fatigue Specimens Precracked in Compression for Measuring Threshold Values and Crack Growth," *J. Test. Eval.*, Vol. 22, 1994, p. 98.

[4] Forth, S. C., Newman, Jr., J. C., and Forman, R. G., "On Generating Fatigue Crack Growth Thresholds," *Int. J. Fatigue*, Vol. 25, 2003, pp. 9–15.

[5] Newman, Jr., J. C., Schneider, J., Daniel, A., and McKnight, D., "Compression Pre-Cracking to Generate Near Threshold Fatigue-Crack-Growth Rates in Two Aluminum Alloys," *Int. J. Fatigue*, Vol. 27, 2005, pp. 1432–1440.

[6] "Damage Tolerance and Fatigue Evaluation of Structure," Federal Aviation Regulations, Title 14 Code of Federal Regulations, Part 25, Section 571.

[7] Pearson, S., "Initiation of Fatigue Cracks in Commercial Aluminum Alloys and the Subsequent Propagation of Very Short Cracks," *Eng. Fract. Mech.*, Vol. 7, No. 2, 1975, pp. 235–247.

[8] Newman, Jr., J. C., "A Nonlinear Fracture Mechanics Approach to the Growth of Small Cracks," *Behavior of Short Cracks in Airframe Components*, AGARD CP-328, North Atlantic Treaty Organization, 1983, pp. 6.1–6.27.

[9] Newman, Jr., J. C., "The Merging of Fatigue and Fracture Mechanics Concepts—A Historical Perspective," *Fatigue and Fracture Mechanics—28th Volume*, ASTM STP 1321, ASTM International, West Conshohocken, PA, 1997, pp. 3–51.

[10] Minakawa, K., and McEvily, A. J., "On Near-Threshold Fatigue Crack Growth in Steels and Aluminum Alloys," *Proceedings of International Conference on Fatigue Thresholds*, Vol. 2, Stockholm, Sweden, 1981, pp. 373–390.

[11] Newman, Jr., J. C., "Analysis of Fatigue Crack Growth and Closure Near Threshold Conditions," *Fatigue Crack Growth Thresholds, Endurance Limits and Design*, ASTM STP 1372, ASTM International, West Conshohocken, PA, 2000, pp. 227–251.

[12] Donald, J. K., and Paris, P. C., "An Evaluation of ΔK_{eff} Estimation Procedures on 6061-T6 and 2024-T3 Aluminum Alloys," *Proceedings of Fatigue Damage of Structural Materials II*, Cape Cod, MA, 1998.

[13] Marci, G., "A Fatigue Crack Growth Threshold," *Eng. Fract. Mech.*, Vol. 42, 1992, pp. 367–385.

[14] Tabernig, B., Powell, P., and Pippan, R., "Resistance Curves for the Threshold of Fatigue Crack Propagation in Particle Reinforced Aluminum Alloys," *Fatigue Crack Growth Thresholds, Endurance Limits and Design*, ASTM STP 1372, ASTM Inter-

national, West Conshohocken, PA, 2000, p. 96.

[15] Gallagher, J., et al., "Advanced High Cycle Fatigue (HCF) Life Assurance Methodologies," AFRL-ML-WP-TR-2005-4102, July 2004.

[16] James, M. A., Forth, S. C., and Newman, J. A., "Load History Effects Resulting from Compression Precracking," *Fatigue and Fracture Mechanics: 34th Volume*, ASTM STP 1461, ASTM International, West Conshohocken, PA, 2005.

[17] Yamada, Y., Newman, III, J. C., and Newman, Jr., J. C., "Elastic-Plastic Finite-Element Analyses of Compression Precracking and Its Influence on Subsequent Fatigue-Crack-Growth in the Near-Threshold Regime," *Fatigue and Fracture Mechanics: 36th Symposium*, Tampa, FL.

RESIDUAL STRESS EFFECTS ON FRACTURE

ASTM Special Technical Publication, Vol. 5, No. 9
Paper ID JAI101540
Available online at www.astm.org

Stephen M. Graham[1] *and Richard Stanley*[1]

Test Results from Round Robin on Precracking and CTOD Testing of Welds

ABSTRACT: A weld fracture toughness round robin test program was initiated by ASTM to evaluate a proposed annex to E1290-93 on fracture toughness testing of ferritic steel weldments. The focus of the round robin was on specimen preparation procedures and their effect on crack tip opening displacement (CTOD). The local compression procedure was used to reduce the influence of residual stress on precrack curvature. Specimens were tested at −196 °C, which is on the lower shelf for this metal, to minimize variability in fracture toughness and maximize influence of residual stress. Seven labs participated in the round robin and among them conducted 51 tests per E1290-93 to measure CTOD. Statistical analysis of the data showed that crack curvature decreased by 5.2 % ±2.1 % for each 1 % increase in local compression, over the range of compressions tested (0–2.9 % with a nominal target value of 1 %). However, mean values of curvature varied significantly between labs, and when results from all labs are considered, local compression of about 1 % did not reliably reduce crack front curvature. It appears that the procedure used is more important than the amount of local compression, as evidenced by the straight cracks obtained by two labs that exercised tight control on local compression. The statistical analysis revealed that the mean value of measured CTOD for all data with less than 10 % curvature was not statistically different than the mean for less than 20 %, as it is in BS7448 (1997). Perhaps the most surprising observation from this round robin is that there does not appear to be a correlation between CTOD measured at −196 °C and amount of local compression or crack front curvature.

Manuscript received November 8, 2007; accepted for publication September 4, 2008; published online October 2008.
[1] Mechanical Engineering, U. S. Naval Academy, 590 Holloway Rd., Annapolis, MD 21402.

Citation: Graham, S. M. and Stanley, R., "Test Results from Round Robin on Precracking and CTOD Testing of Welds," *J. ASTM Intl.*, Vol. 5, No. 9. DOI10.1520/JAI101540. Available online at www.astm.org. Also included in JAI Special Issue STP 1508, *Fatigue and Fracture Mechanics: 36th Volume,* R. W. Neu, K. R. W. Wallin, and S. R. Thompson, guest editors, ASTM International, West Conshohocken, PA, 2009, pp. 275-311.

KEYWORDS: welds, precracking, fracture toughness, local compression, CTOD

Introduction

A weld fracture toughness round robin test program was initiated by ASTM task group E08.08.07 in August 1998 to evaluate a proposed annex to E1290-93[2]on fracture toughness testing of weld metal in ferritic steel weldments. The annex was intended to address issues that are unique to testing of welds, such as terminology, notch placement, specimen straightening, hydrogen release, fatigue precracking in the presence of high residual stress, and post-test microstructural examination. The focus of the round robin was on specimen preparation procedures and their effect on crack tip opening displacement (CTOD). Another objective was to compare a new J-integral based CTOD equation with the traditional E1290-93 equation.

The material used in this round robin was taken from a 17.7 m length of tension leg platform tendon. The nominally grade X60 pipe of A707 steel was of 660 mm (26 in.) outside diameter pipe with a wall thickness of 33 mm (1.3 in.). The pipe contained a longitudinal seam weld created using a twin-wire double submerged arc welding process. A macrograph of the weld is shown in Fig. 1. A 7 m length of the tendon was selected for testing and further divided into three sections labeled *L* for left, *C* for center, and *R* for right, each 2.28 m long. Specimens were machined from the welded pipe in the NF orientation (crack plane normal <u>N</u>ormal to welding direction and crack <u>F</u>ollowing weld) with the notch centered in the weld. The specimens were square SE(B)'s with width and thickness of nominally 25 mm ($W/B=1$). The curvature of the pipe prevented the use of full-thickness specimens, which is preferable when testing welds. The decision was made not to attempt straightening the heavy-section pipe, therefore, the specimens were machined down from 33 mm to a nominal thickness of 25 mm. Forty-five pieces were cut from the weld, 15 from the left end (designated L1–L15), 15 from the center (C1–C15), and 15 from the right end (R1–R15). Five SE(B) specimens were cut from each piece. A randomized test plan was developed to determine what pieces would be sent to each lab.

The round robin referred to the proposed weld test annex for instructions on how specimens were to be prepared and tested. Only the local compression procedure was used to reduce the influence of residual stress on precrack curvature. In this procedure a rectangular or circular indenter is placed on the side of the specimen over the remaining ligament and force is applied to plastically deform the specimen in the thickness direction. However, the proposed annex did not identify which of three possible configurations of indentor was to be used, or whether indentation should be done from one side only, both sides consecutively, or both sides simultaneously. The proposed annex recommended a nominal indent depth of 0.5 % of the specimen thickness on each side (1 %

[2]E1290-93, Standard Test Method for Crack-Tip Opening Displacement (CTOD) Fracture Toughness Measurement.

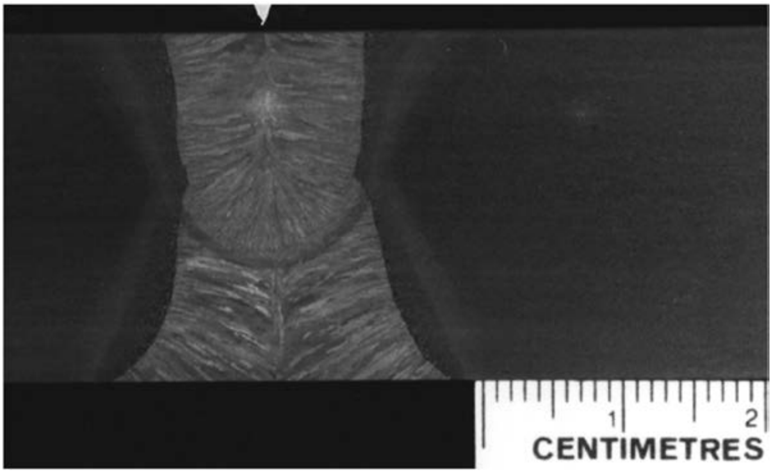

FIG. 1—*Optical macrograph of the round robin weld etched with 5 % Nital* (*Ref* [*1*]).

total plastic strain), however, the labs were not required to use this indent depth. Consequently, the labs were allowed to choose the type of indentor, the specific sequence of indentations, and the indent depth. Specimens were fatigue precracked to $0.45 \leqslant a_0/W \leqslant 0.55$ following the requirements in E1290-93 with the following additional limitation for the final 50 % of fatigue crack extension to account for the large temperature difference between precracking at ambient temperature and testing at LN_2 temperature (−196°C)

$$\frac{K_{\max}}{E} \leqslant \frac{\sigma_{\text{ys-ambient}}}{\sigma_{\text{ys-LN}_2}} \cdot 0.000\,096\sqrt{m} \pm 0.5\ \% \,. \tag{1}$$

The intent of this limitation was to avoid warm prestress effects that can occur if the size of the plastic zone introduced by precracking at high temperature is large compared with the size of the plastic zone produced by testing at low temperature. This requirement resulted in very low final ΔK values. The yield strength ratio in Eq 1 for the weld being tested was 0.66, yielding a maximum permissible $K_{\max}$ of 13.1 MPa$\sqrt{\text{m}}$ (11.9 ksi$\sqrt{\text{in.}}$). There was some misunderstanding concerning this, consequently, some labs precracked at $K_{\max}$ values that exceeded this limitation. Lab E got around this limitation by precracking some specimens at the test temperature −196°C. A memo with supplemental instructions was issued in November 1998 to relax this requirement and allow precracking at higher $K_{\max}$ values. The modified requirement specified that for the final 2.5 % of the final crack length, both of the following conditions must be met:

$$\frac{K_{\max}}{E} < 0.005\sqrt{\text{mm}} \quad \text{or} \quad \frac{K_{\max}}{E} < 0.001\sqrt{\text{in}}, \tag{2}$$

$$K_{\max} < \frac{\sigma_{\text{ys-precracking}}}{\sigma_{\text{ys-test}}} \cdot 0.6K_q, \tag{3}$$

where:

$$K_q = \sqrt{J_q E}, \tag{4}$$

$$J_q = \frac{K^2(1-\nu^2)}{E} + \eta_c \frac{A_c}{Bb}, \tag{5}$$

$$\eta_c = 3.785 - 3.101\left(\frac{a}{W}\right) + 2.018\left(\frac{a}{W}\right)^2, \tag{6}$$

$$K = \frac{PS}{BW^{3/2}} f\left(\frac{a}{W}\right), \tag{7}$$

$$f\left(\frac{a}{W}\right) = 3\sqrt{\frac{a}{W}}\frac{\left\{1.99 - \frac{a}{W}\left(1-\frac{a}{W}\right)\left[2.15 - 3.93\frac{a}{W} + 2.7\left(\frac{a}{W}\right)^2\right]\right\}}{2\left(1+2\frac{a}{W}\right)\left(1-\frac{a}{W}\right)^{3/2}}. \tag{8}$$

These requirements are very similar to those in E399-90, with the exception that $K_{\max}/E$ is half of what is allowed in E399-90. In Eq 5, A_c is the area under the load versus plastic crack mouth opening displacement (CMOD) curve up to the point of fracture. To calculate A_c, CMOD is separated into elastic and plastic components based on the initial measured elastic compliance, which is calculated using a least-squares regression on the linear part of the experimental load versus CMOD data. A comparison of the initial and revised requirements will be presented in the discussion of results.

Ten laboratories offered to participate in the round robin. Each lab was sent a total of 15 fracture toughness specimens, 5 from one piece marked L, 5 from a piece marked C, and 5 from a piece marked R. The first specimen was intended to verify that the local compression procedure produced an acceptably straight precrack. This specimen (referred to as a validation specimen in the proposed annex) was prepared using local compression and precracked at room temperature following the requirements given above to a final precrack length of a_0. Instead of conducting a test on this specimen to measure CTOD, the precracking was continued until the crack extended through at least 40 % of the remaining ligament (W-a_0). The specimen was then broken open and measurements were made of the precrack (a_0) and final crack (a_f). The curvature of the cracks was considered acceptable as long as the precrack met the requirements of E1290-93 and the difference between any two of the inner seven measurements of the final crack length were within 20 % of the nine-point average a_f.

The sequence for the remaining tests was developed using a randomized plan to minimize bias due to location of the specimen blank in the weld. Typical specimen assignment and test sequence are shown in Tables 1 and 2, respec-

TABLE 1—*Specimen assignment for one lab.*

Test temperature	Specimen mark		
	Block *L*	Block *C*	Block *R*
RT	L5-2	C15-1	R10-5
−196°C	L5-5	C15-5	R10-3
−196°C	L5-4	C15-3	R10-2
Validation	L5-3		
1st reserve		C15-4	R10-4
2nd reserve	L5-1	C15-2	R10-1

tively. The block numbers, specimen assignments, and test sequence were randomized, so these tables were different for each lab. Three specimens were to be tested at ambient temperature in order to obtain a δ_m test result and to assess a new CTOD calculation procedure that would require the participants to perform the analytical separation of the CMOD into its two components — elastic and plastic. At the time, the equations for CTOD in E1290-93 were based on a rotation point and did not require separation of CMOD or calculation of J.

Six specimens were to be tested at the boiling point of liquid nitrogen, LN_2 (−196°C). This temperature was chosen on the lower shelf for this metal to minimize variability in fracture toughness and maximize the influence of residual stress. Tests at this temperature resulted in measurements of δ_c. All tests were conducted following the procedures in E1290-93. CTOD was calculated using the equations in E1290-93, and the proposed annex method for calculating CTOD given in Eqs 4–11 [2],

$$\mathrm{CTOD}_q = \frac{J_q}{m\sigma_{\mathrm{flow}}^{\mathrm{weld}}}, \tag{9}$$

TABLE 2—*Test sequence for one lab.*

Test sequence	Test temperature	Parent block
0	Validation	*L*
1	−196°C	*C*
2	−196°C	*C*
3	Ambient	*C*
4	Ambient	*R*
5	−196°C	*R*
6	−196°C	*R*
7	−196°C	*L*
8	−196°C	*L*
9	Ambient	*L*

Note: Remaining five specimens held in reserve.

TABLE 3—*Strength and modulus values for the round robin test weld.*

		Strengths and moduli (MPa)			
Constituent	Temperature (°C)	Elastic modulus	0.2 % offset yield strength	Ultimate strength	Flow strength[a]
Plate	Ambient	205 944	514	593	554
Plate	−196	218 392	848	960	904
Weld	Ambient	205 944	548	593	571
Weld	−196	218 392	888	989	939

[a]Average of yield and ultimate strengths.

$$m = 1.221 + 0.793\frac{a}{W} + 2.751n - 1.418n\frac{a}{W}, \tag{10}$$

where n is the strain hardening exponent for the weld metal that can be determined from a true stress-true strain curve or estimated using the following equation:

$$n = 1.724 - 6.098\frac{\sigma_{ys}}{\sigma_{ult}} + 8.326\left(\frac{\sigma_{ys}}{\sigma_{ult}}\right)^2 - 3.965\left(\frac{\sigma_{ys}}{\sigma_{ult}}\right)^3. \tag{11}$$

Specimens indicated as "reserve" in Table 1 could be used as replacements for specimens that did not meet the validity requirements of E1290-93. The replacement specimen was to be taken from the same block as the invalid specimen and was to be taken in the order shown to maintain the randomized test plan. The tensile properties of the weld at ambient and LN_2 temperatures are given in Table 3.

Round Robin Results

Of the ten labs that volunteered to participate in the round robin, four of them conducted all of the requested tests, three conducted some of the tests, and three did not participate. The tests conducted by each of the labs are summarized in Table 4.

Validation Tests

A total of eight validation specimens were subjected to local compression ranging from 0.5 to 2.9 %. The resulting curvature of the initial and final cracks is compared with the requirements of E1290-93 and the proposed weld annex in Table 5. In all cases, the cracks extended more in the center than at the edges. This is consistent with the weld residual stress field measured by Meith [3], however, the residual stress field is modified by local compression. Mahmoudi [4] showed that local compression performed simultaneously on both sides of a flat plate without a notch using a circular indentor would leave a compressive residual stress in the center. However, the presence of the notch and the posi-

TABLE 4—*Tests conducted by each of the participating labs.*

Lab code	Number of tests at −196°C	Number of tests at room temperature	Number of validation tests
B[a]	8	4	2
C	8	4	0
D	2	3	1
E[a]	6	3	1
F[a]	11	3	1
I	6	2	2
J[a]	10	3	1

[a]Labs that completed the requested tests (6 @ −196°C, 3 @ RT, and 1 validation).

TABLE 5—*Comparison of validation specimen cracks with requirements.*

Lab code	Local compression (%)	Pre-crack curvature[a] (%)	Final crack curvature[b] (%)	Precrack extension ratio[c]	Crack growth ratio[d]
J	1.2	23.3 FAIL	5.9 PASS	1.4 PASS	1.3 PASS
B	2.9	5.5 PASS	7.7 PASS	2.6 PASS	1.0 PASS
B	1.9	10.1 FAIL	11.4 PASS	2.2 PASS	1.1 PASS
F	0.8	4.0 PASS	2.7 PASS	5.7 PASS	0.6 FAIL
I	0.5	36.2 FAIL	8.2 PASS	3.6 PASS	0.7 FAIL
I	1.2	15.8 FAIL	8.4 PASS	6.4 PASS	0.8 FAIL
E	1.2	10 PASS	5.0 PASS	1.5 PASS	1.0 PASS
D	0.9	16.1 FAIL	12.3 PASS	4.6 PASS	1.0 PASS

[a]Difference between maximum and minimum of nine initial crack length measurements divided by average initial crack length. E1290-93 allows a maximum 10 % curvature for the initial crack.

[b]Difference between maximum and minimum of seven inner final crack length measurements divided by average final crack length. Proposed weld annex allows a maximum of 20 % curvature for the final crack.

[c]Mimimum crack extension from notch is lesser of 0.025 W or 1.3 mm. Number shown is actual minimum extension divided by allowable minimum extension.

[d]Proposed weld annex states that minimum allowable crack extension, difference between initial and final average crack lengths, is 40 % of the initial ligament (W-a_o). Number shown is actual difference divided by allowable.

TABLE 6—*Comparison of validation specimen crack curvatures based on thickness B.*

Lab code	Local compression (%)	Pre-crack curvature[a] (%)	Final crack curvature[a] (%)	Precrack extension ratio	Crack growth ratio
J	1.2	12.4 FAIL	6.3 FAIL	1.4 PASS	1.3 PASS
B	2.9	2.8 PASS	6.3 FAIL	2.6 PASS	1.0 PASS
B	1.9	5.2 FAIL	8.2 FAIL	2.2 PASS	1.1 PASS
F	0.8	1.9 PASS	2.6 PASS	5.7 PASS	0.6 FAIL
I	0.5	21.3 FAIL	16.9 FAIL	3.6 PASS	0.7 FAIL
I	1.2	9.4 FAIL	7.4 FAIL	6.4 PASS	0.8 FAIL
E	1.2	5.3 FAIL	4.7 PASS	1.5 PASS	1.0 PASS
D	0.9	8.4 FAIL	8.9 FAIL	4.6 PASS	1.0 PASS

[a]Difference between maximum and minimum of nine initial crack length measurements divided by specimen thickness. Allowable curvature is 5 %.

tion of the indentor can significantly influence the resulting residual stress field [5]. Depending on the diameter of the indentor and its location relative to the crack tip, the residual stresses due to local compression at the crack tip could be tensile or compressive. Since the exact procedure used for local compression by each lab is not known, it is not possible to predict the resulting residual stress field. Only two specimens met all the requirements of the proposed annex, thereby indicating that in most cases, acceptably uniform residual stresses were not achieved by the precrack preparation procedure. All eight specimens easily met the minimum precrack extension requirement, but three failed the crack growth requirement. Only three out of eight specimens had initial precracks straight enough to meet the E1290-93 requirements. However, it is interesting to note that all of the final cracks meet the relaxed requirement of 20 % based on inner seven measurements, and six of those are actually less than 10 %. This is partly because the allowable curvature is proportional to the average crack length, therefore it increases as the crack gets longer.

In order to obtain a better sense of absolute curvature, the results were reanalyzed using the specimen thickness instead of average crack length, and using all nine measurements for both initial and final cracks. Since the initial crack length for these specimens is about $0.5B$ ($W/B=1$ and $a_0/W \sim 0.5$), a curvature equal to 10 % of the crack length (E1290-93 maximum) would translate to 5 % of the thickness. Therefore, an allowable absolute curvature for both initial and final cracks is set at 5 % of B and the curvatures are recalculated, as shown in Table 6. Now it is possible to directly compare initial and final absolute curvatures. Looking at the results this way shows that the final cracks are

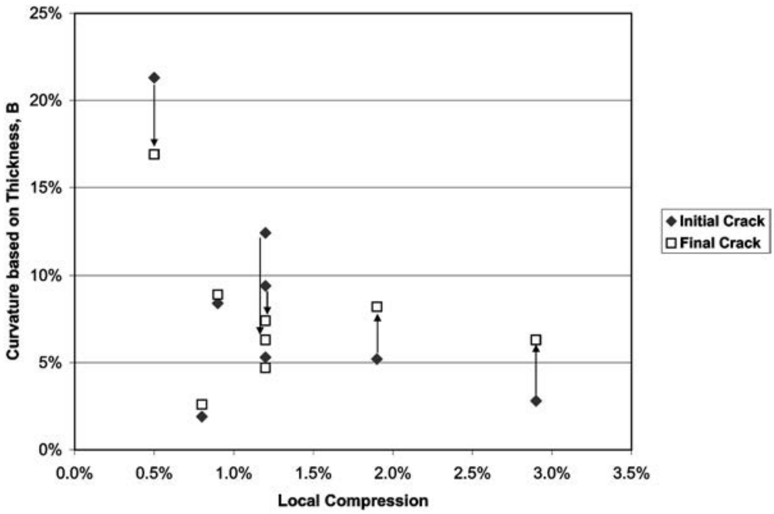

FIG. 2—*Influence of local compression on curvature for validation specimens with thickness used to calculate curvature.*

not necessarily any less curved than the initial cracks. Six of the eight final cracks now fail the 5 % allowable curvature, and in most cases if the initial crack fails, so does the final crack. It can also be seen that increasing the amount of crack extension from the notch did not necessarily decrease the curvature. In one test where the extension was 6.4 times the minimum, the curvature was 9.4 % while in another test with an extension of 1.5 times the minimum, the curvature was 5.3 %. Curvature is plotted as a function of percent local compression in Fig. 2. With the exception of one test, there does seem to be a decrease in absolute curvature as the amount of local compression increases, and it is evident that cracks do not generally get straighter as they grow.

In order to get an engineering sense of how curvature influences the stress intensity factor, the work of Towers and Smith [6] was evaluated relative to the proposed definition of absolute curvature. Towers used finite element analysis (FEA) to determine the stress intensity factor at the center and surface of a compact tension specimen for circular cracks with radii varying from 0.65B to 3.00B. In all cases, the crack length at the surface was equal to the thickness, B, and the specimen width, W, was 2B. They used a three-point measurement of average crack length from E399-83 to calculate a normalized stress intensity factor (K_{FEA}/K_{E399}) and curvature, $(a_{avg}-a_s)/a_{avg}$, where a_{avg} is the three-point average crack length and a_s is the surface crack length. E1290 uses a nine-point measurement of average crack length, so the normalized stress intensity was recalculated using the nine-point measurement for K_{E399}, and curvature was recalculated using the absolute curvature, as defined in Table 6. The resulting normalized stress intensity factor at the center and surface is plotted versus absolute curvature in Fig. 3. For a straight crack the maximum K occurs in the

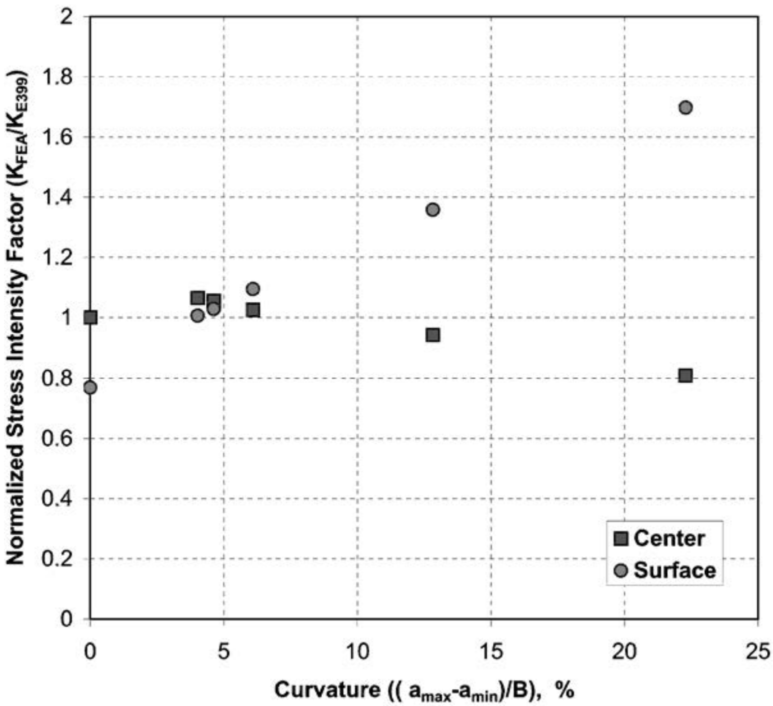

FIG. 3—*Influence of curvature on stress intensity factor.*

center and the surface *K* is 77 % of *K* based on the average crack length. As curvature increases, the normalized *K* at the center exhibits a small elevation and then gradually decreases, while the surface increases steadily. At 5 % curvature, which is the proposed limit on absolute curvature, the center and surface normalized *K* values are very close to each other, and are less than 6 % higher than *K* based on the average crack length. Therefore, at 5 % curvature, the stress intensity factor is actually more uniform across the crack front than it is for a straight crack, and the error incurred by using the nine-point average crack length in the E399 *K* equation is less than 6 %. Although these results are for a compact tension specimen, it is expected that the results would be very similar for a bend specimen.

CTOD tests

The objectives of the CTOD tests at LN_2 temperature were: (1) to evaluate the influence of residual stress, and measures taken to minimize it, on crack front curvature, and (2) to evaluate the influence of specimen preparation and precracking procedures on CTOD. Unfortunately, the actual residual stress in any specimen is unknown, so it can only be inferred through crack curvature. For the purposes of this study, crack front curvature is defined as the difference between the longest and shortest of the nine physical crack length measure-

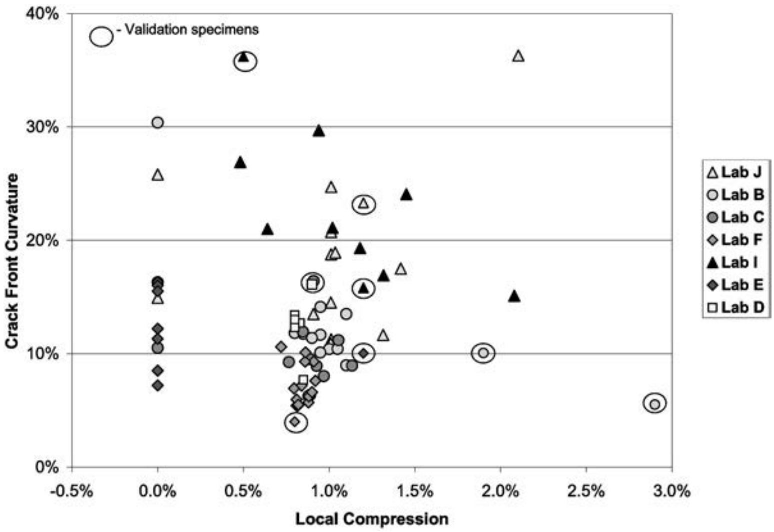

FIG. 4—*Crack front curvature versus percent local compression.*

ments divided by the average. The room temperature tests had the additional objective of comparing CTOD values calculated using the established E1290-93 equations with new equations presented in the proposed weld test annex, which were presented in the introduction. The annex equations were adopted into E1290 in 2002 (E1290-02).

The data were statistically analyzed using analysis of covariance [7] to look for trends between different variables. A detailed description of the statistical analysis is presented in the Appendix. Only the conclusions from the statistical analysis are presented in the following discussion of results.

The relationship between crack front curvature and percent local compression is shown in Fig. 4. The maximum curvature appears to decrease as local compression is increased, however, the minimum curvature does not appear to be influenced by amount of compression. This is consistent with the results for the validation specimens shown in Fig. 2. Analysis of covariance was used to determine if the apparent trend is statistically significant. The analysis, which is discussed in detail in the Appendix, indicates that curvature decreased by 5.2 % ± 2.1 % for each 1 % increase in local compression, over the range of compressions tested. However, interpolated mean curvatures differed among labs even for the same compression. Range and minimum curvature for no local compression (7–30 %) was only slightly different than the range with 1 % ± 0.5 % local compression (4–36 %). However, labs that achieved the tightest control on local compression achieved the straightest cracks. Lab F controlled compression to 0.82 ± 0.10 % and achieved curvatures of less than 10.6 %, with only two specimens above 10 %. As the range in local compression increased for any lab, the range in crack curvature also increased. 26 out of 77 specimens had crack curvature of 10 % or less, and two of those had no local compression at all. When each lab is considered separately, it does appear that

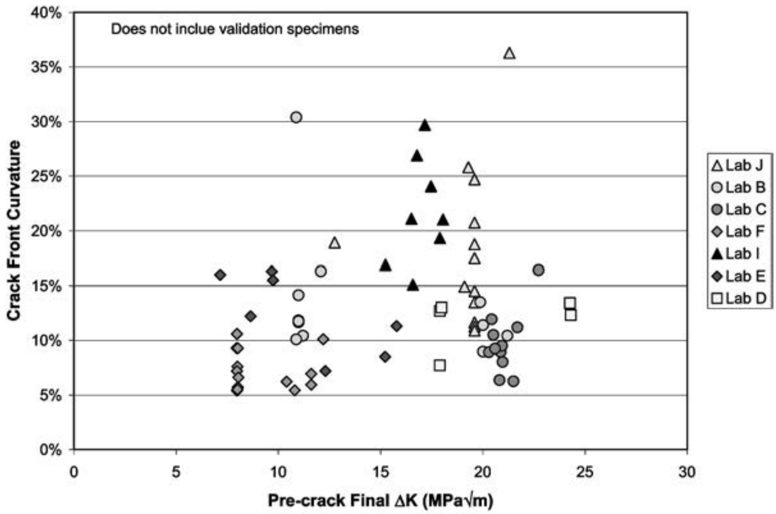

FIG. 5—*Crack front curvature versus final* Δ*K*.

curvature decreases as local compression increases. Labs B and I are the best examples of this. For lab B, curvature was over 30 % with no compression. It decreases to about 12 % at 1 % compression and to about 7 % at almost 3 % compression. Labs J and I show a similar trend, but with more variation, and there is one outlier for lab J where curvature was over 35 % at slightly over 2 % compression. The data for labs C and F is so closely grouped that no trend can be identified. Lab E chose to precrack all but one validation specimen with no compression at all.

A graph of crack front curvature against final ΔK for precracking is shown in Fig. 5. When data from all labs is grouped together, final ΔK appears to have more effect on maximum curvature than percent local compression, but this may be misleading due to differences among labs. When each lab is considered separately, there is no clear trend. When the lab means of the two variables are compared, the estimated slope is an increase of 0.4 % in curvature for a 1 MPa$\sqrt{}$m increase in ΔK, but this correlation is not statistically significant. Lab F had good success with producing straight cracks and all specimens were precracked with a final ΔK of less than 13 MPa$\sqrt{}$m. Lab B also had good success with final ΔK values of about 12 and 20 MPa$\sqrt{}$m, with no obvious difference in curvature between the two. On the other hand, lab C precracked at a final ΔK of around 20 MPa$\sqrt{}$m, and had 7 out of 11 specimens with curvature of less than 10 %. With only one exception, precracking at low ΔK ($<$13 MPa$\sqrt{}$m) lead to curvature of less than 20 %. 59 out of 69 specimens have curvature of less than 20 %. Note that the minimum curvature is about 5 % and is not influenced by final ΔK, so precracking at a higher ΔK does not appear to cause curvature in a crack that otherwise would have been relatively straight.

In Fig. 6 the influence of final ΔK is evaluated by comparing it directly with the room temperature CTOD calculated using the annex equations. The annex

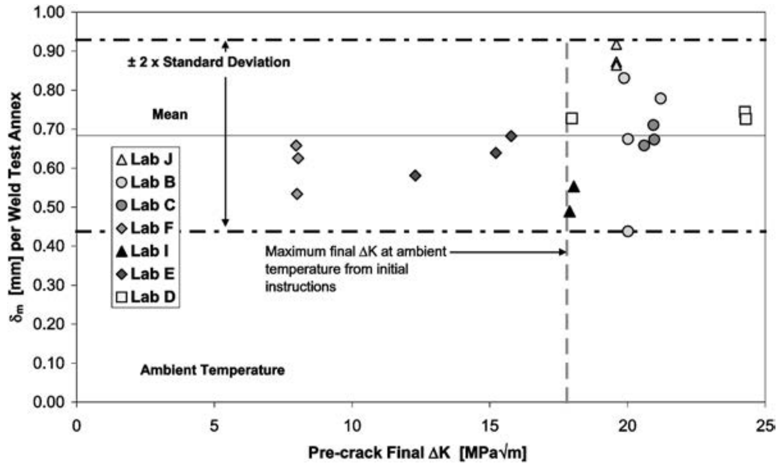

FIG. 6—*CTOD (δ_m) versus final ΔK for ambient temperature tests.*

value of CTOD was chosen instead of the E1290-93 value here and in the following graphs because a benchmark comparison showed there is less variation in the annex CTOD values calculated by the labs. Consequently, the variation in CTOD is related more to the parameter being evaluated than to difficulties in calculating CTOD. More will be presented on the benchmark comparison later. The maximum final ΔK as defined in the initial instructions is shown on graph. Maximum final ΔK for the revised instruction, requirement 1, is 29.3 MPa$\sqrt{}$m, which is beyond the maximum range of the ΔK axis.

There appears to be a slight elevation of δ_m with increasing final ΔK at ambient temperature, but the correlation is far from consistent among the labs. Mean and plus or minus two standard deviations assuming normally distributed data are shown on the graph. Mean for the weld annex equations is 0.683 mm and standard deviation is 0.123 mm. The mean for the E1290-93 equations is lower and the standard deviation is higher (0.607 and 0.160 mm), indicating that there is more scatter in the E1290-93 CTODs. More will be presented on a comparison of the two equations for CTOD later.

The same comparison is presented for the LN_2 temperature tests in Fig. 7. The maximum final ΔK for the initial and revised instructions, requirement 1, are shown as dashed lines on the graph. 30 out of 50 tests exceeded the maximum final ΔK for the initial instructions. It is interesting to note that, although the revised instructions were an attempt to increase the maximum ΔK and allow more data to be valid, they actually had the opposite effect. With the revised instruction, requirement 1, 37 tests exceeded the maximum final ΔK, and only two that were invalid by previous instruction became valid. The range of ΔK for any one lab is too small to determine whether final ΔK influences CTOD, however, when all of the data is considered, it appears that precracking at high ΔK may cause a slight increase in CTOD. Regression of lab means (excluding the outlier from lab F) produced an estimated increase of 0.000 117 mm for each unit of ΔK. This increase may be due to warm prestress

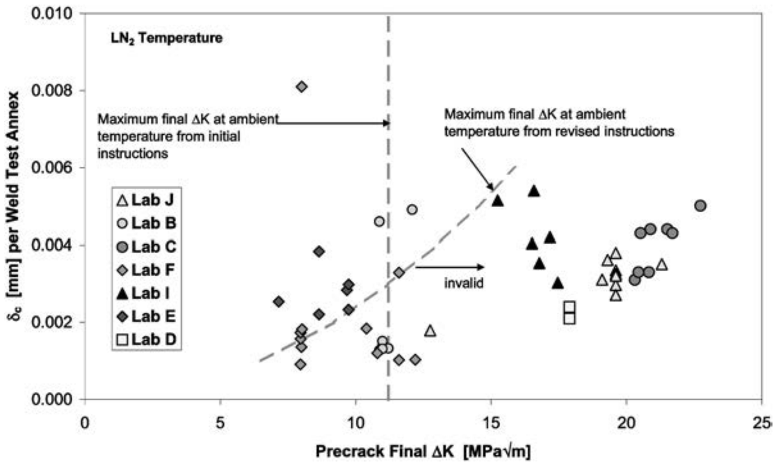

FIG. 7—*CTOD* (δ_c) *versus final* ΔK *for* LN_2 *tests.*

effects [8], however, data presented by Chen et al. [9] indicates that increases in fracture toughness do not become significant until the prestressing load approaches general yielding. The highest final precracking loads for this round robin were less than 30 % of general yielding. Consequently, it is not likely that the slight increase in CTOD is due to warm prestress effects.

The calculated CTOD is correlated directly with curvature in Fig. 8 for the room temperature tests and in Fig. 9 for LN_2 temperature. There is a lot of

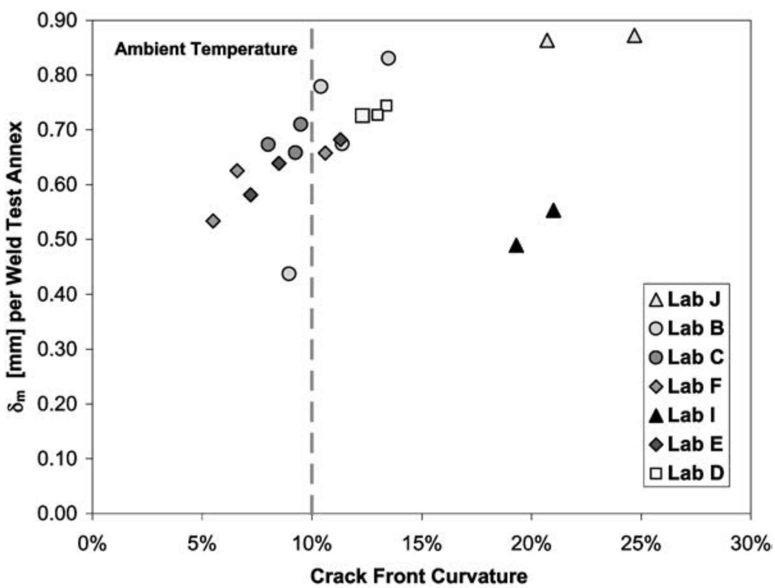

FIG. 8—*CTOD* (δ_m) *versus crack front curvature for ambient temperature tests.*

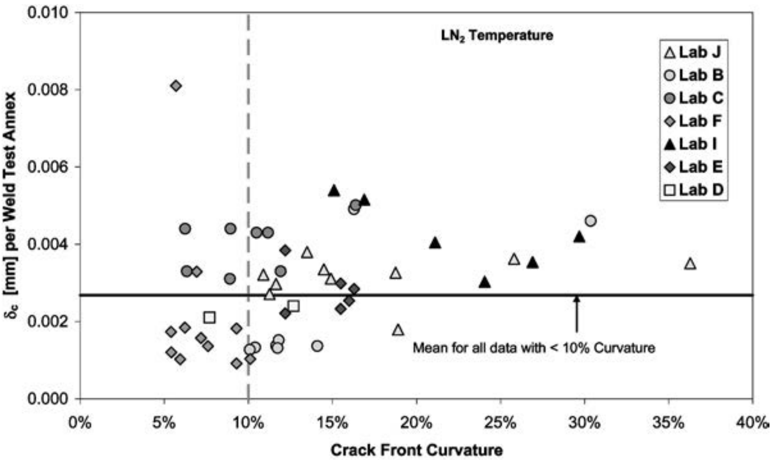

FIG. 9—*CTOD* (δ_c) *versus crack front curvature at* LN_2 *temperature.*

variation in δ_m, which may be due to difficulties in determining the P_m and v_m at first attainment of the maximum load plateau. When considering the data for any one lab, only lab B shows a statistically significant increase in δ_m with increasing curvature. This is partly because the range of curvature for each lab is small. However, were it not for the data from lab I, it would appear that δ_m decreases as the crack curvature drops below 10 %. The estimated slope is 0.0118 ± 0.0152 mm (95 % confidence) per percent of curvature.

It is typical to see large variation in CTOD for welds. Examples of this are seen in the data for labs B and F in Fig. 9 where there are several tests with δ_c of less than 0.002 mm, and then there are one or two tests with δ_c in the range of 0.004–0.008 mm. For lab F the high value occurred with curvature of around 7 %. The mean value based on annex CTOD equations for all cracks with less than 10 % curvature is 0.002 68 mm, and the 95 % confidence bounds are 0.001 72–0.003 63 mm. It is interesting to note that if the limit on curvature were increased to 20 %, as it is in BS7448: Part 2 (1997), the mean would only increase to 0.002 84 mm with 95 % confidence bounds of 0.002 40–0.003 29 mm. The overlap of the confidence bounds shows that, at the 95 % confidence level, there is not a statistically significant difference in the mean values. Note that these confidence bounds are very large relative to the mean values. This is partly due to the large scatter in the data and partly due to the small sample size. There appears to be a small increase in δ_c as curvature increases above 20 %; however, the estimated slope is $0.000\,063 \pm 0.000\,086$ mm (95 % confidence) per percent of curvature, which is not statistically different than zero. The data in Fig. 9 was also examined to determine if location in the weld influenced CTOD, and it was found that there was no discernable difference in the mean or scatter between segments *L*, *C*, and *R*.

There does not appear to be a correlation between CTOD and amount of local compression for either ambient or LN_2 temperatures, as shown in Figs. 10

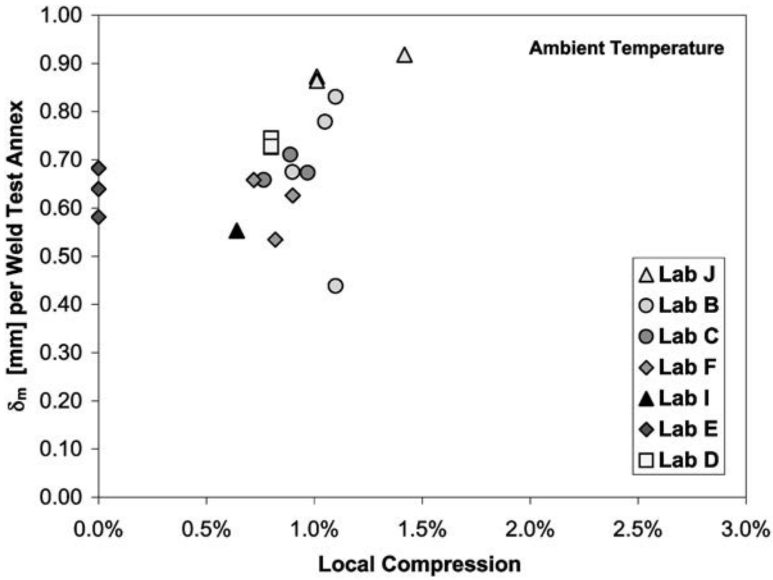

FIG. 10—*CTOD versus local compression at ambient temperature.*

and 11. One would expect compressive residual stresses to increase CTOD and tensile stresses to lower it. It is also expected that residual stresses would have more influence at lower temperatures where there is less plasticity. Comparison

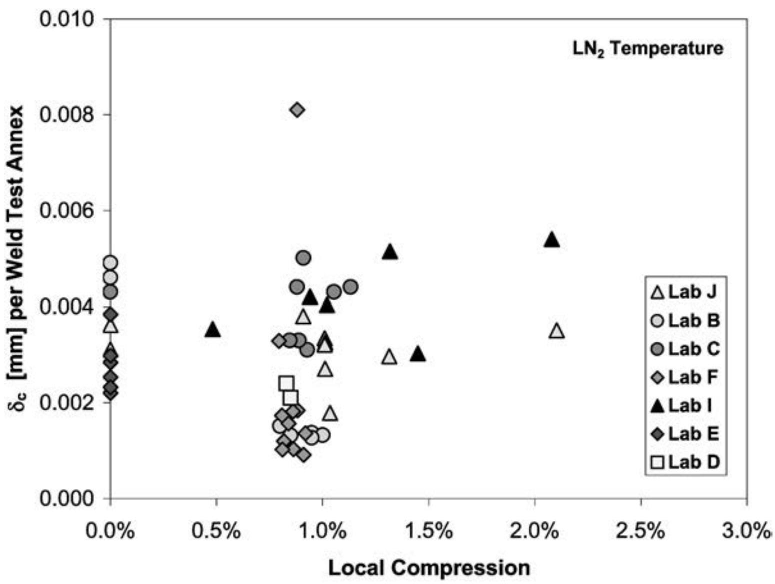

FIG. 11—*CTOD versus local compression at* LN_2 *temperature.*

of the lowest measured CTOD values at LN_2 temperature with and without local compression indicates that local compression increased the tensile residual stresses (or decreased the compressive residual stresses), thereby resulting in a decrease in CTOD. Note in Fig. 11 that the labs with the closest control of their local compression procedure (lab F with exception of two high values and lab B) also tended to measure the lowest values of CTOD. This indicates that they were able to achieve a consistent modification of the residual stress field. Compare these CTOD data with those from lab C that achieved similar amounts of local compression and yet measured significantly higher CTOD values. This variation in mean CTOD values for the labs has repeatedly confounded attempts to draw conclusions from the data and indicates the presence of an uncontrolled variable in this round-robin test program. The parameters used in performing the local compression can have a significant effect on the resulting measured CTOD. Meith [3] showed that moving the position of the center of a 12.7 mm diameter platen on a SE(B) specimen with $W=25.4$ mm from 1.8 mm behind the crack tip to 1.8 mm in front of it decreased the fracture toughness by 56 %. Mahmoudi [4] also showed that platen diameter and location have a significant effect on the load at failure. The results in Fig. 11 indicate that fracture toughness is insensitive to the amount of local compression. This observation is confirmed by Meith [3] where fracture toughness decreased about 60 % compared to the as-received weld when local compression of 0.5 % was applied, and did not change much for local compression up to 2 %. All of this indicates that the size and location of the platen used to perform local compression are more important that the amount of compression.

One of the objectives of this round robin was to compare CTOD values calculated using the E1290-93 equations with new equations in the proposed weld annex. Graphs of CTOD calculated using these two equations are presented in Figs. 12 and 13 for ambient and LN_2 temperatures, respectively. The CTOD values shown in both graphs are as reported by the labs, with the exception of lab I, which conducted the tests and did not analyze the data, and lab E, which did not calculate CTOD using the weld annex equations and had some errors in their E1290-93 analysis. For these two labs, data ware analyzed by the authors. Referring to Fig. 12, lab C did not calculate CTOD per E1290-93 for one test, hence, the data point on the vertical axis. With the exception of the three tests run by lab J and one test by lab I, the weld annex CTOD values are within ±10 % of the E1290-93 values for ambient temperature tests. The weld annex equations tend to yield higher δ_m, with 15 out of 21 specimens having annex δ_m greater than E1290-93 δ_m. It appears that there may be errors in the initial crack lengths for the three specimens from lab J because there is a large difference in measured and theoretical initial compliances. Overestimating the initial crack length causes CTOD per E1290-93 to go down and CTOD per the annex equations to go up. The difference is predominantly caused by the effect of initial crack length on the plastic part of CTOD. For this reason, the difference is most pronounced for ambient temperature tests where the plastic part of CTOD is large relative to the elastic part. At LN_2 temperature, where the plastic part is small relative to the elastic part, errors in initial crack length cause much smaller differences between E1290-93 and annex calculations of

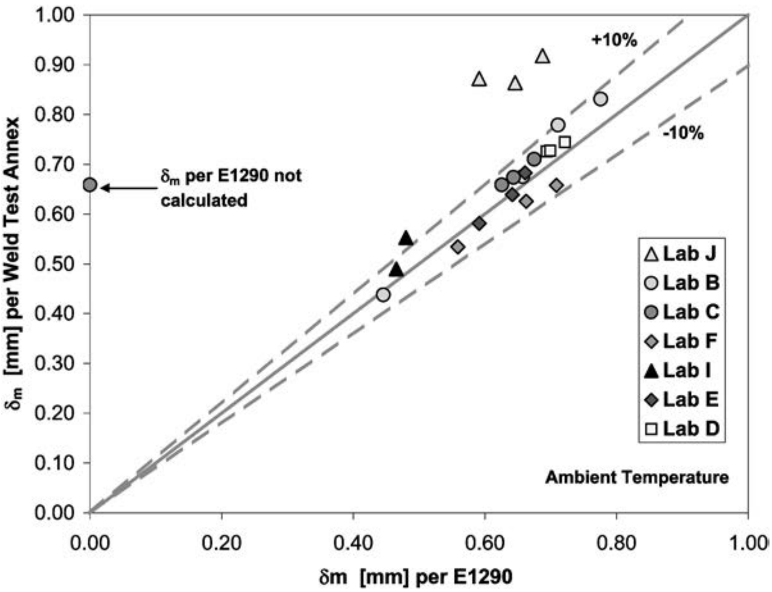

FIG. 12—*CTOD per weld annex versus CTOD per 1290 at ambient temperature as calculated by labs.*

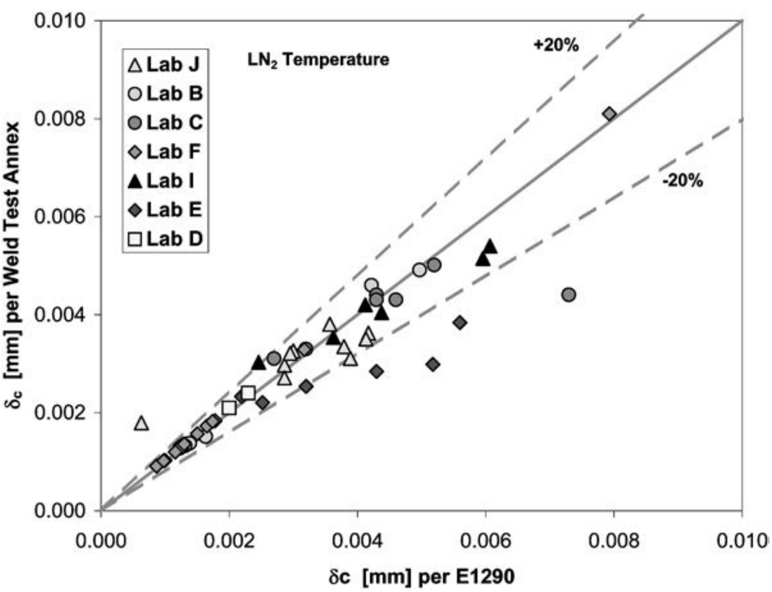

FIG. 13—*CTOD per annex versus CTOD per E1290-93 at* LN_2 *temperature as calculated by labs.*

CTOD. It is important to note that initial crack length does affect the elastic part of CTOD, but it has about the same effect for both E1290-93 and annex equations, so the net difference is small.

Referring to Fig. 13, there is more discrepancy between E1290-93 and annex calculations of CTOD on the lower shelf where the plastic part of CTOD is small. With the exception of three points from lab E, and one point each from labs J and C, the error is within ±20 %. For labs J, I, and E there is a tendency for the weld annex equations to yield lower CTOD values than the E1290-93 equations, and the difference increases as CTOD increases. Labs B, D, and F do not exhibit this tendency. Three E1290-93 CTOD values for lab E came out high relative to the annex CTODs because there was an anomaly similar to a pop-in in each test record that caused an increase in CMOD with no corresponding increase in load. This increased the plastic part of CMOD, which the E1290-93 equations are sensitive to. The anomaly had much less effect on the annex calculations because they are based on plastic area. The raw data for the one test from lab C with a large discrepancy were not available, so the cause for the discrepancy could not be checked. This round robin was started in 1998. Unfortunately, the organizers moved on to other jobs before the round robin was finished, so the data collection and analysis were incomplete. When efforts were made to complete the data analysis after several years of dormancy, it was very difficult to get any additional information. Often the people that ran the tests were no longer at the lab, they did not remember the details about the tests, or the records were lost. The test temperature was solidly on the lower shelf for this alloy, so inadequate temperature control would is not likely to lead to pop-ins because it would be difficult to go colder than −196°C when using liquid nitrogen to chill the specimens, and it would be unusual for pop-ins to occur at higher temperatures while not occurring at −196°C. These discrepancies point out the importance of carefully controlling all variables in a round-robin test program.

It is difficult to determine the cause of the discrepancies between E1290-93 and annex calculations of CTOD by the labs, or whether the discrepancy is due more to the E1290-93 or annex calculation. For example, one test from lab J falls well to the left of the +20 % line in Fig. 13. Is this due to a low value of CTOD by the E1290-93 equation, or a high value by the annex equation? A benchmark was needed to establish verified calculations for both E1290-93 and annex equations. To address this problem, a benchmark analysis was run on all tests where the raw data were available. The benchmark analysis was developed by the authors using MathCAD, and the same analysis was applied to all specimens. The benchmark analysis included both the E1290-93 and annex equations so that comparisons could be made between benchmark and lab analysis for each calculation method. Not all labs provided raw data with their results, and lab E did not calculate CTOD using the annex equations, so it was only possible to perform the annex benchmark for four labs and the E1290-93 benchmark for five labs. The comparison for the annex equations at LN_2 temperature is shown in Fig. 14. With the exception of two points from lab B and two from lab E where the lab values for CTOD are much larger than the benchmark, the values are within ±10 %. This comparison indicates that in most cases the labs were able to effectively calculate CTOD for low temperature tests

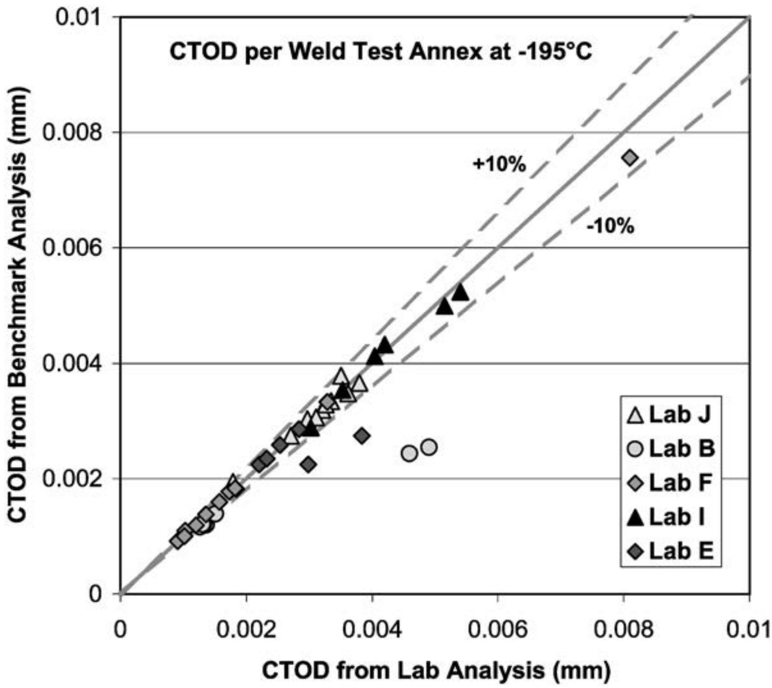

FIG. 14—*CTOD per annex, comparison of benchmark with lab analysis at* LN_2 *temperature.*

using the proposed weld annex equations. The two tests from lab E where lab CTOD values are higher than the benchmark both had significant pop-ins. The benchmark analysis included a significance check for pop-ins, while the lab analysis did not. This accounts for the lower benchmark CTOD values. The cause of the two large annex CTOD values for lab B could not be determined because the details of the lab analysis were not provided, but it appears to be due to errors in the elastic modulus used, and the calculation of m in Eq 10.

At ambient temperature the correlation between benchmark and lab analysis for annex equations is similar to LN_2 temperature, as shown in Fig. 15, with all data falling within the ±10 % lines.

There is considerably more variability in CTOD values at LN_2 temperature using the E1290-93 equations than there was using the proposed weld annex equations, as shown in Fig. 16. There are 21 points that fall outside the ±10 % lines, with most of them having the lab analysis CTOD greater than the benchmark. The CTOD values shown for lab E are as reported, and as mentioned previously, there were errors in their analysis that led to significant overestimation of CTOD for three specimens. Note that the lab calculations of CTOD for two specimens from lab B are also significantly larger than the benchmark. These are the same two specimens that were mentioned in the previous discus-

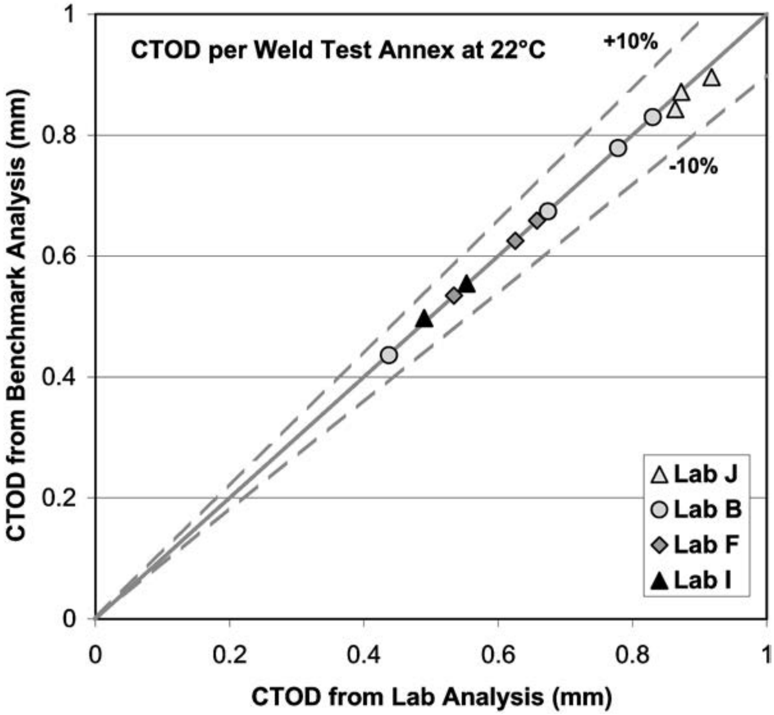

FIG. 15—*CTOD per annex, comparison of benchmark with lab analysis at ambient temperature.*

sion of Fig. 14. The fact that the CTOD values are high compared to the benchmark for both E1290-93 and annex equations explains why they show good correlation in Fig. 13.

In order to get a better sense of the difference between lab and benchmark calculations, the results are replotted as the percent difference between lab and benchmark versus the benchmark CTODs in Fig. 17. The tests where the difference was greater than 20 % were examined to determine the cause. In some cases there were errors in the analysis, such as using the wrong elastic modulus or an inaccurate initial crack length. Many of the tests with large differences had an initial nonlinearity in the load-CMOD record. Comparison of the lab analysis with the benchmark revealed that, in the lab analysis, the initial nonlinearity was not excluded from the data used to perform the linear regression to determine the initial compliance. In most cases observed, the slope starts out high and then decreases until it becomes linear. When the initial nonlinearity is included in the regression, the initial slope is too high (compliance is too low). This results in plastic CMOD values that are too high, as seen in Eq 12. This increases CTOD from the E1290-93 equation and helps explain why many lab values tend to be higher than the benchmark values.

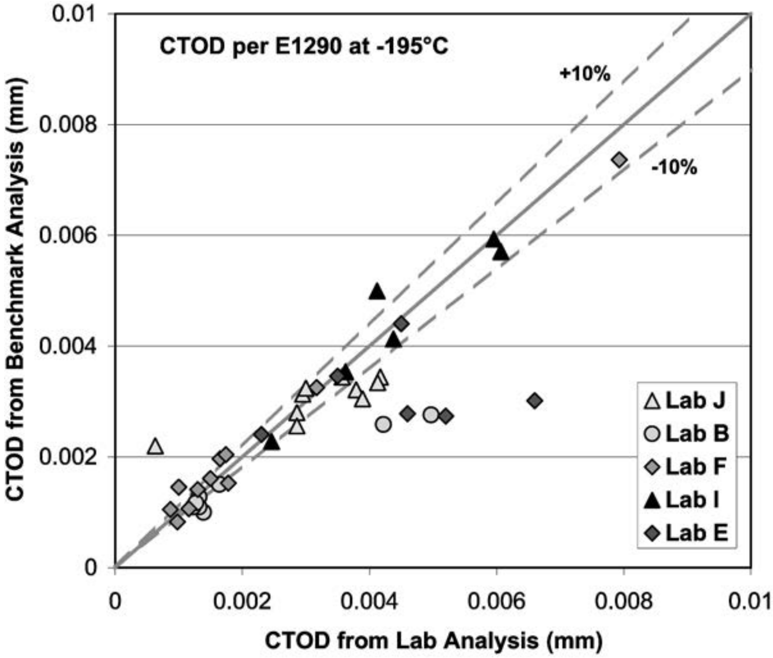

FIG. 16—*CTOD per E1290-93, comparison of benchmark with lab analysis at* LN_2 *temperature.*

$$CMOD_{plastic} = CMOD - (load) \cdot (initial\ compliance). \qquad (12)$$

In the benchmark analysis, great care was taken to carefully select the data in the linear part of the load-CMOD record for the regression. Also, the measured CMODs were shifted by the intercept from the regression to ensure that the projection of the linear part of the load-CMOD curve would go through zero load at zero CMOD. This shift results in zero plastic CMOD during the linear part of the test, which is consistent with the physical behavior of the specimen. A comparison of the lab and benchmark linear regressions for one particular specimen with +27.5 % difference in CTOD is presented in terms of the residual CMOD, which is the difference between the linear fit and the measured CMOD at the same load, in Fig. 18. It is apparent that there is no region over which the lab fit matches the linear part of the data. The benchmark fit matches the data from loads of about 3000 to 8000 N. The slope of the initial part of the residuals curves is caused by the initial nonlinearity in the data, and the slope of the latter part of the lab residual curve is caused by an underestimate of the compliance. The CMOD shift applied to the benchmark analysis brings the residuals close to zero over the central linear part of the load-CMOD curve (it causes a vertical shift in the residuals curve). The effect of the linear fit on the resulting plastic CMOD is shown in Fig. 19. The overestimate of plastic CMOD for the lab calculations that was referred to earlier is apparent in this graph. This behavior was observed for many of the tests that had more than +20 %

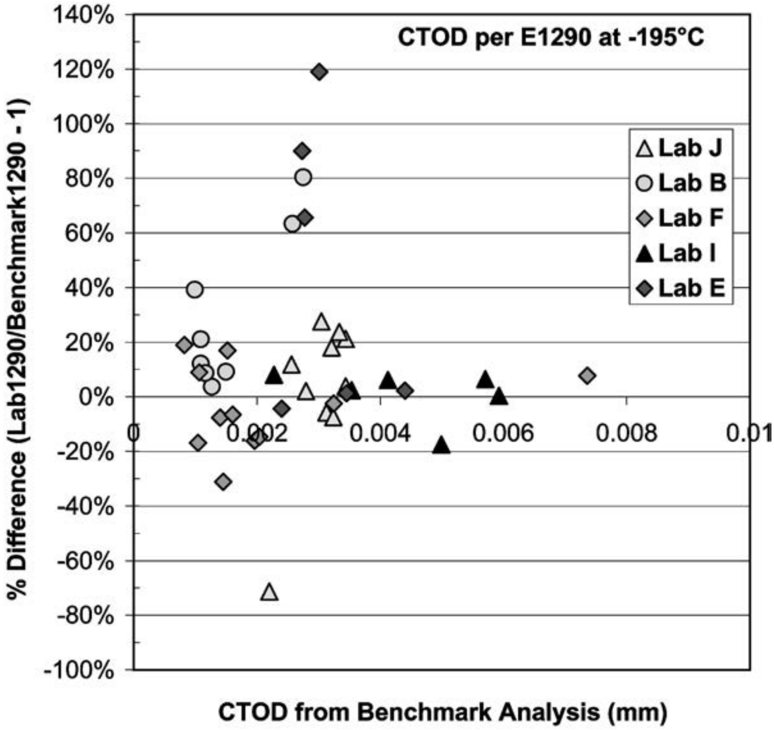

FIG. 17—*Percent difference between lab and benchmark calculations of CTOD using E1290-93 equations.*

difference in CTOD. If the initial nonlinearity had an increasing slope, the effect would be reversed and plastic CMOD would be low compared to the benchmark. This analysis reveals the need for a robust algorithm to determine the linear part of the load-CMOD curve and obtain a fit that excludes the nonlinearities that typically occur near zero and maximum load. Several authors have looked into this problem [10–12]. The authors present algorithms intended for computer implementation that vary from simple iterative approaches where linear regression is repeated with different data subsets until some goodness-of-fit condition is met [10,11] to a complex, statistically based optimization approach [12]. There is clearly a need to implement a robust approach that does not rely on the judgment of the analyst into E1290 and other standards that rely on linear regression.

There is much better correlation between benchmark and lab analysis for E1290-93 equations at room temperature, as shown in Fig. 20, with all data falling within the ±10 % lines. It appears that there were no complications with application of either equation at higher temperatures where the test results in a δ_m value. This is because the plastic part of the CTOD is large, so errors in determining the initial compliance and shifting CMOD have much less effect.

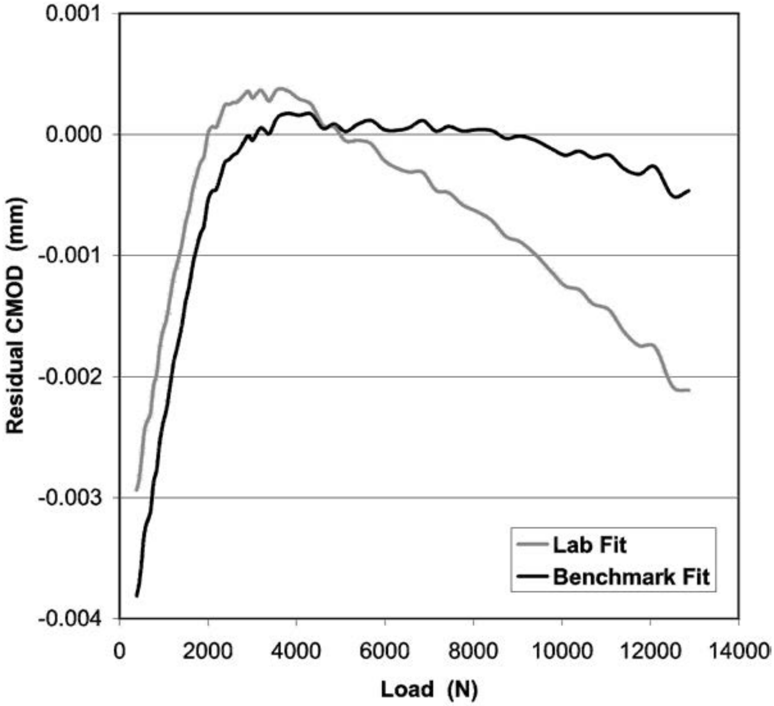

FIG. 18—*Comparison of linear regressions for lab and benchmark in terms of residuals* (*linear fit-measured CMOD*).

Discussion and Conclusions

The ASTM Manual for Conducting an Interlaboratory Study of a Test Method [13] emphasizes the importance of carefully planning and controlling a round-robin study. It is essential that the test procedure be developed in a way that all variables that could influence test results are controlled, and each laboratory must adhere strictly to prescribed procedures of test and measurement. Some of the problems encountered in analyzing the data from this round robin were due to participants deviating from the instructions. For example, lab C did not provide results for validation tests or the raw data and deviated slightly from the test plan, while lab J deviated significantly. Only four of the six labs followed the test plan as laid out, although the sequence of tests could not be checked. Lab E did not use data sheets provided to record data, precracked some specimens at −196°C, only used local compression on validation specimens, and did not calculate CTOD using the annex equations. Three of the six labs precracked at ΔK values that exceeded the allowable. E1290-93 does not specify that ΔK should be reduced when testing at a temperature lower than the precracking temperature, so it appears that they may have followed E1290-93 precracking procedures and not round-robin instructions.

A similar round robin on fracture toughness of welds was conducted to

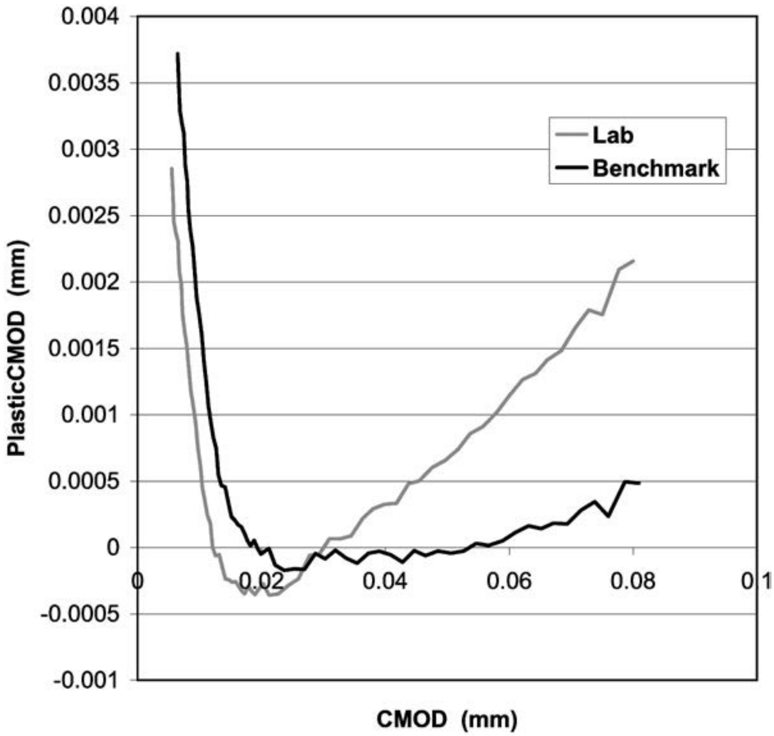

FIG. 19—*Influence of linear regression on plastic CMOD for a test conducted at −196°C.*

evaluate scatter in fracture toughness tests conducted according to Part 2 of BS7448, which was in draft form at the time [14]. That round robin also had problems with the participating labs not strictly following all prescribed procedures. Local compression of 1 % was applied across the specimen ligament by all laboratories. They tested B×2B specimens in the NF orientation at −60°C, which was expected to be in the lower-shelf/lower transition region. Unfortunately, the authors do not provide a transition curve to show where the test temperature is relative to lower shelf. They fit 59 data points with a log-normal distribution and found a mean of 0.061 mm and a standard deviation on the natural log of CTOD of 0.677 ln(mm). In order to compare these results, the −196°C data from this study were fit with a log-normal distribution. The resulting mean is 0.002 63 mm and the standard deviation of the log of CTOD is 0.515 ln(mm). Even though the mean CTOD for this study is quite a bit less than the BS7448 round robin, the standard deviation is comparable, thereby indicating that the scatter in this study is similar to the BS7448 round robin. The authors found that there were statistically significant differences between labs, which is consistent with the findings of this study, and that the differences may be due to variations in how the local compression technique was applied. They also found that 44–64 % of tests were invalid due to excessive bowing of

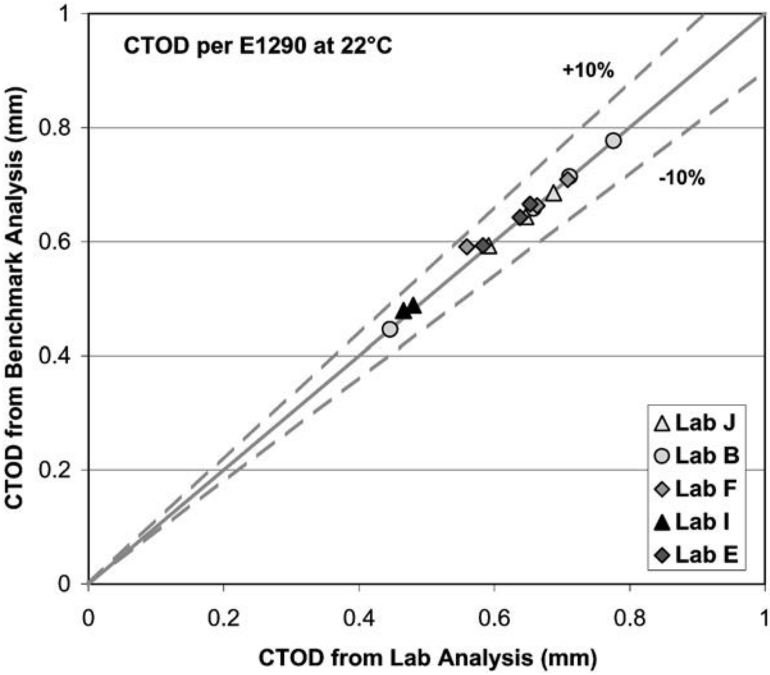

FIG. 20—*CTOD per E1290-93, comparison of benchmark with lab analysis at ambient temperature.*

the pre-crack in the center. The version of BS7448 in use at the time limited curvature to 10 %. They found that measured toughness was insensitive to crack front curvature. These observations are also consistent with this study.

The following conclusions can be drawn from the tests conducted on this particular pipe weld. From these results it is possible to infer the effect of various specimen preparation procedures on measured CTOD for welds, however, there is no guarantee that other welds will behave in the same manner as the test weld. The factors that influence the mechanical properties of welds are many, so each weld is unique.

The analysis of the validation specimens showed that, in most cases, acceptably uniform residual stresses were not achieved by the precrack preparation procedure involving local compression. There does appear to be a decrease in absolute curvature as the amount of local compression increases, and it is evident that cracks do not generally get straighter as they grow for the precracking loads used in this study. Therefore, the residual stress remaining after local compression continues to influence crack growth out to extensions of 40 % of the initial ligament.

Analysis of the CTOD tests showed that, when results from all labs are considered, local compression of 1 % did not consistently and reliably reduce crack front curvature. It appears that the procedure used is more important than the amount of local compression, as evidenced by the straight cracks obtained by two labs that exercised tight control on local compression. Analysis of covariance estimates that curvature decreased by 5.2 % ± 2.1 % for each 1 % increase in local compression for up to 3 % compression. However, interpolated mean curvatures differed among labs even for the same compression. Labs that maintained the tightest control on local compression achieved the straightest cracks.

The final ΔK used in precracking varied significantly among participants. The minimum pre-crack curvature was about 5 % and was not influenced by final ΔK, so precracking at a higher ΔK does not appear to cause curvature in a crack that otherwise would have been relatively straight.

The mean value of δ_c based on annex equations for all cracks with less than 10 % curvature was 0.002 68 mm. If the limit on curvature were increased to 20 %, there is no statistically significant difference in the mean values at the 95 % confidence level.

In general, it appears that the variables that influence CTOD in welds with residual stress were not adequately controlled in this study. The poor correlations of CTOD with percent local compression, final ΔK, and curvature indicate that other variables were involved. These other variables likely have to do with the specific procedure used to perform the local compression.

This study also compared CTOD values calculated using equations in the proposed weld testing annex, which are the equations adopted in E1290-02, with E1290-93 equations. The annex CTOD values for tests exhibiting upper-shelf behavior were within ±10 % of the E1290-93 values, thereby indicating that the labs were able to effectively calculate CTOD using the proposed annex equations.

Problems observed with calculation of CTOD using the E1290-93 equations at low temperatures, where the elastic part of CTOD is larger than the plastic part, were eliminated by using the annex equation. For both equations, the elastic part of CTOD is primarily a function of the critical load and the crack length. Most labs were able to correctly identify the critical load. However, there were some problems with errors in initial crack length, but this affected both equations equally. The primary difference in the equations is in how the plastic part of CTOD is calculated. The E1290-93 equation uses a rotation-point formulation to scale the plastic CMOD, and it is very sensitive to the initial compliance. The annex equation uses the cumulative plastic area, which is less sensitive to initial compliance errors and exhibits much less variation.

Benchmark calculations of CTOD were performed using both annex and E1290-93 equations to provide a reference to compare lab calculations against. Many of the low temperature tests with large differences between lab and benchmark calculations of CTOD using the annex equations had an initial nonlinearity in the load-CMOD record. Comparison of the lab analysis with the benchmark revealed that, in the lab analysis, the initial nonlinearity was not excluded from the data used to perform linear regression to determine the initial compliance. This comparison reveals the need for a robust algorithm to determine the linear part of the load-CMOD curve and obtain a fit that excludes the nonlinearities that typically occur near zero and maximum load.

Appendix: Statistical Data Analysis

The entire data set is characterized by the persistent and marked differences between the results from the various laboratories. These differences are apparent in every variable measured and are far larger than the usual differences between "repeatability" and "reproducibility." Their magnitude severely compromises the utility of the measurements. The most common explanation for such differences is that the sample preparation and/or measurement processes varied significantly among laboratories.

In the face of such large lab to lab differences, it is difficult to assess the relationship between any pair of measured values. The ranges of each variable often differ among the labs, as do the slopes and intercepts of any linear relationships. The statistical method best suited to evaluating the nature of any general relationship between variables is analysis of covariance (ANCOVA) [7]. ANCOVA involves assessing the correlation (fitting a regression line) on the data from each lab separately, then comparing these individual within-lab correlations for consistency and overall significance. Finally, the lab means are assessed for correlations between labs.

ANCOVA was applied to address the following questions for each pair of variables X and Y, where X is taken as the independent variable and Y is the dependent variable.

Within-lab analyses seeks answers to the following.

Question 1: Does the data from within any single laboratory indicate a correlation between X and Y? Are any of these lab-specific correlations significant?

Question 2: Are the within-lab correlations (or lack thereof) consistent from one lab to the next?

Question 3: Regardless of whether within-lab correlations are consistent, is the average slope different from zero?

Question 4: If within-lab correlations are consistent, do the labs' means agree?

Between-lab analyses:

Question 5: Averaging the variable X from each lab, and comparing those to the lab averages for variable Y, do these lab mean values show a correlation?

Question 6: Is this between lab correlation (or absence of such correlation) consistent with the within-lab correlations of X and Y?

Significance levels are set to 0.05, which means that there is no more than a 5 % probability a relationship will detected if none were to exist. The following example demonstrates the process for the case where the variable X is percent local compression and variable Y is crack front curvature.

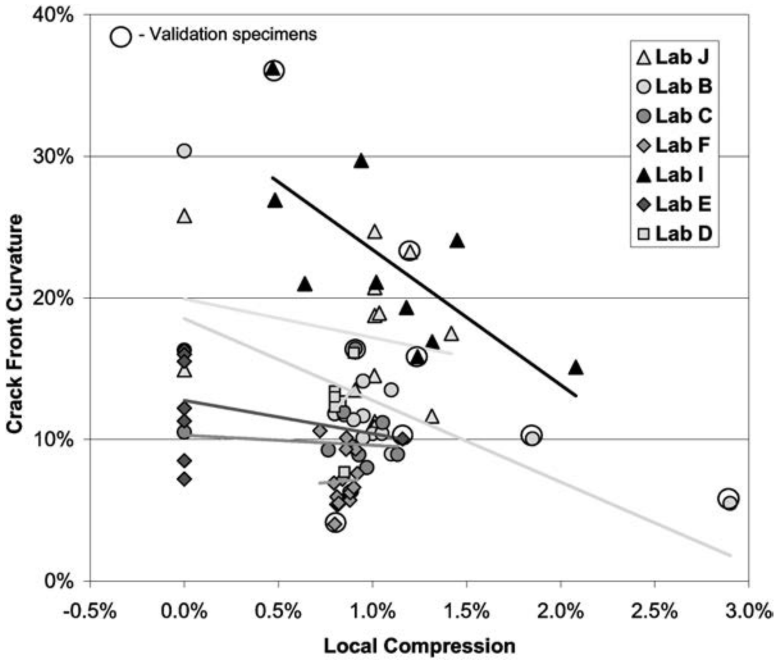

FIG. 21—*Within-lab correlations.*

Is There a Correlation Between Percent Local Compression and Crack Front Curvature?

Question 1: Yes, data from individual labs do show a relationship. After removing what appears to be an outlier from lab J, the crack front curvature was regressed on local compression for each lab separately. The fitted lines are shown in Fig. 21. All of the fitted lines have negative slope (curvature decreasing with increasing local compression) except those for labs F and D. Within those two labs local compression varied only a tiny amount, so their slopes are quite uncertain. (There is inadequate leverage for accurate estimation of their slopes.) The slopes of labs B and I are significantly different from zero. The root-mean-square (rms) deviation on curvature of this multiple slope, multiple intercept model, which measures how closely the data fit the model, is 3.77 % curvature.

Question 2: The analysis starts with the hypothesis that the labs' slopes are not significantly different from one another. To test this hypothesis, the data from each lab are fit using a single slope but separate intercepts. The single slope estimate was -5.2 ± 2.1, meaning that, on average, crack front curvature decreases by 5.2 % for every 1 % increase in local compression. The $\pm$ is used throughout to indicate 95 % confidence limits on the estimate. As the critical value of the t-statistic is 1.99, for 72 degrees of freedom, this is equivalent (within rounding error) to two times the standard error of the slope estimate. Thus, 2.1 is two standard errors of the estimated slope, which is -5.2 %. There-

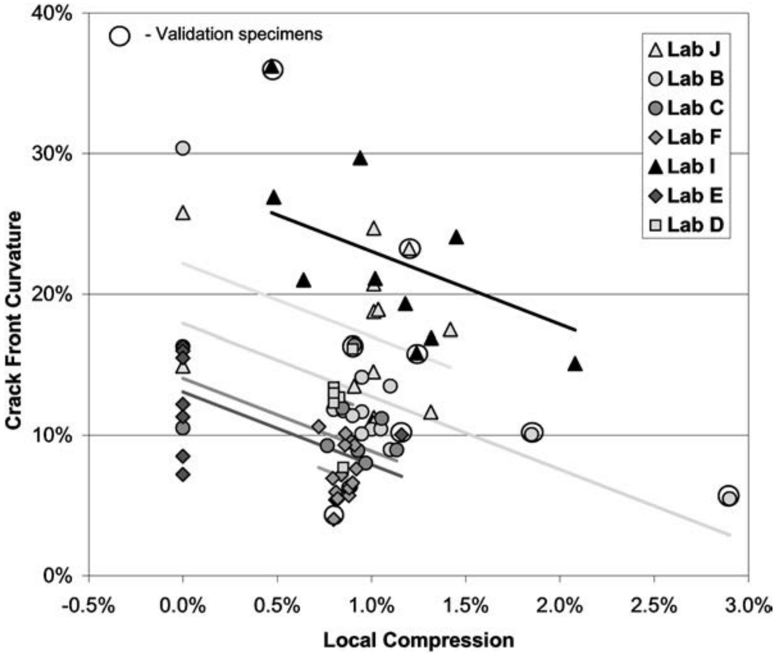

FIG. 22—*Comparison of within-lab correlations where they are forced to have the same slope.*

fore, slope is between −7.3 and −3.1 % with 95 % confidence. This model is displayed in Fig. 22. The residual variation of the data from this simpler model (3.84 %) is larger than that from the multiple-slope model of Fig. 21 (3.77 %), but not by enough that it could not be caused by chance. Significance is established using an F-statistic which is a function of the two rms residuals and the number of samples measured by each lab. Thus, we conclude that the correlations are consistent — there is not strong evidence that the relationships have different slopes.

Question 3: The hypothesis here is that the average slope is significantly different from zero. There are two tests for this, depending on whether or not the slopes are consistent. In this case, the slopes are consistent, so we compare the model of Fig. 22 to that of Fig. 23, where all seven slopes are forced to be zero. The root-mean-square residual from this model is 4.40 %, which is significantly larger than the rms residual for the model of Fig. 22, so the latter is significantly better.

In the event that the slopes were different, we would still be interested in whether the average slope was different from zero. In such a situation, the labs would disagree on the magnitude of the change in the Y variable caused by a unit change in the X variable, but if they were to agree that the change was negative, say, then that would still be a useful finding. One way of testing this is to compute the weighted average of the lab-specific slopes, where the weights are the reciprocal squares of the standard errors of the slopes. (The standard

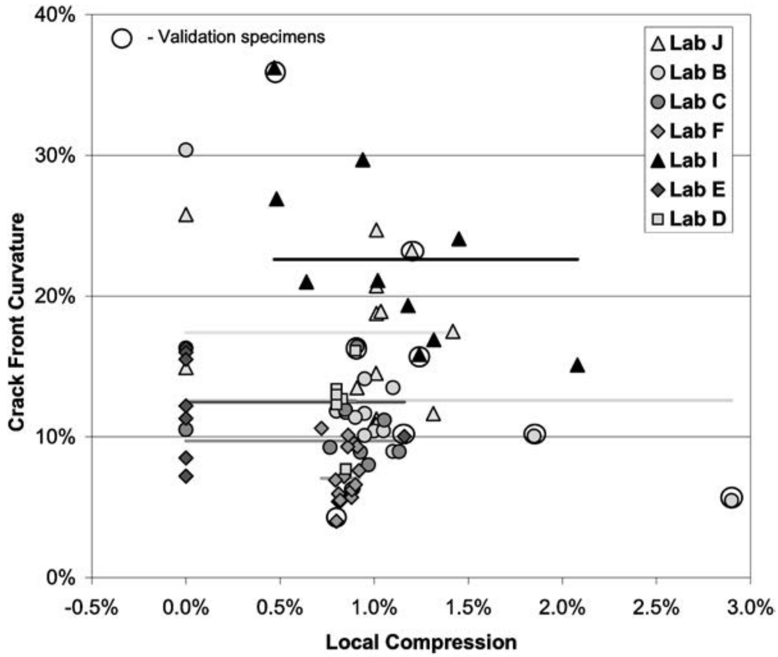

FIG. 23—*Comparison of within-lab correlations where all are forced to have a slope of zero.*

error of a slope is routinely calculated as part of a simple linear regression analysis.) The weighted mean can be compared to zero by dividing by its standard error. The weighted mean of the slopes will always be the same as the single slope estimate of the previous question, but its standard error is different when the slopes are not assumed to be the same.

Question 4: The hypothesis here is that the labs means do not agree. To check this, we regress the crack front curvature against local compression with all the data, with no consideration of which labs the data came from. This is shown in Fig. 24. The rms residual from this model is 6.39 %, far worse than the model of Fig. 22. The slope is only −1.89 % curvature per 1 % local compression.

Question 5: A regression of the lab means of crack front curvature on the lab means of local compression (appropriately weighted by the number of samples each lab measured) produced an estimated slope of +4.8 with a standard error of 7.3, as shown in Fig. 25. But, because the variation among lab means is so much smaller than among the individual measurements, this slope is not significantly different from zero. Thus, there is no discernable relationship between the two sets of means.

Question 6: Although the slope estimate is +4.8 above, its standard error is 7.3. Thus, it is not significantly different from −5.2, the pooled slope estimate from the within-labs regressions of the model in Fig. 22. A combined within and between-lab regression estimate is −5.0, with a standard error of 1.1.

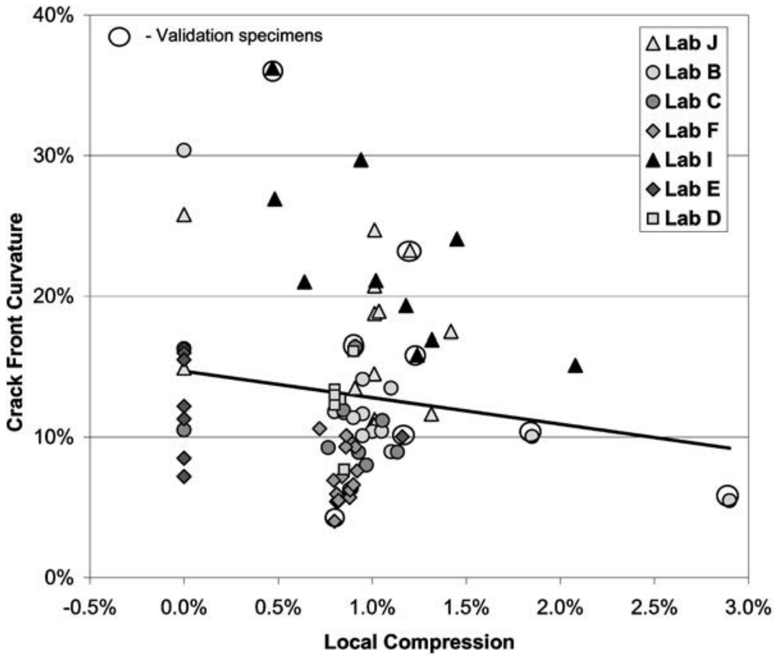

FIG. 24—*Correlation using all data, irrespective of which lab it came from.*

The analysis presented in the preceding example was repeated for various combinations of dependent and independent variables. The results from this analysis are presented in the following summary of conclusions from these bivariate comparisons.

1. Is There a Correlation Between Percent Local Compression and Crack Front Curvature?

(This is the analysis described more thoroughly above.) Yes. Lab J appears to have one outlier. When this result is removed, then, *on average*, curvature decreases approximately 5.2 % for every 1 % increase in total compression. The labs differ from one another (different mean local compressions and different mean curvature), so that prediction of curvature from local compression is of little value without knowledge of specific laboratory characteristics. Although labs differ from one another in both variables, the between labs variations are not correlated. That is, if we consider the lab average local compressions plotted against lab average curvature, there is no apparent relationship. *Validation specimens were included in this analysis.*

2. Is There a Correlation Between Final ΔK and Crack Front Curvature?

No. The labs differ from one another on both ΔK and curvature, but there is no apparent relationship between these two variables, either between or within labs.

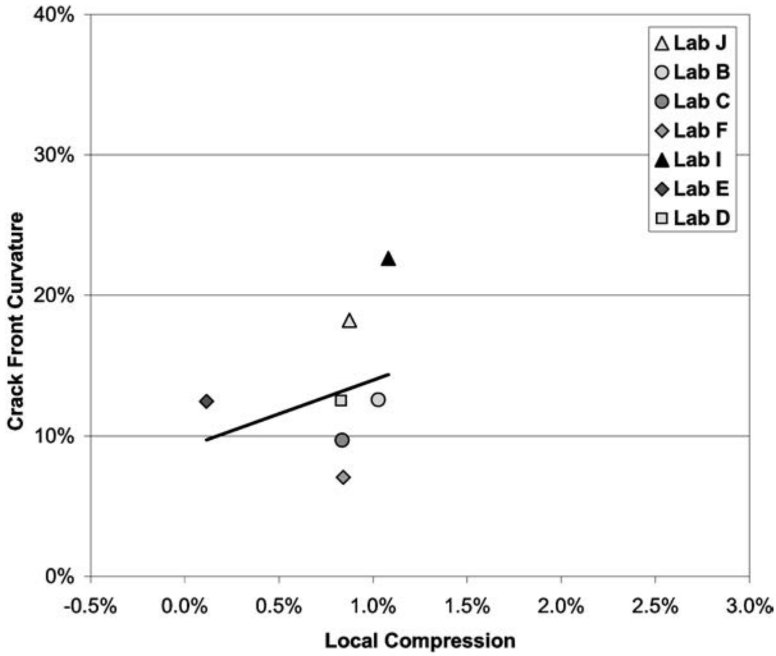

FIG. 25—*Comparison of between lab means.*

3. Is There a Correlation Between Crack Front Curvature and CTOD for LN_2 Tests?

The labs differ from one another on both annex CTOD and curvature. The within-lab correlations are not consistent, even to direction, although, when combined with between lab correlation, there is a weak suggestion that the direction of the correlation may be positive (CTOD increase of $0.000\,063 \pm 0.000\,086$ per 1 % of curvature). An outlier from lab F has been removed from this analysis. When E1290-93 equations for CTOD are used, the within-lab correlations are not so inconsistent, and because of this, the estimate of slope is significantly different from zero ($0.000\,073 \pm 0.000\,054$).

4. Is There a Correlation Between Crack Front Curvature and CTOD for Room Temperature Tests?

The labs differ from one another on both annex CTOD and curvature, and, although some labs indicate correlation, there is no consensus as the nature or direction of the relationships. Estimated slope is 0.0118 ± 0.0152 mm increase in CTOD per percent increase in curvature. When the E1290-93 calculation of CTOD was used as the independent variable, even this hint of a positive correlation is gone.

5. Is There a Correlation between Local Compression and CTOD for LN_2 Tests?

No. The labs differ from one another with respect to both variables, but there is no significant correlation between local compression and annex CTOD, either between or within labs. Lab B notwithstanding, the correlations are all consistent with the hypothesis of no relationship. When E1290-93 version of CTOD is used, the results are the same.

6. Is There a Correlation between Local Compression and CTOD for Room Temperature Tests?

No. The labs differ from one another with respect to both variables, but there is no significant correlation between local compression and CTOD, either between or within labs.

7. Does Final ΔK Influence CTOD at LN_2 or Room Temperature?

At LN_2 temperature there appears to be one CTOD outlier by lab F. Eliminating this, we reach the following conclusions using the Annex equation for CTOD:

a. Labs differed significantly from one another in both final ΔK and CTOD.
b. Some labs found that final ΔK and CTOD were related, but the slope of the relationships differed among labs.
c. Based on the between lab variations of both CTOD and final ΔK, there is a significant slope of $0.000\,117 \pm 0.000\,098$ mm of CTOD per 1 MPa$\sqrt{\text{m}}$ of ΔK.

At ambient temperature, only the first two conclusions above are applicable. Using the E1290-93 CTOD equation, the between-lab relationship at LN_2 (conclusion c) is not significant.

8. Is There a Consistent Difference Between CTOD Calculated Using the Weld Annex Equation and the E1290-93 Equation?

For some labs the differences at LN_2 temperature are consistent, for others only suggestive. Labs B, D, and F obtained virtually identical results when applying the two methods. For the others, the two methods' results were less highly correlated (but still quite correlated), with the E 1290-93 results more variable than those of the weld annex. Regressions for the various labs at LN_2 and room temperature are shown in Figs. 26 and 27, respectively.

At ambient temperature, there was a good deal more variation among lab's correlations. B, F, and D still produced very linear relationships, but this time they did not agree with each other. (Labs B and D were in good agreement — lab F disagreed with these two.) The slopes for the remaining labs are not uniformly less than or equal to one, as they are at LN_2 temperature.

As discussed previously, there is a tendency for the lab calculations of CTOD using the E1290-93 equations to be on the high side. This is apparent

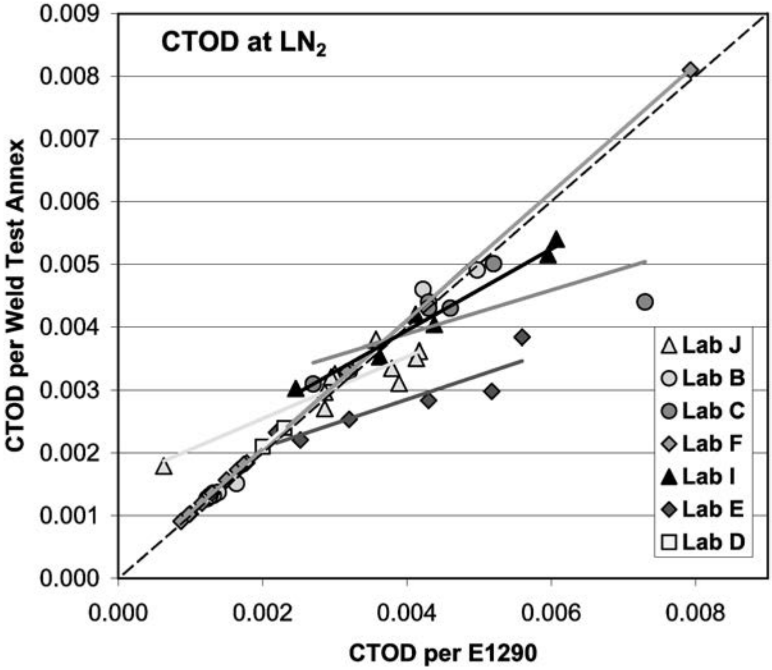

FIG. 26—*Within-lab regressions of CTOD at* LN_2 *temperature calculated using annex and E1290-93 equations as calculated by labs.*

when comparing the lab results with the benchmark calculations. The data points for lab E that stand out with high E1290-93 CTOD values are 60–120 % higher than the benchmark. The results for lab C could not be benchmarked because raw data were not provided. The outlier for lab J resulted from running the analysis with a compliance that was too high. When the benchmark results are used for comparison, the correlation is very close to 1, meaning that there is no significant difference between CTODs calculated by the two equations when the analysis is done carefully.

9. Is There a Difference in the CTOD Values at Either LN_2 or Room Temperature for the Different Labs?

Yes, there are significant differences between labs in CTOD, for both temperatures by the weld test annex, and at ambient temperature by the E1290-93 equation.

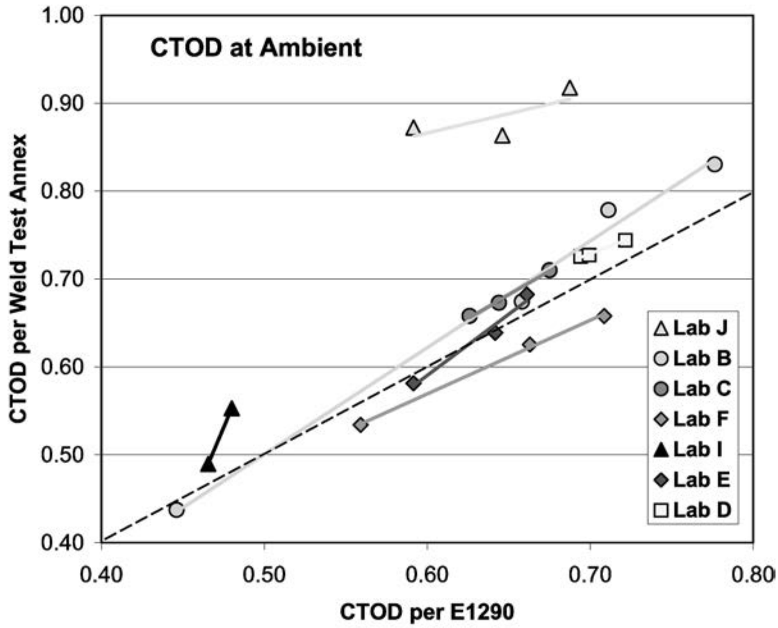

FIG. 27—*Within-lab regressions of CTOD at room temperature calculated using annex and E1290-93 equations as calculated by labs.*

References

[1] Xu, S., Bouchard, R., Braid, J. E. M., Gianetto, J. A., and Tyson, W. R., "ASTM Weld Metal Fracture Toughness Round Robin Testing at MTL/CANMET," CANMET Materials Technology Laboratory Technical Report MTL 99-9(TR), Natural Resources Canada, 1999.

[2] Wang, Y.-Y., Reemsnyder, H. S., and Kirk, M. T., "Inference Equations for Fracture Tougness Testing: Numerical Analysis and Experimental Verification," *J. Eng. Appl. Sci.*, Vol. 1321, 1997, pp. 469–484.

[3] Meith, W. A., Hill, M. R., and Panontin, T. L., "Analytical and Experimental Study of Fracture in Bend Specimens Subjected to Local Compression," *Fatigue & Fracture Mechanics: 33rd Volume, ASTM STP 1417*, Reuter, W. G., and Piascik, R. S., Eds., ASTM International, West Conshohocken, PA, 2002, pp. 425–441.

[4] Mahmoudi, A. H., Stefanescu, D., Hossain, S., Truman, C. E., Smith, D. J., and Withers, P. J., "Measurement and Prediction of the Residual Stress Field Generated by Side-Punching," *J. Eng. Mater. Technol.*, Vol. 128, 2006, pp. 451–459.

[5] Mahmoudi, A. H., Truman, C. E., and Smith, D. J., "Using Local Out-of-Plane Compression (LOPC) to Study the Effects of Residual Stress on Apparent Fracture Toughness," *Eng. Fract. Mech.*, Vol. 75, 2008, pp. 1516–1534.

[6] Towers, O. L., and Smith, A. P., "Stress Intensity Factors for Curved Crack Fronts in Compact Tension Specimens," *Int. J. Fract.*, Vol. 25 (1984), R43–R48.

[7] Sokal, R. R., and Rohlf, F. J., *Biometry: The Principles and Practice of Statistics in Biological Research*, 2nd ed, W. H. Freeman and Co., San Francisco, 1981, pp. 499–530.

[8] Stonesifer, R. B., Rybicki, E. F., and McCabe, D. E., "The Effect of Warm Prestress on the Fracture Toughness of Pressure Vessel Steels," *Advances in Fracture and Fatigue for the 1990's, Volume I: Load History Effects on Fracture Resistance*, Proceedings of the 1989 ASTM Pressure Vessels and Piping Conference, Honolulu, Hawaii, 23–27 July 1989, pp. 23–32.

[9] Chen, J. H., Wang, V. B., Wang, G. Z., and Chen, X., "Mechanism of Effects of Warm Prestressing on Apparent Toughness of Precracked Specimens of HSLA Steels," *Eng. Fract. Mech.*, Vol. 68, 2001, pp. 1669–1686.

[10] McKeighan, P. C., and Hillberry, B. M., "An Algorithm for Determining Tensile Properties from Digitally Recorded Tensile Test Data," *Experimental Techniques*, Vol. 15, No. 6, 1991, pp. 27–30.

[11] Scibetta, M., and Schuurmans, J., "Development and Qualification of an Algorithm for the Determination of the Initial Linear Portion of a Force Versus Displacement Record," *J. Test. Eval.*, Vol. 32, 2004, pp. 500–503.

[12] Roebuck, B., Lord, J. D., Cooper, P. M., and McCartney, L. N., "Data Acquisition and Analysis of Tensile Properties for Metal Matrix Composites," *J. Test. Eval.*, Vol. 22, 1994, pp. 63–69.

[13] *ASTM Manual on Method for Conducting an Interlaboratory Study of a Test Method, ASTM STP 335*, ASTM International, West Conshohocken, PA, 1963.

[14] Hadley, I., and Dawes, M. G., "Fracture Toughness Testing of Weld Metal: Results of a European Round Robin," *Fatigue Fract. Eng. Mater. Struct.*, Vol. 19, 1996, pp. 963–973.

ASTM Special Technical Publication, Vol. 5, No. 6
Paper ID JAI101524
Available online at www.astm.org

Yoichi Yamashita[1] *and Fumiyoshi Minami*[2]

Evaluation of Residual Stress Effects on Brittle Fracture Strength Based on Weibull Stress Criterion

ABSTRACT: This paper studies the method for estimating the residual stress effects on brittle fracture of structural steel based on the Weibull stress criterion. First, brittle fracture tests were conducted for four-point bend notched specimens with and without compressive preloading. It is shown that the compressive preloading apparently decreases the critical crack tip opening displacement (CTOD). The critical CTOD of the preloaded specimen can be predicted from monotonically loaded test results based on the Weibull stress criterion. It has been found that the Weibull stress is an effective fracture parameter for brittle fracture initiation under tensile residual stress. Second, using wide plate specimens with and without welding residual stress subjected to uniform tension and three-point bend fracture toughness specimens, welding residual stresses effect on the brittle fracture strength is investigated. Experiments show that the critical CTOD of wide plate with welding residual stress is significantly smaller than that without residual stress. Constraint loss effect on CTOD of wide plate can be assessed by the equivalent CTOD ratio β. β is defined as $\beta=\delta_{3PB}/\delta_{WP}$, where δ_{3PB} and δ_{WP} are CTODs of the standard fracture toughness specimen and wide plate, respectively, at the same level of the Weibull stress. Fracture assessment result using β is shown within the context of failure assessment diagram. An excessive conservatism observed in the conventional procedure ($\beta=1$) is reasonably reduced by applying the equivalent CTOD ratio β.

Manuscript received November 9, 2007; accepted for publication May 12, 2008; published online June 2008.
[1] Research Laboratory, IHI Corporation, 1, Shin-Nakahara-Cho, Isogo-Ku, Yokohama 235-8501, Japan, e-mail: youichi_yamashita@ihi.co.jp.
[2] Professor, Department of Manufacturing Science, Graduate School of Engineering, Osaka University, 2-1 Yamada-Oka, Suita, Osaka 565-0871, Japan, e-mail: minami@mapse.eng.osaka-u.ac.jp

Citation: Yamashita, Y. and Minami, F., "Evaluation of Residual Stress Effects on Brittle Fracture Strength Based on Weibull Stress Criterion," *J. ASTM Intl.*, Vol. 5, No. 6. DOI10.1520/JAI101524. Available online at www.astm.org. Also included in JAI Special Issue STP 1508, *Fatigue and Fracture Mechanics: 36th Volume,* R. W. Neu, K. R. W. Wallin, and S. R. Thompson, guest editors, ASTM International, West Conshohocken, PA, 2009, pp. 312-339.

KEYWORDS: brittle fracture, compressive preloading, tensile residual stress, critical CTOD, Weibull stress, constraint loss, failure assessment diagram

Introduction

Residual stresses can affect the brittle fracture strength. It is important to assess the residual stress effects on brittle fracture initiation of steel components for the structural integrity. A number of studies were conducted on the effects of preloading or welding residual stresses on the brittle fracture strength [1–14]. As a matter of fact, the linear elastic fracture mechanics is not applicable to the brittle fracture under a large scale yielding condition. The active (primary) CTOD concept [1] postulates that the residual CTOD after preloading has no contribution to fracture, and that the CTOD newly produced by external loads, i.e., the active CTOD, is responsible for fracture resistance at the fracture temperature. However, there still remain arguments on the physical meaning of the active CTOD.

Smith, Pisarski, and Leggatt [2] investigated the welding residual stress effects on the CTOD design curve of mismatched welded joints. They insist that the welding residual stresses have a significant role in the fracture behavior of mismatched welded joints. Ainsworth [3] investigated the significance of thermal and residual stresses in fracture assessments. The behavior of a crack under combined mechanical and thermal/residual loads is described in terms of a reference stress or equivalent mechanical loading. Qi [4], Hooton et al. [5], Smith et al. [6], and Hancock [7] also studied the residual or thermal stresses effects on the fracture. They studied the interaction of primary and secondary stress effects on the fracture in the context of failure assessment diagram in R6 or BS PD6493 and J-Q theory [8,9]. Lei et al. presented the path independent J definition for a crack in a residual stress field [10] and proposed the assessment method for combined conditions of the residual stress and mechanical loading [11]. They found that the conservatism of the reference stress method is dependent on the residual stress distribution along the uncracked ligament when the mechanical load is less than the limit load. Hill and Panontin [12,13] investigated the residual stress effects on the initiation of brittle fracture of a pipe with a circumferential crack subjected to inner pressure and axial loading using J-Q theory. It was confirmed that residual stresses contributed to the fracture driving force and reduced the fracture loads in the early stage of loading history. In addition, the residual stresses severely alter the J-integral value predicted for the onset of brittle fracture. They concluded that this decrease is due to the elevation of constraint by the residual stress.

A probabilistic approach, the so-called Weibull stress [15,16] criterion, was proposed for the assessment of brittle fracture of ferritic materials, where the Weibull stress is used as a fracture driving force. The Weibull stress is defined by integrating the stress field in the fracture process zone around the crack tip, so that it accounts for the stress intensity as well as the effect of the highly stressed region near the crack tip. The critical Weibull stress at brittle fracture initiation follows the Weibull distribution with the shape and scale parameters,

TABLE 1—*Chemical composition of HT780 steel used for compressive preloading* (*mass %*).

C	Si	Mn	P	S	Cu	Cr	Mo	V	B
0.12	0.23	1.06	0.01	0.003	0.03	0.5	0.21	0.04	0.0015

which are considered to be material properties independent of specimen geometry [17].

This paper applies the Weibull stress criterion to brittle fracture under a tensile residual stress field introduced by compressive preloading or welding. A method is studied for estimating the residual stress effect on brittle fracture of structural steel. First, it is verified that the Weibull stress is efficient to estimate the brittle fracture initiation under residual stress field. Using four-point bend (4PB) specimen of a 780-MPa class high strength steel, compressive preloading are introduced at a room temperature. After unloading and cooling, the subsequent fracture test is conducted at a low temperature. Next, the failure assessment method in welding residual stress fields is studied for steel welded components. Using wide plate (WP) specimens with and without welding residual stresses, the welding residual stresses effects on the brittle fracture performance are investigated. Constraint loss in the wide plate is assessed by the equivalent CTOD ratio [17], $\beta = \delta_{3PB}/\delta_{WP}$, where δ_{3PB} and δ_{WP} are CTODs of the standard fracture toughness specimen (3PB) and wide plate, respectively, at the same level of the Weibull stress within the context of failure assessment diagram (FAD) [18].

Experimental Study on Compressive Preloading Effect on Brittle Fracture Strength

Experiments

To investigate the tensile residual stress effects on brittle fracture initiation, compressive preloading at room temperature was applied to the four-point bend specimen. After unloading and cooling, subsequent fracture tests were conducted at −75°C and −100°C. The material used was a 780-MPa class high strength steel (HT 780) with a thickness of 25 mm. The chemical composition and mechanical properties of the HT780 are given in Tables 1 and 2. Figure 1 shows the configuration of the four-point bend specimen employed. The notch

TABLE 2—*Mechanical properties of HT780 steel used for compressive preloading* (*RT*).

Yield stress σ_{Y0}, MPa	Tensile strength σ_T, MPa	vE_{-20}, J	Elongation, % ε_T, %
830	869	245	21

vE_{-20}: Charpy absorbed energy at −20°C.

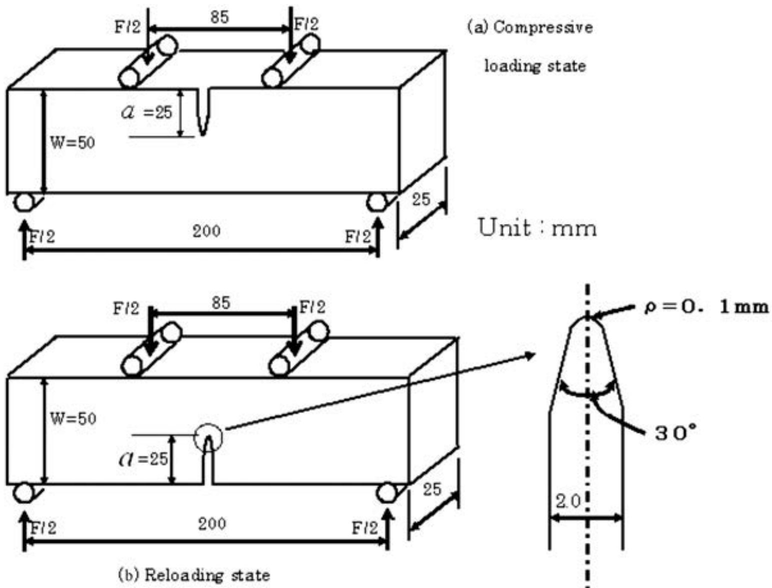

FIG. 1—*Specimen size and geometry of four-point bend specimen used.* (*a*) *Compressive preloading state.* (*b*) *Reloading state.*

depth ratio a/W was 0.5, where W is the specimen height and a is the machined notch length. The machined notch length was 25 mm and notch radius ρ was 0.1 mm.

Calculation of CTODs

Generally, the crack tip opening displacement (CTOD) is defined for fatigue precracked fracture toughness specimen. This study employs notched specimens because of the difficulty in generating tensile residual stress for fatigue precrack due to a surface contact during precompression. The CTOD of the notched specimen is calculated by Eq 1 [19]:

$$\delta(\sigma_Y(T), V_p, F) = \frac{K(F)^2(1-\nu^2)}{2\sigma_Y(T)E} + \frac{0.4(W-a)\,V_p}{0.4W+0.6a} \tag{1}$$

where $K(F)$ is a stress intensity factor under the force F, $\sigma_Y(T)$ is the yield strength at the temperature T, V_p is a plastic component of the crack mouth opening displacement V_g, $E(=206\text{ GPa})$ and $\nu(=0.3)$ are the Young's modulus and Poisson's ratio, respectively. Equation 1 is ordinarily applied to three-point bend specimens; nevertheless, Eq 1 is applied to the four-point bend specimen in this study. In Eq 1, $K(F)$ under four-point bending is calculated by Bakker [20]:

$$K(F) = F(\alpha)\sigma_b\sqrt{\pi a} \tag{2}$$

where $F(\alpha)$ is a correction factor for stress intensity factor, σ_b is nominal bending stress for a gross section of the specimen, and $\alpha(=a/W)$ is the notch depth ratio of the specimen height W. CTODs of compressive preloaded specimens are calculated by Eqs 3–8, where each component of CTOD is drawn in Fig. 2(*a*). Figure 2(*b*) shows the relationship between applied force and plastic component of notch mouth opening displacement:

$$\delta_{\text{preload}} = \delta(\sigma_{\text{Y0}}, V_{\text{p}}\_\text{preload}, F_{\text{preload}}) \tag{3}$$

$$\delta_{\text{unload}} = \delta(2\sigma_{\text{Y0}}, V_{\text{p}}\_\text{unload}, -F_{\text{preload}}) \tag{4}$$

$$\delta_{\text{res}} = \delta_{\text{preload}} + \delta_{\text{unload}} \tag{5}$$

$$\delta_{\text{tensile}} = \delta(\sigma_{\text{Y0}} + \sigma_{\text{Y}}(T), V_{\text{p}}\_\text{tensile}, F_{\text{reload}} - F_{\text{preload}}) \tag{6}$$

$$\delta_{\text{total}} = \delta_{\text{tensile}} + \delta_{\text{preload}} \tag{7}$$

$$\delta_{\text{active}} = \delta_{\text{tensile}} - \delta_{\text{unload}} \tag{8}$$

The symbols are defined as follows:

δ_{preload}: CTOD at precompression state <0,

δ_{unload}: CTOD during unloading >0,

δ_{res}: residual CTOD at unloaded state,

δ_{tensile}: CTOD generated from the point of preloaded state,

δ_{total}: total CTOD considering the history of applied force,

δ_{active}: CTOD at reloading,

V_{p}_preload: plastic component of notch mouse opening displacement at preloaded state,

V_{p}_unload: plastic component of notch mouse opening displacement during unloading,

V_{p}_tensile: plastic component of notch mouse opening displacement generated from the point of preloaded state,

F_{preload}: compressive preload <0, and

F_{reload}: applied force in reloading at fracture temperature.

When Eq 3 is applied to the preloaded state, CTOD has a negative value because notch surface hold a closing displacement. In this study, CTOD is also defined for compressive preloaded state. In determining δ_{preload}, $K(F)$ is calculated in compressive loaded state and has a negative value. V_{p}_preload and F_{preload} have also negative values. Equations 4 and 6 adopt the yield stress of $2\sigma_{\text{Y0}}$ and $\sigma_{\text{Y0}}+\sigma_{\text{Y}}(T)$, respectively, as effective values from compressive yield state to tensile yield state in the notch tip region. V_{p}_unload is given as shown in Fig. 2(*b*). The nomenclature "cr" means the value at brittle fracture initiation.

Examples of the relationships between force and total CTOD calculated with Eqs 1–8 are shown in Fig. 3 based on the crack mouth opening displacement obtained from finite element (FE) analysis. When the force in reloading

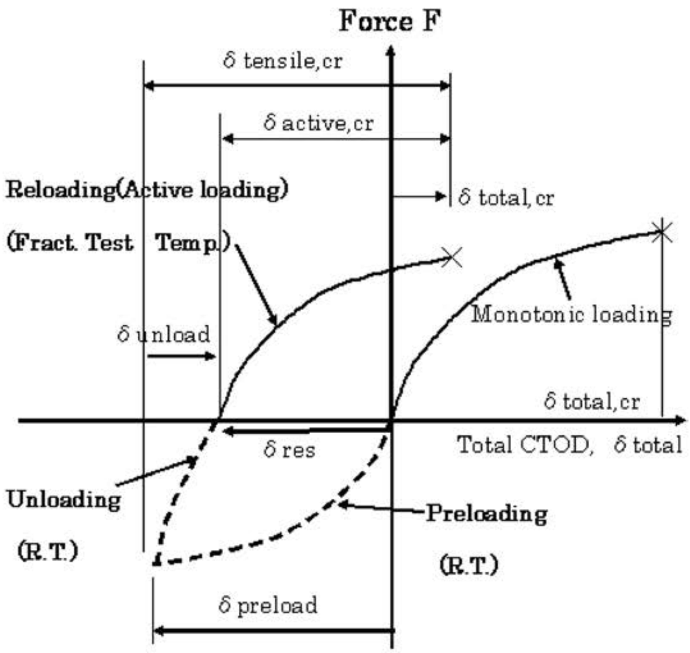

(*a*)

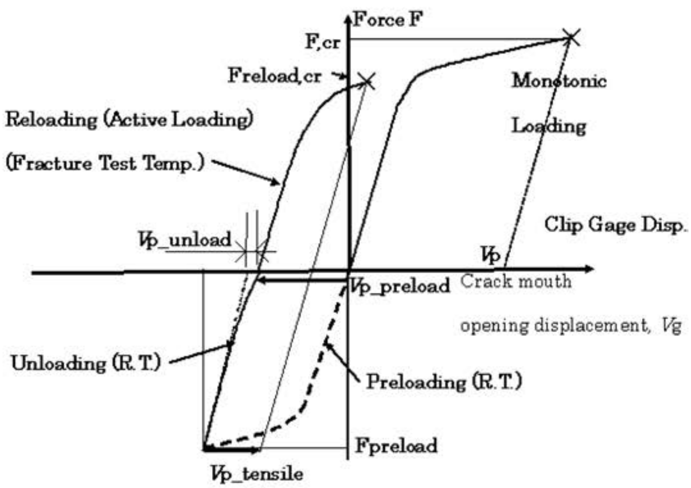

(*b*)

FIG. 2—*Definition of CTODs and notch mouth opening displacement.* (*a*) *Definition of CTODs.* (*b*) *Definition of plastic component of notch mouth opening displacement.*

state is beyond the maximum absolute value of preload, the force-total CTOD relationship for the compressively preloaded specimen is consistent to that for the monotonically loaded specimen.

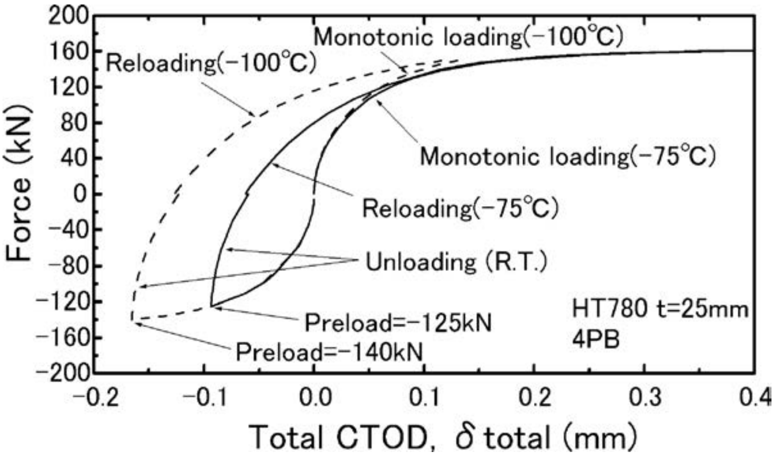

FIG. 3—*Relationships between force and total CTOD calculated by FE model based on Eqs 1–8.*

Test Conditions

Preloading and unloading to produce tensile residual stress was conducted at room temperature. After cooling, fracture tests were conducted at −75°C and −100°C. Three levels of preloading were adopted such as $F_{preload} = -125$, −132, and −140 kN. Absolute values of CTOD $|\delta_{preload}|$ at compressive preloaded state at −125, −132, and −140 kN were smaller than the critical CTOD of the monotonically loaded specimens at −75°C, but larger than the critical CTOD of the monotonically loaded specimens at −100°C.

Test Results

Figure 4 shows cumulative distributions at −75°C of the critical total CTOD. The compressive preloading decreases the critical total CTOD, which is more significant with increasing the absolute value of compressive preload.

The average CTODs at precompression ($\delta_{preload}$) measured for the preloads of −125, −132, and −140 kN were −0.083, −0.11, and −0.16 mm, respectively. The critical CTODs at fracture are shown in Fig. 5. The condition of brittle fracture initiation can be divided into two groups as follow, where $\delta_{cr}(T)$ is the critical CTOD at the monotonic loading condition:

(a) Under the condition of $|\delta_{preload}| < \delta_{cr}(T)$ (test at −75°C).

$$|\delta_{res}| + \delta_{tensile,cr} \geqslant \delta_{cr}(T) \tag{9}$$

This can be expressed as

$$|\delta_{preload}| + \delta_{active,cr} \geqslant \delta_{cr}(T) \tag{10}$$

(b) Under the condition of $|\delta_{preload}| \geq \delta_{cr}(T)$ (test at −100°C).

$$\delta_{unload} + \delta_{active,cr} = \delta_{tensile,cr} \geqslant \delta_{cr}(T) \tag{11}$$

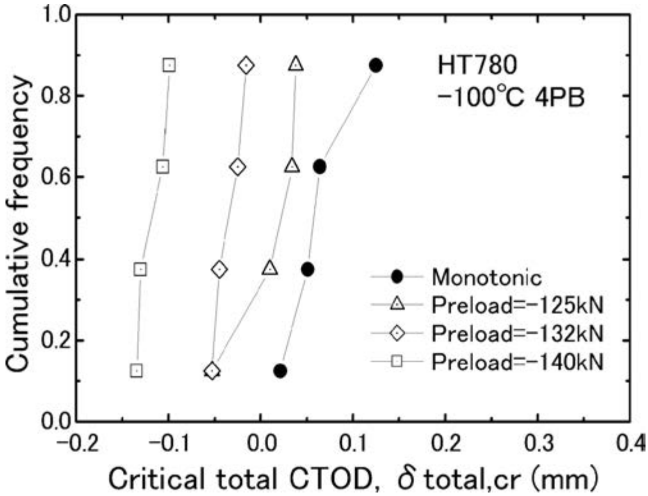

FIG. 4—*Compressive preloading effects on critical total CTOD* (*fracture test temperature at* −75°C).

Equation 10 indicates that brittle fracture occurs when δ_{active} reaches $\delta_{cr}(T)-|\delta_{preload}|$ under the condition of $|\delta_{preload}|<\delta_{cr}(T)$. On the other hand, Eq 11 shows that brittle fracture occurs when CTOD $\delta_{tensile,cr}$, generated from the preloaded state, reaches $\delta_{cr}(T)$; hence $\delta_{tensile,cr}$ is independent of the preload level under the condition of $|\delta_{preload}|\geq\delta_{cr}(T)$.

Sakai [1] shows in a notched wide plate subjected to tensile loading that the critical active CTOD decreases linearly with increasing the residual CTOD when $\delta_{cr}(T)$ is at a large level, and that in the case of rather small $\delta_{cr}(T)$ level, the critical active CTOD is almost constant and nearly equal to $\delta_{cr}(T)$, and independent of the residual CTOD. These results are much the same as the four-point bend results in this paper.

FE Analysis of Compressive Preloading Effect on Near-Tip Stress Fields

FE Analysis

The decrease in the critical total CTOD of the preloaded specimens is due to the existence of tensile residual stresses around the notch tip. The near-crack tip stress fields in the four-point bend specimen were investigated by three-dimensional FE analysis, using the FE code ABAQUS (Ver. 6.6.3). The stress-strain curves at RT, −75°C, and −100°C were determined from the round bar tension tests. In this paper, the stress-strain curve is simulated by Eq 12.

$$\bar{\sigma}=\sigma_Y(1+\bar{\varepsilon}_p/\alpha)^n \tag{12}$$

where $\bar{\sigma}$,σ_Y,ε_p,n, and α are equivalent stress, yield stress, plastic strain, strain hardening exponent, and material constant, respectively.

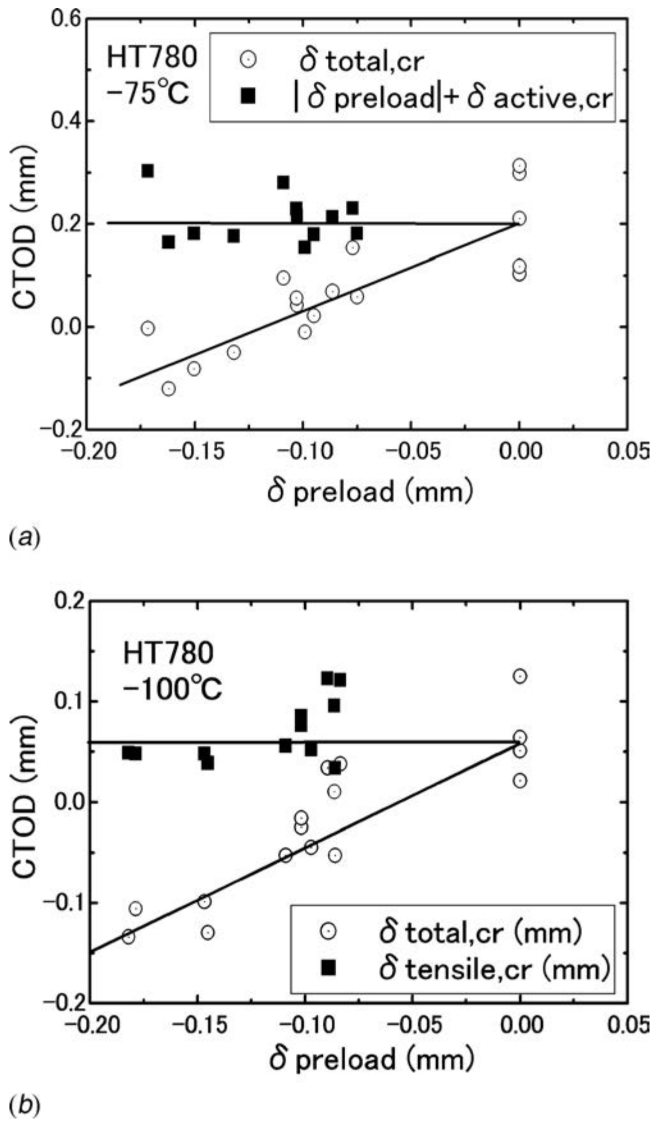

FIG. 5—*Compressive preloading effects on critical total CTOD by experiment*. (*a*) −75°C. (*b*) −100°C.

A quarter of the specimen was modeled because of symmetry. The minimum element size at the notch tip was 0.03 by 0.03 by 0.5 mm^3. In unloading and reloading analysis, the loading direction is reversed. Bauchinger's effect is often considered in this analysis of reloading. However the isotropic hardening rule is adopted in this analysis for convenience. The cooling stage is simulated with the cooperation of the temperature dependence of flow properties. It has been verified that the force versus V_g relationships calculated by the FE analysis is sufficiently consistent with those obtained in the experiment.

Effect of Compressive Preloading on Stress Distribution

Figure 6(*a*) exhibits the stress distributions (notch opening stress σ_{yy}) ahead of the notch tip at the mid-thickness of the specimen under preloaded and unloaded states. It can be seen that tensile residual stresses are produced ahead of the notch tip after unloading. It has been found that the near-tip stress distribution was hardly changed during cooling to the reloading test temperature of $-75°C$ and $-100°C$ from the room temperature (preload temperature). Compressive preloaded specimen hold more activated stress field at early stage of reloading, which was attributed to the tensile residual stress. Figure 6(*b*) exhibits the stress distribution with the force level of 60 kN for specimens subjected to monotonic loading and for reloading after preloading of -125 kN and -140 kN. The activation of the stress field is more significant upon increasing the absolute value of the compressive preload. In addition, it has been verified that the residual stress effect is diminished and the stress distribution for the preloaded specimen becomes consistent with that for the monotonically loaded specimen when the reload level reaches the absolute value of the compressive preload.

Evaluation of Compressive Preloading Effect by the Weibull Stress Criterion

The Weibull Stress Criterion

This paper employs the Weibull stress criterion for the evaluation of compressive preloading effect on the brittle fracture strength. The Weibull stress is given by the integration of the near-tip stresses in the fracture process zone in the form:

$$\sigma_{\mathrm{w}} = \left[\frac{1}{V_0} \int_{V_{\mathrm{f}}} \sigma_1^m dV_{\mathrm{f}} \right]^{1/m} \tag{13}$$

where V_{f} is the volume of a highly stressed region contributing to fracture (fracture process zone), V_0 is a reference volume, and m and σ_1 are the shape parameter and maximum principal stress, respectively. In this paper, $V_0 = 1$ mm is adopted for convenience because the reference volume V_0 does not affect the shape parameter m. The fracture process zone V_{f} was taken from the region ahead of the notch tip where Mises' equivalent stress is equal to or larger than the yield stress and $\sigma_1 > 0$. The critical Weibull stress $\sigma_{\mathrm{w,cr}}$ at the onset of brittle fracture follows the Weibull distribution with two parameters:

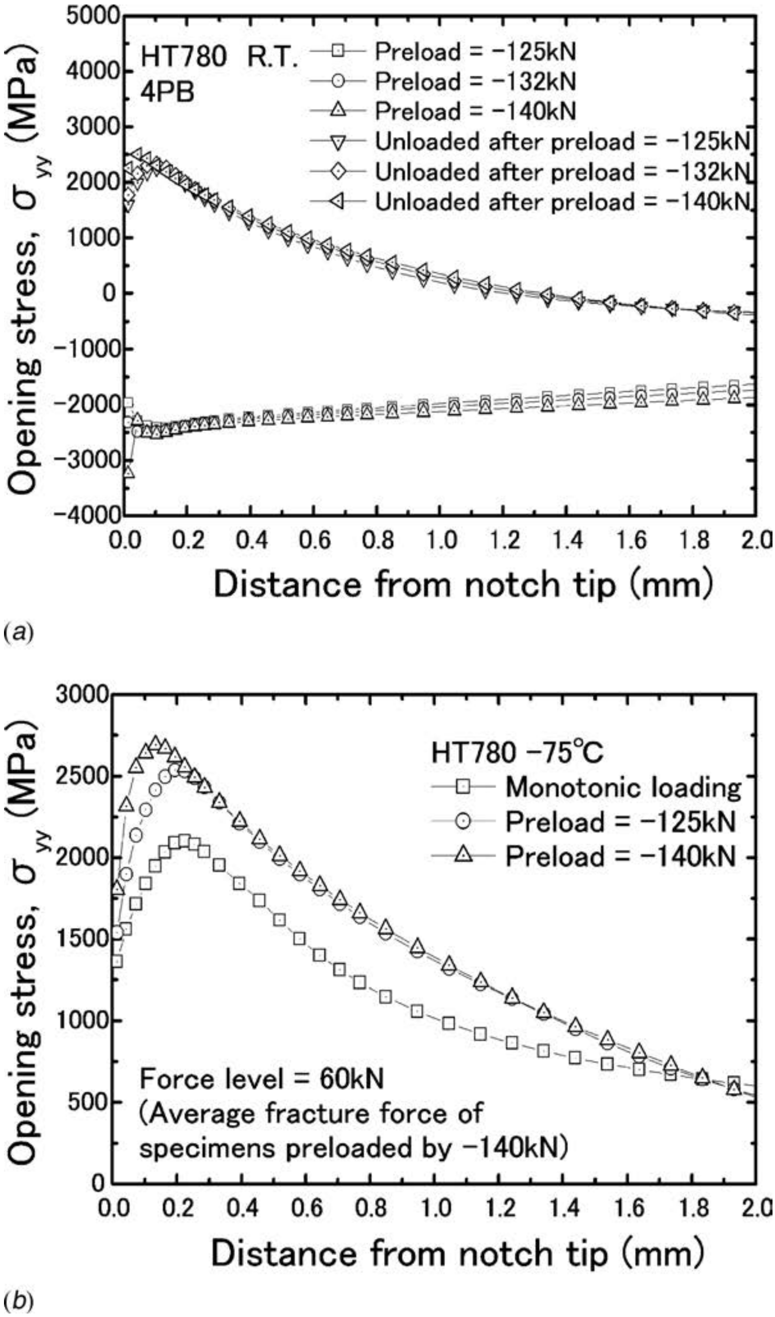

FIG. 6—*Change in notch opening stress distribution with reloading.* (*a*) *At preloaded and unloaded state.* (*b*) –75°C, *force* level = 60 kN.

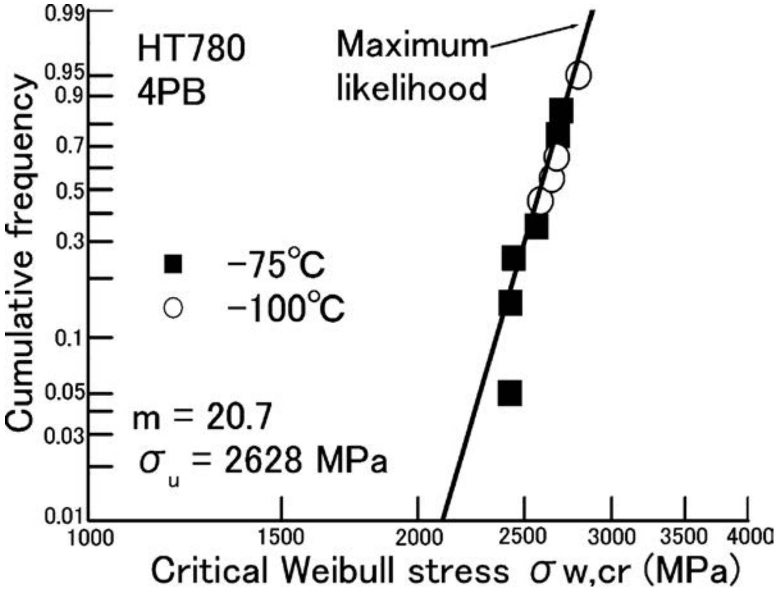

FIG. 7—*Cumulative frequency of critical Weibull stress at brittle fracture initiation at* −75°C *and* −100°C.

$$F(\sigma_{\mathrm{w,cr}}) = 1 - \exp\left[-\left(\frac{\sigma_{\mathrm{w,cr}}}{\sigma_u}\right)^m\right] \tag{14}$$

In this paper, the two parameters m and σ_u were determined by an iteration procedure [21] of the maximum likelihood method using the test data for monotonically loaded specimens. Figure 7 shows the critical Weibull stress distributions at −75°C and −100°C. The Weibull parameters determined were $m = 20.7$ and $\sigma_u = 2628$ MPa.

Prediction of Compressive Preloading Effect on Cleavage Resistance

Using the test results under monotonic loading at −75°C and −100°C, the critical total CTOD of the preloaded specimen are predicted under the assumption that the critical Weibull stress is a material property independent of the loading history and test temperature. The critical CTOD of the preloaded specimen can be determined by finding the CTOD level at which the preloaded specimen gives the same Weibull stress as the monotonically loaded specimen at each fracture probability.

Generally, the compressive preloading increases the material yield strength as a result of plastic hardening, which decreases the material fracture toughness [22]. In this paper, the material hardening due to room temperature plastic deformation is taken into account in the FE analyses. There remains a possibility that the shape parameter m is affected by preloading. Minami and Arimochi [23] reported that the Weibull stress distribution was independent of the

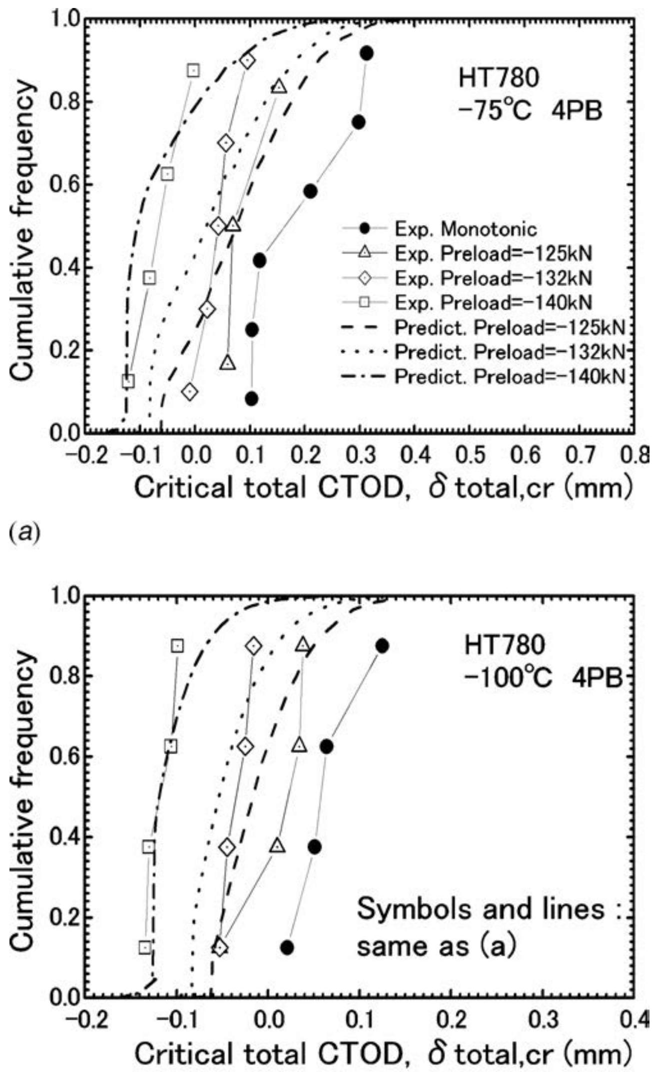

FIG. 8—*Prediction of cumulative frequency of critical total CTOD δ total,cr.* (*a*) *Critical total CTOD $\delta_{\text{total,cr}}$ at* −75°C. (*b*) *Critical total CTOD $\delta_{\text{total,cr}}$ at* −100°C.

prestrain ε_{pre} and loading rate $\dot{P}$ in the range $0<\varepsilon_{\text{pre}}<10\,\%$ and $\dot{P} \leq 300$ mm/s. With these results in mind, the *m* value is assumed to be not influenced by preloading.

Figure 8 shows the predicted results of the critical total CTOD distributions at −75°C and −100°C with the preloads of −125, −132, and −140 kN. The predicted results for the critical total CTOD of the compressively preloaded specimens almost agree with the experimental results.

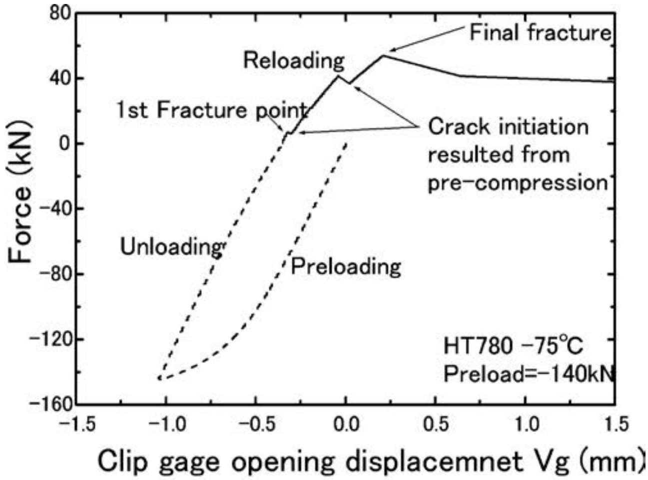

(*a*)

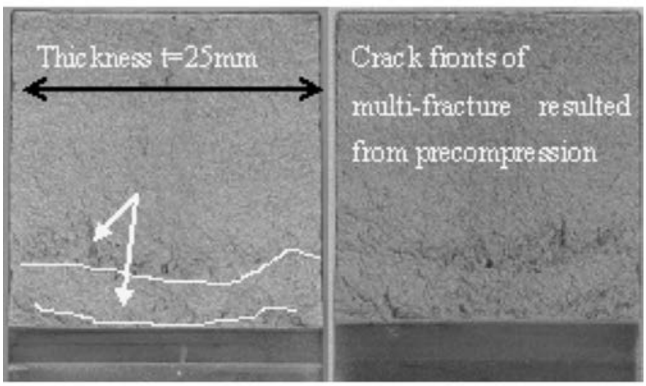

(*b*)

FIG. 9—*Force-clip gage opening displacement curve and the corresponding fracture surface of specimen tested at* −75°C *with* preload = −140 kN. (*a*) *Force-clip gage opening displacement curve.* (*b*) *Fracture surface of specimen tested.*

In addition, it has been found that the fracture probability of the preloaded specimen increases rapidly upon increasing CTOD in early stage of reloading. This is due to the tensile residual stress produced by preloading, as shown in Fig. 6(*a*).

Discussion on Compressive Preloading Effect on the Weibull stress

Brittle Fracture Initiation Behavior

Figure 9(*a*) shows the relationship between the force and V_g with the compres-

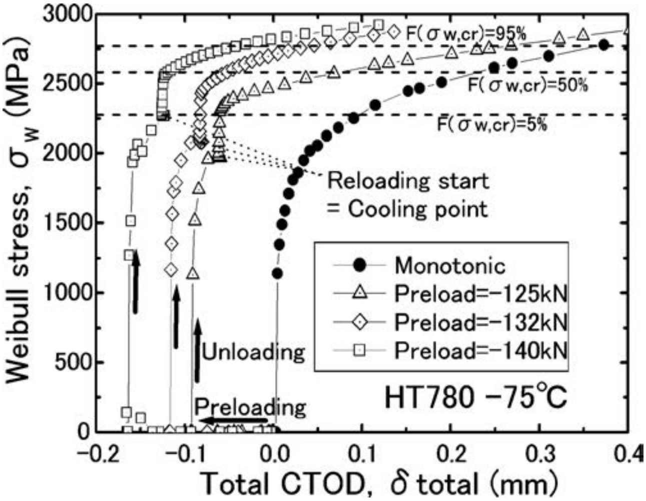

FIG. 10—*Relationships between Weibull stress and total CTOD.*

sive preload of −140 kN. The dotted curve in the figure indicates the preloading and unloading state at room temperature and the solid curve indicates the reloading state at the fracture test temperature of −75°C. Especially, the specimens with compressive preload of −140 kN fractured at a very low load level, where multi-brittle fracture propagation and arrest were observed before final fracture. Multi-type brittle fracture followed by short crack arrests were often observed for the specimen with the preload of −140 kN, as shown in Fig. 9(*b*). A similar fracture behavior is reported by Sakano [24] for the specimen with a crack introduced by the precompression technique. The white lines in Fig. 9(*b*) show the front of each arrested crack. In this case, two arrested crack fronts were observed. These multi-fractures are indicated by the record of the force-V_g curve in Fig. 9(*a*). This paper adopted the first fracture for the evaluation of the critical Weibull stress.

Generally the notched specimen with tensile residual stress does not initiate brittle fracture when it is cooled down to a low temperature from room temperature. Figure 10 shows the relationships between the Weibull stress and the total CTOD for specimens tested at −75°C with and without compressive preloading. It is found that the Weibull stress of the preloaded specimen in low CTOD range is significantly larger than that of the monotonically loaded specimen and that the difference between the Weibull stresses with and without preloading becomes small at a large CTOD level. At the unloading state, the fracture probability of the preloaded specimen was very low. In addition, the cooling stage hardly changed the fracture probability, because the tensile residual stress fields was not changed but only the yield stress was increased by cooling. It can been seen that fracture probability is very low in the preloading, unloading, and cooling stages of the specimen and brittle fracture initiation needs active applied force in the reloading stage at low temperature.

TABLE 3—*Chemical composition of HT780 steel used for wide plate and 3PB (mass %).*

C	Si	Mn	P	S	Cu	Cr	Mo	V	B
0.11	0.24	0.84	0.0007	0.0001	0.16	0.72	0.41	0.04	0.000 01

Welding Residual Stress Effects on Brittle Fracture Initiation

Experiments

Wide plates (WPs) with a center through-thickness crack subjected to uniform tension were used in the experiment. The material used is a 780-MPa class high strength steel (HT780) with a thickness of 25 mm. The chemical composition and mechanical properties of the HT780 steel are given in Tables 3 and 4. Note that this 780-MPa class steel is different from the 780-MPa class steel employed at four-point bend tests. Figure 11 shows the configuration of the WP specimens employed and three-point bend (3PB) specimen for standard fracture toughness tests. The base metal WP specimen and the groove welded WP specimen were employed to investigate welding residual stress effect on brittle fracture initiation. Both WP specimens had a center through-thickness crack of the length of the length $2a=42$ mm including a fatigue crack at both ends of machined notch. For the welded specimen, the notch was machined after welding. And the 6-mm fatigue cracks were introduced at room temperature at both ends of through-thickness notch with the maximum fatigue load of 720 kN, which corresponds to the stress intensity factor of 26 MPa$\sqrt{}$m.

WP specimens were cooled and fracture tests were conducted at −75°C in a lower fracture transition temperature range. Crack mouth opening displacement of WP specimen was measured by using knife edge on specimen's both surfaces to determine the CTOD of WP. The CTOD of the WP specimen was calculated by the BCS model [25]. For the WP specimen with residual stress, the primary CTOD (δ_{WP}), which is caused by primary load only at fracture test temperature, is given by Eq 15 (see Fig. 11(*a*)):

$$\delta_{WP} = \delta_{WP}total - \delta_{WP}res \tag{15}$$

In this case, $\delta_{WP}res$ was calculated by FE analysis mentioned later. $\delta_{WP}total$ is the sum of δ_{WP} and $\delta_{WP}res$. Standard fracture toughness tests using three-point bend (3PB) with $a/W=0.5$ were also conducted at −75°C to determine the critical Weibull stress distribution for HT780 steel used.

TABLE 4—*Mechanical properties of HT780 steel used for wide plate and 3PB (RT).*

Yield stress σ_{Y0}, MPa	Tensile strength σ_T, MPa	vE_{-20}, J	Elongation, % ε_T, %
838	885	248	23

vE_{-20}: Charpy absorbed energy at −20°C.

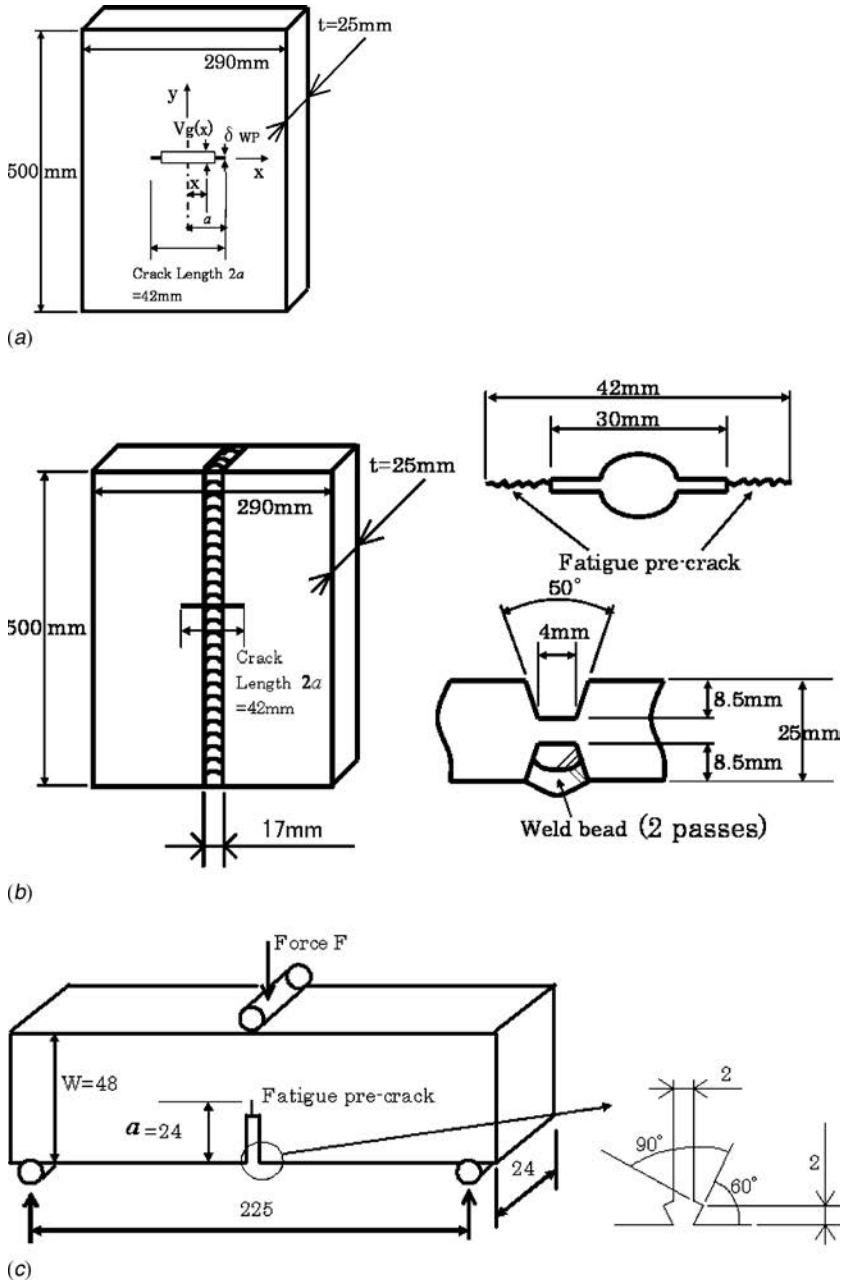

FIG. 11—*Size and geometry of wide plate and three-point bend specimens used.* (*a*) *Wide plate specimen without residual stress.* (*b*) *Wide plate specimen with welding residual stress.* (*c*) *3PB specimen.*

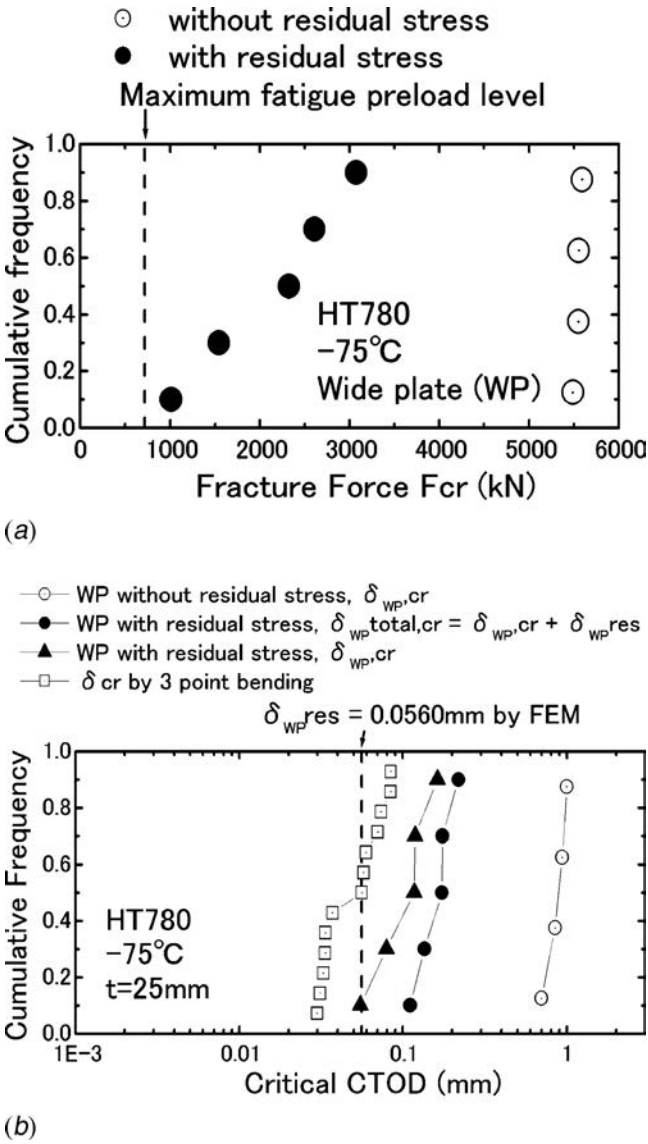

FIG. 12—*Cumulative distributions of fracture force and critical CTOD for WP and 3PB specimens.* (*a*) *Fracture force.* (*b*) *Critical CTODs.*

Results

Figure 12(*a*) shows cumulative distributions of fracture force for the WP specimens. Figure 12(*b*) shows cumulative distributions of the critical CTOD for the WP and 3PB specimens. It can be seen that the brittle fracture strength of the

WP specimen is apparently reduced by the welding residual stress. The critical CTOD of the WP specimens is higher than that of the 3PB specimen even when the WP is subjected to residual stress.

FE Analysis of Residual Stress Effect on Near-Tip Stress Fields

FE Analysis

In order to discuss the residual stress effect and constraint loss effect on the brittle fracture resistance, the three-dimensional FE analysis was performed using the FE code ABAQUS (Ver.6.6). The stress-strain relationships for FE analysis were obtained by round bar tension tests at RT and −75°C and evaluated by the Swift's type relation (Eq 12). Elements employed were isoparametric elements with eight nodes. It was verified that the Weibull stress could calculate reasonably by the first-order elements with minimum element size at the crack tip of 0.025 by 0.025 by 0.5 mm^3. Both WP and 3PB models have seven layers in the thickness direction for the half thickness.

The FE analysis of WP with the residual stress includes the following steps:

Step 1: Introduce the residual stress by eigenstrain tensor due to unit temperature change with the spatially distributed anisotropic thermal expansion properties in the WP specimen [12,13]. At each node in the model, the thermal expansion tensor is set equal to the value of the eigenstrain tensor.

Step 2: Introduce the through-thickness crack with the length of 42 mm by node release procedure. Node release was conduced by releasing crack face tractions to simulate machined notch and fatigue crack. Crack face was introduced progressively using multiple load steps with the piece by piece changes of boundary conditions that correspond to fatigue precrack growth.

Step 3: Load and unload to simulate the preload effect during fatigue precracking. The maximum load level is set to 720 kN, which is the same as the load level at the fatigue precracking in the experiment.

Step 4: Cool from RT to fracture test temperature of −75°C. In this process, the thermal expansion tensor is kept to be zero not changing the eigenstrain field introduced at Step 1.

Step 5: Apply external force for fracture test.

Residual Stress Effect on Stress Distribution

Figure 13 shows the longitudinal residual stress distribution of the WP specimen. The residual stress distribution on the specimen's surfaces measured by the strain changes of block removal method also exhibits in Fig. 13. Residual stress distributions were measured for the both surfaces of WP specimen (surface 1 and surface 2). In the FE analysis, the residual stress distribution is given to simulate the distribution measured on surface 1 adjusting the thermal expansion tensor. Uniform distribution of the residual stress field in the thickness direction of WP was supposed.

Figure 14 shows the change in the opening stress distribution ahead of the crack tip with the same CTOD level for the WP specimens with and without

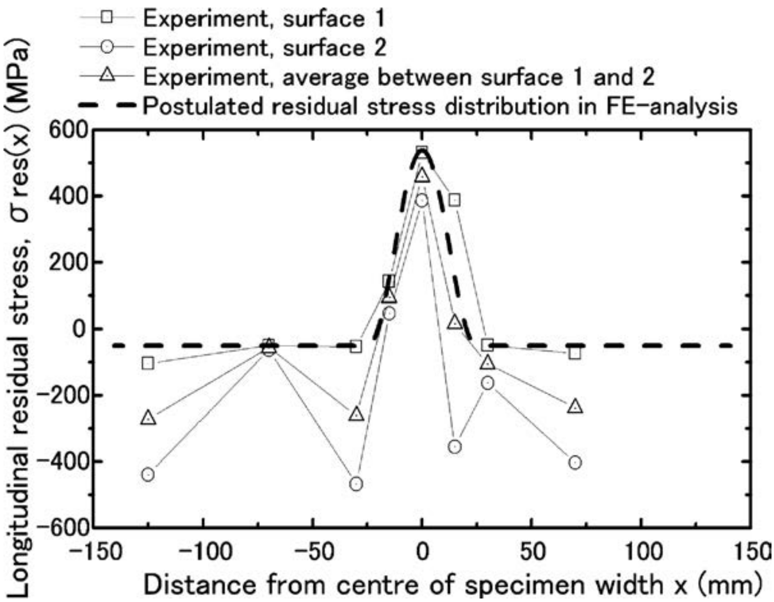

FIG. 13—*Distributions of longitudinal welding residual stress in WP specimen.*

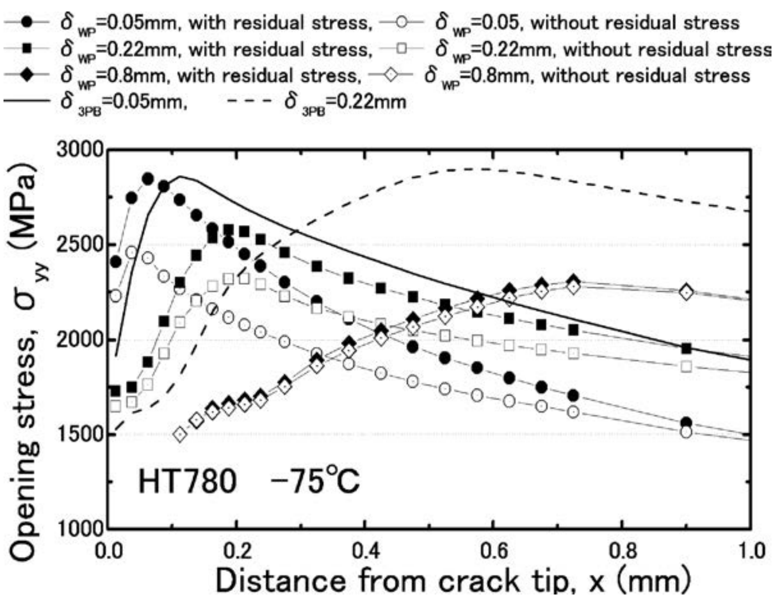

FIG. 14—*Change in opening stress distribution near crack tip of WP with and without residual stress and 3PB.*

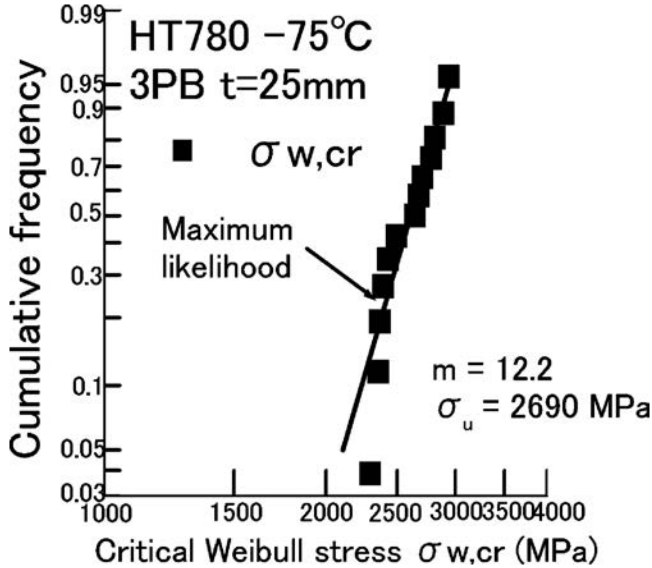

FIG. 15—*Cumulative distribution of the critical Weibull stress for 3PB specimen at* −75°C.

residual stress. The near-tip stress field for WP is activated by the residual stress, which is similar to the case of four-point bend specimen as shown in Fig. 6. The peak stress in the WP with residual stress is almost as large as in the 3PB at low CTOD level, although the WP without residual stress shows lower crack tip stresses due to loss of constraint. At large CTOD, the residual stresses in the WP relax, and so the crack tip stresses become more consistent with those of the WP without residual stress.

Evaluation of Welding Residual Stress Effect on Brittle Fracture Initiation by the Weibull Stress Criterion

Prediction of Welding Residual Stress Effects on Cleavage Resistance

Under the assumption that the Weibull parameters m and σ_u are the material properties, the fracture strengths of the WP specimens with and without residual stress are predicted. Figure 15 shows the critical Weibull stress distribution for the 3PB specimen at −75°C. The Weibull parameters determined were $m=12.2$ and $\sigma_u=2690$ MPa, which were determined by an iteration procedure using the maximum likelihood method. The critical CTOD of the WP specimen can be determined by finding the CTOD of the WP specimen, at which the WP specimen gives the same Weibull stress as the 3PB specimen at each fracture probability. Figure 16 shows the predicted results of the critical CTOD for the WP specimens. In Fig. 16, it is found that the decrease of brittle fracture strength of WP with residual stress in the critical CTOD can be simulated by the

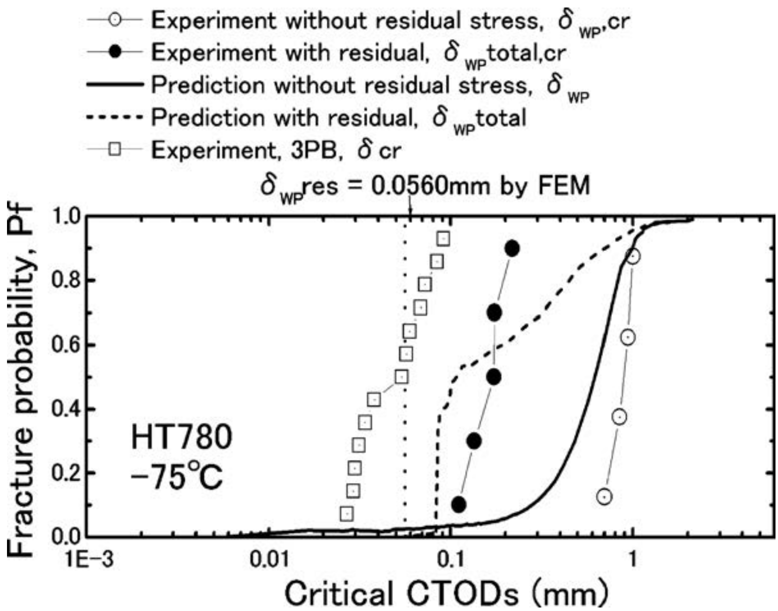

FIG. 16—*Prediction of Critical total CTOD of WP with and without residual stress (critical total CTOD is shown for WP with residual stress).*

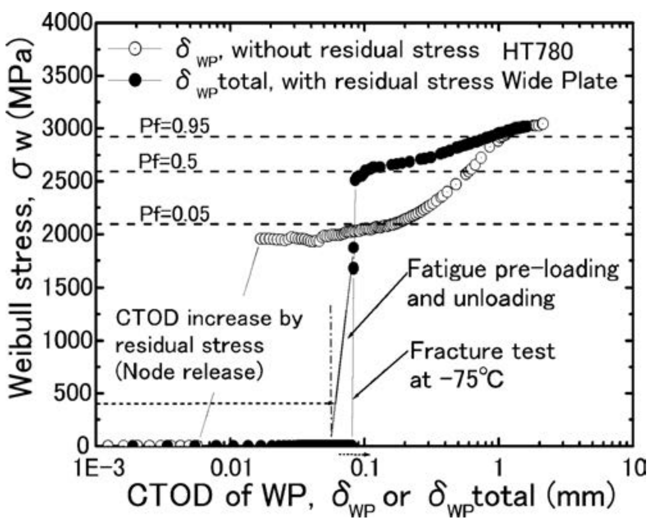

FIG. 17—*Relationship between Weibull stress and CTOD for WP with and without residual stress.*

Weibull stress criterion. Figure 17 shows the relationship between the Weibull stress and CTOD for the WP specimens. Horizontal lines indicate the Weibull stress levels at the fracture probabilities of $P_f = 0.05, 0.5, 0.95$. The Weibull stress of WP with residual stress is significantly larger than that without residual stress in a low CTOD range, which leads to a higher fracture probability of WP with residual stress. In a large CTOD range, however, the difference between the Weibull stresses with and without residual stress becomes small.

Discussion on Fracture Assessment of Component with Residual Stress

Equivalent CTOD Ratio β

Recently, the method for evaluating the constraint loss effect on fracture behavior was proposed by Minami et al. [17] on the basis of the Weibull stress approach. In this methodology, the critical CTOD of the standard fracture toughness specimen is converted to the critical CTOD of the wide plate (structural component) using the equivalent CTOD ratio β. The equivalent CTOD ratio β is defined as δ_{3PB}/δ_{WP}, where δ_{3PB} and δ_{WP} are CTODs of the standard fracture toughness specimen and the wide plate component, respectively, at the same level of the Weibull stress. In this paper, the equivalent CTOD ratio β for wide plate with and without residual stress is defined as follows.

$$\beta = \delta_{3PB}/\delta_{WP} \tag{16}$$

Once β is defined, the critical CTOD of the wide plate (δ_{WP}, cr) can be given as:

$$\delta_{WP,cr} = \delta_{3PB,cr}/\beta \tag{17}$$

where $\delta_{3PB,cr}$ is the critical CTOD of the 3PB specimen measured in fracture toughness testing.

Figure 18 shows the equivalent CTOD ratio β with and without residual stress for the WP specimens tested. In a low CTOD range, β with residual stress is higher than β without residual stress. In a large CTOD range, however, β with residual stress becomes almost the same level as β without residual stress.

Application of Equivalent CTOD Ratio to Failure Assessment Diagram

In this section, the fracture assessment using the equivalent CTOD ratio β is shown within the context of the failure assessment diagram (FAD). This paper uses the FAD curve specified in BS7910:2005. The procedure for constraint loss correction by β in the failure assessment is described below.

(1) Construct the FAD curve.

According to BS7910:2005 [18], the toughness ratio in level 2A assessment is given as

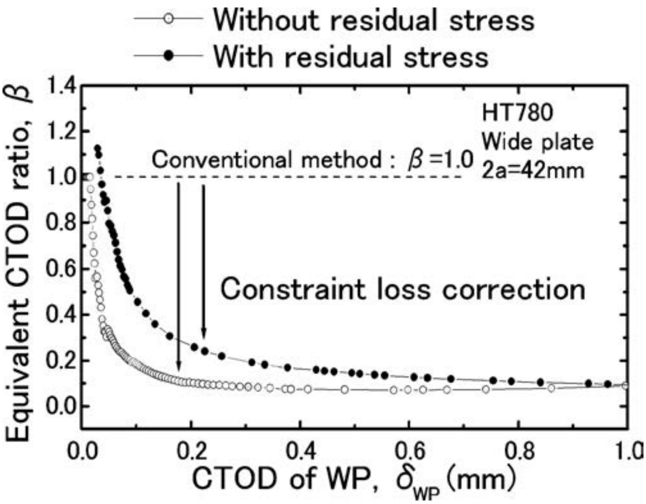

FIG. 18—*Equivalent CTOD ratios for WP with and without residual stress.*

$$\sqrt{\delta_r} = f(L_r) = \sqrt{\frac{\delta^e_{WP}}{\delta_{mat}}} = (1 - 0.14L_r^2) \quad [0.3 + 0.7\exp(-0.65L_r^6)] \tag{18}$$

where δ^e_{WP} is the elastic component of CTOD of wide plate, δ_{mat} is the material fracture toughness, L_r is the load ratio $(=\sigma_{ref}/\sigma_Y)$, and σ_{ref} and σ_Y are the average stress at net section of wide plate and the yield stress of the material.

(2) Calculate the stress intensity factor K_I of WP specimen.

For the wide plate with residual stress, K_I is calculated as the sum of the stress intensity factors produced by the residual stress and applied external force:

$$K_I = K_{res} + K_{apply} \tag{19}$$

where K_{res} and K_{apply} are the stress intensity factors by the residual stress and the applied stress, respectively, and are given as:

$$K_{res} = 2\int_0^a \sigma_{res}(x)m(x,a)dx = \frac{2}{\sqrt{\pi a}}\int_0^a \sigma_{res}(x)\left[\sqrt{\frac{a+x}{a-x}} + \sqrt{\frac{a-x}{a+x}}\right]dx \tag{20}$$

$$K_{apply} = \sigma\sqrt{\pi a}F\left(\frac{2a}{W}\right), \quad F\left(\frac{2a}{W}\right) = F(\xi) = (1 - 0.025\xi^2 + 0.06\xi^4)\sqrt{\sec\left(\frac{\pi\xi}{2}\right)} \tag{21}$$

K_{res} is calculated by the weight function method [26] using the longitudinal welding residual stress distribution $\sigma_{res}(x)$. For the wide plate without residual stress, K_I is just given by Eq 21.

(3) Calculate the elastic component of CTOD (δ^e_{WP}) of the wide plate.

The elastic component of CTOD (δ_{WP}^{e}) of the wide plate is calculated from the stress intensity factor K in the form

$$\delta_{WP}^{e} = \frac{K_I^2}{XE\sigma_y} \quad \begin{cases} E' = E & \text{(Plane stress)} \\ E' = E/(1-\nu^2) & \text{(Plane strain)} \end{cases} \tag{22}$$

where X is a factor generally in the range 1 to 2 that is influenced by the component geometry and the work hardening capacity of the material. The X-value is determined in accordance with BS 7910:2005. $X=1$ is adopted because HT780 steel has the low hardening material property. When secondary stresses are present, a plasticity correction factor ρ is necessary to allow for interaction of the primary and secondary stress contributions, such that:

$$\sqrt{\delta_r} = \sqrt{\frac{\delta_{WP}^{e}}{\delta_{mat}}} + \rho \tag{23}$$

The plasticity correction factor ρ is determined by BS7910:2005, Annex R.

(4) Convert the CTOD toughness $\delta_{3PB,cr}$ of the material to the critical CTOD of the wide plate $\delta_{WP,cr}$, using Eq 17.

(5) Calculate the toughness ratio $\sqrt{\delta_r}$ of wide plate.

In the conventional approach, the critical CTOD ($\delta_{3PB,cr}$), measured in fracture toughness testing is directly used as δ_{mat} and the toughness ratio is evaluated in the form:

$$f(L_r) = \sqrt{\delta_r} = \sqrt{\frac{\delta_{WP}^{e}}{\delta_{mat}}} + \rho = \sqrt{\frac{\delta_{WP}^{e}}{\delta_{3PB,cr}}} + \rho \tag{24}$$

With the constraint loss correction by β, the toughness ratio is evaluated as:

$$f(L_r) = \sqrt{\delta_r} = \sqrt{\frac{\delta_{WP}^{e}}{\delta_{mat}}} = \sqrt{\frac{\delta_{WP}^{e}}{\delta_{WP,cr}}} + \rho = \sqrt{\frac{\delta_{WP}^{e}}{\delta_{3PB,cr}/\beta}} + \rho \tag{25}$$

Figure 19 shows the results of the fracture assessment. Since a number of 3PB toughness data were available for HT780 steel, 0.2MOTE (MOTE: minimum of three equivalent at 20 % fracture probability) value was adopted as the material fracture toughness $\delta_{3PB,cr}$. The maximum, minimum, and 0.2MOTE values of the 3PB critical CTOD are 0.092, 0.027, and 0.030 mm, respectively. β for each experimental fracture points of WP were determined by finding each β corresponding to the measured $\delta_{WP,cr}$ based on Fig. 18. It can be seen that excessive conservatism in the conventional approach is reasonably reduced by applying the equivalent CTOD ratio β for wide plates with and without residual stress.

Conclusions

This paper studied the tensile residual stress effects on brittle fracture strength based on the Weibull stress criterion. From the experiments and the Weibull stress analyses of the four-point bend specimen and the wide plate of a

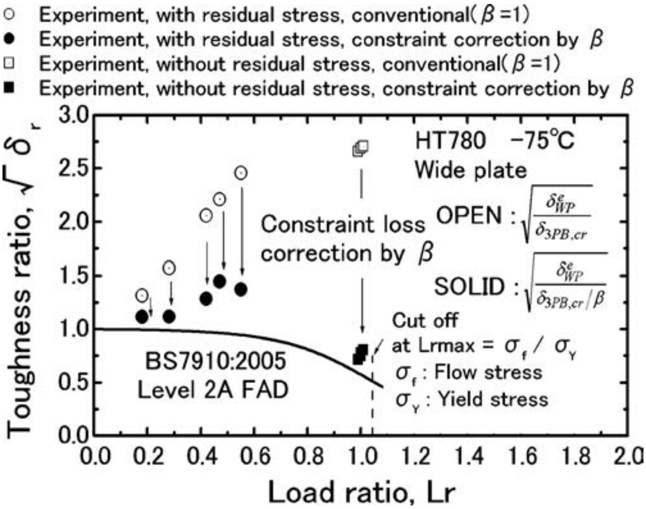

FIG. 19—*Failure assessment of WP with and without residual stress on FAD.*

780-MPa strength class steel, the Weibull stress criterion was found to be effective for the fracture assessment. The results obtained are summarized as follows:

(1) With increasing of compressive preload level, the critical total CTOD calculated from Eqs 1–8 apparently decreases.

(2) The critical CTOD of preloaded specimen can be predicted from the critical Weibull stress distribution of monotonically loaded test results. The Weibull stress is an effective fracture parameter for brittle fracture initiation under tensile residual stress field near the notch tip.

(3) The brittle fracture strength of the WP specimen is apparently reduced by the welding residual stress. The reduction of the critical CTOD of wide plate with residual stress can be predicted by 3PB fracture toughness test data based on the Weibull stress criterion.

(4) The peak stress in the WP with residual stress is almost as large as in the 3PB at low CTOD level, although the WP without residual stress shows lower crack tip stresses due to loss of constraint. At large CTOD, the residual stresses in the WP relax, and so the crack tip stresses become more consistent with those of the WP without residual stress.

(5) Constraint loss effects on CTODs of a wide plate with and without residual stress can be assessed by the equivalent CTOD ratio β. β is defined as $\beta = \delta_{3PB}/\delta_{WP}$, where δ_{3PB} and δ_{WP} are the CTOD of the standard fracture toughness specimen and the CTOD of the wide plate with welding residual stress, respectively, at the same level of the Weibull stress.

(6) Fracture assessment results using β are shown within the context of the CTOD design curve and failure assessment diagram. An excessive conservatism observed in the conventional procedure is reasonably reduced by applying the equivalent CTOD ratio β.

References

[1] Sakai, K., and Iino, N., "Study on Crack Opening Displacement and Brittle Fracture Initiation," *J. Soc. Nav. Archit. Jpn.*, Vol. 127, 1970, pp. 227–237 (in Japanese).

[2] Smith, S. D., Pisarski, H. G., and Leggatt, R. H., "Influence of Residual Stresses on Crack Driving Force for Weld Metal with Under- and Overmatching Yield Strength," *Mis-Matching of Welds, Proc. ESIS 17*, Mechanical Engineering Publications, London, 1994, pp. 573–587.

[3] Ainsworth, R. A., "The Treatment of Thermal and Residual Stresses in Fracture Assessments," *Eng. Fract. Mech.*, Vol. 24, No. 1, 1986, pp. 65–76.

[4] Qi, D. M., "Recommendations on the Treatment of Residual Stresses in PD6493 for the Assessment of the Significance of Weld Defects," *Eng. Fract. Mech.*, Vol. 41, No. 2, 1992, pp. 257–270.

[5] Hooton, D. G., and Budden, P. J., "R6 Developments in the Treatment of Secondary Stresses," *Fatigue and Fracture Mechanics in Pressure Vessels and Piping*, ASME PVP Vol. 304, ASME, New York, 1995, pp. 503–509.

[6] Smith, M. C., and Goldthrope, M. R., "The Treatment of Combined Residual and Thermal Stresses in Defect Assessment-Part 1, Zero Primary Load," *Applications of Fracture Mechanics in Failure Assessment*, ASME PVP Vol. 412, ASME, New York, 2000, pp. 197–215.

[7] Hancock, J. W., "Constraint Based Failure Assessment Diagrams for Primary and Secondary Loading," *Service Experience in Fossil and Nuclear Power Plants*, ASME PVP Vol. 391, ASME, New York, 1999, pp. 251–258.

[8] O'Dowd, N. P., and Shih, C. F., "Family of Crack-Tip Fields Characterized by a Triaxiality Parameter-I. Structure of Fields," *J. Mech. Phys. Solids*, Vol. 39, 1991, pp. 898–1015.

[9] O'Dowd, N. P., and Shih, C. F., "Family of Crack-Tip Fields Characterized by a Triaxiality Parameter-II. Fracture Applications," *J. Mech. Phys. Solids*, Vol. 40, 1992, pp. 939–963.

[10] Lei, Y., O'Dowd, N. P., and Webster, G. A., "Fracture Mechanics Analysis of a Crack in a Residual Stress Field," *Int. J. Fract.*, Vol. 106, 2000, pp. 195–216.

[11] Lei, Y., O'Dowd, N. P., and Webster, G. A., "J Estimation and Defect Assessment for Combined Residual Stress and Mechanical Loading," *Int. J. Pressure Vessels Piping*, Vol. 77, 2000, pp. 312–333.

[12] Hill, M. R., and Panontin, T. L., "Effects of Residual Stress on Brittle Fracture Testing," *Fatigue and Fracture Mechanics: Twenty-Ninth Volume*, ASTM STP 1332, ASTM International, West Conshohocken, PA, 1999, pp. 154–175.

[13] Hill, M. R., and Panontin, T. L., "The Effect of Residual Stresses on Brittle and Ductile Fracture Initiation Predicted by Micromechanical Models," *Int. J. Fract.*, Vol. 82, 1996, pp. 317–333.

[14] Yamashita, Y., Sakano, K., Onozuka, M., and Minami, F., "Prediction of Residual Stress Effects on Fracture Instability using the Local Approach," ASTM STP 1406, ASTM International, West Conshohocken, PA, 2001, pp. 247–260.

[15] Beremin, F. M., "A Local Criterion for Cleavage Fracture of a Nuclear Pressure Vessel Steel," *Metall. Trans. A*, Vol. 14A, 1983, pp. 2277–2287.

[16] Mudry, F., "A Local Approach to Cleavage Fracture," *Nucl. Eng. Des.*, Vol. 105, 1987, pp. 65–76.

[17] Minami, F., Ohata, M., Shimanuki, H., Handa, T., Igi, S., Kurihara, M., Kawabata, T., Yamashita, Y., Tagawa, T., and Hagihara, Y., "Method of Constraint Loss Correction of CTOD Fracture Toughness for Fracture Assessment of Steel Compo-

nents," *Eng. Fract. Mech.*, Vol. 73, 2006, pp. 1996–2020.

[18] BS7910:2005, "Guide on Methods for Assessing the Acceptability of Flaws in Fusion Welded Structures," British Standard Institution, 1991.

[19] BS7448:1991, "Fracture Mechanics Toughness Tests, Part1. Method for Determination of K_{Ic}, Critical CTOD and Critical J values of Metallic Materials," British Standard Institution, 1991.

[20] Bakker, A., "Evaluation of Elastic Fracture Mechanics Parameters for Bend Specimens," *Int. J. Fract.*, Vol. 71, 1995, pp. 323–343.

[21] Minami, F., Brückner-Foit, A., Munz, D., and Trolldenier, B., "Estimation Procedure for the Weibull Parameters Used in the Local Approach," *Int. J. Fract.*, Vol. 54, 1992, pp. 197–210.

[22] Tagawa, T., Itou, A., and Miyata, T., "Quantitative Prediction of Embrittlement due to Pre-Strain for Low Carbon Steels," *Q. J. Jpn. Weld. Soc.*, Vol. 14, 1996, pp. 429–434.

[23] Minami, F., and Arimochi, K., "Evaluation of Prestraining and Dynamic Loading Effects on the Fracture Toughness of Structural Steels by the Local Approach," *J. Pressure Vessel Technol.*, Vol. 123, 2001, pp. 362–372.

[24] Sakano, K., "Precompression Cracking Method for Fracture Toughness Test," *Ishikawajima-Harima Eng. Rev.*, Vol. 11, No. 1, 1978, pp. 1–7.

[25] Bilby, B. A., Cottrell, A. H., Smith, E., and Swinden, K. H., "Plastic Yielding from Sharp Notches," *Proc. R. Soc. London, Ser. A*, Vol. 279, 1964, p. 1.

[26] Tada, H., Paris, P. C., and Irwin, G. R., *The Stress Analysis of Cracks Handbook*, Third Edition, ASM International, Materials Park, OH, 2000.

ASTM Special Technical Publication, Vol. 5, No. 8
Paper ID JAI101713
Available online at www.astm.org

Michael R. Hill[1] *and John E. VanDalen*[1,2]

Evaluation of Residual Stress Corrections to Fracture Toughness Values

ABSTRACT: This paper describes tests carried out to evaluate whether comparable values of fracture toughness may be determined from coupons that contain a range of residual stress. Coupons for fracture toughness testing are taken from a single rolled plate of 7075-T6 aluminum alloy and are fabricated using identical methods. Following fabrication, residual stresses are induced in coupon subsets using laser shock peening. Each coupon subset has a unique laser peening treatment design, such that following fatigue precracking, the stress intensity factor due to residual stress varies over the coupon subsets created from positive to neutral to negative. Subsequent fracture toughness tests show expected trends in the varying toughness values for each coupon subset. Measurements of residual stress on the crack plane, and measurements of the residual stress intensity factor, enable correction of the toughness data through superposition and linear elastic fracture mechanics. The resulting corrected fracture toughness values provide data useful for evaluating residual stress corrections with potential for application to standard fracture test methods. Such corrections would enable measurements of intrinsic fracture toughness in samples that contain significant levels of residual stress.

KEYWORDS: fracture toughness, R-curve, residual stress, aluminum, laser shock peening

Manuscript received February 20, 2008; accepted for publication July 21, 2008; published online August 2008.
[1] Department of Mechanical and Aeronautical Engineering, University of California, One Shields Avenue, Davis, CA 95616, e-mail: mrhill@ucdavis.edu
[2] Hill Engineering, LLC, 5022 Bailey Loop, McClellan, CA 95652.

Citation: Hill, M. R. VanDalen, J. E., "Evaluation of Residual Stress Corrections to Fracture Toughness Values," *J. ASTM Intl.*, Vol. 5, No. 8. DOI10.1520/JAI101713. Available online at www.astm.org. Also included in JAI Special Issue STP 1508, *Fatigue and Fracture Mechanics: 36th Volume*, R. W. Neu, K. R. W. Wallin, and S. R. Thompson, guest editors, ASTM International, West Conshohocken, PA, 2009, pp. 340-354.

TABLE 1—*Mechanical properties of 7075-T6 plate* [8].

S_u (MPa)	S_y (MPa)	E (GPa)	ν	K_{Ic} (MPa$\sqrt{\text{m}}$)
552	490	71	0.33	29.0

Introduction

In cracked bodies under monotonic (tensile) loading, peak- and over-aged high-strength aluminum alloys exhibit low-energy ductile fracture with a rising crack extension resistance curve (R-curve) (e.g., 7050-T7451 [1]). In applications such as aircraft structure, fatigue and fracture of these alloys can occur while the crack tip state may be characterized by small scale yielding. Many product forms of these alloys also contain significant levels of residual stress from heat treatment and metal working operations (e.g., [2]). Since residual stress can significantly affect fracture behavior under small scale yielding (before gross plasticity might reduce its effect [3]), there has been considerable interest in understanding both actual and potential influences of residual stresses on measurements of fracture properties in these alloys (e.g., [4–7]). Despite that interest, there is a paucity of published fracture toughness test data for coupons containing known residual stress distributions.

The present study was designed to provide fracture toughness data for a range of residual stress bearing coupons. This was achieved by developing a set of standard fracture toughness test coupons that contained a range of residual stress distributions, such that when cracked to acceptable initial crack sizes for fracture testing, they contained a range of positive and negative residual stress intensity factors. Identically prepared, but uncracked, fracture toughness coupons were used to obtain residual stress distributions within the coupons on the crack plane as well as measurements of the residual stress intensity factor as a function of crack length. Standard fracture toughness tests were carried out to measure initiation fracture toughness (K_Q) and the stress intensity factor crack-growth resistance curve (R-curve). The residual stress intensity factor data were then combined with test data to assess whether linear elastic fracture mechanics and superposition could be used to obtain consistent fracture toughness data from the coupons.

Methods

Aluminum alloy 7075-T6 was selected for this test program due to its prevalent use in a variety of applications. This alloy exhibits low-energy ductile fracture with a rising R-curve. The material was received as clad plate 4.8 mm thick. Handbook [8] mechanical properties of 7075-T6 are listed in Table 1.

Compact tension, C(T), coupons were used in this study, as defined in several of the ASTM fracture toughness testing standards (e.g., ASTM E561-98, "Standard Practice for R-Curve Determination"). The C(T) coupon is well suited for this work because of its accepted use in fracture toughness testing, simple geometry, and one-dimensional crack, characterized by the crack length a. Coupon geometry had thickness B of 3.81 mm and a characteristic dimension W of

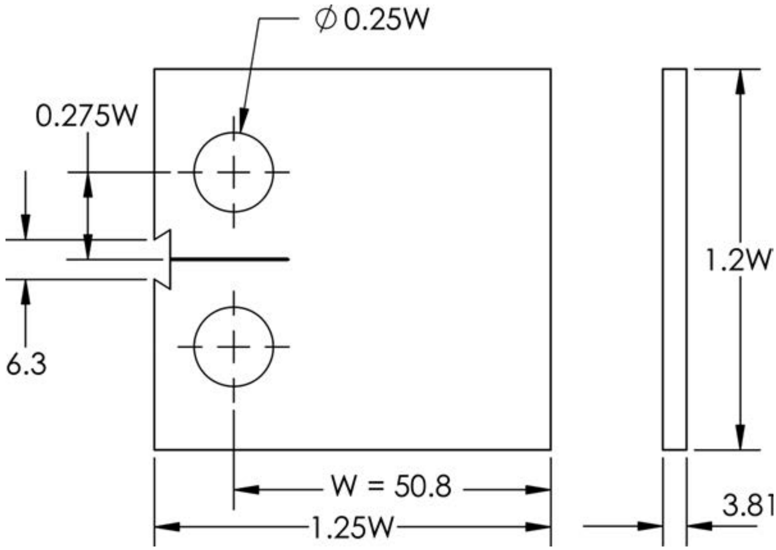

FIG. 1—*7075-T6 C(T) Coupon (dimensions in mm).*

50.8 mm (Fig. 1). Coupons were cut such that crack growth occurred in the L-T orientation. To obtain the 3.8 mm coupon thickness from the stock material, material was machined in equal amounts from each side so that the coupons lay in the T/2 plane and the original clad layer was removed. A starter notch with integral knife edges for crack mouth opening displacement (CMOD) was cut into each coupon using a wire electric discharge machine (EDM). The EDM notch was 0.3 mm wide and had various lengths, as described below.

Laser shock peening (LSP) was used to produce residual stress bearing coupons. In thin geometries, like the C(T) coupons used here, LSP can generate through-thickness compressive residual stress in the treated area. The LSP process uses laser-induced shocks to drive plastic deformation into the surface of a part [9,10]. For this work, LSP was applied using industrial facilities at Metal Improvement Company (Livermore, CA). LSP parameters were chosen to achieve high levels of residual stress in the C(T) coupons. Earlier work in high strength aluminum alloys found that deep residual stress was induced in 19 mm thick coupons using an LSP parameter set of 4 GW/cm^2 irradiance per pulse, 18 ns pulse duration, and three layers of treatment (denoted 4-18-3) [11,12]. It was further found that 4-18-3 provided significant high-cycle fatigue life improvements in 19 mm thick bend bars.

For the present work, LSP was used to obtain two *amounts* of residual stress effect and either *positive* or *negative* residual stress effect on fracture toughness. To obtain sets of coupons with different amounts of residual stress, LSP was applied using a single layer, at 4-18-1, or using three layers, at 4-18-3, where three-layer LSP induces a greater amount of residual stress. To obtain sets of coupons with either positive or negative residual stress effects on fracture, LSP was applied in two different areas, each a square with side length of

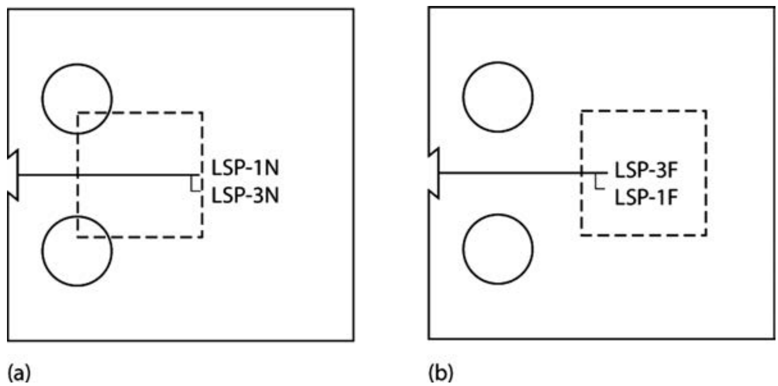

FIG. 2—*Location of LSP regions* (*square regions enclosed by dashed line, having side length of* 22.9 mm) (*a*) *near the front face* (12.7 mm *from the front face*) *and* (*b*) *far from the front face* (12.7 mm *from the back face*) (*also shown are initial crack lengths used for fracture tests of the coupon sets*).

22.9 mm and located either *near to* or *far from* the front face of the C(T) coupon (Fig. 2). Applying LSP near the front face results in compressive residual stress on the crack faces, providing a negative contribution to fracture (i.e., a negative residual stress intensity factor), while applying LSP far from the from the front face results in tensile residual stress on the crack faces, providing a positive contribution to fracture. In total, five coupon conditions were used in this study: as-machined (AM); one-layer LSP applied near the front face (LSP-1N); three-layer LSP applied near the front face (LSP-3N); one-layer LSP applied far from the front face (LSP-1F); and, three-layer LSP applied far from the front face (LSP-3F). LSP coupons were treated on both sides, alternating sides between each layer application until each side was treated with the desired number of layers.

Two-dimensional residual stress distributions were measured on the prospective crack plane of LSP-3N coupons using the contour method [13,14]. Wire EDM was used to cut the coupons in half and expose the crack plane. After cutting, an area-scanning profilometer was used to measure the resulting out-of-plane deformation of the cut surface, on both halves of the coupon. The measured deformations of the two halves were averaged and the inverse averaged deformations were applied as displacement boundary conditions in a three-dimensional, linear elastic finite element model of one-half of the coupon. The stress resulting from the elastic finite element model provided the experimental estimate of the original residual stress distribution. Residual stress measurements were performed on C(T) blanks that had holes, but did not have notches. Replicate coupons were measured to validate LSP process control, and demonstrate the consistency of the contour method.

The slitting method was employed to measure the residual stress intensity factor as a function of crack length, $K_{RS}(a)$, following Schindler's method for a thin rectangular plate [15]. A strain gage with an active grid length of 0.8 mm was applied to the center of the back face of the coupon. Wire EDM was used to incrementally extend a slit through the coupon, with strain recorded after each increment of slit depth. $K_{RS}(a)$ was then computed from the influence function $Z(a)$ provided in Ref [15], the plane stress modulus of elasticity $E' = E$ (given in Table 1), and the derivative of strain with respect to slit depth

$$K_{RS}(a) = \frac{E'}{Z(a)} \frac{d\varepsilon(a)}{da}. \quad (1)$$

The influence function $Z(a)$ of Ref [15] does not account for the holes present in the C(T) coupon, which was assumed to be of negligible effect. In addition, care was taken to account for the different definitions of crack size used by ASTM (measured from the load-line) and Schindler (measured from the edge), which can cause error (or misinterpretation of results, as in Ref [16]).

Fracture toughness tests were performed according to ASTM E561-98 [17] using a servohydraulic load frame under computer control. Typical clevis fixtures were used to apply pin loads to the C(T) coupons, and antibuckling guides were not used. Tests were performed under actuator displacement control at a uniform displacement rate such that the tests were completed in two to five minutes. The first test (on coupon AM-1) was performed at a (load-line) displacement rate of 0.015 mm/s and all subsequent tests were performed at a rate of 0.0075 mm/s; initial stress intensity factor rates in the various coupons ranged from 0.44 to 0.90 $\text{MPa}\sqrt{\text{m}}$. Load frame instrumentation included a load cell calibrated to a full-scale range of 11 kN and a clip-on CMOD gage calibrated to a full-scale range of 2.54 mm. CMOD was measured at integral knife edges placed at the front face of the coupon (Fig. 1). Load and CMOD data pairs were collected and written to a computer file once per second, which was sufficient to capture their development over the duration of the test.

Fatigue precracking was performed per ASTM E561, but accounting for expected influences of residual stress. ASTM E561 requires precracking be performed at constant amplitude load so that the final 0.65 mm of crack growth completes in greater than 5000 cycles, and offers a guideline for precracking with maximum stress intensity $K_{max} = E10^{-4}\ \text{m}^{1/2}$ and $R = 0.1$. Using E from Table 1 and $K_{RS}(a)$ from the slitting measurements, applied loads were computed to meet the K_{max} and stress ratio guidelines in terms of total stress intensity (i.e., in terms of the sum of K_{RS} and K_{app}). These loads were then iterated by trial and error until precracks were completed in roughly 15 000 cycles and in no case less than 10 000 cycles.

Upon completion of the fracture tests, coupons were fatigue cycled at constant load and $R = 0.5$ to mark the extent of fracture, then broken open. The length of the EDM notch a_N, fatigue precrack a_o, and final physical crack extension Δa_{pf} were recorded in accordance with ASTM E561 using a stereo microscope equipped with a two-axis instrumented stage.

Load-CMOD pairs and initial crack length from each test were reduced, as described in E561, to compute a record of applied stress intensity factor $K_{R,app}$ versus effective crack extension Δa_e. Initial load and CMOD data (here taken to be data for loads between 0.44 and 1.3 kN) were fitted to a straight line, the slope of which was used with measured initial crack length to determine an effective elastic modulus E_M that was used in subsequent calculations of effec-

TABLE 2—*Numbers of coupons allocated to test program, by coupon condition.*

Condition	Contour: RS	Slitting: K_{RS}	Fracture: R-Curve and K_Q
AM	2	…	2
LSP-1F	…	1	2
LSP-1N	…	2	2
LSP-3F	…	1	2
LSP-3N	2	2	2

tive crack length a_e. Each pair of load, P, and CMOD, v, measured during the test was used to compute a nondimensional mouth-opening compliance $(E_M Bv)/P$, which was used to determine a_e from a correlation for the C(T) coupon in Table 1 of E561. Effective crack extension Δa_e was then computed by subtracting initial crack size a_o from a_e. Finally, the R-curve was determined by plotting the trend of $K_{R,app}$ versus Δa_e for each test.

R-curves were corrected for residual stress influence by using linear superposition. For each test, the total stress intensity factor $K_{R,tot}$ was determined as the sum of $K_{R,app}$ and K_{RS} as a function of crack length (and crack extension), using interpolation of $K_{RS}(a)$ available from the slitting experiments.

In order to assess residual stress correction of initiation toughness measured in these coupons, data from the R-curve tests were used to compute initiation toughness K_Q for each coupon. K_Q was determined from initial physical crack size and a load P_Q that was found, as described in ASTM E399-90, "Standard Test Method for Plane-Strain Fracture Toughness of Metallic Materials" [18], using a secant line on the load versus CMOD trend having 95 % of the slope of the initial load versus CMOD data. K_Q values were then corrected for residual stress by finding $K_{Q,Tot}$ as the sum of K_Q and $K_{RS}(a_o)$, from the slitting measurements. $K_{Q,Tot}$ values were compared for the five different coupon conditions.

Results

In total, 20 coupons were used in this study, allocated between contour measurements for residual stress (four coupons), slitting measurements for K_{RS} (six coupons), and fracture tests for R-curve and K_Q (ten coupons) (Table 2). Replicate tests were used to assess variability in measurands and measurement methods.

The results of contour measurements made on two AM and two LSP-3N coupons are illustrated in Fig. 3. Residual stress in the AM coupons ranged from −44.8 to 15.9 MPa and had a similar through thickness distribution at all points across the coupon width, which is consistent with residual stress from plate rolling. LSP coupons had a maximum compressive residual stress of −290 MPa that occurred on the surface near the middle of the coupon, and a maximum tensile stress of 350 MPa that occurred at the front face of the coupon. In the peened region (from $x = 12.7$ to $x = 35.6$ mm, where x is measured

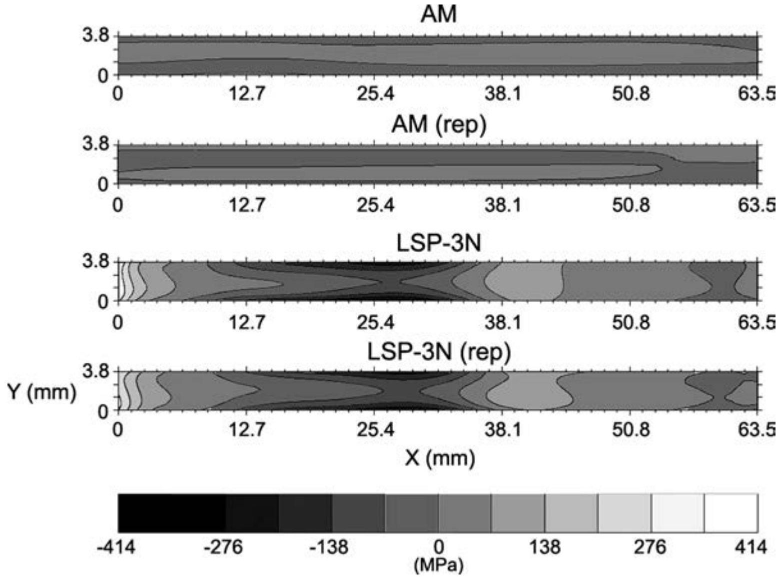

FIG. 3—*Contour measurement results illustrating the residual stress distribution on the plane of the crack for AM and LSP-3N coupons ("rep" indicates a replicate (identical) coupon).*

from the front face of the coupon), residual stress was compressive at the surfaces and grew more positive monotonically with position toward the coupon mid-thickness. Outside of the peened region, residual stress was nearly uniform through thickness but varied with position across the width. The residual stress distribution features inside the LSP region are consistent with double sided peening and outside the LSP region are consistent with plate bending and axial stresses that arise in the coupon to achieve residual stress equilibrium (zero net force and moment across the contour plane). Replicate coupons confirm repeatability of LSP processing and consistency of contour residual stress measurement.

Through thickness average residual stress for each coupon, computed from the contour measurements, is plotted in Fig. 4. AM coupons have a thickness-average of nearly 0 MPa, as expected. Thickness-average stress in the LSP-3N coupon has maximum tension at the front face with a value of 316 MPa and maximum compression of −137 MPa near the middle of the LSP area ($x = 27.4$ mm).

At initial crack lengths useful for fracture tests ($0.35W = 18\text{ mm} \leqslant a_o \leqslant 0.55W = 28\text{ mm}$), slitting measurements show that $K_{RS}(a)$ is either negative or positive, depending on the location of the LSP area (Fig. 5). At these crack lengths, the far-from-front-face LSP coupons (LSP-1F, LSP-3F) have positive K_{RS} and the near-front-face LSP coupons (LSP-1N, LSP-3N) have negative K_{RS}. K_{RS} for the three-layer LSP coupons (LSP-3F, LSP-3N) are roughly double those for the corresponding one-layer LSP coupons (LSP-1F, LSP-1N). For LSP-3F, the positive K_{RS} reaches 35.9 MPa$\sqrt{\text{m}}$, which is quite large, exceeding the

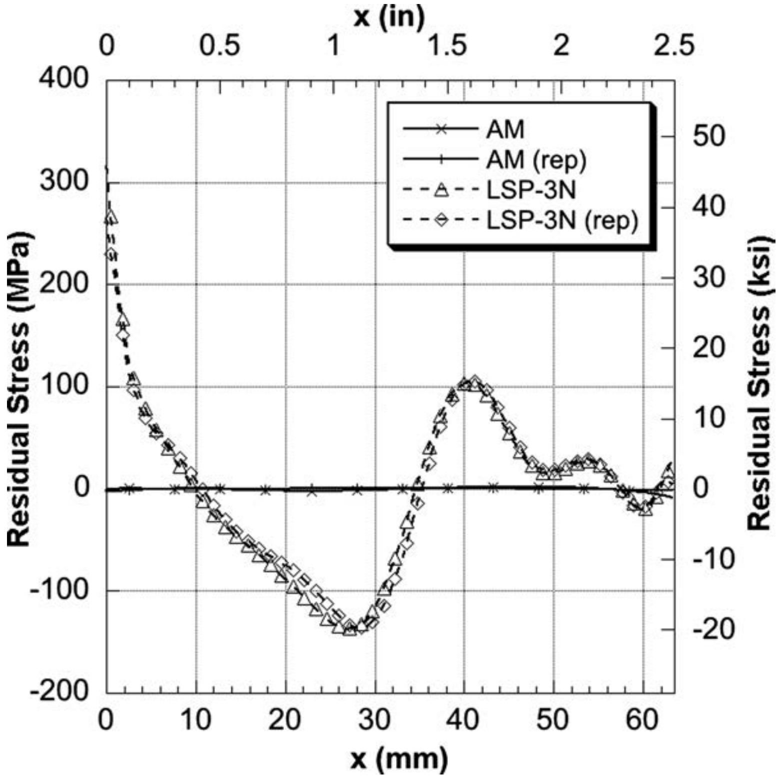

FIG. 4—*Through thickness average stress for AM and LSP-3N coupons computed from contour results* (*"rep" indicates a replicate* (*identical*) *coupon*).

material plane strain fracture toughness of 29.0 MPa$\sqrt{\mathrm{m}}$ (Table 1). The magnitude of the most positive K_{RS} in coupons LSP-1F and LSP-3F (17.7 and 35.9 MPa$\sqrt{\mathrm{m}}$) is nearly twice the magnitude of the most negative K_{RS} in coupons LSP-1N and LSP-3N (−10.5 and −16.8 MPa$\sqrt{\mathrm{m}}$). Replicate coupons illustrate the consistency of the LSP application and of the slitting method.

Based on the slitting results (Fig. 5), target initial crack lengths were selected for the fracture tests. The target crack lengths chosen for each condition are shown (to scale) with the LSP area in Fig. 2. The length of the machined notch is listed for each coupon in Table 3 along with $K_{RS}(a_N)$ from slitting, the loads used for fatigue precracking, and the initial crack size after precracking. Compression-compression precracking was performed for the LSP-1F and LSP-3F coupons due to the high magnitude, positive K_{RS}.

Results of fracture testing showed significant and expected effects from LSP-induced residual stress. Load versus CMOD results for coupons without (AM), with the most positive (LSP-3F), and with the most negative (LSP-3N) residual stress contributions (Fig. 6) show significant effects from residual stress in the range of coupon conditions. R-curves in terms of K_{app} are shown for all coupons in Fig. 7. Results for the two AM coupons exhibit typical elastic-

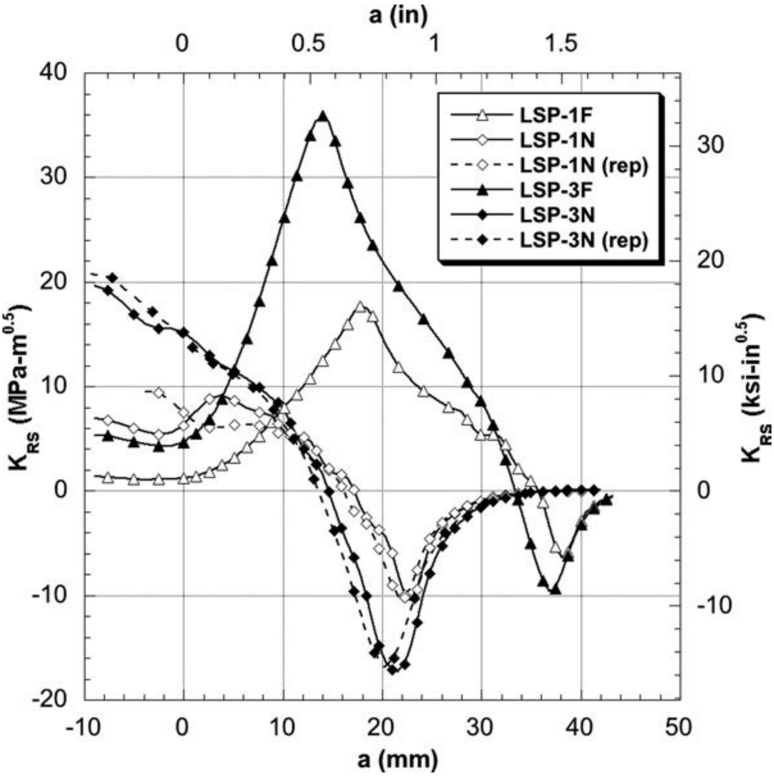

FIG. 5—*K_{RS} as a function of crack length for LSP coupons ("rep" indicates a replicate (identical) coupon; symbols at every other data point are omitted to ensure clarity of data trends).*

plastic blunting behavior until about 30 MPa$\sqrt{m}$, after which monotonically increasing (nearly linear) crack growth resistance is obtained. Compared with the AM results at a given crack length, the LSP-1N and LSP-3N coupons exhibit greater toughness (in terms of K_{app}) and the LSP-1F and LSP3F coupons exhibit reduced toughness, with the three-layer coupons having a larger effect in both cases. Comparing results for the two coupons within each coupon subset shows the data to be repeatable. Residual stress corrected *R*-curves provide similar results for the different coupon subsets (Fig. 8). The LSP-1N and LSP-3N results exhibit significantly greater elastic-plastic blunting than for the AM coupons, which is consistent with the higher level of applied loading at which they initiate crack extension. After blunting, the R-curves of all coupon subsets are in good agreement, though the LSP-3F coupons exhibit a significantly shallower *R*-curve.

Values of initiation toughness are very significantly affected by residual stress in terms of applied load (K_Q) but are nearly invariant in terms of total stress ($K_{Q,Tot}$) (Table 3 and Fig. 9). The mean K_Q for AM coupons was 33.1 MPa$\sqrt{m}$, a value slightly greater than K_{Ic} (Table 1), which is expected given

TABLE 3—*Fracture toughness coupon detail, by coupon condition.*

Coupon	B (mm)	a_N (mm)	$K_{RS}(a_N)$, (MPa$\sqrt{m}$)	Precrack Load Min/Max (kN)	a_o (mm)	$K_{RS}(a_o)$, (MPa$\sqrt{m}$)	K_Q (MPa$\sqrt{m}$)	$K_{Q,Tot}$ (MPa$\sqrt{m}$)	P_{max} (kN)	a_{Pf} (mm)
AM-1	3.81	23.77	0.00	0.18/1.75	26.14	0.00	33.7	33.7	4.58	35.55
AM-2	3.84	23.66	0.00	0.09/0.96	25.90	0.00	32.5	32.5	4.49	28.91
LSP-1F-1	3.85	16.75	15.9	–0.85/–0.04	18.29	17.7	17.2	34.8	6.02	22.50
LSP-1F-2	3.88	16.61	15.9	–0.85/–0.04	17.77	17.0	16.5	33.4	6.41	24.50
LSP-1N-1	3.82	21.04	–5.97	1.09/1.88	23.02	–10.5	46.4	36.0	6.21	32.11
LSP-1N-2	3.88	21.03	–5.97	1.09/1.88	21.94	–8.04	46.8	38.8	6.71	32.06
LSP-3F-1	3.89	17.83	26.3	–1.78/–0.53	20.73	21.4	11.9	33.3	3.91	24.19
LSP-3F-2	3.83	17.77	27.8	–1.78/–0.89	19.80	23.5	7.45	31.0	3.64	23.64
LSP-3N-1	3.84	19.98	–14.8	1.98/2.83	21.27	–17.1	52.8	35.7	7.21	29.24
LSP-3N-2	3.85	19.94	–14.8	1.98/2.83	20.75	–16.4	50.5	34.1	7.51	25.16

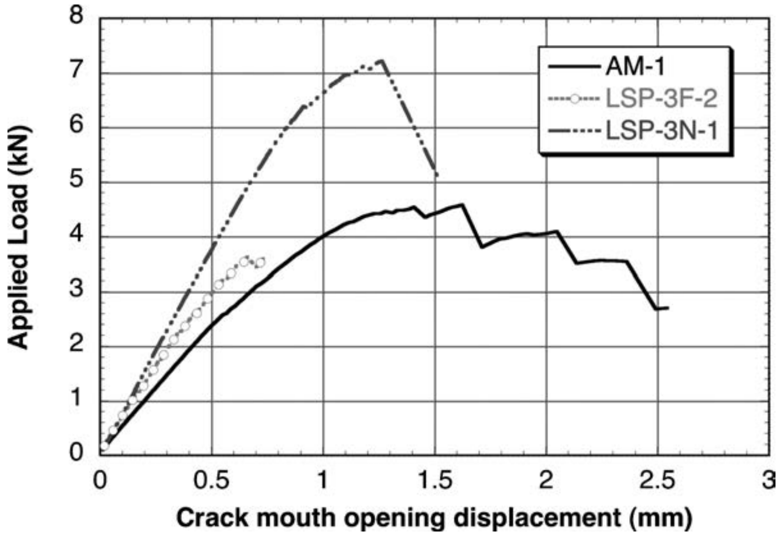

FIG. 6—*Load versus CMOD for coupon AM-1, coupon LSP-3F-2 (which exhibited the smallest applied loads) and LSP-3N-1 (which exhibited the largest applied loads).*

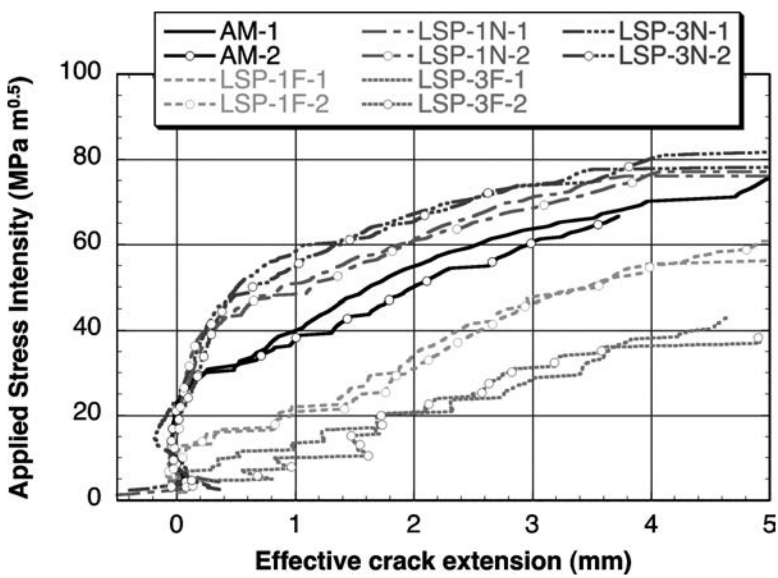

FIG. 7—*R-curve resulting from applied stress intensity factor.*

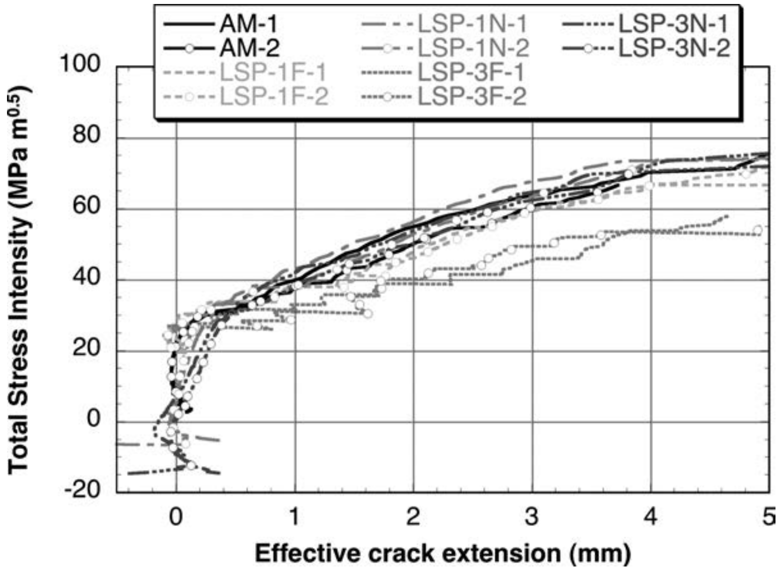

FIG. 8—*R-curve resulting from superposition of applied and residual stress intensity factors.*

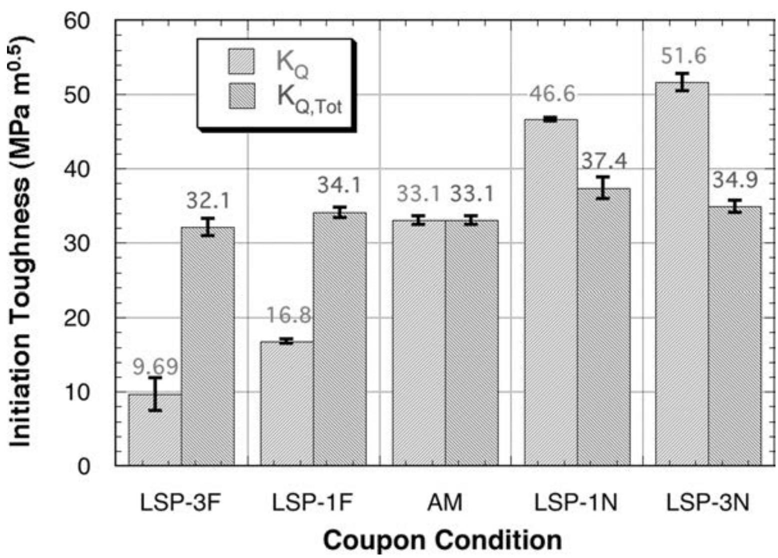

FIG. 9—*Comparison of K_Q and $K_{Q,Tot}$ for the five coupon conditions (bars and values provide mean, error bars indicate range for from two coupons).*

TABLE 4—*Comparison of K_{RS} computed from prenotch strain data with values interpolated from data from residual stress coupons* (*Fig. 5*).

	Computed from Prenotch Data		Interpolated from Residual Stress Coupons			
Coupon	a_{N-} (mm)	$K_{RS}(a_{N-})$ (MPa$\sqrt{m}$)	a_N (mm)	$K_{RS}(a_N)$ (MPa$\sqrt{m}$)	a_o (mm)	$K_{RS}(a_o)$ (MPa$\sqrt{m}$)
LSP-1F-1	16.19	14.79	16.75	15.9	18.29	17.7
LSP-1N-2	20.64	−6.96	21.03	−5.97	21.94	−8.04
LSP-3F-1	16.19	30.37	17.83	26.3	20.73	21.4
LSP-3N-1	19.37	−13.87	19.98	−14.8	21.27	−17.1

the limited coupon thickness. Mean K_Q values for residual stress bearing coupons ranged from 9.69 MPa$\sqrt{m}$ for LSP-3F coupons to 51.6 MPa$\sqrt{m}$ for LSP-3N coupons. Mean $K_{Q,Tot}$ values ranged from 32.1 MPa$\sqrt{m}$ (LSP-3F) to 37.4 MPa$\sqrt{m}$ (LSP-1N), with the latter value being somewhat of an outlier.

Discussion

The present results demonstrate consistent fracture property measurements in residual stress bearing coupons, where residual stress was taken into account; however, the consistency obtained here was dependent on specific methodological choices. First, the material employed is one that exhibits low-energy fracture, and as such, has fracture behavior that is influenced directly (in fact, linearly) by the residual stress intensity factor. It remains to be determined whether consistent toughness data could be obtained in residual stress bearing coupons of a significantly more ductile material. Second, fracture toughness and K_{RS} measurements were performed on coupons prepared identically. A test program employing coupons with greater variability (e.g., hand-forgings or welded materials) would provide less consistent results. Third, the coupon geometry had a large width-to-thickness ratio ($W/B \approx 13$), which allowed significant residual stress influence while avoiding complications arising from non-straight crack-fronts (e.g., as for welded joints [19]). Follow-on work would need to be performed to determine the range of material, coupon geometry, and residual stress fields for which consistent fracture toughness properties can be obtained.

Additional measurements were performed to determine whether a single coupon could provide a useful estimate of $K_{Q,Tot}$. This required estimating $K_{RS}(a_o)$, which was performed by measuring strain during cutting of the machined notch of one coupon in each of the LSP conditions. The notch was cut in the same manner as done for slitting, but cutting was stopped and strain measured at only two notch lengths, including the final notch length a_N. The strain data were used to compute $K_{RS}(a_{N-})$, where a_{N-} was the average between the two notch lengths and the derivative of Eq 1 was computed as the change in strain divided by the change in notch length. Values of $K_{RS}(a_{N-})$ are given in Table 4 and are compared to the values from the replicate coupons that were interpolated at a_N and a_o. The results computed from prenotch strain data generally fit the trend from the residual stress coupons (Table 4 and Fig. 5). For coupon LSP-3F-1, $K_{RS}(a_{N-})$ differs significantly from $K_{RS}(a_o)$, due to both a large difference between a_{N-} and a_o (Table 4) and to the shape of $K_{RS}(a)$ for the LSP-3F condition (Fig. 5). For coupons where the difference between a_{N-} and a_o is small, the difference between $K_{RS}(a_{N-})$ and $K_{RS}(a_o)$ is less than 10 % of the value of K_Q found from the AM coupons. Therefore, it appears possible to approximate $K_{Q,Tot}$ using a single residual stress bearing coupon and prenotch strain measurement, but doing so can introduce large or small bias, depending on the quality of the measurement and the distribution of residual stress in the coupon.

Method selection is an important step when making material property measurements, and the inclusion of residual stress in fracture property testing would require additional standardization activity. Here, the slitting method directly provided the residual stress intensity factor as a function of crack length, which was readily combined with test data. Slitting was straightforward to implement and offered good repeatability (see replicate results in Fig. 5, as well as repeatability of residual stress reported in Ref [20]). Active standardization of the slitting method, within ASTM Task Group E28.13.02, would support its potential use in fracture toughness test standards. Given the good agreement for initiation toughness $K_{Q,Tot}$ and R-curve behavior shown here among coupons containing significantly different distributions of residual stress, further standardization effort is warranted to explore extension of standard fracture toughness tests via superposition of measured residual stress or K_{RS}.

Acknowledgments

The authors wish to thank the following for useful collaborations that enabled this work: Christopher Sanders (UC Davis) for carrying out many of the tests; Lloyd Hackel and Chanh Troung (Metal Improvement Company) for providing LSP; George Schneider (Sikorsky Aircraft Company) for providing material; Bob Schultz and Mark James (Alcoa Technical Center) for helpful discussions. This work was supported by the Federal Aviation Administration, Rotorcraft Damage Tolerance Program, FAA contract DTFACT-06-C-00025 ("Analytical Tools for Residual Stress Enhancement of Rotorcraft Damage Tolerance").

References

[1] Hill, M. R. and Panontin, T. L., "Micromechanical Modeling of Fracture Initiation in 7050 Aluminum," *Eng. Fract. Mech.* Vol. 69, 2002, pp. 2163–2186.

[2] Prime, M. B. and Hill, M. R., "Residual Stress, Stress Relief, and Inhomogeneity in Aluminum Plate," *Scr. Mater.* Vol. 46, 2002, pp. 77–82.

[3] Panontin, T. L. and Hill, M. R., "The Effect of Residual Stresses on Brittle and Ductile Fracture Initiation Predicted by Micromechanical Models," *Int. J. Fract.*Vol. 82, 1996, pp. 317–333.

[4] Bucci, R. J., "Effect of Residual Stress on Fatigue Crack Growth Rate Measurement," *Fracture Mechanics, Proceedings of the 13th National Symposium on Fracture Mechanics*, ASTM STP 743, ASTM International, West Conshohocken, PA, 1981, pp. 28–47.

[5] Reemsnyder, H. S. and Throop, J. F., Eds., *Residual Stress Effects in Fatigue*, ASTM STP 776, ASTM International, West Conshohocken, PA, 1982.

[6] Bucci, R. J., James, M. A., Sklyut, H., Heinimann, M. B., Ball, D. L., and Donald, J. K., "Advances in Testing and Analytical Simulation Methodologies to Support Design and Structural Integrity Assessment of Large Monolithic Parts," SAE Paper No. 2006-01-3179, Toulouse, France, Sept. 2006, Society of Automotive Engineers, Warrendale, PA.

[7] Bush, R. W., Bucci, R. J., Magnusen, P. E., and Kuhlman, G. W., "Fatigue Crack Growth Rate Measurements in Aluminum Alloy Forgings: Effects of Residual Stress and Grain Flow," *Fracture Mechanics, 23rd Symposium*, ASTM STP 1189, ASTM International, West Conshohocken, PA, pp. 568–589.

[8] United States Department of Transportation—Federal Aviation Administration, Metallic Materials Properties Development and Standardization, Report DOT/FAA/AR-MMPDS-01, 2003.

[9] Fabbro, R., Peyre, P., Berthe, L., and Scherpereel, X., "Physics and Applications of Laser-Shock Processing," *J. Laser Appl.* Vol. 10, 1998, pp. 265–279.

[10] Montross, C. S., Wei, T., Ye, L., Clark, G., and Mai, Y.-W., 2002, "Laser Shock Processing and Its Effects on Microstructure and Properties of Metal Alloys: A Review," *Int. J. Fatigue* Vol. 24, 2002, pp. 1021–1036.

[11] Pistochini, T., "Fatigue Life Optimization in Laser Peened 7050-T7451 and 300M Steel," M.S. Thesis, Department of Mechanical and Aeronautical Engineering, University of California, Davis, 2003.

[12] Luong, H., "Fatigue Life Extension and the Effects of Laser Peening on 7050-T7451 Aluminum, 7085-T651 Aluminum, and Ti-6Al-4V Titanium Alloy," M.S. Thesis, Department of Mechanical and Aeronautical Engineering, University of California, Davis, 2006.

[13] Prime, M. B., "Cross-Sectional Mapping of Residual Stresses by Measuring the Surface Contour After a Cut," *J. Eng. Mater. Technol.* Vol. 123, 2001, pp. 162–168.

[14] Prime, M. B., Sebring, R. J., Edwards, J. M., Hughes, D. J., and Webster, P. J., "Laser Surface-Contouring and Spline Data-Smoothing for Residual-Stress Measurement," *Exp. Mech.* Vol. 44, 2004, pp. 176–184.

[15] Schindler, H. J. and Bertschinger, P., "Some Steps Towards Automation of the Crack Compliance Method to Measure Residual Stress Distributions," *Proceedings of the 5th International Conference on Residual Stress, Linköping*, 1997.

[16] Ghidini, T. and Donne, C. D., "Fatigue Crack Propagation Assessment Based on Residual Stresses Obtained Through Cut-Compliance Technique," *Fatigue Fract. Eng. Mater. Struct.* Vol. 30, 2007, pp. 214–222.

[17] ASTM Standard E561–98, "Standard Practice for *R*-Curve Determination," *Annual Book of ASTM Standards*, Vol. 03.01, ASTM International, West Conshohocken, PA.

[18] ASTM Standard E399-90, "Standard Test Method for Plane-Strain Fracture Toughness of Metallic Materials," *Annual Book of ASTM Standards*, Vol. 03.01, ASTM International, West Conshohocken, PA.

[19] Towers, O. L. and Dawes, M. G., "Welding Institute Research on the Fatigue Precracking of Fracture Toughness Specimens," *Elastic-Plastic Fracture Test Methods: The User's Experience*, ASTM STP 856, ASTM International, West Conshohocken, PA, pp. 23–46.

[20] Lee, M. J. and Hill, M. R., "Intralaboratory Repeatability of Residual Stress Determined by the Slitting Method," *Exp. Mech.* Vol. 47, 2007, pp. 745–752.

ASTM Special Technical Publication, Vol. 5, No. 8
Paper ID JAI101608
Available online at www.astm.org

C. J. Aird,[1] *S. Hadidi-Moud,*[1] *C. E. Truman,*[1] *and D. J. Smith*[1]

Impact of Residual Stress and Elastic Follow-Up on Fracture

ABSTRACT: The presence of tensile residual stress in cracked structures combined with external loading leads to circumstances where a structure may fail at a lower applied load than when residual stresses are not present. This is taken into consideration in the fracture assessment codes which are usually invoked to determine whether a cracked structure is fit-for-purpose. These codes typically attempt to decompose the stresses present in the structure under consideration into either “secondary” or “primary” components, in order to simplify the assessment and avoid the need for detailed numerical modeling. It is acknowledged that whether a given residual stress field should be classified as “secondary” or as “primary” is dependent on the level of associated elastic follow-up (EFU). However, although there is a significant body of work related to the influence of EFU on the high temperature creep behavior of uncracked structures, the EFU concept has not yet been rigorously applied to the fracture assessment of cracked structures. This paper represents a first step towards a more rigorous application of the EFU concept to the fracture assessment of cracked structures containing residual stresses. Insight is provided into the influence of residual stress and EFU on fracture by considering the behavior of a simple three-bar assembly. Having introduced the concept, a three-bar type test rig capable of generating fit-up residual stresses with varying levels of EFU in a compact-tension fracture-specimen is presented. Results, produced using this test rig, from two cases with identical levels of initial residual stress but different levels of associated EFU are considered. It is concluded that EFU is important in

Manuscript received December 1, 2007; accepted for publication July 17, 2008; published online August 2008.
[1] Department of Mechanical Engineering, University of Bristol, BS8 1TR, UK, e-mail: david.smith@bristol.ac.uk

Citation: Aird, C. J., Hadidi-Moud, S., Truman, C. E. and Smith, D. J., "Impact of Residual Stress and Elastic Follow-Up on Fracture," *J. ASTM Intl.*, Vol. 5, No. 8. DOI10.1520/JAI101608. Available online at www.astm.org. Also included in JAI Special Issue STP 1508, *Fatigue and Fracture Mechanics* (*36th ASTM National Symposium on Fatigue and Fracture Mechanics*), Richard Neu, Kim Wallin and Steven R. Thompson, guest editors, ASTM International, West Conshohocken, PA, 2008, pp. 355-14.

determining how the residual force in the specimen changes (and therefore how the component of crack driving force associated with the residual force changes) as damage accumulates in the specimen subsequent to fracture initiation.

KEYWORDS: residual stress, elastic follow-up, fracture assessment

Introduction

The presence of tensile residual stress in cracked structures combined with external loading can lead to circumstances where a structure may fail at a lower applied load than when residual stresses are not present. Fracture assessment codes, [1,2], are usually invoked to determine whether a cracked structure is fit-for-purpose. These codes typically attempt to decompose the stresses present in the structure under consideration into either secondary ("fixed-displacement," which do not contribute to plastic collapse) or primary ("fixed-load," which do contribute to plastic collapse) components, in order to simplify the assessment and avoid the need for detailed numerical modeling. (Detailed whole-structure finite element models are difficult and costly to produce and are therefore only used if other more straightforward analysis procedures prove to be unsatisfactory.)

Residual stresses are usually treated as secondary stresses. However, in certain circumstances they must be classed as primary. For example, in a cracked structure where fit-up residual stresses do not self-equilibrate across a ligament, the residual stresses may provide a significant contribution to the plastic collapse of the ligament. Whether they do or not depends on how the residual forces change as crack growth and plastic deformation accumulate in the structure. This in turn depends on the level of "elastic follow-up" (EFU).

The concept of elastic follow-up finds its origin in work focused on assessing the impact of creep damage on uncracked structures carried out by Robinson [3,4]. His initial work concerned the relaxation of bolted joints due to creep. He noted that the amount of initial elastic deformation in the bolt relative to the initial elastic deformation in the bolted flange was important in determining the rate of relaxation due to creep in the bolt.

Although Robinson does not present a definition of elastic follow-up, he uses the term follow-up elasticity to refer to the amount of elastic deformation in the flange. When the flange is rigid the EFU is zero, and as plastic deformation accumulates in the bolt as a result of creep, the force in the bolt reduces while the ends of the bolt remain fixed. When the flange is elastic, EFU is nonzero, and as creep occurs in the bolt, the ends of the bolt move apart under the influence of the elastic flange. Therefore, the relaxation of force in the bolt is not as great as in the case of the rigid flange. As EFU increases, the rate of relaxation of force decreases.

It is against this background that the classification of residual stresses as either primary or secondary is made. For high levels of EFU the residual forces reduce very little as damage accumulates in the structure and the residual stresses should be treated as primary. On the other hand, for low levels of EFU the residual forces reduce a great deal as damage accumulates in the structure, and in these circumstances it may be appropriate to classify the residual stresses as secondary.

Within the context of assessing the impact of creep damage on uncracked structures, there is a significant body of published work demonstrating how stresses can be classified on the basis of the level of EFU. (Although, what EFU is taken to refer to and how it is quantified varies.) Extending the application of the EFU concept beyond uncracked structures to cracked structures containing residual stresses adds an extra level of complexity, as the effects of changing structural stiffness due to crack growth must be taken into consideration. However, although the importance of EFU for the fracture assessment of cracked structures containing residual stresses is acknowledged, the concept has yet to be rigorously applied in this area.

This paper represents a first step towards a more rigorous application of the EFU concept to the fracture assessment of cracked structures containing residual stresses. First, the nature of the residual stress fields which are considered in the fracture assessment of cracked structures is clarified. A simple three-bar structure is then presented in order to illustrate the creation of fit-up residual stresses in a structure, and to show that the level of elastic follow-up influences the relaxation of these stresses resulting from the accumulation of damage in part of the structure. Finally, a three-bar rig capable of generating fit-up residual stresses with varying levels of EFU in a compact tension (C(T)) fracture-specimen is presented. Preliminary results from this rig are presented which show that, for a given initial level of tensile residual stress in the specimen, the degree of residual stress relaxation for a given amount of crack growth and plastic deformation in the specimen depends on the level of associated EFU.

Residual Stress Length Scales

Before considering the influence of residual stress on the fracture of structures, it is first necessary to appreciate that residual stresses exist with metallic structures at a range of different length scales and that not all of these stresses are considered relevant to fracture assessment calculations.

Several researchers have attempted to classify the residual stresses which exist within polycrystalline metallic structures. For example, Masubuchi [5] distinguishes between Type I, II, and III residual stresses, with each type characterized by the length over which the stress field balances. Figures 1 and 2 illustrate these three types of residual stress, which are defined with reference to polycrystalline materials as follows: Type I—macro-residual stresses, σ_I^R, that develop in the body of a structure on a length scale larger than the grain size of the material, Type II—meso-residual stresses, σ_{II}^R, that vary on a length scale of several grains, and Type III—micro-residual stresses, σ_{III}^R, that exist within a grain.

In the context of the fracture assessment of engineering structures containing cracks of the order of several millimetres, Type II and Type III residual stresses provide little contribution to the crack driving force and are therefore generally ignored. However, Type I residual stresses result from misfits on a

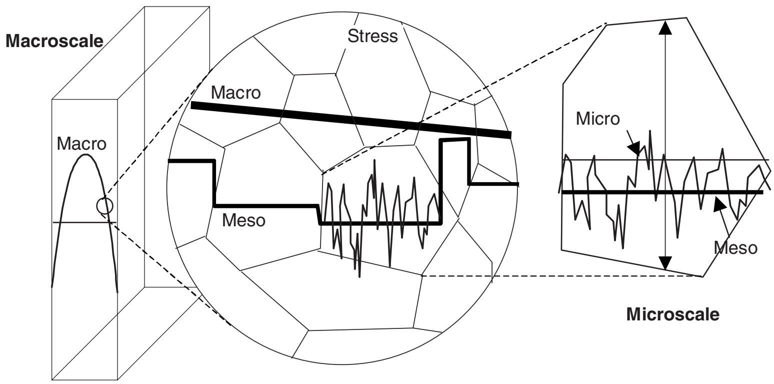

FIG. 1—*An illustration of the relationship between the various residual stresses and the microstructure of a polycrystalline material.*

structural level and may therefore provide a significant contribution to the crack driving force. It is these Type I residual stresses with which we are concerned in this paper.

Behavior of a Simple Structure

As a starting point in our assessment of the influence of Type I residual stresses on the fracture of structures, we now consider the three-bar assembly shown in Fig. 3.

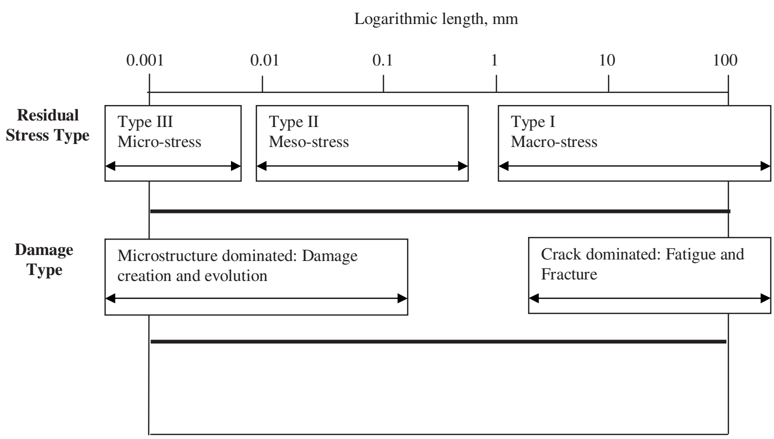

FIG. 2—*Residual stress and structural integrity.*

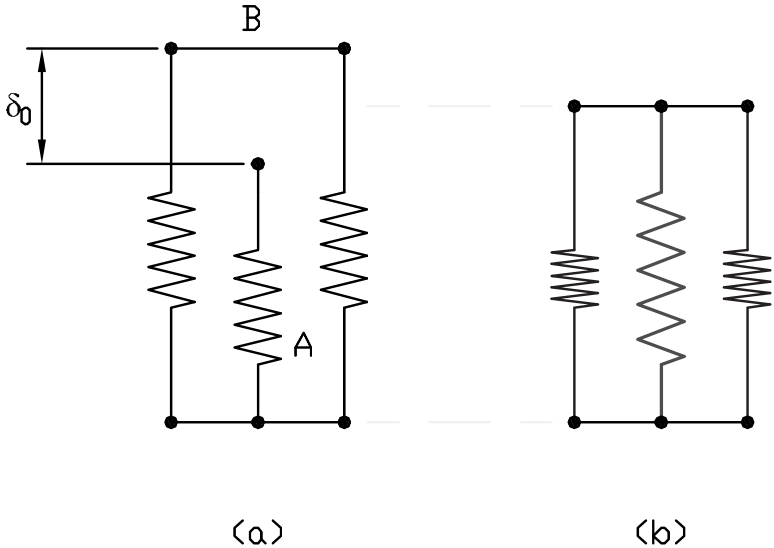

FIG. 3—*Schematic of three-bar structure before and after preloading.*

Creation of Residual Stress

The assembly consists of two main parts: Bar A, and the remainder of the assembly which we refer to as Bar B. These bars are able to deform elastically and have stiffnesses K_A and K_B, respectively. An initial misfit, δ_0, exists between the bars so that joining the bars together introduces fit-up residual stresses into the system, with tension in Bar A and balancing compression in Bar B, as shown in Fig. 3(*b*).

Note that the residual stress in Bar A does not self-equilibrate across a section through the bar. A net-residual-tensile force acts on Bar A, with equilibrium being maintained by a balancing compressive force in Bar B. Therefore, as noted above, the residual stress field associated with this system may have to be classed as primary as, depending on the level of EFU, the residual stresses may provide a significant contribution to the plastic collapse of part of the structure.

With reference to this preloaded structure, we now proceed to offer a definition of elastic follow-up for the purpose of our discussions in this paper.

Elastic Follow-Up

As mentioned above, the earliest use of the term elastic follow-up dates back to a paper by Robinson [3] first published in 1939. Following on from Robinson's early work, which focused on the creep relaxation of bolted joints, the influence of EFU on creep in high temperature pipework systems was investigated by a number of researchers including Teramae [6], Dhalla [7], Roche [8], and Boyle [9]. However, in these papers, the term EFU is used in different ways. Robinson uses follow-up elasticity to refer to the elastic deformation of the flange in the

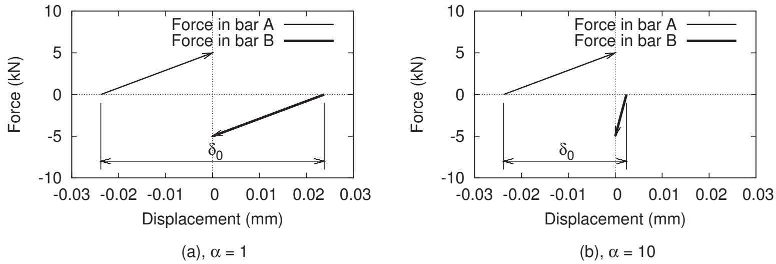

FIG. 4—*Creating residual force in a three-bar structure.*

case of the bolted flange. Goldhoff [10] uses EFU in the same way. However, Roche talks about EFU occurring (rather than already existing) "when the least stressed parts of the piping act as a spring on the most stressed parts in which creep deformation accumulates."

Therefore, given these differences in the use of the term EFU, we must provide a working definition of EFU within the context of this paper. In this paper, we will consider how the process of damage evolution in Bar A (whether crack growth or plastic deformation) is influenced by the residual force imposed on Bar A by the surrounding structure. With this in mind, we describe the elastic deflection of Bar B during the preloading process, δ_B, as the elastic follow-up deflection of Bar B, or the elastic follow-up for short. This allows us to assess the impact of the initial EFU in Bar B on the fracture of Bar A.

Note that for a given initial preload in Bar A the level of EFU in Bar B varies, depending on the stiffness of Bar B. In other words, two assemblies with exactly the same preload in Bar A can have very different levels of EFU in Bar B. This is shown in Fig. 4 where two cases are compared. In the first case, the ratio of the stiffness of Bar B to that of Bar A is 1. In the second case, the ratio is 10 and the level of EFU in Bar B is one-tenth that of the first case. This ratio turns out to be important, and we therefore define $\alpha = K_B/K_A$.

Subsequent Loading

We now consider the subsequent loading of these preloaded assemblies with the aim of establishing how the level of EFU influences the process of damage evolution in Bar A.[2] In the $\alpha = 1$ case, we assume first of all that the entire system responds to the applied load by deforming elastically. In this way, as shown by Fig. 5(*a*), the stress in Bar A increases from its initial preload level of 25 MPa (Point A) up to, in this case, 125 MPa (Point B).

If, however, as the applied load is increased, damage (be it due to crack growth or to plastic deformation) begins to accumulate in Bar A, then when the maximum applied load is reached the bar will no longer lie at Point B. Exactly

[2]With a view to modeling the behavior of welded steel structures, a Young's modulus of 210 GPa was assumed. The geometry was chosen so that the magnitude of the initial residual stress in the assembly was within the range of residual stresses associated with such structures.

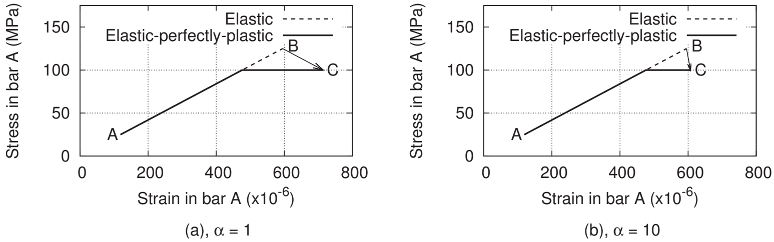

FIG. 5—*Stress and strain response of Bar A during loading of three-bar structure.*

where on the stress-strain diagram the final point will lie depends on the amount of crack growth or plastic deformation. To illustrate this point, we assume that Bar A yields at a stress of 100 MPa and behaves in an elastic-perfectly-plastic manner. This being the case, as the applied load is increased, the stress and strain in the bar increase from their initial preload levels (Point A), and end up at Point C rather than Point B.

In the $\alpha = 10$ case, shown in Fig. 5(*b*), we again consider the elastic system being loaded so that the stress in Bar A increases from its initial preload level of 25 MPa (Point A) up to 125 MPa (Point B). This is identical to the elastic response of Bar A in the $\alpha = 1$ case. However, if it is again assumed that Bar A yields at a stress of 100 MPa, then the position of Point C on the stress-strain diagram is in this case quite different.

Comparing the behavior of Bar A in these two systems shows that if the structure remains elastic then the response is identical. If, however, Bar A is weakened for some reason and both systems are then reloaded as before, then more damage is sustained in Bar A in the system with the higher initial level of EFU. Although this is true, it is the stiffness of Bar B, K_B, which lies behind the initial level of EFU and which accounts for the different behavior in these cases. In fact, if there was no initial residual stress, and therefore no initial EFU (according to the definition given above) in either of these two systems, then repeating the tests would again show the same difference in the gradient of the line BC in the two cases.

The extreme cases correspond to Bar B being much stiffer ($\alpha \to \infty$) or much less stiff ($\alpha \to 0$) than Bar A. As $\alpha \to \infty$ the line BC tends to the vertical. As $\alpha \to 0$ the line BC tends to the horizontal. The boundary conditions associated with Bar A in these extreme cases correspond to fixed-displacement and to fixed-load conditions, respectively.

The Influence of Residual Stress

The preceding analysis has demonstrated that, regardless of the level of residual stress in the assembly, the stiffness of Bar B relative to that of Bar A is an important parameter. However, the focus of this paper is on how residual stress influences fracture. We therefore now turn to consider how the level of residual force changes during the process of loading these two assemblies, again assuming Bar A to yield at a stress of 100 MPa.

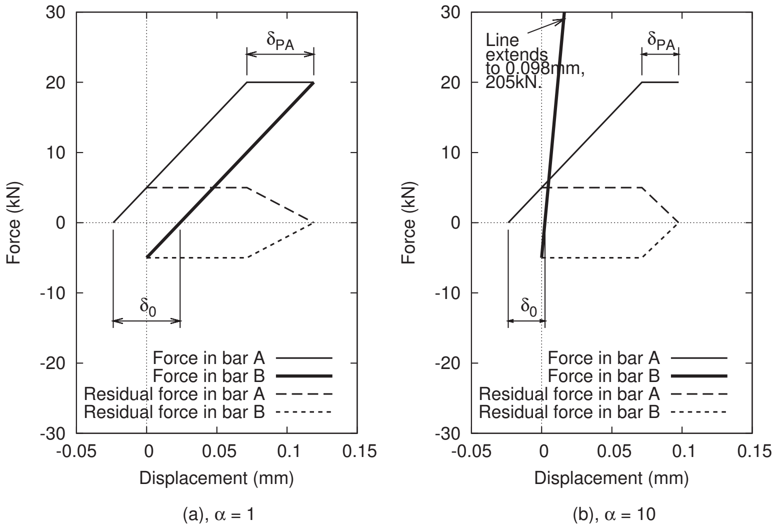

FIG. 6—*Redistribution of misfit residual force during external loading.*

Figure 6(*a*) shows, for the $\alpha=1$ case, how the forces in Bars A and B change as the external load applied to the assembly is increased. Lines are also included which show how the level of residual force in each of the bars changes. Initially, at the zero displacement point, the force in the two bars is equal and opposite. This corresponds to the situation immediately after preloading and before the any external load is applied to the assembly. As the applied load is increased, the level of residual force in the assembly initially remains constant. However, as soon as Bar A begins to yield, the level of residual force starts to reduce. When, as the applied load is increased still further, the amount of plastic deformation in Bar A, δ_{PA}, becomes equal to the initial misfit, δ_0, the residual force is reduced to zero.

Figure 6(*b*) shows the equivalent plot for the $\alpha=10$ case. Note that the initial forces in Bars A and B, which are again equal and opposite, are identical to the initial forces in the $\alpha=1$ case. As in the $\alpha=1$ case, the residual force is reduced to zero when the plastic strain in Bar A becomes equal to the initial misfit. However, since in the $\alpha=10$ case the initial level of EFU is lower than in the $\alpha=1$ case, the initial misfit is also lower and less plastic deformation of Bar A is required to reduce the same level of initial residual force to zero.

Another point to consider is how the level of force required to cause a given amount of plastic strain in Bar A of each of the two preloaded assemblies compares with the level of force required to cause the same amount of damage in the same assemblies without any initial preload. This is a measure of how the residual force in the assembly influences the evolution of damage in the assembly. Although the level of preload is the same in both assemblies, it can be shown that the ratio of the force required to cause a given amount of plastic strain in Bar A in the preloaded case to the force required in the case with no initial preload is different in each assembly. The ratio in the case of the $\alpha=10$

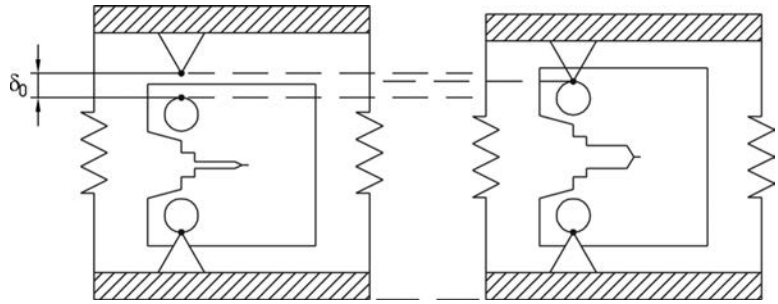

FIG. 7—*Concept of introducing misfit into a fracture mechanics specimen.*

assembly is higher that that corresponding to the $\alpha = 1$ assembly. This suggests that the influence of an initial residual force in the assembly is dependent on the associated level of EFU.

Experimental Studies

We have discussed the behavior of a simple structure and provided insight into concepts of misfit residual stress, the subsequent loading of the structure, and illustrated how a residual stress can relax. These features were explored in an experimental study where it was necessary to consider the design of a test rig. The concept for the test rig is shown in Fig. 7 which illustrates a compact tension, C(T), specimen subjected to a misfit inside an elastic frame. Further details of the rig are described below.

Design of a Test Rig

The test rig was designed with a three-step test-method in mind. First, the rig would be used to preload a fracture-specimen, leaving it in a state of tension at the end of the preloading process. Second, the entire preloaded assembly would then be mounted in a tensile test machine and loaded to a predetermined load level. Finally, on unloading the assembly, the amount of residual stress relaxation would be calculated and the influence of EFU on this relaxation determined.

With reference to Fig. 7, it can be appreciated that the level of preload in the fracture-specimen is a function of the stiffness of the rig, K_B, the stiffness of the specimen, K_A, and the degree of misfit, δ_0 between the specimen and the rig. This can be expressed by

$$F_{AR} = \frac{K_A K_B}{K_A + K_B} \delta_0 \tag{1}$$

where F_{AR} is the residual force in the specimen created as a result of the misfit.

If, during the process of subsequent loading of the preloaded assembly, any of these three values change, then, on unloading, the level of preload remaining in the assembly will change. Since the rig has been designed to remain in the

TABLE 1—*Limiting values of* β *and* χ.

	β	χ
$\alpha \rightarrow \infty$ (Fixed-displacement)	δ_0	K_A
$\alpha \rightarrow 0$ (Fixed-load)	0	0

elastic regime during the process of loading and unloading, the stiffness of the rig, K_B, remains constant. However, any damage occurring in the specimen has the potential to reduce the specimen stiffness, K_A, and the misfit, δ_0. For example, any crack growth will result in the specimen stiffness being reduced and any plastic deformation of the specimen will result in the misfit being reduced. Both of these reductions have the effect of reducing the level of preload (or residual stress) in the specimen as illustrated earlier for the three-bar structure.

To understand how any change in either stiffness or misfit changes the force in the specimen Eq 1 is differentiated with respect to the stiffness of the specimen and the misfit to give

$$\beta = \frac{\partial F_{AR}}{\partial K_A} = \left(\frac{\alpha}{1+\alpha}\right)^2 \delta_0$$

$$\chi = \frac{\partial F_{AR}}{\partial \delta_0} = \left(\frac{\alpha}{1+\alpha}\right) K_A \tag{2}$$

where $\alpha = K_B/K_A$.

There is only a limited range of values for β and χ, the extremes of this range corresponding to α tending to either infinity or to zero. These are given in Table 1.

The specimen experiences fixed-displacement boundary conditions when $\alpha \rightarrow \infty$, with the rig being effectively rigid compared to the specimen. Therefore, on joining the specimen and rig together, the specimen displaces by an amount equal to the initial misfit δ_0 while the rig does not displace at all.

The specimen experiences fixed-load boundary conditions when $\alpha \rightarrow 0$, with the specimen being effectively rigid compared to the rig. Therefore, on joining the specimen and rig together, the rig displaces by an amount equal to the initial misfit δ_0 while the specimen does not displace at all.

Equation 2 reveals that the proximity to fixed-displacement or to fixed-load conditions is a function of α only. By normalizing Eq 2 against the rate of change of preload corresponding to equivalent fixed-displacement conditions [3] the following equations can be derived:

[3]Equivalent fixed displacement conditions correspond to (a) the stiffness of the specimen being identical to that of the general case being normalized, (b) the specimen load attachment points being held at a fixed displacement ($\alpha \rightarrow \infty$) such that the initial level of force in the bar is equal to that of the general case being normalized.

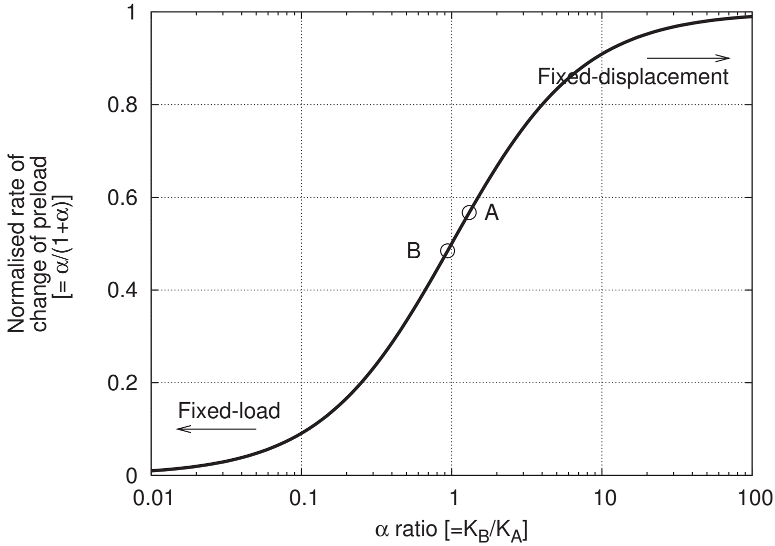

FIG. 8—*Rate of change of preload normalized against equivalent "fixed-displacement" conditions as a function of the stiffness ratio α.*

$$\frac{\beta}{\beta|_{EQUIV\_FIXED\_DISP\_CONDS}} = \frac{\alpha}{1+\alpha}$$

$$\frac{\chi}{\chi|_{EQUIV\_FIXED\_DISP\_CONDS}} = \frac{\alpha}{1+\alpha} \tag{3}$$

Equation 3 is plotted in Fig. 8 which shows that for values of the stiffness ratio greater than about ten there is only a small change in Eq 3. These conditions essentially correspond to fixed-displacement boundary conditions on the fracture-specimen. When the stiffness ratio is less than about 0.1, fixed-load boundary conditions are approached. (Note that Points A and B correspond to the two test arrangements used. These arrangements are discussed in more detail below.)

Experiments

Tests were carried out at room temperature using the preload rig in conjunction with C(T) specimens. A schematic of the overall arrangement is shown in Fig. 9. The specimens used were 15 mm thick by 60 mm high by 50 mm wide 2024-T351 aluminum alloy C(T) specimens with a 5 mm long by 0.1 mm wide notch forming the tip of the 25 mm long crack, and with a crack length to specimen width ratio of 0.5. The specimens were not sidegrooved. Knife edges, attached to the specimens, were used in conjunction with a clip gage to measure the load line displacement during each test.

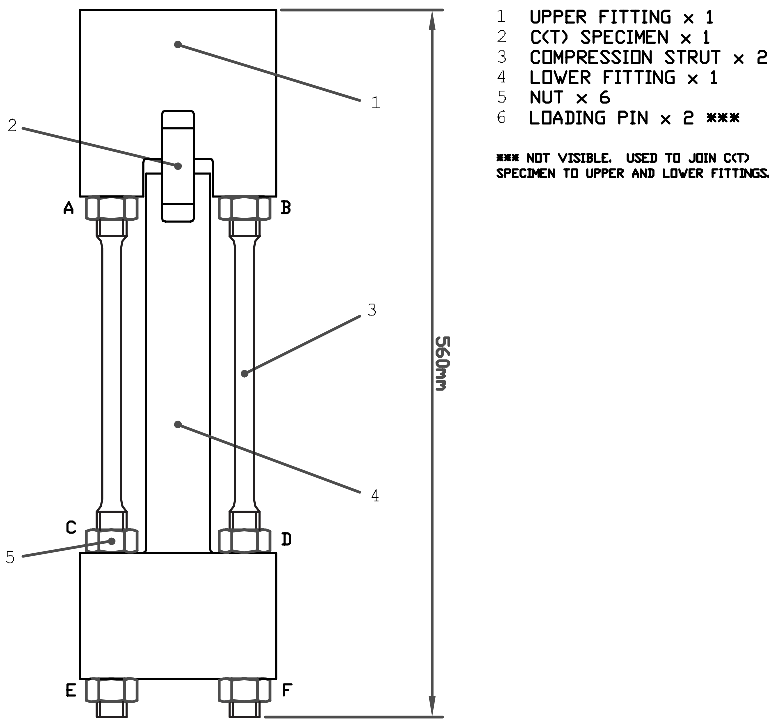

FIG. 9—*Layout of test rig.*

These specimens were chosen as their fracture behavior was well understood [11]. Figure 10 shows the ductile fracture toughness of the alloy as a function of the extent of ductile tearing. Mahmoudi [11] generated these results from experiments using specimens machined from the same aluminum plate as those considered in this paper, to the same drawing, and with cracks introduced using wire electro-discharge machining.

As mentioned above, a three-step test procedure was followed. First, the rig was used to preload a C(T) specimen. This was done as follows. The C(T) specimen was joined to the upper and lower fittings using the two loading pins. Next, the compression struts were screwed into the upper fitting and nuts A and B were tightened. At this point no residual stress existed in the assembly. Then, by screwing nuts C and D down, the upper and lower fittings were forced apart with the result that the fracture-specimen was loaded in tension, to a predetermined level, and the compression struts carried a balancing compressive load. Finally, nuts E and F were screwed onto the ends of the compression struts until contact was made with the lower fitting.

Second, having introduced residual stress into the specimen, the entire assembly was then loaded in tension using a hydraulic tensile test machine. The load was increased until the clip gage reading reached a predetermined level. Finally, the load was reduced to zero and the residual force remaining in the system compared with that at the beginning of the test.

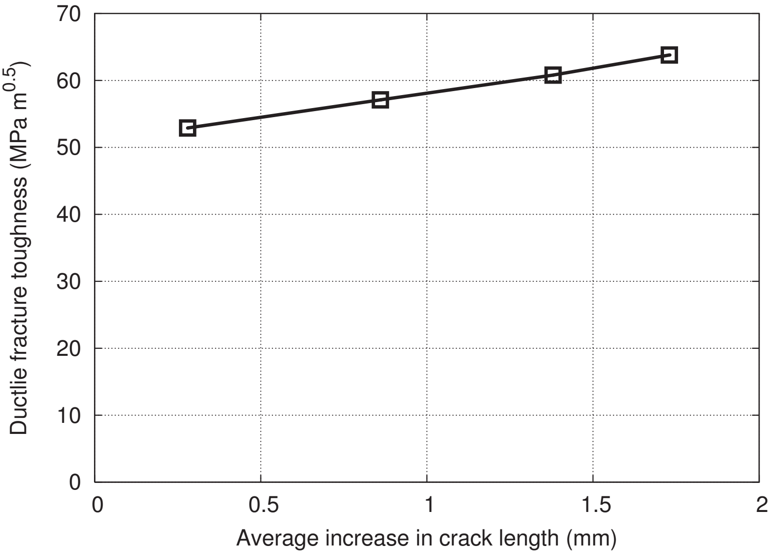

FIG. 10—*Fracture resistance of aluminum alloy 2024-T351 from Ref.* [*11*].

In order to demonstrate the influence of EFU on residual stress relaxation, the test was repeated using loading pins with a lower stiffness, which had the effect of reducing the rig stiffness K_B. These two cases are therefore referred to as the stiff-rig and soft-rig cases, respectively. Table 2 lists the materials used to manufacture each of the test rig components.

Results

Figure 11 shows the force in the C(T) specimen as a function of load line displacement, measured using a clip-gage attached to the specimen, for the stiff-rig case. The points between A and B represent the increase in specimen load during the preloading process. The force at Point B (7.59 kN) corresponds to the initial preload level. The points between B and D correspond to loading of the entire preloaded assembly. (Point C corresponds to the point at which the crack begins to grow.) The points between D and E show the reduction in C(T) specimen force during the unloading phase, with the force at Point E (2.43 kN) corresponding to the final preload level. Finally, the points between E and F show the reduction in force associated with removing the C(T) specimen from

TABLE 2—*Test rig—materials used.*

Upper fitting	EN26 high tensile steel
Compression struts	7075-T6 aluminium
Lower fitting	EN26 high tensile steel
Loading pins, stiff-rig	Nimonic 90
Loading pins, soft-rig	7075-T6 aluminium

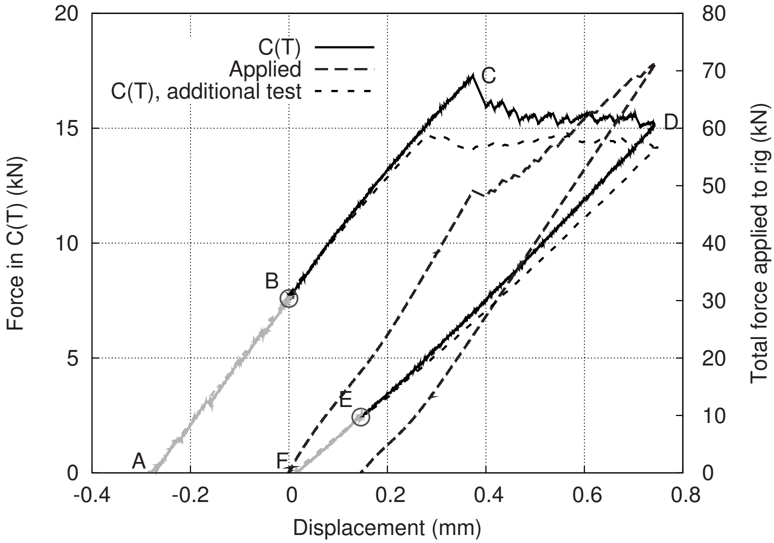

FIG. 11—*Force versus load line displacement, stiff-rig.*

the assembly at the end of the test. The coordinates of Points A to F are given in Table 3. (Results from an additional test are included which show that, given approximately the same initial preload and maximum load-line displacement, the relaxation in residual force is almost identical.)

Figure 12 shows the corresponding plot for the soft-rig case. The coordinates of Points A′ to F′ are given in Table 4.

Note that Points E and E′ in these figures correspond to the final level of residual force in the specimen after the load applied to the assembly is reduced to zero. This can be seen from the lines showing the total force applied to the test rig during each of the tests, which both begin and end at zero. Note that the kinks in these lines correspond to the load in the compression struts changing from compression to tension or vice versa.

TABLE 3—*Coordinates of key points in Fig. 11, stiff-rig.*

	Force (kN)	Disp (mm)
A	0.01	−0.29
B	7.59	0.00
C	17.28	0.37
D	15.25	0.74
E	2.43	0.15
F	0.00	0.02

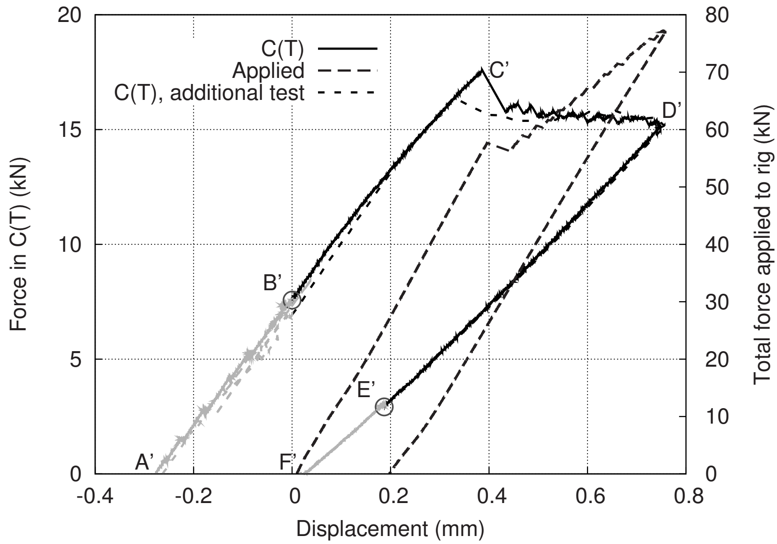

FIG. 12—*Force versus load line displacement, soft-rig.*

Discussion

Consider the C(T) specimen force versus displacement curve for the stiff-rig case shown in Fig. 11. By loading the preloaded assembly beyond the point of fracture initiation (Point C), both crack growth and plastic deformation accumulate in the specimen. This can be seen from the unloading line DF in Fig. 11. Notice first that the slope of line DF is lower than the slope of the initial loading line AC. This reduction in slope corresponds to a reduction in stiffness due to crack growth. The data of Table 3 suggest an initial stiffness of 26.2 kN/mm and a final stiffness of 21.2 kN/mm. Using the standard formula for the compliance of a C(T) specimen taken from Table A7.2 of Ref. [12] and presented in Eq 4, the crack lengths associated with each of these stiffnesses can be calculated. Given the specimen thickness of 15 mm, specimen width of 50 mm, and Young's modulus for the material of 69 GPa, the initial stiffness of 26.2 kN/mm corresponds to an initial crack length of 25.7 mm. Similarly, the

TABLE 4—*Coordinates of key points in Fig. 12, soft-rig.*

	Force (kN)	Disp (mm)
A′	0.01	−0.28
B′	7.57	0.00
C′	17.59	0.39
D′	15.32	0.74
E′	2.92	0.19
F′	0.00	0.03

final stiffness of 21.2 kN/mm corresponds to a crack length of 27.7 mm, an increase in length of 2.0 mm. This confirms that the measured stiffness values are reasonable.

$$stiffness = \frac{BE}{f\left(\frac{a}{W}\right)} \tag{4}$$

where
 B is the specimen thickness;
 E is the Young's modulus;
 a is the crack length; and
 W is the specimen width.
 and

$$f\left(\frac{a}{W}\right) = \left(\frac{1+\frac{a}{W}}{1-\frac{a}{W}}\right)^2 \left[\begin{array}{l} 2.163 + 12.219\left(\frac{a}{W}\right) - 20.065\left(\frac{a}{W}\right)^2 \\ - 0.9925\left(\frac{a}{W}\right)^3 + 20.609\left(\frac{a}{W}\right)^4 - 9.9314\left(\frac{a}{W}\right)^5 \end{array}\right]$$

Second, notice that on complete unloading the specimen remains at Point F rather than returning to Point A. The difference in displacement between these two points corresponds to the reduction in misfit between the specimen and the jig accumulated during the test. Table 3 suggests a reduction in misfit of 0.31 mm. This reduction in misfit results from plastic deformation local to the notch tip and also any incomplete closure of the newly created crack surfaces. However, the fact that the unloading line DF does not increase in gradient as the load in the specimen reduces suggests that any incomplete crack-closure effect is small. Also, post-test inspection of the specimens clearly showed a significant opening-up of the notch, associated with plastic deformation local to the notch tip.

Notice also that the level of residual force in the specimen drops from 7.59 kN at the start of the test (Point B) to 2.43 kN at the end (Point E). As noted previously, the level of residual force in the assembly is a function of three elements: the specimen stiffness, K_A, the rig stiffness, K_B, and the initial misfit, δ_0. Therefore, assuming that the rig is not damaged in any way during the test, the 5.16 kN drop in residual force is a function of the reduction in specimen stiffness (from 26.2 kN/mm to 21.2 kN/mm) and the reduction in initial misfit (reduced by 0.31 mm). Equation 1 above suggests an initial misfit of 0.50 mm, and that by reducing the misfit by 0.31 mm, but keeping the same initial specimen stiffness, the residual force would be expected to drop by 4.73 kN. On the other hand, it suggests that keeping the same initial misfit but reducing the specimen stiffness would lead to a drop of just 0.96 kN. This implies that the 5.16 kN reduction in residual force is due mainly to the change in misfit resulting from the plastic deformation of the specimen.

Now consider the equivalent results for the soft-rig case shown in Fig. 12. Again the same behavior is evident. In this case Table 4 suggests an initial preload of 7.57 kN (0.3 % lower than the stiff-rig case), an initial stiffness of

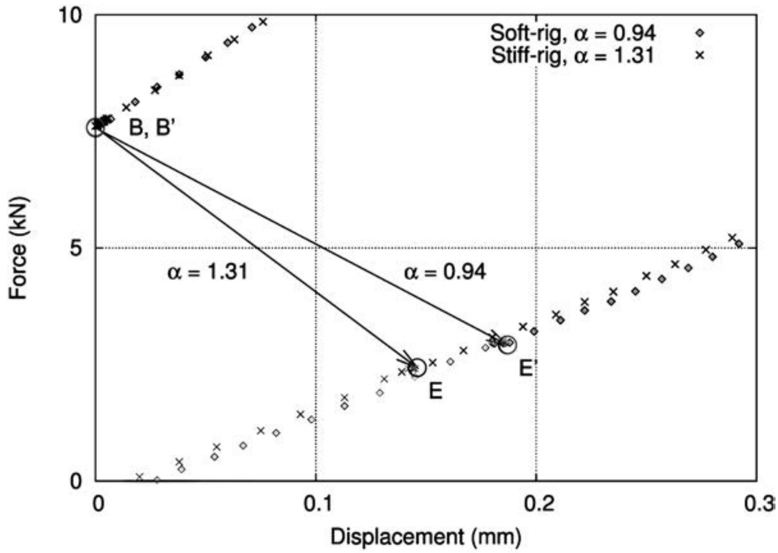

FIG. 13—*Comparison of "relaxation lines" for stiff-rig* (α=1.31) *and soft-rig* (α=0.94) *tests.* (*For clarity error bars are not shown.*)

26.2 kN/mm (identical to the stiff-rig case), a final stiffness of 21.6 kN/mm (1.9 % higher than the stiff-rig case) and a plastic deformation of 0.31 mm (identical to the stiff-rig case). Therefore, given the same misfit and rig stiffness as the stiff-rig case, we would expect a reduction in residual force very close to the 5.16 kN drop seen in the test using the stiff-rig.

However, the reduction in residual force is actually 4.65 kN, ~10 % lower than in the stiff-rig test. The reason for this is that although the change in specimen stiffness and the change in misfit in both tests are almost identical, the change in specimen stiffness relative to that of the rig, and the relative change in misfit are lower in the soft-rig test. In the soft-rig case, Eq 1 suggests an initial misfit of 0.59 mm (greater than the 0.50 mm misfit of the stiff-rig case) so that a reduction in misfit of 0.31 mm corresponds to only a 53 % reduction in misfit compared to a 62 % reduction in the stiff-rig case.

Figure 13 compares the initial and final preload levels in the two tests. (For clarity, error bars are not shown.) Note that the slopes of the "relaxation lines" BE and B′E′ correspond to the jig stiffness in each case. They show the rig to specimen stiffness ratio, α, to be 1.31 in the stiff-rig case and 0.94 in the soft-rig case. Also, the slopes of lines BE and B′E′ are consistent with the different initial normalized rate of change of preload values predicted for the two cases by Eq 3, 0.57 in the case of α=1.31, and 0.49 in the case of α=0.94. See Points A and B in Fig. 8.

Finally, although it has been demonstrated that the rate of residual stress relaxation subsequent to fracture initiation is governed by the initial EFU, it should be noted that the additional specimen force (and therefore the additional crack driving force) required to initiate fracture is not influenced by the initial EFU. This can be deduced from the gradient of the lines AC and A′C′ in Fig. 11 and Fig. 12, respectively which remain very nearly constant up to the point of fracture initiation. These gradients indicate that there is very little plastic deformation, relative to the initial misfit δ_0, prior to initiation, which means that up to the point of initiation the level of residual force (and therefore crack driving force) in the assembly remains fixed in both cases.

Concluding Remarks

This paper has aimed to provide some insight into the influence of residual stress and elastic follow-up on fracture, by considering the behavior of a simple three-bar type assembly. It was noted that two such assemblies could have exactly the same level of preload but different levels of EFU. An experimental arrangement was then presented, along with test results corresponding to two cases with the same initial preload but different levels of associated EFU. From these results, the following main conclusions can be drawn.

First, the level of additional C(T) specimen force (and therefore the additional crack driving force) required to initiate fracture is reduced by the presence of an initial tensile residual force but *is not* influenced by the level of associated EFU. The key point in support of this conclusion is that the gradient of the lines AC and A′C′ in Fig. 11 and Fig. 12, respectively, remains very nearly constant up to the point of fracture initiation. This indicates that there is very little plastic deformation, relative to the initial misfit δ_0, prior to initiation, which means that up to the point of initiation the level of residual force in the assembly remains fixed in both cases.

Second, how the residual force in the specimen changes (and therefore how the component of crack driving force associated with the residual force changes) as damage accumulates in the specimen subsequent to fracture initiation *is* dependent on the level of associated EFU. This can be appreciated by comparing the change in residual force in the stiff-rig ($\alpha=1.31$) and soft-rig ($\alpha=0.94$) tests. See Fig. 13. Although the level of initial residual force in both specimens was very nearly identical, and both specimens were subject to comparable amounts of crack growth and plastic deformation, the reduction in preload was 5.16 kN in the stiff-rig case but 4.65 kN (10 % less) in the soft-rig case.

This means that while the initial additional crack driving force required to initiate fracture was the same in both cases, by the end of the test the additional crack driving force required to initiate further fracture was lower in the case with the higher initial EFU (the soft-rig, $\alpha=0.94$, case). This suggests that residual stresses associated with high levels of EFU are likely to be more damaging than those associated with low levels of EFU.

As mentioned previously, an awareness of this is shown in some of the current structural integrity assessment codes. For example, the R6 code developed by British Energy [1] directs the engineer to treat residual stresses as primary rather than secondary stresses if associated with high levels of EFU. However, no guidance is given regarding how to quantify the level of EFU for the purpose of making this judgement.

The challenge for future work is to consider how the concepts presented in this paper translate to real structures, with a view to improving the means by which EFU effects are accounted for in structural integrity calculations.

Acknowledgments

C. Aird was supported by a Rolls-Royce studentship. S. Haididi-Moud was supported by a grant from the NPCT program. C. Truman was supported by an EPSRC Research Fellowship. D. Smith is grateful for the support of a Royal Society Merit Award.

References

[1] British Energy, "R6, Assessment of the Integrity of Structures Containing Defects, Revision 4," British Energy Generation Limited, 2001.

[2] BSI-British Standards Institute, BS7910 "Guide to Methods for Assessing the Acceptability of Flaws in Metallic Structures," 2005.

[3] Robinson, E. L., "The Resistance to Relaxation of Materials at High Temperature," *Trans. ASME*, Vol. 61, 1939, pp. 543–550.

[4] Robinson, E. L., "Steam-Piping Design to Minimize Creep Concentrations," *Trans. ASME*, Vol. 77, 1955, pp. 1147—1162.

[5] Masubuchi, K., *Analysis of Welded Structures: Residual Stresses, Distortion, and Their Consequences*, Pergamon Press, Oxford, 1980.

[6] Teramae, T., "A Simplified Method for Elastic Follow-Up Analysis of Elevated Temperature Piping Systems," *Int. J. Pressure Vessels Piping*, Vol. 12, 1983, pp. 29–41.

[7] Dhalla, A. K., and Jones, G. L., "ASME Code Classification of Pipe Stresses: a Simplified Elastic Procedure," *Int. J. Pressure Vessels Piping*, Vol. 26, 1986, pp. 145–166.

[8] Roche, R. L., "Estimation of Piping Elastic Follow-Up by Using Conventional Computations," *Int. J. Pressure Vessels Piping*, Vol. 26, 1986, pp. 53–78.

[9] Boyle, J. T., and Nakamura, K., "The Assessment of Elastic Follow-Up in High Temperature Piping Systems—Overall Survey and Theoretical Aspects," *Int. J. Pressure Vessels Piping*, Vol. 29, 1987, pp. 167–194.

[10] Goldhoff, R. M., Zwicky, E. E., and Bahr, H. C., "The Effect of Simulated Elastic Follow-Up on the Relaxation Properties of Bolting Steels," *American Society of Mechanical Engineers Metals Engineering Conference*, 1967.

[11] Mahmoudi, A. H., "Influence of Residual Stress on Fracture," Ph.D. Thesis, University of Bristol, UK, 2005.

[12] Anderson, T. L., *Fracture Mechanics—Fundamentals and Applications*, 3rd ed., CRC, Boca Raton, Florida, 1995.

MULTISCALE AND PHYSICS-BASED APPROACHES

ASTM Special Technical Publication, Vol. 5, No. 9
Paper ID JAI101545
Available online at www.astm.org

M. Marx,[1] *W. Schaef,*[1] *M. Welsch,*[1] *and H. Vehoff*[2]

Focused Ion Beam as New Tool for Local Investigations of the Interaction of Microcracks with Grain Boundaries

ABSTRACT: So far the interaction of microcracks with microstructural elements like grain boundaries or phase boundaries is described qualitatively well by the models of Tanaka and Navarro and De Los Rios. However, an experimentally verified quantitative description is missing due to a lack of systematic experiments. The concept by Marx and Schaef introduced a combination of a focused ion beam technique with high resolution scanning electron microscopy. It is the first method to initiate artificial microcracks with idealized crack parameters relative to selected phase and grain boundaries. This combination of characterizing and manipulating techniques on a microscale enables for the first time a systematic investigation of the interaction between short cracks and micro-structural barriers to check the models quantitatively. However, the geometry of the active slip planes in the adjacent grains, their misorientation angle, and the position of the grain boundary is a three-dimensional problem. Therefore the geometry was reconstructed after the crack propagation measurements by focused ion beam tomography to measure the inclination angles between the surface, the crack plane, and the grain boundary. The results should lead to a better understanding of the physical mechanisms of crack propagation through grain and phase boundaries, which is fundamental to explain the huge scatter in the short crack behavior and to develop materials with fatigue resistant grain boundaries.

Manuscript received November 9, 2007; accepted for publication July 21, 2008; published online October 2008.
[1] Graduate Research Assistant, Institute of Materials Science and Methods, Saarland University, Campus D2 3, D-66041 Saarbruecken, Germany.
[2] Professor, Institute of Materials Science and Methods, Saarland University, Campus D2 3, D-66041 Saarbruecken, Germany.

Citation: Marx, M., Schaef, W., Welsch, M., and Vehoff, H., "Focused Ion Beam as New Tool for Local Investigations of the Interaction of Microcracks with Grain Boundaries," *J. ASTM Intl.*, Vol. 5, No. 9. DOI10.1520/JAI101545. Available online at www.astm.org. Also included in JAI Special Issue STP 1508, *Fatigue and Fracture Mechanics: 36th Volume*, R. W. Neu, K. R. W. Wallin, and S. R. Thompson, guest editors, ASTM International, West Conshohocken, PA, 2009, pp. 377-401.

KEYWORDS: fatigue crack growth, microcracks, grain boundary, phase boundary, focused ion beam

Introduction

For technological applications of construction materials, a reliable method of lifetime prediction with respect to fatigue is a prerequisite. Unfortunately the empirical models for lifetime prediction like the Paris law work only for long cracks. Fatigue life is controlled by the initiation and propagation of microcracks which takes up to 90 % of the lifetime and there is a large scatter in the propagation behavior of microstructurally short cracks [1–3]. The major reason for this is the interaction of the microcracks with microstructural barriers like grain and phase boundaries. While the models of Tanaka [4] and Navarro and De Los Rios [5] describe this interaction qualitatively by a pile up of dislocations in front of the crack tip, one parameter to quantify the resistance of a grain boundary against crack propagation is introduced in the Zhai model which uses the misorientation angle of the active slip planes in the adjacent grains. Nevertheless, a quantitative description of the deceleration of the crack growth rate regarding the interface parameters is missing.

The parameters are local material parameters such as the misorientation of adjacent grains or segregation on the interfaces, and crack parameters like crack length and distance to the grain boundary. It is necessary to investigate the mechanisms of the interaction systematically and locally to create a more physically based model. For such a systematic investigation, cracks must be observed which have predetermined parameters and interact with preselected grain boundaries. This cannot be realized with natural cracks due to their statistical behavior. Hence a method to initiate artificial microcracks was developed which is presented in this paper.

So far in the models the grain boundaries are considered as barriers for the transition of dislocations which are emitted from the crack tip. This blocking effect results in a pile-up of the dislocations in front of a grain boundary and in a shielding of the crack tip from the stress field. Consequently, cracks reduce their propagation rate in front of grain boundaries, some short cracks even stop during a significant number of cycles. However, not every grain boundary shows the same effect. It is assumed that the misorientation of the preferred slip systems in the adjacent grain is essential for the strength of the blocking effect [6,7]. To investigate this influence in detail, grain boundaries with different misorientation angles of the preferred slip systems are selected by electron back scatter diffraction (EBSD). Afterwards cracks are initiated near the grain boundaries of interest by a focused ion beam (FIB) of a dual beam FIB-Scanning Electron Microscope (SEM) station as described in Ref. [8].

Additionally, the interaction of cracks and grain boundaries is measured by imaging the plastic zone by the method of Henning and Vehoff [9] that introduced an orientation gradient mapping technique (OGM) as well as by the electron channeling contrast imaging (ECCI) improved by Welsch and Marx [10]. These techniques reveal accumulated geometrical necessary dislocations and ordered dislocation structures. After the fatigue experiments the three-dimensional geometry of the crack plane the grain boundaries and possibly

TABLE 1—*Chemical composition of the SC and DS alloys, measured by EDX, given in weight %.*

	Ni	Al	Ti	Co	Mo	Ta	W	Re	Cr
CMSX-4	56.5	5.4	0.8	10.5	1.1	2.1	10.5	6	6.9
DS-Alloy	57.6	6.5	0.7	8.5	0.8	3.2	15	0.3	8

enclosed precipitates is investigated by FIB tomography which provides a higher resolution than the common X-ray tomography even if synchrotron radiation is used.

The functionality of the method is shown for several different metallic materials: polycrystalline nickel, low carbon steel, and a directionally solidified (DS) nickel based superalloy were used for the experiments. Nickel was used because for this material a lot of information and data about crack propagation and the according mechanisms are available. Steels and the DS alloy are of technical interest. Especially in the case of DS alloys which are used as high temperature components like turbine blades in the new generation of gas turbines, lifetime prolongation due to an enhanced resistance of the grain boundaries against crack propagation is one aim of the so called "grain boundary engineering."

Experimental Techniques

In this part of the paper the different techniques used to initiate artificial microcracks and to investigate the crack propagation in so far unknown details will be described. These new techniques are further developments of common techniques like ion beam milling, EBSD, and ECCI. Therefore it should be possible to create similar experiments in every well equipped laboratory with an SEM and a FIB. However, at the moment the combination of these techniques is the most promising possibility to identify the crack propagation mechanisms and the influence of the local microstructure in three dimensions. As a future result the crack propagation resistance of microstructural components like grain boundaries, phase boundaries, or precipitates should be quantifiable.

Artificial Crack Initiation by FIB

First the crack initiation method was validated by using a single crystalline (SC) nickel-based superalloy similar to the DS alloy for the preliminary experiments. The preferred crack orientation on a {111} plane remained the same for all specimens. Both nickel-based superalloys have 70 % in volume of γ'-precipitates (Ni_3Al) embedded in a γ-nickel based matrix. The DS alloy has second phases on the grain boundaries for high temperature strengthening. The grain size was about 2 mm perpendicular to the growth direction. The grains were passing through the specimens in the growth direction. The compositions of the alloys, measured by EDX in the SEM, are given in Table 1. Additionally, nickel and low carbon steel were selected for the experiments

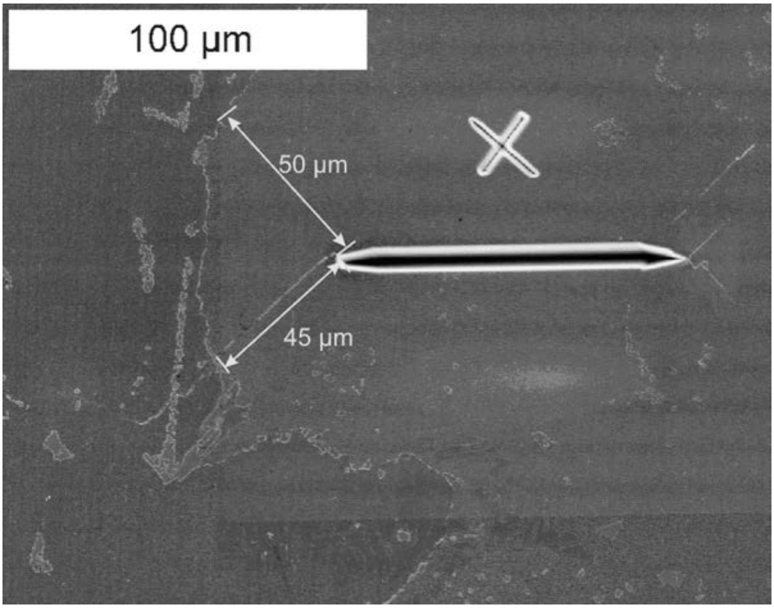

FIG. 1—*Artificial microcrack in a DS nickel-based superalloy with a predicted distance to the grain boundary of about* 50 μm.

because the surface preparation for a sufficient ECCI contrast works best for these materials while the Ni-based superalloys show an additional contrast due to the precipitates which blanket the dislocation induced contrast imaged by ECCI.

The experiment begins with the selection of grain boundaries that are expected to show different interactions with microcracks due to different misorientation angles of the active slip planes. This can be done after the complete sample characterization by EBSD and the calculation of the most favored slip systems within each grain. Afterwards stadium I microcracks are initiated in front of selected grain boundaries by cutting sharp notches with a FIB (Fig. 1). It should be mentioned that for the crack initiation in the α-phase of the low carbon steel (bcc crystal structure) the pencil glide planes must be calculated [11].

Thereby the crack parameters crack length and distance from the crack tip to the grain boundary were fixed. A starting notch is cut in the specimen by the ion beam. This is done by milling a calculated surface pattern several times at the same position to get a sharp and deep notch. Afterwards a crack is initiated at this notch by oscillatory loading. By varying the surface pattern, different notch geometries and consequently different crack geometries like the idealized penny shape surface crack can be produced. In the FIB-SEM the specimen can be rotated and tilted to create a notch exactly parallel to the selected plane (Fig.

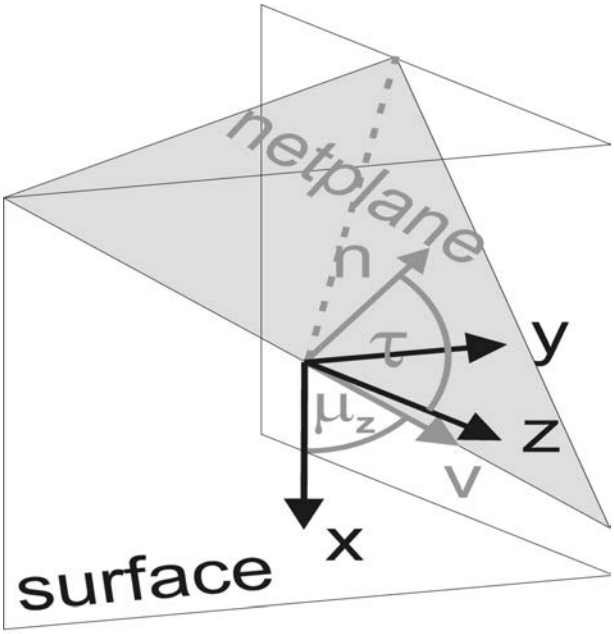

(a)

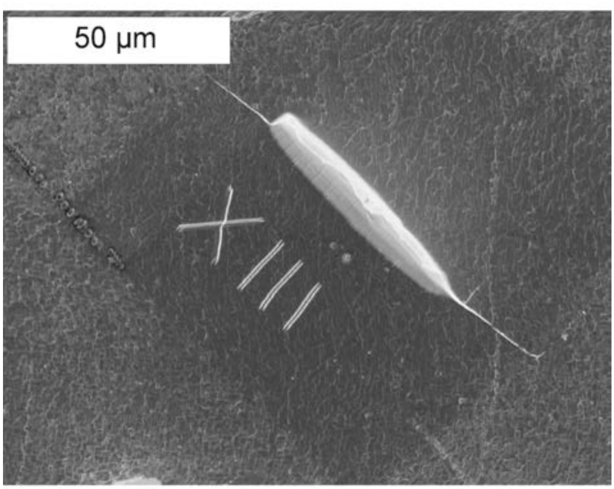

(b)

FIG. 2—(*a*) *Orientation of the preferred slip plane, calculated by the highest Schmid-factor.* (*b*) *Replica of a FIB notch with an artificial crack after* 15 000 cycles.

2(*a*)). The cracks propagate in Stage I on the calculated slip plane as can be seen on the replica image in Fig. 2(*b*). For more details the reader is referred to Ref. [8].

For all experiments, the specimens are cut from the bulk material by spark-

TABLE 2—*Cycles till replica with first observable crack initiation as function of the notch geometry.*

Notch Shape	Initial Crack Length [μm]	Cycles Till Crack Initiation	
		Left Crack Tip	Right Crack Tip
Straight line	160	90 000	90 000
Rectangle with triangular tips	80	30 000	83 000
Penny-shaped	60	15 000	15 000

erosion. The surfaces of the samples are mechanically polished with 3, 1, and 0.25 μm diamond pastes and chemically etched with an Adler solution for a better pattern quality in EBSD and to enhance the grain boundary contrast. For the SC material the loading axis is parallel to the [001]-direction. In the case of the DS-alloy, the loading axis of the samples is parallel to the solidification direction of the grains which is normally near [001]. For all other samples which show no texture after recrystallization the loading direction will not influence the results.

The acceleration voltage is 30 kV with a beam current of 20 nA. The sputtering rate of the ion beam is about $0.14 \mu m^3/nC$. In principle, the depth of an ion-milling pattern can be estimated by the milling time if the sputter rate is known. However, when a notch is created by a sputter process, it is obvious that only limited aspect ratios are possible. Natural short cracks are nearly semicircular depending on crystal anisotropy. Similar cracks can be produced by choosing an elliptical surface profile with an opening of 4 μm.

Fatigue Loading

The specimens are cyclically loaded in a servohydraulic testing machine at room temperature with a frequency of 5 Hz. The load amplitude is about half of the yield strength for all the materials. The R ratio is $R = \sigma_{min}/\sigma_{max} = -0.1$. Crack propagation is measured by a replica technique. Replicas are taken in intervals of 5000 cycles at the beginning. When the cracks start to grow or reach a distance less than 5 μm to the grain boundary, replicas are taken every 1000 cycles. The projected crack length is measured perpendicular to the loading direction. Crack growth is observed usually at both notch tips. The number of cycles needed for crack initiation depends on the notch shape as shown in Table 2 for the nickel-based superalloy.

First it was shown that the crack propagation rate of the artificial cracks da/dN on the basis of the stress intensity factor ΔK is comparable to that of natural cracks (Fig. 3). We have now a simple experimental setup to study the interaction between short cracks and boundaries. The models of the interaction of microcracks with interfaces which are calculated for those idealized Stage I cracks can be checked quantitatively. Then the crack propagation rate towards the grain boundary was measured as a function of the stress intensity factor

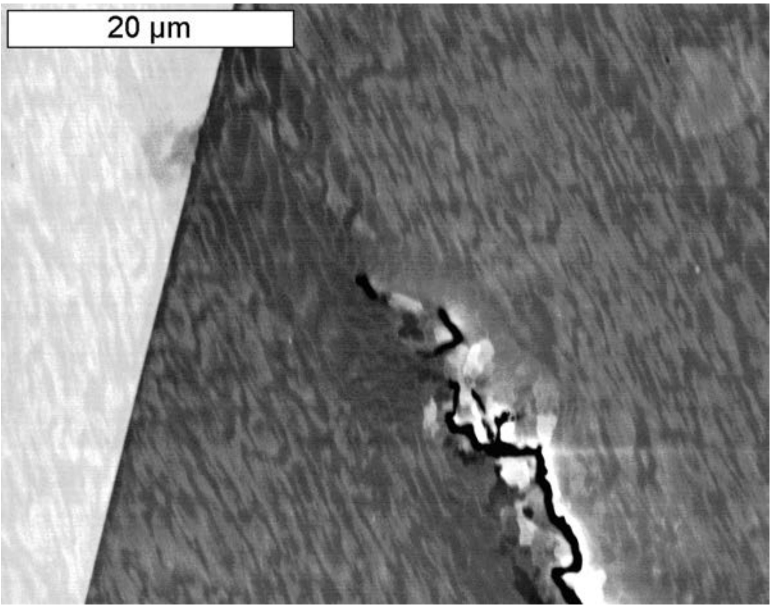

FIG. 3—*Crack with plastic zone in front of a grain boundary in nickel, imaged by ECCI.*

calculated without shielding of the grain boundary and the stress field of the piled up dislocations. This measurement is done for different misorientation angles and crack parameters.

ECCI and OGM Imaging of the Plastic Zone

There are two further developments of the established SEM-based electron diffraction techniques introduced to image the local plastic deformation of metals.

The first technique is the ECCI which allows the imaging of local strains of the crystal lattice with a high in plane resolution [12–14]. This effect is used to make dislocation structures in bulk samples visible. The major application by Wilksinson and Buque is the investigation of lattice defects like persistent slip bands (PSBs) [13,14] and ordered dislocation structures in cyclically deformed specimens [15]. ECCI-imaging can be done in situ to trace the progressive plastic deformation process. A further development of this technique, the ECCI$^+$ technique introduced by Welsch and Marx [10] can be used to image non well-structured local dislocation distributions like geometrically necessary dislocations (GNDs) in plastic zones close to grain bopundaries. It is used to visualize size and shape of plastic zones in front of crack tips as shown in Fig. 3 to study the interaction of cracks with microstructural elements like grain boundaries [8]. However, this method gives only qualitative information about the shape of the high plastic deformation zones.

The ECCI observations are conducted in a CamScan FE-SEM equipped with a field emission gun (FEG) and a “4 quadrants-BSE-detector.” The accel-

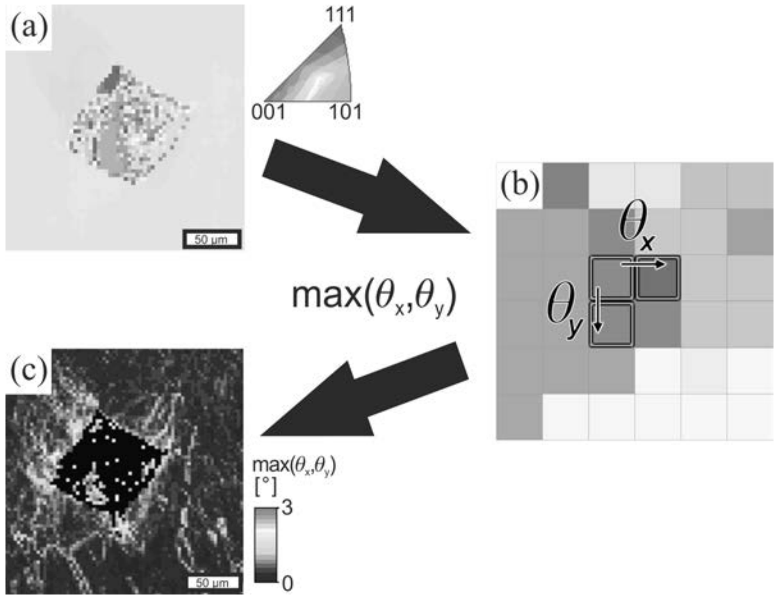

FIG. 4—(*a*) *EBSD measurement of the plastic zone around a micro indent.* (*b*) *Calculation process of the OGM technique.* (*c*) *Resulting OGM showing the plastic deformation zone.*

eration voltage is 20 kV and the resolution for the BSEs is about 50 nm at a working distance of 15 mm. All EBSD measurements are conducted in a CamScan S4-SEM equipped with a standard tungsten filament cathode at an acceleration voltage of 25 keV and an EBSD-resolution of about 1 μm.

The second technique is the EBSD which allows an automated measurement of the local orientation of the crystal lattice with a spatial resolution of about 50 nm depending on the SEM. There are only a few papers in which the local changes of the orientation induced by plastic deformation are described [16,17]. Due to the high accuracy of the EBSD data, not only a qualitative but also a quantitative measurement of the plastic deformation is possible. Based on the orientation map, orientation gradient maps are generated, which were introduced by Henning and Vehoff [9] to visualize the distribution of hardening zones. OGM calculates the maximum orientation difference $\Delta\theta$ between one measuring point and its neighboring measuring points in the x- and y-direction as shown in Fig. 4 for the plastic zone induced by a micro-indent. This gradient can be used as a measure of the GNDs and the plastic deformation. This method can be used to visualize and quantify the local plastic deformation with a lateral resolution of 50 nm.

Although the information depth for both methods ECCI and EBSD is limited to few nanometres due to the relatively short mean free path of the back scattered electrons (BSE), they can be used to image dislocations in bulk materials due to their long-range strain fields which are visible at the surface. The specimen preparation must be done very carefully by combining mechanical polishing with electrolytic polishing. However, SEM is just able to image the surface. The third dimension of the three-dimensional crack and grain boundary geometry is missing. Therefore FIB tomography was used after the experiment to reconstruct the local microstructure and the crack path.

3-D FIB Tomography

In order to derive the 3-D structure of a sample, different tomography techniques have been developed. Classical X-ray tomography covers a size range down to approximately 5 μm. Using synchrotron sources, the resolution limit might be lowered by a factor of 10 to approximately 0.5 μm. In Ref. [18], the shape of microstructurally long cracks is measured in situ and used in deriving a "3-D crack propagation law." However, for long cracks there is little influence of the microstructure on the crack propagation behavior expected. For studying short cracks and their interaction with microstructural barriers higher resolutions are required. This is partly because of the size of the precipitates, and partly because the crack tip opening displacement might be well below 1 μm [19]. Because FIB tomography has been reported to be suitable for the 3-D reconstruction even of small cracks [20], the current study explores this technique in determining the 3-D geometry of crack planes, grain boundaries, and precipitates. Hence, FIB tomography, covering a size range between ~10 nm [21] to ~100 μm should be ideal for local investigations of the crack path.

The technique employs a serial sectioning procedure and is therefore in principal similar to serial metallographic sectioning (e.g., [22]) but with several orders of magnitude better resolution in the z-direction. The slices are performed perpendicular to the sample surface and perpendicular to the crack path on the surface (Fig. 5). A FEI Strata Dual Beam 235 employing an FIB and an FEG electron microscope was employed. An overall width of 30 μm, a depth of nominally 30 μm, and length of 30 μm was chosen. In total, 100 sections were milled (slice spacing of 300 nm). Images are corrected for a 52° sample tilt (angle between the electron and the ion beam). Taking the image resolution and magnification together with the slice spacing into account, a voxel resolution of 31 by 39 by 300 nm is calculated [23].

Results and Discussion

Artificial Crack Initiation

Do natural and artificial microcracks behave similarly? Therefore the growth of a natural crack which initiated at a surface pore was examined. The crack propagation rate was measured quantitatively. The increments in crack length were measured by a replica technique whereby the projected crack length was used. The crack growth rate was determined by a five-point polynomial method and the stress intensity factor ΔK was calculated for semicircular penny-shaped surface cracks [24]. The propagation rate for an FIB crack initiated directly in a slip plane of a single crystalline nickel-based superalloy and the propagation rate of a slip band crack initiated at a surface pore in the same

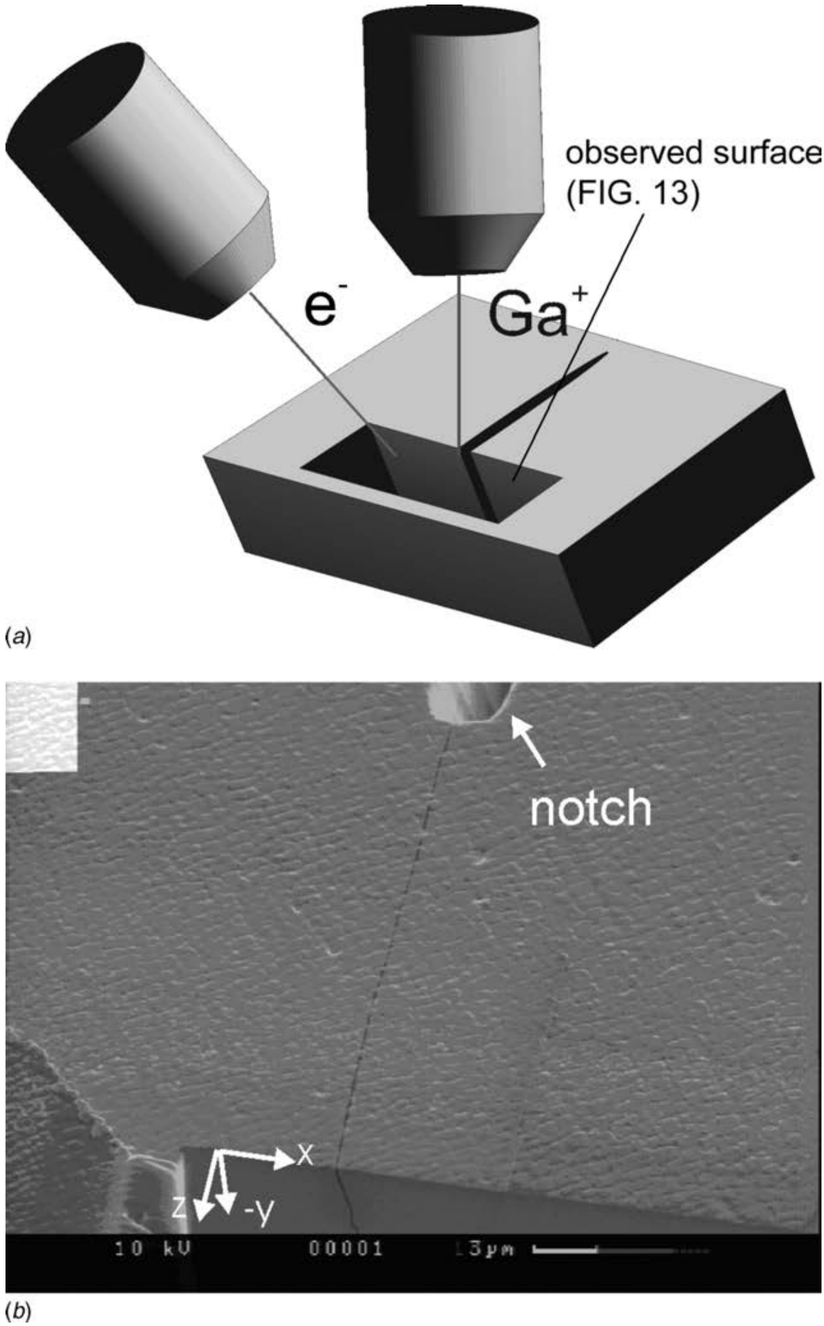

FIG. 5—(*a*) *Slices are milled perpendicular to the sample surface and to the crack path on the surface.* (*b*) *Notch crack and slice of an FIB tomography.*

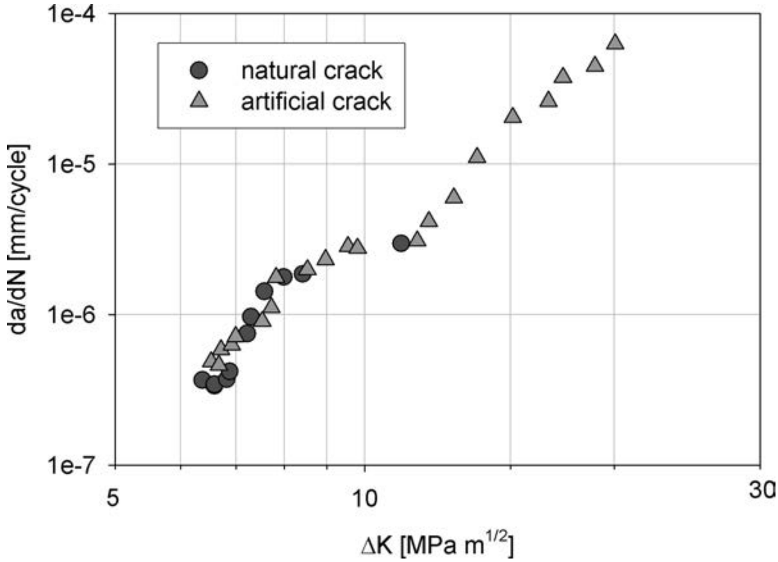

FIG. 6—*Crack propagation rate of an artificial FIB crack compared with a natural crack initiated at a pore.*

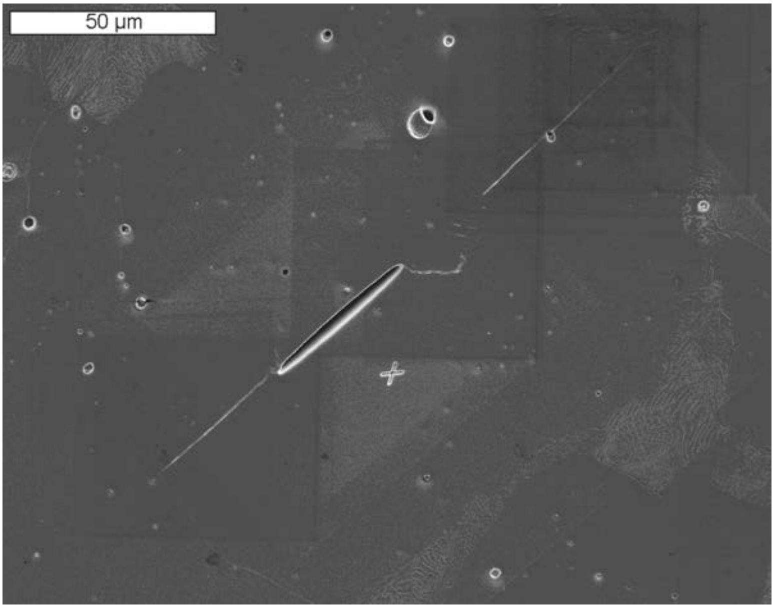

FIG. 7—*Artificial microcrack initiated on a pencil-glide plane in a low carbon steel.*

TABLE 3—*Orientation of the adjacent grains at the selected grain boundaries and resulting misfit.*

Grain Boundary Number I (DSVV1)			Grain Boundary Number II (DSVV2)		
Euler Angles	Left Grain	Right Grain	Euler Angles	Left Grain	Right Grain
φ_1	91.7	166.4	φ_1	4.6	46
Φ	98.7	21.1	Φ	35.1	5.7
φ_2	0.3	289.6	φ_2	1.4	312
Resulting misfit: 21°				Resulting misfit: 32°	

material are shown in Fig. 6. Both curves are in good agreement with each other. This shows that Ga ions which may be implanted in the material during the sputtering process do not affect our experiments in which the crack initiation period is neglected at all. There are no signs of liquid metal embrittlement or internal stresses due to lattice distortion which would result in an increased crack propagation rate.

Interaction of Cracks with Grain Boundaries I: Crack Propagation Rate

In this paper results are presented for two microcracks interacting with different grain boundaries in the DS nickel-based superalloy and for a microcrack in low carbon steel (see Fig. 7). A plate of the DS nickel-based superalloy was characterized by EBSD before cutting the specimens from it. So the orientation misfit angle of the adjacent grains could be calculated for every grain boundary intersecting the surface. The largest grains were selected to ensure that the grains are not "surface grains." Two specimens with different grain boundaries with the grain orientations given in Table 3 were selected where an orientation difference between the adjacent grains of 21°, respectively 32°, was found.

Figure 8(*a*) shows the crack growth rates as a function of the distance between crack and grain boundary, measured perpendicular to the tensile axis. In Sample I (DSVV1) the notch was milled at a distance of 54 μm to the grain boundary, the crack growth rate decelerated beginning at a distance of approximately 12 μm from the grain boundary. However a complete stop of crack propagation could not be observed. The crack growth rate increased immediately after the crack passed the grain boundary. The second notch (DSVV2) was in the middle of a sample of the DS-alloy at a distance of 35 μm to the selected grain boundary. The crack approached the grain boundary after 72 000 cycles; crack arrest could then be observed for a period of 25 000 cycles. The crack growth rate decreased at a distance of approximately 20 to 25 μm from the grain boundary. After passing the grain boundary the crack growth rate increased immediately. The benefit in lifetime for Specimen II was calculated as 30 000 cycles compared to a crack propagating without crossing the grain boundary. Therefore the crack propagation rate was extrapolated by the Paris law. Figure 8(*b*) shows the calculated and extrapolated crack length as a function of the number of cycles and the measured crack length. The measured

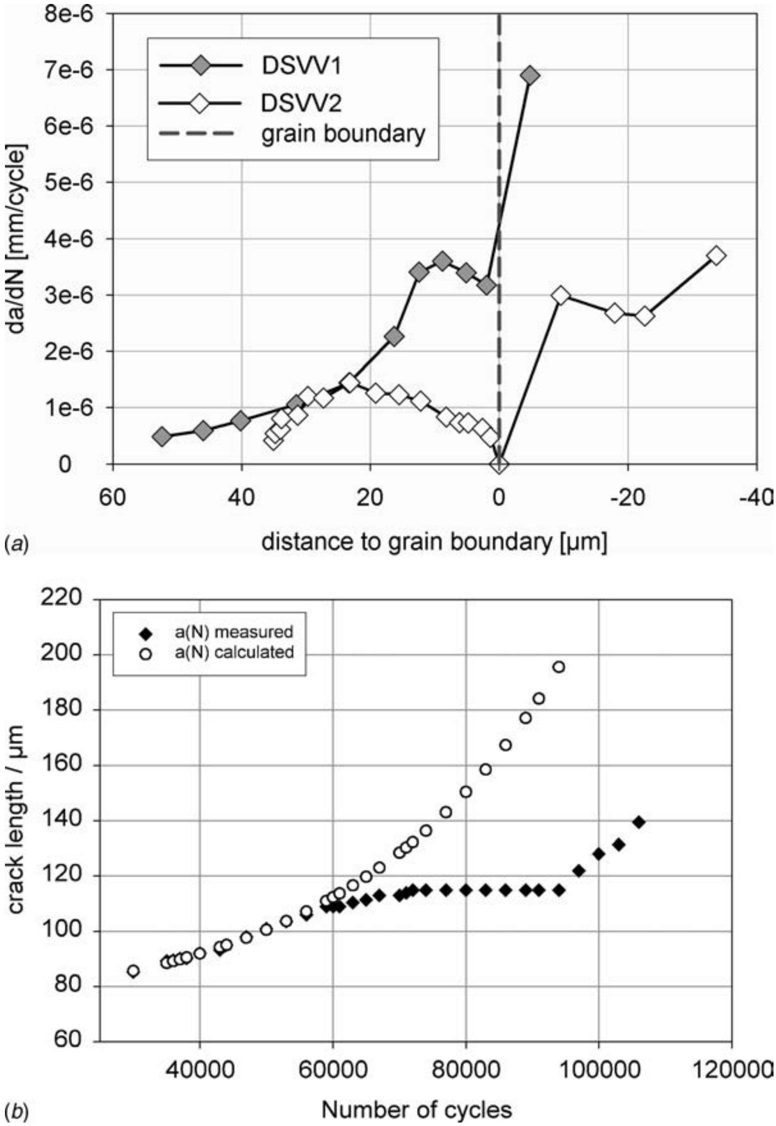

FIG. 8—(*a*) *Crack propagation rate as function of the distance to the grain boundary for the cracks from Table 3.* (*b*) *Extrapolated and measured crack length to evaluate the benefit in lifetime for specimen DSVV2.*

curve is shifted for about 30 000 cycles to a higher number of cycles. These tests clearly prove that grain boundaries have, depending on orientation of the adjacent grains, a strong influence on the crack growth rate over a large distance.

The same behavior was found for the low carbon steel as shown in Fig. 9.

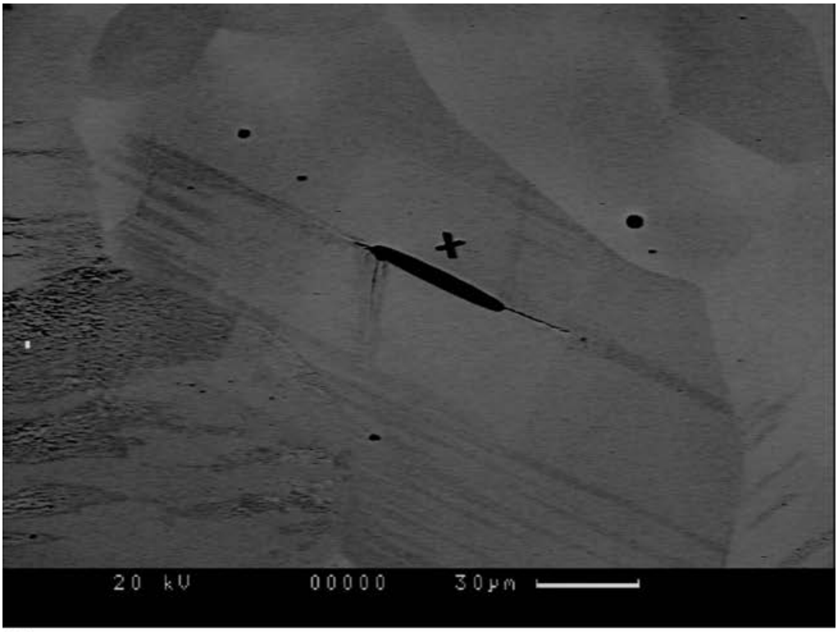

(*a*)

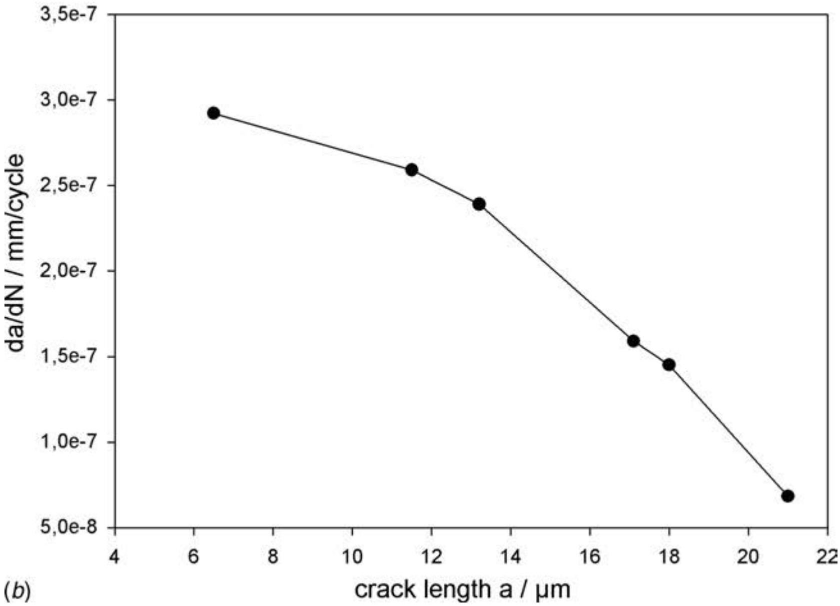

(*b*)

FIG. 9—(*a*) *Artificial microcrack in a low carbon steel interacting with the grain boundaries: slip bands emitting from the crack tips reach the grain boundaries.* (*b*) *Crack propagation rate decelerating in front of the grain boundary* (*grain boundary at* 70 μm).

In this case immediately after the crack started to propagate, the growth rate decelerated before stopping at a distance of 50 μm which is quite a long distance on the scale of typical dislocation interaction and pile-up distances of some microns [25].

Interaction of Cracks with Grain Boundaries II: Plastic Zones

The imaging of plastic zones in front of crack tips by OGM and ECCI is shown here for fatigue cracks in nickel and low carbon steel specimens. Figure 9(*a*) shows an artificial microcrack in a low carbon steel interacting with the surrounding grain boundaries on both sides of the crack. The slip bands are emitted at the artificial notch and reach for the grain boundary on both sides. However, the decrease of the crack propagation rate described above cannot be related to the slip bands and the moment when they are reaching for the grain boundaries. Therefore in situ investigations are necessary where the developing time of these bands will be correlated with the crack propagation rate. Additionally, there are slip bands parallel to the crack slip band and beginning slip bands in the neighboring grain which can be seen as dark lines. Some of them can be seen in the lower right part of Fig. 9(*a*).

The high orientation gradient zone of a fatigue crack tip which is identified as the deformation zone was located at about 60 μm in front of a grain boundary perpendicular to the crack and was observed by OGM (Fig. 10(*a*)). The grain boundaries show a good contrast as white colored lines due to strong changes in orientation between the adjacent grains. It can be seen that the crack orientation is almost parallel to a grain boundary. In the black area no orientation measurement was possible. The crack with its highly deformed crack edges is lying inside this area. Outside the orientation gradients can be detected at a distance up to 100 μm from the crack tip at both sides of the grain boundaries. This is much more than could be imaged by the ECCI (Fig. 10(*b*)). It is visible that the plastic deformation takes place on both sides of the grain boundary parallel to the crack. The deformation is not homogenous but directed in towards the expected crack propagation. Inside the grain in front of the crack plastic deformation can only be found starting at the triple point and can therefore not be correlated with the plastic zone of the crack.

The plastic zone imaged by OGM can be measured to some tens of microns. This correlates quite well with the interaction distance found in the crack propagation rate curves for the nickel-based superalloys (Fig. 8(*a*)) and low carbon steel (Fig. 9(*b*)). Additionally, it was found that the plastic zone of propagating Stage I microcracks spreads in front of some grain boundaries dramatically while in front of some other grain boundaries no spreading of the plastic zone was found (Fig. 11). This indicates a different fatigue resistance of different grain boundaries and should therefore also be quantified in further investigations.

Interaction of Cracks with Grain Boundaries III: 3-D Imaging

The results of the 3-D imaging of two fatigue microcracks interacting with different grain boundaries are presented here. One grain boundary is in the DS

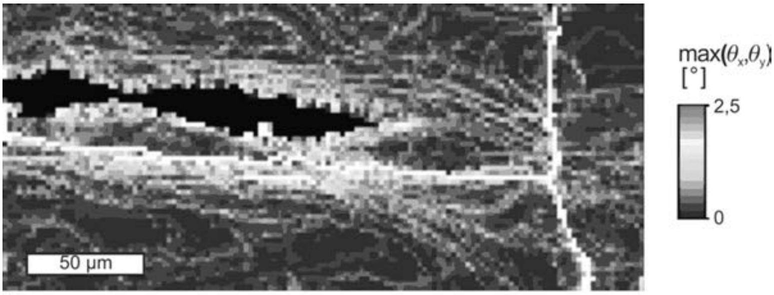

(*a*)

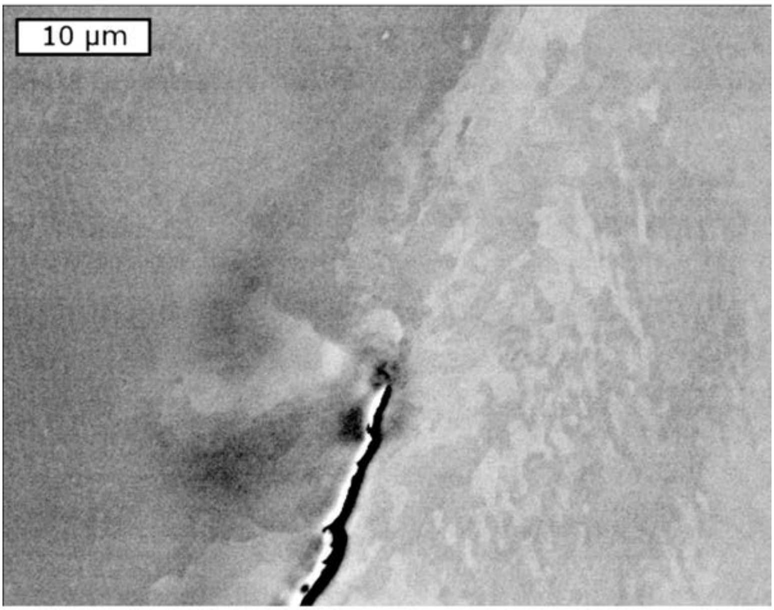

(*b*)

FIG. 10—(*a*) *Crack tip of an intergranular fatigue crack surrounded the plastic zone imaged by OGM.* (*b*) *Crack tip of a similar crack as in Fig. 10*(*a*) *imaged by ECCI.*

nickel-based superalloy and is surfaced by carbide precipitates. The other boundary is a precipitation free boundary in a low carbon steel.

In the DS sample the grain boundaries are decorated by carbides of Ta, Ti, and Hf. Energy dispersive X-ray analysis on carbides exposed at the surface of the sample show type $M_{23}C_6$. The carbides are known to improve the creep resistance at high temperatures. In this study, a sample was investigated, where the crack path was practically parallel to the grain boundary (Fig. 12); nevertheless, the crack arrested for 10 000 cycles without reaching the grain boundary. However, one has to keep in mind that the problem is three-dimensional which may explain the unexpected behavior. A FIB tomography showed that the crack already crossed the grain boundary underneath the surface. In Fig. 13

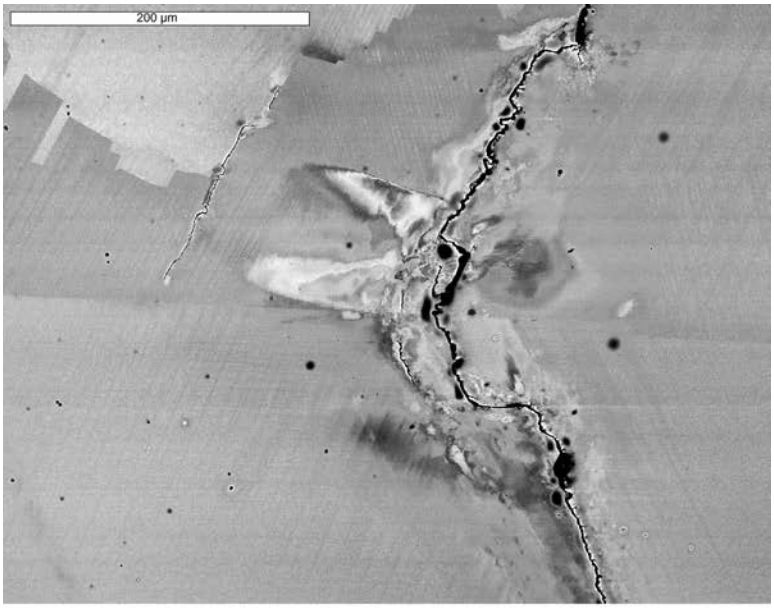

(*a*)

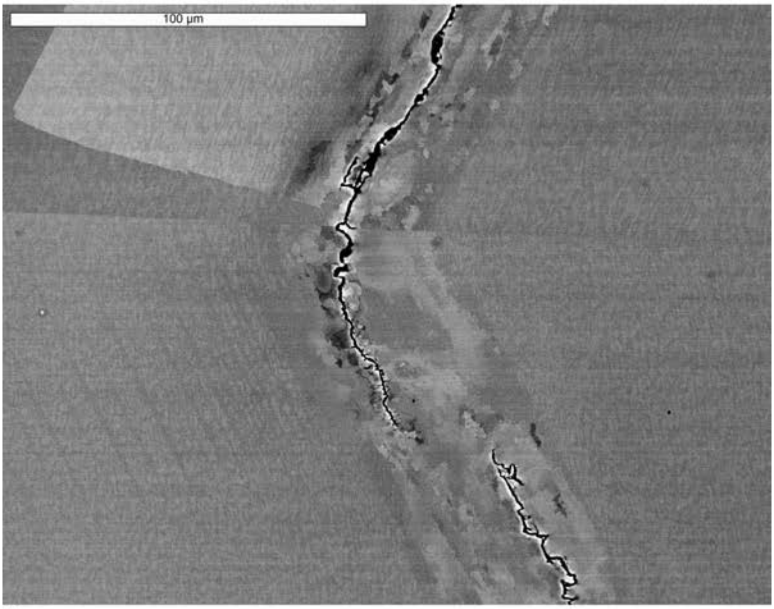

(*b*)

FIG. 11—*Two cracks passing a grain boundary in nickel:* (*a*) *no spreading of the plastic zone;* (*b*) *heavy spreading of the plastic zone due to interaction of the crack with the grain boundary.*

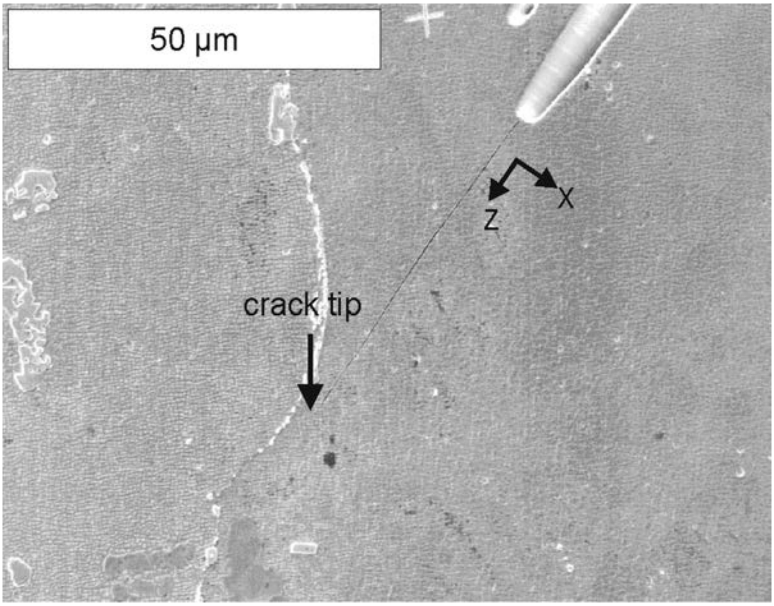

FIG. 12—*Crack propagation experiment in the DS alloy, the tensile axis is vertically oriented. The crack stopped in front of the grain boundary without crossing.*

selected FIB cross sections of this crack are shown. The grain boundary is visible by the precipitates described above. Two kinds of precipitates can be distinguished by their different contrast: small dark (Fig. 13(*a*)) and large light precipitates (Fig. 13(*b*)). The large light precipitates correspond to the type $M_{23}C_6$ already identified on the surface. It is believed that the small precipitates are of the type MC type.

For reconstruction, the crack plane is identified by manual inspection in each slice. However, it was difficult to identify the crack tip due to the small crack opening width even when using the high resolution SEM. Generally, even at the highest resolution, it is difficult to distinguish between slip bands and real crack tip in a crack opening Mode II. The carbide precipitates are taken as a marker of the exact position for the reconstruction of the grain boundary. Figure 14 shows the crack plane, the precipitates, and the position of the grain boundary plane. As can be seen in this figure, the crack already passed the grain boundary underneath the sample surface which explains the aforementioned crack growth stop. Therefore in the ongoing experiments, the exact position of grain boundaries will be taken into account with respect to the propagating microstructurally short cracks.

An important question to answer is by which mechanism a crack overcomes the precipitates during propagation and how this process influences the crack propagation rate. The overcoming can happen either by cutting or by bypassing the precipitates. Figure 15 shows an example where the precipitates are bypassed. The main parameter determining this behavior is the matrix-

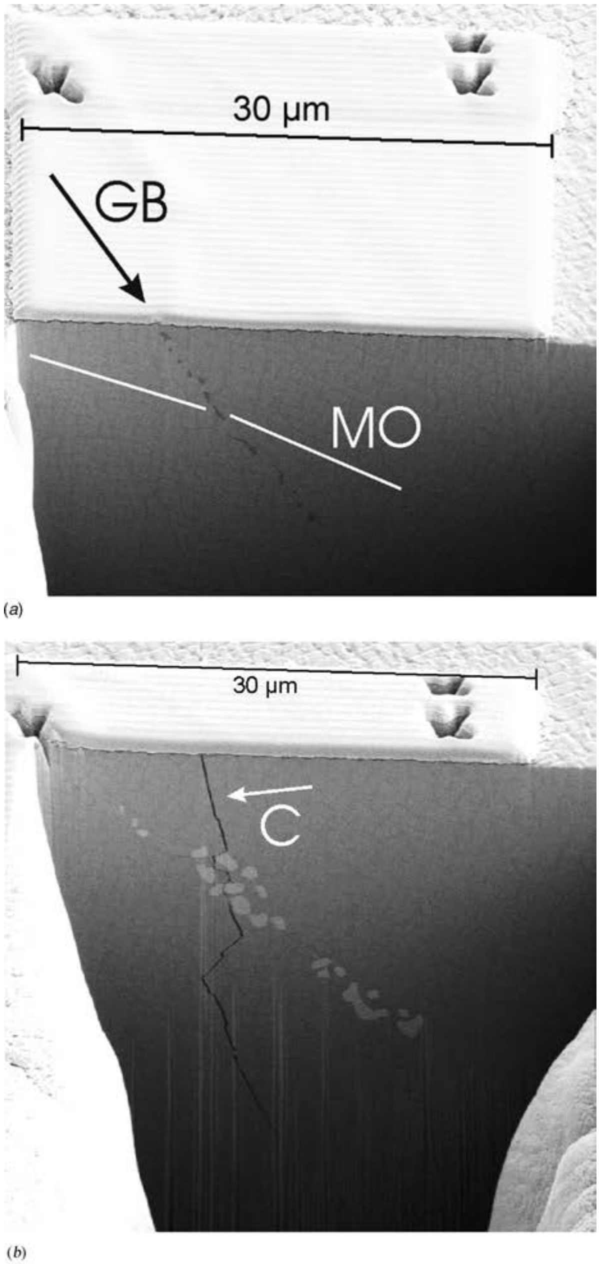

FIG. 13—*FIB serial slicing. In total 100 slices were taken. GB denotes grain boundary and MO denotes orientation of the Ni matrix channels.* (*a*) *Image in front of the crack.* (*b*) *The crack C interacting with a precipitate.*

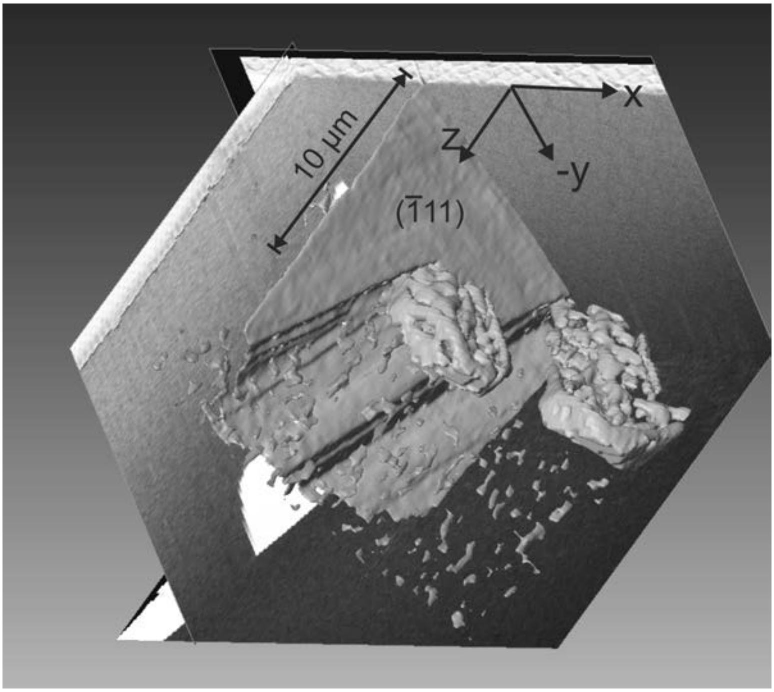

FIG. 14—*Reconstruction of crack plane: the steps in the crack plane result from interaction of the crack with the large precipitates. The position of the crack tip on the surface during the crack arrest is marked by the upper arrow.*

precipitate adherence, the strength of the precipitates, and the capability of the dislocations emitted from the crack tip to pass through the precipitates. Because of the crack-precipitate interaction, the crack deviates from the crack plane while bypassing the precipitates. The active planes were identified using the orientation of the crystal lattice measured by EBSD as follows: In the starting grain the crack propagates along the (−111) plane before reaching the grain boundary. This corresponds to the orientation of the initial FIB notch. In the adjacent grain all steps in the crack plane underneath the grain boundary are parallel to {111} planes. Here the crack propagates by cross slip on the (111) and the (1−11) plane due to bypassing the large precipitates.

In addition, while crossing the grain boundary the crack plane has to rotate because of the Stage I crack growth mechanism. Since the Schmid factors for the active slip planes in both grains, which is the (−111) plane in the first grain and the (111) plane in the second grain, are similar and since the deviation between both planes is just about 3°, the crack path may only slightly deviate while crossing the grain boundary. According to the Zhai model [7] the misorientation of the crack planes at the grain boundary is the main parameter for the resistance of a grain boundary against crack propagation. Therefore, in our case where the misorientation is negligible, it can be assumed that the crack stop is due to the bypassing of the precipitates and not due to any effect of the

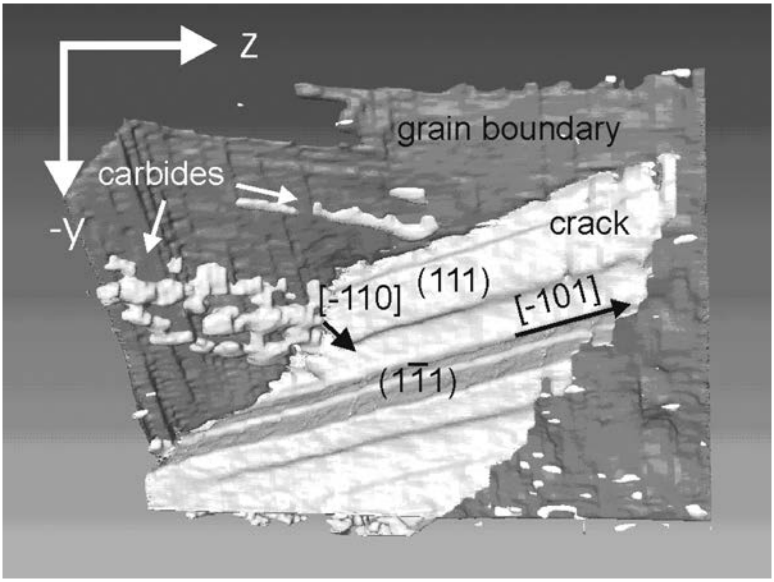

FIG. 15—*Planes of crack propagation (all planes are {111}-planes) indexed by EBSD.*

grain boundary. However, both phenomena (interaction with precipitates and crack plane rotation) lead generally to an increase of the free crack surface. To produce this additional surface more surface energy is needed which results in a significant suppression of crack propagation as shown by the crack growth rate.

A different situation was found in a low carbon steel. As shown in Fig. 16(*a*) the crack growth was straight towards a grain boundary on the calculated slip plane. After passing the grain boundary, the crack started growing on a more statistical path. FIB tomography (Fig. 16(*b*)) showed that there was no behavior under the surface comparable to the crack described above. In the low carbon steel the crack path was straight. Even after cutting the grain boundary there is no change in the crack plane. This example clearly demonstrates that the propagation rates measured at the surface are not in every case representative for the three-dimensional mechanisms and that FIB tomography is needed for a detailed examination of the interaction of cracks and microstructural barriers.

Conclusions and Outlook

The FIB is the only tool to initiate microcracks with almost every defect geometry in nearly every part of real structure elements. Therefore, this is a powerful method for the investigation of individual crack problems in real systems. There is one restriction: this method can only be used to initiate surface defects. However, the largest fraction of critical defects are surface defects.

Furthermore this method combined with EBSD measurements can be used

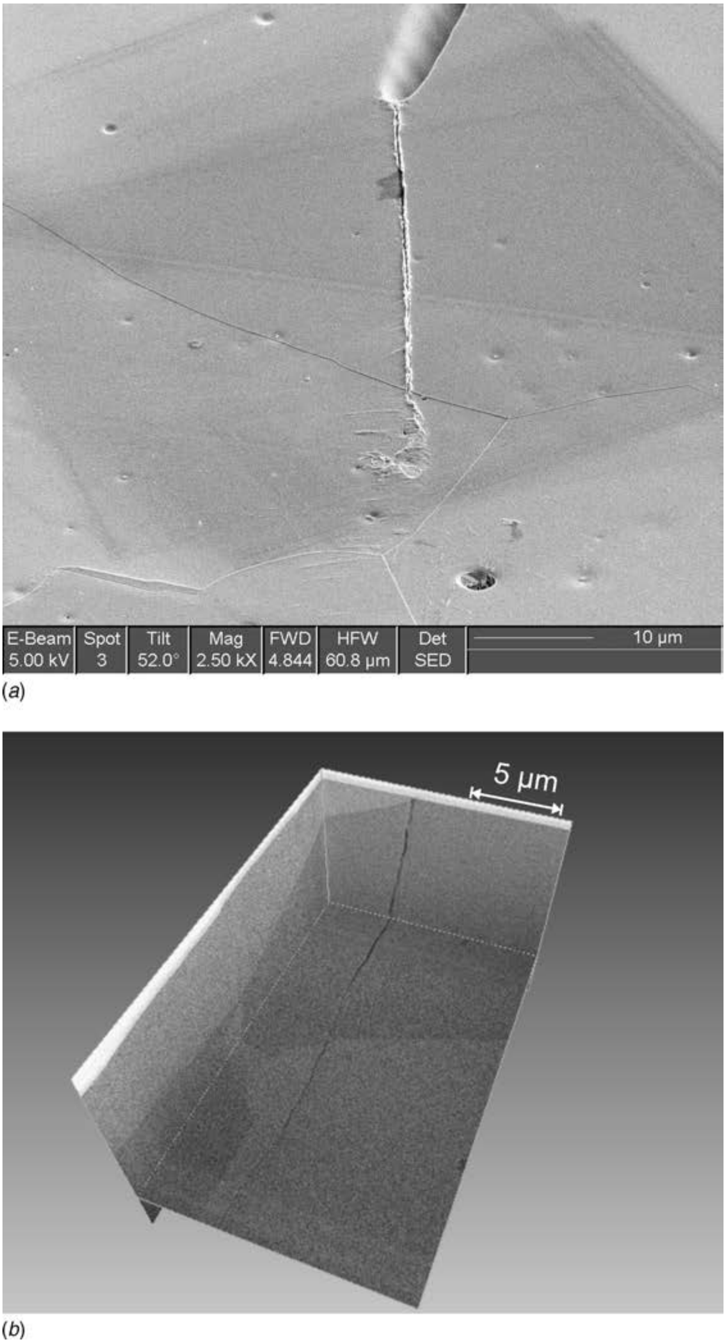

FIG. 16—*FIB tomography of an artificial microcrack in a low carbon steel crossing a grain boundary.*

to investigate the micromechanial mechanisms of crack propagation as described in the models of Navarro, Tanaka and De Los Rios. Therefore, cracks have to be initiated with an idealized geometry directly on the active slip plane to quantify interface and crack parameters for fatigue resistance. The parameters are:

- crystal structure
- local orientation of the grains,
- crack-interface geometry,
- crack length,
- distance from the crack tip to the grain boundary,
- local stress field.

In the upcoming in situ experiments the influence of the grain boundary on the crack tip opening displacement will be measured quantitatively comparable to the procedure described in Refs. [26,27]. Additionally, the plastic zone will be observed in situ by electron channeling contrast and OGM in the SEM. The results will be compared to the work of Deshpande, Needleman and Van der Giessen. They found that the reason for the typical short crack behavior could be seen in internal stresses under cyclic loading resulting from the dislocation structure in the vicinity of the crack tip [25] which are visible in ECCI contrast. The ECCI measurements shown above clearly demonstrate that the plastic zone interacts with the grain boundaries.

Another option of the FIB is local sectioning and hence studying the crack path and the position of the grain boundaries under the surface which is reported to strongly influence crack growth [7]. Present studies of crack growth usually do not take into account the effect of the 3-D grain structure because of the leakage in tomography methods which are capable to resolve grain boundaries directly. If only a surface view is available it is usual to assume that the crack plane and the grain boundary plane are vertical to the interface. In the best defined experiments, the grain structure is measured on both sides of the thin specimen and then interpolated with a flat grain boundary shape as shown in Ref. [28] or bicrystals with known orientations and known slip bands are used [29]. However, both methods require a complicated and restricted experimental setup. On the other hand, FIB tomography can reconstruct nearly all aspects. This was shown for the interaction of a microcrack with a grain boundary in a unidirectional solidified Ni-based superalloy. Thereby the crack can interact with the grain boundary as well as with precipitates which accumulate preferably on the grain boundary. The crack tends to bypass the precipitates by forming geometrically necessary steps in the crack plane whereby this behavior depends on the mechanical properties of the precipitates with respect to the matrix material. The 3-D reconstruction also shows that the subsurface orientation of grain boundaries is an important factor for interpreting crack growth rate observed at the surface. Therefore, FIB tomography extends classical methods such as X-ray tomography with respect to resolution as well as adding different contrast signals revealing different aspects of the true microstructure.

All of these experiments together will give us more details about the mechanisms of the transition of microcracks through microstructural barriers and be helpful on the way to improve the resistance of grain boundaries against crack propagation by grain boundary engineering.

Acknowledgments

The support of this work by the Deutsche Forschungsgemeinschaft (DFG) is gratefully acknowledged.

References

[1] Ritchie, R. O. and Suresh, S., "The Fracture Mechanics Similitude Concept—Questions Concerning its Application to the Behavior of Short Fatigue Cracks," *Mater. Sci. Eng.*, Vol. 57, No. 2, 1983, p. 27.
[2] Ritchie, R. O. and Peters, J. O., "Small Fatigue Cracks: Mechanics, Mechanisms and Engineering Applications," *Mater. Trans., JIM*, Vol. 42, No. 1, 2001, p. 58.
[3] Suresh, S., *Fatigue of Materials*, Cambridge University Press, Cambridge, UK, 1998.
[4] Tanaka, K., Akiniwa, Y., Nakai, Y., and Wei, R. P, "Modelling of Small Fatigue Crack Growth Interacting with Grain Boundary," *Eng. Fract. Mech.*, Vol. 24, 1986, p. 803.
[5] Navarro, A., and De Los Rios, E. R., "Short and Long Fatigue Crack-Growth—A Unified Model," *Philos. Mag. A*, Vol. 57, 1988, p. 15.
[6] Zhang, Y. H., and Edwards, L., "On the Blocking Effect of Grain-Boundaries on Small Crystallographic Fatigue-Crack Growth," *Mater. Sci. Eng., A*, Vol. 188, 1994, p. 121.
[7] Zhai, T., Jiang, X. P., Li, X. J., Garratt, M. D., and Bray, G. H., "The Grain Boundary Geometry for Optimum Resistance to Growth of Short Fatigue Cracks in High Strength Al-Alloys," *Int. J. Fatigue*, Vol. 27, 2005, p. 1202.
[8] Marx, M., Schaef, W., Vehoff, H., and Holzapfel, C., "Interaction of Microcracks with Selected Interfaces: Focused Ion Beam for a Systematic Crack Initiation," *Mater. Sci. Eng., A*, Vol. 435/436, 2006, p. 595.
[9] Henning, M., and Vehoff, H., "Local Mechanical Behavior and Slip Band Formation Within Grains of Thin Sheets," *Acta Mater.*, Vol. 53, 2005, p. 1285.
[10] Welsch, M. T., Henning, M., Marx, M., and Vehoff, H., "Measuring the Plastic Zone Size by Orientation Gradient Mapping (OGM) and Electron Channeling Contrast Imaging (ECCI)," *Adv. Eng. Mater.*, Vol. 9, 2007, p. 34.
[11] Taylor, G. I., and Elam, C. F., "The Distortion of Iron Crystals," *Proc. R. Soc. London*, Vol. 112, 1926, p. 337.
[12] Coates, D. G., "Kikuchi-Like Reflection Patterns Obtained with Scanning Electron Microscopy," *Philos. Mag.*, Vol. 16, 1967, p. 1179.
[13] Wilkinson, A. J., "Quantitative Deformation Studies Using Electron Back Scatter Patterns," *Acta Metall. Mater.*, Vol. 39, 1991, p. 3047.
[14] Wilkinson, A. J., Henderson, M. B., and Martin, J. W., "Examination of Fatigue Crack Plastic Zones Using Scanning-Electron-Microscope-Based Electron Diffraction Techniques," *Philos. Mag. Lett.*, Vol. 74, 1996, p. 145.
[15] Buque, C., Bretschneider, J., Schwab, A., and Holste, C., "Dislocation Structures in Cyclically Deformed Nickel Polycrystals," *Mater. Sci. Eng., A*, Vol. 300, 2001, p. 254.

[16] Lehockey, E. M., Lin, Y., and Lepik, O. E., in *Electron Backscatter Diffraction in Materials Science*, A. J. Schwartz et al., Eds., Kluwer Academic/Plenum Publishers, 2000, p. 247.

[17] Flouriot, S., Forest, S., Cailletaud, G., Koster, A., Remy, L., Burgardt, B., Gros, V., Mosset, S. and Delautre, J., "Strain Location at the Crack Tip in Single Crystal CT Specimens Under Monotonous Loading: 3D Finite Element Analyses and Application to Nickel-Base Superalloys," *Int. J. Fract.*, Vol. 124, 2003, p. 43.

[18] Ferrié, E., Buffière, J. Y., Ludwig, W., Gravouil, A., and Edwards, L., "Fatigue Crack Propagation: In Situ Visualization Using X–ray Microtomography and 3D Simulation Using the Extended Finite Element Method," *Acta Mater.*, Vol. 54, 2006, p. 1111.

[19] Marrow, T. J., Buffiere, J. Y., Withers, P. J., Johnson, G., and Engelberg, D., "High Resolution X-ray Tomography of Short Fatigue Crack Nucleation in Austempered Ductile Cast Iron," *Int. J. Fatigue*, Vol. 26, 2004, p. 717.

[20] Wu, H. Z., Roberts, S. G., Moebus, G., and Inkson, B. J., "Subsurface Damage Analysis by TEM and 3D FIB Crack Mapping in Alumina and Alumina/5vol.%SiC Nanocomposites," *Acta Mater.*, Vol. 51, 2003, p. 143.

[21] Holzer, L., Indutnyi, F., Gasser, P. H., Muench, B., and Wegmann, B. M., "Three-Dimensional Analysis of Porous $BaTiO_3$ Ceramics Using FIB Nanotomography," *J. Microsc.*, Vol. 216, 2004, p. 84.

[22] Clement, P., Angeli, J. P., and Pineau, A., "Short Crack Behavior in Nodular Cast-Iron," *Fatigue Fract. Eng. Mater. Struct.*, Vol. 7, No. 4, 1984, p. 251.

[23] Holzapfel, C., Schaef, W., Marx, M., Vehoff, H., and Muecklich, F., "Interaction of Cracks with Precipitates and Grain Boundaries: Understanding Crack Growth Mechanisms Through Focused Ion Beam Tomography," *Scr. Mater.*, Vol. 56, 2007, p. 697.

[24] Marx, M., Vehoff, H., and Thiele, W. R., in *CAMP 2002—High Temperature Fatigue*, G. Biallas, H. J. Maier, O. Hahn, K. Hermann, and F. Vollertsen, Eds. 2002, p. 142.

[25] Deshpande, V. S., Needleman, A., and Van der Giessen, E., "Discrete Dislocation Plasticity Modeling of Short Cracks in Single Crystals," *Acta Mater.*, Vol. 51, 2003, p. 1.

[26] Marx, M., and Vehoff, H., "Propagation of Microcracks in Single Crystalline Nickel-Based Superalloys: Size Effects on the Crack Opening," *Mater. Sci. Eng., A*, Vol. 387–389, 2004, p. 511.

[27] Marx, M., *Influence of the Microstructure on the Propagation of Micro-Cracks in the Single Crystalline Nickelbase Superalloy CMSX-4*, Shaker-Verlag, Aachen, 2004.

[28] Vehoff, H., Nykyforchyn, A., and Metz, R., "Fatigue Crack Nucleation at Interfaces,"*Mater. Sci. Eng., A*, Vol. 387–389, 2004, p. 546.

[29] Vehoff, H., Ochmann, P., Goeken, M., and Grosse Gehling, M., "Deformation Processes at Crack Tips in NiAl Single- and Bicrystals," *Mater. Sci. Eng., A*, Vol. 239–240, 1997, p. 378.

ASTM Special Technical Publication, Vol. 5, No. 7
Paper ID JAI101567
Available online at www.astm.org

Jeremy E. Schaffer[1]

An Examination of Fatigue Initiation Mechanisms in Thin 35Co-35Ni-20Cr-10Mo Medical Grade Wires

ABSTRACT: Knowledge of the intrinsic defect size distribution, surface grain size distribution, and prior deformation history are important factors in determining fatigue crack initiation mechanisms and total life variability in thin, metallic, medical grade wires. The ASTM F562 alloy system is used extensively as a fine wire coil or cable in the production of cardiac rhythm management leads which require excellent fatigue life, and a good understanding of life variability. In the present investigation, samples of 0.0070 in. diameter ASTM F562, 35Co-35Ni-20Cr-10Mo wires were produced with a variety of grain sizes and strain hardening conditions. Samples were then cyclically loaded to failure in rotary beam testing and preserved for post mortem fractography using high resolution scanning electron microscopy (HR-SEM). Fatigue cracks were found to initiate from three sources: intrinsic microstructural inhomogeneities, persistent slip bands (PSBs), and extrinsic surface defects. The dominance of the various initiation mechanisms was shown to be a function of the constituent particle and grain size as well as the fatigue loading conditions and prior deformation history. In samples exhibiting a surface grain size significantly larger than the constitutive particle distribution, cracks were observed to preferentially nucleate from surface intersecting PSBs rather than near-surface-particles. Understanding of these phenomena is important in the design of robust cardiac lead systems that will outlive the patient.

KEYWORDS: fatigue initiation, fatigue damage, medical wire, CRM device failure, CRM wire, fatigue prediction, high cycle fatigue

---

Manuscript received November 14, 2007; accepted for publication June 10, 2008; published online July 2008.
[1] Fort Wayne Metals Research Products Corporation, Fort Wayne, IN. and Purdue University, West Lafayette, IN.

Citation: Schaffer, J.E., "An Examination of Fatigue Initiation Mechanisms in Thin 35Co-35Ni-20Cr-10Mo Medical Grade Wires," *J. ASTM Intl.*, Vol. 5, No. 7. DOI10.1520/JAI101567. Available online at www.astm.org. Also included in JAI Special Issue STP 1508, *Fatigue and Fracture Mechanics: 36th Volume,* R. W. Neu, K. R. W. Wallin, and S. R. Thompson, guest editors, ASTM International, West Conshohocken, PA, 2009, pp. 402-415.

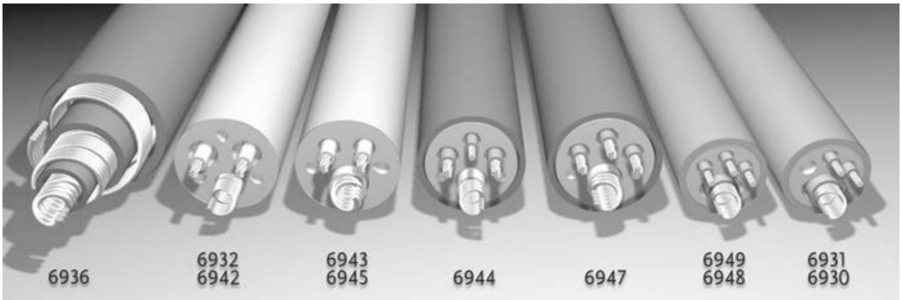

FIG. 1—*Multilumen lead design progression, incorporating ASTM F562 coil and cable elements.* (*Courtesy Medtronic, Inc.*).

Introduction

Fatigue damage is a stochastic process resulting in a high level of unpredictability, even in a laboratory controlled environment. In materials used in implantable medical devices, it is critical to understand variables which may influence fatigue damage and the resultant service life of the implantable device. Cardiac rhythm management (CRM) devices, including implantable pacemakers and defibrillators, are no exception; the materials must remain intact to deliver proper lifesaving therapy [1].

Failure of various CRM system components is anticipated through patient checkup. This practice is evidenced by manufacturer-recommended quarterly device inspection follow-up visits [2]. The components most susceptible to premature failure include the conductor lead and the battery, each with a typical lifetime of approximately three to eleven years. A salient difficulty in today's devices is that the longevity of the lead cannot be predicted and it does not typically give simple indicators that it is nearing the end of its life [2].

Most conductor leads that are in use today consist of a multilumen silicone or polyurethane passage that contains relatively low impedance, wire-based, micro cable or helical coils [3]. The primary structural component of the conductor itself typically comprises high strength MP35N®[2], 35N LT®[3] or a silver cored composite wire of MP35N or 35N LT [4]; failure of this component will result in high circuit impedance and compromised device performance. The individual coil or cables typically receive a conformal fluoropolymer coating in addition to the multilumen jacketing. An example of this construction technique, in which the leads generally comprise ASTM F562 (Standard Specification for Wrought 35Cobalt-35Nickel-20Chromium-10Molybdenum Alloy for Surgical Implant Applications (UNS R30035)) alloy coil and cable assemblies, is shown in Fig. 1.

---

[2]MP35N® is a registered trademark of SPS Technologies, Jenkintown, PA.

[3]35N LT® is a registered trademark of Fort Wayne Metals Research Products Corporation, Fort Wayne, IN.

TABLE 1—*Typical chemistry of alloys falling within ASTM F562-07, MP35N and 35N LT.*

Element	MP35N	35N LT
Carbon	0.008	0.006
Manganese	0.010	0.010
Silicon	0.010	0.101
Phosphorus	0.004	0.003
Sulfur	0.0005	0.0006
Chromium	20.15	20.06
Nickel	36.6	36.75
Molybdenum	10.40	10.32
Iron	0.160	0.120
Titanium	0.680	0.010
Boron	0.0085	0.0080
Cobalt	31.97	32.56

Objectives

The overall goal of this research was to characterize the microstructural parameters that are important in determining total fatigue life and life variability in fine medical wire. The implantable alloy system chosen for this investigation was selected for its widespread use in the field of CRM technology with the expressed intent of bettering design capability for such lifesaving devices. The dearth of information in the area of microstructural fatigue factors and modeling techniques for high strength fine wire materials has been recognized by other authors [5] and was the impetus for the present study.

The specific objective was to analyze fatigue initiation mechanisms under various material and load conditions and provide evidence as to what comprised the primary life-influencing factors.

Material Background

The ASTM F562 alloy system was originally engineered for use as a high strength and fatigue resistant macroscopic fastener alloy, not as a material to serve the medical industry [6]. As a large scale fastener, the presence of 5 to 20 micron nonmetallic inclusions in the alloy is not necessarily deleterious to performance. A new variant of the F562 system, known as 35N LT, was commercially introduced in 2003 directly in response to demand from the medical implant device market. The 35N LT system is processed using carefully controlled melt techniques that eliminate titanium nitride (TiN) particle forming elements and effect a significant downward shift in the inclusion size distribution [4]. The nominal chemistry of standard MP35N and improved 35N LT are shown in Table 1. The 35N LT has recently been approved for use in devices ranging from implantable pacemakers to neurological sensing and stimulation devices.

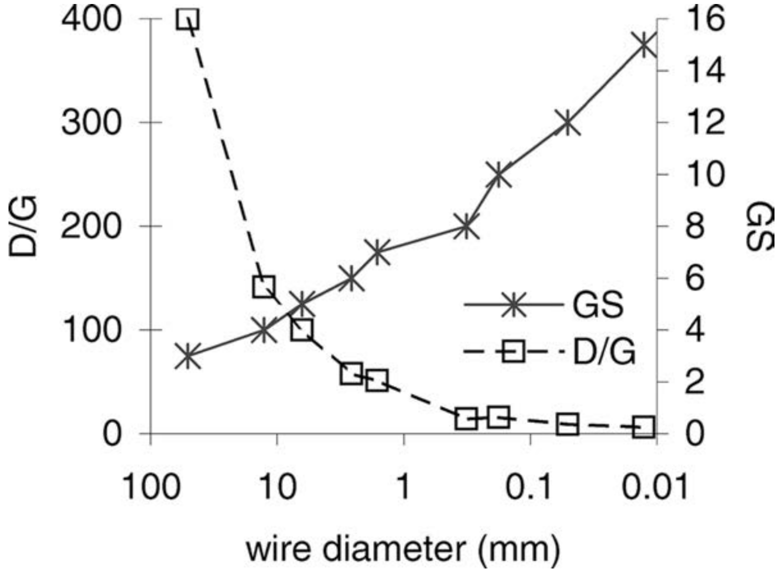

FIG. 2—*Typical wire diameter to grain size ratio in MC, 35N LT medical wire.*

Microscale Effects

The processing of medical wire involves microstructural refinement through significant cold reduction and progressively shorter dwell recrystallization anneals that yield increasingly fine grain distributions. As wire diameters tend towards finer sizes, the average number of grains through a transverse section is reduced. Using nominal production data, the average wire diameter to grain size ratio has been plotted for a typical medical wire process stream, and is shown in Fig. 2. From this plot, it is evident that below a wire diameter of 0.30 mm, less than 10 grains, on average, form the wire thickness and less than 5 grains below 0.10 mm.

Experimental Procedure

Specimen Design

Both materials used for this investigation were initially vacuum induction melt (VIM) cast followed by vacuum arc remelting (VAR). After a homogenization treatment, the VAR ingots were reduced on a rotary forge (GFM) machine and subsequently hot rolled on a continuous rolling mill to 5.6 mm diameter coil. The coil was annealed, shaved to 5.5 mm and pickled in preparation for drawing. Intermediate reduction from 5.5 mm to 1.6 mm were accomplished using carbide drawing dies and powder lubricants. Additional processing to the final diameter of 177 μm was completed using diamond dies and mineral oil lubricants. A qualitative comparison between the surface characteristics of each material was performed using SEM. Generally, the 35N LT was found to possess a more uniform surface due to fewer and smaller intrinsic surface defects. These findings were consistent with results reported in earlier studies [4,7,8].

Specimen Preparation for Rotary Beam Testing

The primary objective of this research was to elucidate important microstructural factors influencing life and life variability in fine medical grade wire. In order to derive results consistent with product used in the field, specimen preparation for rotary beam fatigue testing was minimized. Cold drawn wires typically possess a plasticity induced radius of curvature known in the wire industry as cast. This feature arises primarily due to residual stress imbalance when slight intentional misalignment is induced as the wire exits the final drawing die and serves to stabilize the material as it wraps on a spool. This curvature was mechanically corrected prior to rotary beam evaluation by gently reverse bending each sample before loading them in the chuck fixture. This procedure reduces wobble in the fixture and has been shown over extensive datasets using many materials to reduce geometric instability and test variability [9].

The rotary beam fatigue testers used are equipped with a sensor to detect wire fracture. The equipment function was equivalent to that described by Altman [10] and by Schaffer [8]. As soon as a sample break occurred, the ends were suspended in a plastic tube to prevent mechanical damage. The fatigue fracture ends were cleaned in an ultrasonic bath for 45–60 seconds in high purity acetone before being serially mounted to an aluminum mounting block.

Fractography

In this investigation, three methods of analysis were used to gather information related to causes of failure, general fracture morphology, crack-initiating particle size as well as particle composition, grain size information and persistent slip band spacing. The methods included high resolution, field-emission SEM using a Hitachi model S4800 for nanoscale striation determination, FIB using a FEI Nova 200 for electron channeling contrast and resultant qualitative grain orientation information and SEM with EDS for inclusion particle determination. An example of striation observation along previously deformed slip planes in MP35N using HR-SEM is shown in Fig. 3.

Results

Load Level Dependency

Failure mechanisms were analyzed in four regions of fatigue: single cycle overload, low cycle fatigue (LCF), high cycle fatigue (HCF) and ultra high cycle fatigue (UHCF). The regions were defined as follows: LCF—10^3 to 10^6 cycles, HCF—10^6 to 10^9 cycles, and UHCF—greater than 10^9 cycles.

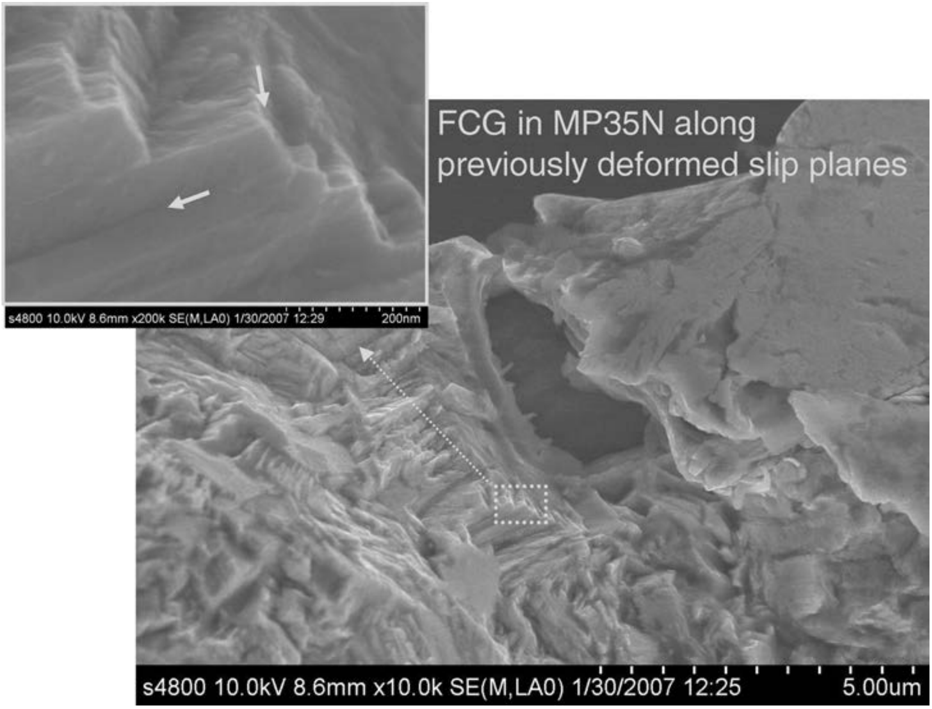

FIG. 3—*FCG along previously deformed slip planes in* 177 μm *MP35N wire.*

Single Cycle Tensile Overload

Inclusions played a role in failure, even at the lower limit of fatigue, a single cycle tension overload test. Following mechanical testing of the 177 μm MP35N wire, specimens were examined and most showed incipient failure at or near inclusion particles. An example of this type of failure mechanism is shown in Fig. 4. The impact on mechanical tensile strength was negligible. This was attributed to a combination of factors including crack tip blunting at the inclusion boundary, small relative inclusion area contribution to the net load-bearing area, and the plane stress conditions in the relatively thin wires. In smaller diameter wires, the same constituent particle distribution would be expected to have greater impact on net section strength.

Low Cycle Fatigue

Prior strain hardening in ASTM F562 medical wire increases material strength with an accompanying decrease in ductility. The high rate of strain hardening in this system is believed to result from a combination of deformation twinning and conventional dislocation interaction [11]. Under LCF conditions, the amount of cold work and resultant properties had a significant effect on initiation mechanisms. Initiation occurred at inclusions, preferentially oriented grains, surface intersecting PSBs and at extrinsic surface defects. In addition to

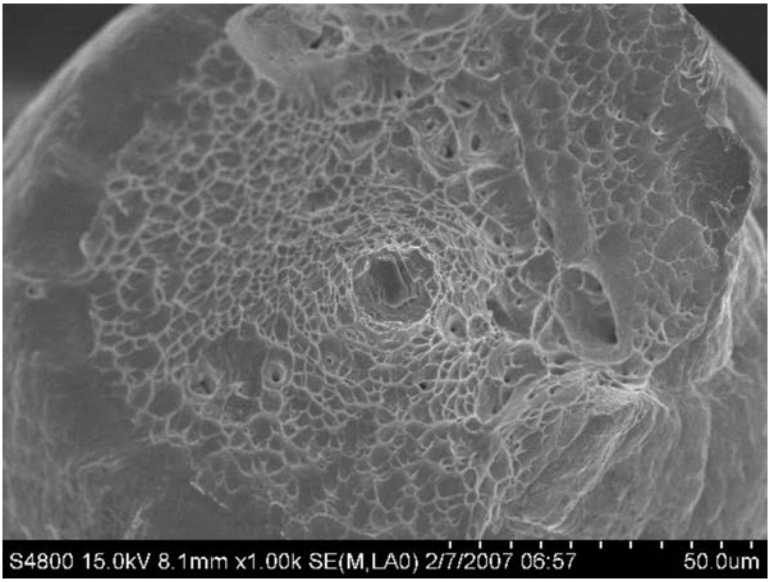

FIG. 4—*Central inclusion-initiated ductile overload in* 177 μm *MP35N wire.*

prior strain hardening, crack initation behavior was found to be strongly dependent on microstructural parameters including grain size and inclusion size.

The annealed samples of MP35N and 35N LT with an equiaxed 3 μm grain size fractured in LCF in multiple locations, independent of inclusion particle size and location. In this low strength, ductile state, irreversible slip was energetically more favorable due to low dislocation density. It is believed that plastic slip occurred in the vicinity of the constituent particles which resulted in crack tip blunting, a reduction in their detrimental impact on total life, and the promotion of multiple site damage (MSD). An example of MSD fracture morphology found in a MP35N failure is shown in Fig. 5.

A significant reduction in grain size, or an increase in strength through cold-work in MP35N, gave rise to particle initiated fracture as shown in Fig. 6. In this case, the material was cold-worked at a level of 36 % reduction of area. The result was a 50 % reduction in LCF lifetime at the 930 MPa test level. In the cold-worked condition, at an initial 3 μm grain size, the 35N LT significantly outlasted the MP35N at mean lifetimes of 2×10^5 versus 9×10^4 cycles, respectively. A comparison between the cumulative distribution function (CDF) of the LCF lifetimes of alloys MP35N and 35N LT in the strain-hardened state is shown in Fig. 7.

In the cold-worked state, the MP35N failed in fewer cycles, and with less lifetime scatter than the 35N LT. This consistency in lifetime was driven by the mostly invariant crack growth rate after initiation at the large, dominant inclusion features. The cracks started at one of numerous, similarly sized inclusion sites in the MP35N and progressed at a relatively constant rate of crack growth as evidenced by fatigue striation measurement [8]. The CDF in Fig. 7 graphi-

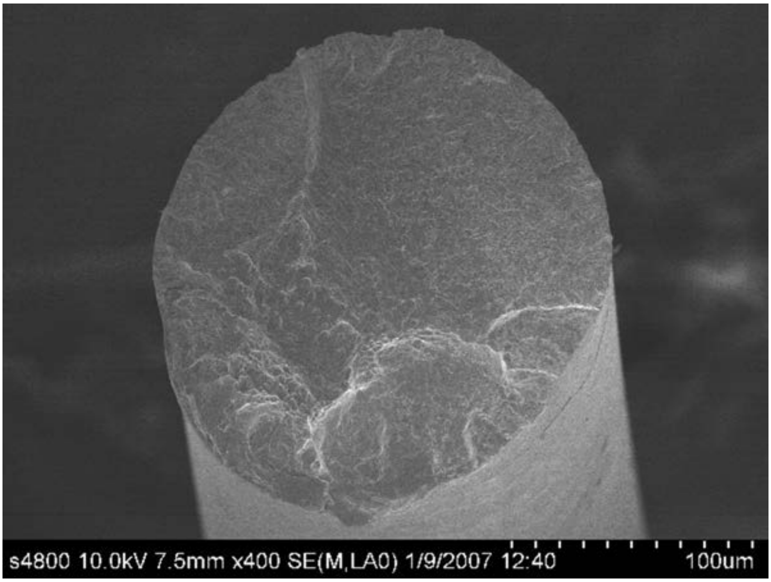

FIG. 5—*MSD, PSB mediated secondary cracking in annealed* 177 μm *MP35N wire tested at a* 930 MPa *alternating stress. Specimen failed in* 9.0×10^4 cycles.

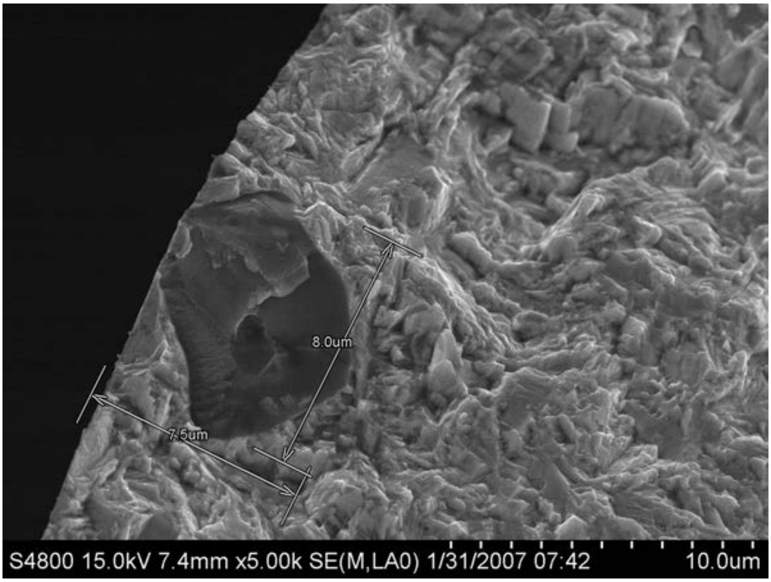

FIG. 6—*Constituent particle* (*TiN inclusion*) *mediated failure in strain hardened* 177 μm *MP35N wire tested at* 930 MPa. *Specimen failed in* 5.8×10^4 cycles.

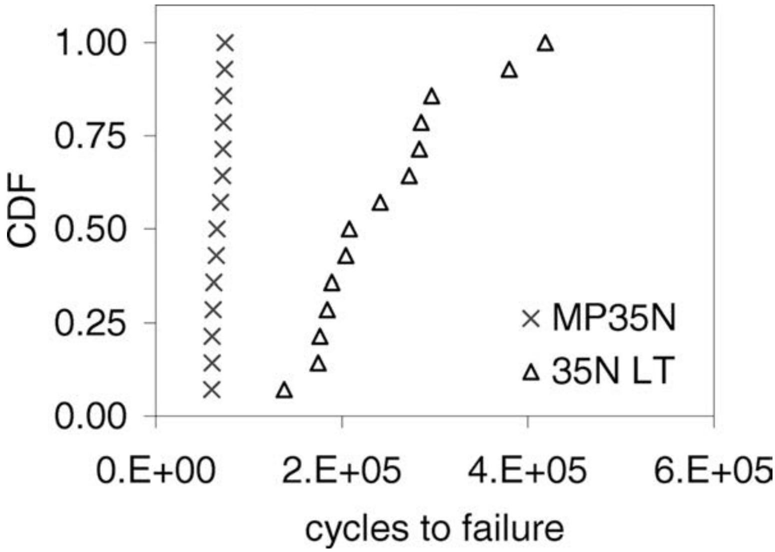

FIG. 7—*CDF of fatigue life at equivalent strain hardening levels in MP35N and 35N LT. Alternating fatigue stress level is* 930 MPa.

cally indicates the increased lifetime and lifetime scatter measured in the cold worked 35N LT. This increase in scatter was attributed to the activation of multiple incipient damage mechanisms in the absence of larger constituent particles. Observed mechanisms of failure included shearing of preferentially oriented grains as shown in Fig. 8, failure at very small inclusion features and less often, failure at extrinsic surface features.

High Cycle Fatigue

The behavior and existence of a fatigue threshold for metallic materials, below which fatigue propagation will not occur has been the subject of numerous recent studies [12–14]. Here, the term "near-threshold" is used to roughly demarcate the LCF region from the high cycle fatigue (HCF) region when the slope of the S-N curve begins to flatten.

As discussed in the LCF regime, fatigue lifetime results were similar in the annealed alloy systems. Under HCF conditions, the annealed material at a 3 μm grain size yielded substantially equivalent lifetime results for both MP35N and 35N LT. Near-threshold behavior was observed at a stress level of 620 MPa with a mean lifetime greater than 1×10^7 cycles. Earlier studies have shown that a significant downward shift in grain size would have generated premature inclusion-based failure in the annealed MP35N [8].

The 35N LT system with 36 % cold-work exhibited near-threshold fatigue behavior at a stress level of 827 MPa with total life ranging from 2.2×10^5 cycles up to 4.2×10^7 cycles. Incipient damage mechanisms were observed to be a mixture of inclusion-free initiation sites similar to Fig. 8, and

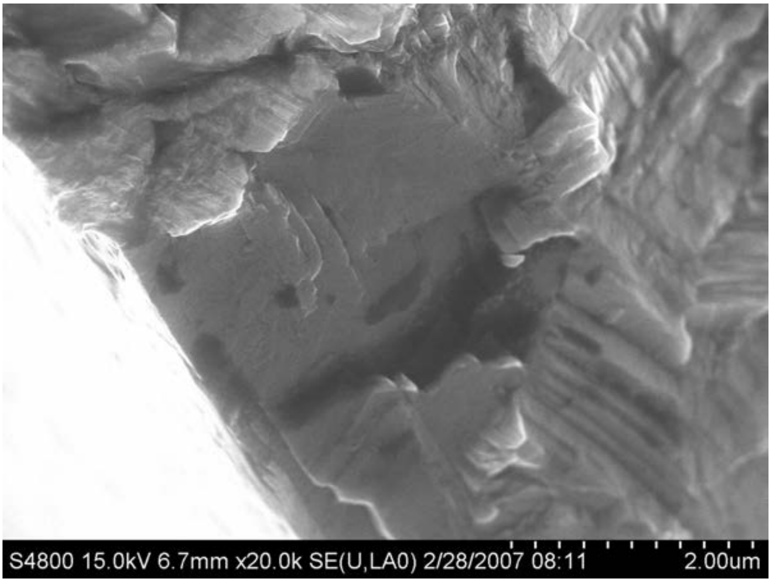

FIG. 8—*Grain orientation mediated fatigue damage* (*no inclusion present*) *in* 177 μm *35N LT wire tested at* 930 MPa. *Specimen failed in* 2.1×10^5 cycles.

crack initiation from 1 to 3 μm aluminum oxide inclusions located at or just beneath the wire surface. Failures that occurred at greater than 1×10^7 cycles were generally noted to occur at small particles located greater than 0.5 μm beneath the drawn free surface of the wire. The separation of initiation mechanisms is evident in the form of the bi-modal CDF as shown in Fig. 9. At the 827 MPa test level, the MP35N failures all occurred at less than 1×10^5 cycles and generally initiated at 4 to 8 μm titanium nitride inclusions located within 0.5 μm of the free surface. Near-threshold behavior in the strain-hardened MP35N was observed at a test level of 690 MPa, significantly lower than for the cold-worked 35N LT samples.

The availability of near-surface damage sites was found to strongly influence total fatigue life. TiN inclusions were present in both sufficient size and quantity in the MP35N under LCF conditions to create a high probability of incipient crack formation at relatively large inclusions located at, or immediately adjacent to, the free surface. In near-threshold behavior, however, the MP35N and 35N LT alloy systems exhibited initiation at both surface and subsurface inclusions. Here, fatigue lifetime was found to be more strongly associated with depth than inclusion size for a given alloy and near-threshold load condition. Least squares regression trend lines were drawn to fit the fatigue lifetime data to inclusion depth (filled circles) and radial inclusion size (open circles) in Figs. 10 and 11 for MP35N and 35N LT, respectively. Within a given dataset, there was little to no observed correlation between radial inclusion size and cycles to failure and a significant positive correlation to inclusion depth. The latter result seems reasonable due to the fact that fatigue and crack tip

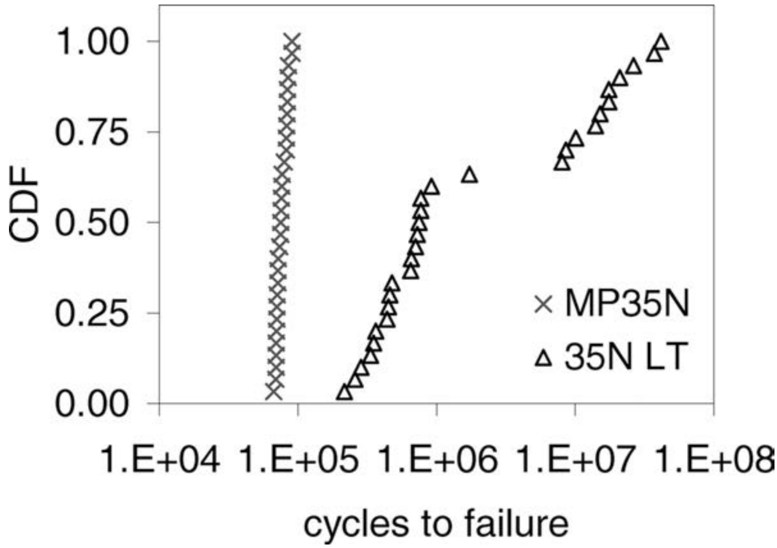

FIG. 9—*CDF of fatigue life at equivalent strain hardening levels in MP35N and 35N LT. Alternating fatigue stress level is* 827 MPa.

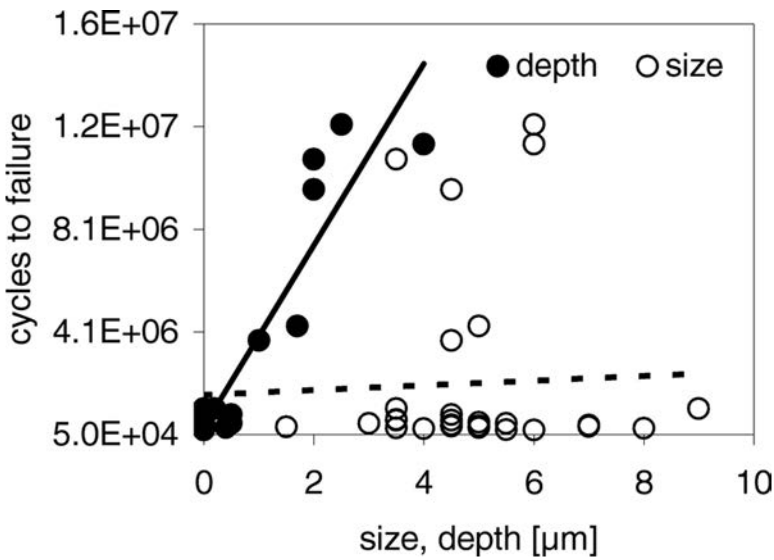

FIG. 10—*Cycles to failure as a function of inclusion depth (filled circles) and size in 36 % cold-worked MP35N alloy tested at an alternating stress of* 620 MPa. *Note that there is little, if any, correlation between fatigue lifetime (cycles) and size.*

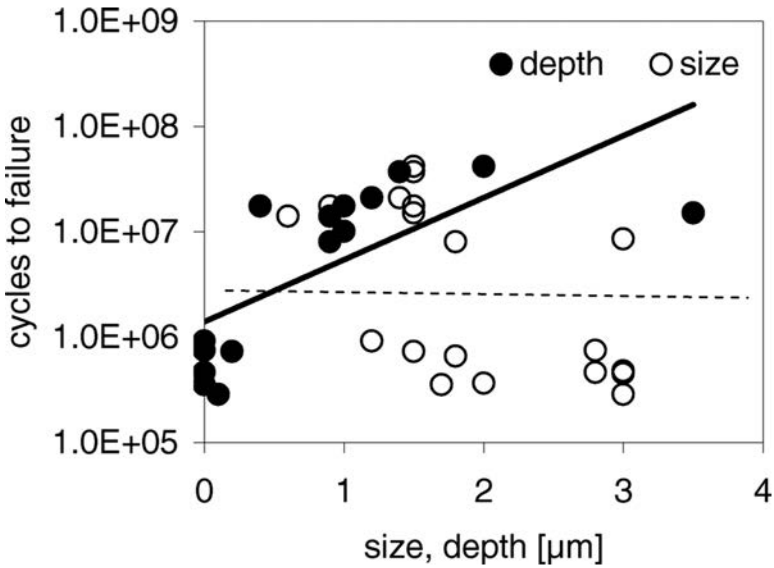

FIG. 11—*Cycles to failure as a function of inclusion depth (filled circles) and size in 36 % cold-worked 35N LT alloy tested at an alternating stress of* 827 MPa. *Note that fatigue lifetime is more correlated to depth (beneath free surface) than inclusion size.*

operating stresses and strains should decrease below the surface [8]. The former indicates that, within a given set of conditions, defect depth from the free surface was more imporatant in fatigue life determination than defect size.

Ultra High Cycle Fatigue

In data extraneous to this study, it was found that the near-threshold fatigue stress of 35N LT closely followed a Hall-Petch relationship (e.g., an increase in fatigue capability with decreasing grain size). In MP35N alloy, competition between inclusion-mediated failure at larger grain sizes precluded its use in this part of the study. Several ultra high cycle fatigue (UHCF) failures were examined in annealed 35N LT material possessing an SEM verified 200 nm grain size. Near-threshold behavior was found at a test level of 1.03 GPa. At these conditions, all samples examined exhibited lifetimes in excess of 0.5×10^9 cycles. Failures in this regime were found to occur predominantly at subsurface preferentially oriented grains and secondarily at subsurface inclusion particles. These findings were consistent with results in other studies suggesting primarily subsurface incipient damage in the gigacycle fatigue range [15]. Due to the long duration of testing in UHCF, samples of the other materials herein were not completed in time for publication.

Conclusions

The overall goal of this research was to characterize the microstructural parameters that are important in determining total fatigue life and life variability in fine medical wire for high fatigue applications. The realized gains in pursuing these objectives may be summarized as follows:

1. In the annealed 3 μm grain size samples, fatigue performance was statistically equivalent regardless of inclusion size distribution. This was attributed to the relative ease of irreversible slip and was evidenced by MSD failures in both alloy systems.
2. In the LCF regime, the cold-work induced hardening diminished the fatigue life performance in the MP35N system while significantly increasing the life of the 35N LT. This effect was attributed to the dominance of inclusion mediated damage in wire with lower ductility.
3. Relatively small inclusion size in the 35N LT increased the fatigue scatter in all failure regimes due to the activation of multiple initiation mechanisms including: surface intersecting PSBs, subsurface particles, and preferentially oriented grains.
4. Consistent availability of large inclusion failure sites in MP35N significantly reduced total fatigue life while increasing lifetime consistency.
5. In the HCF and UHCF regimes, for a given alloy system and load conditions, incipient defect depth from the wire surface was observed to be a stronger determinant of total fatigue lifetime than incipient defect size.

This work is a mere infant step toward a more complete understanding of the complexities of fatigue behavior in metallic fine wire for medical devices. Much more work is needed, including studies on residual stresses and their effect on incipient damage life, non random crystal orientation effects, fatigue behavior in nano-crystalline fine alloy wire, and on variability due to property anisotropy in heavily processed fine wire. The impact of a future model, encompassing raw material through the finish device would be enabling for the medical device engineer, thereby allowing the design of better implantable medical systems with improved resistance to premature failure.

Acknowledgments

With sincere gratitude, the author thanks Professors Eric Stach and Benjamin Hillberry for their insightful guidance. The author would also like to thank the staff of Fort Wayne Metals; without their support and funding, this work would not have been completed.

References

[1] Geddes, L. A. and Roeder, R., *Handbook of Electrical Hazards and Accidents*, CRC Press, Inc., Boca Raton, FL, 2nd ed., 1995.

[2] Smith, T., Halverson, S., Qiao, H., Sargent, A., and Hamann, T., CRDM Product Performance Report, 2006. Product Report 55, Medtronic, Inc., Minneapolis, MN, 2006.

[3] Herre, J. M., "Advances in ICD Lead Technology," *Cardiac Electrophysiology Review*, Vol. 5, No. 1, 2001 pp. 47–51.

[4] Kay, L., Bradley, D., Lippard, H., and Stephenson, T., "Optimization of Melt Chemistry and Properties of 35Cobalt-35Nickel-20Chromium-10Molybdenum Alloy Medical Grade Wire," *Proceedings of ASM International Materials and Processes for Medical Devices Conference, MPMD*, Ahaheim, CA, 2003, pp. 1–7.

[5] Connolley, T., McHugh, P. E., and Bruzzi, M., "A Review of Deformation and Fatigue of Metals at Small Size Scales," *Fatigue Fract. Eng. Mater. Struct.*, Vol. 28, 2005, pp. 1119–1152.

[6] "Superalloys developed by SPS Technologies for Aerospace Fasteners," Product brochure, SPS Technologies, Jenkintown, PA, 1998.

[7] Schaffer, J. E., "A Probabilistic Approach to Modeling Microstructural Variability and Fatigue Behavior in ASTM F562 Medical Grade Wire," *Proceedings of the 9th International Fatigue Congress, Fatigue 2006*, Atlanta, GA, 2006.

[8] Schaffer, J. E., "A Hierarchical Initiation Mechanism Approach to Modeling Fatigue Life Variability in 35Co-35Ni-20Cr-10Mo Medical Grade Fine Wire," Master of Science in Mechanical Engineering, Purdue University, School of Mechanical Engineering, West Lafayette, IN, 2007.

[9] Bouthot, R. J. Private communication, 2007.

[10] Altman, P. A., Meagher, J. M., Walsh, D. W., and Hoffman, D. A., "Rotary Bending Fatigue of Coils and Wires Used in Cardiac Lead Design," *J. Biomed. Mater. Res.*, Vol. 43, 1996, pp. 21–37.

[11] Shaji, E. M., Kalidindi, S. R., Doherty, R. D., and Sedmak, A. S., "Influence of Cold-Work and Aging Heat Treatment on Strength and Ductility of MP35N," *Mater. Sci. Eng., A*, Vol. A272, 1999, pp. 371–379.

[12] Kwofie, S., "Equivalent Stress Approach to Predicting the Effect of Stress Ratio on Fatigue Threshold Stress Intensity Range," *Int. J. Fatigue*, Vol. 26, 2004, pp. 299–303.

[13] Akiniwa, Y., Tanaka, K., and Kimura, H., "Microstructural Effects on Crack Closure and Propagation Thresholds of Small Fatigue Cracks," *Fatigue Fract. Eng. Mater. Struct.*, Vol. 24, 2001, pp. 817–829.

[14] Stanzl-Tschegg, S., "Fatigue Crack Growth and Thresholds at Ultrasonic Frequencies," *Int. J. Fatigue*, Vol. 28, 2006, pp. 1456–1464.

[15] Terent'ev, V. F., "On the Problem of the Fatigue Limit of Metallic Materials," *Metal Science and Heat Treatment*, Vol. 46, 2004, pp. 244–249.

ASTM Special Technical Publication, Vol. 6, No. 2
Paper ID JAI101558
Available online at www.astm.org

Min Liao,[1] *Kyle Chisholm,*[1] *and Mario Mahendran*[1]

Statistical Analysis of Fatigue Related Microstructural Parameters for Airframe Aluminum Alloys

ABSTRACT: This paper presents the results of statistical analysis of the fatigue related microstructural parameters, mainly on constituent particles and pores, in 7050-T7452 aluminum forging materials. The statistical distributions of the particle and pore area data, which were obtained from the metallographic measurements on polished surfaces, were fitted well with three-parameter lognormal functions. Comparative studies were carried out for the particle and pore size distributions between the core and periphery materials, and between the hand and die forging materials. An extreme value theory-based model was investigated to correlate the overall material particle distribution with the fatigue crack-nucleating particle distribution. The results indicated that the particle size is not the only parameter affecting the fatigue process; other parameters, such as grain size and grain orientation, are also important parameters for microstructure-based fatigue modeling. Therefore, orientation image microscopy (OIM) analyses were carried out on pristine 7050 samples, on different planes, to determine the grain orientation distributions. Finally, a preliminary OIM analysis was performed on a fractured sample to measure the misorientation angles between the grains near the crack nucleation and short crack regions. It is expected that the test observations and quantitative microstructural data could help to understand the effects of microstructure on the fatigue process and develop a microstructure-based fatigue modeling.

Manuscript received November 12, 2007; accepted for publication November 10, 2008; published online February 2009.
[1] Structures and Materials Performance Laboratory, Institute for Aerospace Research (IAR), National Research Council Canada (NRC), Ottawa, Ontario, Canada K1A 0R6, E-mail: min.liao@nrc-cnrc.gc.ca

Citation: Liao, M., Chisholm, K., and Mahendran, M., "Statistical Analysis of Fatigue Related Microstructural Parameters for Airframe Aluminum Alloys," *J. ASTM Intl.*, Vol. 6, No. 2. DOI10.1520/JAI101558. Available online at www.astm.org. Also included in JAI Special Issue STP 1508, *Fatigue and Fracture Mechanics: 36th Volume,* R. W. Neu, K. R. W. Wallin, and S. R. Thompson, guest editors, ASTM International, West Conshohocken, PA, 2009, pp. 416-438.

Introduction

The National Research Council Canada (NRC) and other organizations are developing the Holistic Structural Integrity Process (HOLSIP) to augment the traditional safe-life and damage tolerance paradigms, with the ultimate goal to evolve HOLSIP into a new paradigm for both the design and sustainment stages. In HOLSIP, the life of a component is divided into four distinct phases: nucleation, short/small crack, long crack, and final instability. The physics-based life prediction models are employed in HOLSIP to address material microstructure, surface integrity, and synergetic interaction between cyclic and environmental effects. The HOLSIP-based models have demonstrated some success in the life estimation of various components, especially in the case of fatigue and corrosion interaction [1–3].

Recently, NRC is developing the physics-based short/small crack models for Defence Research and Development of Canada (DRDC), which includes generating a material database and validating the model through case studies. The materials selected are the 7050 aluminum alloys since they have been used for the primary structure of the Canadian Forces F/A-18 aircraft. From a brief literature review, it is shown that some material databases in the short/small crack regime have been developed in the previous research for the 7050-T7451 plate [4,5]. However, for the 7050-T7452 forging, there have been very little (almost none) material microstructures characterization and short/small crack modeling found in open publications. Thus, the 7050-T7452 forging was selected as the primary material in the NRC-DRDC short crack project. The T74 temper indicates that the material was solution heat-treated, quenched, and artificially overaged, which provides good stress-corrosion resistance and strength characteristics. The temper Txx52 indicates that a cold compression was performed prior to aging; the compression process can reduce or partially relieve the residual stress in a forged block.

To develop physics-based lifing models for short crack and nucleation, the material microstructure has to be characterized. HOLISP uses the "initial discontinuity state" (IDS) to describe the as-produced state of the material in order to establish the initial analysis condition [6]. Examples of IDS include constituent particles, pores, and machining marks and scratches. Previous research has shown the experimental evidence that these IDS features are responsible for nucleation of fatigue cracks in aluminum alloys 7075 and 2024 [6–12]. Some fatigue modeling, which is based on the particle/pore size distribution, has been developed for life estimation on aluminum alloys [10,13–15]. For the 7050-T7452 forging, NRC fractographic studies [16,17] also indicated that the major crack nucleation features were particles and pores, as shown in Fig. 1.

In previous work [16,17], considerable metallurgical analysis and fractographic studies have been carried out to physically measure the IDS/particles and pores, for 7050-T7452 forging material. In order to further develop a physics-based fatigue model and to establish a database for HOLSIP-based life estimation, this paper carried out the statistical analysis for the measured IDS/particle and pore data, and investigated the correlation between the overall IDS/particle distribution and its fatigue subsets. In addition, other microstruc-

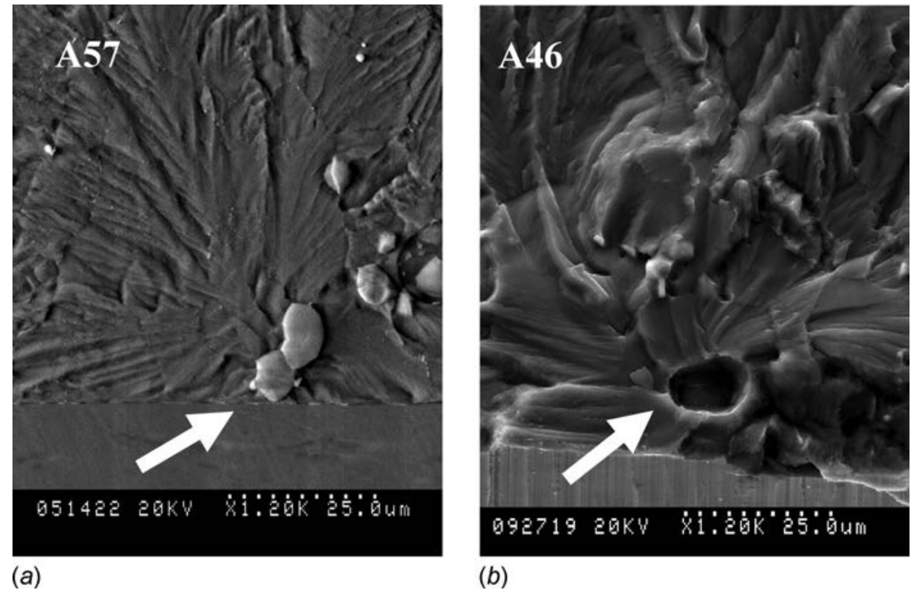

FIG. 1—*Crack nucleation features in 7050-T7452 forging.* (*a*) *Crack nucleation from a particle* ($\sim$112 μm^2). (*b*) *crack nucleation from a pore* ($\sim$400 μm^2).

tural parameters, such as grain size and grain orientation, were studied using the orientation image microscopy (OIM) technique.

Materials and Microstructural Analysis

The polished samples were taken from three forms of material, described as follows [18].

7050-T7452 Hand Forging, Sub-blocks 2, 3, 4, 7, 8, 9

These forgings were originally cut from the 6-in. thick blocks, whose core portions were already used in a previous International Follow-On Structural Test Program (IFOSTP) on the Canadian Forces and Royal Australian Air Force F/A-18 aircraft. The material was originally manufactured by ALCOA Inc. and shipped to NRC in 1996. The original sectioning of all the 6-in. blocks is illustrated in Fig. 2. For scanning electron microscopy (SEM) purposes, a total of 12 samples were manufactured from the sub-blocks 2, 3, 4, 7, 8, 9, XY plane, along the X-direction. On each sample, 49 SEM images were taken from evenly spaced locations, laid out in 7 rows by 7 columns, and each image was 355.5 μm by 461.0 μm in area. It should be noted that the samples are representative of the periphery (non-core) forging blocks.

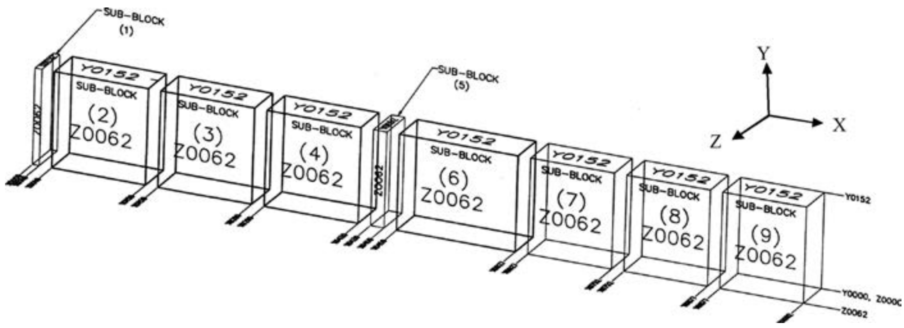

FIG. 2—*Illustration of the original sectioning of the aluminum 7050-T7452 forging* [*18*].

7050-T7452 Hand Forging, Sub-block 6

This sub-block was also left over from the previous IFOSTP project, but it has the core portion in place. In total, 21 samples were removed from the YZ plane, as shown in Fig. 3. Each sample contained 25 images, and each image was 355.5 μm by 461.0 μm in area. It is well known that the core of a block is normally the weakest portion in terms of its fatigue property, and the previous fatigue tests showed that the specimens (7050 plate) taken from the core portion have shorter fatigue lives than those from the periphery material [4]. In order to compare the microstructure features between the core and periphery material, these 21 samples were divided into four groups (Fig. 3):

1) Core group, containing seven samples (3B, 3B2, 3B3, 3B4, 3B5, 3A2, 3A3) taken from the core material;
2) Edge group 1, containing four samples (1A, 2A, 3A, 3A4) from the periphery material;

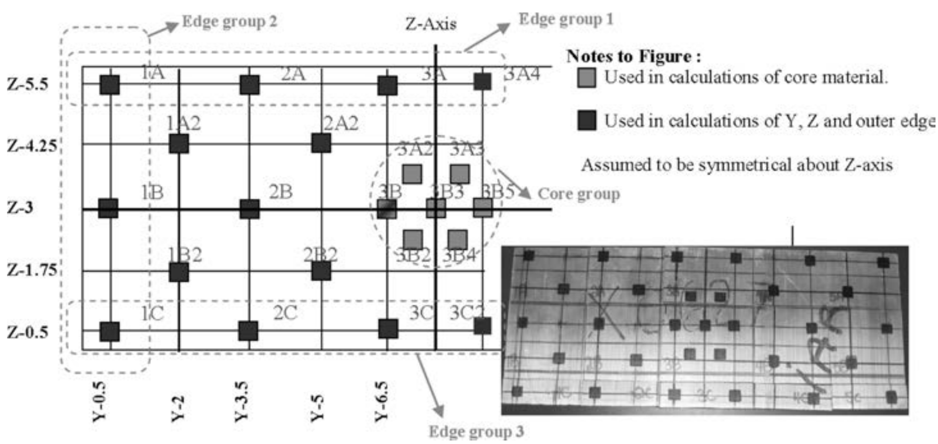

FIG. 3—*Details of the locations that samples removed from the YZ plane of sub-block 6 for image analysis along the Y- and Z-directions* [*16,18*].

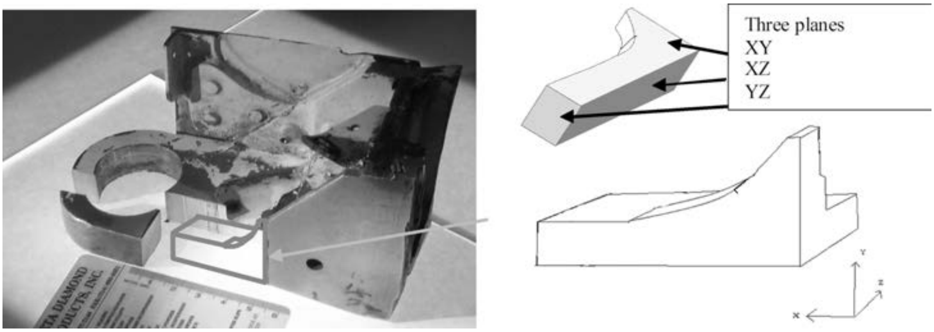

FIG. 4—*Section and samples used for material characterization* [*17*].

3) Edge group 2, containing three samples (1A, 1B, 1C) from the periphery material;
4) Edge group 3, containing four samples (1C, 2C, 3C, 3C2) from the periphery material.

7050-T7452 Die Forging (*Shear Tie Lug*)

A used CF-18 inner wing aft spar, shear tie lug, was given to this project for microstructural analysis. A section of material was cut from the lug, and three samples were taken from three planes of the section, as shown in Fig. 4. Twenty (20) images were taken of the sample from the XY plane, and 14 images from the YZ and XZ planes.

Microstructural Analysis

In the microstructural analysis, the areas of the particle and pore were measured on polished material with the aid of SEM. The SEM images were taken on the polished samples using the magnification of 250×, and then an image analysis was performed using commercial software, Image Pro, to determine the area of the particle or pore. In the image analysis, a threshold of 2 μm^2 was used to screen out any features which were smaller than this value. The detailed test procedures can be found in [16,17]. As an example, Fig. 5 presents an original SEM image and processed image showing particles and pores.

Statistical Analysis of Constituent Particle and Pore Data

Statistical Distribution of Particle and Pore Size

Following a previous statistical study [11,12], a three-parameter (3P) lognormal distribution was found to fit most material IDS/particle data the best, among two-parameter (2P) Weibull, 3P Weibull, Gumbel, Frechet, Pareto, and 2P log-

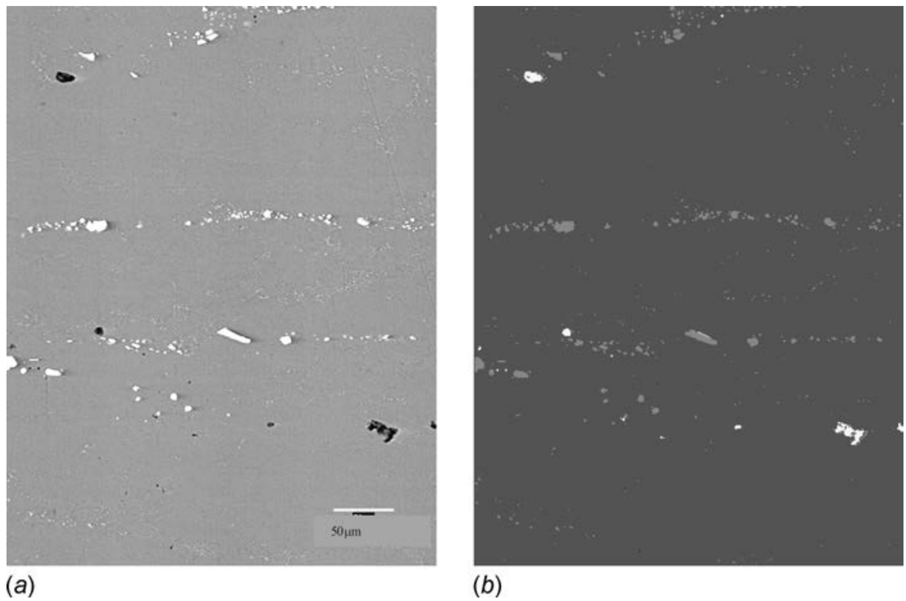

FIG. 5—*Example of SEM images for particle and pore measurements.* (*a*) *Original SEM image* (250×). (*b*) *Processed image showing particles* (*in red*) *and pores* (*in yellow*).

normal distributions. In addition, the lognormal distribution (including 3P and 2P) has been widely accepted for particle [4,10,12], pore [4], as well as other microstructural features, such as grain size [19].

As an example, Fig. 6 shows the different distributions fitting to the particle area data, which were measured from the XY plane of sub-block 2 location X4, on Normal probability paper. In this figure, all the distribution parameters were estimated using maximum likelihood methods, except for the weighted 3P lognormal distribution, which was fitted using least-squares method. It is shown that the 3P lognormal and weighted 3P lognormal provided the best fits to the data, especially in both tails of the distribution.

The 3P lognormal distribution can be expressed as

$$F(x) = \Phi\left[\frac{\ln(x-\tau)-\mu}{\sigma}\right], \quad x > 0, \quad \sigma > 0 \tag{1}$$

where $\Phi(\ldots)$ is the cumulative distribution function of a standard normal distribution, τ is the threshold (location), and μ and σ are the mean and standard deviation of the logarithmic particle/pore size, respectively.

Since the large particles/pores, i.e., the right tail of the particles/pores distribution, are more critical to the fatigue life of the material, a weighted 3P lognormal distribution was also used to further improve the fitting accuracy in the right tail of the particle/pore distribution. The weighted distribution has the same formula as Eq 1, but the parameters were determined by the least-squares method and a weight function as follows:

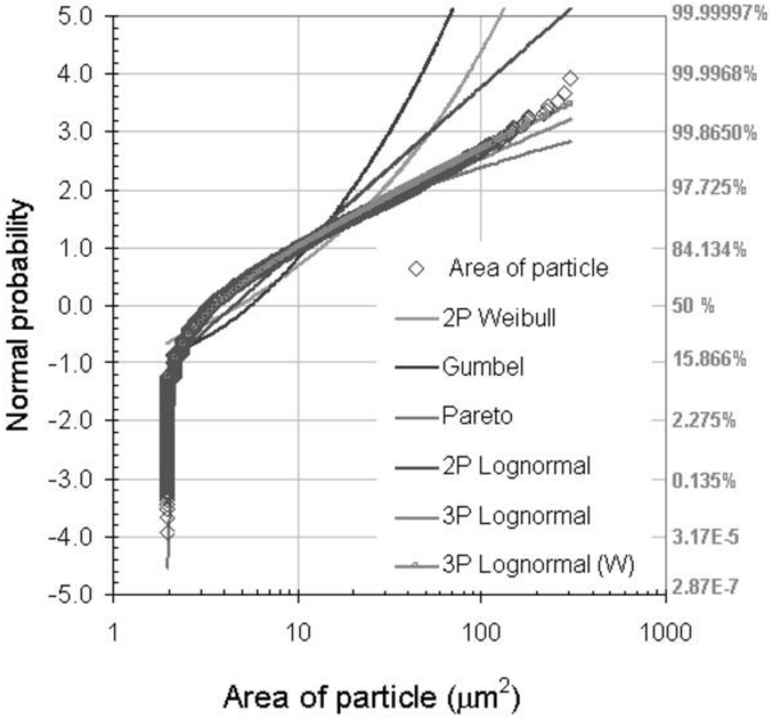

FIG. 6—*Goodness-of-fit plot of different distributions on normal probability paper for particle area (sub-block 2, location X4, XY plane).*

$$w_i = \frac{1}{1 - p_i} \tag{2}$$

where p_i is the empirical cumulative probability of the ordered number i. The goodness-of-fit plotting was carried out for all particle/pore area data. Overall, these figures show that the weighed 3P lognormal distributions provided an even better fit than the regular 3P lognormal distributions.

A MS Excel Macro was developed to process the massive amounts of data and determine the distribution parameters of the 3P lognormal and weighted 3P lognormal distributions. All the parameters are presented in Tables 1–3 for all the investigated materials. General statistics, such as mean, standard deviation, and density of particle/pore, are also presented in these tables.

Table 1 presents the results of the hand forging, which indicated:

- There are more particles than pores in the same area, and a higher density of large particles than pores.
- Average pore area is larger than that of the particle.
- The XY plane has higher density of large particle/pore than the YZ plane.

TABLE 1—*Distribution parameters of particles and pores of 7050-T745 hand forging.*

		Particle		Pores	
		XY plane (sub-blocks 2…9)	YZ plane (sub-block 6)	XY plane (sub-blocks 2–9)	YZ plane (sub-block 6)
General statistics	Mean	7.03	7.27	8.75	9.33
	Std. dev.	14.05	10.64	13.90	11.95
	Sample size	121220	78656	38965	11336
	Density of all particle/poreper 1 mm^2	1258	914	404	132
	Density of large particle (>50 μm^2)per 1 mm^2	19.16	10.60	8.59	2.18
	Density of large particle (>100 μm^2) per 1 mm^2	5.18	1.6725	1.44	0.1394
3P lognormal	Threshold τ	1.872	1.8526	1.8377	1.8448
	Mean μ	0.3963	0.7290	0.8618	1.0625
	Std dev. σ	1.5845	1.4379	1.5600	1.5989
3P lognormal (weighted)	Threshold τ	1.8201	1.4875	1.1579	–0.5552
	Mean μ	0.4554	0.9528	1.2085	1.7862
	Std dev. σ	1.5416	1.2499	1.2574	0.9782

Note:

1) All units are μm^2 except for sample size and density.

2) The lower limit of particle/pore area is about 2 μm^2.

3) For sub-blocks 2–9 (excluding 6), 12 locations were investigated, each location contains 49 images, and each image is 355.5 $\mu m \times 461.0$ μm, which gave a total surveyed area of 96 mm^2.

4) For sub-block 6, 21 locations were investigated, each location contains 25 images, and each image is 355.5 μm by 461.0 μm, which gave a total surveyed area of 86.1 mm^2.

TABLE 2—*Comparison of particle and pore distributions of hand forging, sub-block 6, YZ plane.*

		Particle			Pores		
		Edge Group 1 (1A, 2A, 3A,3A4)	Edge Group 3 (1C, 2C, 3C,3C2)	Core Group (3A2, 3A3, 3B1,3B2, 3B3, 3B4, 3B5)	Edge Group 1 (1A, 2A, 3A, 3A4)	Edge Group 3 (1C, 2C, 3C, 3C2)	Core Group (3A2, 3A3, 3B1,3B2, 3B3, 3B4, 3B5)
General statistics	Mean	7.286	6.523	7.578	9.6683	9.1898	9.7250
	Std. dev.	11.035	8.513	11.200	11.3370	11.0273	12.7516
	Sample size	14065	15405	25303	2017	1878	3812
	Density of all particle/pore per 1 mm^2	858	940	882	123	115	133
	Density of large particle ($>50\ \mu m^2$) per 1 mm^2	10.73	6.71	12.26	1.89	1.71	2.68
	Density of large particle ($>100\ \mu m^2$) per 1 mm^2	2.26	0.67	1.64	0.06	0.00	0.21
3P lognormal	Threshold τ	1.884	1.838	1.863	1.8275	1.8521	1.8550
	Mean μ	0.723	0.664	0.733	1.1715	1.0668	1.0668
	Std. dev. σ	1.420	1.387	1.476	1.5785	1.6170	1.6580
3P lognormal (weighted)	Threshold τ	1.602	1.501	1.284	–2.4571	–2.1942	–1.0702
	Mean μ	0.903	0.880	1.059	2.1245	2.0522	1.8900
	Std. dev. σ	1.272	1.200	1.213	0.8166	0.8244	0.9553

Note: All units are μm^2 except for sample size.

TABLE 3—*Distribution parameters for constituent particles and pores of 7050-T7452 die forging, shear tie lug.*

		Particles			Pores		
		XY plane (4×5 pics, 0.161 mm^2/pic)	YZ plane 2×7 pics, 0.161 mm^2/pic)	XZ plane (2×7 pics, 0.161 mm^2/pic)	XY plane (4×5 pics, 0.161 mm^2/pic)	YZ plane (2×7 pics, 0.161 mm^2/pic)	XZ plane (2×7 pics, 0.161 mm^2/pics)
General statistics	Mean	12.22	13.20	12.61	6.78	8.63	10.58
	Std. dev.	22.68	31.67	26.79	9.42	11.08	19.81
	Sample size	1370	836	790	359	224	146
	Density of all particle/pore per 1 mm^2	418	364	344	110	98	64
	Density of l arge particle ($>50\ \mu m^2$) per 1 mm^2	22.67	17.75	18.19	1.55	2.22	2.66
	Density of large particle ($>100\ \mu m^2$) per 1 mm^2	6.52	11.09	7.54	0.00	0.00	0.44
3P lognormal	Threshold τ	1.8949	1.9103	1.8853	1.8737	1.7846	1.6982
	Mean μ	0.9145	0.9027	0.8880	0.5411	1.0502	1.0165
	Std. dev. σ	1.7833	1.7797	1.6525	1.4876	1.4648	1.4230
3P lognormal (weighted)	Threshold τ	0.6325	1.7518	1.7714	1.6453	1.1187	1.8569
	Mean μ	1.4630	1.0248	0.9746	0.7203	1.3280	0.9029
	Std dev. σ	1.3088	1.6619	1.6361	1.3389	1.1509	1.6106

Note:

1) All units are μm^2 except for sample size.

2) The lower limit of particle and pore area is about 2 μm^2.

Table 2 presents a comparison of the particle and pore distributions between the core and edge portions of the hand forging sub-block 6, which indicated:

- The core group has higher average particle/pore area than the edge groups.
- The core group has higher density of large pore/particle than most edge groups.

Table 3 presents the statistical results for the 7050-T7452 die forging (shear tie lug), which indicated:

- There are more particles than pores, and higher density of large particles than pores.
- In the die forging, the average particle area is larger than that of the pore.
- The average particle area is relatively consistent on different planes. But the average pore area varies on the different planes. The XZ plane has higher pore area (average) and density of large pores, than other planes (note that the XYZ coordinate system (Fig. 4) is not the same as that of the hand forging (Fig. 2).

Comparison of Particle and Pore Distributions among Different Blocks

Overall, it is shown that the number of particles is higher than the number of pores in each sample, for either hand or die forging, core or periphery sample, XY, XZ, or YZ plane.

In the hand forging 7050, the average size of the pores is larger than that of the particles, but in the die forging 7050, the average size of the particles is larger than that of the pores.

The average size of the particles in the hand forging is smaller than that of the die forging, but the average size of the pores in the hand forging is slightly larger than that of the die forging (see Tables 1 and 3). On the other hand, the die forging has slightly higher density of large particles ($>50\ \mu m^2$) as the hand forging, but less density of large pores ($>50\ \mu m^2$) as the hand forging.

The distribution comparisons between the different sub-blocks are presented in Fig. 7 and the results indicate that the probability of having a very large particle or pore [i.e., $P(x>200\ \mu m^2)=1-P(x\leq 200\ \mu m^2)$] in the die forging is greater than the hand forging. Figure 8 presents the particle and pore distributions in sub-block 6, indicating that the probability of having very large pores ($>150\ \mu m^2$) in the core material is greater than the periphery material. However, the probability of having very large particles ($150\ \mu m^2$) in the core material is similar to the periphery material.

Fatigue Crack Nucleating Particle/Pore—IDS Fatigue Subset

The fatigue subsets of the material IDS/particle or pore data were measured from the crack-nucleating particles on the fatigue fracture surface, and characterized by area, or width and height of particle and pore. A number of fatigue tests were carried out using a single edge tension (SENT) specimen [20], some

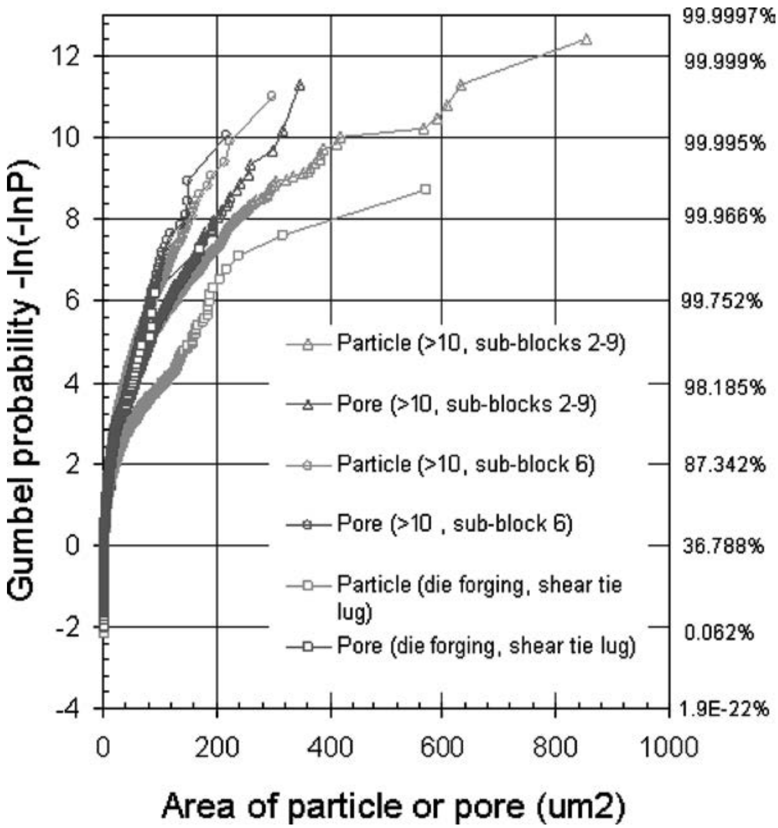

FIG. 7—*Comparison of all pore and particle size, between sub-blocks 2–9, sub-block 6, and die forging (note: due to large amount of data, only the data* >10 μm^2 *are plotted).*

of the crack-nucleating particles were measured from the fracture surface with aid of an SEM, as shown in Fig. 9 (as well as Fig. 1). Physically and statistically, the crack-nucleating particles are a subset of the material IDS/particle distribution which has been analyzed in the previous sections. A correlation should exist between the material IDS/particle distribution and its fatigue subsets. In this paper, an extreme value theory based model is first investigated to determine this correlation, that model was used before for 2024-T351 sheet [12] and 7050-T7451 plate [4].

In brief, the model was based on the extreme value theory (or statistics of extreme)[21]. In the case that the material IDS/particle distribution follows a lognormal distribution, the fatigue subset, i.e., the extreme value of the largest particles, is asymptotic to a Frechet distribution. When the number of sampling particles is large, the extreme value distribution is exactly a Frechet distribution, expressed as [11]

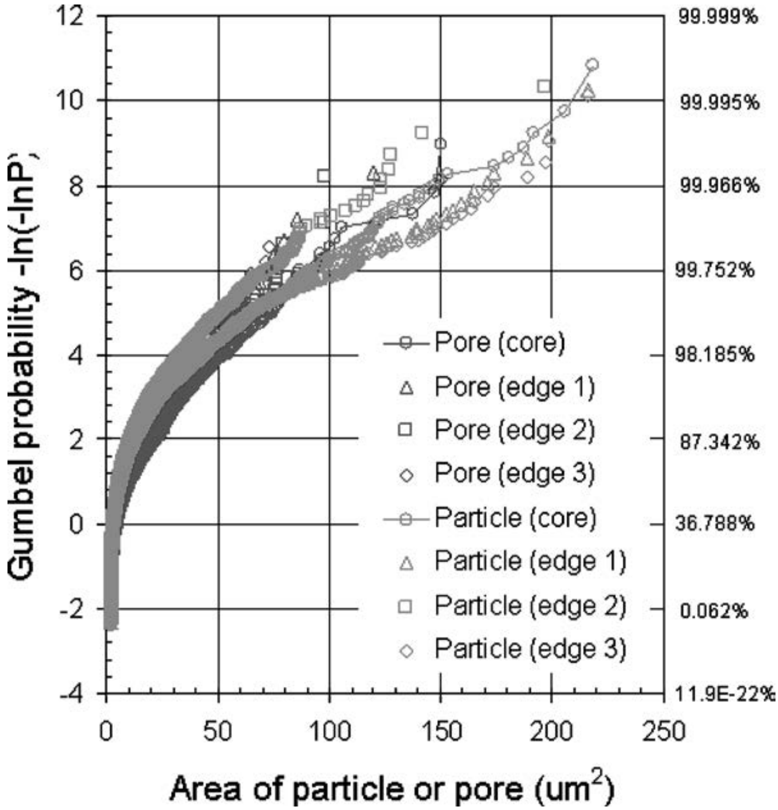

FIG. 8—*Comparison of particle, pore size in between core and edge materials in sub-block 6, YZ plane (note: each point is one measurement).*

$$F_S(x) = \exp\left[-\left(\frac{a}{x-\tau}\right)^b\right], \quad x \geqslant 0, \quad a,b > 0 \tag{3}$$

where

$$a = \exp\left[\sigma\sqrt{2\ln(N_S)} - \sigma\left[\frac{\ln[\ln(N_S) + \ln(4\pi)]}{2\sqrt{2\ln(N_S)}}\right] + \mu\right]$$

$$b = \frac{\sqrt{2\ln(N_S)}}{\sigma} \tag{4}$$

and N_s is the number of particles in the fatigue "hot spot," given by

$$N_S = D_P \times A_{HS} \tag{5}$$

In Eq 5, D_p is the overall particle density, which can be obtained from a basic metallographic examination on a polished surface, and A_{HS} is the area of the highest stress region, which is dependent on geometry, stress level, and gradi-

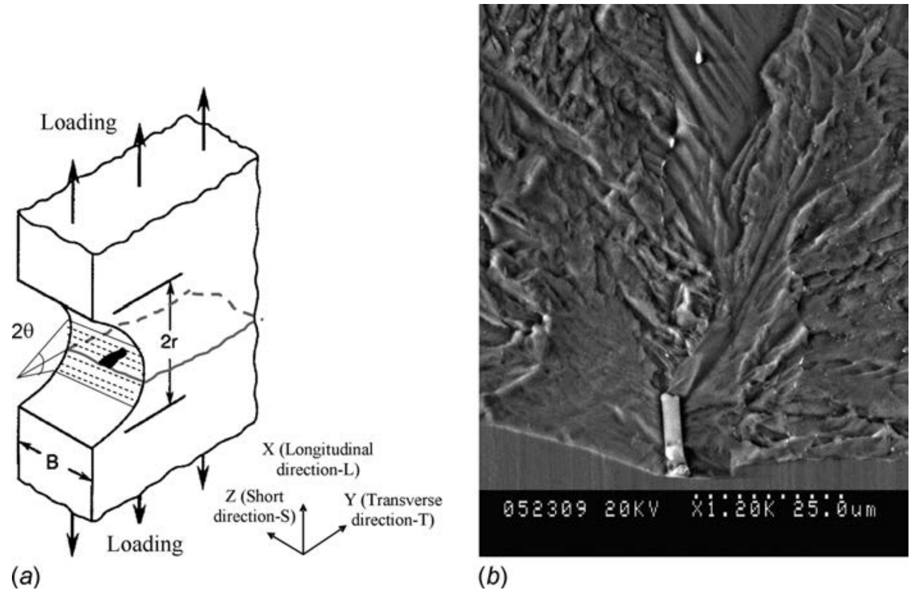

FIG. 9—*Fatigue specimen* (*SENT*) *and crack-nucleating particle.* (*a*) *SENT specimen, notch area.* (*b*) *Crack nucleating particle on fracture surface* (*SEM photo*).

ent and can be determined by a finite element analysis. For the SENT specimens used in this work, the surface area of 95 % of the highest stress zone was determined as part of the bore surface corresponding to a circumferential angle $\theta = 2 \times 19.45°$ [22], as shown in Fig. 9(*a*).

Some of the modeling inputs and results are presented in Table 4. The material IDS distribution used in the model, was the 3P weighted lognormal distribution (Table 2, core group particle, YZ plane). A comparison of the model (Eq 3) and test results is presented in Fig. 10. Overall, the model greatly overestimated the fatigue subset distributions for the 7050 hand forging. In fact, a similar overestimation happened on the smooth 2024 specimen [12] and the open hole 7050-T7451 specimens [4]. The main reason was deemed to be that not all the largest particles in the highest stress region would nucleate cracks. Only those among the largest that are associated with other favorable microstructural features such as grain size, grain orientation, and grain boundary, would nucleate and propagate cracks to final failure. In addition, it was found that either 95 % or 99 % highest stress surface area did not affect the prediction. Using 2D data to represent the 3D particles may also contribute to the overestimation (i.e., Wicksell problem), although the contribution may not be significant [8]. Therefore, a critical density for crack-nucleating particles, (D_{CP}), was back-calculated, which would result in the best "prediction" to the measured fatigue subsets from the fracture surfaces, also shown in Fig. 10. The back calculation was based on the Kolmogorov-Smirnov (K-S) goodness-of-fit criterion, i.e., to minimize the K-S statistic between the model and test distributions. Table 4 presents all the D_{CP} results, which indicate that the critical

TABLE 4—*Inputs and results for statistical modeling of particle (area) distribution for 7050-T7452 hand forging specimen (SENT).*

Fatigue loading (peak stress, stress ratio)	Highest stress region (95 % σ_{MAX}), A_{HS}, mm^2 $A_{HS}=(2\theta/360)\ ^{*}2\pi rt$	Density for all particles, D_P (ST/YZ plane)[a] Table 2	Number of particles in highest stress region $N_s=D_{P}{*}A_{HS}$	Critical density for crack-nucleating particles, D_{CP} K-S test fit	Ratio of D_{CP}/D_P
17–25 ksi, $R-0.35$ ~0.45	13.72	882	12098	5.19	0.59 %

[a]ST/YZ plane—short transverse plane, see Fig. 9(*a*).

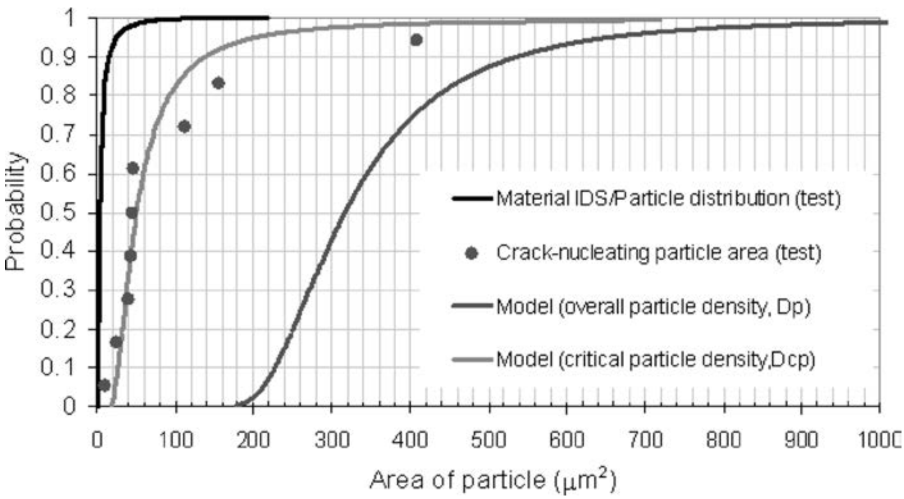

FIG. 10—*Model and test results of crack-nucleating particle (area) distribution for 7050-T7452 hand forging SENT specimen.*

density D_{CP}, is around 0.5 % of the overall particle density, which is similar to the result of [12].

The modeling results again support that fatigue crack nucleation is a process that is fundamentally affected by the material microstructural features such as particle, porosity, and grain structure (size, orientation, and boundary) [6,12,23,24]. The particle or pore may or may not be cracked or debonded from the matrix due to the material manufacturing process. The size and orientation of the surrounded grains affect the dislocation movement, dislocation energy stored, as well as the deformability of the grain structure in association with grain boundaries. The grain boundaries are also well known to block/arrest the growth of microstructural crack. Physically, the crack nucleation process and microstructural short crack growth are dominated by the combination of all these microstructural parameters (not only the particle size). In fact, from the fatigue tests on 7050 and 2024 aluminum alloys, it was found that *larger* particles often result in *shorter* fatigue lives [13,25].

Although the statistical distribution for each parameter may be determined from an independent measurement, the joint statistical distribution of the multiple parameters (particle size, grain size, and grain orientation) needs the data from the dependent/concurrent measurements which contain the statistical correlation information among the multiple parameters. On a fatigue fracture surface, it is impossible to carry out such measurements to determine the joint distribution affecting the fatigue process. Further work was carried out to characterize the grain size and orientation distributions of the 7050 forgings.

Characterization of Grain Size and Orientation Distributions using OIM

In the OIM analysis, 12 polished samples from the 7050 hand forging and three samples from the die forgings were examined using an electron backscatter

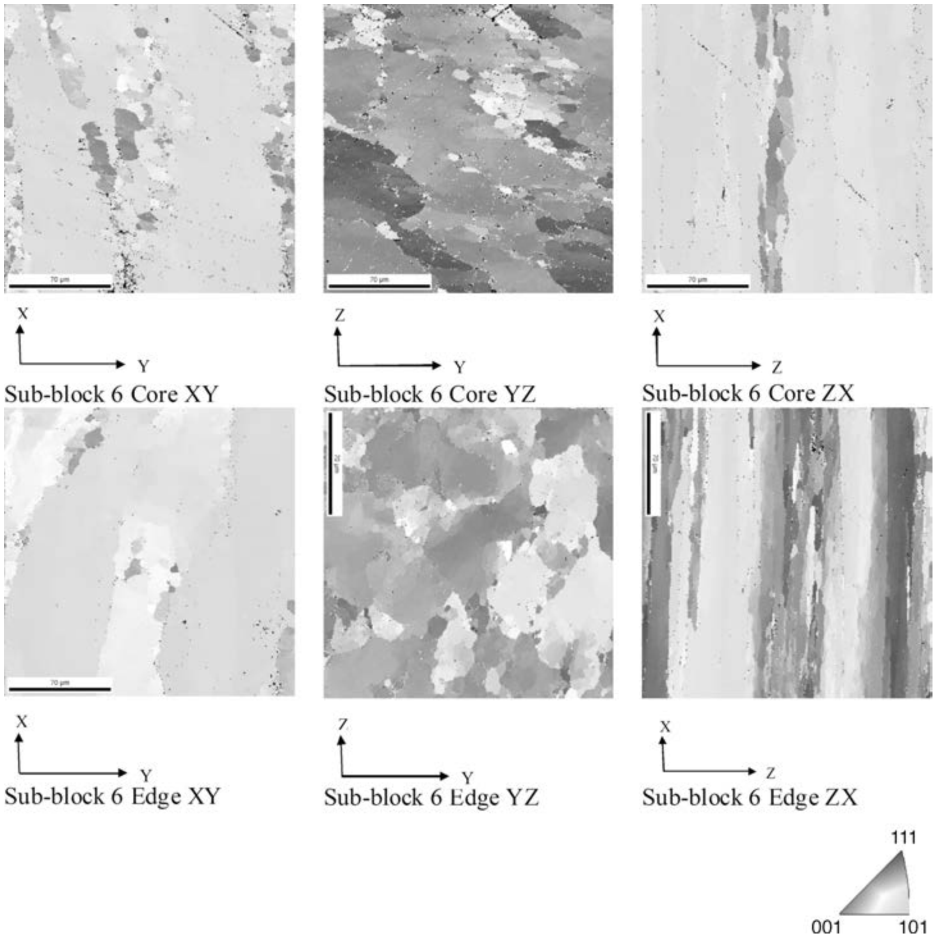

FIG. 11—*Inverse pole figure maps for hand forging 7050 (sub-block 6).*

diffraction (EBSD) detector attached to an SEM, and then the EBSD patterns data were analyzed using the OIM analysis software of EDAX Inc., USA to quantify grain crystallographic orientation as well as other microstructural features. Figure 11 presents the inverse pole figures for some samples taken from the edge and core portions of sub-block 6. It is shown that the grains are elongated along the X-direction. Due to the limit of the OIM examination range, the length of large elongated grains could not be determined, but it is shown that the large elongated grains could easily exceed 100 μm in length. Besides the elongated grains, there are equiaxed small grains with an average size of about 10 μm (Fig. 11). Based on the OIM analysis results, both the core and edge samples showed the similar misorientation angle distribution for the grain boundaries, with an average angle of 22°. Over 50 % of grain boundaries have the misorientation angles which are less than 10°. Meanwhile, the OIM analysis

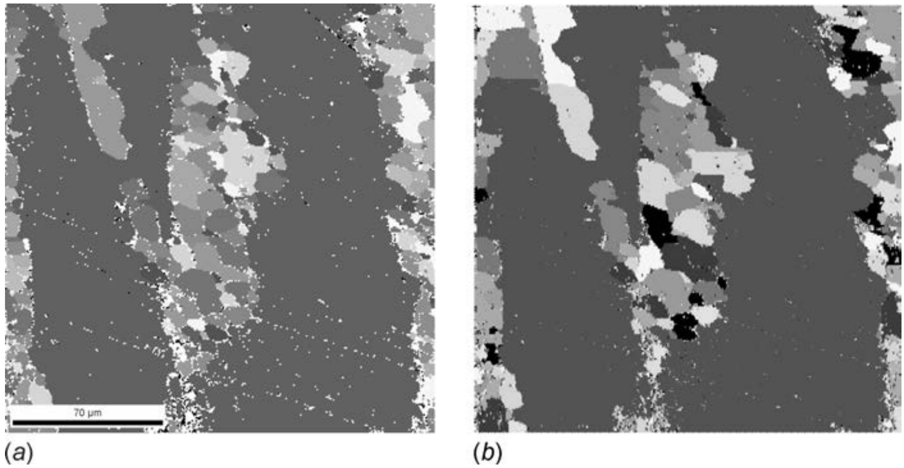

FIG. 12—*Example of an OIM image and the OIM based finite element model.* (*a*) *OIM image example.* (*b*) *OIM-based finite element model.*

software generated a data file (.ang file) which contains all three Euler anglers for each pixel in the image, which can be used for building a microstructural model, such as an anisotropic finite element (FE) model. Figure 12 presents an OIM image based FE model, which contains the same grain orientation information as the OIM results. Currently, more work is underway using this FE model to simulate the fatigue process by taking into account the grain orientation effects.

Figure 13 presents the inverse pole figures for the samples taken from the

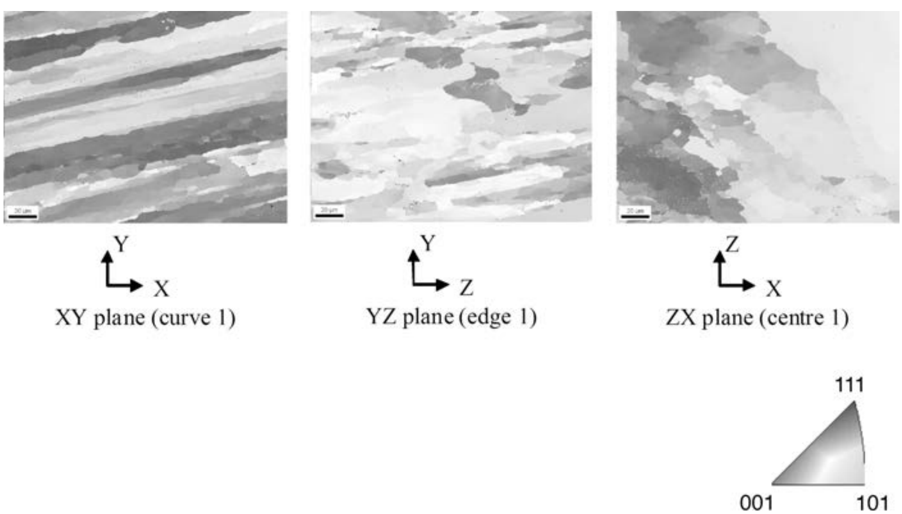

FIG. 13—*Inverse pole figure maps for die forging 7050* (*shear tie lug*).

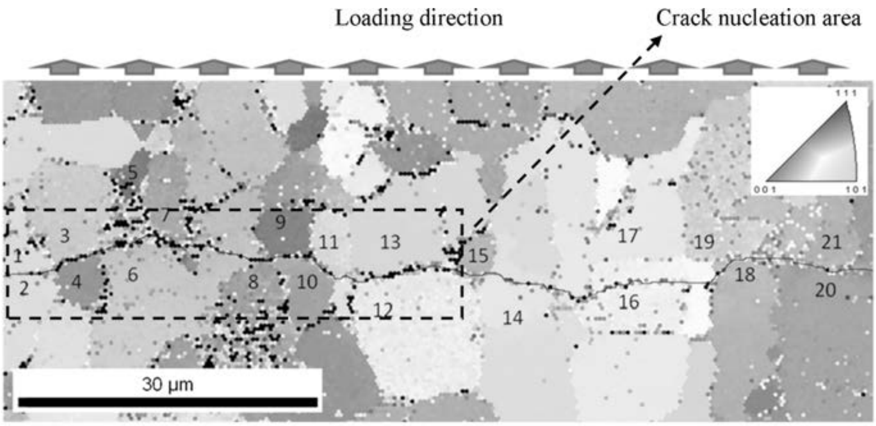

Misorientation angles between grains numbered in the image above, M(x, y) designates the angle between grain x and grain y

M(3, 4)	M(5, 6)	M(6, 7)	M(8, 9)	M(9, 10)	M(10, 11)	M(12, 13)	M(12, 15)	M(14, 15)	M(16, 17)	M(16, 19)	M(16,18)	M(20, 21)
15°	52°	60°	9°	9°	33°	25°	56°	11°	9°	6°	15°	9°

FIG. 14—*Inverse pole figure map and misorientation angles between the grains along the short crack path, the crack nucleation site is around the center of the image.*

die forging (shear tie lug). Compared to the hand forging (Fig. 11), there are fewer small equiaxed grains in the die forging. The majority of grains are elongated along the X-direction, i.e., the main grain flow direction, as well as the Z-direction. All three planes (XY, YZ, and XZ) have similar misorientation angle distributions for the grain boundaries, with an average angle of about 20° and over 50 % of misorientation angles less than 10°.

An OIM analysis was also carried out on a fatigue cracked sample taken from the hand forging SENT coupon. Figure 14 shows the OIM image taken around the center of the surface crack near the crack nucleation site. As required by the OIM scanning, this fractured sample (on the notch surface) was polished to a flat surface, therefore, the crack-nucleating particle/pore on the notch surface may have been removed. From the fractography performed later, the crack nucleation area was identified and marked by a black box in Fig. 14. In the same figure, grains along the crack path are labeled with numbers, and the misorientation angles between the neighboring grains are listed in the table within Fig. 14. After the OIM analysis is done, the sample was opened up and a fractography was carried out using SEM. Figure 15 presents the OIM image along with the SEM photo showing the crack nucleation area. The results of Figs. 14 and 15 indicated that

- in the crack nucleation area (in the black box of Fig. 14), most grain misorientation angles are higher than 15°, while most of the angles are lower than 15° between the grains a short distance away from the nucleation area;
- in the crack nucleation area, the crack propagation is mostly intergranu-

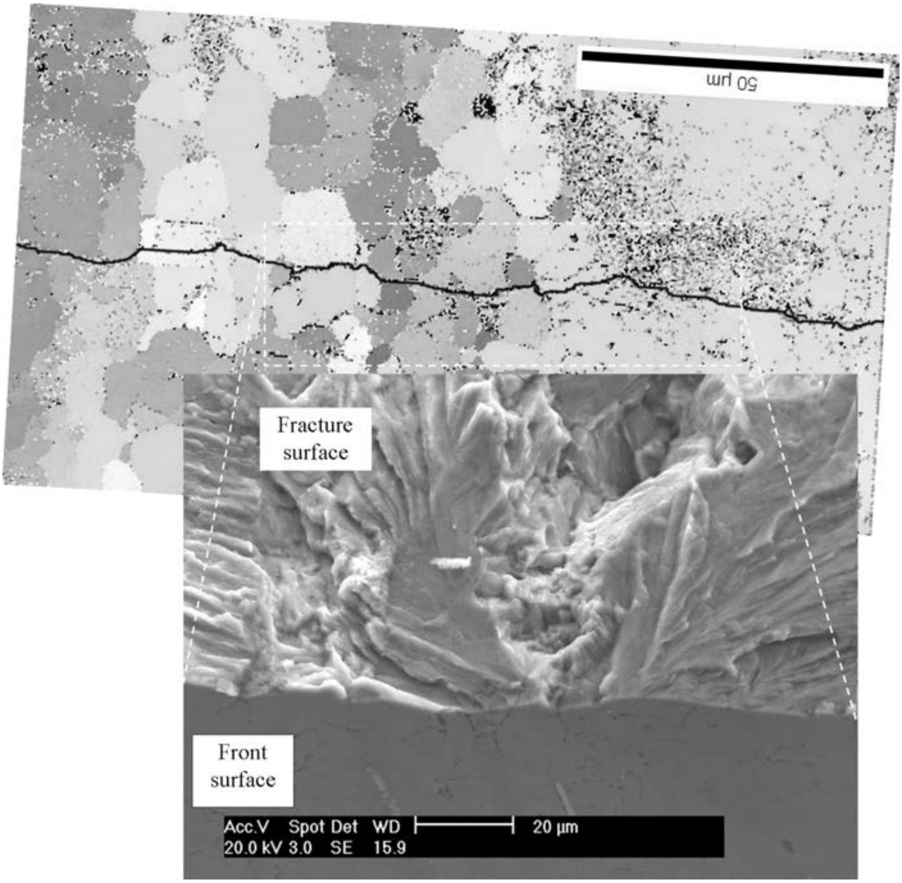

FIG. 15—*OIM image and SEM photo showing the crack nucleation area.*

lar, while the short to long crack propagation is mainly transgranular. The observation and quantitative results are critical experimental evidence that must be taken into account in a microstructural based fatigue modeling.

Discussion

Future work is to carry out more microstructural analysis, including OIM analysis for 7050 grain size and grain orientation distributions, especially on fractured samples. The large cluster of particle/pore should be measured in terms of its size and spatial distance. All these microstructural parameters and distributions will form a database of the 7050 forging material, which will be used (1) to build statistically representative microstructure models, and (2) to help develop a microstructure model for crack nucleation and short/small crack growth analysis.

The current linear elastic fracture mechanics models/tools cannot use a joint (multi-dimensional) distribution of particle size, grain size, and grain orientation. Only a one-dimensional distribution can be used in these models/tools by assuming that the particle size is equal to a crack size. In that case, the crack-nucleating particle/pore size measured from fracture surfaces or the right tail of the material IDS/particle distribution (i.e., the 3P weighted lognormal distribution) could be used for fatigue life estimation [25].

Conclusion

For the 7050 material, the statistical databases of the IDS/particle and pore were established for accurate life prediction based on HOLSIP framework. Overall the 3P lognormal distribution was found to be the best-fit distribution for the material IDS/particle and pore area data, and the weighted 3P lognormal distribution was found to provide an even better fit to the right tail of the distributions. In the 7050 hand and die forgings, there were more particles than pores, and yet the size of the largest particles were also bigger than that of the pores. The particle and pore size in the core ($\sim T/2$) material was slightly larger than the periphery ($\sim T/4$) material. Also, the density of large pore/particle ($> 50\ \mu\text{m}^2$) in the core is higher than in the periphery. This size of particle/pore or larger ones are found to be responsible for most crack nucleation in the NRC fatigue tests.

The extreme value theory-based model determined that the critical density of crack-nucleating particles (D_{cp}), for the hand forging 7050, was about 0.5 % of the density of all particles. This effort also indicated that, in addition to particle size, other microstructural parameters need to be considered for predicting the fatigue subsets of the material IDS/particle size distributions.

The OIM analysis indicated that both the core and edge samples have the similar misorientation angle distributions for the grain boundaries, with an average angle of 20°–22°. Over 50 % of grain boundaries have the misorientation angles of less than 10°. Moreover, the preliminary OIM analysis, on the fractured sample, found that the crack nucleation region showed primary the intergranular propagation, along the grain boundaries with the misorientation angles of larger than 15°, while the short-long crack region showed primary transgranular propagation.

Acknowledgments

This work was carried out with the financial support of Defence Research and Development Canada (DRDC) and National Research Council Canada (NRC), project "Short Crack Model Development" (46_QJ0_56). Thanks to T. Benak, A. Marincak, and Dr. G. Renaud for performing the fatigue test and some modeling; A. Merati, L. Gasser, A. Gagnon, and M. Gallant for performing particle and pore measurements. Special thanks to M. Huang and J. Szpunar of McGill University for performing the OIM analysis.

References

[1] Komorowski, J. P., "New Tools for Aircraft Maintenance," *Aircr. Eng. Aerospace Technol.*, Vol. 75, No. 5, 2003, pp. 453–460.

[2] Brooks, C., Honeycutt, K., Prost-Domasky, S., and Peeler, D., "Monitoring the Robustness of Corrosion and Fatigue Prediction Models," Proceeding of the 2001 USAF ASIP Conference, Williamsburg, VA., 2001.

[3] Liao, M., Bellinger, N. C., Komorowski, J. P., Rutledge, B., and Hiscocks, R., "Corrosion fatigue prediction using holistic life assessment methodology," Proceedings of the 8th International Fatigue Congress, FATIGUE 2002, Stockholm, Sweden, June 2002, Vol. 1, pp. 691–700.

[4] Magnusen, P. E., and Bucci, R. J., "Role of Microstructure on the Fatigue Durability of Aluminum Aircraft Alloys," Contract Report for U.S. Office of Naval Research, 1995.

[5] Molent, L., Sun, Q., and Green, A. J., "Characterisation of Equivalent Initial Flaw Size in 7050 Aluminum Alloys," *Fatigue Fract. Eng. Mater. Struct.*, Vol. 29, 2006, pp. 916–937.

[6] Hoeppner, D. W., Invited Keynote Paper, "Estimation of Component Life by Application of Fatigue Crack Growth Threshold Knowledge," *Fatigue and Creep of Pressure Vessels for Elevated Temperature Service*, 1985, MPC 17, ASME, New York, NY, pp. 1–85.

[7] Suresh, S., *Fatigue of Material*, 2nd ed., Cambridge University Press, Cambridge, 1998, p. 154.

[8] Murakami, Y., *Metal Fatigue: Effects of Small Defects and Nonmetallic Inclusions*, Elsevier, New York, 2002, p. 330.

[9] Newman, J. N., "Short-Crack Growth Behavior in an Aluminum Alloy: An AGARD Cooperative Test Programme," AGARD-R-732, NATO, Advisory Group for Aerospace Research and Development, 1988.

[10] Laz, P. J., and Hillberry, B. M., "Fatigue Life Prediction from Inclusion Initiated Cracks," *Int. J. Fatigue*, Vol. 20, No. 4, 1998, pp. 263–270.

[11] Liao, M., and Merati, A., "Statistical Analysis of the Initial Discontinuity State (IDS) Data of 2024-T351 Aluminum Alloy," Proceedings of the 16th Aerospace Structures and Materials Symposium in 50th CASI Annual General Meeting and Conference, April 2003, Montréal, Québec.

[12] Liao, M., "Probabilistic Modeling of Fatigue Related Microstructural Parameters in Aluminum Alloys," Eng Frac Mech (in press).

[13] Liao, M., Renaud, G., and Bellinger, N. C., "Probabilistic Modeling of Short Crack Growth in Airframe Aluminum Alloys," *J. Aircr.*, Vol. 45, No. 4, 2008, pp. 1105–1111.

[14] Tanaka, K., Kinefuchi, M., and Yokomaku, T., "Modeling of Statistical Characteristics of the Propagation of Small Fatigue Cracks," *Short Fatigue Cracks, ESIS 13*, K. J. Miller and E. R. de los Rois, Eds., 1992, Mechanical Engineering Publications, London, pp. 351–368.

[15] Chan, K. S., "A Microstructural-Based Fatigue-Crack-Initiation Model," *Metall. Mater. Trans. A*, 34A, 2003, pp. 43–58.

[16] Merati, A., and Gasser, L., "Determination of the Statistical Distribution of the IDS of a 7050-T7452 Aluminum Alloys," NRC Technical Report, LM-SMPL-2007-0007, 2007.

[17] Merati, A., and Gagnon, G., "Microstructural Features of 7050-T7452 Die Forged Aluminum for the Case Study of Shear Tie Lug," NRC Technical Report, LM-

SMPL-2007-0009, 2007.

[18] Liao, M., Chisholm, K., and Mahendran, M., "Statistical Analysis of Constituent Particles and Pores in 7050-T7452 Aluminum Alloys," NRC Technical Report, LTR-SMPL-2007-0111, June 2007.

[19] ASTM, Standard E112-96, "Standard Test Methods for Determining Average Grain Size," *Annual Book of ASTM Standards*, ASTM International, West Conshohocken, PA, 1996.

[20] Liao, M., and Benak, T., "Residual Stress Measurements on 7050-T7452 Forging Coupon Specimens," NRC Technical Report, LTR-SMPL-2007-0109, June 2007.

[21] Gumbel, E. J., *Statistics of Extremes*, Columbia University Press, New York, 1958.

[22] Yang, J. N., Manning, S. D., Rudd, J. L., and Bader, B. M., "Investigation of Mechanistically Based Equivalent Initial Flaw Size Approach," ICAF 95, 18th Symposium of ICAF Melbourne Australia, EMAS, 1995.

[23] Chang, R., Morris, W. L., and Buck, O., "Fatigue Crack Nucleation at Intermetallic Particles in Alloys—A Dislocation Pile-up Model," *Scr. Metall.*, Vol. 13, 1979, pp. 191–194.

[24] Miller, K. J., "The Behavior of Short Fatigue Cracks and the Initiation Part II—A General Summary," *Fatigue Fract. Eng. Mater. Struct.*, Vol. 10, Part 2, 1987, pp. 93–113.

[25] Liao, M., Benak, T., Renaud, G., Yanishevsky, M., Marincak, T., Bellinger, N. C., and Mills, T., "Development of Short/Small Crack Model for Airframe Material, 7050 Aluminum Alloys," 11th Joint NASA/FAA/DOD Conference on Aging Aircraft, April, 2008, Phoenix, AZ, 2008. http://www.agingaircraft2008.com/.

ASTM Special Technical Publication, Vol. 5, No. 6
Paper ID JAI101564
Available online at www.astm.org

J. Toribio,[1] *B. González,*[1] *J. C. Matos,*[1] *and F. J. Ayaso*[1]

Multi-Scale Approach to the Fatigue Crack Propagation in High-Strength Pearlitic Steel Wires

ABSTRACT: This paper deals with the influence of the manufacturing process on the fatigue behavior of pearlitic steels with different degrees of cold drawing. The fatigue crack growth rate (da/dN) is related to the stress intensity range (ΔK) by means a compliance method to evaluate the crack depth a in the samples at any instant during the tests. The analysis is focused on the Region II (Paris) of the fatigue behavior in which $da/dN=C(\Delta K)^m$, measuring the constants (C and m) for the different degrees of drawing. From the engineering point of view, the manufacturing process by cold drawing improves the fatigue behavior of the steels, since the fatigue crack growth rate decreases as the strain hardening level in the material increases. In particular, the coefficient m (slope of the Paris Law) remains almost constant and independent of the drawing degree, whereas the constant C decreases as the drawing degree rises. The paper focuses on the relationship between the pearlitic microstructure of the steels (progressively oriented as a consequence of the manufacturing process by cold drawing) and the macroscopic fatigue behavior. To this end, a detailed metallographic analysis was performed on the fatigue crack propagation path after cutting and polishing on a plane perpendicular to the crack front. It is seen that the fatigue crack growth path presents certain roughness at the microscopic level, such a roughness being related to the pearlitic colony boundaries more than to the ferrite/cementite lamellae interfaces.

KEYWORDS: pearlitic steel, high strength steel, fatigue microdamage, Paris' Law

---

Manuscript received November 13, 2007; accepted for publication May 14, 2008; published online June 2008.
[1] Department of Materials Engineering, University of Salamanca, E. P. S., Campus Viriato, Avda. Requejo 33, 49022 Zamora, Spain, e-mail: toribio@usal.es

Citation: Toribio, J., Gonzalez, B., Matos, J. C., and Ayaso, F. J., "Multi-Scale Approach to the Fatigue Crack Propagation in High-Strength Pearlitic Steel Wires," *J. ASTM Intl.*, Vol. 5, No. 6. DOI10.1520/JAI101564. Available online at www.astm.org. Also included in JAI Special Issue STP 1508, *Fatigue and Fracture Mechanics: 36th Volume,* R. W. Neu, K. R. W. Wallin, and S. R. Thompson, guest editors, ASTM International, West Conshohocken, PA, 2009, pp. 439-458.

Introduction

Fatigue propagation is the basic subcritical mechanism of cracking. In pearlitic steel microstructures, the interlamellar spacing is the key parameter controlling fatigue crack growth, since the ferrite/cementite interfaces block the dislocation movement [1]. With regard to fatigue crack growth thresholds, they are strongly dependent on microstructure [2], in particular on the pearlitic colony size [3]. In addition, such a threshold decreases when the stress ratio (R factor) increases at constant temperature, such a decrease being higher at low temperatures [4]. In cold drawn pearlitic steel there is a linear inverse relationship between the stress ratio and the threshold, and the latter decreases when the yield strength increases [5].

In the matter of the Paris regime, although the role of microstructure is not clear for some authors [6], in cold drawn pearlitic steel the Paris' Law shifts to lower values as the drawing degree increases, so that the fatigue crack growth resistance increases with cold drawing [7]. The presence of oriented pearlite promotes a tortuous crack path with local crack deflections and bifurcations [8,9], delaying fatigue crack growth due to the presence of the cementite hard phase.

In this paper the fatigue crack growth in the Paris regime is analyzed in progressive drawn pearlitic steels, determining how the microstructural changes undergone during the drawing process affect both the microscopic and the macroscopic fatigue behavior in the matter of fatigue crack paths, local deflections angles, and fatigue crack growth rate as a function of the degree of drawing.

Experimental Procedure

The materials used were progressively drawn pearlitic steels with eutectoid chemical composition (0.789 % C, 0.681 % Mn, 0.210 % Si, 0.010 % P, 0.218 % Cr, 0.061 % V).

Analysis covered from the hot rolled bar (steel E0 which is not cold drawn at all) to the cold drawn wire (commercial prestressing steel E7 suffering seven cold drawing steps), including the intermediate degrees of drawing too (steels E1 to E6, where the digit indicates the number of drawings steps undergone by each steel after passing through the successive drawing dies).

Pearlitic material microstructure consisted of alternate lamellae of ferrite and cementite whose orientation in relation to the wire axis depended on the drawing level [10–14]. Figures 1 and 2 show longitudinal metallographic sections of the hot rolled bar and the cold drawn wire, cf., [10–13]. As a summary of the effects of cold drawing on the evolution of the pearlite colony or first microstructural level [10,11], cold drawing produces a progressive orientation of the pearlite colony with its main axis approaching the axis of the wire or cold drawing direction, and a slenderizing of the colony itself. In the matter of the pearlitic lamellar microstructure or second microstructural level [12,13], cold drawing produces both a decrease of interlamellar spacing and an orientation of the plates in the cold drawing direction.

Apart from these general trends, the metallographic analysis showed the

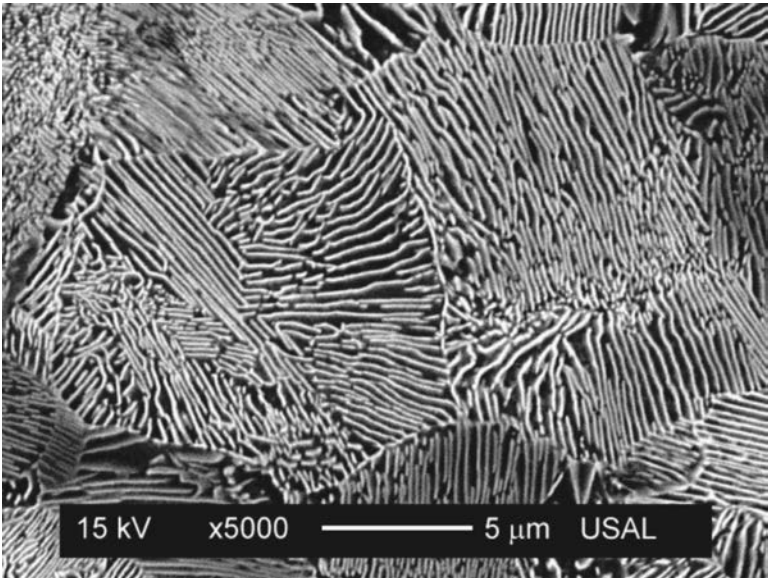

FIG. 1—*Longitudinal metallographic section of the hot rolled bar* (*in the photograph, the horizontal side is associated with the radial direction in the bar and the vertical side corresponds to the bar axis*).

presence of some extremely slender *pearlitic pseudocolonies* (Fig. 3) with anomalous (too large) local interlamellar spacing and even with predamage (microcracks which act as local fracture precursors) which makes them preferential fracture paths with minimum local resistance, in agreement with previous works [14].

The cold drawing process provokes an improvement of conventional mechanical properties of the steel. The yield strength and the ultimate tensile stress increase with cold drawing, whereas the Young's modulus keeps constant through the process. The stress-strain curves of the steels are plotted in Fig. 4 and the main mechanical properties of the steel are summarized in Table 1, where E is the Young's modulus, σ_Y the yield strength, σ_R the ultimate tensile strength, and ε_R the ultimate strain.

The specimens for the fatigue tests were circular rods of 11.0 to 5.1 mm diameter and a mechanical notch was produced to initiate fatigue cracking (Fig. 5). Tests were performed at room temperature, step by step under load control, the load being constant in a step and decreasing from one to another step. Samples were subjected to tensile cyclic loading with an R factor equal to zero, and a frequency of 10 Hz. The maximum load in the first loading stage corresponded to a value of about half the yield strength and was reduced between 20–30 % from one to another step (Fig. 6). Each loading stage was long enough to detect crack advance after the overload retardation effect [15] caused by the previous loading stage (with higher stress intensity level).

Fatigue tests were interrupted and a fracto-metallographic analysis was

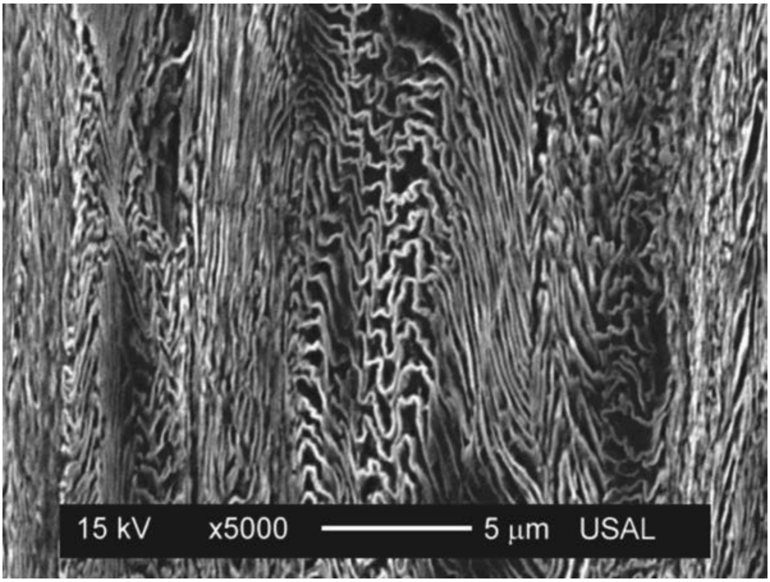

FIG. 2—*Longitudinal metallographic section of the cold drawn wire* (*in the photograph, the horizontal side is associated with the radial direction in the wire and the vertical side corresponds to the wire axis or cold drawing direction*).

performed on the cracked samples by cutting along a plane perpendicular to the crack front in order to examine in detail the fatigue crack path immersed in the steel microstructure. To this end, after grinding and polishing, samples were etched with 4 % Nital during several seconds and later observed by scanning electron microscopy (SEM) with magnification factors of 3000× and 6000×.

TABLE 1—*Mechanical properties of the steels.*

Steel	E (GPa)	σ_Y (GPa)	σ_R (GPa)	ε_R
E0	202	0.70	1.22	0.078
E1	187	0.79	1.27	0.069
E2	189	0.89	1.37	0.059
E3	192	0.92	1.40	0.055
E4	194	1.02	1.50	0.050
E5	199	1.12	1.59	0.049
E6	201	1.20	1.64	0.045
E7	209	1.48	1.82	0.060

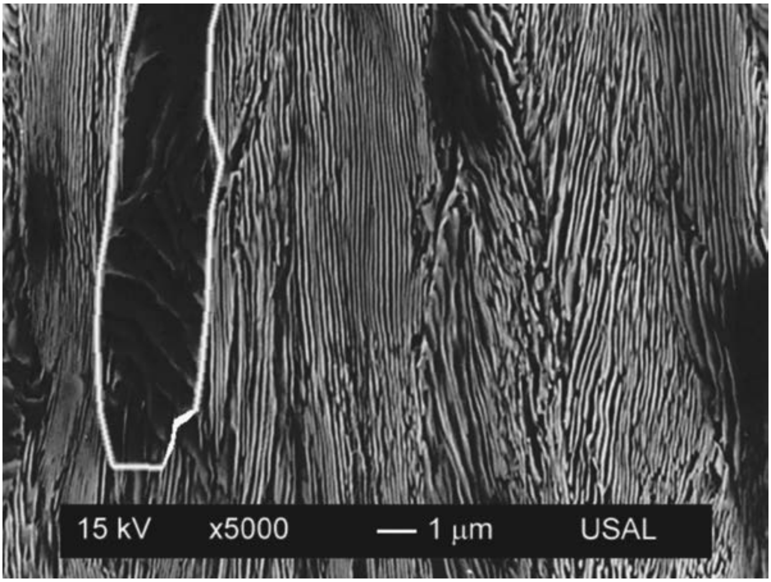

FIG. 3—*Pearlitic pseudocolony in the cold drawn wire* (*in the photograph, the horizontal side is associated with the radial direction in the wire and the vertical side corresponds to the wire axis or cold drawing direction*).

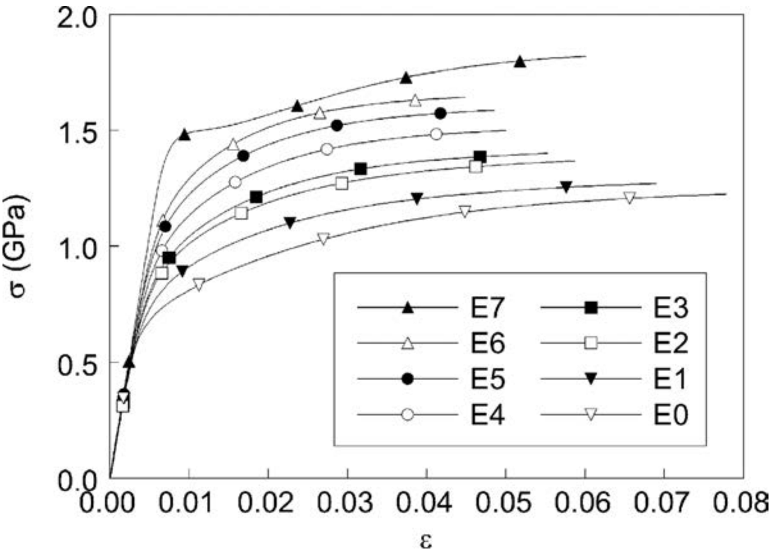

FIG. 4—*Stress-strain curves of the steels.*

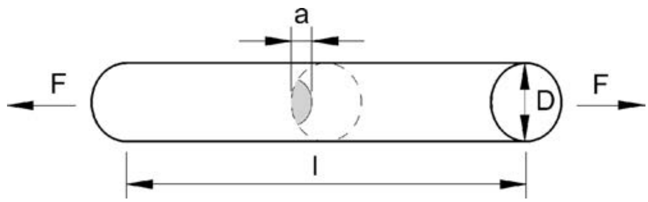

FIG. 5—*Round bar with a surface crack under tension cyclic loading.*

Experimental Results

Fatigue Crack Growth Laws (*Hot Rolled Bar and Prestressing Steel Wire*)

The fatigue crack propagation was analyzed by using the Paris' Law [16]:

$$\frac{da}{dN} = C\Delta K^m \tag{1}$$

by means of fatigue tests under load control, with constant stress range $\Delta\sigma$ during each step and decreasing steps (i.e., the stress range decreases from one to another step), where da/dN is the cyclic crack growth by fatigue and ΔK the stress intensity range, both variables being related by the equation:

$$\Delta K = Y\Delta\sigma\sqrt{\pi a} \tag{2}$$

The dimensionless stress intensity factor Y for the geometry under consideration (cracked wire) was calculated by Astiz [17] by means of the finite element method together with a virtual crack extension technique on the basis of the stiffness derivative, as a function of the relative crack depth, a/D, and the crack aspect ratio, a/b, from the central point of the crack front, $s/s_0=0$ (Fig. 7),

$$Y = \sum_{\substack{i=0 \\ i\neq 1}}^{4} \sum_{j=0}^{3} C_{ij}(a/D)^{i}(a/b)^{j} \tag{3}$$

where the coefficients C_{ij} are given in Table 2.

In the fractographs obtained by fatigue and posterior fracture of the wires, the crack front evolution was observed. The fatigue surfaces of the hot rolled bar and the cold drawn wire are developed in Mode I and the beach marks being clearly detectable by visual inspection (Fig. 8).

The crack front was modeled as an ellipse with its center located at the periphery of the rod. It was defined from a set of real points taken from the actual crack front and using a least squares fitting technique to adjust the theoretical (modeled) crack front to the real one.

The crack length was evaluated by means of the compliance of the samples, the dimensionless compliance ($1/CED$) *versus* the dimensionless crack length (a/D). The compliance (C) for each test was obtained from the last loading step at which the relationship between the applied load (F, measured by means of the load cell) and the relative displacement between two reference points in the

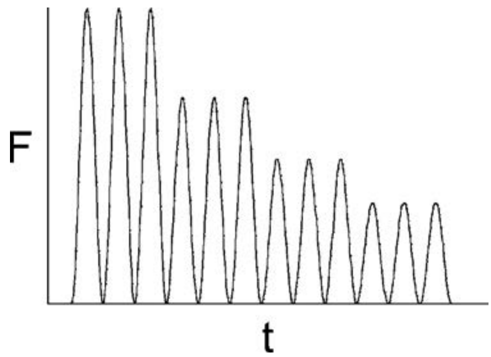

FIG. 6—*Loading scheme during the tests.*

sample (u, evaluated by means of a dynamic extensometer located in front of the crack mouth) allows the computation of the compliance $C = u/F$. Finally, the compliance was related to the crack geometry, relative crack depth a/D and crack aspect ratio a/b (Fig. 9).

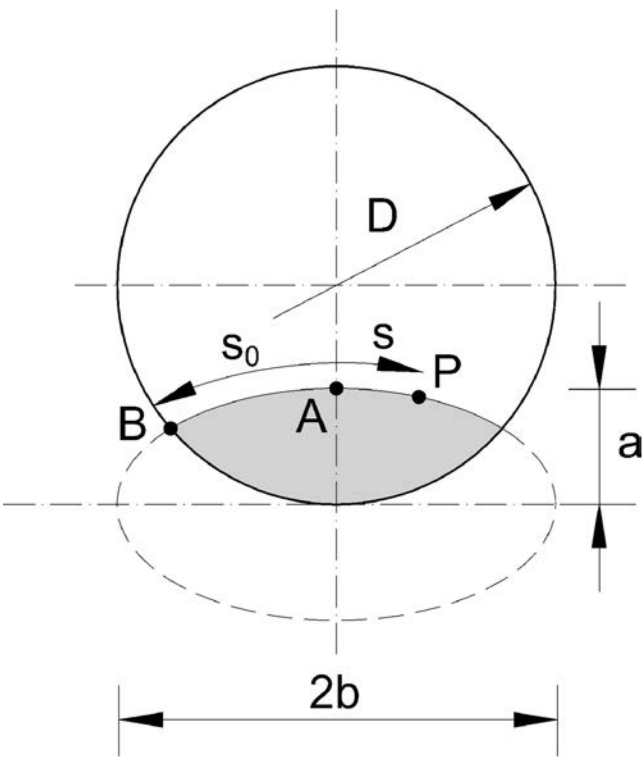

FIG. 7—*Geometric parameters characterizing the crack.*

TABLE 2—*Coefficients* C_{ij} *of Eq 3.*

i/j	0	1	2	3
0	1.118	−0.171	−0.339	0.130
2	1.405	5.902	−9.057	3.032
3	3.891	−20.370	23.217	−7.555
4	8.328	21.895	−36.992	12.676

Figure 10 offers the fatigue crack growth curves ($\mathrm{d}a/\mathrm{d}N - \Delta K$) of both E0 and E7 in the Paris regime. From the engineering point of view, a clear improvement of fatigue performance is observed with cold drawing [18], the two lines being parallel, which indicates that the exponent of the Paris Law is constant during the drawing process, whereas the constant C decreases with cold drawing, Table 3 where international units are used, i.e., when ΔK is used in $\mathrm{MPam}^{1/2}$, $\mathrm{d}a/\mathrm{d}N$ appears in m/cycle. These results are consistent with previous analyses on progressively drawn steels [7], in the sense that the fatigue crack growth rate decreases as the cold drawing degree increases.

Effect of Residual Stress (*Steels with Intermediate Degree of Drawing*)

Steels with intermediate degree of drawing exhibit a retardation of fatigue crack growth in the central area of the wire section (Fig. 11) due to the presence of compressive residual stresses in that area and tensile ones in the vicinity of the wire surface. As a matter of fact, the cold drawing process generates an axisymmetric residual stress profile, so that such internal stresses affect the crack growth under cyclic loading, as discussed in Ref. [19]. Other analyses indicated that tensile residual stresses produce only a slight increase of crack propagation rate, while compressive ones create a big decrease [20]. As a con-

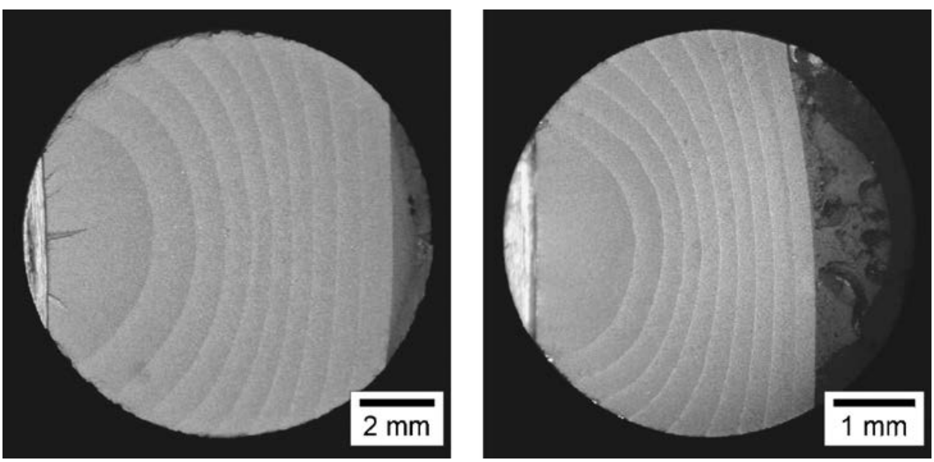

FIG. 8—*Crack shape evolutions in steel wires E0* (*hot rolled bar*) *and E7* (*prestressing steel wire*).

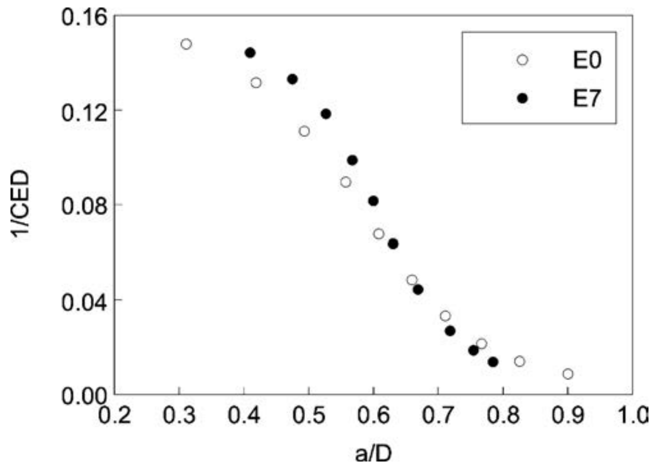

FIG. 9—*Dimensionless compliance.*

sequence, residual stresses produces a *gull*-shaped crack front evolution in the central part of the cross-sectional area of the wires in the case of cold drawn steel, a phenomenon observed in other materials [21]. On the other hand, the hot rolled steel (not cold drawn at all) and the commercial prestressing steel wire (which has undergone a stress-relieving process), the retardation effect (and its associated *gull*-shaped crack front) does not appear (cf., Fig. 8).

To quantify the aforesaid phenomenon, a numerical modeling of the first step of cold drawing was performed by the finite element method using a commercial software (MSC Marc). The problem of a wire passing through a die has

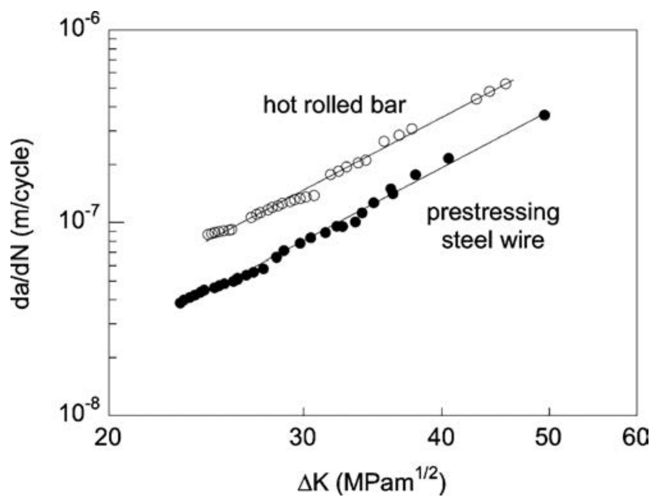

FIG. 10—*Curves* da/dN – ΔK *of materials E0 (hot rolled bar) and E7 (prestressing steel wire).*

TABLE 3—*Paris coefficients* (*S.I.*).

Steel	C	m
Hot rolled bar	$5.11 \cdot 10^{-12}$	3.02
Prestressing steel wire	$2.66 \cdot 10^{-12}$	3.03

cylindrical symmetry, so that only an axial section of the cylinder has to be modeled. Cylindrical coordinates r, θ, and z were used, z being the drawing axis, r the radial coordinate, and θ the annular one. The finite element mesh was refined at the wire axis and at the surface, the two zones where residual stress levels are higher. The stress-strain curve of the drawn steel used in the computations was taken from the standard tension test (cf., Fig. 4), whereas the die was considered as rigid. The drawing process was modeled under displacement control (Fig. 12). Large strains and large displacements were considered in the computations.

Figure 13 shows the cylindrical components of residual stresses after one step of drawing. These distributions can be considered as representative of any degree of drawing in a real manufacturing process. Residual stresses are compressive at the wire center and tensile at the surface, the latter having higher absolute values, and this stress profile can explain the *gull* effect explained above in the matter of crack shape evolution. With regard to the different components, radial, axial and annular stresses are in decreasing series.

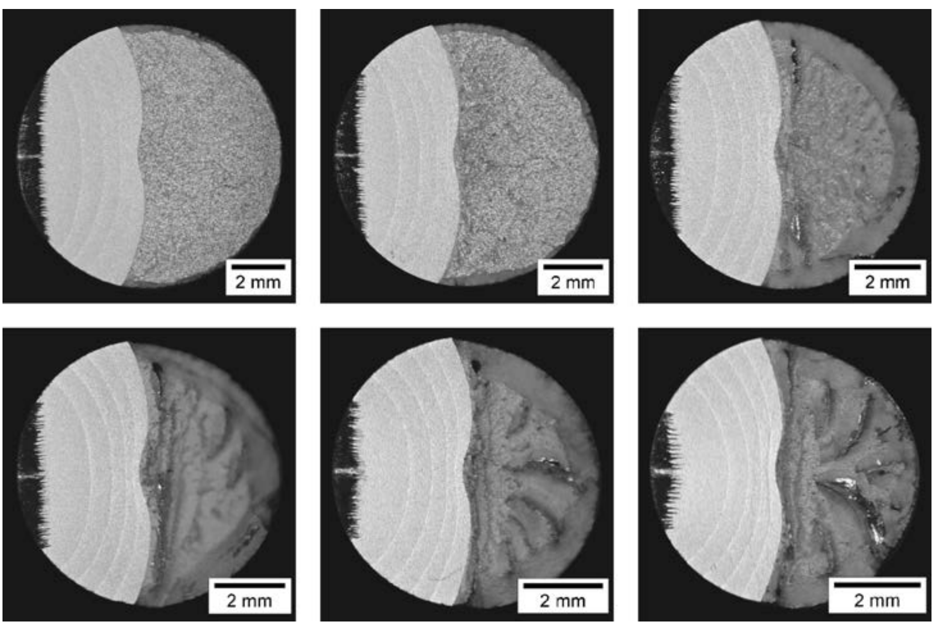

FIG. 11—*Crack shape evolutions in intermediate steps* (*from left to right and top to bottom, steels E1, E2, E3, E4, E5, and E6*).

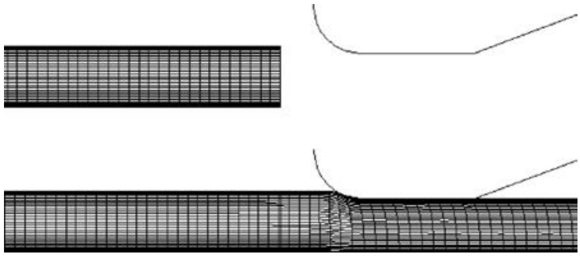

FIG. 12—*Scheme of the drawing process.*

Microscopic Approach: Fatigue Crack Paths

To elucidate the microscopic crack path, metallographic sections (perpendicular to the crack front) were obtained from the fatigue cracked wires. Micrographs were taken showing the fatigue crack growth from left to right, as shown in Fig. 14, where the origin of the fatigue crack is a mechanical notch (left).

The fractographic appearance of fatigue cracks in pearlitic microstructures resembles microplastic tearing, consistent with fatigue damage and crack advance by highly localized plastic strain (Fig. 15). Therefore the fatigue process could be caused by dislocational movement ending at the ferrite-cementite interfaces and promoting the fracture of pearlitic lamellae by plastic collapse. Fatigue cracks are transcolonial and tend to fracture pearlitic lamellae, with

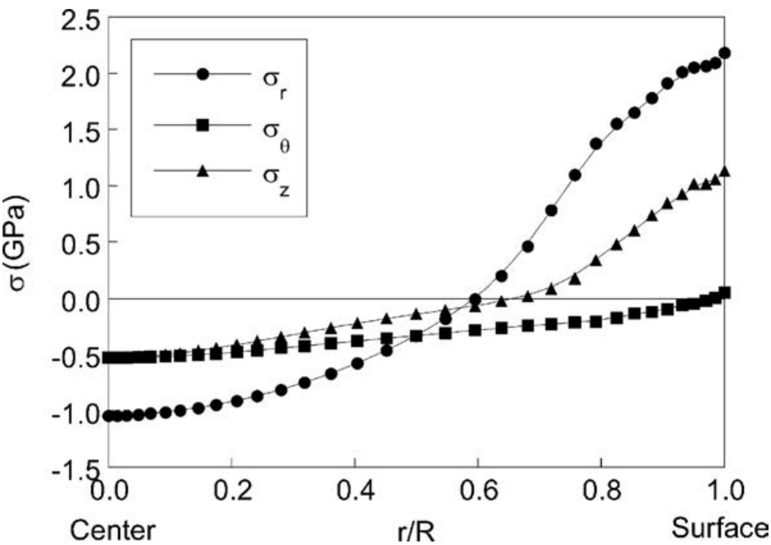

FIG. 13—*Residual stresses in the drawn steel, where r is the radial coordinate and R the wire radius.*

FIG. 14—*Longitudinal section of the wire showing the cracking profile.*

nonuniform crack opening displacement values, micro-discontinuities, branchings, bifurcations, and local deflections, creating microstructural roughness (Fig. 16).

With regard to the role of the drawing degree, in Figs. 17 and 18, the cracking profile is given in the hot rolled bar and the prestressing steel (cold drawn) wire for the same stress intensity range, showing that the frequency of deflections in the fatigue crack path increases with the cold drawing. This tortuous crack path is one of the basic explanations of the improvement of fatigue performance in the cold-drawn wire (Fig. 19).

A computation was made of the ratio of the *real* profile length in the fatigue crack path (L_0) to the *projected* profile length (L). This ratio, a measure of roughness, increases with cold drawing from 1.11 (hot rolled bar) to 1.23 (prestressing steel wire), thereby indicating that there is an increase of the net fatigue fractured surface with the degree of drawing, and the same happens with the frequency and angle of the local crack deflections in the fatigue crack path.

Discussion

Global Crack Advance

To analyze the fatigue crack growth in both steels (E0 and E7), metallographic cuts perpendicular to the fatigue crack path plane were made in both steels. It is seen that in both cases fatigue crack growth is through the pearlitic colonies (i.e., transcolonial), with higher roughness in the cold drawn wire and a growing direction changing from one to another colony. At the microscopic level,

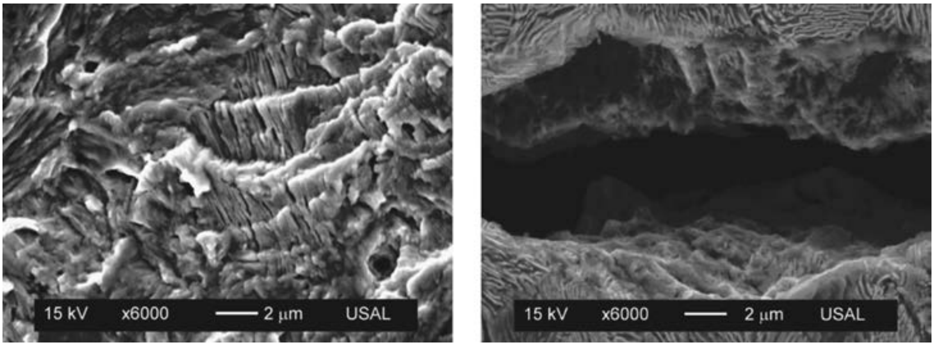

FIG. 15—*Fracture surfaces (steel E1).*

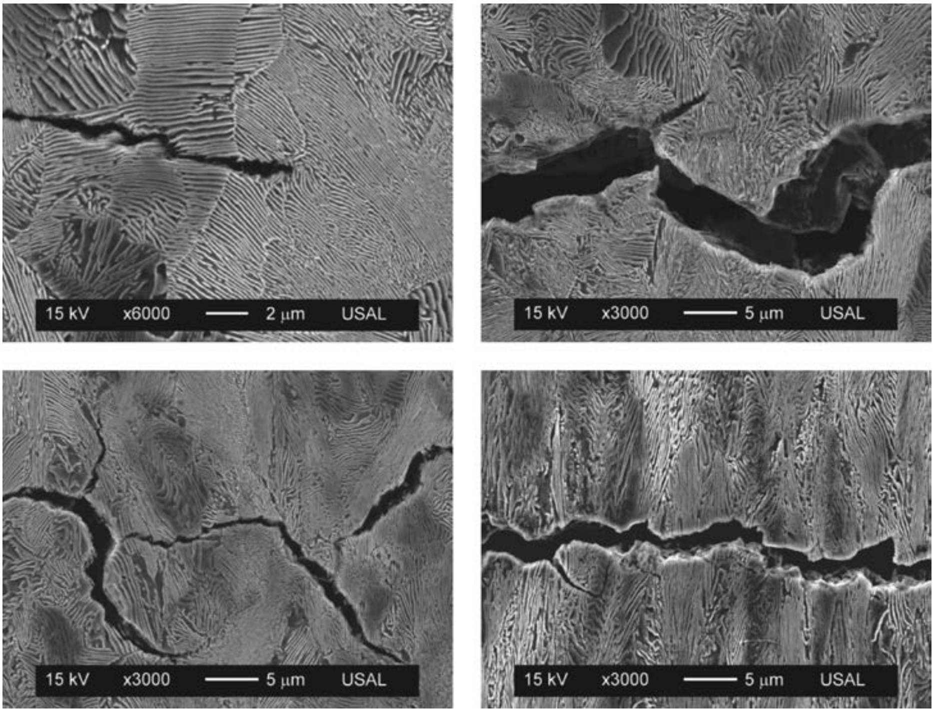

FIG. 16—*Fatigue crack path in pearlitic steel (from left to right and top to bottom, steels E0, E1, E2, and E6).*

fatigue crack growth often exhibits some microcrack branches with a deflection angle of about 45° in relation to the main crack growth direction (transverse to the wire axis). Such deflected branches could appear because fatigue cracking could follow a mechanism similar to that proposed by Miller and Smith [22] for static fracture in pearlitic microstructures. According to this mechanism of

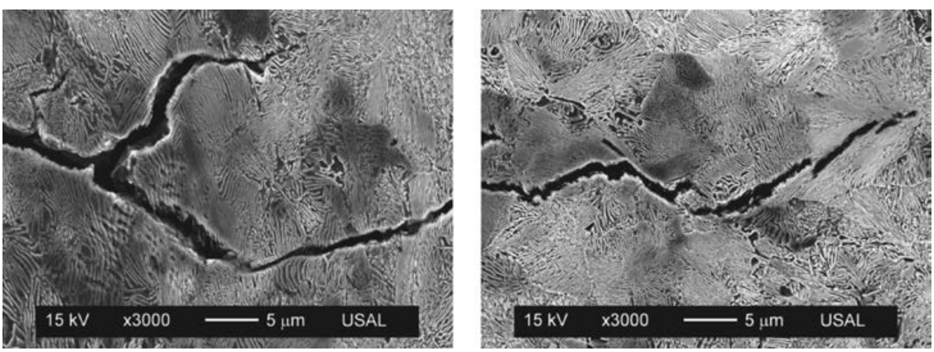

FIG. 17—*Fatigue crack path (hot rolled bar, E0).*

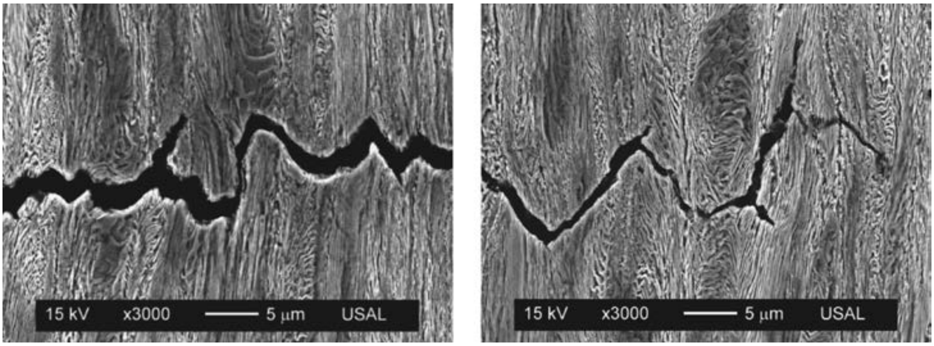

FIG. 18—*Fatigue crack path (prestressing steel wire, E7).*

shear cracking in pearlite, brittle cementite lamellae fail when they are unable to undergo the big shear deformation of the more ductile ferrite.

This subsection tries to analyze the key experimental result: the fact that the crack progresses in Mode I by fatigue even in the cold drawn steel, in spite of its markedly oriented pearlitic microstructure and the presence of pearlitic pseudocolonies acting as local fracture precursors. The reasons for this behavior are threefold:

(i) Crack tip blunting and large geometry changes produced by plasticity. As demonstrated in previous high-resolution numerical analyses by the finite element method [23], large strains and large geometry changes in the vicinity of the crack tip produce big rotations of axes (Fig. 20) and a clear crack tip blunting. Such a blunting is able to counterbalance the effect of the pearlitic pseudocolonies, so that posterior crack growth by fatigue in Mode I after the crack has reached a pearlitic pseudocolony may be possible, as sketched in Fig. 21.

(ii) Geometrical constraint produced by the rest of the points of the crack front that therefore tends to propagate in the original direction, as depicted in Fig. 22. This fact makes the crack deflection by fatigue more difficult.

(iii) The orientation of the pearlitic lamellae. As a mater of fact, although in the cold drawn wire the plates are mainly oriented in the cold drawing direction and thus they are perpendicular to the crack faces, only some of them contain the crack front and tend to produce deflection, while many of them form an angle (or even are perpendicular) to the crack front, in the latter case tending to produce the more

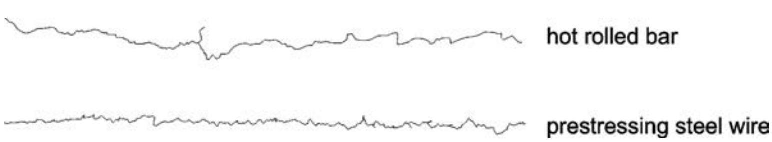

FIG. 19—*Cracking profiles.*

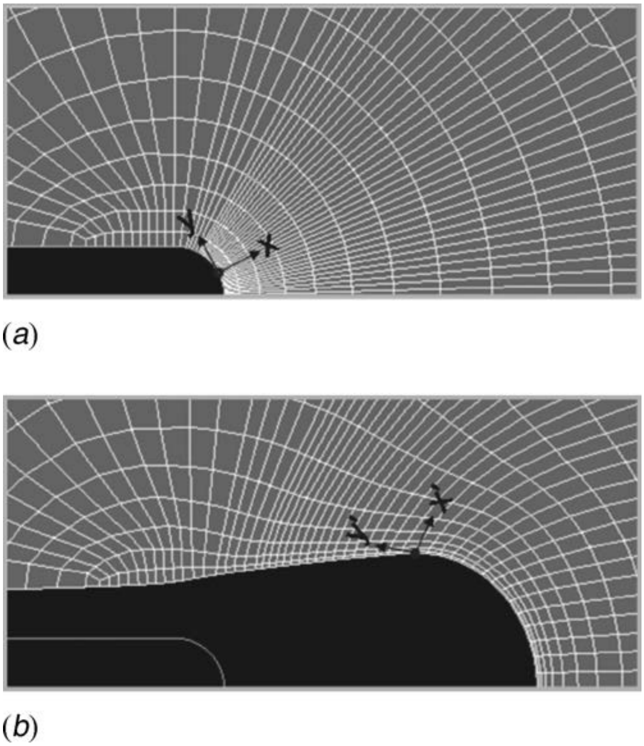

FIG. 20—*Initial undeformed mesh at the crack tip* (a) *and deformed mesh* (b) *at the unloading phase after fatigue cycles, showing large deformations and rotation of axes from x-y to x′-y′.*

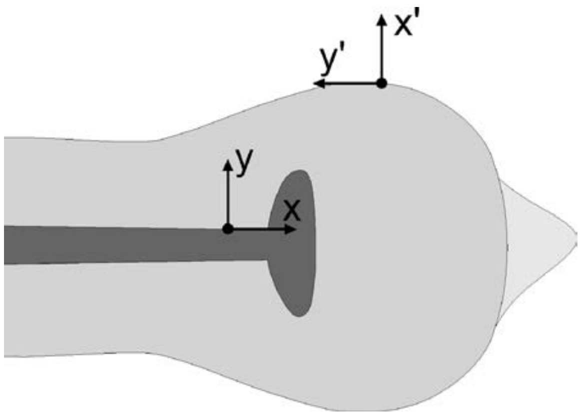

FIG. 21—*Scheme showing crack tip blunting and posterior crack growth by fatigue in Mode I after the crack has reached a pearlitic pseudocolony.*

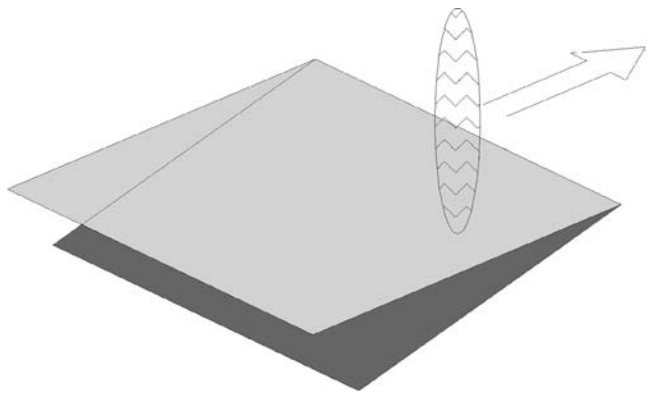

FIG. 22—*Scheme showing crack growth by fatigue in Mode I after the crack has reached a pearlitic pseudocolony, due to the geometrical constraint produced by the rest of the points of the crack front which therefore tends to propagate in the original direction.*

difficult phenomenon of crack bifurcations (two symmetrical branches).

Local Crack Advance

As commented above fatigue cracks are transcolonial and translamellar, tending to fracture the pearlitic lamellae. This is consistent with previous research on two-layer materials [24] in which an initial crack at the interface deviates to advance in one of the two constituents of the composite material, thus fracturing one of the layers. As a consequence of this phenomenon, fatigue crack paths are tortuous, with frequent *local* crack deflections and branches (Figs. 23 and 24), which confirms that a *local* mixed mode propagation takes place in the close vicinity of the crack tip under cyclic loading.

The decrease of pearlite interlamellar spacing with cold drawing [12] provokes a higher number of crack deflections in the fatigue crack path, while the drawing-induced microstructural orientation increases the angle of crack deflection. Therefore, the prestressing steel wire exhibits a fatigue crack path

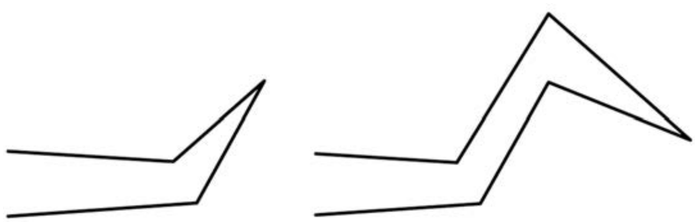

FIG. 23—*Crack deflection.*

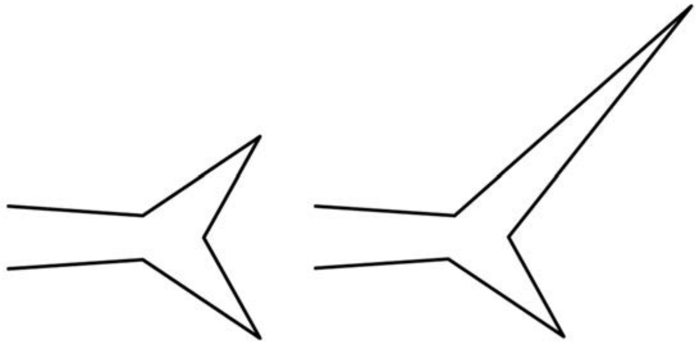

FIG. 24—*Crack branching.*

containing more deflections than the hot rolled bar (Fig. 25), the deflection path being shorter and the deflection angle being higher than in the former than in the latter, i.e.,

$$\theta^{(0)} < \theta^{(7)} \tag{4}$$

$$d^{(0)} > d^{(7)} \tag{5}$$

Thus the fatigue crack propagation rate strongly depends on the orientation of the crack relative to the microstructure (either aligned or not). For cracks parallel to the aligned pearlitic lamellae the resistance of the microstructure against crack propagation is decreased while it is increased for cracks perpendicular to the alignment direction [25].

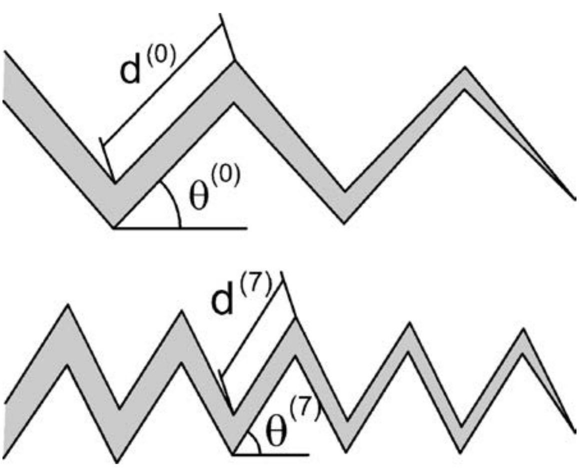

FIG. 25—*Fatigue crack path scheme in steels E0 and E7.*

Conclusions

The cold drawing manufacturing process improves the fatigue performance of eutectoid steel by retarding the fatigue crack growth rate in the Paris regime, thus resulting that the manufacturing process is beneficial from the points of view of damage tolerance and structural integrity of the prestressing steel wires.

Fatigue crack propagation in eutectoid steel wires under tensile loading in the Paris regime develops in Mode I with an elliptical crack front. The crack is able to propagate by fatigue in Mode I (with no crack deflection) even in the cold drawn steel, in spite of the markedly oriented pearlitic microstructure of the material in this case and the presence of pearlitic pseudocolonies (weakest regions). The reasons for this fact are the crack tip blunting and the large geometry changes produced by plasticity in the vicinity of the crack tip, the constraint produced by the rest of the points of the crack front and the different orientations of the pearlitic plates (in relation to the crack line) which would tend to produce crack branching instead of crack deflection.

The steel wires with an intermediate cold drawing degree exhibit a retardation at the crack front center due to the presence of compressive residual stresses in the central area of the crack front (*gull* effect).

The fractographic appearance of the fatigue cracks resembles microplastic tearing, which is consistent with fatigue damage and crack advance by accumulation of plastic strain in the vicinity of the crack tip. From the microscopical point of view, the fatigue cracks are transcolonial and translamellar (i.e., the fatigue crack path crosses the colonies and breaks the lamellae). The crack opening displacement is not uniform along the crack, and many micro-discontinuities, branchings, bifurcations, and local deflections appear, the latter especially in heavily drawn steels.

Thus the cold drawing process produces a tortuous crack path, so that the higher the cold drawing degree, the more tortuous the crack propagation path.

The key microstructural unit governing the fatigue crack growth is the pearlite arrangement (the key parameters being both the interlamellar spacing and the pearlitic plates orientation), since the ferrite-cementite interfaces block the dislocational movement, thereby producing a local retardation of the crack propagation and the aforesaid tortuous crack path.

Acknowledgments

The authors wish to thank the financial support of their research at the University of Salamanca provided by the following institutions: Spanish Ministry for Education and Science (MEC; Grant BIA2005-08965), Regional Government *Junta de Castilla y León* (JCYL; Grants SA067A05 and SA111A07), Spanish Foundation "Memoria de D. Samuel Solórzano Barruso" (Grants for Scientific and Technological Research), and University of Salamanca (Grant USAL 2005-09). In addition, the authors wish to express their gratitude to Mr. Juan Monar (Trefilerías Quijano, Cantabria, Spain) for providing the steel used in the experimental program.

References

[1] Gray, III, G. T., Thompson, A. W., and Williams, J. C., "Influence of Microstructure on Fatigue Crack Initiation in Fully Pearlitic Steels," *Metall. Trans.*, Vol. 16A, 1985, pp. 753–760.

[2] Sankaran, S., Subramanya Sarma, V., Padmanabhan, K. A., Jaeger, G., and Koethe, A., "High Cycle Fatigue Behavior of a Multiphase Microalloyed Medium Carbon Steel: A Comparison Between Ferrite-Pearlite and Tempered Martensite Microstructures," *Mater. Sci. Eng., A*, Vol. 362, 2003, pp. 249–256.

[3] Ravichandran, K. S., "A Rationalization of Fatigue Thresholds in Pearlitic Steels Using a Theoretical Model," *Acta Metall. Mater.*, Vol. 39, 1991, pp. 1331–1341.

[4] El-Shabasy, A. B. and Lewandowski, J. J., "Effects of Load Ratio, *R*, and Test Temperature on Fatigue Crack Growth of Fully Pearlitic Eutectoid Steel (Fatigue Crack Growth of Pearlitic Steel)," *Int. J. Fatigue*, Vol. 26, 2004, pp. 305–309.

[5] Llorca, J. and Sánchez-Gálvez, V., "Fatigue Threshold Determination in High Strength Cold Drawn Eutectoid Steel Wires," *Eng. Fract. Mech.*, Vol. 26, 1987, pp. 869–882.

[6] Subramanya Sarma, V., Padmanabhan, K. A., Jaeger, G., Koethe, A., and Schaper, M., "On the Fatigue Crack Growth Behavior of Two Ferrite-Pearlite Microalloyed Steels," *Mater. Lett.*, Vol. 46, 2000, pp. 185–188.

[7] Toribio, J. and Toledano, M., "Fatigue Behavior of Progressively Drawn Steels," *Proceedings of the 7th International Fatigue Congress*, X. R. Wu and Z. G. Wang, Eds., Beijing, June, 1999, EMAS, West Midlands.

[8] Korda, A. A., Mutoh, Y., Miyashita, Y., and Sadasue, T., "Effects of Pearlite Morphology and Specimen Thickness on Fatigue Crack Growth Resistance in Ferritic-Pearlitic Steels," *Mater. Sci. Eng., A*, Vol. 428, 2006, pp. 262–269.

[9] Korda, A. A., Mutoh, Y., Miyashita, Y., Sadasue, T., and Mannan, S. L., "In Situ Observation of Fatigue Crack Retardation in Banded Ferrite-Pearlite Microstructure Due to Crack Branching," *Scr. Mater.*, Vol. 54, 2006, pp. 1835–1840.

[10] Toribio, J. and Ovejero, E., "Microstructure Evolution in a Pearlitic Steel Subjected to Progressive Plastic Deformation," *Mater. Sci. Eng., A*, Vol. A234-236, 1997, pp. 579–582.

[11] Toribio, J. and Ovejero, E., "Microstructure Orientation in a Pearlitic Steel Subjected to Progressive Plastic Deformation," *J. Mater. Sci. Lett.*, Vol. 17, 1998, pp. 1037–1040.

[12] Toribio, J. and Ovejero, E., "Effect of Cumulative Cold Drawing on the Pearlite Interlamellar Spacing in Eutectoid Steel," *Scr. Mater.*, Vol. 39, 1998, pp. 323–328.

[13] Toribio, J. and Ovejero, E., "Effect of Cold Drawing on Microstructure and Corrosion Performance of High-Strength Steel," *Mech. Time-Depend. Mater.*, Vol. 1, 1998, pp. 307–319.

[14] Toribio, J., Ovejero, E., and Toledano, M., "Microstructural Bases of Anisotropic Fracture Behaviour of Heavily Drawn Steel," *Int. J. Fracture*, Vol. 87, 1997, pp. L83–L88.

[15] Toribio, J., González, B., Matos, J. C., and Ayaso, F. J., "Micro- and Macro-Approach to the Fatigue Crack Propagation in High-Strength Pearlitic Steel Wires," *Key Eng. Mater.*, Vol. 348-349, 2007, pp. 681–684.

[16] Paris, P. C. and Erdogan, F., "A Critical Analysis of Crack Propagation Laws," *J. Basic Eng.*, Vol. 85D, 1963, pp. 528–534.

[17] Astiz, M. A., "An Incompatible Singular Elastic Element for Two- and Three-Dimensional Crack Problems," *Int. J. Fatigue*, Vol. 31, 1986, pp. 105–124.

[18] Toribio, J., González, B., and Matos, J. C., "Fatigue Crack Propagation in Cold Drawn Steel," *Mater. Sci. Eng., A*, Vol. 468-470, 2007, pp. 267–272.

[19] Vasudevan, A. K., Sadananda, K., and Glinka, G., "Critical Parameters for Fatigue Damage," *Int. J. Fatigue*, Vol. 23, 2001, pp. S39–S53.

[20] Toyosada, M., Niwa, T., and Sakai, J., "Physical Meaning of ΔK_{RP} and Fatigue Crack Propagation in the Residual Stress Distribution Field," *Int. J. Fatigue*, Vol. 19, 1997, pp. S161–S166.

[21] Cai, C. Q. and Shin, C. S., "A Normalized Area-Compliance Method for Monitoring Surface Crack Development in a Cylindrical Rod," *Int. J. Fatigue*, Vol. 27, 2005, pp. 801–809.

[22] Miller, L. E. and Smith, G. C., "Tensile Fractures in Carbon Steels," *J. Iron Steel Inst., London*, Vol. 208, 1970, pp. 998–1005.

[23] Toribio, J. and Kharin, V., "Role of Fatigue Crack Closure Stresses in Hydrogen Assisted Cracking," *Advances in Fatigue Crack Closure Measurement and Analysis*, ASTM STP 1343, ASTM International, West Conshohocken, PA, 1999.

[24] Sugimura, Y., Grondin, L., and Suresh, S., "Fatigue Crack Growth at Arbitrary Angles to Bimaterial Interfaces," *Scr. Mater.*, Vol. 33, 1995, pp. 2007–2012.

[25] Wetscher, F., Stock, R., and Pippan, R., "Changes in the Mechanical Properties of a Pearlitic Steel Due to Large Shear Deformation," *Mater. Sci. Eng., A*, Vol. 445-446, 2007, pp. 237–243.

ASTM Special Technical Publication, Vol. 6, No. 1
Paper ID JAI101539
Available online at www.astm.org

Masato Yamamoto,[1] *Takayuki Kitamura,*[2] *and Takashi Ogata*[3]

Effect of Inhomogeneity in Aligned Grains on Creep-Fatigue Crack Opening and Propagation Behavior of Directionally Solidified Superalloy

ABSTRACT: Directionally solidified superalloy, which has elongated large grains, is used for gas-turbine blade application because of its high creep strength. Since the grain size is not small enough in comparison with the component size or the crack size, the inhomogeneous microstructure strongly affects the crack propagation behavior in such a structure. The authors investigate the effect of microstructural inhomogeneity on crack propagation morphology and crack propagation rate (*da*/*dN*) under a creep-fatigue condition. The macroscopic direction of the main crack is perpendicular to the loading axis, though the path is microscopically bumpy due to the effect of inhomogeneous multi-grains. Several subcracks are found around the main crack, and they occasionally coalesce with each other. In order to understand the local fluctuation of (*da*/*dN*) due to the inhomogeneous multigrains, the grain shape and its crystallographic orientation are identified by means of a scanning electron microscope (SEM) and an electron back scattering diffraction (EBSD). The subcracks tend to initiate at the high angle grain boundaries oriented nearly perpendicular to the loading axis. The local

Manuscript received November 8, 2007; accepted for publication September 19, 2008; published online January 2009.
[1] Central Research Institute of Electric Power Industry, Materials Science Research Laboratory, 2-11-1, Iwado-kita, Komae, Tokyo, 201-8511, Japan, e-mail: masatoy@criepi.denken.or.jp
[2] Kyoto University, Department of Mechanical Engineering and Science, Yoshida-honmachi, Sakyo-ku, Kyoto, Kyoto, 606-8501, Japan.
[3] Central Research Institute of Electric Power Industry, Materials Science Research Laboratory, 2-11-1, Iwado-kita, Komae, Tokyo, 201-8511, Japan.

Citation: Yamamoto, M., Kitamura, T., and Ogata, T., "Effect of Inhomogeneity in Aligned Grains on Creep-Fatigue Crack Opening and Propagation Behavior of Directionally Solidified Superalloy," *J. ASTM Intl.*, Vol. 6, No. 1. DOI10.1520/JAI101539. Available online at www.astm.org. Also included in JAI Special Issue STP 1508, *Fatigue and Fracture Mechanics: 36th Volume,* R. W. Neu, K. R. W. Wallin, and S. R. Thompson, guest editors, ASTM International, West Conshohocken, PA 2009, pp. 459-473.

fluctuation of da/dN is influenced by two factors. One is the cracking path; the intergranular crack shows higher da/dN. The other factor is the magnitude of Young's modulus of the grain (in loading direction) at the crack tip. The higher Young's modulus leads to a lower da/dN in transgranular cracking. The detailed observation of local displacement near the crack tip clarified that the magnitude of cyclic displacement inversely related to the Young's modulus of the grain in the loading axis, and results in the high strain concentration at the crack tip in the grain with low Young's modulus. The experiment result suggests that the strain around the crack tip governs the crack propagation rate though it is affected by the inhomogeneous microstructure.

KEYWORDS: creep-fatigue, crack propagation, microstructure, nickel-based directionally solidified superalloy

Introduction

A nickel (Ni)-based directionally solidified (DS) superalloy, which is used for gas-turbine blade application, consists of elongated large grains. Thermal fatigue cracking due to the steep thermal gradient between the outside and inside surfaces of the hollow blade often dominates the blade life [1]. Once the crack propagates through the thickness, the damaged air-cooling system may result in the heavy burnout or the loss of the blade. Therefore, to prevent the through-thickness (around 4 mm) crack propagation, the development of the crack propagation evaluation method up to the crack length of 4 mm is essential. While many researchers [2–8] pointed out that the macroscopic fatigue crack propagation rate of conventional casting superalloys can be characterized by the effective stress intensity factor range, ΔK_{eff}, it is also pointed out that the microscopic crack paths are affected by the inhomogeneously aligned grains or anisotropic slip systems and tend to meander [9–21]. Since the crack size allowed in the component is rather small in comparison with the grain size of DS superalloy, the effect of inhomogeneity due to the aligned crystallographic orientation [22–27] may not be ignorable in component assessment. Therefore, it is essential to take account for the effect of inhomogeneity in identifying parameters that govern the crack propagation. The authors carried out a series of fatigue crack propagation experiments in the DS superalloy [28], and pointed out that (1) fatigue invokes a combination of intergranular and transgranular cracking, and (2) intergranular crack propagates faster than transgranular crack. Recently, Dunne et al. [29] indicated that for DS superalloy the fatigue crack at room temperature tends to initiate at the strain concentration points due to the relative constraint of grains. This suggests that the crack propagation behavior may be governed by the local stress/strain state, which is affected by the inhomogeneities among the grains.

At high temperatures, where the gas turbine blade is used, the time dependency in deformation and damage evolution affects the crack propagation behavior. Because of the complexity, the governing parameters of crack propagation under such a condition are still unclear and awaiting to be investigated. In this study, crack propagation behavior under creep-fatigue condition is continuously observed by means of a charge-coupled device (CCD) with a video

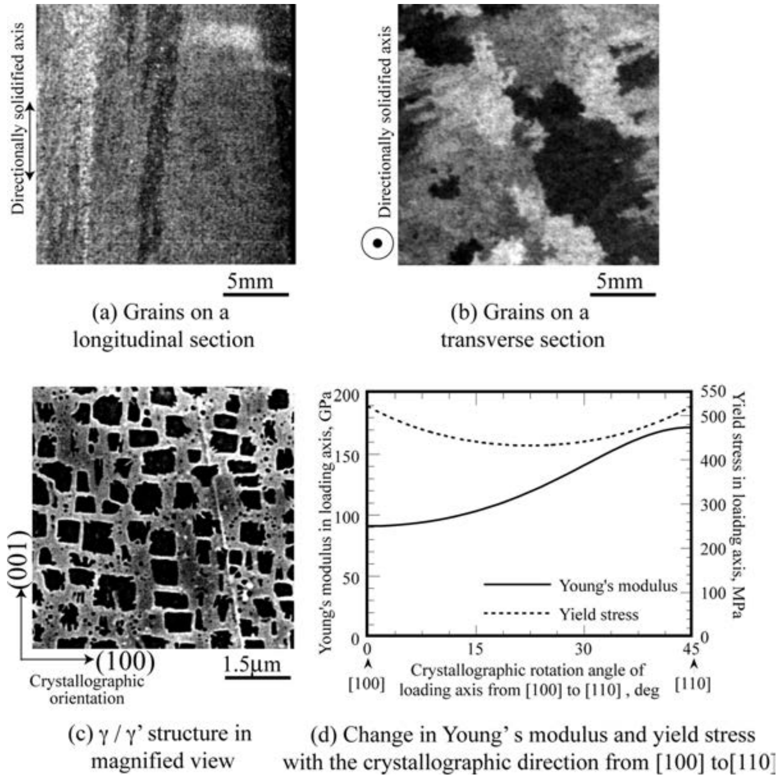

FIG. 1—*Microstructure of directionally solidified superalloy.*

recorder in order to investigate the microstructural effect under the combination of cyclic and time dependent loading.

Experimental Procedure

Figure 1 shows the microstructure of examined Ni-based directionally solidified (DS) superalloy with the chemical composition of C-0.10, Al-3.03, B-0.02, Co-9.56, Cr-13.93, Mo-1.56, Ta-2.77, Ti-4.90, W-3.86, Zr-0.01, Ni-Bal., (unit in Wt %). It consists of elongated large grains, whose average diameter is over 100 mm along the solidification axis (Fig. 1(*a*)) and 0.2–2.0 mm in the transverse direction (Fig. 1(*b*)). All the grains are strengthened by the high volume fraction of γ'-precipitates (Fig. 1(*c*)). The elastic stiffness values of each grains are C_{11}=201.5 GPa, C_{12}=137.1 GPa, C_{44}=98.5 GPa, which are obtained [26] by interpolating the corresponding values of pure γ and γ' [30] according to their volume fractions. The crystallographic direction of solidification axis is [001] while the transverse direction is randomly oriented in the range from [100] to [110]. Figure 1(*d*) shows the change in Young's modulus and yield stress with the change in crystallographic direction from [100] to [110]. The Young's

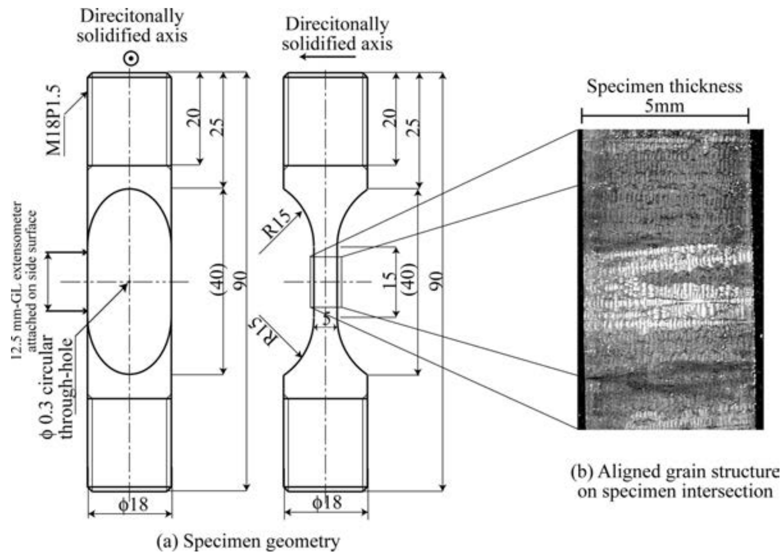

FIG. 2—*Geometry of center cracked plate specimen.*

modulus has the smallest value in [100] and it increases with increasing rotation angle from [100] to [110]. The anisotropy in yield stress is not significant as compared with the anisotropy of Young's modulus.

Figure 2 shows the geometry of a center-cracked plate specimen where the solidification axis is set to be perpendicular to the plate surface. Most of grains pass through the 5 mm thick plate (Fig. 2(*b*)). After the wire-cut machining, the plate surface is polished by #80–#1000 grinding papers and is buffed by diamond paste. A 0.3-mm diameter through hole is introduced as a crack starter at the center of the specimen. Then, the specimen is subjected to cyclic stress of small amplitude (±150 MPa) at 1143 K (the same temperature as in the creep-fatigue experiment) in order to introduce a precrack from the notch root until the crack length reaches 0.1 mm. The precracking and the creep-fatigue examination are conducted by a fatigue testing machine with a closed-loop electric-mechanical system with an induction heating device. The temperature is kept at 1143 K with fluctuation of less than 5 K in the gage section during the experiment. The axial displacement, which means the macroscopic and averaged strain within the gage length, of the specimen is measured and controlled by an extensometer with a gage length of 12.5 mm, which is attached to the side edge of the plate section (Fig. 2). The experiment is conducted under a fully reversed (macroscopic) strain controlled creep-fatigue condition with 6 min strain-hold at the maximum strain of which detail is listed in Table 1.

The specimen surface with an area of 0.8 mm by 0.6 mm is observed by means of a CCD microscope with 1280 by 960 pixels, which is mounted on an electro-servo stage with a micrometre so as to move the observation area with high precision microscope location control. The crack opening behavior is recorded as sequential micrographs every 0.25 seconds.

TABLE 1—*Test condition.*

Environment	Air, Room temperature
Control mode	Total strain control
Gauge length	12.5 mm
Temperature	1143 K
Strain waveform	Fully reversed, Trapezoidal
Total strain range	0.7 %
Strain rate	10^{-3} 1/s
Strain hold	6 min at maximum strain

Figures 3(*a*) and 3(*b*) show the examples of micrographs at the minimum and maximum strain in a cycle, respectively, where the crack tip location can be determined by the latter. The vector in Fig. 3(*c*) shows the local displacement between them, which is evaluated by the pattern-matching method [31,32]. Figure 4 shows the procedure of speckle pattern matching. First, we extract areas (i) and (ii), 256 by 256 pixels, from the same coordinate points of micrographs at the minimum and maximum strain, respectively (Fig. 4(*a*)). The global displacement between these areas is determined by means of correlation function (Fig. 4(*b*)). Second, we extract small areas (iii) and (iv), 16 by 16 pixels, from the areas (i) and (ii), respectively. Here, area (iii) is taken by the center of area (i), and the area (iv) is shifted by the global displacement from the center of area (ii). By the comparison of areas (iii) and (iv), the local displacement of this small area (10 by 10 μm) is obtained with the resolution of 0.1 μm. The plate surface is slightly polished after the experiment to remove the surface oxide and is subjected to the scanning electron microscope (SEM) observation and the electron back scattering diffraction (EBSD) pattern observation.

Results and Discussion

Figure 5 shows the crack propagation process on the specimen surface. The main crack (i) initiates from the edge of the center-through-hole and some subcracks initiate and propagate around it. Although the crack direction is macroscopically perpendicular to the loading axis, several microscopic bumps are observed on the path. Up to the number of cycles $N=799$, four subcracks (cracks (ii) to (v)) are found near the main crack (i). The subcrack (iii), which is parallel to the main crack, coalesces with main crack (i). Subcracks (iv) and (v) ahead of the main crack serially coalesce with the main crack (i) and form a network of crack paths.

Figure 6(*a*) shows the EBSD pattern of the specimen surface after the experiment. The color shows the crystallographic orientation parallel to the loading axis. Since the crystallographic orientation of DS direction (perpendicular to the observed surface) is nearly [001], that of the loading axis is distributed from [100] to [110] as indicated in Fig. 6(*b*). Due to the anisotropic Young's modulus in the loading axis (Fig. 1(*c*)) and the relative constraint among the

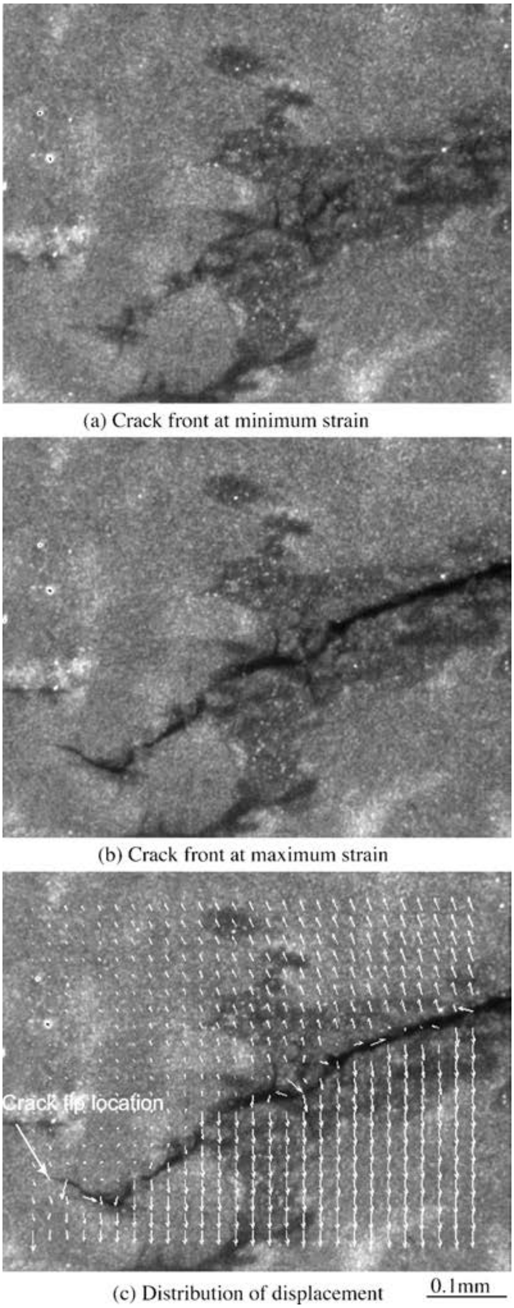

FIG. 3—*Local deformation observed by CCD micrograph.*

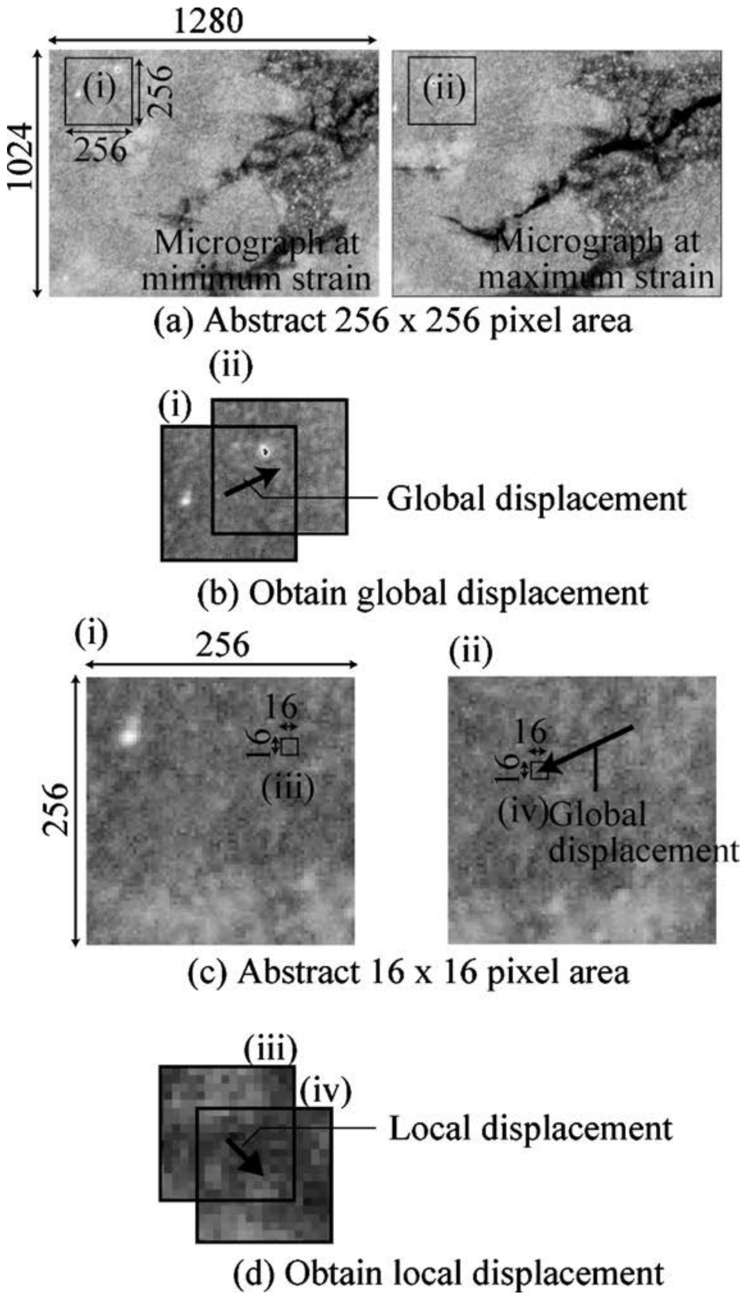

FIG. 4—*Local strain analysis procedure by means of speckle pattern matching.*

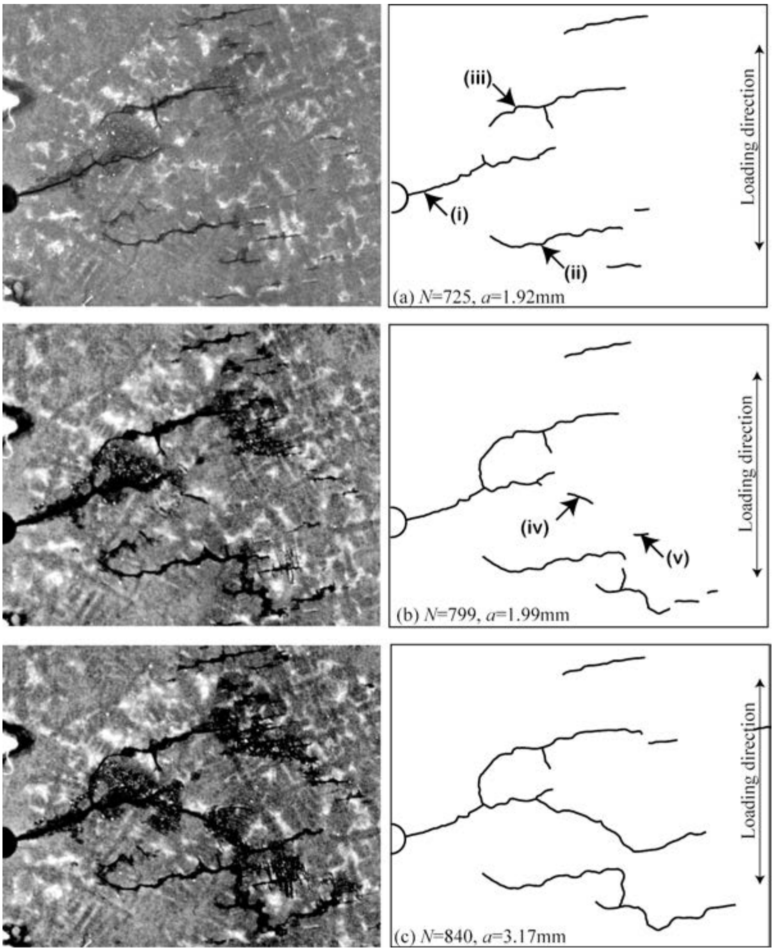

FIG. 5—*Crack propagation process on the specimen surface.*

grains, the grains near [100] will have higher strain and lower stress, while those near [110] will have lower strain and higher stress, than the average. The area nearby the main crack (Fig. 6(*c*)) is observed by SEM with enough high magnification (Fig. 6(*d*)) to observe the cuboidal γ' and grain boundary. Figure 7 shows the sketch of grain boundary network traced out from the EBSD and SEM observations. The brighter color represents the higher angle grain boundaries. The gray bold lines show the crack profile and the dotted ellipsoids show the initiation sites of subcracks (ii) to (v). All the subcracks initiate on high angle (more than 15 degrees) grain boundaries. Furthermore, they are mostly perpendicular to the loading axis. This indicates that (1) the normal stress and strain on the grain boundary governs the crack initiation, and (2) the grain boundary is weaker than the interior of the grain against creep-fatigue cracking.

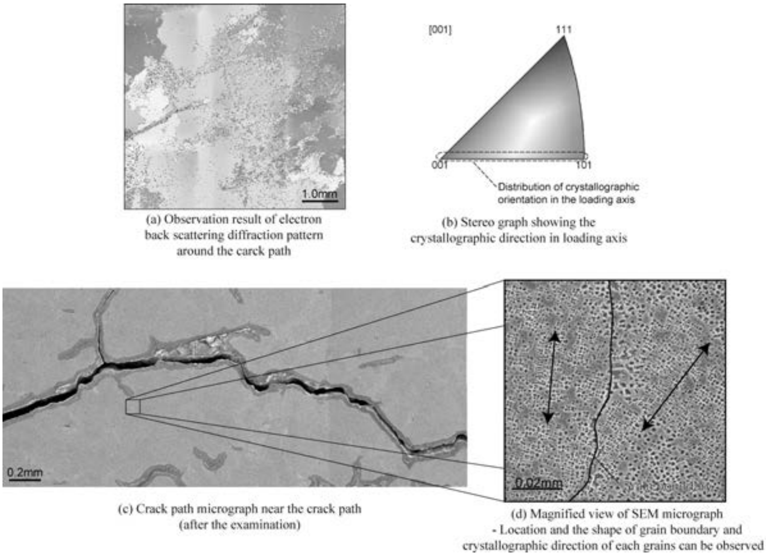

FIG. 6—*EBSD and SEM observation after the crack propagation experiment.*

Figure 8 shows the crack propagation curve. Here, a is the projected length of the main crack (i) on the plane perpendicular to the loading axis. The crack propagation rate, da/dN, shows remarkable fluctuations; high rate at F1 and F2, and low rate at S. Figure 9 shows the main crack path and the aligned grains where the color shows the magnitude of Young's modulus in the loading direction. Reviewing Figs. 5, 8, and 9, the following process can be identified for the main crack.

(1) The crack direction when initiated from the edge of the center-through-hole is perpendicular to the macroscopic loading axis. This means that there is no significant effect of crystallographic anisotropy.
(2) Crack propagates inside the grain (A), which has low Young's modulus value in the loading direction.
(3) Crack propagates along the grain boundary between the grains (A) and (B). As the grain boundary is almost perpendicular to the loading axis, da/dN locally increases here (F1 in Fig. 8).
(4) Crack propagates inside the grain (B). Since this grain has higher Young's modulus in the loading direction than the neighboring two grains in row (grains (A) and (C)), the strain level is kept low and results in the low da/dN (part S in Fig. 8).
(5) While the main crack shows low da/dN at part S, the subcracks (iv) and (v) initiate (Fig. 5(*b*)) at the grain boundaries between grains (B) and (C), and (C) and (D), respectively. Subsequently, cracks (i), (iv), and (v) serially coalesce and propagate rapidly (Fig. 5(*c*), F2 in Fig. 8).

The crack propagation processes consistently suggest that the inhomogeneous microstructures (difference in Young's moduls of each grain, difference

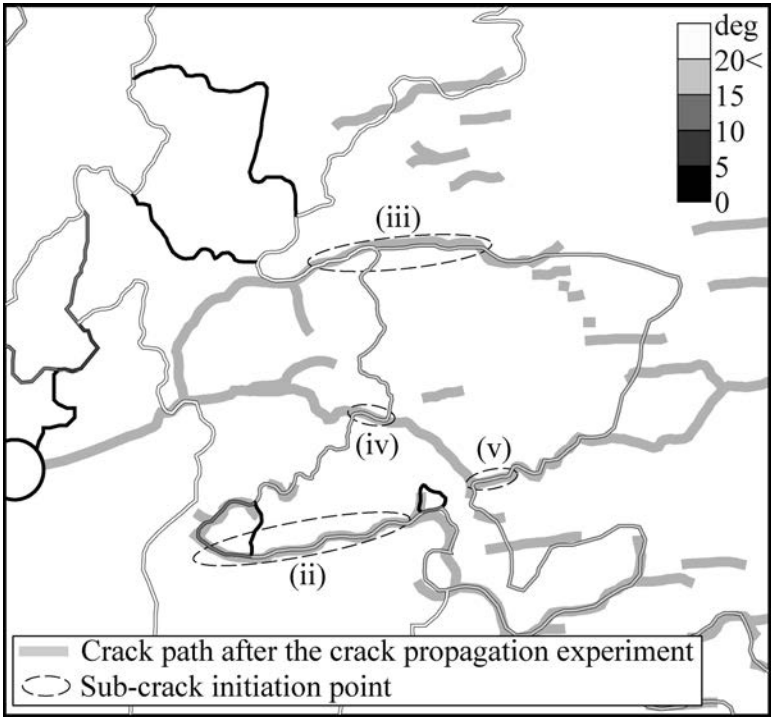

FIG. 7—*Configuration of grain boundary network and the subcrack initiation site.*

in intergranular and transgranular cracking) strongly affect the crack propagation behavior.

Figure 10 shows the magnified CCD micrographs obtained from parts F1 and S. The white vectors show the local displacements between the minimum and maximum strain within a single cycle. At the part F1, (Fig. 10(*a*)), the directions of the white vectors are very different in the neighboring grains, while the ones inside the each grain point out similar directions. Such steep change in the displacement causes the strain concentration at the grain boundary.

In part S (Fig. 10(*b*)), low displacement area can be found ahead of the crack tip in grain (B), which has high Young's modulus in the loading axis direction. On the other hand, grain (C) in the right end has larger vectors. This suggests the correlation between da/dN and the magnitude of strain, which varies by the microstructural effect.

Figure 11 shows the detailed observation results of local displacement in loading axis during the transition from parts S to F2. The micrographs in Figs. 11(*a*) and 11(*b*) are taken at part S ($N=685$) and before the coalescence of cracks (i) and (iv) ($N=799$), respectively. The line segments with circular (●) or triangular (▲) symbols in Figs. 11(*c*) and 11(*d*) show the gages to measure the local displacement in a loading cycle. By the continuous observation of these displacements, the relationship between the locally distributed strain near the

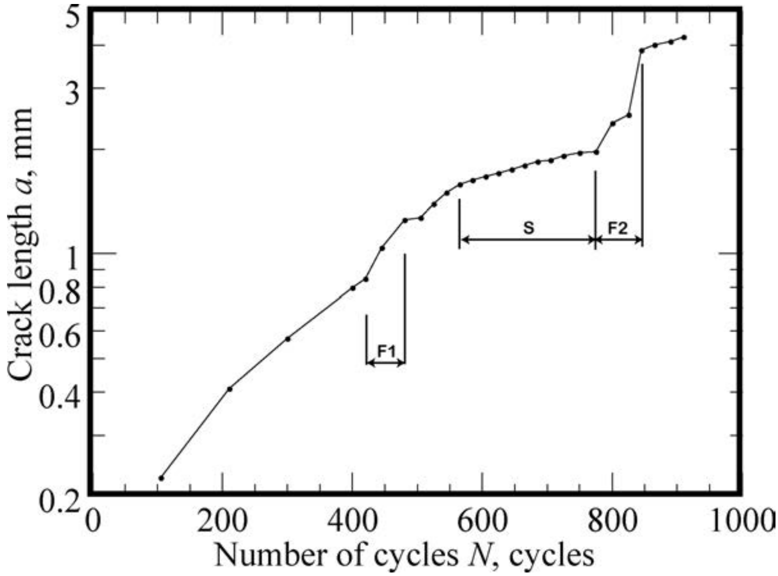

FIG. 8—*Crack propagation curve.*

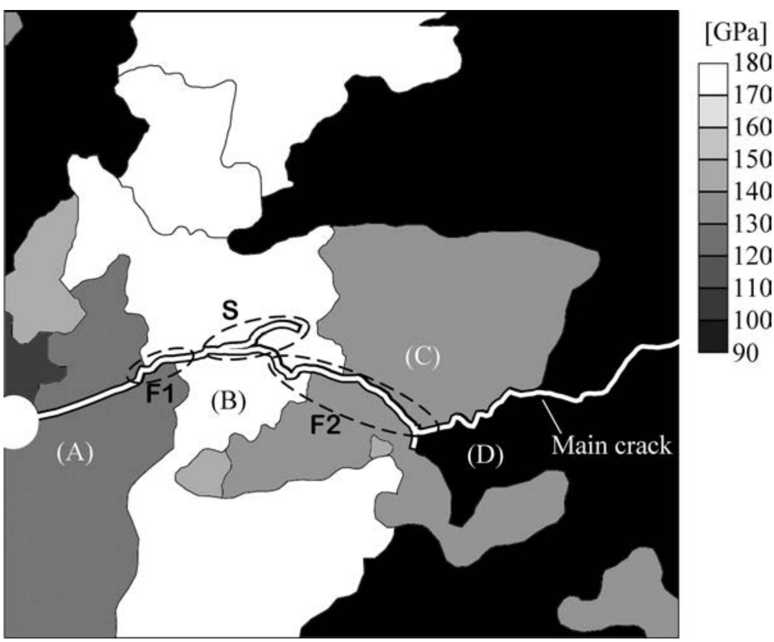

FIG. 9—*Main crack path and local Young's modulus.*

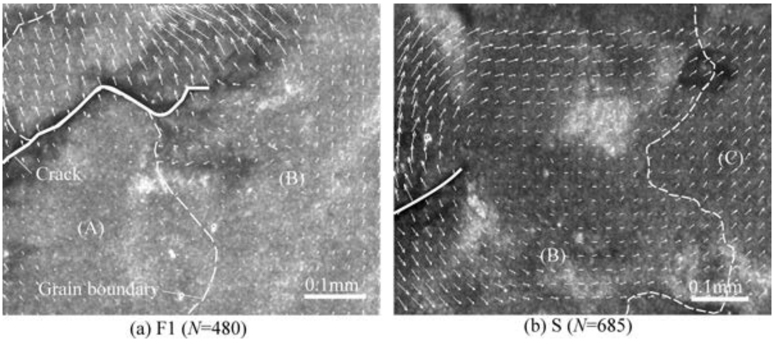

FIG. 10—*Microscopic change in local displacement.*

crack tip and the crack propagation rate can be clarified. Figures 11(*e*) and 11(*f*) show the local displacements along the paths where the open and solid symbols indicate the cracked and uncracked parts, respectively. The displacement of the uncracked part is the largest at the crack tip (large open symbol) and decreases with increasing distance. The overall profile along the path is smooth near the crack tip. These trends in the magnitude of crack opening displacement are representative of the magnitude of evolved strain at the crack tip, which may govern the crack propagation. The change in the displacement level from parts S to F2 is remarkably different between the upper and lower paths. While the displacement near the crack tip of upper path keeps low magnitude in both of Figs. 11(*e*) and 11(*f*), the one of lower path (triangular symbols) at $N=799$ show high magnitudes. This significant difference in local displacement correlates with the change in the main crack path from upper one to lower one, and also correlates to the remarkable change in da/dN from parts S to F2. The above results suggest that (1) there is a close relationship between the strain distribution around the crack tip and da/dN, and (2) the strain level at the crack tip is significantly affected by the microscopic inhomogeneity. In other words, it can be suggested as to the possibility of adopting the traditional fracture mechanics concept to describe the crack propagation by taking into account the effect of the inhomogeneous microstructure.

Conclusion

In order to clarify the microstructural effect on the creep-fatigue crack propagation of the directionally solidified superalloy, the authors carried out a detailed observation of creep-fatigue crack propagation behavior. The results are as follows:

1. The main crack initiates from the edge of the center-through-hole and propagates with the intergranular/transgranular combined manner on the path macroscopically perpendicular to the load axis. Several subcracks are induced at high angle grain boundaries, which is almost perpendicular to the loading axis. The main crack and the subcracks coalesce with each other and form a network of crack paths.

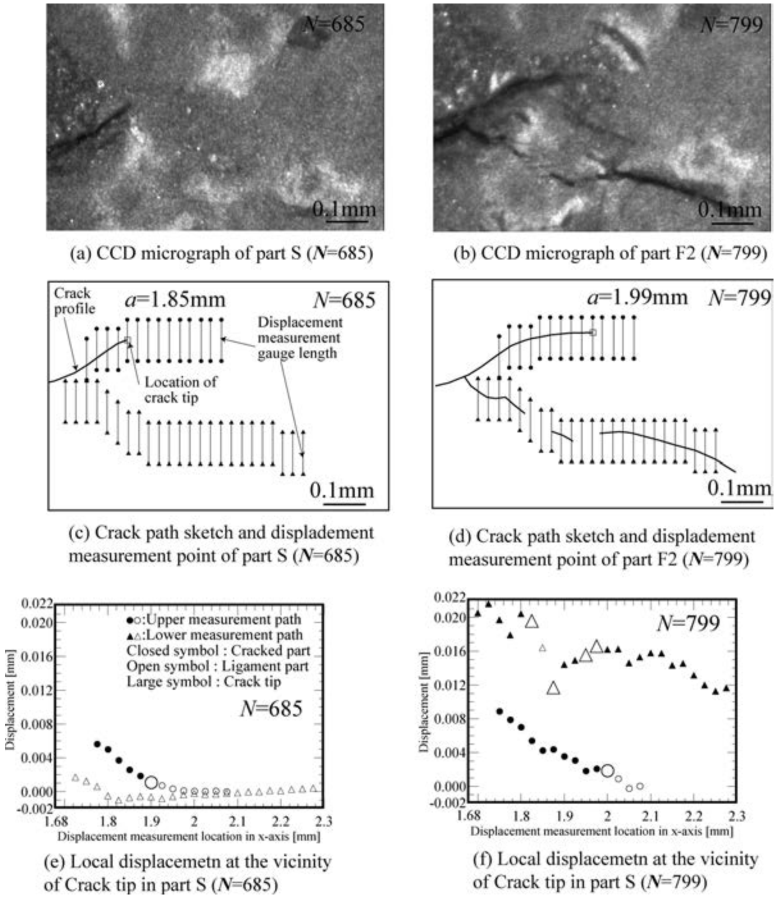

FIG. 11—*Microstructural effect on local displacement near the crack tip.*

2. The propagation rate da/dN of the main crack locally varies due to the effect of the inhomogeneous microstructure. The intergranular crack shows higher da/dN than the transgranular crack. da/dN in the transgranular cracking varies inversely with the magnitude of the Young's modulus of the grain.
3. The cyclic displacement changes locally near the grain boundary. It becomes low if the grain has higher Young's modulus in the loading direction than those in the surrounding grains. This suggests that the inhomogeneity due to crystallographic anisotropy affects the local strain state.
4. The strain distribution due to the microscopic inhomogeneity in the vicinity of the crack tip may affect the locally fluctuated crack propagation rate.

References

[1] Bernstein, H. L., Grant, T. S., McClung, R. C., and Allen, J. M., "Prediction of Thermal Mechanical Fatigue Life for Gas Turbine Blades in Electric Power Generation," *Thermomechanical Fatigue Behavior of Materials, ASTM STP 1186*, H. Sehitoglu, Ed., ASTM International, West Conshohocken, PA, 1993, pp. 212–238.

[2] Okada, M., Tsutsumi, M., Kitamura, T., and Ohtani, R., "Initiation and Growth of Small Cracks in Directionally Solidified Mar-M 247 Under Creep-Fatigue, Part I: Effect of Microstructures," *Fatigue Fract. Eng. Mater. Struct.*, Vol. 21, 1998, pp. 741–750.

[3] Floreen, S. and Kane, R. H., "Controlling Intermediate Temperature Fatigue Crack Growth in Nickel Base Superalloys by Microstructural Variations," *Proceedings of the 4th International Symposium on Superalloys*, 1980, pp. 595–604.

[4] Shahinian, P. and Sadananda, K., "Creep and Fatigue Crack Growth in Several Cast Superalloys," *Proceedings of the 5th International Symposium on Superalloys*, 1984, pp. 741–750.

[5] Hoffelner, W., "Fatigue Crack Growth in High Temperature Alloys," *Proceedings of the 5th International Symposium on Superalloys*, 1984, pp. 771–783.

[6] Skelton, R. P., "Growth of Short Cracks During High Strain Fatigue and Thermal Cycling," *Low-Cycle Fatigue and Life Prediction, ASTM STP770*, C. Amzallag, B. N. Leis, and P. Rabbe, Ed., ASTM International, West Conshohocken, PA, 1982, pp. 337–381.

[7] Hoffelner, W., "Effects of Environment on Crack Growth Behavior of Superalloys Under Various Loading Conditions," *Mater. Sci. Technol.*, Vol. 3, 1987, pp. 765–771.

[8] Shahinian, P. and Sadananda, K., "Creep and Fatigue Crack Growth Behaviour of Some Cast Nickel-Based Alloys," *Mater. Sci. Eng., A*, Vol. 108A, 1989, pp. 131–140.

[9] Ghonem, H., Nicholas, T., and Pineau, A., "Elevated Temperature Fatigue Crack Growth in Alloy 718. II: Effects of Environmental and Material Variables," *Fatigue Fract. Eng. Mater. Struct.*, Vol. 16, No. 6, 1993, 577–590.

[10] Yamamoto, M., Nitta, A., and Ogata, T., "Evaluation of Crack Initiation and Propagation Lives from Internal Defects and Lower Limit of Failure Life in High Temperature Fatigue on Ni-Based Single Crystal Superalloy," *J. Soc. Mater. Sci. Jpn.*, Vol. 50, No. 5, 2001, pp. 510–515.

[11] Chan, K. S. and Leverant, G. R., "Elevated-Temperature Fatigue Crack Growth Behavior of MAR-M200 SIngle Crystals," *Metall. Trans. A*, Vol. 18A, 1987, pp. 593–602.

[12] Lerch, B. A. and Antolovich, S. D., "Fatigue Crack Propagation Behavior of a Single Crystalline Superalloy," *Metall. Trans. A*, Vol. 21A, 1990, pp. 2162–2177.

[13] Okazaki, M., Tabata, T., and Nohmi, S., "Intrinsic Stage I Crack Growth of Directionally Solidified Ni-Based Superalloys During Low-Cycle Fatigue at Elevated Temperature," *Metall. Trans. A*, Vol. 21A, 1990, pp. 2201–2208.

[14] Lupinc, V. and Onfrio, G., "The Effect of Creep and Oxidation on High-Temperature Fatigue Crack Propagation in ⟨001⟩-loaded CMSX-2 Superalloy Single Crystals," *Mater. Sci. Eng., A*, Vol. 202A, 1995, pp. 76–83.

[15] Henderson, M. B. and Martin, J. W., "The Influence of Crystal Orientation on the High Temperature Fatigue Crack Growth of a Ni-Based Single Crystal Superalloy," *Acta Mater.*, Vol. 44, 1996, pp. 111–126.

[16] Telesman, J. and Ghosn, L. J., "Fatigue Crack Growth Behavior of PWA 1484 Single Crystal Superalloy at Elevated Temperatures," *ASME J. Eng. Gas Turbines*

Power, Vol. 118, 1996, pp. 399–405.

[17] Pommier, S., Prioul, C., and Bompard, P., "Influence of a Negative R Ratio on the Creep-Fatigue Behaviour of the N18 Nickel-Based Superalloys," *Fatigue Fract. Eng. Mater. Struct.*, Vol. 20, No. 1, 1997, pp. 93–107.

[18] Schubert, F., Rieck, T., and Ennis, P. J., "The Growth of Small Cracks in the Single Crystal Superalloy CMSX-4 at 750 and 1000C," *Proceedings of the 9th International Symposium on Superalloys*, 2000, pp. 341–346.

[19] Crompton, J. S. and Martin, J. W., "Crack Growth in a Single Crystal Superalloy at Elevated Temperature," *Metall. Trans. A*, Vol. 15A, 1984, pp. 1711–1719.

[20] Bouse, G. K., "Fatigue Crack Propagation Rate Testing of Single Crystal Superalloys NASAIR 100 and CMSX-2 at 982C," *Proceedings of the 5th International Symposium on Superalloys*, 1984, pp. 751–759.

[21] Wright, P. K., "Oxidation-Fatigue Interactions in a Single-Crystal Superalloy," *Low Cycle Fatigue, ASTM STP 942*, H. D. Solomon, G. R. Halfored, L. R. Kaisand, and B. N. Leis, Eds., ASTM International, West Conshohocken, PA, 1988, pp. 558–575.

[22] Muller, S., Rosler, J., Sommer, C., and Hartnagel, W., "The Influence of Load Ratio, Temperature, Orientation and Hold Time on Fatigue Crack Growth of CMSX-4," *Proceedings of the 9th International Symposium on Superalloys*, 2000, pp. 347–356.

[23] Okada, M., Tsutsumi, M., Kitamura, T., and Ohtani, R., "Initiation and Growth of Small Cracks in Directionally Solidified Mar-M 247 Under Creep-Fatigue, Part II: Effect of Angle Between Stress Axis and Solidification Direction," *Fatigue Fract. Eng. Mater. Struct.*, Vol. 21, 1998, pp. 751–760.

[24] Sumigawa, T., Kitamura, T., and Ohishi, K., "Slip Behaviour Near a Grain Boundary in High-Cycle Fatigue of Poly-Crystal Copper," *Fatigue Fract. Eng. Mater. Struct.*, Vol. 27, No. 6, 2004, pp. 495–503.

[25] Kamaya, M. and Kitamura, T., "Stress Intensity Factors of Microstructually Small Crack," *Int. J. Fract.*, Vol. 124, 2003, pp. 201–213.

[26] Yaguchi, M. and Busso, E., "On the Accuracy of Self-Consistent Elasticity Formulations for Directionally Solidified Polycrystal Aggeregates," *Int. J. Solids Struct.*, Vol. 42, 2005, pp. 1073–1089.

[27] Yaguchi, M., Yamamoto, M., Ogata, T., and Ohno, N., "An Anisotropic Constitutive Model for a Directionally Solidified Superalloy," *Key Eng. Mater.*, Vol. 340–341, 2007, pp. 901–906.

[28] Yamamoto, M. and Kitamura, T., "Effect of Microstructure on Crack Propagation in High-Temperature Fatigue of Directionally Solidified Ni-Based Superalloy," *Fatigue Fract. Eng. Mater. Struct.*, Vol. 29, 2006, pp. 431–439.

[29] Dunne, F. P. E., Wilkinson, A. J., and Allen, R., "Experimental and Computational Studies of Low Cycle Fatigue Crack Nucleation in a Polycrystal," *Internationl Journal of Plasticity*, Vol. 23, 2007, pp. 273–295.

[30] Pollock, T. M. and Argon, A. S., "Directional Coarsening in Nickel-Based Single Crystals with High Volume Fractions of Coherent Precipitates," *Acta Metall. Mater.*, Vol. 42, 1994, pp. 1859–1874.

[31] Fincham, A. M. and Spedding, G. R., "Low Cost, High Resolution DPIV for Measurements of Turbulent Fluid Flow," *Exp. Fluids*, Vol. 23, 1997, pp. 449–462.

[32] Ronneberger, O., Raffel, M., and Kompenhans, J., "Advanced Evaluation Algorithms for Standard and Dual Plane Particle Image Velocimetry," *Proceedings of the 9th International Symposium on Applications of Laser Technologies to Fluid Mechanics*, Lisbon, 1998, p. 10.1.

ASTM Special Technical Publication, Vol. 5, No. 6
Paper ID JAI101531
Available online at www.astm.org

M. Dadfarnia,[1] *P. Sofronis,*[1] *B. P. Somerday,*[2] *and I. M. Robertson*[3]

Hydrogen/Plasticity Interactions at an Axial Crack in Pipeline Steel

ABSTRACT: The technology of large scale hydrogen transmission from central production facilities to refueling stations and stationary power sites is at present undeveloped. Among the problems which confront the implementation of this technology is the deleterious effect of hydrogen on structural material properties, in particular at gas pressure of 15 MPa which is the desirable transmission pressure suggested by economic studies for efficient transport. To investigate the hydrogen embrittlement of pipelines, a hydrogen transport methodology for the calculation of hydrogen accumulation ahead of a crack tip in a pipeline steel is outlined. This work addresses the interaction of hydrogen with an axial crack on the inside surface of the pipe. The approach accounts for stress-driven transient diffusion of hydrogen and trapping at microstructural defects whose density evolves dynamically with deformation. The results address the effect of hydrostatic constraint, stress, and plastic strain on the time it takes for the steady state hydrogen profiles to be established.

KEYWORDS: hydrogen embrittlement, diffusion, elastoplasticity, pipeline, finite element analysis

---

Manuscript received November 14, 2007; accepted for publication May 14, 2008; published online June 2008.

[1] Department of Mechanical Science and Engineering, University of Illinois at Urbana-Champaign, 1206 West Green Street, Urbana, IL 61801.
[2] Sandia National Laboratories, P.O. Box 969, MS 9403, Livermore, CA 94551.
[3] Department of Material Science and Engineering, University of Illinois at Urbana-Champaign, 1304 West Green Street, Urbana, IL 61801.

Citation: Dadfarnia, M., Sofronis, P, Somerday, B. P., and Robertson, I. M., "Hydrogen/Plasticity Interactions at an Axial Crack in Pipeline Steel," *J. ASTM Intl.*, Vol. 5, No. 6. DOI10.1520/JAI101531. Available online at www.astm.org. Also included in JAI Special Issue STP 1508, *Fatigue and Fracture Mechanics: 36th Volume,* R. W. Neu, K. R. W. Wallin, and S. R. Thompson, guest editors, ASTM International, West Conshohocken, PA, 2009, pp. 474-495.

Nomenclature

a = crack length
b = crack tip opening displacement in the deformed state
b_0 = crack tip opening displacement in the undeformed state
C_0 = hydrogen concentration in interstitial sites at the crack face under 15 MPa pressure measured in atoms per m^3
C_L = hydrogen concentration in interstitial sites measured in atoms per m^3
C_T = hydrogen concentration in trapping sites measured in atoms per m^3
c = total hydrogen concentration measured in hydrogen atom per solvent atom
D = hydrogen diffusion coefficient through interstitial sites
D_{eff} = Effective hydrogen diffusion coefficient
D_{ij}^{e} = elastic part of deformation rate tensor
D_{ij}^{p} = plastic part of deformation rate tensor
D_{ij}^{h} = deformation rate for lattice straining due to hydrogen
D_{ij} = total deformation rate = $D_{ij}^{e}+D_{ij}^{p}+D_{ij}^{h}$
d = constant in Abel-Nobel equation of state
E = Young's modulus
f = fugacity of hydrogen gas
h = pipeline thickness
j = hydrogen flux
K = solubility of hydrogen in steel
K_I = stress intensity factor
K_T = equilibrium constant
L = domain size
N_A = Avogadro's number
N_T = trap density
N_L = number of solvent atoms per unit volume
n = work hardening coefficient
P = hydrogen pressure
R = universal gas constant
r = radius in polar coordinate
T = T-stress
t = time
t_{ss} = effective time to steady state
V_H = partial molar volume of hydrogen
V_M = molar volume of the host lattice
W_B = trap binding energy

x_i = coordinate system
α = number of sites per trap
β = number of NILS per host atom
δ_{ij} = Kronecker delta
Δv = volume increase per hydrogen atom = V_H/N_A
ε_0 = yield strain
ε^p = equivalent plastic strain
Θ = temperature
θ = polar angle in polar coordinate
θ_L = occupancy of the interstitial sites
θ_T = occupancy of the trapping sites
ν = Poisson's ratio
ξ_i = nondimensional coordinate = x_i/L
ρ = nondimensional hydrostatic stress = $\sigma_{kk}V_H/3RT$
σ_0 = yield stress
σ_e = equivalent stress
σ_{ij} = Cauchy's stress
Ω = mean atomic volume of the host lattice
τ = nondimensional time = Dt/L^2
ϕ = nondimensional NILS concentration = C_L/C_0

Introduction

Hydrogen embrittlement is a severe degradation of the mechanical properties of metals and alloys [1,2]. In the presence of hydrogen, materials usually fail at load levels much lower than those they can sustain in a neutral environment [3–7]. In general, hydrogen embrittlement is a three-step process: adsorption of hydrogen atoms on the surface, transport of hydrogen solutes to regions stressed in tension ahead of crack tips, and failure of the material in the embrittled zone. The macroscopic ductility dependence on temperature and strain rate, the incubation period, and the critical hydrogen concentration build-up before fracture reflect the hydrogen transport kinetics [8] rather than the mechanisms of failure. Therefore, the analysis of the hydrogen transport processes is an essential prerequisite to any attempt to understand failures induced by hydrogen [9].

Kitagawa and Kojima [10] were the first who coupled the nonlinear diffusion phenomena with elastoplastic deformation ahead of a crack tip. Sofronis and McMeeking [11] studied transient diffusion of hydrogen and hydrogen trapping at microstructural defects in iron and steel in the area around a blunting crack tip. In their model, they considered drift due to hydrostatic stress and trapping generated by plastic deformation. By including the effect of hydrogen-induced dilatation on the material constitutive model, Lufrano and Sofronis [12] extended the model of Sofronis and McMeeking, and analyzed the interaction of hydrogen with local plasticity at cracked and round-notched geometries. Krom et al. [13] extended the model of Sofronis and McMeeking by introducing a strain rate factor in the diffusion equation to account for the hydrogen balance in normal interstitial lattice sites (NILS) and trapping sites. Taha and Sofronis [14], using Krom's modified transport model, investigated the interaction between hydrostatic stress, plastic strain, and hydrogen concentration and its dependence on strength and strain rate in both high and low solubility systems.

In the work to date, solution to the coupled problem between hydrogen diffusion and material elastoplasticity was obtained on the assumption of a uniform nonzero initial hydrogen concentration in NILS throughout the material before loading. This type of initial condition pertains to specimens which are first charged with hydrogen and then subjected to stress. However, in the case of an axial crack on the inner diameter (ID) surface of a pipeline carrying pressurized hydrogen, hydrogen diffuses in the material through the crack faces concurrently with the development of pressure-induced stress ahead of the crack tip. Modeling this problem requires that the pipeline wall material be assumed hydrogen-free at time $t=0$ and all surfaces in contact with hydrogen (inner surface of the pipeline and crack faces) at time $t \geq 0$ be at equilibrium with the hydrogen gas pressure in the pipe as dictated by Sievert's law.

Our previous attempts [15–17] to address the mechanics of hydrogen uptake through the surfaces of an axial crack on the interior wall-surface of a pipe were based on a boundary layer approach under small scale yielding (SSY) conditions of Mode I loading in plane strain. In that formulation, the load on the outer boundary of the domain was applied by displacements associated with the stress intensity factor experienced by the crack tip. The purpose of the present work is to study the interaction of hydrogen transport with the elastic and plastic deformation of the material directly at the pipeline setting, that is, as the hydrogen diffuses through the faces of an axial crack on the interior wall-surface of an actual pipe carrying hydrogen under high pressure.

The organization of the paper is as follows: The mathematical modeling issues of the coupled hydrogen diffusion and elastoplastic problems are explained in the next section. The formulation of the problems and the numerical solution for two crack depths (crack size) are presented. Next, the full-field solution for the pipeline geometry is compared with the solution obtained using a modified boundary layer approach for a cracked specimen loaded under Mode I plane strain small scale yielding conditions. The approach is termed modified because the imposed macroscopic displacements account also for the second, the so-called T-stress, a term in the Williams [18] asymptotic expansion for the linear elastic stress-field at a crack tip.

Hydrogen Transport in an Elastoplastic Material

Hydrogen is assumed to reside either at normal interstitial lattice sites (NILS) or at reversible trapping sites such as microstructural defects [11]. According to Oriani's theory [19], the two populations are always in equilibrium such that the occupancy of the interstitial sites θ_L, and the occupancy of the trapping sites θ_T are related through $\theta_T/(1-\theta_T)=\theta_L/(1-\theta_L)K_T$, where $K_T=\exp(W_B/R\Theta)$ represents the equilibrium constant, W_B is the trap binding energy, $R=8.314$ J/mol K is the universal gas constant, and Θ is the absolute temperature. The hydrogen concentration in trapping sites C_T, measured in hydrogen atoms per unit volume, can be expressed as $C_T=\theta_T\alpha N_T$, where α denotes the number of sites per trap and $N_T=N_T(\varepsilon^p)$ denotes the trap density in number of traps per unit volume and is a function of the amount of the local plastic strain ε^p. Similarly, the hydrogen concentration C_L in NILS, measured in hydrogen atoms per unit volume, can be phrased as $C_L=\theta_L\beta N_L$, where β denotes the number of NILS per solvent atom, $N_L=N_A/V_M$ denotes the number of solvent atoms per unit volume with N_A being Avogadro's number, and V_M the molar volume of the host lattice measured in units of volume per mole.

Transient diffusion of hydrogen is governed by [11–13]

$$\frac{D}{D_{eff}}\frac{dC_L}{dt}+\alpha\theta_T\frac{dN_T}{d\varepsilon^p}\frac{d\varepsilon^p}{dt}-DC_{L,ii}+\left(\frac{DV_H}{3R\Theta}C_L\sigma_{kk,i}\right)_{,i}=0 \tag{1}$$

where $()_{,i}=\partial()/\partial x_i$, d/dt is the time derivative, D is the hydrogen diffusion coefficient through NILS, D_{eff} is an effective diffusion coefficient given by $D_{eff}=D/(1+\partial C_T/\partial C_L)$, V_H is the partial molar volume of hydrogen in solid solution, σ_{ij} is the Cauchy stress, and a repeated index implies the standard summation convention over the range.

The hydrogen transport, Eq 1, can be expressed in a nondimensionalized form by considering the following nondimensional parameters:

$$\xi_i=\frac{x_i}{L},\quad \tau=\frac{Dt}{L^2},\quad \phi=\frac{C_L}{C_0},\quad \rho=\frac{\sigma_{kk}V_H}{3R\Theta} \tag{2}$$

where L is a nondimensionalizing length, and C_0 is a reference hydrogen concentration that is taken as the equilibrium hydrogen concentration, as dictated by Sievert's law at a given hydrogen pressure. Using the nondimensional parameters Eq 2, Eq 1 can be expressed as:

$$\frac{D}{D_{eff}}\frac{d\phi}{d\tau}+\frac{\alpha\theta_T}{C_0}\frac{dN_T}{d\varepsilon^p}\frac{d\varepsilon^p}{d\tau}-\frac{\partial^2\phi}{\partial\xi_i\,\partial\xi_i}+\frac{\partial}{\partial\xi_i}\left(\phi\frac{\partial\rho}{\partial\xi_i}\right)=0 \tag{3}$$

The elasticity of the material is assumed linearly elastic and isotropic with moduli independent of the local hydrogen concentration. In the plastic regime, the material hardens isotropically and flows according to von-Mises yielding in which the flow stress is assumed independent of hydrogen.

For the description of the material deformation, the total deformation rate tensor D_{ij} which equals the symmetric part of the velocity gradient in spatial coordinates is decomposed as $D_{ij}=D^e_{ij}+D^p_{ij}+D^h_{ij}$, where D^e_{ij}, D^p_{ij}, and D^h_{ij} denote the elastic, plastic, and hydrogen components, respectively. The deformation rate due to hydrogen solute atoms is purely dilatational [20] and is phrased as $D^h_{ij}=\delta_{ij}d[\ln(1+c\Delta v/3\Omega)]/dt$, where δ_{ij} is the Kronecker delta, $c=(C_L+C_T)/N_L$ is the total hydrogen concentration measured in hydrogen atoms per solvent atom, $\Delta v=V_H/N_A$ is the volume increase per hydrogen atom introduced into solution, and Ω is the mean atomic volume of the host metal atom.

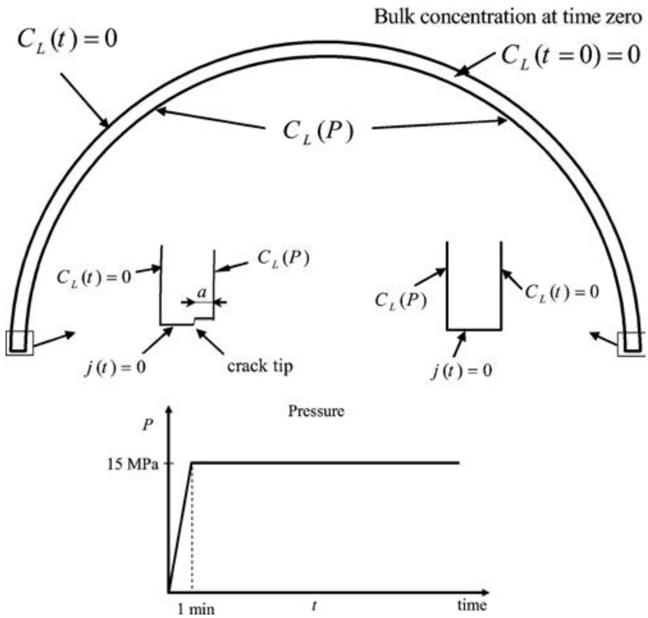

FIG. 1—*Description of the initial and boundary conditions for the hydrogen diffusion problem in the pipeline. The parameter j denotes hydrogen flux and* $C_L(P)$ *is normal interstitial lattice site hydrogen concentration at the inner wall-surface of the pipeline in equilibrium with the hydrogen gas pressure P as it increases to* 15 MPa *in one minute. At time zero, the material is hydrogen free,* $C_L(t=0)=0$.

The hydrogen diffusion initial/boundary-value problem and the elastic-plastic boundary problem are coupled [11]. The finite element procedures for the solution of the coupled problems are outlined in the works by Sofronis and McMeeking [11] and Liang and Sofronis [21].

Full-Field Solution

In this section, the initial/boundary-value problem of hydrogen diffusion coupled with material elastoplasticity is solved in the presence of an axial crack on the inner wall-surface of a pipe under plane strain conditions. The solution is termed as "*full-field solution*" since the formulation of the problem is done over the entire cross-sectional area of the pipe in the presence of an axial crack (Fig. 1). The outside diameter of the pipe is 40.64 cm; the wall thickness $h=9.52$ mm; and the depth of the axial crack, $a=1.9$ mm ($a/h=0.2$) (Fig. 1). In the absence of hydrogen, a finite crack-tip opening displacement (CTOD), $b_0=1.5\ \mu$m, is assumed for the finite element calculations.

The material properties used in the simulations are for a new X70/X80 type pipeline steel, which has an acicular ferrite microstructure with the pertinent properties given in Table 1. This medium strength ferritic steel was selected because it possesses the appropriate strength and is low cost; important factors

TABLE 1—*Material properties used in the simulations.*

Properties	Symbol	Value
Young's modulus	E	201.88 GPa
Poisson's ratio	ν	0.3
Yield stress	σ_0	595 MPa
Work hardening exponent	n	0.059
Number of sites per trap	α	1
Number of NILS per host atom	β	1
Trap binding energy [22]	W_B	60 kJ/mol
Molar volume of the host lattice	V_M	7.116 cm^3/mol
Partial molar volume of H	V_H	2 cm^3/mol
Diffusion coefficient	D	1.271×10^{-8} m^2/s
Volume change per H atom	$\Delta\nu/\Omega$	0.281
Solubility at temperature of 300 K	K	0.005435 mol $H_2/m^3\sqrt{MPa}$

in selecting a steel for new pipeline construction. The uniaxial stress-strain curve has been measured experimentally and is approximated by a power-law relationship of the form $\sigma_e = \sigma_0(1 + \varepsilon^p/\varepsilon_0)^n$, where ε^p is the plastic strain and strain at the onset of yielding $\varepsilon_0 = \sigma_0/E$. The temperature of the system is taken $\Theta = 300$ K. The trap density N_T is assumed to increase with plastic strain according to the experimental results of Kumnick and Johnson [22]. Certainly the numerical calculation results will be sensitive to the determination of the parameters (e.g., α and β) involved in the assumed model for trapping. However, it is not expected that uncertainties in the experimental determination of other parameters such as yield strength, partial molar volume of hydrogen, and solubility will have a marked effect on the conclusions of this work.

The mechanical load imposed on the surface of the inner wall by the hydrogen pressure opens up the crack, thus creating a tensile region ahead of the crack tip. The resulting stress field attracts hydrogen solute atoms as they diffuse into the material.

Figure 1 describes the hydrogen-related boundary and initial conditions of the problem. Due to symmetry, only half of the pipeline cross-sectional area is analyzed. The hydrogen concentration is set to zero at the external surface of the pipe, i.e., $C_L = 0$, and the hydrogen flux to zero at the plane of symmetry, i.e., $j = 0$. On the inner surface and the crack faces, the NILS hydrogen concentration C_L is always assumed to be in equilibrium with the hydrogen gas in the pipe. This equilibrium surface concentration is given by

$$C_L = K\sqrt{f} \tag{4}$$

where K is the solubility of hydrogen in the lattice and f is the fugacity of the hydrogen gas. According to the Abel-Noble equation of state for hydrogen [23], the relationship between fugacity and pressure is

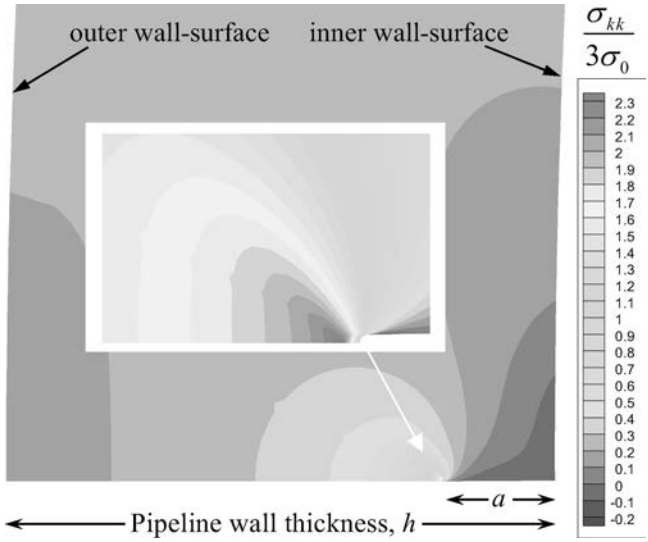

FIG. 2—*Contour plot of the normalized hydrostatic stress* $\sigma_{kk}/3\sigma_0$ *near the cracked region of the pipeline at hydrogen pressure of* 15 MPa*. The parameter* $\sigma_0 = 595$ MPa *is the yield stress of the material and* $a = 0.2h = 1.9$ mm *is the crack size. The inset shows the hydrostatic stress near the crack tip.*

$$f = P \exp\left(\frac{Pd}{RT}\right) \tag{5}$$

where d is a constant equal to 15.84 cm^3/mol.

At time zero, we assume there is no hydrogen in the pipe and thus the concentration in the metal is zero. In the simulations, hydrogen diffusion begins at time $t > 0$ as the hydrogen pressure is increased incrementally at a constant rate of 15 MPa/min over one minute and is then kept constant at 15 MPa (Fig. 1). The NILS hydrogen concentration in equilibrium with the hydrogen gas at 15 MPa is $C_L = C_0 = 2.659 \times 10^{22}$ H atoms/m^3 ($=3.142 \times 10^{-7}$ H atoms per solvent atoms) and has been used as the normalizing concentration parameter in Eqs 1 and 2.

The contour plot of the normalized hydrostatic stress in the pipe and around the crack is shown in Fig. 2 for a hydrogen pressure of 15 MPa. The corresponding crack tip opening displacement, b, defined by the 90° intersection method, is equal to 6.61 μm, which is four times the assumed initial crack tip opening displacement b_0. The maximum normalized hydrostatic stress ahead of the crack tip is $\sigma_{kk}/3\sigma_0 = 2.4$, and this decreases to about 1.73 at a distance of about $10b$ from the crack tip. Figure 3 shows the contour plot of the equivalent plastic strain in the pipe near the crack tip. At a hydrogen pressure of 15 MPa, the plastic zone is confined to the crack tip and its size is small compared to the thickness of the pipe.

The distribution of hydrogen concentration reaches steady state after 2

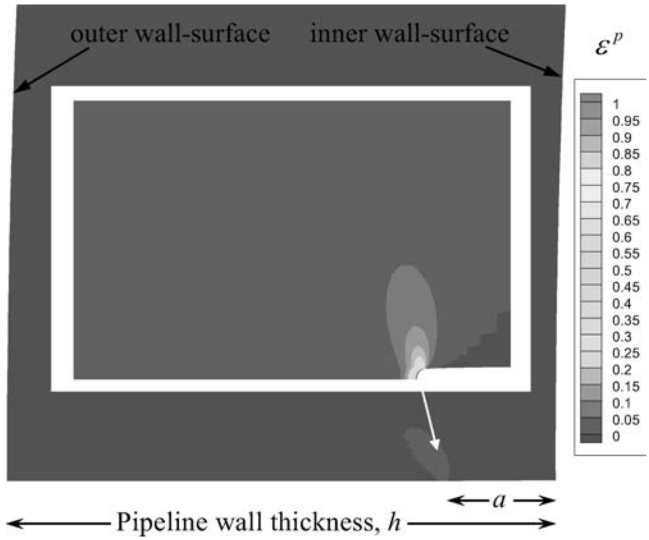

FIG. 3—*Contour plot of equivalent plastic strain* ε^p *near the cracked region of the pipeline at hydrogen pressure of* 15 MPa. *The crack size is* $a = 1.9$ mm *and the inset shows the plastic strain near the crack tip.*

hours. The contour plots of the hydrogen concentration fields at steady state under pressure 15 MPa are shown in Figs. 4 and 5. Figure 4 shows the normalized NILS concentration C_L/C_0. The distribution of C_L near the notch root varies in accordance with the hydrostatic stress (inset of Fig. 2). The equivalent plastic strain attains its peak value at the crack tip and decreases rapidly away from it. The profile of the trapped concentration C_T follows closely that of the plastic strain (Fig. 3) and since the trap density increases monotonically with plastic strain [22] the site of accumulation of trapped hydrogen is near the crack tip (Fig. 5).

The total hydrogen concentration in the region near the crack tip is essentially governed by trapped hydrogen (Fig. 6). In the region away from the crack tip, where the plastic strain is small, the trap density N_T is small relative to the NILS density βN_L and, consequently, the magnitude of the trapped concentration is small compare to the NILS hydrogen concentration. Therefore, as shown in Fig. 6, the total hydrogen population away from the crack tip is predominantly NILS hydrogen.

Figure 7 shows the normalized hydrogen concentration C_L/C_0 at NILS against normalized distance R/b from the crack tip along the axis of symmetry as the system evolves toward steady state. The parameter b denotes the instantaneous crack tip opening displacement which increases from 1.5 μm to 6.61 μm as the hydrogen pressure increases from zero to 15 MPa in 60 s. After that, the pressure and b remain constant. The effect of hydrostatic stress on the shape of the hydrogen concentration profile at NILS can be clearly seen in this figure.

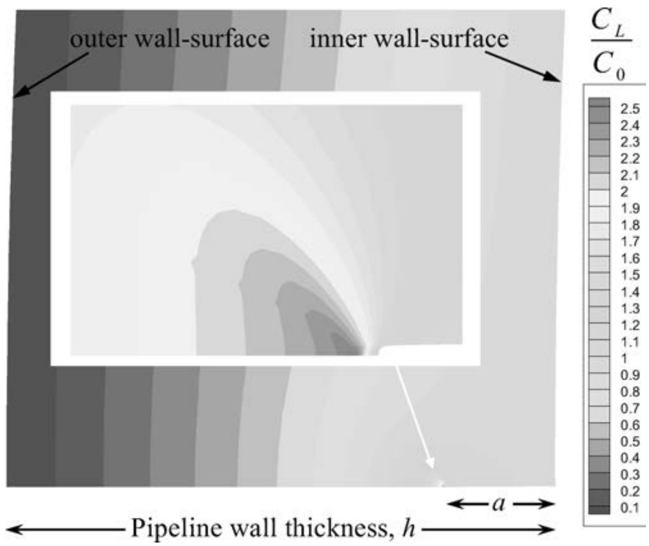

FIG. 4—*Contour plot of normalized NILS hydrogen concentration* C_L/C_0 *at steady state under hydrogen pressure of* 15 MPa. *The inset shows the concentration near the crack tip. The parameter* $C_0 = 2.659 \times 10^{22}$ H atoms/m^3 (=3.142×10^{-7} H atoms *per solvent atoms) denotes the hydrogen concentration on the inner wall-surface and crack face in equilibrium with the hydrogen gas. The crack size is* $a = 1.9$ mm.

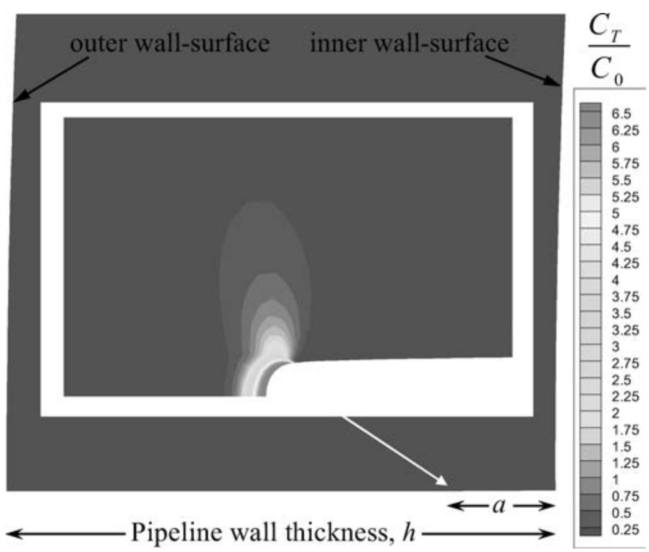

FIG. 5—*Contour plots of steady state normalized hydrogen concentration* C_T/C_0 *at trapping sites near the cracked region of the pipeline at hydrogen pressure of* 15 MPa. *The crack size is* $a = 1.9$ mm *and the inset shows the concentration near the crack tip.*

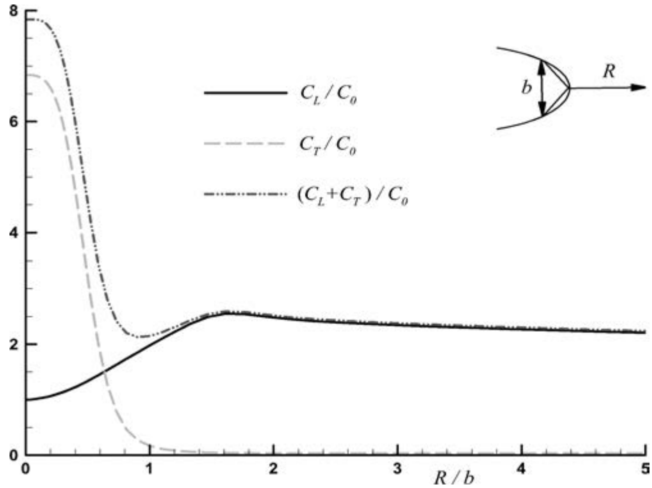

FIG. 6—*Plot of normalized hydrogen concentrations at steady state versus normalized distance* R/b *ahead of the crack tip for crack size* $a = 1.9$ mm. *The parameters* C_L, C_T, *and* $(C_L + C_T)$ *are hydrogen concentration in NILS, hydrogen concentration in trapping sites, and total hydrogen concentration, respectively. The parameter b denotes the crack tip opening displacement at hydrogen pressure of* 15 MPa.

We define the effective time to steady state t_{ss} to be the time at which the peak value of NILS hydrogen concentration reaches 98 % of the final steady-

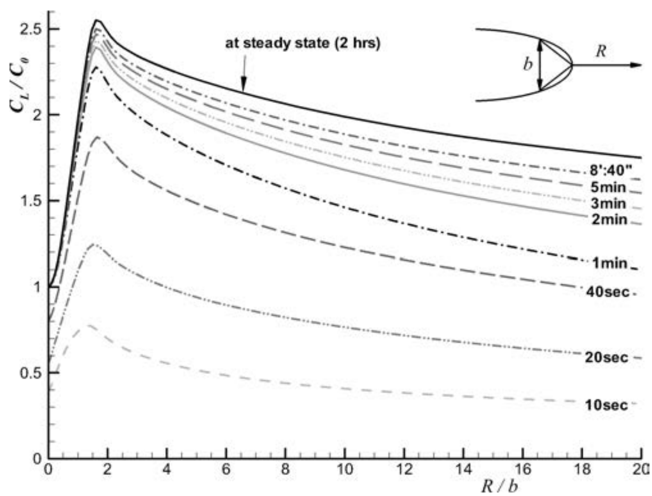

FIG. 7—*Evolution of normalized hydrogen concentration* C_L/C_0 *in NILS versus normalized distance* R/b *ahead of the crack tip for crack size* $a = 1.9$ mm. *The parameter b denotes the crack tip opening displacement which varies with time as the hydrogen pressure increases toward its final value of* 15 MPa *over one minute.*

state peak value. The parameter t_{ss} is a measure of the time at which steady state in the fracture process zone has almost been reached while in the rest of the specimen diffusion to steady-state continues. For the pipe geometry and the material properties considered, the effective time to steady state is calculated to be $t_{ss} = 520$ s. The corresponding normalized hydrogen concentration at this time is shown in Fig. 7.

Modified Boundary Layer (MBL) Approach

So far, the solution to the coupled hydrogen transport and elastoplastic deformation problem was presented for the actual pipe geometry. This solution which was termed *full-field solution* pertains to the specific pipe dimensions. To assess the fracture behavior of a pipe in terms of the hydrogen pressure and the calculated parameters, e.g., local stress, strain, and hydrogen concentration, one needs to investigate the transferability of these parameters as calculated from laboratory specimens to the actual pipe. The relevant question here is under what conditions the stress, deformation, and hydrogen concentration field in the actual pipe and laboratory specimen are similar. Thus, we seek to explore whether a similarity between the full-field solution under a given pressure and the corresponding small scale yielding solution obtained in a laboratory specimen exists. In the SSY boundary layer approach, the domain of analysis is loaded by the applied stress intensity factor experienced by the crack tip in the actual pipeline under the given hydrogen pressure. Further, in order to accurately account for the hydrostatic constraint that develops in the actual pipe, we included in the loading of the boundary layer domain the T-stress, which is the first nonsingular constant term in the Williams [18] asymptotic Mode I singular elastic solution at a crack tip. This *modified boundary layer approach* (MBL) has been used by Hancock and co-workers [24–26] and Parks [27] to study the role of hydrostatic constraint [28] on material fracture toughness. Lastly, for the analysis of the hydrogen diffusion problem through the MBL formulation, the size of the domain needs to be specified. The uncracked wall ligament $L(=h-a)$ is an appropriate characteristic size for the domain. Indeed, enforcing in the MBL approach the zero concentration boundary condition at distance L from the crack tip models quite accurately the location of the zero concentration boundary condition prevailing at the exterior surface of the pipe.

We used the commercial code ABAQUS/Standard [29] to determine the stress-intensity factor and the T-stress for the cracked pipe geometry. The full pipe domain was modeled with eight-noded isoparametric plain-strain elements and a focused mesh at the crack tip with independent coincident nodes was used. For crack size $a = 1.9$ mm $(a/h = 0.2)$ and hydrogen gas pressure of 15 MPa, for which the full-field solution was obtained, the stress-intensity factor was found to be $K_I = 34.12$ MPa$\sqrt{\text{m}}$ and the normalized T-stress was $T/\sigma_0 = -0.316$.

Figure 8 shows the schematic of the domain and boundary conditions used in the MBL approach [30]. The distance L is taken equal to the uncracked ligament $h-a = 7.62$ mm of the pipeline and the initial crack opening displace-

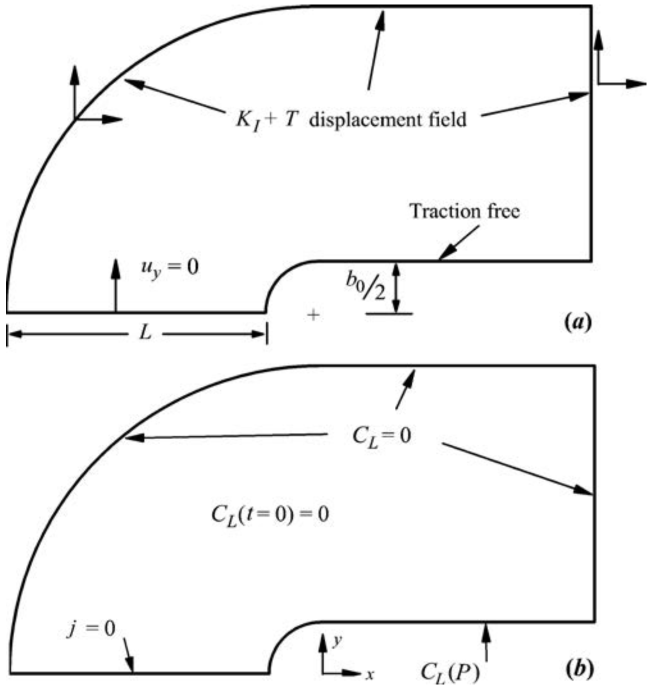

FIG. 8—*Description of* (*a*) *boundary conditions for the elastoplastic problem, and* (*b*) *initial and boundary conditions for the diffusion problem at a blunting crack tip for the modified boundary layer* (*MBL*) *formulation. The parameter* b_0 *denotes the crack tip opening in the absence of hydrogen. The parameter* $C_L(P)$ *denotes NILS hydrogen concentration at the crack face in equilibrium with the hydrogen gas pressure P and j is hydrogen flux.*

ment is taken $b_0 = 1.5\ \mu\text{m}$, the same as the CTOD used to obtain the full-field solution for the pipeline crack.

As shown in Fig. 8(*a*), the asymptotic displacements of the Williams' singular linear elastic field [18] were imposed on the outer boundary of the domain such that

$$u_x(r,\theta) = K_I \frac{1+\nu}{E}\sqrt{\frac{r}{2\pi}}\cos(\theta/2)[3-4\nu-\cos(\theta)] + T\frac{1-\nu^2}{E} r\cos(\theta) \qquad (6)$$

$$u_y(r,\theta) = K_I \frac{1+\nu}{E}\sqrt{\frac{r}{2\pi}}\sin(\theta/2)[3-4\nu-\cos(\theta)] - T\frac{\nu(1+\nu)}{E} r\sin(\theta) \qquad (7)$$

where r and θ are, respectively, the radius and polar angle of the outer boundary, E is Young's modulus, and ν is Poisson's ratio. To simulate the actual pipeline environment, the stress intensity factor K_I and the T-stress were increased linearly from zero to $K_I = 34.12\ \text{MPa}\sqrt{\text{m}}$ and $T = -0.316\sigma_0$, respectively over one minute, and they were then kept constant. On the crack surface, the NILS

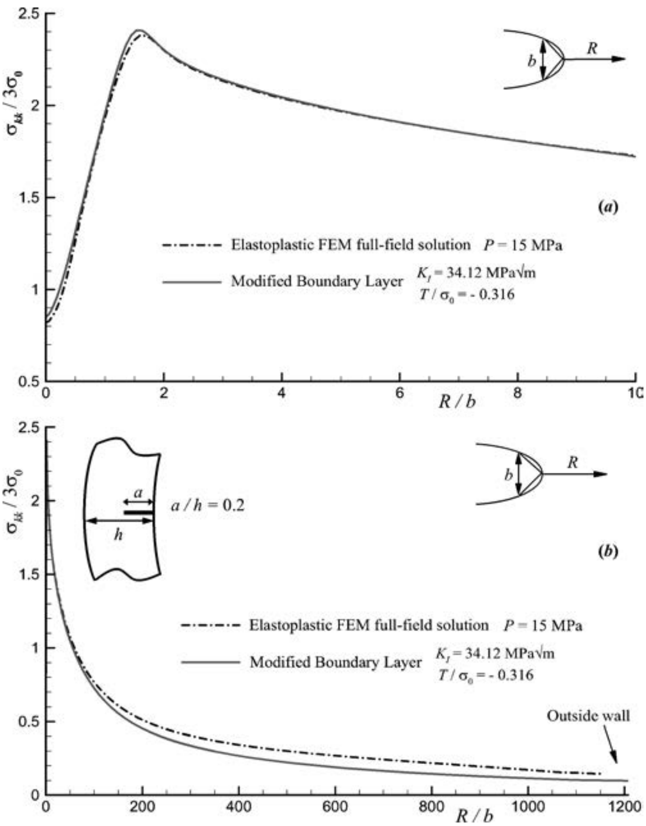

FIG. 9—*The normalized hydrostatic stress* $\sigma_{kk}/3\sigma_0$ *ahead of the crack tip from the full-field solution with a crack size* $a = 1.9$ mm *compared with the modified boundary layer* (*MBL*) *solution at hydrogen pressure* 15 MPa*:* (*a*) *near the crack tip,* (*b*) *over the entire uncracked pipeline ligament. The parameter b which is* 6.61 μm *in the full-field solution and* 6.31 μm *in the MBL solution denotes the crack tip opening displacement.*

hydrogen concentration C_L in equilibrium with the hydrogen gas was prescribed. Its magnitude increased in accordance with Eqs 4 and 5 as the pressure of hydrogen P increased from zero to 15 MPa in one minutes. At this time, $t = 1$ min, the NILS concentration on the crack surface is $C_L = C_0 = 2.659 \times 10^{22}$ H atoms/m^3 (=3.142×10^{-7} H atoms per solvent atoms). Figure 8(*b*) shows schematically the hydrogen-related initial/boundary conditions used in the MBL formulation for the hydrogen transport problem. A zero concentration boundary condition, i.e., $C_L = 0$, was assigned at the outer boundary of the domain whereas a zero flux condition, i.e., $j = 0$, was prescribed on the axis of symmetry ahead of the crack tip.

The normalized hydrostatic stress along the axis of symmetry ahead of the crack tip is shown plotted against normalized distance R/b from the tip in Fig. 9 at an applied stress intensity $K_I = 34.12$ MPa$\sqrt{\text{m}}$ and T-stress equal to

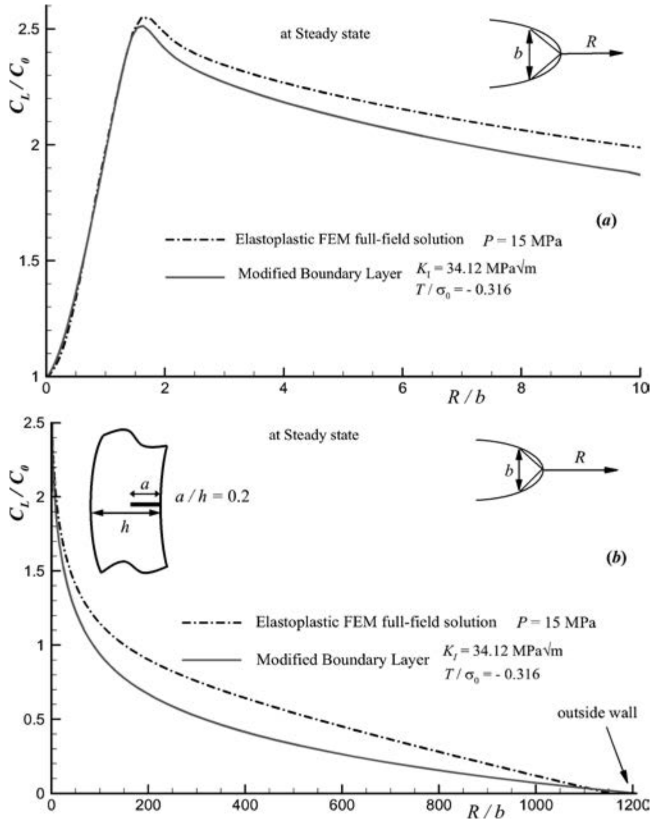

FIG. 10—*Normalized NILS hydrogen concentration C_L/C_0 versus normalized distance R/b ahead of the crack tip at steady state for full-field* (*crack size* $a = 1.9$ mm) *and MBL solutions:* (*a*) *near the crack tip,* (*b*) *over the entire uncracked ligament. The parameter b denotes the crack tip opening displacement for each case.*

$-0.316\sigma_0$, values which correspond to hydrogen gas pressure of 15 MPa in the pipe. Superposed on the same figure is the corresponding full-field solution. The crack tip opening displacement b in the MBL solution is 6.31 μm, a value slightly less than the corresponding value furnished by the full-field solution (6.61 μm). The hydrostatic stress profiles from both solutions near the crack tip are almost coincident, an indication of self- similarity due to the prevalence of small scale yielding conditions in the full-field solutions (Dadfarnia et al. [17]). However, away from the crack tip, Fig. 9(*b*) shows that the MBL solution deviates from the full-field solution. It is emphasized that the excellent agreement between the MBL and full-field solutions for the hydrostatic stress shown in Fig. 9(*a*) is related to the accounting for the *T*-stress effect in the problem formulation (Hancock and co-workers, [25,26]).

Figure 10 shows the steady-state normalized concentration C_L/C_0 in NILS ahead of the crack tip plotted against normalized distance R/b for both MBL

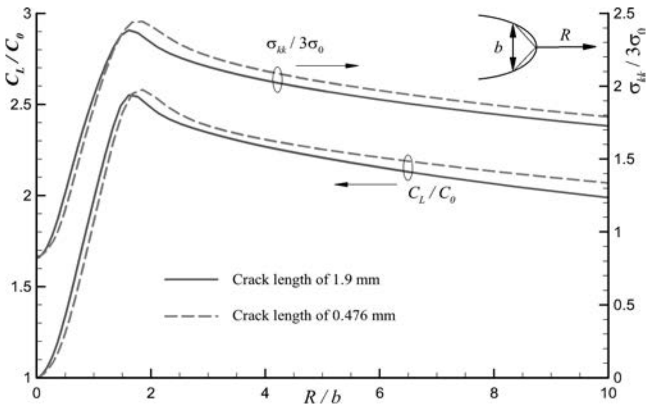

FIG. 11—*Comparison of the full-field solutions for the normalized hydrostatic stress* $\sigma_{kk}/3\sigma_0$ *and the steady state normalized NILS hydrogen concentration* C_L/C_0 *near the crack tip for two crack sizes. The parameter b denotes the crack tip opening displacement for each case.*

and full-field solutions. There is only a 2 % difference between the two solutions at the concentration peak location. Also, the effective time to steady state as calculated through the MBL approach was $t_{ss}=400$ s which is 120 s shorter than in the full-field solution.

Effect of Crack Size

In order to investigate the effect of the crack size on the evolution of the hydrogen concentration profiles, additional simulations were carried out for a shallower crack. Specifically, a crack with a size equal to 5 % of the wall thickness ($a/h=0.05$), i.e., $a=0.476$ mm was considered. As before, the hydrogen pressure in the pipe was increased to 15 MPa in 60 s and then kept constant. The initial crack tip opening displacement $b_0=0.2\ \mu$m increased to $b=1.06\ \mu$m at time $t=60$ s when the hydrogen pressure reached 15 MPa. The effective time to steady state was calculated $t_{ss}=95$ s, i.e., once the pressure reached 15 MPa, it took only 35 seconds for the maximum hydrogen concentration to reach 98 % of the peak value at steady state.

The full-field solutions for the hydrostatic stress and steady state hydrogen concentrations at NILS ahead of the crack tip for crack sizes $a=0.476$ mm ($a/h=0.05$) and $a=1.9$ mm ($a/h=0.2$) are presented in Fig. 11. The stress intensity factor and the normalized T-stress for the shorter crack are $K_I=14.38\ \text{MPa}\sqrt{\text{m}}$ and $T/\sigma_0=-0.292$, respectively. The hydrostatic stress profiles ahead of the crack tip are coincident for both crack sizes. As a result, the associated peak values of the hydrogen concentration are also the same. The slight difference is attributed to the difference in the T-stress, which is $T/\sigma_0=-0.292$ for the short crack ($a/h=0.05$) and $T/\sigma_0=-0.316$ for the long crack ($a/h=0.2$). A more negative T-stress produces a smaller hydrostatic stress peak.

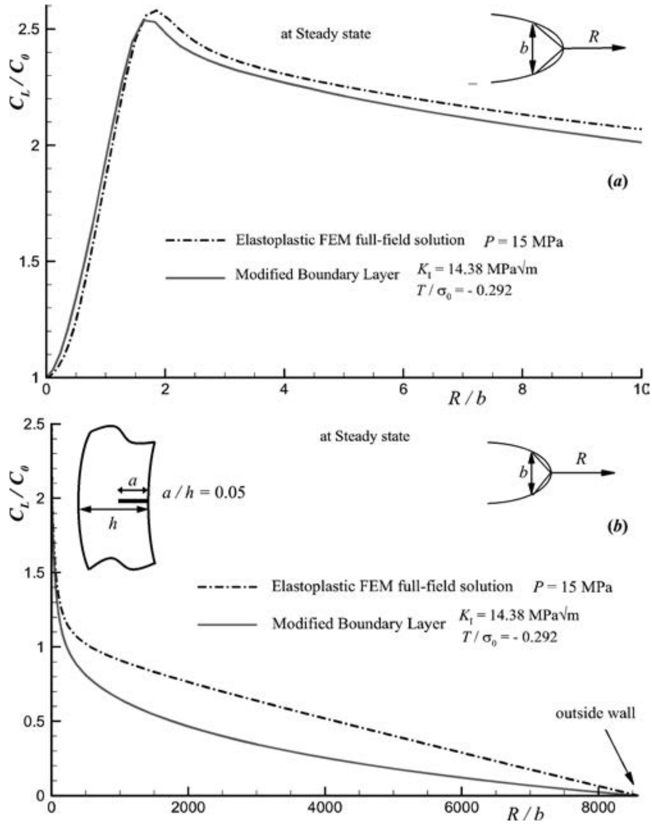

FIG. 12—*Normalized NILS hydrogen concentration* C_L/C_0 *versus normalized distance* R/b *ahead of the crack tip at steady state for full-field* (*crack size* $a = 0.476$ mm) *and MBL solutions:* (*a*) *near the crack tip,* (*b*) *over the entire uncracked ligament. The parameter b denotes the crack tip opening displacement for each case.*

In Fig. 12, the results for the NILS concentration as obtained from the MBL and full-field solutions are presented for the short crack, $a = 0.476$ mm ($a/h = 0.05$). For the sake of brevity, we do not report the comparison between the full-field and MBL solutions for the hydrostatic stress for this case. The crack-tip opening displacement calculated from the MBL approach was nearly the same as that from the full-field solution, i.e., $b = 1.06$ μm. Again, as was the case for the longer crack, both the hydrostatic stress and hydrogen profiles (Figs. 10(*a*) and 12(*a*)) of the full-field and MBL solutions close to the crack tip are coincident whereas the profiles deviate at distances further away from the tip (Figs. 10(*b*) and 12(*b*)). Also, the effective time to steady state from the MBL approach, $t_{ss} = 130$ s, turned out to be different from the full-field solution $t_{ss} = 95$ s.

Figure 13 shows the stress intensity factor and the normalized T-stress as a function of the normalized crack size a/h at hydrogen pressure of 15 MPa. For

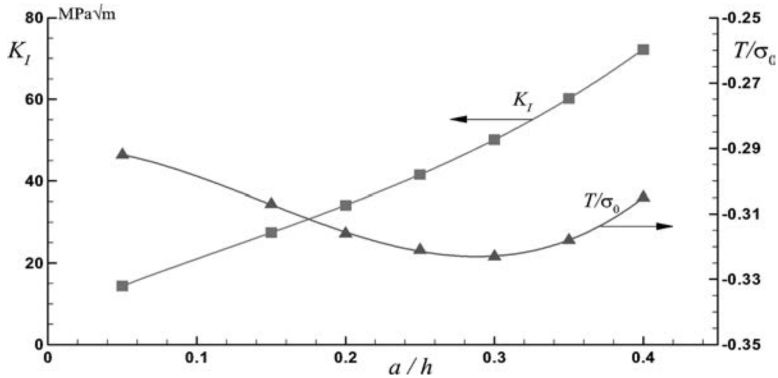

FIG. 13—*Stress intensity factor and normalized T-stress as a function of the normalized crack size a/h. The parameter h denotes the pipeline wall thickness.*

large crack sizes ($a/h > 0.45$), the plastic zone extends as far as the outer wall surface of the pipe and therefore the conditions for the boundary layer formulation, i.e., presence of small scale yielding, are not warranted. For the normalized crack sizes a/h in the range of 0.05–0.40, the normalized T-stress did not vary markedly, $-0.29 < T < -0.32$. Therefore, for $a/h < 0.4$, the near tip profiles of the hydrostatic stress and steady state normalized hydrogen concentration at NILS as shown in Fig. 11 are independent of the crack size.

Concluding Discussion

The coupled transient hydrogen diffusion initial/boundary-value problem and the large strain elastoplastic boundary value problem were solved for a pipe of an outer diameter 40.64 cm, wall thickness $h = 9.52$ mm, and with an axial crack on the inner wall surface. Solutions were obtained under hydrogen pressure of 15 MPa and material properties for an X70/80 type steel specifically for two crack sizes: $a = 0.476$ mm ($a/h = 0.05$) and $a = 1.9$ mm ($a/h = 0.2$). The finite element calculation results indicate that small scale yielding conditions are prevalent for cracks shorter than $a/h < 0.4$ and hence, the solution for the hydrogen concentration profiles scales with the applied stress intensity as demonstrated by Dadfarnia et al. [17], independently of the crack size. In these small scale yielding solutions, the normalized NILS hydrogen concentration ahead of the crack tip peaks at a value equal to 2.55.

The simulations show that steady-state diffusion throughout the wall thickness is attained after two hours from the time diffusion begins regardless of the crack size. Defining the effective time to steady state t_{ss} as the time at which the hydrogen concentration at NILS at the hydrostatic-stress peak location reaches 98 % of the final steady state value, we found that t_{ss} does depend on the crack size since the crack size along with the hydrogen pressure on the crack faces and ID surface determines the profile of the hydrostatic stress whose gradient drives the diffusion process through the pipeline wall. In particular, t_{ss} equals

95 s and 520 s for crack sizes $a = 0.476$ mm and $a = 1.9$ mm, respectively.

The present work attempted to provide a measure of the magnitude of the hydrogen concentration ahead of a crack as well as the time at which steady state is reached. It is very likely that both parameters are associated with the embrittlement of the material. Certainly, one can argue that hydrogen reaches steady state conditions very quickly in comparison to the long term service of a pipeline. Precise identification of the embrittlement conditions requires the coupling of the present simulations with a micromechanics model for fracture. Experimental work and theoretical calculations of fracture initiation and growth originating from an axial crack in a pipeline is the subject of an ongoing investigation.

Experimental studies of hydrogen transport and trapping at crack tips are scarce, and one likely reason is because of the complexity of such measurements. For example, the most accurate experiments must have high spatial resolution, probe the high-constraint region in the interior of the specimen, and be conducted in situ with high-pressure hydrogen (or its isotopes). The authors are not aware of any attempts to measure the transient evolution of hydrogen concentration fields at a crack tip. There have been some attempts to quantify the magnitude of the hydrogen concentration at a crack tip [31,32]. Results from these studies must be considered qualitative, due to complications associated with spatial resolution and surface measurements. However, these studies confirm that hydrogen concentrates in the hydrostatic stress field and plastic zone ahead of the crack tip.

Since conditions of small scale yielding were prevalent in the calculations for the full-field solution, the modified boundary layer (MBL) approach was used to solve the coupled elastoplasticity/diffusion problem in the neighborhood of a crack. It has been demonstrated that using the MBL approach with a diffusion domain of size equal to the uncracked wall ligament, one can predict the peak normalized hydrogen concentration in NILS at steady state within 2 % deviation from the actual value in the full-field solution. Thus the modified boundary layer approach offers an expedient way to study hydrogen transport around cracks in pipes.

Lastly, attention should be drawn to the effect of the hydrogen diffusion coefficient on the time to steady state [17]. Looking at the nondimensionalized hydrogen transport Eq 3, one notices that there is no explicit dependence on the hydrogen diffusion coefficient D. Therefore, the solution $\phi(\xi_i, \tau)$ to Eq 3 is independent of the hydrogen diffusion coefficient D. This implies that the effective nondimensionalized time τ_{ss} to steady state is also independent of D. Then, using the relationship $t_{ss} = \tau_{ss} L^2 / D$ between τ_{ss} and t_{ss} of Eq 2, one concludes that the actual effective time to steady state t_{ss} is inversely proportional to the diffusion coefficient D (i.e., $t_{ss} \propto 1/D$). This is an important result in view of the existing ambiguity around the magnitude of the diffusion coefficient in bcc ferritic systems in which a large range of diffusivities have been reported around room temperature [33].

Acknowledgments

The authors gratefully acknowledge support from (i) the Sandia National Laboratories under U.S. Department of Energy contract no. DE-AC04-94AL85000; (ii) U.S. Department of Energy Grant GO15045; and (iii) National Science Foundation Grant DMR 0302470.

References

[1] Hirth, J. P., "Effect of Hydrogen on the Properties of Iron and Steel," *Metall. Trans. A* Vol. 11, No. 6, 1980, pp. 861–890.

[2] Birnbaum, H. K., Robertson, I. M., Sofronis, P., and Teter, D., "Mechanisms of Hydrogen Related Fracture—A Review," *2nd International Conference on Corrosion Deformation Interactions*, CDI'96, Nice, France, 24–26 September, 1996, T. Magnin, Ed., The Institute of Materials, Great Britain, 1997, pp. 172–195.

[3] Thompson, A. W., "Materials For Hydrogen Service," *Hydrogen, Its Technology & Implications*, K. E. Cox and K. D. Williamson, Eds., Vol. 2 Transmission and Storage, CRC Press, Cleveland, 1977, pp. 85–124.

[4] Lee, T. D., Goldenberg, T., and Hirth, J. P., "Effect of Hydrogen on Fracture of U-Notched Bend Specimens of Spheroidized AISI 1095 Steel," *Metall. Trans. A*, Vol. 10, No. 4, 1979, pp. 199–208.

[5] Onyewuenyi, O. A. and Hirth, J. P., "Effects of Hydrogen on Notch Ductility and Fracture in Spheroidized AISI 1090 Steel," *Metall. Trans. A*, Vol. 14, No. 2, 1983, pp. 259–269.

[6] Robinson, S. L. and Stoltz, R. E., "Toughness Losses and Fracture Behavior of Low Strength Carbon-Manganese Steels in Hydrogen," *Hydrogen Effects in Metals*, I. M. Bernstein and A. W. Thompson, Eds., The Metallurgical Society of AIME, Warrendale, PA, 1981, pp. 987–995.

[7] Cialone, H. J. and Holbrook, J. H., "Sensitivity of Steels to Degradation in Gaseous Hydrogen," *Hydrogen Embrittlement: Prevention and Control*, ASTM STP 962, L. Raymond, Ed., ASTM International, West Conshohocken, PA, 1998, pp. 134–152.

[8] Birnbaum, H. K., "Hydrogen Related Failure Mechanisms in Metals," *Environmental Sensitive Fracture of Engineering Materials*, Z. A. Foroulis, Ed., *Proceedings of Symposium on Environmental Effects on Fracture*, Chicago, IL, October 24–26, 1977, Metallurgical Society of AIME, Warrendale, PA, 1978, pp. 326–360.

[9] Birnbaum, H. K. and Sofronis, P., "Hydrogen-Enhanced Localized Plasticity—A Mechanism for Hydrogen Related Fracture," *Mater. Sci. Eng., A*, Vol. 176, 1994, pp. 191–202.

[10] Kitagawa, H. and Kojima, Y., "Diffusion of Hydrogen Near an Elastoplastically Deformed Crack Tip," *Atomistic Fracture*, R. A. Latanision, and J. R. Pickens, Eds., *Proceedings of a NATO Advanced Research Institute on Atomistics of Fracture*, Calcatoggio, Corsica, France, May 22–31, 1981, Plenium Press, New York, 1983, pp. 799–811.

[11] Sofronis, P. and McMeeking, R. M., "Numerical Analysis of Hydrogen Transport Near a Blunting Crack Tip," *J. Mech. Phys. Solids*, Vol. 37, No. 3, 1989, pp. 317–350.

[12] Lufrano, J. and Sofronis, P., "Enhanced Hydrogen Concentration Ahead of Rounded Notches and Cracks—Competition Between Plastic Strain and Hydrogen Stress," *Acta Mater.*, Vol. 46, No. 5, 1998, pp. 1519–1526.

[13] Krom, A. H. M., Koers, R. W. J., and Bakker, A., "Hydrogen Transport Near a Blunting Crack Tip," *J. Mech. Phys. Solids*, Vol. 47, No. 4, 1999, pp. 971–992.
[14] Taha, A. and Sofronis, P., "A Micromechanics Approach to the Study of Hydrogen Transport and Embrittlement," *Eng. Fract. Mech.*, Vol. 68, No. 6, 2001, pp. 803–837.
[15] Dadfarnia, M., Sofronis, P., Robertson, I., Somerday, B. P., Muralidharan, G., and Stalheim, D., "Numerical Simulation of Hydrogen Transport at a Crack Tip in a Pipeline Steel," *Proceedings of the ASME International Pipeline Conference 2006*, Calgary, Alberta, Canada, September 25–29, 2006, ASME, New York, NY, 2007, pp. 193–199.
[16] Dadfarnia, M., Sofronis, P., Robertson, I., Somerday, B. P., Muralidharan, G., and Stalheim, D., "Micromechanics of Hydrogen Transport and Embrittlement in Pipeline Steels," *Proceedings of the ASME Materials Division: Presented at 2006 ASME International Mechanical Engineering Congress and Exposition*, November 5–10, 2006, Chicago, IL, ASME, New York, NY, 2007, pp. 741–750.
[17] Dadfarnia, M., Somerday, B. P., Sofronis, P., Robertson, I. M., and Stalheim, D., "Interaction of Hydrogen Transport and Material Elastoplasticity in Pipeline Steels," submitted to *J. Pressure Vessel Technol.*, 2008.
[18] Williams, M. L., "On the Stress Distribution at the Base of a Stationary Crack," *J. Appl. Mech.*, Vol. 24, 1957, pp. 109–114.
[19] Oriani, R. A., "The Diffusion and Trapping of Hydrogen in Steel," *Acta Metall.*, Vol. 18, No. 1, 1970, pp. 147–157.
[20] Peisl, H., "Lattice Strains Due to Hydrogen in Metals," *Hydrogen in Metals I, Topics in Applied Physics*, G. Alefeld and J. Völkl, Eds., Springer-Verlag, Berlin, Vol. 28, 1978, pp. 53–74.
[21] Liang, Y. and Sofronis, P., "Micromechanics and Numerical Modeling of the Hydrogen-Particle-Matrix Interactions in Nickel-Base Alloys," *Modell. Simul. Mater. Sci. Eng.*, Vol. 11, 2003, pp. 523–551.
[22] Kumnick, A. J. and Johnson, H. H., "Deep Trapping States for Hydrogen in Deformed Iron," *Acta Metall.*, Vol. 28, No. 1, 1980, pp. 33–39.
[23] San Marchi, C., Somerday, B. P., and Robinson, S. L., "Permeability, Solubility and Diffusivity of Hydrogen Isotopes in Stainless Steels at High Gas Pressures," *Int. J. Hydrogen Energy*, Vol. 32, 2007, pp. 100–116.
[24] Al-Ani, A. M. and Hancock, J. W., "J-Dominance of Short Cracks in Tension and Bending," *J. Mech. Phys. Solids*, Vol. 39, 1991, pp. 23–43.
[25] Betegon, C. and Hancock, J. W., "Two-Parameter Characterization of Elastic-Plastic Crack-Tip Fields," *J. Appl. Mech.*, Vol. 58, 1991, pp. 104–110.
[26] Du, Z. Z. and Hancock, J. W., "The Effect of Non-Singular Stresses on Crack-Tip Constraint," *J. Mech. Phys. Solids*, Vol. 39, 1991, pp. 555–567.
[27] Parks, D. M., "Advances in Characterization of Elastic-Plastic Crack-Tip Fields," *Topics in Fracture and Fatigue*, A. S. Argon, Ed., Springer-Verlag, Berlin, 1992, pp. 59–98.
[28] Larsson, S. G. and Carlsson, A. J., "Influence of Non-Singular Stress Terms and Specimen Geometry on Small Scale Yielding at Crack Tips in Elastic-Plastic Material," *J. Mech. Phys. Solids*, Vol. 21, 1973, pp. 263–278.
[29] ABAQUS/Standard, *User's Manual*, Version 6.4. Abaqus Inc., Providence, RI, 2003.
[30] Liang, Y., Sofronis, P., and Dodds, R. H., Jr., "Interaction of Hydrogen with Crack-Tip Plasticity: Effects of Constraint on Void Growth," *Mater. Sci. Eng., A*, Vol. 366, No. 2, 2004, pp. 397–411.
[31] Robinson, S. L., Moody, N. R., Costa, J. C., Pontau, A. E., and Gerberich, W. W., "Hydrogen Isotope Concentration Enhancements at a Blunt Notch," *Scr. Metall.*

Mater., Vol. 24, No. 1, 1990, pp. 111–116.

[32] Chene, J. and Brass, A. M., "Deuterium and Tritium Applications to the Quantitative Study of Hydrogen Local Concentration in Metals and Related Embrittlement," *Hydrogen Effects in Materials*, A. W. Thompson and N. R. Moody, Eds., TMS, Warrendale, PA, 1996, pp. 47–59.

[33] Völkl, J. and Alefeld, G., "Diffusion of Hydrogen in Metals." *Hydrogen in Metals I, Topics in Applied Physics*, G. Alefeld and J. Völkl, Eds., Springer-Verlag, Berlin, Vol. 28, 1978, pp. 53–74.

REACTOR COMPONENTS AND MATERIALS

ASTM Special Technical Publication, Vol. 5, No. 9
Paper ID JAI101561
Available online at www.astm.org

M. Scibetta,[1] *J. Schuurmans,*[1] *and E. Lucon*[1]

Experimental Study of the Fracture Toughness Transferability to Pressurized Thermal Shock Representative Loading Conditions

ABSTRACT: Fracture toughness testing on standard specimens in the ductile to brittle transition regime is well established and was first standardized by ASTM in 1997. However, its applicability to structural components and its potential conservatism, due to the high constraint condition in standard specimens, remain a subject of concern. In this work a study of the transferability of the fracture toughness measurements from laboratory specimens to structural components is performed. The structural component of interest is the Reactor Pressure Vessel subjected to an accidental loading condition called Pressurized Thermal Shock (PTS). As the actual component cannot be reasonably tested, an original experimental set-up is developed to simulate PTS representative loading conditions. A semi-elliptical crack is introduced by fatigue in a disk shape specimen which is biaxial loaded in the ductile to brittle transition regime. The developed disk specimen is called PTS-D specimen. Master Curve tests on 15 PTS-D specimens are performed and compared to standard size specimens having deep and shallow cracks. The reference temperature obtained on PTS-D is equivalent to the one obtained on half-inch compact tension specimens. To support the experimental results, finite element calculations are performed. It turns out that, in the tested range, constraint in PTS-D specimens is high. However, loss of constraint appears earlier than in standard specimens. It is found that the Beremin approach combined with analytical tool allows rationalizing all test results.

Manuscript received November 14, 2007; accepted for publication August 1, 2008; published online September 2008.

[1] SCK·CEN, Boeretang 200, 2400 Mol, Belgium.

Citation: Scibetta, M., Schuurmans, J., and Lucon, E., "Experimental Study of the Fracture Toughness Transferability to Pressurized Thermal Shock Representative Loading Conditions," *J. ASTM Intl.*, Vol. 5, No. 9. DOI10.1520/JAI101561. Available online at www.astm.org. Also included in JAI Special Issue STP 1508, *Fatigue and Fracture Mechanics: 36th Volume,* R. W. Neu, K. R. W. Wallin, and S. R. Thompson, guest editors, ASTM International, West Conshohocken, PA, 2009, pp. 499-517.

KEYWORDS: fracture toughness, master curve, pressurized thermal shock, transferability, loss of constraint, reactor pressure vessel

Introduction

The understanding of cleavage fracture mechanisms in the ductile to brittle transition region for ferritic steels has improved drastically over the last 30 years. Now, the well established Master Curve approach is used to determine the fracture toughness, the reference temperature and the specimen size dependence, using as few as six standard Single Edge Bend (SE(B)) or Compact Tension (C(T)) specimens [1]. This approach leads to the determination of the fracture toughness under relatively high constraint conditions. However, in actual components the constraint is likely to be low [2]. This low constraint can lead to some additional safety margin as a low constraint configuration typically shows an apparent higher fracture toughness. The quantification of the additional safety margin can be done using empirical or physical models based on the T-stress or Q-factor approaches or on local approach models [3–5].

The validation of this methodology consists in verifying the transferability of fracture toughness measured on standard size laboratory specimens to structural components. Such validation exercises published in the open literature on large structural components are relatively limited due to the large cost of such experimental programs.

When concentrating on Reactor Pressure Vessels (RPV) submitted to an accidental loading condition called Pressurized Thermal Shock (PTS), one-to-one scale experiments have never been performed as the cost of such a program would be prohibitive. However, within the Network for Evaluating Structural Components (NESC), two projects were developed to reproduce PTS loading conditions on relatively large cylinders containing artificial defects. In the NESC-I project, one test was performed with a shell of 1395 mm outer diameter and 175 mm thickness. Loading was produced by the combination of inertial effect by spinning the cylinder at 2280 rpm and thermal loading by injection of cold water [6]. In the NESC-II project, two tests were performed on cylinders of 581 mm outer diameter and 189 mm thickness. Loading was produced by a complex combination of internal pressure axial loading and thermal loading [7].

Those large scale PTS experiments are very useful to demonstrate the adequacy of the structural integrity assessment. However, due to the stochastic nature of brittle fracture, many repeated tests are needed to obtain conclusive results. Therefore, the NESC I and II projects are unable to address the effect of constraint on the transferability issue of fracture toughness from laboratory specimens to the PTS situation.

To address this specific issue, multiple tests need to be performed at an affordable cost with loading conditions approaching PTS accidental conditions. This has been addressed using the so-called cruciform specimen developed within the heavy-section steel technology program at ORNL [8] and used in the subsequent NESC-IV and Vocalist program [9]. The cruciform geometry has two arms of 102 mm square cross section. Each arm is 800 mm long. It allows loading the central portion using biaxiality ratios of 1:1, 1:0.6, and 1:0.

TABLE 1—*Chemical analyses on the base material* (*weight %*).

Material	C	Mn	Si	S	P	Cr	Ni	Mo	V	Cu	Co
Lemoniz	0.21	0.62	0.26	0.007	0.008	0.35	0.66	0.58	0.01	0.05	0.015

In NESC-IV, six cruciform tests with a biaxiality ratio of 1:1 were performed on surface-breaking semi-elliptic defects in a RPV longitudinal weld and four uniaxial tests on embedded flaw. The number of specimens tested remains limited because of the cost to prepare each specimen and the amount of material required. The cost of specimen preparation results from several Electrical Discharge Machining (EDM) cutting, welding the four extension bars, precracking, and testing. For biaxial loading, the experimental results did not exhibit loss of constraint. However, finite element calculations predict a variation of constraint level along the crack front. The final recommendation of the NESC-IV program [9] is to provide a more statistically reliable data set for benchmarking the constraint loss assessment methods.

This study aims at further assessing constraint loss under PTS relevant loading conditions. In a first step a new specific geometry is developed in order to cut down the unit price of the test. The new geometry is a simple disk of 200 mm diameter and 50 mm thickness (see Fig. 2). The PTS representative loading condition disk specimen is named PTS-D.

Fifteen PTS-D specimens are tested in the transition region and compared to tests on shallow and deep crack standard specimens. Finite element calculations are also performed to evaluate constraint in each specimen to interpret test results in terms of constraint.

Material

The base material of the RPV of Lemoniz 1 is selected for this study. The Lemoniz 1 unit, whose construction was cancelled, is a Spanish 900 MW Pressurized Water Reactor of Westinghouse design, similar to the North Anna unit in the United States. A study of the cladding of this material was the reason for purchasing a block of material by Tractebel [10].

The Lemoniz base material is A508 Class 2 normalized at 893°C for 23 h, austenitized at 857°C for 9 h before water quenching, and tempered at 660°C for 12 h before air cooling. The chemical and mechanical properties are summarized in Tables 1 and 2. Young's modulus and yield strength used for Master Curve are given in Eqs 1 and 2.

The temperature dependence of the Young's modulus is taken equal to:

$$E = 207 - 0.06T \tag{1}$$

with E in GPa and T in °C. The temperature dependence of yield strength is obtained from the exponential fit:

$$\sigma_{YS} = 398 + 45.2\exp(-0.014\,13T) \tag{2}$$

with T in °C and σ_{YS} in MPa. The fit is valid between −150°C and 300°C and has an accuracy of 5 %.

TABLE 2—*Mechanical properties of the base material. σ_{YS} is the yield strength, σ_{TS} the tensile strength, RA the reduction of area, ε_t the total elongation, T_{41J} the* 41 Joule *transition temperature, USE the upper shelf energy, and NDT the nil-ductility transition temperature.*

	Tensile properties at room temperature				Charpy		Drop weight
Material	σ_{YS}, MPa	σ_{TS}, MPa	RA, %	ε_t, %	T_{41J}, °C	USE, J	NDT, °C
Lemoniz	459	607	70	27	−19	204	−18

Test Matrix

Testing of conventional specimens is performed to obtain the fracture toughness of the material in the ductile to brittle transition region. These results are used to allow comparison with PTS-D specimens. In addition to the conventional PreCracked Charpy V-notch (PCCv) and 0.5T-C(T) covered by the ASTM Standard E1921-05, some shallow crack specimens were added to investigate the sensitivity to loss of constraint on T_0. The number of specimens is large enough to obtain a reference temperature with enough accuracy. The test matrix is given in Table 3.

All specimens are cut from the block in the LS orientation. This orientation is selected to represent axial crack used in PTS study. Due to material availability, PCCv, C(T), and PTS-D specimens are machined at different position across the thickness from $1/8T$ to $7/8T$. The fracture toughness variation along the thickness of this forging is under investigation. Preliminary results have shown that the variation of toughness in this range is limited to a maximum of 15°C.

PTS Representative Loading Condition

During a PTS event, the stresses along the vessel thickness are result from the internal pressure (primary load), the thermal gradient (secondary loading), and residual stresses. Internal pressure induces almost constant axial and circumferential stresses along the vessel thickness. The ratio between axial to circumferential stresses is 0.5.

For stresses induced by a thermal gradient the circumferential to axial stress ratio is close to 1. The stress along the thickness is nonuniform and can

TABLE 3—*Test matrix for fracture toughness testing.*

Specimen type	Number of machined specimens	Test temperature, °C
PCCv ($a/W \approx 0.5$)	12	−115 to −75
PCCv ($a/W \approx 0.1$)	12	−140 to −110
0.5 T−C(T) ($a/W \approx 0.5$)	10	−80 to −90
PTS-D ($a/W \approx 0.25$)	15	−120 to −90

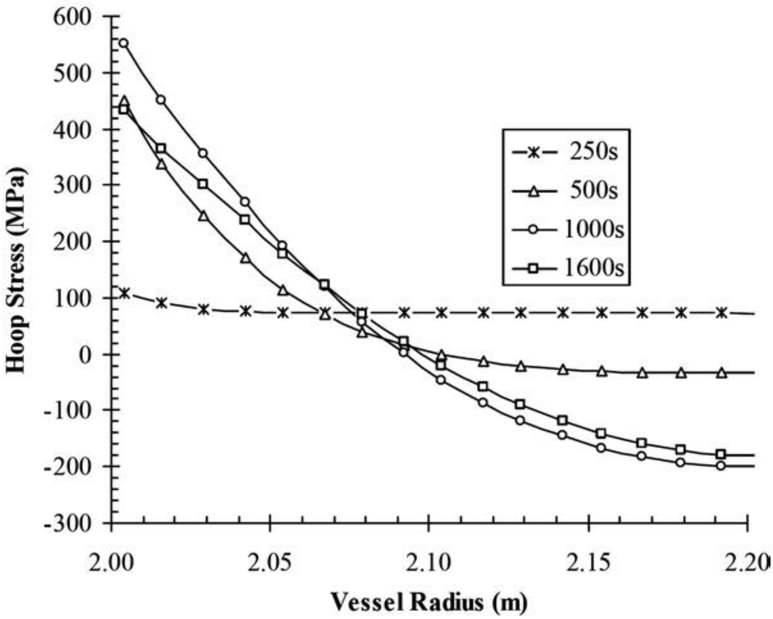

FIG. 1—*Typical stress profile along the thickness for a given transient for different times after the loss of cooling accident* (*Figure provided by Tractebel-Suez.*)

be approximated by a bending moment. The average circumferential and axial stresses from thermal and residual stresses are zero.

Several PTS transients were studied by Tractebel. For all severe transients they found that the bending stress dominates over membrane stress, resulting in a circumferential to axial stress ratio close to 1. An example of typical stress profile provided by Tractebel is illustrated in Fig. 1. The most severe stresses are obtained 1000 s after a loss of cooling accident, where bending dominates over membrane stress. Another typical stress distribution, illustrated in [9], is very similar to the profile shown in Fig. 1.

Development of the PTS-D

It may be possible to approximate PTS loading conditions without having to test a full vessel. The general idea (see also the cruciform beam experiment) is to use bending to approximate the far-field biaxial stress of the PTS. If successful, the approach will reduce drastically the specimen size and the cost of the experiment.

The objective of this project is to develop a cost effective set-up to reproduce PTS loading conditions (in particular, biaxial loading) with specimens having a thickness approaching actual RPV wall but using limited amount of material. The constraint for this project is the use of available infrastructure, i.e., a 500 kN servohydraulic machine, an environmental chamber with inter-

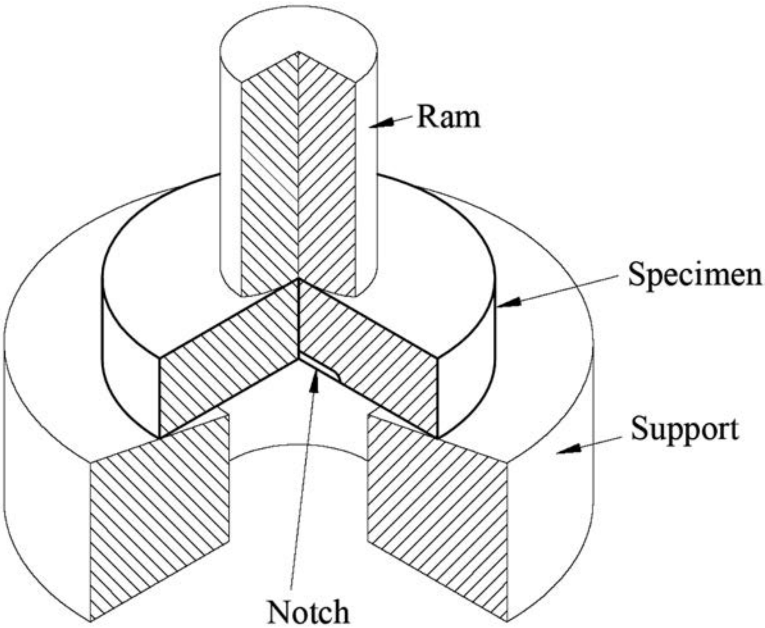

FIG. 2—*Isometric view of the PTS-D specimen simply supported and loaded at its center using a ram.*

nal dimension 400 by 400 by 550 mm^3 and a 2 MN static hydraulic machine. As a consequence of these constraints, the selected thickness has been fixed to 50 mm, which is about one-fourth of the actual wall thickness.

Several options were evaluated such as the cruciform beam, loading through the use of dissimilar material having different thermal expansion coefficients, and the introduction of a thermal gradient using a heater in conjunction with the environmental chamber. None of these options was fully satisfactory. The last option evaluated was the loading of a 200 mm diameter disk which is simply supported on its bottom surface circumference and loaded at the center of the upper surface. The schematic of the configuration is illustrated in Fig. 2.

The selected geometry has several advantages such as:

- pure biaxial loading with 1:1 biaxiality ratio,
- use of a minimum quantity of material for specimen machining,
- no need for welding extension arms contrary to the cruciform specimen,
- no need for Electrical Discharge Machining (EDM) of load diffusion slots, contrary to the cruciform specimen,
- compact set-up allowing the use of a well controlled environmental chamber,
- easy machining of specimen and test set-up.

TABLE 4—*Results of linear elastic finite element calculations for a semi-elliptical crack. a is the crack depth, c is the half-crack width, compliance is the crack mouth opening compliance, K_a is the stress intensity factor at the deepest point and K_c is the stress intensity factor at the free surface.*

a mm	c mm	c/a	Compliance mm/kN	force/K_a kN/MPa$\sqrt{m}$	force/K_c kN/MPa$\sqrt{\text{m}}$
4.00	17.44	4.36	4.42×10^{-5}	19.2	33.5
5.42	18.28	3.37	5.74×10^{-5}	18.0	26.8
6.83	19.12	2.80	6.90×10^{-5}	17.4	23.0
8.25	19.97	2.42	7.95×10^{-5}	17.2	20.5
9.67	20.81	2.15	8.91×10^{-5}	17.2	18.7
11.08	21.66	1.95	9.80×10^{-5}	17.4	17.4
12.50	22.50	1.80	10.6×10^{-5}	17.8	16.4
13.92	23.34	1.68	11.4×10^{-5}	18.3	15.7

Precracking Method for PTS-D

The introduction of a crack by fatigue is quite straightforward. A 4 mm deep and 35 mm width sharp notch is machined with a milling cutter as shown in Fig. 2. The specimen is loaded cyclically with the same set-up as in Fig. 2. To follow crack propagation and to control the stress intensity factor, linear elastic finite element calculations are performed using a semi-elliptical crack with various crack depths and crack widths. Results are summarized in Table 4.

For the practical use of Table 4 in automated software, compliance and stress intensity factor at the deepest point are fitted using a polynomial Eqs 3 and 4. The overall accuracy in the investigated crack size range is estimated, on the bases of a mesh size sensitivity study, to be better than 5 %:

$$C = \frac{1}{WE}(0.048 + 5.59(a/W) - 5.59(a/W)^2) \tag{3}$$

where C is the crack mouth opening compliance, a the crack length, W the specimen thickness and E the Young's modulus:

$$K_a = \frac{F}{W^{1.5}} \frac{1}{2.33 - 11.3(a/W) + 49.4(a/W)^2 - 64.1(a/W)^3} \tag{4}$$

where K_a is the stress intensity factor at the deepest point.

During fatigue loading, the crack mouth opening displacement is monitored with a dedicated clip gauge. This allows periodical measurement of the compliance to monitor the crack growth and to adjust the force to obtain the desired stress intensity factor.

Fracture Toughness Evaluation of PTS-D

Fracture toughness is here taken equal to the maximum stress intensity factor along the crack front (or the J-integral) at the fracture initiation point. In practice, as can be seen in the fatigue results section, fatigue has propagated the crack such that the stress intensity factor is relatively constant along the crack front. Therefore, fracture toughness of PTS-D specimen can be evaluated from the force versus Crack Mouth Opening Displacement (CMOD) record using Eq 4 when tests are performed in the linear elastic regime. When deviation from linearity is observed, fracture toughness needs to be evaluated using:

$$J = \frac{(1-\nu^2)}{E} K^2 + J_{pl} \tag{5}$$

where ν is the Poisson ratio, E the Young's modulus and J_{pl} the plastic component of the J-integral.

From a practical point of view J_{pl} can be evaluated using:

$$J_{pl} = \eta \frac{U_{pl}}{W^2} \tag{6}$$

where U_{pl} is the plastic energy under the force versus CMOD record and η (eta factor) a constant that needs to be identified. The η-factor has been evaluated using finite element calculations with crack size and material properties representative for the performed experiment. The following material properties are therefore selected:

- Young's modulus $E = 211\,800$ MPa,
- Poisson's ratio $\nu = 0.3$,
- Yield strength 520 MPa,
- Ultimate tensile strength 710 MPa,
- Uniaxial true stress versus true strain power law hardening above the yield strength with a strain hardening exponent of 0.110 836 5,
- $a/W = 0.236$ and $c/W = 0.41$.

The computation of J was performed using the energy release rate. An average J integral over the crack can be computed using the energy release rate:

$$J = -\left.\frac{\partial U}{\partial A}\right|_{\Delta} \tag{7}$$

where ∂A is the increase in crack area. In practice, the central difference approximation of the derivate was used.

Under these conditions, the η-factor is evaluated to be 0.25.

To analyze the results according to the Master Curve, the specimen thickness should be defined. In standard specimens the thickness corresponds to the crack front length. For the PTS-D specimen the stress intensity factor is nearly constant along the crack front, and the same definition can be used. The crack front length can be approximated using the simple Ramanujan's approximation of the complete elliptical integral of the second kind [11]:

$$B = \frac{\pi}{2}\left[3(a+c) - \sqrt{(3a+c)(a+3c)}\right] \tag{8}$$

where B is the crack front length, a the crack depth, and c half the crack width. For the elliptical crack eccentricity considered here, the error is less than 2×10^{-4} %.

Precracking and Fracture Toughness Testing of Shallow Crack SE(B)

Shallow crack testing is not covered by the current ASTM Standard E1921-05. Therefore the deviations from the standard for precracking and fracture toughness testing are documented in this paragraph. For PCCv ($a/W \approx 0.1$), a specific precracking procedure is used. For precracking, the initial sharp notch to start the fatigue crack could affect the stress field ahead of a shallow crack [12]. Therefore, the initial dimensions of the specimen are $B=10$, $W=13.5$, $L=55$, with a sharp notch of 3 mm depth. After precracking over a distance of about 1.5 mm, the specimen width W is reduced to 10 mm by machining. The initial notch of 3 mm depth is therefore removed. As an integral notch for the clip gauge would affect the stress state ahead of a shallow crack [12], attachable knifes are used to measure the CMOD. The knifes are 1 mm thick; therefore, the displacement is measured 1 mm above the specimen surface. This distance can be accounted for using the plastic rotation factor r_p:

$$CMOD = CMOD_Z \frac{a_0 + r_p(W - a_0)}{a_0 + r_p(W - a_0) + Z} \tag{9}$$

where $CMOD_Z$ is the measured clip gauge displacement, a_0 the initial crack length, Z the distance between the knife edge and the specimen surface and r_p the plastic rotation factor equal to 0.44 for a_0/W between 0.45 and 0.55. For shallow cracks, the plastic rotation factor depends on the crack length to width ratio and on the material strain hardening exponent [13]. The r_p value for the material of interest ($n=10$) and $a_0/W=0.15$ is 0.261 [13]. However, a value of 0.5 is found in [14] using the same procedure. On the other hand, a r_p value of 0.27 for $a_0/W=0.15$ is found in [14] using the ratio between the CMOD and the Load Line Displacement (LLD). The plastic rotation factor can also be obtained from the following equation [15]:

$$\frac{\eta_{LLD}}{\eta_{CMOD}} \frac{S}{4W} = r_p + (1 - r_p)a_0/W \tag{10}$$

This definition is believed to be more appropriate for our application. The assumption of a rigid body rotating around a rotation point does not hold close to the crack tip. Using the results published in [13] in conjunction with Eq 10, the plastic rotation factor for the material of interest ($n=10$) and $a_0/W=0.15$ is 0.37. From experimental and computational evidence, the following equation is suggested in [14]:

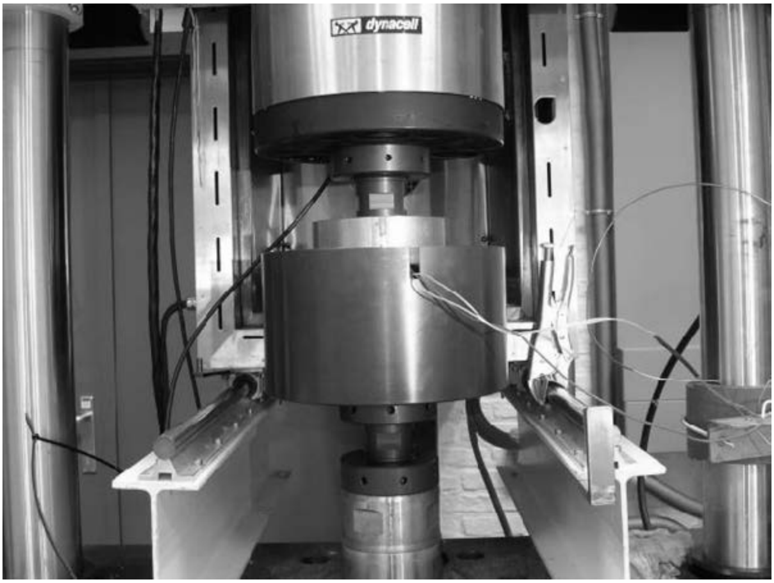

FIG. 3—500 kN *8803 Instron machine equipped for PTS specimen precracking.*

$$r_p = 0.3 + 0.5a_0/W \quad \text{for } a_0/W < 0.3 \tag{11}$$

yielding a value of 0.375 for $a_0/W = 0.15$.

It should be noted that in our case ($a_0 = 1.5, W = 10$, $Z = 1$, $r_p = 0.37$) an error of 10 % on r_p only affects the measured CMOD by 2 % and the measured fracture toughness by 1 %. Therefore a value of 0.37 for r_p is taken in this analysis.

The η-factor based on the load line given in the ASTM Standard E1921-05 is inadequate for shallow SE(B). In this case, the η-factor depends on the crack length to width ratio and on the strain hardening exponent of the material [13]. In [13], an alternative approach has been developed for a shallow crack relying on a specific η-factor based on the CMOD. This formulation has been extended in [15] and is given by the following equation:

$$\eta_{CMOD} = \frac{S}{4W}(3.785 - 3.101(a_0/W) + 2.018(a_0/W)^2) \tag{12}$$

Result of the PTS-D Precracking

The precracking of the specimens is performed on a 500 kN INSTRON servo-hydraulic machine available at SCK·CEN (see Fig. 3). The crack size during the precracking is monitored using the compliance of the specimen based on the crack mouth opening. Crack mouth opening is measured using a clip gauge. Two 1 mm thick razor blades (knifes) are screwed across the crack lips to allow clip gauge mounting.

The initial precracking force is 467 kN, which corresponds to a stress intensity factor of 24.3 MPa$\sqrt{}$m. Higher forces could not be applied as it reduces the operating frequency drastically. Specimens were precracked starting with a frequency of 9 Hz. Close to the final crack sharpening (crack depth of about 12.5 mm), a stress intensity factor of 13.3 MPa$\sqrt{}$m is imposed, which corresponds to an applied force of 238 kN. Due to the lower applied force, finishing frequency can be increased to 15 Hz, which speed up precracking. The average and standard deviation for the number of cycles, the initial and final measured compliance are, respectively, $1.0\times10^{6}\pm50\ \%$, $4.6\times10^{-5}\ \mathrm{mm/kN}\pm5\ \%$ and $9.5\times10^{-5}\ \mathrm{mm/kN}\pm4\ \%$. The number of cycles to achieve a specified crack length varies significantly from specimen to specimen.

During specimen preparation, it was found that the fatigue crack in three specimens was just at the junction between the base and the weld material. Therefore, results obtained from these specimens might not be representative of the Lemoniz base metal.

After fracture toughness testing, specimens were broken open at liquid nitrogen temperature. The average and standard deviation for the measured crack depth and crack width are, respectively 11.9 ± 0.6 mm and 41.4 ± 2 mm. The reproducibility of the precracking procedure is therefore relatively good.

The average half-crack width to crack depth ratio (c/a) is 1.74. In Table 4, the stress intensity factor at the deepest point and at the free surface for this ratio is nearly equal. The fatigue crack front shape naturally evolves to reach a relative constant K along the crack front. In the ASME code III, Appendix G postulates defects to have a c/a ratio equal to 3. This ratio was originally our target. However, this ratio is impossible to reach as the crack will always tend to grow over the depth before growing along the width, As shown in Table 4, $K_a > K_c$ ($F/K_a < F/K_c$) in the initial condition.

Fracture Toughness Results

Fracture toughness results are obtained on 0.5T-C(T), PCCv, PCCv with shallow cracks and PTS-D. Testing of PTS-D specimens was performed on a 2 MN machine and crack mouth opening was measured using a clip gauge using a configuration similar to the one for precracking (see Fig. 3). The other geometries were tested on a universal servo-mechanic testing machine with 50 kN capacity. Testing of all geometries is performed in an environmental chamber to ensure proper control of the temperature. The average crack depth for the shallow specimen is larger than the 1 mm target value. The average and standard deviation on the shallow crack length is 1.51 ± 0.13 mm.

All fracture toughness results normalized to a thickness of one inch are shown in Fig. 4. In addition, 5, 50, and 95 % confidence bound derived from the 0.5T-C(T) geometry are also provided in Fig. 4.

Fracture toughness results are analyzed using the ASTM Standard E1921-05. Results are summarized in Table 5. The standard is not strictly speaking applicable to shallow crack and PTS-D specimen. Therefore, no censoring limit has been applied to these geometries. The censoring limit aiming at avoiding loss of constraint will be investigated in the next paragraph.

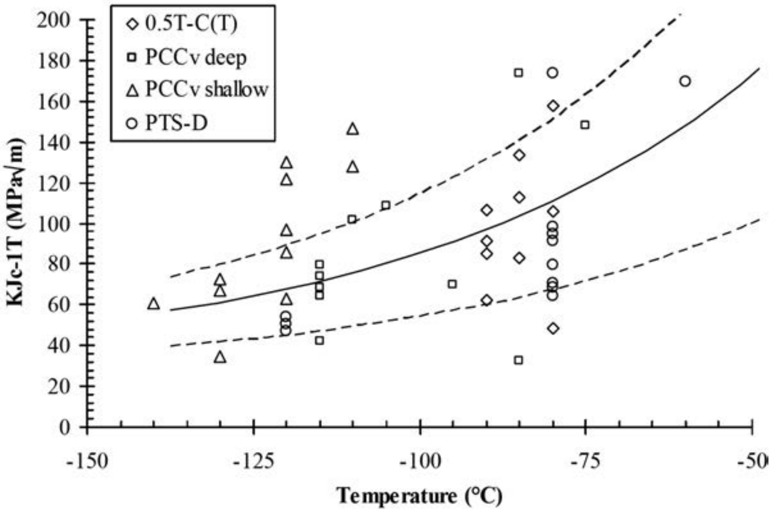

FIG. 4—*Fracture toughness results normalized to one-inch thickness.*

Loss of Constraint Evaluation

In Linear Elastic Fracture Mechanics (LEFM), the stress field ahead of the crack tip is governed by the level of the singularity, i.e., the stress intensity factor. In elastic plastic fracture mechanics when deviating from small scale yielding conditions, the second term of the LEFM stress field, called T-stress, governs the stress level ahead of the crack tip and can be used as a measure of constraint. As standard deep crack 0.5T-C(T) and SE(B) are high constraint geometries with a positive T-stress, they are considered to provide conservative (smaller) fracture toughness measurements for structural applications.

T-stress solutions for 0.5T-C(T), SE(B), and semi-elliptical cracks can be found in [16] and are reproduced in Figs. 5–8. The T-stress is proportional to the applied stress, which means that constraint depends on the loading level. For both 0.5T-C(T) and SE(B), the T-stress decreases and becomes negative for shallow cracks. The T-stress is positive for deep cracks and larger for 0.5T-C(T)

TABLE 5—*Summary of fracture toughness results on the Lemoniz base material. N is the total number of tests, r is the total number of valid results which are inside the validity window and n is an index that should be larger than 1 to have a valid reference temperature per ASTM E1921-05.*

Type	Test temp. range, °C	N	r	N	$T_0 \pm 2\sigma$ °C
0.5T – C(T)	−80 to −90	10	10	1.67	−87 ± 11
PCCv deep	−115 to −75	12	10	1.5	−91 ± 12
PCCv shallow	−140 to −110	12	12	1.98	−117 ± 10
PTS-D	−120 to −60	12	12	1.88	−83 ± 10

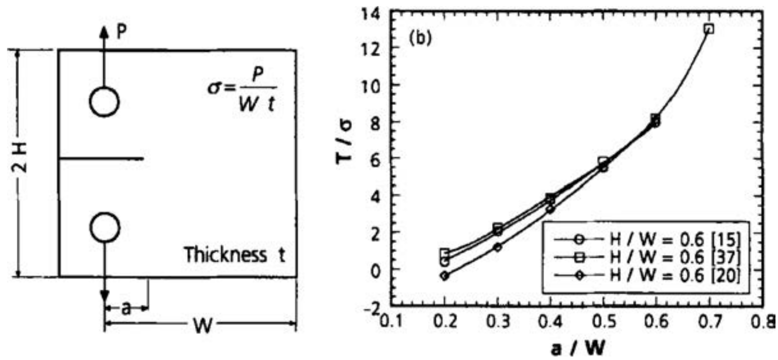

FIG. 5—*T-stress for 0.5T-C(T)* [*16*]

than for SE(B), which is the reason generally put forward to explain the difference in measured reference temperature (SE(B)s leading to about 10°C lower reference temperature than 0.5T-C(T), see scope of ASTM E1921-05).

For semi-elliptical cracks, the T-stress varies with the angular position and is a minimum at about 75°. Comparison of Figs. 7 and 8 illustrates the effect of biaxial loading. It is clear that biaxial loading tends to reduce loss of constraint.

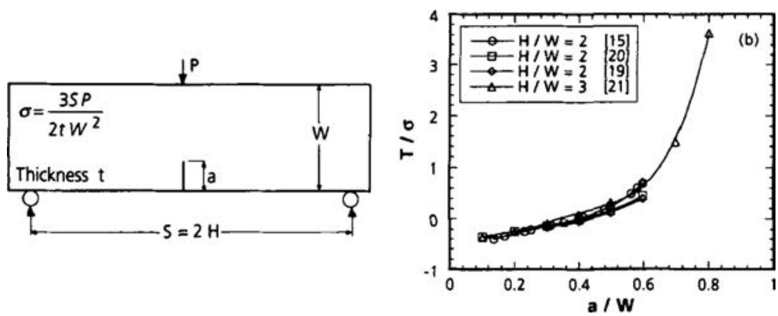

FIG. 6—*T-stress for SE(B)* [*16*]

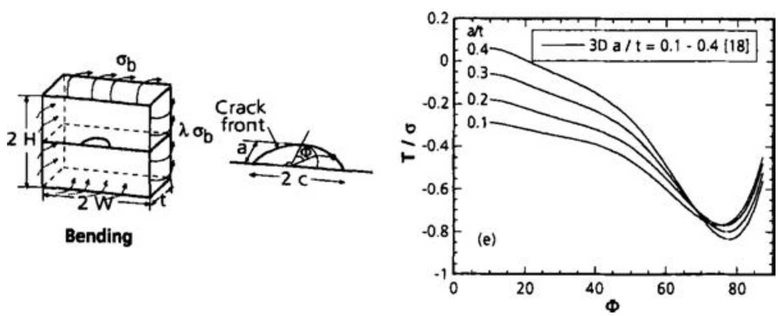

FIG. 7—*T-stress along the crack front for* $c/a = 3.33$ *and biaxiality ratio* $\lambda = 0$ [*16*].

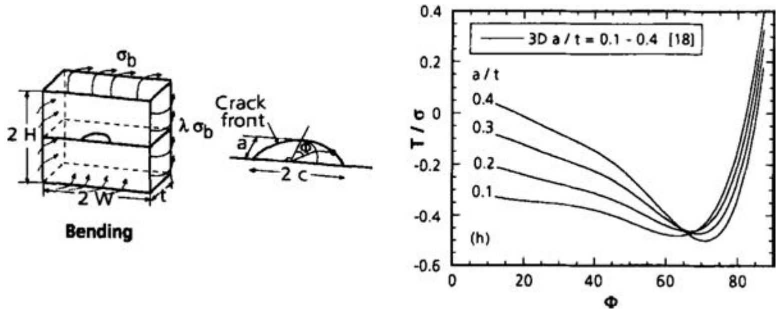

FIG. 8—*T-stress along the crack front for* $c/a = 3.33$ *and biaxiality ratio* $\lambda = 1$ [*16*].

The average crack depth to plate thickness ratio of the test is 0.24, therefore, the T-stress is negative along the whole crack front except near the free surface.

In large scale yielding the limit load is reached. In [3], it is suggested to substitute the stress by the limit load stress which yields a T-stress independent of the loading level. In addition an empirical correlation is suggested to correct the reference temperature or to correct individual measured K_{Jc} values:

$$T_0 = T_{0,deep} + \frac{T_{stress}}{10\ \mathrm{MPa}/{}^\circ\mathrm{C}} \quad \text{for } T_{stress} < 0 \tag{13}$$

The application of this simple model to the four geometries investigated here is summarized in Table 6. The T-stress is calculated for each specimen and the average is given in Table 6. For C(T) and SE(B), the T stress is calculate from the fracture load using Figs. 5 and 6, respectively. For PTS-D specimens, the fracture load F is converted to a bending stress σ_b using a proportional factor of 0.562 MPa/kN established using an elastic finite element calculation. The bending stress is converted to an average T-stress along the crack front (Φ between 0° and 60°) using Fig. 7.

To better assess loss of constraint, the local approach to fracture can be used [17]. Many models exist such as the Beremin model [17], the Bordet model [18], the Prometey model [19], the Anderson and Dodds model [20], or the WST model [21]. All models yield similar trends, therefore only the original and simple Beremin approach is used in this work. The Weibull stress is defined as [17]:

TABLE 6—*Application of the T-stress model to the experimental data set. The fracture load is used as input to calculate the T stress.*

Type	T_0, °C	Average T-stress, MPa	T_0 corrected, °C
0.5T – C(T)	−87	250	87
PCCv deep	−91	55	−91
PCCv shallow	−117	−310	−86
PTS-D	−83	−165	−66.5

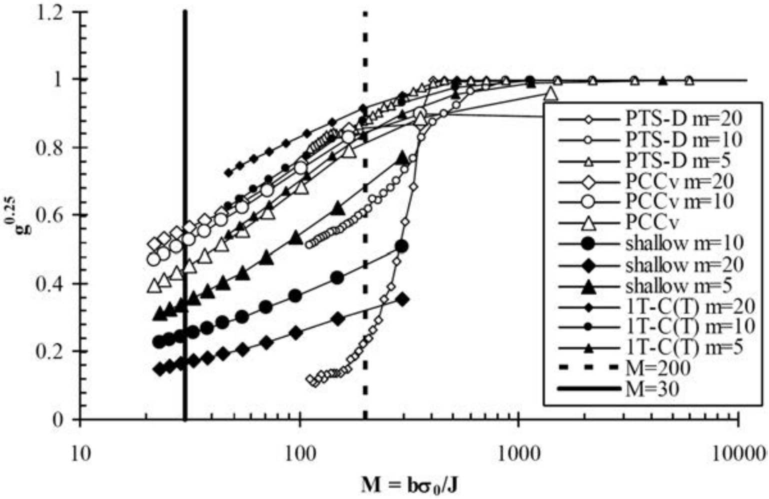

FIG. 9—*Loss of constraint evaluation for different geometries as a function of loading level* (*M*).

$$\sigma_W^m = \int_{Vp} \sigma_1^m \frac{dV}{V_0} \tag{14}$$

where V_0 is a reference volume taken equal to $50^3\ \mu m^3$, σ_1 the maximum principal stress, m the Weibull exponent that typically ranges from 5 to 20, and V_p the volume of integration for which the plastic deformation is larger than zero.

In order to compare the constraint of different geometries, the dimensionless g-function is introduced in [22]. This function is constant when no loss of constraint is observed and decreases with loss of constraint. According to [22], fracture toughness should be normalized by the g-function to the power of $\frac{1}{4}$ to obtain constraint insensitive results. The g-function is defined in [22] as:

$$g(M) = C\frac{\sigma_W^m}{BK^4} \tag{15}$$

where $M = b\sigma_{YS}/J$, b is the ligament equal to $W-a$, B is the crack front length, and C a constant.

The g function is constant in small scale yielding and tends to decrease for lower M values indicating loss of constraint. The g function has been normalized to 1 for 0.5T-C(T) small scale yielding conditions. 3D finite element calculations are performed on the four different geometries. Results are presented in Fig. 9.

The g function given in Fig. 9 is evaluated for the different geometries and summarized in Table 7. In Table 7, the selection of the m value should in principle be based on the procedure described in [22]. However for simplicity, a typical value of 10 has been adopted in this work. The $g^{0.25}$ function is used to normalize the fracture toughness and allows correction of the reference tem-

TABLE 7—*Application of the Beremin model to the experimental data set.*

Type	T_0, °C	Average M	$g^{0.25}$ for $m=10$	T_0 corrected for $m=10$, °C
0.5 T–C(T)	−87	173	0.86	−79
PCCv deep	−91	124	0.78	−78
PCCv shallow	−117	188	0.44	−74
PTS-D	−83	1320	1	−83

perature for loss of constraint. It is assumed that the correction only applies above 30 MPa$\sqrt{}$m. This assumption is used to ensure that the median fracture toughness always remains above 30 MPa$\sqrt{}$m, ensuring that the reference temperature is always defined and reducing the tendency to overcorrect in the Beremin approach.

Instead of applying a mean correction, each fracture toughness data point can be corrected for size and loss of constraint. The applied correction equation is:

$$K_{Jc,1T,SSY} = (K_{Jc} - K_{\min})\left(\frac{B}{B_{1T}}\right)^{0.25} g^{0.25} + K_{\min} \tag{16}$$

Data corrected for size and loss of constraint are given in Fig. 10. In addition, 5, 50, and 95 % confidence bounds derived from the 0.5T-C(T) geometry are also provided. Master Curve analysis based on the ASTM Standard E1921-05 is performed. No data have been censored as the loss of constraint correction allows use of fracture toughness data above the measurement capacity limit. However,

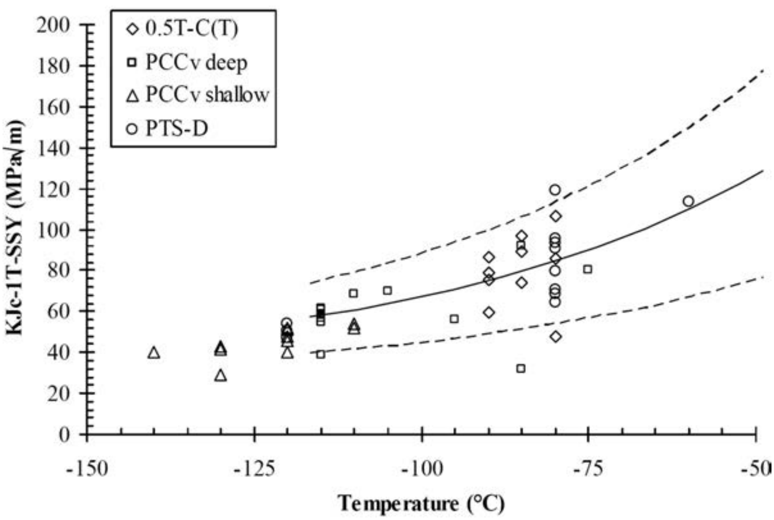

FIG. 10—*Fracture toughness results normalized to* 1 in. *and corrected for loss of constraint using the Beremin model with* $m=10$.

TABLE 8—*Summary of fracture toughness results on the Lemoniz base material. Data are corrected for loss of constraint using the Beremin model with* $m=10$. *N is the total number of tests, r is the total number of valid results which are inside the validity window, and n is an index that should be larger than 1 to have a valid reference temperature per ASTM E1921-05.*

Type	Test temp. range, °C	N	r	n	$T_0 \pm 2\sigma$ °C
0.5T-C(T)	−80 to −90	10	10	1.5	−67 ± 12
PCCv deep	−115 to −75	12	6	0.85	−62 ± 15
PCCv shallow	−140 to −110	12	0	0	N.A.
PTS-D	−120 to −60	12	9	1.5	−67 ± 12

many data points were outside the validity window of ±50°C around T_0 and were not used for the analysis. The analysis is summarized in Table 8.

Discussion

Experimental fracture toughness results in Fig. 4 show a very low data point at −85°C obtained on a PCCv deep crack. The specimen and test procedure were checked but no anomalies were found.

Fracture toughness results on shallow PCCv in Fig. 4 clearly show higher apparent fracture toughness compared to 0.5T-C(T), which is confirmed by the Master Curve analysis in Table 5. This is a clear effect of constraint loss that can be rationalized using both the T-stress and the Beremin approach.

A small difference of the reference temperature between PCCv and 0.5T-C(T) is observed. This difference is expected but cannot be rationalized using just the simple T-stress approach as both geometries have a positive T-stress.

Experimental fracture toughness results on PTS-D in Fig. 4 show that all results are below the median curve except two data points that have a rather large toughness. The reference temperature is equivalent to the 0.5T-C(T) and therefore no actual loss of constraint is observed on the global behavior between PTS-D and 0.5T-C(T). The T-stress approach does not allow one one to rationalize the data as the T-stress is negative and loss of constraint is predicted for this geometry. The Beremin model is much more effective. It demonstrates that loss of constraint exists for this geometry. However, loss of constraint cannot be observed in the testing range except for the two high points. Loss of constraint occurs more abruptly than for other geometries and for lower M values. The Beremin model correlates all four geometries, as shown in Fig. 10. Correcting each fracture toughness data point with the Beremin model results in a shift of the reference temperature of about 20°C for the 0.5T-C(T). The resulting reference temperatures for the different geometries are then within ±3°C.

Conclusions

An experimental investigation of the transferability of fracture toughness from laboratory specimens to specimens simulating PTS conditions has been performed and has been supported by analytical work. The main findings of this works are:

- PTS loading conditions are predominantly biaxial bending. The developed PTS-D geometry and specimen can simulate such conditions.
- Semi-elliptical cracks develop naturally by fatigue. However, the ratio between the two axes cannot be controlled as cracks propagate such that the stress intensity factor is constant along the crack front.
- Equations for the stress intensity factor, the J-integral, and the compliance have been established and support monitoring of crack growth during fatigue loading and fracture toughness evaluation during testing.
- Shallow crack testing of PCCv specimens clearly demonstrates loss of constraint compared to deep crack 0.5T-C(T) and PCCv.
- PTS-D specimens show no loss of constraint within the testing range.
- The T-stress parameter supports correlation of the test results to a certain extent but is unable to rationalize the reason for the low loss of constraint observed with the PTS-D and the difference in T_0 between 0.5T-C(T) and PCCv.
- The Beremin local approach to fracture is rather simple to use and allows a much better correlation of all the data, i.e., PCCv, PCCv shallow, 0.5T-C(T), and PTS-D.

Acknowledgments

This work has been partly financed by Electrabel and Tractebel-Suez; their support is kindly appreciated.

References

[1] ASTM, Standard E1921-05, "Standard Test Method for Determination of Reference Temperature, To, for Ferritic Steels in the Transition Range," *Annual Book of ASTM Standards*, ASTM International, West Conshohocken, PA, 2005.

[2] ISO/DIS 27306:2008, "Metallic Materials—Method of Constraint Loss Correction of CTOD Fracture Toughness for Fracture Assessment of Steel Components," International Organization for Standardization, Geneva, Switzerland.

[3] Wallin, K., "Quantifying T-Stress Controlled Constraint by the Master Curve Transition Temperature T0," *Eng. Fract. Mech.*, Vol. 68, 2001, p. 303.

[4] Sherry, A. H., Wilkes, M. A., Beardsmore, D. W., and Lidbury, D. P. G., "Material Constraint Parameters for the Assessment of Shallow Defects in Structural Components—Part I: Parameter Solutions," , Vol. 72, No. 15, 2005, pp. 2373–2395.

[5] Sherry, A. H., Hooton, D. G., Beardsmore, D. W., and Lidbury, D. P. G., "Material Constraint Parameters for the Assessment of Shallow Defects in Structural Components. Part II: Constraint-Based Assessment of Shallow Defects," *Eng. Fract. Mech.*, Vol. 72, No. 15, 2005, pp. 2396–2415.

[6] Bass, R., Wintle, J., Hurst, R. C., and Taylor, N., NESC-I Project Overview, 2002, EUR 19051EN.

[7] Siegele, D., Schäfer, R., Varfolomeyev, I., and Blauel, J. G., "Analyses of Fracture Toughness Tests and Application to NESC II Thermal Shock Experiments," SMiRT 16, Washington DC, August 2001.

[8] Bass, B. R., McAfee, W. J., Williams, P. T., and Pennell, W. E., "Fracture Assessment

of Shallow-Flaw Cruciform Beams Tested Under Uniaxial and Biaxial Loading Conditions," *Nucl. Eng. Des.*, Vol. 188, No. 3, 1999, pp. 259–288.

[9] Taylor, N. G., Nilsson, K.-F., Minnebo, P., Bass, B. R., McAfee, W. J., Williams, P. T., Swan, D. I., and Siegele, D., NESC-IV project: "An Investigation of the Transferability of Master Curve Technology to Shallow Flaws In Reactor Pressure Vessel Applications," Final Report, 2005, EUR 21846EN.

[10] SCK·CEN Scientific Report 2005, SCK·CEN, Mol, Belgium, 2005 http://www.sckcen.be/sckcen_en/publications/scientrep/05/index.shtml

[11] http://en.wikipedia.org/wiki/Circumference

[12] Lucon, E., Scibetta, M., Chaouadi, R., and van Walle, E., "Fracture Toughness Measurements in the Transition Region Using Sub-Size Precracked Charpy and Cylindrical Bar Specimens," *Small Specimen Test Techniques: Fourth Volume, ASTM STP 1418*, ASTM International, West Conshohocken, PA, 2002, pp. 3–17.

[13] Kirk, M. T., and Dodds, R. H., "J and CTOD Estimation Equations for Shallow Cracks in Single Edge Notch Bend Specimens," *J. Test. Eval.*, Vol. 21, No. 4, July 1993, pp. 228–238.

[14] Stumpter, J. D. G., "Jc Determination for Shallow Notch Weld Bend Specimens," *Fatigue Fract. Eng. Mater. Struct.*, Vol. 10, No. 6, 1987, pp. 479–498.

[15] Scibetta, M., "3-D Finite Element Simulation of the PCCv Specimen Statically Loaded in Three-Point Bending," report BLG-860 revision 1, SCK·CEN Mol, Belgium, March 2000.

[16] Sherry, A. H., France, C., and Goldhorpe, M., "Compendium of T-Stress Solutions for Two and 3D Cracked Geometries," *Fatigue Fract. Eng. Mater. Struct.*, Vol. 18, No. 1, 1995, p. 155.

[17] Beremin, F. M., "A Local Criterion for Cleavage Fracture of a Nuclear Pressure Vessel Steel," *Metallur. Trans. A*, Vol. 14A, 1983, pp. 2277–2287.

[18] Bordet, S. R., Karstensen, A. D., Knowles, D. M., and Wiesner, C. S., "A New Statistical Local Criterion for Cleavage Fracture in Steel. Part I: Model Presentation," *Eng. Fract. Mech.*, Vol. 72, No. 3, February 2005, pp. 435–452.

[19] Margolin, B. Z., Shvetsova, V. A., Gulenko, A. G., and Kostylev, V. I., "Prometey Local Approach to Brittle Fracture: Development and Application," *Eng. Fract. Mech.*, Vol. 75, No. 11, July 2008, pp. 3483–3489.

[20] Anderson, T. L., and Dodds, R. H., "Simple Constraint Corrections for Subsize Fracture Toughness Specimens," *Small Specimen Test Techniques Applied to Nuclear Reactor Vessel Thermal Annealing and Plant Life Extension, ASTM STP 1204*, W. R. Corwin, F. M. Haggag, and W. L. Server, eds., American Society for Testing and Materials, West Conshohocken, PA, 1993.

[21] Wallin, K., and Laukkanen, A., "New Developments of the Wallin, Saario, Törrönen Cleavage Fracture Model," *Eng. Fract. Mech.*, In Press, Corrected Proof, Available online 3 August 2007.

[22] Petti, J. P., and Dodds, R. H., "Calibration of the Weibull Stress Scale Parameter, σu, Using the Master Curve," *Eng. Fract. Mech.*, Vol. 72, No. 1, January 2005, pp. 91–120.

ASTM Special Technical Publication, Vol. 5, No. 4
Paper ID JAI101562
Available online at www.astm.org

Xinglong Zhao,[1] *David Lidbury,*[2] *João Quinta da Fonseca,*[1] *and Andrew Sherry*[1]

Introducing Heterogeneity into Brittle Fracture Modeling of a 22NiMoCr37 Ferritic Steel Ring Forging

ABSTRACT: Microstructural observations of the 22NiMoCr37 "EURO" reactor pressure vessel (RPV) steel ring forging reveal that there is a banded structure along the radial direction, composed of alternate layers rich in bainite and ferrite of wavelength ~1.5 ±0.75 mm. Heterogeneity at this meso (millimetre)-scale as well as at the micro (micrometre)-scale is currently not considered by conventional fracture mechanics. This paper describes the development of two numerical approaches aimed at incorporating such heterogeneity into the Beremin local approach model of cleavage failure, a model that has been used extensively for predicting the brittle fracture of ferritic RPV steels. The approaches developed combine the crystal plasticity finite element method (CPFEM) with continuum finite element analysis (FEA). CPFEM is applied to predict stress distributions at the microscale and to obtain phase-specific yield and flow properties for continuum FEA that derives stresses at the mesoscale. The results confirm that deformation heterogeneity on the micro- and mesoscales influences the local development of stress. At the microscale, the stress distribution within a representative volume of material located within the crack-tip plastic zone is shown to follow a normal distribution with a ratio of mean stress to standard deviation tending towards 0.1. These results indicate local stress levels that are within approximately ±20 % of those derived using continuum FEA. At the mesoscale, a

Manuscript received November 13, 2007; accepted for publication March 6, 2008; published online April 2008.
[1] Materials Performance Centre, School of Materials, University of Manchester, Sackville Street, Manchester M60 1QD, United Kingdom.
[2] Serco Assurance, Birchwood Park, Warrington WA3 6GA, United Kingdom.

Citation: Zhao, X., Lidbury, D., Quinta da Fonseca, J., and Sherry, A., "Introducing Heterogeneity into Brittle Fracture Modeling of a 22NiMoCr37 Ferritic Steel Ring Forging," *J. ASTM Intl.*, Vol. 5, No. 4. DOI10.1520/JAI101562. Available online at www.astm.org. Also included in JAI Special Issue STP 1508, *Fatigue and Fracture Mechanics: 36th Volume*, R. W. Neu, K. R. W. Wallin, and S. R. Thompson, guest editors, ASTM International, West Conshohocken, PA 2009, pp. 518-539.

periodic variation of stress is predicted within the larger representative volume. This variation is less dramatic than that observed at the microscale, though it still gives a spatial variation in maximum principal stress of approximately ± 7 % between bainite- and ferrite-rich microstructural regions. These results suggest a significant influence of deformation heterogeneity on local stress levels, particularly at the microscale. However, the conventional Beremin cleavage fracture model, modified to account for microscale stress distribution, predicts only a modest influence of deformation heterogeneity on cleavage fracture probability, increasing P_f by just 5 %. This highlights the need to account for both the spatial variation in cleavage initiation sites as well as the distribution in stress throughout the microstructure. The paper describes one approach for this development.

KEYWORDS: RPV steel, brittle fracture, Beremin model, microstructural heterogeneity, crystal plasticity

Introduction

Ferritic materials, such as the low alloy steels used to fabricate the reactor pressure vessel (RPV) in a nuclear plant, undergo a transition in fracture mechanism with temperature. At high temperatures, crack growth from a preexisting flaw occurs in a stable ductile manner by the nucleation, growth, and coalescence of voids within the fracture process zone. At low temperatures, crack growth occurs in an unstable manner by the initiation of a fast-running crack from a brittle second phase particle within the plastically deformed metal matrix. Initiating particles are typically inclusions (e.g., manganese sulphide) or carbides that are randomly distributed within the ferrite-bainite microstructure typical of these materials. The crack path is either transgranular, on the low energy {100} "cleavage" planes, or intergranular, along grain boundaries that have been embrittled, e.g., through the segregation of elements such as phosphorus. At intermediate temperatures, limited amounts of ductile tearing can precede brittle fracture.

An understanding of the fracture behavior within the ductile-to-brittle transition temperature regime is critical for the safe and reliable operation of reactors. While pressurized water reactors will normally operate at temperatures that render the RPV material fully ductile, particular abnormal loading conditions (e.g., pressurized thermal shock) as well as start-up/shut-down conditions, combined with the through-life embrittlement of the material by thermal and fast neutrons, mean that the vessel may be exposed to temperatures within the cleavage fracture regime from time to time. Due to the severity of the consequences of the brittle fracture of the RPV, safety justifications must ensure that such an event remains *incredible*; i.e., defined as a 10^{-7} probability of brittle fracture per year [1].

Safety cases rely on the principles of fracture mechanics to demonstrate a sufficiently low probability of failure. Complementary and supporting evidence can also be obtained using the mechanistic modeling approaches, collectively referred to as Local Approaches. These approaches are based on a mechanistic understanding of the fracture process phrased within a micromechanical model that utilizes the local crack-tip stress and strain fields to calculate a failure probability.

The Beremin Local Approach cleavage fracture model [2] is based on the assumption that cleavage occurs by the build-up of plastic strain in material around hard second phase particles leading to particle cracking and the formation of a microcrack. The resulting microcrack, when greater than a critical size, propagates across neighboring grains, eventually leading to complete failure. The observation of single fractured cleavage initiating particles on the fracture surfaces of ferritic steel specimens tested within the cleavage fracture regime has indicated that cleavage fracture may be considered as a "weakest link" process. Consequently, the Beremin model is phrased within a weakest link statistical framework, in which the probability of cleavage failure P_R is defined by either a two- or three-parameter Weibull distribution:

$$P_R = 1 - \exp\left[-\left(\frac{\sigma_W}{\sigma_u}\right)^m\right] \quad \text{or} \quad 1 - \exp\left[-\left(\frac{\sigma_W - \sigma_{W,min}}{\sigma_u - \sigma_{W,min}}\right)^m\right] \tag{1}$$

where σ_u and m are transferable materials parameters and σ_W is the so-called Weibull stress (with threshold value $\sigma_{W,min}$ in the three-parameter distribution), which is an integral of the maximum principal stress within the fracture process zone (often taken as the crack-tip plastic zone):

$$\sigma_W = \sqrt[m]{\sum_j (\sigma_I^j)^m \frac{V_j}{V_o}} \tag{2}$$

where σ_I^J is the value of the maximum principal stress within an element of volume V_j within the fracture process zone. The parameter V_o is a small statistically independent volume, sufficiently large to contain at least one cleavage initiation site, and is a characteristic of the material. The derivation of the distribution of σ_I within the fracture process zone is normally carried out using continuum finite element analysis (FEA) of the cracked geometry and loading condition of interest, invoking von Mises flow theory for isotropic material.

The Beremin model has been successfully applied to predict the cleavage fracture probability of standard and non-standard fracture mechanics specimens (e.g., see Refs. [3,4]). However, the assumption of isotropic material that follows a standard von Mises flow theory with a random and homogeneous distribution of potential cleavage initiation sites may not always be appropriate. At the mesoscale (millimetre scale), forged RPV steels can exhibit a banded microstructure, while rolled steel can exhibit segregation lines [5]. At the microscale (micrometre scale) RPV steels contain a mixture of bainite packets and ferrite grains. Such microstructural heterogeneity has a consequent influence on the local yield, flow, and fracture behavior of the material, through factors including grain size, bainite structure, carbide size, etc. [6–8].

This paper presents two modeling developments for taking account of the influence of such microstructural heterogeneity on the yield, flow, and fracture properties of a ferritic pressure vessel steel. The paper provides a description of the numerical approaches developed to calculate stress distributions in single- and dual-phase RPV materials, taking account of heterogeneity at the micro-

TABLE 1—*Chemical analyses of EURO material* (wt.%).

Fe	C	Si	Mn	P	S	Cu	Cr	Mo	Ni
Bal	0.22	0.25	0.88	0.007	0.003	0.07	0.39	0.51	0.84

and mesoscales. The paper also describes an approach for incorporating the influence of initiating carbide size distribution on cleavage fracture probability.

Material

The material referenced in this work is a section of a 22NiMoCr37 ferritic steel ring forging of 280 mm thickness known as Euro Reference Material "A," or henceforth the "EURO" material [9]. The material corresponds to quenched and tempered ASTM A508-3 low alloy ferritic steel. The composition of the material is given in Table 1.

Microstructure

The microstructure of the EURO material consists of ferrite and tempered bainite. Figure 1 illustrates the microstructure in the circumferential-radial (C-R) plane of the ring forging. Ferrite is α iron and bainite consists of packets composed of slightly misoriented α iron laths decorated with carbides. At the mesoscale, the microstructure appears banded with alternate ferrite- and bainite-rich regions. The band spacing is variable and within the range 0.75 mm to 2.25 mm. The bands are oriented perpendicular to the radial direction (R) and parallel to the circumferential (C) and axial (A) directions in the original ring forging. At the microscale, the microstructure exhibits bainite

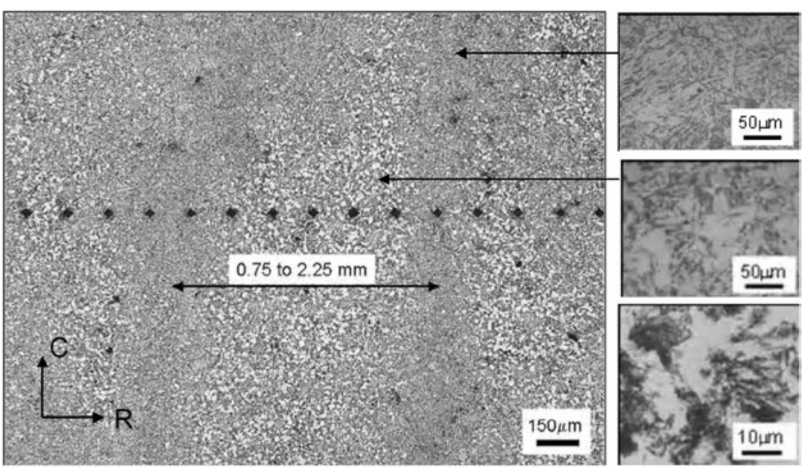

FIG. 1—*Optical micrograph of EURO material in C-R plane, and associated extraction replica showing carbide distribution (lower right).*

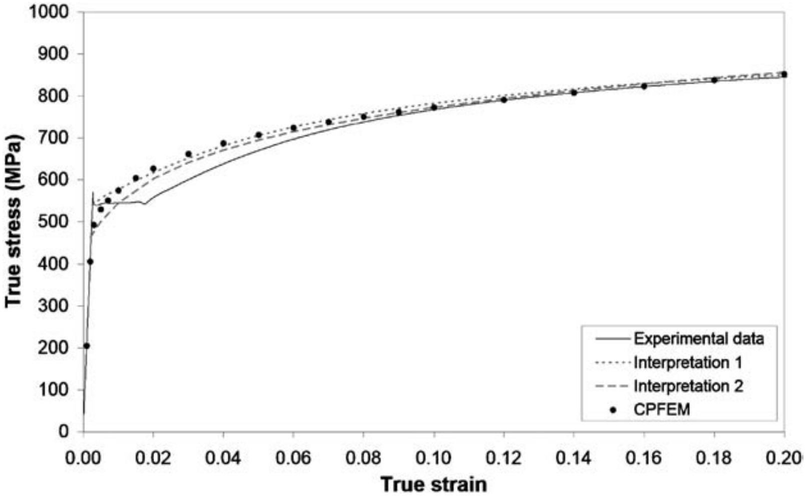

FIG. 2—*True stress versus true strain behavior of EURO material at* −91°C *alongside two interpretations of the data for FEA and fitted CPFEM data.*

packet and ferrite grains of approximate size 15 μm. Quantitative metallographic examination of extraction replicas in the transmission electron microscope has revealed the average volume density of carbides to be approximately 7.6×10^{17} m^{-3}, with the following size distribution [10,11]:

$$F(r) = \exp\left[-\left(\frac{r}{b}\right)^{-a}\right], \quad a = 2.7,\ b = 3.6 \times 10^{-8}\ \text{m} \tag{3}$$

where $F(r)$ is the probability of finding a carbide with radius greater than r.

Material Properties

The tensile stress-strain curve for the EURO material at a temperature of −91°C (within the lower transition regime) is illustrated in Fig. 2 [12]. The raw data give a 0.2 % proof stress close to 550 MPa. The material exhibits Lüders strain and this is variously treated in finite element calculations. Interpretation 1 removes the Lüders strain from the post-yield portion of the curve, maintaining the yield stress close to 550 MPa. Interpretation 2 uses a power-law expression fitted to the work hardening portion of the curve, thus smoothing out the Lüders strain and giving a lower yield stress of approximately 460 MPa. Included in Fig. 2 is the calibrated CPFEM stress versus strain curve, which was fitted to Interpretation 1. This calibration is described in the "Numerical Approaches" section.

The Vicker's hardness properties of the EURO material are location specific and reveal a spatial and periodic variation in properties that is related to the mesoscale banding observed in the microstructure (the hardness indents are visible in Fig. 1). Ferrite-rich regions have a mean hardness of approximately 200 H_v, some 15 % lower than that of the bainite-rich regions, which is approximately 235 H_v. The local yield strength of each microstructural region is assumed to be proportional to the local hardness properties. Based on these hardness measurements, the yield strength of the ferrite-rich regions is assumed to be 510 MPa; i.e., 92.5 % the macroscopic yield strength. The yield stress of the bainite-rich regions is assumed to be 592 MPa; i.e., 107.5 % the macroscopic yield strength.

Numerical Approaches

Modeling Microscale Heterogeneity

Engineers treat metals as homogeneously deforming continua. In reality, most engineering alloys are polycrystalline, containing grains that are elastically and plastically anisotropic. This anisotropy leads to incompatibilities between grains during deformation and consequently deformation at the microstructural scale is heterogeneous. As a result, the stress and strain in each grain is different from the mean stresses and strains in the polycrystal. The stress and strain in each grain are mainly a function of the single crystal anisotropy and the orientation of the grain, but they are also affected by the constraint imposed by neighboring grains. These stresses can be modeled using polycrystalline deformation modeling such as CPFEM [13].

In CPFEM, the grains making up a representative volume (RV) of the polycrystal are represented by a finite element mesh. Each finite element is assigned the properties of a single crystal and a crystallographic orientation. The RV must contain a sufficient number of grains (and orientations), so that the mechanical behavior of the volume is equivalent to that of the bulk. The stress is permitted to vary linearly within each crystal plasticity finite element; i.e., each grain is treated as a discrete continuum. Within the current approach, the discrete polycrystalline aggregate is modeled as a mesh of 20-noded, isoparametric brick elements, each with eight integration points. The RV considered is a cube containing 10 by 10 by 10 elements, each representing an individual (randomly oriented) grain of diameter 15 μm.

In the single-phase formulation of the CPFEM model, where all elements (grains) have the same yield and flow characteristics, the RV of the EURO material is assumed to consist of grains of random orientation; i.e., crystallographic texture is not modeled. In the dual-phase formulation, where all elements (grains) have the yield and flow characteristics of either ferrite or bainite, the RV is assumed to consist of an aggregate of ferrite and bainite grains of random orientation. The following volume fractions of bainite f_b within the RV were studied: f_b=0.00 (100 % ferrite), 0.10, 0.35, 0.50, 0.65, 0.90, and 1.00 (100 % bainite).

Microscale Representative Volume Yield and Flow Behavior—In the CPFEM, plastic deformation is assumed to occur by slip that is rate sensitive according to the following expression [14,15]:

$$\frac{\dot{\gamma}}{\dot{\gamma}_0} = \left(\frac{\tau}{\tau_0}\right)^{\frac{1}{k}} \tag{4}$$

where $\dot{\gamma}$ is the slip rate, $\dot{\gamma}_0$ is a nominal reference slip rate, τ is the resolved shear stress, and τ_0 the instantaneous slip resistance in any given slip system. The rate sensitivity k has a small positive value (typically 0.02) for all systems. Slip hardening behavior is modeled using a modified Voce type law, which describes a power-law decay of the hardening rate from an initial to a final rate. It is given by:

$$\Theta = \Theta_{IV} + \Theta_0\left[\left|1 - \frac{\tau}{\tau_s}\right|^{\alpha} \mathrm{sgn}\left(1 - \frac{\tau}{\tau_s}\right)\right] \tag{5}$$

where Θ_0 is the initial hardening rate, Θ_{IV} is the Stage IV or final hardening rate, τ is the resolved shear stress and τ_s a saturation slip resistance. It is assumed that slip occurs on the $\{112\}$ and $\{110\}$ planes in a $\langle 111 \rangle$ direction; i.e., a total of 24 slip systems.

The macroscopic stress-strain behavior of the single-phase RV conforms to the stress-strain curve illustrated in Fig. 2 for CPFEM. Values for the initial slip resistance and work hardening parameters were determined by calibrating the parameters of the CPFEM model against Interpretation 1 of the EURO materials stress-strain curve using a Taylor factor[3] $M = 2.6$. This process resulted in the following model parameters: $\Theta_0 = 65\,000$ MPa, $\Theta_{IV} = 25$ MPa, $\tau_s = 575$ MPa, and $\alpha = 8$. The initial slip resistance was assumed to be 210 MPa for all slip systems. The values used for the three elastic compliance moduli were: $S_{11} = 7.67$ MPa^{-1}, $S_{12} = -2.83$ MPa^{-1}, and $S_{66} = 8.57$ MPa^{-1}. The resulting macroscopic stress-strain curve is compared with that of the EURO material in Fig. 2.

For dual-phase microstructures, the yield stresses of bainite and ferrite were set equal to 592 MPa and 510 MPa, respectively, based on the spatial variation in hardness properties described in the previous section, "Material Properties." Thus, the calibration for pure bainite set the yield and flow properties to conform to the CPFEM curve illustrated in Fig. 2 elevated by 7.5 %. Conversely, for pure ferrite the calibration produced a macroscopic yield and flow curve that lies 7.5 % below the CPFEM curve shown in Fig. 2.

Microscale Representative Volume Boundary Conditions—The approach for using the calibrated CPFEM model alongside the Beremin cleavage fracture model to account for grain-scale stress heterogeneity is illustrated as a flow diagram in Fig. 3. This flow diagram is referred to in the following description of the boundary conditions applied to the RV.

To calculate the stress distribution due to crystal plasticity at a given location within the plastic zone at the tip of a crack, the CPFEM RV is used as a sub-model to a standard elastic-plastic FEA of the geometry of interest in which the boundary conditions applied to the RV are the three principal strains, i.e.,

[3]The Taylor factor is defined as the ratio of the uniaxial yield stress and the critical resolved shear stress on the slip systems.

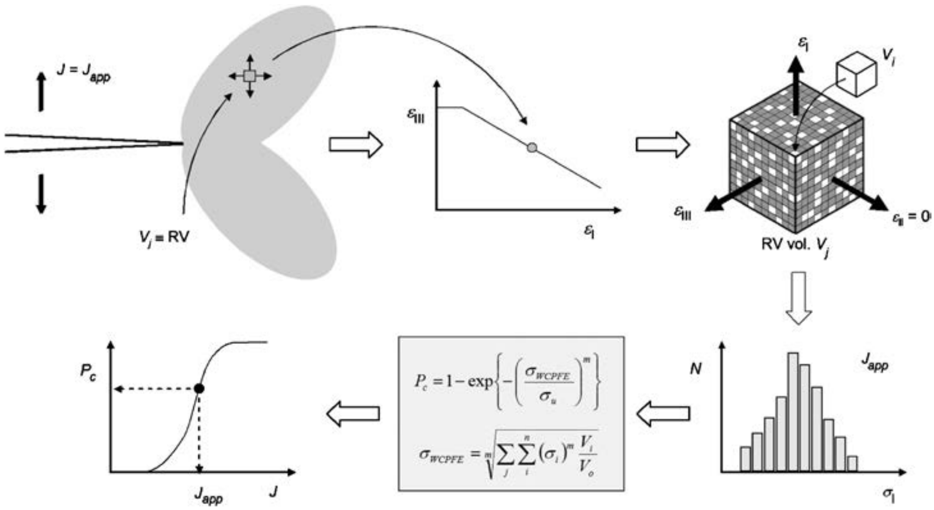

$$P_c = 1 - \exp\left\{-\left(\frac{\sigma_{WCPFE}}{\sigma_u}\right)^m\right\}$$

$$\sigma_{WCPFE} = \sqrt[m]{\sum_j \sum_i^n (\sigma_i)^m \frac{V_i}{V_o}}$$

FIG. 3—*Flow diagram showing the definition of boundary conditions for the RV from the variation in principal strains within the plastic zone and the derivation of cleavage fracture probability from the derived stress distribution within* V_j.

ε_{I}, $\varepsilon_{\mathrm{II}}$, and $\varepsilon_{\mathrm{III}}$, at the location of interest derived from the elastic-plastic FEA. While the intermediate principal strain $\varepsilon_{\mathrm{II}}$ is always set equal to zero for plane strain conditions, the maximum ε_{I} and minimum $\varepsilon_{\mathrm{III}}$ principal strains are dependent upon the particular location of interest. These strains include elastic and plastic components.

- Elastic component. The elastic strains in the maximum and minimum principal directions are *not* equal, being dependent upon the location of the point of interest relative to the crack tip; i.e., $\varepsilon_{\mathrm{I}}^{\mathrm{el}} \neq -\varepsilon_{\mathrm{III}}^{\mathrm{el}}$. This is due to the local variations in stress triaxiality and differences in Poisson's ratio under elastic and plastic conditions.
- Plastic component. Conservation of material during plastic deformation demands that the maximum principal plastic strain $\varepsilon_{\mathrm{I}}^{\mathrm{pl}}$ (which is positive) be of the same magnitude as the minimum principal plastic strain $\varepsilon_{\mathrm{III}}^{\mathrm{pl}}$ (which is negative).Consequently, the total maximum and minimum

principal strains are not of the same magnitude; i.e., $\varepsilon_{\mathrm{I}} \neq -\varepsilon_{\mathrm{III}}$. The RV boundary conditions must correctly reflect the actual relationship between ε_{I} and $\varepsilon_{\mathrm{III}}$ at all locations within the crack-tip plastic zone as a function of increased loading. While this would seem to infer that an almost infinite number of separate CPFEM analyses are required to simulate all points within the plastic zone, each correctly reflecting the local ε_{I} and $\varepsilon_{\mathrm{III}}$ condition at the position of interest, this is not necessarily the case. Figure 4 illustrates the variation in ε_{I} and $\varepsilon_{\mathrm{III}}$ directly ahead of ($\theta = 0°$), and directly behind ($\theta = 180°$) a crack tip calculated using the Hutchinson, Rice, and Rosengren (HRR) field solutions [16,17]] for the EURO material at an applied value of the J-integral of 120 kJ/m^2 using the following Ramberg-Osgood stress-strain behavior:

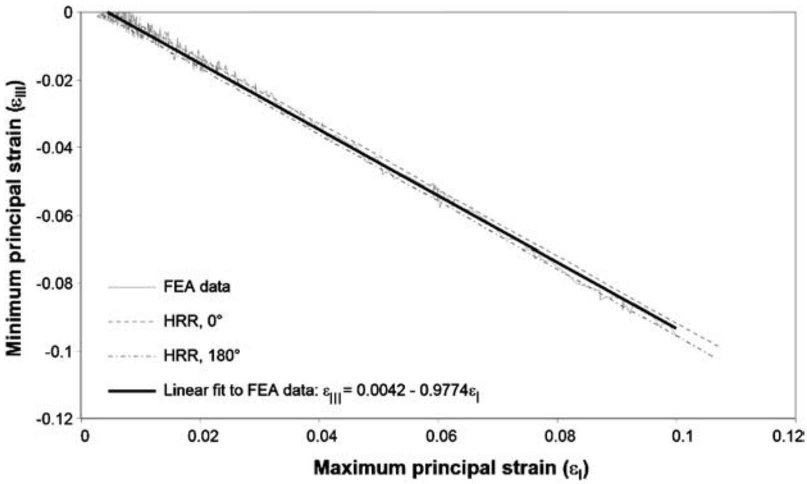

FIG. 4—*Relationship between maximum and minimum principal strains as defined by the HRR field solution and FEA of a compact-tension specimen.*

$$\frac{\epsilon}{\epsilon_0} = \frac{\sigma}{\sigma_0} + \alpha\left(\frac{\sigma}{\sigma_0}\right)^n \tag{6}$$

where ε is the true strain, σ is the true stress, σ_0 is the yield stress, and $\varepsilon_0 = \sigma_0/E$, E being Young's modulus[4]. The relationship between $\varepsilon_{\rm I}$ and $\varepsilon_{\rm III}$ is shown to be approximately bi-linear. Under elastic conditions, $\varepsilon_{\rm I}$ increases rapidly with little increase in $\varepsilon_{\rm III}$. Under elastic-plastic conditions, $\varepsilon_{\rm I}$ and $\varepsilon_{\rm III}$ follow a linear relationship that is only weakly dependent upon location. Examination of the $\varepsilon_{\rm I}$ versus $\varepsilon_{\rm III}$ data derived from an elastic-plastic FEA of a compact-tension specimen at a similar level of applied J using Interpretation 1 of the EURO stress-strain curve (Fig. 2), reveals the majority of data to be bounded by the two HRR lines (Fig. 4). These FEA data are for *all* positions within the crack-tip plastic zone; i.e., from the near tip region (high $\varepsilon_{\rm I}$, $\varepsilon_{\rm III}$) extending to the elastic-plastic boundary (low $\varepsilon_{\rm I}$, $\varepsilon_{\rm III}$).

These data suggest that a *single* CPFEM analysis using the $\varepsilon_{\rm I}$ versus $\varepsilon_{\rm III}$ relationship defined by a linear regression line fitted to the FEA data shown in Fig. 4 may provide a reasonable approximation of the $\varepsilon_{\rm I}$-$\varepsilon_{\rm III}$ relationship for all locations within the crack-tip plastic zone over the range of load levels of interest. This linear regression line is given by:

$$\varepsilon_{\rm III} = 0.0042 - 0.9774\varepsilon_{\rm I} \tag{7}$$

Similar equations can be derived for the $\varepsilon_{\rm I}$-$\varepsilon_{\rm III}$ relationships obtained from analysis of the HRR field solutions [18]. As shown schematically in Fig. 3, for a given level of applied J, each location within the crack-tip plastic zone relates to

[4]The following parameters in Eq 5 provide close agreement with Interpretation 2 of the EURO material curve in Fig. 2: $E = 210$ GPa, $\sigma_0 = 450$ MPa, $\alpha = 1$, and $n = 7$.

a particular position on the ε_{I} versus ε_{III} line. Application of this boundary condition to the RV provides a prediction of the stress distribution due to crystal plasticity at this location within the plastic zone. A single CPFEM calculation using the Eq 7 boundary condition provides series of such stress distributions, each one relating to a different position on the ε_{I} versus ε_{III} line and hence to a specific location within the crack-tip plastic zone at a particular level of applied J. These stress distributions provide the lookup tables necessary to incorporate stress heterogeneity into the Beremin model.

In the current CPFEM analyses, the strain increment used was $\varepsilon_{I}=0.0001$ with a maximum value of ε_{I} being equal to 0.1. The boundary condition Eq 7 was applied using two linear ε_{I}-ε_{III} relationships: for the first 42 steps ($\varepsilon_{I} \leq 0.0042$), strain increments were $\varepsilon_{I}=0.0001$, $\varepsilon_{II}=0.0000$, and $\varepsilon_{III}=0.0000$; from step 43 and after, strain increments were $\varepsilon_{I}=0.0001$, $\varepsilon_{II}=0.0000$, and $\varepsilon_{III}=-0.000\,977\,4$. This reproduces the FEA data regression line, as shown in Fig. 4.

Microscale Beremin Model Formulation—When introducing grain scale heterogeneity into the Weibull stress calculation, it is assumed that only the tensile stress in the direction of the maximum macroscopic principal stress can initiate cleavage fracture. While the continuum FEA provides a single principal stress for a given position within the plastic zone, CPFEM provides a corresponding distribution of stresses, each stress being associated with an individual grain of volume V_i within the RV which has a volume V_j, as shown in Fig. 3.

Microscale heterogeneity can thus be introduced into the Beremin model through the Weibull stress, by replacing σ_I^j within Eq 2 by a distribution of σ_I^j in V_j. The distribution of σ_I^j in V_j is found to follow a normal distribution. When including this effect, the Weibull stress as expressed in Eq 2 can be rewritten as Eq 8. In Eq 8, V_j is considered as the total volume of the RV. The normal stress distribution is divided into n bins (Fig. 3), each of which will have an associated volume V_i (the sum of all such volumes V_1 to V_{1000} will equal V_j), and a mean stress σ_i in the maximum principal direction. The probability of grains having stress of value σ_i is equal to the volume fraction V_i/V_j. In calculating the Weibull stress, this volume fraction is approximated by a normal distribution. Thus:

$$\sigma_{\mathrm{WCPFEM}} = \sqrt[m]{\sum_j \sum_i^n (\sigma_i)^m \frac{V_i}{V_o}} = \sqrt[m]{\sum_j \frac{\left[\sum_i^n (\sigma_i)^m V_i/V_j\right]}{(\sigma_I^j)^m} (\sigma_I^j)^m \frac{V_j}{V_o}}$$
$$= \sqrt[m]{\sum_j \left(\frac{\sigma_{wj}}{\sigma_I^j}\right)^m (\sigma_I^j)^m \frac{V_j}{V_o}} \quad (8)$$

If, in all the grains, the mean stress distribution has the same relative spread, $\sigma_N/\mu=\alpha$ (a constant), it can be shown that $\sigma_{wj}/\sigma_I^j=C$, a constant:

$$\sigma_{wj} = \left[\sum_{i}^{n} \frac{(\sigma_i)^m V_i}{V_j} \right]^{1/m} \tag{9}$$

$$= \left[\int_0^{\infty} \sigma_i^m P(\sigma_i) d\sigma_i \right]^{1/m} \tag{10}$$

$$\approx \left[\int_{\sigma_{\mathrm{I}}^j - 4\sigma_N}^{\sigma_{\mathrm{I}}^j + 4\sigma_N} \frac{\sigma_i^m}{\sigma_N \sqrt{2\pi}} \exp\left[-\frac{(\sigma_i - \sigma_{\mathrm{I}}^j)^2}{2\sigma_N^2} \right] d\sigma_i \right]^{1/m} \tag{11}$$

$$= \left[(\sigma_{\mathrm{I}}^j)^m \int_{\sigma_{\mathrm{I}}^j - 4\sigma_N}^{\sigma_{\mathrm{I}}^j + 4\sigma_N} \frac{\left(\sigma_i/\sigma_{\mathrm{I}}^j\right)^m}{\sigma_N \sqrt{2\pi}} \exp\left[-\frac{(\sigma_{\mathrm{I}}^j)^2 \left(\sigma_i/\sigma_{\mathrm{I}}^j - 1\right)^2}{2\sigma_N^2} \right] d\sigma_i \right]^{1/m} \tag{12}$$

$$= \sigma_{\mathrm{I}}^j \left[\int_{1-4\alpha}^{1+4\alpha} \frac{x^m}{\alpha \sqrt{2\pi}} \exp\left[-\frac{(x-1)^2}{2\alpha^2} \right] dx \right]^{1/m} = \sigma_{\mathrm{I}}^j C \tag{13}$$

where $P(\sigma_i) = V_i / V_j$ is the probability density of σ_i, $x = \sigma_i / \sigma_{\mathrm{I}}^j$, and Eq 8 can be rewritten as:

$$\sigma_{\mathrm{WCPFEM}} = C \sqrt[m]{\sum_j (\sigma_{\mathrm{I}}^j)^m \frac{V_j}{V_{\mathrm{o}}}} = C\sigma_{\mathrm{W}} \tag{14}$$

Modeling of Mesoscale Heterogeneity

As illustrated in Fig. 1, the microstructure of the EURO material is made up of alternating bands of ferrite- and bainite-rich material, the hardness (and hence yield stress) of which vary by up to approximately 15 %. The modeling approach used to simulate this mesoscale heterogeneity is based on continuum FEA in which the yield and flow properties vary spatially according to a sinusoidal relationship of wavelength 1.5 mm (the average spacing of ferrite- and bainite-rich regions). Once again, a RV approach is adopted, though the size of the RV is somewhat larger than that described above to model microscale heterogeneity.

Mesoscale Representative Volume Yield and Flow Behavior—The tensile properties of the different microstructural regions were obtained from the CPFEM modeling of dual phase microstructures described earlier in this section. By assuming a linear relationship between the phase composition and the average stress within the CPFEM RV at a given strain, the effect of phase composition on flow behavior along the position perpendicular to the band can be modeled. Thus, the center of bainite-rich band was assumed to have a yield stress of 592 MPa, while that of the ferrite-rich region was assigned a yield stress of 510 MPa. At intermediate regions, the yield stress was scaled linearly between these to extreme values, such that at the mid-position between the bands, the yield stress was 551 MPa.

An ABAQUS user-defined material subroutine [19] was written so that the yield and flow properties of the finite elements element varied sinusoidally along the R-direction, with the highest strength being that of the bainite-rich region and the lowest strength being that of ferrite-rich region.

Mesoscale Representative Volume Boundary Conditions—The mesoscale RV was represented by a 2D plane strain model of dimensions 6 by 6 mm^2 in the C-R plane; i.e., the same plane as that illustrated in Fig. 1. Eight-noded quadrilateral elements were used in the analysis, with a uniform square element size of 0.15 mm. The model was oriented such that the y-direction corresponded to the circumferential C-direction of the ring forging and the x-direction corresponded to the radial R-direction; i.e., the ferrite-bainite bands were oriented parallel to the y-direction in the model.

The boundary conditions applied to the boundary of the model followed Eq 7 with a maximum principal strain $\varepsilon_I = 6\ \%$, a realistically high strain level in the crack tip plastic zone, being applied to the y-direction (C-direction of the ring forging), i.e., parallel to the ferrite-bainite bands, which is the usual loading direction (C-direction) of the fracture toughness tests.

Results

Stress Distribution for Single-Phase Microscale Heterogeneity

For the analysis of single-phase microscale heterogeneity, the distribution of stress in the global maximum principal stress direction σ_x, calculated within the CPFEM RV at an applied strain of 1 % and 10 %, respectively, is shown in Fig. 5. Here, the stresses from all 1000 CPFEM elements, defined as the mean of the eight integration points' values, have been sorted into 13 bins. As shown, the stress is observed to vary within the RV by a significant degree. In order to quantify this distribution, a FORTRAN program was developed to assess the best statistical fit to the σ_x data, with a simplex downhill search method being applied to search for the minimum residual for various statistical distribution functions [20]. As inferred above, the stress was found to be best represented by a normal distribution. The normal probability density function is expressed by Eq 15, where μ is the mean stress and σ_N the standard deviation, which reflects the spread of data:

$$f(x) = \frac{1}{\sigma_N\sqrt{2\pi}} \exp\left[-\frac{(x-\mu)^2}{2\sigma_N^2}\right] \tag{15}$$

where $x = \sigma_x$. The resulting normal distributions are shown in Fig. 5.

In order to assess the significance of the precise boundary conditions used on the derived stress distributions, the relationship between ε_I and ε_{III} derived using the HRR field solutions for $\theta = 0°$ and 180° were also applied to the RV (Fig. 4). The predicted mean stress within the RV was shown to vary by approximately 500 MPa. The mean stress derived using Eq 7 was shown to lie midway

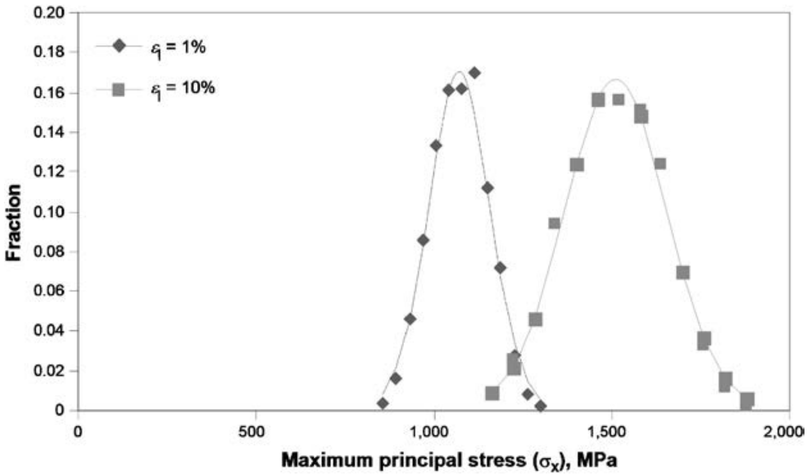

FIG. 5—*Distribution of average grain stress in CPFEM RV for* $\varepsilon_1 = 1$ % *and* 10 %. *Normal distributions are shown.*

between those derived using the relationship between ε_{I} and $\varepsilon_{\mathrm{III}}$ obtained from the HRR field solutions for $\theta = 0°$ and 180° as boundary conditions to the RV.

The relationship between the relative spread of the data, i.e., σ_N/μ, and the applied maximum principal strain is shown in Fig. 6 for each set of boundary conditions. It is apparent that, except for a transient region induced by the onset of plastic deformation at low applied strains, the relative spread of the data saturates above $\varepsilon_{\mathrm{I}} \sim 3$ %.

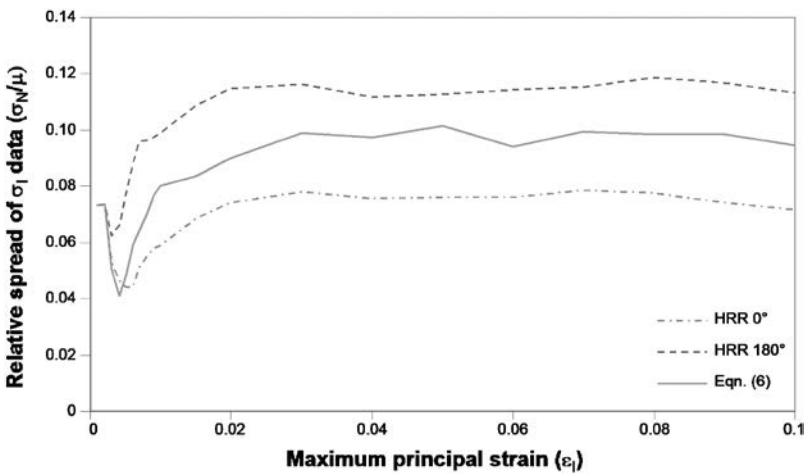

FIG. 6—*Influence of boundary conditions on the relative spread of maximum principal stress data as a function of applied maximum principal strain.*

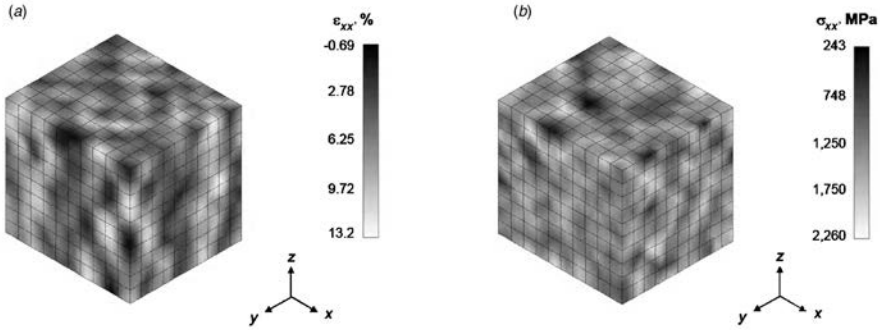

FIG. 7—*Contour plots showing the spatial variation of* (*a*) *strain in the x-direction and* (*b*) *stress in the x-direction for a dual-phase representative volume element containing 50 % bainite.*

Stress Distribution for Dual Phase Microscale Heterogeneity

To evaluate the influence of phase composition on the mean of the maximum principal stress within an aggregate of grains, a series of CPFEM analyses were performed for bainite fractions $f_b = 0$ (pure ferrite), 0.10, 0.35, 0.50, 0.65, 0.90, and 1.00 (pure bainite) with ferrite and bainite grains randomly assigned to elements within the CPFEM model.

Figures 7(*a*) and 7(*b*) show contour plots which illustrate the distribution of strain and stress in the x-directions within the dual-phase RV with $f_b = 0.5$. The contour plots demonstrate that both stress and strain vary significantly over the scale of the elements; i.e., the grain scale.

Figure 8 summarizes the statistical analyses undertaken with respect to the predicted maximum principal stress distributions within the dual phase RV at an applied $\varepsilon_I = 6$ %. This plot represents each dataset as a separate box, each box enclosing 90 % of the data. The bottom and top of each box represent the 5th and 95th percentiles of the data and the three lines drawn inside each box represents the 25th, 50th, and 75th, percentiles of the data. Included in Fig. 8 is a histogram showing the actual stress distribution predicted for $f_b = 0.50$. Figure 8 demonstrates that the median of the maximum principal stress distribution increases modestly with increasing bainite fraction. The mean maximum principal stress predicted for $f_b = 0.00$ (100 % ferrite) is approximately 7 % lower than that for the $f_b = 1.00$ (100 % bainite). For pure ferrite ($f_b = 0$) the range in stress is predicted to be just over 650 MPa. Pure bainite exhibits the largest scatter in maximum principal stress which is over 900 MPa.

The relative spread in maximum principal stresses within RV σ_N/μ was found to be largely independent of f_b and similar to that shown in Fig. 6, i.e., the value of σ_N/μ saturates at approximately 0.1, independent of the proportion of bainite within the RV.

The mean principal stresses are plotted as a function of f_b in Fig. 9. The mean of the maximum principal stress within the ferrite grains and that within the bainite grains are also shown for each proportion of bainite modeled. It is

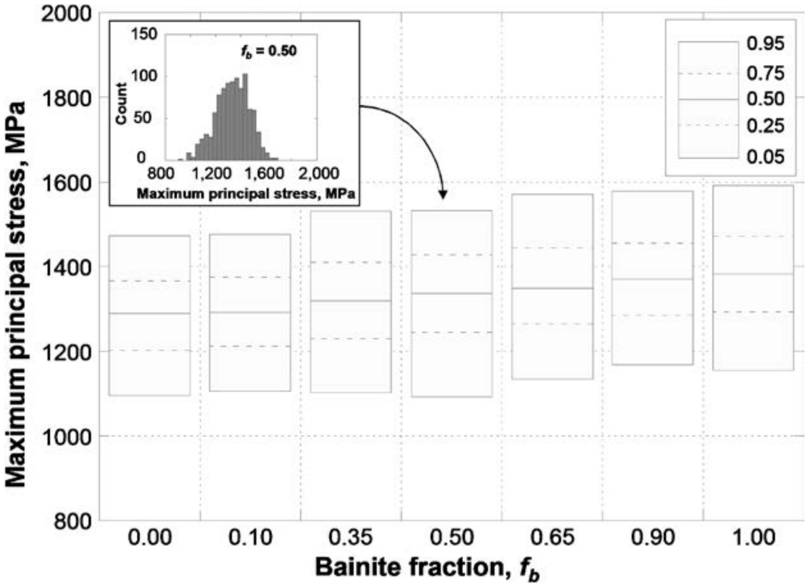

FIG. 8—*Summary plot showing statistical distribution of maximum principal stresses in RVE as a function of bainite fraction for* $\varepsilon_I = 0.6$. *The inset shows the distribution of maximum principal stress with the RV for* $f_b = 0.50$.

apparent that for a given value of f_b, the bainite grains support a higher stress than the ferrite grains. This is expected, since the yield and flow stress of bainite is assumed to be higher than that of ferrite (previous section, "Microscale

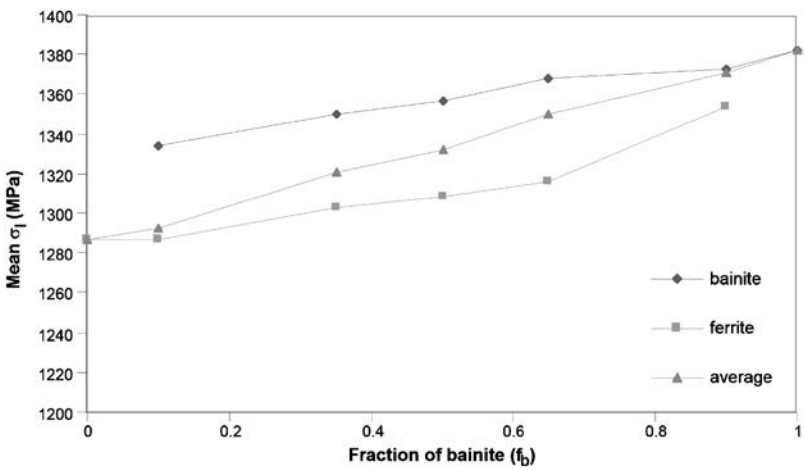

FIG. 9—*Variation of mean maximum principal stress within microscale model as a function of phase composition for* $\varepsilon_I = 0.6$.

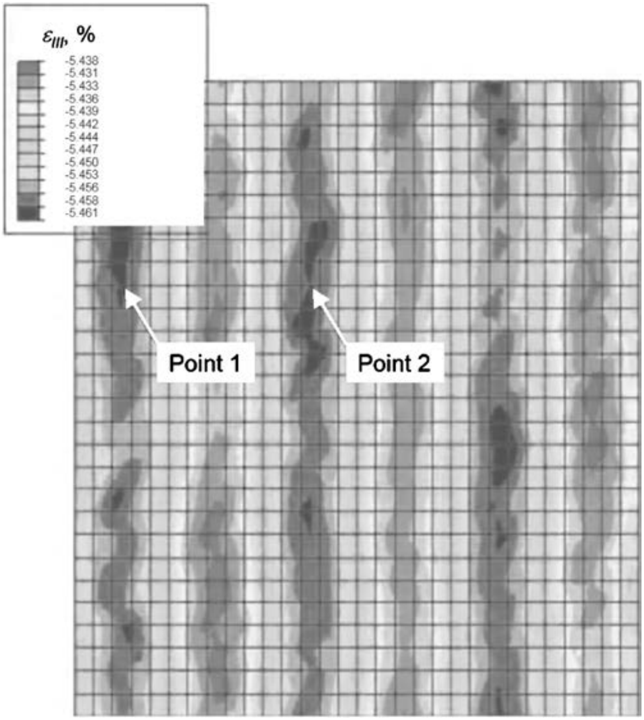

FIG. 10—*Contour plot showing predicted distribution of the minimum principal strain in the mesoscale RVE. Points 1 and 2 indicate the positions* $x=0$ *and* $x=L$ *at the center of the ferrite bands, respectively.*

Representative Volume Field and Flow Behavior”). For $f_b=0.5$, i.e., equal proportions of ferrite and bainite, the mean maximum principal stress within the bainite grains is predicted to be approximately 4 % higher than that within the ferrite grains.

Stress Distribution for Dual-Phase Mesoscale Heterogeneity

Figure 10 illustrates a contour plot showing the distribution of minimum principal strain within the mesoscale RV. As shown the larger (negative) strains are accumulated within the ferrite phase.

Figure 11 illustrates the variation in maximum principal stress as a function of normalized distance x/L, where L is the wavelength of the banded structure and x is defined as the distance from the center of the ferrite band (Point 1 in Fig. 10). The von Mises stress is shown to be approximately 10 % higher in the bainite phase ($x/L=0.5$) than in the ferrite phase ($x/L=0$ and 1). This is to be expected since bainite has a higher yield stress than that of ferrite (previous section, “Mesoscale Representative Volume Yield and Flow Behavior”). The maximum principal stress is shown to be highest within the bainite phase, being approximately 7 % higher than that in the ferrite phase.

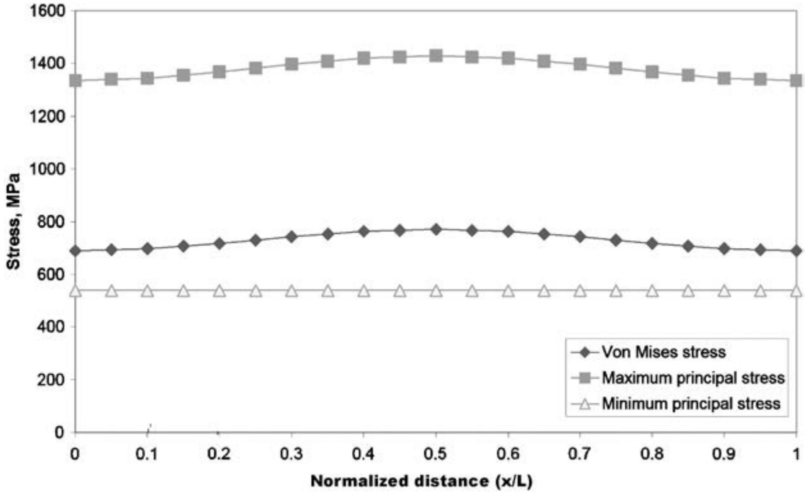

FIG. 11—*Variation of stress as a function of normalized distance within ferrite-bainite banded microstructure. Note the center of ferrite band at* $x/L=0$ *and 1 and the center of bainite band at* $x/L=0.5$.

Discussion

The purpose of studying the influence of deformation heterogeneity on stress distributions at the microscale and mesoscale was to establish a method for including such variations in brittle fracture modeling using fracture models such as the Beremin model.

The stress results presented in the previous section reveal that accounting for deformation heterogeneity at the *microscale* for single phase and dual phase microstructure leads to a normal distribution in maximum principal stress within the RV with a relative spread $\sigma_N/\mu \approx 0.1$. It is worth noting that $\sigma_N/\mu \approx 0.1$ equates to a scatter in maximum principal stress of approximately ±20 % (95 % confidence intervals). At the mesoscale, the predicted variation in stress is less significant for the EURO material studied. In this case a variation in maximum principal stress of less than ±4 % is predicted (Fig. 11).

One might expect the spatial variation in maximum principal stress predicted at the micro- and the mesoscales to influence stress-controlled fracture modes such as cleavage. This aspect is assessed below with reference to the microscale stress distributions derived from the CPFEM analyses, since the scatter in stress is higher than that derived at the mesoscale using continuum FEA. The Beremin cleavage fracture model [2] provides the framework for this assessment.

Using the boundary conditions defined by Eq 7 with a single-phase RV and $\varepsilon_I = 1$ %, the Weibull stress defined by Eqs 14 and 15 gives $\mu = 1071$ MPa and $\sigma_N = 86$ MPa, i.e., $\sigma_N/\mu = 0.08036$. The stress range is divided into 13 groups ($n = 13$), and the stress range considered covers 99.5 % of all possible results. With this particular Weibull stress distribution, σ_{wi}/σ_I^j is found to be equal to

$C = 1.05$. Using the boundary conditions derived from the HRR field at $\theta = 0°$ and 180° with $\varepsilon_I = 1\ \%$, C is found to be equal to 1.03 and 1.07.

These results suggest that microscale stress heterogeneity, even to the magnitude derived by the CPFEM approach, has only a modest effect on the predicted Weibull stress, and consequently cleavage fracture probability as predicted by the Beremin approach. There are likely to be two reasons for this.

First, as shown in Fig. 5, the distribution in σ_I within the RV follows a normal distribution which is quite narrow: the standard deviation is about 0.1 of the mean stress. The integration of a normal stress distribution within the Weibull stress calculation means that the detrimental influence of the higher stress levels on cleavage probability will be offset to some extent by the lower stress levels. The cumulative result is that the derived Weibull stress is little different to the conventional Weibull stress derived using continuum FEA.

Secondly, the Beremin model assumes a homogeneous distribution of cleavage initiation sites, assuming that each volume within the plastic zone contains at least one microcrack [2]. In reality, as shown by the Griffith relationship, the condition for cleavage fracture requires that a stress σ be achieved at a microcrack of critical size d_c, i.e.:

$$d_c = \frac{2\pi E' \gamma}{\sigma^2} \tag{16}$$

where $E' = E/(1-\nu^2)$ under plane strain conditions, ν being Poisson's ratio and γ the material surface energy (often augmented by the work done in plastic strain development, ω_p). This microstructural aspect has not been included within the modified Beremin approach described in subsection "Microscale Beremin Model Formulation," and the modeling approach only assesses the influence of material heterogeneity on local stress. The influence of the resulting stress heterogeneity on predicted cleavage fracture behavior has been shown to be modest for the EURO RPV material.

The Griffith relationship given by Eq 16 suggests that the coincidence of a high local stress with a large microcrack (or brittle particle) will lead to a low fracture toughness value. Conversely, a low local stress coincident with a small microcrack will result in higher fracture toughness values. It is therefore the *combined* influence of the spatial distribution in stress and microcracks that leads to the scatter in fracture toughness properties for ferritic materials.

An important extension to the approach described above is to acknowledge the actual volume fraction and size distribution of cleavage initiating particles within the RV. The method used to extend the model in this way follows that of Mathieu et al. [11] and is briefly described below, where reference is made to Fig. 12 that schematically illustrates the method.

A RV of randomly oriented grains is defined, within which the orientation of each grain in the macroscopic x, y, z coordinate system is known (Fig. 12). The principal stresses in each element within the RV are calculated using CPFEM as a function of increasing applied macroscopic stress Σ[5]. At each

[5]When applied to a cracked geometry, this analysis would use the principal strain boundary condition defined by Eq 7.

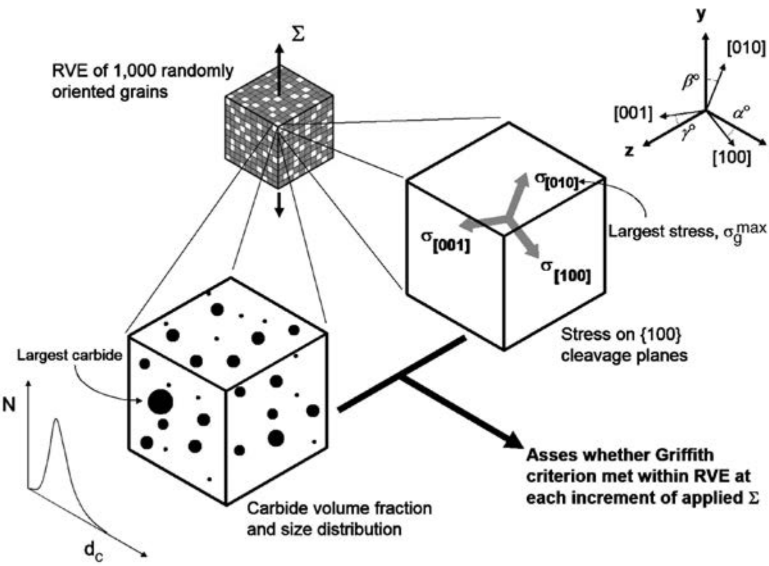

FIG. 12—*Schematic illustration of fracture model used to combine distributions in stress and carbide size on cleavage fracture probability.*

increment in the CPFEM analysis, the principal stresses within each element are resolved perpendicular to the three {100} cleavage planes, i.e., as shown in Fig. 12, $\sigma_{[100]}$, $\sigma_{[010]}$, and $\sigma_{[001]}$ are calculated. The maximum of $\sigma_{[100]}$, $\sigma_{[010]}$, and $\sigma_{[001]}$ within each element (σ_g^{max}) at each increment in the analysis is noted. A spatial distribution of carbides is then assigned to elements within the RV, which is consistent with the measured volume fraction and size distribution of particles for the material of interest; i.e., for the EURO material Eq 3 is used. The maximum carbide within each element is identified and the critical cleavage stress σ_g^c for that element calculated using the Griffith relationship, Eq 16, with an assumed value of γ. The increment in the analysis when $\sigma_g^{max} > \sigma_g^c$ within any of the elements within the RV is identified, and the critical stress Σ^c defined for that assigned distribution of carbides. A new spatial distribution of carbides is then assigned to elements within the RV and a new value of Σ^c calculated. To ensure that the spatial distribution is random and consistent with Eq 3, the inverse function of Eq 3, i.e., Eq 17, is employed, and the particle size is determined by the random number p. By assuming a grain size of 15 μm, a total of 2.565×10^6 particles are generated for the RVE each time. This step is repeated 1000 times to provide a statistically significant number of results in order to rank the critical applied stress Σ^c as a cumulative distribution function.

$$F^{-1}(p) = b[-\ln(p)]^{-\frac{1}{a}}, \quad p \in [0,1] \tag{17}$$

Results from such an analysis, using boundary conditions of uniaxial tensile loading, are illustrated in Fig. 13, where the results for $\gamma = 3$ and 4 J/m^2 are

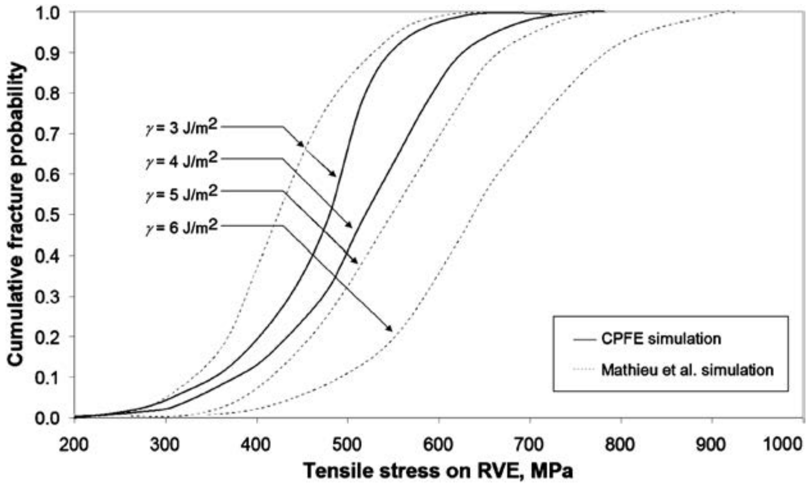

FIG. 13—*Variation of cumulative fracture probability of RVE as a function of macroscopic applied stress* Σ.

compared with results from the work of Mathieu et al. [10]. The modest difference between the results for γ=3 J/m^2 is likely to arise from the mesh refinement used to model each grain within the RV. In the current work, each grain is assumed to be cubic and is modeled by a single CPFEM element, whereas in Mathieu et al.'s work, each grain is represented by a number of elements such that the grain shape is more realistic.

Conclusions

This paper has described two approaches for calculating the influence of deformation heterogeneity on stress development in ferritic pressure vessel steel (the EURO material). Crystal plasticity finite element modeling has been developed to calculate stress heterogeneity at the microscale for both single- and dual-phase microstructures. Continuum FEA has been used to calculate stress heterogeneity at the mesoscale for dual-phase microstructures. The influence of local stress heterogeneity on cleavage fracture probability has been assessed using a modified Beremin model to account for local stress distributions. The following conclusions may be drawn under the assumptions used in this study.

1. For a single-phase randomly oriented microstructure, the *microscale* (grain scale) distribution in maximum principal stress follows a normal distribution. The ratio of standard deviation σ_N to the mean stress μ of the distribution saturates at $\sigma_N/\mu \approx 0.1$ for principal strains greater than approximately 3 %.
2. For a dual-phase randomly oriented microstructure, the *microscale* distribution in maximum principal stress also follows a normal distribution. The σ_N/μ ratio also saturates at approximately 0.1.
3. For a *mesoscale* ferrite-bainite banded structure, the mean principal

stress follows a sinusoidal distribution, the stress being consistently higher in the bainite than in ferrite though by less than 7 % when a maximum principal strain of 6 % is applied parallel to the ferrite-bainite bands.

4. The influence of *microscale* stress heterogeneity on the Weibull stress, and hence on cleavage fracture probability, is modest when a homogeneous distribution of cleavage initiating particles is assumed; i.e., using conventional Beremin model modified to account for stress heterogeneity alone.
5. The combined influence of local distributions of stress and cleavage initiating particle sizes may be accounted for by using the Griffith relationship combined with the crystal plasticity finite element approach and an appropriate statistical distribution of cleavage initiating particles.

References

[1] Bullough, R., et al., "The Demonstration of Incredibility of Failure in Structural Integrity Safety Cases," *Int. J. Pressure Vessels Piping*, Vol. 78, 2001, pp. 539–552.

[2] Beremin, F. M., "A Local Criterion for Cleavage Fracture of a Nuclear Pressure Vessel Steel," *Metall. Trans. A*, Vol. 14A, 1983, pp. 2277–2287.

[3] Sherry, A. H., Lidbury, D. P. G., Bass, B. R., and Williams, P. T., "Developments in Local Approach Methodology with the Application to Analysis/Re-Analysis of the NESC-1 PTS Benchmark Experiment," *Int. J. Pressure Vessels Piping*, Vol. 78, 2001, pp. 237–249.

[4] Lidbury, D. P. G., Sherry, A. H., Bass, B. R., Gilles, P., Connors, D., Eisele, U., Keim, E., Keinanen, H., Lauerova, D., Marie, S., Nagel, G., Nilsson, K., Siegele, D., and Wadier, Y., "Validation of Constraint Based Methodology in Structural Integrity," *Fatigue Fract. Eng. Mater. Struct.*, Vol. 29, 2006, pp. 829–849.

[5] Silva, R. J. C. and Fernandes, F. M. B., "Characterisation of Segregation Band Distributions in Hot-Rolled Alloy Steels," *Key Eng. Mater.*, Vol. 230-2, 2002, pp. 327–330.

[6] Im, Y.-R., et al., "Effect of Microstructure on the Cleavage Fracture Strength of Low Carbon Mn–Ni–Mo Bainitic Steels," *J. Nucl. Mater.*, Vol. 324, No. 1, 2004, pp. 33–40.

[7] Keehan, E., Karlsson, L., et al., "New Developments with C-Mn-Ni High-Strength Steel Weld Metals, Part A – Microstructure," *Weld. J.* (*Miami, FL, U.S.*), Vol. 85, No. 9, 2006, pp. 200S–210S.

[8] Keehan, E., Karlsson, L., et al., "New Developments with C-Mn-Ni in High-Strength Steel Weld Metals - Part B, Mechanical Properties," *Weld. J.* (*Miami, FL, U.S.*), Vol. 85, No. 10, 2006, pp. 218S–224S.

[9] Wallin, K., "Master Curve Analysis of the 'Euro' Fracture Toughness Dataset," *Eng. Fract. Mech.*, Vol. 69, 2002, pp. 451–481.

[10] Ortner, S. R., Duff, J., and Beardsmore, D. W., "Characterization of Euro 'A' Reference Steel for Application of EOH Model of Brittle Fracture," Serco Assurance Internal Report, 2005.

[11] Mathieu, J.-P., Berveiller, S., Inal, K., and Diard, O., "Microscale Modeling of Cleavage Fracture at Low Temperatures: Influence of Heterogeneities at the

Granular Scale," *Fatigue Fract. Eng. Mater. Struct.*, Vol. 29, 2006, pp. 725–737.

[12] Keim, E. (AREVA NP GmbH), private communication, 2003.

[13] Asaro, R. and Needleman, A., "Texture Development and Strain Hardening in Rate Dependent Polycrystals," *Acta Metall.*, Vol. 33, No. 6, 1985, pp. 923–953.

[14] Bate, P. S., "Modelling Deformation Microstructure with the Crystal Plasticity Finite-Element Method," *Philos. Trans. R. Soc. London, Ser. A*, Vol. 357, 1999, pp. 1589–1601.

[15] Bate, P. S. and Quinta da Fonseca, J., "Texture Development in the Cold Rolling of IF Steel," *Mater. Sci. Eng., A*, Vol. 380, Nos. 1–2, 2004, pp. 365–377.

[16] Hutchinson, J. W., "Singular Behaviour at the End of a Tensile Crack in a Hardening Material," *J. Mech. Phys. Solids*, Vol. 16, 1968, 13–31.

[17] Rice, J. R. and Rosengren, G. F., "Plane Strain Deformation Near a Crack Tip in a Power Law Hardening Material," *J. Mech. Phys. Solids*, Vol. 16, 1968, pp. 1–12.

[18] Zhao, X., Lidbury, D. P. G., Fonseca, J., and Sherry, A. H., "Assessing the Effect of Intrinsinc Microscale Heterogeneity on Brittle Fracture of a Ferritic Steel," Paper No. PVP2007-26752, *Proceedings of ASME PVP2007*, ASME Pressure Vessels & Piping Conference, San Antonio, Texas, 22–26 July, 2007.

[19] ABAQUS Version 6.6-1, ABAQUS Inc. (now Simulia), 2006.

[20] William, H., in *The Numerical Recipes in FORTRAN 77: The Art of Scientific Computing*, Cambridge University Press, Cambridge, 1992.

ASTM Special Technical Publication, Vol. 6, No. 2
Paper ID JAI101555
Available online at www.astm.org

B. W. Leitch[1] *and S. St. Lawrence*[1]

Stress-Triaxiality in Zr-2.5Nb Pressure Tube Materials

ABSTRACT: The crack growth resistance of irradiated Zr-2.5Nb pressure tubes is controlled by the initiation of voids and their subsequent growth and coalescence. The presence of particles that contribute to void nucleation is determined by the operating conditions/history of the pressure tube and by the concentration of pre-existing species, which is a function of the manufacturing process. The susceptibility of the pressure tubes to void nucleation is determined by the number and distribution of particles, the deformation properties of the matrix, and the stress state at the crack tip. The effect of irradiation on zirconium material is to increase the yield stress but to reduce the work hardening ability of the matrix and to promote strain localization, which, in turn, leads to void nucleation. Void nucleation is also enhanced by high values of stress triaxiality at or near the crack tip. For irradiated pressure tube material, both small-scale curved compact tension specimens and large-scale burst test sections are used to characterize the crack growth resistance. However, the measured fracture toughness can depend on the specimen geometry due to differences in constraint. The present investigation uses three-dimensional finite element analyses to characterize stress triaxiality at the crack tip in these different specimen geometries. Results of the numerical analyses are compared to the experimental evidence that provide qualitative evidence of differences in stress triaxiality at the crack tip for different specimen geometries.

KEYWORDS: stress triaxiality, J-integral, elastic plastic fracture, Zr-2.5Nb alloy, pressure tubes, burst test

Manuscript received November 23, 2007; accepted for publication November 14, 2008; published online February 2009.
[1] Atomic Energy of Canada Ltd., Chalk River Laboratories, Chalk River, ON, K0J 1P0, Canada.

Citation: Leitch, B. W. and St. Lawrence, S.J, "Stress-Triaxiality in Zr-2.5Nb Pressure Tube Materials," *J. ASTM Intl.*, Vol. 6, No. 2. DOI10.1520/JAI101555. Available online at www.astm.org. Also included in JAI Special Issue STP 1508, *Fatigue and Fracture Mechanics: 36th Volume,* R. W. Neu, K. R. W. Wallin, and S. R. Thompson, guest editors, ASTM International, West Conshohocken, PA, 2009, pp. 540-557.

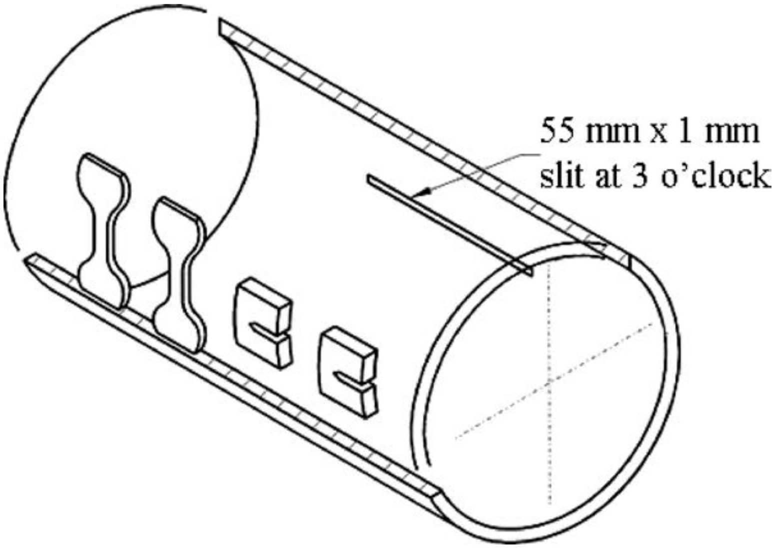

FIG. 1—*Schematic diagram indicating transverse tensile and curved compact tension specimen sampling from burst test section.*

Introduction

The CANDU[2] nuclear power generation system uses natural uranium as the power source. The natural uranium fuel is contained within a series of horizontal tubes. The thermal energy generated by the fuel in the pressurized tubes is extracted using a heavy-water, primary heat transport system. The heat is transferred to a secondary heat transport system via steam-generators, and hence to steam turbines to produce electrical power. The horizontal tubes are enclosed in a large external vessel containing a separate quantity of heavy-water which moderates the reaction. During normal conditions, these tubes operate with an inlet temperature of 265°C and an outlet temperature of 300°C. An internal pressure of 10 MPa maintains the primary transport in a fluid state. The pressurized tubes are rigidly fixed at one end and are free to expand horizontally over bearing pads positioned at the opposite end of the tube. These tubes are manufactured from a zirconium alloy, Zr-2.5Nb, are extruded from a forged billet, and have a 27 % cold work reduction process applied before machining to the final dimensions. The tubes are 6.3 m in length, have an internal diameter of 103.4 mm, and a wall thickness of 4.2 mm.

The fracture toughness of the pressure tubes is needed for leak-before-break analysis and has been characterized using standard ASTM specimens and testing procedures [1,2], with the notable difference that the compact tension specimens are curved rather than flat since they are machined directly

[2]CANDU is a registered trademark of Atomic Energy of Canada Limited (AECL).

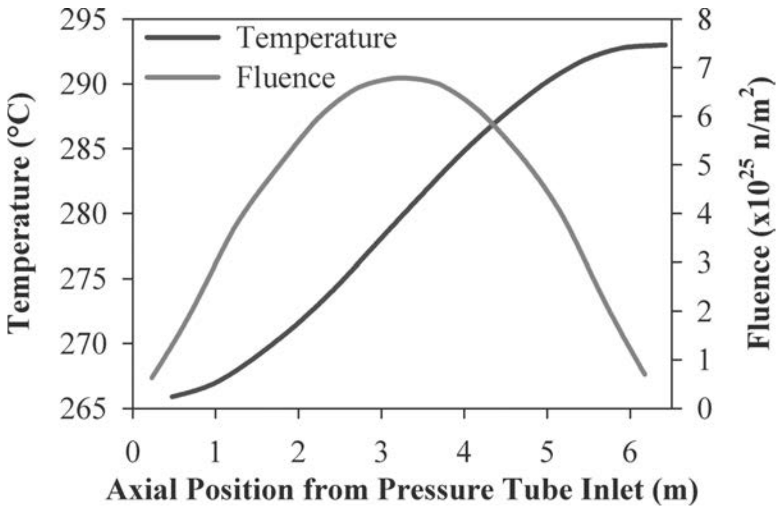

FIG. 2—*Axial distribution of temperature and fluence along the length of an internally pressurized tube.*

from the wall of the pressure tubes as shown in Fig. 1. However, despite the adherence to these standards, careful consideration must still be given to the fracture toughness values determined using these curved compact tension specimens (CCTS) and how these values are related to the pressure tubes within their normal operating environment. The fracture toughness of axially cracked pressure tubes is an important parameter in determining the critical crack length of that tube and, therefore, an accurate assessment of the toughness is needed [3–5].

A previous paper [6], where the stress state of the small-scale specimens and internally pressurized tubes were examined at the same J-integral value, indicated that there did not appear to be any common constraint parameter that could be used to correlate the small specimen results to the full diameter tube results. T [7–11] and Q stress [12,13] and other constraint parameters [14–17] were examined, but a definitive correlation factor or relationship was not evident. In this paper, the anisotropic material behavior of the hexagonal close packed (hcp) crystalline zirconium alloy is considered in the analyses, as well as its effect on the triaxiality [18–22] factor as defined by σ_h/σ_{vm}, where σ_h is the hydrostatic (or mean) stress and σ_{vm} is the von Mises (or equivalent) stress. The previous analyses concentrated on the determination of the constraint fields in the CCTS and tubes where the same average J-integral value was attained. The present analyses use the experimental test loads and crack length values as boundary conditions for the analytical models and examines the stress state and the value of the triaxiality factor for any commonality.

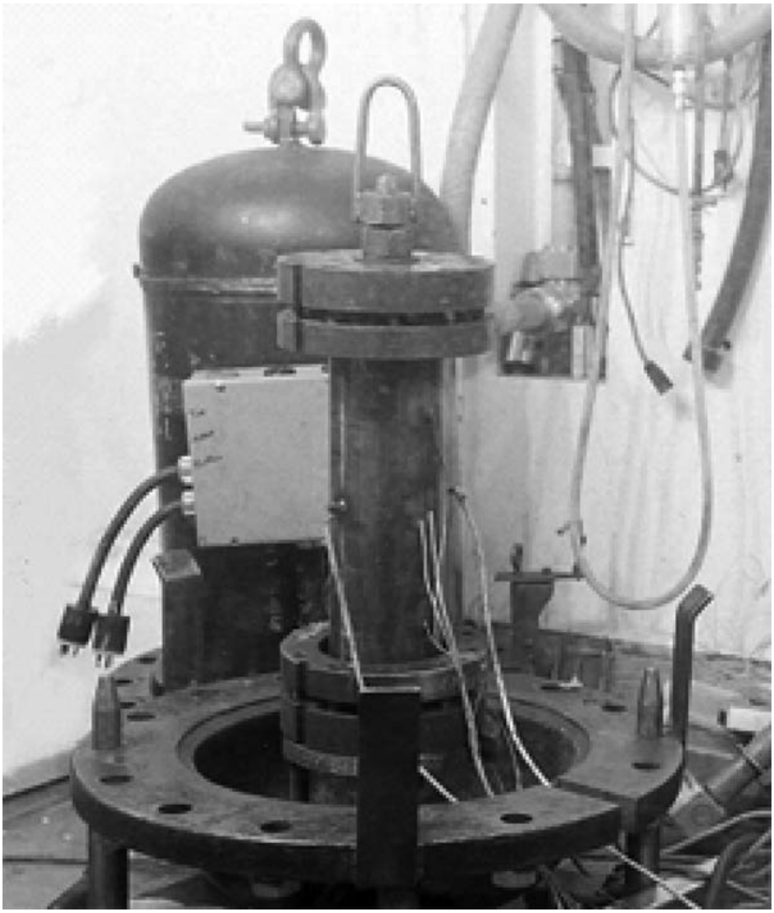

FIG. 3—*Burst test specimen with mechanical end caps and potential drop leads. The bell jar is visible behind the specimen.*

CCTS and Internally Pressurized Tube Experiments

The zirconium tubes are subjected to a long-term aggressive environment of stress, temperature, and irradiation. The nominal stress in the tube is 120 MPa and the axial temperature and fluence variations are indicated in Fig. 2.

A burst test is performed using a 500 mm long section of tube with a spark-machined through-wall axial flaw at the midlength that is fatigue-sharpened at room temperature to a crack length of ~55 mm. The starter flaw is then sealed using a composite patch that is attached to the inside surface using silicone rubber. The ends of the specimen are sealed with mechanical end caps, as shown in Fig. 3. The specimen is then placed in a protective bell jar and heated to the test temperature of 250°C. After soaking at that temperature, the specimen is pressurized to failure with argon gas at a rate that results in an initial rate of increase of the stress intensity factor of 0.75 $\mathrm{MPa}\sqrt{\mathrm{m}}\cdot\mathrm{s}^{-1}$. During

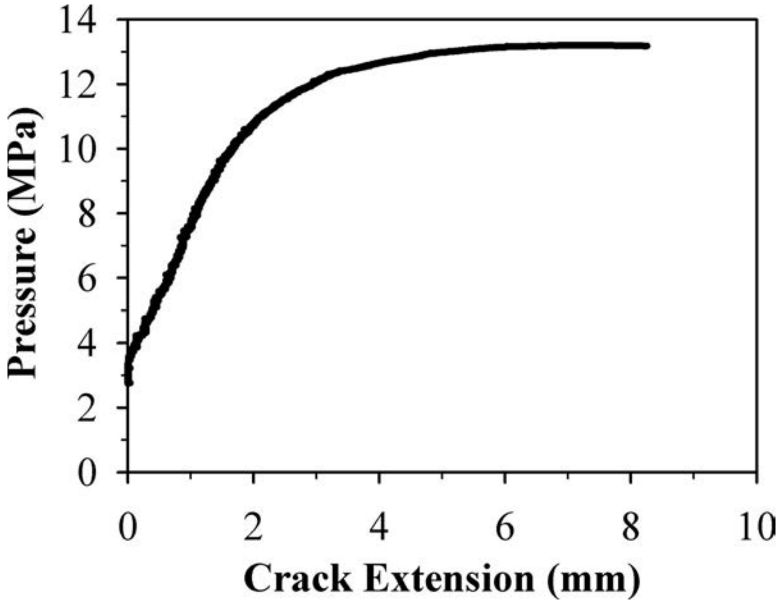

FIG. 4—*Pressure versus crack extension for burst test specimen from pressure tube 735.*

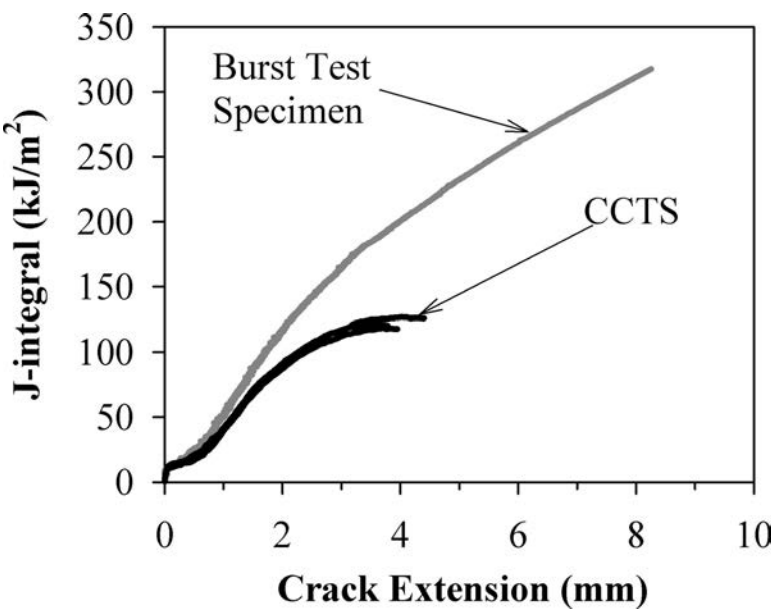

FIG. 5—*Crack growth resistance* (*J-R*) *curves from burst test and curved compact tension specimens of pressure tube 735.*

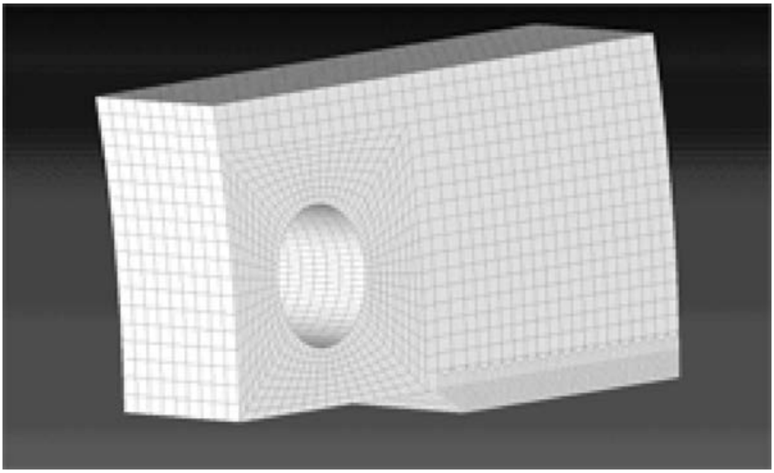

FIG. 6—*Three-dimensional finite element mesh of the CCTS.*

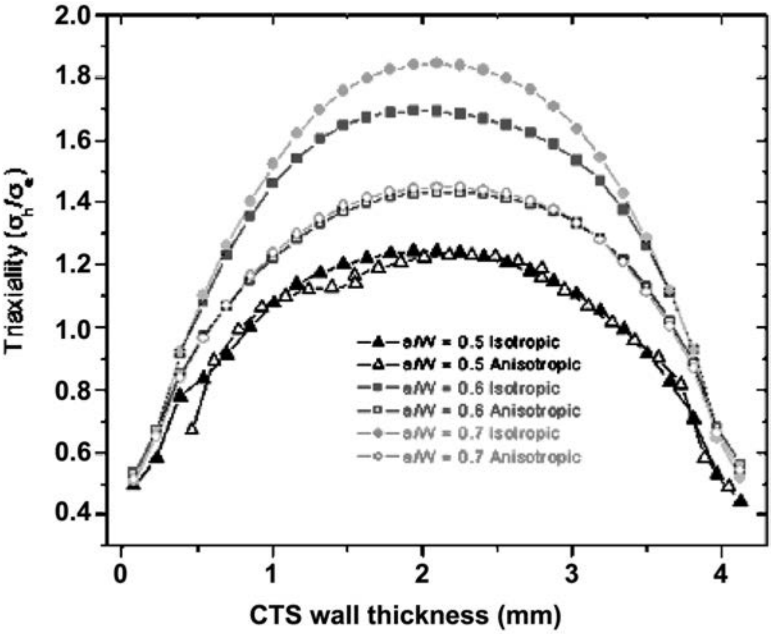

FIG. 7—*Triaxiality measured at* $r = 2J/\sigma_y$ *ahead of the crack for the CCTS isotropic and anisotropic material property analyses.*

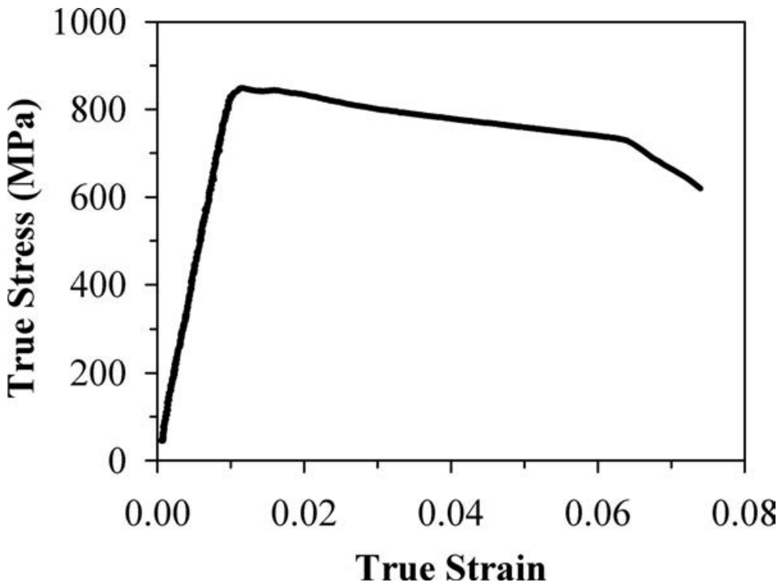

FIG. 8—*True stress versus true strain for a transverse tensile specimen from pressure tube 735 at a test temperature of* 250°C. *The ultimate tensile strength,* σ_{UTS}, *of* 849 MPa *occurs at a uniform elongation of less than 0.2 %.*

the test, the total crack extension is monitored using the potential drop method. Figure 4 shows the pressure versus crack extension during a burst test of a pressure tube specimen. The extended plateau in the pressure versus crack extension curve is typical for a tube of intermediate toughness, as is the large amount of stable crack growth before instability.

Following each burst test, CCTS are machined from the test specimen, as indicated in Fig. 1. The location of the CCTS is at 9:00 o'clock, diametrically opposite to the starter flaw at 3:00 o'clock. The location of the CCTS is chosen to reduce variability resulting from differences in toughness around the circumference of the tube, which allows for a more direct comparison between the two specimen geometries. The toughness of a pressure tube can vary between the top (12:00 o'clock) and bottom (6:00 o'clock) due to flow by-pass resulting from diametral expansion. The planar dimensions of the CCTS are in accordance with ASTM standard [1]. The orientation of the specimens is chosen for crack growth in the axial direction on the radial-axial plane. Prior to testing, the specimens are fatigue-sharpened at room temperature to a starting crack ratio of $a/W=0.5$ and tested at 250°C to a maximum crack ratio of approximately $a/W=0.7$. At the end of the test, the fracture surfaces are heat tinted to mark the final crack extension. The specimens are tested in an air furnace in stroke control at a constant displacement rate of 0.5 $\mathrm{mm \cdot min^{-1}}$. During the test, crack extension is again monitored using the dc potential drop method.

The pressure tube selected for this analysis, identified as 735, was chosen

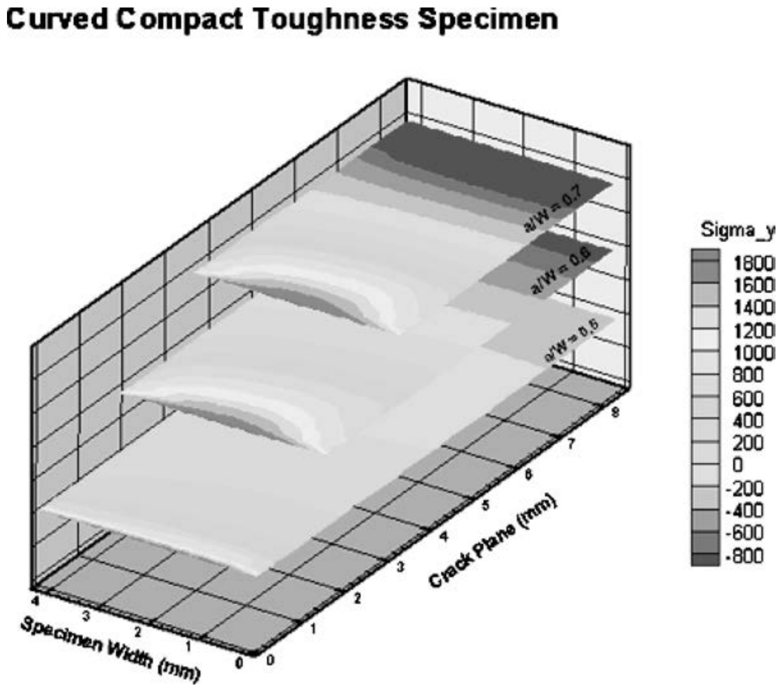

FIG. 9—*CCTS stress normal to the crack plane* (*MPa*) *for* $a/W = 0.5$*, 0.6, and 0.7.*

because it is considered to be of intermediate toughness and is from the same source that was used previously [4]. The wide variation in toughness for Zr-2.5Nb pressure tubes is due in part to a variation in chlorine and phosphorus concentration (25). Generally, material with less than 1 wt ppm Cl exhibits high toughness, between 1 wt ppm and 3 wt ppm Cl intermediate toughness and Cl $\geqslant$ 3 wt ppm lower toughness. Glow discharge mass spectroscopy (GDMS) was used to determine the concentration of Cl and P using off-cut material removed from the pressure tube prior to installation in reactor. For tube 735, the concentrations of Cl and P were found to be 2 wt ppm and 37 wt ppm, respectively.

For pressure tube 735, the shape of the *J-R* curve for both the small- and large-scale specimens is characteristic of intermediate toughness material, with evidence of three distinct stages of crack growth as shown in Fig. 5. For both specimen geometries, there is initially a stage of low resistance to crack growth at small crack extensions, followed by a stage of increasing crack growth resistance (increase in slope) up to approximately 2 mm to 3 mm of crack extension. At still larger crack extensions, there is a reduction in slope until the onset of instability for the burst test specimen or until the test is terminated in the case of the small-scale specimens. The higher crack growth resistance of the burst test specimen compared to the CCTS is characteristic of a tube of intermediate toughness [23,24].

Three-Dimensional Finite Element Analyses

Curved Compact Toughness Specimens

Three-dimensional (3-D) finite element models of the CCTS were constructed. Figure 6 shows the finite element mesh of the CCTS model. Assuming axial symmetry in the CCTS, only half of the specimen was constructed. Finite element models for crack ratios of $a/W = 0.5$, 0.6, and 0.7 were created. Following the experimental load/crack extension data, appropriate pin load values for each crack extension ratio were applied to the finite element models. The finite element program H3DMAP [25] was used to analyze the models since this program has the capability to calculate the anisotropic response of the zirconium hcp material [26].

Nominal isotropic elastic-plastic material properties of Young's modulus $(E) = 90$ GPa, Poisson's ratio $(\nu) = 0.34$, and a yield stress $(\sigma_y) = 500$ MPa were assumed. The triaxiality factor, $\sigma_{h/}\sigma_{vm}$, is plotted (Fig. 7) at a location $r = 2J/\sigma_y$ ahead of the crack tip.

The 3-D analyses were repeated using the anisotropic elasticplastic material properties of zirconium. The following anisotropic material properties were used [26]:

Young's Modulus	$E_{11}=82$ GPa	$E_{22}=93$ GPa	$E_{33}=81$ Gpa
Shear Modulus	$G_{12}=32$ GPa	$G_{23}=29$ GPa	$G_{13}=28$ GPa
Poisson's Ratio	$\nu_{12}=0.29$	$\nu_{23}=0.38$	$\nu_{13}=0.34$
Yield Stress	$\sigma_{y11}=650$ MPa	$\sigma_{y22}=877$ MPa	$\sigma_{y33}=750$ MPa

where (w.r.t. Fig. 1),

11 signifies the axial direction,

22 signifies the transverse or hoop direction, and

33 signifies the radial direction.

An elastic/perfectly plastic stress-strain curve was using the finite element analyses as this reflects the response of an irradiated zirconium material. A typical, irradiated material tensile test result (true-stress/true-strain) is shown in Fig. 8. For such material, very little hardening takes place after the yield stress is attained. Again, the triaxiality factor was extracted from the crack plane ahead of the crack tip, at the $r = 2J/\sigma_y$ location and plotted in Fig. 7. (For the anisotropic analysis results, the triaxiality factor was determined using a nominal $\sigma_y = 500$ MPa.)

The stress acting normal to the crack plane immediately ahead of the crack tip for each of the CCTS a/W ratios is shown in Fig. 9. Similarly, the hydrostatic and the von Mises (equivalent) stresses in this crack plane are shown in Figs. 10 and 11. The triaxiality factor is shown in Fig. 12. These figures were generated from analyses using anisotropic material properties.

Pressurized Tube

3-D finite element models of the zirconium tube were constructed. Applying symmetry boundary conditions, only a quarter of the tube was generated, as

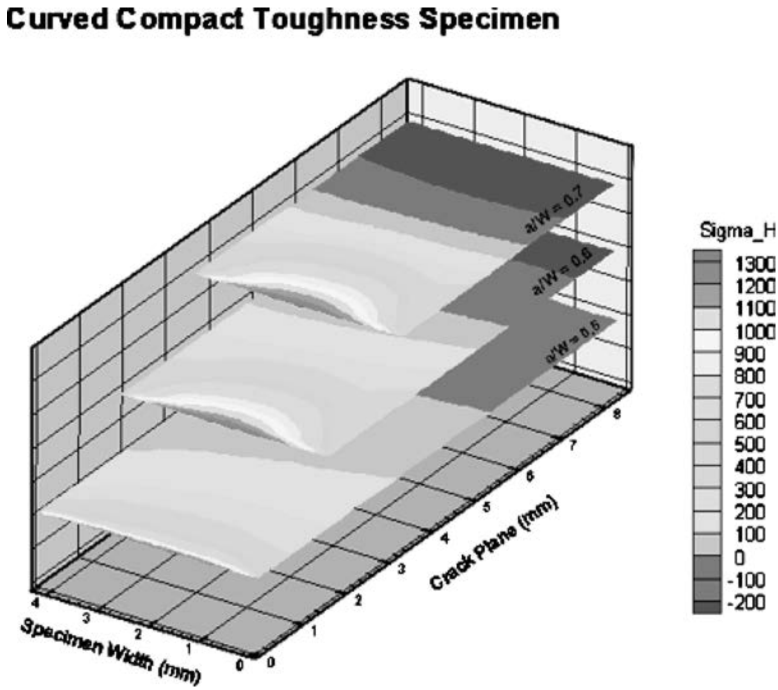

FIG. 10—*Hydrostatic stress in the crack plane (MPa) for CCTS* $a/W = 0.5$*, 0.6, and 0.7.*

shown in Fig. 13. Total axial crack lengths of 56.0, 57.7, and 60 mm were modeled. These crack lengths were selected from the pressurized tube experimental results as they are equivalent to the crack extension for a CCTS at a/W ratios of 0.5, 0.6, and 0.7, respectively. Therefore, similar crack extensions have taken place in both specimen geometries, which provides a common reference point.

It should be noted that the identical 3-D crack tip mesh configurations were used in the CCTS and tube models.

Internal pressure values (and corresponding pressure-induced end-loads) were applied to the tube model. No pressure was applied to the crack faces because in the actual test the crack does not experience the internal pressure load. (In an actual leaking tube, the crack face will experience the internal pressure, and this particular loading condition will be considered in future work.)

As a consequence of the CCTS isotropic and anisotropic analyses, only the anisotropic material properties were used in the tube analyses. Figure 14 shows the tube triaxiality factors measured at $r = 2J/\sigma_y$. The normal, hydrostatic, and von Mises stresses in the plane immediate ahead of the crack tip are shown in Figs. 14–16. Figure 17 shows the triaxiality factor for the burst test specimen.

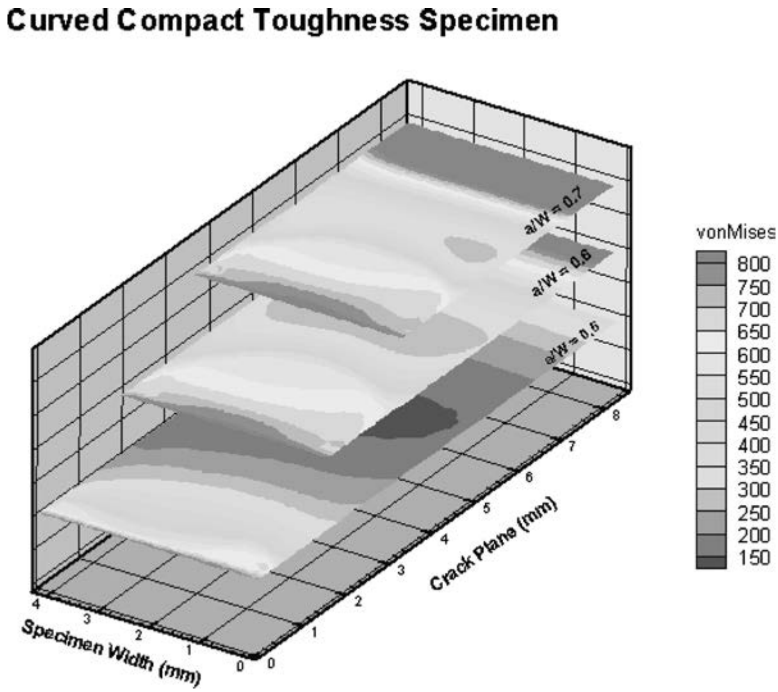

FIG. 11—*von Mises stress (MPa) for the CCTS* $a/W=0.5$*, 0.6, and 0.7.*

Discussion

Comparing Figs. 7 and 12, the anisotropic material properties reduce the triaxiality factor values of the CCTS at $a/W=0.6$ and 0.7 analyses from 1.7 and 1.83, respectively, to a common peak value of 1.4. The peak triaxiality value for the CCTS at $a/W=0.5$ is 1.2 for both the isotropic and anisotropic analyses. The anisotropic triaxiality values for the tube are almost identical, with a peak value of 1.3.

Examining the stress state in the crack plane ahead of the crack, as the crack extends in the CCTS, a predominately increasing bending stress evolves. The compressive stress (Fig. 9) on the back region of the CCTS model increases in magnitude and volume. However, for the pressure tube there is no compressive stress values on the crack plane, as shown in Fig. 15.

A similar condition is evident for the hydrostatic stress (Figs. 10 and 16). The CCTS model has a small negative hydrostatic stress value that increases as the crack extends. The tube again has no negative hydrostatic stress values. As the crack extends axially, the hydrostatic stress in the crack plane of the tube changes slightly.

As the von Mises equivalent stress is a scalar, it is only a very general indicator of the stress condition. The crack tip von Mises value is greater in the tube model (see Fig. 17), than that of the CCTS model (Fig. 11), although in terms of total magnitude, the CCTS model has the greater volume.

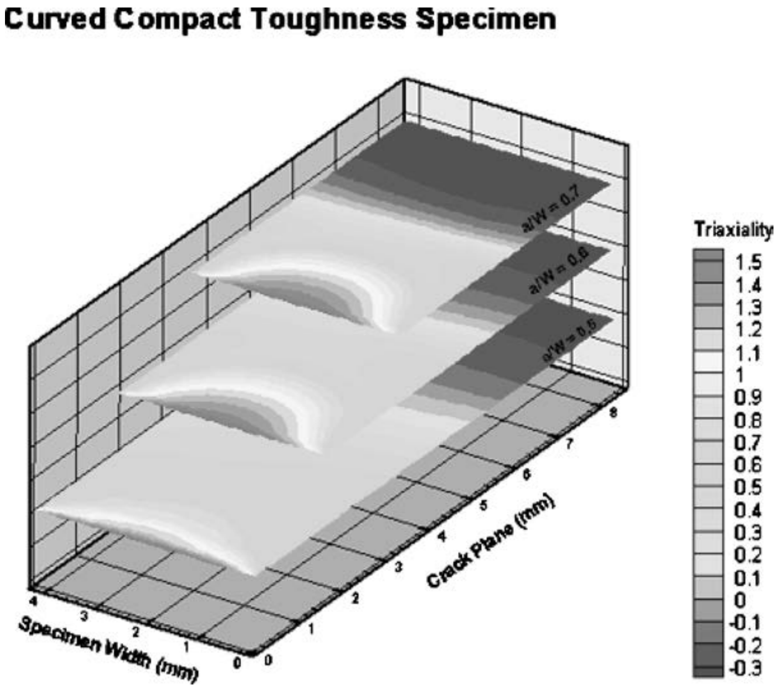

FIG. 12—*Triaxiality values in the crack plane.*

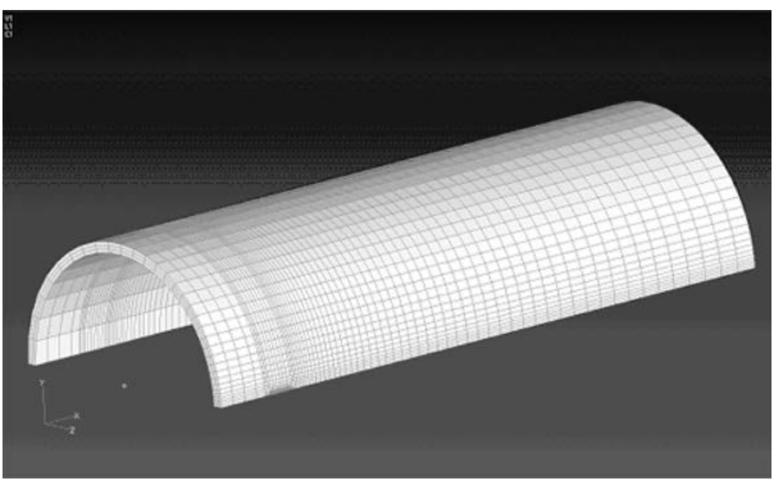

FIG. 13—*Three-dimensional finite element model of pressurized tube.*

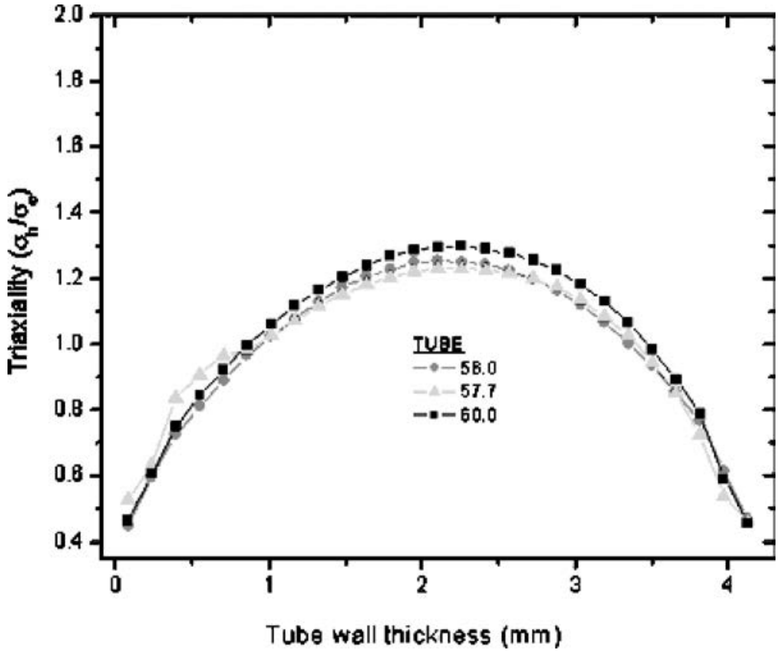

FIG. 14—*Pressure tube anisotropic material properties. Triaxiality at* $r = 2J/\sigma_y$.

The CCTS model shows larger triaxiality values over a greater volume (Fig. 12) than the tube (Fig. 18). Using triaxiality as an indicator of the propensity for void initiation, it would appear that the CCTS has more potential to generate voids at the crack tip than the tube, which is qualitatively supported by experimental evidence showing differences in the fracture surfaces of burst test specimens and matching CCTS [4,23].

The toughness of irradiated pressure tube material in a burst test is determined by the changes in the crack growth behavior. For tubes of low to intermediate toughness, the crack growth resistance at small crack extensions is dominated by a low energy absorbing flat fracture due to the crack tunnelling forward in the region of highest constraint (e.g., highest triaxility) at the midsection. As the crack extends further, a higher energy absorbing transition zone is formed between the flat fracture at the midsection and the region of lowest constraint at the surface. The shear or slant fracture at the surface has a relatively low energy absorbing capacity and its growth through the specimen thickness results in a decrease in crack growth resistance at larger crack extensions. The crack growth resistance is determined by the ability of the crack to tunnel forward at small crack extensions, i.e., at ~3 mm to 4 mm of crack growth, and to initiate slant fracture [4]. For tubes of intermediate toughness, full shear fracture generally develops at larger crack extensions, well beyond the range considered in this analysis. Although the general characteristics of crack growth in a CCTS are similar, the flat fracture zone is typically wider and the shear lips narrower than in the corresponding burst test specimen at the

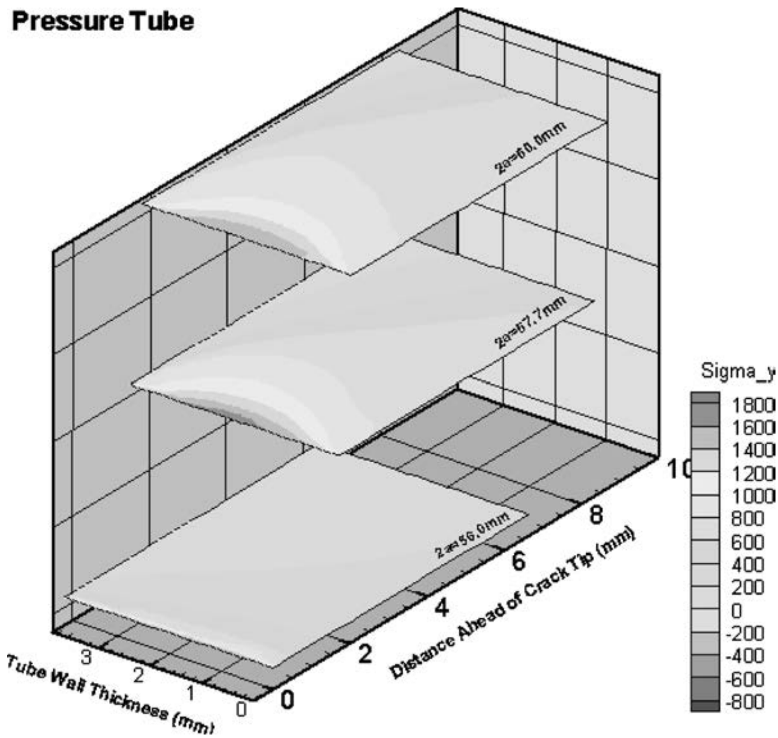

FIG. 15—*Stress (MPa) normal to the crack plane ahead of the axial crack in the tube.*

same crack extension [4]. The difference in the relative portion of flat fracture reflects the difference in triaxility between the bend-type CCTS compared to the biaxial burst test specimen.

Conclusions

The triaxiality factor values of the CCTS and the internally pressurized tube are relatively similar at $r = 2J/\sigma_y$. However, when the triaxiality and stress state ahead of the crack is considered, significant differences are evident between the two geometries. A previous examination of other constraint parameters also highlighted this difference [6].

The convenience of the CCTS technique allows a relative comparison of the temperature and fluence effects on the fracture toughness material to be evaluated. Directly applying these CCTS fracture results to an internally pressurized tube is challenging [24]. The general loading condition of the geometry will influence not only the crack region but also the dynamic response of the specimen when failure occurs. Essentially, a single-edged notch bend specimen is being used to predict when an internally pressurized tube [27] containing a double-edged crack subjected to biaxial loading will fail.

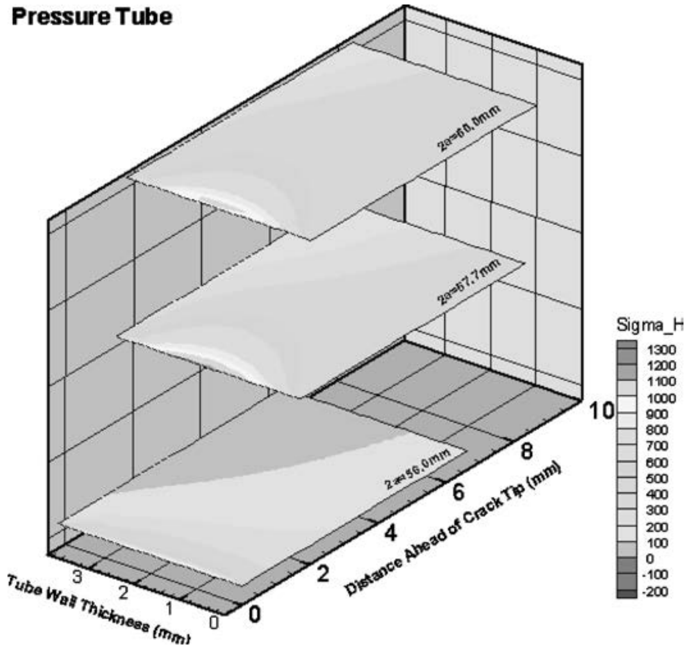

FIG. 16—*Hydrostatic stress (MPa) in the tube.*

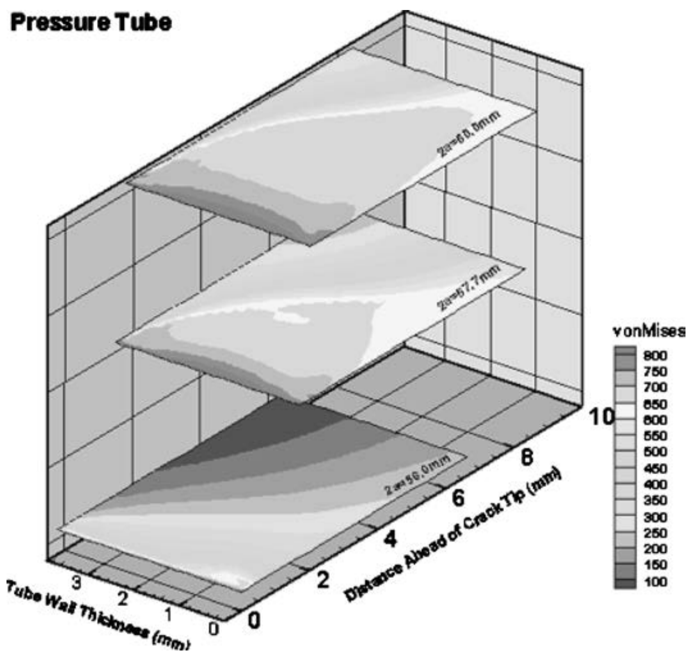

FIG. 17—*von Mises stress (MPa) on the crack plane of the tube.*

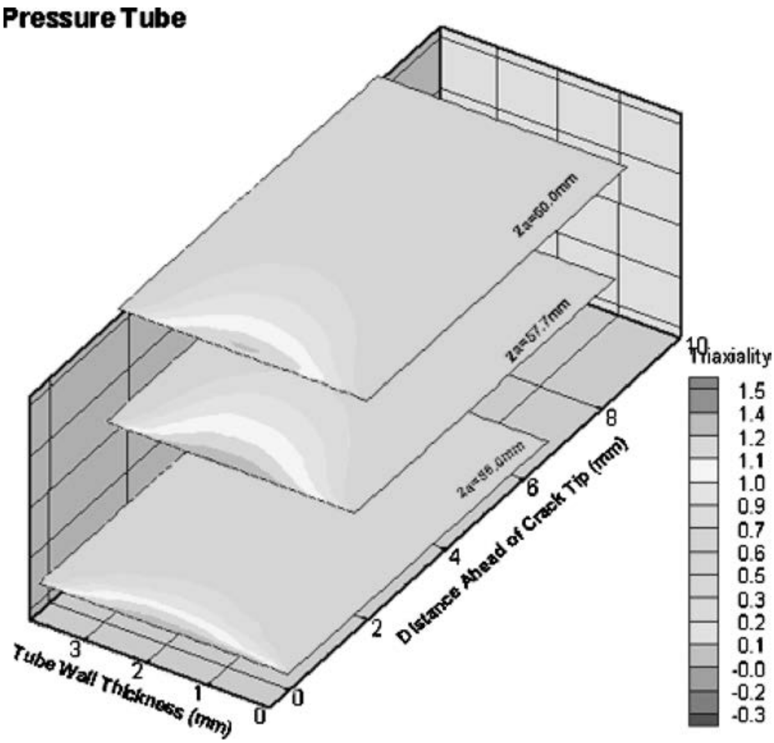

FIG. 18—*Triaxiality factors in the crack plane of the tube.*

Further experimental and analytical work is necessary to address these differences.

References

[1] ASTM, Standard E813-81, "Standard Test for J_{IC}, a Measure of Fracture Toughness," *Annual Book of ASTM Standards*, ASTM International, West Conshohocken, PA, 1981.

[2] ASTM, Standard E399-83, "Methods of Test for Plane-Strain Fracture Toughness of Metallic Materials," *Annual Book of ASTM Standards*, ASTM International, West Conshohocken, PA, 1983.

[3] Simpson, L. A., and Clarke, C. F., "An Elastic-Plastic R-Curve Description of Fracture in Zr-2.5Nb Pressure Tube Alloy," *Elastic-Plastic Fracture, ASTM STP 668*, J. D. Landes, J. A. Begley, and G. A. Clarke, Eds., ASTM International, West Conshohocken, PA, 1977, pp. 643–658.

[4] Davies, P. H., and Shewfelt, R. S. W., "Link Between Results of Small- and Large-Scale Toughness Tests on Irradiated Zr-2.5Nb Pressure Tube Material," *Zirconium in the Nuclear Industry: Eleventh International Symposium, ASTM STP 1295*, E. R. Bradley and G. P. Sabol, Eds., ASTM International, West Conshohocken, PA, 1996, pp. 492–517.

[5] Davies, P. H., and Stearns, C. P., "Axial Fracture Toughness Testing of Zr-2.5Nb Pressure Tube Material," *Fracture Mechanics: Sixteenth Symposium, ASTM STP 868*, M. F. Kannien and A. T. Hooper, Eds., ASTM International, West Conshohocken, PA, 1985, pp. 308–327.

[6] Leitch, B. W., "Fracture Analyses of an Internally Pressurized Tube Containing an Axial, Through-Wall Crack," *Fatigue and Fracture Mechanics*, 29th Volume, ASTM STP 1332, T. L. Panontin and S. D. Sheppard, Eds., ASTM International, West Conshohocken, PA, 1998.

[7] Kfouri, A. P., "Some Evaluations of the Elastic T-Term Using Eshelby's Method," *Int. J. Fract. Mech.*, Vol. 30, 1986, pp. 301–315.

[8] Larsson, S. G., and Carlsson, A. J., "Influence of Non-singular Stress Terms and Specimen Geometry on Small-Scale Yielding at Crack Tips in Elastic-Plastic Materials," *J. Mech. Phys. Solids*, Vol. 21, 1973, pp. 447–473.

[9] Sham, T.-L., "The Determination of the Elastic T-Term using Higher Order Weight Functions," *Int. J. Fract.*, Vol. 48, 1991, pp. 81–102.

[10] Nakamura, T., and Parks, D. M., "Determination of Elastic T-Stress along 3-D Crack Fronts Using an Interaction Integral," *Int. J. Solids Struct.*, Vol. 29, No. 13, 1992, pp. 1579–1611.

[11] Wang, Y.–Y., and Parks, D. M., "Evaluation of the Elastic T-Stress in Surface-Cracked Plates Using the Line-Spring Method," *Int. J. Fract.*, Vol. 56, 1992, pp. 25–40.

[12] O'Dowd, N. P., and Shih, C. F., "Family of Crack-Tip Fields Characterized by a Triaxiality Parameter: Part I -Structure of Fields," *J. Mech. Phys. Solids*, Vol. 39, 1991, pp. 989–1015.

[13] O'Dowd, N. P., and Shih, C. F., "Family of Crack-Tip Fields Characterized by a Triaxiality Parameter: Part II–Fracture Applications," *J. Mech. Phys. Solids*, Vol. 40, 1992, pp. 939–963.

[14] Cruse, T. A., "Lateral Constraint in a Cracked, Three Dimensional Elastic Body," *Int. J. Fract. Mech.*, Vol. 6, 1970, pp. 326–328.

[15] Ruggieri, C., and Dodds, R. H., "WSTRESS Numerical Computation of the Probabilistic Fracture Parameters," Civil Engineering Studies (SRS 608), University of Illinois, UILU-ENG-95-2013, 1995.

[16] Dodds, R. H., Anderson, T. L., and Kirk, T. L., "A Framework to Correlate a/W Ratio Effects on Elastic Plastic Fracture Toughness (J_c)," *Int. J. Fract.*, Vol. 48, 1991, pp. 1–22.

[17] Anderson, T. L., and Dodds, R. H., Jr., "Specimen Size Requirements for Fracture Toughness Testing in the Transition Region," Materials and Mechanics Center, Texas A&M University, MM-6586-90-5, 1990.

[18] McClimtock, F. A., "A Criterion of Ductile Fracture of Voids by the Growth of Holes," *J. Appl. Mech.*, Vol. 35, 1968, pp. 363–371.

[19] Rice, J. R., and Tracy, D. M., "On the Ductile Enlargement of Voids in Triaxial Stress Fields," *J. Mech. Phys. Solids*, Vol. 17, 1969, pp. 201–217.

[20] Du, Z.-Z., and Hancock, J. W., "The Effect of Non-Singular Stress on the Crack-Tip Constraint," *J. Mech. Phys. Solids*, Vol. 39, 1991, pp. 555–567.

[21] Henry, B. S., and Luxmore, A. R., "The Stress Triaxiality Constraint and the Q-Value as a Ductile Fracture Parameter," *Eng. Fract. Mech.*, Vol. 57, No. 4, 1997, pp. 375–390.

[22] Bao, Y., "Dependence of Ductile Crack Formation in Tensile Tests on Stress Triaxiality, Stress and Strain Ratios," *Eng. Fract. Mech.*, Vol. 72, 2005, pp. 505–522.

[23] Davies, P. H., Himbeault, D. D., and Shewfelt, R. S. W., "Crack Growth Resistance of Irradiated Zr-2.5Nb Pressure Tube Material at Low Hydrogen Levels," *Effects of*

Radiation on Materials, 20th International Symposium, ASTM STP 1405, S. T. Rosinski, M. L. Grossbeck, T. R. Allen, and A. S. Kumar, Eds., ASTM International, West Conshohocken, PA, 2001, pp. 846–868.

[24] Davies, P. H., "Predicting Crack Instability Behaviour of Burst Tubes from Small Specimen for Irradiated Zr-2.5Nb Pressure Tubes," *Fatigue and Fracture Mechanics, 28th Volume, ASTM STP 1321*, J. H. Underwood, B. D. Macdonald, and M. R. Mitchell, Eds., ASTM International, West Conshohocken, PA, 1997, pp. 535–561.

[25] Sauve, R. G., and Metzger, D. R., "A Hybrid Explicit Solution Technique for Quasi-Static Transients," *Computer Technology: Applications and Methodology, ASME PVP*, Montreal, July 1996, ASME, New York, Vol. 326, pp. 151–158.

[26] Sauve, R. G., Badie, N., and Lovic, T. G., "A Material Model and Algorithm for Three-Dimensional Anisotropic Elastoplasticity," *Computer Technology, Finite Element Applications: Linear, NonLinear, Optimization and Fatigue and Fracture, ASME PVP*, July 1998, ASME, New York, Vol. 370, pp. 165–174.

[27] McAfee, W. J., Bass, B. R., Bryson, J. W., Jr., and Pennell, W. E., "Biaxial Loading Effects on the Fracture Toughness of Reactor Pressure Vessel Steel," Oak Ridge National Laboratory, NUREG/CR-6273, ORNL/TM-12866, 1995.

FATIGUE CRACK GROWTH

ASTM Special Technical Publication, Vol. 5, No. 8
Paper ID JAI101549
Available online at www.astm.org

Koji Ikematsu,[1] *Takuhiro Mishima,*[1] *Minwoo Kang,*[1]
Yuuta Aono,[1] *and Hiroshi Noguchi*[1]

Effect of Prestrain on Fatigue Crack Growth of Age-Hardened Al 6061-T6

ABSTRACT: The effect of prestrain on fatigue crack growth characteristic (FCGC) of age-hardened Al 6061-T6 was investigated. Al 6061-T6 specimens were subjected to tension to produce plastic strain. Extruded bars were prepared to investigate FCGC. Specimens with an artificial hole from the bar were used to observe Mode I fatigue crack. On the other hand, coarse-grained plain specimens were used and observed for Mode II fatigue crack. Fatigue tests were performed under a rotating bending load ($R=-1$). The experimental results showed the Mode I fatigue crack growth rates decelerated a little due to prestrain. However, in the case of Mode II, fatigue crack growth rates of prestrain specimens accelerated about ten times due to prestrain. The Mode II fatigue crack easily propagates on the slip bands, because precipitation particles on the slip bands are sheared by prestrain. The result means the influence of prestrain on Mode II fatigue should be taken into account for damage-tolerant design.

KEYWORDS: metal fatigue, fatigue crack growth rate, Mode II fatigue crack, Al-alloy, prestrain

Introduction

A number of mechanical parts are subjected to plastic working (prestrain) during the manufacturing process. This influences the mechanical properties and the surface conditions of materials. Damage-tolerant design requires the effect of the plastic deformation on the fatigue behavior. The influence of prestrain on

Manuscript received November 11, 2007; accepted for publication July 8, 2008; published online August 2008.
[1] Department of Mechanical Engineering Science, Kyushu University, Nishi-ku, Fukuoka, Japan.

Citation: Ikematsu, K., Mishima, T., Kang, M., Aono, Y., and Noguchi, H., "Effect of Prestrain on Fatigue Crack Growth of Age-Hardened Al 6061-T6," *J. ASTM Intl.*, Vol. 5, No. 8. DOI10.1520/JAI101549. Available online at www.astm.org. Also included in JAI Special Issue STP 1508, *Fatigue and Fracture Mechanics: 36th Volume,* R. W. Neu, K. R. W. Wallin, and S. R. Thompson, guest editors, ASTM International, West Conshohocken, PA 2009, pp. 561-573.

TABLE 1—*Fatigue test conditions.*

Test ID	Mode of Fatigue Crack	Grain Diameter [μm]	Size of Artificial Hole, $d=h$ [μm]	Prestrain [%]
Test A	Mode I and II	50	none	0, 5.8
Test B	Mode I	50	500	0, 0.34, 2.3, 4.8
Test C	Mode II	800	none	0, 3.7

Note: d = The size of the hole in diameter. h = The size of the hole in depth.

the fatigue characteristics of steel has been studied by many researchers. However, to apply the result of these investigations on steel to other materials, more details of the fatigue process of the materials must be considered. In the case of carbon steel, excepting fatigue crack nucleation, only the Mode I fatigue crack growth appears under tension-compression loading. Although, in age-hardened Al-alloy, many previous studies have revealed that the fatigue crack usually propagates with a switching between Mode I and II [1–4]. Especially, the long Mode II fatigue crack is a unique characteristic of Al 6061-T6, and the fatigue design of Al 6061-T6 should take this Mode II into account. Those studies also revealed that fatigue crack morphology varies upon aging. Otsuka et al. showed that the Mode II crack growth behavior is material sensitive [5]. The effects of loading Mode and sequence on the fatigue behavior of Al 6061-T6 was studied by Lin et al. [6]. Hence, prestrain generated by plastic working is considered to affect the fatigue behavior of the material, but the design guide for this material disregards the influence of prestrain [7].

Thus we must evaluate the effect of prestrain on fatigue characteristics by adding the fatigue characteristic of the Mode II crack to that of the Mode I crack. In the case of Al 6061-T6, the Mode II fatigue crack growth is considered to be easy to propagate and accelerate because of the presence of the slip bands due to prestrain. Therefore, the fatigue life will become shorter if the Mode II crack growth rate or the ratio of the Mode II crack growth to the total crack growth increases as a result of prestrain.

The objective of this study is the investigation of influence of prestrain on Mode I and Mode II FCGC of Al 6061-T6. For this purpose, fatigue tests were carried out. First, the investigation of the fatigue crack that changes to another Mode using plain specimens (Test A) was performed. The crack growth rate scattered widely because fatigue crack growth rates of Mode I and Mode II were different. To separate Modes I and II, fatigue tests were carried out as follows. For the Mode I crack, an artificial hole was formed in the specimen and the Mode I fatigue crack growth rate was measured (Test B). For the Mode II crack, coarse-grained aluminum alloy specimens were produced by solution treatment (Test C). The relationship between the crack growth rate and the difference in the growth Modes are discussed.

Experimental Procedure

The material used in this study was age-hardened Al 6061-T6. It was produced by extrusion. Tables 1 and 2 list the chemical composition and mechanical

TABLE 2—*Mechanical properties of Al 6061-T6.*

E [GPa]	σ_B [MPa]	$\sigma_{0.2}$ [MPa]	δ [%]
68.2	345	330	13.5

Note: E=Young's modulus, σ_B=Tensile strength, $\sigma_{0.2}$=Proof stress, δ=Engineering fracture strain.

properties of the used material, respectively.

All fatigue tests were performed using an Ono-type machine for rotating bending fatigue tests (14.8 Nm, 50 Hz). The difference between the three test conditions is shown in Table 3.

Figure 1 shows the shapes and dimensions of specimens. Figure 2 shows the procedure for preparing and testing specimens. The grain size of the as-received material is about 50 μm in diameter. The specimens for Test C were heated at 530 °C for 24 h as the solution treatment to coarsen the grains in order to investigate Mode II fatigue crack growth. Then T6 age hardening was applied at 180 °C for 8 h to recover the static characteristic. After the solution

TABLE 3—*Chemical composition* (*wt %*) *of Al 6061–T6.*

Si	Fe	Cu	Mn	Mg	Cr	Zn	Ti	Al
0.64	0.17	0.29	0.02	0.94	0.11	0.01	0.01	Bal.

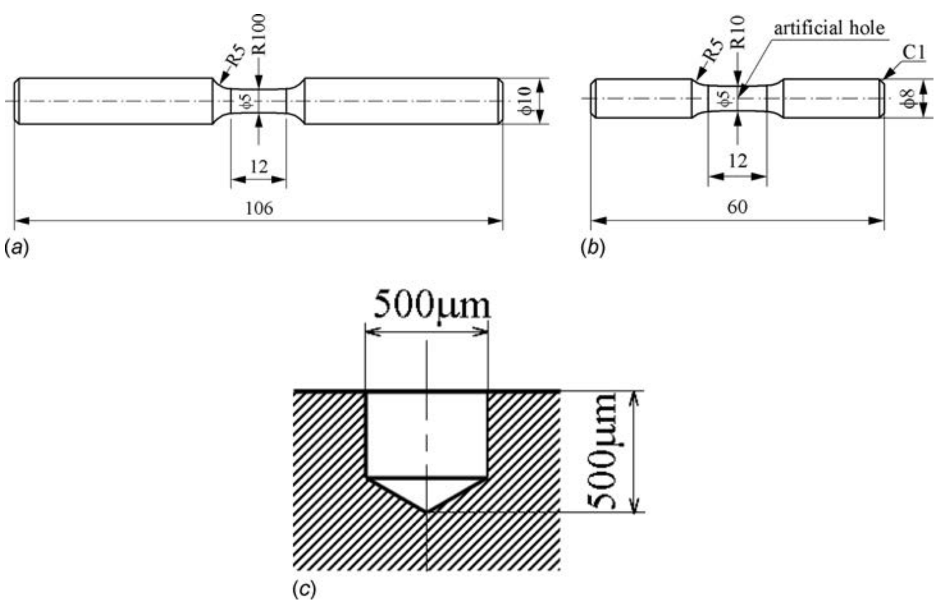

FIG. 1—*Shapes and dimensions of and of prestrained specimens and of prestrained specimens;* (*a*) *tensile prestrained specimen;* (*b*) *rotating bending fatigue specimens;* (*c*) *aritificial hole.*

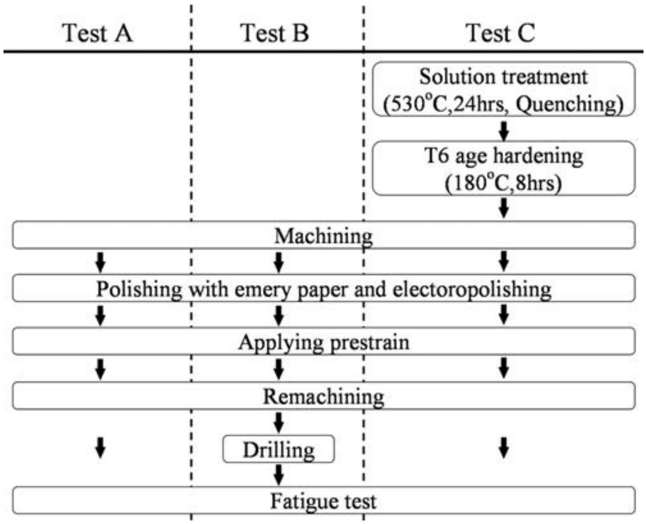

FIG. 2—*Procedure for preparing and testing specimens.*

treatment, the grain size grew to about 800 μm in diameter, but was still unchanged in the axial direction because grains in the extrusion bar were very long in the axial direction. Photographs of etched cross sections before and after the solution treatment are shown in Fig. 3. The central part of all specimens was electropolished to remove the work-hardened layer.

Prestrain was applied to the specimens in Fig. 1(*a*) by a static tensile test. The prestrain is defined as the equivalent plastic strain remaining after tensile deformation. All the prestrained specimens were remachined at the chucking part only, and the central part of the specimen was preserved to retain the effect of prestrain and the surface state as shown in Fig. 1(*b*). Then, the artificial hole

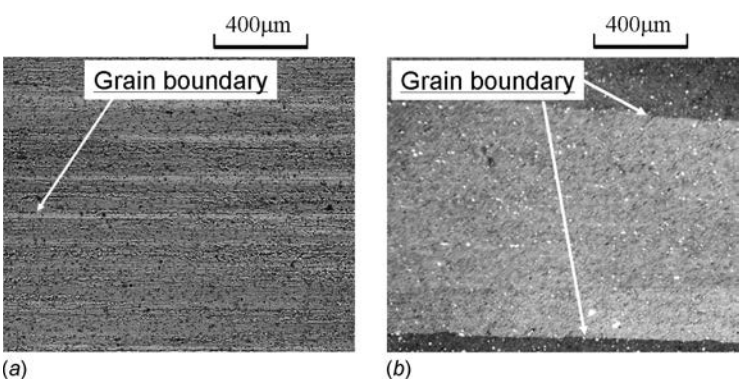

FIG. 3—*Cross sections of 6061-T6 before and after solution treatment;* (*a*) *as-received;* (*b*) *coarsened-grain.*

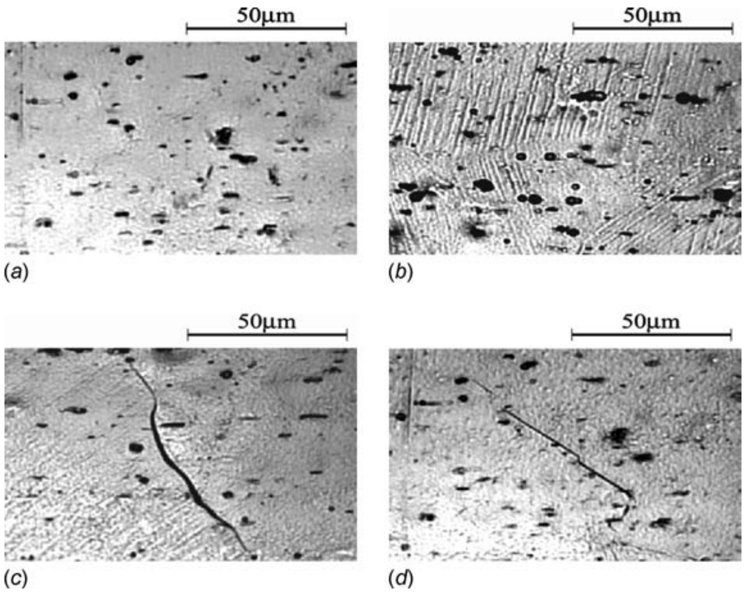

FIG. 4—*Surface states of prestrained specimens;* (*a*) *0 % prestrain;* (*b*) *slip bands due to prestrain;* (*c*) *Precrack in grain boundary;* (*d*) *Precrack in grain.*

was introduced with a microdrill in the central part of the specimens for Test B to investigate the Mode I fatigue crack as shown in Fig. 1(*c*).

The replica method was successively used to monitor the surface condition and the fatigue crack behavior. The replicas of specimen surface roughness were produced by copying on acetyl cellulose films with methyl acetate.

Experimental Results

Result of Test A: Plain Specimen from As-Received Extruded Bar

Figure 4 shows the surface states of specimens before and after applying prestrain. Many slip bands and microcracks (precracks) due to prestrain are observed. Precracks were observed in both the grain and the grain boundary. Enough depth was observed in precracks on replica films. But the slip bands were shallow and vanished by electropolishing of 3 μm depth.

Figure 5 shows the fatigue crack path of the as-received Al 6061-T6 plain specimen as examined by the replica method. The crack propagation was very complicated in that Mode I and II cracks were observed during the whole fatigue life. However, generally speaking, the propagation was Mode II or a mixed mode in the early stage, and gradually changed to Mode I, although Mode II cracks occasionally appeared even after a crack became long. Mode change seemed to occur when a crack passed through a grain boundary. Figure 6 shows fatigue crack growth rates of 0 % and 5.8 % prestrained specimens. The

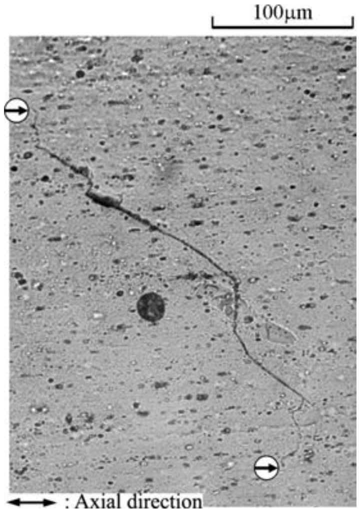

FIG. 5—*Fatigue crack path of as-received plain specimen: 0 % prestrain,* $\sigma_a = 190$ MPa, $N = 1.8 \times 10^5$ cycles, $N_f = 4.02 \times 10^5$ cycles.

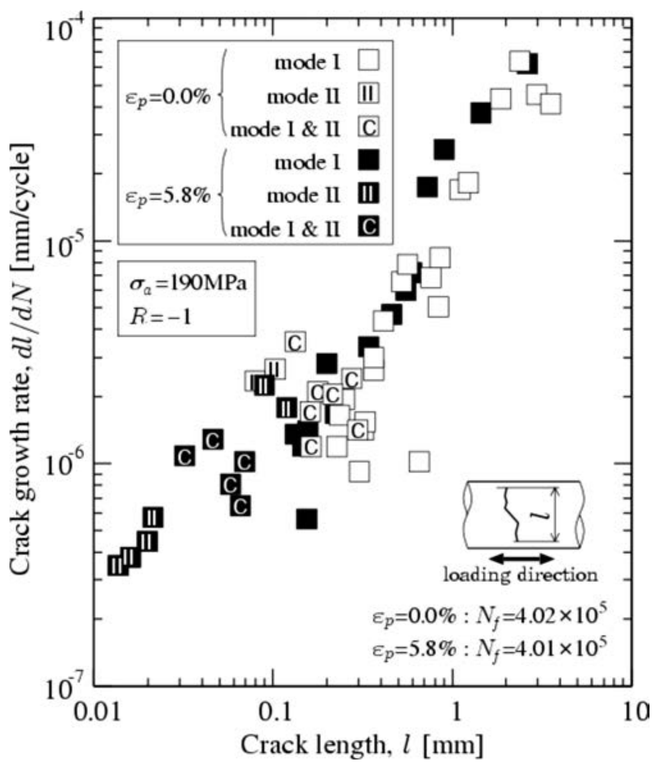

FIG. 6—*Crack growth rate and its mode for as-received plain specimens.*

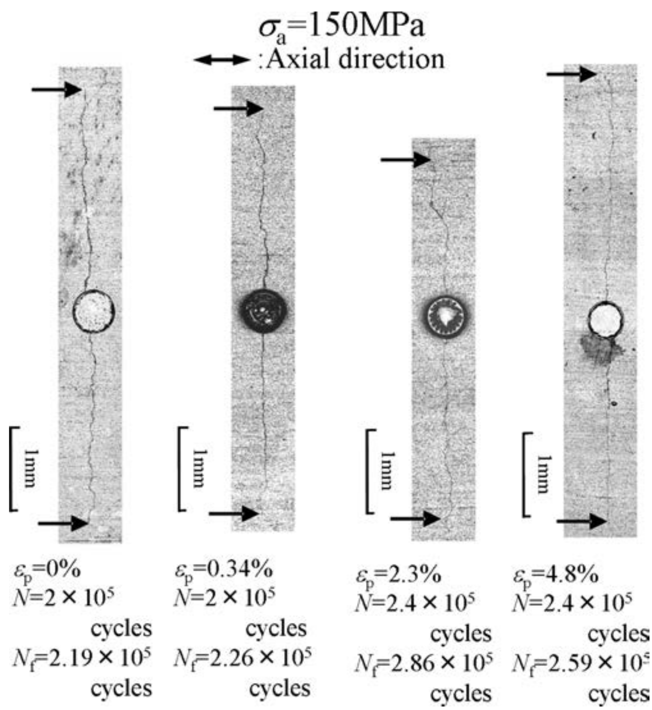

FIG. 7—*Fatigue crack paths of as-received specimens with artificial hole.*

plotted marks represent the Mode of the crack. The crack growth rate in both specimens was scattered and the Mode II and mixed Mode cracks appeared when the crack length was less than about 0.4 mm. In contrast, only Mode I cracks propagated after the cracks became longer than 0.4 mm in both cases. Moreover, no difference was found between the two crack growth rates. The test condition was not appropriate for the observation of each Mode of crack propagation separately.

Two types of specimens to observe single Modes of crack propagation were prepared. For the Mode I crack, an artificial hole was introduced in the central part of the specimen. The artificial hole raises the stress concentration and is regarded as a long crack. Therefore, the Mode of the fatigue crack is expected to be Mode I, which is maintained when the crack passes through grain boundaries of the as-received extruded bar. For Mode II crack, the specimens whose grain size was coarsened by solution treatment were provided. The fatigue crack nucleation is expected to be Mode II and not to change within a grain [8].

Result of Test B: Specimen with an Artificial Hole From As-Received Bar

Figure 7 shows fatigue crack paths of specimens with an artificial hole under the stress amplitude of 150 MPa. Every fatigue crack is in a state immediately

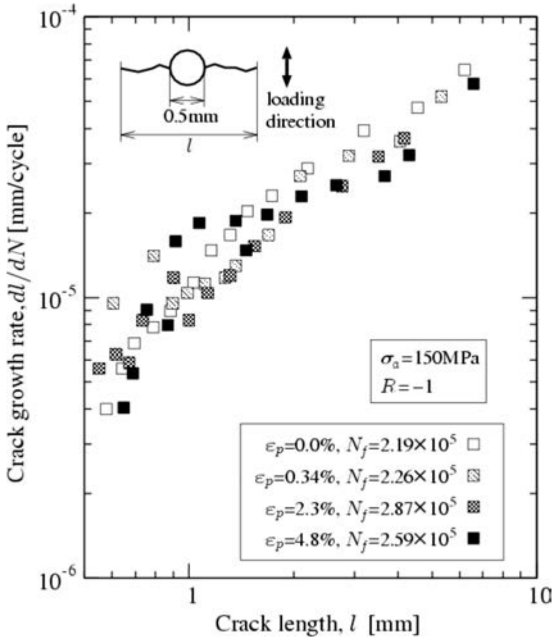

FIG. 8—*Mode I fatigue crack growth rate of as-received specimens with artificial hole.*

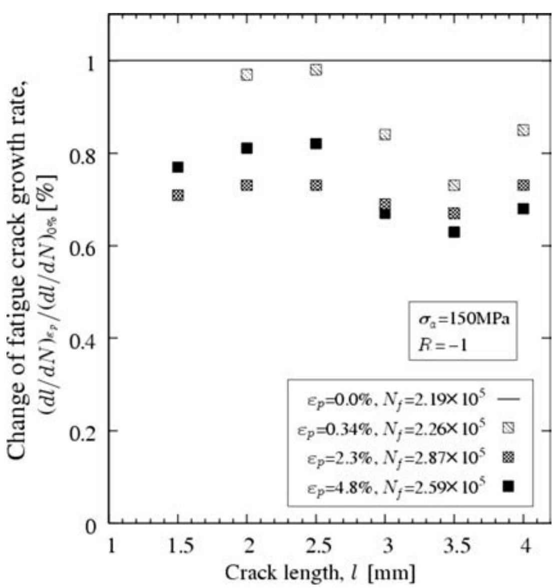

FIG. 9—*Change of Mode I fatigue crack growth rate as a result of applying prestrain.*

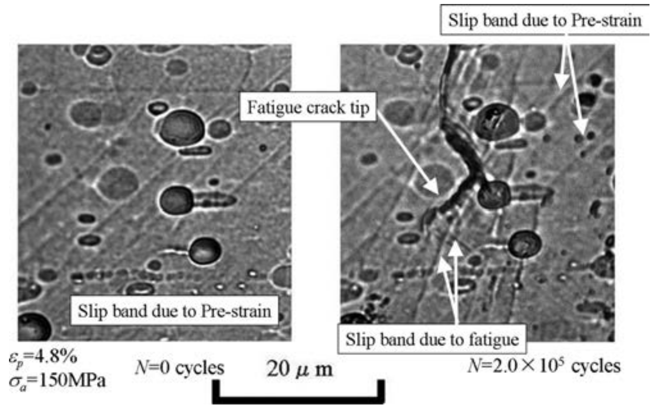

FIG. 10—*Slip bands by prestrain and fatigue crack propagation of as-received specimen with a hole.*

preceding final fracture but prestrains are different. It is found that most of the propagations were Mode I except at crack nucleation and there was no effect of prestrain on the crack Mode.

Figure 8 shows Mode I fatigue crack growth rates. The crack growth rates were scattered when the crack was shorter than about 1.5 mm. It is considered that the area near a hole is influenced by stress concentration, but after the crack became sufficiently long, the mode I fatigue crack growth rates of prestrained specimens became stable and lower than those of 0 % prestrained specimen.

Figure 9 shows the relationship between fatigue crack length and crack growth rate relative to that of 0 % prestrain. The decrease in the crack growth rate as a result of applying prestrain was about 5–40 % regardless of the prestrain value.

Figure 10 shows slip bands due to prestrain and Mode I fatigue crack propagation. The slip bands due to prestrain and those due to Mode I fatigue crack propagation crossed. This disagreement of slip bands is considered to cause the decrease in the crack growth rate after applying prestrain. On the other hand, when the crack propagates on the slip bands due to prestrain, the crack growth rate is considered to be accelerated. These mechanisms resulted in the scatter of the crack growth rate.

Result of Test C: Coarse-Grained Plain Specimen

The fatigue crack paths are shown in Fig. 11. The crack mode of both 0 % and 3.7 % prestrained specimens was Mode II from nucleation to final fracture. In the case of the 3.7 % prestrained specimen, the crack was curved. Detail observation shows that the curved path followed slip bands due to prestrain and the crack propagated in Mode II.

Figure 12 shows the Mode II fatigue crack growth rate. The Mode II fatigue crack growth rates of 3.7 % prestrained specimens were higher than that of the

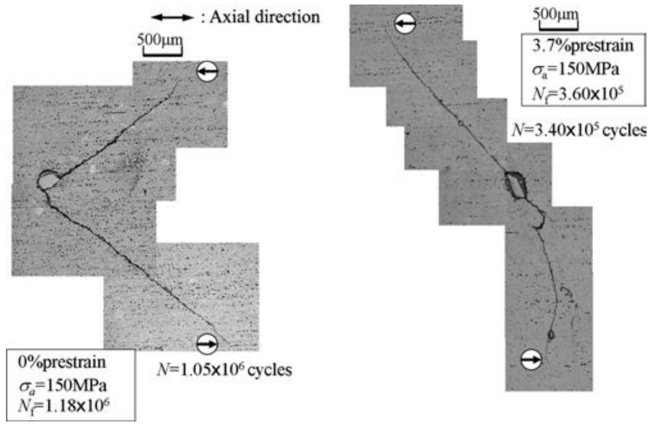

FIG. 11—*Fatigue crack paths of coarse-grained plain specimens.*

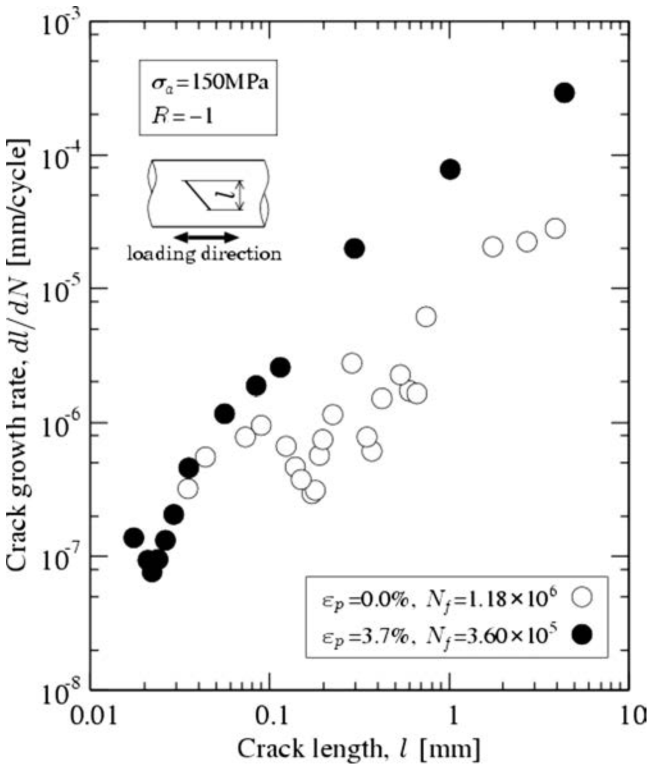

FIG. 12—*Mode II fatigue crack growth rate of coarse-grained plain specimens.*

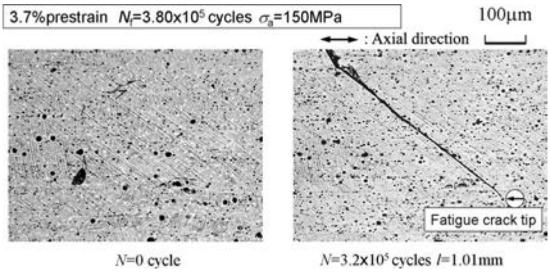

FIG. 13—*Slip bands due to prestrain and fatigue crack of coarse-grained plain specimens.*

0 % prestrained specimen. The scatter of crack growth rates of the 0 % prestrained specimen was wide and this is considered to be related to crack path. Figure 13 shows slip bands due to prestrain and fatigue cracks. For the 3.7 % prestrained specimen, Mode II fatigue crack of prestrain specimen has grown up along slip bands due to prestrain. Figure 14 shows comparison of fatigue crack paths. The fatigue crack path of 3.7 % prestrained specimen was straighter than that of 0 % prestrain specimen. Slip bands due to prestrain accelerated Mode II fatigue crack growth rate.

Discussion

A summary of the effect of prestrain is as follows:

1. The average Mode I crack growth rate became about 20–30 % lower as a result of prestrain as shown in Fig. 9. However, the change of crack growth rate doesn't affect the fatigue life, because it is within the scatter of the fatigue life. This was almost independent of the value of prestrain.
2. The Mode II crack growth rate was accelerated by prestrain, but when grain size was small, Mode II cracks occasionally appeared.

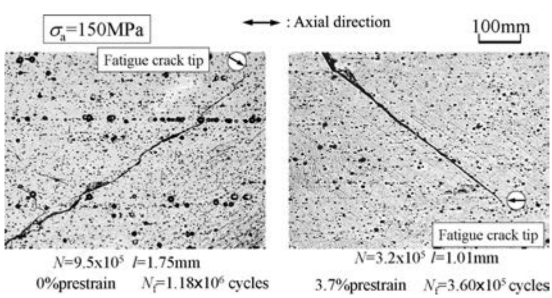

FIG. 14—*Comparison of Mode II fatigue crack paths of coarse-grained plain specimens.*

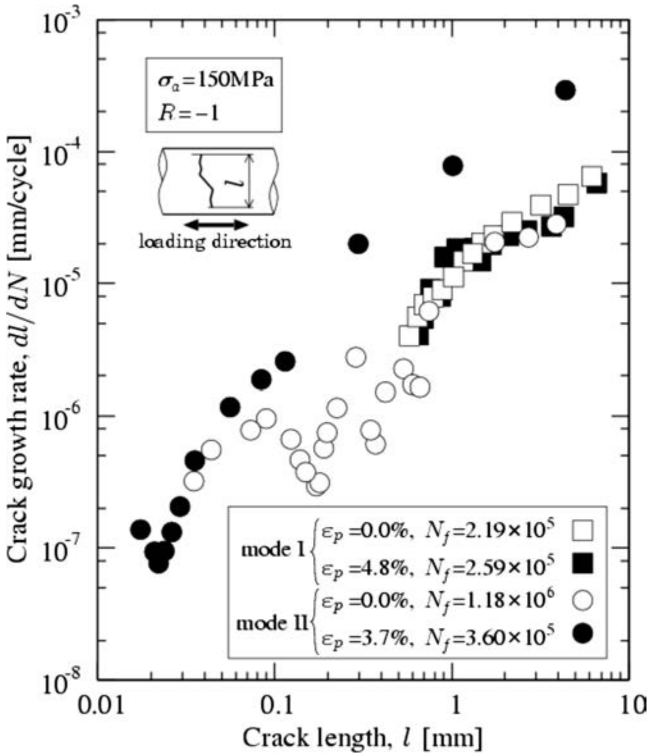

FIG. 15—*Mode I and Mode II fatigue crack growth rate of Test B and C.*

Figure 15 shows Mode I and Mode II fatigue crack growth rates. The Mode II crack growth rate of 3.7 % prestrained specimen was the highest. Therefore, Mode II cracks can shorten fatigue life.

It is, however, strange that Mode I cracks mainly appear when the grain size is small, independent of prestrain. The crack Mode seems to change when the crack passes through the grain boundary. Baxter et al. reported that a persistent slip band was terminated when the slip band encountered a grain boundary [8]. The propagation of a Mode II crack across a grain boundary is considered to be difficult.

It was also found that slip bands lead to mode II cracks. Therefore, the occurrence of the Mode II crack is considered to be facilitated by slip bands due to prestrain.

Hornbogen et al. [9] studied the influence of aging of austenitic alloy to fatigue crack growth. They reported that the slip from the crack tip shears the precipitation particles, but a part of the slip deformation reverses in the unloading section of a loading cycle. They interpreted that the deceleration of the crack growth rate is caused by the above mechanism. This phenomenon appears near the threshold stress intensity range [1–4]. However, in this study, the stress level is higher enough than the threshold level and the fatigue life of the

0 % prestrained specimen is about 10^6. Therefore the slip bands due to prestrain are not reversible and accelerate the Mode II crack growth in the higher stress level.

Conclusion

The effect of prestrain on fatigue crack growth characteristic of age-hardened Al-alloy 6061-T6 was investigated using prestrained specimens. The main results obtained are as follows.

1. The Mode I fatigue crack growth rates of prestrained specimens were a little lower than that of the 0 % prestrained specimen.
2. The Mode II fatigue crack growth rates of prestrained specimens were higher than that of the 0 % prestrained specimen.
3. We should pay attention to the acceleration of Mode II crack growth rates due to prestrain when we achieve damage-tolerant design.

References

[1] Suresh, S., Vasudevan, A. K., and Bretz, P. E., "Mechanisms of Slow Fatigue Crack Growth in High Strength Aluminum Alloys: Role of Microstructure and Environment,"*Metall. Trans. A*, Vol. 15A, 1984, pp. 369–379.

[2] Carter, R. D., Lee, E. W., Starke, E. A. Jr., and Beevers, C. J., "The Effect of Microstructure and Environment on Fatigue Crack Closure of 7475 Aluminum Alloy," *Metall. Trans. A*, Vol. 15A, 1984, pp. 555–563.

[3] Nisitani, H., and Kawagoishi, N., "Characteristics of Surface Crack Growth in Rotating Bending Tests of Age-Hardened or Annealed Al-Alloy," *Trans. Jpn. Soc. Mech. Eng., Ser. A*, Vol. 50, No. 455, 1984, pp. 1334–1340 (in Japanese).

[4] Blankenship, C. P. Jr., and Starke, E. A. Jr., "The Fatigue Crack Growth Behavior of the Al-Cu-Li-Alloy Weldalite 049," *Fatigue Fract. Eng. Mater. Struct.*, Vol. 14, No. 1, 1990, pp. 103–114.

[5] Otsuka, A., Tohgo, K., Sakakibara, K., and Yoshida, T., "Mode II Fatigue Crack Growth Mechanism and Its Dependency on Material in Aluminum Alloys," *J. Soc. Mater. Sci. Jpn.*, Vol. 34, No. 385, 1985, pp. 1174–1179 (in Japanese).

[6] Lin, H., Nayeb-Hashemi, H., and Berg, C. A., "Cumulative Damage Behavior of Anisotropic Al-6061-T6 as a Function of Axial-Torsional Loading Mode Sequence," *J. Eng. Mater. Technol.*, Vol. 116, 1994, pp. 27–34.

[7] Yahr, G. T., "Fatigue Design Curves for 6061-T6 Aluminum," *J. Pressure Vessel Technol.*, Vol. 119, 1997, pp. 211–215.

[8] Baxter, W. J., and McKinney, T. R., "Growth of Slip Bands During Fatigue of 6061-T6 Aluminum," *Metall. Trans. A*, Vol. 19, 1988, pp. 83–91.

[9] Hornbogen, E., and Zum Gahr, K. H., "Microstructure and Fatigue Crack Growth in a γ-FeNi-Al Alloy," *Acta Metall.* Vol. 24, 1976, pp. 581–592.

ASTM Special Technical Publication, Vol. 5, No. 7
Paper ID JAI101648
Available online at www.astm.org

M. Carboni,[1] *S. Beretta,*[1] *and M. Madia*[1]

Analysis of Crack Growth at *R*=−1 Under Variable Amplitude Loading on a Steel for Railway Axles

ABSTRACT: Railway axles are designed for infinite life, but occasional failures have been and are observed in service. The failures, which are usually due to fatigue crack propagation, are typically positioned at the press fits which correspond to the wheels, gears, brakes, or they appear at the axle body close to the notches and transitions. The way to addressing this problem is to adopt the concept of "damage tolerance" in order to determine the inspection intervals of the axle depending on the NDT method. The issue open to discussion is the choice of the correct algorithm for simulating crack growth at $R=-1$ at variable amplitude loading especially when considering mild steels such as A1N. The aim of the present research is to discuss the application of state-of-the-art algorithms to estimate the effect of block loading at $R=-1$ (derived from real load spectra experienced by the axle) upon constant crack growth rate. More specifically the current research addresses: (i) crack growth experiments at $R=-1$ under constant amplitude loading on two novel types of small-scale specimens; (ii) crack growth experiments under block loading on small-scale specimens; and (iii) the prediction of the experimental evidences by well-known and wide-spread analytical tools.

KEYWORDS: railway axles, A1N steel, damage tolerance, crack growth, variable amplitude loading, NASGRO®

Manuscript received December 27, 2007; accepted for publication June 26, 2008; published online August 2008.
[1] Dept. of Mechanical Engineering, Politecnico di Milano, Via La Masa 34, I-20156 Milano, Italy E-mail: michele.carboni@polimi.it (corresponding author).

Citation: Carboni, M., Beretta, S., and Madia, M., "Analysis of Crack Growth at *R*=-1 Under Variable Amplitude Loading on a Steel for Railway Axles," *J. ASTM Intl.*, Vol. 5, No. 7. DOI10.1520/JAI101648. Available online at www.astm.org. Also included in JAI Special Issue STP 1508, *Fatigue and Fracture Mechanics: 36th Volume,* R. W. Neu, K. R. W. Wallin, and S. R. Thompson, guest editors, ASTM International, West Conshohocken, PA, 2009, pp. 574-591.

Introduction

Railway axles are designed to have an infinite lifetime [1]. Even if this is accepted as adequate, the fact remains that occasional failures have been and are observed in service all around Europe and the United States. Failures typically occur at the press-fits for wheels, gears, and brakes or at the axle body close to notches and transitions. Such failures always occur due to fatigue crack propagation but the nucleation of these can be due to various factors [2]. In the case of railway axles, the presence of wide-spread corrosion [3,4] or possible damage caused by the ballast impacts [5] may constitute such factors.

These kind of failures are usually tackled by employing the "damage tolerance" methodology, whose philosophy consists [6,7] in determining the most opportune inspection interval given the "Probability of Detection" (POD) of the adopted nondestructive testing (NDT) technique or, alternatively, in defining the needed NDT specifications given a programmed inspection interval. A comprehensive up-to-date description of how the damage tolerance methodology is applied to railway axles can be found in Ref. [2]. However, it is worth noting that several aspects have yet to be widely investigated. For example, the application of analytical tools for life prediction of cracked bodies, the specification of the stress intensity factor [8] of cracks in or close to press-fits and the determination of effective load spectra [9,10]. Considering here the first topic, one of the main points is then to verify the existence of appreciable load interaction effects on crack growth under stress spectra at $R=-1$ and the other one is to check the ability of existing algorithms for correctly predicting growth rates. Some research [11] has already been done considering the case of a high strength steel usually adopted to produce railway axles, while Refs. [12–14] show more general applications of well-known and wide-spread analytical tools. The conclusions drawn in the cited references seem to be contradictory about the performances of these predictive tools.

The aim of the present research is to discuss the application of state-of-the-art algorithms to estimate the effect of block loading at $R=-1$ (derived from real load spectra experienced by the axle) upon crack growth rate, especially considering mild steels such as A1N, which is widely used for manufacturing railway axles [1]. More specifically, the present study addressed: (i) crack growth experiments at $R=-1$ under constant amplitude loading on two novel types of small-scale specimens; (ii) crack growth experiments under block loading on small-scale specimens; and (iii) the prediction of the experimental evidences by well-known and wide-spread analytical tools.

Experimental Tests on Traditional Small-Scale SE(B) Specimens

The material analyzed in the present study is a mild carbon steel, named A1N. Mechanical properties of A1N are [14,15]: ultimate tensile strength UTS $=591$ MPa and monotonic yield strength $\sigma_{y,\mathrm{monotonic}}=388$ MPa. Cyclic properties were modeled by the cyclic Ramberg–Osgood relationship

$$\varepsilon = \frac{\sigma}{E_{\mathrm{cyc}}} + \left(\frac{\sigma}{H}\right)^n, \tag{1}$$

where $E_{\mathrm{cyc}} = 200\,000$ MPa, $n = 0.168\,472$ and $H = 1036.24$ MPa. Furthermore, the 0.2 % cyclic proof stress resulted to be $\sigma_{y,\mathrm{cyc}0.2} = 365$ MPa while the cyclic linear elastic limit $\sigma_{\mathrm{cyc,el}} = \sigma_{y,\mathrm{cyc}0.005} = 195$ MPa (0.005 % cyclic proof stress).

Crack Growth Tests

Crack growth properties of A1N steel have been extensively studied by the current authors [14]. In some of these studies crack growth and ΔK-decreasing [16] tests were carried out using SE(B) specimens (Fig. 1(*a*), width equal to 24 mm, thickness equal to 12 mm, and starting notch length equal to 8 mm) taken from three different steel batches (more details about the tests are reported in Ref. [14]). Fig. 1(*b*) shows the obtained growth data at $R = -1$ together with the effective crack propagation curve (derived from three tests at $R \geqslant 0.85$) and the growth curve obtained from two full-scale crack propagation tests on axles [14]. A large scatter can be observed from data at $R = -1$ in both da/dN and ΔK directions and especially if the threshold region is considered. The treatment of this kind of scatter has been addressed elsewhere [15]. As can be noted from Fig. 1(*b*), a significant scale effect between small-scale and full-scale specimens can be observed, an effect which is probably due to the different constraint at the crack tip. This effect led to the design of novel small-scale fracture mechanic specimens characterized by a higher constraint at the crack tip which could be used as "companion specimens" [17] of railway axles during tests in the lab.

Design of Novel Fracture Mechanic Specimens

In order to describe the constraint at the crack tip in railway axles when using small-scale fracture mechanic specimens, two novel geometries were designed. The initial idea for this design was based around the theory that the more material there is surrounding the crack tip, the higher the constraint and the plain strain condition of cracks in axles is approached by the cracks in specimens. The first specimen was produced by simply modifying the traditional SE(T) so it had bigger dimensions than the typically adopted ones. Fig. 2(*a*) and 2(*b*) show the typical SE(T) specimen, adopted in the present research, which had a width equal to 50 mm and thickness equal to 20 mm. Dedicated finite element method (FEM) analyses [18] were carried out in order to derive the boundary correction function that resulted, as expected, to coincide with that reported in the literature for SE(T) specimens [19].

The second specimen was derived by modifying the traditional C(T) specimen: (i) in terms of its dimensions (also in this case the width was typically equal to 50 mm, while the thickness was equal to 25.4 mm); (ii) two threaded rigid pins were connected so that the specimen could also be used at negative stress ratios (Fig. 2(*c*) and 2(*d*)). Dedicated FEM linear elastic three-dimensional (3D) analyses (Fig. 3(*a*)) were carried out [18] using ABAQUS®

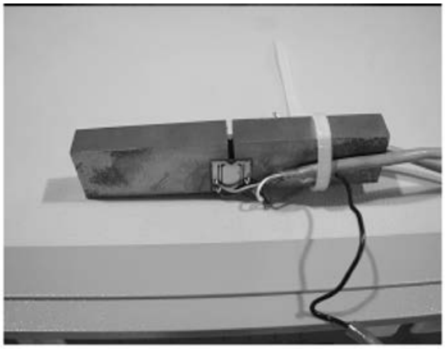

(a)

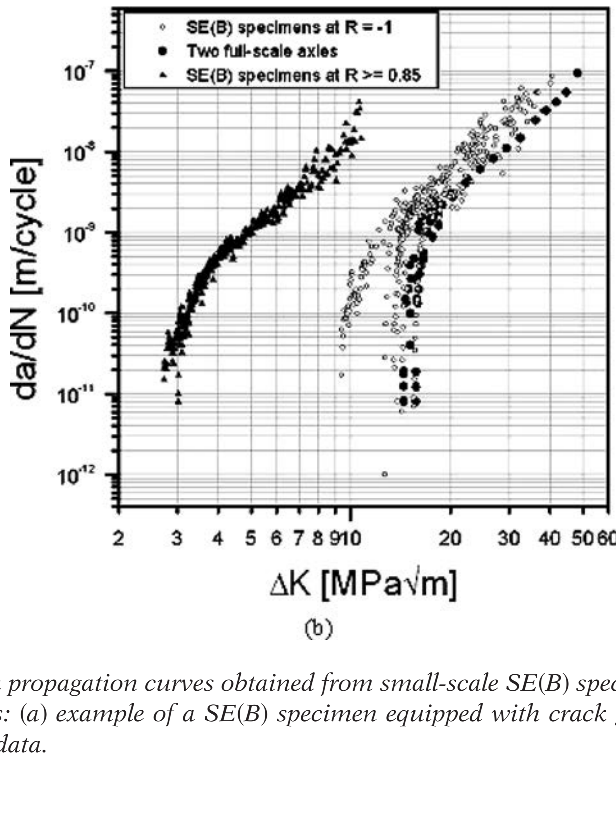

(b)

FIG. 1—*Crack propagation curves obtained from small-scale SE*(*B*) *specimens and two full-scale axles:* (*a*) *example of a SE*(*B*) *specimen equipped with crack gauges, and* (*b*) *crack growth data.*

v6.5 [20], applying the submodeling technique and adopting quadratic elements with 20 nodes and reduced integration (C3D20R [20]). The analyses allowed the pins to be effectively designed to protect them against fatigue failure, to check the deformed shape of the specimen (Fig. 3(*b*)) and to compare the boundary correction functions for the traditional [19] and the modified C(T) specimens finding a maximum error equal to 2 % (Fig. 3(*c*), this is due to the calibrated flexibility of the pins).

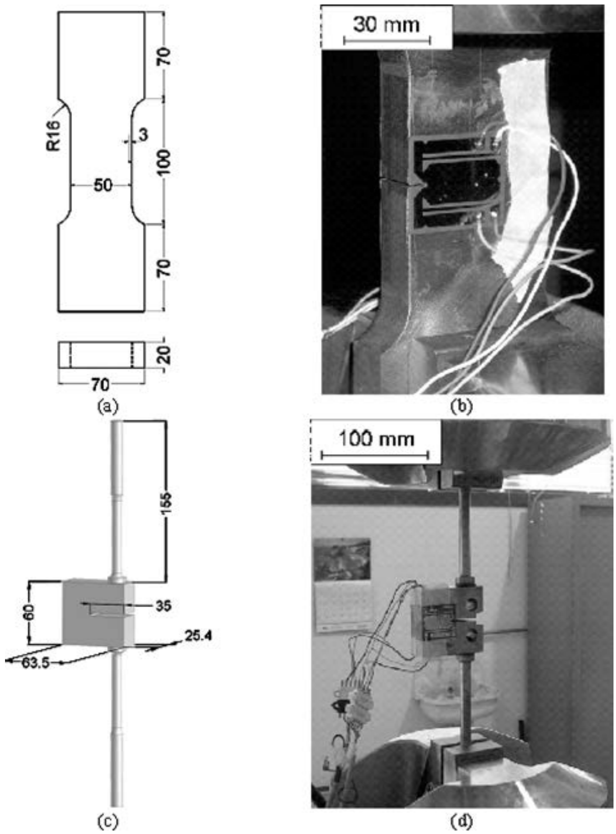

FIG. 2—*Two novel small-scale fracture mechanics specimens for describing high constraint at crack tip in railway axles:* (*a*) *and* (*b*) *SE*(*T*)*;* (*c*) *and* (*d*) *modified C*(*T*)*.*

Experimental Tests and Strip-Yield Simulations at Constant Amplitude Loading

In the present research, all the experimental tests on the modified small-scale specimens were carried out at $R=-1$ using an uniaxial servohydraulic testing machine with a maximum applicable load equal to 250 kN. Crack length and advance were measured by means of crack gages (Fig. 2(*b*) and 2(*d*)) connected to a dedicated control unit. All the small-scale specimens were machined from previously fatigue tested full-scale axles.

Fig. 4 shows the comparison between the crack growth curves obtained at constant amplitude loading from three modified C(T) specimens, two SE(T) specimens and the full-scale axles. As can be seen, crack growth data from small-scale specimens fit very well onto full-scale ones. This fact seems to support the initial idea that the constraint at the crack tip of specimens which are thick can effectively describe the constraint of a crack tip in full-scale axles, since the plane strain conditions of both the systems become similar. The modi-

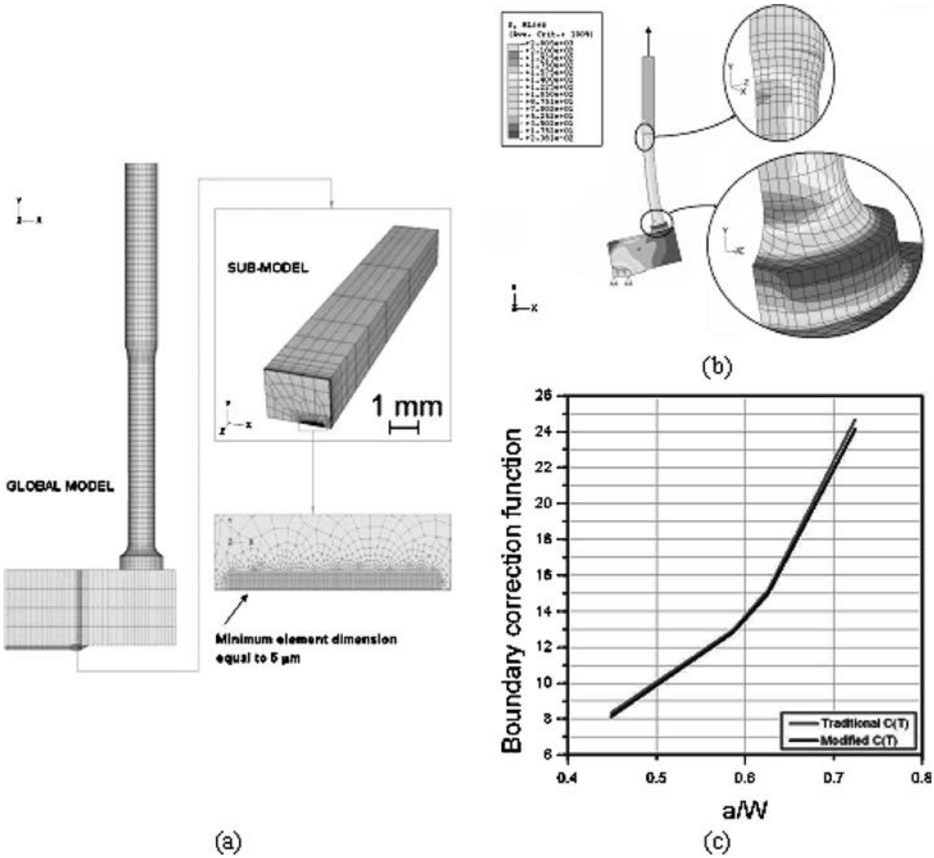

FIG. 3—*FE analysis of the modified C*(*T*) *specimen:* (*a*) *adopted mesh;* (*b*) *deformed shape; and* (*c*) *comparison between the boundary correction functions of the traditional and modified C*(*T*) *specimens.*

fied SE(T) and C(T) specimens were then adopted as companion specimens for railway axles in the subsequent part of the research.

A further noteworthy analysis, obtained from tests carried out on SE(T) specimens, regarded the estimation of the opening load of the crack in terms of the U-factor defined as [6]

$$U = \frac{\Delta K_{\mathrm{eff}}}{\Delta K} = \frac{K_{\max} - K_{\mathrm{op}}}{K_{\max} - K_{\min}} = \frac{\Delta S_{\mathrm{op}}}{\Delta S}, \tag{2}$$

where $\Delta K_{eff} = K_{max} - K_{op} = Y \cdot \Delta S_{op} \cdot \sqrt{(\pi a)}$ is the effective stress intensity factor range and $\Delta K = K_{max} - K_{min} = Y \cdot \Delta S \cdot \sqrt{(\pi a)}$ = the applied stress intensity factor range.

The ΔS_{op} value was estimated in three different ways: (i) experimentally, applying a clip gage at the crack mouth of the specimen and elaborating the acquired data by means of the "compliance offset" global compliance method

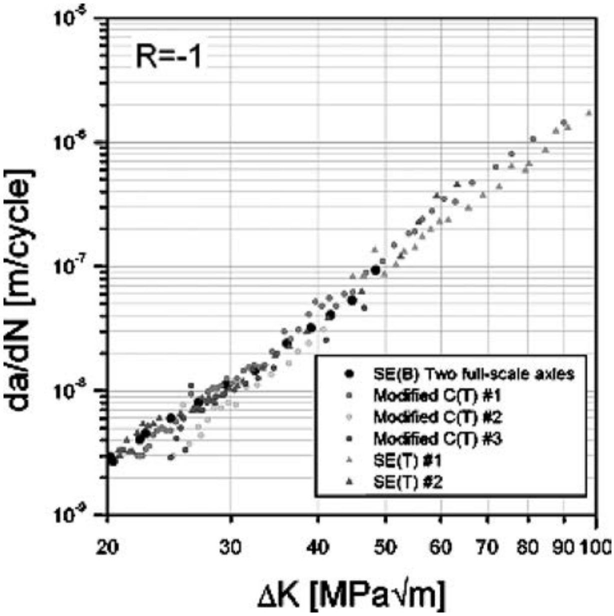

FIG. 4—*Crack growth curves obtained at constant amplitude loading from the modified small-scale specimens.*

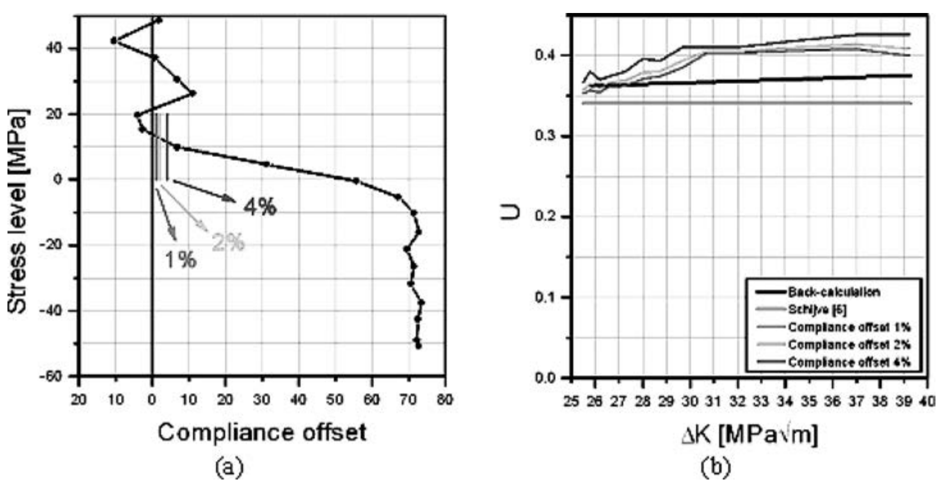

FIG. 5—*Estimation of the opening load on SE(T) specimens: (a) an example of the application of the "compliance offset" method, and (b) comparison between the obtained results.*

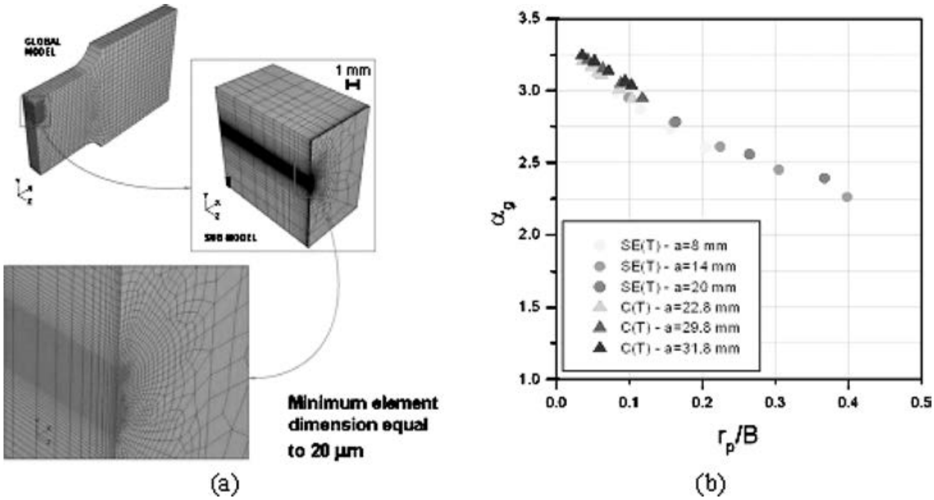

FIG. 6—*Numerical characterization of constraint in small-scale specimens:* (*a*) *FE model, and* (*b*) *global constraint factor.*

proposed by ASTM E647-05 [16] (Fig. 5(*a*) shows an example of elaboration); (ii) experimentally, backcalculating the opening stress value by comparing the growth curves shown in Fig. 4 and the effective growth curve shown in Fig. 1(*b*); (iii) applying Schijve's empirical expression $U=0.55+0.33\cdot R+0.12\cdot R^2$ valid for negative stress ratios [6]. The comparison of the results obtained by the three applied methods is shown in Fig. 5(*b*). As can be observed, the back-calculation is in-between Schijve's expression and compliance offset results, a result concordant with the literature [12,13].

Numerical Characterization of the Constraint of Novel Specimens

In the present research, the strip-yield (SY) model [21] was the predictive tool adopted to simulate crack growth curves. This two-dimensional model calculates the multiaxial state of stress at the crack tip by introducing a "constraint factor" α. This means that the material in the plastic zone yields at a stress level equal to $\alpha\cdot\sigma_o$, where σ_o is the flow stress [21]. Limit values for the constraint factor are $\alpha=1$ for plane stress conditions and $\alpha=3$ for plane strain conditions. Typically, a global constraint factor α_g (i.e. the mean value of the constraint factor along the crack front) is introduced into the SY model.

In order to quantify the α_g value for the modified SE(T) and C(T) specimens in A1N steel, elastoplastic 3D finite element analyses were carried out (Fig. 6(*a*)). The material was described by means of its cyclic (Ramberg–Osgood) behavior. More details about the numerical analyses can be found in Refs. [18,22]. According to Newman [23], α_g can be defined as

$$\alpha_g \sigma_0 A_0 = \int_{A_0} \sigma_n dA_n, \tag{3}$$

where: σ_n = the stress in the nth yielded element of the plastic zone, A_n = the projected area of the same element on the ligament, and A_o = the projected area of the whole plastic zone on the ligament.

It is important to add, for the following analyses, that the COD value of crack surfaces, as discovered in previous studies [22], is not directly influenced by the α_g value, but the relevant parameter is the product $\alpha_g \cdot \sigma_o$.

Analyses were carried out using different crack lengths in SE(T) and modified C(T) specimens which were subjected to different stress levels. Fig. 6(*b*) shows the global constraint factor trend as a function of the ratio between the plastic zone dimension r_p and the thickness B, so that all the curves collapse onto one as suggested by Guo [24]. The plastic zone dimension was calculated by the usual formula [25]

$$r_p = \frac{\pi}{8} \cdot \left(\frac{K_{\max}}{\sigma_0} \right)^2. \tag{4}$$

In the most general case, there are three constraint factors which should be introduced into the SY model: α_t for the tensile yielding of the elements of the plastic zone, α_c for the compressive yielding of the elements of the plastic zone, and α_w for the compressive yielding of the elements of the plastic wake. The original SY model (developed for light weight alloys subjected to positive stress ratios) assumes the "Newman's constraint model" [21] where $\alpha_t = \alpha_g$, $\alpha_c = \alpha_w = 1$, and σ_o equal to the mean value between the yield and the ultimate stress values (even if here $\sigma_o = \sigma_{\text{cyc,el}} = \sigma_{y,\text{cyc}0.005}$ will be adopted). Many other constraint models have been developed and are available in the literature: in the present research, the "symmetrical constraint model" [26,27] characterized by $\alpha_t = \alpha_c = \alpha_g$ (this choice is due to the observation that at $R = -1$ the cyclic constraint should be symmetrical), $\alpha_w = 1$ and $\sigma_o = \sigma_{\text{cyc,el}} = \sigma_{y,\text{cyc}0.005}$ and the "cyclic proof stress constraint model" characterized by $\alpha_t = 2.5$ [28], $\alpha_c = \alpha_w = 1$, and $\sigma_o = \sigma_{y,\text{cyc}0.2}$ [22,28] were utilized.

SY Simulations of Constant Amplitude Crack Growth Tests

A first series of simulations was carried out in order to predict constant amplitude crack growth tests by using the simple "PoliSY" code developed by the authors and incorporating a SY model with constraints [29]. This SY model has been developed over the years, as a "starting point" tool for the analysis of constraint models and of the strains close to the crack tip [26,27]. It is called "simple" because it is only able to consider constant amplitude load conditions. The advantages of adopting this simple SY model during the present preliminary analyses are: (i) its optimized internal procedures for negative stress ratios and structural steels [29] and (ii) its "open" code, which allowed the different parameters and conditions to be fully tested and experimented with.

Fig. 7(*a*) shows the comparison between the experimental data obtained from the modified small-scale specimens (Fig. 4) and the three constraint mod-

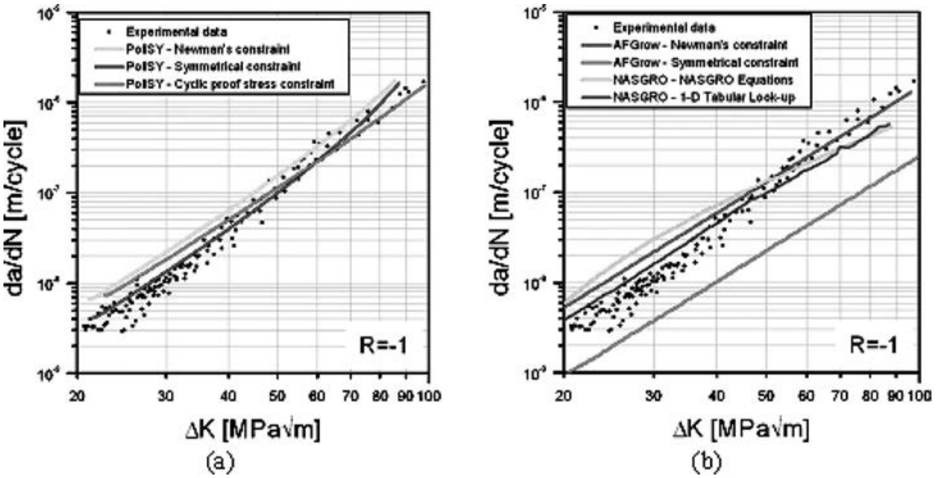

FIG. 7—*Simulations of constant amplitude crack growth tests on SE*(*T*) *specimens:* (*a*) *PoliSY SY model, and* (*b*) *NASGRO and AFGrow SY models.*

els: (i) Newman's constraint ($\alpha_t = 2.86$ from Fig. 6, $\alpha_c = \alpha_w = 1$ and $\sigma_o = \sigma_{y,\mathrm{cyc}0.005} = 195$ MPa); (ii) symmetrical constraint ($\alpha_t = \alpha_c = 2.86$ from Fig. 6, $\alpha_w = 1$ and $\sigma_o = \sigma_{y,\mathrm{cyc}0.005} = 195$ MPa); and (iii) cyclic proof stress constraint ($\alpha_t = 2.5$, $\alpha_c = \alpha_w = 1$ and $\sigma_o = \sigma_{y,\mathrm{cyc}0.2} = 365$ MPa). The best match seems to be achieved by the symmetrical constraint model, while Newman's model seems to slightly overestimate crack rates and the cyclic proof stress constraint is in-between but seems to show a different slope compared to the experimental data. This last observation can be explained by considering the different constraint conditions tested when adopting the cyclic proof stress model: in Newman's model and that of symmetrical constraint $\alpha_g \cdot \sigma_o = 558$ MPa, while for the cyclic proof stress constraint model $\alpha_g \cdot \sigma_o = 913$ MPa.

Since the present research deals with variable amplitude loading, a second series of simulations of the same experimental data was carried out by the well-known and wide-spread software packages AFGrow v. 4.0011.14 [30] and NASGRO v. 3.0.21 [31]. Unfortunately, these two software packages are not open coded and so it was not always possible to apply the relevant constraint models. For example, AFGrow only allows two constraint factors to be set (one for tension and one for compression): Fig. 7(*b*) shows the results obtained adopting Newman's model and that of symmetrical constraint. As Fig. 7(*b*) shows, Newman's constraint slightly overestimates growth rates while the symmetrical constraint significantly underestimates them. Exactly the same prediction could be achieved by PoliSY applying a constraint model characterized by $\alpha_t = \alpha_c = \alpha_w = 2.86$ ($\sigma_o = 195$ MPa), so suggesting that the compressive constraint factor defined in AFGrow is applied both in the plastic zone and in the plastic wake. Considering NASGRO, only one constraint factor can be set for the analyses, so the symmetrical constraint model was not taken into consideration. The application of Newman's constraint gave exactly the same prediction shown by PoliSY (Fig. 7(*a*), growth rates slightly overestimated), so the cyclic proof stress constraint model was assumed in the following and the comparison of different methods for introducing the behavior of the material into the software was carried out. The two methods which are considered here are: (i) one-dimensional (1D) tabular look-up, where the effective crack propagation curve (Fig. 1(*b*)) is presented to the software as a table of values, and (ii) NASGRO equations [32], where the crack propagation curve is provided in terms of the empirical parameters of the expressions

$$\frac{da}{dN} = c\left[\left(\frac{1-f}{1-R}\right)\Delta K\right]^{n} \frac{\left(1-\dfrac{\Delta K_{\mathrm{th}}}{\Delta K}\right)^{p}}{\left(1-\dfrac{K_{\max}}{K_{\mathrm{crit}}}\right)^{q}}, \tag{5}$$

$$\Delta K_{\mathrm{th}} = \Delta K_{\mathrm{tho}} \frac{\sqrt{\dfrac{a}{a+a_0}}}{\left[\dfrac{1-f}{(1-A_0)(1-R)}\right]^{(1-C_{\mathrm{th}}R)}}. \tag{5$'$}$$

In Eq 5 C, n, p, and q are empirical constants, ΔK_{th} is the threshold value for ΔK, $K_{\max}$ and K_{crit} are the maximum and the critical SIF values, respectively, R is the stress ratio and the $f = S_{\mathrm{op}}/S_{\max}$ parameter takes the closure phenomenon into account [32]. In Eq 5′ ΔK_{th0} is the threshold SIF range at $R=0$, a is the crack depth, a_0 is the El-Haddad parameter, A_0 is a constant used in Newman's equation for f [32], whereas C_{th} is an empirical constant which distinguishes positive ($C_{\mathrm{th+}}$) from negative ($C_{\mathrm{th-}}$) R values. Note that Eq 5′, in general, is valid in the range $-2 \leqslant R \leqslant 0.7$ [32]. Eq 5 is able to describe crack growth rate as a function of the SIF for all the three propagation regimes (threshold, linear and critical), whereas, Eq 5′ describes the threshold SIF variation as a function of the stress ratio. In the case of A1N steel, calibration has already been achieved by the authors in previous experiments [14,15,33]. Fig. 7(*b*) displays the results obtained by the two methods and shows that the 1D tabular look-up performs better. This observation is in accordance with similar results available in the literature [13].

The software package, excluding PoliSY, which provided the best prediction of constant amplitude tests on modified SE(T) and C(T) specimens was then NASGRO introducing the material data as 1D tabular look-up and adopting the cyclic proof stress constraint model. This configuration was then applied to the prediction of all the variable amplitude tests.

Experimental Tests and SY Simulations at Variable Amplitude Loading

Variable amplitude crack propagation tests were carried out by applying HI-LOW block loads and typical load spectra, representative of the service of railway axles, to companion specimens.

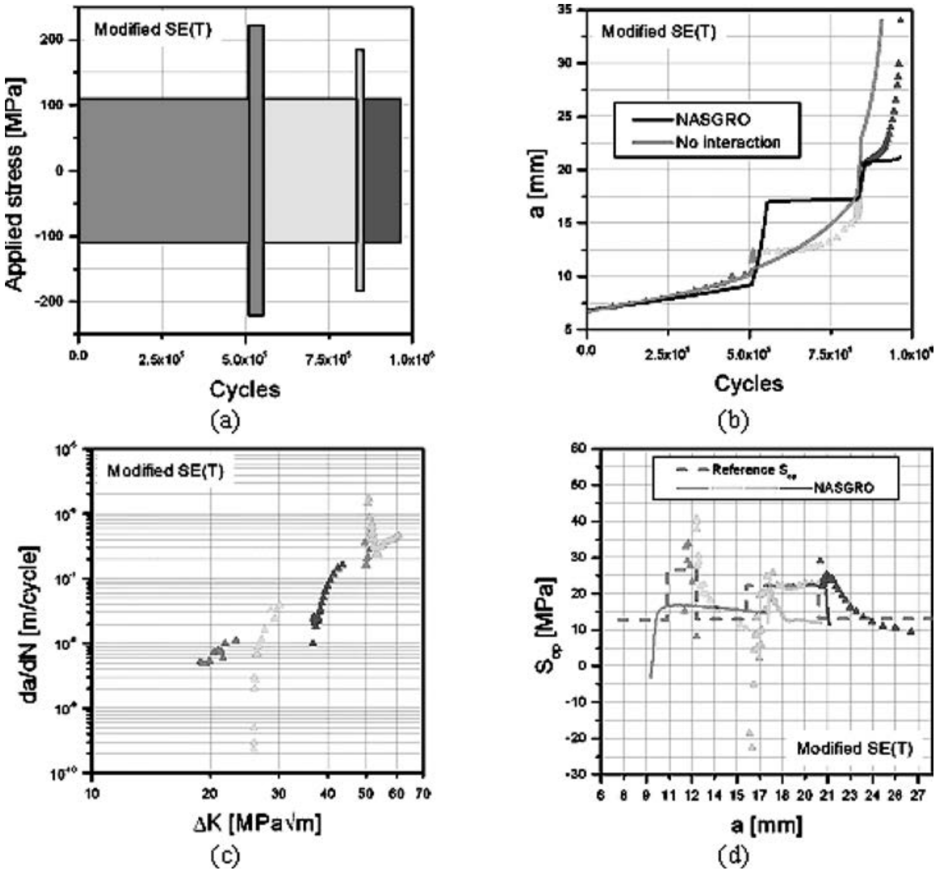

FIG. 8—*Crack propagation tests under HI-LOW block loads on SE*(*T*) *specimens:* (*a*) *block loads;* (*b*) *crack propagation curve;* (*c*) *crack growth rate curve; and* (*d*) *opening load trend.*

HI-LOW Block Loads

Two specimens, one modified SE(T) and one modified C(T), were subjected to the HI-LOW block loads shown in Figs. 8(*a*) and 9(*a*), respectively. The resulting crack propagation curves are reported in Figs. 8(*b*) and 9(*b*). It is possible to observe the expected load interaction effects which consist in an acceleration just after a LOW-HI load transition and a retardation just after a HI-LOW load transition. The use of NASGRO to simulate the relevant block load tests (Figs. 8(*b*) and 9(*b*)) highlighted that the predicted crack propagation curves were significantly different from the experimental ones. Table 1 reports, for both specimens, the percentage of error relating to the partial crack growth advances corresponding to each load level and to the test as a whole (i.e., the mean behavior of all the partial advances put together). As the results show, NASGRO seems to better predict C(T) specimens, even if the error of partial

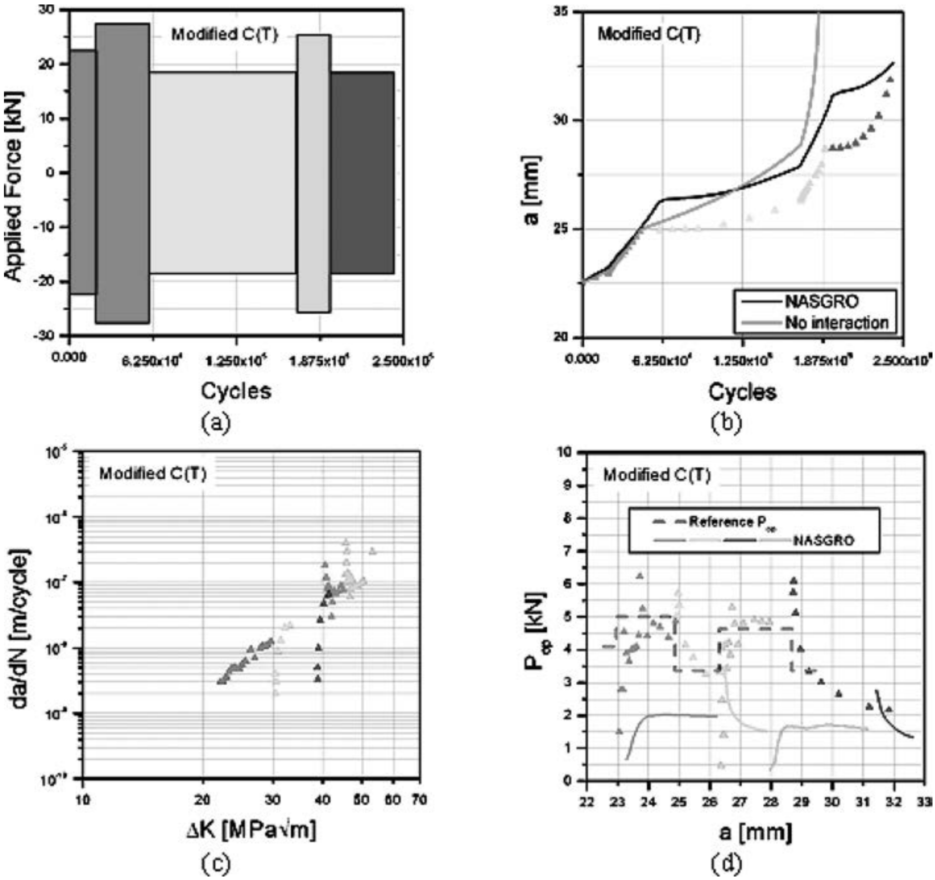

FIG. 9—*Crack propagation tests under HI-LOW block loads on modified C(T) specimens: (a) block loads; (b) crack propagation curve; (c) crack growth rate curve, and (d) opening load trend.*

advances is as high as 20–35 %. Furthermore, the last block seems more critical than the others for both the specimens since the error magnitudes get much higher. It is important to add that the predictions were also carried out by a very simple model derived from the bare Paris' law (Figs. 8(*b*) and 9(*b*)) which is not able to take load interaction effects into account. In the case of the SE(T) specimen (Fig. 8(*b*)), the resultant curve shows an estimation of the experimental data comparable to the one provided by the SY model (similar average error). The curve obtained from the C(T) specimen (Fig. 9(*b*)) shows a very good agreement with the experimental data under constant amplitude loading and during the first HI-block, whereas it diverges for the remaining HI-LOW block loads, where the SY model seems to work better.

The obtained crack growth rate curves are reported in Figs. 8(*c*) and 9(*c*). These figures result in the load interaction effects being even more evident. An

TABLE 1—*Errors between simulated* (Δa_{sim}) *and experimental* (Δa_{sper}) *crack advances in HI-LOW block load tests.*

	Modified SE(T)			Modified C(T)		
	Δa_{sper} (mm)	Δa_{sim} (mm)	Error (%)	Δa_{sper} (mm)	Δa_{sim} (mm)	Error (%)
Red block	3.63	2.80	−29.70	0.57	0.85	33.14
Orange block	1.94	7.45	73.96	1.83	2.84	35.65
Cyan block	3.69	0.21	−1680.20	1.37	1.72	20.41
Green block	4.42	3.44	−28.47	2.38	3.18	25.20
Blue block	13.55	0.46	−2860.58	3.20	1.49	−114.85
Whole test	27.23	14.41	−88.92	9.34	10.09	7.42

analysis of the variation of the opening load, during the tests, was carried out. Figs. 8(*d*) and 9(*d*) show the results of this analysis: an experimental opening load trend was obtained point by point by means of a backcalculation from the effective crack propagation curve, while the reference opening load is the theoretical one, calculated by means of Schijve's expression $U=0.55+0.33\cdot R+0.12\cdot R^2$ [6], for the given load level. The most interesting observation is that all the well-known characteristics of opening load trends with changing load levels are well described by the obtained experimental results. Figs. 8(*d*) and 9(*d*) also report the opening load level calculated by NASGRO for each block load. As can be seen in the previously mentioned figures, the C(T) trends are qualitatively correct but quantitatively down shifted, the SE(T) trend is also qualitatively different (displayed in Fig. 8(*b*)).

Load Spectrum

The adopted load spectrum (Fig. 10(*a*)) was derived [34] from measurements carried out during service and is representative of 125.000 km. Such a spectrum was applied to a modified SE(T) and to a modified C(T) in terms of block loads (Fig. 10(*a*)) arranged by a Gassner's sequence (Fig. 10(*b*)) characterized by $R=-1$. Fig. 11(*a*) and 11(*b*) show the resulting crack propagation curves. It is worth noting that before applying the load spectrum to specimens some constant amplitude load was applied in order to derive the correspondent crack propagation law. Regarding the experimental results, the most interesting consideration is that the adopted load spectrum slows down crack growth rates compared to constant amplitude load, in particular this effect is significant in case of the modified C(T) specimen.

Simulations were carried out using both the SY model, implemented in NASGRO, and the simple "no interaction" crack propagation model (Fig. 11(*a*) and 11(*b*)). As in the case of HI-LOW blocks, SY prediction was shown to be slightly more precise in C(T) specimens, at least when the test as a whole was considered. Furthermore, the no interaction model yields much better predictions compared to the more sophisticated SY model. This last result may be a consequence of the chosen Gassner's sequence. More general conclusions

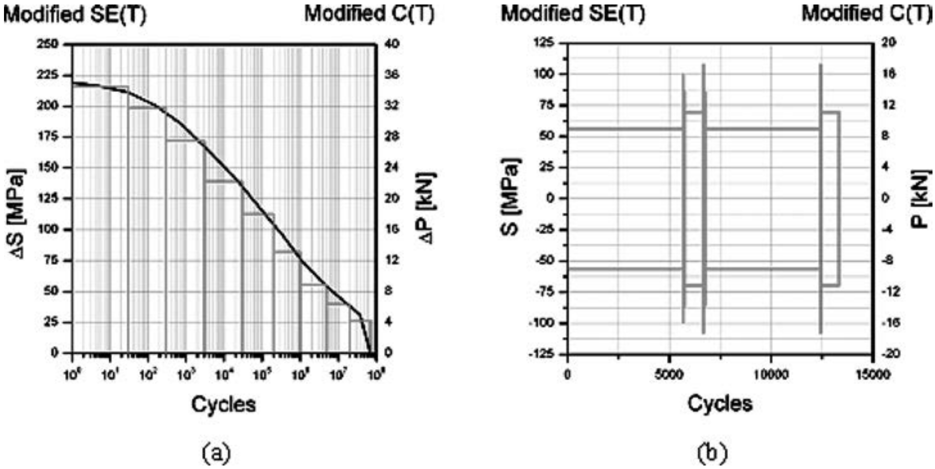

FIG. 10—*Load spectrum representative of* 125.000 km *of typical railway service:* (*a*) *spectrum and its discretization in block loads, and* (*b*) *arrangement of block loads into a Gassner's sequence* ($R = -1$).

would be probably achieved if different randomizations of the block loads and the application of time histories were taken into consideration.

Conclusions

The present research addresses the application of state-of-the-art algorithms to estimate the effect of block loading at $R = -1$ upon constant crack growth rate

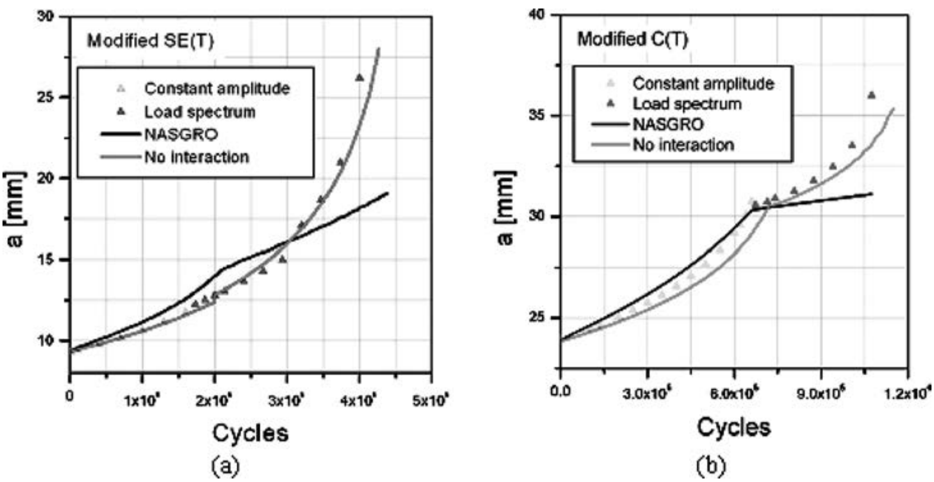

FIG. 11—*Crack propagation curves for specimens subjected to load spectrum:* (*a*) *SE*(*T*), *and* (*b*) *C*(*T*).

considering the A1N mild steel, which is widely used for manufacturing railway axles. The obtained results can be so summarized:

- crack propagation curves obtained at constant amplitude loading by traditional small-scale fracture mechanics specimens show a significant scale effect in respect to those coming from full-scale tests on railway axles;
- two novel small-scale companion specimens, characterized by higher constraint at the crack tip, were successfully designed in order to reduce this scale effect. Moreover, the modified C(T) specimen is able to be tested at negative stress ratios;
- considering the application of suitably calibrated SY models to prediction of constant amplitude loading tests, the NASGRO® software package resulted to perform better than the others when the 1D tabular look-up is adopted to provide material's data;
- a very simple no interaction model permitted to predict, in an effective way, crack propagation curves obtained by the application of HI-LOW block loads and a discretized load spectrum better than using the more sophisticated SY model.

References

[1] EN13261. *Railway Applications—Wheelsets and Bogies—Axles—Product Requirements*, BSI, 2003.

[2] Zerbst, U., Vormwald, M., Andersch, C., Mädler, K., and Pfuff, M., "The Development of a Damage Tolerance Concept for Railway Components and Its Demonstration for a Railway Axle," *Eng. Fract. Mech.*, Vol. 72, 2003, pp. 209–239.

[3] Hoddinot, D. S., "Railway Axle Failure Investigations and Fatigue Crack Growth Monitoring of an Axle," *Proc. Inst. Mech. Eng., F J. Rail Rapid Transit*, Vol. 218, 2004, pp. 283–292.

[4] Lonsdale, C. P., and Stone, D. H., "North American Axle Failure Experience," *Proc. Inst. Mech. Eng., F J. Rail Rapid Transit*, Vol. 218, 2004, pp. 293–298.

[5] Gravier, N., Viet, J. J., and Leluan, A., *Revue General des Chemins de Fer*, Vol. 3, 1999, pp. 33–40.

[6] Schijve, J., *Fatigue struct. mater.*, Kluwer, New York, 2004.

[7] Broek, D., "The Practice of Damage Tolerance Analysis," *Fatigue and Fracture*, ASM Handbook 19, ASM International, Metals Park, OH, 1996.

[8] Beretta, S., Madia, M., Schoedel, M., and Zerbst, U., "SIF Solutions for Cracks at Notches Under Rotating Bending," *Proceedings of the 16th European Conference on Fracture* (*ECF16*), Alexandropoulos, Greece, 2006.

[9] WIDEM EU Project, *Wheelset Integrated Design and Effective Maintenance*, Website: www.widem.org.

[10] Beretta, S., and Carboni, M., "Inspection Intervals of Railway Axles: Influence of Stress Spectrum," *Proceedings of the 8th Int. Conference on Engineering Structural Integrity Assessment* (*ESIA8*), Manchester, UK, 2006.

[11] Beretta, S., and Carboni, M., "Simulation of Fatigue Crack Propagation in Railway Axles," *J. ASTM Int.*, Vol. 2, 2005, pp. 1–14.

[12] Skorupa, M., "Load Interaction Effects During Fatigue Crack Growth Under Variable Amplitude Loading—A Literature Review, Part II: Qualitative Interpretation,"

Fatigue Fract. Eng. Mater. Struct., Vol. 22, 1999, pp. 905–926.

[13] Skorupa, M., Machniewicz, T., Schijve, J., and Skorupa, A., "Application of the Strip-Yield Model from the NASGRO Software to Predict Fatigue Crack Growth in Aluminium Alloys Under Constant and Variable Amplitude Loading," *Eng. Fract. Mech.*, Vol. 74, 2007, pp. 291–313.

[14] Beretta, S., Carboni, M., Cantini, S., and Ghidini, A., "Application of Fatigue Crack Growth Algorithms to Railway Axles and Comparison of Two Steel Grades," *Proc. Inst. Mech. Eng., F J. Rail Rapid Transit*, Vol. 218, 2004, pp. 317–326.

[15] Beretta, S., and Carboni, M., "Experiments and Stochastic Model for Propagation Lifetime of Railway Axles," *Eng. Fract. Mech.*, Vol. 73, 2006, pp. 2627–2641.

[16] ASTM, Standard E647–05, "Standard Test Method for Measurement of Fatigue Crack Growth Rates," *Annual Book of ASTM Standards*, Vol. 3(1), ASTM International, West Conshohocken, PA, CD-ROM version.

[17] Conle, A., and Nowack, H., "Verification of a Neuber-Based Notch Analysis by the Companion-Specimen Method," *Exp. Mech.*, Vol. 17, 1977, pp. 57–63.

[18] Barbieri, C., Beretta, S., and Carboni, M., "Modelling Crack Propagation in Railway Axles Made in A1N Steel," *Proceedings of the 19th Italian Group on Fracture Congress*, Milan, Italy, 2007 (in Italian).

[19] Tada, H., Paris, P., and Irwin, G., *The Stress Analysis of Cracks Handbook*, 3rd Ed., Del Research Corporation, Hellertown, PA, 2000.

[20] ABAQUS® *Online Documentation Version 6.5-1*, ABAQUS, Inc., 2004.

[21] Newman, J. C., Jr., "A Crack Closure Model for Predicting Fatigue Crack Growth Under Aircraft Spectrum Loading," *Methods and Models for Predicting Fatigue Crack Growth Under Random Loading*, ASTM STP 748, J. B. Chang, and C. M. Hudson, Eds., ASTM International, West Conshohocken, PA, 198, pp. 53–84.

[22] Beretta, S., Carboni, M., and Madia, M., "Modelling of Fatigue Thresholds for Small Cracks in a Mild Steel by a Strip-Yield Model," submitted *Eng. Fract. Mech.*, 2007.

[23] Newman, Jr. J. C., Bigelow, C. A., and Shivakumar, K. N., "Three-Dimensional Elastic-Plastic Finite-Element Analyses of Constraint Variations in Cracked Bodies," *Eng. Fract. Mech.*, Vol. 46, 1993, pp. 1–13.

[24] Guo, W., Wang, C. H., and Rose, L. R. F., "The Influence of Cross-Sectional Thickness on Fatigue Crack Growth," *Fatigue Fract. Eng. Mater. Struct.*, Vol. 22, 1999, pp. 437–444.

[25] Anderson, T. L., *Fracture Mechanics—Fundamentals and Applications*, 3rd ed., CRC Press, Bona Raton, 2005.

[26] Beretta, S., and Carboni, M., "A Strip-Yield Algorithm for the Analysis of Closure Evaluation Near the Crack Tip," *Eng. Fract. Mech.*, Vol. 72, 2005, pp. 1222–1237.

[27] Carboni, M., "Strain-Gauge Compliance Measurements Near the Crack Tip for Crack Closure Evaluation: Applicability and Accuracy," *Eng. Fract. Mech.*, Vol. 74, 2007, pp. 563–577.

[28] Savaidis, G., Dankert, M., and Seeger, T., "An Analytical Procedure for Predicting Opening Loads of Cracks at Notches," *Fatigue Fract. Eng. Mater. Struct.*, Vol. 18, 1995, pp. 425–442.

[29] Beretta, S., Carboni, M., and Lombardo, F., "A Model for Simulating Fatigue Crack Propagation Considering Cyclic Plasticity at the Crack Tip," *Proceedings of the 16th Italian Group on Fracture Congress*, Catania, Italy, 2002 (in Italian).

[30] Harter, J. A., *AFGrow Users Guide and Technical Manual*, AFRL-VA-WP-TR-2002-XXXX, U.S. Air Force Research Laboratory Technical Report, 2002.

[31] NASGRO® Consortium, *Fatigue crack growth computer program "NASGRO®" version 3.0. User Manual*, JSC-22267B, NASA Technical Report, 2001.

[32] Newman, J. C., Jr., "A Crack Opening Stress Equation for Fatigue Crack Growth," *Int. J. Fract.*, Vol. 24, 1984, pp. R131–R135.
[33] Carboni, M., and Beretta, S., "The Effect of 'Probability of Detection' Upon the Definition of Inspection Intervals for Railway Axles," *Proc. Inst. Mech. Eng., F J. Rail Rapid Transit*, Vol. 221, 2007, pp. 409–417.
[34] Fisher, G., and Grubisic, V., *Bemessung von Radsatzwellen—Einflussgrssen und Vorgehen bei der Auslegung*, Bericht FB-226, LBF, Darmstadt, 2005.

ASTM Special Technical Publication, Vol. 5, No. 7
Paper ID JAI101557
Available online at www.astm.org

Aaron T. Nardi[1] *and Stephen L. Smith*[2]

Laser Generated Crack-Like Features Developed for Assessment of Fatigue Threshold Behavior

ABSTRACT: Developing methods to evaluate damage tolerance in high cycle fatigue is an important issue for the propeller industry. Traditional methods to establish threshold stress intensity factors for aluminum and martensitic steel have relied mainly on load shedding through-crack test specimens resulting in a pre-cracking history and the associated closure effects. For threshold determination of real life defects, a surface-crack test method, devoid of pre-cracking and closure issues, is needed. To this end, laser generated crack-like features (LGCLFs) were created and have been used successfully to evaluate the threshold crack growth properties of cracks in 7075-T651 with and without shot peening in axial $R = 0.1$ loading. For this work, a laser part marking system was used to generate a LGCLF semi-circular in shape, and measuring ~0.015 in. (0.381 mm) deep by ~0.030 in. (0.762 mm) long, with a notch height of 0.0007–0.001 in. (17.8–25.4 μm) with a tip radius of 0.000 14 in. (3.5 μm). When evaluated metallographically, these laser notches exhibited a very thin recast layer and a negligible heat affected zone. Specimens produced with these flaws were tested in $R=0.1$ tension-tension fatigue to produce a stress versus life plot of the data. A NASGRO crack growth model was used to generate stress versus cycle data points for the same geometry over the same stress range with a 7075-T651 material model and a crack growth threshold of 1.35 ksi $\cdot$(in.)$^{0.5}$ resulting in very good

Manuscript received November 12, 2007; accepted for publication April 3, 2008; published online July 2008.

[1] Materials Research and Test Engineer, United Technologies Research Center, 411 Silver Lane, M/S 129-22, East Hartford, CT, USA, 06108, electronic-mail: nardiat@utrc.utc.com
[2] Mechanical Metallurgy Fellow, Hamilton Sundstrand Division Of United Technologies, 1 Hamilton Road, M/S 1-3-B46, Windsor Locks, CT, USA, 06096, electronic-mail: stephenl.smith@hs.utc.com

Citation: Nardi, A. T. and Smith, S. L., "Laser Generated Crack-Line Features Developed for Assessment of Fatigue Threshold Behavior," *J. ASTM Intl.*, Vol. 5, No. 7. DOI10.1520/JAI101557. Available online at www.astm.org. Also included in JAI Special Issue STP 1508, *Fatigue and Fracture Mechanics: 36th Volume,* R. W. Neu, K. R. W. Wallin, and S. R. Thompson, guest editors, ASTM International, West Conshohocken, PA 2009, pp. 592-605.

agreement with the test data. This threshold compares favorably with the small crack threshold of 1.27–1.33 ksi·(in.)$^{0.5}$ produced by *da/dN* testing performed by NASA at R=0.1 using a compressive pre-cracking method. Testing with samples shot peened prior to generating a LGCLF exhibited significantly higher endurance stresses and failure initiations were not from the LGCLF.

KEYWORDS: damage tolerance, laser pre-cracking, laser generated defects, LGCLF, threshold stress intensity

Introduction

Developing methods to evaluate damage tolerance in high cycle fatigue (HCF) is an important issue for the propeller industry [1]. Traditional methods to establish threshold stress intensity factors for aluminum and martensitic steel have relied mainly on through-crack test specimens that have shown difficulty with specimen configuration, pre-cracking history and the associated closure effects [2–4]. For threshold determination of real life defects, a surface-crack test method, devoid of pre-cracking and closure issues, is needed. Hence, surface-crack fatigue tests with sharp notches created by a laser were investigated.

This concept was initially conceived during an investigation into the fatigue effects due to part marking. The need for a method of direct part marking in a computer assisted manner was required to meet customer driven requirements for two-dimensional (2D) data matrix marks or 2D bar codes. These marks can be generated in numerous ways, but the most preferable manner is by direct laser marking (sometimes referred to as laser etching or laser engraving). The cost of laser part marking equipment for marking metallic parts is on the order of $30K–$100K depending on system options. The time required to create these marks are on the order of fractions of a minute, but more often fractions of seconds. Typically no surface preparation would be needed and fixture requirements are based on correct positioning only.

Previous investigations into laser marking have shown significant fatigue debits in most materials, limiting the use of this marking technique on fatigue critical hardware [5]. Testing was performed with 7075-T6 aluminum and 1070 steel (220 ksi or 1517 MPa UTS) incorporating 2D data matrix marks from a number of standard laser marking devices. Tests were also performed with a laser assisted method, known as laser bonding, in which a glass frit material is applied to the surface then fired with the laser. All tests were performed by standard load controlled high cycle fatigue testing methods in either four-point bend or axial loading with a stress ratio of $R=0.1$. The data was reduced to stress vs. cycle resulting in a distinct correlation between mark depth and shape and the endurance limit. Further analysis suggested that the marks could be characterized as cracks with a stress intensity factor calculated based on the mark shape when cross sectioned perpendicular to the stress axis. The resulting stress intensity values corresponding to the endurance limit stresses correlated well with the threshold stress intensity factors expected for the materials [6].

These results highlighted a concern about the depth control in laser part marking of fatigue critical components and further led to the development of a crack-like flaw. Although further work in ongoing with flaws of varying geometry, the initial work was performed on a semi-circular surface flaw. The result was a semi-circular cross section flaw 0.030 in. (0.762 mm) in length by 0.015 in. (0.381 mm) deep. This flaw was made with a laser intended for laser marking by using a laser milling technique. This technique consisted of making successive cuts over the same 0.030 in. (0.762 mm) line at varying power levels, pulse conditions, and travel lengths until the final geometry was generated. This flaw was created in 7076-T6 and 7075-T73 material successfully and is currently being used in an investigation underway between Hamilton Sundstrand, NASA, and the FAA to determine the damage tolerance properties of shot peened 7075-T73 and D6AC steel for use in aircraft propeller applications. Work has also been performed to develop smaller and larger semi-circular flaws as well as linear flaws on steel, aluminum, titanium, and nickel based superalloys. This process is a material removal process that will result in a crack opening height greater than a fatigue crack, eliminating the potential for crack closure effects. It is also limited to creating surface flaws.

Laser Marking and Notching

The laser marking equipment used to prepare the specimens were procured and utilized by the Connecticut Center for Advanced Technology (CCAT). CCAT investigated a number of laser technologies and developed the laser parameters required to successfully create the geometry desired while minimizing the effect to the surrounding microstructure. The laser equipment described herein were a Nd:YVO_4 vanadate (using neodymium doped yttrium vanadate crystal gain media) laser system, or a ytterbium fiber laser (ytterbium doped silicate glass fiber gain media) system. The vanadate laser has a wavelength of approximately 1064 nm, which is the same as a Nd:YAG laser. The fiber laser has a wavelength of 1070 nm, resulting in similar absorption properties to the 1064 nm wavelength lasers in metals. This furthermore results in similar material removal characteristics between the YAG, vanadate, and fiber lasers. As is typical for marking lasers, these lasers are pulsed, which means that rather than generating a continuous laser beam, a device called a Q-switch, similar to a shutter on a camera, is used to block the beam or let it pass. When the beam is blocked, it stays in the gain media longer and develops more power such that when the switch opens, a high power pulse is emitted. Lower switch frequencies like 20–50 kHz develop more peak pulse power because the switch is closed for a longer period of time. As the laser is pulsed at frequencies approaching 80 kHz, it begins to approximate a continuous laser because dwell time in the gain media is reduced. Therefore, for comparable power settings, a lower pulse frequency will generally produce greater material expulsion rates.

The vanadate lasers used were 10 W lasers and were only used for the laser marking work. The fiber laser was a 20 W laser and was used for both laser marking and making laser crack-like features. All equipment used for the testing described herein utilized laser scanner heads comprised of sets of mirrors driven by computer controlled galvos, which direct the laser onto a flat field focusing lens to intensify the beam. The focusing length was in the range on

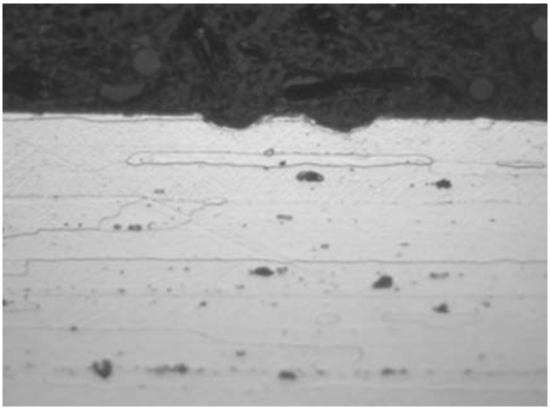

FIG. 1—*Typical laser mark cross section on 7075-T6 aluminum alloy.*

7 in. (178 mm) from the lens face, and the marking field was approximately 4.75 in. (120 mm) square. Further work has been performed to create more complex shaped crack-like features by mounting the fiber laser source on a six-axis CNC laser machining station and using the focusing and part manipulation of the machine to generate the features. This has resulted in complex shape and angled ring crack-like features in cylindrical coupons.

Generating the thumbnail shaped flaw required numerous iterations to determine which laser parameters to vary to get the correct shape and to clean the material out of the feature. The associated problems are related to the melting and expulsion of the metal. In this type of process with this wavelength and pulse length, short duration pulses are directed at the material quickly melting the material such that heat affected zones (HAZs) are minimized. In shallow mark depths, the material expulsion occurs easily due to the flaw depth to opening height ratio. Efficient material removal can therefore be achieved in a single laser pass (see Fig. 1). This photo shows two laser marks approximately 0.0005 in. deep and 0.001 in. wide. Removing the material from very deep features like those that have been used as crack-like features is more difficult (see Fig. 2). This figure is a cross section of a typical semi-circular LGCLF in 7075-T6 material that has been etched with Kellers etchant. The recast material can be seen predominantly on the side walls of the flaw, and a grain boundary is evident surrounding the flaw.

The problem of material expulsion is difficult to predict because the depth versus opening height of the feature must be considered in a cross-sectional view such as these, but the length must also be considered. In very shallow marks, the metal boils and is expelled easily. The material expulsion characteristics can vary with pulse frequency where some pulse frequencies allow the material to resolidify on the surface, and others eject it more cleanly, but there is little likelihood of it solidifying within the mark. Deep narrow flaws, however, have more difficulty expelling material due to the aspect ratio. The other expelling difficulty is in the direction of the flaw. As the beam begins to cut, the material may start to be expelled; then as the beam traverses the molten metal

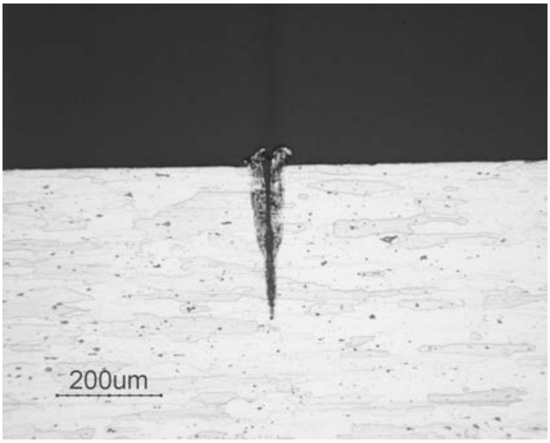

FIG. 2—*Thumbnail shaped LGCLF in cross section on 7075-T6 aluminum alloy.*

from the newly formed area, can be expelled not only up and out of the feature, but also along the length of the feature filling in a previously clean area. For this reason, multiple smaller cut depth passes are required both for material expulsion and for creating the 2D shape of the notch (the thumbnail shape desired). It is not known at this point exactly how clean the feature must be in order to act like a crack. The recast material is likely micro-cracked and brittle due to the high oxide concentration and may therefore not need to be completely removed.

Newer lasers with very short pulse widths (pico- and femto-second lasers) claim to be able to completely vaporize material. This is done by compressing the pulse energy in a given pulse to a very short time frame on the order of 10^{-9} to 10^{-15} s versus 10^{-6} s for the lasers investigated here. This increases the peak power and reduces the elapsed time, which in theory eliminates the melting and boiling of the metal and rather vaporizes it. It is not known, however, if the sharpness of the possible cracks in the recast material is required in order for the feature to truly act like a crack. Recast layer cracking is a commonly found in electrical discharge machining, for instance and is known to reduce fatigue capability[7]. The recast layer in the area of interest for a laser generated crack-like feature (LGCLF) has proven difficult to image due to the geometry, but similar images with laser marked samples have shown this characteristic (see Fig. 3). These cracks, which may exist in all laser recast layers, may be the cause of the crack-like performance. The other possibility is the brittle nature of the recast material may be sufficient to form a crack during initial cycling even at low stresses. This distinction is important and is being investigated, but in either case a fine crack is likely to be present even at early fatigue cycles in order to exhibit the crack-like performance seen in this study.

Figure 4 shows a micro-section of a flaw in 7075-T6 that was shot peened to evaluate the effect of peening on the threshold properties of the alloy. The LGCLF was put in the part after the peening had been applied to simulate damage that might occur to a part in the field. In this case the sample was

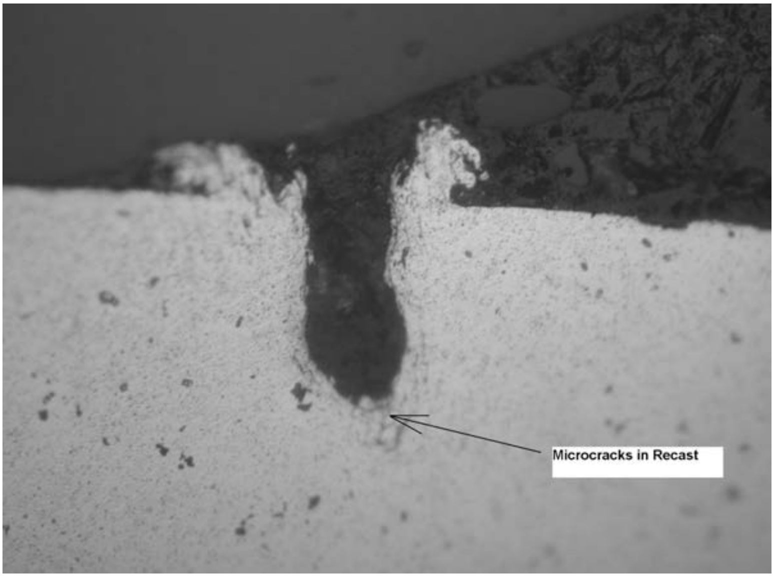

FIG. 3—*Laser mark in 7075-T73 approximately* 0.0035 in. *deep showing micro-cracks in recast.*

cycled initially at a ΔK of 1.7 ksi$\cdot$(in.)$^{0.5}$ (1.6 MPa$\cdot$(m)$^{0.5}$) and after running out to 10×10^6 cycles was raised to 2.5 ksi$\cdot$(in.)$^{0.5}$ (2.3 MPa$\cdot$(m)$^{0.5}$), where it ran another 10×10^6 cycles then to 2.9 ksi$\cdot$(in.)$^{0.5}$ (2.9 MPa$\cdot$(m)$^{0.5}$), where it finally failed outside the location of the flaw. In this case although some propagation had occurred from the tip of the flaw it appears to either have been arrested by the shot peening, or be propagating at a very retarded rate. Similar tests with non-shot-peened samples exhibited failures in 244 000 cycles at 1.7 ksi$\cdot$(in.)$^{0.5}$ (1.6 MPa$\cdot$(m)$^{0.5}$), which match up well with predicted propagation rates.

The LGCLFs investigated here were 0.015 in. (0.381 mm) deep semi-circular surface flaws. These flaws were created with 27 individual laser passes. The laser passes were in groups of three with the first pass being a 20 kHz pulse frequency aimed at material removal, and the second two passes at 80 kHz aimed at cleaning out some of the recast created by the first pass. The first group of three passes were made at the highest power level with the shortest travel length. Each successive group of three passes were made at successively lower power settings, and successively larger travel lengths, with the last group of three being at the lowest power and 0.030 in. (0.762 mm) in length. The resulting in plane cross-sectional geometry can be seen in Fig. 5. This figure shows a fracture surface photograph in the area where the flaw was created.

Investigations have been made into creating a LGCLF for D6AC steel, Ti-6Al-4V titanium, and a nickel based superalloy. The work with D6AC is related to the 7075 aluminum work, and is also part of a program between the FAA, NASA, and Hamilton Sundstrand regarding propeller damage tolerance. This

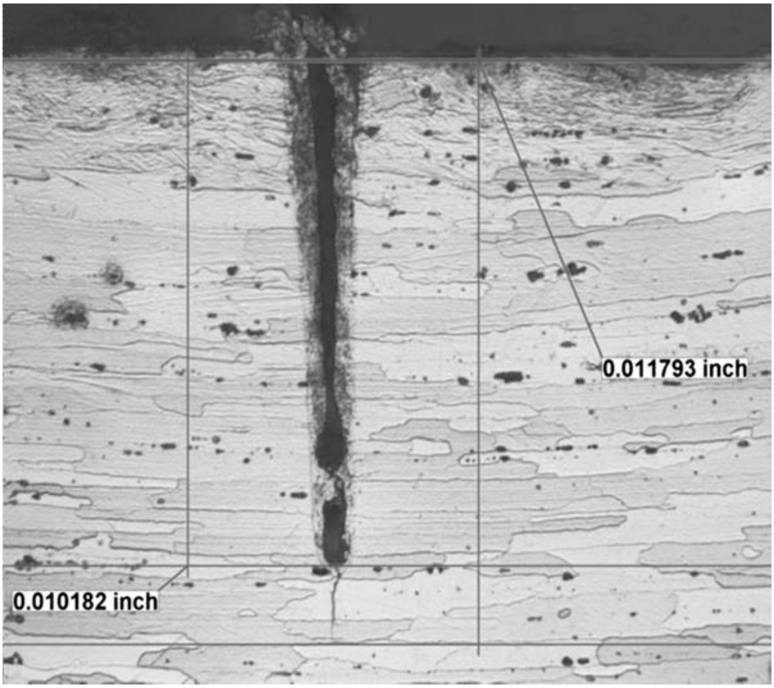

FIG. 4—*LGCLF in shot-peened 7075-T6 after specimen failure from remote location.*

flaw is also a semicircular flaw with similar dimensions to the 7075 flaw discussed previously. This flaw cross section can be seen in Fig. 6. In this photograph, the sample has been etched with nital etch to highlight the recast and HAZ. Flaws in the titanium and nickel alloys were created for other United Technologies Corporation programs. The titanium samples are of specific interest relative to the flaw generation, because this flaw is a ring flaw around the circumference of a 1 in. (25.4 mm) bar. Figures 7 and 8 show these titanium LGCLFs etched with Kellers and at 90° and 45° incident angles to the sample, respectively. This work was performed with the same low power pulsed laser,

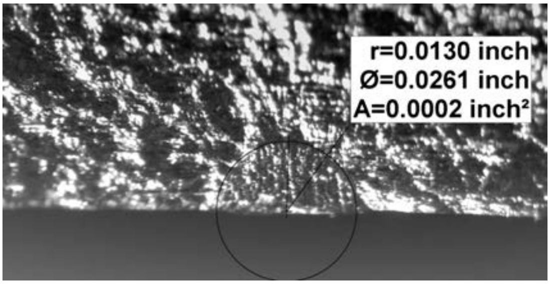

FIG. 5—*Fracture surface of thumbnail shaped LGCLF cycled at* $R = 0.1$.

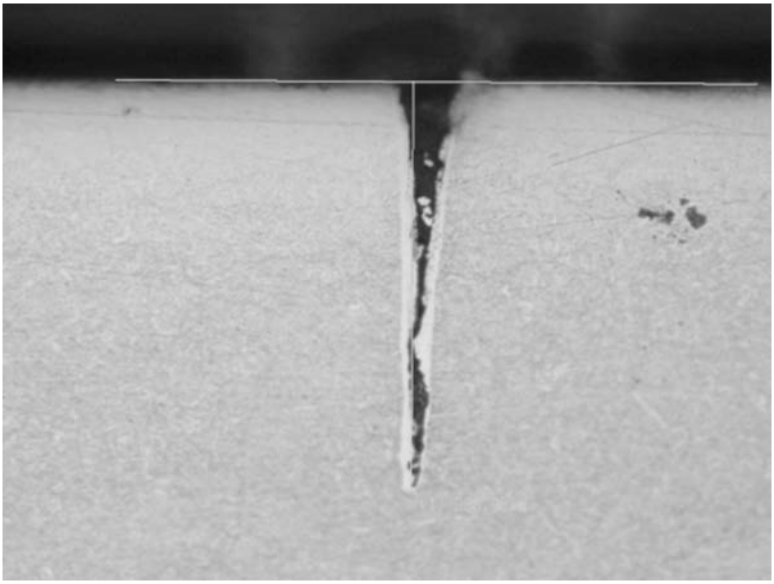

FIG. 6—*Micro-photograph of semi-circular D6AC LGCLF, etched with nital.*

but was fixed to a multi-axis laser machining station. The nickel based superalloy flaw was a semi-circular flaw created at an angle of approximately 60° to the surface. Figure 9 is a photo of this flaw taken on a static overload fracture surface. This flaw was broken open in order to evaluate the flaw geometry.

Fatigue Testing Experimental Procedure

Initial fatigue testing of LGCLFs were performed on 7075-T6 coupons approximately 3 in. long, 0.75 in. wide, and 0.15 in. thick. These coupons were ma-

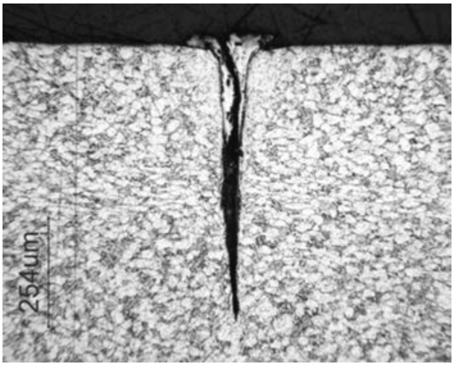

FIG. 7—*Micro-photograph of Ti-6Al-4V LGCLF ring crack in a solid bar, etched with Kellers.*

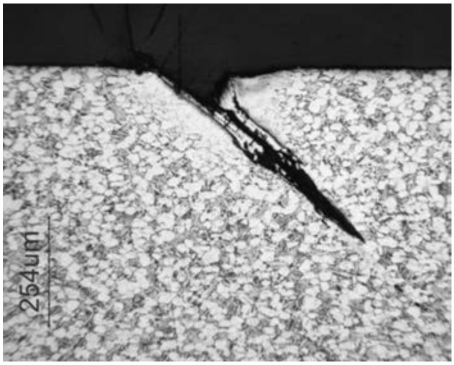

FIG. 8—*Micro-photograph of Ti-6Al-4V LGCLF ring crack, at* 45° *to perpendicular, in a solid bar, etched with Kellers.*

chined to have a 0.375 in. wide test section approximately 1 in. long. The final screening test specimen, seen in Fig. 10, was cycled in tension-tension fatigue at $R = 0.1$ under load controlled conditions using servo-hydraulic test equipment. Earlier work with laser marking was done using a similar specimen under four-point bend conditions. This bend configuration was avoided for the LGCLFs in order to avoid steep stress gradients across the flaw geometry and the use of stress intensity factor solutions for *C*-direction growth in a semi-circular surface flaw (see Fig. 11).

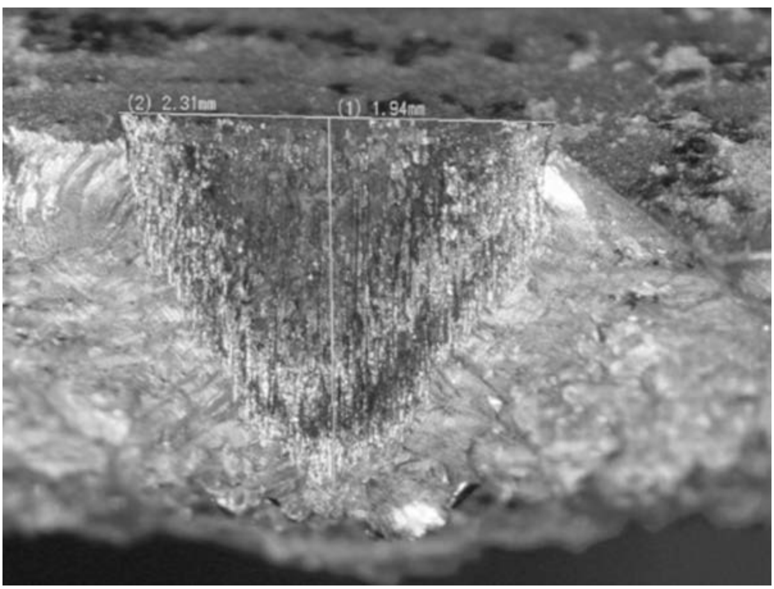

FIG. 9—*Fracture surface of LGCLF in a nickel based superalloy overloaded to document flaw shape.*

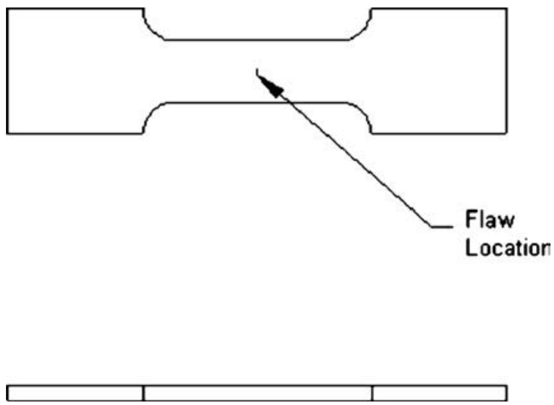

FIG. 10—*Axial $R = 0.1$ fatigue specimen used for final screening tests.*

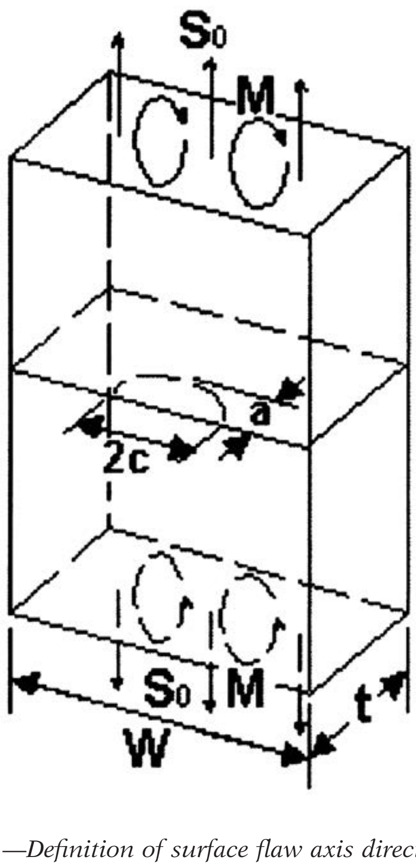

FIG. 11—*Definition of surface flaw axis direction.*

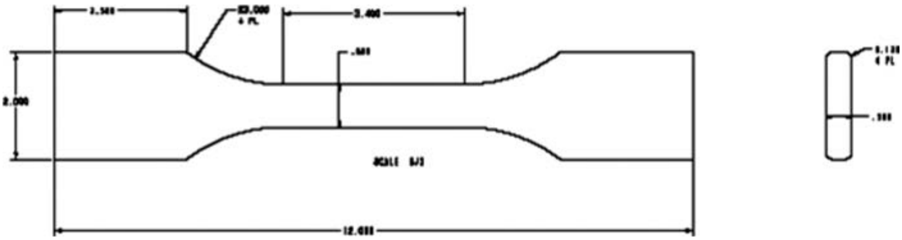

FIG. 12—*Drawing of NASA damage tolerance test specimen.*

This axial fatigue specimen was utilized due to availability of material stock. The specimen would not be the ideal geometry for standard material tests due to a sharper fillet radius and less reduced area in the test section than typically desired. These specimens worked well in spite of these issues due to the fact that the flaws generated were sufficient to cause the failures to occur at the flaw location. Most test specimens were made and polished to an 8 Ra longitudinal surface finish prior to the LGCLF being introduced. Some specimens were also shot peened prior to the flaw being introduced in order to understand the benefit of compressive residual stresses to the growth of a crack from the LGCLF. More specifically, this study was to evaluate the benefits of shot peening on the propagation from field induced damage.

All specimens of the geometry described above were used to prove out the LGCLF process for use in further studies of crack growth from shot-peened and non-shot-peened 7075-T73 aluminum as part of a damage tolerance program funded by the FAA and under the guidance of Hamilton Sundstrand, NASA Johnson, and the FAA. NASA created larger, more standard, fatigue specimens for this study. These specimens, shown in Fig. 12, were prepared by completely machining and preparing the specimens prior to introducing the LGCLF. Similarly some specimens were polished, and others were shot peened. Due to the thickness of the specimens (about 0.4 in.) the shot-peening depth was on the order of 0.05 in. deep compared to about 0.02 in. deep on the 0.1 in. thick specimens. Only one of the non-peened 7075-T73 specimens from the Joint NASA, FAA, Hamilton Sundstrand project has been tested to date. This specimen was tested in constant amplitude load controlled fatigue at $R = 0.1$ with a DC potential drop system attached to monitor crack growth. The other specimens may be run under constant amplitude, K-increasing, or K-decreasing modes.

The test data from the small scale screening specimens were reduced to standard S/N plots. The notch geometry was also modeled in NASGRO and various stresses were run to generate stress versus cycle data points that could be plotted on the same S/N curve as the test data. The 7075-T6 material data in NASGRO was used to as a starting point, and the coefficients affecting the threshold were altered until the NASGRO curve fit to the test data. From this an effective threshold was determined. The NASA Johnson testing yielded results in the form of da/dN and ΔK, and could therefore be plotted on a curve with fracture data from literature and previous compact tension tests.

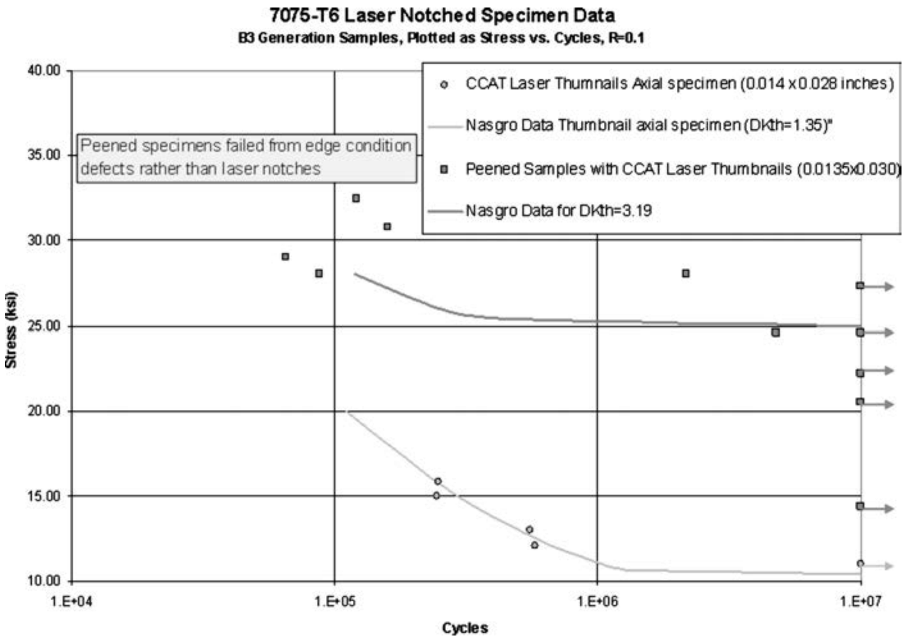

FIG. 13—*S/N data from screening coupon tests made from 7075-T6 showing the performance in the presence of a* 0.014×0.028 in. *LGCLF, with and without shot peening.*

Results

The test data from screening tests shown graphically in Fig. 13 can be seen to follow the NASGRO predicted curve reasonably well assuming the LGCLF can be modeled as a crack. The threshold that NASGRO needed to properly predict the endurance limit was 1.35 ksi$\sqrt{}$(in.). The remainder of the curve is generated based on standard NASGRO material coefficients and also fits the data well. The value of 1.35 ksi$\sqrt{}$(in.) is consistent with previous work with small crack properties of 7075-T6 and 7075-T73.

The shot-peened specimen data shown in Fig. 13 was reduced in a similar way and required a threshold of 3.19 ksi$\sqrt{}$in. in NASGRO to properly fit the data. This would be representative of a minimum threshold; however, the samples failed from edge and fillet stress concentrations rather than the LGCLF. This more than two-fold increase in apparent threshold from shot peening is consistent with previous data for 7000 series aluminum alloys with heavy shot peening [8,9]. Future testing of specimens at NASA Johnson should, however, provide a more resolved value of crack growth threshold under shot-peened conditions.

An example of *da/dN* data generated by NASA using a compressive pre-cracking and *K*-increasing test procedure to understand the threshold behavior is shown in Fig. 14 represented by red squares. Although not agreed upon throughout the industry, this test method is one of the better test methods to capture the small crack threshold of aluminum alloys. Also plotted is the data

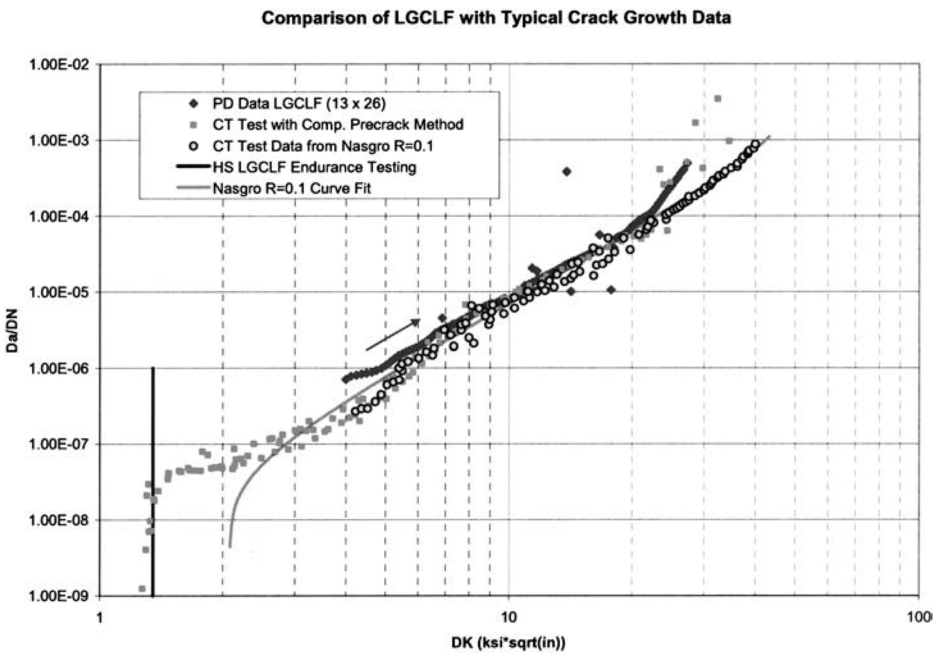

FIG. 14—*Comparison of 7075-T73 data from a constant amplitude load test of a LGCLF using DC potential drop, standard compact tension testing in literature, compressive pre-cracking and K-increasing tests, the NASGRO long crack curve fit.*

from the first NASA test run with a surface LGCLF tested with a DC potential drop system. These data points are shown as blue diamonds. This data was generated only in the region 2 and 3 portions of the curve. The endurance limit from standard S/N data for the same flaw is represented as a vertical line at a ΔK value of 1.35 $\text{ksi}\cdot(\text{in.})^{0.5}$. The remainder of the data is literature data and NASGRO curve fit data for compact tension testing equating to long crack properties.

Conclusions

Based on the data presented and the data currently being collected by NASA Johnson the possibility of using laser generated crack-like defects in test specimens looks promising. Although the exact mechanism that drives the crack-like performance is not entirely known, it is likely due to the sharpness of micro-cracks in the recast layer that may exist as created or may require low cycles of low tensile stress to initiate. In addition, the physical sharpness of the feature may either aid or dominate the crack growth characteristics. In either case, it is expected that the plastic zone sizes would be minimized and a steady-state condition would develop rapidly after external load is applied to the specimen. It is also not known how the same flaw would perform in reversed loading as the flaw at the surface is more open than a typical fatigue crack. Experiments using features with an open crack tip but filled with recast may be beneficial in reversed loading.

The benefits of such a feature include quick repeatable flaw generation and the ability to create very complex flaw geometries in complex specimens or parts that do not require pre-cracking. The technology has application in fracture mechanics as a way to induce flaws in specimens without a pre-existing stress history and to perform damage tolerance assessments on parts that might undergo full scale testing by creating a flaw in high stress areas of interest. There is also the possibility of creating a test method by which a standard high cycle fatigue test procedure like ASTM E466 is performed on a series of specimens with given flaw sizes and reduced in a similar manner to the screening specimens in this study. This would further allow calibration of particular flaw geometries to existing crack growth analysis methods, and would allow users interested primarily in threshold properties the ability to generate that data with only standard HCF testing equipment.

Acknowledgments

The authors would like to thank Scott Davis, Laser Specialist, Connecticut Center for Advanced Technology, Scott Forth, Senior Fracture Engineer, NASA Johnson, and Jack Kattler, Structure Lab Senior Technician, Hamilton Sundstrand, for their assistance.

References

[1] Forth, S., Le, D., and Turnberg, J., "An Evaluation of the Applicability of Damage Tolerance to Dynamic Systems," *Aging Aircraft Conference*, Feb. 2005.

[2] Forth, S., "Mechanical Data for Use in Damage Tolerance Analyses," NASA/TM-2004-213503 ARL-TR-3375.

[3] Forth, S., Newman, J., and Forman, R., "Anomalous Fatigue Crack Growth Data Generated Using the ASTM Standards," *J. ASTM Int.*, Vol. 3, No. 3, 2006, Paper ID JAI13180.

[4] Newman, J. et al., "Compresion Pre-Cracking to Generate Near Threshold Fatigue-Crack-Growth Rates in Two Aluminum Alloys," *International Conference on Fatigue Damage of Structural Materials V*, Sept. 2004.

[5] Legg, K., "Direct Part Marking of Aerospace Materials Sensitive to Temperature, Notches and Fatigue," *Presented at Workshop for Part Marking*, Nov. 2006.

[6] Forth, S., "The Purpose of Generating Fatigue Crack Growth Threshold Data," *Presented at Workshop for ASTM E08*, Nov. 15, 2006, ASTM International, West Conshohocken, PA.

[7] *ASM Handbook*, Vol. 16, "Non-Traditional Machining Processes-Electrical Discharge Machining," J. R. Davis, Ed., ASM International, Materials Park, OH, 1989.

[8] Mutoh, Y. et al., "The Effect of Residual Stresses Induced by Shot-Peening on Fatigue Crack Propagation in Two High Strength Aluminum Alloys," *Fatigue Fract. Eng. Mater. Struct.*, Vol. 10, 1987, pp. 261–272.

[9] Hammond, D., "Fatigue Fracture in the Presence of Shot Peening Residual Stresses, Initiation, Propagation, and Relaxation," Ph.D. Thesis, School of Mechanical Engineering, Cranfield Institute of Technology, Cranfiled, UK, 1988.

ELEVATED TEMPERATURE
AND
ENVIRONMENTAL EFFECTS

ASTM Special Technical Publication, Vol. 5, No. 8
Paper ID JAI101548
Available online at www.astm.org

V. N. Shlyannikov,[1] *B. V. Ilchenko,*[1] *and N. V. Boychenko*[1]

Biaxial Loading Effect on Higher-Order Crack Tip Parameters

ABSTRACT: The higher-order asymptotic crack-tip fields are considered for a Mode I in power-law plastic and creeping materials under plane strain conditions. Using an asymptotic expansion and separation of variables for the stress function, a series solution is obtained for stress components at a crack tip. In addition, full-field finite element analysis based on a modified layer approach is employed to model the effects of biaxial loading on nonlinear behavior. Loadings were applied related to a range of biaxial stress ratio $(-2, +2)$. The radial and angular stress distributions and higher-order amplitude coefficients for plastic materials are obtained. Crack tip higher-order fields under various conditions of biaxial loading and spanning the range of times from small scale creep to extensive creep are presented. Account is taken of the radial distance accompanying crack tip blunting. The phenomenon of stress redistributions along crack plane on creep time as a function of biaxial stress ratio is stated. The regions of dominance of the HRR-type field under various biaxial stress ratio, crack distance, hardening exponent, and creep time are found. Good agreement analytical findings with finite element results conforms that HRR-solution corresponds only to the equibiaxial tension which is a particular case of biaxial loading. It is further demonstrated that the higher-order both for plastic and creeping fields are controlled through constraint parameter A_2 by biaxial stress ratio. By fitting numerical results for plastic and creeping materials, two empirical formulas were obtained to describe the higher-order terms amplitude coefficients A_2 distributions depending on biaxial stress ratio, crack distance, hardening exponent, and creep time.

Manuscript received January 29, 2008; accepted for publication July 16, 2008; published online August 2008.
[1] Research Center for Power Engineering Problems of the Russian Academy of Sciences, Lobachevsky Street, 2/31, P.O. 190, Kazan, 420111, Russia, e-mail: shlyannikov@mail.ru

Citation: Shlyannikov, V. N., Ilchenko, B. V., and Boychenko, N. V., "Biaxial Loading Effect on Higher-Order Crack Tip Parameters," *J. ASTM Intl.*, Vol. 5, No. 8. DOI10.1520/JAI101548. Available online at www.astm.org. Also included in JAI Special Issue STP 1508, *Fatigue and Fracture Mechanics: 36th Volume,* R. W. Neu, K. R. W. Wallin, and S. R. Thompson, guest editors, ASTM International, West Conshohocken, PA, 2009, pp. 609-640.

KEYWORDS: biaxial loading, higher-order terms, constraint parameter, crack-tip field, plane strain, plastic and creeping materials

Introduction

The J-integral is considered as the basic approach of nonlinear fracture mechanics for rate-independent materials under monotonic loading conditions. It is established [1] that the application of the J-integral must meet the conditions stating that the regions in which finite strain effects are important and in which the occurring microscopic processes must each be included well within the region of the small-strain solution dominated by singularity fields. This condition in literature is called J-dominance. It has been known that J depends on the geometry and loading of the cracked body and hence J-integral alone does not describe the stress and strain state at the crack tip univalently. Wide investigations of so-called constraint effects are carried out with the aim of improving approximation of the near-tip crack fields. Various approaches have been proposed to quantify crack-tip constraint and as a result a second parameter has been introduced.

It is necessary to keep in mind that the analysis of constraint effects at fracture first of all is related to the background and the limitation of the HRR-fields [2,3] application. The singular HRR-field is asymptotically exact as the crack tip is approached. It has been pointed out in the latter reference that in the region affected by the blunting which is within a few crack-tip opening displacements, the J-integral is path dependent, but the plastic singular fields retain their validity as outer fields surrounding and controlling this area.

The characteristic size R of the dominance zone of the singularity fields depends strongly on geometry and hardening. Up to now it is clear that the geometry of a cracked body is influenced by a second, nonsingular term (so-called T-stress) parallel to the crack flank. The T-stress is considered as inherent property in various fracture specimen geometries or structure components. The magnitude of the T-stress is defined through a biaxiality factor, proposed by Leevers and Radon [4]. They have tabulated the crack-length dependence of an elastic parameter expressing the degree of stress biaxiality inherent to the six of standard specimen geometries.

Most numerical investigations concerning taking into consideration the nonsingular T-stress use the modified boundary layer approach to describe the crack-tip stress fields. This approach has been intensively used for both pure Mode I and mixed mode loading conditions. Larsson and Carlsson [5] were the first to make use of the T-stress in modified boundary layer finite element analyses. The main idea is that the mesh is loaded by tractions related to both the elastic singular field, governed by stress intensity factor K, and the constant T-stress field for fracture specimen configurations. The nonsingular stress for each specimen is obtained as the difference between stresses for the corresponding specimen and boundary layer solution. By comparing results for two type analyses Larsson and Carlsson [5] have shown that including the T-stress gave an improved representation of the elastic-plastic crack-tip stress fields.

Several numerical investigations have been carried out by use of the modified boundary layer approach to examine crack-tip stress fields and account for the loss of J-dominance at the crack tip under conditions of small to large (through intermediate) scale yielding. Betegon and Hancock [6] as well as O'Dowd and Shih [7] have analyzed Mode I plane strain crack by using the elastic K-T field as remote boundary conditions. These analyses imply that if fracture depends on crack-tip stress field it may be possible to describe crack behavior by using two parameters, namely J-integral and T-stress. The common point of view of their results is that for small negative values of T-stress, the actual crack-tip stress fields fell below the HRR-field, and as T became more negative, the stresses fell much further; while for zero or positive T-stress J-dominance is maintained and these solutions lie close together. Shlyannikov [8] has found that the near-tip second stress fields are dependent on magnitude and sign of the T-stress, but this parameter itself does not describe the remote boundary conditions univalently whereas the same value of T-stress can correspond to several different plastic fields.

O'Dowd and Shih [7] have introduced as alternative constraint methodology a biparametrical approach on the base of J and a hydrostatic stress parameter Q. Afterwards Yuan [9], and Yuan and Brocks [10] applied this approach to the detailed finite element analyses of three-dimensional cracked geometries. It has been shown that the Q term is a dimensionless measure of deviation of the actual crack-tip stress field from the HRR-field and it is a better parameter than T as it can extend into full plastic state. O'Dowd and Shih [7] have proposed relations between T and Q, while Anderson [11] by applying their finite element results has obtained a family of J-Q toughness loci. The Q-stress, like T-stress, is supposed to characterize effects of in-plane constraint in elastic-plastic fracture mechanics. Both quantities obviously affect the hydrostatic stress and, hence, stress triaxiality in the same way, i.e., negative values lower, positive values raise the hydrostatic stress. Yuan and Brocks [10] have shown that the second term in the near tip three-dimensional stress fields appears to depend on the distance to the tip and to the free surface of the specimen. Hence, the whole three-dimensional crack front fields cannot be correctly described by a two-parameter formulation as the load increases. However, they have found a unique linear relationship between Q and the hydrostatic stress in all three-dimensional crack front fields.

Various investigators [7,10,12] have produced results for estimation of the effect of fracture specimen geometry and sizes as well as different loading conditions on the constraint effects in the crack tip regions.

A two-term, [13,14] as well as a three-term, [12,15] generalized asymptotic expansion of the stress function were used to describe the stress field in the vicinity of the crack tip in a power hardening material and also to interpret the constraint effects due to finite specimen geometry and loading configurations. Asymptotic analyses based on a higher-order terms power expansion under plane strain conditions confirmed that the second and third term can be expressed by one additional amplitude parameter. The results showed also that contrary to the T-stress of elastic fracture mechanics, the angular function of the second term $\tilde{\sigma}_{ij}$ in Q-stress formulation is not only dependent on the polar angle θ but also on the distance to the crack tip r as reported [12,16–18].

Although there has been a wide range of studies on the effects of constraint for Mode I, at the same time very little research has been reported in the literature concerning the biaxial loading influence. Most of the above analyses on the constraint effect are focused on the determination of second-order term amplitude under uniaxial tension or bending. Thus, the influence of the nominal stress biaxial ratio on dimensionless angular higher-order stress functions has not been studied so far, with the exception of O'Dowd and Shih's [7] and Yuan and Brocks's [10] investigations. In particular, it is not clear whether the *T*-stress is a unique parameter characterizing stress fields in a wide range of biaxial loading configurations under Mode I both plane strain and plane stress conditions. Moreover, only limited studies were conducted in the past to study the effect of loading biaxiality on both the higher order crack-tip fields and constraint parameter behavior for creeping materials.

The main objective of the present paper is to study the effect of biaxial loading on an angular variation of higher-order terms and crack-tip constraint parameters for general Mode I plane strain conditions. Plane strain asymptotic solution for angular variation of the higher-order terms is obtained by using the Nikishkov method [19]. To assess the validity of three-term asymptotic solution for various biaxial loading conditions, detailed finite element analysis is conducted for elastic-plastic and creeping materials. Behavior of different constraint parameters utilizing the amplitude of second term A_2, Q-stress correction term and the local triaxiality parameter h have been presented. The relations between a dimensionless amplitude factor of the second-order field and biaxial stress ratio η at different crack distance and creep time are determined for both plastic and creeping materials.

Higher-Order Term Asymptotic Expansion

The stress field in an elastic body containing a crack is presented by Williams [20] as a power series expansion

$$\sigma_{ij} = A_{ij}(\theta)r^{-1/2} + B_{ij}(\theta) + C_{ij}(\theta)r^{1/2} \tag{1}$$

The first term in this asymptotic solution is singular at the crack tip, whereas the higher-order terms are finite and bounded. The second term in the expansion (1) was named by Rice [21] as *T*-stress and the stress field in this case can be expressed in the following form

$$\sigma_{ij} = \frac{K}{\sqrt{2\pi r}} f_{ij}(\theta) + T\delta_{1i}\delta_{1j} \tag{2}$$

Generalization of the elastic asymptotic *T*-stress solutions for both biaxial and mixed mode loading was made by Eftis and Subramonian [22] and Theocaris and Michopoulos [23].

The higher-order terms approach was later extended on elastic-plastic fracture area under both small scale yielding and large scale yielding conditions. Li and Wang [13] and Sharma and Aravas [14] solved the plane boundary value problem with a two-term power expansion for power law hardening material assuming deformation theory of plasticity

$$\sigma_{ij}(r,\theta)=\left(\frac{J}{\alpha\sigma_y\varepsilon_y I_n r}\right)^{1/(m+1)}\tilde{\sigma}_{ij}^{(0)}(\theta)+Q\left(\frac{r\sigma_y}{J}\right)^{p}\tilde{\sigma}_{ij}^{(1)}(\theta) \tag{3}$$

where σ_y is yield stress and the first term represents the known HRR-solution. Note that the analytical results by Sharma and Aravas [14] as well as Yuan and Yang [24] provide dependences between the second-order term exponent p and strain hardening exponent m for plane strain and plane stress, respectively. An alternative form was presented later by O'Dowd and Shih [7] in which the leading HRR-term was replaced by the small scale yielding solution with $T=0$, that is

$$\sigma_{ij}=\left[\sigma_{ij}\left(\frac{r\sigma_y}{J},\theta\right)\right]^{SSY,T=0}+Q\sigma_y\tilde{\sigma}_{ij}(r,\theta) \tag{4}$$

O'Dowd and Shih [7] have therefore introduced some simplifications based on detailed finite element analyses. With reference to the T-stress concept they set

$$\sigma_{ij}=\left[\sigma_{ij}\left(\frac{r\sigma_y}{J},\theta\right)\right]^{REF}+Q\sigma_y\delta_{ij} \tag{5}$$

The second crack-tip field parameter, Q, is obtained as the difference parameter between the full stress field and the reference solution

$$Q=\frac{\sigma_{\theta\theta}-\sigma_{\theta\theta}^{REF}}{\sigma_y},\quad \text{at}\quad \frac{r\sigma_y}{J}=2,\quad \theta=0 \tag{6}$$

The reference solution can be taken as the plane strain field with zero transverse stress, $[\sigma_{ij}]^{SSY,T=0}$ in small scale yielding (SSY) or as the HRR stress field, $[\sigma_{ij}]^{HRR}$, under fully plastic conditions.

Because the validity of all concepts mentioned above depends on the chosen reference field a local parameter of crack tip constraint and stress triaxiality is proposed by Henry and Luxmoore [25] as a secondary fracture parameter

$$h(r,\theta,z)=\sigma_{kk}\Big/\left(3\sqrt{\frac{3}{2}s_{ij}s_{ij}}\right) \tag{7}$$

where σ_{kk} and s_{ij} are hydrostatic and deviatiric stresses, respectively. Being the function of both the first invariant of the stress tensor and the second invariant of the stress deviator, it is a local measure of in-plane and out-of-plane constraint effects that is independent of any reference field.

Three-Term Asymptotic Solution

As pointed out previously, the HRR-type one-term singularity field generally dominates in a very small region or does not exist near a crack tip for real structures. Some attempts were made to improve the description of the near-tip stress field by introducing an additional parameter. Thus, a more mathematically rigorous approach for the introduction of a second fracture mechanics parameter is proposed on the base of the higher-order elastic-plastic asymptatic expansions. Yang et al. [16] and Nikishkov [19] performed a complete analysis of three-term asymptotic fields for Mode I plane strain conditions. They have shown that the first three terms of the asymptotic expansion are sufficient to represent the stress field in the crack tip vicinity in a power-law hardening material. Some details of these solutions follow.

It is assumed the stress components near a crack tip are separable and can be expressed as a series as

$$\bar{\sigma}_{ij} = A_1 \lfloor \bar{r}^{s1} \tilde{\sigma}_{ij}^{(1)}(\theta) + A_2 \bar{r}^{s2} \tilde{\sigma}_{ij}^{(2)}(\theta) + A_3 \bar{r}^{s3} \tilde{\sigma}_{ij}^{(3)}(\theta) + \ \ldots \rfloor \tag{8}$$

where r and θ are polar coordinates centered at the crack tip, the index 1,2,3 corresponds to the first-order, second-order, and third-order fields, respectively. The first term of Eq 8 is the HRR solution, where dimensionless angular functions $\tilde{\sigma}_{ij}^{(1)}(\theta)$ have been determined by solution of the nonlinear fourth-order differential equation and are well known in the literature. A_1, A_2, A_3 are undetermined amplitude factors, S_1, S_2, S_3 are the exponents of stress functions. In the polar coordinate system, the equilibrium equations have the following form:

$$\sigma_{rr,r} + \frac{1}{r}\sigma_{r\theta,r} + \frac{1}{r}(\sigma_{rr} - \sigma_{\theta\theta}) = 0$$

$$\sigma_{r\theta,r} + \frac{1}{r}\sigma_{\vartheta\theta,\theta} + \frac{2}{r}\sigma_{r\theta} = 0 \tag{9}$$

Substitution of Eq 8 into Eq 9 yields the relationships among the angular stress functions

$$\left. \begin{array}{l} (s_k + 1)\sigma_{rr}^{(k)} - \sigma_{\theta\theta}^{(k)} + \sigma_{r\theta,\theta}^{(k)} = 0 \quad (k = 1,2,3) \\ \sigma_{\theta,\theta}^{(k)} + (s_k + 2)\sigma_{r\theta}^{(k)} = 0 \end{array} \right\} \tag{10}$$

Formulas 10 are the final governing equations for the first-order, second-order, and third-order asymptotic fields and the stress exponents. They are exactly the same as those given by Nikishkov [19] for power-law hardening materials. According to these solution properties the amplitudes of the second-order and third-order fields are not independent of each other and have a simple relationship

$$A_3 = A_2^2 \tag{11}$$

and for hardening exponent $m \geq 3$, the stress exponents are related by

$$s_1 = -1/(m+1), \quad s_3 = 2s_2 - s_1 \tag{12}$$

It is noted that the amplitude factor A_2 cannot be determined in the asymptotic analysis. Therefore in this work the values of A_2 are determined by matching the three-term stress solutions in Eq 8 with known crack-tip fields, such as finite element results.

The first term in Eq 8 corresponds to the HRR field [2,3] with the amplitude coefficient A_1

$$A_1 = \left(\frac{J}{\alpha \sigma_y \varepsilon_y I_n} \right)^{1/(m+1)} \tag{13}$$

and dimensionless scaling integral I_n

$$I_n(\theta, M_p, m) = \int_{-\pi}^{\pi} \Omega(m, \theta) d\theta$$

$$\Omega(m, \theta) = \frac{m}{m+1} \tilde{\sigma}_e^{m+1} \cos\theta - \left[\tilde{\sigma}_{rr} \left(\tilde{u}_\theta - \frac{d\tilde{u}_r}{d\theta} \right) - \tilde{\sigma}_{r\theta} \left(\tilde{u}_r + \frac{d\tilde{u}_\theta}{d\theta} \right) \right] sin\,\theta - \frac{1}{m+1} (\tilde{\sigma}_{rr} \tilde{u}_r + \tilde{\sigma}_{r\theta} \tilde{u}_\theta) \cos\theta \tag{14}$$

where $\tilde{\sigma}_e$ is the Mises equivalent stress. The dimensionless constant I_n and the θ-variation functions of the suitably normalized functions $\tilde{\sigma}_{ij}$ and $\tilde{u}_i$ depend only on the hardening exponent.

One of the purposes of our work is to reveal the asymptotic results that can accurately characterize the mechanical fields near a crack tip in creeping materaials. It should be noted that creep fracture mechanics has often relied on the straightforward application of the Hoff analogy [26] by which the HRR solution for power-law creeping materials can be obtained by replacing the J-integral by $C(t)$-integral, and by replacing strains and displacements by strain rates and displacement rates, respectively. Based on this argument, Nguyen et al. [27,28] and Chao et al. [29] extended the J-A_2 three-term solution of Yang et al. [16] and Nikishkov [19] for elastic-plastic hardening materials to a three-term near-tip solution for a plane strain Mode-I crack in power-law creeping materials with two parameters: C-integral and a constraint parameter A_2. Hence, the three-term asymptotic fields under the steady-state creep are described by the same Eq 8 as those for elastic-plastic state, but with different amplitude factors A_1, A_2, A_3. The angular functions of stress $\tilde{\sigma}_{ij}^{(k)}(\theta)$ in Eq 8 for creeping materials are the same as those for power-law hardening materials. It means that the solution constructions are similar for two kinds of materials. In the case of the creeping material the first term amplitude factor A_1 can be obtained by replacing appropriate parameters. Using the Hoff analogy to contrast the power-law creep relation with the power-law hardening relation, Ridel and Rice [30] presented the HRR-type singularity field for power-law creep materials with amplitude A_1

$$A_1(t) = \left(\frac{C(t)}{\dot{\varepsilon}_0 \sigma_0 I_n} \right)^{1/(n+1)} \tag{15}$$

where σ_0 is a reference stress, $\dot{\varepsilon}_0$ is a reference creep strain rate and n is the creep exponent. The amplitude factor $C(t)$, which depends upon the applied time, magnitude of the remote loading, crack configuration and material properties, is defined by Bassani and McClintock [31].

To complete the three-term asymptotic solution, it is necessary to calculate amplitude factor A_2. A few methods have been proposed for this pupose, e.g., the point-matching technique of Chao [32], the least square approach of Nikishkov [19], the weight function approach of Chao and Zhu [33]. In the present work, the stress components $\bar{\sigma}_{rr}$ and $\bar{\sigma}_{\theta\theta}$ of Eq 8 at $\theta=0°$ for different crack distance $\bar{r}$ are used to determine a value of A_2 by matching the three-trem solution with appropriate finite element results for $\bar{\sigma}_{rr}^{FEM}$ and $\bar{\sigma}_{\theta\theta}^{FEM}$. Thus, the stresses $\bar{\sigma}_{rr}$, $\bar{\sigma}_{\theta\theta}$, or some combinations of them, e.g., $(\bar{\sigma}_{\theta\theta}/\bar{\sigma}_{rr})$ can be used for fitting. Based on the stress asymptotic expansion 8, one has

$$\frac{\bar{\sigma}_{\theta\theta}}{\bar{\sigma}_{rr}} = \frac{\bar{r}^{s_1}\tilde{\sigma}_{\theta\theta}^{(1)} + A_2\bar{r}^{s_2}\tilde{\sigma}_{\theta\theta}^{(2)} + A_2^2\bar{r}\tilde{\sigma}_{\theta\theta}^{(3)}}{\bar{r}^{s_1}\tilde{\sigma}_{rr}^{(1)} + A_2\bar{r}^{s_2}\tilde{\sigma}_{rr}^{(2)} + A_2^2\bar{r}\tilde{\sigma}_{rr}^{(3)}} \tag{16}$$

Substituting the finite element stress component into the three-term solution 8, one obtains the first term amplitude factor A_1

$$A_1^{FEM} = \bar{\sigma}_{\theta\theta}^{FEM}/(\bar{r}^{s_1}\tilde{\sigma}_{\theta\theta}^{(1)} + A_2\bar{r}^{s_2}\tilde{\sigma}_{\theta\theta}^{(2)} + A_2^2\bar{r}^{s_3}\tilde{\sigma}_{\theta\theta}^{(3)}) \tag{17}$$

In this system of linear equations the governing paremeters are the second-term amplitude factor A_2 and ratio $\bar{\sigma}_{\theta\theta}^{FEM}/\bar{\sigma}_{rr}^{FEM}$. Note that the value of numerically determined the first term amplitude coefficient A_1^{FEM} by Eq 17 will be used for the comparison with appropriate analytical solutions for A_1 concerning the elastic-plastic Eq 13 and creeping Eq 15 materials.

The higher-order terms in Eq 8 control the deviation of the crack-tip fields from the HRR solution. The intensity of this deviation, in terms of the value of A_2, in a cracked body depends on crack tip distance, the loading configuration, material properties, and so on. Let us introduce the measure of such deviation, like Nikishkov [19] in the form of the sum of second and third terms in Eq 8

$$Q_{\theta\theta} = A_1(A_2\bar{r}^{s_2}\tilde{\sigma}_{\theta\theta}^{(2)} + A_2^2\bar{r}^{s_3}\tilde{\sigma}_{\theta\theta}^{(3)})$$

$$Q_e = A_1(A_2\bar{r}^{s_2}\tilde{\sigma}_e^{(2)} + A_2^2\bar{r}^{s_3}\tilde{\sigma}_e^{(3)}) \tag{18}$$

Before proceeding to the determination of both the second-order term amplitude and its angular variations stress expansion is normalized in such a way that direct comparisons with the solution developed by Hutchinson [2] can be made. It then follows purely from dimensional considerations that for elastic-plastic problem the distance from the crack tip r must scale by the yield stress σ_y when the loading is governed solely by J-integral

$$\bar{r} = (\sigma_y r/J) = (r/a)(\sigma_y E/\sigma^2\pi) \tag{19}$$

where σ is applied nominal stress and a is crack length. In the case of creeping material the loading governing parameter is the C-integral and a dimensionless radial coordinate is

$$\bar{r} = (\sigma_0\dot{\varepsilon}_0 r/C) = (r/a) \Bigg/ \left(\pi\sqrt{n}\left(\frac{\sqrt{3}}{2}\frac{\sigma}{\sigma_0}\right)^{n+1}\right) \tag{20}$$

where σ_0 is a reference stress, $\dot{\varepsilon}_0$ is a reference creep strain rate and n is the creep exponent. Note that for creeping material, the amplitude factors in the three-term solution Eq 8 depend generally on the creep time, magnitude of the applied loading, crack geometry, and material properties. Due to the complexities we consider in the present work different creeping stages. In this case it is usefull to normalize a current creep time t by the characteristic time t_T for

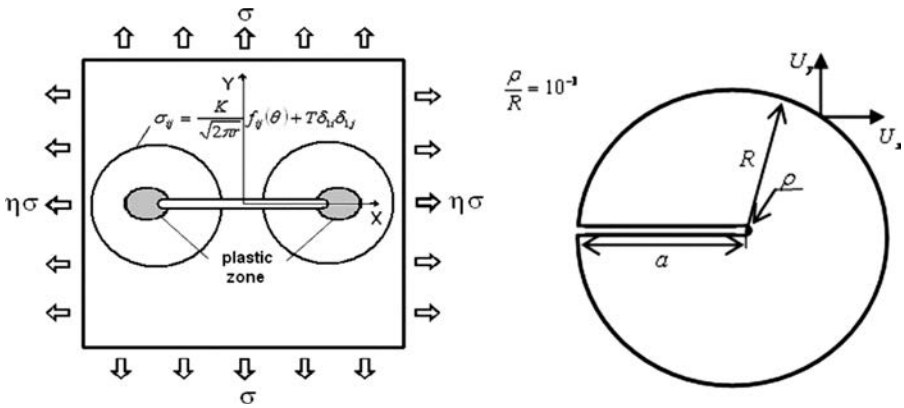

FIG. 1—*Biaxially loaded cracked panel.*

transition from small-scale creep to extensive creep which is given as [34]

$$\frac{t}{t_T} = \frac{t(n+1)EC}{(1-\nu^2)K_I^2} \tag{21}$$

where K_I is elastic stress intensity factor, ν is the Poisson's ratio, E is the Young's modulus.

The results for elastic-plastic and creeping materials of angular stress distributions for both general FEM-numerical solutions and asymptotic problems of the order 1,2,3 are normalized so that

$$\tilde{\sigma}_{e,max}^{FEM} = \left(\frac{3}{2} s_{ij}^{FEM} s_{ij}^{FEM}\right)_{max}^{1/2} = 1, \quad \tilde{\sigma}_{e,max}^{(k)} = \left(\frac{3}{2} s_{ij}^{(k)} s_{ij}^{(k)}\right)_{max}^{1/2} = 1, \quad k = 1,2,3 \tag{22}$$

Following the procedure for obtaining the three-term asymptotic solutions of Yang et al. [16] and Nikishkov [19] three-term asymptotic fields for elastic-plastic and creeping materails are reported here.

The Modified Boundary Layer Approach

The geometry considered in this section is traditional for the modified boundary layer formulation. A biaxially loaded cracked panel (Fig. 1) is imagined which contains an annular region where the local stress field under arbitrary remote loading may be essentially characterized by a scalable eigensolution (Williams [20], Eftis and Subramonian [22])

$$
\begin{cases}
\sigma_{xx} = \dfrac{K_1}{\sqrt{2\pi r}} \cos\dfrac{\theta}{2}\left[1 - \sin\dfrac{\theta}{2}\sin\dfrac{3\theta}{2}\right] + T \\
\sigma_{yy} = \dfrac{K_1}{\sqrt{2\pi r}} \cos\dfrac{\theta}{2}\left[1 + \sin\dfrac{\theta}{2}\sin\dfrac{3\theta}{2}\right] \\
\sigma_{xy} = \dfrac{K_1}{\sqrt{2\pi r}} \sin\dfrac{\theta}{2}\cos\dfrac{\theta}{2}\cos\dfrac{3\theta}{2}
\end{cases}
\tag{23}
$$

$$
T = \sigma(1 - \eta)\cos 2\beta \tag{24}
$$

Here T is the nonsingular second-order term or the T-stress, σ is the nominal stress applied in the Y-axis direction, β is the inclined crack angle referred to the Y-axis, η is the biaxial stress ratio, r and θ are polar coordinates centered at the crack tip. It is clear that T-stress does not describe the remote boundary conditions univalently whereas the same value of T-stress can correspond to several different loading conditions. Indeed, the value of $T=0$ can be achieved at $\eta=1$ for any β or at $\beta=\pi/4$ for any η. A circular disk (Fig. 1) containing the crack tip in a large panel is removed, modeling the near tip region with the modified boundary layer formulation.

The displacement components are based on the first two terms of the elastic crack tip field which are given by Eftis and Subramonian [22]

$$
\begin{cases}
u_x = \dfrac{K_1}{G}\sqrt{\dfrac{r}{2\pi}}\cos\dfrac{\theta}{2}\left[\dfrac{1}{2}(\kappa - 1) + \sin^2\dfrac{\theta}{2}\right] \\
+ \dfrac{(1-\eta)\sigma}{8G}\{r[\cos(\theta + 2\beta) + \kappa\cos(\theta - 2\beta) - 2\sin\theta\sin 2\beta] + (\kappa + 1)a\cos 2\beta\} \\
u_y = \dfrac{K_1}{G}\sqrt{\dfrac{r}{2\pi}}\sin\dfrac{\theta}{2}\left[\dfrac{1}{2}(\kappa + 1) - \cos^2\dfrac{\theta}{2}\right] \\
+ \dfrac{(1-\eta)\sigma}{8G}\{r[\sin(2\beta - \theta) + \kappa\sin(2\beta + \theta) - 2\sin\theta\cos 2\beta] + (\kappa + 1)a\sin 2\beta\}
\end{cases}
\tag{25}
$$

$$
K_1 = \frac{\sigma\sqrt{\pi a}}{2}[(1 + \eta) - (1 - \eta)\cos 2\beta] \tag{26}
$$

are prescribed on the outer boundary of the domain. In above equations, K_1 is the Mode I stress intensity factor. Further, G and a are the shear modulus and the crack length, and $\kappa=3-4\nu$ for plane strain. In the particular case of $\beta=\pi/2$ Eqs 25 and 26 are simplified for plane strain in a well known manner. These elastic displacements corresponding to the Mode I were applied along the circular boundary of the R radius.

The biaxial loads are applied through the stress intensity factors and the transverse T-stress. The crack tip is located at the center of the disk. The panel could be subjected to two perpendicular loads: one parallel to the Y-axis σ_{yy}^{∞} and another parallel to the X-axis σ_{xx}^{∞}. The magnitude of the traverse load σ_{xx}^{∞} can

TABLE 1—*Values of varied parameters in numerical calculations for elastic-plastic material.*

Line No.	1	2	3	4	5	6	7	8	9	10	11	12	13
η	2.0	1.75	1.5	1.25	1.0	0.75	0.5	0.25	0.0	−0.25	−0.5	−0.66	−0.9
$\bar{T}$	0.53	0.39	0.26	0.13	0.0	−0.13	−0.26	−0.39	−0.53	−0.66	−0.8	−0.87	−1.0

also be described by nominal stress biaxial ratio $\eta = \sigma_{xx}^{\infty}/\sigma_{yy}^{\infty}$. The panel was subjected to biaxial loading with a large number of different values for η. To apply the load in each particular analysis, a fixed value was selected for σ_{yy}^{∞} throughout total analysis. Varied parameters of biaxial loading Mode I conditions for elastic-plastic material at $\beta = \pi/2$ and resulting T-stress values are listed in Table 1, where $\bar{T} = T/\sigma_y$ is normalized by the yield stress σ_y.

For creeping material we consider three different biaxial stress states: equibiaxial tension-compression ($\eta = -1$), uniaxial tension ($\eta = 0$), and equibiaxial tension-tension ($\eta = +1$). Each type of biaxial loading is analyzed at nine stages of creep time which is varied from $t = 0$ up to $t = 5 \cdot 10^4$ hours. Our computations terminated at $t = 5 \cdot 10^4$ hours, which is the time when the creep zone radius equals about 80 % of the plate outer boundary. All values of creep time t are normalized by reference time t_T. We define the reference time, t_T, as the time corresponding to the transition from the small scale creep to the extensive creep. Table 2 gives the values of creep time in both natural and dimensionless form.

The ANSYS [35,36] finite element code is used to solve modified boundary layer problems. A large circular domain containing a notch along one of its radii, which is entirely represented by 3-D plane strain is considered. Due to symmetry, only one-half of the panel was simulated in the finite element code ANSYS. A mesh consisted of 40 fans of elements circumferentially and 45 element rings radially. Radial sizes of elements are varied according to the geometric progression. A finite element mesh consisting of 1905 nodes and 1849 eight-nodes quadrilateral elements was used. To consider the details of large deformation and blunting of the crack tip, a typical mesh was used to model the region near the notch tip. The radius of outermost boundary circular domain R (along which the modified boundary condition is given), is about $10^3\rho$, where ρ is the initial notch root radius. In the undeformed configuration, the center of curvature of the notch coincides with the center of the circular domain.

TABLE 2—*Values of varied creep time in numerical calculations for creeping material.*

No.	1	2	3	4	5	6	7	8	9
t [hour]	$1 \cdot 10^2$	$3 \cdot 10^2$	$5 \cdot 10^2$	$1 \cdot 10^3$	$3 \cdot 10^3$	$5 \cdot 10^3$	$1 \cdot 10^4$	$3 \cdot 10^4$	$5 \cdot 10^4$
t/t_T	0.0925	0.2775	0.4625	0.925	2.775	4.625	9.25	27.75	46.25

Models of Materials Behavior

Our attention in this work is focused on two-dimensional Mode I stationary crack problems under plane strain conditions. In general, the material deformation behavior is described by additive decomposition of the elastic, plastic and creep strains

$$\varepsilon_{total} = \varepsilon_{elastic} + \varepsilon_{plastic} + \varepsilon_{creep} \tag{27}$$

Here the elastic, plastic, and creep strains are evaluated independently. All are based upon the current stress state but not on each other. The creep strain combined with the plastic strain comprise the inelastic strain. The creep strains themselves are not evaluated against a yield stress, do not require a higher stress value for more creep strain to occur, and do not cause plastic hardening of the material. However, the plastic strains are evaluated against a yield stress, require a higher stress value for more plastic strain to develop, and cause plastic hardening of the material. In our work two different strain treatments are used for calculating total strain. The first of them is obtained by combining elastic and isotropic hardening, while the second one is combined elastic, isotropic hardening and creep.

The Ramberg-Osgood model

$$\frac{\varepsilon}{\varepsilon_y} = \frac{\sigma}{\sigma_y} + \alpha\left(\frac{\sigma}{\sigma_y}\right)^m \tag{28}$$

was employed to define the stress-strain curve corresponding to the elastic-plastic material properties. In Eq 28, σ_y is the yield stress, m is the hardening coefficient and α and ε_y are two fitting parameters. The parameter ε_y is usually taken to be σ_y/E. Two fitting parameters are determined by means of least squares minimization. It is well known that this fit type yields a good approximation of the true stress-strain curve for high plastic strains but for low plastic strains, the stresses are lower than the experimental data. In our case the typical relative difference between experimental and fitting values of the true strain is less than 5 %.

In the multi-axial case the corresponding constitutive equations of the J_2-deformation theory of plasticity are

$$\frac{\varepsilon_{ij}}{\varepsilon_y} = (1+\nu)\frac{S_{ij}}{\sigma_y} + \frac{1-2\nu}{3}\frac{\sigma_{pp}}{\sigma_y}\delta_{ij} + \frac{3}{2}\alpha\left(\frac{\sigma_e}{\sigma_y}\right)^{m-1}\frac{S_{ij}}{\sigma_y} \tag{29}$$

or in incremental form

$$\dot{\varepsilon}_{ij} = (1+\nu)\dot{\sigma}_{ij} - \nu\dot{\sigma}_{kk}\delta_{ij} + \frac{3}{2}m\alpha\left(\frac{\sigma_e}{\sigma_y}\right)^{m-2}\frac{S_{ij}}{E}\frac{\dot{\sigma}_e}{\sigma_y} \tag{30}$$

A purely power-law creeping material behavior governed by Norton constitutive relation and under uniaxial tension, the total strain rate is related to the stress by

$$\dot{\varepsilon} = \dot{\varepsilon}_0 \left[\frac{\sigma}{\sigma_0} \right]^n \quad \text{or}\, \dot{\varepsilon} = B\sigma^n \tag{31}$$

where σ_0 is a reference stress, $\dot{\varepsilon}_0$ is a reference creep strain rate and n is the creep exponent. Note that a combined constant $B = \dot{\varepsilon}_0 / \sigma_0^n$ is often used. Under multi-axial stress state, based on the J_2-deformation theory, the extension of the uniaxial creep relation can be written as

$$\dot{\varepsilon}_{ij} = \frac{3}{2} \dot{\varepsilon}_0 \left(\frac{\sigma_e}{\sigma_0} \right)^{n-1} \frac{S_{ij}}{\sigma_0} \tag{32}$$

In Eqs 28–32 ν is the Poisson ratio, δ_{ij} is the Kronecker delta, $\dot{\varepsilon}_{ij}$ are the components of the strain rate tensor, σ_{ij} are the component of the stress tensor, S_{ij} are the components of the deviatoric stress tensor, $\sigma_e = (3/2 S_{ij} S_{ij})^{1/2}$ is the Mises effective stress. Typically, the material constants E, ν, σ_y, m, n, σ_0, $\dot{\varepsilon}_0$, or B are obtained experimentally from uniaxial tests at the temperature of interest. For the present problem, the Young's modulus, Poisson's ratio, and the yield stress were considered to be 205 GPa, 0.3 and 380 MPa. The strain hardening exponent m was 4.96. The creep parameter and the creep exponent are $B = 1.4 \cdot 10^{-10}$ and $n = 3$. The Ramberg-Osgood model was introduced into the finite element code using a piecewise linear model available in ANSYS for describing material properties.

After the solution of an elastic-plastic problem, the ANSYS output file is used as an input data for FORTRAN programs developed to determine the dimensionless angular distributions and the amplitude of the second order term according to Eqs 8, 16, and 17.

Results and Discussion

Radial Stress Distributions for Elastic-Plastic Material

In the present work the full field numerical solution $\bar{\sigma}_{ij}^{FEM}(r, \theta)$ to the two parameter boundary layer formulation is taken to be the exact solution. First, the stress distribution ahead of the crack-tip ($\theta = 0$) under Mode I at $\beta = \pi/2$ was investigated. The state of biaxiality is given by $\eta = \sigma_{xx}^{\infty} / \sigma_{yy}^{\infty}$. The stresses $\bar{\sigma}_{\theta\theta}$ and $\bar{\sigma}_{rr}$ with several levels of T-stress and η are displayed together with HRR solution in Fig. 2 where the stresses are normalized by the yield stress σ_y and the radial distance r is normalized by J/σ_y. It can be seen that finite strain effects dominate for the normalized radial distance $r\sigma_y/J < 2$, while higher-order terms can be significant at large distances. For this reason, it is necessary to show the fields in the interval $0 < r\sigma_y/J < 12$. In the region of $r\sigma_y/J > 2$ where stress relaxation due to the crack tip blunting does not exist, the near-tip stresses depend on the sign and amplitude of the T-stress, and have nearly equidistant shift with the HRR field. With positive T-stress and $\eta > 1$, the stresses are larger than the ones of the HRR distribution, but the difference is little. However, with negative T-stress and $\eta < 1$, the stresses considerably decrease below the ones of the HRR solution as the absolute value of T-stress increases.

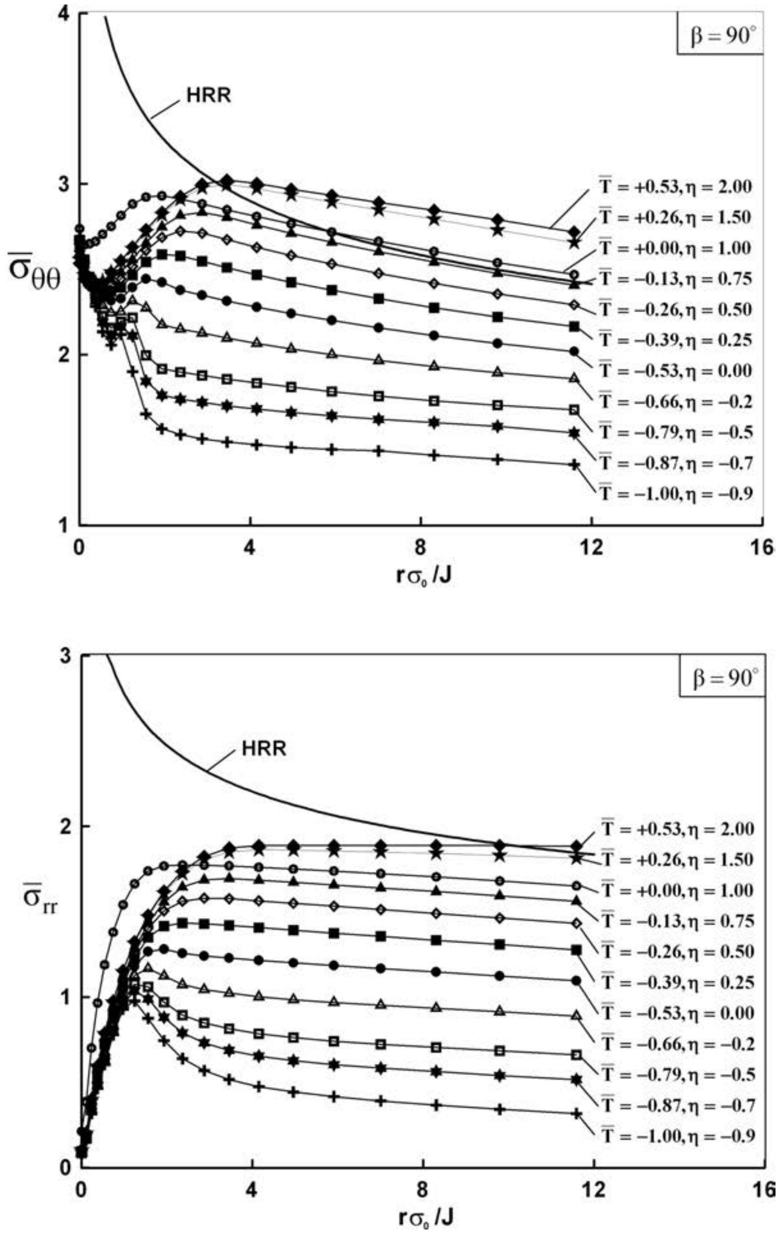

FIG. 2—*Radial distribution of stresses along $\theta = 0°$ under plane strain biaxial loading.*

Our results show that at the same negative and positive T-stress magnitudes, the tangential stress distributions do not coincide with each other because the same magnitudes of the T-stress can be obtained by the combination of different values of the biaxial stress ratio η and crack angle β. Note that the investigation of Hutchinson [2] is concerned with the plastic deformation at the crack tip in two-dimensional stress field which is *uniaxial tension* in a direction perpendicular to the crack far from it. For the uniaxial tension when $\eta=0$ at $\beta=\pi/2$ the nonsingular term is $\bar{T}=-\bar{\sigma}(1-\eta)=-\bar{\sigma}$ and cannot approach zero. Only under *equi-biaxial tension* when $\eta=1.0$ the nonsingular term $\bar{T}=\bar{\sigma}(1-\eta)=0$ approaches zero. However, the solution which has been used in the work [2] for elastic stress intensity factor $K_I=0.5\sigma\sqrt{\pi a}(1+\eta-(1-\eta)\cos 2\beta)$ reduces for pure Mode I at $\beta=\pi/2$ to $K_I=\sigma\sqrt{\pi a}$ and is independent of biaxial stress ratio η. Therefore, strictly speaking, it is necessary to make the comparison of these or those full field solutions with the HRR-type fields only for the case of the *equi-biaxial tension* when $T/\sigma_y=0$ but not for that of the *uniaxial tension* when $T/\sigma_y=-\sigma/\sigma_y$.

Our numerical solutions clearly indicate that the crack-tip fields cannot be adequately predicted under biaxial loading by inclusion of the T-stress as a second crack-tip parameter. It is found that the near-tip second stress fields are dependent on magnitude and sign of the T-stress, but this parameter itself does not describe the remote boundary conditions univalently whereas the same value of T-stress can correspond to several different plastic fields. So hereafter, we shall interpret our numerical results in terms of load biaxiality η instead of the T-stress.

Angular Stress Distributions for Elastic-Plastic Material

In order to demonstrate the angular distributions of a stress field, in this section the full field finite element results, HRR-fields and the three-term solutions are reported and compared. The full field finite element distributions of the stress components for crack angle $\beta=\pi/2$ are represented in Fig. 3. The full field finite element solution is indicated by the symbols while the HRR field is indicated by a solid line. It is observed that in Fig. 3 the full field finite element solutions of all stress components $\tilde{\sigma}_{\theta\theta}$, $\tilde{\sigma}_{rr}$, and $\tilde{\sigma}_{r\theta}$ at $\beta=\pi/2$ deviate substantially from those of HRR fields. Results which are represented in Fig. 3, monotonic character of T-stress change from $\bar{T}=-1.0$ up to $\bar{T}=0.53$ coincides with the biaxial stress ratio variation from $\eta=-0.9$ to $\eta=2.0$.

Note that up to now the classical HRR-solution has not been put in correspondence to any type of biaxial loading. From the analysis of the Eq 24 it follows that for pure Mode I ($\beta=\pi/2$) the nonsingular second-order term $\bar{T}$ can be equal to zero only in case of equi-biaxial tension with $\eta=+1$. Figure 4 shows full field finite element angular variations of stress components and the HRR field at radial distances $r\sigma_y/J=4.05$ and $r\sigma_y/J=11.3$ under different biaxial loading conditions. It can be seen that the HRR field is close only to the equi-biaxial tension angular stress distributions.

In order to have a further appreciation of the quality of the three-term expansion, Fig. 5 shows the angular stress variations of the three-term solutions $\tilde{\sigma}_{\theta\theta}$ and $\tilde{\sigma}_{rr}$ according to Eqs 8 and 10. It is observed that the load biaxiality ratio η has certain influence on the dimensionless stress angular distribu-

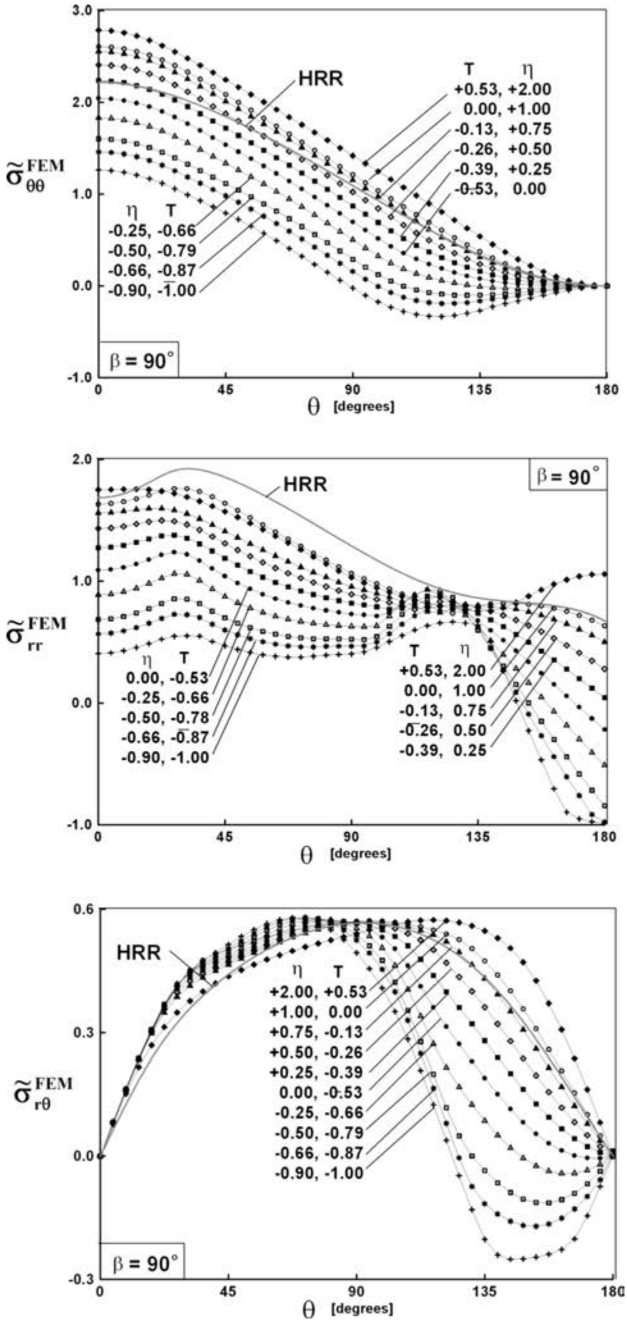

FIG. 3—*Angular distributions of the stress components obtained from FEM analysis under biaxial loading.*

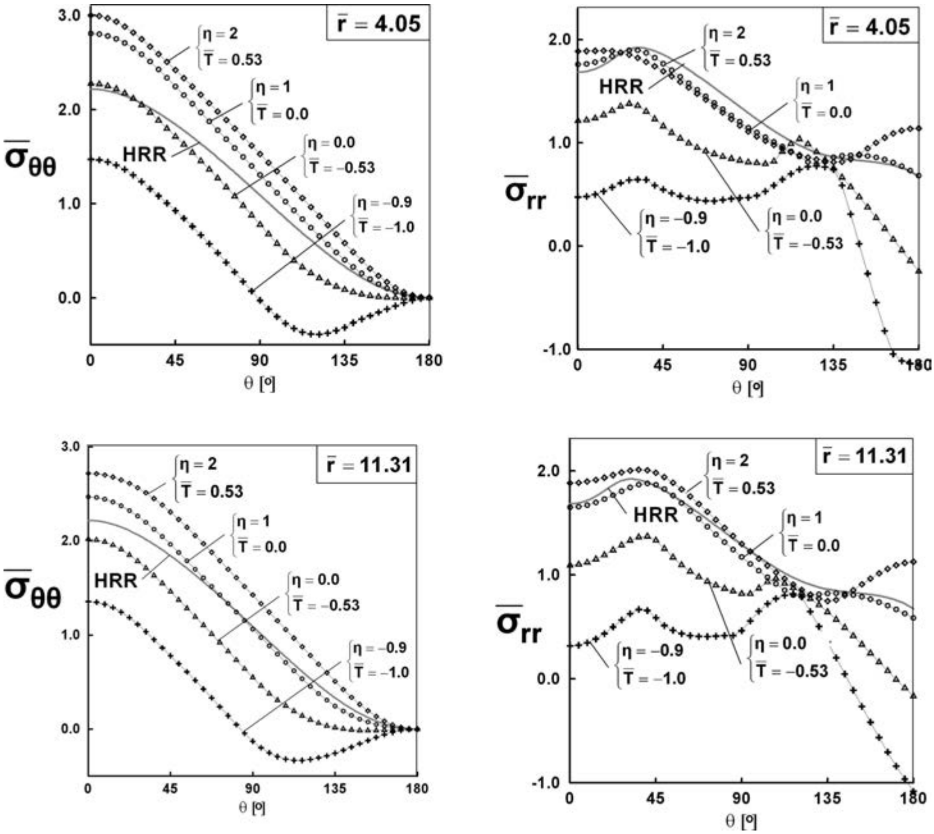

FIG. 4—*Angular stress distributions under different biaxial stress states.*

tions. Besides all calculated stress components have strong dependence on the crack tip distance scaled by J/σ_y. On the basis of both numerical (Fig. 4) and analytical (Fig. 5) results, we can conclude that a three-term expansion indeed provides a more accurate description of the actual near-tip fields for power-law elastic-plastic material. As it follows from Fig. 5, to speak about the regions of dominance of the HRR solution is only possible in case of the equi-biaxial tension when $\eta = +1$ and $\bar{T} = 0$. Other biaxial loading types do not fall under determinancy domain of the HRR solution because in these cases the deviation of the HRR-field with respect to the three-term asymptotic solution is quite large.

Constraint Parameters Behavior for Elastic-Plastic Material

The tangential and radial stresses near the crack tip were obtained in this paper to explore the influence of the biaxial load coefficient η and crack tip distance $\bar{r}$ on constraint effect under Mode I plane strain conditions. The values of the first A_1 and second A_2 amplitude parameters are determined by the fitting pro-

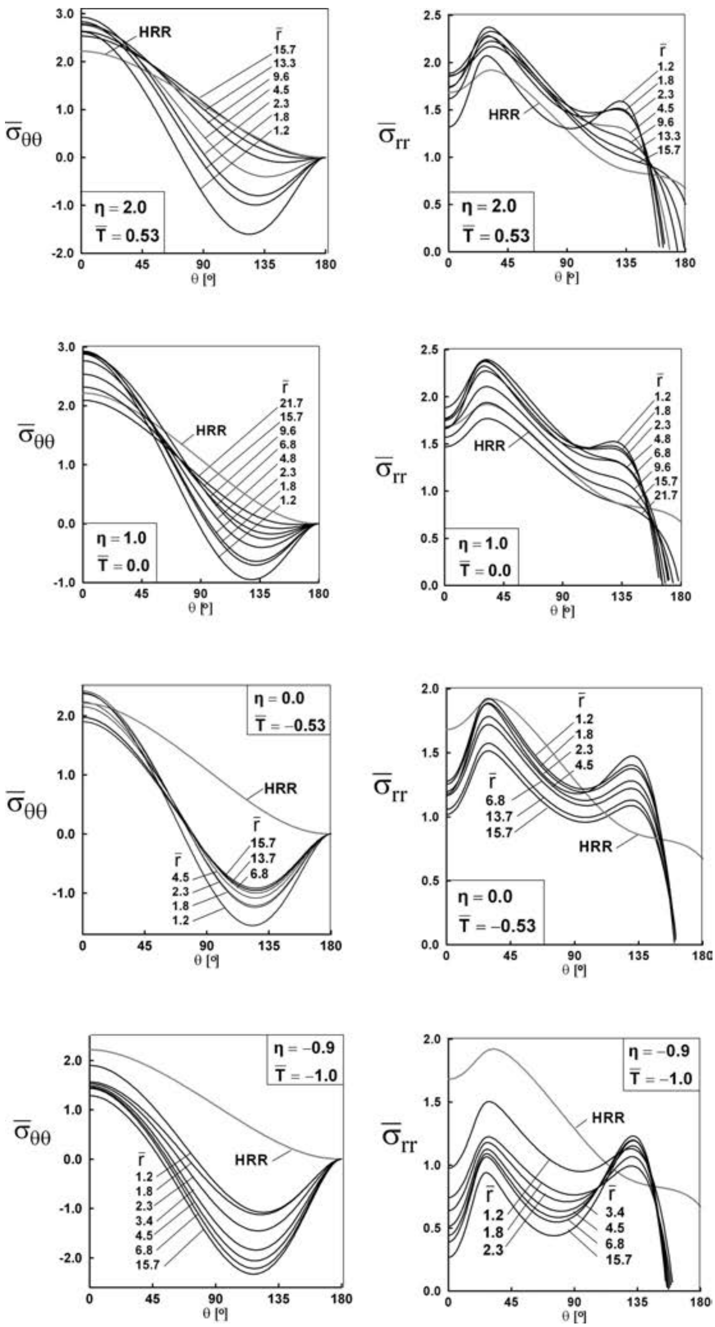

FIG. 5—*Dependencies of angular stress distributions on crack distance.*

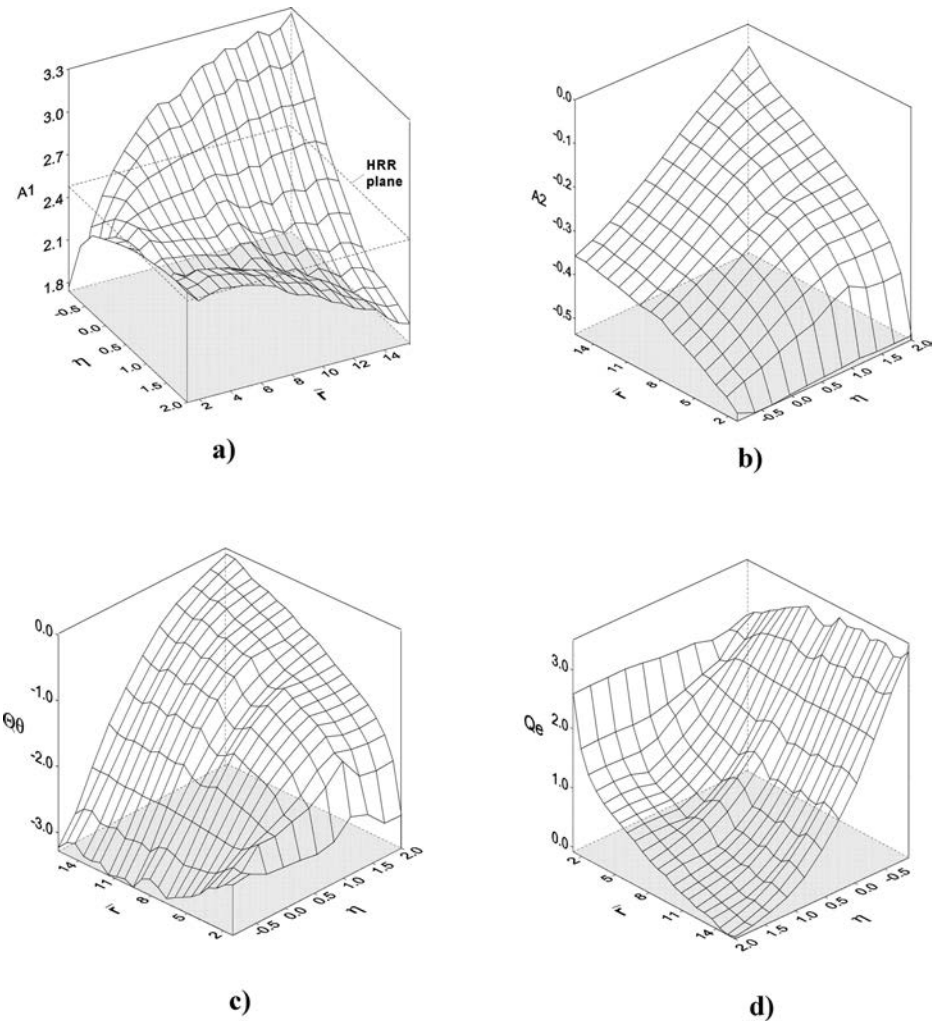

FIG. 6—*Constraint parameters behavior under biaxial loading.*

cedure applying Eqs 16 and 17 in common with the finite element results for elastic-plastic material. The effect of biaxial stress ratio η and crack tip distance $\bar{r}$ on the computed values of amplitude parameters A_1 and A_2 are presented in Fig. 6. It can be seen in Fig. 6(*a*) that the behavior of A_1 is not uniform and generally does not coincide with the theoretical value $A_1 = 2.494$ which was obtained by Eq 13 on the basis of the HRR solution.

The values of second-order term amplitude factor of the three-term expansion for variable η and $\bar{r}$ are presented in Fig. 6(*b*). The amplitude A_2 monotonous increases with the increase of η and $\bar{r}$. The values of A_2 amplitude mainly are negative for all studied biaxial stress states, and vary substantially with respect to $\bar{r}$ especially at positive η. It is interesting to note that the second-order term amplitude factor A_2 almost approaches zero under the equi-biaxial tension $\eta=+1$ when $\bar{T}=0$, but small quantitative differences remain. This observation is essentially due to the fact that in order to apply the three-term solution when one calculates A_1 the finite element results were used instead in the less precisely analytical formula 13.

It is pertinent to note that the loss of constraint is directly related to the change of the biaxial load ratio η from positive to negative value. Figure 6(*b*) shows that for $\eta=-0.9$ and $\bar{T}=-1$ the lowest constraint takes place. The significant influence of load biaxiality on constraint effects is realized through amplitude A_2 and is completely ignored in the HRR-model. Therefore HRR-approach is expected to have very limited applicability of characterizing biaxial load and in-plane constraint effects. The three-term expansion can indeed account for the main features of the deviation of the finite element results from the HRR solution quite well.

The higher-order stress factor $Q_{\theta\theta}$ and Q_e defined by Eq 18 as the sum of the second and the third terms in asymptotic expansion 8 or the difference between the finite element solution and the HRR field is depicted in Fig. 6(*c*), and Fig. 6(*d*) for tangential and effective stresses, respectively. It can be seen that finite-strain effects on the near-tip stress are significant at the crack distance $r\sigma_y/J<3$ for both considered parameters. The weak dependence of $Q_{\theta\theta}$ on crack distance $\bar{r}$ for $\eta<0$ can be seen. Figure 6(*d*) shows that Q_e-stress is almost independent on biaxial stress ratio in finite strain zone. It developed that, when the full range of the crack tip distance is considered, the biaxial loading, produced by both positive and negative stresses, has a more direct influence on the crack-tip stress fields. The distributions for all biaxial load states can be identified with members of the Q-family of fields. To illustrate this point look back at Fig. 6(*c*). For Mode I plane strain loading conditions it can be clearly stated that the biaxial ratio $\eta<0$ corresponds to a low-constraint state when $Q_{\theta\theta}<0$, while $0\leq\eta\leq1$ corresponds to an intermediate state and $1\leq\eta\leq2$ corresponds to a high-constraint state at $Q_{\theta\theta}\approx0$.

By comparing the sum of the second and third terms in the three term asymptotic expansion 8 and the first term of this solution, a quantification of the deviation of the current biaxial stress state from the HRR conditions by applying the constraint parameter $Q_{\theta\theta}$ is achieved. It is found by numerical calculation that the value of this sum can be averaged up to 52 % with respect to the first HRR-term under generally biaxial stress states. By force of these circumstances the necessity of including the higher-order terms in asymptotic expansion for characterizing constraint effects under biaxial loading is clear.

By fitting the numerical calculations, the general constraint parameter $Q_{\theta\theta}$ determined by Eq 18 as a function of varied crack distance, load biaxiality and hardening exponent of elastic-plastic material can be expressed in the form

$$Q_{\theta\theta}=F(\bar{\eta};\bar{r};n),\quad \text{where}\, F=-1.67739\cdot F_n\cdot\bar{r}^{-(\tau+1/(n+1))}+F_\eta\cdot\bar{r}^{-\tau}-3.47206$$

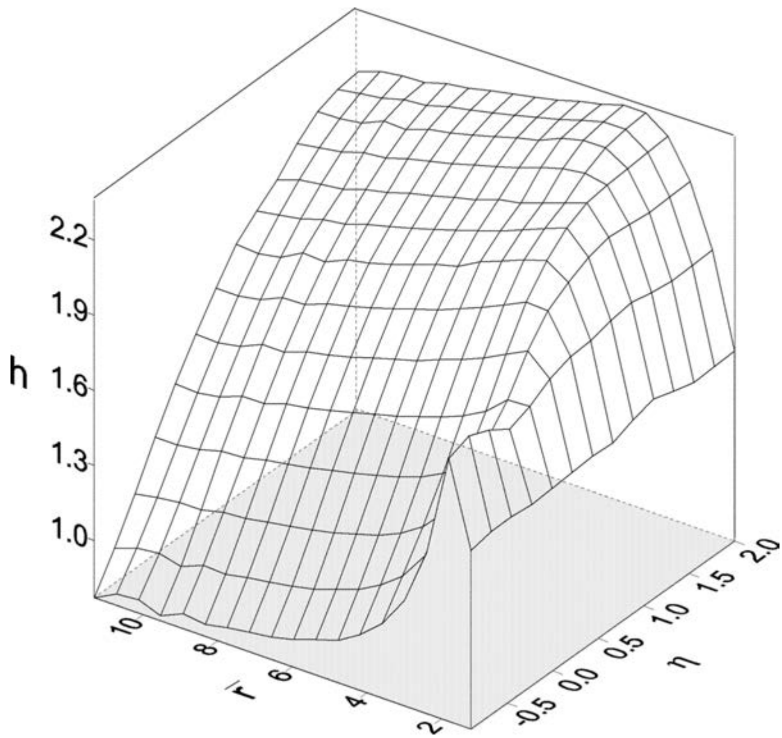

FIG. 7—*Stress triaxiality parameter behavior under biaxial loading.*

$$F_n = \frac{1}{n+1}(3.08913 \cdot n + 11.1638); \quad \tau = 1.01041^n - 0.900617; \quad \bar{\eta} = \frac{\sigma}{\sigma_y}(1 - \eta)\cos 2\beta$$

$$F_\eta = 10.1155 + 0.780826 \cdot \bar{\eta} - 0.938127 \cdot \bar{\eta}^2 + 0.193731 \cdot \bar{\eta}^3 + 0.127252 \cdot \bar{\eta}^4 - 0.0780075 \cdot \bar{\eta}^5$$

The typical relative difference between the numerical and fitting values of the constraint parameter $Q_{\theta\theta}$ is less than 3 % inside the fitting area.

The behavior of the stress triaxiality parameter h which was obtained by Eq 7 for different loading conditions is represented in Fig. 7. It should be noted that h-curves for different values of the load biaxiality have the same shape and differ from each other by equidistant shifting on some magnitude. This implies that for crack distance more than finite strains and blunting zone, the h-η relation is numerically unique because the triaxiality parameter is independent of any reference field and incorporates all stress components. It is expected that this parameter would be useful to describe in-plane constraint effects with simplicity point of view.

Radial Stress Distributions for Creeping Material

The finite element model described in the previous section was employed to study the effect of biaxial loading on the near crack tip stresses in Mode I plane strain conditions. The creeping material properties were described earlier and the state of biaxiality again is given by $\eta = \sigma_{xx}^{\infty}/\sigma_{yy}^{\infty}$.

The tangential stress distributions $\bar{\sigma}_{\theta\theta}$ ahead of the crack-tip ($\theta=0$) for three types of biaxial stress states are displayed in Fig. 8 where the full-field solution stresses are normalized by the yield stress σ_y and the radial distance r is normalized by $C/(\sigma_0\dot{\varepsilon}_0)$. Numbering of lines in Fig. 8 corresponds to the creep time in Table 2. As shown in Fig. 8, when crack distance scaled by $r/[C/(\sigma_0\dot{\varepsilon}_0)]$ increases from 0.002 to 0.1, the tangential stress level monotonically decreases as the creep time increases. This plot shows how both positive and negative biaxial loads affect the tangential stresses in Mode I. Observe that the influence of creep time on the tangential full field stress distributions depends on the biaxial nominal stress state. In all calculations, the tangential stress behavior in the radial direction within $r/[C/(\sigma_0\dot{\varepsilon}_0)<0.001]$ is characterized as an evident unloading state, while beyond $r/[C/(\sigma_0\dot{\varepsilon}_0)>0.002]$ the radial stress distributions are approximately uniform. Note that in this region the stress gradient is depending on the biaxial stress state. Moreover, the change of stress gradients with respect to the creep time is large at $\eta=+1$ and is very small at $\eta=-1$. Thus, under the equibiaxial tension-compression stress state with $\eta=-1$ the full field tangential stress is nearly unaffected by the creep time when $r/[C/(\sigma_0\dot{\varepsilon}_0)>0.002]$.

The general trend of the full field tangential stress redistribution in the radial direction under different biaxial stress state with respect to creep time is illustrated in Fig. 9. The transition time $t_T=1053h$, which is calculated from Eq 21. It is interesting to note that at the short creep time $t/t_T=0.46$ or small scale creep conditions, the maximum values of the tangential stresses correspond to the equi-biaxial tension $\eta=+1$. At the transition creep time $2.76>t/t_T>0.92$ all stress distributions for different biaxial loading nearly coincide with each other. For long time $t/t_T=9.2$ or extensive creep conditions already the equi-biaxial tension-compression stress state $\eta=-1$ has maximal values of the tangential stresses within the region of considered crack tip distances. In summary, from small scale creep (i.e., $t<t_T$) to extensive creep (i.e., $t>9.2t_T$), the equi-biaxial tension and the equi-biaxial tension-compression have contrary tendencies of changing in stress distributions. This is reasonable because under a constant remote loading, creep deformations leading to blunting and continuously evolving crack tip fields will continue to accumulate with different intensity depending on biaxial stress state.

Angular Stress Distributions for Creeping Material

As well as in the elastic-plastic material case, in order to background the validity of the three-term expansion 8, in this section the full field finite element results, HRR-type fields and the three-term asymptotic solutions are considered and compared for creeping material. The full field finite element solution is indicated by the symbols while the HRR field is indicated by the thin solid line

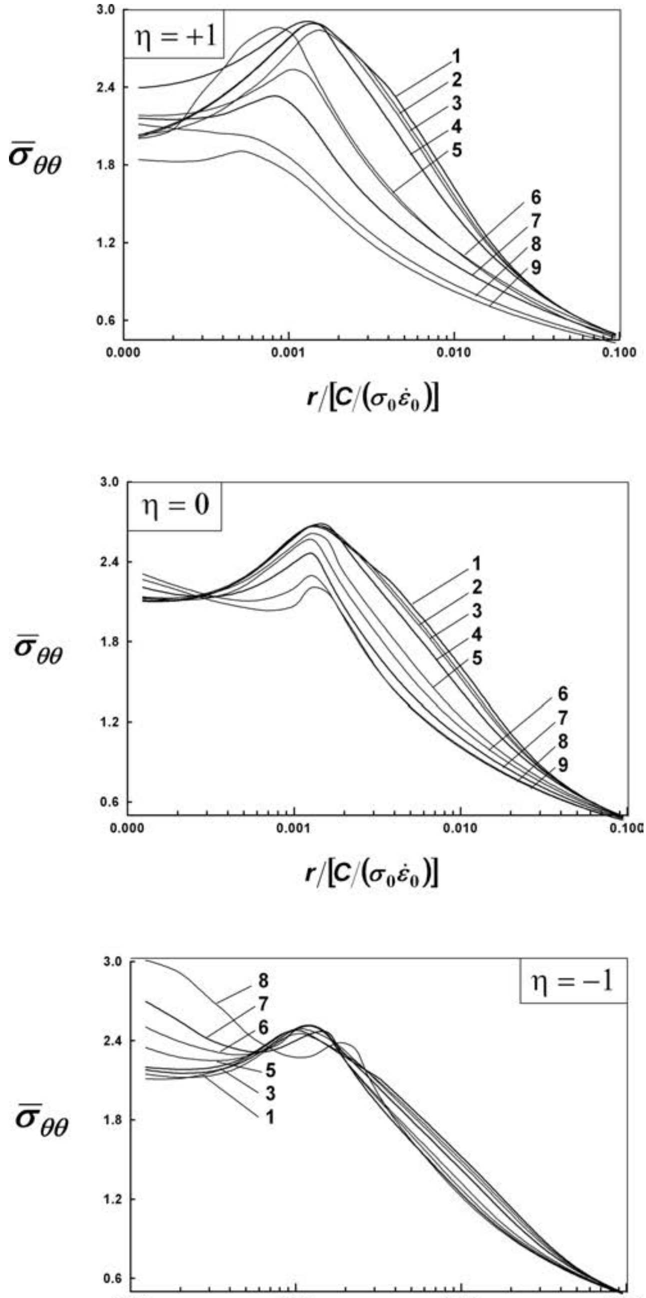

FIG. 8—*Radial stress distributions along $\theta = 0°$ under biaxial loading.*

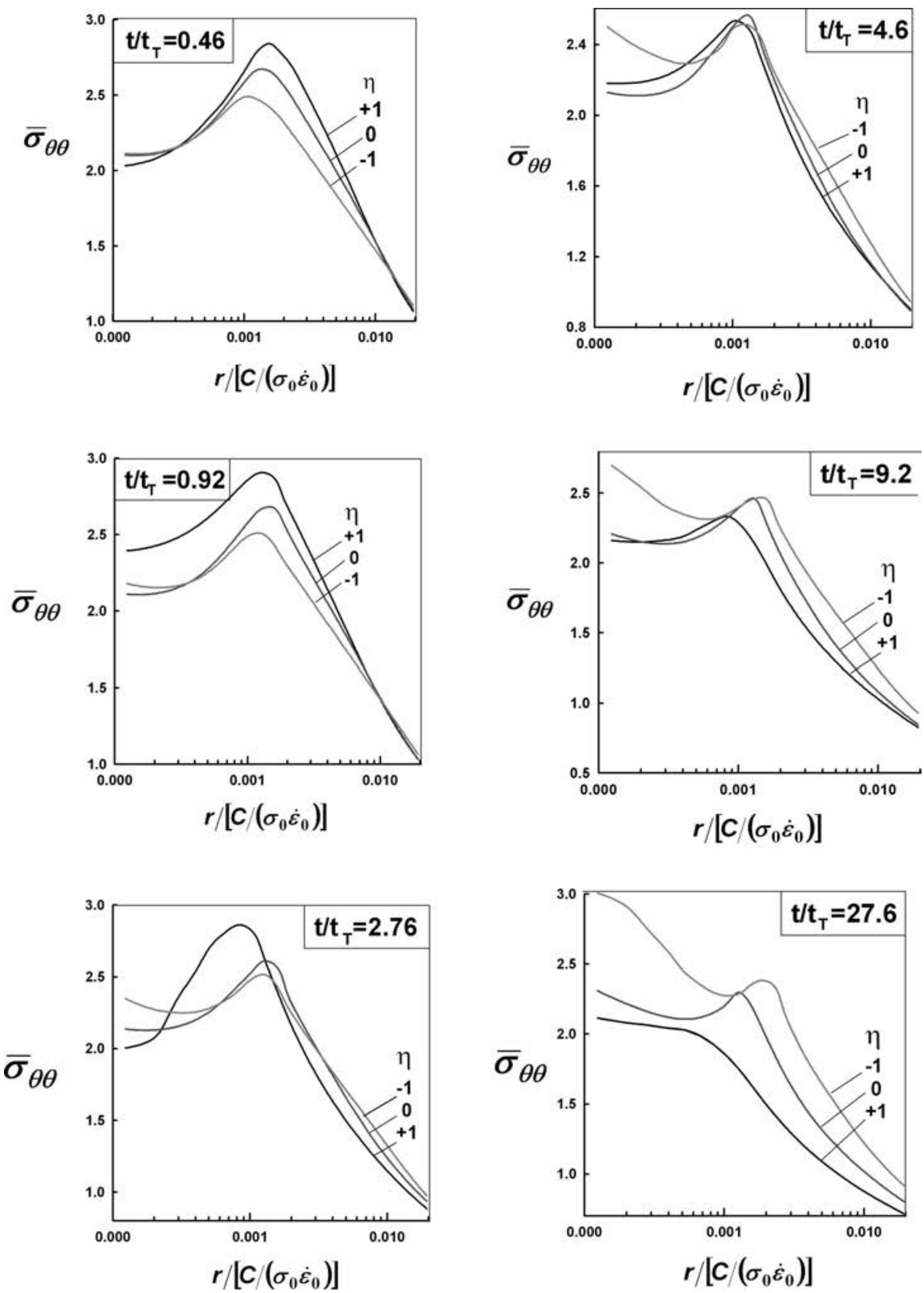

FIG. 9—*Tangential stress redistribution on creep stages.*

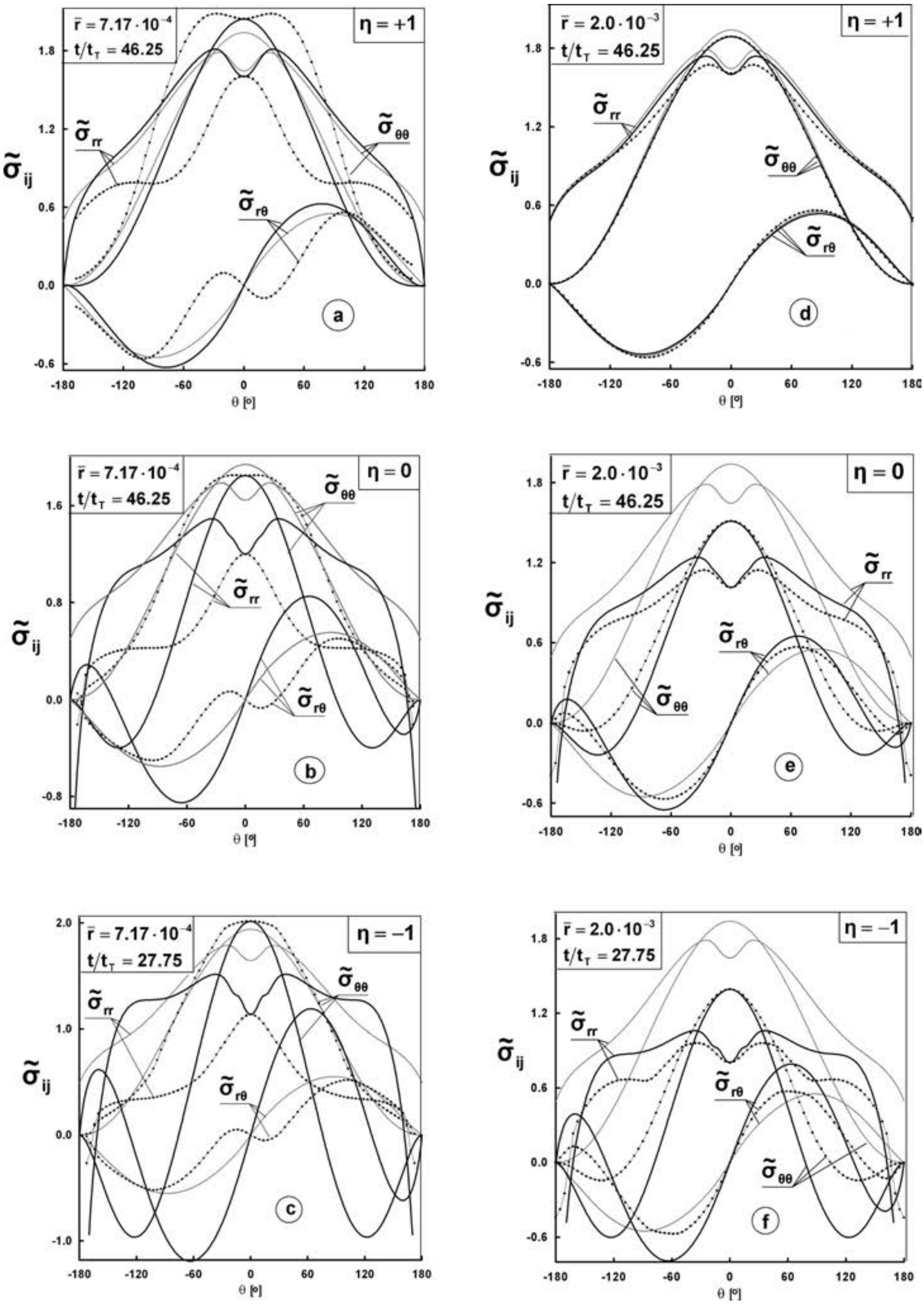

FIG. 10—*Angular stress distributions under different biaxial stress states.*

and the three-term solution by the thick line. Figure 10 shows angular distributions of the normal $\tilde{\sigma}_{rr}$, $\tilde{\sigma}_{\theta\theta}$, and shear $\tilde{\sigma}_{r\theta}$ stress components at the position from crack tip $r/[C/(\sigma_0\dot{\varepsilon}_0)]=7.17\cdot10^{-4}$ and $r/[C/(\sigma_0\dot{\varepsilon}_0)]=2\cdot10^{-3}$ for different biaxial stress states at long creep time $t/t_T=46.2$.

Near the crack tip within the finite strain or unloading zone at $r/[C/(\sigma_0\dot{\varepsilon}_0)]=7.17\cdot10^{-4}$ neither the HRR field nor the three-term asymptotic solution coincide with the finite element results. However, at a radial distance more than the unloading zone $r/[C/(\sigma_0\dot{\varepsilon}_0)]=2\cdot10^{-3}$ the three-term solutions are in good agreement with full field FEM results for the times considered here from $t/t_T=0.46$ to $t/t_T=46.2$. The quality of the approximation by a three-term expansion (8) is better in all interval of angular coordinate changing. The HRR-type fields deviate from both the FEM results and the higher-order term solutions for all the times except for the equi-biaxial tension at $\eta=+1$. Although not shown here, for extensive creep when $9.2<t/t_T<46.2$ the same biaxial loading and crack distance effects similar to the creep time $t/t_T=46.2$ were observed for the dimensionless stress components angular distributions. Good agreement of analytical findings with finite element results confirms again that HRR-solution corresponds only to the equi-biaxial tension $\eta=+1$ which is the particular case of general biaxial loading. The results and analyses of polar stress distributions indicate clearly that the three-term solution 8 is correct for all times from the small scale creep to the extensive creep.

Constraint Parameter Behavior for Creeping Material

Figure 11 is the variation of the amplitude A_1 and A_2 in the three-term asymptotic solution 8 as the function of the crack tip distance at different creeping stages under biaxial loading ($\eta=+1;0;-1$). The results in this figure are obtained by Eqs 16 and 17 from the finite element analysis with the account of the three-term asymptotic solution with respect to the dimensionless higher-order stress components $\tilde{\sigma}_{rr}^{(k)}$, $\tilde{\sigma}_{\theta\theta}^{(k)}$, $\tilde{\sigma}_{r\theta}^{(k)}$ ($k=1,2,3$). In this figure the crack-tip distance is normalized by $r/\rho=10^3 r/[C/(\sigma_0\dot{\varepsilon}_0)]$, while the creep time is normalized by the transition time t_T.

At the transition time from small scale creep to extensive creep, i.e., $t=t_T$ C-integral approaches the steady-state value C_0. We are not aware of any published theoretical work that provides expression of C-integral under different biaxial stress state. Only *uniaxial* tension for a crack of length $2a$ in an infinity body and subjected to a remote stress σ, C_0 for the plane strain extensive problem is very accurately given by [37]

$$C_0=\sigma_0\dot{\varepsilon}_0 a\pi\sqrt{n}\left(\frac{\sqrt{3}}{2}\frac{\sigma}{\sigma_0}\right)^{n+1}$$

In the case of the uniaxial tension $\eta=0$ accounting for this value for C_0 $=8.395\cdot10^{-5}$, the amplitude A_1 from Riedel and Rice's estimation formula 15 is determined as $A_1=0.959$ and represented in Fig. 11 as the corresponding plane. It is necessary to note that the analytical Riedel-Rice solution is only a particular case of our numerical results.

Figure 11 depicts the variations of amplitude A_2 of the three-term

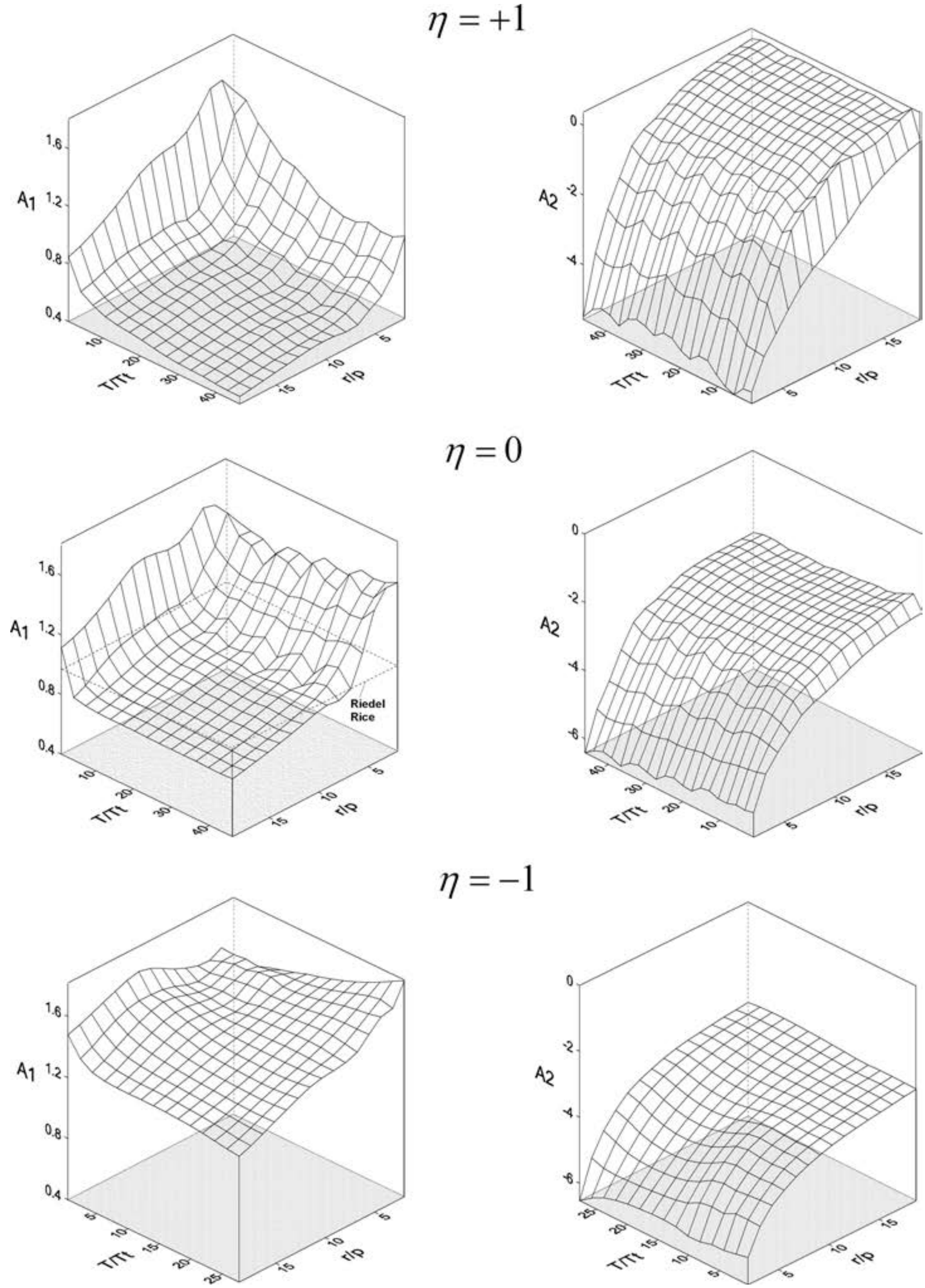

FIG. 11—*Amplitude factors behavior under biaxial loading.*

asymptotic solution with the distance from the crack tip at the different creep time for three biaxial stress states. It is found that the creep time has certain influence on A_2 only in short time within the finite strain zone. One can conclude that the amplitude A_2 in the three-term asymptotic solution for power-law creeping materials is approximately independent of the time at extensive creep conditions, i.e., the creep time has no role in the crack-tip stress fields. On the other hand, the distance from the crack tip has significant effects on the constraint parameter A_2 as shown in Fig. 11.

The value of amplitude A_2 is negative for all the studied creep stages, and varies substantially with the biaxial loading. From comparison of different biaxial stress states it is clear that the general tendency is that the absolute value of A_2 decreases with change ratio η from +1 up to −1. Therefore, for a given creep time t/t_T and crack distance r/ρ, the loss of constraint is directly related to A_2 by means of biaxial stress ratio η. As pointed out previously for elastic-plastic material, again in creeping material the value of A_2 approximately achieves zero under equi-biaxial tension at $\eta=+1$ that confirms the undertone of the HRR-type solution.

By fitting the numerical calculations, the constraint parameter in the form of amplitude A_2 determined by Eqs 16 and 17 as the function of varied crack distance $\bar{r}=r/[C/(\sigma_0\dot{\varepsilon}_0)]$, load biaxiality η and creep time $\bar{t}=t/t_T$ for creeping material can be represented in the following expression $A_2=F(\bar{t},\eta,\bar{r})$, where for $\eta=0$ $A_2=0.76\bar{t}^{0.19}-1.237+F_t/\bar{r}^{0.47}$, $F_t=-0.048\bar{t}+0.00128\bar{t}^2-1.38\cdot10^{-5}\bar{t}^3-2.49$; for $\eta=-1$ $A_2=0.047\bar{t}^{0.77}-2.22+F_t/\bar{r}^{0.569}$, $F_t=-0.0253\bar{t}+2.65\cdot10^{-4}\bar{t}^2-4.09\cdot10^{-6}\bar{t}^3-1.457$; for $\eta=+1$ $A_2=2.184\bar{t}^{0.216}+1.3+F_t/\bar{r}^{0.33}$, $F_t=-0.101\bar{t}+0.003\bar{t}^2-4.29\cdot10^{-5}\bar{t}^3-5.26$.

Figure 12 represents a comparison of the numerical and fitting A_2-values. In Fig. 12 the numerical solutions are indicated by the symbols while fitting results are indicated by solid lines. As can be seen from Fig. 12, the fitting equations approximate the finite element data with good precision for both biaxial loading conditions and creep times.

The behavior of the higher-order stress factor $Q_{\theta\theta}$ and Q_e defined by Eq 18 as the sum of the second and the third terms in asymptotic expansion 8 or difference between the finite element solution and the HRR field in qualitative sense repeats the behavior of amplitude A_2 and for this reason they are not shown here. Likewise to the elastic-plastic material, for the creeping material quantum of this sum can be average up to 58 % with respect to the first HRR-type term under generally biaxial stress states. The behavior of the stress triaxiality parameter h obtained by Eq 7 deserves attention too. Figure 13 depicts the variations of the constraint parameter h with the distance from the crack tip at several creep stages under biaxial loading. One can conclude that for power-law creeping material within the unloading zone, the stress triaxiality parameter h is approximately independent on the stress biaxiality at both small scale and extensive creep. The finite-strain effect on the triaxiality stress is not significant at the crack distance $r/[C/(\sigma_0\dot{\varepsilon}_0)]<1\cdot10^{-3}$. Beyond this distance the strong dependence of h on load biaxiality can be seen. It should be noted that only at the short creep time $t/t_T<0.92$, the triaxiality stress distributions are similar while they become more different with increasing creep time t/t_T. The

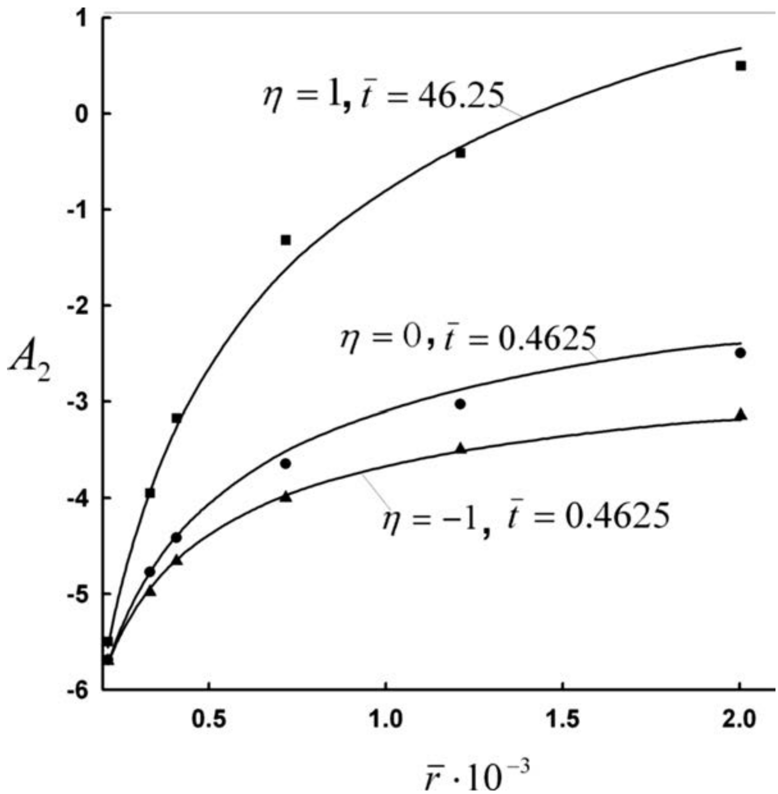

FIG. 12—*Comparison of the numerical and fitting A_2 values.*

general tendency is that the absolute value of h for the equi-biaxial tension $\eta = +1$ increases drastically with t/t_T, whereas the values of h for other biaxial stress states, i.e., $\eta=0$ and $\eta=-1$ do not.

Conclusions

The higher-order asymptotic crack-tip fields are investigated in the present work for a plane strain Mode I crack in both elastic-plastic and creeping materials under the biaxial loading conditions. The numerical solutions clearly indicate that the effects of higher-order terms on the crack-tip fields in both elastic-plastic and creeping materials cannot be adequately predicted under biaxial loading by the inclusion of the T-stress as a second crack-tip parameter. It is found that the near-tip second stress fields are dependent on the magnitude and sign of the T-stress, but this parameter itself does not describe univalently the remote boundary conditions.

Good agreement of analytical findings on the base of the three-term expansion with finite element results conforms that HRR-solution for elastic-plastic

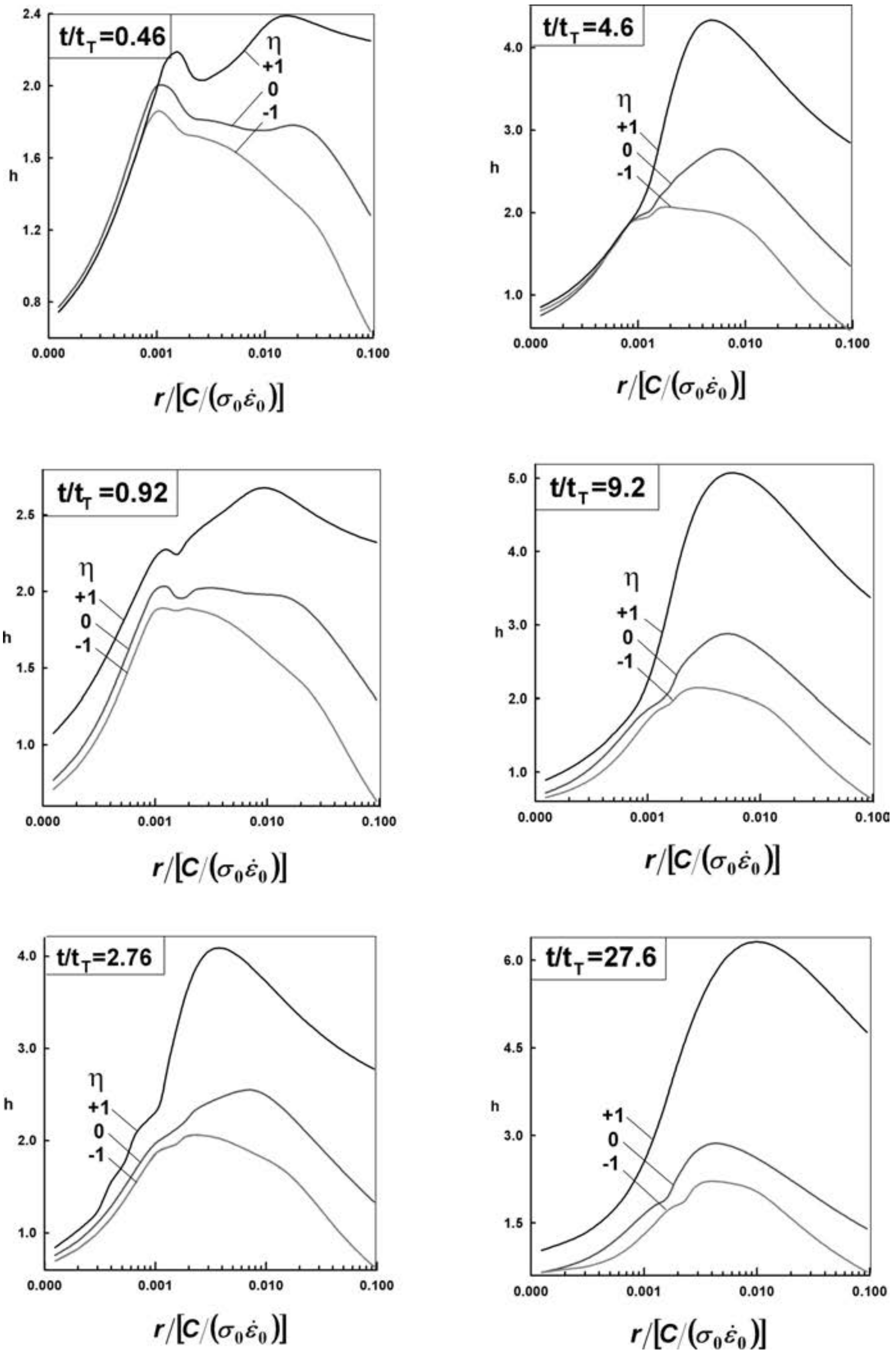

FIG. 13—*Stress triaxiality parameter distributions on creep stages.*

material and the HRR-type solution for creeping material is particular case of general biaxial loading which corresponds to the equi-biaxial tension.

Several constraint concepts are analyzed with respect to their capability of characterizing the load biaxiality effect. It is found that the influence of the nominal biaxial stress state is realized only through the higher-order terms which have a sense of the constraint parameters in different approaches. Because value of the sum of the second and the third terms in asymptotic expansion can be average up to 52–58 % with respect to the first HRR term under generally biaxial stress states the necessity to include the higher-order terms solution for characterizing constraint effects under biaxial loading is clear.

References

[1] Hutchinson, J. W., "Fundamentals of the Phenomenological Theory of Nonlinear Fracture Mechanics," *J. Appl. Meteorol.*, Vol. 50, 1983, pp. 1042–1051.

[2] Hutchinson, J. W., "Singular Behaviour at the End of a Tensile Crack in a Hardening Material," *J. Mech. Phys. Solids*, Vol. 16, 1968, pp. 13–31.

[3] Rice, J. R., and Rosengren, G. F., "Plane Strain Deformation Near a Crack Tip in Power Law Hardening Material," *J. Mech. Phys. Solids*, Vol. 16, 1968, pp. 1–12.

[4] Leevers, P. S., and Radon, J. C., "Inherent Stress Biaxiality in Various Fracture Specimen Geometries," *International Journal of Fracture*, Vol. 19, 1982, pp. 311–325.

[5] Larsson, S. G., and Carlsson, A. J., "Influence of Non-Singular Stress Terms and Specimen Geometry on Small-Scale Yielding at Crack Tips in Elastic-Plastic Materials," *J. Mech. Phys. Solids*, Vol. 21, 1973, pp. 263–272.

[6] Betegon, C., and Hancock, J. W., "Two-Parameter Characterization of Elastic-Plastic Crack-Tip Fields," *J. Appl. Mech.*, Vol. 58, 1991, pp. 104–110.

[7] O'Dowd, N. P., and Shih, C. F., "Family of Crack-Tip Fields Characterized by a Triaxiality Parameter—I. Structure of Fields," *J. Mech. Phys. Solids*, Vol. 39, 1991, pp. 989–1015.

[8] Shlyannikov, V. N., "Method of Higher-Order Terms Determination in Plastic Crack Tip," *Strength Mater.*, Vol. 3, 2006, pp. 43–59.

[9] Yuan, H., "Effects of Biaxial Loadings on Three-Dimensional Crack Front Fields," In *Structural Integrity: Experiments-Models-Applications*, EMAS, Warley, 1994, Vol. I, pp. 493–503.

[10] Yuan, H., and Brocks, W., "Quantification of Constraint Effects in Elastic-Plastic Crack Front Fields," *J. Mech. Phys. Solids*, Vol. 46, 1998, pp. 219–241.

[11] Anderson, T. L., *Elastic-Plastic Fracture Mechanics. Fracture Mechanics. Fundamentals and Applications*, CRC, Boca Raton, Florida, 1995, pp. 139–181.

[12] Nikishkov, G. P., Brückner-Foit, A., and Munz, D., "Calculation of the Second Fracture Parameter for Finite Cracked Bodies Using a Three-Term Elastic-Plastic Asymptotic Expansion," *Eng. Fract. Mech.*, Vol. 52, 1995, pp. 685–701.

[13] Li, Y., and Wang, Z., "High-Order Asymptotic Field of Tensile Plane-Strain Nonlinear Crack Problems," *Sci. Sin., Ser. A*, Vol. 29, 1986, pp. 941–955.

[14] Sharma, S. M., and Aravas, N., "Determination of Higher-Order Terms in Asymptotic Elastoplastic Crack Tip Solutions," *J. Mech. Phys. Solids*, Vol. 39, 1991, pp. 1043–1072.

[15] Zhu, X. K., and Chao, Y. J., "Characterization of Constraint of Fully Plastic Crack-Tip Fields in Non-Hardening Materials by the Three-Term Solution," *Int. J. Solids Struct.*, Vol. 36, 1999, pp. 4497–4517.

[16] Yang, S., Chao, Y. J., and Sutton, N. A., "Higher Order Asymptotic Fields in a Power Law Hardening Material," *Eng. Fract. Mech.*, Vol. 45, 1993, pp. 1–20.

[17] Yuan, H., Lin, G., and Cornec, A., "Quantifications of Crack Constraint Effects in an Austenitic Steels," *International Journal of Fracture*, Vol. 71, 1995, pp. 273–291.

[18] Yuan, H., and Lin, G., "Elastoplastic Crack Analysis for Pressure-Sensitive Dilatant Materials—Part I: Higher-Order Solutions and Two-Parameter Characterization," *International Journal of Fracture*, Vol. 61, 1993, pp. 295–330.

[19] Nikishkov, G. P., "An Algorithm and Computer Program for the Three-Term Asymptotic Expansion of Elastic-Plastic Crack-Tip Stress and Displacement Fields," *Eng. Fract. Mech.*, Vol. 50, 1995, pp. 65–83.

[20] Williams, M. L., "On the Stress Distribution at the Base of Stationary Crack," *J. Appl. Mech.*, Vol. 24, 1957, pp. 111–114.

[21] Rice, J. R., "Limitations to the Small Scale Yielding Approximation for Crack Tip Plasticity," *J. Mech. Phys. Solids*, Vol. 22, 1974, pp. 17–26.

[22] Eftis, J., and Subramonian, N., "The Inclined Crack Under Biaxial Load," *Eng. Fract. Mech.*, Vol. 10, 1978, pp. 43–67.

[23] Theocaris, P. S., and Michopoulos, J. G., "A Closed-Form Solution of a Slant Crack Under Biaxial Loading," *Eng. Fract. Mech.*, Vol. 17, 1983, pp. 97–133.

[24] Yuan, F. G., and Yang, S., "Crack-Tip Fields in Elastic-Plastic Material Under Plane Stress Mode I Loading," *International Journal of Fracture*, Vol. 85, 1997, pp. 131–155.

[25] Henry, B. S., and Luxmoore, A. R., "The Stress Triaxiality Constraint and the Q-value as Fracture Parameter," *Eng. Fract. Mech.*, Vol. 57, 1997, pp. 375–390.

[26] Hoff, N. J., "Approximate Analysis of Structures in the Presence of Moderately Large Creep Deformation," *Quarterly Applied Mechanics*, Vol. 12, 1954, pp. 49–55.

[27] Nguyen, B. N., Onck, P. R., and van der Giessen, E., "On Higher-Order Crack-Tip Fields in Creeping Solids," *J. Appl. Mech.*, Vol. 67, 2000, pp. 372–382.

[28] Nguyen, B. N., Onck, P. R., and van der Giessen, E., "Crack-Tip Constraint Effects on Creep Fracture," *Eng. Fract. Mech.*, Vol. 65, 2000, pp. 467–490.

[29] Chao, Y. J., Zhu, X. K., and Zhang, L., "Higher-Order Asymptotic Crack-Tip Fields in Power-Law Creeping Material," *Int. J. Solids Struct.*, Vol. 38, 2001, pp. 3853–3875.

[30] Riedel, H., and Rice, J. R., "Tensile Crack in Creeping Solids," *Fracture Mechanics*, ASTM STP 700, ASTM International, West Conshohocken, PA, 700, 1980, pp. 112–130.

[31] Bassani, J. L., and McClintock, F. A., "Creep Relaxation of Stress Around a Crack Tip," *Int. J. Solids Struct.*, Vol. 17, 1981, pp. 479–492.

[32] Chao, Y. J., Yang, S., and Sutton, N. A., "On the Fracture of Solids Characterized by One or Two Parameters: Theory and Practice," *J. Mech. Phys. Solids*, Vol. 42, 1994, pp. 629–647.

[33] Chao, Y. J., and Zhu, X. K., "Constraint-Modified J-R Curves and Applications to Predict Ductile Crack Growth," *International Journal of Fracture*, Vol. 100, 2000, pp. 3853–3875.

[34] Li, F. Z., Needleman, A., and Shih, C. F., "Characterization of Near Tip Stress and Deformation Fields in Creeping Solids," *International Journal of Fracture*, Vol. 36, 1988, pp. 163–186.

[35] ANSYS Structural Analysis Guide. 001245. 5th ed., SAS IP, Inc., 1999.

[36] ANSYS Theory Reference. 001242. 11th ed., SAS IP, Inc., 1999.

[37] He, M. Y., and Hutchinson, J. W., "Bounds for Fully Plastic Crack Problems for Infinite Bodies," *Elastic-Plastic Fracture*, ASTM STP 803, ASTM International, West Conshohocken, PA, Vol. 1, 1983, pp. 277–290.

ASTM Special Technical Publication, Vol. 5, No. 9
Paper ID JAI101535
Available online at www.astm.org

H. Koeberl,[1] G. Winter,[2] H. Leitner,[1] and W. Eichlseder[1,2]

Comparison of the Temperature and Pre-Aging Influences on the Low Cycle Fatigue and Thermo-Mechanical Fatigue Behavior of Copper Alloys (CuCoBe/CuCo2Be)

ABSTRACT: Typically thermo-mechanical fatigue (TMF) loaded components in power plants and steel works are made of copper alloys and are used in different applications (e.g. cooling systems in continuous casting, transformers). So a careful analysis and comparison of the experimental results and microstructure of thermo-mechanical loaded copper components, which are based on a systematic variation of the relevant influence factors, have been conducted to develop empirical models for computing the fatigue life. At specific low cycle fatigue (LCF) and thermo-mechanical fatigue test series on the copper alloys CuCoBe and CuCo2Be, the influence of pre-aging and temperature were investigated by means of the cyclic deformation and lifetime behavior. Based on stress-strain loops from LCF tests at different temperatures and aging conditions a non-linear combined material model was adopted to describe the cyclic deformation behavior. The simulated loading parameters of stress and strain were the basis for the subsequent lifetime simulation. A new energy based damage parameter for copper alloys has been developed to fulfill the requirements of lifetime simulation.

KEYWORDS: material model, energy based damage parameters, lifetime model

---

Manuscript received December 4, 2007; accepted for publication August 10, 2008; published online September 2008.

[1] Chair of Mechanical Engineering, University of Leoben, Austria.
[2] CD-Laboratory for Fatigue Analysis, University of Leoben, Austria.

Citation: Koeberl, H., Winter, G., Leitner, H., and Eichlseder, W., "Comparison of the Temperature and Pre-Aging Influences on the Low Cycle Fatigue and Thermo-Mechanical Fatigue Behavior of Copper Alloys (CuCoBe/CuCo2Be)," *J. ASTM Intl.*, Vol. 5, No. 9. DOI10.1520/JAI101535. Available online at www.astm.org. Also included in JAI Special Issue STP 1508, *Fatigue and Fracture Mechanics: 36th Volume,* R. W. Neu, K. R. W. Wallin, and S. R. Thompson, guest editors, ASTM International, West Conshohocken, PA, 2009, pp. 641-656.

Introduction

Cyclic loading of metallic engineering components at constant increasing or fluctuating temperatures causes a complex evolution of damage which is difficult to describe. In many engineering components thermo-mechanical loading occurs, e.g., cooling components in metal processing and forming, turbine blades, cylinder heads, etc. The steady rise of engine power and productivity often causes higher operating temperatures. At the same time the thermal expansion of this material is restricted due to the complex geometry of the components.

Thermo-mechanical fatigue induced through cyclic loading by temperature variation results in simultaneous elongation constrained. This constraint leads to local plastic deformation resulting in the fatigue of the material. Because of the low number of bearable thermo-mechanical cycles and the macroscopic plastic deformation, the thermo-mechanical fatigue takes place in the low cycle fatigue (LCF) region of the classical S-N curve.

Due to the preponderance of temperature differences and stresses during a TMF cycle there is an appearance of several damage mechanisms. Apart from the classical fatigue damage in terms of plastic deformation, corrosive influences (for example oxidation) and creep damage also occur as a result of the elevated temperature. In order to work out a methodology for simulating the fatigue and lifetime behavior of thermo-mechanically loaded components, experiments like tensile or isothermal LCF tests were conducted to provide a basic understanding of CuCoBe and CuCo2Be, which are both standard materials in thermo-mechanical loaded cooling components.

Based on stress-strain loops from LCF tests at different temperatures and aging conditions, a nonlinear combined material model was adopted to describe the cyclic deformation behavior. Simultaneous damage mechanisms were described by different models. Many of the empirical models are strain based criteria like the Manson-Coffin [1,2] criterion with numerous modifications.

To find a correlation between the number of cycles to failure and loading parameters, different damage parameters are available stated in lifetimes [3]. From the perspective of fracture mechanics, e.g., with cyclic J-integrals, a description of the TMF lifetime can be obtained. Cumulative models, like the Chaboche model [4], try to cumulate the damage for each cycle; therefore these models need a lot of computing time for complex structures. Due to the interplay of strain and stress values under TMF loading, they are able to account for more specific influences as well as their interactions. It is shown in former works of Riedler [5,6], that energy based criteria are qualified for lifetime approaches. To estimate the lifetime, a damage parameter, based on the energy (elastic and plastic) of a hysteresis loop to find a correlation between the number of cycles to failure and loading parameters, has been developed.

Damage Mechanisms Due to TMF

Damage mechanisms which have occurred via a TMF process are affected by different temperature dependent mechanisms during every cycle. Whereby the

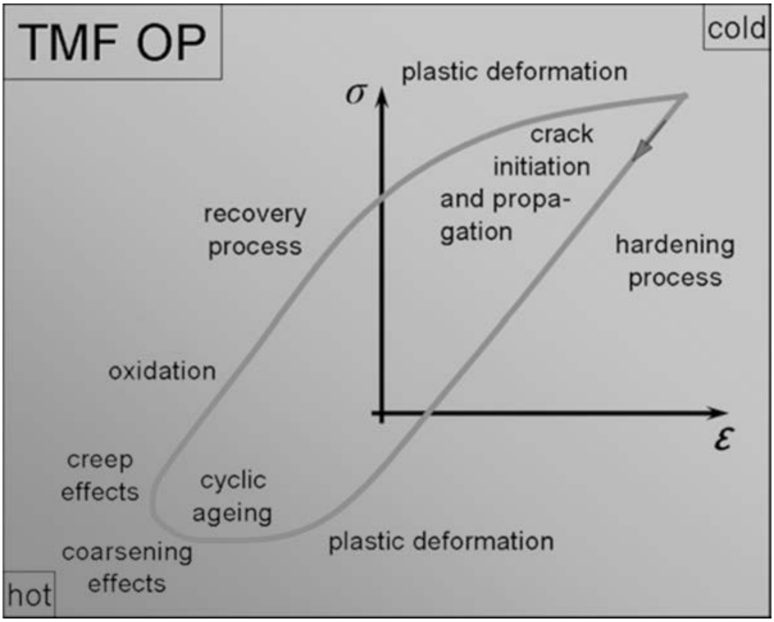

FIG. 1—*Active damage mechanisms during OP cycles* [7].

damage mechanisms, listed previously, occurs at elevated temperatures by an individual or cumulative interaction.

The influence on cyclic thermo-mechanical deformation behavior depends on thermal activated dislocation aspects at lower temperatures, cyclic aging processes at mid-temperature ranges and diffusion conveyed creep at higher temperatures. So, under both loading modes, IP-TMF (in-phase, i.e., temperature and stress are in-phase) as well as OP-TMF (out-of-phase, i.e., temperature and stress are opposite), the training of the microstructure and oxidation were predominantly formed in a range at the maximum temperature (see Figs. 1 and 2).

Oxidation, for example, that intensifies act at high temperatures, can cause embrittlement, or cause weakness in strength. As a result early crack initiation and accelerated crack propagation during an OP-TMF cycle is enhanced.

In out-of-phase testing conditions, the mechanical strain works against the thermal strain, which results in compression at maximum temperature. In in-phase tests the mechanical and thermal strain are cumulative, which results in tension at maximum temperature. The used phase shift in this study is out-of-phase (OP).

$$K_{TM} = \frac{\Delta\varepsilon_t^{mech}}{\Delta\varepsilon_t^{th}} \qquad (1)$$

The relationship between mechanical and thermal strain is defined by the degree of strain constraining K_{TM} (Eq 1), where $\Delta\varepsilon_t^{mech}$ is the total mechanical

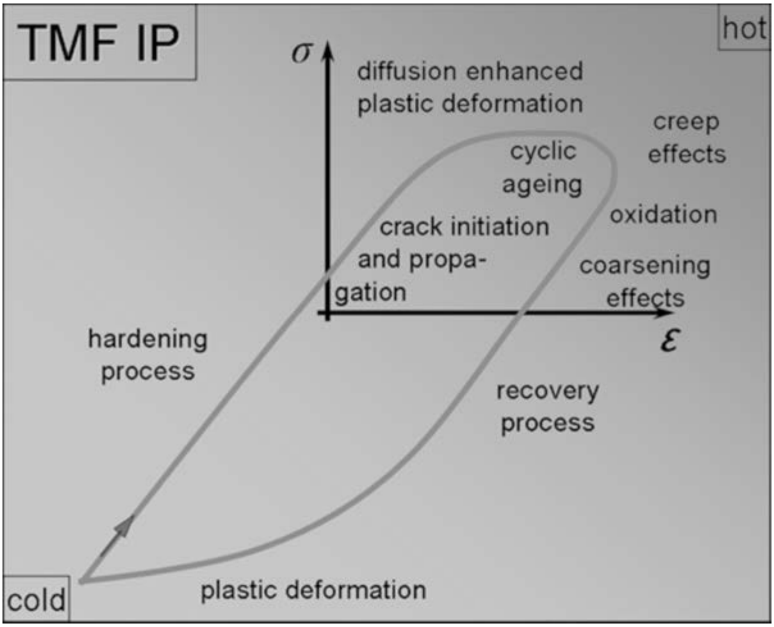

FIG. 2—*Active damage mechanisms during IP cycles* [7].

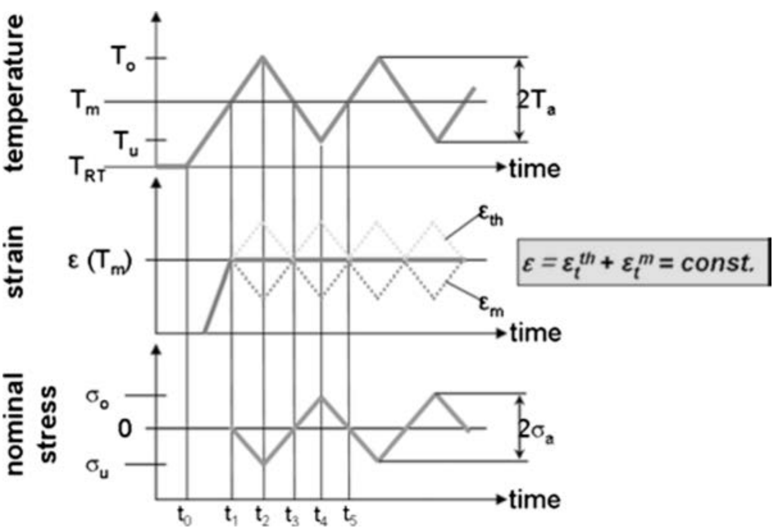

FIG. 3—*Temperature-strain-time characteristics with respect to OP-TMF.*

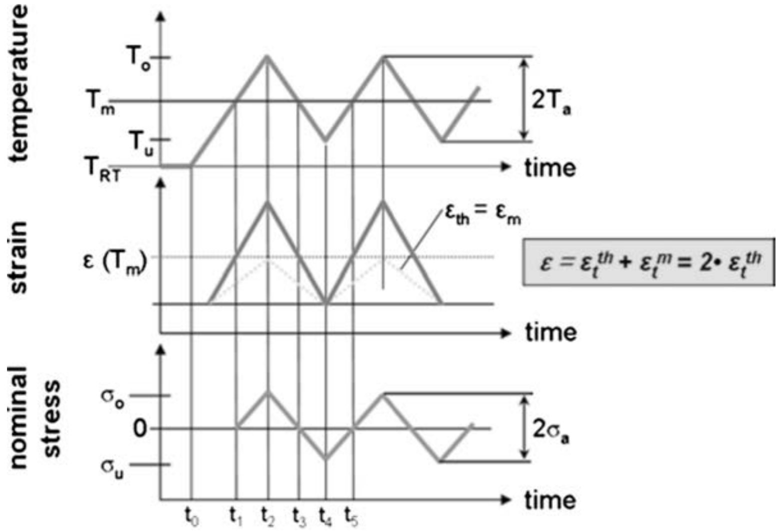

FIG. 4—*Temperature-strain-time characteristics with respect to IP-TMF.*

strain range and $\Delta\varepsilon_t^{th}$ is the total thermal strain range (see Figs. 3 and 4).

Experimental Setup Methods

The investigated materials for this research are CuCoBe and CuCo2Be, also called cobalt-beryllium-bronzes. In this study, CuCoBe was a wrought alloy and CuCo2Be was a cold worked rod. Both are copper-based alloys containing cobalt (2 wt. % in CuCo2Be) and beryllium with small traces of nickel and iron. Such materials can be strengthened by different heat treatments like solution annealing. Thereby a high oversaturated alpha-phase is formed and after cooling down to room temperature also a fine distributed cobalt- and beryllium-rich phase is generated see.

To describe the effect, respectively, the influence of pre-aging on the yield strength of these materials, tensile test specimens were preaged at different temperatures (room temperature, 125, 225, 275, and 325°C) with different pre-aging times (from 10 h to 1500 h).

LCF tests were conducted at different temperatures (room temperature 125, 225, 325, and 375°C) and variable pre-aging conditions. The tests were made on a Schenk servo-hydraulic test rig (nominal force 250 kN) with Instron FastTrack control. The clamping was controlled via hydraulic clamping grips, see Fig. 5(*a*). The specimens (Fig. 6) were strain test controlled with an Instron extensometer with a gage length of 12.5 mm and a range of ±2.5 mm. These tests were made with a strain rate of 1 %/s (0.01 %/s), in accordance with DIN EN 3988.

TMF tests were conducted for CuCo2Be (without any pre-aging conditions) on a test rig developed at the *Institute of Mechanical Engineering* (Fig. 5(*b*)).

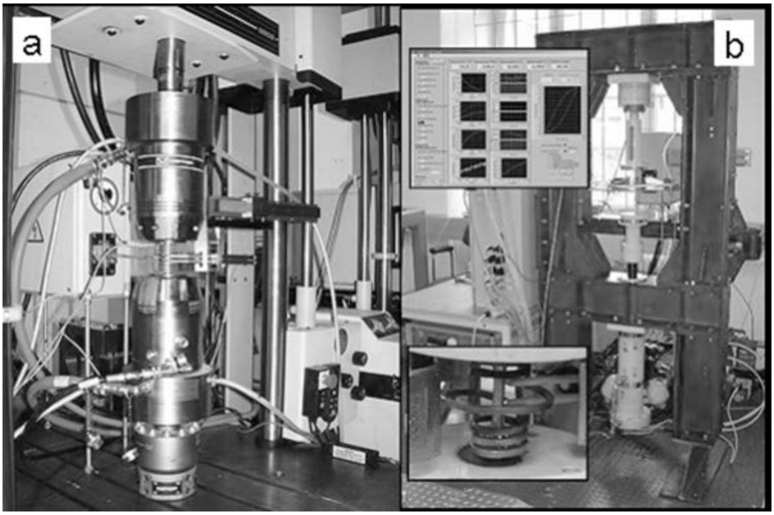

FIG. 5—*Servo-hydraulic test rigs:* (*a*) *LCF and* (*b*) *TMF.*

With this test rig it was possible to allow defined phase shifts and frequency superimpositions, between thermal and mechanical strains. LCF and TMF tests were temperature controlled with an induction coil, operated by a Huettinger generator [8].

Because of relatively low working and therefore testing temperatures for the CuCo2Be alloy, a strain constrainment of $K_{TM}=3$ was used to estimate a rational testing time (max. 15 000 cycles). The heating rate was 10°C/s up to the respective maximum temperature (200, 225, 250, 275, 300, and 325°C). The dwell time at the maximum temperature was 10 s–100 s after which the samples were left to cool down to $T_{\min}=60°C$, as described in Ref [9]. Additionally, metallographic analyses were conducted to show the changes in the microstructure.

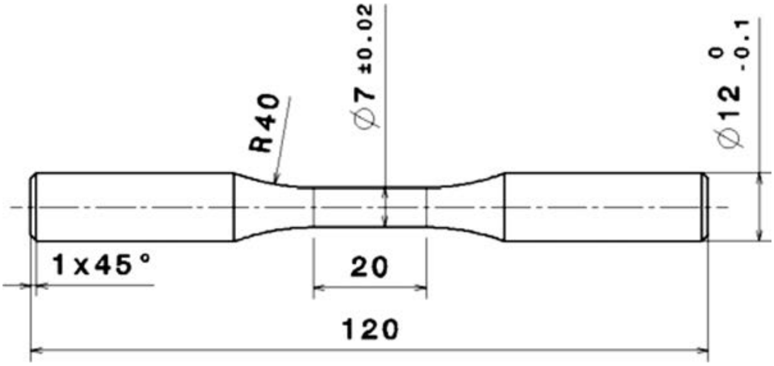

FIG. 6—*LCF-TMF test specimen* [*mm*].

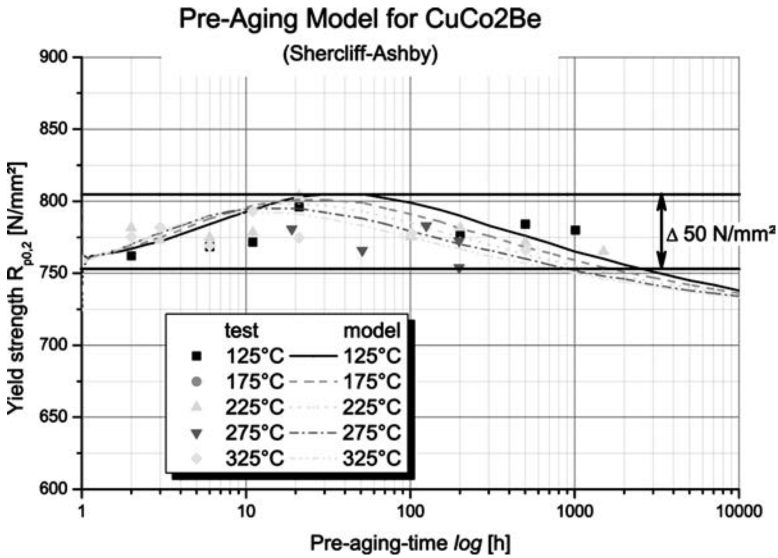

FIG. 7—*Pre-aging model (Shercliff-Ashby) for CuCo2Be.*

Results

Preaging (CuCo2Be) and Microstructure

Typically metals show a different temperature- and time-dependent aging behavior. These can significantly change the mechanical properties. This behavior can be described by the yield strength at different pre-aging temperatures as a function of the pre-aging time, according to Shercliff-Ashby [10,11]. As shown in Fig. 7, the effect of pre-aging at working temperatures up to 325°C on the CuCo2Be alloy is in a range of 50 MPa for all aging temperatures, which is less than 7 % of the yield strength. So pre-aging has no distinctive influence on the cyclic deformation behavior.

Figure 8 shows the microstructure of nonaged and preaged specimens, revealing primary copper oxide dendrites and eutectic copper ($Cu_2O + Cu$) [12] by using a light optical microscope and a system for image analysis (OLYMPUS analySIS3.2). The finely dispersed copper-oxide Cu_2O in the eutectic phase can only be visually detected at high magnification (500× to 1000×). From the micrographs the distribution of primary copper dendrites for the CuCo2Be (Fig. 8(*a*)) and CuCoBe (Fig. 8(*b*)) alloys after forming, (see Damage Mechanisms Due to TMF section) is the same. But there is a significant distinction in the distribution of eutectic copper oxide, identifiable in the reduced finely distributed Cu_2O phase in the CuCoBe alloy. By comparing the microstructure (CuCo2Be) for standard and preaged, at 10 h (Fig. 8(*c*)) and 500 h pre-aging time (Fig. 8(*d*)) at 325°C, specimens show a coarsening of the microstructure during the pre-aging process in the first ten hours. Longer pre-aging times do not lead to a further coarsening of the microstructure. For a precise detection

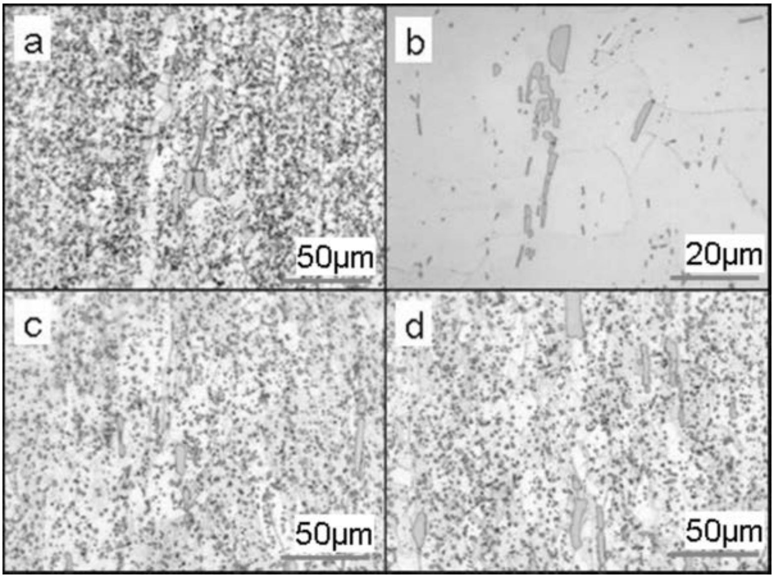

FIG. 8—*Microstructure of nonpre-aged specimens: CuCo2Be* (*a*) (*1000 times magnified*) *and CuCoBe,* (*b*) (*500 times*), *and pre-aged specimens: CuCo2Be,* 10 h (*c*), *and* 500 h (*d*) (*1000 times*).

of the precipitation of beryllium, cobalt and inter-phases, with respect to their influences on the yield strength and lifetime, an analysis via transmission electron microscope (HRTEM or EFTEM) will be done in further publications.

The amount of primary Cu_2O (% area) decreases from 7 % without pre-aging to 6 % after 10 h pre-aging at 325°C, thereafter staying almost constant up to 500 h pre-aging at 325°C. The amount of eutectic Cu_2O decreases from 2 % before to 1.5 % after 10 h pre-aging staying constant almost up to 500 h pre-aging at 325°C. The influence of pre-aging for further considerations can thus be eliminated, because there is no change in microstructure during the pre-aging process, i.e., there is no influence on the yield strength and the deformation behavior respectively.

Comparison of LCF and TMF Lifetime

During a thermo-mechanical cycle, different temperatures and mechanical loadings are applied to the material. This temperature dependent process, that occurs during a common TMF cycle, causes plastic deformation, cycling aging, creep effects, oxidation effects, coarsening of the microstructure, and crack initiation with resultant propagation. As explained previously, the influence of pre-aging is negligible, irrespective of the low testing temperature. The main damage mechanisms for CuCoBe and CuCo2Be are pure fatigue and oxidation damage.

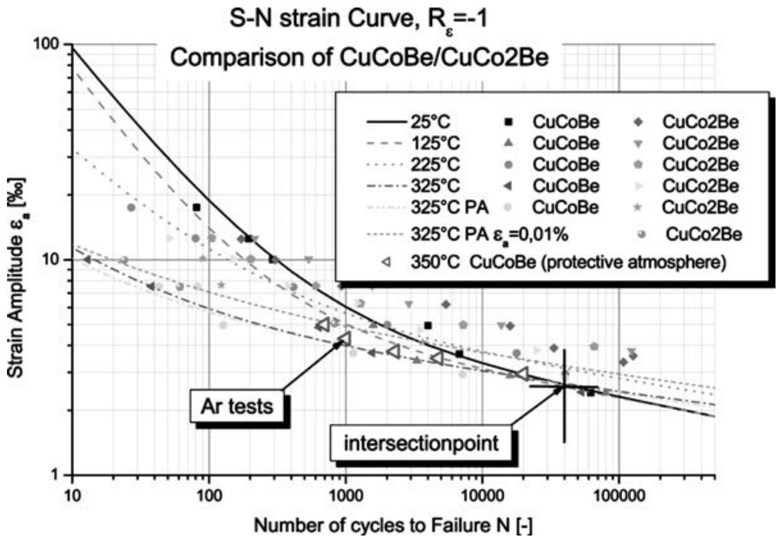

FIG. 9—*Comparison of LCF tests for CuCoBe and CuCo2Be according to the Manson-Coffin-Basquin model.*

$$\varepsilon_{a,t} = \varepsilon_{a,pl} + \varepsilon_{a,el} = \frac{\sigma_f'}{E} \cdot (N_f)^b + \varepsilon_f' \cdot (N_f)^c \tag{2}$$

where $\varepsilon_{a,t}$, $\varepsilon_{a,pl}$, and $\varepsilon_{a,el}$ describe the total, plastic, and elastic strain amplitude, respectively, σ_f' the fatigue strength coefficient, ε_f' the cyclic ductility coefficient, b the fatigue strength exponent, c the cyclic ductility exponent, E the Young's modulus, and N_f the number of cycle to failure.

In the LCF experiments the influence of oxidation increases with rising test temperatures and decreasing strain rate. Figure 9 shows a comparison of strain lifetime curves (strain S-N curves) at different testing temperatures according to the Manson-Coffin-Basquin model (Eq 2), strain rates and different pre-aging (PA) conditions. The influence of oxidation was also investigated and therefore some tests were conducted under a protective Ar atmosphere.

There was no influence of testing temperature on the lifetime behavior of CuCo2Be of up to 125°C. The S-N strain curves at higher temperatures are displaced to the left indicating a reduction in lifetime. At temperatures of 225°C the lifetime reduces by ~40 % in comparison to that of 125°C. At 325°C the reduction in lifetime amounts to ~70 % of the lifetime at room temperature. This reduction can be explained by the increasing influence of oxidation which has a factor of two for lifetimes (Fig. 9) during the testing period.

The influence on lifetime of a low strain rate is noticeable only at high temperatures. This causes creep and oxidation effects, which start above the materials activation energy (~400°C). At room temperature a change in strain rate has no effect on lifetime. By testing with a very slow strain rate at a high temperature the crack surface can be oxidized for a longer time which leads to

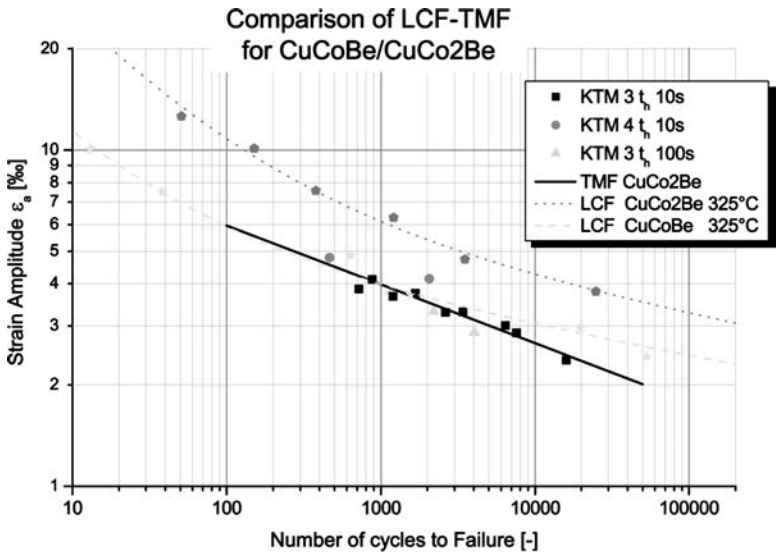

FIG. 10—*Comparison of all TMF tests* (*CuCo2Be*) *and LCF tests at* 325°C (*CuCoBe and CuCo2Be*).

a reduction in lifetime. CuCoBe demonstrates a different lifetime behavior to CuCo2Be. The total strain amplitude tolerable is a factor of 1.5 lower than that for CuCo2Be, which is up to one decade in terms of lifetime. Typically CuCo2Be shows nearly parallel lifetime curves with CuCoBe and a collective intersection point at 40 000 cycles (see Fig. 9).

To investigate the influence of oxidation, some specimens were preaged or rather oxidized at the surface for 500 h at 325°C and tested with a standard strain rate of 1 %/s and a lower strain rate of 0.01 %/s. Parallel tests, in an inert atmosphere, were conducted to determine the full range of oxygen influence. By oxidizing the specimen surface the velocity of crack initiation and crack growth increases and because of this the lifetime decreases. As a result, there was a reduction of ~50 % in lifetime when the preaged specimens, 500 h at 325°C, were compared to those tested in an inert atmosphere. This influence may be of further interest when considering damage parameters like Neu-Sehitoglu [13].

The S-N strain curves for the TMF and LCF tests for the CuCoBe and CuCo2Be alloys at 325°C are shown in Fig. 10. Due to higher mechanical strains, resulting from higher thermal strains and varied strain constrainment, lifetime decreases. This is because of higher plastic deformation, during each cycle. Besides the influence of plastic deformation, the effect of oxidation increases by raising the maximum temperature. For longer dwell times at the maximum temperature the oxidation influence leads to a significant reduction in lifetime. This reduction in lifetime is about 30 %, depending on the maximum temperature.

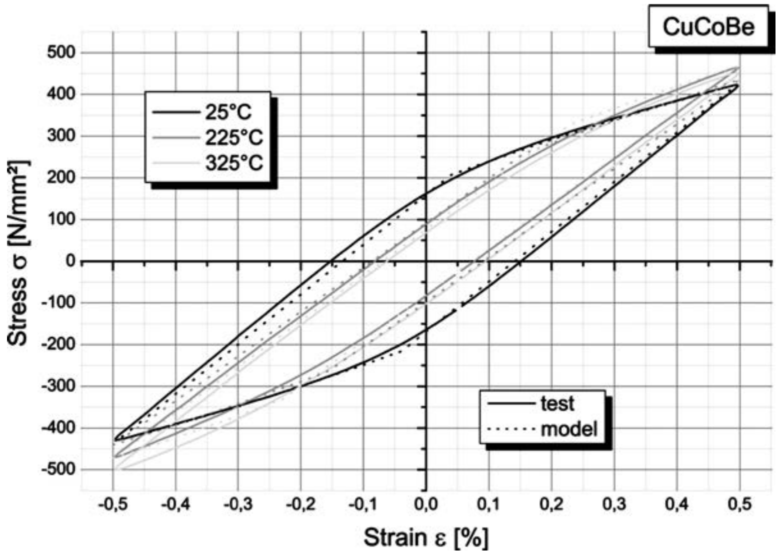

FIG. 11—*LCF simulation of CuCoBe.*

Simulation of the Cyclic Deformation Behavior

The description of the elastic-plastic cyclic deformation behavior for both the investigated materials is the basis for lifetime assessment by using simulated loading parameters. Using the finite-element method and a suitable material and damage model, the local loading parameters can be calculated and used to estimate the lifetime. To describe the elastic-plastic deformation behavior of the two copper alloys, a standard material model, the combined hardening model, which is implemented in the software package ABAQUS® has been used. The combined hardening model describes the kinematic and isotropic deformation performance in dependency of the temperature.

$$\dot{\boldsymbol{\alpha}} = C\frac{1}{\sigma^0 + k}(\boldsymbol{\sigma} - \boldsymbol{\alpha})\dot{\bar{\varepsilon}}_{pl} - \gamma\boldsymbol{\alpha}\dot{\bar{\varepsilon}}_{pl} \tag{3}$$

The evolution law of the kinematic hardening component, which describes the translation of the yield surface in stress space through the back stress tensor $\dot{\alpha}$ is given by Eq 3 and in this case it is effectual [14]. σ^0 is the first deviate of the elastic to the plastic region, C the initial kinematic hardening modulus, γ the rate of decay of the kinematic hardening modulus, k isotropic hardening (change of size of yield surface) and $\dot{\bar{\varepsilon}}^{pl}$ the total plastic strain rate of the hysteresis.

The parameters for the material model were derived by using stress-strain loops from LCF tests at half the number of cycles to failure $N_{f/2}$. A comparison of the hysteresis loops from the experiments at $N_{f/2}$ and the simulated hysteresis loops for a total strain amplitude of 0.5 % under different temperatures is given in Fig. 11. The hysteresis loops calculated with the adapted material

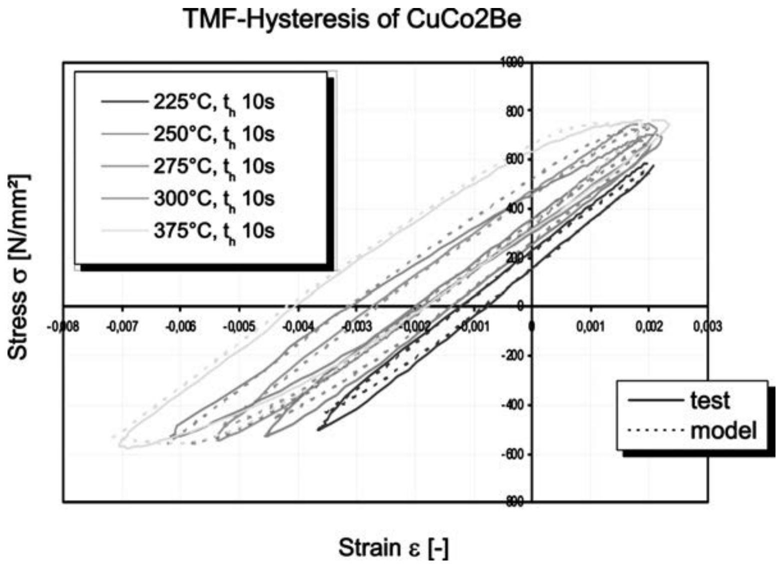

FIG. 12—*TMF simulation of CuCo2Be.*

model show good agreement with those obtained from the experiments.

Using the investigated material model at different maximum temperatures to simulate the TMF hysteresis loops also reveals a good correlation with the experimental hysteresis loops (using the LCF data). Figure 12 shows a comparison of the hysteresis loops at different maximum temperatures for a dwell time of 10 s. These calculated TMF-hysteresis loops are the basis for further lifetime assessments by using the local loading parameters obtained from the hysteresis loop.

Models for Lifetime Assessments

Many of the empirical models are strain-based criteria like the Manson-Coffin criterion [1,2] with numerous modifications. Criteria, based on damage parameters, are used to find a correlation between the number of cycles to failure with respect to the loading parameters. The mechanical fracture view allows a description of the lifetime mostly via cyclic J-integrals. Cumulative models, such as the Chaboche models, try to accumulate damage for each cycle. Therefore, a lot of computing time is needed for complex structures. Another method involves the accumulation of damaged parts (pure fatigue, oxidation, creep), e.g., Miller [15] or Neu-Sehitoglu [13].

In this case energy based damage parameters show the best ratio between applicability and effort because they can describe the TMF lifetime using only a few parameters. To describe the lifetime according to cyclic loading parameters, a new, Koeberl modified Prillhofer-Riedler [16] damage parameter, was developed.

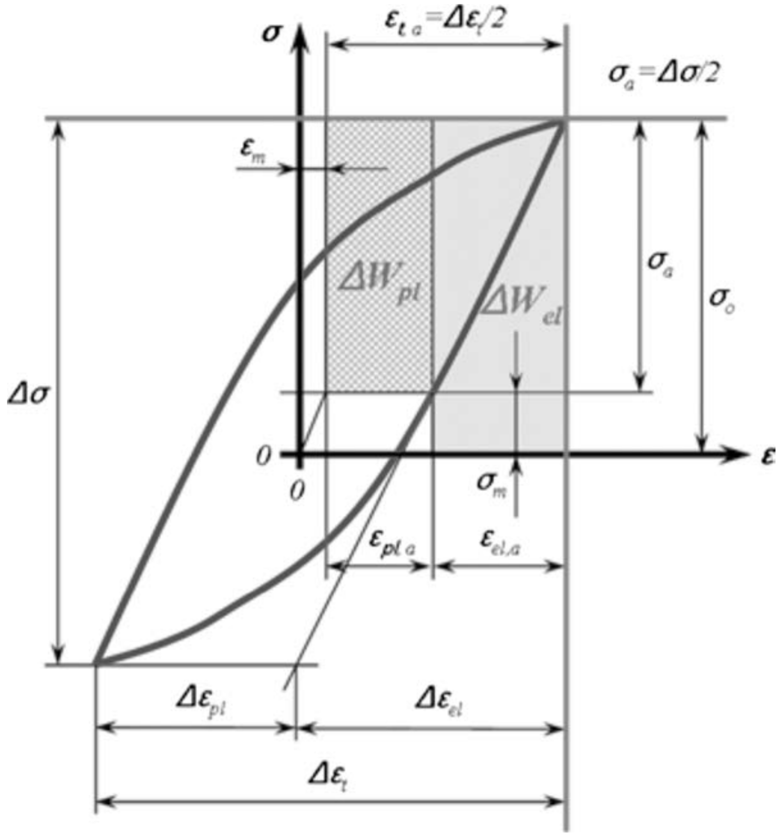

FIG. 13—*General definition of elastic and plastic energy.*

$$P_{KPR} = (\varepsilon_{el,a} + c_{pl} \cdot \varepsilon_{pl,a}) \cdot \sigma_a \cdot \xi_s \cdot \xi_e \tag{4}$$

This damage parameter (P_{KPR} (Eq 4)) is based on the idea of separating elastic and plastic strain components as in the two-parametric Manson-Coffin-Basquin strain lifetime curve. This damage parameter is defined as follows:

$\varepsilon_{el,a}$ describes the elastic, $\varepsilon_{pl,a}$ the plastic strain amplitude, c_{pl} the plastic strain factor ($0 \leq c_{pl} \geq 1$ for LCF and $0 \leq c_{pl} \geq 10$ for TMF) and σ_a the stress amplitude at $N_{f/2}$, see also Fig. 13 (σ_o maximum stress, σ_m mean stress, and ε_m the mean strain). The elastic energy component in Eq 4 specifies the nonreversible elastic energy in the cyclic deformation (i.e., hysteresis energy based on the elastic and plastic energy components).

$$\xi_s = \left(\frac{\sigma_{Rp0.2}}{\sigma_a}\right)^2 \tag{5}$$

$$\xi_e = \left(\frac{\varepsilon_{pl,a}}{\varepsilon_{t,a}}\right)^{c_\varepsilon} \tag{6}$$

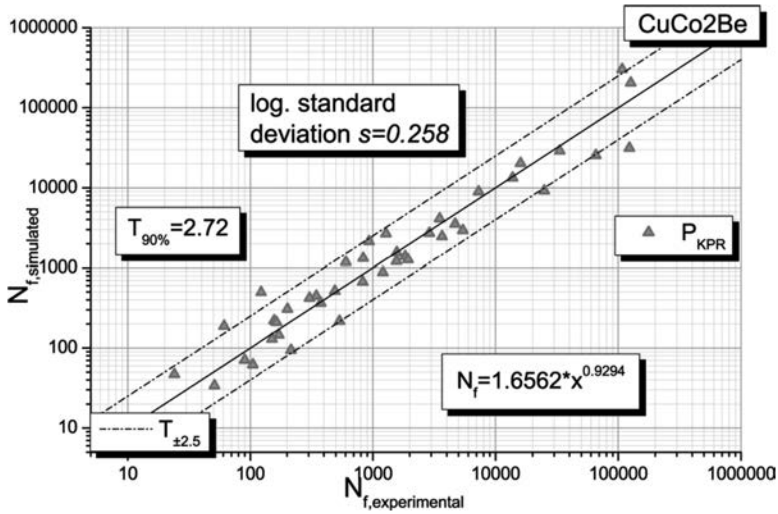

FIG. 14—*Strain, temperature, and strain rate ranges simulated over the experimental lifetime of the LCF tests* (*CuCo2Be*).

The parameter ξ_s (Eq 5) can be described in term of the squared dependency of σ_a at $N_{f/2}$ by using the yield strength ($\sigma_{Rp0.2}$) and ξ_e (Eq 6) is the dependency of the plastic strain amplitude $\varepsilon_{pl,a}$ and the total strain amplitude $\varepsilon_{t,a}$ where c_ε ($0 \leq c_\varepsilon \geq 1$) is the power of. With $\sigma_{Rp0.2} = 775$ MPa for CuCo2Be, and 550 MPa for CuCoBe, respectively.

$$P_{KPR} = \kappa_1 \cdot N_f^{\kappa_2} \tag{7}$$

The lifetime dependency can be described by using a power law as given in Eq 7, where κ_1 and κ_2 are empirical material constants and N_f characterizes the number of cycles to failure.

Lifetime Assessment with P_{KPR}

In general, there is a clear dependency between P_{KPR} and the number of cycles to failure. Figure 14 shows the application of P_{KPR} for the LCF test at room and elevated temperatures. The comparison of the estimated lifetime, by using the loading parameters from the simulation, with the lifetime according to the experimental tests gives a good correlation agreement. The logarithmic standard deviation ($s = 0.258$) is low and the scatter band for 90 % of all tests ($T_{90\ \%} = 2.72$) is acceptable.

For the TMF tests the P_{KPR} results show a good correlation. This depends on the similar deformation behavior of the hysteresis loops under LCF and TMF loading. Figure 15 shows the test results for all TMF tests. The exact specification of the cyclic deformation behavior and the created material model for copper alloys is a reason for the accurate estimation, as well as the precise

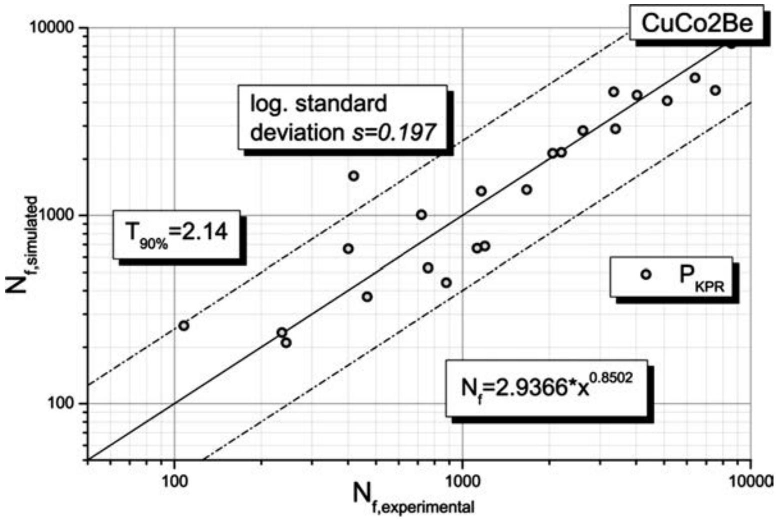

FIG. 15—*Comparison of lifetime results by simulation and experimental lifetime for TMF tests of CuCo2Be.*

lifetime assessment for LCF tests. The logarithmic standard deviation ($s = 0.197$) was very low and the scatter band for 90 % of all tests ($T_{90\ \%} = 2.14$) was good.

Conclusion

An extensive test program was conducted to investigate the influences relevant to the cyclic deformation and lifetime behavior of CuCo2Be and CuCoBe alloys under LCF and TMF loading. Based on stress-strain loops of LCF tests at different temperatures, a kinematic material model was adopted to describe the cyclic deformation behavior in order to gain the stress and strain values for different loading conditions. This was the basis for a subsequent lifetime calculation. To describe the lifetime behavior a new damage parameter, the Koeberl-Prillhofer-Riedler parameter P_{KPR} was developed. This damage parameter delivers a good estimation for lifetime under both LCF and TMF loading.

Acknowledgments

The research work of this paper was performed at the Chair of Mechanical Engineering (Leoben, Austria) within the framework of the Austrian Research Council (FFG) Bridge Project No. "810120/7351-SCK/SAI."

References

[1] Manson, S. S., "Behavior of Materials Under Conditions of Thermal Stress," NACA

Report, 1170, 1954.
[2] Coffin, L. F., "A Study of the Effects of Cyclic Thermal Stresses on a Ductile Metal," *Trans. ASME*, Vol. 76, 1954, pp. 931–950.
[3] Köberl, H., Winter, G., Riedler, M., and Eichlseder, W., "Failure Mechanism of Pure Nickel (Ni 200/201) Under Thermo-Mechanical Loading," *Key Eng. Mater.*, Vol. 348–349, 2007, pp. 793–796, online at http://www.scientific.net, Trans Tech Publications, Suiss.
[4] Lemaitre, J., and Chaboche, J. L., *Mechanics of Solid Materials*, Cambridge Univ. Press, 1990.
[5] Riedler, M., "Methodikfindung zur Simulation von thermomechanisch beanspruchten Motorbauteilen aus Aluminiumlegierungen," Ph.D. Thesis, University of Leoben 2005.
[6] Riedler, M., Minichmayr, R., and Eichlseder, W., "Methods for the Thermo-Mechanical Fatigue Simulation Based on Energy Criteria," *Proceedings of the 6th International Conference of Assessment of Reliability of Materials and Structures: Problems and Solutions*, RELMAS 2005, St. Petersburg, 2005, pp. 496–503.
[7] Löhe, D., Beck, T., and Lang, K.-H., "Important Aspects of Cyclic Deformation, Damage and Lifetime Behaviour in Thermomechanical Fatigue of Engineering Alloys," *5th International Conference on Low Cycle Fatigue*, P. D. Portella, H. Sehitoglu, and K. Hatanaka, Eds., DVM, Berlin, 2005, pp. 161–175.
[8] Hähner, P., Affeldt, E., Beck, T., Klingelhöffer, H., Loveday, M., and Rinaldi, C., "Validated Code-of-Practice for Strain-Controlled Thermo-Mechanical Fatigue Testing," EUR *22281 EN–DG* JRC-Institute for Energy, Luxembourg, Office for Official Publications of the European Communities, ISBN 92-79-02216-4, 2006.
[9] Prillhofer, B., Riedler, M., and Eichlseder, W., "The Influence of Preaging, Temperature and Strain Rate on Low Cycle and Thermo-Mechanical Fatigue of CuCo2Be," *Copper 06—Better Properties for Innovative Products*, Compiègne, France, 2006.
[10] Shercliff, H. R., and Ashby, M. F., "Process Model for Age Hardening of Aluminium Alloys—I. The Model," *Am. Mineral.*, Vol. 38, No. 10, 1990, pp. 1789–1802.
[11] Shercliff, H. R., and Ashby, M. F., "Process Model for Age Hardening of Aluminium Alloys—II. Applications of the Model,," *Am. Mineral.*, Vol. 38, No. 10, 1990, pp. 1803–1812.
[12] Austrian Foundry Institute (OGI), technical report, material analysis. OGI-A.-Nr. 45. 521, 2006.
[13] Neu, R. W., and Sehitoglu, H., "Thermo-Mechanical Fatigue, Oxidation and Creep, Part II: Life Prediction," *Metall. Mater. Trans. A*, 20A, 1989, pp. 1769–1783.
[14] Minichmayr, R., "Modellierung und Simulation des thermomechanischen Ermüdungsverhalten von Aluminiumbauteilen," Ph.D. Thesis, Department of Product Engineering, University of Leoben, 2005.
[15] Miller, M. P., McDowell, D. L., Oehmke, R. L. T., and Antolovich, S. D., "A Life Prediction Model for Thermo-Mechanical Fatigue Based on Micro Crack Propagation," *Thermo-Mechanical Fatigue Behavior of Materials, ASTM STP 1186*, H. Sehitoglu, Ed., ASTM International, West Conshohocken, PA, 1993, pp. 35–49.
[16] Prillhofer, B., "Charakterisierung, Modellierung und Simulation des thermomechanischen Ermüdungsverhaltens von CuCo2Be," M.Sc. Thesis, Department of Product Engineering, University of Leoben, 2006.

COMPONENTS AND STRUCTURES

ASTM Special Technical Publication, Vol. 5, No. 9
Paper ID JAI101695
Available online at www.astm.org

V. N. Shlyannikov,[1] *B. V. Ilchenko,*[1] *and R. R. Yarullin*[1]

Carrying Capacity Prediction of Steam Turbine Rotors with Operation Damage

ABSTRACT: This study is concerned with assessing the integrity of cracked steam turbine rotor which operates under creep conditions. Damage accumulation and growth for turbine rotor took place on the inner surface of hole in a shaft. In this case the crack front was nearly half-elliptical shape. The model based on the critical distance concept is presented for expressing crack growth rate in terms of creep damage accumulation in a process zone ahead of the crack tip. An engineering approach to the prediction of residual lifetime of a turbine rotor which is sensitive to the loading history at maintenance is proposed. Full-size stress-strain state analysis of turbine rotor is represented for different stages of lifetime under considering loading conditions. As a result accumulated creep strain in critical zones of turbine rotor depending on time of loading is defined. The creep fracture mechanics parameters that are found numerically are used to characterize the local strain rate and stress fields at any instant around the crack tip in a turbine rotor subjected extensive creep conditions. The meaning of the critical creep ductility appropriate to the stress state at the crack tip is defined as the difference between permissible and accumulated creep strains at different times of loading. Approximate estimations of carrying capacity are presented for the different stress-strain state of a steam turbine rotor at the operation. It is found that the individual mean lifetime of a turbine rotor can be predicted with reasonable accuracy from knowledge of the stress-strain distributives and the material uniaxial creep ductility and creep rupture strength.

KEYWORDS: plastic and creep strain, crack-tip field, fracture process zone, crack growth, turbine rotor, life time

Manuscript received February 5, 2008; accepted for publication August 2, 2008; published online September 2008.

[1] Research Center for Power Engineering Problems of the Russian Academy of Sciences, Lobachevsky Street 2/31, post box 190, Kazan 420111, Russia, e-mail: shlyannikov@mail.ru (corresponding author).

Citation: Shlyannikov, V. N., Ilchenko, B. V., and Yarullin, R. R., "Carrying Capacity Prediction of Steam Turbine Rotors with Operation Damage," *J. ASTM Intl.*, Vol. 5, No. 9. DOI10.1520/JAI101695. Available online at www.astm.org. Also included in JAI Special Issue STP 1508, *Fatigue and Fracture Mechanics: 36th Volume,* R. W. Neu, K. R. W. Wallin, and S. R. Thompson, guest editors, ASTM International, West Conshohocken, PA, 2009, pp. 659-671.

Introduction

A large and growing portion of electricity is produced by aging thermal power plants. Extending the life of steam turbines and ensuring high reliability requires life assessment technology, scheduled repairing, modification, and upgrading of components in order to provide a stable power supply. Although high quality materials are used for the steam turbines, various forms metallurgical degradation due to creep and fatigue affect the parts and components during long-time operation at high temperature. Our work is concerned primary with situations where creep controls the failure mechanism.

There are the several kinds of examination methods for damage assessment of steam turbines, namely, the destructive method, the nondestructive method, and numerical modeling, but they are not always effective and accurate due to their individual advantages and disadvantages. We have paid our attention on the combined method including the numerical stress-strain distribution in the parts and components of power steam turbine by using finite element analyses (FEA) and limited experimental data related to elastic-plastic and creeping material properties under uniaxial tension.

Models of Materials Behavior

In our work the material deformation behavior is described by additive decomposition of the elastic, plastic, and creep strains:

$$\varepsilon_{total} = \varepsilon_{elastic} + \varepsilon_{plastic} + \varepsilon_{creep} \tag{1}$$

Here the elastic, plastic, and creep strains are evaluated independently. The first and second terms of Eq 1 are obtained by combining elastic and isotropic hardening. The Ramberg-Osgood model

$$\frac{\varepsilon}{\varepsilon_y} = \frac{\sigma}{\sigma_y} + \alpha\left(\frac{\sigma}{\sigma_y}\right)^m \tag{2}$$

was employed to define the stress-strain curve corresponding to the elastic-plastic material properties. In Eq 2, σ_y is the yield stress, m is the hardening coefficient, and α and ε_y are two fitting parameters. The parameter ε_y is usually taken to be σ_y/E.

In the multi-axial case the corresponding constitutive equations of the J_2-deformation theory of plasticity are in incremental form:

$$\dot{\varepsilon}_{ij} = (1+\nu)\dot{\sigma}_{ij} - \nu\dot{\sigma}_{kk}\delta_{ij} + \frac{3}{2}m\alpha\left(\frac{\sigma_e}{\sigma_y}\right)^{m-2}\frac{S_{ij}}{E}\frac{\dot{\sigma}_e}{\sigma_y} \tag{3}$$

A purely power-law creeping material behavior governed by Norton constitutive relation and under uniaxial tension, the total strain rate is related to the stress by

$$\dot{\varepsilon} = \dot{\varepsilon}_0 \left[\frac{\sigma}{\sigma_0} \right]^n \text{ or } \dot{\varepsilon} = B\sigma^n \tag{4}$$

where σ_0 is a reference stress, $\dot{\varepsilon}_0$ is a reference creep strain rate, and n is the creep exponent. Note that a combined constant $B = \dot{\varepsilon}_0 / \sigma_0^n$ is often used. Under multi-axial stress state, based on the J_2-deformation theory, the extension of the uniaxial creep relation can be written as

$$\dot{\varepsilon}_{ij} = \frac{3}{2} \dot{\varepsilon}_0 \left(\frac{\sigma_e}{\sigma_0} \right)^{n-1} \frac{S_{ij}}{\sigma_0} \tag{5}$$

In Eqs 2–5, ν is the Poisson ratio, δ_{ij} is the Kronecker delta, $\dot{\varepsilon}_{ij}$ are the components of the strain rate tensor, σ_{ij} are the components of the stress tensor, S_{ij} are the components of the deviatoric stress tensor, and $\sigma_e = ((3/2)S_{ij}S_{ij})^{1/2}$ is the Mises effective stress. Typically, the material constants E, ν, σ_y, m, n, σ_0, $\dot{\varepsilon}_0$, and B are obtained experimentally from uniaxial tests at the temperature of interest. For the considering power steam turbine rotor, the Young's modulus, Poisson's ratio, and the yield stress were considered to be 199 GPa, 0.3, and 460 MPa, respectively. The strain hardening exponent m was 3.96. The creep parameter and the creep exponent are $\dot{\varepsilon}_0 = 1.46 \times 10^{-8}$, $B = 4.35 \times 10^{-15}$, and $n = 3.34$.

Elastic-Plastic Stress and Creep Strain Fields in Turbine Rotor

The subjects of our consideration are rotor of 100 MW power steam turbine (Fig. 1). The critical zones of this turbine are disk and blade attachment, key, and shaft. Damage accumulation and growth for turbine rotor took place on the inner surface of hole in a shaft. In this case the crack front was a nearly half-elliptical shape (Fig. 1).

Fatigue and creep lifetime prediction for power steam turbine traditionally has involved numerical study in real structure components in order to determine the stress-strain fields and crack modeling based on the theoretical relationship and experimental data. The finite element method was used to carry out stress-strain analysis in order to determine the total stress-strain state and creep strain distribution at the critical region.

This part of our study is concerned with assessing the integrity of cracked steam turbine rotors which operate under creep conditions. Turbine rotor is subjected to a inertia loading at temperature of 550°C. Damage accumulation and growth have occurred on the inner surface of hole in a turbine rotor. A disk-blades assembly of power steam turbine is assumed mounted on a circular rotor (Fig. 2). The blades are assembled into the disk by rivet joints. The disk is divided into identical sectors, each of which accommodates a blade. The disk-blades assembly is assumed loading by inertia forces. It is supposed that temperature distribution is constant along the disk radius. Finite element mesh of a full-size 3-D model of a turbine rotor is shown in Fig. 2. The ANSYS [1,2] finite element code is used to solve both elastic-plastic and creep 3-D problems.

The finite element analyses are made by using 20-node isoparametric three-dimensional solid elements. Full-size stress-strain state analysis of a turbine

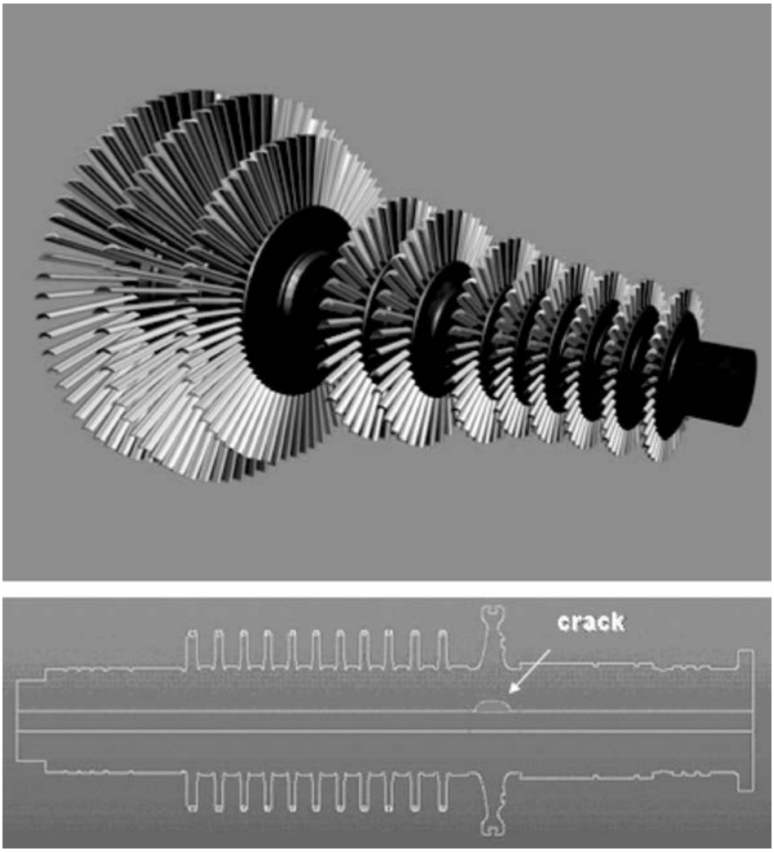

FIG. 1—100 MW *power steam turbine rotor with operation damages on inner surface of hole in a shaft.*

rotor is represented in Fig. 2 for different stages of lifetime under considered loading conditions. As a result, accumulated creep strain in critical zones of turbine rotor depending on time of loading is defined (Table 1). As it was supposed, the critical zones are the disk and blade rivet attachment and the inner surface of hole in a shaft. The operation of turbine rotor with crack in rivet attachment is not possible; therefore, we paid our attention on the shaft.

Three-dimensional finite element models of the power steam turbine rotor containing a semi-elliptical surface crack are shown in Fig. 3. Special attempts have been made to form finite element mesh of turbine rotor with the semi-elliptical crack on inner surface of turbine rotor (Fig. 3). The sub-modeling technology is employed to analyze of detailed stress-strain state in the crack tip vicinity. To consider the details of large deformation of the crack tip, a typical mesh was used to model the region near the notch tip. In Fig. 3 are shown both crack tips on inner surface of shaft and also one crack tip in a large scale. The sub-model of the shaft consists of 16 layers. The thickness of the layer in both

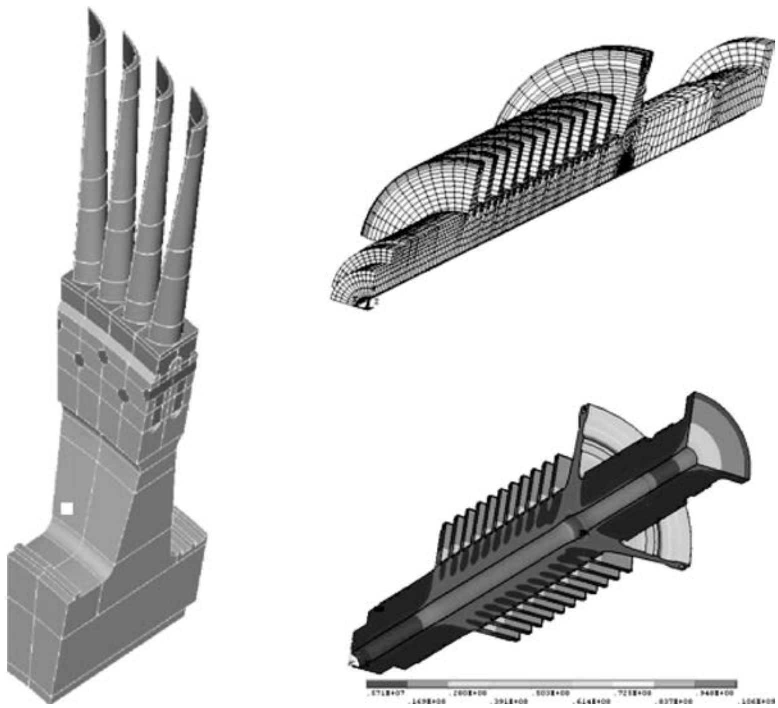

FIG. 2—*Turbine rotor finite element model and stress concentration zones.*

free-surface and deepest point directions is gradually reduced to accommodate the strong variations of the stress gradients along curvilinear crack front. In the plane perpendicular to the crack front, the element size gradually increases with increasing radial distance r from the crack tip, while the angular increment of each element layer is kept constant at 7.5°, throughout the mesh.

In our calculations the crack form varied from semi-circular to semi-elliptical surface cracks. We consider several planes which were placed along the curvilinear crack front (Fig. 4). It is proposed to set the position of any plane of the semi-elliptical crack front by two coordinates, i.e., crack distance r and angle ϕ, which varied from $\varphi=0^{\circ}$ (surface point of crack front) up to φ

TABLE 1—*Structural integrity estimation of power steam turbine rotor.*

Variant	Operation time, h	ε	ε^{FEM}	ε_f	σ^{FEM}, MPa	t_{cr}, h
1	100 000	0.007	0.004 67	0.002 33	176.3	299 800
2	150 000	0.008	0.006 74	0.001 26	168.3	162 100
3	200 000	0.009	0.008 45	0.000 55	164.2	70 760
4	230 000	0.010	0.009 61	0.000 39	156.8	50 170

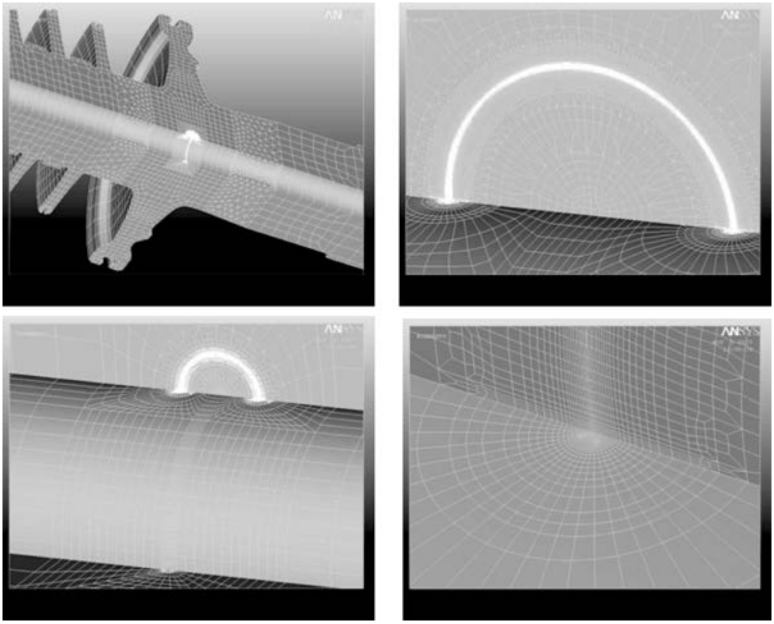

FIG. 3—*Finite element mesh of power steam turbine rotor with semi-elliptical crack.*

$=90°$ (deepest point of crack front). In each section on the elliptic plane the Cartesian coordinates rearranged into a polar one centered at the crack tip (Fig. 4).

It should be noted that creep fracture mechanics has often relied on the straightforward application of the Hoff analogy [3] by which the Hutchinson,

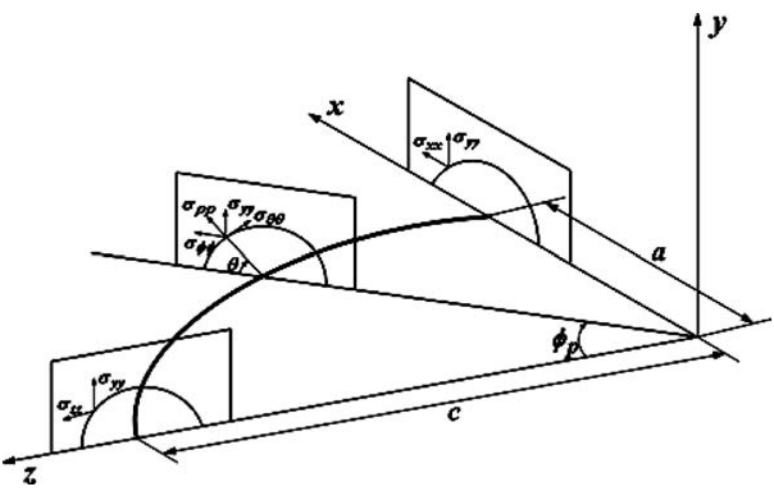

FIG. 4—*Transformation of coordinates on elliptic plane.*

Rice, and Rosengren (HRR) [4–6] solution for power-law creeping materials can be obtained by replacing the J-integral by the $C(t)$-integral, and by replacing strains and displacements by strain rates and displacement rates, respectively. Using the Hoff analogy for an isotropic creeping body containing a crack subject to symmetric mode I loading, Ridel and Rice [7] presented the HRR-type singularity field for power-law creep materials:

$$\sigma_{ij} = \sigma_0 \left(\frac{C(t)}{\sigma_0 \dot{\varepsilon}_0 I_n r} \right)^{1/(n+1)} \tilde{\sigma}_{ij}(\theta, n) \tag{6}$$

where r and θ are polar coordinates centered at the crack tip, σ_0 is a reference stress, $\dot{\varepsilon}_0$ is a reference creep strain rate, n is the creep exponent, $\tilde{\sigma}_{ij}(\theta)$ is dimensionless angular functions, and I_n a dimensionless constant depending only on the creep exponent. The amplitude factor $C(t)$, which depends upon the applied time, magnitude of the remote loading, crack configuration, and material properties, is defined by Bassani and McClintock [8].

Before proceeding to the determination of both the elastic-plastic stress and creep strain distributions, all numerical FEM results are normalized in such a way that direct comparisons with the solution related to different crack front position by can be made. It then follows purely from dimensional considerations that for elastic-plastic problem, the distance from the crack tip r must scale by the yield stress σ_y when the loading is governed solely by J-integral

$$\bar{r} = (\sigma_y r / J) \tag{7}$$

In the case of the creep problem the loading governing parameter is the C-integral and the dimensionless polar radius is

$$\bar{r} = (\sigma_0 \dot{\varepsilon}_0 r / C) \tag{8}$$

The elastic-plastic stresses and the total strains are normalized by the yield stress σ_y and the yield strain ε_y, respectively:

$$\bar{\sigma}_{ij} = \frac{\sigma_{ij}^{FEM}}{\sigma_y}, \quad \bar{\varepsilon}_{ij} = \frac{\varepsilon_{ij}^{FEM}}{\varepsilon_y} \tag{9}$$

The results for elastic-plastic and creeping problems of angular stress distributions for both general FEM numerical solutions are normalized so that

$$\tilde{\sigma}_{e,max}^{FEM} = \left(\frac{3}{2} s_{ij}^{FEM} s_{ij}^{FEM} \right)_{max}^{1/2} = 1, \quad \tilde{\sigma}_{e,max}^{(k)} = \left(\frac{3}{2} s_{ij}^{(k)} s_{ij}^{(k)} \right)_{max}^{1/2} = 1, \quad k = 1,2,3 \tag{10}$$

Once the full field FEM olution $\bar{\sigma}_{ij}^{FEM}(r, \theta, n)$ is found, the angular variation of dimensionless stress can be easily obtained by resolving Eq 6 relatively $\tilde{\sigma}_{ij}(\theta, n)$:

$$\tilde{\sigma}_e(\theta, n) = 1 \Rightarrow \tilde{\sigma}_{ij}(\theta, n) = \frac{\bar{\sigma}_{ij}^{FEM} (\sigma_0 \dot{\varepsilon}_0 I_n)^{1/(n+1)}}{(C/\bar{r})^{1/(n+1)}} \tag{11}$$

In this equation the value of $(C/\bar{r})^{1/(n+1)}$ plays the role of a scale factor which normalizes the effective stress $\tilde{\sigma}_e^{(1)}(\theta)$ so that $(3\tilde{s}_{ij}^{(1)}\tilde{s}_{ij}^{(1)}/2)^{1/2} = 1$.

Due to the complexities, we consider in the present work both elastic-plastic state and the different creeping stages of power steam turbine rotor

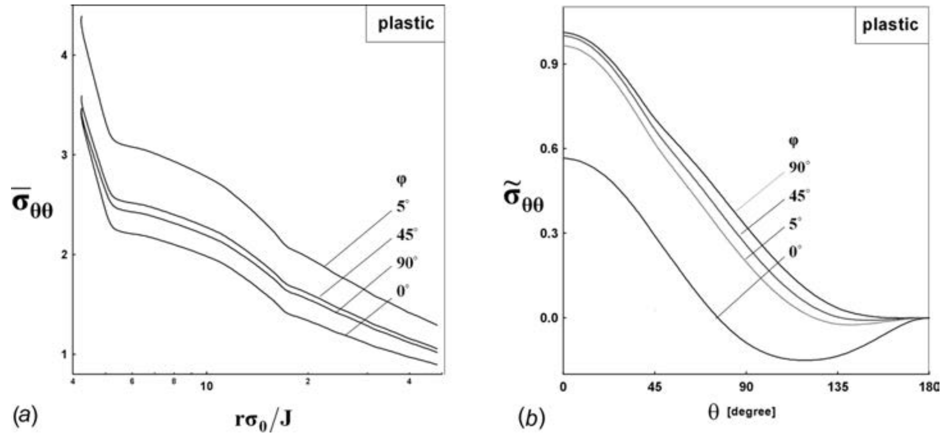

FIG. 5—*Elastic-plastic* (*a*) *radial and* (*b*) *angular tangential stress distributions for different crack front positions.*

operation time. Figure 5(*a*) represents the radial dimensionless tangential stress distributions from the line ahead of the crack tip ($\theta = 0°$) up to crack surface ($\theta = 180°$) at some distance from the crack tip at creep time $t = 1$ h (purely elastic-plastic state of turbine rotor). Figure 5(*b*) shows the angular dimensionless tangential stress distributions at crack distance $\bar{r} = 7.61$ at the same creep time. The strong influence of the crack plane position along crack front on the stress fields for aspect ratio $\xi = a/c = 1$ is easily seen.

Figure 6 represents the tangential and the shear dimensionless plastic and creep strain distributions in the shaft of the turbine rotor with a semi-elliptical crack at the different creep times. As it follows from three-dimensional stress-strain analysis, the maximum plastic and creep strains occur at the surface point of the crack front with respect to the deepest crack point in the turbine rotor.

Figure 7 represents the plastic and the creep zones along the semi-elliptical crack front in the turbine rotor. From the results of calculation, it seems reasonable to assume that the surface and deepest point of the crack front would be governed by different local stress-strain conditions. Regions of the crack front close to the free surface may be considered as local plane stress conditions, while the deepest point is close to the plane strain state. The above analyses demonstrate the transition of stress-strain state from the plane stress to the plane strain state.

Fracture Process Zone Size

In the present work is considered a cracked body in the steady (secondary) creep of polycrystalline material undergoing creep-constrained grain boundary cavitation. In this case a phenomenological constitutive law is proposed by Hutchinson [9] which includes two main governing parameters, where n is the creep exponent and ρ is the density of cavitating facets. At high temperatures

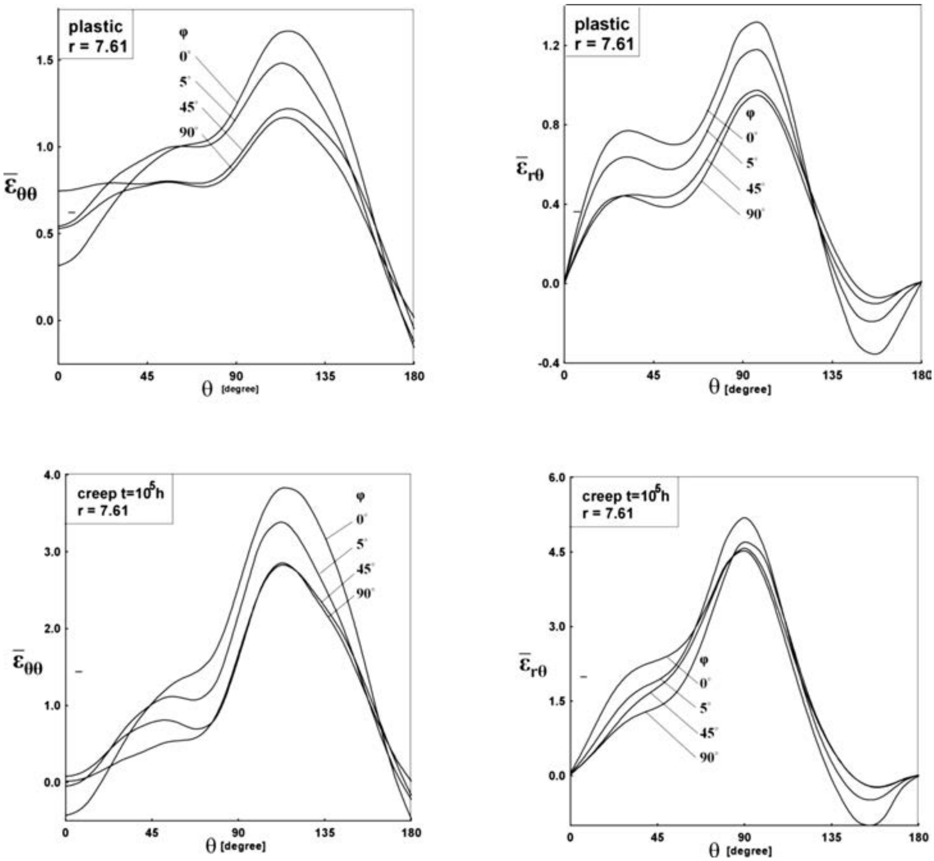

FIG. 6—*Angular tangential and shear strain distributions along crack front.*

grain boundary cavitation is one of the primary mechanisms of deformation and fracture in polycrystalline materials, which is a nucleation and growth process associated with grain boundary voids. Whether these voids then grow or collapse depends on many factors including the temperature and local stress state at the boundary. If the voids do grow they can do so by one of several mechanisms including diffusion, coupled diffusion, power-law creep, and purely power-law creep. Mentioned above, different deformation and fracture mechanisms can be described by corresponding combinations of governing parameters n and ρ which reflect the mechanical properties of definite structural material. When $\rho=0$ the Hutchinson law is reduced to the Norton equation 4.

In our investigation a case when the creep process takes place in full rotor but damage accumulation and growth are concentrated in the process zone adjacent to initial main crack is considered. For formulating fracture criteria the satisfaction of the requirements that stress-strain criteria are applied over a microstructural distance related to the fracture mechanism is necessary. In [10]

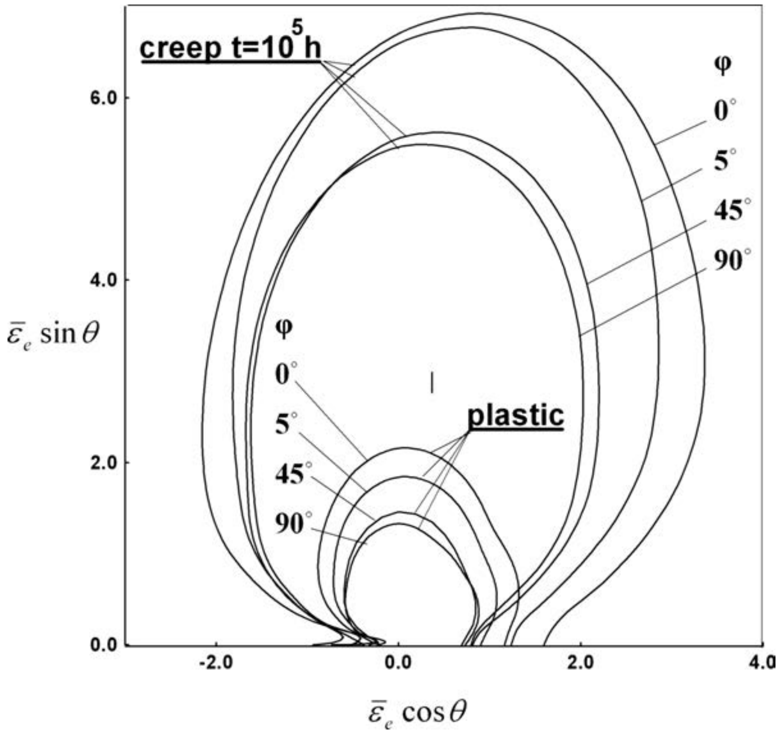

FIG. 7—*Plastic and creep strain zones at crack front in power steam turbine rotor.*

the conditions of applicability of the strain energy density rate (SEDR) function to ductile fracture due to void growth and coalescence, wherein multiple voids interact within the fracture process zone (FPZ) are discussed. The length of the FPZ is introduced and measured as the distance between main crack front and the point where the SEDR reaches certain critical value that can be obtained from a uniaxial creep test data (Eq 12). The FPZ is formed by process involving void growth and coalescence under conditions in which take place multiple interacting voids in a "void-sheet" ahead of the main crack tip. The length of the FPZ is assumed to be large compared to the size of several voids which have coalesced ahead of the critical SEDR point, while shear or rapture ligaments for other voids located between macrocrack tip and this point have occurred. The macroscopic effect of mechanisms of nucleation, growth, and coalescence of voids is a new free surface creation (increment of the crack length) which is apparent in various degrees in all materials from quasi-brittle to the quasi-plastic. Thus, the physical meaning of FPZ size may be revealed as the increment of the crack length in an elementary act (being a sum of several failed voids and spaces between them) of fracture events.

The next part of our study is concerned with assessing the integrity of cracked steam turbine rotor which operates under creep conditions. What we are interested in here is describing creep crack growth rate and predicting lifetime of turbine rotor at the operation conditions. The model based on the critical distance concept is presented for expressing crack growth rate in terms of creep damage accumulation in a process zone ahead of the crack tip. Some details are in the follows.

Several broadly compatible models of creep crack growth have been discussed in the literature. In the approach of Nikbin-Smith-Webster [11] a process zone is postulated at the crack tip. It is supposed that this zone encompasses the region over which creep damage accumulated ahead of a growing crack. It also is assumed that local fracture will occur at the crack tip when the stress-strain state in the element reaches a certain critical value. This fracture parameter can be measured from standard uniaxial test data in terms of the strain energy density rate as it proposed by Shlyannikov [10]:

$$\dot{W}_f = \sigma_0 \dot{\varepsilon}_0 \frac{n}{n+1} \left(\frac{\sigma_f}{\sigma_0} \right)^{n+1} \text{ or } \dot{W}_f = B \frac{n \sigma_f^{n+1}}{n+1} \tag{12}$$

where σ_f is creep rupture strength. The value of $\dot{W}_f$ is the material properties. On the other hand, making use of the Eq 4, the current value of the strain energy density rate for a given structure can be written as

$$\dot{W}_{cr} = \frac{n}{n+1} \frac{C^*}{I_n r_{cr}} \tilde{\sigma}_e^{n+1}(\theta, n) \tag{13}$$

In this case $\dot{W}_{cr}$ is stress-strain state parameter. A fracture process zone size can be introduced equaling Eqs 12 and 13. That is:

$$\dot{W}_f = \left. \dot{W}_{cr} \right|_{r=r_{cr}} \text{ or } \sigma_0 \dot{\varepsilon}_0 \frac{n}{n+1} \left(\frac{\sigma_f}{\sigma_0} \right)^{n+1} = \frac{n}{n+1} \frac{C^*}{I_n r_{cr}} \tilde{\sigma}_e^{n+1} \tag{14}$$

Resolving this equation with respect to crack distance it is easily obtain the creep fracture process zone size

$$r_{cr} = \frac{C^*}{\sigma_0 \dot{\varepsilon}_0} \frac{\tilde{\sigma}_e^{n+1}}{I_n} \left(\frac{\sigma_0}{\sigma_f} \right)^{n+1} \tag{15}$$

Crack Growth Model

When secondary creep dominates Eq 15, the size of the process zone can be inserted into NSW model [11] to give an expression for creep crack growth rate as

$$\dot{a} = (n+1) \frac{\dot{\varepsilon}_0}{\varepsilon_f} \left(\frac{C^*}{\dot{\varepsilon}_0 \sigma_0 I_n} \right)^{n/(n+1)} r_{cr}^{1/(n+1)} \tag{16}$$

where ε_f is the creep ductility appropriate to the state of stress local to the crack tip.

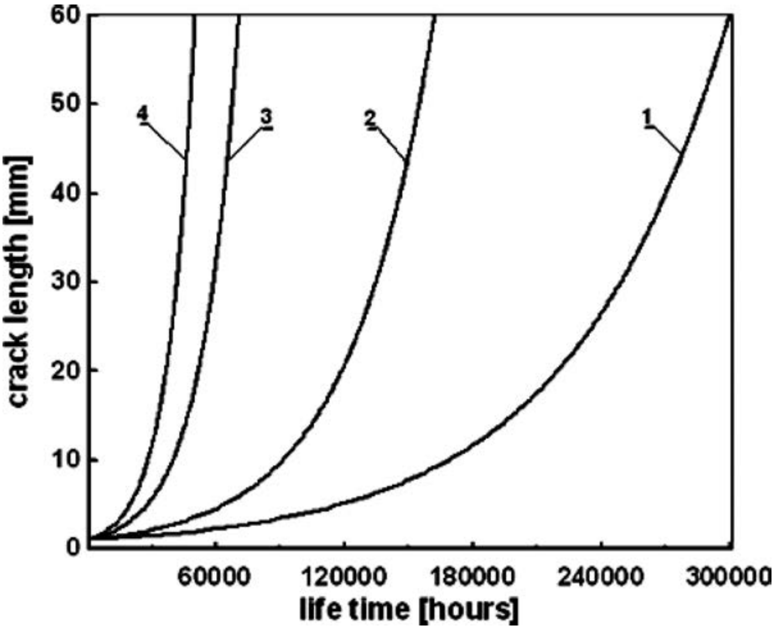

FIG. 8—*Residual life time prediction on the crack growth stage in turbine rotor at different preliminary operation times.*

From the results of calculation concerning the determination of amplitude factors in the turbine rotor, it is found that for the deepest point of semi-elliptical crack front may be approximately describe by He-Hutchinson solution [12]:

$$C^* = \dot{\varepsilon}_0 \sigma_0 (0.5\pi a)\sqrt{n}\left[\frac{\sqrt{3}}{2}\frac{\sigma}{\sigma_0}\right]^{n+1} \tag{17}$$

Substituting this equation into Eq 16 there results an equation of crack growth rate under extensive creep conditions:

$$\dot{a} = \frac{da}{dt} = (n+1)\frac{\dot{\varepsilon}_0 \sigma_0}{\varepsilon_f \sigma_f}\frac{\tilde{\sigma}_e}{I_n}(0.5\pi a)\sqrt{n}\left[\frac{\sqrt{3}}{2}\frac{\sigma}{\sigma_0}\right]^{n+1} \tag{18}$$

This equation includes the value of creep ductility ε_f. We suppose the meaning of the critical creep ductility ε_f appropriate to the stress state at different times of loading is defined as the difference between permissible $[\varepsilon]$ and accumulated ε^{FEM} in service creep strains before crack appearance:

$$\varepsilon_f = [\varepsilon] - \varepsilon^{FEM} \tag{19}$$

On this basis, approximate estimations of carrying capacity are presented for the different stress-strain state of steam turbine rotor at the operation (Table 1).

Figure 8 represents residual lifetime prediction on the crack growth stage in a turbine rotor at different preliminary operation times as the example of creep crack propagation evaluation by Eq 18. These show the crack length as a function of creep crack propagation time. It is found that individual mean lifetimes of turbine rotor can be predicted with reasonable accuracy from knowledge of the stress-strain distributions and the material uniaxial both creep ductility and creep rupture strength.

Conclusions

Full-size stress-strain state analysis of power steam turbine rotor is represented for different stage of lifetime under considering loading conditions. As a result accumulated creep strain in critical zones of turbine rotor depending on time of loading is defined. The creep fracture mechanics parameters that are found numerically are used to characterize the local strain rate and stress fields at any instant around the crack tip in power steam turbine rotor subjected to extensive creep conditions. An engineering approach to the prediction of residual lifetime of power steam turbine components which is sensitive to the loading history in service is proposed.

[1] *ANSYS Structural Analysis Guide*, 001245, 5th Ed., SAS IP, Inc., 1999.

[2] *ANSYS Theory Reference*, 001242, 11th Ed., SAS IP, Inc., 1999.

[3] Hoff, N. J., "Approximate Analysis of Structures in the Presence of Moderately Large Creep Deformation," *Q. J. Mech. Appl. Math.*, Vol. 12, 1954, pp. 49–55.

[4] Hutchinson, J. W., "Singular Behaviour at the End of a Tensile Crack in a Hardening Material," *J. Mech. Phys. Solids*, Vol. 16, 1968, pp. 13–31.

[5] Rice, J. R., and Rosengren, G. F., "Plane Strain Deformation Near a Crack Tip in Power Law Hardening Material," *J. Mech. Phys. Solids*, Vol. 16, 1968, pp. 1–12.

[6] Hutchinson, J. W., "Fundamentals of the Phenomenological Theory of Nonlinear Fracture Mechanics," *J. Appl. Mech.*, Vol. 50, 1983, pp. 1042–1051.

[7] Riedel, H., and Rice, J. R., "Tensile Crack in Creeping Solids," in: *Fracture Mechanics, ASTM STP 700*, ASTM International, West Conshohocken, PA, 1980, pp. 112–130.

[8] Bassani, J. L., and McClintock, F. A., "Creep Relaxation of Stress Around a Crack Tip," *Int. J. Solids Struct.*, Vol. 17, 1981, pp. 479–492.

[9] Hutchinson, J. W., "Constitutive Behavior and Crack Tip Fields for Materials Undergoing Creep-Constrained Grain Boundary Cavitation," *Acta Metall.*, Vol. 31, 1983, pp. 1079–1088.

[10] Shlyannikov, V. N., *Elastic-Plastic Mixed Mode Fracture Criteria and Parameters*, Springer-Verlag, Berlin, 2003.

[11] Nikbin, K. M., Smith, D. J., Webster, G. A., "An Engineering Approach to the Prediction of Creep Crack Growth," *J. Eng. Mater. Technol.*, Vol. 108, 1986, pp. 186–191.

[12] He, M. Y., and Hutchinson, J. W., in: *Elastic-Plastic Fracture, ASTM STP 803*, Vol. 1, ASTM International, West Conshohocken, PA, 1983, pp. 227–290.

ASTM Special Technical Publication, Vol. 5, No. 9
Paper ID JAI101619
Available online at www.astm.org

Raghu V Prakash[1] *and Akash Bagla*[1]

Fatigue Crack Growth in Open and Nut-Loaded Bolts with and without Pretension Loading

ABSTRACT: Results of an experimental study to understand crack growth in open threaded bolts and nut-loaded bolts with and without pretension are presented in this paper. Experimental crack growth rates are compared with predicted solutions obtained from known stress intensity factor solutions. For the experiment, a specially designed fixture was used for loading the bolt and the level of pretension was varied by controlling the displacement on the arm of the C section of the fixture. Programmed Hi–Lo fatigue load sequence was applied on a bolt to ensure that decodable marker bands are left behind on the fracture surface, to study the crack growth characteristics. Fatigue crack growth rate was estimated using a scanning electron microscope by identifying crack increment during high stress ratio cycles. This has been compared with predicted crack growth rates using available stress intensity factor solutions. Crack growth at the center of the bolt correlates well with Toribio's (Int. J. Fract., Vol. 53, 1992, pp. 367–385) finite element based predictions for open threaded bolts. Crack growth rate is much higher at the surface than at the center. In case of nut-loaded bolts, available *K* solutions are found to be inadequate to provide an accurate estimate of crack growth rates at the center of the bolt. Further study is required to characterize the effect of friction, pitch angle, and thread geometry to understand crack growth in bolts.

Manuscript received January 24, 2008; accepted for publication July 16, 2008; published online October 2008.

[1] Associate Professor and Graduate Student, respectively, Department of Mechanical Engineering, Indian Institute of Technology Madras, Chennai 600 036, India, e-mail: raghuprakash@iitm.ac.in

Citation: Prakash, R. V. and Bagla, A., "Fatigue Crack Growth in Open and Nut-Loaded Bolts with and without Pretension Loading," *J. ASTM Intl.*, Vol. 5, No. 9. DOI10.1520/JAI101619. Available online at www.astm.org. Also included in JAI Special Issue STP 1508, *Fatigue and Fracture Mechanics: 36th Volume,* R. W. Neu, K. R. W. Wallin, and S. R. Thompson, guest editors, ASTM International, West Conshohocken, PA, 2009, pp. 672-694.

KEYWORDS: fatigue crack growth, open thread bolts, nut-loaded bolts, pretension loading, marker band technique, stress intensity factor

Introduction

Threaded fasteners such as bolts are still widely in use in mechanical assemblies to interconnect two dissimilar components. Despite several advances in fastener technology, bolted joints are in use, even today, in view of the flexibility they offer in assembly and in service. Though failures of fasteners are not frequent, thanks to the careful design considerations, the consequence of some failures can be severe; hence, considerable attention is being given to the design of bolted fasteners. In cases of components subjected to dynamic loading, the bolts experience fatigue loading, resulting in fatigue crack initiation at the thread root, which acts as a stress concentrator. In cases such as pressure vessels and internal combustion engines, bolts are subjected to pretension loading during initial assembly to ensure pressure tightness, which results in tensile mean stress; further, some of the bolts experience high temperature in addition to mechanical loading, thus making the entire fatigue process as complex. Understanding fatigue behavior of bolts subjected to dynamic loading is important from the viewpoint of structural safety.

Fatigue failure at the bolts takes place at the first thread of the bolted joint ($\sim$65 % of bolt failures) and it takes place by the process of crack initiation at the thread root, followed by crack growth prior to attainment of critical crack size to fracture. Crack propagation can be influenced by the presence of corrosive fluids, in which case it leads to accelerated cracking. It is generally said that when the crack size (a) is small in relation to the diameter of the bolt (D), the stress concentration factor at the thread root has a significant contribution to crack growth, and the effect diminishes when the crack size becomes large (almost equal to half the diameter of bolt) and in such cases, fatigue crack growth in bolts can be approximated by the stress intensity factor (K) expressions for an unnotched round bar [1].

Several K solutions are available in the literature [2,3] relating to single fatigue crack in notched and unnotched round bars, with straight crack front as well as circular crack front; K solutions have been worked out for tension, bending loading. Figure 1 presents typical crack fronts observed in notched bars. Obviously, the stress intensity factor is dependent on the shape of the crack front. It is observed that the straight crack front has a higher value of K than the circular crack front at all crack length "a" to diameter "D" (a/D) ratios [1]. In the case of semicircular crack fronts, it was observed that the K value at the deepest point was less than the K value at free surface of the notched bar. Very few researchers [4,5] have investigated the effect of crack aspect ratio—defined as ratio of depth "a" to chord distance "b" [refer to Fig. 1(c)] for a semicircular crack front. The stress intensity factor tends to decrease with increasing values of aspect ratio (a/b). From the viewpoint of modeling, it is important to assume an initial shape to a crack front for a fatigue crack in a bolt thread, and redefine the shape as the crack progresses prior to its attaining the fracture shape. Traditionally, it is assumed that the initial shape is semicir-

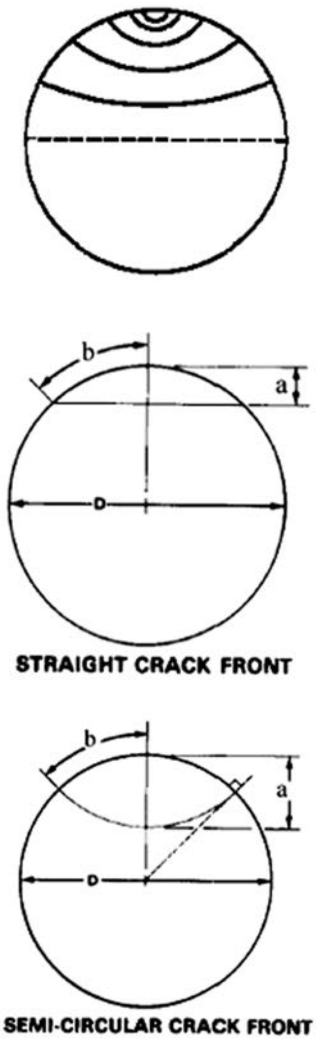

FIG. 1—*Typical crack fronts observed in notched bars.*

cular, but it has been shown, through experimental studies, that the crack which initiates as semicircular or semielliptic in shape at the time of initiation changes over to straight crack front with the growth of crack in the geometry. Forman and Shivakumar [6] suggested a set of equations to describe the crack aspect ratio for straight, semicircular crack fronts for the cases of tensile, bending loading.

While several researchers have examined the effect of crack front on K values for circular bars, very few works concentrate on the stress intensity for threaded members. The problem is complex in view of the pitch angle (also

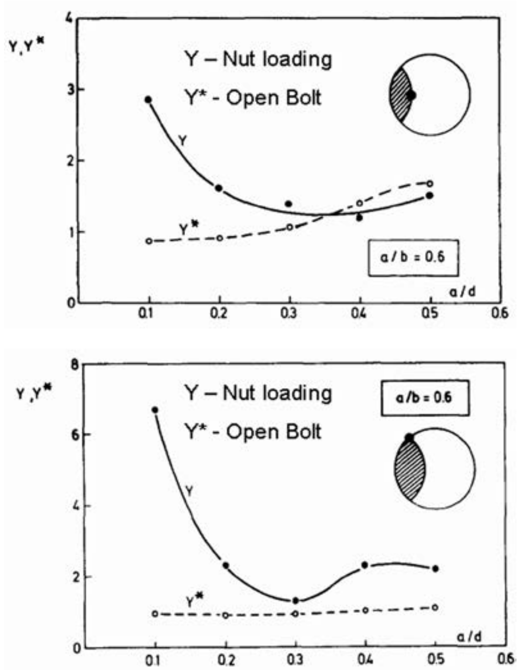

FIG. 2—*Stress intensity factor comparison for open thread bolt* (Y^*) *and nut-loaded bolt* (Y) *at* (*a*) *the midthickness region and* (*b*) *at near surface* [7].

referred to as helix angle), and varying contact surfaces for force transfer during tension-compression loading for the case of a nut-loaded bolt.

Toribio [7,8] analyzed the stress intensity solution for threaded bolts subjected to simple tension loading as well as for the case of nut-loaded bolt. The loading on the contact face was assumed to be varying from value "p" at first engagement thread to value "$p/2$" for second thread. It may be noted that subsequent threads share reduced loads compared to second thread. Based on the finite element study, Toribio concluded that the stress intensity factor for a crack in a nut-loaded bolt (as represented by Y in Fig. 2) is much higher than for an open threaded bolt (Y^* in Fig. 2). Contact pressure variation at the helical interface was not considered in the analysis. The above-presented text suggests that stress intensity solutions to predict crack growth in nut-loaded bolts are scarce; this affects our ability to predict crack growth rates in bolts subjected to fatigue loading. The aim of this study is to experimentally derive the crack growth rates for fatigue cracks in bolts loaded by a nut with and without preload and compare the data with those derived analytically from known stress intensity factor solutions. A programmed marker block loading consisting of Hi–Lo blocks of constant amplitude loading is applied on bolts and based on the marker band spacing the empirical stress intensity factor is derived. This is compared with available stress intensity factor solutions from the literature.

To understand the effect of nut loading on stress distribution at a thread root, which in turn affects the stress intensity factor, a finite element analysis was carried out simulating the case of an open thread root and a nut-loaded thread root.

Finite Element Analysis of Open Bolt and Nut-Loaded Bolt

Stress distribution near the thread root provides an estimate of local stresses that governs the stress intensity factor as well as fatigue crack growth rates. Most often in the literature, stress intensity solution for fatigue crack in bolts has been derived using the notched bar geometry. Such solutions can, at best, simulate the behavior of a fatigue crack in open thread configuration. However, experience suggests that most of the bolt failures take place at the first thread engagement and the role of nut loading is significant. To understand the effect of stress distortion due to nut loading, a geometric model of a thread root was generated using ANSYS® finite element software. The model is considered to be axisymmetric for simplicity; thus the pitch angle is assumed to be small in comparison with other geometric features. The root diameter of 8.16 mm was modeled for M10 bolt. A total of 9722 elements of type Plane-2 and 19 563 nodes were used for modeling an open bolt. The model was constrained at one end (can be either at the top or bottom end) and uniform pressure loading was applied to the other end. The displacement along the x and y directions in the constrained end was arrested.

For modeling a nut-loaded bolt, contact elements of type CONTA 172 and target elements of type TARGET 169 are used. The coefficient of friction between the contact elements is assumed to be a constant of 0.2. A uniform pressure load was applied along one end of the bolt and the same reacted by the axisymmetric nut end. The displacement along the x and y directions for restraining ends of bolt and nut were equated to zero. Tilt along the axis of loading of bolt and nut was arrested, thus making the bolt and nut displace primarily along the axis of symmetry. Figure 3 presents the generated mesh for open bolt and nut-loaded bolt. Elastic–plastic analysis considering the material stress–strain curve obtained from tensile testing of bolt material was used as input for material description during analysis. The stress–strain data relating to postyield behavior for low carbon, boron steel material was fed into the ANSYS package for material constants.

Experimentation

Industry standard, ISO class 8.8, M10 high tension steel bolts were used for this study. The bolt material had yield strength of ~650 MPa and ultimate tensile strength of ~850 MPa with a proof stress of 600 MPa. The bolts had undergone the standard practice of thread forming operation under controlled conditions of production. The surface of the thread faces was examined using an optical stereo microscope prior to testing and found to be free from any imperfections in surface finish.

A straight edge crack initiator was machined at a thread root by wire electric discharge machining (EDM) process to a depth of 0.5 mm from the root

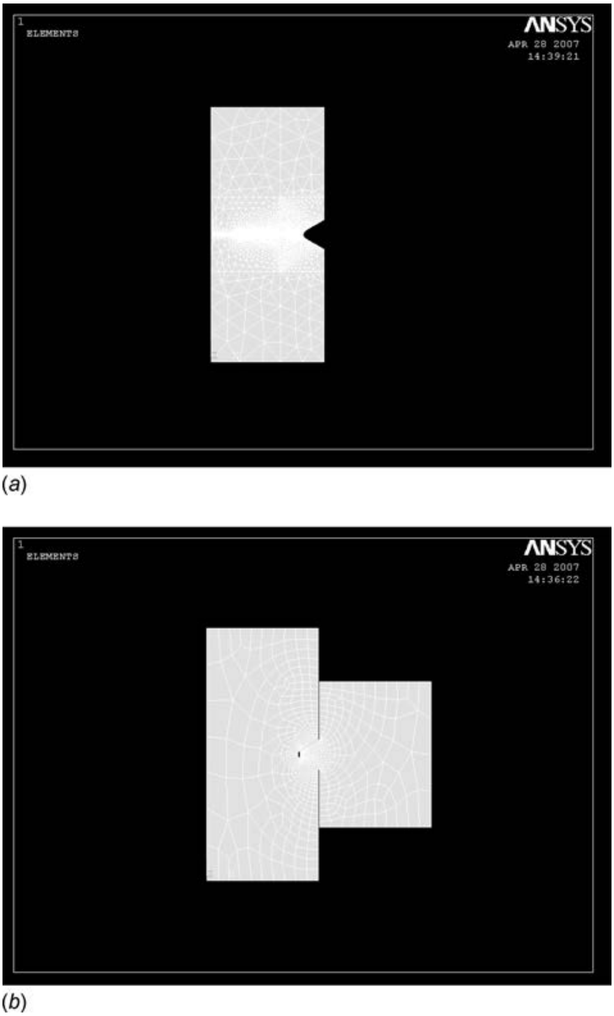

FIG. 3—*Mesh generation for* (*a*) *open thread bolt and* (*b*) *nut-loaded bolt.*

surface of the thread. Experiments were carried out on open threaded bolts and on nut-loaded bolts. In the case of nut-loaded bolts the first thread engagement of nut was manually aligned to crack initiator. The loading arrangement was a simple thread adapter for bolts loaded without preloading (Fig. 4).

A special fixture was developed for preloading of nuts. Normally, preloading is carried out by engaging the bolts inside a nut, which in turn is stretched by a known displacement to induce a prestress on the threaded bolts, by an arrangement similar to the one shown in Fig. 5. In such a case, one could add the preload component to the applied load and obtain the total load acting on the bolt. In the case of pressure vessels, internal combustion engines, which have preloaded fastening, the point of threading is away from the point from

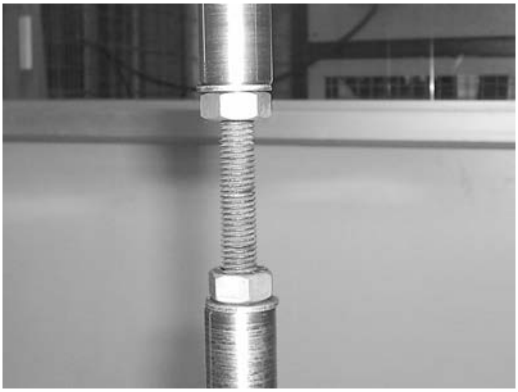

FIG. 4—*Fixture used for fatigue testing of open thread bolts.*

where the internal pressure variation takes place and, as a consequence, a force and moment acts on the threaded bolts. To simulate this effect, a C-clamp type fixture was developed as shown in Fig. 6. The material of the C clamp is AISI 4340 steel having a base yield strength of 550 MPa and UTS of 630 MPa. The C clamp has a slit at one end and by controlling the separation distance, one could achieve a known level of pretensioning on the bolt that is attached at the open end of the C clamp. The C clamp had a diameter of 150 mm and a wall thickness of 8 mm.

As the clamp distance controls the extent of pretension on the bolt, a bolt sample with one quarter of thread length was strain gauged and the pretension load was calibrated for known C clamp end distance. Figure 7 presents the calibration chart for the pretension load versus clamp clearance distance when the specimen was not loaded at the center in the test machine.

The C-clamp fixture with varying levels of preload was loaded on a 100 kN-MTS servohydraulic test system and a correlation curve between applied load and load sensed by the bolt was established (Fig. 8). It may be noted that at the commencement of loading, the entire loading train gets internally readjusted for alignment and as a consequence one could notice a different slope for the first loading half-cycle. A subsequent cycle of loading and unloading resulted in a fixed slope between load applied on the machine and load experienced by the bolt. It can also be noted from Fig. 8 that the load sensed by the bolt is greater than the sum of preload and machine load, in view of the moment component in the loading. It may be noted that Hobbs et al. [9] indicated that eccentric loading of bolts introduces mean stress to the bolt which is different from the axially loaded bolts; however, the authors have indicated that this does not affect the failure mode in bolts significantly. Upon complete unloading to zero loads, the load transferred to the bolt returns to original preload level, which indicates that the loading on the bolt has been completely elastic. A similar trend was observed for varying levels of pretension in the bolt. Care was exercised during this loading–unloading calibration not to have elastic–plastic loading of the threaded bolt. Figure 9 presents the loading—unloading response of bolts for various levels of pretension. Thus, with knowledge of the

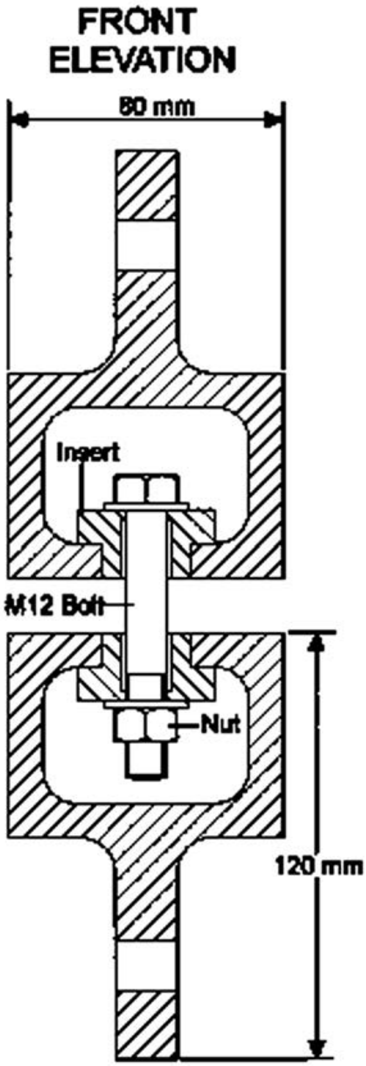

FIG. 5—*Preloading fixture for bolts* [9].

slope of the data, one could estimate the amplitude of the load applied on the bolt for a given pretension level and machine load amplitude.

Marker Band Loading

Data on fatigue crack growth provides a valuable input for understanding the crack driving force in complex geometries. If crack growth in cycles having high mean stresses can be identified, one could treat it as a case of crack growth

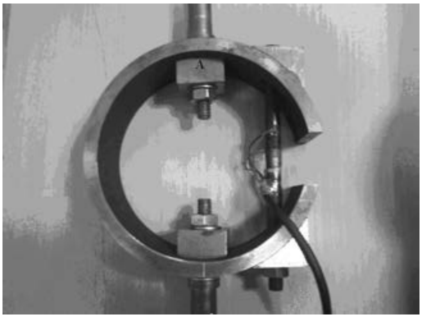

FIG. 6—*Preloading fixture used for bolt fatigue evaluation. The gap at the open section of fixture controls the extent of preloading on the bolt.*

in the absence of crack closure and use it to estimate the stress intensity factor. In this work, a two-step Hi–Lo loading block was used to generate marker bands on the fracture surface of the bolt. Figure 10 presents the schematic of marker block loading. Typically, 500 cycles of Hi-amplitude ($R = 0.1$) loads and 5000 cycles of low amplitude ($R = 0.6$) loads were applied to the load assembly. The blocks were repeated until specimen failure. In some cases, the number of cycles of Hi and Lo amplitude was altered as per data in Table 1, to examine the identification of marker bands on fracture surface. It may be noted that identifiable marker bands on the fracture surface are dependent on the load level applied, number of cycles of loading at each block of loading, and on the crack

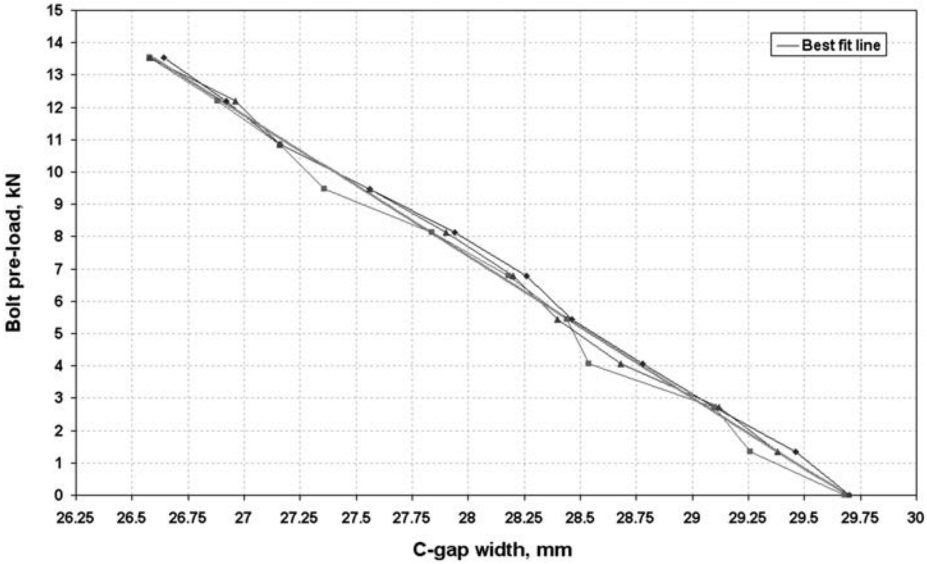

FIG. 7—*Calibration chart for preload levels with the variation of gap in C section in the fixture.*

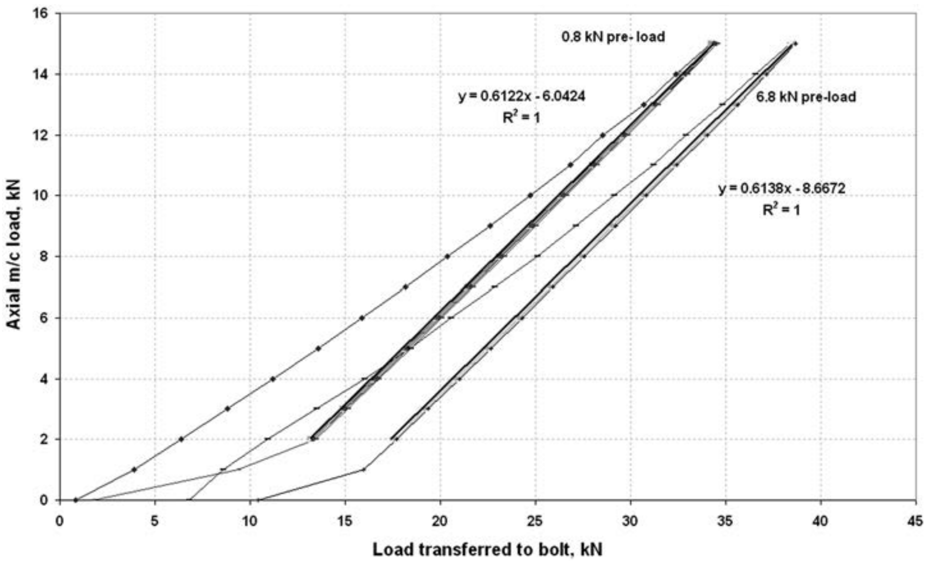

FIG. 8—*Load sensed by the bolt as a function of nominal load applied on the test fixture for two different levels of pretension.*

growth rate. Some materials such as Al–Cu alloy 2014 are more amenable for marker banding, while some others are not amenable for marker banding; marker band formation is dependent on the mechanism of crack growth in a material and ductile materials generally show clear marker bands, while brittle materials show poor marker bands.

The fracture surfaces of specimen failures were examined under a FEI Quanta-200 scanning electron microscope (SEM) in view of the better reso-

TABLE 1—*Loading conditions for fatigue loading of bolts.*

Bolt	Type of loading	Stress ratio (R)	Max. load (kN)	Cycles (N)	Remarks
I	Open	0.1	20.88	500	Beach marks observed
		0.6	20.88	5000	
II	Open	0.1	15.00	500	Beach marks observed
		0.6	15.00	5000	
III	Open	0.1	12.00	50	Beach marks not observed
		0.6	12.00	500	
IV	Nut loaded	−0.1	18.00	150	Beach marks observed
		0.6	18.00	3000	
V	Nut loaded	−0.1	21.00	150	Beach marks not observed
		0.6	21.00	3000	
VI	Nut loaded	−0.1	24.00	300	Beach marks not observed

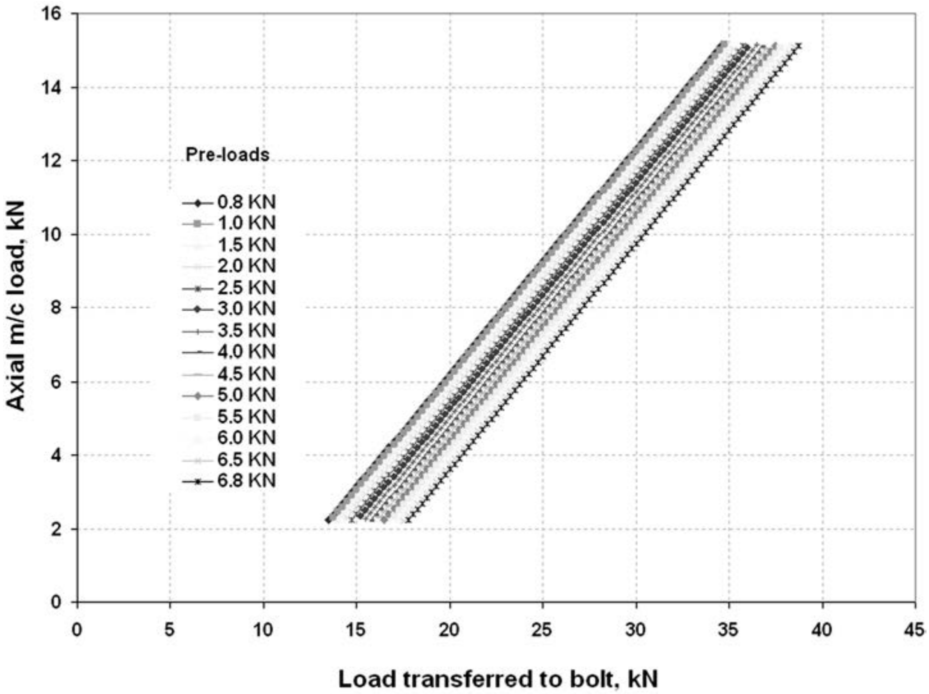

FIG. 9—*Load sensed by the bolt for various levels of pretension applied on the bolt through the test fixture.*

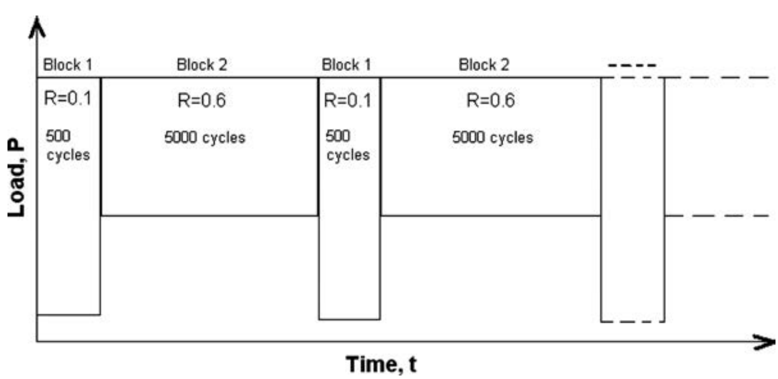

FIG. 10—*Schematic of Hi–Lo block load sequence used to induce marker bands on the fracture surface of fatigue cracked bolts.*

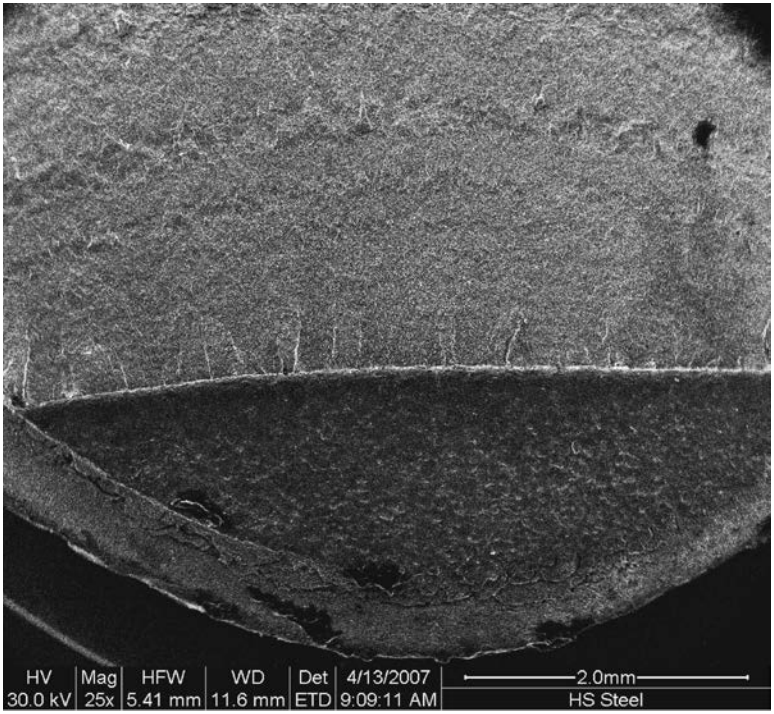

FIG. 11—*Typical SEM fractograph of bolt failure surface. Magnification: 25 times*

lution in a SEM compared to a conventional optical microscope. Typically, 30 kV electron beam voltage was used and a magnification factor of 25 to 200 times was used for observations of marker bands. Figure 11 presents a typical micrograph of a bolt specimen failure. The bright region corresponds to low amplitude loading ($R=0.6$) and dark region corresponds to high amplitude loading ($R=0.1$). Thus by estimating the distance between two dark bands, one could estimate the crack growth rate during "n" applied cycles of low-amplitude loading. Crack growth rate for Lo-amplitude cycles can be estimated as

$$\left(\frac{da}{dN}\right)_j \approx \left(\frac{\Delta a}{\Delta N}\right)_j = \frac{a_j - a_{j-1}}{N_j - N_{j-1}}.$$

The stress intensity factor range can be calculated as

$$\Delta K_j = F\Delta\sigma\sqrt{\pi a_{\mathrm{avg}}}$$

where:

$$a_{\mathrm{avg}} = (a_j + a_{j-1})/2,$$

F = geometry correction factor, and

$\Delta\sigma$

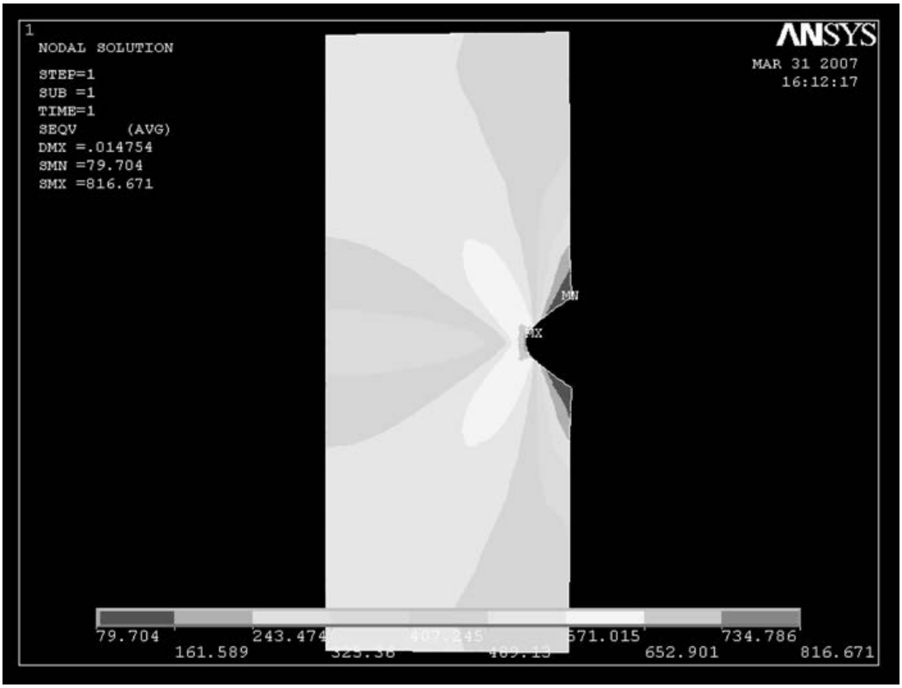

FIG. 12—*Stress plot for open thread bolt geometry.*

= applied stress range.

As the crack growth measurements are made primarily for the Lo amplitude (high mean stress cycles), it can be said that the data are not distorted by events such as crack closure, which are normally associated with fatigue crack growth. In view of the above-presented assumption, no crack closure characterization study was attempted in the present investigation.

Results and Discussion

Finite Element Analysis

Figure 12 presents the stress distribution at the thread root of an open bolt. It can be observed that the stress distribution is symmetrical about the plane of thread root, which implies that the fatigue crack is likely to grow in a plane perpendicular to the axis of loading, if the pitch angle for the bolt is small, which is justifiable in cases of small pitch threads.

Figure 13 presents the stress distribution for a nut-loaded bolt. As expected, the stress distribution is not symmetrical between the top half and bottom half of the thread root. The principal stress direction is shifted toward the face that

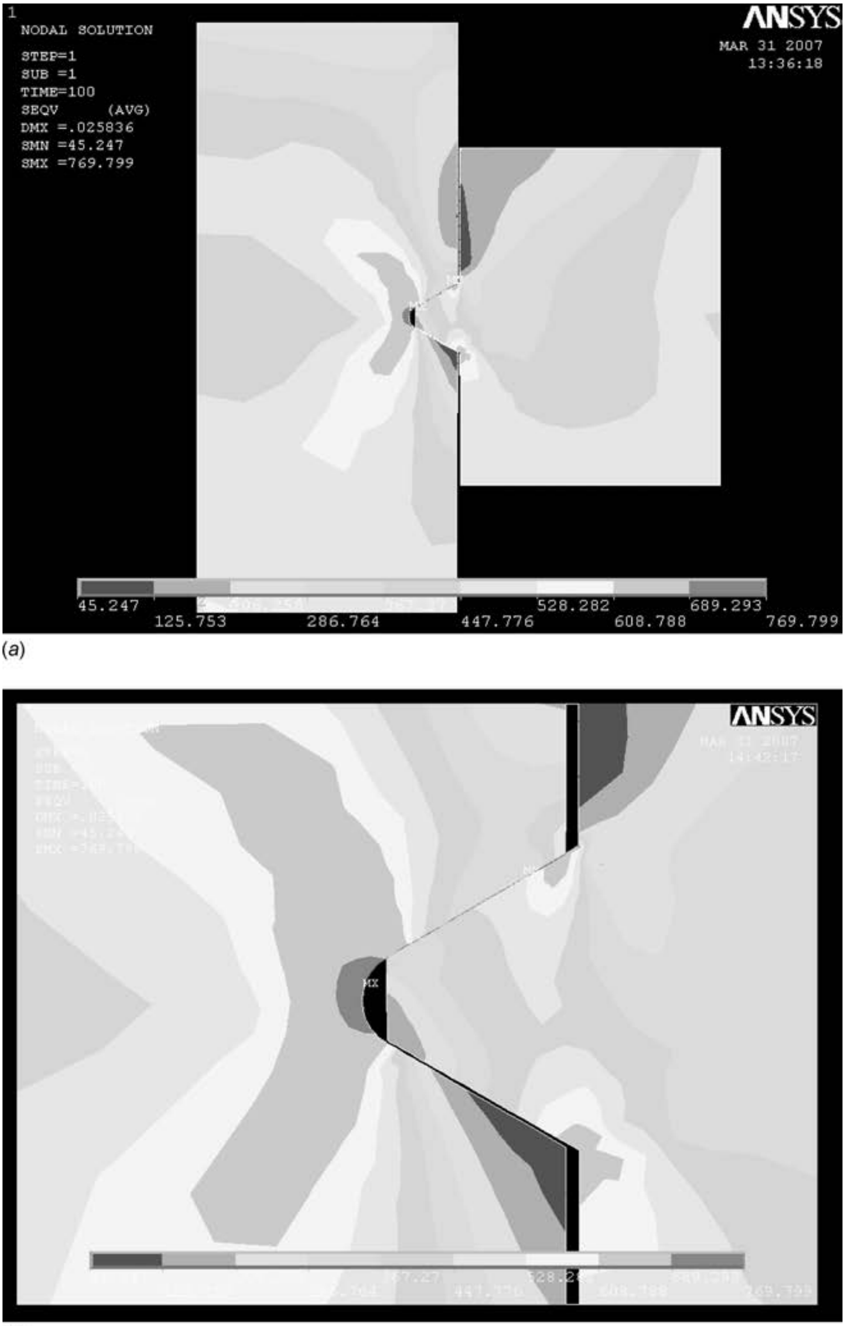

(a)

(b)

FIG. 13—*Stress plot for nut-loaded bolt geometry:* (*a*) *General distribution and* (*b*) *near the thread root.*

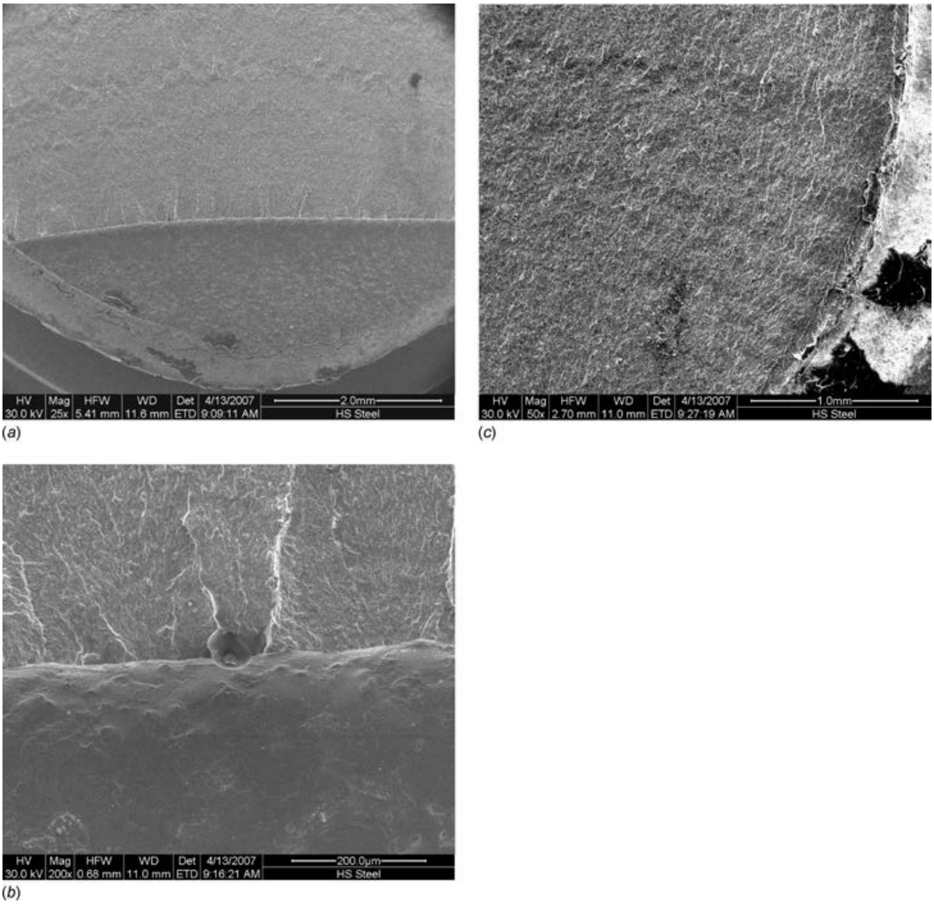

FIG. 14—(*a*) *SEM picture of open thread bolt specimen fracture. Magnification: 25 times.* (*b*) *Crack initiation from sputter point of EDM machining process and* (*c*) *marker bands near the surface. Magnification: 50 times.*

makes contact. The lower face of the bolt shows separation while the upper face takes most of the load by contact. Thus one could expect crack growth at an angle to the axis of the loading in the case of nut loading. Incidentally, for the sake of simplicity, in the present finite element model the nut-loaded bolt was modeled as the one with zero helix angle. The exact direction of maximum principal stress would depend on the pitch angle of the thread, friction coefficient of contact between the thread and nut (which is likely to be variable as a function of crack depth). These would affect the crack growth rates in nut-loaded bolts.

Fatigue Crack Growth

Figure 14 presents the SEM image of an open threaded bolt subjected to a

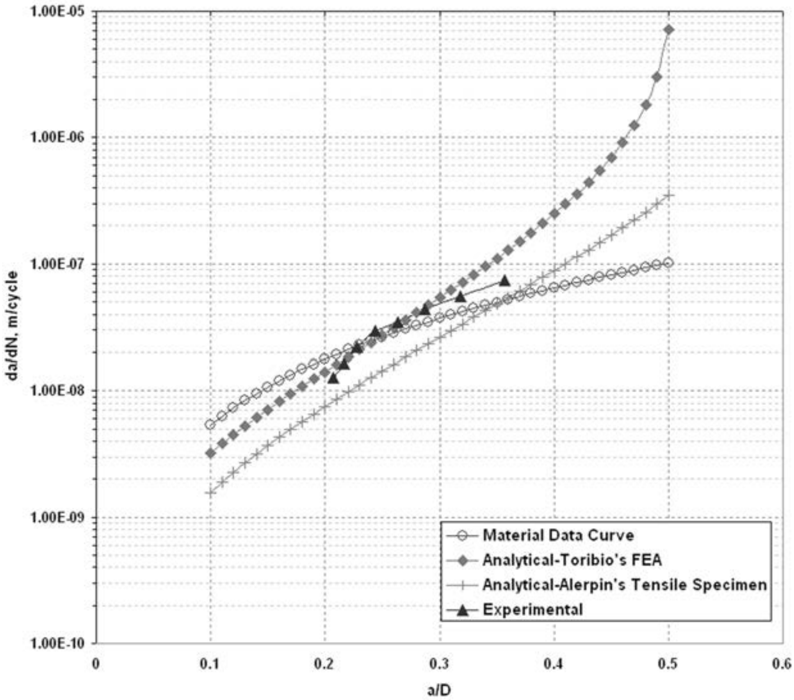

FIG. 15—*Crack growth rate as a function of a/D for open loaded bolt.*

cyclic loading between 20.88 and 2.088 kN of Hi-block loading. Fatigue crack initiated from one of the sputter points induced by the spark erosion process of machining a prenotch [Fig. 14(*b*)]. Crack propagation was observed to be semielliptic in nature. The crack aspect ratio was observed to be 0.53 for the most prominent marker band. The marker bands were barely visible near the surface compared to midthickness region. Figure 14(*c*) presents the image at 50 times. Marker bands are identified by the dotted white lines on the image.

Figure 15 presents the crack growth rate data plotted as a function of (a/D). Also presented in the same plot are crack growth rates estimated based on Toribio's FEA stress intensity factor solutions and Mackay and Alerpin's tensile specimen correction data [10]. It can be noted that the marker bands were obtained from the a/D range of 0.21–0.36. From the graph it can be observed that the experimental crack growth rate data have slight deviation from the finite element analysis (FEA) solution provided by Toribio, but the difference is more when Alerpin's correction factor is considered.

Figure 16 presents the crack growth rate as a function of stress intensity factor range, ΔK. It can be observed that Alerpin's analytical solution does not correlate with experimental crack growth rate data, while Toribio's solutions are in close conformity with experimental data. The deviation of Alerpin's solution could be due to the consideration of plain tensile specimen geometry to predict crack growth in threaded fasteners.

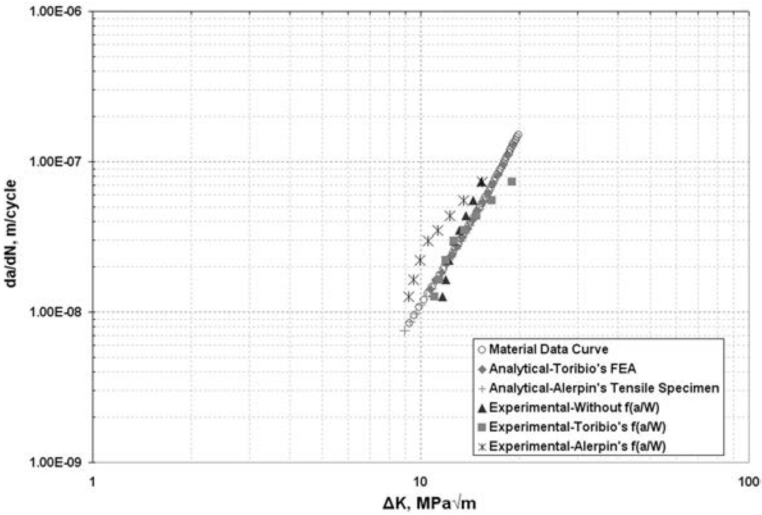

FIG. 16—*Crack growth rate as a function of stress intensity factor range for open thread bolt.*

Figure 17 presents the SEM image of fracture for another thread fastener loaded in open bolt configuration at a peak load of 15 kN. Marker bands could be observed at both the center of the specimen as well as at the free surface. The fatigue crack initiated once again from the sputter point of wire EDM prenotch machining process and propagated as a semielliptical crack front. The crack aspect ratio was observed to be ~0.68 for the most prominent marker band. Figure 17(*b*) shows the image at close to surface of the bolt. From the SEM image one can notice that the crack growth rate is higher at the free edge compared to midthickness region.

Figure 18 presents the crack growth rate at midthickness and at free surface versus a/D for this open thread bolt geometry. Also presented in the same graph are analytical predictions for a/D ranging between 0.1 and 0.5. It can be observed that the crack growth rate at the midthickness region is marginally different from the analytical predictions based on Toribio's stress intensity factor (SIF). But the experimental crack growth rates at the free surface are almost one order higher than predictions based on Toribio's solution. This is again reflected in da/dN versus ΔK plot shown in Fig. 18(*b*). Higher crack growth rate at the free surface of the threaded bolt could be due to the absence of constraint to deformation and crack growth. Thus, available SIF solution for the free edge of the bolt is not adequate to predict crack growth rates accurately.

Nut-Loaded Bolt

Figure 19 presents the fractograph of a nut-loaded bolt having a preflaw and tested at a maximum load of 15 kN using Hi–Lo block loading. Marker bands were observed at the crack center. Crack initiation was from an inclusion at the

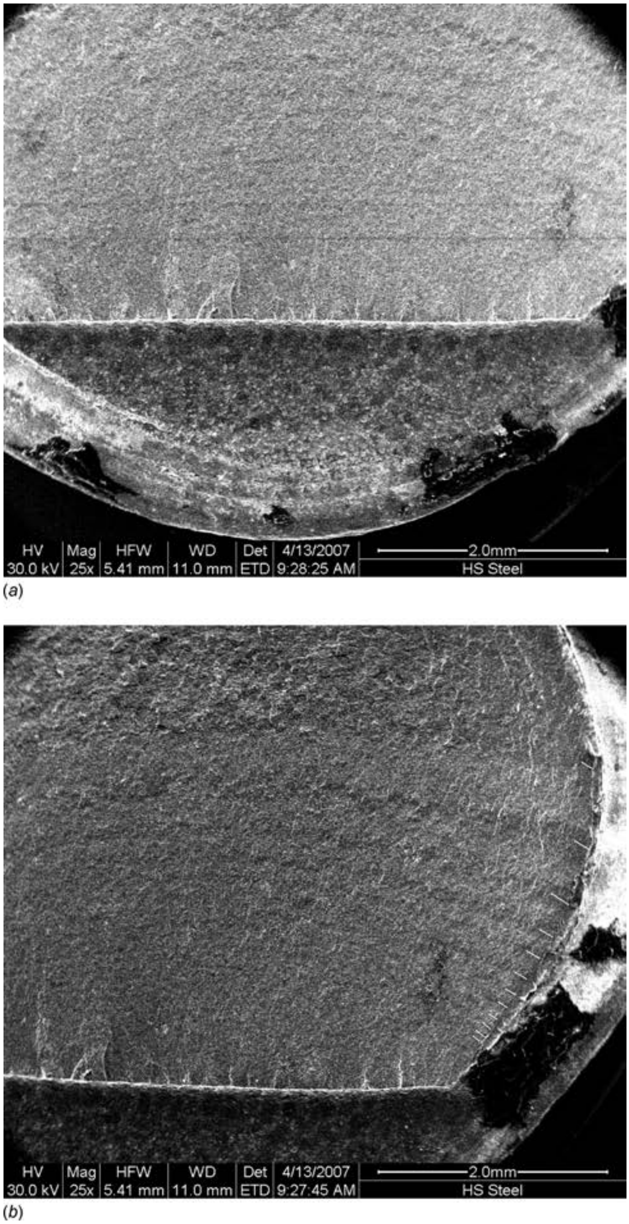

FIG. 17—(*a*) *SEM image of fracture of open thread bolt tested at* 15 kN *maximum load. The marker bands are clearly visible on the fracture surface.* (*b*) *Fatigue crack growth rate at free surface is higher than at the crack center.*

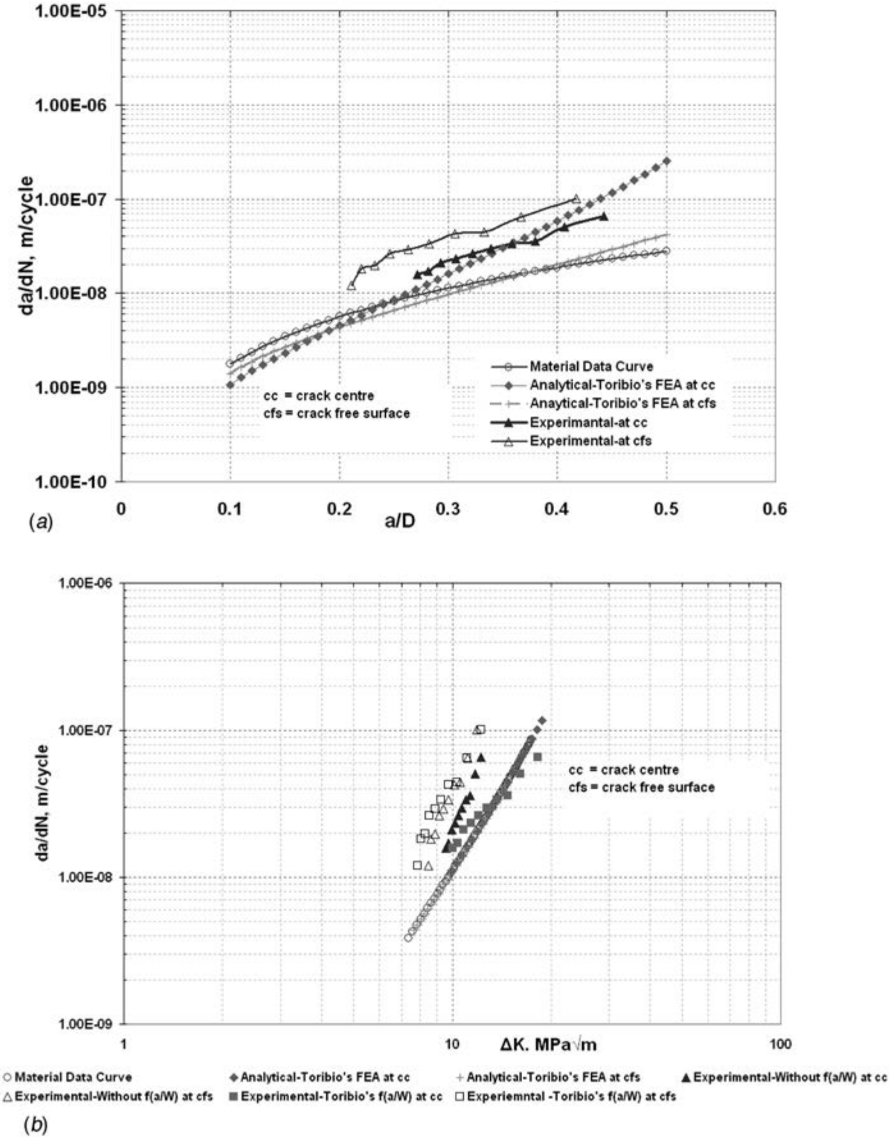

FIG. 18—(*a*) *Crack growth rate vs. a/D for open thread bolt.* (*b*) *Crack growth rate vs. stress intensity factor range* ΔK *for an open thread bolt.*

notch and propagated as a semielliptical crack front. The crack aspect ratio was estimated to be ~0.47 for the most prominent marker band. The marker bands were not clear at the free surfaces of the specimen.

Figure 20(*a*) presents the crack growth rate data versus a/D for nut-loaded condition. Experimental data were obtained clearly for as a/D ratio of 0.33–

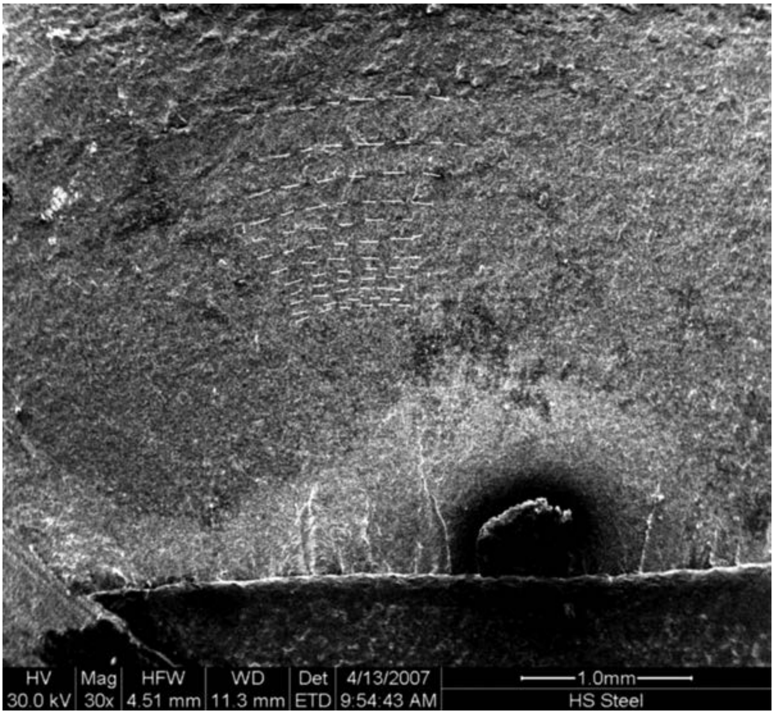

FIG. 19—*SEM image of crack growth in nut-loaded bolt.*

0.47. Analytical predictions were made using Toribio's SIF solutions. From the figure, it can be observed that the experimental crack growth rate is always lower than the analytical predictions based on Toribio. This is also shown in the crack growth rate plotted against SIF range [Fig. 20(*b*)]. The observed differences could be ascribed to the pitch angle of the thread, mixed mode crack growth in nut-loaded bolt, which reduces the effective stress intensity factor compared to the case of a pure opening mode stress intensity solution provided by Toribio. Interestingly, experimental estimation of crack closure stress for fatigue cracks in round notched bars by Shin and Qai [11] suggests that the influence of crack closure (as indicated by $\Delta K\,\mathrm{eff}/\Delta K$) is of the order of 70 % of applied maximum load (implying 30 % crack closure level) and the effect of crack closure reduces with increasing (a/D) ratio. This suggests that crack closure could not be the reason for the difference in crack growth rates between experimental data and predicted data.

As indicated in the remarks column (column 6) of Table 1, in some cases, marker bands could not be identified on the fracture surface. This may be due to the combination of load levels, number of cycles of loading applied at each stress ratio of Hi-/Lo-block loading. This problem became significant in the case of pretension bolts as the marker block loading in gross loading conditions did not leave identifiable marker bands on the fracture surface.

The failure life reduced due to the pretension effect, and the extent of crack

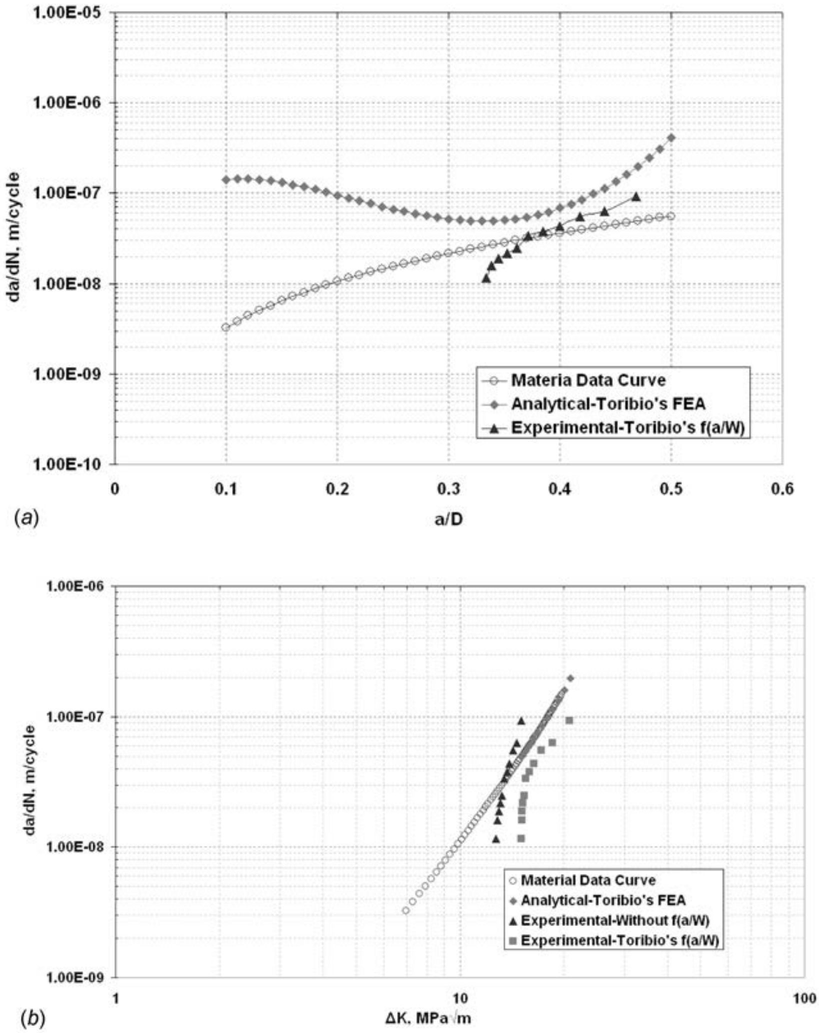

FIG. 20—(*a*) *Crack growth rate as a function of a/D for nut loaded bolt.* (*b*) *Crack growth rate as a function of stress intensity factor range.*

growth was much less compared to bolts with no pretension loads. However, the nature of fracture was similar to the other bolts, possibly because the experiments involved use of starter notches. Work is in progress to generate marker bands on the fracture surface which would enable identification of crack growth during block loading. It is also proposed to instrument the crack growth process through the use of a clip-on-type displacement gauge near the crack region to estimate crack growth in pretension bolts, in the event the marker band technique is not conducive.

Summary

Fatigue crack growth rate was measured experimentally by beach marking technique for open and nut-loaded bolts. Finite element analysis results showed that the elastoplastic stress distribution in the nut-loaded bolts is not symmetrical as in the open bolts.

Open Bolt

1. The experimental crack growth rate data are in close agreement with the analytical results for the crack growth at the center of the crack. Thus, the analytical solutions proposed by Toribio can be applied in practice. The small deviation observed in crack growth rates may be due to the fact that the helix angle is not considered in the analytical models.
2. The experimental crack growth at the free surface showed a much larger deviation when compared with the analytical solution. This suggests analytical methods are inadequate to predict the crack growth rate.
3. The experimental crack growth rate at the crack free surface is higher than the experimental crack growth rate at the crack center. This could be due to the absence of constraint at the free surface.

Nut-Loaded Bolt

The experimentally observed crack growth rate at the crack center is much less compared to the analytical solution. Thus, the analytical solutions, when applied to real-life situations may lead to erroneous predictions. The friction between the contact threaded members and the presence of nut encouraging the mixed mode and/or the crack closure effect may play a significant role in influencing the crack growth rate. Many of the above-mentioned factors are not considered in the analytical models.

Further research is in progress to investigate the effect of thread geometry, helix angle, and friction coefficient on fatigue crack growth behavior in bolts.

References

[1] James, L. A., and Mills, W. J., "Review and synthesis of stress intensity factor solutions applicable to cracks in bolts," *Eng. Fract. Mech.*, Vol. 30, No. 5, 1988, pp. 641–654.

[2] Blackburn, W. S., "Calculation of stress intensity factors for straight cracks in grooved and ungrooved shafts," *Eng. Fract. Mech.*, Vol. 8, 1976, pp. 731–736.

[3] Astiz, M. A., and Elices, M., "On the application of the stiffness derivative method to two- and three-dimensional fracture problems," *Proceedings of the Second International Conference on Numerical Methods in Fracture Mechanics*, Swansea, UK, 1980, pp. 93–106.

[4] Raju, I. S., and Newman, J. C., "Stress intensity factors for circumferential surface cracks in pipes and rods," *Fracture Mechanics: Seventeenth Volume, ASTM STP 905*, ASTM International, West Conshohocken, PA, 1986, pp. 789–805.

[5] Nord, K. J., and Chung, T. J., "Fracture and surface flaws in smooth and threaded round bars," *Int. J. Fracture*, Vol. 30, 1986, pp. 47–55.
[6] Forman, R. G., and Shivakumar, V., "Growth behavior of surface cracks in the circumferential plane of solid and hollow cylinders," *Fracture Mechanics: Seventeenth Volume, ASTM STP 905*, ASTM International, West Conshohocken, PA, 1986, pp. 59–74.
[7] Toribio, J., "Stress intensity factor solutions for a cracked bolt loaded by a nut," , Vol. 53, 1992, pp. 367–385.
[8] Toribio, J., Sanchez-Galvez, V., Assize, M. A., and Campos, J. M., "Stress intensity factor solutions for a cracked bolt under tension, bending and residual stress loading," *Eng. Fract. Mech.* 39, No. 2, 1991, pp. 359–371.
[9] Hobbs, J. W., Burguete, R. L., Heyes, P., and Patterson, E. A., "The effect of eccentric loading on the fatigue performance of high tensile bolts," *Int. J. Fatigue* 22, 2000, pp. 531–538.
[10] Mackay, T. L., and Alerpin, B. J., "Stress intensity factors for fatigue cracking in high strength bolts," *Eng. Fract. Mech.*, Vol. 21, No. 2, 1985, pp. 391–397.
[11] Shin, C. S., and Cai, C. Q., "Evaluating fatigue crack propagation properties using a cylindrical rod specimen," *Int. J. Fatigue*, Vol. 29, 2007, pp. 397–405.

ASTM Special Technical Publication, Vol. 5, No. 9
Paper ID JAI101523
Available online at www.astm.org

Justus Medgenberg[1] *and Thomas Ummenhofer*[1]

In-situ Fatigue Damage Investigations in Welded Metallic Components by Infrared Techniques

ABSTRACT: The paper reviews the state of the art of thermal damage assessment in metals and proposes a specialized form of lock-in thermography as an efficient tool for the quantification of early fatigue damage phenomena in welded steel structures in the regime of mid- to high-cycle fatigue. It can be proved that advanced thermographic techniques are sensitive to early damage phenomena in the weld toe. They provide a new experimental mean for *in-situ* investigation of early inhomogeneous fatigue damage phenomena as mesoplasticity and fatigue cracks. The results demonstrate that non-contacting full field temperature measurements using highly sensitive infrared technology can be applied successfully to detect localized fatigue damage at around 10 % to 20 % of the total fatigue lifetime of the tested specimens. The applied method is based on the separation of thermoelastic and thermoplastic temperature effects which cause characteristic local temperature signatures. In contrast to other well-known approaches—as, e.g., measuring the rise of mean temperature during fatigue loading—the applied method offers a very high spatial resolution and resolves extremely localized phenomena. The methodology can be applied to monitor the fatigue process during conventional fatigue testing. The additional effort for the specimen preparation and the installation of the testing setup is minimal.

Manuscript received November 6, 2007; accepted for publication August 1, 2008; published online October 2008.
[1] Institut fuer Bauwerkserhaltung und Tragwerk, Technische Universitaet Carolo-Wilhelmina, Pockelsstrasse 3, Braunschweig, 38106 Braunschweig, Germany, e-mail: J.Medgenberg@tu-bs.de; T.Ummenhofer@tu-bs.de

Citation: Medgenberg, J. and Ummenhofer, T., "*In-situ* Fatigue Damage Investigations in Welded Metallic Components by Infrared Techniques," *J. ASTM Intl.*, Vol. 5, No. 9. DOI10.1520/JAI101523. Available online at www.astm.org. Also included in JAI Special Issue STP 1508, *Fatigue and Fracture Mechanics* (*36th ASTM National Symposium on Fatigue and Fracture Mechanics*), R. W. Neu, K. W. R. Wallin and S. R. Thompson, guest editors, ASTM International, West Conshohocken, PA, 2008, pp. 695-18.

KEYWORDS: Fatigue damage, fatigue crack, crack initiation, thermography

Introduction

Within repeatedly loaded steel structures, geometric notches, stiffness changes, or weld seams constitute the critical details for potential fatigue damage. In particular, weld seams pose significant problems for a reliable fatigue lifetime prediction since various influence factors as flaws in the weld toe, geometric effects, and residual stresses need to be taken into account simultaneously. Accordingly, fatigue lifetimes of welded structures are often subjected to significant scatter and large discrepancies between predicted and achieved fatigue lifetimes. Surprisingly, the experimental approaches for the investigation of welded joints are still rather rudimentary. Often the only purpose of fatigue testing is to evaluate the number of load cycles until failure, which yields a single data point in the S/N-curve (Woehler curve). This means that little information is gained from a test which might last hours or days. Sometimes testing is more refined, e.g., by applying strain gauges which allow monitoring of changes in stiffness of the tested component. The fatigue process, if at all, is investigated after failure by microscopic analysis of the fracture surface. Thus, the existing experimental approaches provide an insufficient understanding of the fatigue process. For the investigation and analysis of the fatigue process during fatigue testing the application of high resolution infrared thermography offers a promising tool. The application is fast, noncontacting, and requires only minimal specimen preparation. Infrared thermography offers superb thermal and spatial resolution and is a convenient tool to monitor local damage processes. The following paper reviews the state of the art of experimental assessment of thermomechancial coupling phenomena and presents results obtained during fatigue testing of unwelded and welded specimens of mild ferritic-pearlitic steel S355J2G3 with the material properties given in Tables 1 and 2.

Experimental Investigations of Thermomechanical Coupling and Damage Phenomena-State of the Art

In the past, various efforts have been made to relate mechanical properties to the measured temperature changes during mechanical loading or to the intrinsic heat generation due to dissipation effects. Most reported applications of thermal measurements for material characterization fall into one of the following categories:

TABLE 1—*Material parameters of the used steel S355J2G3.*

Young's modulus E, MPa	Lower yield limit $\sigma_{y,l}$, MPa	Upper yield limit $\sigma_{y,u}$, MPa	Ultimate strength σ_u, MPa	Poisson's ratio ν
214 300	352	464	546	0.275

TABLE 2—*Composition of the used steel S355J2G3 in % of the total mass.*

C	Si	Mn	P	S	N	Cr	Al	Cu	Ni
0.179	0.315	1.487	0.016	0.008	0.006	0.051	0.034	0.029	0.018

- thermoelastic stress analysis
- notch and crack tip investigations in fracture mechanics
- dissipation measurements and damage assessment during monotonic and cyclic loading.

Thermoelastic Stress Analysis

Ever since the theoretical derivations of Lord Kelvin (William Thomson) [1] and the experimental findings of Joule [2], it is known that the rate of the elastic volume work exerted upon a solid body equals an equivalent heat generation within the body. Under adiabatic conditions the resulting thermoelastic temperature variations are proportional to the sum of the principal stresses or strains; i.e., to the first invariant of the strain tensor. Pure shear strains do not contribute to the thermoelastic coupling. The temperature changes in solids caused by thermoelasticity are small: For steel a change of the principal stress sum of 1 MPa causes a temperature change of only about 1 mK, presuming adiabatic conditions.

The most elegant way to measure the temperature changes is based on radiometric full-field measurements by means of infrared (IR) cameras. The first commercial IR cameras became available in the 1980s and 1990s and led to the development of the so-called Thermoelastic Stress Analysis (TSA). At the beginning, scanning devices as the SPATE system were used. Noise reduction was achieved by using hardware lock-in amplifiers. Typically the time needed for the acquisition of a full field image was in the range of hours. Current (commercially available) infrared cameras provide detector sizes up to 1024 by 1024 pixels at frame rates above 100 Hz and thermal resolution in the mK range. With respect to the data processing, the built-in hardware lock-in amplifiers of the first generation devices have been replaced by digital data processing methods. [3–5] give a comprehensive review of the state of the art of the thermoelastic stress analysis technique and its theory at the end of the 20th century. Here an overview of the main topics of worldwide research activities is given.

In the past the extraction of the full stress or strain tensor of the thermal data has been one of the most important goals of worldwide research activities in the field of TSA [6–12]. Despite all efforts, this problem remains mostly unsolved and the methods reported so far are limited to special applications and testing conditions or require additional measurement techniques. The problem of non-adiabatic conditions during testing has been addressed by [13,14]. It has been shown for harmonic loading that areas which are strongly influenced by heat diffusion can be identified by a phase shift in the temperature signal [13,14]. So far only a few attempts have been made to compensate the effects of heat diffusion [15–17] for a 2-D case. The existing correction schemes are still insufficient for complex (but realistic) loading scenarios with 3-D stress gradients.

As an extension of the classical theory, [18,19] reported a dependence of the thermoelastic temperature signal on the mean stress, which [20,21] attributed to the temperature dependence of the Young's modulus. The dependence is taken into account by additional coupling terms which—for harmonic loading—become dependent on the stress amplitude and the mean load. Theoretically, this opens the opportunity to quantify residual stresses, mean stresses, or both from thermoelastic temperature records [22–24]. However, besides some studies under laboratory conditions, no practical investigations have been reported so far, which can be explained by the difficulties to quantify the mean load effect properly under realistic conditions.

With the spread of numerical methods as the finite element method, TSA results have been used more and more to verify numerical models of the tested components. Two general approaches can be distinguished: For the first approach adiabatic conditions are assumed and possible effects of heat diffusion are not taken into account. In this case the TSA results can be compared directly to the principal stress sum obtained from a standard numerical simulation of the mechanical problem [25]. The second approach considers the effects of heat diffusion based on a fully coupled transient mechanical-thermal model. In this case the calculated temperature changes are directly compared with the temperature measurements obtained during mechanical loading [13,26]. The advantage of this methodology is the correct consideration of heat diffusion but its application requires the correct evaluation of all thermal and mechanical material properties. Therefore, the adjustment of the numerical model becomes relatively demanding.

Application of Thermal Methods to Crack Detection and Crack Tip Investigations

The detection of fatigue cracks in metal structures is one of the most important tasks of nondestructive testing. The application of thermography during mechanical loading offers various opportunities of crack detection and more advanced applications in fracture mechanics. Two aspects of the presence of cracks in ductile material need to be distinguished. First it has been recognized that the fatigue crack initiation and growth lead to strong inhomogeneities in the measured temperature distribution. The strong plastic dissipation at the crack tip causes a local increase of the stabilized mean temperature [27]. This effect can be used to estimate the moment of crack initiation during fatigue tests.

The second aspect concerns the influence of cracks on the local thermoelastic coupling. [28] shows that crack closure and crack tip plasticity in the vicinity of a mechanical loaded crack lead to nonlinearities in the thermoelastic temperature evolution. In [28] the TSA measurements are compared with extensive numerical studies of the first and second harmonic of the first invariant of the stress tensor. The studies reveal that the nonlinearities in the temperature signal caused by crack closure exceed by far the nonlinearities due to crack tip plasticity. [29] evaluated the applicability of the SPATE system for the detection of hidden internal cracks in aeronautical structures. For this approach the disturbance of the surface principal stress sum due to a hidden crack has been investigated both experimentally and numerically.

Another field of investigation is concerned with the quantitative relation of thermoelastic and thermoplastic measurements to classical approaches in fracture mechanics. [30,31] used TSA measurements to estimate the effective stress intensity factor and compared them with classical compliance methods. For welded specimens, [31] noticed a substantial difference in the mode I stress intensity factor, which was attributed to the residual stress field in the vicinity of the weld seam. The investigations concentrated on the cross-section of the weld detail so that overall a 2-D situation was given.

Plastic Dissipation and Damage Assessment

In contrast to the thermoelastic coupling, thermoplastic dissipation causes a net heat generation and leads to a local or global temperature rise during repeated fatigue loading. Numerous investigators related the observed mean temperature rise or derived parameters to specific fatigue properties [17,32,33], or the mechanical damping [34] of the tested specimens. Mostly the results have been reported for unnotched specimens with a homogeneous distribution of plastic strains. The investigations differ primarily in the tested material and the applied measurement techniques. The main parameter of interest is the evolution of the mean temperature during testing, which can be used to estimate the bulk dissipation due to plasticity. It has been shown by numerous researchers that the fatigue limit of metals can be estimated from temperature measurements. For this purpose, fatigue tests with stepwise increasing load amplitudes are performed and the stabilized mean temperature of the specimen at each load step is evaluated. A sharp increase of the mean temperature has been noticed at load amplitudes close to the fatigue limit [35–37]. The strong increase of the stabilized temperature close to the fatigue limit indicates the sudden massive onset of plastic deformations. The procedure has also been transferred to the fatigue testing of entire components [38]. Reference [39] showed that the fatigue limit cannot only be determined by the mean temperature rise but also by a change in the first and second natural frequencies of the harmonic thermoelastic/thermoplastic temperature signal. Until now these investigations have not been developed further with respect to the investigations of localized phenomena. To extend the rather empirical approaches based entirely on temperature data, different researchers focus on the deduction of the heat source distribution [40,41]. It can be estimated from the temperature records by inversion of the heat diffusion equation, which generally requires the simplification to a 1-D or 2-D case.

Only few attempts have been made so far to apply thermal measurements for the detection of localized damage phenomena in the pre-crack phase. Early investigations on steel and fiberglass-epoxy are presented by [27]. In this study the evolution of the mean temperature in the vicinity of strong stress concentrators (saw cuts) was measured and it was concluded that thermal studies allowed predicting the likely position of crack initiation and investigation of fatigue crack growth. [42] focused on the detection of fatigue cracks in unnotched specimens made of 35CrMo4 with an unknown location of crack initiation. The proposed data processing for crack detection is based on the spatial standard deviation of the recorded infrared pictures. The experiments reported by [43] aimed at assessing the local hot spots at welds using TSA measurements. The results suffered from the insufficient thermal and spatial resolution of the available equipment and unspecific data processing. The application has therefore not been developed further. Based on a detailed numerical investigation of thermomechanical coupling, we have shown in a previous paper [26] that besides the mean temperature rise, cyclic plasticity causes characteristic nonlinearities in the temperature evolution. They have been found to be in the range of a few mK and are therefore very difficult to detect experimentally.

Summary and Conclusion

Extensive theoretical, numerical, and experimental work has been published on TSA and related thermal techniques for the assessment of thermomechanical coupling phenomena during static testing and fatigue loading. The results reported so far demonstrate the strong interdependence of mechanical exposure, local material behavior, and thermal answer of solid materials under mechanical loading and thus prove the high potential of thermal methods in experimental mechanics. Mechanical phenomena such as thermoelasticity, plasticity, cracks, localization phenomena, etc., have been assessed within different materials. Additionally, various special topics of the measuring technique and data processing have been addressed. Almost all the reported applications which aim at the assessment of damage focus either on the investigation of macroscopic cracks in the millimeter or centimeter range or on the indirect assessment of plastic dissipation by assessing the mean temperature. Overall very few attempts have been made to investigate localized damage phenomena which are characteristic of the early fatigue damage process.

Experimental Studies

Experimental Arrangement

In order to study how localized fatigue damage can be assessed by infrared thermography, we performed fatigue tests on different specimen geometries. The experimental setup (Fig. 1) used for the studies consists of a digitally controlled servo-hydraulic testing machine (MTS load frame 810, 250 kN), a high resolution infrared camera (FLIR Phoenix, 640 by 512, InSb detector), and a video microscope (Opto Zoom 125 with 1320 by 1024 pixel QImaging CCD-camera) which can be used for accompanying light microscopic investigations on the specimen surface. A positioning unit (MICOS LS180) is used to perform automated testing procedures. During the testing of the welded specimens (compare the “Investigation on Welded Specimens” section), a brass half-sphere has been attached around the specimens to ensure a uniform thermal background radiation.

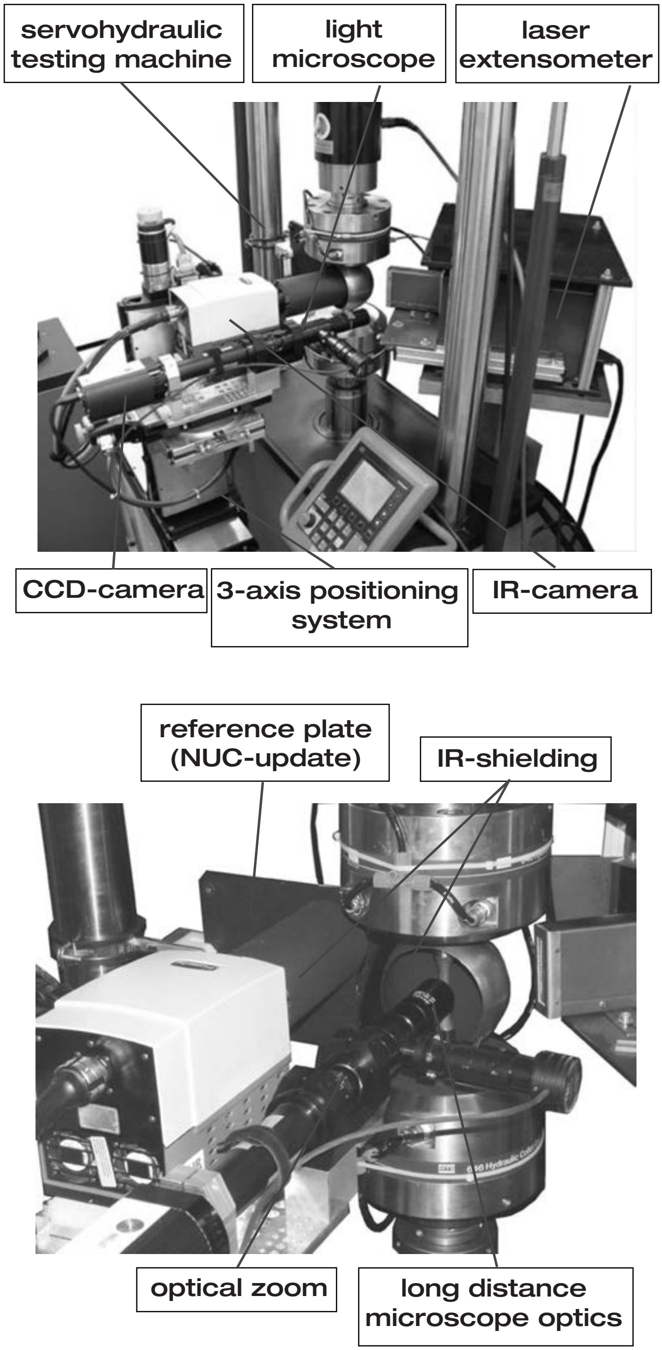

FIG. 1—*Experimental setup and pieces of equipment.*

The settings of the infrared camera have been adjusted to achieve a frame rate of 412.5 Hz at an integration time of 2 ms using a subwindow of the detector of 192 by 300 pixels. During the fatigue testing, sequences of 2000 infrared images were acquired and stored on hard disk every 15 000, 20 000, or 30 000 load cycles. The loading was not interrupted for the recording, so that it can be assumed that all thermal measurements were performed during thermal equilibrium of the specimens; i.e., at constant mean temperature.

Data Processing

Data processing of the recorded infrared sequences was performed offline after termination of the testing. The purpose of the data processing is to extract minor nonlinearities in the overall thermoelastic temperature evolution. It can be divided into the following processing steps:

a) nonuniformity correction, bad pixel replacement and temperature calibration
b) motion compensation
c) extraction of nonlinearities.

A schematic overview of the data processing is given in Fig. 2. The first processing step, i.e., the correction of the images for the detector nonuniformity and corrupt pixels, is a standard procedure used for processing of thermal radiation images [44]. Therefore, it is not explained in more detail here.

The second step constitutes the conversion of the corrected gray values into equivalent temperature values. This is performed by applying a calibration curve which has been obtained using a black body radiation source. The black body has been coated with a high emissivity graphite spray (Kontakt Chemie, Graphit 33) which has also been used for the preparation of the test specimens. For the calibration the mean gray-values in a certain area have been evaluated at different temperatures of the black body between 18°C and 35°C. Assuming that the testing conditions (temperature, humidity) within the laboratory do not change significantly, a direct conversion of the gray values into temperatures is adequate. This has the advantage that the adjustment of a radiation model becomes obsolete.

The third step of the data processing is a motion compensation, which becomes necessary since the specimen surface moves orthogonally to the camera axis due to the mechanical loading of the specimen. Even though the motion blur was generally less than 3 pixels, i.e., 1 % of the total image dimension, it has been found to be detrimental to the evaluation of the nonlinearities in the temperature evolution. The negative effect is caused by the influence of small heterogeneities in the surface emissivity. The passing-by of spots with different emissivity due to the mechanical loading causes apparent cyclic temperature changes of the corresponding pixels. They are superimposed on the temperature changes induced by thermomechanical coupling. The motion compensation is based on normalized cross-correlation of each image with respect to an unloaded reference image of the scenery. Only solid body motion has been considered, whereas possible effects of the deformation of the specimens have been neglected. Since the standard normalized cross-correlation renders only discrete values for the pixel offset, an interpolation scheme has been imple-

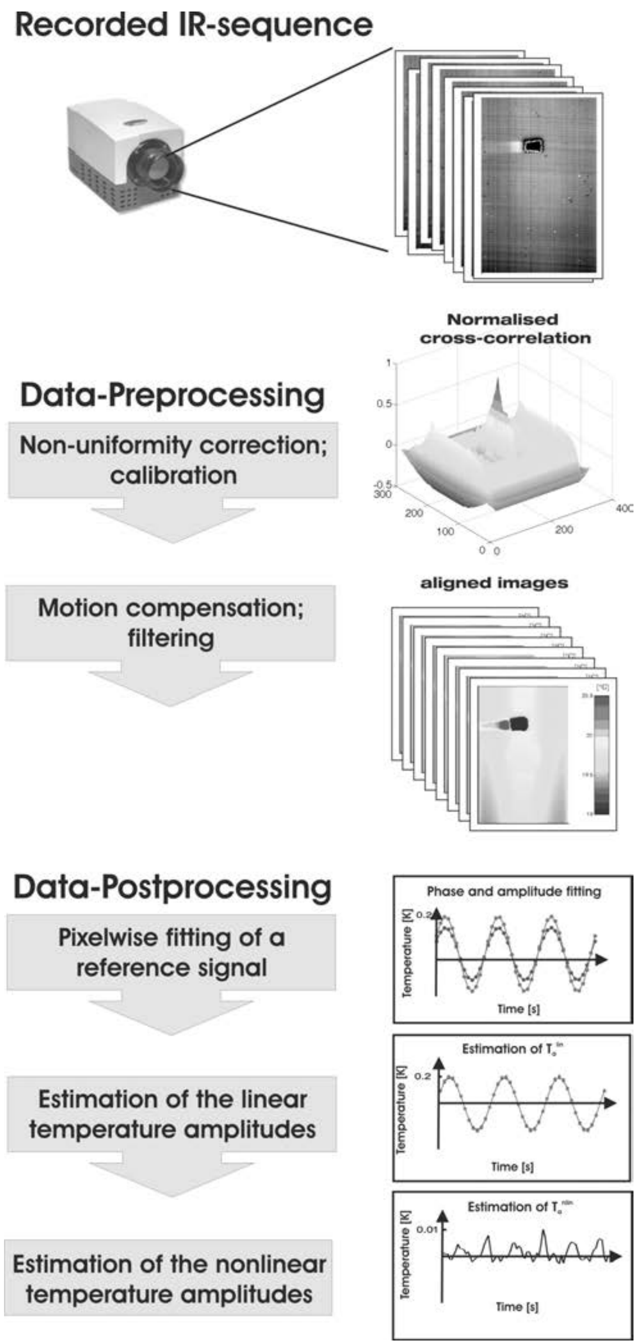

FIG. 2—*Schematic of the data processing of the infrared sequences.*

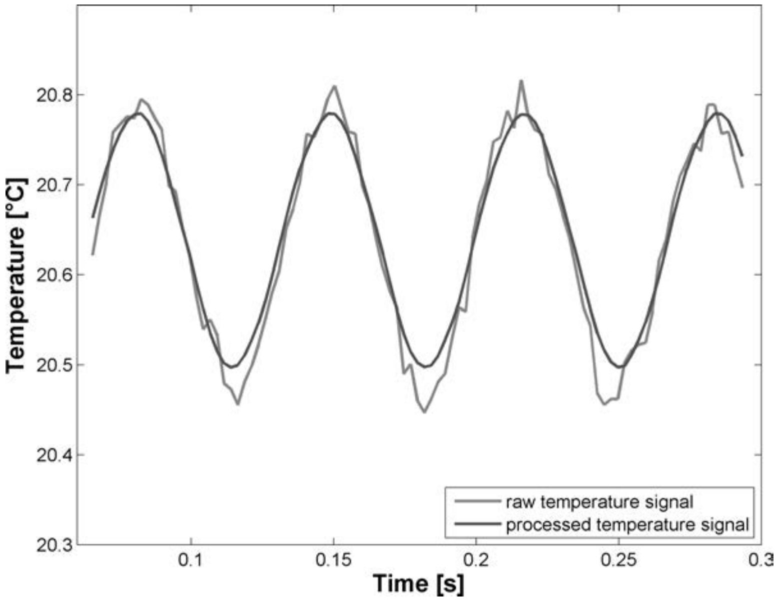

FIG. 3—*Examples of temperature signals before and after data processing.*

mented. The scheme yields the displacement vector with a sub-pixel accuracy between approximately 1/10 and 1/100 of a pixel. The application of the normalized cross-correlation requires at least one high contrast feature within the images. However, the coating of the specimens with graphite spray causes a very uniform gray-value distribution in the infrared regime. Therefore, a small piece of the specimen surface has been left uncoated by applying a self-adhesive marker prior to coating (compare also to the white stripe in Fig. 8). The uncoated metallic area is strongly reflective in the infrared and yields a sharp, high contrast feature within the images. Due to the poor emissivity of the blank metal surface, temperature records within the uncoated area are not possible. Additional noise reduction is achieved by applying a spatial mean filter of 3 by 3 or 5 by 5 pixels to each of the images. After filtering, the variation of temperature with respect to time is very smooth and quasi-noise-free at the cost of reduced spatial resolution and loss of minor details. Figure 3 shows exemplarily the temperature signal in a single point on the specimen surface before and after data processing.

The last step of data processing involves the separation of the nonlinearities in the temperature evolution. This is performed based on a specialized approach in the time domain. Based on numerical simulations it could be shown that in the absence of cracks or plastic dissipation the thermoelastic temperature variations behave to a large extent linearly with respect to load variations. This remains true even if further nonlinear aspects as heat diffusion, temperature or stress dependency of the material parameters, or the temperature dependence of the thermoelastic coupling itself are taken into consideration. The idea behind the developed methodology is to separate linear and minor nonlinear signal portions by comparing the pixelwise temperature evolution to a reference signal which is known to vary linearly with respect to the applied loading. Here only nearly sinusoidal temperature signals are considered. In this case the linear portion of the temperature signal is obtained by estimating the phase and amplitude of the reference signal, which give an optimal fit to the recorded temperature evolution. The nonlinear portion of the temperature signal is then given as the remaining signal after subtraction of the fitted reference signal. Suitable reference signals are, e.g., the recorded control-variable of the testing machine (in our case the load signal) or the temperature evolution in a section of the specimen where linear elastic material behavior can be presumed for the moment of the thermal measurements. The fitting to the temperature evolution at each pixel is performed as follows. First, for easier handling, the reference signal is scaled so that its amplitude equals unity. Then the zero crossings of both the reference signal and the temperature evolution of the considered pixel are evaluated. Next the reference signal is interpolated on a new time scale so that its discrete values represent the same phase instances as the values of the pixel signal. Afterwards the amplitude of the reference signal is scaled so that the least-squares residual between the reference and the pixel signal becomes minimized (least-squares fitting). The scaling factor represents the linear part of the pixel temperature evolution and is referred to as linear temperature amplitude T_a^{lin} from now on. Finally, the difference signal between the pixel signal and the fitted reference is calculated by subtraction of both signals. A suitable parameter for the classification of the difference signal is its mean amplitude, which is referred to as nonlinear temperature amplitude T_a^{nlin}. The described procedure has been found to work well for nearly harmonic temperature signals with overall minor nonlinearities. Nonlinearities as small as 1 mK could be properly detected based on the described approach.

Investigations on Plain Cylindrical Specimens

In order to verify the sensitivity of the chosen approach with respect to the cyclic material behavior fatigue tests on unnotched cylindrical specimens (Fig. 4) of mild steel (S355J2G3) with the material properties given in Tables 1 and 2 have been performed. The specimens have been polished mechanically and tested under annealed conditions. In the mid-section the specimens have been equipped with a strain gauge (Tokyo Sokki Kenkyujo, Type: PFL-20-11-3L) which gave the strains in longitudinal direction. The strain gauge has been temperature compensated by a half-bridge completion circuit with an unloaded strain gauge. This second strain gauge has been applied to a piece of the same steel and brought in close thermal contact to the specimen. The front side of the specimen has been coated with graphite spray as preparation for the thermographic investigations.

The fatigue tests have been accomplished under load control with a load ratio of $R = -1$ at a testing frequency of 2.5 Hz, which was small enough to prevent excessive self-heating of the specimens due to plastic dissipation. Additionally, the grips of the testing machine have been constantly flushed with cooled water which guaranteed quasi-stable thermal boundary conditions for

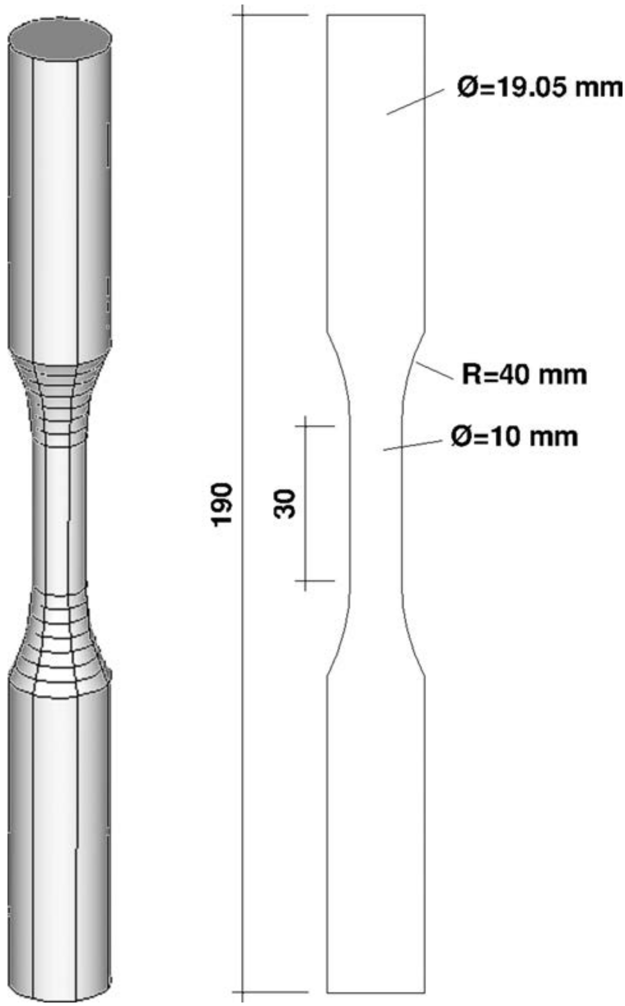

FIG. 4—*Geometry of the cylindrical specimen made of S355J2G3.*

the specimens. The load amplitudes varied between 235 and 275 MPa, which guarantees that only elastic deformations occurred during the first load cycles.

Figure 5 shows the typical cyclic stress strain behavior of the specimens. Figure 5(*a*) gives the evolution of the total strain amplitude ε_a^{tot} with respect to the applied load cycles as measured by the strain gauges. Figures 5(*b*) and 5(*c*) show the corresponding evolution of the plastic strain amplitudes ε_a^P and the mean strains ε_m, respectively.

The plastic strain amplitude has been obtained from the total strain amplitude ε_a^{tot} through

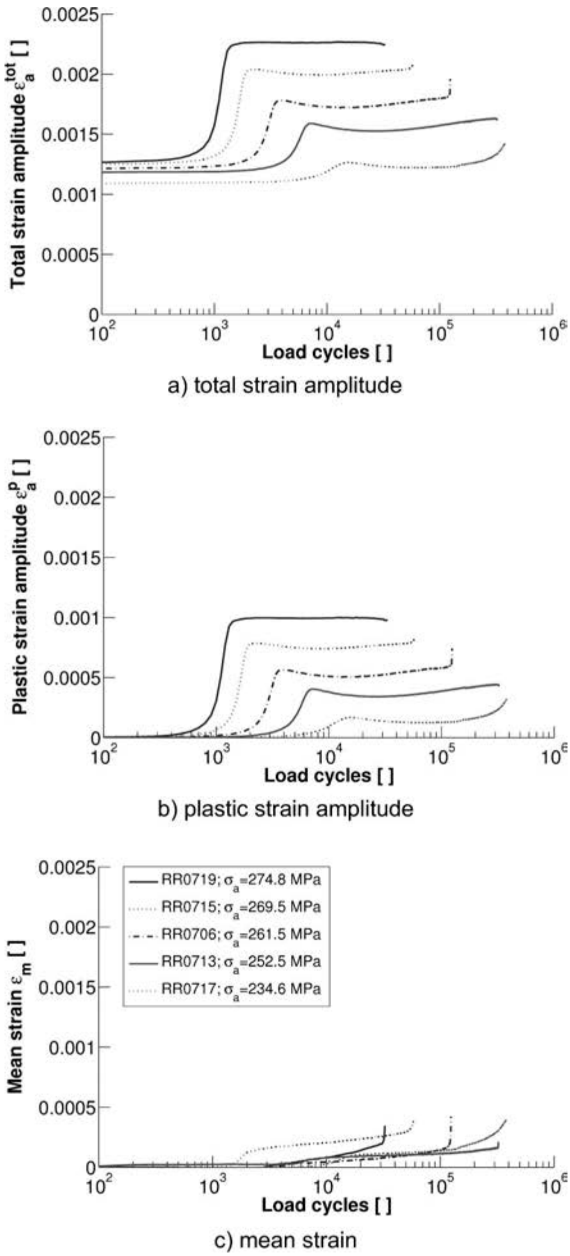

FIG. 5—*Evolution of the total strain amplitude, the plastic strain amplitude, and the mean strain in the middle section of the cylindrical specimen type during fatigue testing at* $R=-1$, $f_L=2.5$ Hz, *and load amplitudes between 235 and* 275 MPa.

$$\varepsilon_a^P = \varepsilon_a^{tot} - \sigma_a/E \tag{1}$$

where σ_a is the total applied stress amplitude and E is the Young's modulus. The mean strain is given as

$$\varepsilon_m = (\varepsilon_{max}^{tot} - \varepsilon_{min}^{tot})/2 \tag{2}$$

Four phases can be generally distinguished in the cyclic softening and hardening behavior. During the primary phase the steel behaves completely linear elastically and no plastic strains can be detected macroscopically. This phase is terminated by the onset of plastic deformations which cause a rapid rise of the total and plastic strain amplitudes (compare Figs. 5(*a*) and 5(*b*)). The period of primary softening is short compared to the entire fatigue process. Typically it comprises less than 1000 load cycles. Afterwards the plastic strain amplitudes are quasi-saturated and change only little. For some of the specimens a tendency to hardening can be observed which manifests in a slight decrease of the plastic strain amplitudes during ongoing loading (Fig. 5(*b*), e.g., specimen RR0713). Close to crack initiation a second softening phase can be observed. However, it might be possible that the apparent rise of the strain amplitudes is caused by the initiation of fatigue cracks. Eventually all specimens failed due to fatigue cracks in the center section.

Figure 6(*a*) gives the corresponding mean temperature evolution within the middle section of the specimens during fatigue testing. The data represent the absolute temperature difference with respect to the initial temperature. Figures 6(*b*) and 6(*c*) show the corresponding evolution of the linear and nonlinear temperature amplitudes. The evolution of the temperature increase (Fig. 6(*a*)) shows that together with the onset of primary softening the absolute temperature of the specimens rises significantly by several degrees K. This can be attributed to the plastic dissipation within the specimens which causes strong self-heating of the specimens until a dynamic equilibrium is reached. The temperature increase becomes more pronounced with higher plastic strain amplitudes. The testing of one of the specimens (RR0717) was unintentionally interrupted by an error in the testing machine. During the break, the hydraulic system of the testing machine and the specimen itself cooled down. After restarting of the test the temperature rose quickly again. This compares to findings of [45]. However, the mean temperature measured before the break was not completely reached again. This demonstrates the sensitivity of the absolute temperature increase towards the specific testing conditions, which complicates quantitative approaches. Note that at the same time no change of the plastic strains can be observed, which verifies that the cyclic behaviour was not significantly influenced by the break.

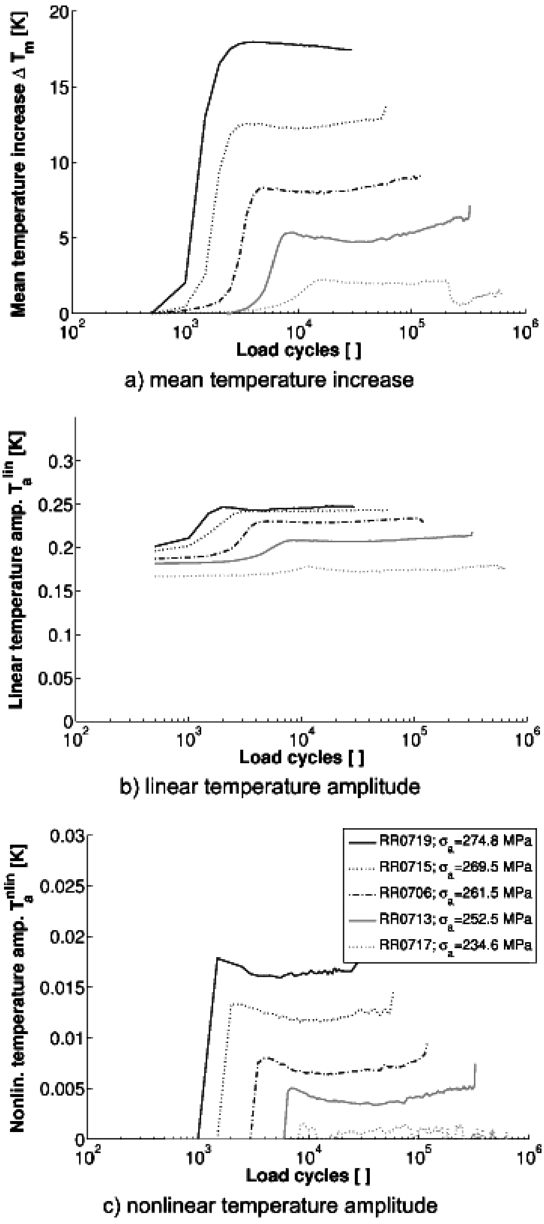

FIG. 6—*Evolution of the mean temperature with respect to the initial temperature, the linear and nonlinear temperature amplitudes in the middle section of the cylindrical specimen type during fatigue testing at* $R=-1$, $f_L=2.5$ Hz, *and load amplitudes between 235 and* 275 MPa.

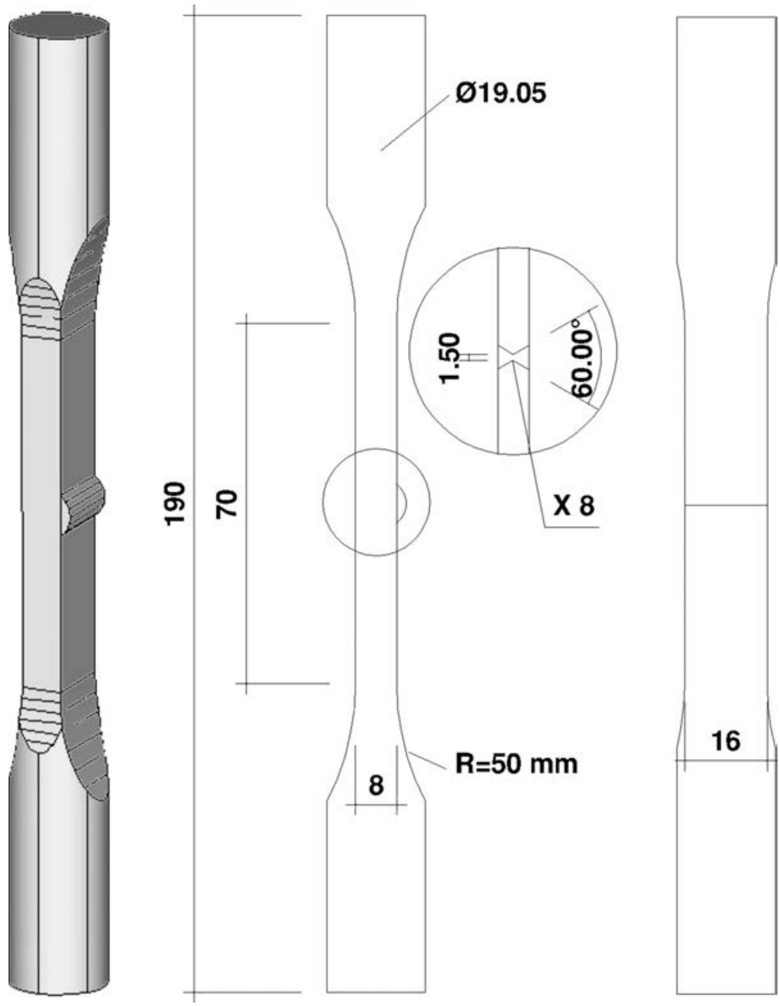

FIG. 7—*Geometry of the welded specimen made of S355J2G3.*

The linear temperature amplitudes (Fig. 6(*b*)) show a significant increase up to 25 % with the onset of cyclic softening. This phenomenon cannot be explained by the classical theory of thermoelastic coupling and plastic dissipation. Instead the results show that further coupling between thermoelasticity and the hardening state might be present. Within the context of the classical theory this phenomenon can be incorporated by assuming that the coefficient of thermal expansion depends on the hardening state. Further evidence of this dependency is e.g. given by the investigations of [46,47]. The evolution of the nonlinear temperature amplitudes (Fig. 6(*c*)) verifies that the onset of plastic dissipation goes along with small but detectable nonlinearities in the temperature evolution. The amplitudes of the nonlinearities increase with increasing

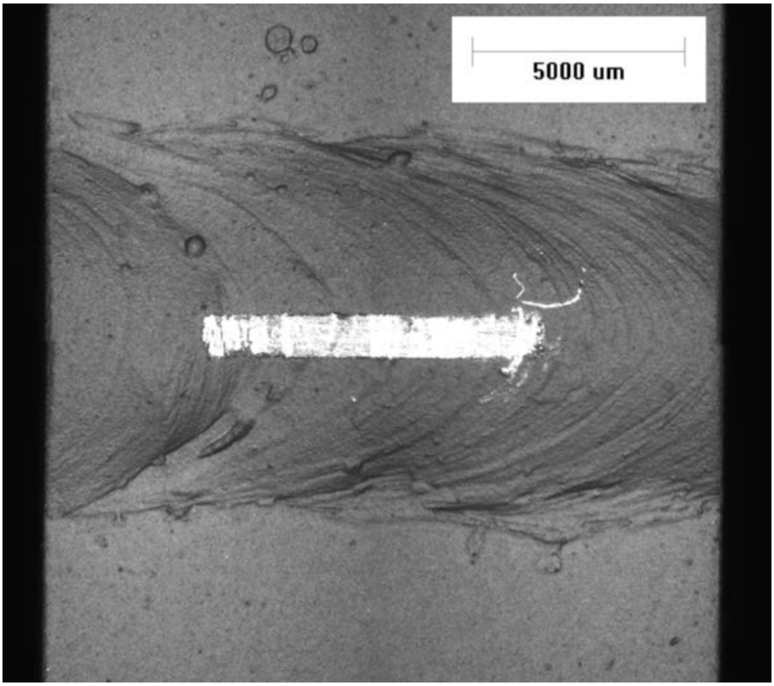

FIG. 8—*Visual detail image of the weld seam.*

plastic strain amplitudes and follow closely the general evolution of the plastic strains (Fig. 5(*b*)). As long as heat diffusion remains negligible their analysis provides a means to quantify the bulk plastic dissipation. In case heat diffusion needs to be considered (e.g., due to strong gradients at stress concentrations), any quantitative evaluations require an additional correction scheme. Further results obtained on mildly notched cylindrical specimens verify that within geometric notches the extension, onset and strength of plastic dissipations and plastic strains can be assessed qualitatively by the analysis of the nonlinearities [48].

Investigations on Welded Specimens

The second test series was concerned with the investigation of fatigue damage processes on welded specimens (Fig. 7). For this purpose specimens of the same steel but with a butt weld in the center section have been prepared. The two parts of the specimen have been joined by manual arc welding, using temporal extension plates at both sides of the specimen. One side of the originally symmetric weld seam has been leveled after welding to prevent crack initiation from the back side of the specimen. For the thermographic investigations a graphite coating has been applied to the investigated side of the specimen. A detailed view of the weld seam is given in Fig. 8. As described before, the white stripe in the middle of the weld bead represents an uncoated reference area

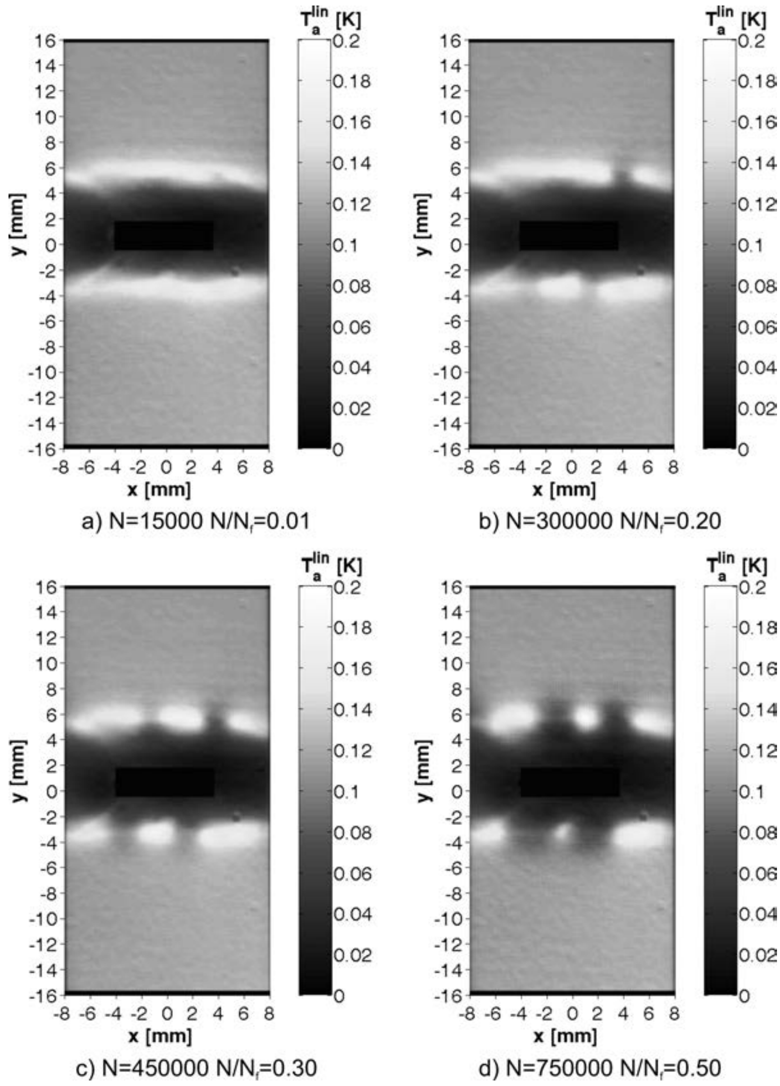

FIG. 9—*Distribution of the linear temperature amplitudes at the front side of the welded specimen type. Four different stages of the fatigue testing. Crack initiation at the front side.* N = number *of load cycles,* N_f = number *of load cycles at failure.*

used for the motion compensation scheme. Since in this area no temperature measurements are possible, all corresponding amplitude values have been set to zero in Fig. 9–11.

The specimens have been tested without annealing at load amplitudes between 125 and 150 MPa in the nominal cross-section of the specimens using a

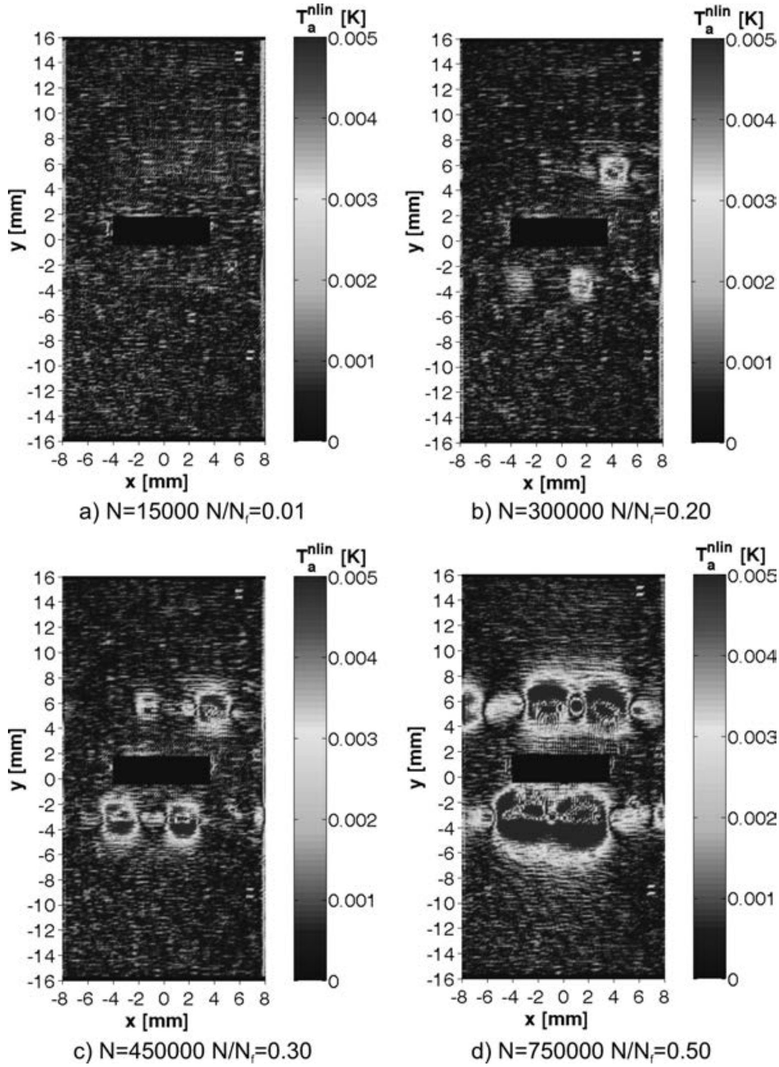

FIG. 10—*Distribution of the nonlinear temperature amplitudes at the front side of the welded specimen type. Four different stages of the fatigue testing. Crack initiation at the front side.* N = number *of load cycles,* N_f = number *of load cycles at failure.*

load ratio $R = -1$. All specimens failed because of fatigue cracks within the weld toes. Beside one specimen the fatigue cracks originated at the investigated side of the specimen.

Figures 9 and 10 show the evolution of the linear and nonlinear temperature amplitudes of a specimen tested at a nominal load amplitude of 140 MPa, which failed from the investigated side. The processing of the recorded infrared sequences has been performed with the technique described in the "Data Pro-

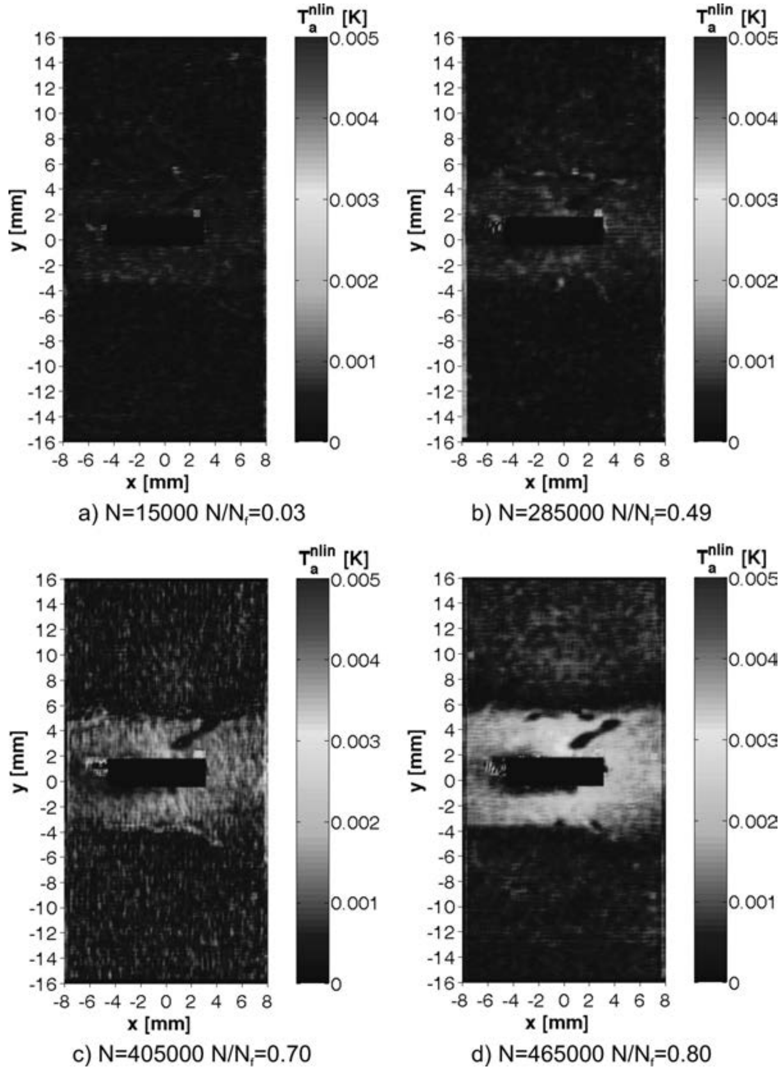

FIG. 11—*Distribution of the nonlinear temperature amplitudes at the front side of the welded specimen type. Four different stages of the fatigue testing. Crack initiation at the back side of the specimen.* N = number *of load cycles,* N_f = number *of load cycles at failure.*

cessing" section. The image of the linear temperature-amplitudes at the beginning of the testing (Fig. 9(*a*)) reveals the inhomogeneous stress concentration at the weld toe and the less stressed welding bead. The material throughout the entire weld seam still behaves completely linearly and the corresponding nonlinear temperature amplitudes (Fig. 10(*a*)) are close to zero. With ongoing loading multiple points in the center of the weld toes can be identified where the linear temperature amplitudes decrease locally (Fig. 9(*b*)). Almost simultaneously the nonlinear temperature amplitudes increase in these points (Fig. 10(*b*)). During the further fatigue process additional hot-spots develop and grow until final failure of the specimens (Figs. 9(*c*) and 9(*d*) and Figs. 10(*c*) and 10(*d*)).

The process is accompanied by a strong increase of the nonlinear temperature amplitudes. Generally for specimens with a small number of failure load cycles we could not distinguish between individual initiation sites. In this case the damage process starts quite homogeneously over almost the entire width of the specimen and spreads rapidly. For specimens with a high number of failure load cycles individual initiation sites within the weld toe could generally be distinguished. Normally the first local cracks could be found between 10 % and 30 % of the entire fatigue lifetime. The subsequent growth and joining of the individual initiation sites comprises a major part of the fatigue process. For all specimens the fatigue process started quasi-simultaneously within both weld toes. The final failure occurred at the side of the weld seam where the damage progress proceeded a little faster. Visual inspection of the other weld toe failed to identify the damage state observed before by thermography. Final rupture was initiated when in one of the weld toes the cracks ran across the entire specimen width. A comparable behavior could be observed for all specimens where crack initiation occurred at the front side. A characteristic of the results is that the beginning of fatigue crack initiation generally manifests itself in a decrease of the linear temperature amplitudes. Detectable nonlinearities do not evolve until a couple of thousand load cycles afterwards. This constitutes a clear contrast to the findings on the plain specimens discussed before. In contrast to the fatigue behavior of the cylindrical specimens discussed before no undoubted evidence for cyclic plastic deformations within the weld toes or in the nominal cross-section of the specimens could be detected. The observed nonlinearities are stronger and grow much faster as can be explained by cyclic plasticity.

The findings show that the fatigue process at the weld seams is strongly governed by crack propagation which comprises the major part of the fatigue life. Nevertheless, it should be noted that the manually welded specimens involve very sharp notches at the weld toes. Therefore, the relative lifetime until crack initiation might be much longer for other specimen geometries.

As a comparison to the results discussed above Fig. 11 shows the evolution of the nonlinear temperature amplitudes of the specimen which failed from the back. The specimen has been tested at a load amplitude of 127 MPa. Clearly the characteristics of these results differ strongly from the findings discussed before. The fatigue crack initiation at the back side becomes apparent if the growing fatigue cracks cause stress redistributions within the specimen. In this case the entire weld seam becomes subjected to stress amplitudes which are above the cyclic yield limit so that wide areas of the weld seam start to plasticize. In this case the observed nonlinearities originate from plastic deformations due to the reduced cross-section of the specimen and not from structural nonlinearities due to crack opening and closure as before.

Conclusion

For the presented studies, fatigue damage phenomena in low alloy steel have been investigated by infrared thermography. Results obtained on plain cylindrical specimens and welded specimens have been discussed. Contrary to former approaches of thermal measurements during fatigue testing of metals, the focus has been put onto the resolution of localized effects. For this purpose a data processing methodology which separates linear coupling phenomena due to thermoelasticity and nonlinear phenomena, e.g., due to plastic dissipation, has been developed. For the fatigue tests on plain cylindrical specimens the nonlinear behavior corresponds to the evolution of the plastic deformations evaluated by strain gauge measurements. During fatigue testing on welded specimens we were able to observe the local fatigue process in the weld toe starting from the first individual fatigue cracks. The cracks can be identified by both a variation of the linear thermoelastic coupling and the occurrence of strong nonlinearities. In this case no undoubted indication of significant cyclic plasticity within the weld toe prior to crack initiation could be observed. The application of thermography to study local fatigue damage phenomena during fatigue testing has been found to be very valuable for the understanding of the fatigue processes e.g. in comparative studies. For the future more work is planned to distinguish individual phenomena from the recorded surface temperature evolutions and to develop portable devices which allow for insitu fatigue damage inspections.

Acknowledgments

The authors would like to thank the Deutsche Forschungsgemeinschaft (DFG) for their financial support of the presented investigations.

[1] Thomson, W., "On the Dynamical Theory of Heat-With Numerical Results Deduced from Mr. Joule's Equivalent of a Thermal Unit and M. Regaut's Observations on Steam," *R. Soc. Edinburgh, Trans. R. Soc.*, 1853, pp. 261–288.
[2] Joule, J., "On Some Thermodynamic Properties of Solids," *Philos. Trans. R. Soc. London*, Vol. 149, 1859, p. 91–131.
[3] Harwood, N., and Cummings, W., "Thermoelastic Stress Analysis," Adam Hilger, Bristol, 1991.
[4] Dulieu-Barton, J., and Stanley, P., "Development and Applications for Thermoelastic Stress Analysis," *J. Strain Anal. Eng. Des.*, Vol. 33, No. 2, 1998, pp. 93–104.
[5] Pitarresi, G., and Patterson, E., "A Review of the General Theory of Thermoelastic Stress Analysis," *J. Strain Anal. Eng. Des.*, Vol. 38, No. 5, 2003, pp. 405–417.
[6] Huang, Y., Abdelmohsen, H., and Rowlands, R., "Determination of Individual Stresses Thermoelastically," *Exp. Mech.*, Vol. 30, No. 1, 1990, pp. 88–94.
[7] Feng, Z., et al., "Thermoelastic Determination of Individual Stress Components in Loaded Composites," *Exp. Mech.*, Vol. 32, No. 2, 1992, pp. 89–95.
[8] Rauch, B., and Rowlands, R., "Recent Advances in Determining Individual Stresses from Thermoelastically Measured Isopaches," *In*: K. A. Galione, ed., *Proceedings of the 50th Spring Conference on Experimental Mechanics, Dearborn, Michagan*, pp. 740–748.
[9] Feickert, W., "Ermittlung des Vollständigen Spannungszustands mit dem Ver-

fahren der Thermoelastischen Spannungsanalyse, VDI—Fortschritt Berichte," Vol. 18, No. 154.
[10] Barone, S., and Patterson, E., "Full-Field Separation of Principal Stresses by Combined Thermo- and Photoelasticity," *Exp. Mech.*, Vol. 36, No. 4, 1996, pp. 318–324.
[11] Stanley, P., and Dulieu-Smith, J., "Devices for the Experimental Determination of Individual Stresses from Thermoelastic Data," *J. Strain Anal. Eng. Des.*, Vol. 31, No. 1, 1996, pp. 53–63.
[12] Inoue, H. "Stress Separation in Thermoelastic Stress Analysis Using Nonlinearity of the Thermoelastic Effect," *JSME Int. J., Ser. A*, Vol. 47, No. 3, 2004, pp. 305–311.
[13] Offermann, S. et al., "Thermoelastic Stress Analysis Under Nonadiabatic Conditions," *Exp. Mech.*, Vol. 37, No. 4, 1997, pp. 409–413.
[14] Quinn, S., and Dulieu-Barton, J., "Identification of the Sources of Non-adiabatic Behaviour for Practical Thermoelastic Stress Analysis," *J. Strain Anal. Eng. Des.*, Vol. 37, No. 1, 2002, pp. 59–71.
[15] Salerno, A., and Desiderati, S., "Procedure Proposal for the Correction of Nonadiabatic Thermoelastic Stress Analysis Results," *Rev. Sci. Instrum.*, Vol. 75, No. 2, 2004, pp. 507–514.
[16] Gallotti, A., and Salerno, A., "Automatic Procedure for the Correction of Thermoelastic Stress Analysis Data Acquired in Nonadiabatic Conditions," *Rev. Sci. Instrum.*, Vol. 76, No. 12, 2005, pp. 124903.
[17] Yang, B., *Thermography Detection on the Fatigue Damage*, Ph.D. Thesis, University of Tennesse, Knoxville, TN, 2003.
[18] Machin, A., Sparrow, J., and Stimson, M.-G., "Mean Stress Dependence of the Thermoelastic Constant," *Strain J. Brit. Soc. Strain Measurement*, Vol. 23, 1987, pp. 27–29.
[19] Machin, A., Sparrow, J., and Stimson, M.-G., "The Thermoelastic Constant," *Proc. SPIE*Vol. 731, 1987, pp. 26–31.
[20] Wong, A., Jones, R., and Sparrow, J., "Thermoelastic Constant or Thermoelastic Parameter?," *J. Phys. Chem. Solids*, Vol. 48, No. 8, 1987, pp. 749–753.
[21] Wong, A., Sparrow, J., and Dunn, S., "On the Revised Theory of the Thermoelastic Effect," *J. Phys. Chem. Solids*, Vol. 49, No. 4, 1988, pp. 395–400.
[22] Gyekenyesi, A., and Baaklini, G., "Thermoelastic Stress Analysis: The Mean Stress Effect in Metallic Alloys," NASA/TM 1999–209376.
[23] Gyekenyesi, A., and Baaklini, G., "Quantifying Residual Stresses by Means of Thermoelastic Stress Analysis," NASA/TM 2001–210697.
[24] Quinn, S., Dulieu-Barton, J., and Langlands, J., "Progress in Thermoelastic Residual Stress Measurement," *Strain J. Brit. Soc. Strain Measurement*, Vol. 40, No. 3, 2004, pp. 127–133.
[25] Greene, R., and Patterson, E., "Integrating Thermoelastic and Numerical Stress Methods for Reliable Analysis," *J. Strain Anal. Eng. Des.*, Vol. 38, No. 4, 2003, pp. 303–312.
[26] Ummenhofer, T., and Medgenberg, J., "Numerical Modelling of Thermoelasticity and Plasticity in Fatigue-Loaded Low Carbon Steels Studies for a Thermographic Approach," *QIRT Journal*, Vol. 3, No. 1, 2006, pp. 71–93.
[27] Charles, J., Appl, F., and Francis, J., "Using the Infrared Camera in Experimental Fatigue Studies," *Exp. Mech.*, Vol. 15, No. 4, 1975, pp. 133–138.
[28] Huss, A., "Rissdetektion und -bewertung mit dem Verfahren der Thermoelastischen Spannungsanalyse," *VDI-Fortschritt Berichte*, Vol. 18, No. 147, 1994.
[29] Silva, L., et al., "Applicability of the SPATE Technique to the Detection of Hidden Cracks," *NDT & E Int.*, Vol. 33, 2000, pp. 7–13.
[30] Diaz, F., Yates, J., and Patterson, E., "Measuring Stress Intensity Factors During

Fatigue Crack Growth Using Thermoelasticity," *Fatigue Fract. Eng. Mater. Struct.*, Vol. 27, No. 7, 2004, pp. 571–583.

[31] Diaz, F., Yates, J., and Patterson, E., "Some Improvments in the Analysis of Fatigue Cracks Using Thermoelasticity," *Int. J. Fatigue*, Vol. 26, No. 4, 2004, pp. 365–376.

[32] Liaw, P., et al., "Thermographic Detection of Fatigue Damage of Pressure Vessel Steels at 1,000 Hz and 20 Hz," *Scr. Mater.*, Vol. 42, No. 4, 2000, pp. 389–395.

[33] Jiang, L. et al., "Characterization of the Temperature Evolution During High-Cycle-Fatigue of the Ultimet Superalloy. Experiment and Theoretical Modelling," *Metall. Mater. Trans. A*, Vol. 32A, No. 9, 2001, pp. 2279–2296.

[34] Audenino, A., Crupi, V., and Zanetti, E., "Correlation Between Thermography and Internal Damping in Metals," *Int. J. Fatigue*, Vol. 25, No. 4, 2003, pp. 343–351.

[35] Harig, H., *Zur Bedeutung der Thermometrie bei der Mechanischen Prüfung Metallischer Werkstoffe* [Habilitation], TU Berlin, Berlin, 1975.

[36] Eschermann, K., *Infrarot-Temperaturmessungen an Schwingend Beanspruchten Stahlproben*, Ph.D. Thesis, Fachbereich Werkstoffwissenschaften, TU Berlin. Berlin, 1980.

[37] La Rosa, G., and Risitano, A., "Thermographic Methodology for Rapid Determination of the Fatigue Limit of Materials and Mechanical Components," *Int. J. Fatigue*, Vol. 22, No. 1, 2000, pp. 65–73.

[38] Luong, M., "Fatigue Limit Evaluation of Metals Using an Infrared Thermographic Technique," *Mech. Mater.*, Vol. 28, No. 1, 1998, pp. 155–163.

[39] Krapez, J., and Pacou, D., "Thermography Detection of Damage Initation During Fatigue Tests," *Proc. SPIE*, Vol. 4710, 2002, pp. 435–449.

[40] Stärk, F., *Thermometrische Untersuchungen zum Zyklischen Verformungsverhalten Metallischer Werkstoffe*, MPA, Thesis, Universität Stuttgart, Stuttgart, 1980.

[41] Boulanger, T. et al., "Calorimetric Analysis of Dissipative and Thermoelastic Effects Associated with the Fatigue Behavior of Steels," *Int. J. Fatigue*, Vol. 26, No. 3, 2004, pp. 221–229.

[42] Plekhov, O. et al., "Fatigue Crack Initiation and Growth in a 35CrMo4 Steel Investigated by Infrared Thermography," *Fatigue Fract. Eng. Mater. Struct.*, Vol. 28 No. 1–2, 2005, pp. 169–178.

[43] Askegaard, V., "Prediction of Initial Crack Location in Welded Fatigue Test Specimens by the Thermoelastic Stress Analysis Technique," Technical University of Denmark, Serie R; 276, 1991.

[44] Flir 2005: User's manual for ThermaCam RDac.

[45] Meyendorf, N. et al., "Thermo-acoustic Fatigue Characterization," *Ultrasonics*, Vol. 40, No. 1, 2002, pp. 427–434.

[46] Rosenfield, A., and Averbach, B., "Effect of Stress on the Expansion Coefficient," *J. Appl. Phys.*, Vol. 27, No. 2, 1956, pp. 154–156.

[47] Rosenholtz, J., and Smith, D., "The Effect of Compressive Stresses on the Linear Thermal Expansion of Magnesium and Steel," *J. Appl. Phys.*, Vol. 21, 1950, pp. 396–399.

[48] Medgenberg, J., and Ummenhofer, T., "Detection of Localized Fatigue Damage in Steel by Thermography," *Proc. SPIE*, Vol. 6541, 2007.

ASTM Special Technical Publication, Vol. 5, No. 4
Paper ID JAI101568
Available online at www.astm.org

Dwight A. Burford,[1] *Bryan M. Tweedy,*[1] *and Christian A. Widener*[1]

Fatigue Crack Growth in Integrally Stiffened Panels Joined Using Friction Stir Welding and Swept Friction Stir Spot Welding

ABSTRACT: Fatigue crack growth rates in AA2024-T3 sheet joined to AA7075-T6 stiffeners by friction stir welding have been compared with rates measured in panels joined with rivets and in unstiffened parent material panels. Friction stir panels were prepared with both continuous friction stir welding (FSW) and swept friction stir spot welding (FSSW). Fatigue cracks in edge crack panels with continuous FSW joints tended to grow into the parent material away from the stiffeners. This behavior was attributed to the reduced stress levels corresponding to the increased thickness of continuous FSW joints and the support of the attached stiffener. Fatigue cracks in edge crack panels were found to follow the joint line in panels made with discrete fasteners (both rivets and swept FSSW joints). The measured crack growth rates in riveted panels increased at an increasing rate as the crack approached the riveted joints. In contrast, crack growth rates in panels joined with FSSW decreased at a decreasing rate as the crack approached the swept spot joints. Test results indicate that the swept FSSW process produced favorable residual stresses that inhibited fatigue crack growth along the joint line.

KEYWORDS: friction stir welding, friction stir spot welding, fatigue crack growth rate, edge crack panel, lap joint, residual stress

Manuscript received November 14, 2007; accepted for publication March 5, 2008; published online April 2008.

[1] Senior Research Scientist and Director, Senior Research Engineer, and Research Scientist, respectively, Advanced Joining and Processing Lab, National Institute for Aviation Research, Wichita State University, Wichita, Kansas.

Citation: Burford D. A., Tweedy, B. M., and Widener, C. A., "Fatigue Crack Growth in Integrally Stiffened Panels Joined Using Friction Stir Welding and Swept Friction Stir Spot Welding," *J. ASTM Intl.*, Vol. 5, No. 4. DOI10.1520/JAI101568. Available online at www.astm.org. Also included in JAI Special Issue STP 1508, *Fatigue and Fracture Mechanics: 36th Volume,* R. W. Neu, K. R. W. Wallin, and S. R. Thompson, guest editors, ASTM International, West Conshohocken, PA, 2009, pp. 719-742.

Nomenclature

FSW = friction stir welding
FSSW = friction stir spot welding
HAZ = heat affected zone
mm/min = millimeters per minute
ipm = inches per minute
rpm = revolutions per minute

Introduction

Friction stir welding (FSW) and friction stir spot welding (FSSW) are emergent joining technologies that are being developed for a variety of applications in different industries, including the aerospace industry [1–3]. Applications utilizing these technologies are typically developed on a case-by-case basis to take advantage of associated manufacturing and implementation cost savings, such as part count reduction, improved material buy-to-fly ratios, cycle time reduction, reduced material lead-time requirements, flexible material sourcing options, and lowered environmental impacts.

A number of different forms of FSSW have been developed, including a simple plunge or "poke" spot welding process patented by Mazda [4], a refill process developed by GKSS [5], a swing spot welding process developed by Hitachi [6], and a circular spot pattern introduced by TWI in Great Britain [7].

Although unique, each of these FSSW technologies produces a similar result: a discrete joint. In all cases, parent material is locally stirred thermo-mechanically with specially designed metal working tools to form a metallurgical bond between two or more components in a lap joint configuration. Therefore, in this paper the various forms of FSSW are referred to as *in situ* fastener joining technologies. The class of joints they produce are referred to in this paper collectively as *in situ* integral fasteners.

In situ integral fasteners provide unique benefits over riveting and continuous FSW joints. These include, but are not limited to, the following:

- *Consolidated joints versus fastened joints*. Holes drilled for installed fasteners serve as stress concentrations. Conversely, the combined parent material consolidated in FSSW joints effectively forms pad-up regions (either annular or solid) that act to lower local in-plane stress levels (described in the *Approach* section).
- *A reduction in loose debris*. Drill chips are common to drilling holes for installed fasteners. Consequently, the operations needed to clean them out of airframe structure and from production areas are also common. FSSW greatly reduces the amount of the material discarded as chips in making a joint because the parent material is retained for forming the joint, i.e., the *in situ* integral fastener.
- *A potential reduction in fastener interaction as a function of separation distance*. Rivets, for example, are spaced a minimum distance (e.g., $4D$) to reduce the interaction of their stress fields under load. Conversely,

FSSW joints can be placed side by side to form continuous joints similar to continuous FSW without the adverse interaction of the stress concentrations encountered with installed fasteners.

- *Rapid installation and reduced cycle time. In situ* integral fasteners typically require fewer operations than installed fasteners, e.g., by eliminating the drilling step.
- *Simplified tooling requirements*. FSSW requires lower lateral forces over short ranges as compared to continuous FSW. As such, only discrete points are required to react the load; this is in contrast to the monolithic tools that are often found in continuous FSW.
- *Installation via a robot versus a gantry machine*. Continuous FSW most often requires a purpose-built FSW machine that can sufficiently control the weld tool along the entire length of the joint line. Appropriately developed, *in situ* integral fasteners can be installed via robots in an array of discrete locations similar to rivets, providing a low-cost solution and greater flexibility in production facilities.
- *Distortion control options*. Similar to riveting, FSSW affords the opportunity to randomize the sequence of fastener installation for lowering distortion in large panels.
- *A discontinuous heat affected zone* (*HAZ*). Similar to rivets, *in situ* integral fasteners are separated by parent material. As such, a row of *in situ* integral fasteners does not introduce a continuous HAZ in precipitation-strengthened alloys and work hardened alloys as does FSW. It also induces a discontinuous or intermittent residual stress pattern when compared to FSW.
- *Introduction of favorable residual stresses associated with discrete joints*. FSSW produces a compressive residual stress field surrounding the *in situ* integral fastener. Consequently, the results discussed in this paper show that lower fatigue crack growth rates can be achieved with the swept spot technique tested.
- *Tailored joint sizes and shapes*. FSSW provides more latitude when designing for joint properties than do rivet systems. Some of the *in situ* integral fastener systems, namely, swept spots, allow non-circular shapes, such as ovals, crescents, etc., to be formed and oriented for optimizing joint performance.
- *Compatible with sealants on the faying surface*. Similar to riveting, FSW has been shown to be compatible with fay surface sealants in lap joints to enhance corrosion protection [8–11]. Therefore, in terms of corrosion prevention, FSW and FSSW have a marked advantage over resistance spot welding, which is not compatible with fay surface sealants applied for corrosion protection. FSSW has been successfully tested with surface treatments, including anodize, alodine, and cladding [12]. FSSW through fay surface sealants is currently under development for *in situ* integral integral fasteners with positive results being reported [13].

In prior work, the static strength of friction stir welded panels was found to be equivalent to or better than the strength of riveted panels tested in tension, compression, and in diagonal shear [14]. The present work was undertaken to extend this work by evaluating fatigue crack growth behavior in FSW and FSSW joints as compared to riveted joints.

The *in situ* integral fastener investigated in this study was the Octaspot™ swept spot introduced by Tweedy et al. [15]. This swept spot technique is similar to the TWI technique and is described in more detail elsewhere [12]. It is referred to as a swept spot because it involves making a tight circular, circumscribed friction stir weld to form a discrete joint.

Approach

The primary objective of this work was to investigate the fatigue crack growth rate and behavior in thin aluminum lap joints fabricated by FSW and swept FSSW in comparison to similar joints fabricated using standard rivets. Testing was limited to lap joints between conventional aluminum alloys AA2024-T3 and AA7075-T6, which are common in airframe construction. Stiffeners made from 1 mm (0.040 in.) thick bare AA7075-T6 sheet were joined to 1 mm (0.040 in.) thick bare AA2024-T3 sheet test coupons.

Edge Crack Fatigue Coupon Test and Test Method

The test coupon configuration and test method selected for this study was based on work conducted by Smith et al. [16]. In their study, Smith and his co-workers investigated the effects of dents on fatigue crack growth rates in 1 mm (0.040 in.) thick AA2024-T3 aluminum sheet. An edge crack, initially 7.6 mm (0.3 in.) in length, was grown by constant amplitude loading cycles through two dents located as shown in Fig. 1(*a*).

For the present study, the coupon was modified slightly by attaching a stiffener strip across the central portion of the coupon parallel to the crack growth direction, as shown in Fig. 1(*b*). NAS1097AD5-4 countersunk rivets (3.18 mm or 0.125 in. diameter) and swept FSSW spots (integral *in situ* fasteners) were placed at the same location the dents were placed in Smith's work.

The machined coupons were 203 mm (8 in.) wide by 508 mm (20 in.) long with the grain direction oriented perpendicular to the loading axis. Doublers were machined from 6.4 mm (0.25 in.) thick aluminum plate and bonded to the test coupon, with two rows of fastener holes (15 holes total) at each end of the coupons. A coupon is shown mounted in the fatigue crack growth rate test setup shown in Fig. 2.

Crack Growth Rate Measurements

A 22 kN (5 kip) servo-hydraulic MTS testing machine was used to generate crack growth data. Constant amplitude cyclic testing was conducted at a frequency of 10 Hz. The ratio of the minimum stress to the maximum stress was 0.2 (i.e., $R = 0.2$). The minimum load was 1.8 kN (400 lbf) (8.7 MPa (1250 psi)) and the maximum load was 8.9 kN (2000 lbf) (43.1 MPa (6250 psi)). Following

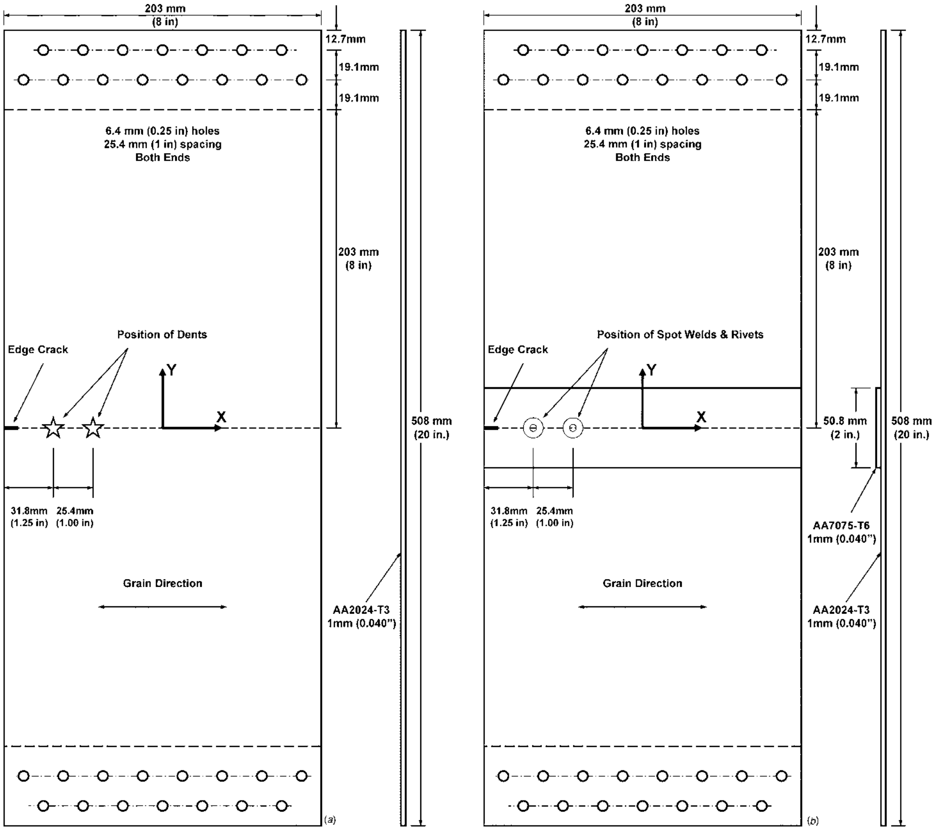

FIG. 1—*Edge-crack panels with an initial edge pre-crack nominally* 7.6 mm (0.3 in.) *in length, located as shown:* (*a*) *dent study test panel* [*16*] *and* (*b*) *swept spot and riveted test panel* (*NTS*).

the work of Smith et al. [16], the same cyclic loading was used to grow the pre-crack from an initial saw-cut notch length of nominally 7.6 mm (0.3 in.) to a length of nominally 9.4 mm (0.37 in.).

A Hirox optical microscope (BH-1000 BGA) was used to record crack growth length as a function of both fatigue cycles and crack growth at a magnification of 160×. Figure 2 shows the microscope mounted adjacent to the MTS fatigue test machine. The microscope was mounted on a table equipped with a mechanical translation system, and it was connected to a video monitor for measuring the crack tip throughout the test.

Swept Spot in situ Fastener Configuration

An Octaspot™ swept spot [12] was used to join the bare 1 mm (0.040 in.) thick AA7075-T6 stiffeners to the bare 1 mm (0.040 in.) thick AA2024-T3 sheet coupons. A schematic of the various stages in the swept spot path is shown in Fig.

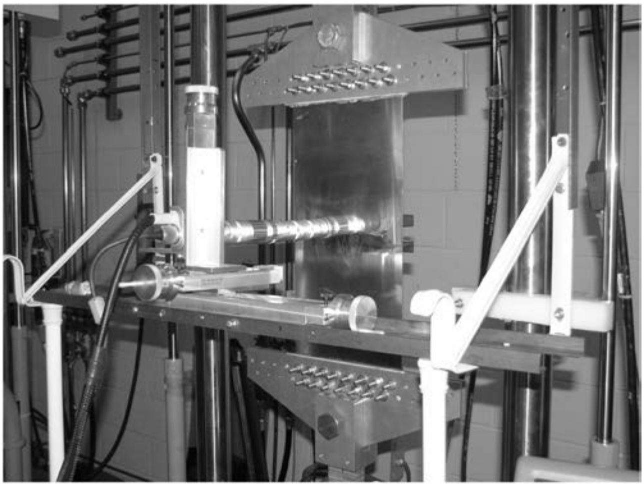

FIG. 2—*Fatigue crack growth measurement test fixture mounted in an MTS servo-hydraulic load frame. The measurement system features a traveling microscope for measuring crack growth as a function of cyclic loading. Crack length is measured on the non-stiffened side, i.e., in the AA2024-T3 sheet.*

3(*a*). The process parameters for the swept spots were: 1350 rpm, 7.4 mm/s (17.5 ipm) (around the periphery), 1° tool tilt lead angle, 2.5 mm (0.10 in.) path radius, and 5.1 kN (1150 lbf) load control. A typical Octaspot™ joint tested in this study is shown in Fig. 3(*b*) in the as-fabricated condition. A cross section taken through the center of a representative joint in this study is shown in Fig. 3(*c*).

The joint includes a centrally located exit hole surrounded by the joint material, which was formed by combining parent material from the upper and lower sheets. In addition to establishing a link between the stiffener (top) and sheet (bottom), the fine-grained joint material acts as an annular embossment or pad-up on either component, outlined in Fig. 3(*d*). Thus, to pass through the joint, a crack in either component would have to pass through a dual layer of material. A more favorable path would be to circumvent the embossment by passing around the joint.

A schematic of the tool that was used in making both the continuous friction stir welds and the swept spots for this study is shown in Fig. 4. It has a 6.4 mm (0.25 in.) diameter shoulder, a concave shoulder face, and a 1.4 mm (.054 in.) long tapered probe with three flats. The friction stir welds were made at 1200 rpm and 6.8 mm/s (16 ipm) under load control.

3D Strain Distribution Measurements

An ARAMIS optical 3D deformation analysis system, shown in Fig. 5, was used to measure full field strain distributions in edge crack panels as a function of uniaxial stretching to nominally 1.5 % total strain. The back surface of the

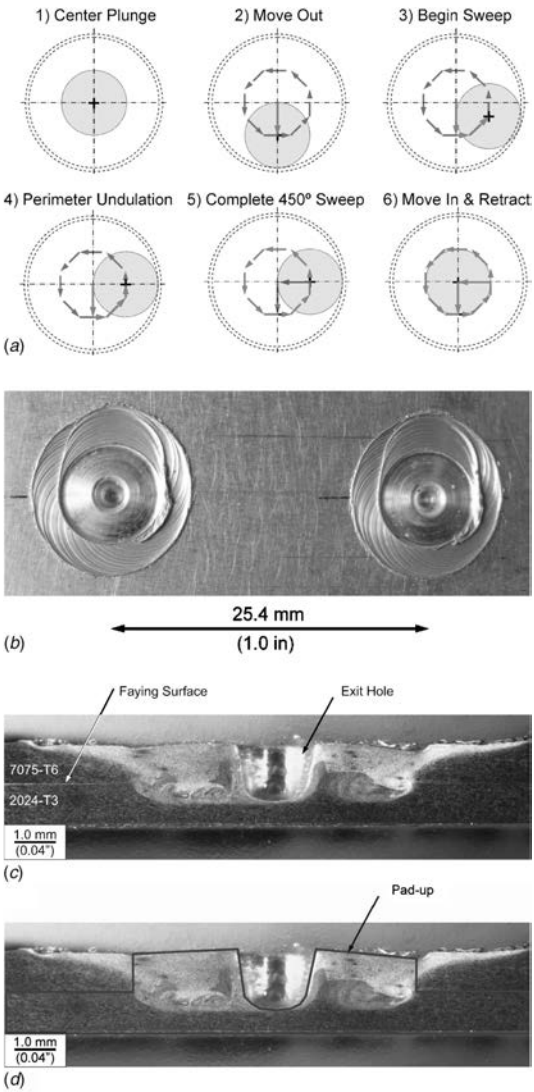

FIG. 3—(*a*) *Octaspot™ swept spot path:* (*1*) *initial center plunge,* (*2*) *movement to the periphery of the joint,* (*3*) *beginning of octagonal movement around the periphery of the joint,* (*4*) *slight undulation with octagonal movement,* (*5*) *continued sweep for a total of 450°, and* (*6*) *movement to the center and extraction of tool.* (*b*) *Photograph of a typical Octaspot™ friction stir spot weld.* (*c*) *Cross section of a typical Octaspot™ friction stir lap joint between* 0.040 in. *thick* (1 mm) *AA2024-T3 aluminum upper and lower sheets.* (*d*) *Overlay of "pad-up" on cross section shown in* (*c*).

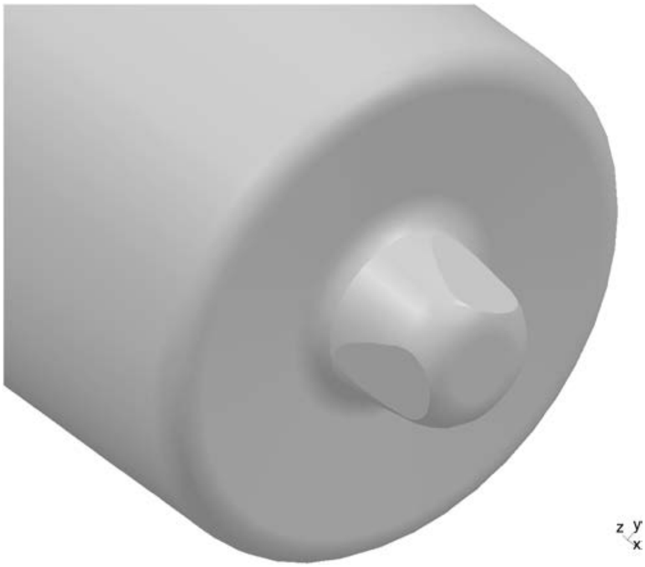

FIG. 4—*Weld tool used to produce Octaspot™ swept spot joints between* 1 mm (0.040 in.) *thick bare AA7075-T6 stiffeners and bare* 1 mm (0.040 in.) *thick AA2024-T3 sheet stock. It features a* 6.4 mm (0.25 in.) *diameter shoulder, a concave shoulder face, and a tapered probe with three flats* (*Tool # 05-0054-0250-01*).

panels (i.e., opposite the stiffener) was coated with a random pattern of black speckles on a white background. The speckles were applied to have approximately 50 % coverage in the random pattern. Positional changes in the pattern as a function of strain were recorded in time sequence by two digital cameras and strains were then computed based on photogrammetry methods [17].

X-Ray Diffraction Residual Stress Measurements

X-ray diffraction residual stress measurements on two OctaSpot™ swept spots in a single panel were performed by Lambda Research [18]. Per the report submitted by Lambda, measurements were taken at the surface and at nominal depths of 127, 254, and 381×10^{-3} mm (5.0, 10.0, and 15.0×10^{-3} in.). The measurements were made in the transverse direction to the crack growth direction on the backside of both swept spots (in the AA2024-T3 sheet). Twelve measurements were made on either side of the joints in addition to the measurement taken at the center of the spot weld. The locations included ±1.1, 2.3, 3.4, 4.6, 5.7, 6.9, 8.0, 9.1, 10.3, 11.4, 12.6, and 13.7 mm (±0.045, 0.090, 0.135, 0.180, 0.225, 0.270, 0.315, 0.360, 0.405, 0.450, 0.495, and 0.540 in.). X-ray diffraction residual stress measurements and calculations were performed in accordance with SAE HS-784 and ASTM E915.

For the subsurface measurements, material was removed electrolytically. Lambda reported that all data obtained as a function of depth were corrected for the effects of the penetration of the radiation employed for residual stress

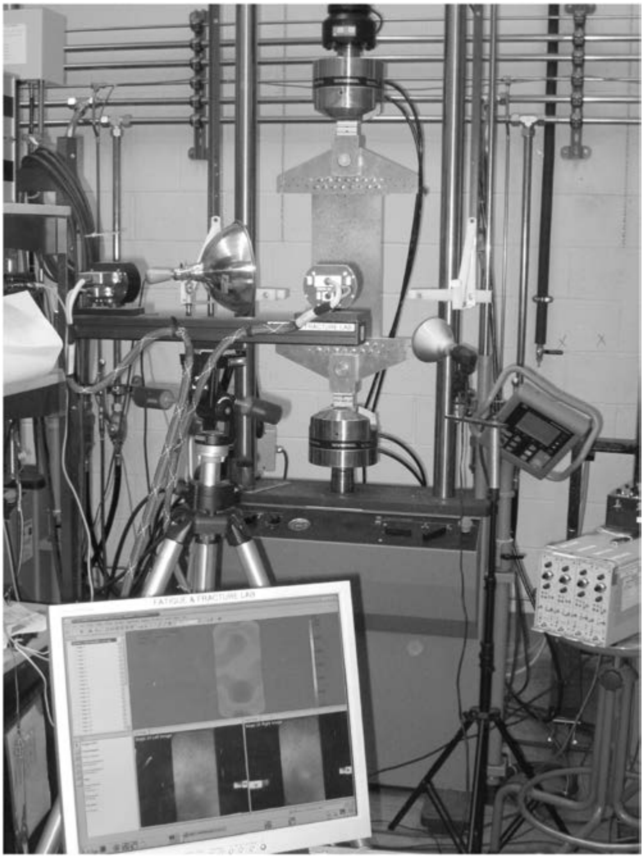

FIG. 5—*ARAMIS optical 3D deformation analysis system shown monitoring strain as a function of uniaxial stretching of edge crack panels in the MTS servo-hydraulic load frame.*

measurement into the subsurface stress gradient [19]. Stress gradient corrections applied to the last depth measured were based upon an extrapolation to greater depths. They further reported that corrections for sectioning stress relaxation, as well as for stress relaxation caused by layer removal, were applied as appropriate [20].

Results and Discussion

Crack Growth Rates in Riveted and FSSW Panels

The fatigue crack growth rate test results from the initial rivet and FSSW test panels are presented in Fig. 6. For comparison, the crack growth curves of three pristine (no dents or fasteners) panels from Smith et al. [16] are also

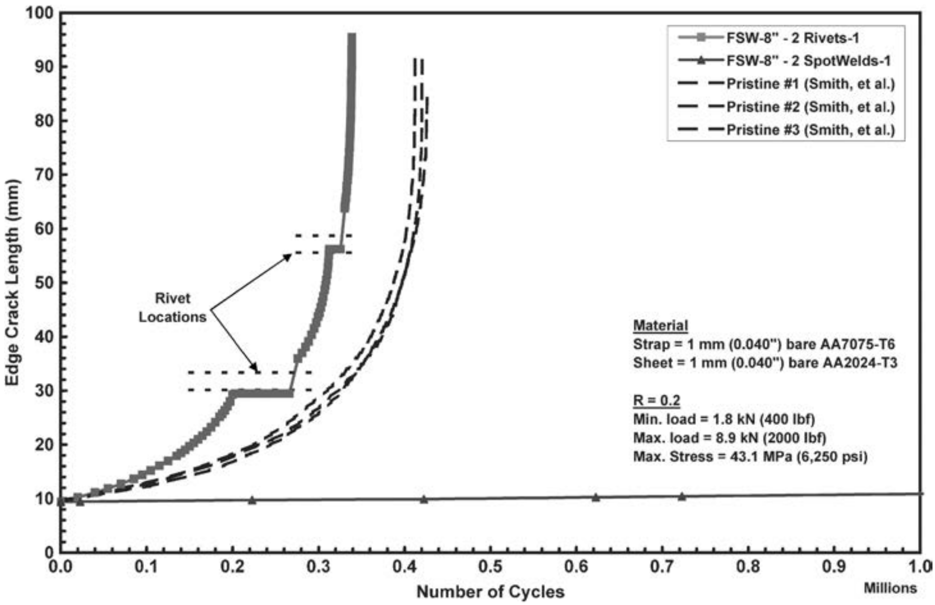

FIG. 6—*Edge crack length as a function of fatigue cycles in riveted and FSSW edge crack panels* (*Fig. 1*(*b*)) *during constant amplitude cyclic loading. Data for pristine panels from Smith et al., are shown for comparison* [*16*].

included. The crack in the riveted panel is observed to accelerate as it approaches the rivet holes, growing faster than the three pristine parent material panels. This behavior is attributed to the crack reacting with the stress concentration associated with the rivet hole. Once the crack reaches the rivet holes a delay in crack growth is observed. This delay is attributed to the time required to initiate a crack on the opposite side of the rivet hole (which is expected to vary from rivet to rivet, being dependent upon hole quality, etc.).

The rate at which the crack grew in the swept spot panel was much less than that of either the pristine (unstiffened) panels or the riveted panel. Specifically, the crack grew only 14 mm (0.55 in.) in 4.7×10^6 cycles at the noted stress levels. To encourage crack growth, the initial stress levels of the test were then doubled for this specimen. A second rivet panel was also tested at the increased stress levels for comparison. The test results from these double-loaded test panels are presented in Fig. 7. In the riveted panel the edge crack again accelerated as it approached the rivet holes. Conversely it decelerated slightly as it approached the swept spots in the FSSW panel.

To determine if this behavior is associated with residual stresses, panels fastened with rivets and swept spots were stretched 6.1 mm (0.24 in.) in the test setup shown in Fig. 5 prior to fatigue crack growth testing. The objective of this stretcher leveling step was to relieve any in-plane residual stresses that may

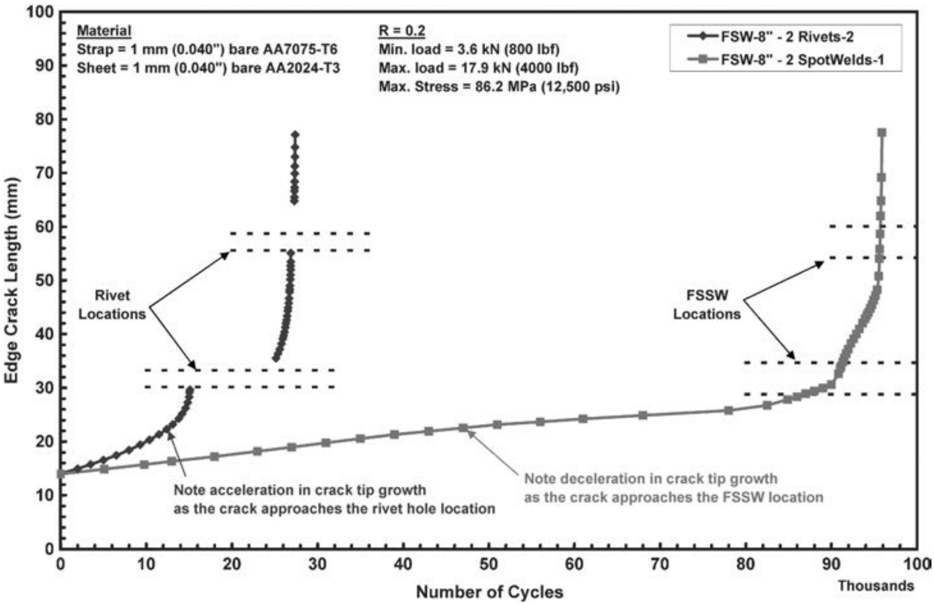

FIG. 7—*Edge crack length as a function of fatigue cycles in a single riveted panel and a single FSSW edge-crack panel during constant amplitude cyclic loading. Note: Loading is double that in the original dent study performed by Smith et al.* [*16*].

have been induced in the panel by FSSW. The strain distributions in the stretched panels were documented with an ARAMIS optical 3D deformation analysis system.

The strain distribution map of the *Y*-component (stretch direction) of strain in the riveted panel is shown in Fig. 8 (see Fig. 1(*b*) for rivet locations). Note that the high strain region is associated with the location of the two fasteners (compare with Fig. 1(*b*)). A strain distribution map of the *X*-component (transverse to the stretch direction) for the same stretched riveted panel is shown in Fig. 9. The rivets clearly dominate the strain pattern in the stretched panels.

The *Y*-component strain distribution map of a stretched panel with two swept spots is shown in Fig. 10 (see Fig. 1(*b*) for locations). For this panel, the high strain region is not associated with the location of the two swept spots. Rather, the locations of the joints show a lower strain level than the region immediately around them. The *X*-component distribution map of the same panel joined with swept spots is shown in Fig. 11. Note that this figure shows less severe gradients in strain than does the *X*-component map for the riveted panels presented in Fig. 9.

After the panels were stretched, they were subjected to the same cycle crack growth conditions for the panels shown in Fig. 6. The crack growth curve of the stretched panels are shown in Fig. 12 (the data from Fig. 6 are included for comparison). Note that the fatigue crack growth rate in the stretched FSSW panel is similar to that of the pristine panels tested by Smith et al. [16]. The

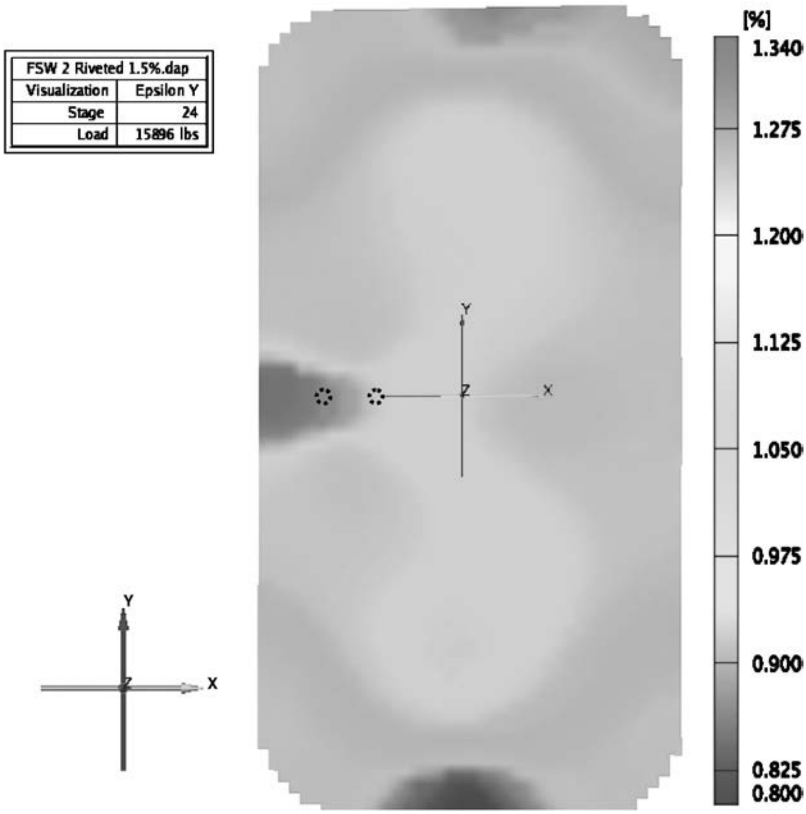

FIG. 8—*ARAMIS strain map for a riveted panel stretcher-leveled* 6.1 mm (0.24 in.)*: Y-component of plastic strain; measured under load. Note strain concentration at the location of the two rivets. Fastener location indicated by dashed lines* (*see Fig. 1*).

only noticeable deviation between the crack growth curves of the stretched swept spot panels and the referenced pristine panels occurs at the location of the first swept spot. At this location the crack growth rate in the swept spot panel is observed to slow as it encounters the first joint and then, once past the joint, it returns to a rate comparable to that measured in the pristine panels.

The crack growth rate in both the stretched and unstretched riveted panels behaved in a similar manner, as shown in Fig. 6. However, the delay in crack growth associated with the first rivet location may have been extended by the stretching process, but due to the variable nature of crack initiation in conjunction with the stress concentration associated with the hole, further work would be required to confirm this effect.

The crack growth curves presented in Fig. 12 suggest that residual stresses are primarily responsible for the greatly reduced fatigue crack growth rate in the unstretched panel with swept spots (Fig. 6). The curves further suggest that the pad-up effect produced by the swept spots (see Fig. 3(*d*)) contributes to a

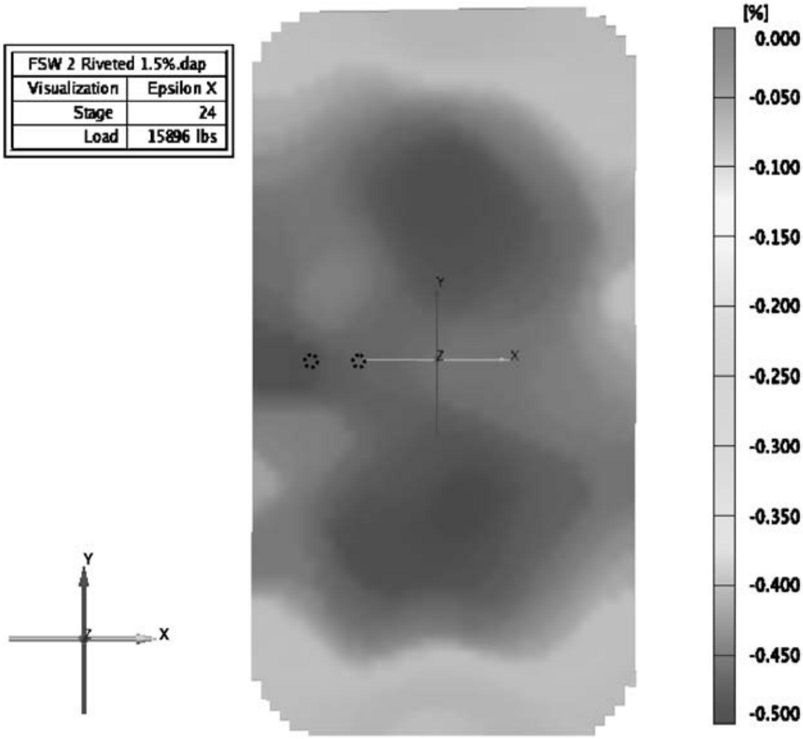

FIG. 9—*ARAMIS strain map of a riveted panel stretcher-leveled* 6.1 mm (0.24 in.)*: X-component of plastic strain; measured under load. Fastener location indicated by dashed lines* (*see Fig. 1*).

lesser extent in slowing crack growth than does residual stresses. In the stretched condition, the panels behave similar to panels without fasteners except for the slight slowing in crack growth around the swept spots.

To confirm that the test results presented in Fig. 7 were not unique to the panels tested, two additional riveted panels and two additional swept spot panels were tested under the same cyclic loading conditions. The fatigue crack growth curve data for these additional panels, along with the data from the original panels, are presented in Fig. 13. Based on the nature of fatigue crack growth, these test results appear consistent and representative of the different fastener systems.

Crack Growth Rates in FSW Panels

Edge crack panels were also fabricated with continuous FSW joints oriented along the crack growth path, as shown in Figs. 14(*a*) and 14(*b*). Panels were tested that had welds produced by traveling in the same direction as the crack growth direction and in the opposite direction.

In the first test of a continuous welded panel, the pre-crack failed to grow

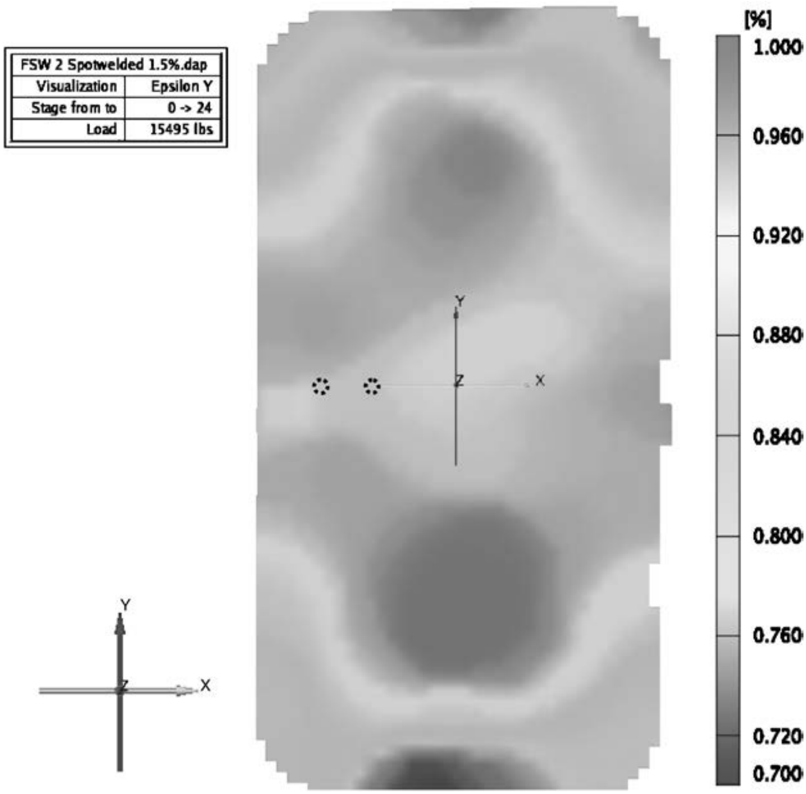

FIG. 10—*ARAMIS strain map of a FSSW panel stretcher-leveled* 6.1 mm (0.24 in.)*: Y-component of plastic strain; measured under load. Note the lower strain level at the location of the two swept spots. Fastener location indicated by dashed lines* (*see Fig. 1*).

under the original cyclic loading conditions of a maximum load of 8.9 kN (2000 lbf) (43.1 MPa (6250 psi)) and load ratio $R=0.2$. Therefore, the stress levels were doubled, as was done with the discrete fastener panels featured in Figs. 7 and 13.

Figure 15 includes the crack growth data from the first continuous FSW panel plotted with the data from Fig. 7. The continuous panel demonstrates a substantially lower growth rate than either the riveted or swept spot panels. Upon inspection of the failed panel, it was observed that the fatigue crack in the panel grew away from the continuous joint region into the parent material, as shown in Fig. 16.

To evaluate this behavior further, the strain distributions in stretched continuous FSW panels were documented with an ARAMIS optical 3D deformation analysis system. A map of the Y-component (stretch direction) of strain for a stretched FSW panel is shown in Fig. 17. For this panel, the strain in the region adjacent to the joint is noticeably less than in regions away from the joint line. The highest strain regions occur on either side of the joint between

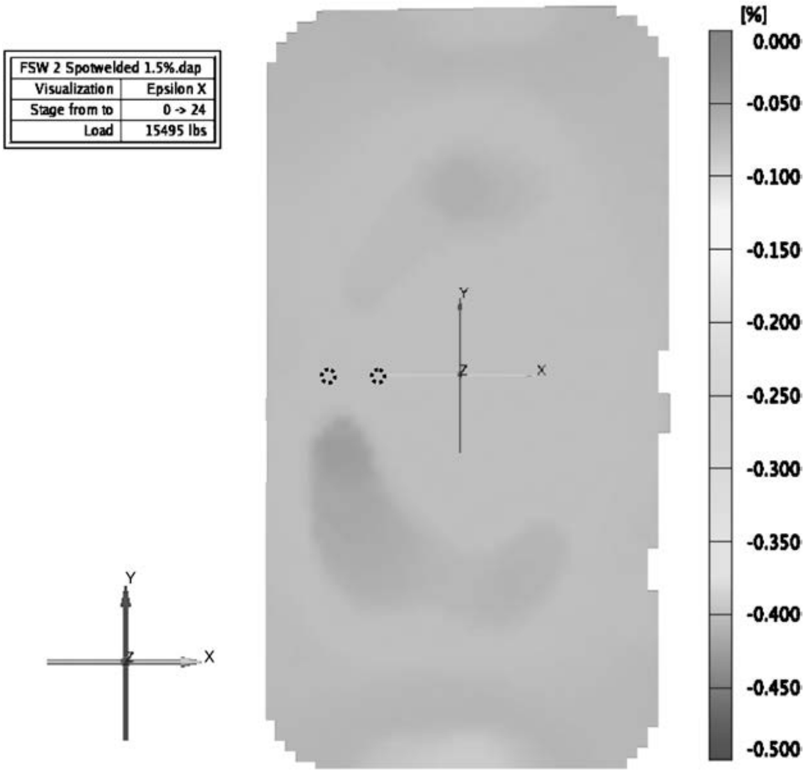

FIG. 11—*ARAMIS strain map of a FSSW panel stretcher-leveled* 6.1 mm (0.24 in.)*: X-component of plastic strain; measured under load. Fastener location indicated by dashed lines* (*see Fig. 1*).

the grips and the stiffener. Similarly, the *X*-component of strain, shown in Fig. 18, is also highest away from the stiffener location. Therefore, notwithstanding any possible influence the FSW process may have on fatigue properties in the sheet material, such as forming a HAZ or producing residual stresses, the reduced stress level imposed by the presence of the stiffener dominates fatigue crack growth in the configurations tested. Effectively, a FSW lap joint introduces a pad-up region by joining the parent material. Once formed, the joint acts to lower the local in-plane stresses and, in turn, inhibits fatigue crack growth adjacent to the joint.

X-Ray Diffraction Residual Stress Measurements

The residual stresses associated with OctaSpot™ swept spots were evaluated using X-ray diffraction. The specimen tested is shown in Fig. 19. Measurements were taken on the back side (the AA2024-T3 side) of the coupon.

Transverse residual stress measurements were made at 25 locations along the direction of crack growth on the original surface of the coupon. These

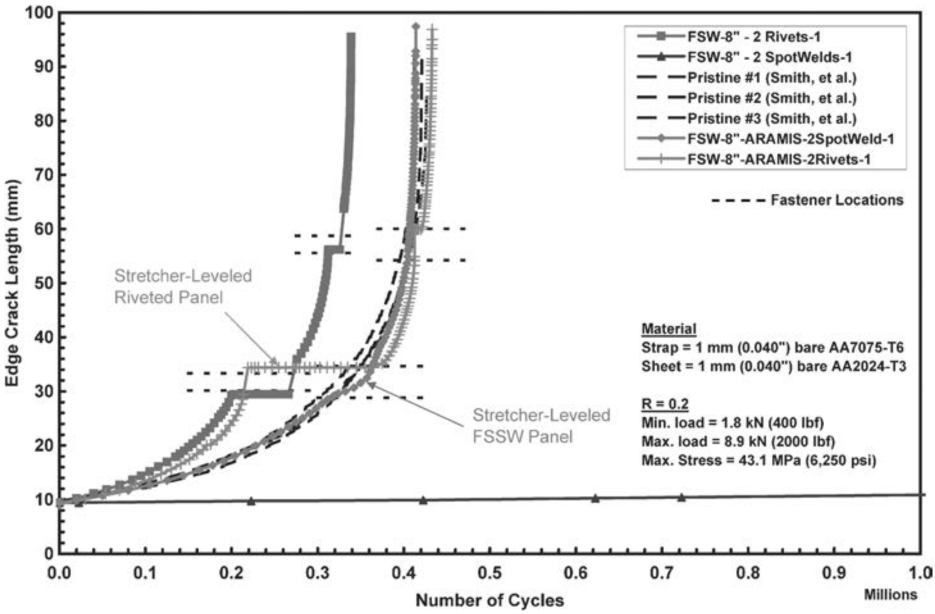

FIG. 12—*Edge-crack length as a function of fatigue cycles for riveted and swept FSSW edge crack panels during constant amplitude cyclic loading. Data for pristine panels from Smith et al.* [*16*] *are shown for comparison.*

include a measurement at the center of the spot and 12 locations on either side along the crack growth direction. Additional measurements were taken at the same 25 locations but at the following nominal depths: 127, 254, and 381 $\times 10^{-3}$ mm (5.0, 10.0, and 15.0×10^{-3} in.). This array of 25 measurement locations for the swept spot closest to the edge is indicated in Fig. 20. For reference, Fig. 20 includes the locations of x-ray measurements relative to the inflections in the crack growth versus constant amplitude cycles featured in Fig. 7. It also includes the centerline and the nominal diameter of each swept spot for reference (see Fig. 3(*c*) for a typical joint cross section). The measured residual stress distributions are provided in Fig. 21.

Per the report submitted by Lambda Research [18], the highest tension stress for both welds was at a depth of 0.13 mm (0.005 in.). The highest compressive stress for both welds was at the surface. The compressive stress level between the two welds is relatively uniform and the subsurface material appears to have relatively uniform cold working.

At the center of the swept spot joint transverse tensile stresses are present in the AA2024-T3 sheet material at the bottom of the exit hole. Around the exit hole the transverse stresses turn compressive and level off past the extent of the consolidated portion of each joint. Between the joints the transverse stress level remains compressive, while on the respective opposite sides it tends toward zero as a function of distance away from the joint.

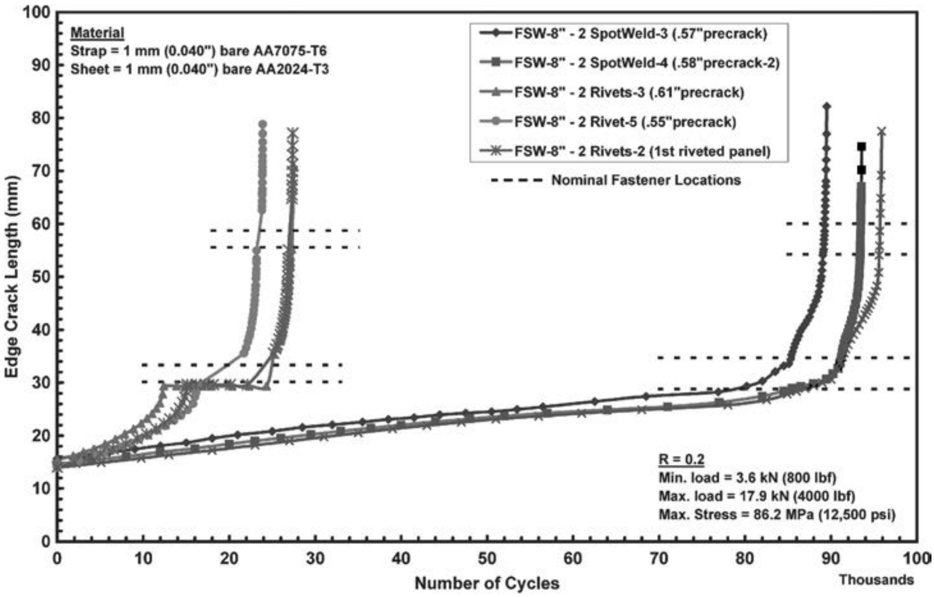

FIG. 13—*Edge-crack length as a function of fatigue cycles in three riveted panels and three FSSW edge crack panels during constant amplitude cyclic loading. Note: Loading is double that in the original dent study performed by Smith et al.* [*16*]. *Compare results with Fig. 7.*

Summary and Conclusions

In this paper, fatigue crack growth rates in flat, stiffened edge-crack panels were investigated in the initial phase of a test program to evaluate the relative performance of joints produced by FSSW and riveted joints based on a test procedure developed in an earlier study. Lower crack growth rates were observed in FSSW pre-crack panels than were observed in unstiffened panels and panels joined with rivets. By testing panels that were stress relieved with stretcher-leveling, it was concluded that a beneficial residual stress field is produced around swept OctaSpot™ joints, the *in situ* fastener system studied in this program. It was also concluded that the pad-up effect, resulting from mechanically forming discrete integral joints between the sheet and stiffener (i.e., *in situ* fasteners), contributes to the observed lowered crack growth rates in FSSW panels to a lesser extent than does the residual stress effect. Conversely, it appears that the pad-up effect associated with continuous FSW joints imposes a sufficient stiffening effect to reduce the stress level adjacent to the joint and, in turn, cause the crack to turn away from the stiffener into higher stress areas. Therefore, the observed reduced crack growth rates along continuous FSW lap joints holds potential for overriding any possible deleterious affects from, for example, the presence of a continuous HAZ. In summary, swept FSSW joints and continuous FSW joints provide effective methods for reducing

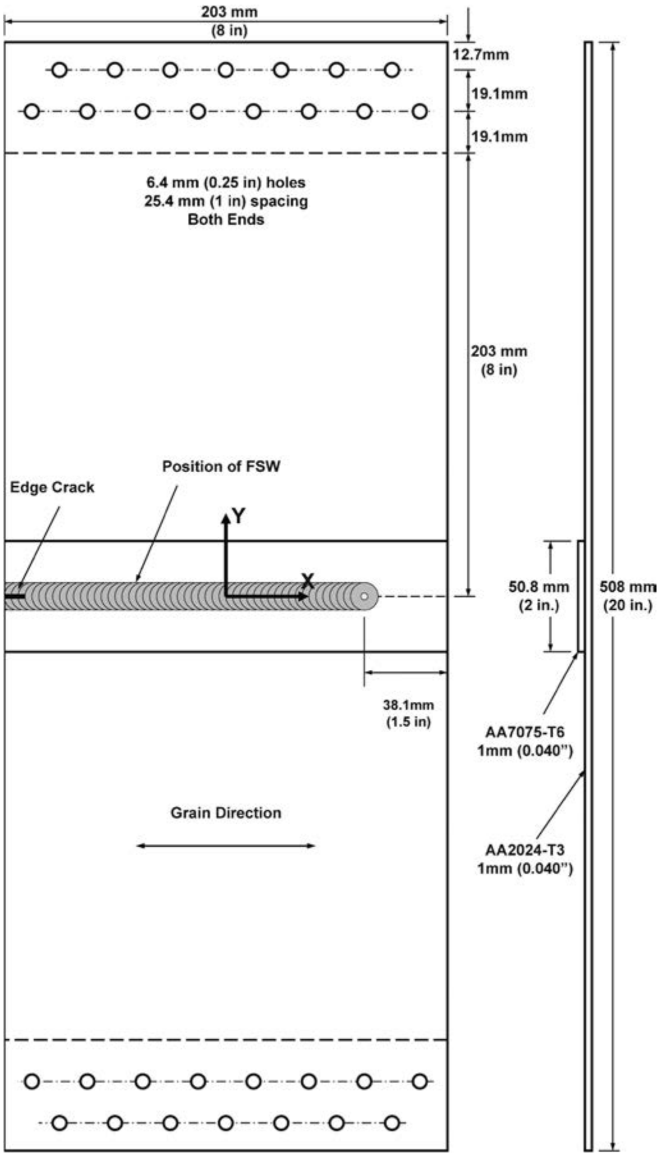

FIG. 14—*Edge-crack panels with an edge pre-crack nominally* 7.6 mm (0.3 in.) *in length, located as shown:* (*b*) *FSW coupon with weld running off of the panel, and* (*b*) *FSW coupon with weld running onto the panel* (*NTS*).

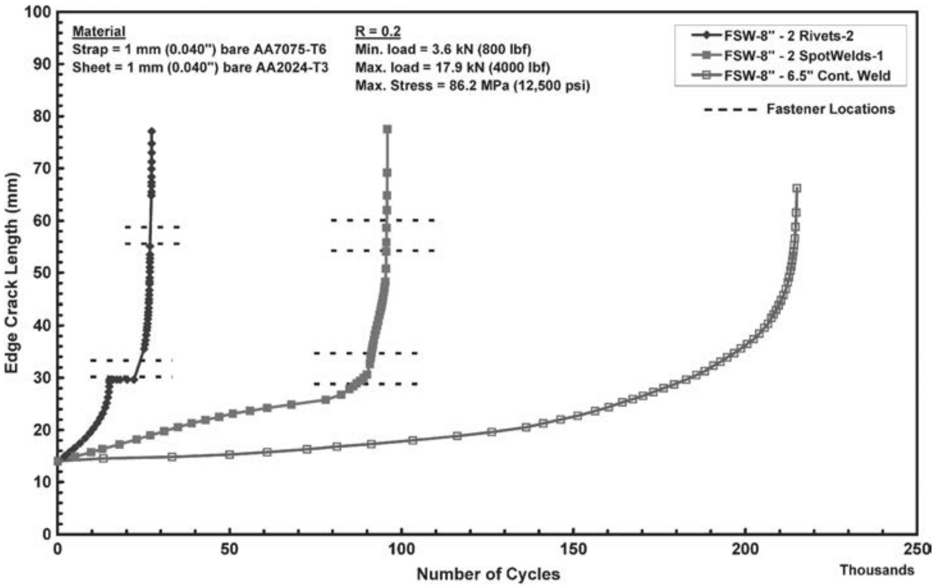

FIG. 15—*Edge-crack length as a function of fatigue cycles in three edge crack panel configurations during constant amplitude cyclic loading: a two-rivet configuration (Fig. 1(b)), a two-spot weld configuration (Fig. 1(b)), and a continuous weld configuration (cf. Fig. 14). Note: Loading is double that in the original dent study performed by Smith et al. [16]. Compare results with Fig. 7.*

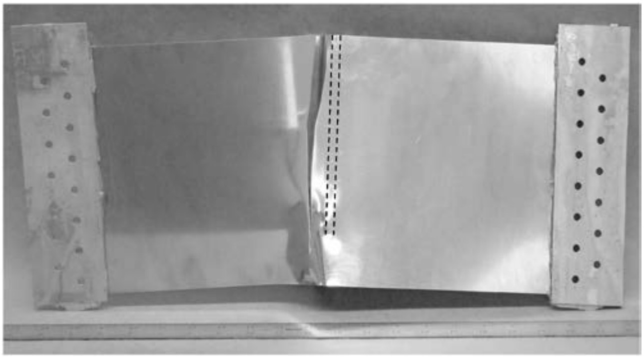

FIG. 16—*Failed continuous FSW test panel: fatigue crack growth curve provided in Fig. 15. Note that the fatigue crack grew away from the joint and stiffener location. Joint location indicated by dashed lines (see Fig. 14).*

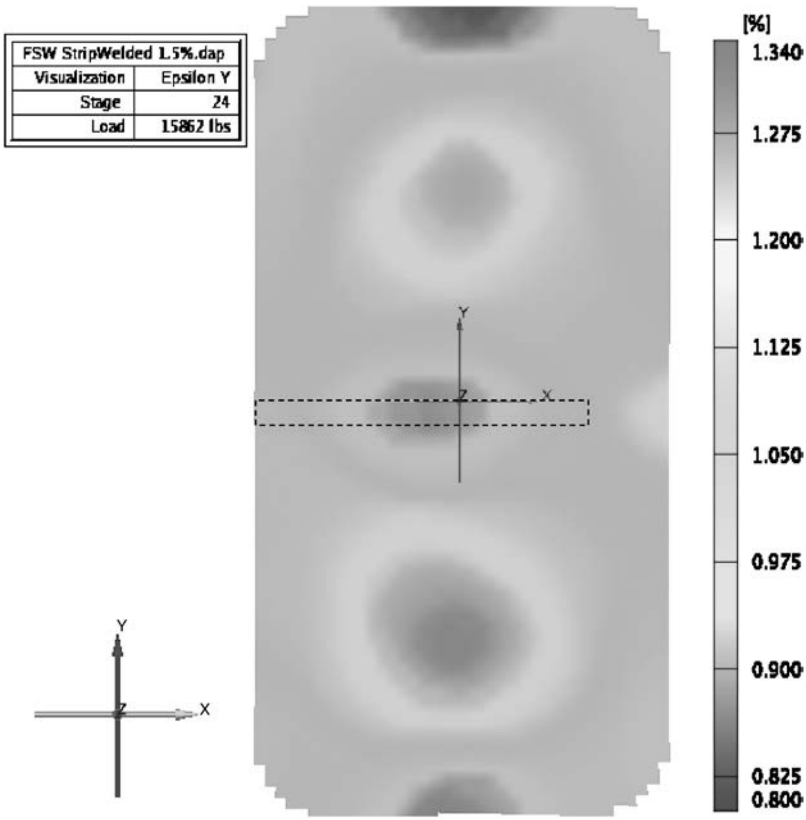

FIG. 17—*ARAMIS strain map of FSW panel stretcher-leveled* 6.1 mm (0.24 in.)*: Y-component of plastic strain; measured under load. Note the lower strain level adjacent to the continuous FSW and stiffener as compared to the strain levels shown in Figs. 8 and 10. Joint location indicated by dashed lines* (*see Fig. 14*).

the stress concentration associated with the drilled holes required for installing conventionally installed fasteners.

Acknowledgments

The authors gratefully acknowledge the contribution of the staff and students in the Advanced Joining & Processing Lab and the Fracture & Fatigue Lab of the National Institute of Aviation Research (NIAR). This work was made possible by grants from the State of Kansas and the Federal Aviation Administration (FAA).

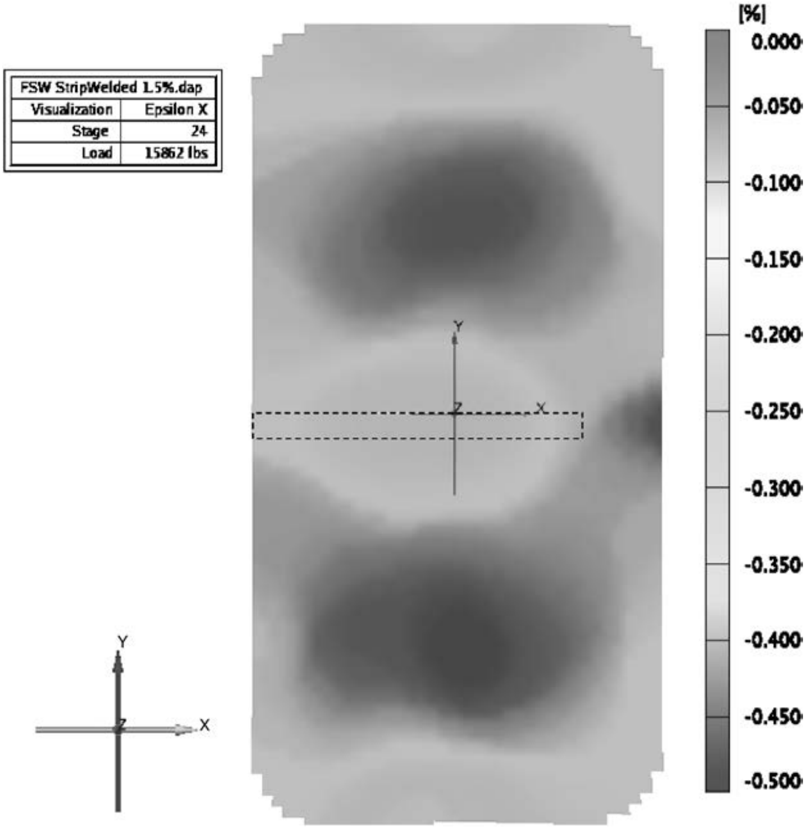

FIG. 18—*ARAMIS strain map of FSW panel stretcher-leveled* 6.1 mm (0.24 in.)*: X-component of plastic strain; measured under load. Note the lower strain level adjacent to the continuous FSW and stiffener as compared to the strain levels shown in Figs. 9 and 11. Joint location indicated by dashed lines* (*see Fig. 14*).

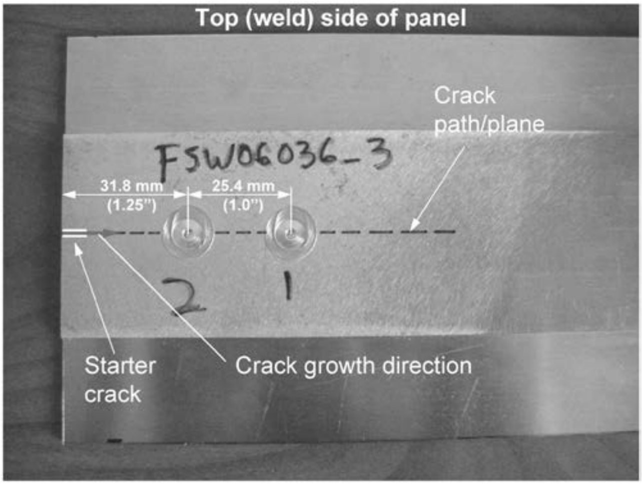

FIG. 19—*X-ray diffraction measurement locations relative to the two swept OctaSpots™* (*see Fig. 1*(*a*) *for spot locations*). *A strip of* 1 mm (0.04 in.) *thick AA7075-T6 is shown attached to a sheet of* 1 mm (0.04 in.) *thick AA2024-T3. Residual stress measurements were taken on AA2024-T3 side of the panel* (*opposite the side shown*).

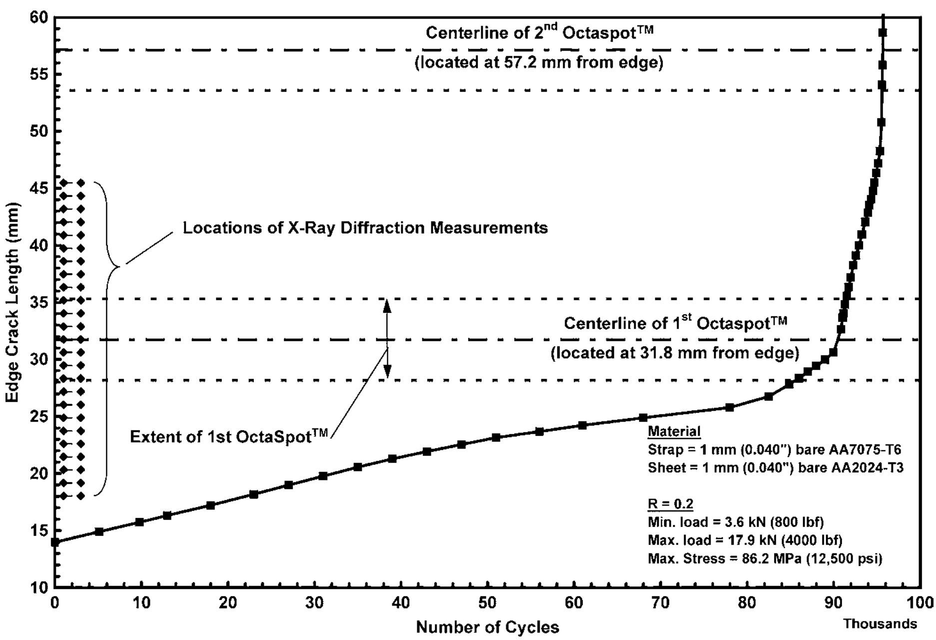

FIG. 20—*Location of x-ray diffraction measurement positions superimposed over the fatigue crack growth curve for the swept spot coupon presented in Fig. 7.*

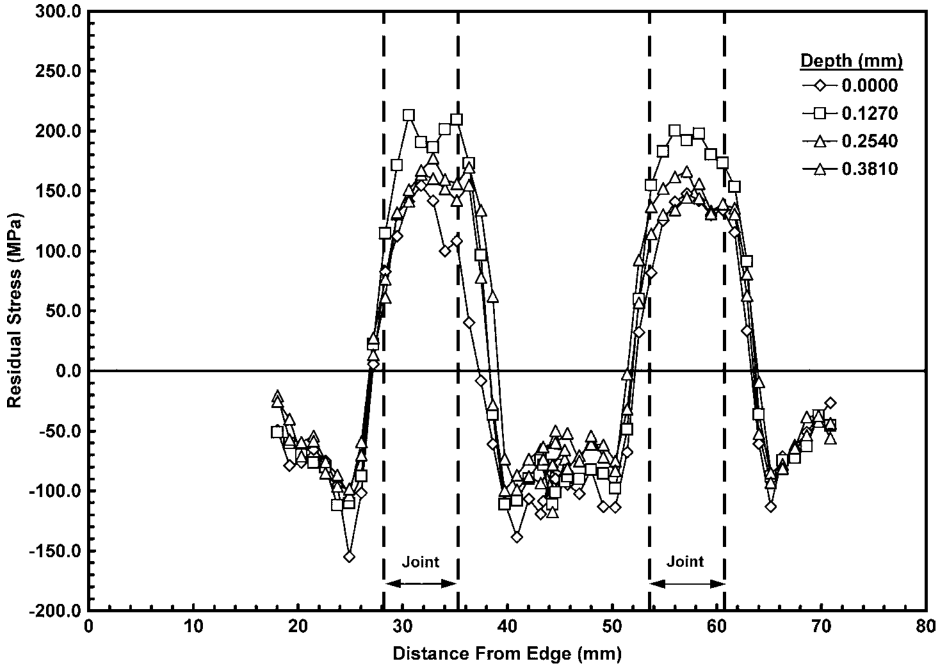

FIG. 21—*Residual stress distribution measured in an edge crack panel with two swept FSSW joints. The measurements were taken transverse to the crack growth direction in the plane of the sheet and as a function of distance from the coupon edge (see Figs. 1(b) and 19) and depth below the surface on the AA2024-T3 sheet side of the coupon.*

References

[1] Thomas, W. M., Nicholas, E. D., Needham, J. C., Murch, M. G., Temple-Smith, P., and Dawes, C. J., "Friction Welding," U.S. Patent 5460317, Oct. 1995, filed Aug. 1994.

[2] Arbegast, W. J., "Application of Friction Stir Welding and Related Technologies," *Friction Stir Welding and Processing*, R. S. Mishra and M. W. Mahoney, Eds., ASM International, Materials Park, OH, 2007, pp. 273–308.

[3] Badarinarayan, H., Hunt, F., and Okamoto, K., "Friction Stir Spot Welding," *Friction Stir Welding and Processing*, R. S. Mishra and M. W. Mahoney, Eds., ASM International, Materials Park, OH, 2007, pp. 235–272.

[4] Iwashita, T., "Method and Apparatus for Joining," U.S. Patent 6601751, 2003, filed April 2001.

[5] Shilling, C., and Dos Santos, J., "Method and Device for Joining at Least Two Adjoining Work Pieces by Friction Welding," U.S. Patent Application 2002/0179682, filed 16 May 2002.

[6] Okamoto, K., Hunt, F., and Hirano, S., "Development of Friction Stir Welding Technique and Machine for Aluminum Sheet Metal Assembly—Friction Stir Welding of Aluminum for Automotive Applications," 2005 SAE World Congress, Detroit, MI, Society of Automotive Engineers, April 2005, Paper 2005-01-1254.

[7] Addison, A. C., and Robelou, A. J., “Friction Stir Spot Welding: Principle Parameters and Their Effects,” Proceedings of the 5th International FSW Symposium, Metz, France, 14–16 September 2004, TWI Ltd., Granta Park, Great Abington, Cambridgeshire, CB1 6AL, UK.

[8] Mahoney, M. W., “Interface Preparation for Weld Joints,” U.S. Patent 6543670, 8 April 2003.

[9] Van Aken, D. C., Baumann, J. A., Lederich, R. J., and Talwar, R., “Method and Sealant for Weld Joints,” U.S. Patent 6905060, 14 June 2005.

[10] Christner, B., “Welded joints with polymer sealants,” U.S. Patent 7225966, 5 June 2007.

[11] Van Aken, D. C., and Kato, Y., “Sealants for Structural Member Joints and Methods of Using Same,” U.S. Patent Application 20070044406, 1 March 2007.

[12] Brown, J., Tweedy, B., Widener, C., Horn, W., Talia, G., and Burford, D., “The Effect of Surface Treatments on the Faying Surface of Friction Stir Spot Welds,” *Friction Stir Welding and Processing IV*, R. S. Mishra, M. W. Mahoney, T. J. Lienert, and K. V. Jata, Eds., The Minerals, Metals & Materials Society (TMS), Warrondale, PA, 2007, ISBN 978-0-87339-661-5, pp. 333–340.

[13] Brown, J. Burford, D. Horn, W., and Talia, G. “Evaluation of Swept Friction Stir Spot Welding Through Sealants and Surface Treatments,” 8th International Conference on Trends in Welding Research™, 2–6 June, 2008, Pine Mountain, Georgia.

[14] Tweedy, B. M., Sellmeyer, S., Jahn, A., and Burford, D. A., “Static Strength Comparison of Riveted versus Friction Stir Welded Stiffened Panels,” 1–4 May 2006, 47th AIAA/ASME/ASCE/AHS/ASC Structures, Structural Dynamics, and Materials Conference, Newport, Rhode Island, Paper AIAA-2006-2266.

[15] Tweedy, B. M., Widener, C. A., Merry, J. D., Brown, J. M., and Burford, D. A., “Factors Affecting the Properties of Swept Friction Stir Spot Welds,” Paper 08M-178, 2008 SAE World Congress, Detroit, MI, Society of Automotive Engineers, April 16, 2008 (to be published).

[16] Smith, B. L., Shivalli, P., and Kumar, B., “The Effect of Dents on the Stable Crack Growth in 2024-T3 Bare Sheet Aluminum Alloy under Constant Amplitude Loading,” 6th AIAA Aviation Technology, Integration and Operations Conference (ATIO), 25–27 September 2006, Wichita, KS, AIAA Paper 2006-7728.

[17] http://www.gom.com/EN/measuring.systems/aramis/system/system.html, Last accessed February 2008.

[18] Lambda Research Report No. 1418-13874, 10 October 2007.

[19] Koistinen, D. P., and Marburger, R. E., “A Simplified Procedure for Calculating Peak Position in X-Ray Residual Stress Measurements on Hardened Steel,” *Trans. ASM*, Vol. 51, 1959, pp. 537–550.

[20] Moore, M. G., and Evans, W. P., “Mathematical Correction for Stress in Removed Layers in X-Ray Diffraction Residual Stress Analysis,” *Trans. SAE*, Vol. 66, 1958, pp. 340–345.

ASTM Special Technical Publication, Vol. 5, No. 5
Paper ID JAI101544
Available online at www.astm.org

Allison Nolting,[1] *Leon M. Cheng,*[1] *and James Huang*[1]

Mechanical Evaluation of Mixed As-Cast and Friction Stir Processed Zones in Nickel Aluminum Bronze

ABSTRACT: The performance of nickel aluminum bronze (NAB) propellers can be limited by the resistance of the alloy to fatigue. Friction stir processing (FSP) is a potential method for improving the fatigue life and fracture toughness of this material through grain structure refinement. As friction stir processing is a surface treatment, as-cast, thermo-mechanically affected zone (TMAZ), and FSP zone microstructures can all occur in components with thick cross sections and when FSP is performed on only selected areas of the component surface. The boundary between modified and unmodified microstructures produced by traditional processing techniques (i.e., heat affected zones produced by welding) are often the source of in-service failures as they can contain defects, residual stresses, deleterious microstructures or any combination thereof. In this paper, the mechanical behavior of FSP nickel aluminum bronze specimens containing as-cast, TMAZ, and FSP microstructures are evaluated using monotonic tensile tests and rotating bending fatigue tests. Analysis of the fatigue specimen fracture surfaces indicate that fatigue cracks initiated and propagated through the as-cast microstructure before penetrating the TMAZ and the FSP microstructures. The tensile specimens failed in the as-cast structure away from the FSP zone and the TMAZ. These results indicate that the as-cast material is weaker than both the FSP and the TMAZ, implying that localized friction stir processing is not detrimental to the mechanical behavior of a NAB component, even in the boundary region.

Manuscript received November 9, 2007; accepted for publication April 3, 2008; published online May 2008.
[1] Defence Scientists, Defence R&D Canada–Atlantic, 9 Grove St., Dartmouth, Nova Scotia, Canada.

Citation: Nolting, A., Cheng, L. M., and Huang, J., "Mechanical Evaluation of Mixed As-Cast and Friction Stir Processed Zones in Nickel Aluminum Bronze," *J. ASTM Intl.*, Vol. 5, No. 5. DOI10.1520/JAI101544. Available online at www.astm.org. Also included in JAI Special Issue STP 1508, *Fatigue and Fracture Mechanics: 36th Volume,* R. W. Neu, K. R. W. Wallin, and S. R. Thompson, guest editors, ASTM International, West Conshohocken, PA, 2009, pp. 743-760.

KEYWORDS: friction stir processing, nickel aluminum bronze, fatigue, metallography, tensile

Introduction

Friction stir processing (FSP) is a potential method to locally enhance the mechanical properties of nickel aluminum bronze (NAB). It has been shown that FSP can significantly improve the strength of the material [1–3]. However, in other processing techniques, the boundary region is often the source of in-service failure. The purpose of this work is to investigate whether the presence of a mixed microstructure will be detrimental to the overall mechanical performance of a NAB component.

Nickel aluminum bronze alloys have essentially replaced manganese bronzes in the production of ship propellers because they have higher strength and resistance to erosion and cavitation damage than other bronze alloys. The composition of a C95800 bronze, which is commonly used for ship propellers, is given in Table 1. NAB has a complex microstructure that is sensitive to cooling rate and includes many different phases. Large components, such as propellers, often experience slow cooling rates [1], resulting in microstructures that are similar to those obtained by equilibrium cooling conditions. The final microstructure of equilibrium cooled NAB contains mainly fcc α phase and lamellar α and Ni rich κ_{iii} eutectoid [5,6]. Other κ phases can be present, including globular κ_{ii} (which is nominally Fe_3Al and is located at grain boundaries) and fine κ_{iv} (which is nominally Fe_3Al and precipitates in the α phase) [5,6].

Friction stir processing is used to locally alter the microstructure of NAB from as-cast to wrought without causing gross deformation of the component geometry. The friction stir processed microstructure has higher yield and ultimate tensile strength (UTS), and shorter fracture elongations, than the as-cast microstructure [1–4]. Friction stir processing can be used to locally increase the strength of a component in high stress areas and to eliminate casting defects, such as porosity. It is conducted by forcing a rotating pin tool into the surface of an alloy [2,4,6,7]. The movement of the tool causes adiabatic and frictional heating that soften the work piece material and allows the movement of the pin to break up and refine the α phase. If the temperature in the stir zone (SZ) exceeds approximately 800°C, then the eutectoid microstructure transforms to bcc β phase during processing [2,4]. The cooling rate after FSP is faster than during the casting process, resulting in transformed β phase between the α

TABLE 1—*Composition of C95800 Nickel Aluminium Bronze* [*4*].

	element (wt. %)						
	Cu	Al	Ni	Fe	Mn	Si	Pb
Min/max	79.0 min	8.5–9.5	4.0–5.0	3.5–4.5	0.8–1.5	0.10 max	0.03 max
Nominal	81	9	5	4	1	–	–
Typical	81.2	9.39	4.29	3.67	1.20	0.05	<0.005

phase, instead of eutectoid microstructure [4]. The SZ is surrounded by a thermo-mechanically affected zone (TMAZ) that contains distorted α phases that are approximately the same size as the α phase in the as-cast material [6]. The distortion of the α phases varies around the FSP zone and is considerably different between the advancing and retreating sides of the processed zone. Depending on the temperature and concurrent deformation in the TMAZ zone during FSP, the eutectoid microstructure can revert to transformed β structure.

Friction stir processing can be used to improve the mechanical properties of castings in areas subject to high stresses or cyclic loading, such as the root of propeller blades. The reduction of defects (such as porosity) and the refinement of grain structure caused by friction stir processing can result in improved performance and fatigue life for FSP components. Palko et al. [1] conducted tensile tests on as-cast and FSP Ni Al bronze, and found 100 % and 90 % increases in the yield and ultimate strengths, respectively. The increased strength was accompanied by a 30 % decrease in the ductility of the material. Fuller et al. [2] performed tensile tests on undersized specimens taken from different locations in a piece of FSP Ni Al bronze. They reported a 100–150 % increase in the yield strength of the FSP material as compared to the as-cast structure. The ultimate strength improved by approximately 50 %, and the ductility was found to be lowest in the TMAZ. In a separate paper, Fuller et al. [3] reported that FSP resulted in yield strength increases between 140 % and 172 % and ultimate strength increases between 40 % and 134 %.They also conducted rotating bending and uniaxial fatigue tests on FSP and as-cast Ni Al bronze. They found significant increases in the fatigue lives of the specimens that had been friction stir processed. The percentage increase cannot be reported, as the FSP specimens did not fail at stress ranges that corresponded to fatigues lives of approximately 10^4 cycles in the as-cast specimens.

The open literature indicates that there are very significant benefits to be gained from using FSP. However, before implementing this technology into expensive and critical components, such as ship propellers, it is important to assess the potential risks associated with the technology. The friction stir process creates high thermal and strain gradients in the TMAZ [3,4]. Temperature gradients in the heat affected zones of conventional processes such as welding can result in the creation of residual stresses and the evolution of unfavorable microstructures that can cause in-service fatigue, corrosion damage, or both. The high temperature and strain gradients seen in the TMAZ have the potential to produce residual stresses, microstructures, or a combination of the two which could serve as initiation sites for fracture or fatigue cracks. As FSP is a localized process, areas that contain as-cast, TMAZ, and FSP microstructures (referred to as mixed-microstructure specimens) are unavoidable and will be present at the edge of the processed area. In a proper design, the areas of mixed microstructure should be located in areas of low stress; however, poorly designed or conducted FSP could result in the presence of mixed microstructures in areas subjected to high stresses. It is important to determine if the presence of mixed microstructures will diminish the overall mechanical behavior, potentially resulting in accelerated damage evolution. This work examines the mechanical properties mixed-microstructure FSP NAB specimens in order to assess the risk associated with the implementation of this technology.

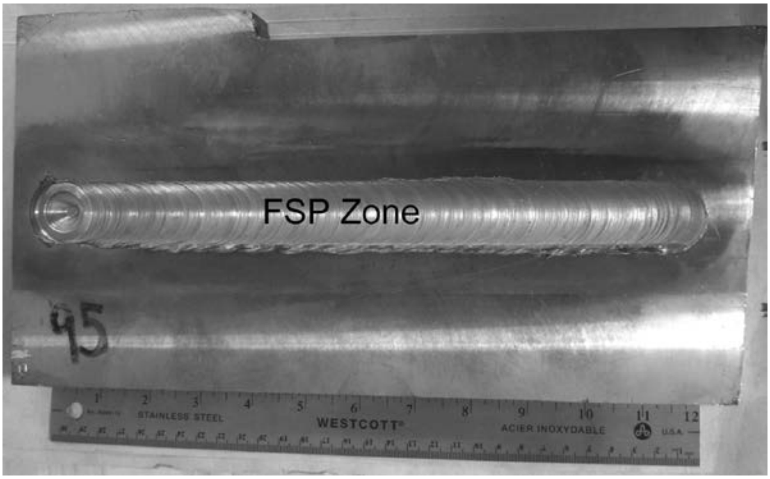

FIG. 1—*Friction stir processed cast NAB plates.*

Test Methods

Friction Stir Processed Plates

Three 356 by 152 by 25 mm cast UNS C95800 nickel aluminum bronze plates (Fig 1) were supplied by the Naval Surface Warfare Centre, Carderock MD (NSWC Carderock). The chemistry of the plates met MIL Standard MIL-B-24480A. Double-pass friction stir processing was performed by NSWC along the centerline of each of the plates using a half-inch stepped spiral Densimet® pin tool. A polished cross section of a friction stir processed plate is shown in Fig. 2.

Metallography

Metallographic specimens were sectioned with a diamond blade precision saw and mounted in Bakelite. The surfaces were polished to a 0.25 μm finish and etched with a solution composed of 5 g of $FeCl_3$, 5 mL of HCl, and 100 mL of H_2O. The specimens were examined with an Olympus PMG3 inverted research metallurgical microscope.

Tensile Testing

The tensile test specimens are shown in Fig. 3. Tensile tests were conducted in a closed-loop Instron 8801 100 kN servo-hydraulic load frame at a constant displacement rate of 0.04 mm/s. The global strain in the specimens was monitored using an extensometer with a gage length of 25.4 mm. To measure the localized strain in the FSP region, a strain gage (Micromeasurements Group, Model # CEA-06-125UW-120) was bonded to the specimen in the middle of the FSP zone, as shown in Fig. 4(*a*). A strain gage was also bonded to the opposite

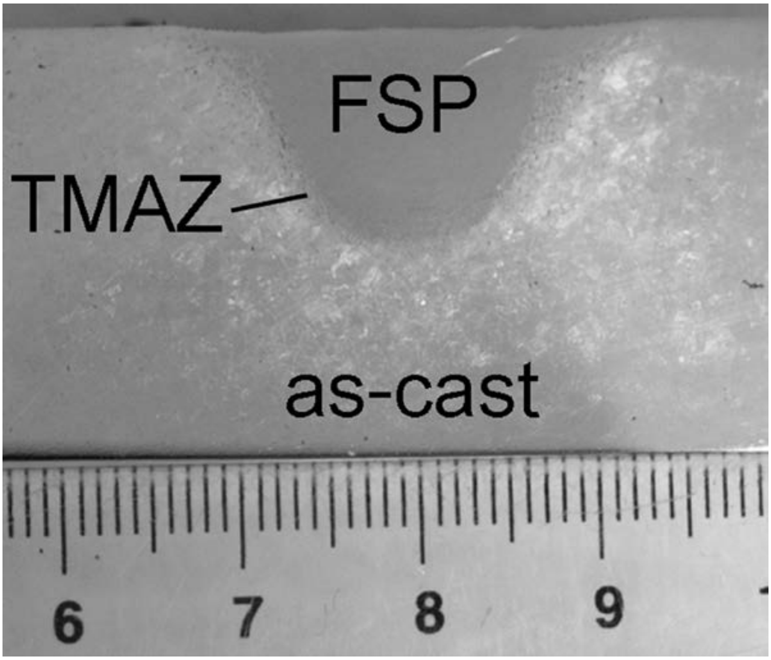

FIG. 2—*Cross section of the NAB plate.*

face of the specimen (Fig. 4(*a*)). The strain gage located on the FSP zone will be referred to as the "front gage" and the other strain gage will be referred to as the "back gage." The FSP zone was located by polishing and lightly etching one side of the tensile specimen to reveal the FSP zone cross section. Load and strain gage signals were monitored using a DAQBook 2000 data acquisition

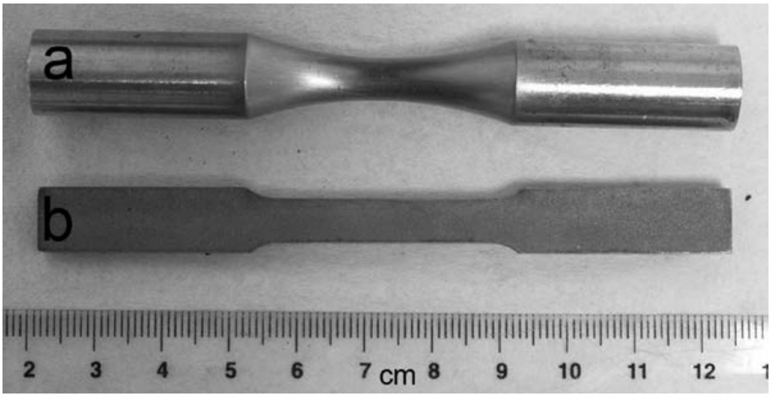

FIG. 3—*Test specimen geometry:* (*a*) *rotating bending fatigue specimen and* (*b*) *tensile test specimen.*

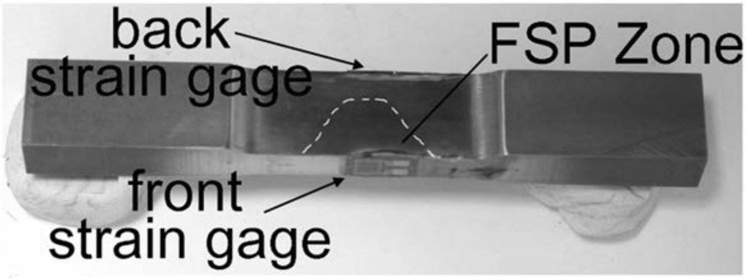

(a)

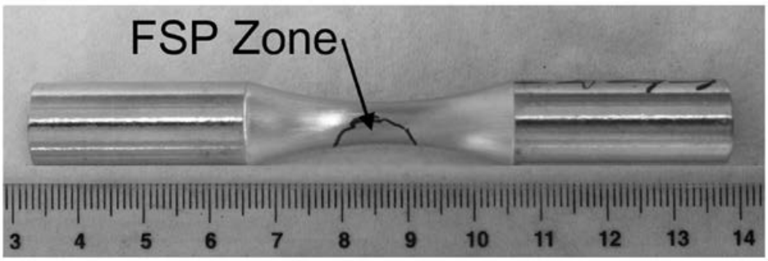

(b)

FIG. 4—*Location of FSP area on:* (*a*) *tensile test specimens and* (*b*) *fatigue test specimens.*

system with a DBK43A eight-channel strain gage module and DAQView™ software. Two as-cast specimens were also strain gaged in order to verify the data acquisition system.

The tensile specimen shown in Fig. 4(*a*) is 15 mm thick and has a FSP zone with a maximum depth equivalent to 66 % of the specimen thickness. Two other mixed-microstructure tensile specimens were tested. The specimens were 9 mm thick and had maximum FSP zone depths that were 13 % and 28 % of the specimen thickness, respectively. The mixed-structure specimens will be referred to in further discussions by these percentages.

Fatigue Testing

The rotating bending fatigue specimens shown in Fig. 3 were machined in accordance to ASTM E466-96 [8]. The approximate location of the FSP zone within a typical fatigue specimen is shown in Fig. 4(*b*). A polished and etched cross section taken from the middle of the gage section of a mixed-structure fatigue specimen is shown in Fig. 5. As the maximum stresses in a rotating bending fatigue specimen are located at the surface of the gage section, it is important that all three microstructures (FSP, TMAZ, and as-cast) be present on the surface of the specimen. Fig. 5 confirms that this is indeed true.

Fatigue testing was conducted on an RBF-200 model rotating bending fa-

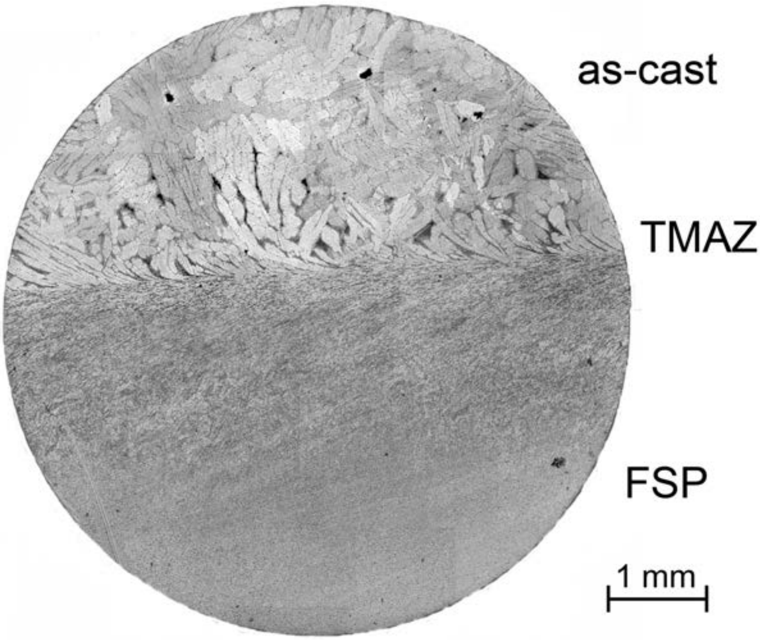

FIG. 5—*Optical photography montage of the entire cross section of a FSP fatigue specimen taken near the middle of the gage section.*

tigue tester manufactured by Fatigue Dynamics Inc. Tests were conducted at approximately 600 rpm and failure was defined by the deflection of the applied load on the test apparatus. Complete separation of the specimens did not occur before this deflection was exceeded. The hydraulic load frame was used to separate some of the specimens for fractographic evaluation. Examination of the fracture surfaces was conducted with a stereomicroscope and a scanning electron microscope. Other specimens were sectioned along the axis of the specimen in order to observe the path of the fatigue crack through the microstructure.

Results

Metallography

An optical micrograph of the as-cast structure is shown in Fig. 6. The microstructure shows large areas of primary α phase (light etch) containing fine κ_{iv} precipitates. The α phase is surrounded by lamellar α and κ_{iii} phases, and globular κ_{ii} precipitates are found near the α grain boundaries. Micrographs taken in the FSP zone (Fig. 7) show that the microstructure was homogenized and refined. The lamellar α and κ_{iii} eutectoid was replaced with transformed β structure, and the κ_{iv} precipitates were not observed in the α phase during

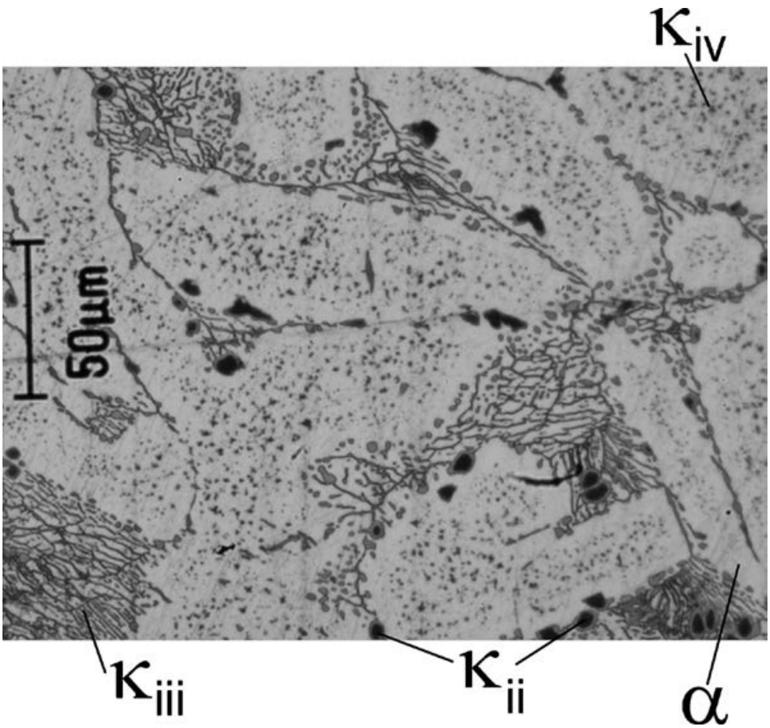

FIG. 6—*Typical microstructure of the as-cast* Ni Al *bronze plates.*

examination with an optical microscope up to 200× magnification. The microstructural changes indicate that the temperature in the FSP was sufficient to transform the eutectoid microstructure (approximately 860°C for C95800).

A montage of micrographs showing the transition from the FSP zone to the as-cast microstructure at the bottom of the FSP zone is presented in Fig. 8. The microstructure in the TMAZ has been distorted by the friction stir processing but the maximum diameter of the α phases remain essentially the same size as in the as-cast microstructure. A closer view of the TMAZ is shown in Fig. 9. The eutectoid microstructure has evolved into transformed β in areas close to the FSP zone; however, the κ_{iv} precipitates are still present in the primary α. This indicates that the maximum temperatures in the TMAZ were between approximately 800°c and 860°C.

Tensile Tests

The global stress-strain curves for the as-cast and mixed microstructure specimens are shown in Fig. 10. A summary of the mechanical properties obtained from the three tensile tests is given in Table 2. Although there was a negligible difference in the yield strength of the specimens with 13 % and 28 % FSP zones, the yield strength generally increased with increasing percentage of FSP

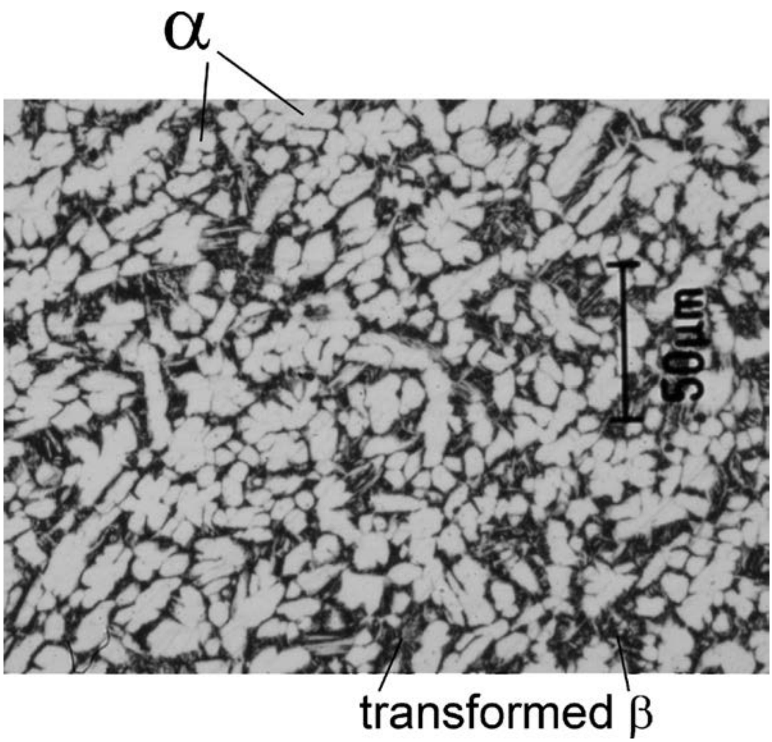

FIG. 7—*Typical FSP microstructure.*

microstructure. The elongation at fracture decreased with increasing FSP microstructure. The average ultimate tensile strength (UTS) was essentially the same for the as-cast and mixed-microstructure specimens.

The strain gages used to obtain localized stress-strain curves debonded from the specimens before completion of the tensile tests. Therefore, only the initial portion of the localized stress strain curve was captured. The data obtained from the 13 % FSP zone mixed-microstructure specimen, which are typical of all the mixed-microstructure tensile tests, are shown in Fig. 11. The discrepancy in the initial slope of the stress-strain curves for the different strain monitoring devices was an artifact of the data acquisition systems, and was also observed on the strain-gaged as-cast specimens. The stress-strain curves from the global and back strain gage yielded at approximately the same stress. The front strain gage, which was located on the FSP microstructure, did not yield before the strain gage debonded. The yield stress of the as-cast NAB specimens were measured to be approximately 210 MPa. Based on the range of yield strength increases reported by Palko et al. [1] and Fuller et al. [3] (90 % to 173 %, respectively) the FSP microstructure is estimated to have a yield strength between 400 MPa and 570 MPa. This indicates that the FSP microstructure experienced very little, if any, yielding during the tensile test. Observation of the 66 % FSP mixed-structure specimen after tensile testing supports

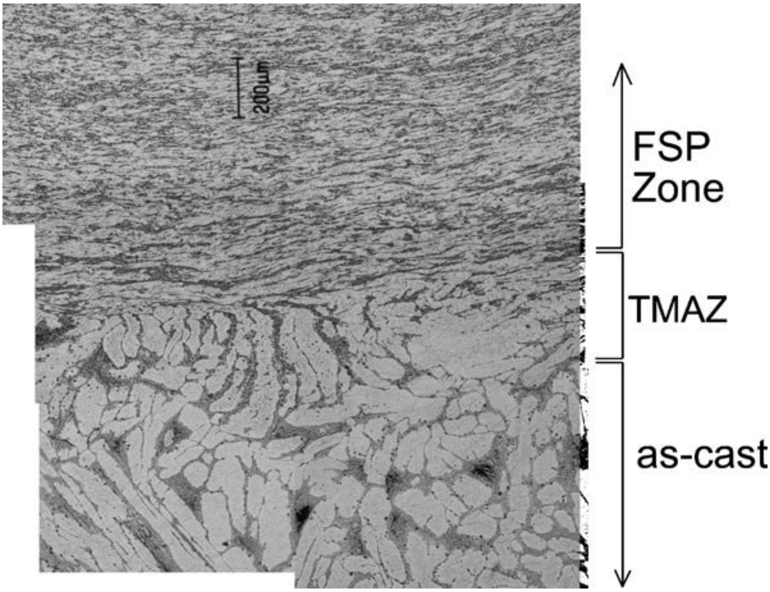

FIG. 8—*Optical microscopy montage of the microstructure at the interface between the as-cast and FSP zones.*

this assumption. After tensile testing, the 66 % FSP specimen showed "orange peel" texture on the surface of the as-cast material. The dimensions of the FSP zone appeared to be unaffected by the test (Fig. 12). The thickness of the gage section in the purely as-cast material after testing was 13.8 mm, while it was 14.4 mm at the location with the highest percent FSP zone, indicating that the strain was localized in the as-cast microstructure. The difference in the strain between the FSP zone and the as-cast material will produce a high strain gradient in the TMAZ, which has the potential to act as a fracture initiation site. The 13 % and 28 % FSP mixed-structure specimens both fractured near the edge of the FSP zone; however, the 66 % FSP mixed-structure specimen failed away from the FSP zone. Fracture surfaces of the 66 % and 13 % FSP mixed-microstructure specimens were similar to the fracture surfaces of the fully as-cast specimens, indicating that failure occurred in the as-cast microstructure.

The mechanical behavior of the mixed-microstructure tensile specimens fell between that of the as-cast and FSP microstructures. However, the UTS was similar in the as-cast and mixed-microstructure specimens. Strain was concentrated and failure occurred in the as-cast microstructures. This implied that the as-cast material has the weakest microstructure and that the tensile performance of the mixed microstructures is as good as, if not better than, that of the as-cast NAB.

Fatigue Tests

The results of the rotating bending fatigue tests conducted on specimens with fully as-cast microstructure and mixed microstructure are shown in Fig. 13.

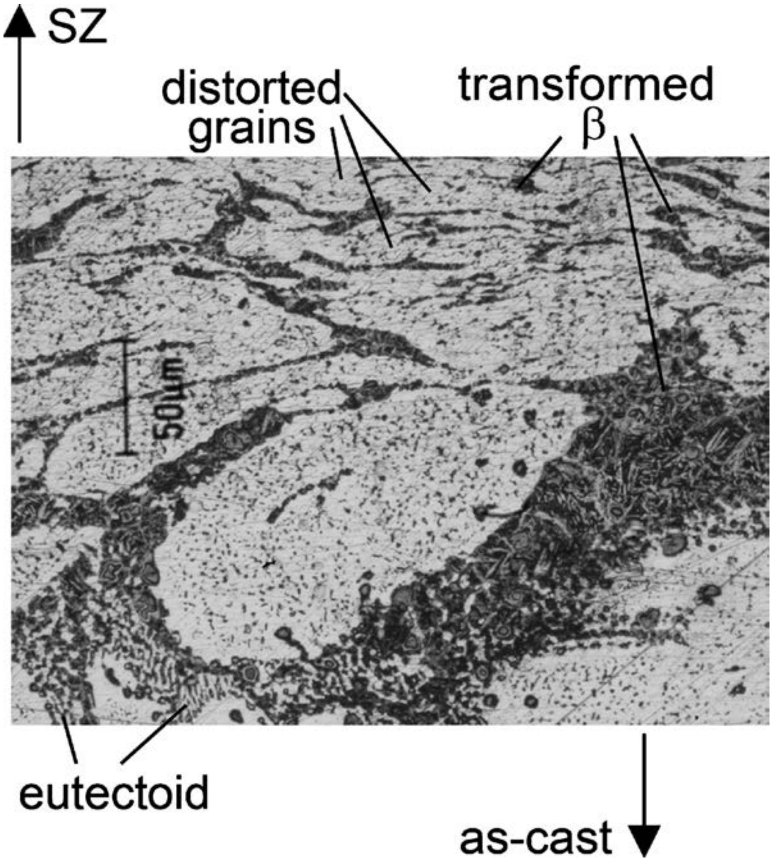

FIG. 9—*Typical microstructure in the thermo-mechanically affected zone.*

Data reported by Fuller et al. [3] for fully as-cast and fully FSP microstructures are also included in Fig. 13. The fatigue lives of the as-cast specimens from this body of work and Ref. [3] are in good agreement. The mixed-microstructure specimens have approximately twice the fatigue life of the as-cast specimens at maximum stresses above 250 MPa. Below 250 MPa, the fatigue lives were approximately the same for the as-cast and mixed-microstructure specimens. The mixed-microstructure performs as well as, if not better than, the purely as-cast specimens, indicating that the presence of the TMAZ and mixed microstructure are not detrimental to the overall fatigue behavior of the material. The data for the fully FSP microstructure specimens reported by Fuller et al. [3] indicate that significant improvements in fatigue life can be realized by the implementation of FSP. It should be noted that Fuller et al. [3] tested FSP specimens manufactured with a variety of processing parameters, which is why the FSP data produced by Fuller et al. [3] appears to have significant scatter.

The fracture surfaces of some of the fatigue specimens were observed under a scanning electron microscope. Representative micrographs of the as-

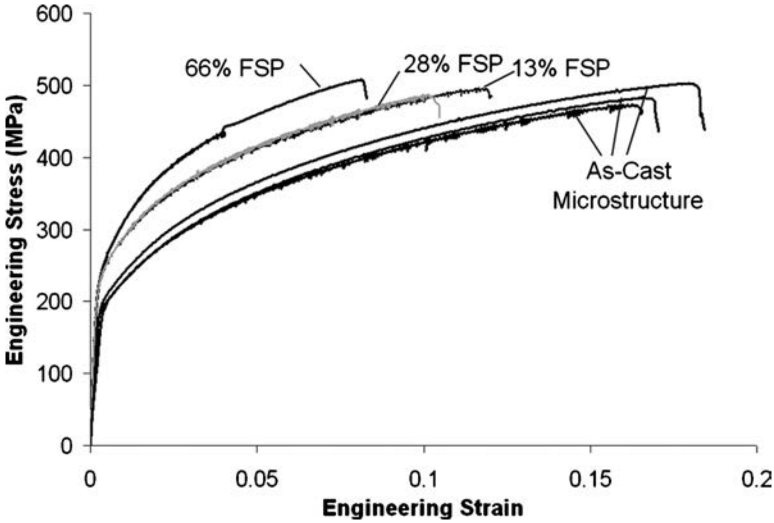

FIG. 10—*Global stress-strain curves for the as-cast and mixed-structure specimens.*

cast and mixed-microstructure fracture surfaces are shown in Figs. 14 and 15, respectively. The arrows on Figs. 14(*a*) and 15(*a*) indicate the fatigue crack initiation sites and the dashed line in Fig. 15(*a*) encompasses the area of fatigue crack growth. Fig. 14(*b*) shows the ductile fatigue propagation in an area far from the fatigue crack initiation, while Figure 14(*c*) shows an area close to the fatigue crack initiation where striations are present. The fatigue crack in the mixed-microstructure specimen (Fig. 15(*a*)) initiated in the as-cast microstructure and propagated into the FSP microstructure. The fracture surface produced by the propagation of the fatigue crack in the as-cast microstructure is

TABLE 2—*Summary of mechanical properties of the as-cast and mixed-microstructure specimens.*

Specimen	Yield strength, MPa	UTS, MPa	Fracture elongation %
As-cast #1	208	484	17
As-cast #2	213	488	18
As-cast #3	210	457	17
13 % FSP (mixed microstructure)	245	496	12
28 % FSP (mixed microstructure)	244	487	10
66 % FSP (mixed microstructure)	250	508	8

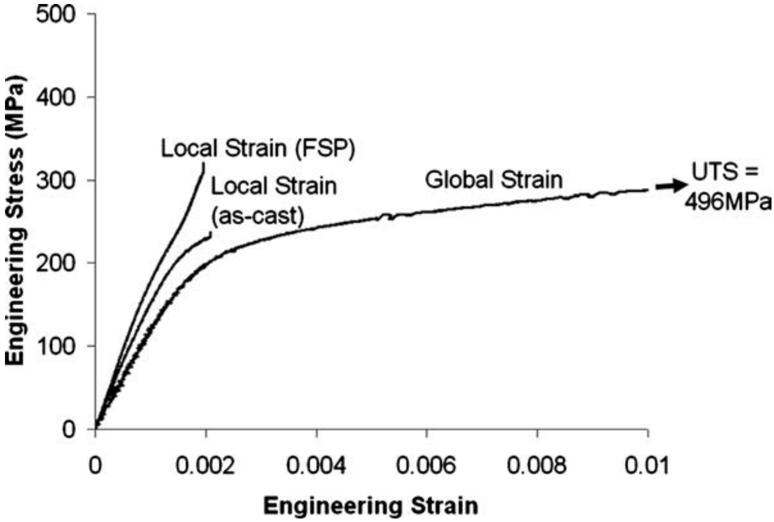

FIG. 11—*Localized and global stress strain curves for the* 13 % *FSP mixed-structure specimen.*

shown in Fig. 15(*b*). The transition from the as-cast to the FSP microstructures is shown in Fig. 15(*c*). A fractograph taken from where the crack propagated into the FSP material is shown in Fig. 15(*d*).

The fatigue crack initiation sites were located by fractographic examination using a scanning electron microscope and by observation of the gage sections during testing. In both the as-cast and mixed-microstructure specimens, fatigue cracks were only observed to initiate in the as-cast structure. Multiple fatigue cracks were often observed in the gage length of the specimens after the fatigue tests were completed. Typically, multiple initiation sites are more likely to occur at long fatigue lives; however, they were observed on specimens that had fatigue lives as low as 10^4 cycles. The multiple initiation sites might be attributed to a microstructural feature in which fatigue cracks can easily ini-

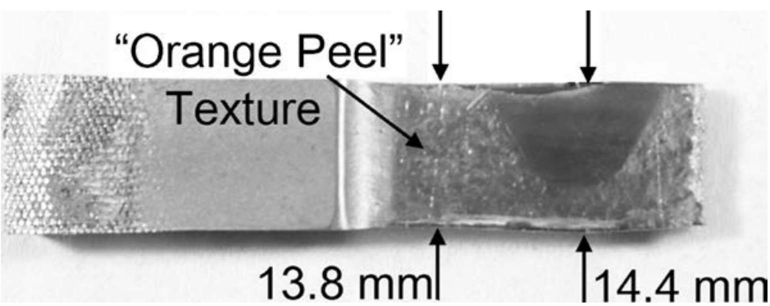

FIG. 12—66 % *FSP mixed-structure specimen after tensile testing* (*surface polished at etched prior to testing*).

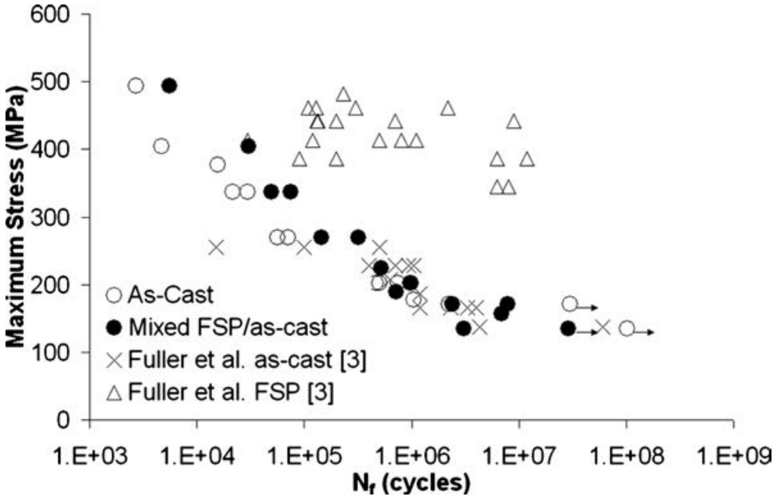

FIG. 13—*Rotating bending fatigue test results.*

tiate. The presence of this feature at multiple sites on the surface of the specimen could lead to multiple crack initiation sites. It was also observed that the fatigue cracks followed very crooked paths through the as-cast microstructure. This implies that the cracks followed a path of least resistance through a weak microstructural feature. A few of the fatigue specimens were longitudinally sectioned to observe the path of the fatigue cracks through the microstructure. Figure 16 shows two fatigue cracks in the gage section of an as-cast fatigue specimen. The crack appeared to follow a path mainly through the eutectoid structure (marked in white), resulting in crooked propagation path as the crack diverted to follow the eutectoid microstructure. Propagation through the α phase often occurred at angles that minimized the length of the path through the α phase. This indicates that the eutectoid is the weakest microstructure in the NAB with respect to fatigue initiation and propagation. It is possible that the transformation of the coarse eutectoid microstructure to high temperature β (during processing) then to fine β transformation products (after cooling) in the SZ and part of the TMAZ increases the resistance to crack initiation and propagation in these microstructures. This is supported by the observation that fatigue cracks did not initiate in the TMAZ or FSP microstructures. A cross section of a fatigue crack that has propagated into the FSP microstructure is shown in Fig. 17. The path of the crack is considerably straighter than in the as-cast microstructure, and travels through both the α and the transformed β microstructures.

Conclusions

The results of the tensile and fatigue testing indicated that the bulk tensile and fatigue properties of the mixed-microstructure specimens fall between those of as-cast and the fully FSP microstructures. This indicates that, with the excep-

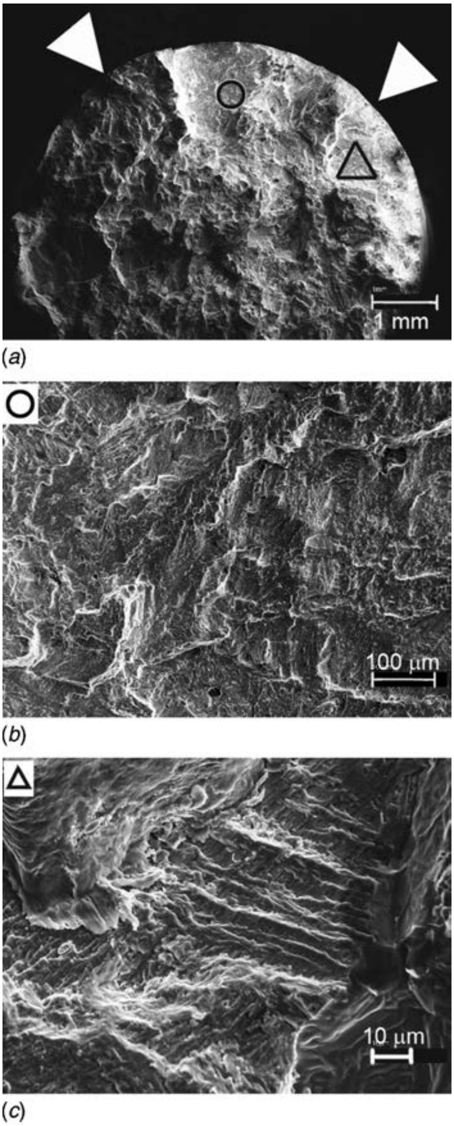

FIG. 14—(*a*) *Fracture surface of a typical as-cast rotating bending fatigue specimen.* (*b*) *Higher magnification of the fracture surface near "O" on* (*a*). (*c*) *Higher magnification view of the fracture surface near "Δ" on* (*a*).

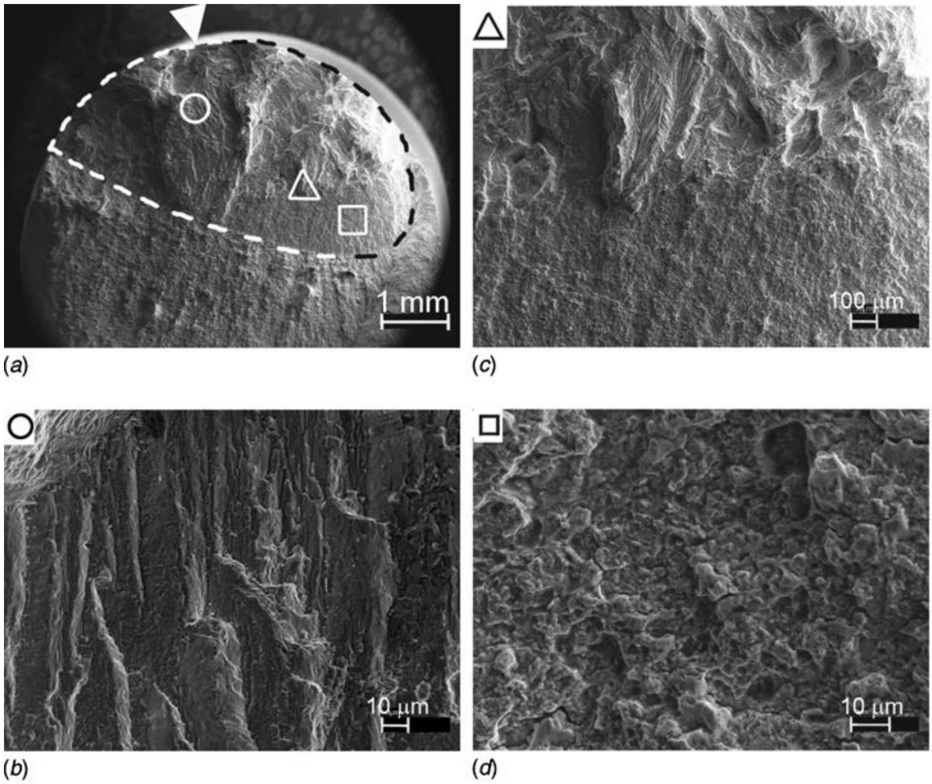

FIG. 15—(*a*) *Fracture surface of a typical mixed microstructure rotating bending fatigue specimen and higher magnification views* (*b*) *in the as-cast microstructure near "O" on* (*a*), (*c*) *in the transition from as-cast to FSP microstructures near "Δ" on* (*a*), *and* (*d*) *in the FSP microstructure near "◇" on* (*a*).

tion of elongation, the mechanical behavior of the mixed microstructure is as good as, if not better than, the as-cast material. Of the FSP, TMAZ, and as-cast microstructures present in the mixed-microstructure specimens, tensile failure and fatigue crack initiation were observed to occur in the as-cast microstructure. This implies that the TMAZ microstructure is stronger and more fatigue resistant than the as-cast microstructure and that any microstructural changes or residual stresses that may be present in the TMAZ do not have a significant determental affect on the mechanical behavior of the bulk material. Consequently, if mixed microstructures are present in areas of high stress, the mechanical behavior would be at least as good as, if not better than, the mechanical behavior of the as-cast microstructure. This research helps to clarify how FSP NAB will perform in a real component where the FSP is performed locally at areas of high stress.

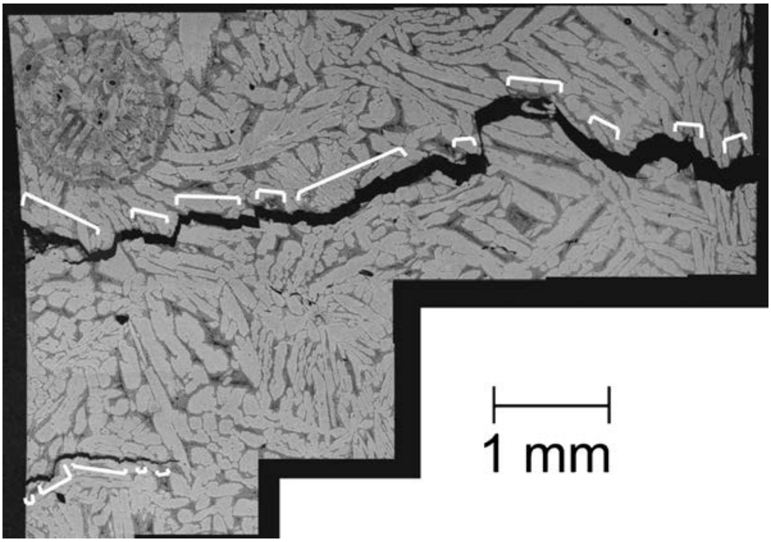

FIG. 16—*Cross section of a fatigue crack which propagated through as-cast structure.*

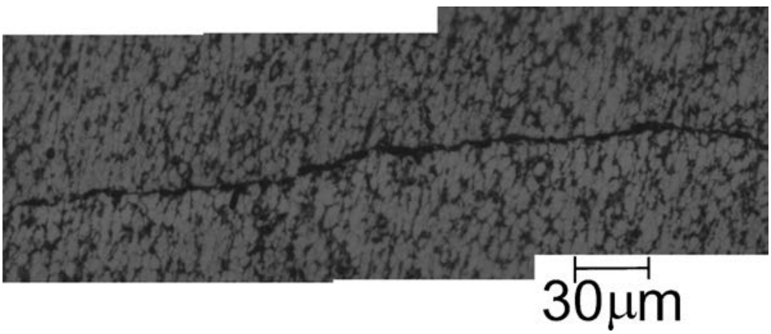

FIG. 17—*Cross section of a fatigue crack that propagated through the SZ of a mixed-microstructure specimen.*

Acknowledgments

The authors would like to thank Dr. Julie Christodoulou of the US Office of Naval Research, and the Naval Surface Warfare Centre, Carderock Division for supplying the FSP material. We would also like to thank Patricia Fraser for her assistance in conducting the testing.

References

[1] Palko, W. A., Fielder, R. S., and Young, P. F., "Investigation of the Use of Friction Stir Processing to Repair and Locally Enhance the Properties of Large Ni Al Bronze Propellers," *Mater. Sci. Forum*, Vol. 426–432, 2003, pp. 2909–2914.

[2] Fuller, M. D., Swaminathan, S., Zhilyaev, A. P., and McNelley, T. R., "Microstructural Transformations and Mechanical Properties of Cast Ni Al Bronze: Effects of Fusion Welding and Friction Stir Processing," *Mater. Sci. Eng., A*, Vol. 463, 2007, pp. 128–137.

[3] Fuller, C. B., Mahoney, M. W., Bingel, W. H., Calabrese, M., and London, B. "Tensile and Fatigue Properties of Friction Stir Processed Ni Al Bronze," *Mater. Sci. Forum*, Vol. 539–543, 2007, pp. 3751–3756.

[4] Culpan, E. A. and Rose, G., "Microstructural Characterization of Cast Nickel Aluminium Bronze," *J. Mater. Sci.*, Vol. 13, 1978, pp. 1647–1657.

[5] Oh-Ishi, K. and McNelley, T. R., "Microstructural Modification of As-Cast Ni Al Bronze by Friction Stir Processing," *Metall. Mater. Trans. A*, Vol. 35A, 2004, pp. 2951–2961.

[6] McNelley, T. R., Oh-Ishi, K., and Zhilyaev, A. P., "Microstructures and Properties of Copper Alloys After Friction Stir Welding/Processing," in *Friction Stir Welding and Processing*, R. S. Mishra, and M. W. Mahoney, Eds., ASM International, Materials Park, OH, 2007, Chap. 8, pp. 155–174.

[7] Oh-Ishi, K., Zhilyaev, A. P., and McNelley, T. R., "A Microtexture Investigation of Recrystallization During Friction Stir Processing of As-Cast NiAl Bronze," *Metall. Mater. Trans. A*, Vol. 37A, July 2006, pp. 2239–2251.

[8] ASTM Standard E466-96, "Standard Practices for Conducting Force Controlled Constant Amplitude Axial Fatigue Tests of Metallic Materials," ASTM International, West Conshohocken, PA, 2000.

ASTM Special Technical Publication, Vol. 5, No. 5
Paper ID JAI101559
Available online at www.astm.org

A. E. Nolting,[1] *P. R. Underhill,*[1] *and D. L. DuQuesnay*[1]

Fatigue Behavior of Adhesively Bonded Aluminium Double Strap Joints

ABSTRACT: The fatigue life and failure mode of double strap joints constructed from bare and clad aluminum alloys were examined. Substrate failures were found to occur at lower stress levels, while the failure mode at higher stresses was debonding of the patches. The stress/strain state at the edge of the patch was altered by changing the patch thickness, patch modulus, or by tapering the edges of the patch. The specimens were modeled using finite element analysis. The results of the finite element analysis revealed a power law relationship between fatigue life and either the peak principal strain in the adhesive for adhesive failures, or the nominal axial stress in the substrate for substrate failures. The fatigue life and failure mode of a double strap joint specimen can be determined by calculating the failure life for that specimen under adhesive and substrate failure. The failure mode with the shortest life will indicate the failure mode and fatigue life of that specimen.

KEYWORDS: fatigue, adhesive, finite element, aluminum, cladding

Background

As both commercial and military aircraft are being used beyond their intended service lives, there has been considerable research into the management of damage caused by fatigue cracks, corrosion, or both. Inspections for weakened areas have been incorporated into regular maintenance routines and damage tolerance analysis techniques are used to evaluate the impact of corrosion and fatigue cracks on the safe operation of the aircraft. Many techniques have been

Manuscript received November 12, 2007; accepted for publication April 3, 2008; published online May 2008.
[1] Emerging Materials Section, Defence R&D Canada-Atlantic, 9 Grove St., Dartmouth, NS B3A 3C5 Canada.

Citation: Nolting, A. E., Underhill, P. R., and DuQuesnay, D. L., "Fatigue Behavior of Adhesively Bonded Aluminum Double Strap Joint," *J. ASTM Intl.*, Vol. 5, No. 5. DOI10.1520/JAI101559. Available online at www.astm.org. Also included in JAI Special Issue STP 1508, *Fatigue and Fracture Mechanics: 36th Volume,* R. W. Neu, K. R. W. Wallin, and S. R. Thompson, guest editors, ASTM International, West Conshohocken, PA, 2009, pp. 761-777.

developed to repair damaged areas, one of which is the application of patches to restore stiffness and strength. Patches can be attached to the aircraft using mechanical fasteners or adhesives. Mechanical fasters (e.g., rivets) require additional holes that can further weaken the structure and can serve as initiation sites for future in-service damage. Crevice corrosion can occur in the space between the patch and the structure. Attaching a patch with adhesives can avoid the need to drill extra holes, and can prevent crevice corrosion by sealing the gap between the patch and the structure. Concerns of patch delamination caused by failure at the adhesive-substrate interface [1] has lead to the perception that adhesively bonded patches are less reliable than mechanically fastened patches. However, since no additional holes are drilled in the application of the adhesively bonded patch, the aircraft is no worse off then it was before the repair was made. As damage tolerance analysis currently does not include the increase in life gained by the presence of the patch, this theoretically would not pose a threat to the safe operation of the aircraft, provided the delamination was detected. Developments in the durability and strength of adhesive bonds have led some researchers to suggest that the presence of the patches should be incorporated into damage tolerance analysis [1]. If this practice is to be adopted, it is necessary to have a very thorough understanding of how and when adhesively bonded patches can fail.

When conducting damage tolerance analysis of patch repairs on clad aluminum substrates, the effect of the cladding layer on the fatigue life of the aluminum must be considered. Cladding is applied to structural alloys, such as the 2xxx and 7xxx series aluminum alloys, to provide corrosion protection. The cladding layers are soft, near pure aluminum alloys, which are anodic to the substrate aluminum. The presence of a cladding layer on a structural aluminum alloy changes the crack initiation location of the material from large silicon and iron containing precipitates [2–6] in the structural alloy to the soft cladding layer [2,7,8]. This results in an overall decrease in the fatigue life through a decrease in the time to crack initiation [2,7–10] and a decrease in the endurance limit in the clad aluminum alloys. Multiple crack initiation is also likely to be observed on clad aluminum alloys [2,7,9].

It has also been observed by DuQuesnay et al. [11] and Aakkula and Saarela [12] that the presence of a cladding layer on bonded aluminum joints can switch the failure mode of the joints from adhesive failure to failure of the substrate material. In both studies, substrate fatigue cracks initiated near the edge of the patch. DuQuesnay et al. [11] observed that the substrate failures only occurred at low applied stress levels and that similar specimens constructed with unclad substrates failed through the adhesive. Accompanying the change in the failure mode of the clad specimens was a decrease in the fatigue life with respect to the bare (unclad) specimens. DuQuesnay et al. [11] also found that the run-out stress of the clad specimens was lower than that of the bare specimens.

This paper examines the fatigue life and failure mode of adhesively bonded clad aluminum joints subjected to constant amplitude cyclic loading. The adhesive and substrate failures are assumed to be competing failure modes, with substrate failures prevailing at lower stresses and adhesive failures occurring at higher stresses. It is assumed that fatigue life of each failure mode can be

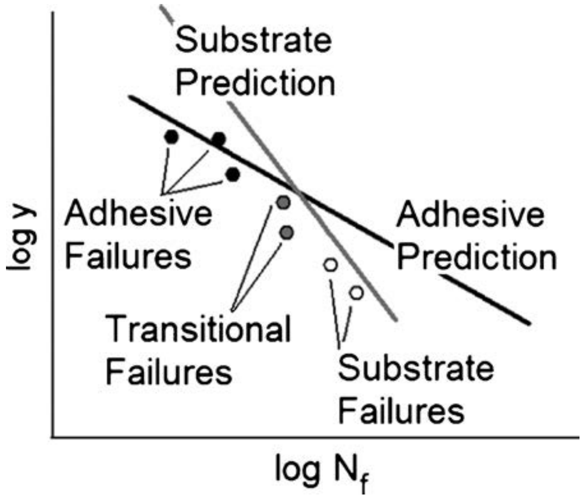

FIG. 1—*Competing failure mechanisms for the failure mode of bonded joints.*

modeled with a Basquin type relationship [13] with the appropriate stress or strain variable. A schematic of the assumed fatigue behavior is shown in Fig. 1, with "y" being the appropriate stress/strain parameter. The stress or strain levels where the two failure modes meet are expected to yield transitional mode failures (which are essentially adhesive failures with cladding pull-off observed on the bonded faces). The stress and strain in the adhesive and cladding layers are modeled using finite element analysis (FEA) in order to identify the appropriate stress or strain variable and the Basquin constants that best predict each failure mode. The predicted fatigue lives for each failure mode are then plotted with fatigue test data to determine how the Basquin relationships can be used to predict the fatigue life and failure mode of the bonded joints.

Test Methods

Fatigue tests were conducted on adhesively bonded double strap joints constructed with a variety of geometries and materials. All test results are discussed with respect to the results of the "baseline" specimen tests, the geometry of which is shown in Fig. 2(*a*). The baseline specimens were manufactured from clad and bare 2024-T351 aluminum alloys. Specimens constructed with clad and bare substrate material are referred to as "baseline clad" and "baseline bare" specimens, respectively. Although many patch repairs that are conducted on aircraft use carbon/epoxy or boron/epoxy patches, aluminum was used for the patch material on the double lap shear specimens in order to minimize residual stresses that might arise from the high temperature cure of the epoxy adhesive. The aluminum used for the patches was always in the bare condition. Clad substrate specimens with deviations from the baseline geometry and materials were tested in order to alter the stress and strain distribution at the edge of the patches. These deviations included patch stiffness (3.2 mm thick brass

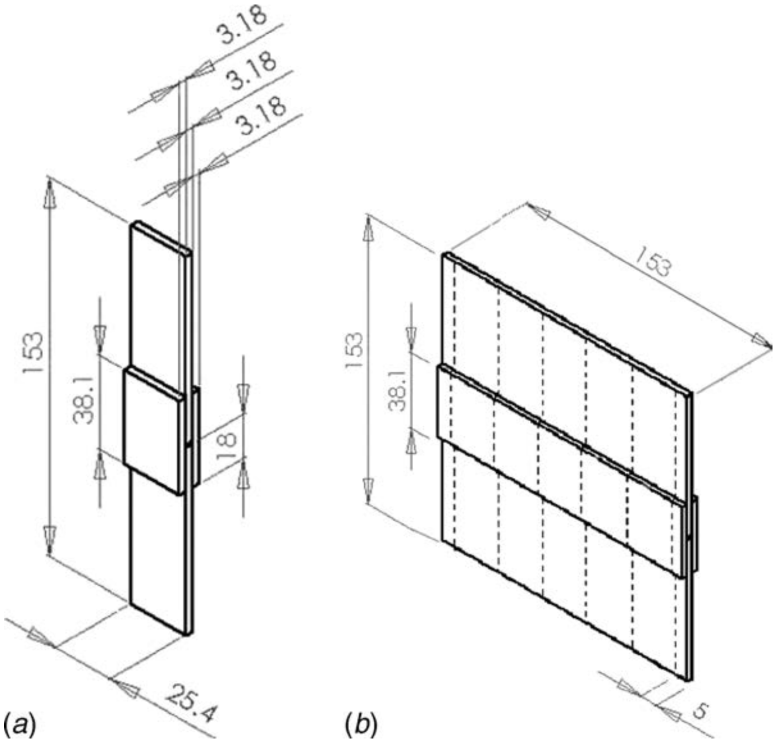

FIG. 2—*Geometry of baseline double strap fatigue joints* (*all dimension in millimeters.*) (*a*) *An individual specimen and* (*b*) *the "plates" from which the individual specimens were cut.*

and steel patches), patch thickness (1.6 mm and 4.8 mm), and patch taper angle (30° and 10°). For the tapered patch specimens, the length of the untapered section of the patches was kept the same as the base specimens, resulting in a longer overall patch length. To determine if substrate failures could be avoided by removing some or all of the cladding layer, specimens that had half or all of the cladding layer milled off of the substrate surfaces were tested. The cladding layer was measured to be approximately 0.09 mm thick. Removing 50 % of the cladding layer corresponded to milling approximately 0.05 mm of material off the surfaces of the substrate. For the specimens that had the cladding layer completely removed, 0.15 mm of material (which corresponds to 150 % of the cladding thickness) was milled off the surfaces of the substrate material. The partial or complete removal of the cladding layer was confirmed with an optical microscope.

The specimens were manufactured in sheets, as shown in Fig. 2(*b*), and were sectioned on a horizontal band saw after bonding to create five specimens per sheet. The specimens that had the cladding layer milled off were manufactured as single specimens in order to facilitate even milling of the surfaces. Seven millimetres of material were removed from each side of these specimens to avoid edge effects on the fatigue behavior. The cut surfaces of all of the specimens were milled to a width of 25.4 mm and sanded with 400 grit sandpaper longitudinally along the specimen.

The specimens were bonded using FM73 epoxy film adhesive in a knit carrier with a nominal mass of 300 g/m^2 and a nominal thickness of 0.25 mm. The bonding surfaces were cleaned, degreased, and grit blasted with 50 μm alumina in a nitrogen gas stream at a pressure of 275 kPa. The specimens were given a warm water treatment to introduce a controlled oxide layer on the bonding surfaces. A solution containing mercaptopropyltrimethoxysilane was then applied to the bonding surfaces and allowed to dry. The adhesive, substrates, and patches were assembled, clamped, and cured at 120°C for 2 h. Residual stresses between the patch and the substrate caused by the elevated temperature cure were minimized by using aluminum for both the patch and substrate material. A more detailed description of the bonding technique is given in [14,15].

Fatigue testing was conducted in load control on servo-hydraulic load frames using closed-loop FLEX control software [16] in atmospheric temperature and humidity. The test frequencies ranged from 5 Hz to 30 Hz and were chosen to maximize the test speed while maintaining errors of less that 1 % of the applied load. The stress ratio of the loading cycles R is the ratio of the minimum applied stress to the maximum applied stress. All of the tests were conducted at $R=0$, with the maximum stress ranging from 22 MPa nominal shear to the endurance limit levels. The nominal shear stress was calculated by dividing the applied load by the overlap area (as calculated by multiplying the measured overlap length by the measured specimen width) of the side of the specimen with the shortest overlap. Fatigue tests were conducted until fracture of the specimens occurred, or until the specimen reached 5×10^6 cycles without fracture.

The failure mode for each specimen was defined as adhesive, substrate, or “transitional.” An adhesive failure was defined as failure through the adhesive with no visible signs of damage to the cladding layer on the bonded surfaces. Substrate failures referred to specimens that failed from cracks that propagated in the substrate near the edge of the patch. The third failure mode, i.e., transitional, was essentially an adhesive failure; however, the fracture surfaces revealed areas where the cladding had been pulled off the substrate. Pull-off occurred near the edge of the patch and the severity of the pull-off (defined by an increased number of pull-off sites, the size of the pull-off sites, and the distance from the edge of the patch) increased with decreasing applied stress. The severity of cladding pull-off was ranked from 1 to 5, where 5 was the most severe. Examples of cladding pull-offs are shown in Fig. 3.

Finite Element Analysis

The stress and strain in the adhesive and cladding layers of the patches were modeled using ANSYS finite element software. The two-dimensional model used quarter symmetry and PLANE82 triangular plane strain elements. Digital images of specimen cross sections were analyzed to determine the average thick-

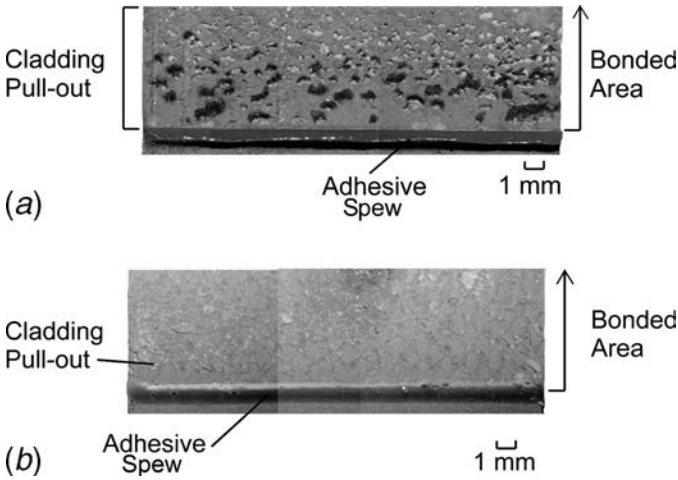

FIG. 3—*Examples of cladding pull-out.* (*a*) *Severe pull-out* (*Rank 5*) *and* (*b*) *mild pull-out* (*Rank 1*).

ness of the adhesive and cladding layers. The FE mesh was designed so that there were three layers of elements in the adhesive and two layers of elements in the cladding. The size of the mesh gradually increased in the substrate and increasing degrees of refinement were employed near the edge of the patch, where the stress and strain gradients were highest. To check the convergence of the model, the refinement at the edge of the patch was increased and two calculations (one with a low and one at a high applied stress level) were conducted. The peak stresses calculated with the highly refined model were within 1 % of the peak stresses calculated using the unmodified model. It was concluded that the unmodified model converged.

The material behavior was initially modeled with linear material properties. The material parameters, elastic modulus (E), and Poisson's ratio (ν), are given in Table 1. The material properties for 2024-T351 were obtained from published research [17], while nominal brass and steel material properties were taken from [18]. The cladding alloy, 1230 aluminum, is a near-pure non-heat treatable aluminum alloy for which reliable mechanical properties could not be located. The material properties for annealed 99.9 % pure aluminum were used to model the behavior of the cladding. The product data sheet distributed by the manufacturer of FM73 adhesive presents the material properties in terms of shear stress and shear strain, and therefore they list a shear modulus (G) in-

TABLE 1—*Linear material properties.*

Property	2024-T351 Al alloy	Aluminum cladding	FM73 adhesive	Steel	Brass
E, MPa	72 400	69 000	2310	205 000	115 000
ν	0.33	0.33	0.37	0.3	0.3

stead of E. Poisson's ratio for FM73 was taken as the average of three published values [19–21] and the elastic modulus was calculated using the manufacturer's published value of G [22] and the relationship $E = 2G(1+\nu)$. The model was verified by comparing the resulting stress distribution with analytical equations developed by Taheri et al. [23] and Shahin et al. [24]. The FEA and the analytical equations [23,24] were in good agreement in the area of interest.

Examination of the FEA results indicated that the yield strength of the cladding and adhesive layers were exceeded for some of the simulated test. The model was therefore modified to incorporate non-linear material properties for the cladding and adhesive layers. A bilinear isotropic material model was used for the adhesive. The secondary shear modulus G_2 was calculated to be 19 MPa from the shear stress-shear strain curve supplied by the manufacturer [22] and the equation $E_2 = 2G_2(1+\nu)$. To validate the non-linear adhesive model, the FE model described above was used to create a multi-element square shape in ANSYS. A load was applied along the faces of the square and applied shear stress and shear strain calculated by the FEA were compared to the shear stress versus shear strain curve supplied by the manufacturer. The FEA and the manufacturer's data were in good agreement, thus validating the non-linear adhesive model.

The cladding layer was modeled using a table of stress-strain points. The cladding behavior was modeled using a stress-strain curve for annealed 99.9 % pure aluminum obtained from the Atlas of Stress Strain Curves [25]. The non-linear cladding model was verified in a similar manner as the non-linear adhesive model. The FEA analysis and the stress strain curve were in good agreement, thus validating the non-linear cladding model.

The FEA model was used to evaluate the peel, shear, and Von Mises stresses and the X, Y, and principal strains in the adhesive and cladding layers. The stresses and strains were calculated 0.01 mm from the substrate/adhesive and adhesive/cladding interfaces in the adhesive and cladding layers, respectively. A FEA was conducted for each individual fatigue test and the peak values, as well as the distributions, of the six stress and strain parameters were evaluated.

Results

The results of the fatigue tests for the different specimen variations are presented in Figs. 4–9. The clad baseline specimen data are plotted in the each of the figures (except Fig. 9, where the bare baseline specimen data are plotted) to provide a reference for discussion of the results. The following postulates are made when discussing the data:

(1) Increasing the peak stress at the edge of the patch will result in shorter fatigue lives.
(2) Increasing the peak stress at the edge of the patch will result in a tendency towards adhesive failure.
(3) Increasing the stiffness of the patch will increase the peak stress at the edge of the patch.
(4) Tapering the edge of the patch will decrease the peak stresses at the edge of the patch.

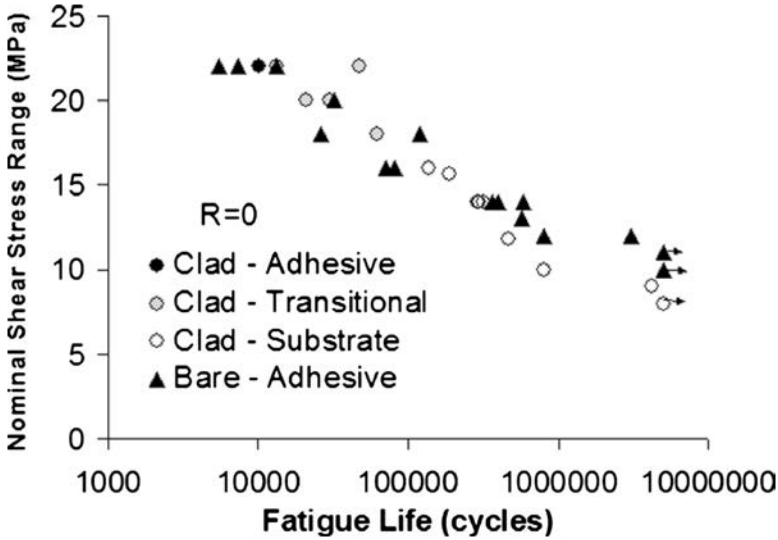

FIG. 4—*Fatigue data for bare and clad baseline specimens. Open, gray, and solid symbols represent substrate, transitional, and adhesive failures, respectively.*

(5) Removing part of the cladding layer will not affect crack initiation in the cladding layer and therefore will have no affect of fatigue life or failure mode.
(6) Removing the entire cladding layer will prevent the occurrence of substrate failures.

The baseline data for the bare and clad specimens are presented in Fig. 4. All of the bare specimens failed in the adhesive and the bare specimens had a higher endurance limit that the clad specimens. Adhesive failures occurred through the adhesive (cohesive failure) not at the metal/adhesive interface. The clad specimens failed by adhesive failure at the highest applied stress range and by substrate failure at the lower applied stress ranges. Transitional failures were observed at intermediate stress ranges, with the severity of cladding pull-off increasing with decreasing applied stress range. The fatigue lives of the bare and clad baseline specimens were similar between 14 MPa and 22 MPa.

It was expected that increasing the patch thickness would increase the peak stress in the adhesive. Figure 5 shows the results of fatigue tests conducted on specimens with varying patch thicknesses. The 3.2 mm thick patch represents the baseline specimens. The specimens with thinner (1.6 mm) patches failed by transitional failure at 22 MPa nominal shear stress and by substrate failure at stresses at or below 20 MPa. The specimens with thicker (4.8 mm) patches failed by adhesive failures at lower stresses than the baseline specimens. As the thinner and thicker patches are expected to produce lower and higher stresses in at the edge of the patch, respectively, this observation supports postulate #2. The fatigue lives of the thick patch specimens were shorter than the baseline specimens at higher stresses, while the thinner patches had longer fatigue lives at higher applied stresses. This observation supports postulate #1. However,

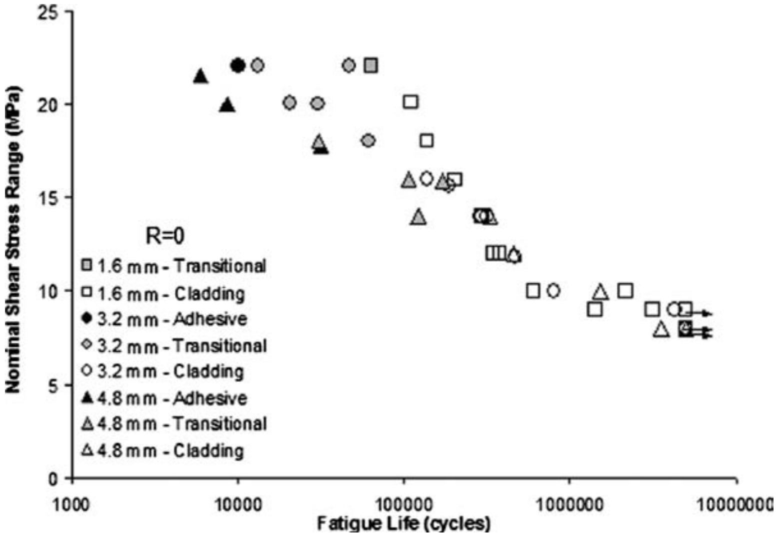

FIG. 5—*Fatigue data for specimens with varying patch thickness.*

when the failure mode for all of the specimens became substrate failure, i.e., at the lowest applied shear stresses, the data consolidated to a single curve and the endurance limits for all of the specimen geometries were similar.

Both the brass and the steel patches have higher elastic moduli than the aluminum patches of the baseline specimens and therefore should both produce higher peak stresses at the edge of the patch; however, the fatigue lives of all of the specimens in Fig. 6 were similar. The failure modes of the specimens did support postulate #2, as the steel specimens failed in the adhesive at lower stress levels than the baseline specimens, and the brass specimens experienced transitional failures at lower stress levels than the baseline specimens. Once again, at stresses where all of the specimens failed in the substrate, the data consolidated to a single curve and had similar endurance limits.

It was postulated that the specimens with more gradual tapers would have lower peak stresses at the edge of the patch, resulting in longer fatigue lives and a tendency towards substrate failures. The data for the tapered patches is shown in Fig. 7 and the 90° taper data represent the clad baseline specimens. The specimens with a 10° taper failed exclusively by substrate failure. At a given stress level, they had longer fatigue lives than the specimens that failed by adhesive or transitional failures. The specimens with a 30° taper had longer fatigue lives than the baseline specimens and transitional failures at lower applied stresses. Again, it is interesting to note that the fatigue data fall onto a common curve when the failure mode of all of the specimens is through the substrate.

The final specimen variation that was examined was removal of half or all of the cladding layer from the bonding surfaces. The specimens with half of the cladding layer milled off had similar fatigue lives as the baseline clad specimens (Fig. 8). However, adhesive failures were observed in the 50 % cladding-

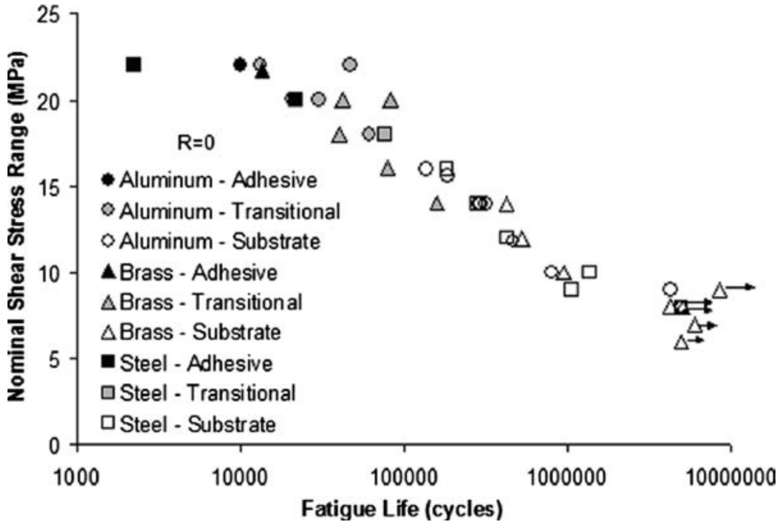

FIG. 6—*Fatigue data for specimens with varying patch material.*

removed specimens at all but the lowest applied stresses. This implies that removing the cladding layer can suppress the occurrence of substrate failures, however it has little effect on the fatigue life. The specimens with all of the cladding layer removed are plotted against the bare baseline data in Fig. 9. The fatigue lives were similar and the failure mode for all of the specimens was fully adhesive. The endurance limit was slightly lower for the specimens with the cladding completely removed. This could be attributed to the small loss of cross

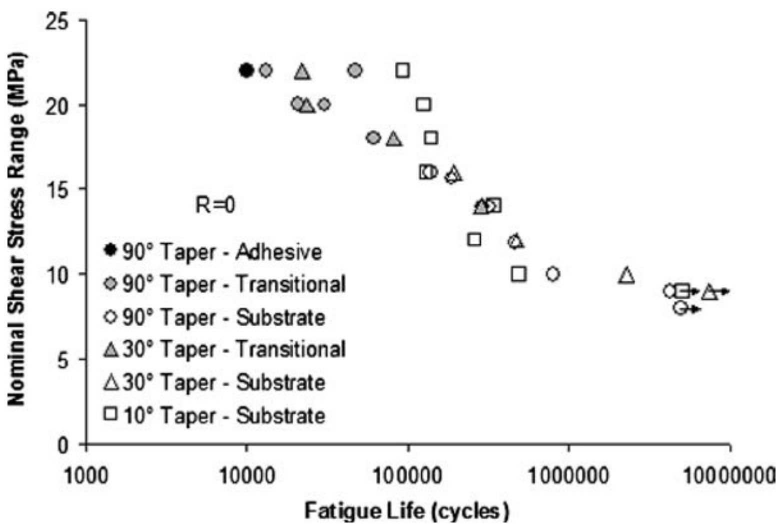

FIG. 7—*Fatigue data for specimens with varying taper angle.*

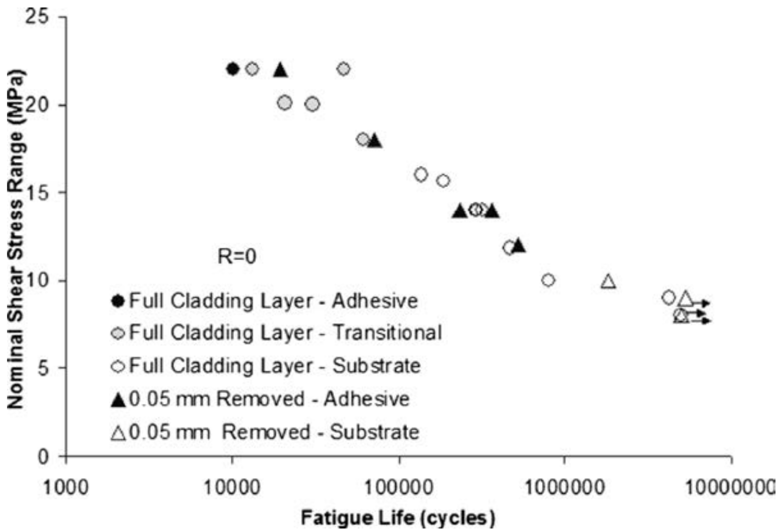

FIG. 8—*Fatigue data for specimens with* 50 % *of the cladding layer removed.*

section after milling (about 1 %) causing a slight increase in the peak stress at the edge of the patch. The results of this test series indicates that the occurrence of substrate failures can be decreased by removing some of the cladding layer or prevented by removing all of the cladding layer.

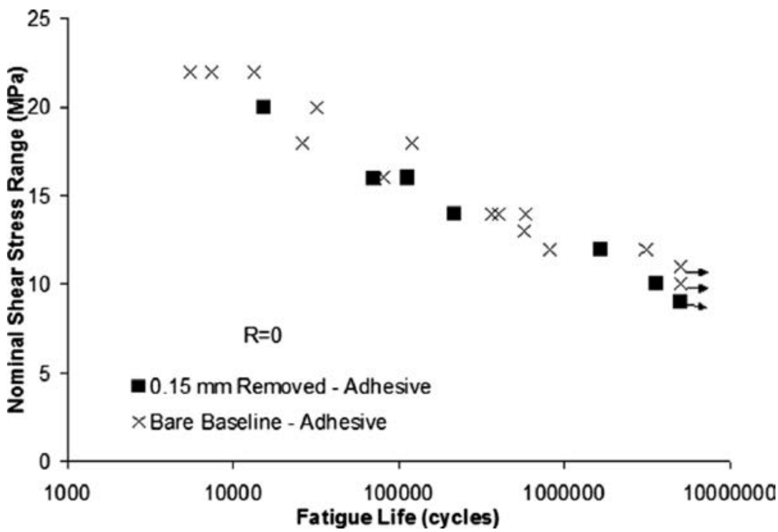

FIG. 9—*Fatigue data for specimens with all of the cladding layer removed, plotted with the bare baseline specimens.*

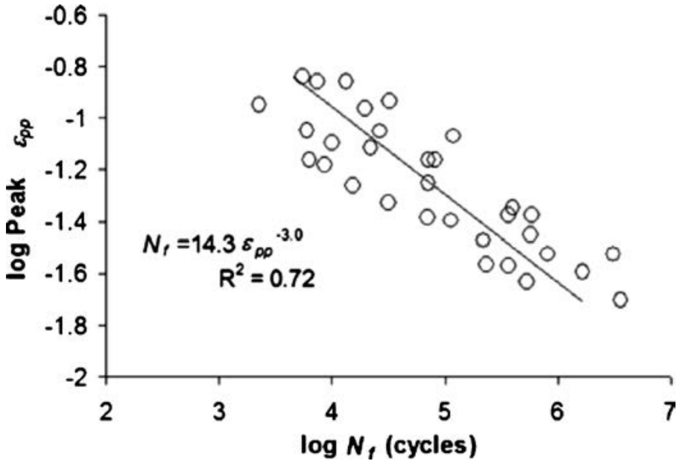

FIG. 10—*Adhesive failure data, peak principal strain in the adhesive layer versus fatigue life.*

The peak stresses and strains in the specimens, as calculated from the FEA, supported postulates #3 and #4. At a given applied load, specimens with stiffer and thicker patches had higher peak stresses and strains. The tapered specimens experienced a decrease in the peak stresses and strains at the edge of the patches.

The fatigue data from all of the specimens that failed by fully adhesive failure were analyzed to determine which stress or strain variables correlated best with the fatigue life on a log-log plot (i.e., Basquin relationship). It was found that the peak principal strain in the adhesive layer produced the best correlation using a least-squares regression. The data and the regression are shown in Fig. 10 and the Basquin relationship was determined to be $N_f = 14.3\varepsilon_{pp}^{-3.0}$. The preliminary linear FE model indicated that the adhesive was stressed beyond its yield stress near the edge of the patch. The behavior of the adhesive was then modeled with a bi-linear material model. The post-yield line used to describe the adhesive behavior had a very low slope. Consequently, large changes in applied load resulted in very slight changes in the peak stress at the edge of the patch and significant changes in the peak strain. Therefore, it is not surprising that the strain correlated with the fatigue life data better than the stress. The principal strain incorporates both shear and peel strains at the edge of the patch and therefore gives a more accurate depiction of the entire strain state in the material. It is reasonable that the peak principal strains correlate best with the fatigue life data.

The fatigue data for all of the specimens that failed in the substrate were analyzed using the same techniques as the adhesive failure data. It was found that the substrate failures correlated best with the nominal axial stress S_{nom} in the substrate. The substrate failure data is plotted in Fig. 11, and the relationship was found to be $N_f = 5.7\times10^{13}S_{\mathrm{nom}}^{-3.7}$. It is interesting to note that the finite element analysis is not required to calculate S_{nom}; it is simply the applied load

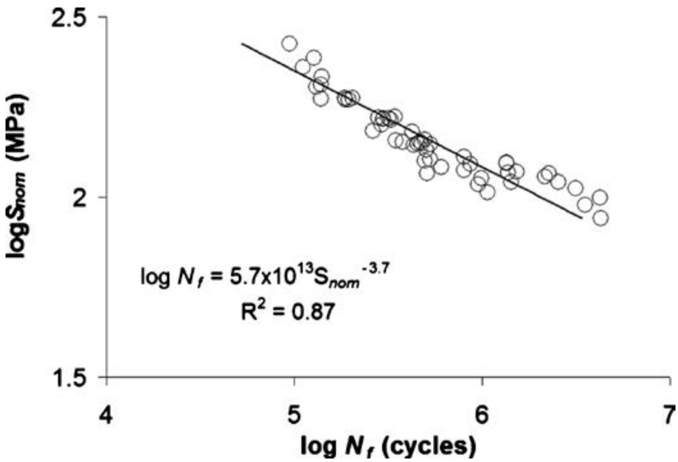

FIG. 11—*Substrate failure data, nominal axial stress in the substrate versus failure life.*

divided by the cross-sectional area of the substrate. Using this nominal value to predict the fatigue life implies that the stress and strain concentration at the edge of the patch does not affect the fatigue behavior under substrate loading. However, the fact that the substrate failures always occur at the edge of the patch demonstrates that the stress concentration does have an effect on the fatigue behavior. The ease of using S_{nom} to calculate N_f and the strong ($R^2 = 0.87$) correlation between S_{nom} and N_f make it a good variable for calculating fatigue life.

The Basquin relationships were used to predict the fatigue lives for the adhesive and substrate failure modes for each of the specimens that were tested. The fatigue data and the fatigue life predictions were plotted for each specimen configuration to determine if the Basquin relationships could predict the fatigue life and failure modes of the specimens. The prediction with the shortest fatigue life at a given stress level is taken to be the failure mode and fatigue life for specimens at that stress level. Figure 12 shows these plots for the steel and brass patched specimens, which represent the range of the best and the worst fatigue life predictions, respectively. In Figs. 12(*a*) and 12(*b*), the lines that represent the fatigue life predictions intersect through the transitional data. The data are plotted against the nominal shear stress in the tensile specimens. Since the nominal shear stress is proportional to the nominal axial stress, the substrate failure prediction plots as a straight line. The line representing the adhesive failure prediction is curved because the peak principal strain at the edge of the patch is not linearly related to the nominal shear stress. The predicted fatigue lives agree well with the data and the fatigue mode is predicted with reasonable accuracy.

Discussion

When designing a patch repair for an aircraft, it is desirable to minimize the stresses at the edge of the patch by introducing a taper at the edge of the patch.

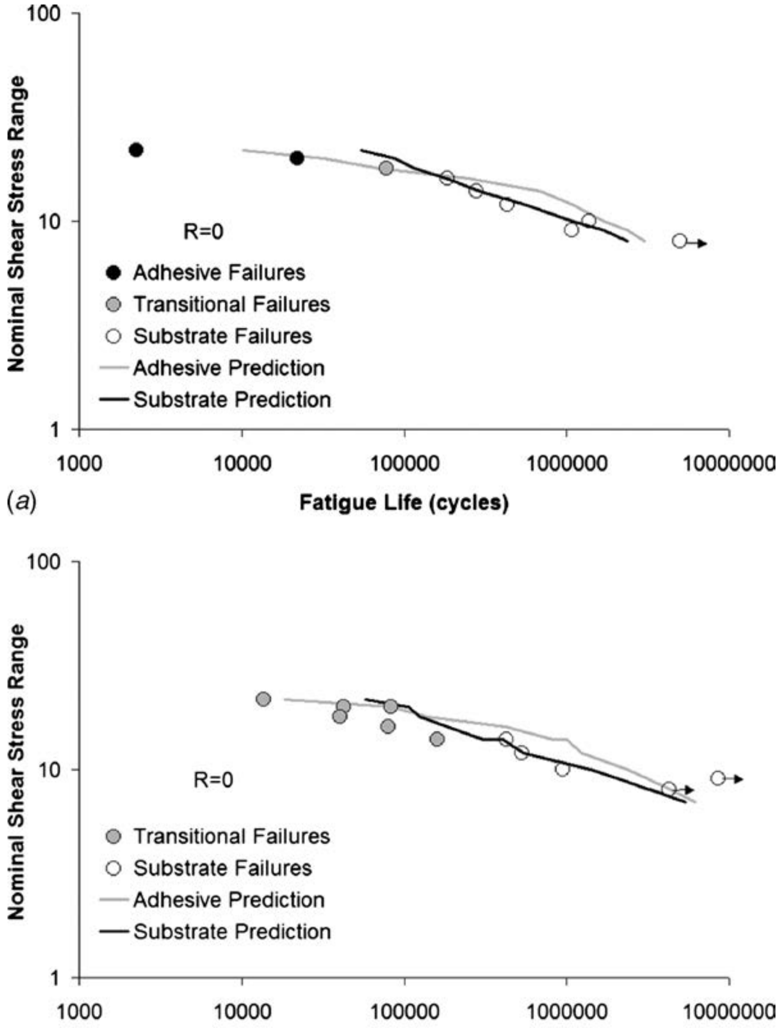

FIG. 12—*Fatigue data and fatigue life predictions for* (*a*) *specimens with steel patches* (*representing the best prediction*) *and* (*b*) *specimens with brass patches* (*representing the worst prediction*).

This is done to produce a smooth stress transition and to prolong the service life of the patch system [1]. However, this body of work has shown that if the stresses at the edge of the patch are sufficiently low, the failure mode can change from through the adhesive to through the substrate (if the base material is clad). Another scenario where substrate failure can occur is if an area is patched multiple times because of successive patch adhesive failures. If a patch delaminates and a new patch is applied, the new patch is expected to have a similar fatigue life as the first patch. However, if damage has occurred in the substrate, even if it was not enough damage to cause failure, it will still be present when the new patch is applied. Therefore, the number of cycles required to cause a substrate failure will be less than it was required the original first patch was applied. The damage in the substrate will continue to accumulate for multiple patch delamination/reapplication cycles. Although some of the fatigue damage in the substrate may be removed when the surface is prepared for bonding, there is still the possibility that accumulated damage could eventually lead to a substrate failure. Consequently, the longer an area is patched, the more likely it is to fail through the substrate, and even though substrate failures have not been report as yet, they should still be a consideration for safe aircraft maintenance practices.

There are two strategies available for avoiding substrate failures. The first is to limit the stress in the substrate to below the endurance limit for substrate failures. Although this option would be effective, keeping the stresses below the endurance limit may require operation limitations and consequently will not be a viable option for all structures. The second strategy for avoiding fatigue failures is to remove the cladding from the area where the patch is applied. This body of work has shown that removing the cladding layer prevents fatigue failures from occurring in the substrate. Although milling was the method used to remove cladding on the double strap joints tested here, chemical and abrasive removal techniques might be more appropriate for *in situ* cladding removal, and will be the topic of future investigations. It is recommended that the cladding layer be removed before any adhesively bonded patch repairs are applied.

Conclusions

It was found that increasing the peak strain at the edge of the double strap joint patches resulted in shorter fatigue lives and a tendency toward adhesive failures at higher stress levels. When specimen failure occurred in the substrate, the stress-life data consolidated to a single curve, despite the change in stress and strain distribution at the edge of the patch. The fatigue lives of the double strap joints by adhesive and substrate failure can be calculated using the equations $N_f = 14.3\varepsilon_{\mathrm{pp}}^{-3.0}$ and $N_f = 5.7\times10^{13} S_{\mathrm{nom}}^{-3.7}$, respectively. A finite element analysis is required to determine the peak principal strain ($\varepsilon_{\mathrm{pp}}$) used to determine the adhesive failure life. The nominal stress in the substrate can be calculated by dividing the applied load by the cross-sectional area and therefore does not require assistance from a finite element model. The predicted failure mode and fatigue life of a specimen is determined from the failure mode that predicts the shortest fatigue life at a given applied load. The equation for the fatigue life of specimens that fail through the adhesive layer is most likely depended on the specimen geometry and it is recommended that this equation be verified for each geometry of interest. It is expected that the fatigue life prediction for specimens that fail in the substrate will not be geometry dependent.

To maintain safe operation of an aircraft, it is important to insure that any patches bonded to the aircraft will not cause damage to the substrate. This is best accomplished by removing the cladding layer from the substrate before the patch is applied. Special care must be taken to make sure that the entire cladding layer is removed, as it has been shown that partial removal of the cladding layer will not prevent fatigue failures from occurring in the substrate.

References

[1] Baker, A., "Bonded Composite Repair of Fatigue-Cracked Primary Aircraft Structure," *Compos. Struct.*, Vol. 47, No. 1, 1999, pp. 431–443.

[2] Merati, A., "A Study of Nucleation and Fatigue Behavior of an Aerospace Aluminum Alloy 2024-T3," *Int. J. Fatigue*, Vol. 27, No. 1, 2005, pp. 33–44.

[3] Nakai, M. and Eto, T., "New Aspects of Development of High Strength Aluminum Alloys for Aerospace Applications," *Mater. Sci. Eng., A*, Vol. 285, 2000, pp. 62–68.

[4] Broek, D., *Elementary Engineering Fracture Mechanics*, 4th Ed., Kluwer Academic Publishers, Dordrecht, 1986.

[5] Bhandarkar, M. D. and Lisagor, W. B., "Metallurgical Characterization of the Fracture of Aluminum Alloys," *Fractography in Failure Analysis, ASTM STP 645*, B. M. Strauss and W. H. Cullen, Jr., Eds., American Society for Testing and Materials, West Conshohocken, PA, 1978, pp. 176–209.

[6] Axter, S. E., Jones, W. B., and Polonis, D. H., "Microstructural Origins of Dynamic Fracture in 2024 Aluminum Alloy," *Metallography*, Vol. 8, No. 5, 1975, pp. 425–438.

[7] Schijve, J., Jacobs, F. A., and Tromp, P. J., "The Significance of Cladding for Fatigue of Aluminium Alloys in Aircraft Structures," Report # NLR TR 76065 U, The National Aerospace Laboratory NLR the Neatherlands, 1976, pp. 1–24.

[8] Wu, X. R., Newman, J. C., Zhao, W., Swain, M. H., Ding, C. F., and Phillips, E. P., "Small Crack Growth and Fatigue Life Predictions for High-Strength Aluminum Alloys: Part I—Experimental and Fracture Mechanics," *Fatigue Fract. Eng. Mater. Struct.*, Vol. 21, No. 11, 1998, pp. 1289–1306.

[9] Pellegrini, H. V., Bishop, C. M., and Bennett, J. M., "Uncommon Failures in Aluminum Alloys," *Metal Progress*, Vol. 115, No. 3, 1979, pp. 38–41.

[10] Suresh, S., Sugimura, Y., and Ogawa, T., "Fatigue Cracking in Materials with Brittle Surface Coatings," *Scr. Metall. Mater.*, Vol. 29, 1993, pp. 237–242.

[11] DuQuesnay, D. L., Underhill, P. R., and Britt, H. J., "Fatigue Failure of Adhesively Patched 2024-T3 and 7075-T6 Clad and Bare Aluminum Alloys," *Fatigue Fract. Eng. Mater. Struct.*, Vol. 28, No. 4, 2005, pp. 381–389.

[12] Aakkula, J. J. and Saarela, O., "Crack Growth in Aluminium Plates Repaired with Composite Reinforcements," *Proceedings of the 18th Symposium of the International Committee on Aeronautical Fatigue*, 3–5 May 1995, Melbourne, Australia, J. M. Grandage, and G. S. Jost, Eds., pp. 703–716.

[13] Basquin, O. H., "The Exponential Law of Endurance Tests," *Proceedings of the Annual Meeting—ASTM*, ASTM International, West Conshohocken, PA, Vol. 10, 1910, pp. 625–630.

[14] Underhill, P. R., Rider, A. N., and DuQuesnay, D. L., "Warm Water Treatment of Aluminum for Adhesive Bonding," *Int. J. Adhes. Adhes.*, Vol. 23, 2003, pp. 307–313.

[15] Nolting, A., "Fatigue Behaviour of Adhesively Bonded Aluminum Double Strap Joints," PhD thesis, 2006, Royal Military College of Canada.

[16] Pompetzki, M. A., Saper, R. H., and Topper, T. H., "Software for High Frequency Control of Variable Amplitude Fatigue Tests," *Can. Metall. Q.*, Vol. 25, No. 2, 1986,

pp. 191–194.

[17] DuQuesnay, D. L., Topper, T. H., Yu, M. T., and Pompetzki, M. A., "The Effective Stress Range as a Mean Stress Parameter," *Int. J. Fatigue*, Vol. 14, No. 1, 1992, pp. 45–50.

[18] *Metals Handbook*, Vol. 2, Properties and Selection: Nonferrous Alloys and Special Purpose Materials, 10th ed., ASM International, Metals Park, OH, 1990.

[19] Baker, W., Jones, R., Davis, C., and Galea, S., "Finite Element Modeling to Determine Thermal Residual Strain Distribution of Bonded Composite Repairs for Structural Health Monitoring Design," *Proc. SPIE*, Vol. 4934, 2002, pp. 128–139.

[20] Cheuk, P. T., Tong, L., Rider, A. N., and Wang, J., "Analysis of Energy Release Rate for Fatigue Cracked Metal-To-Metal Double-Lap Shear Joints," *Int. J. Adhes. Adhes.*, Vol. 25, 2005, pp. 181–191.

[21] Klug, J., Maley, S., and Sun, C. T., "Characterization of Fatigue Behavior of Bonded Composite Repairs," *J. Aircr.*, Vol. 36, No. 6, 1999, pp. 1016–1022.

[22] Cytec Engineered Materials, "FM73 Toughened Epoxy Film," Technical Data Sheet, June 1998.

[23] Zou, G. P., Shahin, K., and Taheri, F., "An Analytical Solution for the Analysis of Symmetric Composite Adhesively Bonded Joints," *Compos. Struct.*, Vol. 65, 2004, pp. 499–510.

[24] Shahin, K., Zou, G. P., and Taheri, F., "Novel Analytical Solutions for Adhesively Bonded Joints Integrated with Shape Memory Alloy Wires," *The Fifth Canadian-International Composites Conference*, 16–19 August 2005, Vancouver, British Columbia, Canada.

[25] Boyer, H. E., *Atlas of Stress-Strain Curves*, ASM International, Metals Park OH, 1987.

ASTM Special Technical Publication, Vol. 5, No. 5
Paper ID JAI101566
Available online at www.astm.org

Richard D. Widdle, Jr.,[1] *Lee C. Firth,*[1] *and Paul W. Reed*[2]

A Simplified Modeling Approach for Predicting Global Distortion in Large Metallic Parts Caused by the Installation of Interference Fit Bushings

ABSTRACT: One technique for improving the fatigue life of a fastener hole in a built-up metallic structure is to use an interference fit bushing. The installation of these bushings produces residual compressive stresses around the hole that improve the fatigue life. It also causes residual strains and therefore distortion of the part. The distortion is both in-plane growth of the part and out-of-plane deflection, or cupping. The resulting distortion can cause difficulty in downstream assembly, such as misalignment of fastener holes or a misfit of mating surfaces. For small parts with only a few bushings, it is possible to predict the distortion by explicitly modeling the installation process by using a finite element approach. However, for a large part with many bushings, it is not practical to build a model with a detailed finite element representation of each bushing installation. In this work, a simplified approach is presented for predicting the global distortion of large shell-like parts that is caused by installing many interference fit bushings. The simplified approach consists of representing the bushings with equivalent springs in a shell-based finite element model of a large part. In this approach, the equivalent springs are not constructed with spring elements that are commonly found in finite element codes. Rather, the equivalent springs are constructed with a number of shell elements in two layers. The properties of the elements

Manuscript received November 13, 2007; accepted for publication April 3, 2008; published online May 2008.
[1] Boeing Engineering Operations and Technology, Phantom Works, P.O. Box 3707MC 42-26, Seattle WA 98124.
[2] Boeing Commercial Airplanes, Materials and Process Technology, P.O. Box 3707MC 0P-AH, Seattle WA 98124.

Citation: Widdle, Jr., R. D., Firth, L. C., and Reed, P. W., "A Simplified Modeling Approach for Predicting Global Distortion in Large Metallic Parts Caused by the Installation of Interference Fit Bushings," *J. ASTM Intl.*, Vol. 5, No. 5. DOI10.1520/JAI101566. Available online at www.astm.org. Also included in JAI Special Issue STP 1508, *Fatigue and Fracture Mechanics: 36th Volume,* R. W. Neu, K. R. W. Wallin, and S. R. Thompson, guest editors, ASTM International, West Conshohocken, PA, 2009, pp. 778-793.

that make up the equivalent springs are estimated from experiments on small test coupons. The same springs, with the same calibrated parameters, are then applied to the larger part of interest. Results indicate that this approach can be used to estimate the distortion that can be expected in a large part that is cause by the installation of interference fit bushings.

KEYWORDS: bushing, fatigue, interference fit, cold work, finite element

Introduction

One technique for improving the fatigue life of a fastener hole in a metal part is to use an interference fit bushing [1]. Installation of such bushings produces a residual stress state that improves fatigue life. Residual stresses produce corresponding residual strains and therefore distortion of the part. This distortion can cause difficulties in downstream assembly, such as misalignment of fastener holes or a mismatch of mating surfaces. The manufacturing process can account for the distortion upstream if it can be estimated beforehand. Additionally, if a designer has the ability to estimate the effects of installing interference fit bushings, there is the potential to minimize the impact on the design.

Of interest in this work is the technique of passing a tapered mandrel through a bushing to cause permanent radial expansion, resulting in an interference fit. It is possible to explicitly model the installation of interference fit bushings, and similar hole cold-working processes, using a finite element approach. For example, Kang et al. [2], Dutta et al. [3], and Kim et al. [4] used the finite element method to investigate the three-dimensional stress state near a fastener hole that has been cold-expanded by a mandrel. Karabin et al. [5], O'Brien [6], and Ozdemir et al. [7] studied the split sleeve cold-expansion method. In each of the investigations cited, a detailed three-dimensional finite element model was created and solved to find the residual stress state near the hole. The analyses were restricted to a small region near the fastener hole.

Investigators have also employed closed form methods to assess the effects of cold-working fastener holes. Wang et al. [8] reviewed several of these approaches. A more recent development has been provided by Zhang et al. [9]. Each of these approaches relies on either a plane stress or plane strain assumption. However, as pointed out by Kang et al. [2] and Ozdemir et al. [7], the residual stresses induced by these hole cold-working processes vary through the thickness of the part. Therefore, a two-dimensional closed form solution will not be able to predict the out-of-plane distortion of the part that results from the nonuniformity of the through thickness stresses.

For large parts with many bushings, it is not practical to build a model with a detailed finite element simulation of each bushing installation because of the large model size and solution time that would be required. For example, the finite element model used by Kang et al. [2] was approximately 25 by 25 by 6 mm and was composed of 8020 elements. When the size of a part is on the order of metres rather than millimetres the same level of mesh refinement would not be practical. Therefore, the objective of this investigation is to de-

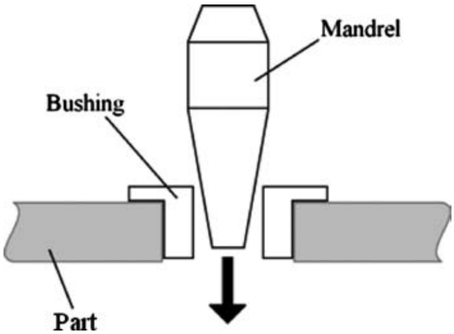

FIG. 1—*Schematic of the bushing installation process with the part and bushing shown in cross section.*

velop a simplified approach to predict the distortion of large metallic, shell-like parts caused by the installation of interference fit bushings. This is done not by modeling the installation process, but by approximating the affect on the part.

The simplified approach that has been developed consists of representing the installed bushings with equivalent springs in a shell-based finite element model of the part. The equivalent springs are not intended to represent the bushing, but the effects of the bushing on the part by applying approximately the same loads as the installed bushing. They are not the spring elements found in a typical finite element code. Rather, the equivalent springs are constructed with a number of shell elements that are arranged in two layers.

The process of installing interference fit bushings is described next. This is followed by a description of the simplified modeling approach. Finally, the technique used for applying the simplified method is illustrated by example. The technique consists of first calibrating the parameters of the equivalent spring, which represent installed bushings, by using experimental results from small test coupons. The calibrated springs are then applied to a structure of interest. The structure of interest here, which is used for illustration, is referred to as the "T-Section."

Interference Fit Bushing Installation Process

The process of installing the bushings is illustrated schematically in Fig. 1. The bushing is placed in a hole in the part and a puller (not shown) draws the mandrel through the bushing. The mandrel is tapered and the largest diameter is bigger than the inner diameter of the uninstalled bushing. As the mandrel is drawn through the hole, the bushing is expanded. The mandrel and bushing are sized such that there is permanent radial expansion of the bushing. The result is a compressive stress state around the hole that favors an improved fatigue life. The particular interference fit bushing system investigated is the Force-Mate bushing system, manufactured by Fatigue Technologies Incorporated.

The final step in the installation is to ream the hole to the proper diameter. Removing material during the reaming process affects the stress state in and

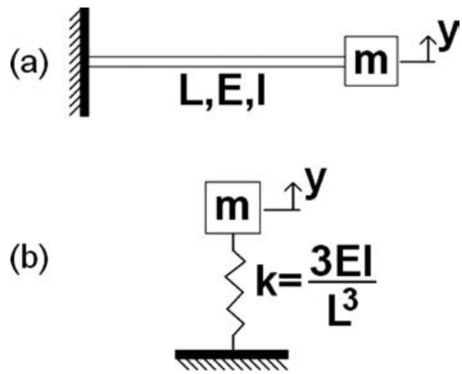

FIG. 2—*A common example of an equivalent spring representation of a mechanical component:* (*a*) *mass m attached to a beam of length L, Young's modulus E, and moment of inertia I, and* (*b*) *mass m attached to an equivalent spring of stiffness k that represents the beam.*

around the bushing, and therefore affects the distortion of the part. While this effect is important in determining the final configuration, it is not addressed in this paper. Rather, the focus of this work is on the predictive ability of the simplified, equivalent spring approach and only the distortion caused by the installation is considered. The effects of reaming can easily be incorporated into the method through appropriate calibration of the equivalent springs.

Simplified Modeling—Equivalent Spring Approach

During the installation process, an interference fit bushing is deformed plastically making it larger in diameter. As a result, there are residual compressive stresses in the material near the interface between the bushing and the native material. This causes expansion, or growth, in the part. Additionally, since the radial stresses are not necessarily uniform along the axial direction of the bushing [2,7], there is a net moment that causes bending, or cupping, deflection.

After the installation process, the bushing can be thought of as a spring that is applying forces and moments to the part. To predict global distortion of a part within a finite element model, it is not necessary to model the details of the bushing. Instead, the bushing can be represented by any component that applies the correct forces and moments to the structure at the inner surface of the fastener hole. In other words, the bushing can be modeled by an equivalent spring that has the same size and stiffness properties as the actual bushing.

Representing part of a structure with an equivalent spring is a common modeling technique. Consider, for example, a mass attached to the end of a beam as shown in Fig. 2. Representing the beam with a spring, that has the same stiffness as the beam, produces the same equation of motion for the mass.

In this investigation the part is represented by shell elements. An installed bushing is represented with an equivalent spring that is constructed with two layers of shell elements, as shown in the cross section in Fig. 3. This is in

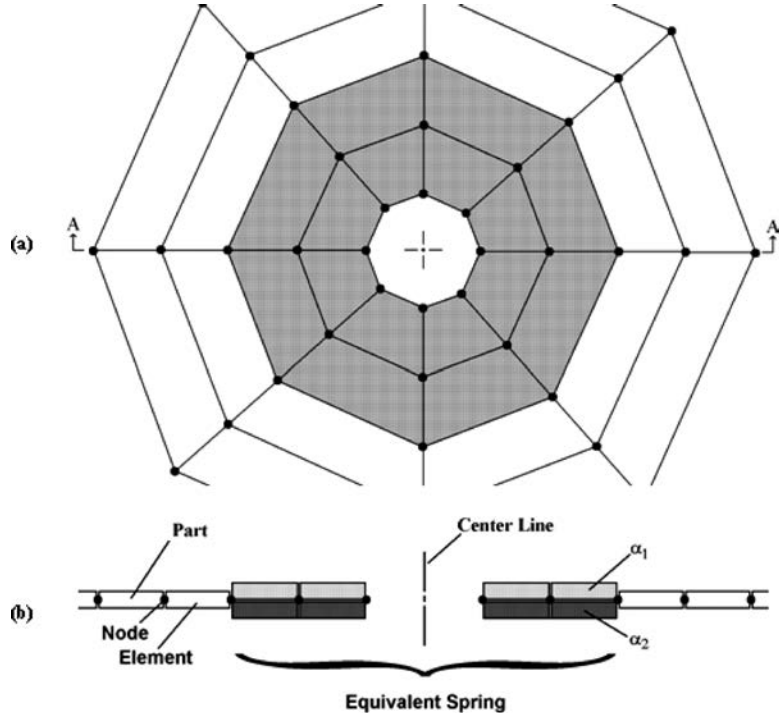

FIG. 3—*Schematic of the equivalent spring approach, (a) top view and (b) cross section (A-A) view. The part is represented by shell elements. The bushing is represented by two layers of shell elements with different coefficients of thermal expansion, α_1 and α_2, with reference surfaces that are offset from their neutral surfaces.*

contrast to representing a structural component with single spring element that may be available within a finite element package. In other words, the equivalent springs are "constructed" out of shell elements.

The two layers of shell elements representing the spring have different coefficients of thermal expansion, and their reference surface (the plane of the nodes) is offset from their neutral surfaces. When the temperature of the finite element model is changed, one layer expands (or contracts) by a different amount than the other. The result is a net expansion in the plane of the elements and deflection transverse to the plane of the elements, i.e., growth and cupping deformation.

This equivalent spring representation of the bushing can be thought of as a bimetallic washer, similar to the bimetallic springs that are found in common household thermostats. Note, however, that the change of temperature in the simplified modeling approach has no physical significance; it is only a technique to produce the appropriate internal forces and moments. The properties of the part are specified such that they are unaffected by temperature changes in the analysis.

By selecting the temperature change, ΔT, applied to the model and the

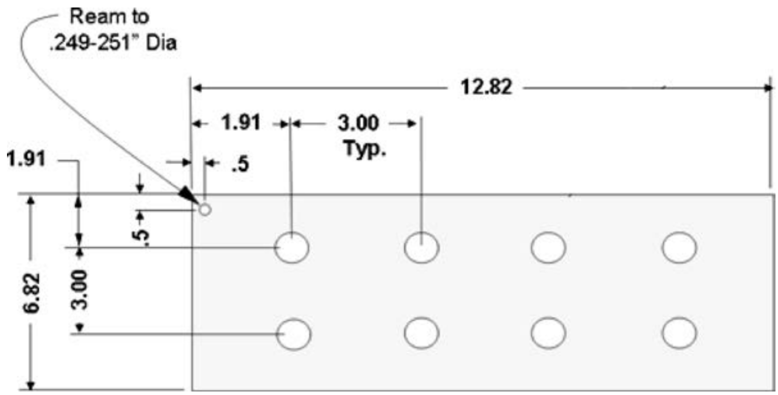

FIG. 4—*Geometry of the test plates with the rectangular hole pattern. The quarter-inch hole in the corner is an orientation reference. Dimensions given in inches.*

coefficients of thermal expansion, α_1 and α_2, the forces and moments applied to the part by the bushing can be approximated. In the modeling work described below, $\Delta T = 1$. The appropriate values for α_1 and α_2 are found by conducting experiments and correlating them with a model of the experimental configuration.

In the experiments, several bushings are installed in small rectangular plates, as described in the next section. The resulting distortion is measured. A shell-based model of the test plates is constructed with an equivalent spring representation of the bushings, and the coefficients α_1 and α_2 were adjusted until the model prediction approximately matched the experimental results. The fitted parameters are then used in simplified models for a different part. The experiments on the rectangular test plates and the corresponding finite element models are described in the next section.

The software packages Truegrid (XYZ Scientific Applications, Inc.) and HyperMesh (Altair Engineering) are used to construct the finite element models described below and LS-DYNA (Livermore Software Technology Corp.) is used to solve them. The finite element models consist of shell elements, with the part material represented with a fully integrated shell element, LS-DYNA shell element type 16. A Hughes-Liu shell element with selectively reduced integration, LS-DYNA shell element Type 6, is used to construct the equivalent spring. The Hughes-Liu shell element is formulated as a degenerate eight-noded brick element that allows for the reference surface to be offset from the neutral surface [10,11].

Rectangular Test Plates

Equivalent spring properties are estimated from experiments on rectangular test plates. The technique is described below with the experimental results from four plates.

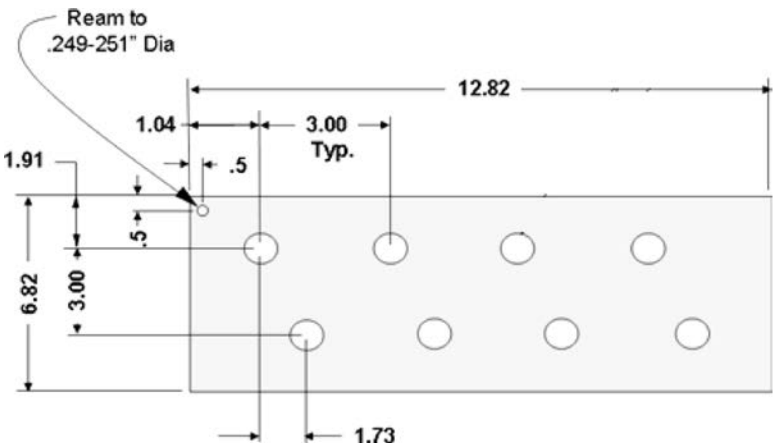

FIG. 5—*Geometry of the test plates with the staggered hole pattern. The quarter-inch hole in the corner is an orientation reference. Dimensions are given in inches.*

Experimental Setup

Four test plates were machined from titanium plate. The holes were drilled and reamed per the specifications of the bushing manufacturer. Two of the plates were 0.180 in. (4.57 mm) thick. The other two were 0.220 in. (0.559 mm) thick. One plate of each thickness was machined to have a rectangular hole pattern, as shown in Fig. 4. The other plates were made to have a staggered hole pattern as shown in Fig. 5. A quarter-inch hole was drilled in one corner of each plate as a reference to ensure the correct orientation.

To find the deformation caused by installing the bushings, the geometry of each plate was measured before and after installation using a scanning laser measurement system (FARO Laser ScanArm Platinum, FARO Technologies, Inc.). The scanning system produced an estimate of the relative positions of a sample of points on the surface of the part being scanned. The position estimates are in three dimensions and envelope the surface of the part. This is sometimes referred to as a "point cloud." The accuracy of this system, as stated by the manufacturer, is ±0.0027 in. (0.069 mm).

The distortion of each part was estimated with the software PolyWorks (InnovMetric Software). Within the program, the before and after point clouds are moved with respect to each other as rigid bodies. Their relative positions are adjusted using an iterative closest point method [12]. Finally, the relative positions of points in the two clouds are used to estimate the deflection caused by the bushing installation.

Simplified Finite Element Models

The simplified finite element mesh for the test plates with the staggered hole pattern is shown in Fig. 6. The model consists of shell elements representing the titanium plate (blue), and the bushings (red) are represented with equivalent springs that are constructed as described above. Single point constraints

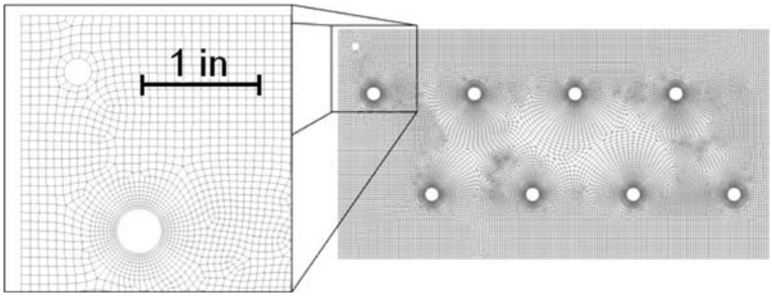

FIG. 6—*Finite element mesh used for the simplified model of the test plates with the staggered hole pattern. Elements representing the titanium plate are shown in blue, while the equivalent springs are red.*

are applied to three corner nodes to eliminate rigid body motion. A similar level of mesh refinement was used for all of the simplified models of the test plates and the T-Section part.

Since the thickness of the plate appears in the model as a property of the shell elements, the same finite element mesh is used for both plate thicknesses. The level of mesh refinement used was found to be acceptable by using a higher level of mesh refinement without significant changes in the results. Again, the thickness of the test plates was either 0.180 in. (4.57 mm) or 0.220 in. (5.59 mm). The thickness of each layer of the equivalent springs was 0.132 in. (3.35 mm) and 0.152 in. (3.86 mm) for the 0.180 in. (4.57 mm) and 0.220 in. (5.59 mm) plates, respectively. These thicknesses correspond to half the bushing thickness. The elastic properties that were used for the titanium plate and steel bushings are given in Table 1 [13].

Results

To make a quantitative comparison, three measurements are considered, as illustrated in Fig. 7. The three measurements are the change in width, change in length, and the out-of-plane deflection at the center of the plate with respect to the corners. The length and width measurements are made at the middle of the part edge and are measured in the x-y-plane. These parameters are estimated within the PolyWorks software and are listed in Table 2.

The magnitudes of the measured changes in width are smaller than the accuracy of the measurement system that is quoted by the manufacturer, ±0.0027 in. (±0.069 mm). Furthermore, the changes in width were measured to be negative, indicating a net contraction in that direction. This is unlikely

TABLE 1—*Assumed elastic properties used in the simplified finite element models* [*13*].

	Titanium Plate	Steel Bushings
Young's Modulus, GPa (psi)	110 (15.9×10^6)	200 (29.0×10^6)
Poisson's Ratio	0.31	0.33

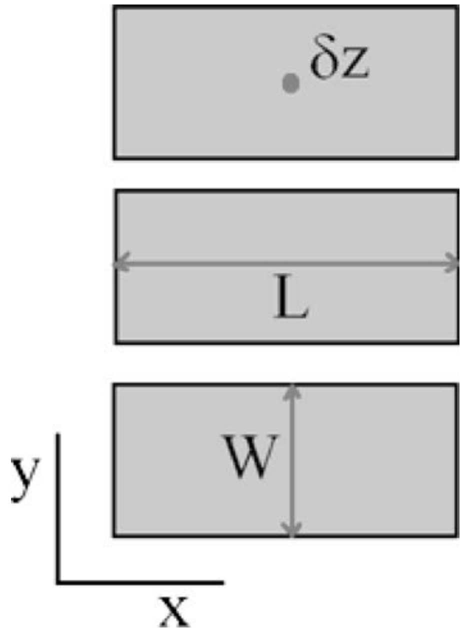

FIG. 7—*Test plate locations for the measurement of width* (*W*), *length* (*L*), *and z-displacement* (δz) *used to quantitatively compare the measured deformation and the deformation predicted by the model.*

considering that the bushings are being forced to expand. It is believed that this is due to systematic error in the measurement system, or that the measurements were not taken precisely at the mid-plane of the part. In the case of the latter, rotation of the edge plane due to cupping distortion would result in different growth measurements depending on where on the edge the measurement was taken.

The measured changes in the length of each plate, although positive, are also smaller than the accuracy of the measurement system. Significant systematic error in these measurements is likely given the observations made about the changes in width above. However, for the purpose of estimating the equivalent spring properties, the measured changes in length were taken to be correct. Although this assumption is a likely contributor to modeling error that will be

TABLE 2—*Measured in-plane and out-of-plane deflections of the test plates.*

Plate	Configuration	δz, in. (mm)		δL, in. (mm)		δW, in. (mm)	
1	0.180 in., Square	−0.020	(−0.508)	0.0016	(0.0406)	−0.0008	(−0.0203)
2	0.180 in., Staggered	−0.016	(−0.406)	0.0004	(0.0102)	−0.0007	(−0.0178)
3	0.220 in., Square	−0.020	(−0.508)	0.0033	(0.0838)	−0.0006	(−0.0152)
4	0.220 in., Staggered	−0.015	(0.318)	0.0027	(0.0686)	−0.0004	(−0.0102)

(a)

(b)

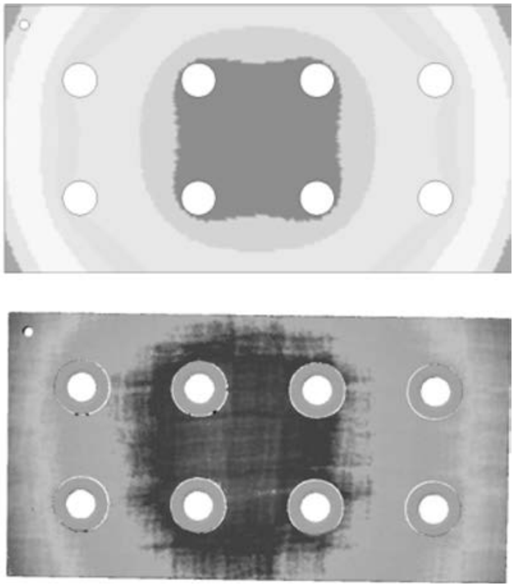

FIG. 8—*A qualitative comparison of the out-of-plane deflection determined from the* (*a*) *simplified model and* (*b*) *experiment, due to installation of bushings in the* 0.180 in. (4.57 mm) *plate with the square hole pattern. Red indicates deflection out of the page, while blue is into the page.*

described in the next section, it does provide a good first approximation. Improvements to the estimated equivalent spring properties, which would require increased accuracy in the measurement technique, would be required to make better predictions.

Thermal expansion coefficients are listed in Table 3 for the equivalent springs that were estimated for the test plates. The coefficients were adjusted manually until the change in length and out-of-plane deflection approximately matched. It is challenging to achieve a precise match between the experiment and model, and an automated optimization routine may be able provide a better fit. However, the iteration was expedited by noticing that plate growth depends primarily on the average expansion of the spring, while out-of-plane deflection depends mostly on the difference between the expansions of the two shell layers.

A qualitative comparison of the model and experimental results is given in Figs. 8 and 9 for two of the test plates. In the figures, red corresponds to deflection out of the page, while blue regions are deflected into the page. The modeling results shown in the figure were produced after the coefficients of thermal expansion were calibrated to approximately match the experimental data.

Here, the word "qualitative" is taken to mean the essential character of the deformation. As indicated in the figures, there is good qualitative agreement

TABLE 3—*Estimated coefficients of thermal expansion for the elements of the equivalent springs, and the corresponding measured and predicted deflections of the rectangular plates. The units of the thermal expansion coefficients are per one temperature unit.*

Alpha 1	Alpha 2	Plate Thickness, in. (mm)	Hole Arrangement	Measurement	Model	Experiment	Difference
0.0012	0.0028	0.180 (4.57)	Square	δz, in. (mm)	−0.0188 (−0.0478)	−0.0200 (−0.508)	0.0012 (0.0305)
				δL, in. (mm)	0.0015 (0.0381)	0.0016 (0.0406)	−0.0001 (−0.0025)
			Staggered	δz, in. (mm)	−0.0190 (−0.483)	−0.0160 (−0.406)	−0.0030 (−0.0762)
				δL,in. (mm)	0.0010 (0.0254)	0.0004 (0.0102)	0.0006 (0.0152)
0.003	0.005	0.220 (5.59)	Square	δz, in. (mm)	−0.0203 (−0.516)	−0.0200 (−0.508)	−0.0003 (−0.0076)
				δL, in. (mm)	0.0030 (0.076)	0.0033 (0.0838)	−0.0003 (−0.0076)
			Staggered	δz, in. (mm)	−0.0204 (−0.518)	−0.0150 (−0.381)	−0.0054 (−0.1372)
				δL, in. (mm)	0.0030 (0.076)	0.0027 (0.0686)	0.0003 (0.0076)

(a)

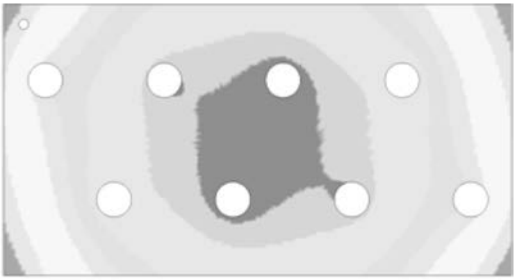

(b)

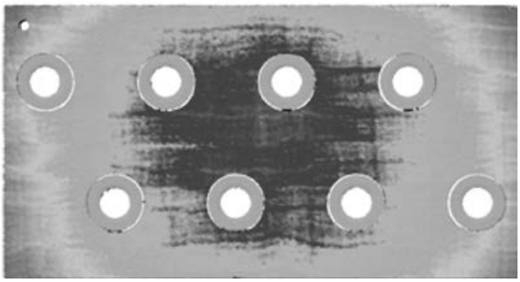

FIG. 9—*A qualitative comparison of the out-of-plane deflection determined from the* (*a*) *simplified model and* (*b*) *experiment, due to installation of bushings in the* 0.220 in. (5.59 mm) *plate with the staggered hole pattern. Red indicates deflection out of the page, while blue is into the page.*

between the model and experiment, in that the plate centers are deflected into the page. Also, the staggered hole pattern produces a skewed deformation pattern in both the model and experiment.

T-Section Part

The simplified modeling approach was used to predict the distortion of a part that is referred to here as the "T-Section." An image of the part generated by the scanning system is shown in Fig. 10. The T-Section was constructed specifically to assist in the investigation of distortion caused by interference fit bushings. It was scanned with the laser scanner before and after bushing installation. The PolyWorks software was again used to estimate the resulting distortion of the part as described above. Finally, the simplified modeling approach was used to predict the distortion.

A comparison of model and experimental results for the T-Section is shown in Figs. 11 and 12 and the results are summarized in Table 4. The predicted and measured y-deflection is shown in Fig. 11(*a*). The fringe patterns match qualitatively. The quantitative agreement is also good. The values of deflection in the model and experiment are shifted with respect to one another by a constant because the point of zero deflection has been selected differently in each set of results—an artifact of the particular software packages used. However, the

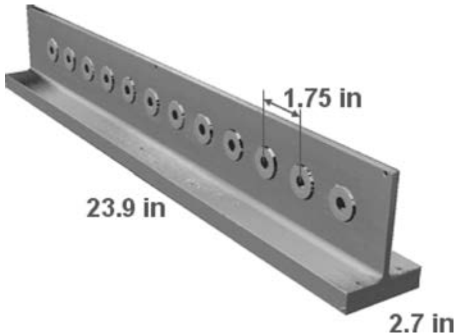

FIG. 10—*T-Section part with* 0.75 in. *bushings installed.*

range of the y-deflections is approximately the same for the model and experimental results.

The z-deflections are compared in Fig. 11(*b*). In this case, the results appear to show some qualitative difference. The major difference is the deflected shape of the left edge (positive y). The model predicts that the left edge in Fig. 11(*b*) deflects in the positive z-direction, with the corners deflecting much more than

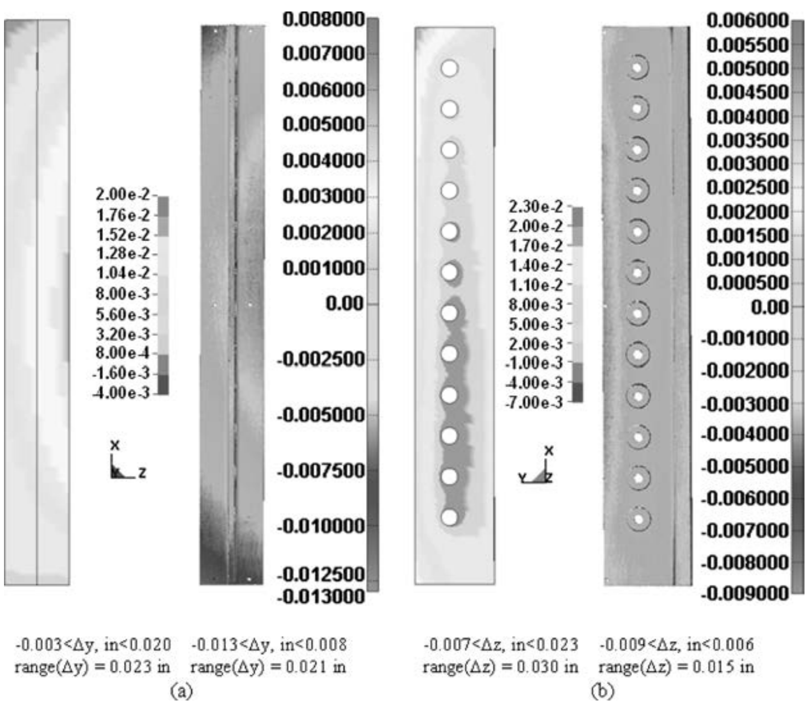

FIG. 11—*Model versus experiment for the T-Section. Fringes of* (*a*) *y-displacement and* (*b*) *z-displacement, in inches. Bushing flanges are on the positive z side of the part.*

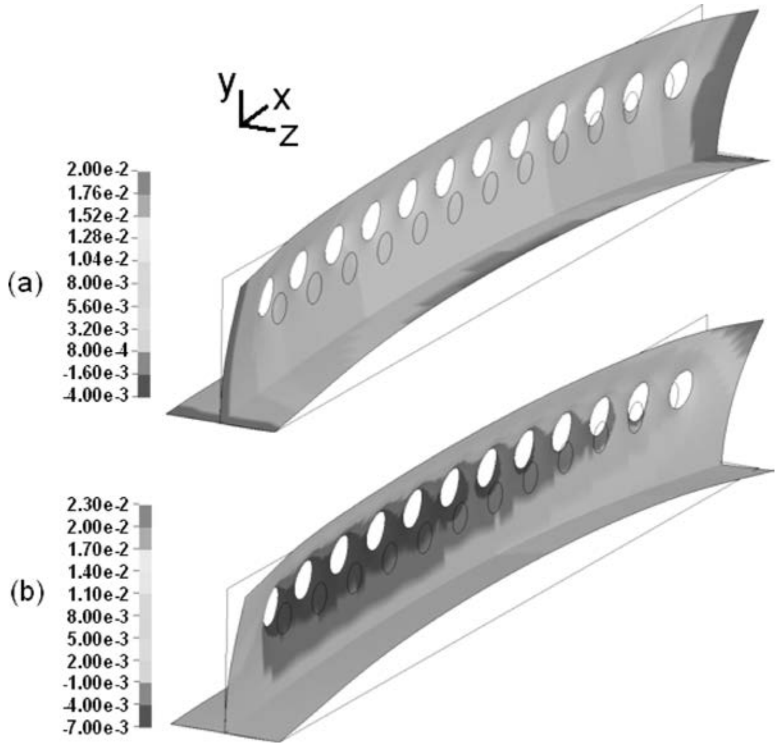

FIG. 12—*Fringes of (a) y-deflection and (b) z-deflection for the T-Section. The depicted deflections are 50 times the actual. Bushing flanges are on the positive z side of the part.*

the middle. The experimental results also show the left edge deflected in the positive z-direction with respect to the bushings, but the middle is deflected more than the corners. Also, the range of deflections is predicted to be about six thousandths of an inch larger than were measured. Notice, however, that the magnitude of the measured deflections is small and close to the published accuracy of the measurement system, ±0.0027 in. (±0.069 mm).

To aid in visualization, the deflected shape has been shown exaggerated in Fig. 12. The deflection of the part has been magnified 50 times and is shown twice, once with fringes of y-displacements and again with fringes of

TABLE 4—*Summary of measured and predicted T-Section part deflections.*

Measure of Deflection	Deflection, in. (mm)		Error, in. (mm)
	Model	Experiment	Model - Experiment
range (Δy)	0.023 (0.584)	0.030 (0.762)	−0.007 (−0.178)
range (Δz)	0.021 (0.533)	0.015 (0.381)	0.006 (0.152)

z-displacements. The outline of the undeflected part is shown in black. Note that in the figure the bushing flanges would be on the near side of the part. Cupping is induced in the part that is towards the flange side (near side). The radial expansion of the bushings causes the T-Section to arch in the positive y-direction.

Conclusions

A simplified modeling approach has been developed that makes it practical to predict the distortion of large shell-like metallic parts that is caused by the installation of the interference fit bushings. The simplified method predicted the overall character of the deflection well. However, there was some discrepancy in the predicted magnitude of the deflections.

The simplified equivalent spring approach can give designers a good idea of the type of deflection to expect when bushings are installed. The accuracy of the predicted deflection depends in part on how well the equivalent springs are calibrated. It is expected that the accuracy of the prediction can be improved with more accurate calibration measurements and an automated identification of the equivalent spring parameters.

Acknowledgments

The efforts of a number of people made this work possible. In addition to model geometry, material property data, and funding, Tanni Sisco, Jeff Wilkerson, Bill Merrick, and Matt Knighton provided a great deal of helpful feedback on the analysis work.

References

[1] Champoux, R. L. and Landy, M. A., “Fatigue Life Enhancement and High Interference Bushing Installation Using the ForceMate Bushing Installation Technique,” *Fatigue in Mechanically Fastened Composite and Metallic Joints*, ASTM STP 927, John M. Potter, Ed., ASTM International, West Conshohocken, PA, 1986, pp. 39–52.

[2] Kang, J., Johnson, S. W., and Clark, D. A., “Three-Dimensional Finite Element Analysis of the Cold Expansion of Fastener Holes in Two Aluminum Alloys,” *J. Eng. Mater. Technol.*, Vol. 124, No. 2, 2002, pp. 140–145.

[3] Dutta, N., Rasty, J., and Rassaian, M., “Finite Element Analysis of Elastic-Plastic Zone Around Cold-Expanded Holes,” *Post-Conference Proceedings of the 1997 Society for Experimental Mechanics (SEM) Spring Conference*, June 2–5, 1997, Bellevue, WA, pp. 108–115.

[4] Kim, C., Kim, D.-J., Seok, C.-S., and Yang, W.-H., “Finite Element Analysis of the Residual Stress by Cold Expansion Method Under the Influence of Adjacent Holes,” *J. Mater. Process. Technol.*, Vol. 153-154, 2004, pp. 986–991.

[5] Karabin, M. E., Barlat, F., and Schultz, R. W., “Numerical and Experimental Study of the Cold Expansion Process in 7085 Plate Using a Modified Split Sleeve,” *J. Mater. Process. Technol.*, Vol. 189, 2007, pp. 45–57.

[6] O'Brien, E. W., "Beneficial Residual Stress from the Cold Expansion of Large Holes in Thick Light Alloy Plate," *J. Strain Anal. Eng. Des.*, Vol. 35, No. 4, 2000, pp. 261–276.
[7] Ozdemir, A. T. and Edwards, L., "Through-Thickness Residual Stress Distribution After the Cold Expansion of Fastener Holes and Its Effect on Fracturing," *J. Eng. Mater. Technol.*, Vol. 126, 2004, pp. 129–135.
[8] Wang, Z. and Zhang, X., "Predicting Fatigue Crack Growth Life for Cold-Worked Holes Based on Existing Closed-Form Residual Stress Models," *Int. J. Fatigue*, Vol. 25, 2003, pp. 1285–1291.
[9] Zhang, Y., Fitzpatrick, M. E., and Edwards, L., "Analysis of the Residual Stress Around a Cold-Expanded Fastener Hole in a Finite Plate," *Strain J. Brit. Soc. Strain Measurement*, Vol. 41, 2005, pp. 59–70.
[10] *LS-DYNA Keyword User's Manual*, Version 970, Livermore Software Technology Corporation, April 2003.
[11] *LS-DYNA Theory Manual*, J. O. Hallquist, Ed., Livermore Software Technology Corporation, March 2006.
[12] Bergevin, R., Soucy, M., Gagnon, H., and Laurendeau, D., "Towards a General Multi-View Registration Technique," *IEEE Trans. Pattern Anal. Mach. Intell.*, Vol. 18, No. 5, 1996.
[13] *Department of Defense Handbook: Metallic Materials and Elements for Aerospace Vehicle Structures*, United States Department of Defense, MIL-HDBK-5J, January 31, 2003.

ASTM Special Technical Publication, Vol. 5, No. 10
Paper ID JAI101530
Available online at www.astm.org

A. Lamik,[1] *H. Leitner,*[1] *W. Eichlseder,*[1] *and F. Riemelmoser*[2]

A Concept for the Fatigue Life Prediction of Components from an Aluminum-Steel Compound

ABSTRACT: The goal of this research project is the development of a simulation model for lifetime estimation of components from AA6016-T4/FeP06 material compound. Since such components are manufactured predominantly by rolling (for manufacturing of the material compound) and deep-drawing, the influence of the plastic deformations during the manufacturing process on the fatigue behavior must be investigated. In particular, the influence of the rolling reduction on the behavior of FeP06 steel has a relevant effect on the fatigue life of this aluminum-steel compound. Simulation models for fatigue life estimation of this material compound must therefore consider the influence of the elastic plastic deformation which occurs during, e.g., rolling and deep-drawing processes. For this purpose, a new model for the generation of yield curve as a function of the rolling reduction of the material FeP06 was determined. The proposed yield curve model shows good results at low and high rolling reduction compared to the models of Voce and Swift. The lifetime estimation shows a substantial improvement of accuracy (600 %) by the consideration of the influence of the rolling reduction.

KEYWORDS: material compound, rolling reduction, AA6016-T4/FeP06, simulation model, hardening

---

Manuscript received November 19, 2007; accepted for publication October 3, 2008; published online November 2008.
[1] Chair of Mechanical Engineering, University of Leoben, A-8700 Leoben, Austria, e-mail: Abdelrhani.lamik@mu-leoben.at
[2] ARC Leichtmetallkompetenzzentrum Ranshofen GmbH, A-5282 Ranshofen, Austria.

Citation: Lamik, A., Leitner, H., Eichlseder, W., and Riemelmoser, F., "A Concept for the Fatigue Life Prediction of Components from an Aluminum-Steel Compound, *J. ASTM Intl.*, Vol. 5, No. 10. DOI10.1520/JAI101530. Available online at www.astm.org. Also included in JAI Special Issue STP 1508, *Fatigue and Fracture Mechanics: 36th Volume,* R. W. Neu, K. R. W. Wallin, and S. R. Thompson, guest editors, ASTM International, West Conshohocken, PA, 2009, pp. 794-813.

Introduction

In wide areas of mechanical engineering, a permanent development of components and modules concerning low weight and reliability are required. In many cases, due to the manifold requirements, a solution with a specific single material cannot be reached. New application areas can be found by the use of material compounds. The advantages of each individual material of the material compound can be utilized.

In addition to the described requirements above, the components must exhibit appropriate fatigue strength, i.e., sufficient durability under cyclic load as described by the S/N-curve.

For lifetime calculation, three concepts are available:

- Nominal stress concept: to characterize the allowable stress in the components a nominal stress has to be defined. Moreover, position and a characteristic cross section must be defined.
- Local stress concept.
- Fracture mechanics concept: it's assumed that the components to be analyzed are cracked. An overview of these different lifetime calculation concepts is given in Refs. [1,2].

The local stress concept is totally adequate for lifetime calculation of components from thin sheet. Lifetime calculation software does not consider the influence of the rolling reduction during the rolling process on the material behavior. The first approach of lifetime estimation of the structure from thin sheet metal was established by Herrmann et al. and Le Roch as well as by Masendorf et al., whereas the influence of the rolling reduction on the cyclic material behavior was not considered [3,4]. The local stress of the structure from thin sheet was investigated by means of a linear elastic Finite Element Method (FEM) calculation [3]. The local elastic plastic stress was estimated by the mean of Neuber rule [5] and the cyclic stress-strain-curve of unformed material. The suggested concept considers neither the variation of the material behavior through forming (e.g., deep drawing) nor through the rolling process. It's assumed that the thickness of the sheet is constant and that the components have an ideal geometry.

A forming simulation was carried out to determine the stress distribution [4]. It serves for the consideration of the thickness reduction during the forming process. The forming ratio was still not considered. The position of the critical stress is identified using the Dang Van criteria [6].

The influence of the forming ratio on the cyclic material behavior was first investigated by Masendorf [7]. He found that for all investigated material, the mechanical properties increase by increasing the forming ratio. The strain S/N curve is translated to higher fatigue life in the transition range to the fatigue strength.

The characterization of the AA6016-T4/FeP06 material compound was introduced in Ref. [9]. In this work, the main section deals with the influence of the rolling reduction on the fatigue behavior during the manufacturing process. Additionally, the influence of the mean stress and rolling direction on the fatigue behavior of the A6016/FeP06 material compound was studied.

In this investigation, each component of the material compound was first

TABLE 1—*Chemical composition of FeP06 (in weight percent).*

C	Si	Mn	P	S	Al	Ti
0.002	0.01	0.12	0.006	0.011	0.045	0.072

analyzed separately, and then the material compound itself was analyzed.

Material Data

For this investigation, the following materials were used:

- Cold-rolled IF-steel FeP06 according to EN10130, 2.5 mm of thickness
- Cold-rolled AA6016-T4, 2 mm of thickness

The chemical composition of both materials is shown in Tables 1 and 2.

Mechanical Testing

The static mechanical properties were evaluated by employing a computer-controlled servo-hydraulic machine (Instron 8802). The load was measured using a load cell Dynacell with a 100 kN nominal load. For strain measurement, an Instron extensometer of type 2620 was used.

The fatigue tests were performed using a MICROTRON resonant testing machine with a nominal load of 20 kN.

Overview of the Manufacturing of the Material Compound

The material compound was manufactured using the roll-bonding process. Before rolling, the aluminum and steel sheets were degreased. Then, the surface of the sheets was scratch brushed. The pressure in the roll gap elongates the strips and causes the interface layers to break up simultaneously (see Fig. 1(*a*) and Fig. 1(*b*)). The underlying metal is then exposed, and is extruded under the action of the roll pressure through widening cracks in the surface layers Fig. 1(*c*). The freshly created metal surfaces come into intimate contact and are welded, Fig. 1(*d*). The welding quality is affected by the rolling reduction, the metal under consideration, the temperature of welding, pressure, time of welding, lattice structure, solubility of oxygen in the metal, metal purity, and surface preparation. The mechanism of cold pressure welding is explained in detail in Refs. [9–12]. An investigation of the deformation behavior and bonding strength of the bimetal strip is presented in detail in Refs. [13–15]. The effect of annealing treatment on mechanical properties of aluminum clad steel sheet is evaluated in Ref. [16].

TABLE 2—*Chemical composition of AA6016-T4 (in weight percent).*

Si	Fe	Cu	Mn	Mg	Zn	Ti
1.0–1.5	0.2	0.2	0.2	0.25–0.6	0.2	0.15

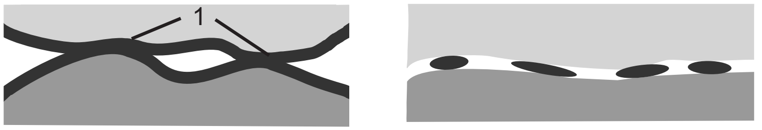

(a) Interface layers come together (b) Break up of the two interface layers

(c) Extension of material in the crack (d) Freshly created surfaces come into intimate contact

FIG. 1—*Schematic illustration of the mechanism of cold pressure welding.*

In order to complete the welding process, the material compound undergoes a suitable heat treatment (solution annealing at 540°C) (see Fig. 2). This enhances the diffusion process and leads to good bond strength. Furthermore, bonding does not occur until a certain threshold deformation is reached. In the actual work, the threshold deformation for AA6016-T4/FeP06 is equal to a 20 % reduction of the thickness (rolling reduction).

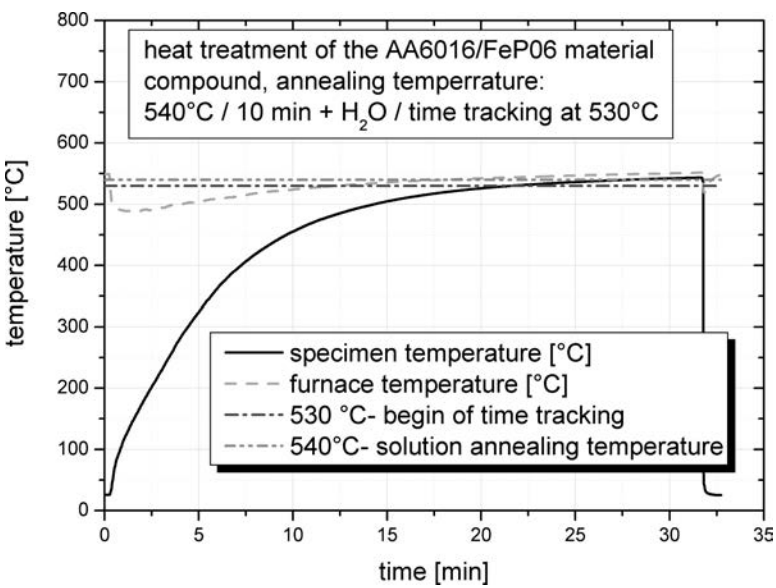

FIG. 2—*Heat treatment of the AA6016/FeP06 material compound.*

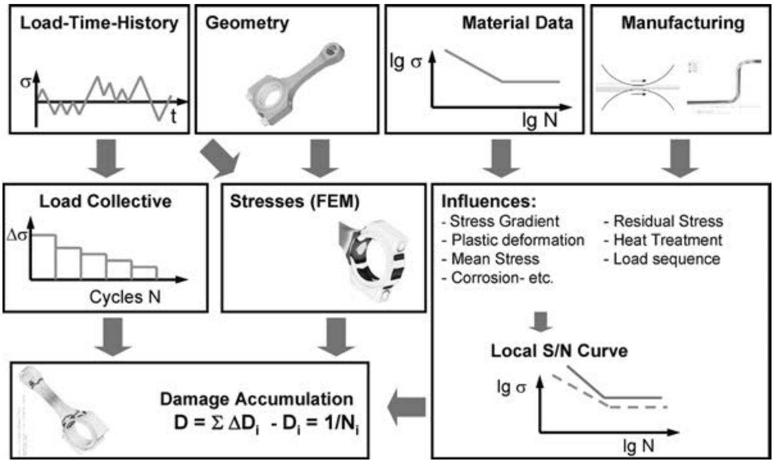

FIG. 3—*Lifetime calculation concept on the base of local stresses.*

Lifetime Estimation on the Base of Local Stresses

Since it is not possible to define a characteristic cross section for complex structures, the lifetime calculation based on nominal stresses cannot be applied. Hence, the lifetime calculation is carried out using local stresses as shown in Fig. 3 [17,18].

The stress distribution is obtained by a FEM simulation which uses the load history and the components geometry as input parameters. To determine the local material behavior, a basic S/N curve is needed which is derived from fatigue tests on specimens under defined loadings. These basic material data are adjusted to the local conditions by means of several fatigue hypotheses.

Furthermore, the load spectrum derived from the load history is also needed for the lifetime calculation. The damage value results from the damage accumulation. Therefore, the local load spectrum, the local stress distribution, and the local fatigue behavior are needed.

Transferability of Material Behavior from Specimens to Component

The strength behavior of material in a component under operating conditions is not identical with the strength determined on idealized specimens under laboratory conditions. The local fatigue strength in the component is influenced by stress concentrations, plastic deformation, mean stress, rolling direction, sequence effects, etc. The local effects have to be classified to their fatigue behavior; afterwards, their influences can be considered by simulation step by step.

The influence of the stress concentrations is taken into account according to Eichlseder [17]. The computational S/N curve model of Eichlseder is based on the experimentally established S/N curve of unnotched specimens under both tension/compression and bending load. This model calculates the fatigue

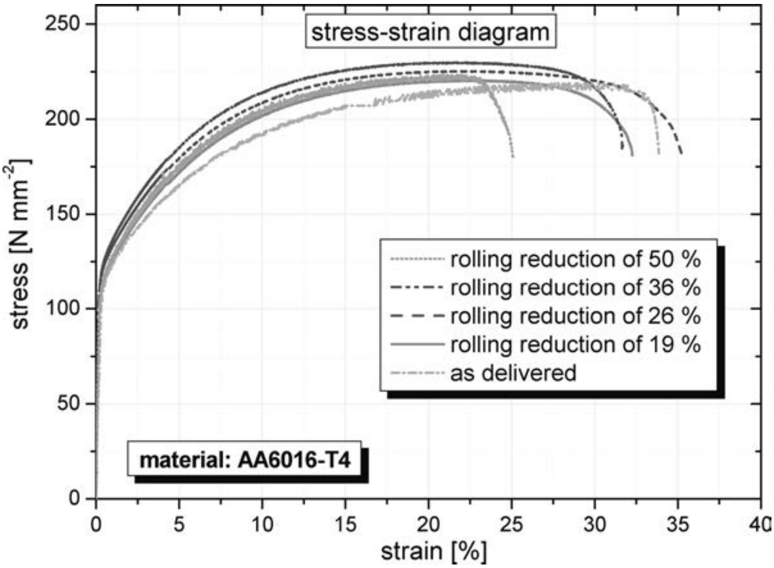

FIG. 4—*Influence of the rolling reduction on the static material behavior of AA6016-T4.*

strength σ_D, the number of cycles at the fatigue limit N_D, and the slope k of the S/N curve is dependent on the local stress gradient.

In this work, the properties of the S/N curve (σ_D, N_D, and k) are calculated as a function of the rolling reduction. The influence of the mean stress, rolling direction on the fatigue behavior is also investigated.

Influence of the Rolling Reduction on the Fatigue Behavior

According to a literature study [13,16] and many experimental investigations, it's been found that a heat treatment (solution annealing at 540°C) of the material compound is optimal to obtain a good bond strength. A material hardening occurs during the manufacturing of the material compound using cold rolling. Due to the heat treatment at 540°C, a recrystallization of the AA6016 occurs, i.e., its mechanical behavior is assumed to be independent from the manufacturing process of the material compound, and there is no influence of the rolling reduction on the mechanical properties of this material (see Fig. 4). In fact, 540°C is too low to cause a recrystallization of the material FeP06. Hence, the influence of the cold rolling reduction which causes a hardening of the material FeP06 is taken as the main influence factor that has to be considered in this simulation model.

In order to investigate the influence of the plastic deformation due to the rolling process on the static and cyclic behavior of the steel, a series of rolling experiments were carried out using several rolling reductions.

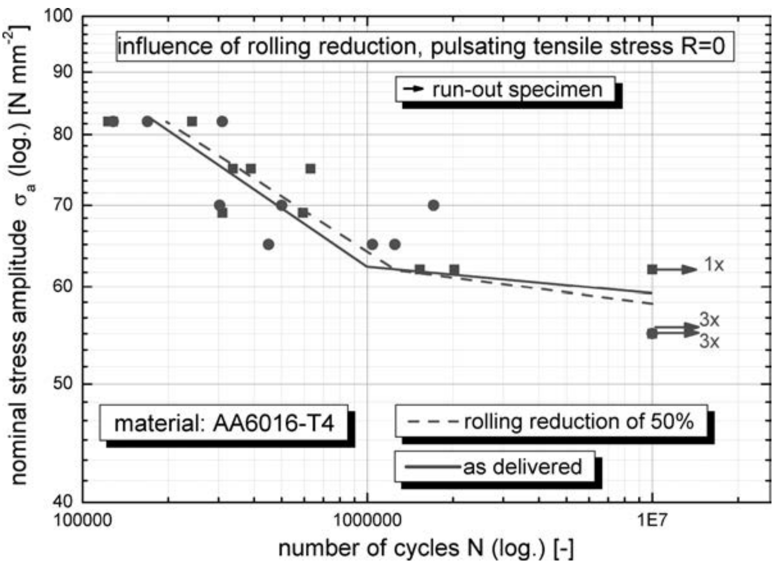

FIG. 5—*Influence of the rolling reduction on the static material behavior of AA6016-T4.*

Influence of Rolling Reduction on Static and Cyclic Behavior of AA6016-T4

Figures 4 and 5, respectively, show the influence of the rolling reduction on the static and cyclic material behavior of the AA6016-T4. As a result of the heat treatment at 540°C (recrystallization effect), this influence is still marginal for both static and fatigue behavior. Although the ultimate strain by a rolling reduction of 50 % declines, the fatigue behavior is marginally changed (see Fig. 5). Hence, the influence of the rolling reduction on fatigue life of the AA6016-T4 will not be considered in the simulation model presented.

Influence of Rolling Reduction on Static and Cyclic Behavior of FeP06

Influence on Static Material behavior—Figure 6 shows the results of the tensile tests on specimens which were machined from plates with different rolling reductions (as delivered, 16, 19, 25, and 37 %). The influence of the rolling process on the mechanical properties is significant.

The yield strength ($R_{p0.2}$) and the ultimate tensile stress (UTS) were established as an empirical function of the rolling reduction (RR), see Eq 1 and 2.

$$R_{p0.2} = 3 \cdot RR + 257 \qquad (1)$$

$$UTS = 3.5 \cdot RR + 276 \qquad (2)$$

Influence on Cyclic Material Behavior, Pulsating Tensile Stress—Several fatigue tests (see Fig. 7) have been performed in order to find a model to describe the fatigue behavior of the material FeP06 as a function of the rolling

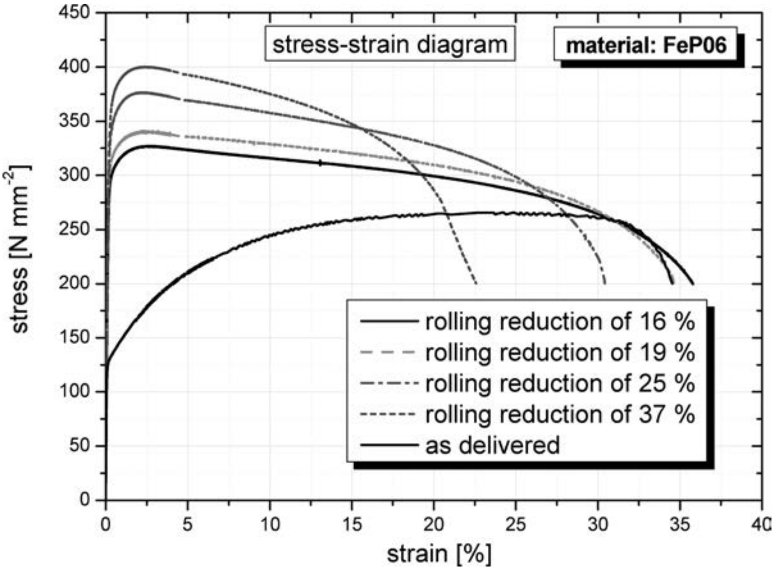

FIG. 6—*Influence of the rolling reduction on the static behavior of the material FeP06.*

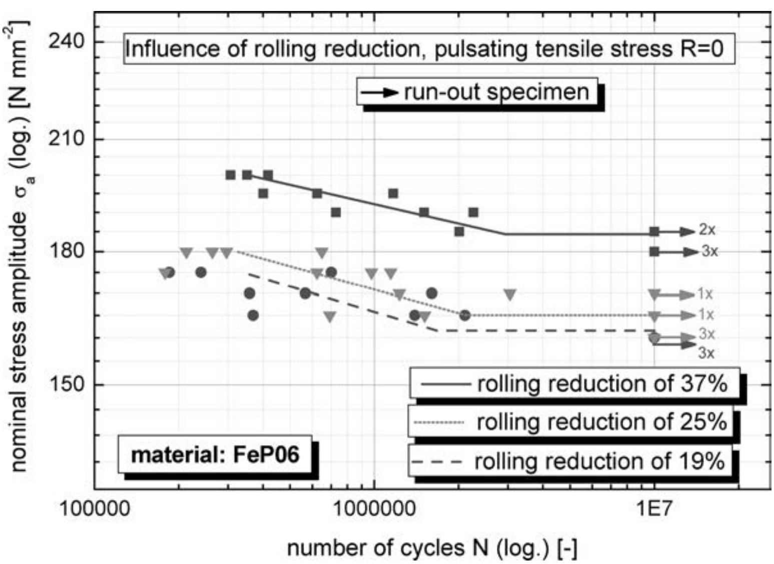

FIG. 7—*Influence of the rolling reduction on the cyclic behavior of the material FeP06, pulsating tensile stress.*

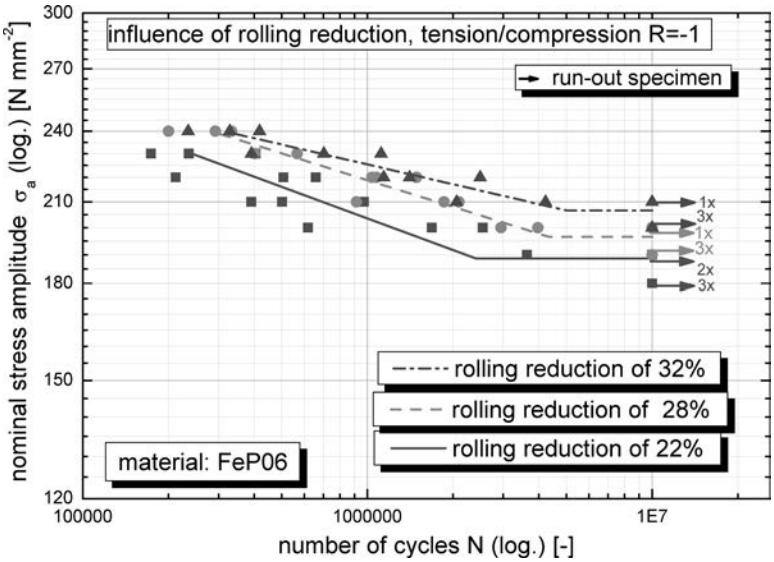

FIG. 8—*Influence of the rolling reduction on the cyclic behavior of the material FeP06, tension/compression.*

reduction.

On the basis of these results the properties of the S/N curve (fatigue limit σ_D, slope k, and the number of cycles at fatigue limit N_D) are established as a function of the rolling reduction (RR) using a linear approximation (see Eqs 3–5).

$$\sigma_D = 1.27 \cdot RR + 136 \tag{3}$$

$$k = 0.34 \cdot RR + 13.66 \tag{4}$$

$$N_D = 69643 \cdot RR + 359643 \tag{5}$$

Influence on Cyclic Material Behavior, Tension/Compression—Figure 8 shows S/N curves for the material FeP06 under tension/compression ($R = -1$) at different rolling reductions. The relation between the properties of the S/N curve and the rolling reduction is shown in Eqs 6–8.

$$\sigma_D = 1.76 \cdot RR + 146.5 \tag{6}$$

$$k = 0.58 \cdot RR + 1.16 \tag{7}$$

$$N_D = 265000 \cdot RR - 3000000 \tag{8}$$

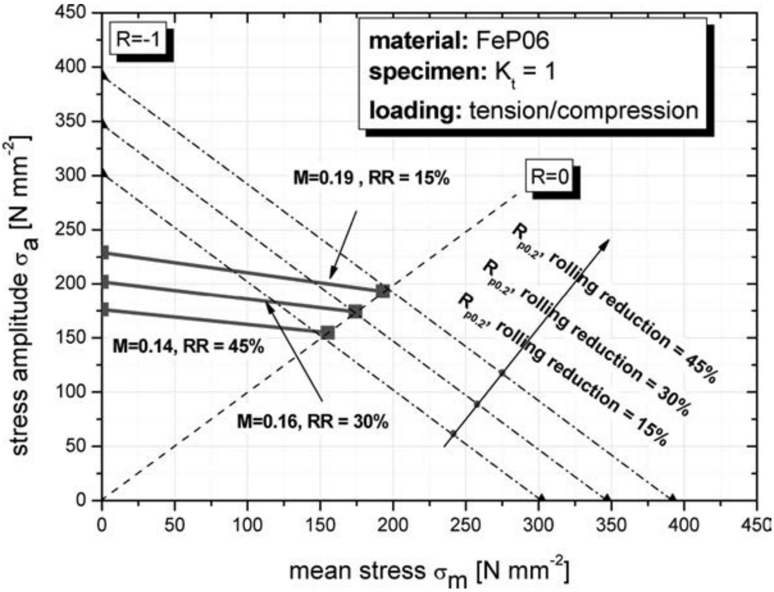

FIG. 9—*Haigh diagram under uniaxial cyclic tension/compression loading, FeP06.*

Influence of the Mean Stress on the Cyclic Behavior

For characterizing the mean stress sensitivity under normal mean stresses of the material FeP06, two S/N curves were determined at stress ratios of $R = -1$, $R = 0$. For AA6016-T4, three S/N curves were determined at stress ratio of $R = -1$, $R = 0$ and $R = 0.5$. The fatigue tests were carried out on unnotched specimens.

Influence of Mean Stress on the Behavior of FeP06

The Haigh diagram under cyclic tension/compression loading (see Fig. 9) indicates that the peak stress evaluated at a stress ratio of $R = 0$ exceeds the yield point at the fatigue limit. Therefore, one can assume that cyclic hardening occurs at high normal mean stresses. The mean stress sensitivity M can be determined by means of:

$$M = \frac{\sigma_a(R = -1)}{\sigma_a(R = 0)} - 1 \tag{9}$$

Figure 9 indicates that the mean stress sensitivity increases by increasing normal mean stress. Another conclusion which can be drawn from the Haigh diagram is that the slope of the S/N curve decreases with increasing mean stress.

The relationship between the mean stress sensitivity and the rolling reduction of the fatigue strength was calculated using Eqs 3 and 6 for several rolling reductions. The mean stress sensitivity M was calculated using Eq 9. The varia-

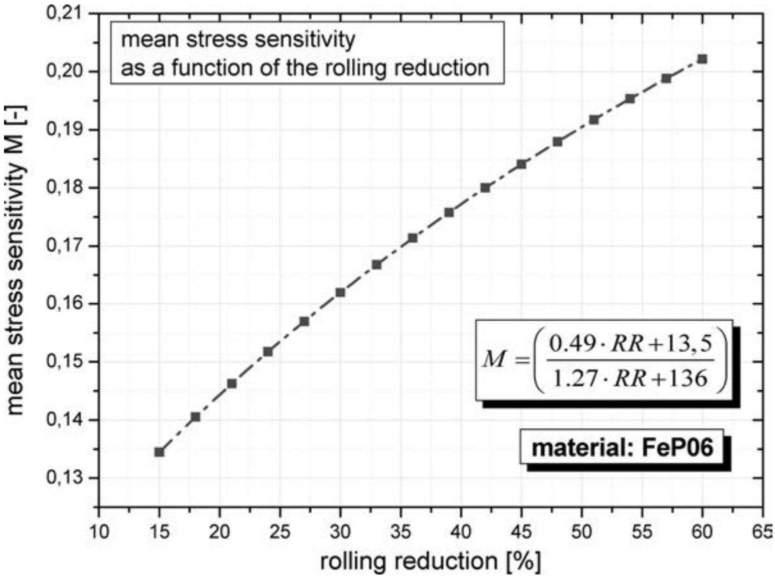

FIG. 10—*Mean stress sensitivity as a function of the rolling reduction* (*RR*).

tion of M as a function of the rolling reduction is shown in Fig. 10. The mean stress sensitivity increases with the increase of the rolling reduction. This confirms the theory that the higher the strength, the more sensitive the material to the mean stress.

Influence of Mean Stress on the Behavior of AA6016-T4

The Haigh diagram under cyclic tension/compression (see Fig. 11) indicates that the peak stress evaluated at a stress ratio of $R = 0.5$ exceeds the yield point even at the fatigue limit. Therefore, one can assume that cyclic hardening occurs at high mean stresses. The mean stress sensitivity M can be determined by means of Eq 9.

Figure 11 indicates that the mean stress sensitivity increases with increasing mean stress.

Influence of the Rolling Direction on the Fatigue Behavior

Several specimens which were machined from the plate with their axes following two different orientations (0° and 90°) with respect to the rolling direction were tested.

The rolling direction has a considerable influence on the static and cyclic behavior of the material FeP06. The yield strength is 293 MPa for specimens taken at 0° to the rolling direction. This value increases to 343 MPa for specimens taken in the other direction (90°) (see Fig. 12). The fatigue strength is increased from 153 MPa to 165 MPa (see Fig. 13). For the material AA6016-T4,

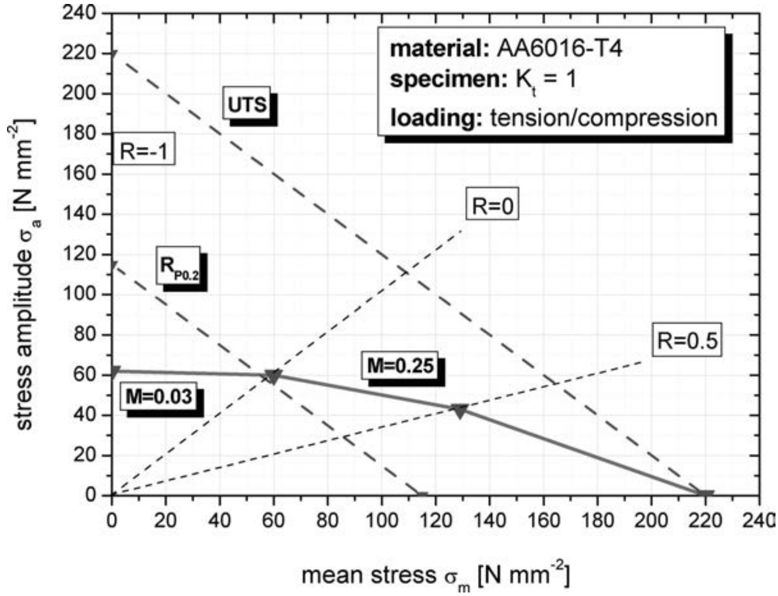

FIG. 11—*Haigh diagram under uniaxial cyclic tension/compression loading, AA6016-T4.*

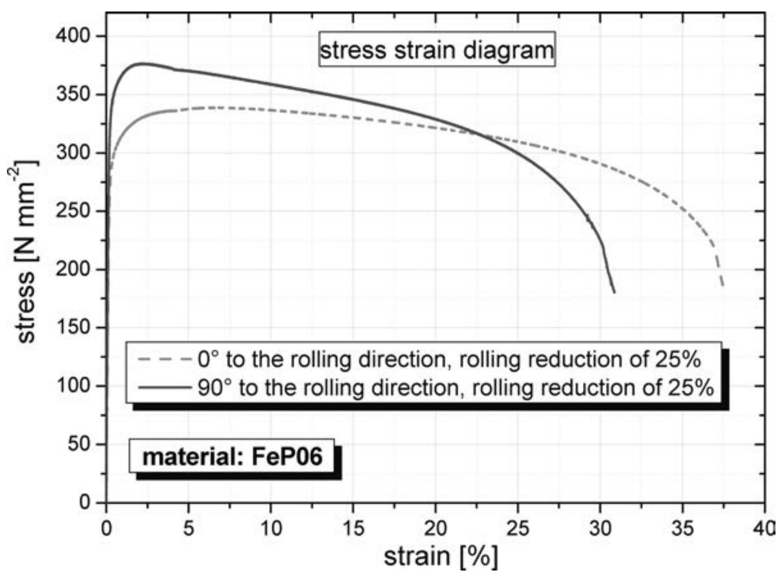

FIG. 12—*Influence of the rolling direction on the static behavior of the material FeP06.*

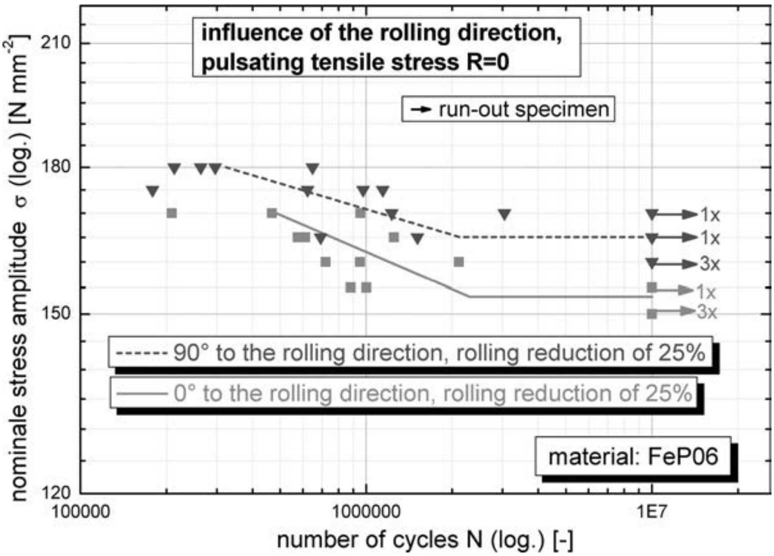

FIG. 13—*Influence of the rolling direction on the cyclic behavior of the material FeP06.*

no effect of the rolling direction on both static and cyclic material behavior was observed.

Simulation of Deep Drawing Process

As the intended use of this material compound for manufacturing components is by means of the deep drawing technique, a simple drawn part (see Fig. 14) is

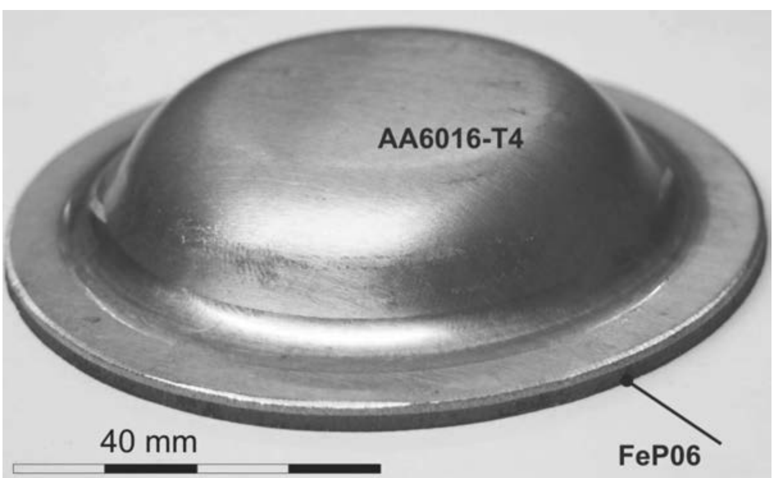

FIG. 14—*Photograph of a simple deep-drawed part (cup).*

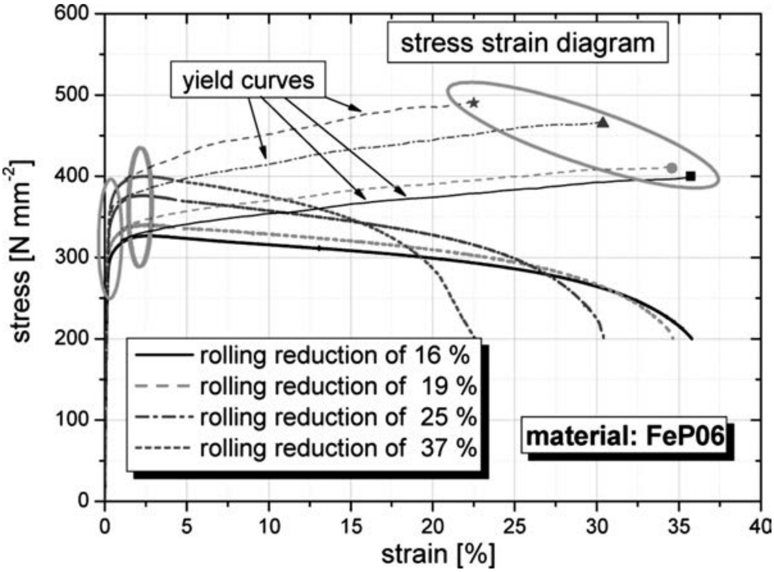

FIG. 15—*Calculation of the yield curve on the base of the tensile test.*

used to verify the simulation model. The peeling tests show that the strength of the interface layer is higher than the least layer (aluminum). Due to these results, it was not necessary to model the interface layer. In fact, an ideal bond between the steel and aluminum is assumed.

Generation of the Yield Curve of AA6016-T4 and FeP06

To simulate a deep drawing process, the elastic plastic behaviors of both materials FeP06 and AA6016-T4 have to be known. The tensile tests show a marginal influence of the rolling reduction on the static behavior of AA6016-T4, thus the yield curve is assumed to be independent from the plastic deformation during the rolling process. Due to the considerable influence of the deformation on the static properties of the material FeP06, a model to generate a yield curve as a relation of the rolling reduction has to be generated. On the basis of the simple tensile tests, a model of the yield curves as a function of the rolling reduction is introduced. From the results of the tensile tests, the yield strength, the ultimate tensile strength and the fracture stress were deduced as a function of the rolling reduction (see Fig. 15, green ellipse). The true fracture stress is calculated by dividing the fracture force by the fracture surface, which is measured using a light microscope. For a given rolling reduction, one is able to determine the yield strength, the ultimate tensile strength, and the fracture stress. Using these three properties and on the basis of the relation of Swift [19], it's possible to calculate the yield curve depending on the rolling reduction (see Eqs 10 and 11):

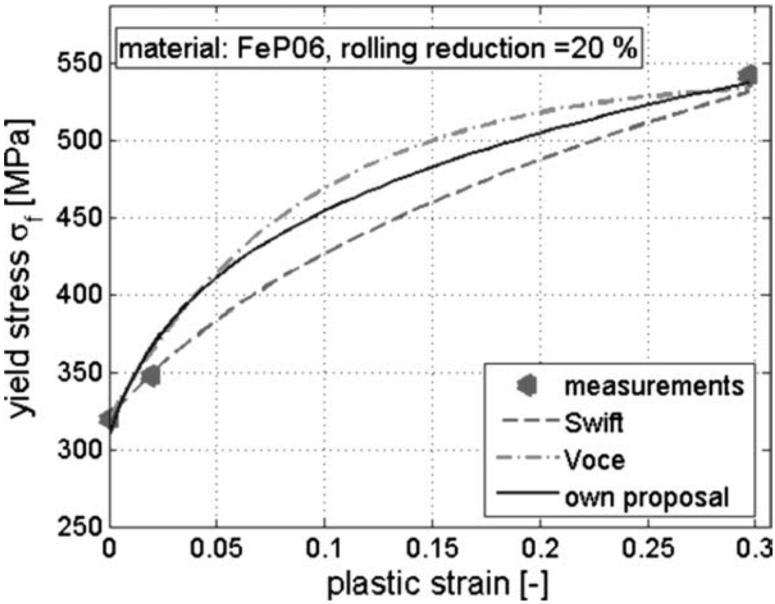

FIG. 16—*Comparison of several approaches for yield curves determination, RR of 20 %.*

$$\sigma_f = R_{p0.2} \cdot \left(1 + \frac{\varepsilon_p}{0.012}\right)^n \tag{10}$$

where σ_f, ε_p, YS and UTS are the true stress, the true strain, the yield stress, and the ultimate tensile stress, respectively. The exponent n is defined as follows (see Eq 11):

$$n = \frac{\ln(YS/UTS)}{\ln(\varepsilon_{FS}/\varepsilon_{UTS})}. \tag{11}$$

where ε_{FS} and ε_{UTS} are, respectively, the true strain after fracture and true strain before reduction.

Comparison of Several Approaches for Yield Curves Determination

To verify the accuracy of the proposed model for the yield curve generation, several approaches were compared with it. In the range of low rolling reduction (*RR*), both the model of Swift and Voce describe well the hardening behavior of FeP06 at high rolling reduction; however, both models become inaccurate. The proposed yield curve model shows a good match at low *RR* and a satisfying accuracy at high *RR* compared to the models of Voce and Swift, see Figs. 16 and 17.

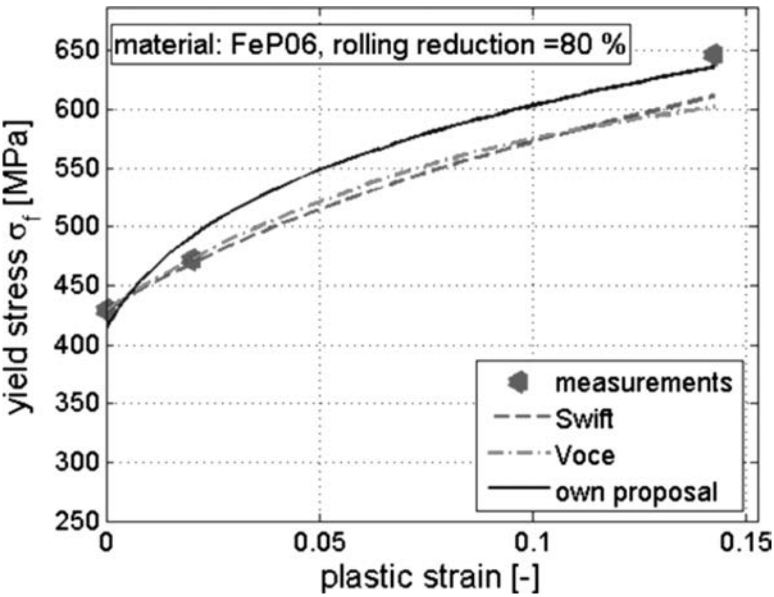

FIG. 17—*Comparison of several approaches for yield curves determination, RR of 80 %.*

Comparison with Experiments

To ensure that the simulation of the cup is valid, a comparison of calculated versus measured thinning at the symmetric line is carried out (see Fig. 18). The calculated distribution of the wall thickness after forming was in good agreement with the experimental results. The simulation of the deep drawing process is carried out using the finite element software ABAQUS, which the thickness of the part is automatically generated. The thinning of the part is measured using a 3-D table for coordinate measurement.

The investigation of thinning along the measurement curve leads to the following conclusion: the maximum thinning is located along the border of the bottom dome (position B). The decay in thinning is around 12 %. The peak of deformation is accurately predicted by the simulation.

A Concept for the Fatigue Life Estimation Applied on a Cup Shaped Component

The investigation accomplished up to now showed a considerable dependence of the fatigue strength and the yield curve on the rolling reduction of the material FeP06. For a lifetime calculation of components made of an AA6016-FeP06 material compound, a simulation has to be carried out in order to calculate the local stress. This has not only to consider the geometry of the component, but also the influence of the rolling reduction.

Figure 19 shows a concept of a lifetime calculation of component made

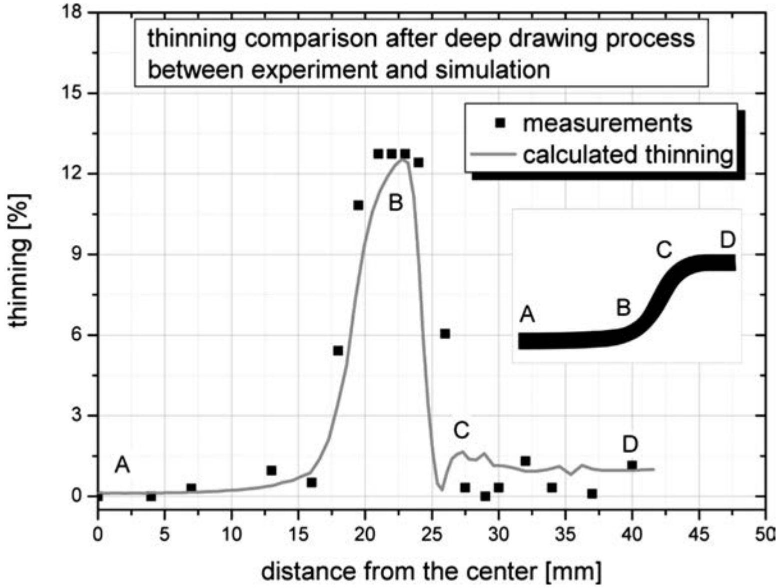

FIG. 18—*Comparison between distributions of wall thickness obtained by simulation an experiment.*

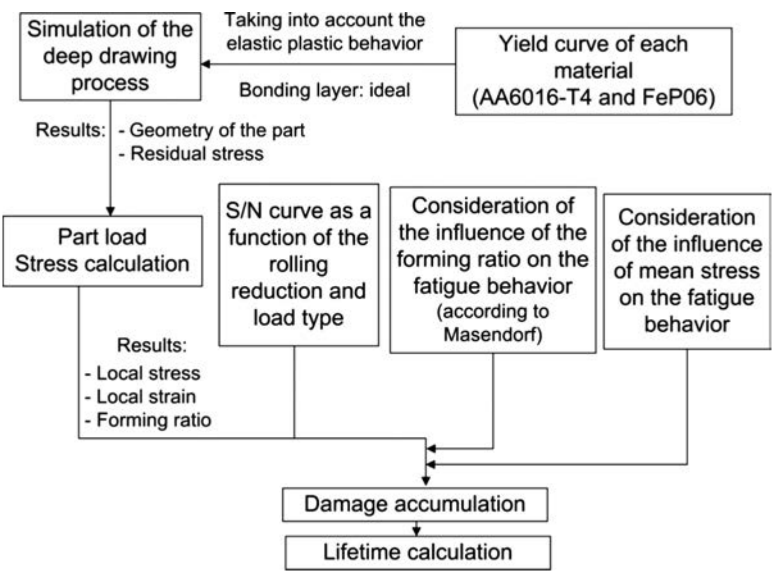

FIG. 19—*Concept of a model for lifetime calculation.*

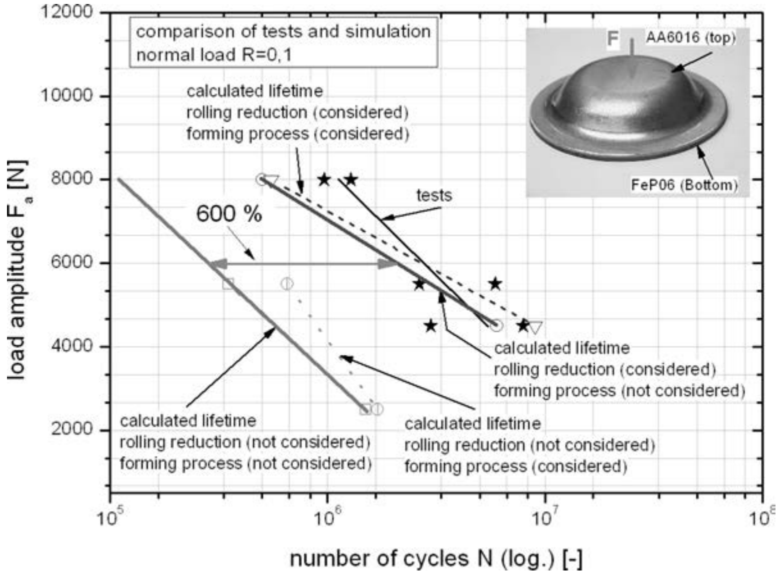

FIG. 20—*Concept of a model for lifetime calculation.*

from this material compound. With this calculation concept it's the first time that the influence of the manufacturing process (rolling reduction) on the fatigue behavior of the component by the means of simulation has been considered.

Another influence factor on the fatigue life of components from thin sheet metal is the forming ratio. This was investigated in detail in Ref. [7] and will also be considered in the actual model.

First, the forming simulation (deep drawing simulation) by mean of the yield curve is carried out. Using this simulation, the component geometry and the residual stress can be deduced.

The component is loaded by an alternating force perpendicularly to the top surface of the cup. The local stress, local strain, and the forming ratio are then determined. By means of the local stress, the local strain and the local S/N curves (which depend on the rolling reduction), damage value is calculated using a linear damage accumulation method according to Miner [20].

Verification of the Proposed Concept for Lifetime Estimation

The material compound is manufactured by means of the deep drawing technique. We therefore used a simple drawn part, in this case a component with a cup shape, to verify the simulation model. Several fatigue tests were performed at stress ratio of $R=0.1$. The results of the fatigue tests were compared to the simulation results. The lifetime estimation shows a considerable improvement of 600 % of accuracy by the consideration of the influence of the rolling reduction, see Fig. 20.

Conclusion

Due to the conflict between the requirements (low weight and high strength), the design of components from a thin sheet of metal manufactured of different compounds, still poses optimization problems. To reduce the development effort, it is important to minimize the number of prototypes. Therefore, the use of a simulation model to predict behavior is necessary for component optimization. A computation concept is presented for the lifetime estimation of cyclic loaded components from an Al6016-T4/FeP06 material compound. This considers the influence of the rolling reduction as the main influence factor on the lifetime of such components. A yield curve as a function of the rolling reduction of the material FeP06 was also generated in this study, which is necessary for each elastic plastic deep drawing simulation. The proposed yield curve model shows significant improved results at low and high rolling reduction compared to the models of Voce and Swift.

To verify this simulation model, fatigue tests on the component itself have been performed. The lifetime estimation shows a substantial improvement of accuracy (600 %) by the consideration of the influence of the rolling reduction. In order to approve the general applicability of this model, other materials have also to be tested.

Acknowledgments

The authors would like to thank the Austrian National Foundation for funding this research work in the framework of the project: Austrian Light Weight Structures.

References

[1] Haibach, E., "Verfahren Und Daten Zur Bauteilberechnung," VDI; ISBN 3–18–400828–2; 1989.
[2] Radaj, D., "ErmüDungsfestigkeit," Springer Verlag, Berlin, 1995.
[3] Herrmann, F., Kiehn, H., and Stäblein, R., "Lebensdauer Von Blechen Mit Sicken," *Forschungsvereinigung Automobiltechnik EV*, Bericht Nr.128, Frankfurt.
[4] Le Roch, Y., Berard, J. Y., Duval, J. L., Mouatassim, El, and DI Pasqual, E., "Coupled Sheet Metal Forming and Fatigue Simulation," IDDRG "Sheet Metal Forming Beyond 2000," *Proceedings of the 20th Biennial Congress*, 17–19 June, 1998, Genval, Brussels.
[5] H. Neuber, "Theory of Stress Concentration for Shear-Strained Prismatical Bodies with Arbitrary Nonlinear Stress-Strain-Law," ASME, *ASME J. Appl. Mech.*, Vol. 28 (1961).
[6] Dan Van, K., "On a New Multiaxial Fatigue Limit Criterion: Theory and Application," *Biaxial and Multiaxial Fatigue EGF3*, Mechanical Engineering publications, London, 1989, pp. 479–496.
[7] Masendorf, R., "Einfluss Der Umformung Auf Die Zyklischen Werkstoffkennwerte Von Feinblech," Technische Universität Clausthal, Dissertation, 2000.
[8] Lamik, A., Leitner, H., Eichlseder, W., and Riemelmoser, F., "A Study of the Fatigue Behaviour of an Aluminium-Clad Steel Material Compound," *Strain Journal*, 2007.

[9] Cave, J. A., and Williams, J. D., "the Mechanism of Cold Pressure Welding by Rolling," Department of Mechanical Engineering, Ashby Institute, The Queen's University of Belfast, *Journal of the Institute of Metals*, Vol. 101, 1973, pp. 203–213.

[10] K. J. B. Mcewan, and D. R. Milner, "Pressure Welding of Dissimilar Metals," Department of Industrial Metallurgy at Birmingham University, *Br. Weld. J.*, Vol. 9, July 1962, pp. 406–420.

[11] N. FröMel, and M. Paulus, "Modifiziertes Kaltwalzplattierverfahren," *Metall*, Vol. 36 No. 7, 1982, pp. 771–773.

[12] N. Bay, "Friction and Adhesion in Metal Forming and Cold Welding," Dissertation, Technical University of Denmark, 1985.

[13] H. Danesh Manesh, and A. Karimi Taheri, "Bond Strength and Formability of an Aluminium-Clad Steel Sheet," *J. Alloys Compd.*, Vol. 361, 2003, pp. 138–143.

[14] H. Danesh Manesh, and A. Karimi Taheri, "An Investigation of Deformation Behavior and Bonding Strength of Bimetal Strip During Rolling," *Mechanics of Materials*, Vol. 37, 2005, pp. 531–542.

[15] Mori, T., and Kurimoto, S., "Press-Formability of Stainless Steel and Aluminum Clad Sheet," *J. Mater. Process. Technol.*, Vol. 56, 1996, pp. 242–253.

[16] Danesh Manesh, H., and Karimi Taheri, A., "the Effect of Annealing Treatment on Mechanical Properties of Aluminium Clad Steel Sheet," *Mater. Des.*, Vol. 24, 2003, pp. 617–622.

[17] Eichlseder, W., "Fatigue Analysis by Local Stress Concept Based on Finite Element Results," *Computers & Structures*, Vol. 80, 2002, pp. 2109–2113.

[18] Fröschl, J., and Eichlseder, W., "Betrachtungen zur Schwingfestigkeit multiaxial beanspruchter Bauteile," Christian Doppler Laboratorium für Betriebsfestigkeit, Lehrstuhl für Allgemeinen Maschinenbau, Montanuniversität Leoben.

[19] Gronostajski, Z., "The Constitutive Equations for FEM Analysis," *J. Mater. Process. Technol.*, Vol. 106, 2000, pp. 40–44.

[20] Miner, M. A., "Cumulative Damage in Fatigue," *ASME J. Appl. Mech.*, Vol. 12, 1945, pp. 159–164.

ASTM Special Technical Publication, Vol. 5, No. 6
Paper ID JAI101571
Available online at www.astm.org

C. N. David,[1] *M. A. Athanasiou,*[1] *K. G. Anthymidis,*[1] *and P. K. Gotsis*[1]

Impact Fatigue Failure Investigation of HVOF Coatings

ABSTRACT: Dynamic impact-wear and coating fatigue at cyclic loading conditions demonstrates a very demanding failure mode, which occurs in a number of mechanical applications and it becomes very critical when the application concerns aggressive working environments. The coating impact testing is a novel experimental technique developed to investigate the fatigue behavior of coating-substrate compounds, which was not possible with the common testing methods previously available. The objective of this study is to investigate the influence of the impact load on the fatigue strength of thermal spray high velocity oxy-fuel (HVOF) coatings. Furthermore, the overall aim of the current research is to prove the reliability of the impact testing method to assess the coating lifetime against fatigue, to interpret the coating failure modes, and thereby to explore its capability, whether this nonstandard test can be used in industrial scale as a reliable technique in the development and optimization of fatigue resistant coatings. Based on the above method the current research provides experimental results concerning the coating fracture in terms of cohesive and adhesive failure modes. The fatigue strength of the tested coatings is determined in terms of fatigue-like diagrams by means of scanning electron and white light interference microscopy, as well as by electron dispersive x-ray analysis (EDX) at discrete loads and number of loading cycles. From the conducted experiments, it was shown that the optimum HVOF coating against fatigue is the WC-CoCr.

KEYWORDS: HVOF coatings, impact fatigue, cohesive-adhesive coating failure

---

Manuscript received November 14, 2007; accepted for publication May 14, 2008; published online June 2008.

[1] Mechanical Engineering Department, Technical University of Serres, 62124Serres, Greece, e-mail: david@teiser.gr

Citation: David, C. N., Athanasiou, M. A., Anthymidis, K. G., and Gotsis, P. K., "Impact Fatigue Failure Investigation of HVOF Coatings," *J. ASTM Intl.*, Vol. 5, No. 6. DOI10.1520/JAI101571. Available online at www.astm.org. Also included in JAI Special Issue STP 1508, *Fatigue and Fracture Mechanics: 36th Volume,* R. W. Neu, K. R. W. Wallin, and S. R. Thompson, guest editors, ASTM International, West Conshohocken, PA, 2009, pp. 814-824.

Introduction

The modern power generation steam turbines are being designed to have higher efficiencies and to meet the stringent environmental regulations, ensuring plant reliability, availability, and maintainability without compromising cost. High efficiencies can be achieved at higher temperatures. Therefore, the operating temperature is expected to rise from 550°C to 650°C and from the material perspective to implement turbine components protected by spallation and oxidation resistant coatings.

To guarantee the reliability of coated steam turbines components, used in power plants, the lifetime assessment of the coatings and their failure prediction become very important. Microhardness, scratch adhesion and pin-on-disk sliding tests are commonly used for rapid evaluation of the mechanical properties of coatings [1]. However, they do not model the dynamic cyclic impact fatigue. The impact test method has been introduced as a convenient experimental technique to assess the fatigue strength of coatings being exposed in successive impact loads [2–5].

According to this method a coated specimen is exposed to a cyclic impact load. The superficially developed Hertzian pressure induces a complex stress field within the coating, as well as in the interfacial zone between the layer and the substrate. Both these stress states are responsible for distinct failure modes such as the cohesive or adhesive one. The exposure of the layered compound against impulsive stresses creates the real conditions for the appearance of the coating fatigue phenomena based upon structural transformation, cracking generation, and cracking growth, which are responsible for the gradual microchipping and the degradation of the coating.

Experimental Procedure

The objective of this experimental study was to investigate the influence of the impact stress state on the performance and fatigue strength of thermal spray HVOF coatings. Furthermore, the overall aim of the current research was to prove the reliability of the impact test, as a new testing method, to assess the coating lifetime against high cycle fatigue, to interpret the failure modes of coatings, and thereby to examine its capability, whether this nonstandard test can be used as a useful method for the development and optimization of fatigue resistant coatings working under impact Hertzian loading.

Thermal spray coatings have been applied in many different industries to provide wear and corrosion protection. It is common knowledge today that high velocity oxy-fuel (HVOF) deposition systems are capable of producing coatings with high density, higher hardness, and superior bond strength compared to other thermal spray methods. This paper is concerned with HVOF thermal spray coatings, deposited on high-strength Cr-steel (P91). In Table 1 specific properties of the investigated coating steel layered compounds are shown. The coating impact test was used as the most convenient experimental method to assess the fatigue strength of the examined coating systems under cyclic impact loading.

Figure 1 shows the impact test rig where the experiments have been con-

TABLE 1—*Specific properties of the investigated coating steel layered compounds.*

Coating/substrate	WC-CoCr/P91 Steel	Ni20%Cr/P91 Steel	CrC25%Ni/P91 Steel
Hardness (HV)	520/270	340/271	851/257
Thickness (μm)	100	100	130
Deposition method	HVOF	HVOF	HVOF

ducted [6,7]. The stress strain problem related to the impact test is the Hertzian contact, which is developed between the spherical indentor (cemented carbide ball consists of 88 % WC and 12 % Co) with a diameter of 5 mm and the examined layered space (Fig. 2(*a*)). To minimize the friction in the contact area during the impact lubricant film is used. The resulted impact craters were analyzed using both scanning electron microscopy and 3D-optical profilometry (Fig. 2(*b*)). A window of the impact force signal in time domain acquired during a typical experiment is shown in Fig. 2(*c*). The impact frequency amounts to 50 Hz and was the same for all conducted experiments. In order to determine experimentally the coating fatigue life curve (Fig. 2(*d*)) a number of experiments with varied impact force amplitude and a number of cycles have to be carried out [2,4].

In the impact craters resulting from such experiments three different zones inside and around the impact cavity can be identified [5]. A central zone in the mid of the impact cavity, where the coating is strained with compressive stresses and gradual cohesive degradation takes place. The intermediate zone inside the piled up rim formed around the impact cavity, where tensile and shear stresses are building up and both cohesive and adhesive coating failure arises. Finally, the outer zone of the impact cavity, where macrocracks might propagate and coating adhesive failure occurs depending on the coating brittleness. Gradual intrinsic coherence coating release and coating microchipping leading to progressive degradation of the film is characterized as cohesive failure mode. Abrupt coating fracture and suddenly exposure of the substrate material, due to poor coating adhesion with the substrate, designates the adhesive failure mode. Both coating failure modes and their extent were assessed by SEM observations, EDX analysis, as well as by white light interference microscopy (3D-optical profilometry). The appearance of the substrate material due to coating removal in a local area of the impact crater was selected as failure

FIG. 1—*Impact test rig.*

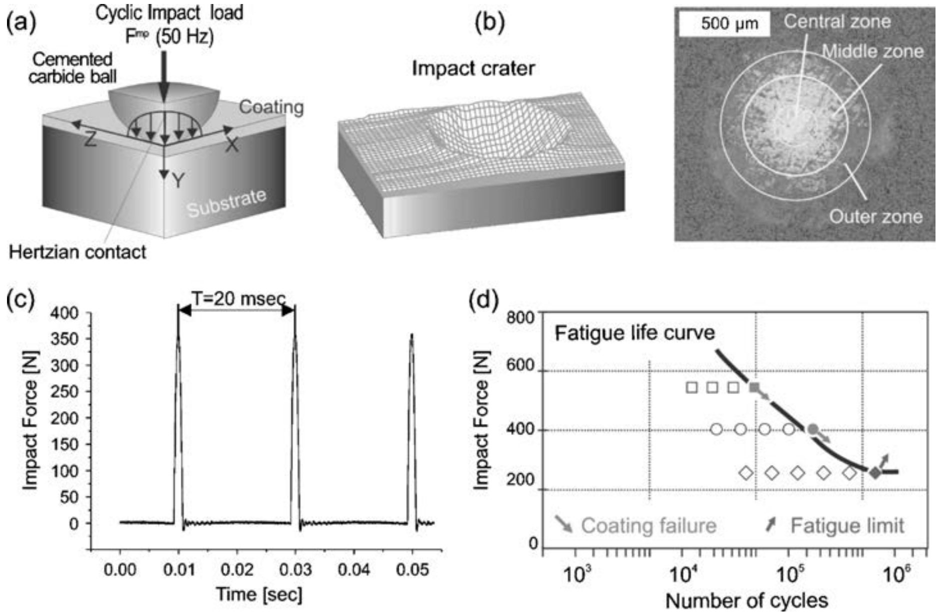

FIG. 2—(*a*) *Working principle of the impact testing,* (*b*) *scanned impact craters,* (*c*) *impact force signal,* (*d*) *coating fatigue life curve.*

criterion. The failure was identified by EDX analysis inside the crater in terms of iron detection belonging to the substrate. The proposed testing method has been proved to be repeatable regarding the coating fatigue strength identification, due to the fact that for each of the examined samples, a couple of experiments have been carried out in order to determine the fatigue curve. From these experiments we observe that in all fatigue diagrams the resulted fatigue curves have the typical shape of fatigue life curves.

During the indentation of the impact ball in the crater, friction and microslip mainly exist at the intermediate area of the impact cavity and superficial abrasive wear also takes place there. However, from the experimental analysis it is observed that coating failure in adhesive mode arises in this zone. Although friction is present here, the result is that the induced shear and tensile stresses cause the coating fatigue. Furthermore, coating failure occurs in the center of the impact cavity, where the friction due microslip is negligible and in the crater vicinity where no contact exists, as well. Hence, it can be concluded that the major coating failure mechanism is the coating fatigue and the friction does not significantly affect the coating failure in this test.

Discussion of Experimental Results

The main failure of the examined coating-substrate compounds occurred in the central zone of the impact crater with gradual coating degradation. However, depending on the impact load amplitude the tensile and shear stresses in the

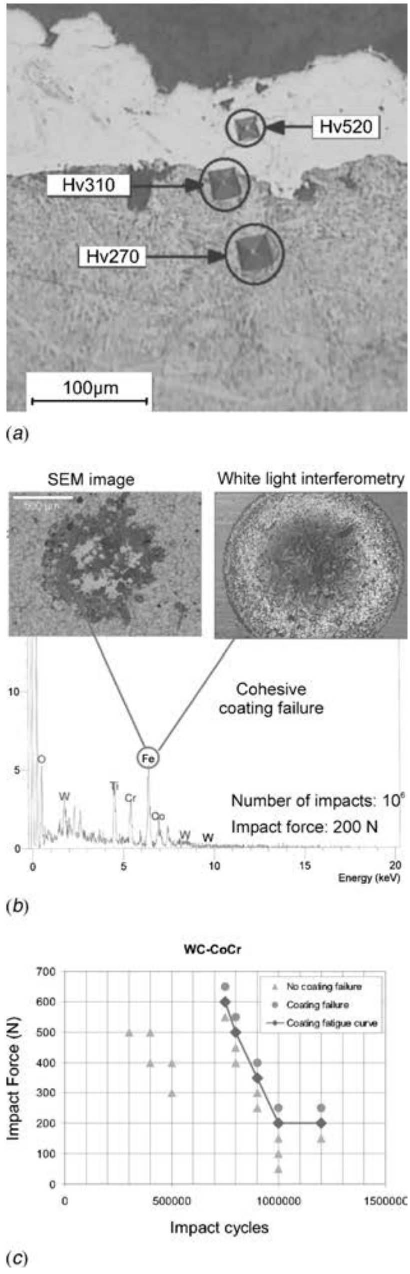

FIG. 3—(*a*) *Microhardness measurement of the* WC-CoCr/P91 *steel layered compound,* (*b*) *SEM and white light interferometry image of the impact crater and EDX analysis indicating the* WC-CoCr *coating failure* (*cohesive failure mode*), (*c*) WC-CoCr *fatigue life curve.*

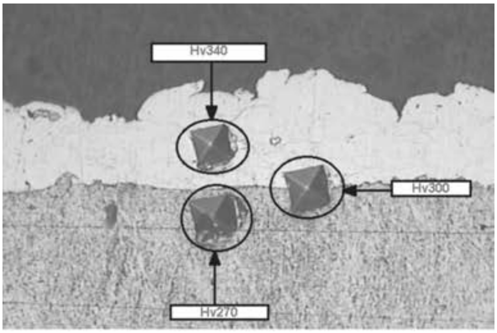

(*a*)

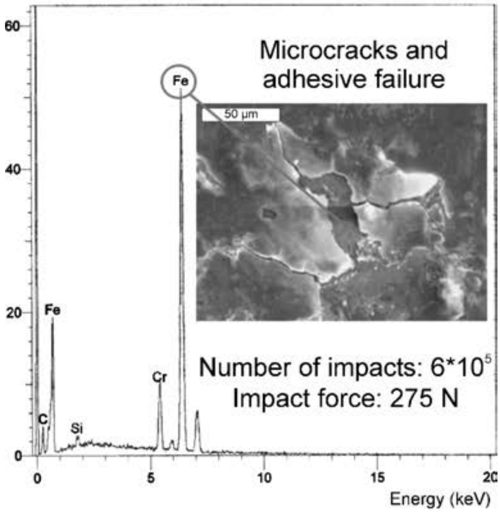

(*b*)

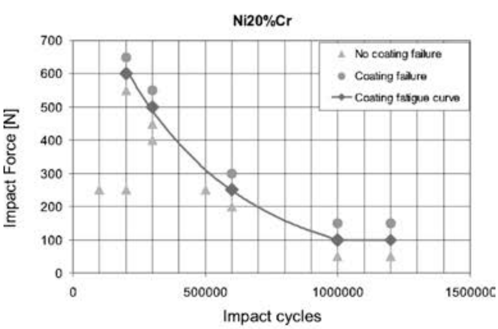

(*c*)

FIG. 4—(*a*) *Microhardness measurement of the* Ni20%Cr/P91 *steel layered compound,* (*b*) *SEM image of the impact crater with coating microcracks and EDX analysis indicating the* Ni20%Cr *coating failure* (*adhesive failure mode*), (*c*) Ni20%Cr *fatigue life curve.*

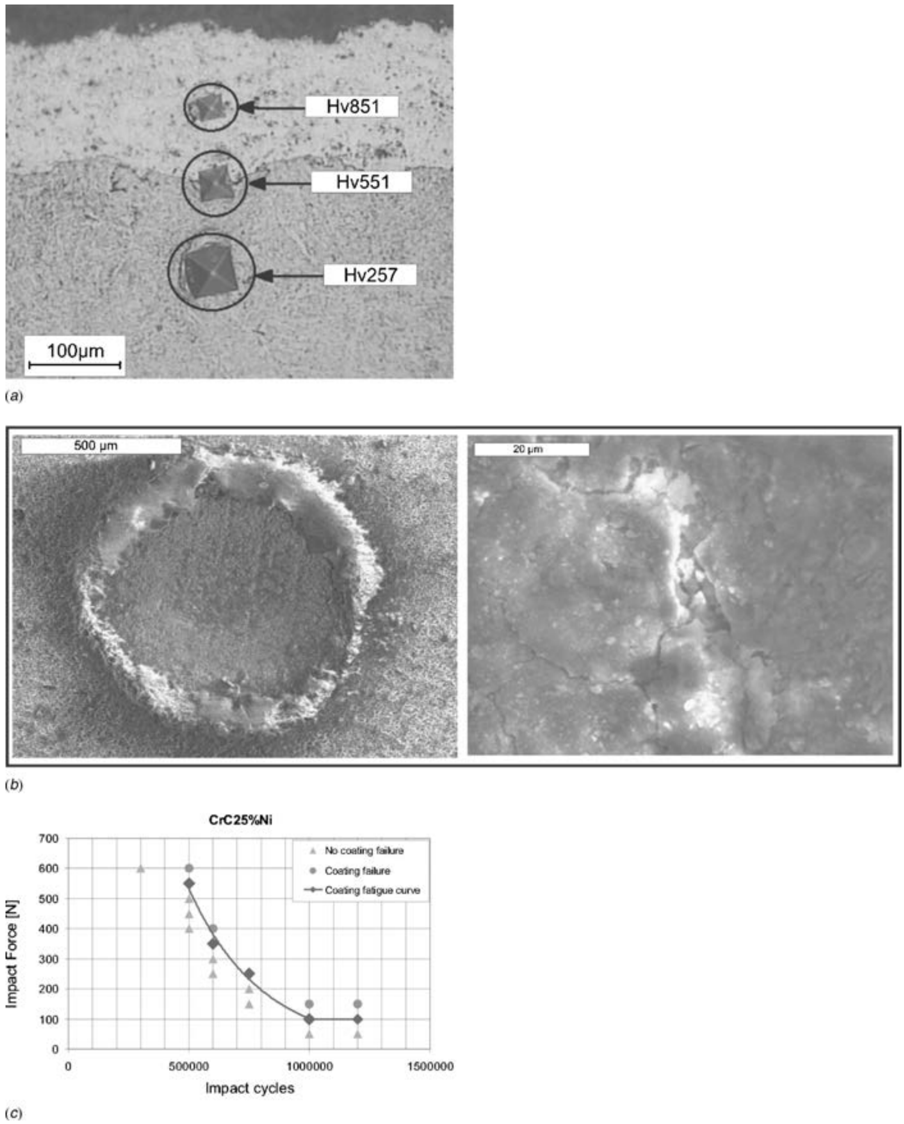

FIG. 5—(*a*) *Microhardness measurement of the* CrC25%Ni/P91 *steel layered compound,* (*b*) *SEM image of impact crater with total coating removal after* $5 \cdot 10^5$ *impact cycles at* 600 N *impact force and magnified SEM image with coating microcracks inside the crater at lower impact force* 550 N, (*c*) CrC25%Ni *fatigue life curve.*

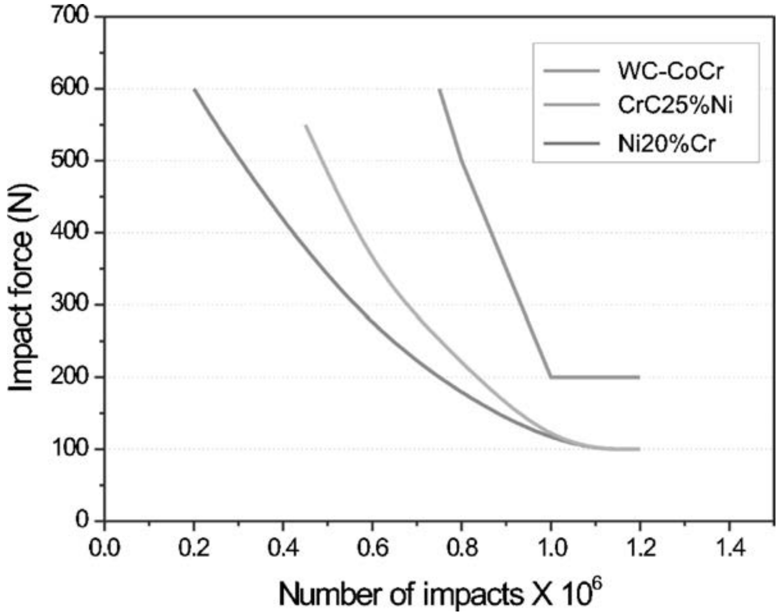

FIG. 6—*Comparison of the impact fatigue curves of the examined HVOF thermal spray coatings.*

intermediate zone of the impact crater take high values. In this case microcracks propagate and sheet-like debris of the coating layer (flakes) can occur.

Figure 3(*a*) illustrates the cross section of the examined WC-CoCr thermal spray coating deposited on P91 steel substrate. The microhardness value (520 HV) indicates the relatively high wear resistance of this coating. Furthermore, the observed homogeneous coating microstructure, in relation with its composition, is responsible for the high coating toughness. In Fig. 3(*b*) the impact crater is depicted by SEM and white light interferometry images. The EDX analysis, inside the crater, indicates the coating cohesive failure initiation in local regions, where Fe belonging to the steel substrate is detected. The fatigue strength evaluation of this coating, after the conclusion of the necessary experiments to find out the coating fatigue curve, is outlined in Fig. 3(*c*). From the results it is concluded that the coating sustains the dynamic impact load to high cycles, presenting also enhanced fatigue limit (200 N). The overall coating behavior can be attributed to the enhanced fracture toughness of this coating and the perfect adhesion with the substrate. However, superficial abrasive wear as reported in other works [8] has been observed.

Particular attention was paid also to the coating adhesive failure mode, which occurs in the coating-substrate interfacial zone. This kind of failure has been observed by the investigation of the Ni20%Cr coating compound (Fig. 4(*a*)) [9]. High tensile and shear stresses developed in the intermediate vicinity of the impact crater, due to the plastic deformation of the substrate, have initiated the development of a large number of microcracks and caused thereby

TABLE 2—*Fatigue strength evaluation of the investigated coating steel layered compounds.*

Coatings	Experiments	Failure Mode	Behavior	Bonding with Substrate	Fatigue Strength	Fatigue Limit	Failure Mechanism
WC-CO	24	cohesive	ductile	perfect	high	200 N	Micro chipping, gradual degradation
Ni20%Cr	19	adhesive	ductile	poor	small	100 N	Large macro cracks in the interface and coating removal in flakes
CrC25%Ni	19	adhesive	brittle	good	medium	100 N	Coating micro cracks and intrinsic coherence release

the coating abruption and the substrate exposure (Fig. 4(*b*)). Microcracks arise inside the coating layer and propagate perpendicular to its surface, when the coating is not tough enough to accommodate the stresses, induced by the ball indenter, and to follow the flexure and deformation of the substrate. When the above damage mechanism is present, and in the case where the bonding of the coating with the substrate is faulty, adhesive failure takes place in the form of sheet-like debris. Figure 4(*c*) outlines the fatigue life curve of this coating determined by impact testing.

Figure 5 shows a typical example of adhesive fatigue failure as it has been observed at the brittle CrC25%Ni coating, which has considerably higher hardness (Fig. 5(*a*)) in comparison to the previous one, Ni20%Cr. In the magnified view of the failure area inside the impact cavity, microcracks are visible after $5 \cdot 10^5$ impacts at 550 N indicating the coating failure initiation (Fig. 5(*b*) right part). At the same impact cycles with increased impact load (600 N), the total removal of the coating and the exposure of the substrate is observed. An overview of the fatigue strength of this coating is given in Fig. 5(*c*).

From the above experiments we conclude that the adhesive failure (abrupt coating removal like flakes from the substrate) appears in low cycle fatigue at high impact force amplitude. Instead of that cohesive failure occurs in high cycle fatigue at low impact force (gradual coating degradation). Figure 6 outlines the fatigue strength performance of the three examined thermal spray coatings by means of the experimental determined coating fatigue curves. Apparently, the WC-CoCr coating demonstrates higher fatigue strength against cyclic impact loading in comparison to the other two HVOF coatings. An overview of the fatigue strength of the examined coatings and their failure modes is presented in Table 2.

Conclusions

The work presented here explores the impact testing method in understanding the failure mechanisms of HVOF thermal spray coatings and provides a feedback approach for optimizing the design of surface engineered components being used in cycle power plants (steam turbine components). More specifically the paper reports the results of a novel experimental approach adopted to investigate the performance of HVOF coating systems and to deliver a reliable testing method for coating development. The current impact testing investigations revealed the good fatigue strength of HVOF thermal spray coatings.

Acknowledgments

The authors are greatly indebted to the Research Committee of the Technical University of Serres, Greece, for financing this research project.

References

[1] Loeffler, F., "Methods to Investigate Mechanical Properties of Coatings," *Thin Solid Films*, Vol. 339, 1999, pp. 181–186.

[2] Bouzakis, K., Vidakis, N., and David, K., "The Concept of an Advanced Impact Tester Supported by Evaluation Software for the Fatigue Strength Characterization of Hard Layered Media," *Thin Solid Films*, Vol. 351, 1999, pp. 1–8.

[3] Bouzakis, K., David, K., Siganos, A., Leyendecker, T., and Erkens, G., "Investigation of the Fatigue Failure Progress of PVD Elastoplastic Coatings with Various Roughness During the Impact Testing," *International Conference on Metallurgical Coatings and Thin Films*, San Diego, CA, 30 April 2001, p. 116.

[4] Knotek, O., Bosserhoff, B., Schrey, A., Leyendecker, T., Lemmer, O., and Esser, S., "A New Technique for Testing the Impact Load of Thin Films: The Coating Impact Test," *Surf. Coat. Technol.*, Vol. 54-55, 1992, pp. 102–107.

[5] Bantle, R. and Matthews, A., "Investigation Into the Impact Wear Behavior of Ceramic Coatings," *Surf. Coat. Technol.*, Vol. 74-75, No. Part 2, 1995, pp. 857–868.

[6] David, C., Anthymidis, K., and Tsipas, D., "A Comparative Study of the Fatigue Resistance of Aluminide Coatings on P91 Steel Substrate Under Cyclic Impact Loading," *Particle and Continuum Aspects of Mesomechanics*, ISTE Ltd., 2007, pp. 721–728.

[7] David, C., Anthymidis, K., Agrianidis, P., and Tsipas, D., "Determination of the Fatigue Resistance of HVOF Thermal Spray WC-CoCr Coatings by Means of Impact Testing," *J. Test. Eval.*, Vol. 35, No. 6, 2007, pp. 630–634.

[8] Ahmed, R., "Contact Fatigue Failure Modes of HVOF Coatings," *Wear*, Vol. 253, 2002, pp. 473–487.

[9] Padilla, K., et al., "Fatigue Behavior of a 4140 Steel Coated with a NiMoAl Deposit Applied by HVOF Thermal Spray," *Surf. Coat. Technol.*, Vol. 150, 2002, pp. 151–162.

Author Index

Subject Index

G

H

I

J

L

M

N

Cover image courtesy of AFRL/RXSA

www.astm.org

ISBN: 978-0-8031-3416-4
Stock #: STP1508